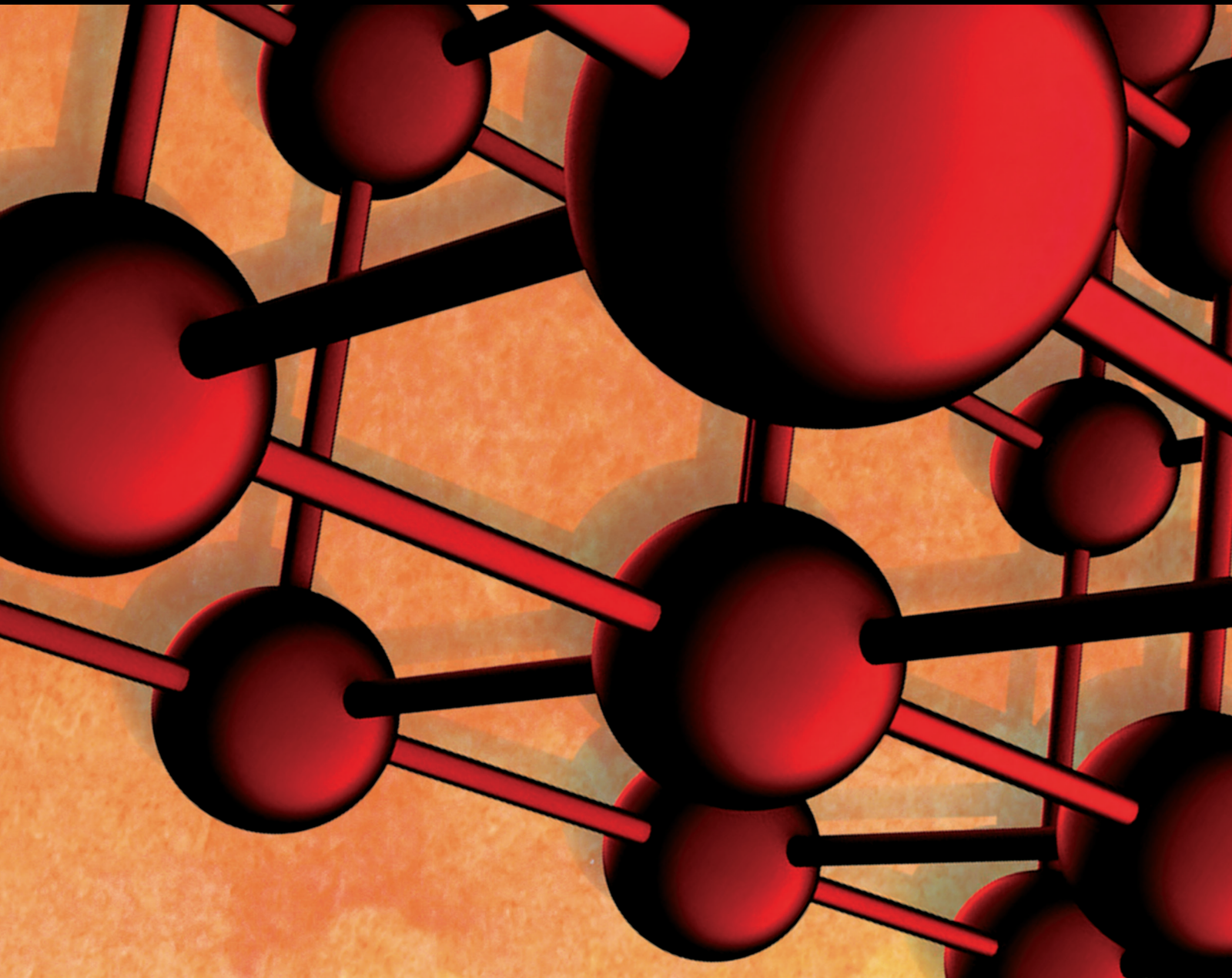


Advances in Materials Science and Engineering

# Advanced Functional Graded Materials: Processing and Applications

Lead Guest Editor: K. Raja

Guest Editors: Saravana Jaganathan, H.N. Reddappa, and Naresh Kakur





---

# **Advanced Functional Graded Materials: Processing and Applications**



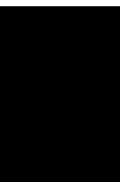
Advances in Materials Science and Engineering

---

**Advanced Functional Graded Materials:  
Processing and Applications**

Lead Guest Editor: K. Raja

Guest Editors: Saravana Jaganathan, H.N.  
Reddappa, and Naresh Kakur




---

Copyright © 2024 Hindawi Limited. All rights reserved.

This is a special issue published in "Advances in Materials Science and Engineering." All articles are open access articles distributed under the Creative Commons Attribution License, which permits unrestricted use, distribution, and reproduction in any medium, provided the original work is properly cited.

# Chief Editor
























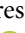
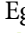


Amit Bandyopadhyay , USA

## Associate Editors

Vamsi Balla , India  
Mitun Das , USA  
Sandip Harimkar, USA  
Ravi Kumar , India  
Peter Majewski , Australia  
Enzo Martinelli , Italy  
Luigi Nicolais , Italy  
Carlos R. Rambo , Brazil  
Michael J. Schütze , Germany  
Kohji Tashiro , Japan  
Zhonghua Yao , China  
Dongdong Yuan , China  
Wei Zhou , China

## Academic Editors

Antonio Abate , Germany  
Hany Abdo , Saudi Arabia  
H.P.S. Abdul Khalil , Malaysia  
Ismael Alejandro Aguayo Villarreal , Mexico  
Sheraz Ahmad , Pakistan  
Michael Aizenshtein, Israel  
Jarir Aktaa, Germany  
Bandar AlMangour, Saudi Arabia  
Huaming An, China  
Alicia Esther Ares , Argentina  
Siva Avudaiappan , Chile  
Habib Awais , Pakistan  
NEERAJ KUMAR BHOI, India  
Enrico Babilio , Italy  
Renal Backov, France  
M Bahubalendruni , India  
Sudharsan Balasubramanian , India  
Markus Bambach, Germany  
Irene Bavasso , Italy  
Stefano Bellucci , Italy  
Brahim Benmokrane, Canada  
Jean-Michel Bergheau , France  
Guillaume Bernard-Granger, France  
Giovanni Berselli, Italy  
Patrice Berthod , France  
Michele Bianchi , Italy  
Hugo C. Biscaia , Portugal

Antonio Boccaccio, Italy  
Mohamed Bououdina , Saudi Arabia  
Gianlorenzo Bussetti , Italy  
Antonio Caggiano , Germany  
Marco Cannas , Italy  
Qi Cao, China  
Gianfranco Carotenuto , Italy  
Paolo Andrea Carraro , Italy  
Jose Cesar de Sa , Portugal  
Wen-Shao Chang , United Kingdom  
Qian Chen , China  
Francisco Chinesta , France  
Er-Yuan Chuang , Taiwan  
Francesco Colangelo, Italy  
María Criado , Spain  
Enrique Cuan-Urquizo , Mexico  
Lucas Da Silva , Portugal  
Angela De Bonis , Italy  
Abílio De Jesus , Portugal  
José António Fonseca De Oliveira  
Correia , Portugal  
Ismail Demir , Turkey  
Luigi Di Benedetto , Italy  
Maria Laura Di Lorenzo, Italy  
Marisa Di Sabatino, Norway  
Luigi Di Sarno, Italy  
Ana María Díez-Pascual , Spain  
Guru P. Dinda , USA  
Hongbiao Dong, China  
Mingdong Dong , Denmark  
Frederic Dumur , France  
Stanislaw Dymek, Poland  
Kaveh Edalati , Japan  
Philip Eisenlohr , USA  
Luis Evangelista , Norway  
Michele Fedel , Italy  
Francisco Javier Fernández Fernández , Spain  
Spain  
Isabel J. Ferrer , Spain  
Massimo Fresta, Italy  
Samia Gad , Egypt  
Pasquale Gallo , Finland  
Sharanabasava Ganachari, India  
Santiago Garcia-Granda , Spain  
Carlos Garcia-Mateo , Spain

Achraf Ghorbal , Tunisia  
Georgios I. Giannopoulos , Greece  
Ivan Giorgio , Italy  
Andrea Grilli , Italy  
Vincenzo Guarino , Italy  
Daniel Guay, Canada  
Jenő Gubicza , Hungary  
Xuchun Gui , China  
Benoit Guiffard , France  
Zhixing Guo, China  
Ivan Gutierrez-Urrutia , Japan  
Weiwei Han , Republic of Korea  
Simo-Pekka Hannula, Finland  
A. M. Hassan , Egypt  
Akbar Heidarzadeh, Iran  
Yi Huang , United Kingdom  
Joshua Ighalo, Nigeria  
Saliha Ilican , Turkey  
Md Mainul Islam , Australia  
Ilia Ivanov , USA  
Jijo James , India  
Hafsa Jamshaid , Pakistan  
Hom Kandel , USA  
Kenji Kaneko, Japan  
Rajesh Kannan A , Democratic People's  
Republic of Korea  
Mehran Khan , Hong Kong  
Akihiko Kimura, Japan  
Ling B. Kong , Singapore  
Pramod Koshy, Australia  
Hongchao Kou , China  
Alexander Kromka, Czech Republic  
Abhinay Kumar, India  
Avvaru Praveen Kumar , Ethiopia  
Sachin Kumar, India  
Paweł Kłosowski , Poland  
Wing-Fu Lai , Hong Kong  
Luciano Lamberti, Italy  
Fulvio Lavecchia , Italy  
Laurent Lebrun , France  
Joon-Hyung Lee , Republic of Korea  
Cristina Leonelli, Italy  
Chenggao Li , China  
Rongrong Li , China  
Yuanshi Li, Canada

Guang-xing Liang , China  
Barbara Liguori , Italy  
Jun Liu , China  
Yunqi Liu, China  
Rong Lu, China  
Zhiping Luo , USA  
Fernando Lusquiños , Spain  
Himadri Majumder , India  
Dimitrios E. Manolakos , Greece  
Necmettin Maraşlı , Turkey  
Alessandro Martucci , Italy  
Roshan Mayadunne , Australia  
Mamoun Medraj , Canada  
Shazim A. Memon , Kazakhstan  
Pratima Meshram , India  
Mohsen Mhadhbi , Tunisia  
Philippe Miele, France  
Andrey E. Miroshnichenko, Australia  
Ajay Kumar Mishra , South Africa  
Hossein Moayedi , Vietnam  
Dhanesh G. Mohan , United Kingdom  
Sakar Mohan , India  
Namdev More, USA  
Tahir Muhmood , China  
Faisal Mukhtar , Pakistan  
Dr. Tauseef Munawar , Pakistan  
Roger Narayan , USA  
Saleem Nasir , Pakistan  
Elango Natarajan, Malaysia  
Rufino M. Navarro, Spain  
Miguel Navarro-Cia , United Kingdom  
Behzad Nematollahi , Australia  
Peter Niemz, Switzerland  
Hiroschi Noguchi, Japan  
Dariusz Oleszak , Poland  
Laurent Orgéas , France  
Togay Ozbakkaloglu, United Kingdom  
Marián Palcut , Slovakia  
Davide Palumbo , Italy  
Gianfranco Palumbo , Italy  
Murlidhar Patel, India  
Zbyšek Pavlík , Czech Republic  
Alessandro Pegoretti , Italy  
Gianluca Percoco , Italy  
Andrea Petrella, Italy



Claudio Pettinari , Italy  
Giorgio Pia , Italy  
Candido Fabrizio Pirri, Italy  
Marinos Pitsikalis , Greece  
Alain Portavoce , France  
Simon C. Potter, Canada  
Ulrich Prah, Germany  
Veena Ragupathi , India  
Kawaljit Singh Randhawa , India  
Baskaran Rangasamy , Zambia  
Paulo Reis , Portugal  
Hilda E. Reynel-Avila , Mexico  
Yuri Ribakov , Israel  
Aniello Riccio , Italy  
Anna Richelli , Italy  
Antonio Riveiro , Spain  
Marco Rossi , Italy  
Fernando Rubio-Marcos , Spain  
Francesco Ruffino , Italy  
Giuseppe Ruta , Italy  
Sachin Salunkhe , India  
P Sangeetha , India  
Carlo Santulli, Italy  
Fabrizio Sarasini , Italy  
Senthil Kumaran Selvaraj , India  
Raffaele Sepe , Italy  
Aabid H Shalla, India  
Poorva Sharma , China  
Mercedes Solla, Spain  
Tushar Sonar , Russia  
Donato Sorgente , Italy  
Charles C. Sorrell , Australia  
Damien Soulat , France  
Adolfo Speghini , Italy  
Antonino Squillace , Italy  
Koichi Sugimoto, Japan  
Jirapornchai Suksaeree , Thailand  
Baozhong Sun, China  
Sam-Shajing Sun , USA  
Xiaolong Sun, China  
Yongding Tian , China  
Hao Tong, China  
Achim Trampert, Germany  
Tomasz Trzepieciński , Poland  
Kavimani V , India

Matjaz Valant , Slovenia  
Mostafa Vamegh, Iran  
Lijing Wang , Australia  
Jörg M. K. Wiezorek , USA  
Guosong Wu, China  
Junhui Xiao , China  
Guoqiang Xie , China  
YASHPAL YASHPAL, India  
Anil Singh Yadav , India  
Yee-wen Yen, Taiwan  
Hao Yi , China  
Wenbin Yi, China  
Tetsu Yonezawa, Japan  
Hiroshi Yoshihara , Japan  
Bin Yu , China  
Rahadian Zainul , Indonesia  
Lenka Zaji#c#kova# , Czech Republic  
Zhigang Zang , China  
Michele Zappalorto , Italy  
Gang Zhang, Singapore  
Jinghuai Zhang, China  
Zengping Zhang, China  
You Zhou , Japan  
Robert Černý , Czech Republic

# Contents

---

**Retracted: Application of Nanoflexible Photoelectric Devices in Welding Tooling Equipment Systems**

Advances in Materials Science and Engineering  
Retraction (1 page), Article ID 9893723, Volume 2024 (2024)

**Retracted: Construction of Facial Expression Recognition Technology of Intelligent Service Robot Based on Nanofiber Flexible Wearable Electronic Skins**

Advances in Materials Science and Engineering  
Retraction (1 page), Article ID 9849245, Volume 2024 (2024)

**Retracted: Effects of Polypropylene Waste Addition as Coarse Aggregates in Concrete: Experimental Characterization and Statistical Analysis**

Advances in Materials Science and Engineering  
Retraction (1 page), Article ID 9813686, Volume 2024 (2024)

**Retracted: Predicting the Spread of Vessels in Initial Stage Cervical Cancer through Radiomics Strategy Based on Deep Learning Approach**

Advances in Materials Science and Engineering  
Retraction (1 page), Article ID 9898737, Volume 2023 (2023)

**Retracted: Analysis of Temperature Distribution and Mechanical Properties of Friction Stir Welding of Al-Cu Joints Using Hardened H13 Steel Tools**

Advances in Materials Science and Engineering  
Retraction (1 page), Article ID 9891727, Volume 2023 (2023)

**Retracted: Investigation on Durability Behavior of Fiber Reinforced Concrete with Steel Slag/Bacteria beneath Diverse Exposure Conditions**

Advances in Materials Science and Engineering  
Retraction (1 page), Article ID 9890527, Volume 2023 (2023)

**Retracted: Wind Tunnel Testing and Validation of Helicopter Rotor Blades Using Additive Manufacturing**

Advances in Materials Science and Engineering  
Retraction (1 page), Article ID 9870519, Volume 2023 (2023)

**Retracted: Application of Composite Nano-Bone Transplantation and Massage Exercise Rehabilitation Training in Patients Undergoing Limb Replantation**

Advances in Materials Science and Engineering  
Retraction (1 page), Article ID 9867852, Volume 2023 (2023)

**Retracted: Clinical Application of Graphene Composite in Internal Fixation of Ankle Fracture in Sports**

Advances in Materials Science and Engineering  
Retraction (1 page), Article ID 9865864, Volume 2023 (2023)

**Retracted: Mechanical and Morphological Studies of *Sansevieria trifasciata* Fiber-Reinforced Polyester Composites with the Addition of SiO<sub>2</sub> and B<sub>4</sub>C**

Advances in Materials Science and Engineering  
Retraction (1 page), Article ID 9864182, Volume 2023 (2023)

**Retracted: An Improved Inverse Kinematics Solution for a Robot Arm Trajectory Using Multiple Adaptive Neuro-Fuzzy Inference Systems**

Advances in Materials Science and Engineering  
Retraction (1 page), Article ID 9864019, Volume 2023 (2023)

**Retracted: Methane Extraction and Resource Utilization Based on Multisource Data Fusion**

Advances in Materials Science and Engineering  
Retraction (1 page), Article ID 9854105, Volume 2023 (2023)

**Retracted: Image-Based Precision Measurement Technology for the Quality Inspection of Crane Boom Materials**

Advances in Materials Science and Engineering  
Retraction (1 page), Article ID 9852428, Volume 2023 (2023)

**Retracted: Molecular Dynamics Simulation Calculation Method for Elasticity and Plasticity of Metal Nanostructures**

Advances in Materials Science and Engineering  
Retraction (1 page), Article ID 9852319, Volume 2023 (2023)

**Retracted: Control of Material Procurement Cost of Enterprises under the Background of the Low-Carbon Economy**

Advances in Materials Science and Engineering  
Retraction (1 page), Article ID 9851310, Volume 2023 (2023)

**Retracted: Statistical Analysis on the Mechanical Properties of ATH Nanofiller Addition on the Woven Jute/Polyester Hybrid Composites by the Grey-Taguchi Method**

Advances in Materials Science and Engineering  
Retraction (1 page), Article ID 9848631, Volume 2023 (2023)

**Retracted: Investigation of Insulation Properties Using Microwave Nondevastating Methodology to Predict the Strength of Polymer Materials**

Advances in Materials Science and Engineering  
Retraction (1 page), Article ID 9843560, Volume 2023 (2023)

**Retracted: Prediction of *Escherichia coli* Bacterial and Coliforms on Plants through Artificial Neural Network**

Advances in Materials Science and Engineering  
Retraction (1 page), Article ID 9841463, Volume 2023 (2023)

# Contents

---

**Retracted: Investigation of Groundwater Hydro-Geochemistry, Excellence, and Anthropoid Wellbeing Hazard in Dry Zones Using the Chemometric Method**

Advances in Materials Science and Engineering  
Retraction (1 page), Article ID 9841367, Volume 2023 (2023)

**Retracted: Experimental Analysis and Optimization of Tribological Properties of Self-Lubricating Aluminum Hybrid Nanocomposites Using the Taguchi Approach**

Advances in Materials Science and Engineering  
Retraction (1 page), Article ID 9840714, Volume 2023 (2023)

**Retracted: Preparation and Supercritical CO<sub>2</sub> Foaming of Modified Nanocrystalline Cellulose Reinforced Polylactic Acid Bionanocomposites**

Advances in Materials Science and Engineering  
Retraction (1 page), Article ID 9840239, Volume 2023 (2023)

**Retracted: Based on the Application Practice of Multifunctional Nanomaterials in Art Design and Industrial Manufacturing Concept**

Advances in Materials Science and Engineering  
Retraction (1 page), Article ID 9839276, Volume 2023 (2023)

**Retracted: Preparation of Graphene Nanosilver Composites for 3D Printing Technology**

Advances in Materials Science and Engineering  
Retraction (1 page), Article ID 9835192, Volume 2023 (2023)

**Retracted: Modelling and Analysis of Surface Roughness Using the Cascade Forward Neural Network (CFNN) in Turning of Inconel 625**

Advances in Materials Science and Engineering  
Retraction (1 page), Article ID 9834301, Volume 2023 (2023)

**Retracted: Maintenance Methodologies Embraced for Railroad Systems: A Review**

Advances in Materials Science and Engineering  
Retraction (1 page), Article ID 9830489, Volume 2023 (2023)

**Retracted: Processing and Properties of AlCoCrFeNi High Entropy Alloys: A Review**

Advances in Materials Science and Engineering  
Retraction (1 page), Article ID 9829015, Volume 2023 (2023)

**Retracted: Research on the Innovation of Procurement Mode of Nanomaterials Based on E-Commerce**

Advances in Materials Science and Engineering  
Retraction (1 page), Article ID 9827137, Volume 2023 (2023)

**Retracted: Thermogravimetric Analysis and Mechanical Properties of Pebble Natural Filler-Reinforced Polymer Composites Produced through a Hand Layup Technique**

Advances in Materials Science and Engineering  
Retraction (1 page), Article ID 9825096, Volume 2023 (2023)



**Retracted: Construction of Nanomaterials and the Role of Rutin in the Treatment of Cerebral Hemorrhage**

Advances in Materials Science and Engineering  
Retraction (1 page), Article ID 9823761, Volume 2023 (2023)

**Retracted: A Multisensor Data Fusion Based Anomaly Detection (Ammonia Nitrogen) Approach for Ensuring Green Coastal Environment**

Advances in Materials Science and Engineering  
Retraction (1 page), Article ID 9821313, Volume 2023 (2023)

**Retracted: Study of Wear Behavior on AA6061 Reinforced with Hybrid Ceramic Composites through Optimization**

Advances in Materials Science and Engineering  
Retraction (1 page), Article ID 9821259, Volume 2023 (2023)

**Retracted: Process Optimization of Spark Plasma Sintering Parameters for Tungsten Carbide/Silicon Nitride/AA2219 Composites by Taguchi Method**

Advances in Materials Science and Engineering  
Retraction (1 page), Article ID 9820671, Volume 2023 (2023)

**Retracted: Performance and Exhaust Emission Characteristics of C.I Engine Using Biofuels and Its Diesel Blend with Nano-Additives**

Advances in Materials Science and Engineering  
Retraction (1 page), Article ID 9820313, Volume 2023 (2023)

**Retracted: Streamline Effect Improvement of Additive Manufactured Airfoil Utilizing Dynamic Stream Control Procedure**

Advances in Materials Science and Engineering  
Retraction (1 page), Article ID 9818150, Volume 2023 (2023)

**Retracted: Parametric Optimization of Abrasive Water Jet Cutting on AA 5083 through Multiobjective Teaching-Learning Method**

Advances in Materials Science and Engineering  
Retraction (1 page), Article ID 9816979, Volume 2023 (2023)

**Retracted: Development of Microbiology Plantation-Based Multimodal Segmentation for Smart Garden Using Machine Learning**

Advances in Materials Science and Engineering  
Retraction (1 page), Article ID 9815405, Volume 2023 (2023)

**Retracted: Optimization on Tribological Behaviour of AA7075/Zirconium Boride Composites Using Taguchi Technique**

Advances in Materials Science and Engineering  
Retraction (1 page), Article ID 9815329, Volume 2023 (2023)

# Contents

---

**Retracted: Machine Learning Approach: Prediction of Surface Roughness in Dry Turning Inconel 625**  
Advances in Materials Science and Engineering  
Retraction (1 page), Article ID 9812703, Volume 2023 (2023)

**Retracted: Optimizing the Parameters of Zirconium Carbide and Rice Husk Ash Reinforced with AA 2618 Composites**  
Advances in Materials Science and Engineering  
Retraction (1 page), Article ID 9810167, Volume 2023 (2023)

**Retracted: Tribological Behavior of AA7075 Reinforced with Ag and ZrO<sub>2</sub> Composites**  
Advances in Materials Science and Engineering  
Retraction (1 page), Article ID 9808135, Volume 2023 (2023)

**Retracted: Utilization of Flex Controlled Robotics on Prosthetic Hand instead of Damaged Body Parts**  
Advances in Materials Science and Engineering  
Retraction (1 page), Article ID 9803902, Volume 2023 (2023)

**Retracted: Influence of Metallic Particles on Properties of Aluminium Composites through Taguchi Technique**  
Advances in Materials Science and Engineering  
Retraction (1 page), Article ID 9798764, Volume 2023 (2023)

**Retracted: Investigation on Heat Deflection and Thermal Conductivity of Basalt Fiber Reinforced Composites Prepared by Hand Layup Method**  
Advances in Materials Science and Engineering  
Retraction (1 page), Article ID 9797109, Volume 2023 (2023)

**Retracted: Experimental Studies on Mechanical and Thermal Properties of Polyester Hybrid Composites Reinforced with Sansevieria Trifasciata Fibers**  
Advances in Materials Science and Engineering  
Retraction (1 page), Article ID 9791674, Volume 2023 (2023)

**Retracted: The Influence of Chemically Treated Hemp Fibre on the Mechanical Behavior and Thermal Properties of Polylactic Acid Made with FDM**  
Advances in Materials Science and Engineering  
Retraction (1 page), Article ID 9791541, Volume 2023 (2023)

**Retracted: A Study of Structural Parameters Effects on Pressure Differential to Roll Titanium Diaphragm for a Spacecraft Propellant Tank**  
Advances in Materials Science and Engineering  
Retraction (1 page), Article ID 9790582, Volume 2023 (2023)

**Retracted: Effect of Reinforcement on Tensile Characteristics in AA 5052 with ZrC and Fly Ash-Based Composites**  
Advances in Materials Science and Engineering  
Retraction (1 page), Article ID 9781204, Volume 2023 (2023)

**Retracted: Experimental Investigation on the Average Surface Roughness (Ra) of AlSi10Mg Alloy Manufactured by Laser Powder Bed Fusion Method**

Advances in Materials Science and Engineering  
Retraction (1 page), Article ID 9768637, Volume 2023 (2023)

**Retracted: Optimization of Process Parameter on AA8052 Friction Stir Welding Using Taguchi's Method**

Advances in Materials Science and Engineering  
Retraction (1 page), Article ID 9759187, Volume 2023 (2023)

**Retracted: Application of IoT-Based Drones in Precision Agriculture for Pest Control**

Advances in Materials Science and Engineering  
Retraction (1 page), Article ID 9763026, Volume 2023 (2023)

**Retracted: Nanorobots with Hybrid Biomembranes for Simultaneous Degradation of Toxic Microorganism**

Advances in Materials Science and Engineering  
Retraction (1 page), Article ID 9753635, Volume 2023 (2023)

**Retracted: Tiny Spherical Robot with a Magnetic Field-Based Interference Detection and Prevention Framework**

Advances in Materials Science and Engineering  
Retraction (1 page), Article ID 9878642, Volume 2023 (2023)


**Retracted: An Enhanced Drone Technology for Detecting the Human Object in the Dense Areas Using a Deep Learning Model**

Advances in Materials Science and Engineering  
Retraction (1 page), Article ID 9873705, Volume 2023 (2023)

**Retracted: An Artificial Intelligence Mechanism for the Prediction of Signal Strength in Drones to IoT Devices in Smart Cities**

Advances in Materials Science and Engineering  
Retraction (1 page), Article ID 9864760, Volume 2023 (2023)

**[Retracted] Influence of Metallic Particles on Properties of Aluminium Composites through Taguchi Technique**


B. Venkatesh, Anantha Raman Lakshmi pathi, T. Prakash, Pothamsetty Kasi V. Rao, Rajesh Verma, N. Nagabhooshanam, and Simon Yishak   
Research Article (12 pages), Article ID 9637728, Volume 2023 (2023)

**Retracted: Effect of SiC Particle Incorporated Dielectric Medium on Electrical Discharge Machining Behavior of AA6061/B4Cp/SiCp AMCs**

Advances in Materials Science and Engineering  
Retraction (1 page), Article ID 9803294, Volume 2023 (2023)

## Contents

**[Retracted] Study of Wear Behavior on AA6061 Reinforced with Hybrid Ceramic Composites through Optimization**

Omar Shabbir, S. V. Alagarsamy, C. Krishnamurthy, A. Nagaraj, Pradeep Kumar Singh, and Sisay Ketema Sida 


Research Article (10 pages), Article ID 7558886, Volume 2023 (2023)

**[Retracted] Effects of Polypropylene Waste Addition as Coarse Aggregates in Concrete: Experimental Characterization and Statistical Analysis**

D. C. Naveen, K. Naresh , B. S. Keerthi Gowda , Madhu Sudana Reddy G , C. Durga Prasad , and Ragavanantham Shanmugam 




Research Article (11 pages), Article ID 7886722, Volume 2022 (2022)

**[Retracted] A Study of Structural Parameters Effects on Pressure Differential to Roll Titanium Diaphragm for a Spacecraft Propellant Tank**

Tianju Ma, Sendong Gu , Jipeng Zhao, Bin Yu, Jianjun Zhang, and Wenbo Yang


Research Article (10 pages), Article ID 2003905, Volume 2022 (2022)

**[Retracted] Analysis of Temperature Distribution and Mechanical Properties of Friction Stir Welding of Al-Cu Joints Using Hardened H13 Steel Tools**

J. Pratap Kumar , Anil Raj, A. R. Venkatraman, Arul Kulandaivel , G. Ashwin Prabhu, S. K. Narendranathan, and Nagaraj Ashok 

Research Article (14 pages), Article ID 4973839, Volume 2022 (2022)

**[Retracted] Investigation on Heat Deflection and Thermal Conductivity of Basalt Fiber Reinforced Composites Prepared by Hand Layup Method**

R. Meenakshi Reddy, S. Ravi, Pradeep Kumar Singh, H. Dineshkumar, K. Arun Bhaskar, Vallapureddy Siva Nagi Reddy, A. H. Seikh, M. H. Siddique, and Ashok Nagaraj 

Research Article (6 pages), Article ID 1294374, Volume 2022 (2022)

**[Retracted] Optimization on Tribological Behaviour of AA7075/Zirconium Boride Composites Using Taguchi Technique**

S. Krishna Mohan, R. Meenakshi Reddy, V. Kamalakar, Pranavan S, M. Amareswar, A. H. Seikh, M. H. Siddique, T. L. Kishore, and Bhupender Singh 


Research Article (7 pages), Article ID 4058442, Volume 2022 (2022)

**[Retracted] Parametric Optimization of Abrasive Water Jet Cutting on AA 5083 through Multiobjective Teaching-Learning Method**

R. Meenakshi Reddy, K. Logesh, S. V. Alagarsamy, A. Nagaraj, Rishabh Chaturvedi, Mylavarapu Kalyan Ram, A. H. Seikh, M. H. Siddique, and Beruk Hailu 

Research Article (7 pages), Article ID 1123256, Volume 2022 (2022)



**[Retracted] Investigation of Groundwater Hydro-Geochemistry, Excellence, and Anthropoid Wellbeing Hazard in Dry Zones Using the Chemometric Method**

Mohamed Saad Ahmed, G. Ramkumar, S. Radjarejseri, Ram Prasad, Pilla Ravi Kishore, Mika Sillanpaa, and Endalkachew Mergia Anbese 



Research Article (10 pages), Article ID 4903323, Volume 2022 (2022)




**[Retracted] Modelling and Analysis of Surface Roughness Using the Cascade Forward Neural Network (CFNN) in Turning of Inconel 625**

Rajesh A. S. , M. S. Prabhuswamy, and Ishwarya Komalnu Raghavan   
Research Article (9 pages), Article ID 7520962, Volume 2022 (2022)


**[Retracted] Machine Learning Approach: Prediction of Surface Roughness in Dry Turning Inconel 625**

A. S. Rajesh , M. S. Prabhuswamy, and M. Rudra Naik   
Research Article (7 pages), Article ID 6038804, Volume 2022 (2022)




**[Retracted] Development of Microbiology Plantation-Based Multimodal Segmentation for Smart Garden Using Machine Learning**

S. Prasath, Ramkumar Govindaraj, Ram Subbiah, Sulaiman Ali Alharbi, Hesham S. Almoallim, S. Priya, and Begna Dejene Mulugeta   
Research Article (6 pages), Article ID 1066535, Volume 2022 (2022)

**[Retracted] Experimental Analysis and Optimization of Tribological Properties of Self-Lubricating Aluminum Hybrid Nanocomposites Using the Taguchi Approach**

Vinoth Kumar Selvaraj, S. Jeyanthi, Raja Thiyagarajan, M. Senthil Kumar, L. Yuvaraj, P. Ravindran, D. M. Niveditha, and Yigezu Bantirga Gebremichael   
Research Article (13 pages), Article ID 4511140, Volume 2022 (2022)


**[Retracted] Processing and Properties of AlCoCrFeNi High Entropy Alloys: A Review**

P.M. Gopal , K. Soorya Prakash, V. Kavimani , and Gopal Rajendiran   
Review Article (13 pages), Article ID 1190161, Volume 2022 (2022)


**[Retracted] Process Optimization of Spark Plasma Sintering Parameters for Tungsten Carbide/Silicon Nitride/AA2219 Composites by Taguchi Method**

Sultan Althahban, Gurusamy Pathinettampadian, Faez Qahtani, Yosef Jazaa, S. Mousa, Sanipina Anjani Devi, Melvin Victor De Pours, R. Subbiah, and Hana Beyene Mamo   
Research Article (8 pages), Article ID 4829499, Volume 2022 (2022)

**[Retracted] Construction of Facial Expression Recognition Technology of Intelligent Service Robot Based on Nanofiber Flexible Wearable Electronic Skins**



Feigao Li , Chenyang Li, and Yue Liu  
Research Article (10 pages), Article ID 8669298, Volume 2022 (2022)

**[Retracted] Effect of Reinforcement on Tensile Characteristics in AA 5052 with ZrC and Fly Ash-Based Composites**


K. Mallikarjuna, M. K. Harikeerthan, B. S. Shubhalakshmi, K. S. Vinay Kumar, Ravindra Pratap Singh, Maddali Srikanth, Y. Krishna Srinivasa Subba Rao, Suresh Kumar, and Aggegnenu Shara Shata   
Research Article (7 pages), Article ID 7070304, Volume 2022 (2022)

## Contents

**[Retracted] Prediction of *Escherichia coli* Bacterial and Coliforms on Plants through Artificial Neural Network**

S. Prasath Alais Surendhar, Govindaraj Ramkumar , Ram Prasad, Piyush Kumar Pareek, R. Subbiah, Abdullah A. Alarfaj, Abdurahman Hajinur Hiraad, S. S. Priya, and Raja Raju   
Research Article (13 pages), Article ID 9793790, Volume 2022 (2022)



**[Retracted] Methane Extraction and Resource Utilization Based on Multisource Data Fusion**

Wensheng Chen  and Zhongliang Lu  
Research Article (8 pages), Article ID 7419076, Volume 2022 (2022)




**[Retracted] Application of Nanoflexible Photoelectric Devices in Welding Tooling Equipment Systems**

Wenping Tan , Honghua Liu , Hongmei Li, and Shen Cao  
Research Article (14 pages), Article ID 7010891, Volume 2022 (2022)


**[Retracted] Predicting the Spread of Vessels in Initial Stage Cervical Cancer through Radiomics Strategy Based on Deep Learning Approach**

Piyush Kumar Pareek, Prasath Alais Surendhar S, Ram Prasad, Govindaraj Ramkumar , Ekta Dixit, R. Subbiah, Saleh H. Salmen, Hesham S. Almoallim, S. S. Priya, and S. Arockia Jayadhas   
Research Article (13 pages), Article ID 1008652, Volume 2022 (2022)



**[Retracted] Performance and Exhaust Emission Characteristics of C.I Engine Using Biofuels and Its Diesel Blend with Nano-Additives**

S. Jacob , L. Karikalan , J. Isaac Joshua Ramesh Lalvani, Aman Sharma, and Maghalengam Kannappan   
Research Article (5 pages), Article ID 9185388, Volume 2022 (2022)


**[Retracted] Image-Based Precision Measurement Technology for the Quality Inspection of Crane Boom Materials**

Honghua Liu, Wenping Tan , Shen Cao, and Hongmei Li  
Research Article (13 pages), Article ID 8379621, Volume 2022 (2022)



**[Retracted] Tiny Spherical Robot with a Magnetic Field-Based Interference Detection and Prevention Framework**

Mohamad Reda A. Refaai , S. Meenatchi, B. Ramesh, N. I. Haroon Rashid, N. B. Soni, and Manikandan Ganesan   
Research Article (10 pages), Article ID 3908975, Volume 2022 (2022)

**[Retracted] Tribological Behavior of AA7075 Reinforced with Ag and ZrO<sub>2</sub> Composites**

C. R. Mahesha, Suprabha R, M. Mahaveer Sree Jayan, Shilpa Kulkarni, Aman Sharma, Essam A. Al-Ammar, S. M. A. K. Mohammed, Ram Subbiah, and Agonafir Alemayehu   
Research Article (8 pages), Article ID 7105770, Volume 2022 (2022)

**[Retracted] Nanorobots with Hybrid Biomembranes for Simultaneous Degradation of Toxic Microorganism**

Mohamad Reda A. Refaai , M. N. Manjunatha, S. Radjarejesri, B. Ramesh, Ram Subbiah, and Nahom Adugna 





Research Article (12 pages), Article ID 2391843, Volume 2022 (2022)

**[Retracted] Statistical Analysis on the Mechanical Properties of ATH Nanofiller Addition on the Woven Jute/Polyester Hybrid Composites by the Grey-Taguchi Method**

CR Mahesha, Suprabha R, D. Raja Ramesh, Rajesh A S, Melvin Victor De Poures, Ram Subbiah, Wadi B. Alonazi, S. Sivakumar, and Agegnehu shara shata 


Research Article (6 pages), Article ID 1752203, Volume 2022 (2022)

**[Retracted] Wind Tunnel Testing and Validation of Helicopter Rotor Blades Using Additive Manufacturing**

Inamul Hasan , R. Mukesh, P. Radha Krishnan , R. Srinath, Dhanya Prakash Babu , and Negash Lemma Gurmu 


Research Article (13 pages), Article ID 4052208, Volume 2022 (2022)

**[Retracted] Optimizing the Parameters of Zirconium Carbide and Rice Husk Ash Reinforced with AA 2618 Composites**

C. R. Mahesha, R. Suprabha, S. Thenmozhi, V. Gowri, Chirumamill Mallika Chowdary, V. Savithiri, B. V. V. L. Kala Bharathi, Ram Subbiah, and Ishwarya Komalnu Raghavan 



Research Article (11 pages), Article ID 1962523, Volume 2022 (2022)

**[Retracted] Thermogravimetric Analysis and Mechanical Properties of Pebble Natural Filler-Reinforced Polymer Composites Produced through a Hand Layup Technique**

Raj Kumar, S. Mohan Kumar, M. E. Shashi Kumar, V. Ravi Kumar, Rajesh Kivade, Jonnalagadda Pavan, A. H. Seikh, M.H. Siddique, and Abdi Diriba 





Research Article (8 pages), Article ID 1837741, Volume 2022 (2022)

**[Retracted] Streamline Effect Improvement of Additive Manufactured Airfoil Utilizing Dynamic Stream Control Procedure**

R. Srinath, R. Mukesh, Manish C. Poojari, Inamul Hasan , and Wubetu Amare Alebachew 

Research Article (12 pages), Article ID 1252681, Volume 2022 (2022)



**[Retracted] Maintenance Methodologies Embraced for Railroad Systems: A Review**

Priyanka Prabhakaran , Anandakumar Subbaiyan, Dineshkumar Gopalakrishnan , Harsha Vardhana Balaji.M, S. Ramkumar , Suresh Veluswamy, Dinesh Kumar Murugesan, Satheeshkumar Seerangagounder, Sivakumar Arunachalam, Prabhu Velusamy , and Priyanka Bhaskaran

Review Article (15 pages), Article ID 7655245, Volume 2022 (2022)


# Contents

**[Retracted] An Enhanced Drone Technology for Detecting the Human Object in the Dense Areas Using a Deep Learning Model**

Mohamad Reda A. Refaai , Dhruva R. Rinku, I. Thamarai, S. Meera, Naresh Kumar Sripada, and Simon Yishak 



Research Article (12 pages), Article ID 4162007, Volume 2022 (2022)

**[Retracted] Preparation of Graphene Nanosilver Composites for 3D Printing Technology**

Xiujuan Liang and Haixu Ji 


Research Article (11 pages), Article ID 2086250, Volume 2022 (2022)

**[Retracted] Application of Composite Nano-Bone Transplantation and Massage Exercise Rehabilitation Training in Patients Undergoing Limb Replantation**

Yan Tang  and Junxia Fu 



Research Article (8 pages), Article ID 2065744, Volume 2022 (2022)

**[Retracted] An Improved Inverse Kinematics Solution for a Robot Arm Trajectory Using Multiple Adaptive Neuro-Fuzzy Inference Systems**

Mohamad Reda A. Refaai 




Research Article (12 pages), Article ID 1413952, Volume 2022 (2022)

**[Retracted] Application of IoT-Based Drones in Precision Agriculture for Pest Control**

Mohamad Reda. A. Refaai , Vinjamuri SNCH Dattu, N. Gireesh, Ekta Dixit, CH. Sandeep, and David Christopher 


Research Article (12 pages), Article ID 1160258, Volume 2022 (2022)

**High Speed Grinding of EN31 Steel with Alumina Nanofluid Coolant**

T. Sathish, R. Saravanan , V. Vijayan , R. Karthick, N. Karthikeyan, and S. Rajkumar 

Research Article (12 pages), Article ID 3324008, Volume 2022 (2022)

**[Retracted] Research on the Innovation of Procurement Mode of Nanomaterials Based on E-Commerce**

Baorui Song and Xiaozhi Wang 

Research Article (9 pages), Article ID 2415668, Volume 2022 (2022)

**[Retracted] Based on the Application Practice of Multifunctional Nanomaterials in Art Design and Industrial Manufacturing Concept**

Wensi Cai  and Yuze Li

Research Article (11 pages), Article ID 1653828, Volume 2022 (2022)



**[Retracted] Clinical Application of Graphene Composite in Internal Fixation of Ankle Fracture in Sports**

Xiaowei Xu , Rongna Wang, Dachao Zhang , and Yingge Feng

Research Article (9 pages), Article ID 2504511, Volume 2022 (2022)



**[Retracted] An Artificial Intelligence Mechanism for the Prediction of Signal Strength in Drones to IoT Devices in Smart Cities**

Mohamad Reda A. Refaai , Vinjamuri S. N. C. H. Dattu, H. S. Niranjana Murthy, P. Pramod Kumar, B. Kannadasan, and Abdi Diriba   
Research Article (13 pages), Article ID 7387346, Volume 2022 (2022)








**[Retracted] Molecular Dynamics Simulation Calculation Method for Elasticity and Plasticity of Metal Nanostructures**

Kunrong Zeng  and Kaifeng Chen   
Research Article (11 pages), Article ID 6264256, Volume 2022 (2022)



**[Retracted] Construction of Nanomaterials and the Role of Rutin in the Treatment of Cerebral Hemorrhage**

Xin Li  and Zhenzhong Gao  
Research Article (11 pages), Article ID 7044153, Volume 2022 (2022)


**[Retracted] Investigation of Insulation Properties Using Microwave Nondevastating Methodology to Predict the Strength of Polymer Materials**

Anitha Gopalan , S Ramesh , Nirmala P , Govindaraj Ramkumar , Satyajeet Sahoo , S. Agnes Shifani , and S. Arockia Jayadhas   
Research Article (9 pages), Article ID 1673263, Volume 2022 (2022)



**[Retracted] A Multisensor Data Fusion Based Anomaly Detection (Ammonia Nitrogen) Approach for Ensuring Green Coastal Environment**

Chong Qu, Zhiguo Zhou, Zhiwen Liu, Shuli Jia, Liyong Ma , and Mary Immaculate Sheela L   
Research Article (6 pages), Article ID 4632137, Volume 2022 (2022)


**[Retracted] Preparation and Supercritical CO<sub>2</sub> Foaming of Modified Nanocrystalline Cellulose Reinforced Polylactic Acid Bionanocomposites**

Dan Chen , Ping Zhang, Jiajun Wang, and De Gao  
Research Article (14 pages), Article ID 2805670, Volume 2022 (2022)

**[Retracted] Utilization of Flex Controlled Robotics on Prosthetic Hand instead of Damaged Body Parts**

Mohamad Reda A. Refaai , Ashraf Elfasakhany, P. Rajalakshmy, Bikash Chandra Saha, A. S. Prakaash, and Dadapeer Basheer   
Research Article (7 pages), Article ID 3496122, Volume 2022 (2022)

**[Retracted] The Influence of Chemically Treated Hemp Fibre on the Mechanical Behavior and Thermal Properties of Polylactic Acid Made with FDM**

N. I. Haroon Rashid, R. Meenakshi Reddy, A. R Venkataramanan, Melvin V. D. Pours, A. Thanikasalam, Ashraf Elfasakhany, and Agonafir Alemayehu   
Research Article (9 pages), Article ID 6953136, Volume 2022 (2022)


## Contents

**[Retracted] Control of Material Procurement Cost of Enterprises under the Background of the Low-Carbon Economy**

Yan Ma 



Research Article (12 pages), Article ID 5643665, Volume 2022 (2022)

**[Retracted] Effect of SiC Particle Incorporated Dielectric Medium on Electrical Discharge Machining Behavior of AA6061/B4Cp/SiCp AMCs**

Johny Khajuria, N. Nagabhooshanam, Pankaj Sharma, Atul Kumar, Santosh Kumar Sahu, Peyyala Sree Devi, and Kuma Gowwomsa Erko 

Research Article (9 pages), Article ID 2661158, Volume 2022 (2022)

**[Retracted] Experimental Studies on Mechanical and Thermal Properties of Polyester Hybrid Composites Reinforced with Sansevieria Trifasciata Fibers**

R. Premkumar, K. Sathish Kumar, J. Maniraj, A. Felix sahayaraj, I. Jenish, Fayaz Hussain , Nidhal Ben Khedher, Walid Aich, and V. Suresh 



Research Article (6 pages), Article ID 8604234, Volume 2022 (2022)

**[Retracted] Mechanical and Morphological Studies of *Sansevieria trifasciata* Fiber-Reinforced Polyester Composites with the Addition of SiO<sub>2</sub> and B<sub>4</sub>C**

P. Hariprasad, M. Kannan, C. Ramesh, A. Felix Sahayaraj, I. Jenish , Fayaz Hussain, Nidhal Ben Khedher, Attia Boudjemline, and V. Suresh 


Research Article (5 pages), Article ID 1634670, Volume 2022 (2022)

**[Retracted] Experimental Investigation on the Average Surface Roughness (Ra) of AlSi10Mg Alloy Manufactured by Laser Powder Bed Fusion Method**

Mohamad Reda A. Refaai , D. Prakash, Jaya Christiyana K G, DVSSSV Prasad, E. Archana, and Agegnehu Shara Shata 


Research Article (5 pages), Article ID 5874875, Volume 2022 (2022)

**[Retracted] Optimization of Process Parameter on AA8052 Friction Stir Welding Using Taguchi's Method**

Pankaj Sharma, S. Baskar, Puneet Joshi, T. A. Raja, Santosh Kumar Sahu, Medapati Sreenivasa Reddy, and M. Rudra Naik 

Research Article (8 pages), Article ID 3048956, Volume 2022 (2022)

**[Retracted] Investigation on Durability Behavior of Fiber Reinforced Concrete with Steel Slag/Bacteria beneath Diverse Exposure Conditions**

Madhan Kumar M, Vidhya Lakshmi Sivakumar, Subathra Devi V, N. Nagabhooshanam, and Subash Thanappan 

Research Article (10 pages), Article ID 4900241, Volume 2022 (2022)

## Retraction

# Retracted: Application of Nanoflexible Photoelectric Devices in Welding Tooling Equipment Systems

### Advances in Materials Science and Engineering

Received 8 January 2024; Accepted 8 January 2024; Published 9 January 2024

Copyright © 2024 Advances in Materials Science and Engineering. This is an open access article distributed under the Creative Commons Attribution License, which permits unrestricted use, distribution, and reproduction in any medium, provided the original work is properly cited.

This article has been retracted by Hindawi following an investigation undertaken by the publisher [1]. This investigation has uncovered evidence of one or more of the following indicators of systematic manipulation of the publication process:

- (1) Discrepancies in scope
- (2) Discrepancies in the description of the research reported
- (3) Discrepancies between the availability of data and the research described
- (4) Inappropriate citations
- (5) Incoherent, meaningless and/or irrelevant content included in the article
- (6) Manipulated or compromised peer review

The presence of these indicators undermines our confidence in the integrity of the article's content and we cannot, therefore, vouch for its reliability. Please note that this notice is intended solely to alert readers that the content of this article is unreliable. We have not investigated whether authors were aware of or involved in the systematic manipulation of the publication process.

Wiley and Hindawi regrets that the usual quality checks did not identify these issues before publication and have since put additional measures in place to safeguard research integrity.

We wish to credit our own Research Integrity and Research Publishing teams and anonymous and named external researchers and research integrity experts for contributing to this investigation.

The corresponding author, as the representative of all authors, has been given the opportunity to register their agreement or disagreement to this retraction. We have kept a record of any response received.

### References

- [1] W. Tan, H. Liu, H. Li, and S. Cao, "Application of Nanoflexible Photoelectric Devices in Welding Tooling Equipment Systems," *Advances in Materials Science and Engineering*, vol. 2022, Article ID 7010891, 14 pages, 2022.

## *Retraction*

# **Retracted: Construction of Facial Expression Recognition Technology of Intelligent Service Robot Based on Nanofiber Flexible Wearable Electronic Skins**

### **Advances in Materials Science and Engineering**

Received 8 January 2024; Accepted 8 January 2024; Published 9 January 2024

Copyright © 2024 Advances in Materials Science and Engineering. This is an open access article distributed under the Creative Commons Attribution License, which permits unrestricted use, distribution, and reproduction in any medium, provided the original work is properly cited.

This article has been retracted by Hindawi following an investigation undertaken by the publisher [1]. This investigation has uncovered evidence of one or more of the following indicators of systematic manipulation of the publication process:

- (1) Discrepancies in scope
- (2) Discrepancies in the description of the research reported
- (3) Discrepancies between the availability of data and the research described
- (4) Inappropriate citations
- (5) Incoherent, meaningless and/or irrelevant content included in the article
- (6) Manipulated or compromised peer review

The presence of these indicators undermines our confidence in the integrity of the article's content and we cannot, therefore, vouch for its reliability. Please note that this notice is intended solely to alert readers that the content of this article is unreliable. We have not investigated whether authors were aware of or involved in the systematic manipulation of the publication process.

Wiley and Hindawi regrets that the usual quality checks did not identify these issues before publication and have since put additional measures in place to safeguard research integrity.

We wish to credit our own Research Integrity and Research Publishing teams and anonymous and named external researchers and research integrity experts for contributing to this investigation.

The corresponding author, as the representative of all authors, has been given the opportunity to register their agreement or disagreement to this retraction. We have kept a record of any response received.

### **References**

- [1] F. Li, C. Li, and Y. Liu, "Construction of Facial Expression Recognition Technology of Intelligent Service Robot Based on Nanofiber Flexible Wearable Electronic Skins," *Advances in Materials Science and Engineering*, vol. 2022, Article ID 8669298, 10 pages, 2022.

## Retraction

# Retracted: Effects of Polypropylene Waste Addition as Coarse Aggregates in Concrete: Experimental Characterization and Statistical Analysis

### Advances in Materials Science and Engineering

Received 8 January 2024; Accepted 8 January 2024; Published 9 January 2024

Copyright © 2024 Advances in Materials Science and Engineering. This is an open access article distributed under the Creative Commons Attribution License, which permits unrestricted use, distribution, and reproduction in any medium, provided the original work is properly cited.

This article has been retracted by Hindawi following an investigation undertaken by the publisher [1]. This investigation has uncovered evidence of one or more of the following indicators of systematic manipulation of the publication process:

- (1) Discrepancies in scope
- (2) Discrepancies in the description of the research reported
- (3) Discrepancies between the availability of data and the research described
- (4) Inappropriate citations
- (5) Incoherent, meaningless and/or irrelevant content included in the article
- (6) Manipulated or compromised peer review

The presence of these indicators undermines our confidence in the integrity of the article's content and we cannot, therefore, vouch for its reliability. Please note that this notice is intended solely to alert readers that the content of this article is unreliable. We have not investigated whether authors were aware of or involved in the systematic manipulation of the publication process.

Wiley and Hindawi regrets that the usual quality checks did not identify these issues before publication and have since put additional measures in place to safeguard research integrity.

We wish to credit our own Research Integrity and Research Publishing teams and anonymous and named external researchers and research integrity experts for contributing to this investigation.

The corresponding author, as the representative of all authors, has been given the opportunity to register their agreement or disagreement to this retraction. We have kept a record of any response received.

### References

- [1] D. C. Naveen, K. Naresh, B. S. Keerthi Gowda, M. S. Reddy G, C. D. Prasad, and R. Shanmugam, "Effects of Polypropylene Waste Addition as Coarse Aggregates in Concrete: Experimental Characterization and Statistical Analysis," *Advances in Materials Science and Engineering*, vol. 2022, Article ID 7886722, 11 pages, 2022.

## *Retraction*

# **Retracted: Predicting the Spread of Vessels in Initial Stage Cervical Cancer through Radiomics Strategy Based on Deep Learning Approach**

### **Advances in Materials Science and Engineering**

Received 26 December 2023; Accepted 26 December 2023; Published 29 December 2023

Copyright © 2023 Advances in Materials Science and Engineering. This is an open access article distributed under the Creative Commons Attribution License, which permits unrestricted use, distribution, and reproduction in any medium, provided the original work is properly cited.

This article has been retracted by Hindawi, as publisher, following an investigation undertaken by the publisher [1]. This investigation has uncovered evidence of systematic manipulation of the publication and peer-review process. We cannot, therefore, vouch for the reliability or integrity of this article.

Please note that this notice is intended solely to alert readers that the peer-review process of this article has been compromised.

Wiley and Hindawi regret that the usual quality checks did not identify these issues before publication and have since put additional measures in place to safeguard research integrity.

We wish to credit our Research Integrity and Research Publishing teams and anonymous and named external researchers and research integrity experts for contributing to this investigation.

The corresponding author, as the representative of all authors, has been given the opportunity to register their agreement or disagreement to this retraction. We have kept a record of any response received.

### **References**

- [1] P. K. Pareek, P. A. S. Surendhar, R. Prasad et al., "Predicting the Spread of Vessels in Initial Stage Cervical Cancer through Radiomics Strategy Based on Deep Learning Approach," *Advances in Materials Science and Engineering*, vol. 2022, Article ID 1008652, 13 pages, 2022.

## *Retraction*

# **Retracted: Analysis of Temperature Distribution and Mechanical Properties of Friction Stir Welding of Al-Cu Joints Using Hardened H13 Steel Tools**

### **Advances in Materials Science and Engineering**

Received 26 December 2023; Accepted 26 December 2023; Published 29 December 2023

Copyright © 2023 Advances in Materials Science and Engineering. This is an open access article distributed under the Creative Commons Attribution License, which permits unrestricted use, distribution, and reproduction in any medium, provided the original work is properly cited.

This article has been retracted by Hindawi, as publisher, following an investigation undertaken by the publisher [1]. This investigation has uncovered evidence of systematic manipulation of the publication and peer-review process. We cannot, therefore, vouch for the reliability or integrity of this article.

Please note that this notice is intended solely to alert readers that the peer-review process of this article has been compromised.

Wiley and Hindawi regret that the usual quality checks did not identify these issues before publication and have since put additional measures in place to safeguard research integrity.

We wish to credit our Research Integrity and Research Publishing teams and anonymous and named external researchers and research integrity experts for contributing to this investigation.

The corresponding author, as the representative of all authors, has been given the opportunity to register their agreement or disagreement to this retraction. We have kept a record of any response received.

### **References**

- [1] J. Pratap Kumar, A. Raj, A. R. Venkatraman et al., “Analysis of Temperature Distribution and Mechanical Properties of Friction Stir Welding of Al-Cu Joints Using Hardened H13 Steel Tools,” *Advances in Materials Science and Engineering*, vol. 2022, Article ID 4973839, 14 pages, 2022.

## *Retraction*

# **Retracted: Investigation on Durability Behavior of Fiber Reinforced Concrete with Steel Slag/Bacteria beneath Diverse Exposure Conditions**

### **Advances in Materials Science and Engineering**

Received 26 December 2023; Accepted 26 December 2023; Published 29 December 2023

Copyright © 2023 Advances in Materials Science and Engineering. This is an open access article distributed under the Creative Commons Attribution License, which permits unrestricted use, distribution, and reproduction in any medium, provided the original work is properly cited.

This article has been retracted by Hindawi, as publisher, following an investigation undertaken by the publisher [1]. This investigation has uncovered evidence of systematic manipulation of the publication and peer-review process. We cannot, therefore, vouch for the reliability or integrity of this article.

Please note that this notice is intended solely to alert readers that the peer-review process of this article has been compromised.

Wiley and Hindawi regret that the usual quality checks did not identify these issues before publication and have since put additional measures in place to safeguard research integrity.

We wish to credit our Research Integrity and Research Publishing teams and anonymous and named external researchers and research integrity experts for contributing to this investigation.

The corresponding author, as the representative of all authors, has been given the opportunity to register their agreement or disagreement to this retraction. We have kept a record of any response received.

### **References**

- [1] M. Kumar M, V. L. Sivakumar, S. Devi V, N. Nagabhooshanam, and S. Thanappan, "Investigation on Durability Behavior of Fiber Reinforced Concrete with Steel Slag/Bacteria beneath Diverse Exposure Conditions," *Advances in Materials Science and Engineering*, vol. 2022, Article ID 4900241, 10 pages, 2022.



## *Retraction*

# **Retracted: Wind Tunnel Testing and Validation of Helicopter Rotor Blades Using Additive Manufacturing**

### **Advances in Materials Science and Engineering**

Received 26 December 2023; Accepted 26 December 2023; Published 29 December 2023

Copyright © 2023 Advances in Materials Science and Engineering. This is an open access article distributed under the Creative Commons Attribution License, which permits unrestricted use, distribution, and reproduction in any medium, provided the original work is properly cited.

This article has been retracted by Hindawi, as publisher, following an investigation undertaken by the publisher [1]. This investigation has uncovered evidence of systematic manipulation of the publication and peer-review process. We cannot, therefore, vouch for the reliability or integrity of this article.

Please note that this notice is intended solely to alert readers that the peer-review process of this article has been compromised.

Wiley and Hindawi regret that the usual quality checks did not identify these issues before publication and have since put additional measures in place to safeguard research integrity.

We wish to credit our Research Integrity and Research Publishing teams and anonymous and named external researchers and research integrity experts for contributing to this investigation.

The corresponding author, as the representative of all authors, has been given the opportunity to register their agreement or disagreement to this retraction. We have kept a record of any response received.

### **References**

- [1] I. Hasan, R. Mukesh, P. Radha Krishnan, R. Srinath, D. P. Babu, and N. Lemma Gurmu, "Wind Tunnel Testing and Validation of Helicopter Rotor Blades Using Additive Manufacturing," *Advances in Materials Science and Engineering*, vol. 2022, Article ID 4052208, 13 pages, 2022.

## *Retraction*

# **Retracted: Application of Composite Nano-Bone Transplantation and Massage Exercise Rehabilitation Training in Patients Undergoing Limb Replantation**

### **Advances in Materials Science and Engineering**

Received 26 December 2023; Accepted 26 December 2023; Published 29 December 2023

Copyright © 2023 Advances in Materials Science and Engineering. This is an open access article distributed under the Creative Commons Attribution License, which permits unrestricted use, distribution, and reproduction in any medium, provided the original work is properly cited.

This article has been retracted by Hindawi, as publisher, following an investigation undertaken by the publisher [1]. This investigation has uncovered evidence of systematic manipulation of the publication and peer-review process. We cannot, therefore, vouch for the reliability or integrity of this article.

Please note that this notice is intended solely to alert readers that the peer-review process of this article has been compromised.

Wiley and Hindawi regret that the usual quality checks did not identify these issues before publication and have since put additional measures in place to safeguard research integrity.

We wish to credit our Research Integrity and Research Publishing teams and anonymous and named external researchers and research integrity experts for contributing to this investigation.

The corresponding author, as the representative of all authors, has been given the opportunity to register their agreement or disagreement to this retraction. We have kept a record of any response received.

### **References**

- [1] Y. Tang and J. Fu, "Application of Composite Nano-Bone Transplantation and Massage Exercise Rehabilitation Training in Patients Undergoing Limb Replantation," *Advances in Materials Science and Engineering*, vol. 2022, Article ID 2065744, 8 pages, 2022.

## *Retraction*

# **Retracted: Clinical Application of Graphene Composite in Internal Fixation of Ankle Fracture in Sports**

### **Advances in Materials Science and Engineering**

Received 26 December 2023; Accepted 26 December 2023; Published 29 December 2023

Copyright © 2023 Advances in Materials Science and Engineering. This is an open access article distributed under the Creative Commons Attribution License, which permits unrestricted use, distribution, and reproduction in any medium, provided the original work is properly cited.

This article has been retracted by Hindawi, as publisher, following an investigation undertaken by the publisher [1]. This investigation has uncovered evidence of systematic manipulation of the publication and peer-review process. We cannot, therefore, vouch for the reliability or integrity of this article.

Please note that this notice is intended solely to alert readers that the peer-review process of this article has been compromised.

Wiley and Hindawi regret that the usual quality checks did not identify these issues before publication and have since put additional measures in place to safeguard research integrity.

We wish to credit our Research Integrity and Research Publishing teams and anonymous and named external researchers and research integrity experts for contributing to this investigation.

The corresponding author, as the representative of all authors, has been given the opportunity to register their agreement or disagreement to this retraction. We have kept a record of any response received.

### **References**

- [1] X. Xu, R. Wang, D. Zhang, and Y. Feng, "Clinical Application of Graphene Composite in Internal Fixation of Ankle Fracture in Sports," *Advances in Materials Science and Engineering*, vol. 2022, Article ID 2504511, 9 pages, 2022.

## *Retraction*

# **Retracted: Mechanical and Morphological Studies of *Sansevieria trifasciata* Fiber-Reinforced Polyester Composites with the Addition of SiO<sub>2</sub> and B<sub>4</sub>C**

### **Advances in Materials Science and Engineering**

Received 26 December 2023; Accepted 26 December 2023; Published 29 December 2023

Copyright © 2023 Advances in Materials Science and Engineering. This is an open access article distributed under the Creative Commons Attribution License, which permits unrestricted use, distribution, and reproduction in any medium, provided the original work is properly cited.

This article has been retracted by Hindawi, as publisher, following an investigation undertaken by the publisher [1]. This investigation has uncovered evidence of systematic manipulation of the publication and peer-review process. We cannot, therefore, vouch for the reliability or integrity of this article.

Please note that this notice is intended solely to alert readers that the peer-review process of this article has been compromised.

Wiley and Hindawi regret that the usual quality checks did not identify these issues before publication and have since put additional measures in place to safeguard research integrity.

We wish to credit our Research Integrity and Research Publishing teams and anonymous and named external researchers and research integrity experts for contributing to this investigation.

The corresponding author, as the representative of all authors, has been given the opportunity to register their agreement or disagreement to this retraction. We have kept a record of any response received.

### **References**

- [1] P. Hariprasad, M. Kannan, C. Ramesh et al., “Mechanical and Morphological Studies of *Sansevieria trifasciata* Fiber-Reinforced Polyester Composites with the Addition of SiO<sub>2</sub> and B<sub>4</sub>C,” *Advances in Materials Science and Engineering*, vol. 2022, Article ID 1634670, 5 pages, 2022.

## *Retraction*

# **Retracted: An Improved Inverse Kinematics Solution for a Robot Arm Trajectory Using Multiple Adaptive Neuro-Fuzzy Inference Systems**

### **Advances in Materials Science and Engineering**

Received 26 December 2023; Accepted 26 December 2023; Published 29 December 2023

Copyright © 2023 Advances in Materials Science and Engineering. This is an open access article distributed under the Creative Commons Attribution License, which permits unrestricted use, distribution, and reproduction in any medium, provided the original work is properly cited.

This article has been retracted by Hindawi, as publisher, following an investigation undertaken by the publisher [1]. This investigation has uncovered evidence of systematic manipulation of the publication and peer-review process. We cannot, therefore, vouch for the reliability or integrity of this article.

Please note that this notice is intended solely to alert readers that the peer-review process of this article has been compromised.

Wiley and Hindawi regret that the usual quality checks did not identify these issues before publication and have since put additional measures in place to safeguard research integrity.

We wish to credit our Research Integrity and Research Publishing teams and anonymous and named external researchers and research integrity experts for contributing to this investigation.

The corresponding author, as the representative of all authors, has been given the opportunity to register their agreement or disagreement to this retraction. We have kept a record of any response received.

### **References**

- [1] M. R. A. Refaai, "An Improved Inverse Kinematics Solution for a Robot Arm Trajectory Using Multiple Adaptive Neuro-Fuzzy Inference Systems," *Advances in Materials Science and Engineering*, vol. 2022, Article ID 1413952, 12 pages, 2022.

## *Retraction*

# **Retracted: Methane Extraction and Resource Utilization Based on Multisource Data Fusion**

### **Advances in Materials Science and Engineering**

Received 26 December 2023; Accepted 26 December 2023; Published 29 December 2023

Copyright © 2023 Advances in Materials Science and Engineering. This is an open access article distributed under the Creative Commons Attribution License, which permits unrestricted use, distribution, and reproduction in any medium, provided the original work is properly cited.

This article has been retracted by Hindawi, as publisher, following an investigation undertaken by the publisher [1]. This investigation has uncovered evidence of systematic manipulation of the publication and peer-review process. We cannot, therefore, vouch for the reliability or integrity of this article.

Please note that this notice is intended solely to alert readers that the peer-review process of this article has been compromised.

Wiley and Hindawi regret that the usual quality checks did not identify these issues before publication and have since put additional measures in place to safeguard research integrity.

We wish to credit our Research Integrity and Research Publishing teams and anonymous and named external researchers and research integrity experts for contributing to this investigation.

The corresponding author, as the representative of all authors, has been given the opportunity to register their agreement or disagreement to this retraction. We have kept a record of any response received.

### **References**

- [1] W. Chen and Z. Lu, "Methane Extraction and Resource Utilization Based on Multisource Data Fusion," *Advances in Materials Science and Engineering*, vol. 2022, Article ID 7419076, 8 pages, 2022.

## *Retraction*

# **Retracted: Image-Based Precision Measurement Technology for the Quality Inspection of Crane Boom Materials**

### **Advances in Materials Science and Engineering**

Received 26 December 2023; Accepted 26 December 2023; Published 29 December 2023

Copyright © 2023 Advances in Materials Science and Engineering. This is an open access article distributed under the Creative Commons Attribution License, which permits unrestricted use, distribution, and reproduction in any medium, provided the original work is properly cited.

This article has been retracted by Hindawi, as publisher, following an investigation undertaken by the publisher [1]. This investigation has uncovered evidence of systematic manipulation of the publication and peer-review process. We cannot, therefore, vouch for the reliability or integrity of this article.

Please note that this notice is intended solely to alert readers that the peer-review process of this article has been compromised.

Wiley and Hindawi regret that the usual quality checks did not identify these issues before publication and have since put additional measures in place to safeguard research integrity.

We wish to credit our Research Integrity and Research Publishing teams and anonymous and named external researchers and research integrity experts for contributing to this investigation.

The corresponding author, as the representative of all authors, has been given the opportunity to register their agreement or disagreement to this retraction. We have kept a record of any response received.

### **References**

- [1] H. Liu, W. Tan, S. Cao, and H. Li, "Image-Based Precision Measurement Technology for the Quality Inspection of Crane Boom Materials," *Advances in Materials Science and Engineering*, vol. 2022, Article ID 8379621, 13 pages, 2022.

## *Retraction*

# **Retracted: Molecular Dynamics Simulation Calculation Method for Elasticity and Plasticity of Metal Nanostructures**

### **Advances in Materials Science and Engineering**

Received 26 December 2023; Accepted 26 December 2023; Published 29 December 2023

Copyright © 2023 Advances in Materials Science and Engineering. This is an open access article distributed under the Creative Commons Attribution License, which permits unrestricted use, distribution, and reproduction in any medium, provided the original work is properly cited.

This article has been retracted by Hindawi, as publisher, following an investigation undertaken by the publisher [1]. This investigation has uncovered evidence of systematic manipulation of the publication and peer-review process. We cannot, therefore, vouch for the reliability or integrity of this article.

Please note that this notice is intended solely to alert readers that the peer-review process of this article has been compromised.

Wiley and Hindawi regret that the usual quality checks did not identify these issues before publication and have since put additional measures in place to safeguard research integrity.

We wish to credit our Research Integrity and Research Publishing teams and anonymous and named external researchers and research integrity experts for contributing to this investigation.

The corresponding author, as the representative of all authors, has been given the opportunity to register their agreement or disagreement to this retraction. We have kept a record of any response received.

### **References**

- [1] K. Zeng and K. Chen, "Molecular Dynamics Simulation Calculation Method for Elasticity and Plasticity of Metal Nanostructures," *Advances in Materials Science and Engineering*, vol. 2022, Article ID 6264256, 11 pages, 2022.



## *Retraction*

# **Retracted: Control of Material Procurement Cost of Enterprises under the Background of the Low-Carbon Economy**

### **Advances in Materials Science and Engineering**

Received 26 December 2023; Accepted 26 December 2023; Published 29 December 2023

Copyright © 2023 Advances in Materials Science and Engineering. This is an open access article distributed under the Creative Commons Attribution License, which permits unrestricted use, distribution, and reproduction in any medium, provided the original work is properly cited.

This article has been retracted by Hindawi, as publisher, following an investigation undertaken by the publisher [1]. This investigation has uncovered evidence of systematic manipulation of the publication and peer-review process. We cannot, therefore, vouch for the reliability or integrity of this article.

Please note that this notice is intended solely to alert readers that the peer-review process of this article has been compromised.

Wiley and Hindawi regret that the usual quality checks did not identify these issues before publication and have since put additional measures in place to safeguard research integrity.

We wish to credit our Research Integrity and Research Publishing teams and anonymous and named external researchers and research integrity experts for contributing to this investigation.

The corresponding author, as the representative of all authors, has been given the opportunity to register their agreement or disagreement to this retraction. We have kept a record of any response received.

### **References**

- [1] Y. Ma, "Control of Material Procurement Cost of Enterprises under the Background of the Low-Carbon Economy," *Advances in Materials Science and Engineering*, vol. 2022, Article ID 5643665, 12 pages, 2022.

## *Retraction*

# **Retracted: Statistical Analysis on the Mechanical Properties of ATH Nanofiller Addition on the Woven Jute/Polyester Hybrid Composites by the Grey–Taguchi Method**

### **Advances in Materials Science and Engineering**

Received 26 December 2023; Accepted 26 December 2023; Published 29 December 2023

Copyright © 2023 Advances in Materials Science and Engineering. This is an open access article distributed under the Creative Commons Attribution License, which permits unrestricted use, distribution, and reproduction in any medium, provided the original work is properly cited.

This article has been retracted by Hindawi, as publisher, following an investigation undertaken by the publisher [1]. This investigation has uncovered evidence of systematic manipulation of the publication and peer-review process. We cannot, therefore, vouch for the reliability or integrity of this article.

Please note that this notice is intended solely to alert readers that the peer-review process of this article has been compromised.

Wiley and Hindawi regret that the usual quality checks did not identify these issues before publication and have since put additional measures in place to safeguard research integrity.

We wish to credit our Research Integrity and Research Publishing teams and anonymous and named external researchers and research integrity experts for contributing to this investigation.

The corresponding author, as the representative of all authors, has been given the opportunity to register their agreement or disagreement to this retraction. We have kept a record of any response received.

### **References**

- [1] C. R. Mahesha, S. R. D. Raja Ramesh et al., “Statistical Analysis on the Mechanical Properties of ATH Nanofiller Addition on the Woven Jute/Polyester Hybrid Composites by the Grey–Taguchi Method,” *Advances in Materials Science and Engineering*, vol. 2022, Article ID 1752203, 6 pages, 2022.

## *Retraction*

# **Retracted: Investigation of Insulation Properties Using Microwave Nondevastating Methodology to Predict the Strength of Polymer Materials**

### **Advances in Materials Science and Engineering**

Received 26 December 2023; Accepted 26 December 2023; Published 29 December 2023

Copyright © 2023 Advances in Materials Science and Engineering. This is an open access article distributed under the Creative Commons Attribution License, which permits unrestricted use, distribution, and reproduction in any medium, provided the original work is properly cited.

This article has been retracted by Hindawi, as publisher, following an investigation undertaken by the publisher [1]. This investigation has uncovered evidence of systematic manipulation of the publication and peer-review process. We cannot, therefore, vouch for the reliability or integrity of this article.

Please note that this notice is intended solely to alert readers that the peer-review process of this article has been compromised.

Wiley and Hindawi regret that the usual quality checks did not identify these issues before publication and have since put additional measures in place to safeguard research integrity.

We wish to credit our Research Integrity and Research Publishing teams and anonymous and named external researchers and research integrity experts for contributing to this investigation.

The corresponding author, as the representative of all authors, has been given the opportunity to register their agreement or disagreement to this retraction. We have kept a record of any response received.

### **References**

- [1] A. Gopalan, S. Ramesh, P. Nirmala et al., "Investigation of Insulation Properties Using Microwave Nondevastating Methodology to Predict the Strength of Polymer Materials," *Advances in Materials Science and Engineering*, vol. 2022, Article ID 1673263, 9 pages, 2022.

## *Retraction*

# **Retracted: Prediction of *Escherichia coli* Bacterial and Coliforms on Plants through Artificial Neural Network**

### **Advances in Materials Science and Engineering**

Received 26 December 2023; Accepted 26 December 2023; Published 29 December 2023

Copyright © 2023 Advances in Materials Science and Engineering. This is an open access article distributed under the Creative Commons Attribution License, which permits unrestricted use, distribution, and reproduction in any medium, provided the original work is properly cited.

This article has been retracted by Hindawi, as publisher, following an investigation undertaken by the publisher [1]. This investigation has uncovered evidence of systematic manipulation of the publication and peer-review process. We cannot, therefore, vouch for the reliability or integrity of this article.

Please note that this notice is intended solely to alert readers that the peer-review process of this article has been compromised.

Wiley and Hindawi regret that the usual quality checks did not identify these issues before publication and have since put additional measures in place to safeguard research integrity.

We wish to credit our Research Integrity and Research Publishing teams and anonymous and named external researchers and research integrity experts for contributing to this investigation.

The corresponding author, as the representative of all authors, has been given the opportunity to register their agreement or disagreement to this retraction. We have kept a record of any response received.

### **References**

- [1] S. Prasath Alais Surendhar, G. Ramkumar, R. Prasad et al., "Prediction of *Escherichia coli* Bacterial and Coliforms on Plants through Artificial Neural Network," *Advances in Materials Science and Engineering*, vol. 2022, Article ID 9793790, 13 pages, 2022.

## *Retraction*

# **Retracted: Investigation of Groundwater Hydro-Geochemistry, Excellence, and Anthropoid Wellbeing Hazard in Dry Zones Using the Chemometric Method**

### **Advances in Materials Science and Engineering**

Received 26 December 2023; Accepted 26 December 2023; Published 29 December 2023

Copyright © 2023 Advances in Materials Science and Engineering. This is an open access article distributed under the Creative Commons Attribution License, which permits unrestricted use, distribution, and reproduction in any medium, provided the original work is properly cited.

This article has been retracted by Hindawi, as publisher, following an investigation undertaken by the publisher [1]. This investigation has uncovered evidence of systematic manipulation of the publication and peer-review process. We cannot, therefore, vouch for the reliability or integrity of this article.

Please note that this notice is intended solely to alert readers that the peer-review process of this article has been compromised.

Wiley and Hindawi regret that the usual quality checks did not identify these issues before publication and have since put additional measures in place to safeguard research integrity.

We wish to credit our Research Integrity and Research Publishing teams and anonymous and named external researchers and research integrity experts for contributing to this investigation.

The corresponding author, as the representative of all authors, has been given the opportunity to register their agreement or disagreement to this retraction. We have kept a record of any response received.

### **References**

- [1] M. S. Ahmed, G. Ramkumar, S. Radjarejesri et al., "Investigation of Groundwater Hydro-Geochemistry, Excellence, and Anthropoid Wellbeing Hazard in Dry Zones Using the Chemometric Method," *Advances in Materials Science and Engineering*, vol. 2022, Article ID 4903323, 10 pages, 2022.

## *Retraction*

# **Retracted: Experimental Analysis and Optimization of Tribological Properties of Self-Lubricating Aluminum Hybrid Nanocomposites Using the Taguchi Approach**

### **Advances in Materials Science and Engineering**

Received 26 December 2023; Accepted 26 December 2023; Published 29 December 2023

Copyright © 2023 Advances in Materials Science and Engineering. This is an open access article distributed under the Creative Commons Attribution License, which permits unrestricted use, distribution, and reproduction in any medium, provided the original work is properly cited.

This article has been retracted by Hindawi, as publisher, following an investigation undertaken by the publisher [1]. This investigation has uncovered evidence of systematic manipulation of the publication and peer-review process. We cannot, therefore, vouch for the reliability or integrity of this article.

Please note that this notice is intended solely to alert readers that the peer-review process of this article has been compromised.

Wiley and Hindawi regret that the usual quality checks did not identify these issues before publication and have since put additional measures in place to safeguard research integrity.

We wish to credit our Research Integrity and Research Publishing teams and anonymous and named external researchers and research integrity experts for contributing to this investigation.

The corresponding author, as the representative of all authors, has been given the opportunity to register their agreement or disagreement to this retraction. We have kept a record of any response received.

### **References**

- [1] V. K. Selvaraj, S. Jeyanthi, R. Thiyagarajan et al., "Experimental Analysis and Optimization of Tribological Properties of Self-Lubricating Aluminum Hybrid Nanocomposites Using the Taguchi Approach," *Advances in Materials Science and Engineering*, vol. 2022, Article ID 4511140, 13 pages, 2022.

## *Retraction*

# **Retracted: Preparation and Supercritical CO<sub>2</sub> Foaming of Modified Nanocrystalline Cellulose Reinforced Polylactic Acid Bionanocomposites**

### **Advances in Materials Science and Engineering**

Received 26 December 2023; Accepted 26 December 2023; Published 29 December 2023

Copyright © 2023 Advances in Materials Science and Engineering. This is an open access article distributed under the Creative Commons Attribution License, which permits unrestricted use, distribution, and reproduction in any medium, provided the original work is properly cited.

This article has been retracted by Hindawi, as publisher, following an investigation undertaken by the publisher [1]. This investigation has uncovered evidence of systematic manipulation of the publication and peer-review process. We cannot, therefore, vouch for the reliability or integrity of this article.

Please note that this notice is intended solely to alert readers that the peer-review process of this article has been compromised.

Wiley and Hindawi regret that the usual quality checks did not identify these issues before publication and have since put additional measures in place to safeguard research integrity.

We wish to credit our Research Integrity and Research Publishing teams and anonymous and named external researchers and research integrity experts for contributing to this investigation.

The corresponding author, as the representative of all authors, has been given the opportunity to register their agreement or disagreement to this retraction. We have kept a record of any response received.

### **References**

- [1] D. Chen, P. Zhang, J. Wang, and D. Gao, "Preparation and Supercritical CO<sub>2</sub> Foaming of Modified Nanocrystalline Cellulose Reinforced Polylactic Acid Bionanocomposites," *Advances in Materials Science and Engineering*, vol. 2022, Article ID 2805670, 14 pages, 2022.

## *Retraction*

# **Retracted: Based on the Application Practice of Multifunctional Nanomaterials in Art Design and Industrial Manufacturing Concept**

### **Advances in Materials Science and Engineering**

Received 26 December 2023; Accepted 26 December 2023; Published 29 December 2023

Copyright © 2023 Advances in Materials Science and Engineering. This is an open access article distributed under the Creative Commons Attribution License, which permits unrestricted use, distribution, and reproduction in any medium, provided the original work is properly cited.

This article has been retracted by Hindawi, as publisher, following an investigation undertaken by the publisher [1]. This investigation has uncovered evidence of systematic manipulation of the publication and peer-review process. We cannot, therefore, vouch for the reliability or integrity of this article.

Please note that this notice is intended solely to alert readers that the peer-review process of this article has been compromised.

Wiley and Hindawi regret that the usual quality checks did not identify these issues before publication and have since put additional measures in place to safeguard research integrity.

We wish to credit our Research Integrity and Research Publishing teams and anonymous and named external researchers and research integrity experts for contributing to this investigation.

The corresponding author, as the representative of all authors, has been given the opportunity to register their agreement or disagreement to this retraction. We have kept a record of any response received.

### **References**

- [1] W. Cai and Y. Li, "Based on the Application Practice of Multifunctional Nanomaterials in Art Design and Industrial Manufacturing Concept," *Advances in Materials Science and Engineering*, vol. 2022, Article ID 1653828, 11 pages, 2022.



## *Retraction*

# **Retracted: Preparation of Graphene Nanosilver Composites for 3D Printing Technology**

### **Advances in Materials Science and Engineering**

Received 26 December 2023; Accepted 26 December 2023; Published 29 December 2023

Copyright © 2023 Advances in Materials Science and Engineering. This is an open access article distributed under the Creative Commons Attribution License, which permits unrestricted use, distribution, and reproduction in any medium, provided the original work is properly cited.

This article has been retracted by Hindawi, as publisher, following an investigation undertaken by the publisher [1]. This investigation has uncovered evidence of systematic manipulation of the publication and peer-review process. We cannot, therefore, vouch for the reliability or integrity of this article.

Please note that this notice is intended solely to alert readers that the peer-review process of this article has been compromised.

Wiley and Hindawi regret that the usual quality checks did not identify these issues before publication and have since put additional measures in place to safeguard research integrity.

We wish to credit our Research Integrity and Research Publishing teams and anonymous and named external researchers and research integrity experts for contributing to this investigation.

The corresponding author, as the representative of all authors, has been given the opportunity to register their agreement or disagreement to this retraction. We have kept a record of any response received.

### **References**

- [1] X. Liang and H. Ji, "Preparation of Graphene Nanosilver Composites for 3D Printing Technology," *Advances in Materials Science and Engineering*, vol. 2022, Article ID 2086250, 11 pages, 2022.

## *Retraction*

# **Retracted: Modelling and Analysis of Surface Roughness Using the Cascade Forward Neural Network (CFNN) in Turning of Inconel 625**

### **Advances in Materials Science and Engineering**

Received 26 December 2023; Accepted 26 December 2023; Published 29 December 2023

Copyright © 2023 Advances in Materials Science and Engineering. This is an open access article distributed under the Creative Commons Attribution License, which permits unrestricted use, distribution, and reproduction in any medium, provided the original work is properly cited.

This article has been retracted by Hindawi, as publisher, following an investigation undertaken by the publisher [1]. This investigation has uncovered evidence of systematic manipulation of the publication and peer-review process. We cannot, therefore, vouch for the reliability or integrity of this article.

Please note that this notice is intended solely to alert readers that the peer-review process of this article has been compromised.

Wiley and Hindawi regret that the usual quality checks did not identify these issues before publication and have since put additional measures in place to safeguard research integrity.

We wish to credit our Research Integrity and Research Publishing teams and anonymous and named external researchers and research integrity experts for contributing to this investigation.

The corresponding author, as the representative of all authors, has been given the opportunity to register their agreement or disagreement to this retraction. We have kept a record of any response received.

### **References**

- [1] R. A S, M. S. Prabhuswamy, and I. Komalnu Raghavan, "Modelling and Analysis of Surface Roughness Using the Cascade Forward Neural Network (CFNN) in Turning of Inconel 625," *Advances in Materials Science and Engineering*, vol. 2022, Article ID 7520962, 9 pages, 2022.

## *Retraction*

# **Retracted: Maintenance Methodologies Embraced for Railroad Systems: A Review**

### **Advances in Materials Science and Engineering**

Received 26 December 2023; Accepted 26 December 2023; Published 29 December 2023

Copyright © 2023 Advances in Materials Science and Engineering. This is an open access article distributed under the Creative Commons Attribution License, which permits unrestricted use, distribution, and reproduction in any medium, provided the original work is properly cited.

This article has been retracted by Hindawi, as publisher, following an investigation undertaken by the publisher [1]. This investigation has uncovered evidence of systematic manipulation of the publication and peer-review process. We cannot, therefore, vouch for the reliability or integrity of this article.

Please note that this notice is intended solely to alert readers that the peer-review process of this article has been compromised.

Wiley and Hindawi regret that the usual quality checks did not identify these issues before publication and have since put additional measures in place to safeguard research integrity.

We wish to credit our Research Integrity and Research Publishing teams and anonymous and named external researchers and research integrity experts for contributing to this investigation.

The corresponding author, as the representative of all authors, has been given the opportunity to register their agreement or disagreement to this retraction. We have kept a record of any response received.

### **References**

- [1] P. Prabhakaran, A. Subbaiyan, D. Gopalakrishnan et al., "Maintenance Methodologies Embraced for Railroad Systems: A Review," *Advances in Materials Science and Engineering*, vol. 2022, Article ID 7655245, 15 pages, 2022.

## *Retraction*

# **Retracted: Processing and Properties of AlCoCrFeNi High Entropy Alloys: A Review**

### **Advances in Materials Science and Engineering**

Received 26 December 2023; Accepted 26 December 2023; Published 29 December 2023

Copyright © 2023 Advances in Materials Science and Engineering. This is an open access article distributed under the Creative Commons Attribution License, which permits unrestricted use, distribution, and reproduction in any medium, provided the original work is properly cited.

This article has been retracted by Hindawi, as publisher, following an investigation undertaken by the publisher [1]. This investigation has uncovered evidence of systematic manipulation of the publication and peer-review process. We cannot, therefore, vouch for the reliability or integrity of this article.

Please note that this notice is intended solely to alert readers that the peer-review process of this article has been compromised.

Wiley and Hindawi regret that the usual quality checks did not identify these issues before publication and have since put additional measures in place to safeguard research integrity.

We wish to credit our Research Integrity and Research Publishing teams and anonymous and named external researchers and research integrity experts for contributing to this investigation.

The corresponding author, as the representative of all authors, has been given the opportunity to register their agreement or disagreement to this retraction. We have kept a record of any response received.

### **References**

- [1] P. Gopal, K. Soorya Prakash, V. Kavimani, and G. Rajendiran, "Processing and Properties of AlCoCrFeNi High Entropy Alloys: A Review," *Advances in Materials Science and Engineering*, vol. 2022, Article ID 1190161, 13 pages, 2022.

## *Retraction*

# **Retracted: Research on the Innovation of Procurement Mode of Nanomaterials Based on E-Commerce**

### **Advances in Materials Science and Engineering**

Received 26 December 2023; Accepted 26 December 2023; Published 29 December 2023

Copyright © 2023 Advances in Materials Science and Engineering. This is an open access article distributed under the Creative Commons Attribution License, which permits unrestricted use, distribution, and reproduction in any medium, provided the original work is properly cited.

This article has been retracted by Hindawi, as publisher, following an investigation undertaken by the publisher [1]. This investigation has uncovered evidence of systematic manipulation of the publication and peer-review process. We cannot, therefore, vouch for the reliability or integrity of this article.

Please note that this notice is intended solely to alert readers that the peer-review process of this article has been compromised.

Wiley and Hindawi regret that the usual quality checks did not identify these issues before publication and have since put additional measures in place to safeguard research integrity.

We wish to credit our Research Integrity and Research Publishing teams and anonymous and named external researchers and research integrity experts for contributing to this investigation.

The corresponding author, as the representative of all authors, has been given the opportunity to register their agreement or disagreement to this retraction. We have kept a record of any response received.

### **References**

- [1] B. Song and X. Wang, "Research on the Innovation of Procurement Mode of Nanomaterials Based on E-Commerce," *Advances in Materials Science and Engineering*, vol. 2022, Article ID 2415668, 9 pages, 2022.

## *Retraction*

# **Retracted: Thermogravimetric Analysis and Mechanical Properties of Pebble Natural Filler-Reinforced Polymer Composites Produced through a Hand Layup Technique**

### **Advances in Materials Science and Engineering**

Received 26 December 2023; Accepted 26 December 2023; Published 29 December 2023

Copyright © 2023 Advances in Materials Science and Engineering. This is an open access article distributed under the Creative Commons Attribution License, which permits unrestricted use, distribution, and reproduction in any medium, provided the original work is properly cited.

This article has been retracted by Hindawi, as publisher, following an investigation undertaken by the publisher [1]. This investigation has uncovered evidence of systematic manipulation of the publication and peer-review process. We cannot, therefore, vouch for the reliability or integrity of this article.

Please note that this notice is intended solely to alert readers that the peer-review process of this article has been compromised.

Wiley and Hindawi regret that the usual quality checks did not identify these issues before publication and have since put additional measures in place to safeguard research integrity.

We wish to credit our Research Integrity and Research Publishing teams and anonymous and named external researchers and research integrity experts for contributing to this investigation.

The corresponding author, as the representative of all authors, has been given the opportunity to register their agreement or disagreement to this retraction. We have kept a record of any response received.

### **References**

- [1] R. Kumar, S. M. Kumar, M. E. S. Kumar et al., "Thermogravimetric Analysis and Mechanical Properties of Pebble Natural Filler-Reinforced Polymer Composites Produced through a Hand Layup Technique," *Advances in Materials Science and Engineering*, vol. 2022, Article ID 1837741, 8 pages, 2022.

## *Retraction*

# **Retracted: Construction of Nanomaterials and the Role of Rutin in the Treatment of Cerebral Hemorrhage**

### **Advances in Materials Science and Engineering**

Received 26 December 2023; Accepted 26 December 2023; Published 29 December 2023

Copyright © 2023 Advances in Materials Science and Engineering. This is an open access article distributed under the Creative Commons Attribution License, which permits unrestricted use, distribution, and reproduction in any medium, provided the original work is properly cited.

This article has been retracted by Hindawi, as publisher, following an investigation undertaken by the publisher [1]. This investigation has uncovered evidence of systematic manipulation of the publication and peer-review process. We cannot, therefore, vouch for the reliability or integrity of this article.

Please note that this notice is intended solely to alert readers that the peer-review process of this article has been compromised.

Wiley and Hindawi regret that the usual quality checks did not identify these issues before publication and have since put additional measures in place to safeguard research integrity.

We wish to credit our Research Integrity and Research Publishing teams and anonymous and named external researchers and research integrity experts for contributing to this investigation.

The corresponding author, as the representative of all authors, has been given the opportunity to register their agreement or disagreement to this retraction. We have kept a record of any response received.

### **References**

- [1] X. Li and Z. Gao, "Construction of Nanomaterials and the Role of Rutin in the Treatment of Cerebral Hemorrhage," *Advances in Materials Science and Engineering*, vol. 2022, Article ID 7044153, 11 pages, 2022.

## *Retraction*

# **Retracted: A Multisensor Data Fusion Based Anomaly Detection (Ammonia Nitrogen) Approach for Ensuring Green Coastal Environment**

### **Advances in Materials Science and Engineering**

Received 26 December 2023; Accepted 26 December 2023; Published 29 December 2023

Copyright © 2023 Advances in Materials Science and Engineering. This is an open access article distributed under the Creative Commons Attribution License, which permits unrestricted use, distribution, and reproduction in any medium, provided the original work is properly cited.

This article has been retracted by Hindawi, as publisher, following an investigation undertaken by the publisher [1]. This investigation has uncovered evidence of systematic manipulation of the publication and peer-review process. We cannot, therefore, vouch for the reliability or integrity of this article.

Please note that this notice is intended solely to alert readers that the peer-review process of this article has been compromised.

Wiley and Hindawi regret that the usual quality checks did not identify these issues before publication and have since put additional measures in place to safeguard research integrity.

We wish to credit our Research Integrity and Research Publishing teams and anonymous and named external researchers and research integrity experts for contributing to this investigation.

The corresponding author, as the representative of all authors, has been given the opportunity to register their agreement or disagreement to this retraction. We have kept a record of any response received.

### **References**

- [1] C. Qu, Z. Zhou, Z. Liu, S. Jia, L. Ma, and M. I. Sheela L, "A Multisensor Data Fusion Based Anomaly Detection (Ammonia Nitrogen) Approach for Ensuring Green Coastal Environment," *Advances in Materials Science and Engineering*, vol. 2022, Article ID 4632137, 6 pages, 2022.



## *Retraction*

# **Retracted: Study of Wear Behavior on AA6061 Reinforced with Hybrid Ceramic Composites through Optimization**

### **Advances in Materials Science and Engineering**

Received 26 December 2023; Accepted 26 December 2023; Published 29 December 2023

Copyright © 2023 Advances in Materials Science and Engineering. This is an open access article distributed under the Creative Commons Attribution License, which permits unrestricted use, distribution, and reproduction in any medium, provided the original work is properly cited.

This article has been retracted by Hindawi, as publisher, following an investigation undertaken by the publisher [1]. This investigation has uncovered evidence of systematic manipulation of the publication and peer-review process. We cannot, therefore, vouch for the reliability or integrity of this article.

Please note that this notice is intended solely to alert readers that the peer-review process of this article has been compromised.

Wiley and Hindawi regret that the usual quality checks did not identify these issues before publication and have since put additional measures in place to safeguard research integrity.

We wish to credit our Research Integrity and Research Publishing teams and anonymous and named external researchers and research integrity experts for contributing to this investigation.

The corresponding author, as the representative of all authors, has been given the opportunity to register their agreement or disagreement to this retraction. We have kept a record of any response received.

### **References**

- [1] O. Shabbir, S. V. Alagarsamy, C. Krishnamurthy, A. Nagaraj, P. K. Singh, and S. Ketema Sida, "Study of Wear Behavior on AA6061 Reinforced with Hybrid Ceramic Composites through Optimization," *Advances in Materials Science and Engineering*, vol. 2023, Article ID 7558886, 10 pages, 2023.

## *Retraction*

# **Retracted: Process Optimization of Spark Plasma Sintering Parameters for Tungsten Carbide/Silicon Nitride/AA2219 Composites by Taguchi Method**

### **Advances in Materials Science and Engineering**

Received 26 December 2023; Accepted 26 December 2023; Published 29 December 2023

Copyright © 2023 Advances in Materials Science and Engineering. This is an open access article distributed under the Creative Commons Attribution License, which permits unrestricted use, distribution, and reproduction in any medium, provided the original work is properly cited.

This article has been retracted by Hindawi, as publisher, following an investigation undertaken by the publisher [1]. This investigation has uncovered evidence of systematic manipulation of the publication and peer-review process. We cannot, therefore, vouch for the reliability or integrity of this article.

Please note that this notice is intended solely to alert readers that the peer-review process of this article has been compromised.

Wiley and Hindawi regret that the usual quality checks did not identify these issues before publication and have since put additional measures in place to safeguard research integrity.

We wish to credit our Research Integrity and Research Publishing teams and anonymous and named external researchers and research integrity experts for contributing to this investigation.

The corresponding author, as the representative of all authors, has been given the opportunity to register their agreement or disagreement to this retraction. We have kept a record of any response received.

### **References**

- [1] S. Althahban, G. Pathinettampadian, F. Qahtani et al., "Process Optimization of Spark Plasma Sintering Parameters for Tungsten Carbide/Silicon Nitride/AA2219 Composites by Taguchi Method," *Advances in Materials Science and Engineering*, vol. 2022, Article ID 4829499, 8 pages, 2022.

## *Retraction*

# **Retracted: Performance and Exhaust Emission Characteristics of C.I Engine Using Biofuels and Its Diesel Blend with Nano-Additives**

### **Advances in Materials Science and Engineering**

Received 26 December 2023; Accepted 26 December 2023; Published 29 December 2023

Copyright © 2023 Advances in Materials Science and Engineering. This is an open access article distributed under the Creative Commons Attribution License, which permits unrestricted use, distribution, and reproduction in any medium, provided the original work is properly cited.

This article has been retracted by Hindawi, as publisher, following an investigation undertaken by the publisher [1]. This investigation has uncovered evidence of systematic manipulation of the publication and peer-review process. We cannot, therefore, vouch for the reliability or integrity of this article.

Please note that this notice is intended solely to alert readers that the peer-review process of this article has been compromised.

Wiley and Hindawi regret that the usual quality checks did not identify these issues before publication and have since put additional measures in place to safeguard research integrity.

We wish to credit our Research Integrity and Research Publishing teams and anonymous and named external researchers and research integrity experts for contributing to this investigation.

The corresponding author, as the representative of all authors, has been given the opportunity to register their agreement or disagreement to this retraction. We have kept a record of any response received.

### **References**

- [1] S. Jacob, L. Karikalan, J. I. JoshuaRamesh Lalvani, A. Sharma, and M. Kannappan, "Performance and Exhaust Emission Characteristics of C.I Engine Using Biofuels and Its Diesel Blend with Nano-Additives," *Advances in Materials Science and Engineering*, vol. 2022, Article ID 9185388, 5 pages, 2022.

## *Retraction*

# **Retracted: Streamline Effect Improvement of Additive Manufactured Airfoil Utilizing Dynamic Stream Control Procedure**

### **Advances in Materials Science and Engineering**

Received 26 December 2023; Accepted 26 December 2023; Published 29 December 2023

Copyright © 2023 Advances in Materials Science and Engineering. This is an open access article distributed under the Creative Commons Attribution License, which permits unrestricted use, distribution, and reproduction in any medium, provided the original work is properly cited.

This article has been retracted by Hindawi, as publisher, following an investigation undertaken by the publisher [1]. This investigation has uncovered evidence of systematic manipulation of the publication and peer-review process. We cannot, therefore, vouch for the reliability or integrity of this article.

Please note that this notice is intended solely to alert readers that the peer-review process of this article has been compromised.

Wiley and Hindawi regret that the usual quality checks did not identify these issues before publication and have since put additional measures in place to safeguard research integrity.

We wish to credit our Research Integrity and Research Publishing teams and anonymous and named external researchers and research integrity experts for contributing to this investigation.

The corresponding author, as the representative of all authors, has been given the opportunity to register their agreement or disagreement to this retraction. We have kept a record of any response received.

### **References**

- [1] R. Srinath, R. Mukesh, M. C. Poojari, I. Hasan, and W. Amare Alebachew, "Streamline Effect Improvement of Additive Manufactured Airfoil Utilizing Dynamic Stream Control Procedure," *Advances in Materials Science and Engineering*, vol. 2022, Article ID 1252681, 12 pages, 2022.

## *Retraction*

# **Retracted: Parametric Optimization of Abrasive Water Jet Cutting on AA 5083 through Multiobjective Teaching-Learning Method**

### **Advances in Materials Science and Engineering**

Received 26 December 2023; Accepted 26 December 2023; Published 29 December 2023

Copyright © 2023 Advances in Materials Science and Engineering. This is an open access article distributed under the Creative Commons Attribution License, which permits unrestricted use, distribution, and reproduction in any medium, provided the original work is properly cited.

This article has been retracted by Hindawi, as publisher, following an investigation undertaken by the publisher [1]. This investigation has uncovered evidence of systematic manipulation of the publication and peer-review process. We cannot, therefore, vouch for the reliability or integrity of this article.

Please note that this notice is intended solely to alert readers that the peer-review process of this article has been compromised.

Wiley and Hindawi regret that the usual quality checks did not identify these issues before publication and have since put additional measures in place to safeguard research integrity.

We wish to credit our Research Integrity and Research Publishing teams and anonymous and named external researchers and research integrity experts for contributing to this investigation.

The corresponding author, as the representative of all authors, has been given the opportunity to register their agreement or disagreement to this retraction. We have kept a record of any response received.

### **References**

- [1] R. Meenakshi Reddy, K. Logesh, S. V. Alagarsamy et al., "Parametric Optimization of Abrasive Water Jet Cutting on AA 5083 through Multiobjective Teaching-Learning Method," *Advances in Materials Science and Engineering*, vol. 2022, Article ID 1123256, 7 pages, 2022.

## *Retraction*

# **Retracted: Development of Microbiology Plantation-Based Multimodal Segmentation for Smart Garden Using Machine Learning**

### **Advances in Materials Science and Engineering**

Received 26 December 2023; Accepted 26 December 2023; Published 29 December 2023

Copyright © 2023 Advances in Materials Science and Engineering. This is an open access article distributed under the Creative Commons Attribution License, which permits unrestricted use, distribution, and reproduction in any medium, provided the original work is properly cited.

This article has been retracted by Hindawi, as publisher, following an investigation undertaken by the publisher [1]. This investigation has uncovered evidence of systematic manipulation of the publication and peer-review process. We cannot, therefore, vouch for the reliability or integrity of this article.

Please note that this notice is intended solely to alert readers that the peer-review process of this article has been compromised.

Wiley and Hindawi regret that the usual quality checks did not identify these issues before publication and have since put additional measures in place to safeguard research integrity.

We wish to credit our Research Integrity and Research Publishing teams and anonymous and named external researchers and research integrity experts for contributing to this investigation.

The corresponding author, as the representative of all authors, has been given the opportunity to register their agreement or disagreement to this retraction. We have kept a record of any response received.

### **References**

- [1] S. Prasath, R. Govindaraj, R. Subbiah et al., "Development of Microbiology Plantation-Based Multimodal Segmentation for Smart Garden Using Machine Learning," *Advances in Materials Science and Engineering*, vol. 2022, Article ID 1066535, 6 pages, 2022.

## *Retraction*

# **Retracted: Optimization on Tribological Behaviour of AA7075/Zirconium Boride Composites Using Taguchi Technique**

### **Advances in Materials Science and Engineering**

Received 26 December 2023; Accepted 26 December 2023; Published 29 December 2023

Copyright © 2023 Advances in Materials Science and Engineering. This is an open access article distributed under the Creative Commons Attribution License, which permits unrestricted use, distribution, and reproduction in any medium, provided the original work is properly cited.

This article has been retracted by Hindawi, as publisher, following an investigation undertaken by the publisher [1]. This investigation has uncovered evidence of systematic manipulation of the publication and peer-review process. We cannot, therefore, vouch for the reliability or integrity of this article.

Please note that this notice is intended solely to alert readers that the peer-review process of this article has been compromised.

Wiley and Hindawi regret that the usual quality checks did not identify these issues before publication and have since put additional measures in place to safeguard research integrity.

We wish to credit our Research Integrity and Research Publishing teams and anonymous and named external researchers and research integrity experts for contributing to this investigation.

The corresponding author, as the representative of all authors, has been given the opportunity to register their agreement or disagreement to this retraction. We have kept a record of any response received.

### **References**

- [1] S. K. Mohan, R. M. Reddy, V. Kamalakar et al., "Optimization on Tribological Behaviour of AA7075/Zirconium Boride Composites Using Taguchi Technique," *Advances in Materials Science and Engineering*, vol. 2022, Article ID 4058442, 7 pages, 2022.

## *Retraction*

# **Retracted: Machine Learning Approach: Prediction of Surface Roughness in Dry Turning Inconel 625**

### **Advances in Materials Science and Engineering**

Received 26 December 2023; Accepted 26 December 2023; Published 29 December 2023

Copyright © 2023 Advances in Materials Science and Engineering. This is an open access article distributed under the Creative Commons Attribution License, which permits unrestricted use, distribution, and reproduction in any medium, provided the original work is properly cited.

This article has been retracted by Hindawi, as publisher, following an investigation undertaken by the publisher [1]. This investigation has uncovered evidence of systematic manipulation of the publication and peer-review process. We cannot, therefore, vouch for the reliability or integrity of this article.

Please note that this notice is intended solely to alert readers that the peer-review process of this article has been compromised.

Wiley and Hindawi regret that the usual quality checks did not identify these issues before publication and have since put additional measures in place to safeguard research integrity.

We wish to credit our Research Integrity and Research Publishing teams and anonymous and named external researchers and research integrity experts for contributing to this investigation.

The corresponding author, as the representative of all authors, has been given the opportunity to register their agreement or disagreement to this retraction. We have kept a record of any response received.

### **References**

- [1] A. S. Rajesh, M. S. Prabhuswamy, and M. Rudra Naik, "Machine Learning Approach: Prediction of Surface Roughness in Dry Turning Inconel 625," *Advances in Materials Science and Engineering*, vol. 2022, Article ID 6038804, 7 pages, 2022.



## *Retraction*

# **Retracted: Optimizing the Parameters of Zirconium Carbide and Rice Husk Ash Reinforced with AA 2618 Composites**

### **Advances in Materials Science and Engineering**

Received 26 December 2023; Accepted 26 December 2023; Published 29 December 2023

Copyright © 2023 Advances in Materials Science and Engineering. This is an open access article distributed under the Creative Commons Attribution License, which permits unrestricted use, distribution, and reproduction in any medium, provided the original work is properly cited.

This article has been retracted by Hindawi, as publisher, following an investigation undertaken by the publisher [1]. This investigation has uncovered evidence of systematic manipulation of the publication and peer-review process. We cannot, therefore, vouch for the reliability or integrity of this article.

Please note that this notice is intended solely to alert readers that the peer-review process of this article has been compromised.

Wiley and Hindawi regret that the usual quality checks did not identify these issues before publication and have since put additional measures in place to safeguard research integrity.

We wish to credit our Research Integrity and Research Publishing teams and anonymous and named external researchers and research integrity experts for contributing to this investigation.

The corresponding author, as the representative of all authors, has been given the opportunity to register their agreement or disagreement to this retraction. We have kept a record of any response received.

### **References**

- [1] C. R. Mahesha, R. Suprabha, S. Thenmozhi et al., "Optimizing the Parameters of Zirconium Carbide and Rice Husk Ash Reinforced with AA 2618 Composites," *Advances in Materials Science and Engineering*, vol. 2022, Article ID 1962523, 11 pages, 2022.

## *Retraction*

# **Retracted: Tribological Behavior of AA7075 Reinforced with Ag and ZrO<sub>2</sub> Composites**

### **Advances in Materials Science and Engineering**

Received 26 December 2023; Accepted 26 December 2023; Published 29 December 2023

Copyright © 2023 Advances in Materials Science and Engineering. This is an open access article distributed under the Creative Commons Attribution License, which permits unrestricted use, distribution, and reproduction in any medium, provided the original work is properly cited.

This article has been retracted by Hindawi, as publisher, following an investigation undertaken by the publisher [1]. This investigation has uncovered evidence of systematic manipulation of the publication and peer-review process. We cannot, therefore, vouch for the reliability or integrity of this article.

Please note that this notice is intended solely to alert readers that the peer-review process of this article has been compromised.

Wiley and Hindawi regret that the usual quality checks did not identify these issues before publication and have since put additional measures in place to safeguard research integrity.

We wish to credit our Research Integrity and Research Publishing teams and anonymous and named external researchers and research integrity experts for contributing to this investigation.

The corresponding author, as the representative of all authors, has been given the opportunity to register their agreement or disagreement to this retraction. We have kept a record of any response received.

### **References**

- [1] C. R. Mahesha, S. R. M. M. Sree Jayan et al., "Tribological Behavior of AA7075 Reinforced with Ag and ZrO<sub>2</sub> Composites," *Advances in Materials Science and Engineering*, vol. 2022, Article ID 7105770, 8 pages, 2022.

## *Retraction*

# **Retracted: Utilization of Flex Controlled Robotics on Prosthetic Hand instead of Damaged Body Parts**

### **Advances in Materials Science and Engineering**

Received 26 December 2023; Accepted 26 December 2023; Published 29 December 2023

Copyright © 2023 Advances in Materials Science and Engineering. This is an open access article distributed under the Creative Commons Attribution License, which permits unrestricted use, distribution, and reproduction in any medium, provided the original work is properly cited.

This article has been retracted by Hindawi, as publisher, following an investigation undertaken by the publisher [1]. This investigation has uncovered evidence of systematic manipulation of the publication and peer-review process. We cannot, therefore, vouch for the reliability or integrity of this article.

Please note that this notice is intended solely to alert readers that the peer-review process of this article has been compromised.

Wiley and Hindawi regret that the usual quality checks did not identify these issues before publication and have since put additional measures in place to safeguard research integrity.

We wish to credit our Research Integrity and Research Publishing teams and anonymous and named external researchers and research integrity experts for contributing to this investigation.

The corresponding author, as the representative of all authors, has been given the opportunity to register their agreement or disagreement to this retraction. We have kept a record of any response received.

### **References**

- [1] M. R. A. Refaai, A. Elfasakhany, P. Rajalakshmy, B. Chandra Saha, A. S. Prakaash, and D. Basheer, "Utilization of Flex Controlled Robotics on Prosthetic Hand instead of Damaged Body Parts," *Advances in Materials Science and Engineering*, vol. 2022, Article ID 3496122, 7 pages, 2022.

## *Retraction*

# **Retracted: Influence of Metallic Particles on Properties of Aluminium Composites through Taguchi Technique**

### **Advances in Materials Science and Engineering**

Received 26 December 2023; Accepted 26 December 2023; Published 29 December 2023

Copyright © 2023 Advances in Materials Science and Engineering. This is an open access article distributed under the Creative Commons Attribution License, which permits unrestricted use, distribution, and reproduction in any medium, provided the original work is properly cited.

This article has been retracted by Hindawi, as publisher, following an investigation undertaken by the publisher [1]. This investigation has uncovered evidence of systematic manipulation of the publication and peer-review process. We cannot, therefore, vouch for the reliability or integrity of this article.

Please note that this notice is intended solely to alert readers that the peer-review process of this article has been compromised.

Wiley and Hindawi regret that the usual quality checks did not identify these issues before publication and have since put additional measures in place to safeguard research integrity.

We wish to credit our Research Integrity and Research Publishing teams and anonymous and named external researchers and research integrity experts for contributing to this investigation.

The corresponding author, as the representative of all authors, has been given the opportunity to register their agreement or disagreement to this retraction. We have kept a record of any response received.

### **References**

- [1] B. Venkatesh, A. R. Lakshmi pathi, T. Prakash et al., "Influence of Metallic Particles on Properties of Aluminium Composites through Taguchi Technique," *Advances in Materials Science and Engineering*, vol. 2023, Article ID 9637728, 12 pages, 2023.

## *Retraction*

# **Retracted: Investigation on Heat Deflection and Thermal Conductivity of Basalt Fiber Reinforced Composites Prepared by Hand Layup Method**

### **Advances in Materials Science and Engineering**

Received 26 December 2023; Accepted 26 December 2023; Published 29 December 2023

Copyright © 2023 Advances in Materials Science and Engineering. This is an open access article distributed under the Creative Commons Attribution License, which permits unrestricted use, distribution, and reproduction in any medium, provided the original work is properly cited.

This article has been retracted by Hindawi, as publisher, following an investigation undertaken by the publisher [1]. This investigation has uncovered evidence of systematic manipulation of the publication and peer-review process. We cannot, therefore, vouch for the reliability or integrity of this article.

Please note that this notice is intended solely to alert readers that the peer-review process of this article has been compromised.

Wiley and Hindawi regret that the usual quality checks did not identify these issues before publication and have since put additional measures in place to safeguard research integrity.

We wish to credit our Research Integrity and Research Publishing teams and anonymous and named external researchers and research integrity experts for contributing to this investigation.

The corresponding author, as the representative of all authors, has been given the opportunity to register their agreement or disagreement to this retraction. We have kept a record of any response received.

### **References**

- [1] R. M. Reddy, S. Ravi, P. K. Singh et al., "Investigation on Heat Deflection and Thermal Conductivity of Basalt Fiber Reinforced Composites Prepared by Hand Layup Method," *Advances in Materials Science and Engineering*, vol. 2022, Article ID 1294374, 6 pages, 2022.

## *Retraction*

# **Retracted: Experimental Studies on Mechanical and Thermal Properties of Polyester Hybrid Composites Reinforced with Sansevieria Trifasciata Fibers**

### **Advances in Materials Science and Engineering**

Received 26 December 2023; Accepted 26 December 2023; Published 29 December 2023

Copyright © 2023 Advances in Materials Science and Engineering. This is an open access article distributed under the Creative Commons Attribution License, which permits unrestricted use, distribution, and reproduction in any medium, provided the original work is properly cited.

This article has been retracted by Hindawi, as publisher, following an investigation undertaken by the publisher [1]. This investigation has uncovered evidence of systematic manipulation of the publication and peer-review process. We cannot, therefore, vouch for the reliability or integrity of this article.

Please note that this notice is intended solely to alert readers that the peer-review process of this article has been compromised.

Wiley and Hindawi regret that the usual quality checks did not identify these issues before publication and have since put additional measures in place to safeguard research integrity.

We wish to credit our Research Integrity and Research Publishing teams and anonymous and named external researchers and research integrity experts for contributing to this investigation.

The corresponding author, as the representative of all authors, has been given the opportunity to register their agreement or disagreement to this retraction. We have kept a record of any response received.

### **References**

- [1] R. Premkumar, K. Sathish Kumar, J. Maniraj et al., “Experimental Studies on Mechanical and Thermal Properties of Polyester Hybrid Composites Reinforced with Sansevieria Trifasciata Fibers,” *Advances in Materials Science and Engineering*, vol. 2022, Article ID 8604234, 6 pages, 2022.

## *Retraction*

# **Retracted: The Influence of Chemically Treated Hemp Fibre on the Mechanical Behavior and Thermal Properties of Polylactic Acid Made with FDM**

### **Advances in Materials Science and Engineering**

Received 26 December 2023; Accepted 26 December 2023; Published 29 December 2023

Copyright © 2023 Advances in Materials Science and Engineering. This is an open access article distributed under the Creative Commons Attribution License, which permits unrestricted use, distribution, and reproduction in any medium, provided the original work is properly cited.

This article has been retracted by Hindawi, as publisher, following an investigation undertaken by the publisher [1]. This investigation has uncovered evidence of systematic manipulation of the publication and peer-review process. We cannot, therefore, vouch for the reliability or integrity of this article.

Please note that this notice is intended solely to alert readers that the peer-review process of this article has been compromised.

Wiley and Hindawi regret that the usual quality checks did not identify these issues before publication and have since put additional measures in place to safeguard research integrity.

We wish to credit our Research Integrity and Research Publishing teams and anonymous and named external researchers and research integrity experts for contributing to this investigation.

The corresponding author, as the representative of all authors, has been given the opportunity to register their agreement or disagreement to this retraction. We have kept a record of any response received.

### **References**

- [1] N. I. Haroon Rashid, R. Meenakshi Reddy, A. R. Venkataramanan et al., "The Influence of Chemically Treated Hemp Fibre on the Mechanical Behavior and Thermal Properties of Polylactic Acid Made with FDM," *Advances in Materials Science and Engineering*, vol. 2022, Article ID 6953136, 9 pages, 2022.

## *Retraction*

# **Retracted: A Study of Structural Parameters Effects on Pressure Differential to Roll Titanium Diaphragm for a Spacecraft Propellant Tank**

### **Advances in Materials Science and Engineering**

Received 26 December 2023; Accepted 26 December 2023; Published 29 December 2023

Copyright © 2023 Advances in Materials Science and Engineering. This is an open access article distributed under the Creative Commons Attribution License, which permits unrestricted use, distribution, and reproduction in any medium, provided the original work is properly cited.

This article has been retracted by Hindawi, as publisher, following an investigation undertaken by the publisher [1]. This investigation has uncovered evidence of systematic manipulation of the publication and peer-review process. We cannot, therefore, vouch for the reliability or integrity of this article.

Please note that this notice is intended solely to alert readers that the peer-review process of this article has been compromised.

Wiley and Hindawi regret that the usual quality checks did not identify these issues before publication and have since put additional measures in place to safeguard research integrity.

We wish to credit our Research Integrity and Research Publishing teams and anonymous and named external researchers and research integrity experts for contributing to this investigation.

The corresponding author, as the representative of all authors, has been given the opportunity to register their agreement or disagreement to this retraction. We have kept a record of any response received.

### **References**

- [1] T. Ma, S. Gu, J. Zhao, B. Yu, J. Zhang, and W. Yang, "A Study of Structural Parameters Effects on Pressure Differential to Roll Titanium Diaphragm for a Spacecraft Propellant Tank," *Advances in Materials Science and Engineering*, vol. 2022, Article ID 2003905, 10 pages, 2022.



## *Retraction*

# **Retracted: Effect of Reinforcement on Tensile Characteristics in AA 5052 with ZrC and Fly Ash-Based Composites**

### **Advances in Materials Science and Engineering**

Received 26 December 2023; Accepted 26 December 2023; Published 29 December 2023

Copyright © 2023 Advances in Materials Science and Engineering. This is an open access article distributed under the Creative Commons Attribution License, which permits unrestricted use, distribution, and reproduction in any medium, provided the original work is properly cited.

This article has been retracted by Hindawi, as publisher, following an investigation undertaken by the publisher [1]. This investigation has uncovered evidence of systematic manipulation of the publication and peer-review process. We cannot, therefore, vouch for the reliability or integrity of this article.

Please note that this notice is intended solely to alert readers that the peer-review process of this article has been compromised.

Wiley and Hindawi regret that the usual quality checks did not identify these issues before publication and have since put additional measures in place to safeguard research integrity.

We wish to credit our Research Integrity and Research Publishing teams and anonymous and named external researchers and research integrity experts for contributing to this investigation.

The corresponding author, as the representative of all authors, has been given the opportunity to register their agreement or disagreement to this retraction. We have kept a record of any response received.

### **References**

- [1] K. Mallikarjuna, M. K. Harikeerthan, B. S. Shubhalakshmi et al., "Effect of Reinforcement on Tensile Characteristics in AA 5052 with ZrC and Fly Ash-Based Composites," *Advances in Materials Science and Engineering*, vol. 2022, Article ID 7070304, 7 pages, 2022.

## *Retraction*

# **Retracted: Experimental Investigation on the Average Surface Roughness (Ra) of AlSi10Mg Alloy Manufactured by Laser Powder Bed Fusion Method**

### **Advances in Materials Science and Engineering**

Received 26 December 2023; Accepted 26 December 2023; Published 29 December 2023

Copyright © 2023 Advances in Materials Science and Engineering. This is an open access article distributed under the Creative Commons Attribution License, which permits unrestricted use, distribution, and reproduction in any medium, provided the original work is properly cited.

This article has been retracted by Hindawi, as publisher, following an investigation undertaken by the publisher [1]. This investigation has uncovered evidence of systematic manipulation of the publication and peer-review process. We cannot, therefore, vouch for the reliability or integrity of this article.

Please note that this notice is intended solely to alert readers that the peer-review process of this article has been compromised.

Wiley and Hindawi regret that the usual quality checks did not identify these issues before publication and have since put additional measures in place to safeguard research integrity.

We wish to credit our Research Integrity and Research Publishing teams and anonymous and named external researchers and research integrity experts for contributing to this investigation.

The corresponding author, as the representative of all authors, has been given the opportunity to register their agreement or disagreement to this retraction. We have kept a record of any response received.

### **References**

- [1] M. R. A. Refaai, D. Prakash, K. G. Jaya Christiyani, D. Prasad, E. Archana, and A. S. Shata, "Experimental Investigation on the Average Surface Roughness (Ra) of AlSi10Mg Alloy Manufactured by Laser Powder Bed Fusion Method," *Advances in Materials Science and Engineering*, vol. 2022, Article ID 5874875, 5 pages, 2022.

## *Retraction*

# **Retracted: Optimization of Process Parameter on AA8052 Friction Stir Welding Using Taguchi's Method**

### **Advances in Materials Science and Engineering**

Received 26 December 2023; Accepted 26 December 2023; Published 29 December 2023

Copyright © 2023 Advances in Materials Science and Engineering. This is an open access article distributed under the Creative Commons Attribution License, which permits unrestricted use, distribution, and reproduction in any medium, provided the original work is properly cited.

This article has been retracted by Hindawi, as publisher, following an investigation undertaken by the publisher [1]. This investigation has uncovered evidence of systematic manipulation of the publication and peer-review process. We cannot, therefore, vouch for the reliability or integrity of this article.

Please note that this notice is intended solely to alert readers that the peer-review process of this article has been compromised.

Wiley and Hindawi regret that the usual quality checks did not identify these issues before publication and have since put additional measures in place to safeguard research integrity.

We wish to credit our Research Integrity and Research Publishing teams and anonymous and named external researchers and research integrity experts for contributing to this investigation.

The corresponding author, as the representative of all authors, has been given the opportunity to register their agreement or disagreement to this retraction. We have kept a record of any response received.

### **References**

- [1] P. Sharma, S. Baskar, P. Joshi et al., "Optimization of Process Parameter on AA8052 Friction Stir Welding Using Taguchi's Method," *Advances in Materials Science and Engineering*, vol. 2022, Article ID 3048956, 8 pages, 2022.

## Retraction

# Retracted: Application of IoT-Based Drones in Precision Agriculture for Pest Control

### Advances in Materials Science and Engineering

Received 20 June 2023; Accepted 20 June 2023; Published 21 June 2023

Copyright © 2023 Advances in Materials Science and Engineering. This is an open access article distributed under the Creative Commons Attribution License, which permits unrestricted use, distribution, and reproduction in any medium, provided the original work is properly cited.

This article has been retracted by Hindawi following an investigation undertaken by the publisher [1]. This investigation has uncovered evidence of one or more of the following indicators of systematic manipulation of the publication process:

- (1) Discrepancies in scope
- (2) Discrepancies in the description of the research reported
- (3) Discrepancies between the availability of data and the research described
- (4) Inappropriate citations
- (5) Incoherent, meaningless and/or irrelevant content included in the article
- (6) Peer-review manipulation

The presence of these indicators undermines our confidence in the integrity of the article's content and we cannot, therefore, vouch for its reliability. Please note that this notice is intended solely to alert readers that the content of this article is unreliable. We have not investigated whether authors were aware of or involved in the systematic manipulation of the publication process.

Wiley and Hindawi regrets that the usual quality checks did not identify these issues before publication and have since put additional measures in place to safeguard research integrity.

We wish to credit our own Research Integrity and Research Publishing teams and anonymous and named external researchers and research integrity experts for contributing to this investigation.

The corresponding author, as the representative of all authors, has been given the opportunity to register their agreement or disagreement to this retraction. We have kept a record of any response received.

### References

- [1] M. R. A. Refaai, V. S. Dattu, N. Gireesh, E. Dixit, C. Sandeep, and D. Christopher, "Application of IoT-Based Drones in Precision Agriculture for Pest Control," *Advances in Materials Science and Engineering*, vol. 2022, Article ID 1160258, 12 pages, 2022.

## Retraction

# Retracted: Nanorobots with Hybrid Biomembranes for Simultaneous Degradation of Toxic Microorganism

### Advances in Materials Science and Engineering

Received 20 June 2023; Accepted 20 June 2023; Published 21 June 2023

Copyright © 2023 Advances in Materials Science and Engineering. This is an open access article distributed under the Creative Commons Attribution License, which permits unrestricted use, distribution, and reproduction in any medium, provided the original work is properly cited.

This article has been retracted by Hindawi following an investigation undertaken by the publisher [1]. This investigation has uncovered evidence of one or more of the following indicators of systematic manipulation of the publication process:

- (1) Discrepancies in scope
- (2) Discrepancies in the description of the research reported
- (3) Discrepancies between the availability of data and the research described
- (4) Inappropriate citations
- (5) Incoherent, meaningless and/or irrelevant content included in the article
- (6) Peer-review manipulation

The presence of these indicators undermines our confidence in the integrity of the article's content and we cannot, therefore, vouch for its reliability. Please note that this notice is intended solely to alert readers that the content of this article is unreliable. We have not investigated whether authors were aware of or involved in the systematic manipulation of the publication process.

Wiley and Hindawi regrets that the usual quality checks did not identify these issues before publication and have since put additional measures in place to safeguard research integrity.

We wish to credit our own Research Integrity and Research Publishing teams and anonymous and named external researchers and research integrity experts for contributing to this investigation.

The corresponding author, as the representative of all authors, has been given the opportunity to register their agreement or disagreement to this retraction. We have kept a record of any response received.

### References

- [1] M. R. A. Refaai, M. N. Manjunatha, S. Radjarejesri, B. Ramesh, R. Subbiah, and N. Adugna, "Nanorobots with Hybrid Biomembranes for Simultaneous Degradation of Toxic Microorganism," *Advances in Materials Science and Engineering*, vol. 2022, Article ID 2391843, 12 pages, 2022.

## Retraction

# Retracted: Tiny Spherical Robot with a Magnetic Field-Based Interference Detection and Prevention Framework

### Advances in Materials Science and Engineering

Received 20 June 2023; Accepted 20 June 2023; Published 21 June 2023

Copyright © 2023 Advances in Materials Science and Engineering. This is an open access article distributed under the Creative Commons Attribution License, which permits unrestricted use, distribution, and reproduction in any medium, provided the original work is properly cited.

This article has been retracted by Hindawi following an investigation undertaken by the publisher [1]. This investigation has uncovered evidence of one or more of the following indicators of systematic manipulation of the publication process:

- (1) Discrepancies in scope
- (2) Discrepancies in the description of the research reported
- (3) Discrepancies between the availability of data and the research described
- (4) Inappropriate citations
- (5) Incoherent, meaningless and/or irrelevant content included in the article
- (6) Peer-review manipulation

The presence of these indicators undermines our confidence in the integrity of the article's content and we cannot, therefore, vouch for its reliability. Please note that this notice is intended solely to alert readers that the content of this article is unreliable. We have not investigated whether authors were aware of or involved in the systematic manipulation of the publication process.

Wiley and Hindawi regrets that the usual quality checks did not identify these issues before publication and have since put additional measures in place to safeguard research integrity.

We wish to credit our own Research Integrity and Research Publishing teams and anonymous and named external researchers and research integrity experts for contributing to this investigation.

The corresponding author, as the representative of all authors, has been given the opportunity to register their agreement or disagreement to this retraction. We have kept a record of any response received.

### References

- [1] M. R. A. Refaai, S. Meenatchi, B. Ramesh, N. I. H. Rashid, N. B. Soni, and M. Ganesan, "Tiny Spherical Robot with a Magnetic Field-Based Interference Detection and Prevention Framework," *Advances in Materials Science and Engineering*, vol. 2022, Article ID 3908975, 10 pages, 2022.

## *Retraction*

# **Retracted: An Enhanced Drone Technology for Detecting the Human Object in the Dense Areas Using a Deep Learning Model**

### **Advances in Materials Science and Engineering**

Received 20 June 2023; Accepted 20 June 2023; Published 21 June 2023

Copyright © 2023 Advances in Materials Science and Engineering. This is an open access article distributed under the Creative Commons Attribution License, which permits unrestricted use, distribution, and reproduction in any medium, provided the original work is properly cited.

This article has been retracted by Hindawi following an investigation undertaken by the publisher [1]. This investigation has uncovered evidence of one or more of the following indicators of systematic manipulation of the publication process:

- (1) Discrepancies in scope
- (2) Discrepancies in the description of the research reported
- (3) Discrepancies between the availability of data and the research described
- (4) Inappropriate citations
- (5) Incoherent, meaningless and/or irrelevant content included in the article
- (6) Peer-review manipulation

The presence of these indicators undermines our confidence in the integrity of the article's content and we cannot, therefore, vouch for its reliability. Please note that this notice is intended solely to alert readers that the content of this article is unreliable. We have not investigated whether authors were aware of or involved in the systematic manipulation of the publication process.

Wiley and Hindawi regrets that the usual quality checks did not identify these issues before publication and have since put additional measures in place to safeguard research integrity.

We wish to credit our own Research Integrity and Research Publishing teams and anonymous and named external researchers and research integrity experts for contributing to this investigation.

The corresponding author, as the representative of all authors, has been given the opportunity to register their agreement or disagreement to this retraction. We have kept a record of any response received.

### **References**

- [1] M. R. A. Refaai, D. R. Rinku, I. Thamarai, S. Meera, N. K. Sripada, and S. Yishak, "An Enhanced Drone Technology for Detecting the Human Object in the Dense Areas Using a Deep Learning Model," *Advances in Materials Science and Engineering*, vol. 2022, Article ID 4162007, 12 pages, 2022.

## Retraction

# Retracted: An Artificial Intelligence Mechanism for the Prediction of Signal Strength in Drones to IoT Devices in Smart Cities

### Advances in Materials Science and Engineering

Received 20 June 2023; Accepted 20 June 2023; Published 21 June 2023

Copyright © 2023 Advances in Materials Science and Engineering. This is an open access article distributed under the Creative Commons Attribution License, which permits unrestricted use, distribution, and reproduction in any medium, provided the original work is properly cited.

This article has been retracted by Hindawi following an investigation undertaken by the publisher [1]. This investigation has uncovered evidence of one or more of the following indicators of systematic manipulation of the publication process:

- (1) Discrepancies in scope
- (2) Discrepancies in the description of the research reported
- (3) Discrepancies between the availability of data and the research described
- (4) Inappropriate citations
- (5) Incoherent, meaningless and/or irrelevant content included in the article
- (6) Peer-review manipulation

The presence of these indicators undermines our confidence in the integrity of the article's content and we cannot, therefore, vouch for its reliability. Please note that this notice is intended solely to alert readers that the content of this article is unreliable. We have not investigated whether authors were aware of or involved in the systematic manipulation of the publication process.

Wiley and Hindawi regrets that the usual quality checks did not identify these issues before publication and have since put additional measures in place to safeguard research integrity.

We wish to credit our own Research Integrity and Research Publishing teams and anonymous and named external researchers and research integrity experts for contributing to this investigation.

The corresponding author, as the representative of all authors, has been given the opportunity to register their agreement or disagreement to this retraction. We have kept a record of any response received.

### References

- [1] M. R. A. Refaai, V. S. N. C. H. Dattu, H. S. Niranjana Murthy, P. Pramod Kumar, B. Kannadasan, and A. Diriba, "An Artificial Intelligence Mechanism for the Prediction of Signal Strength in Drones to IoT Devices in Smart Cities," *Advances in Materials Science and Engineering*, vol. 2022, Article ID 7387346, 13 pages, 2022.



## *Retraction*

# **Retracted: Influence of Metallic Particles on Properties of Aluminium Composites through Taguchi Technique**

### **Advances in Materials Science and Engineering**

Received 26 December 2023; Accepted 26 December 2023; Published 29 December 2023

Copyright © 2023 Advances in Materials Science and Engineering. This is an open access article distributed under the Creative Commons Attribution License, which permits unrestricted use, distribution, and reproduction in any medium, provided the original work is properly cited.

This article has been retracted by Hindawi, as publisher, following an investigation undertaken by the publisher [1]. This investigation has uncovered evidence of systematic manipulation of the publication and peer-review process. We cannot, therefore, vouch for the reliability or integrity of this article.

Please note that this notice is intended solely to alert readers that the peer-review process of this article has been compromised.

Wiley and Hindawi regret that the usual quality checks did not identify these issues before publication and have since put additional measures in place to safeguard research integrity.

We wish to credit our Research Integrity and Research Publishing teams and anonymous and named external researchers and research integrity experts for contributing to this investigation.

The corresponding author, as the representative of all authors, has been given the opportunity to register their agreement or disagreement to this retraction. We have kept a record of any response received.

### **References**

- [1] B. Venkatesh, A. R. Lakshmi pathi, T. Prakash et al., "Influence of Metallic Particles on Properties of Aluminium Composites through Taguchi Technique," *Advances in Materials Science and Engineering*, vol. 2023, Article ID 9637728, 12 pages, 2023.

## Research Article

# Influence of Metallic Particles on Properties of Aluminium Composites through Taguchi Technique

**B. Venkatesh,<sup>1</sup> Anantha Raman Lakshmipathi,<sup>2</sup> T. Prakash,<sup>3</sup> Pothamsetty Kasi V. Rao,<sup>4</sup> Rajesh Verma,<sup>5</sup> N. Nagabhooshanam,<sup>6</sup> and Simon Yishak<sup>7</sup>**

<sup>1</sup>Department of Mechanical Engineering, Vardhaman College of Engineering, Hyderabad, Telangana, India

<sup>2</sup>Department of Mechanical Engineering, Madanapalle Institute of Technology and Science, Madanapalle, Andhra Pradesh, India

<sup>3</sup>Department of Mechanical Engineering, SNS College of Technology, Coimbatore 641035, Tamil Nadu, India

<sup>4</sup>Department of Mechanical Engineering, Koneru Lakshmaiah Education Foundation, Vaddeswaram, Andhra Pradesh, India

<sup>5</sup>Department of Electrical Engineering, College of Engineering, King Khalid University, Abha, Saudi Arabia

<sup>6</sup>Department of Mechanical Engineering, Aditya Engineering College, Surampalem 533437, Andhra Pradesh, India

<sup>7</sup>College of Engineering and Argo-Industrial Technology, Sawla Campus, Arba Minch University, Arba Minch, Ethiopia

Correspondence should be addressed to Simon Yishak; [simon.yishak@amu.edu.et](mailto:simon.yishak@amu.edu.et)

Received 27 June 2022; Revised 20 August 2022; Accepted 8 September 2022; Published 10 May 2023

Academic Editor: K. Raja

Copyright © 2023 B. Venkatesh et al. This is an open access article distributed under the Creative Commons Attribution License, which permits unrestricted use, distribution, and reproduction in any medium, provided the original work is properly cited.

In this work, aluminium composites have been evaluated in terms of their characteristics and behaviour. Stirring metallics and a specific quantity of ceramic-derived silicon nitride resulted in AA6061 composites ( $\text{Si}_3\text{N}_4$ ). The mechanical, corrosion, and tribological properties of composites were investigated. Tensile, corrosion, and hardness characteristics have been improved in composites with a constant weight percent of ceramic and advanced metallic fortification. The improved hardness of the composite has decreased wear and friction. Furthermore, by using ceramic strengthening with the metal, the impact strength of the composites was condensed. In addition to the research, the design of experiments method was used to optimize the important wear test elements such as reinforcement %, applied stress, sliding distance, and speed. Analysis of variance was used to find the most significant testing features and its interface with wear performance and the friction coefficient of the composite specimen.

## 1. Introduction

Two or more separate materials are combined in a composite material, which has an identifiable interface between the two [1]. The ability to combine characteristics in conventional monolithic materials is constrained. Composites, on the other hand, have been built for increased particular stiffness and specific strength, wear and fatigue resistance, creep and corrosion resistance, as well as a variety of other advantages [2, 3]. To achieve these features, the volume fraction of strengthening can be controlled, and the desired amount of strength and stiffness can be selected for the reinforcements. Composites are accessible in a variety of forms in today's competitive market. MMCs (metal-metal-ceramic-ceramic) are only a few examples, but there are many more (PMCs). As a result of their high hardness and operating

performance, MMCs play a key role in the industrial sector [4–6]. Reinforcement phases can be added to MMCs using one or more of the following methods: spray and codeposition, powder metallurgy, thermal spraying, LMR, and compacted techniques, such as squeeze casting, or a combination of these techniques. As a result of its affordability, stir casting remains a popular manufacturing technology [7]. Stirrer motion guarantees that reinforcement is evenly distributed throughout the matrix, and material is able to accept reinforcement and volume by 30%. The possibility of obtaining the required materials is an additional benefit [8, 9]. A surge in the usage of lighter materials in manufacturing is owing to the higher strength-to-weight ratio, simple fabrication, and rate reductions associated with MMCs composites. As a result of the rise of globalisation and the improvement of production, alloys are ideal lightweight

materials [10–14]. As a result, there is a great need for structures that are both strong and light in weight. Boron carbide, silicon carbide, alumina, and other ceramic-based reinforcements are among the most often employed in the current market for MMCs' reinforcement [15].

The research presented here shows that composites based on aluminium AA6082 with silicon nitride reinforcement have been created [16, 17]. It is a sign that adding reinforcement has improved the material's density and porosity. Additionally, composites have gained in hardness and tensile strength. More than two reinforcements in the matrix gave rise to the name "hybrid composite," and one study examined a hybrid composite consisting of 1.0 volume% Silicon Carbide and 0.5 vol. % Boron Carbide [18–20]. There is a minor reduction in impact strength with this percentage and combination of hardness and tensile strength. All important structural applications in automotive manufacturing have been served by AA7075, a 7-series aluminium alloy [21, 22]. According to the most recent AA7075 research, mechanical parameters, including tensile as well as yield strength, improved by 33.8% and 13.56% when the basic material was reinforced with titanium boride ( $\text{TiB}_2$ ). Nearly 10% more hardness can be achieved by incorporating ceramic-based strengthening like SiC into the aluminium matrix [23–25]. These self-lubricating aluminium mixtures were produced employing the powder metallurgy approach in the field of Al matrix [26, 27]. The mechanical and tribological characteristics of this nano-structured composite are enhanced by the inclusion of graphene up to 5% weight. By reinforcing silicon carbide and alumina particles with composites, the researcher has examined aluminium alloys based on structure, including AA6061 and AA7075. When mechanical characteristics like tensile properties and hardness and tribological characteristics like wear loss are concerned, both composite samples exhibit a noticeable improvement [28]. As a result, the density of samples has reached the expected level [29, 30]. Many characteristics, such as granular dimensions, wt. % of strengthening, applying load, distance as well as speed and industrial technique, were shown to influence the wear performance of Al composites [31, 32].

Growing the volume portion of strengthening declines the wear rate, while raising the particle size does the opposite. Due to correct precipitation and effective hardening, the composite used with age treatment will have better wear resistance [33, 34]. When brake pads are used, the tribo-layer generated on the pin material during the wear test has a greater impact on wear behaviour. It is apparent that the aluminium alloy with ceramic and metallic particle strengthening increases properties, as well as composite density when compared to the basic aluminium alloy [35–37]. The corrosion behaviour of these aluminium alloys in diverse media has received just a few research information. In light of this, the most pertinent information has been provided [38, 39]. Aluminum alloy AA6061 corrosion behaviour in acidic and alkaline environments at various concentrations and temperatures has been examined. Tafel polarisation and impedance spectroscopy were used in the electrochemical techniques used in the

experiment (EIS) [40]. The results reveal that the AA6061 aluminium alloy is more susceptible to corrosion in alkaline media (NaOH) than in acidic media (Ph). AA6061 aluminium alloy with an alumina-based composite has been studied in salt water, acidic, and alkaline media conditions [41, 42]. Corrosion resistance of the composite is superior to that of other media in salt water, although the unreinforced state is superior in acidic and alkaline environments. Both reinforced and unreinforced aluminium alloys demonstrate improved corrosion resistance after heat treatment [43–45]. A passive oxide layer has been found to improve corrosion resistance when applied to heat-treated AA6061 with silicon carbide reinforcement, according to earlier research.

The best wear process parameter for various operating conditions was also identified. The effects of grain size, weight, and sliding distance were studied using a factorial design of experiments. SiC emery broadside wear rate improved with rising applied load, coarse magnitude, and distance, while  $\text{Al}_2\text{O}_3$  paper wear rate decreased only with decreasing sliding distance. The material's rate of wear was altered in a number of ways by the variables. Another study on Al–5% SiC found that the applied load is the most critical factor when using Taguchi's  $L_{27}$  orthogonal arrangement strategy and increased wear resistance using SiC strengthening in an aluminium matrix. Taguchi's  $L_{27}$  orthogonal arrangement design (Al/SiC/Gr) was active in examining the ideal wear constraint of a hybridized aluminium composite (Al/SiC/Gr), which was established by ANOVA. The sliding distance (57.12%) was shown to be the most important process factor in the study.  $L_{27}$  orthogonal arrangement plan and the analysis of variance were utilised to optimize an Al-based composite strengthened with 5–15% SiC. The sliding distance (49.12%) is the most significant processing factor that influences wear. By means of Taguchi's  $L_{27}$  design and ANOVA, a structure-based hybrid aluminium alloy (AA6061) composite was discovered to have the best wear rate and frictional coefficient.

The best wear rate and coefficient of friction can be attained by using a variety of processing factors, including 4.5 m/s sliding speed, 15 N applied load, 20 minute sliding time, and 15% reinforcement. By investigating how reinforcement content (measured as a percentage of volume) affects qualities, this investigation also sought to identify the optimal value with the greatest impact on specimen tribological characteristics including rate of wear and frictional coefficient. The most crucial parameter does not have a name. An examination of the literature reveals that metallic-derived reinforcement alone or in grouping with ceramic-derived reinforcement has received relatively little research attention. Ceramic and metallic reinforcements can be added to aluminium matrix for the purpose of this investigation. Since ceramic particles in metal matrix increase the rate of wear and frictional coefficient as well as the hardness and strength of the material, this is a good reason to incorporate metallic reinforcement. With metallic reinforcement, a composite's impact strength improved without sacrificing any of the material's structural integrity [31–40].

An experiment's planning, design, and analysis are all covered by this statistical technique. To determine the best answer, the design of experiment method is employed. Systematic design, factor design, and lenience design are all stages in the optimization process. The wear testing in our study was made more efficient by the use of parameter design. Designing optimum process parameters and determining product parameters based on optimal processing factor values is a key part of the parameter designing process. The Taguchi approach is a powerful tool for determining the optimum strategy with high-quality structures from a range of design of experimental methods. It is a usual practise to do a large number of experiments in which just one variable is changed while the other remains constant. Using the Taguchi technique, fewer experiments are required to get an optimum answer. The Taguchi method allows for the interplay of several factors. As a result of the aforementioned principles, the Taguchi technique outperforms conventional experimentation [40–45]. Minitab-16 software was used to name all the data, and ANOVA was used to generate the percentages. Thus, this work aims to fabricate the aluminium composite reinforced with ceramic and metallic fibres and to study its various characterization including physical, corrosion, and wear behaviour.

## 2. Experimental Procedure

**2.1. Material Details.** The ingot is melted at 750°C in a muffle furnace for 45 minutes with AA6061 raw material, as shown in Figure 1 in a graphite crucible, weighing 700 g. An AA6061 is a class of metal that seems to have a high strength-to-weight proportion and may be heat-treated. It is utilised in industrial and structural applications due to its excellent mechanical properties. After that, the strengthening was heated in a different furnace for about an hour at 500°C for silicon nitride, whose composition is shown in Table 1 and for about 15 minutes at 100°C for copper nitrate. The primary goal of heating and strengthening is to reduce the humidity and improve the blend of the reinforcement with the composites. Oxygen from the dispersoid surface was scavenged by 2 wt. % pure magnesium, thinning the gas layer and improving moistening and response-aided moistening with the dispersoid surface. Owing to the continual exciting action of a multiblade stirrer inside the furnace, stir casting provided a standardized dispersion of fortification in the composites. At 300 rpm, the stirrer was running for 15 minutes, and the processing parameters are shown in Table 2. The molten fluid was then poured into a 120 mm long by 25 mm wide heated metal mould. The composite sample was removed from the mould once it had cooled to room temperature.

## 3. Testing Details

**3.1. Tensile Test.** Copper ( $\text{Cu}(\text{NO}_3)_2$ ) and silicon ( $\text{Si}_3\text{N}_4$ ) were used to reinforce the aluminium composite with different weight percentages, but the final product was successful. To achieve the standard subsize dimension, the cast specimens were CNC machined. In accordance with the



FIGURE 1: Stir casting process.

ASTM E8/E 8M-08 B557 standard, the tensile strength of the composite was measured using an electronic tensile testing machine. The experimentation was conducted at room temperature.

**3.2. Hardness Test.** An indentation is used to measure a metal's resistance to plastic deformation. In order to calculate the impact of metallic strengthening on the mixture specimen's hardness, the macro of the specimen was subjected to a Brinell hardness test. 10 mm ball was loaded with 500 kg and held for 20 s in Brinell hardness. Macrohardness testing, as shown in Figure 2 was performed using the specimen, which was produced in accordance with ASTM E10.

**3.3. Impact Test.** A material's impact strength measures its capacity to withstand a sudden application of force. A composite specimen was subjected to the IZOD impact test. A  $66 \times 12.8 \times 3.4$  mm cast specimen was CNC machined to measure the entire energy fascinated by the composite specimen. The experiment was conducted at room temperature. According to ASTM D256, the specimen was created.

**3.4. Salt Spray Test-Corrosion Test.** The corrosion performance of the composite specimen was examined using the ASTM B117-2011 salt spray method. An accelerated corrosion test known as the salt spray test (fog test) is employed to determine the corrosion resistance of constituents to salt spray or salt fog at raised temperatures. As part of the salt spray testing process, a salt water solution is continually

TABLE 1: Characteristics of reinforcements.

Reinforcement particles	Average particle size ( $\mu\text{m}$ )	Hardness (GPa)	Density ( $\text{g}/\text{cm}^3$ )	Melting point ( $^{\circ}\text{C}$ )
Silicon nitride	10–40	34.8	4.32	2150
Copper nitrate	10–40	—	4.36	150

TABLE 2: Stir casting processing factors.

Processing factors	Values
Stirring time	20 min
Molten composite temperature	750 $^{\circ}\text{C}$
Preheated temperature of permanent mould	720 $^{\circ}\text{C}$
Stirring speed	350 rpm
Preheated temperature of $\text{Cu}(\text{NO}_3)_2$	120 $^{\circ}\text{C}$ soaking time 20 min
Preheated temperature of $\text{Si}_3\text{N}_4$	750 $^{\circ}\text{C}$ soaking time 60 min

applied to test specimens in a surrounding salt spray testing system or chamber. As the test progressed, the environment that had been created was maintained. The weight loss technique was employed to calculate the corrosion rate of each sample. An electronic weighting device with a precision of 0.1 mg was used to determine the specimen's weight prior to testing. Weighing and cleaning were then completed to ascertain the specimen's weight. We utilise the Table 3 in this situation.

**3.5. Pin-on-Disc Test.** Wear tests were executed in accord with the ASTM G99 in dry, unlubricated sliding conditions. Pinned-on-disc wear testing was utilised to determine these parameters in Figure 3. The composite was used to make a cylinder-shaped pin with a width of 10 mm and a span of 25 mm. EN32 steel with an HRC65 hardness was used to make the discs.  $L_{27}$  Taguchi orthogonal design was used to improve the process parameters. The frictional coefficient, wear rate, and wt. % reinforcement are all impacted by the same processing parameter. Table 4 lists the processing factor levels. An analysis of variance was employed to calculate the statistical significance of the different factors and the interactions among them.

## 4. Result and Discussion

**4.1. Density and Porosity.** Table 5 shows the results of density and porosity. Electronic weighing equipment with a 0.1 mg resolution was utilized to measure the experimental density using a composite sample of 60 mm height and 9.5 mm diameter. Density of AA6061 reinforced with 12 wt. %  $\text{Si}_3\text{N}_4$  and different percentages of metallic reinforcement  $\text{Cu}(\text{NO}_3)_2$  are shown. A general impression is that the density of materials grew as the percentage of metallic reinforcement varied. With 12 wt. %  $\text{Si}_3\text{N}_4$  reinforcement and 6 wt. %  $\text{Cu}(\text{NO}_3)_2$ , a sample with the combined state is more dense than the sample with 12 wt. %  $\text{Si}_3\text{N}_4$  reinforcement and no  $\text{Cu}(\text{NO}_3)_2$  with 3.26338  $\text{g}/\text{cm}^3$  density. To increase the density of a composite, metallic materials are added to



FIGURE 2: Hardness tester.

TABLE 3: Salt spray analysing factor.

Test factors	Values
Solution pH value	6.5–6.95
Sample loading position in the chamber	45 $^{\circ}$ angle
Concentration of solution	4.9–5.6% of NaCl
Chamber temperature	35.6–36.8 $^{\circ}\text{C}$
Volume of salt solution collected	1.2–1.5 ml/hr
Air pressure	15–19 psi

a lower-density material. Composite matrix porosity decreased when metallic strengthening engaged the space vacated by the insertion of metallic reinforcement. Because of this, the volume or compactness of the composite, measured by the number of atoms, has grown.

Magnesium-based binders have been shown to increase the wettability and lower the threshold pressure for strengthening, therefore increasing the strong contact between the matrix and the particles. Increasing density and decreasing porosity levels are the result of this. With (1), it is possible to determine the composite's density.

$$\rho_C = \rho_m \phi_m + \rho_r \phi_r, \quad (1)$$

where  $\rho_C$ ,  $\rho_m$ , and  $\rho_r$  are the density of composites, matrix, and reinforcement correspondingly.



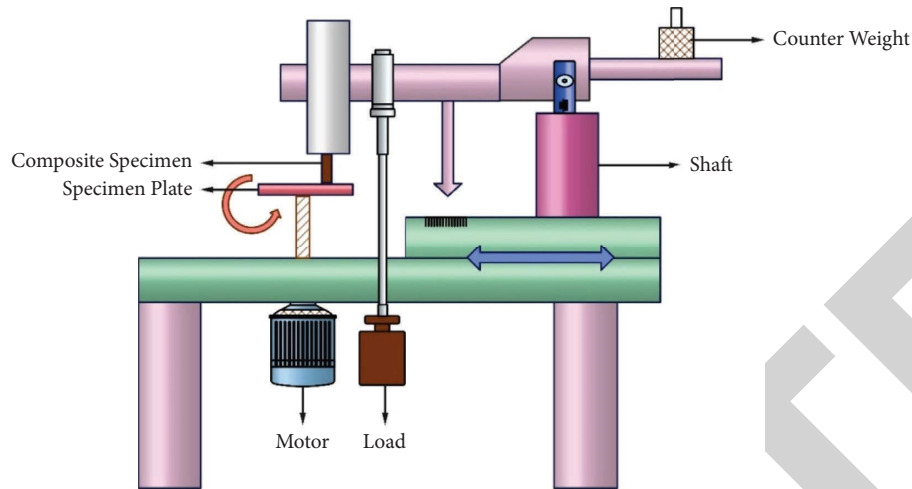


FIGURE 3: Diagram of pin-on-disc.

TABLE 4: Control factors and its levels.

Control factors	Levels		
	1	2	3
A: copper nitrate reinforcement (wt. %)	3	6	9
B: applied load (Newton)	15	20	25
C: sliding distance (metre)	1250	1750	2250
D: sliding speed (revolution per minute)	250	350	450

TABLE 5: Density and porosity for variant reinforcement.

Wt. % reinforcement of copper nitrate	Theoretical density (g/cm <sup>3</sup> )	Experimental density (g/cm <sup>3</sup> )	Porosity (%)
0	3.6834	3.843	4.61
3	3.8714	3.781	3.53
6	3.7438	3.678	3.70
9	3.6412	3.618	3.72

Equation (2) was used to determine the sample's porosity

$$\text{Porosity} = \frac{\rho_T - \rho_E}{\rho_T} \times 100\%, \quad (2)$$

where  $\rho_T, \rho_E$  are theoretical and experimental density of composites correspondingly

## 4.2. Mechanical Properties

**4.2.1. Macrohardness.** Density and hardness have a mathematical relationship that is proportionate to one another. Soft base material is hardened by adding of copper nitrate, which acts as a "hard phase." Plastic distortion theory states that the accumulated displacement increases as foreign particles such as reinforcements, are added. As a result of the reinforcing, composites now have a higher hardness rating. To further improve composite material resistance to penetration, up to 9 weight% of reinforcing steel is added to the matrix for better macrohardness. Figure 4 shows the connection between the % of metallic strengthening and the hardness value. By increasing the amount of metallic nitrate in the matrix, the hardness of the composites is decreased.

Adding more metallic nitrate has no effect on its solubility or reactivity. Consequently, the toughness of the hybrid composite with 9% copper nitrate is superior.

**4.2.2. Tensile Strength.** Synthesized aluminium hybrid composites with varied weight percentages of metallic reinforcement are shown in Figure 5 to have a positive connection with tensile strength. Initially, the composites with 12%  $\text{Si}_3\text{N}_4$  was 254 MPa in initial tensile strength. The tensile strength of the matrix has grown to 268 MPa following the addition of copper nitrate metallic reinforcement. Hard metallic reinforcement is present at the grain boundary to increase the tensile strength, and this causes the dislocation to pile up with the grains. As a result, the matrix's internal resistance and carrying capacity have both increased. To summarise, the results show that copper nitrate constrains the dislocations in a soft matrix, changing its plastic deformation behaviour. Up to 9 weight % of dislocation density can be attributed to this phenomena. Up to 9% ceramic nitrate can be used as an additional metal nitrate reinforcement to improve both the tensile strength and hardness of a material, according to this study. In the

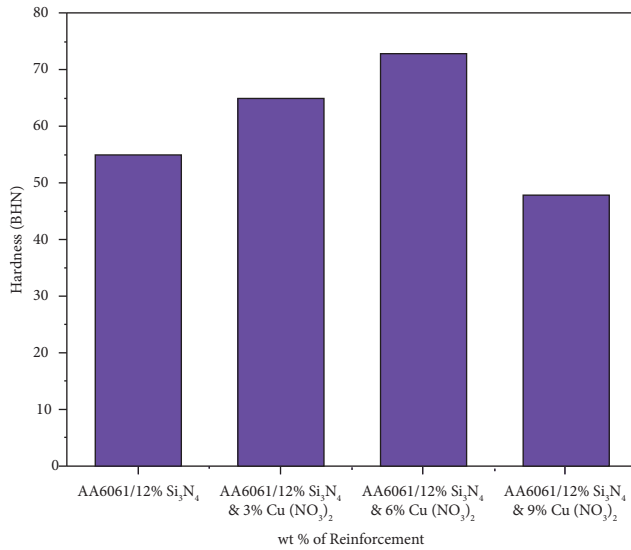


FIGURE 4: Variation in macrohardness as a function of Cu (NO<sub>3</sub>)<sub>2</sub> weight percentage.

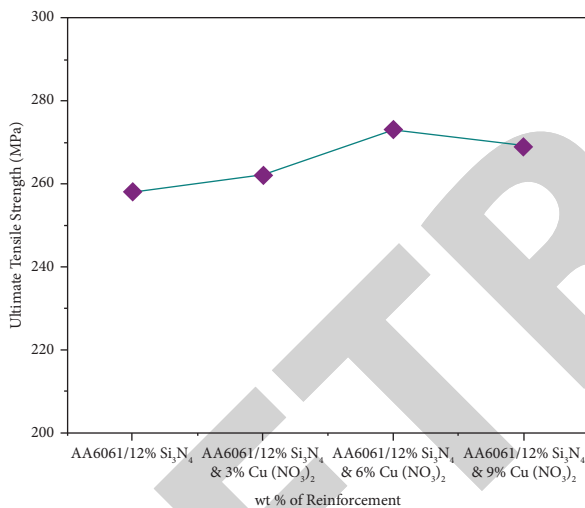


FIGURE 5: Tensile strength varies depending on the weight fraction of Cu(NO<sub>3</sub>)<sub>2</sub>.

presence of additional metallic reinforcement, the soft phase expands, but the mechanical qualities remain unchanged. Hybrid composite containing 9 weight % copper nitrate has virtuous wear and mechanical characteristics.

Hence, the improved performance and characteristics of the hybrid composite with 9 weight % copper nitrate. Samples with increasing or decreasing amounts of reinforcement are shown in Figure 6. Compared to 0, 3, 6, 9 wt. % Cu (NO<sub>3</sub>)<sub>2</sub>, the composite with 8 wt. % Cu (NO<sub>3</sub>)<sub>2</sub> mixed together with AA6061/12 wt. % Si<sub>3</sub>N<sub>4</sub> exhibits lower ultimate stress. The specimen's wear and friction characteristics rise as the tensile strength increases. As a result, the optimal amount of Cu (NO<sub>3</sub>)<sub>2</sub> in the composite was 6%. Composite failure is caused by void nucleation and its coalescence, which disrupts the matrix-reinforcement relationship, resulting in composite failure.

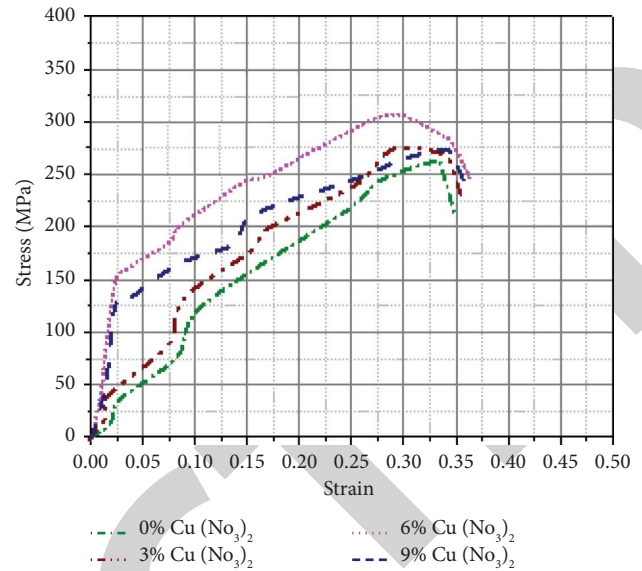


FIGURE 6: Stress—strain for different wt. % of Cu (NO<sub>3</sub>)<sub>2</sub>.

**4.2.3. Impact Strength.** Composites based on AA6061 have been utilised widely in an extensive range of fields, including ballistics, corrosion, the harshest environments, and heavy-duty applications. According to ASTM specifications, a CNC milling machine was used to cut and process the plate into the V-notch specimen. The notch angle and cross-sectional area were both set to 10 mm<sup>2</sup>. Unreinforced AA6061's impact strength is superior to that of reinforced composite, as shown by the instrumental impact test. The unstrengthened squeeze out AA6061 alloy has an impact strength of 92 Joule at atmospheric temperature, but the strengthened AA6061 alloy with 12 wt. % silicon nitrate has a strength of just 5 J.

The composite impact strength and weight percentage of metallic reinforcement are shown in Figure 7. This is due to the reinforcement being grouped or agglomerated in places where crack nucleation and propagation are more likely to occur. Due to its lower energy absorption than an unreinforced alloy, the AA6061 ceramic-reinforced composite eventually fractures. Cracking and decohesion at particle interfaces also lead to fast microcrack growth and reduced impact strength.

**4.2.4. Corrosion.** The salt spray method was used to examine the corrosion behaviour of AA6061 reinforced with ceramic and metal. The weight loss technique and physical reflection on the visible outward of the specimen were used to analyse the behaviours. The strengthened AA6061 was subjected to a salt spray test. Even after 36 hours, there is no evidence of rust on the sample surface. It was only after 48 hours of exposure that the rust began to appear. Since the corrosion process begins after only 48 hours of exposure, it can be deduced that using copper nitrate as an additional metallic reinforcement has a significant impact on weight reduction.

Copper nitrate reinforcement has improved the composite's corrosion resistance. The copper metal's passive behaviour is whether helps the AA6061-based composite resist corrosion. In comparison, the corrosion resistance is

improved, owing to the occurrence of copper nitrate elements. Indeed, the occurrence of corundum file (Alumina) on the aluminium alloys' surfaces, as well as the presence of copper, has improved corrosion resistance in all environmental conditions. Few studies in the literature have shown

that the presence of copper in aluminium alloys improves corrosion resistance. The outcome of the salt spray test is indicated in Figure 8. Table 6 displays the results of the corrosion tests. The following was used to compute the sample corrosion rate:

$$\text{Corrosion rate (mmpy)} = \frac{8.75 \times 10^4 \times \text{weight loss (gm)}}{\text{Composite density (gm/cm}^3) \times \text{Exposed area (cm}^2) \times \text{Exposure time (hr)}} \quad (3)$$

**4.2.5. Mechanism of Wear Test.** Table 7 shows wear test of produced composites. Hybrid composite pins of various compositions were exposed to dry sliding wear trials with diverse loads, such as 15 N, 20 N, and 25 N. At speeds of 250 rpm, 350 rpm, and 450 rpm, a sliding distance of 1250 m, 1750 m, and 2250 m was achieved. Prior to testing, the end surface of the test sample is smooth and refined with a metallographic alloy. To remove any residues of composite from the specimen and counter face disc, acetone was used. Weighing the specimen earlier and afterwards testing and getting an accurateness of 0.1 mg can be used to compute the wear loss. The normal load was used to calculate the frictional coefficient, while the data acquisition system provided the tangential load. Five times each test was performed before the average value was calculated and examined. Reinforced AA6061/12 wt Si<sub>3</sub>N<sub>4</sub> with 3, 6, or 9 wt. % for unreinforced AA6061. The roughness of the surface 0.279 m, 0.406 m, 0.39 m, and 0.386 m were measured using the Ra-value using the surface roughness tester. On the worn surface, counter face pits allowed us to see the microcutting and microploving that had occurred. abrasive and adhesive damage is indicated by the appearance of a plough mark and a crack. There is a crack in the material due to the weakening of the reinforcement-to-matrix linkage as load and sliding distance increase. The main output is the response function's average value at a specified parameter level. The S/N (Signal/Matrix) ratio is used to determine the parameter's quality attributes. First, smaller is preferable in terms of size. Second, higher is better. Third, nominal is best in order to achieve the best quality attributes, we adopted the smaller-is-better principle to preserve less wear loss and friction. The S/N ratio was obtained by transforming the loss function logarithmically, as illustrated in the relationships in the following equation:

$$\frac{S}{N} = -10 \log \frac{1}{n} (\epsilon_y)^2, \quad (4)$$

where  $n$  = no. of observation and  $y$  = experiment.

**4.3. Impact of Testing Factors on Wear Loss.** To illustrate the relationship among various process variables and the wear and frictional coefficients of the composites, shown in Figures 9(a) and 9(b). For example, if a process parameter's mean plot graph curve is close to the horizontal and it has no effect on composites, then it has a bigger impact. It was revealed that the difference in the mean S/N ratio between

its highest and lowest values was the most important control parameter. S/N ratios that are more than two standard deviations off of a given value should be used as controls. A decreased wear rate and a better sound-to-noise coefficient of friction were used to analyse the process parameter in this investigation. Testing elements like the wt. % of reinforcement, applying load, distance as well as speed were examined employing the Taguchi method. That which was most crucially derived from the analysis of variance. The significance level was chosen at 5% with a 95% confidence interval. Because of the strong wear resistance of the metallic reinforcement, the weight percentage of reinforcement ( $p = 35.68\%$ ) had the greatest impact on wear loss, as indicated in Table 8. Cu(NO<sub>3</sub>)<sub>2</sub> and Si<sub>3</sub>N<sub>4</sub> strengthen the surface, making it extremely hard and durable. Wear rate falls as reinforcement percentage increases, so this is why. Wear loss was influenced by sliding distance, speed, and applied load ( $p = 29.16$  and  $22.04\%$ , respectively). Weight % reinforcement and applied load (3.10%) and weight % reinforcement and sliding distance (-2.6%) only have a minimal impact on composite's wear rate (-2.04%).

**4.4. Impact of Testing Factors on the Friction Coefficient.** Table 9 displays the ANOVA results for friction coefficient. Nearly 73.22% of the coefficient of friction was impacted by the weight percentage of metallic reinforcement. There was a 9.647% influence from the sliding distance. Other parameter interactions, such as the load applied and the sliding velocity, were not considerably altered. By means of the weight proportion of strengthening rises, so did the coefficient of friction. There is a pooled error of 9.647% in the ANOVA table related to the results. If you want to know how much variation there is in the mean and variance, you can use this approach. This method uses absolute numbers instead of unit values. According to the interaction of variables, the friction coefficient of hybridized MMC is significantly influenced (4.56%) by the interplay of load and reinforcing percentage.

**4.5. Confirmation Test.** Using a linear equation, it is possible to evaluate the relationship among two or more forecast values and responsible variables. Calculating the wear rate and friction coefficient of hybrid composites can be done by utilising equations. It has a regression coefficient of 0.88. A positive load indicator implies that the composite's wear



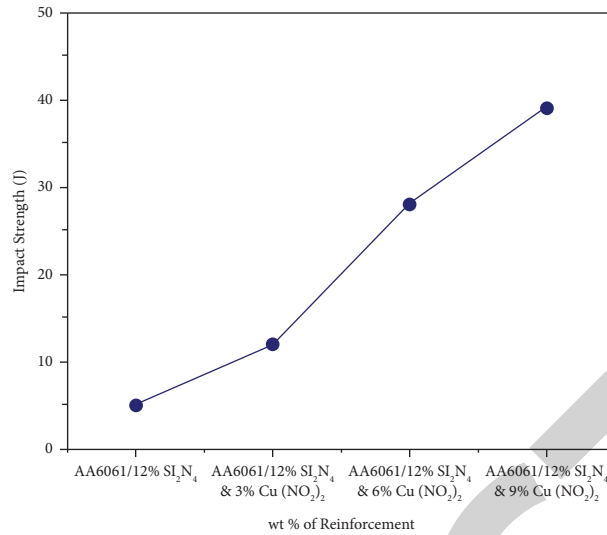


FIGURE 7: Impact strength varies with Cu (NO<sub>3</sub>)<sub>2</sub> weight percentage.

TABLE 6: Composites with differing levels of reinforcement possess varying rates of corrosion.

Wt. % of reinforcement of copper nitrate	Starting weight (gm)	Ending weight (gm)	Weight loss (gm)	Density (g/cm <sup>3</sup> )	Corrosion rate (mmpy)
0	2.6127	2.9612	0.0070	2.1624	0.98251
3	2.4512	2.4768	0.0039	2.9624	0.58942
6	2.4316	2.6313	0.0035	2.2710	0.04342
9	2.1496	2.787	0.0020	2.7891	0.23946

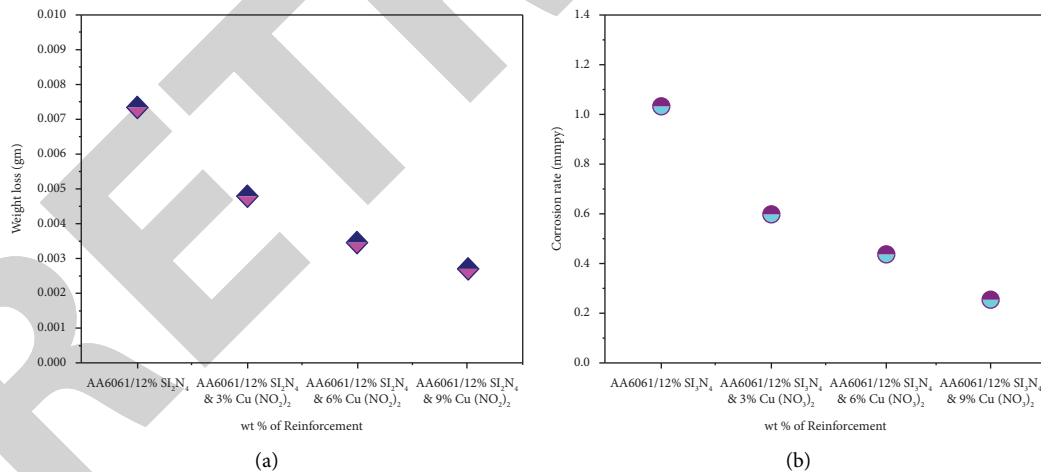


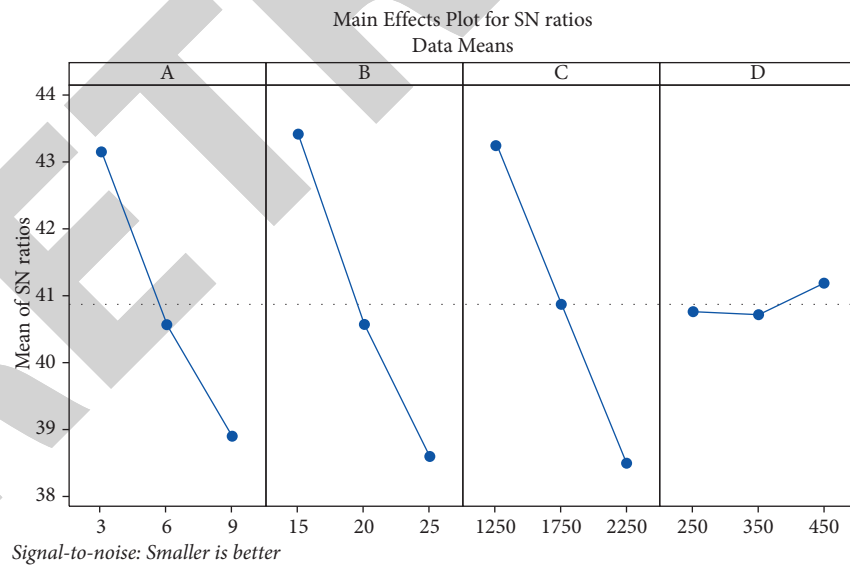
FIGURE 8: (a) Weight loss vs wt. % of metallic reinforcement and (b) corrosion rate vs wt. % of metallic reinforcement.

rate and friction coefficient will increase. When the speed increases, the wear rate of composites declines, according to the regression equation. The friction coefficient is reduced by increasing the weight percentage of the reinforcing component. Hybridized composites' abrasion resistance and load carrying capacity both rose as the reinforcing weight percentage increased. Mathematical modelling and

experimental reference process parameter values were compared to see if their comparison would affect the processing factor expected to be affected by it. As shown in Table 10, these numbers are broken out. The wear loss and friction coefficient were evaluated. From 8.4% to 11.42%, the wear rate and friction coefficient inaccuracy percentages were found.

TABLE 7:  $L_{27}$  orthogonal arrangement considered by Taguchi.

Ex. no	A	B	C	D	Wear loss (gm)	S/N ratio (db)	Friction coefficient	S/N ratio (db)
1	3	15	1250	250	0.0050	46.0206	0.6984	3.11792
2	3	15	1750	350	0.0062	44.1522	0.7632	2.34723
3	3	15	2250	450	0.0058	44.7314	0.7585	2.40089
4	3	20	1250	350	0.0048	46.3752	0.6755	3.40749
5	3	20	1750	450	0.0059	44.5830	0.7764	2.19829
6	3	20	2250	250	0.0102	39.8280	0.7653	2.32337
7	3	25	1250	450	0.0059	44.5830	0.6958	3.15031
8	3	25	1750	250	0.0091	40.8192	0.6859	3.27478
9	3	25	2250	350	0.0140	37.0774	0.7625	2.35520
10	6	15	1250	350	0.0061	44.2934	0.5582	5.06420
11	6	15	1750	250	0.0069	43.2230	0.5826	4.69259
12	6	15	2250	250	0.0108	39.3315	0.6831	3.31031
13	6	20	1250	350	0.0073	42.7335	0.6101	4.29198
14	6	20	1750	250	0.0090	40.9151	0.6913	3.20667
15	6	20	2250	450	0.0124	38.1316	0.6685	3.49797
16	6	25	1250	250	0.0092	40.7242	0.6861	3.27225
17	6	25	1750	350	0.0121	38.3443	0.6586	3.62757
18	6	25	2250	450	0.0135	37.3933	0.7952	1.99047
19	9	15	1250	450	0.0043	47.3306	0.3249	9.76501
20	9	15	1750	250	0.0068	43.3498	0.5604	5.03004
21	9	15	2250	350	0.0125	38.0618	0.5826	4.69259
22	9	20	1250	250	0.0118	38.5624	0.4624	6.69964
23	9	20	1750	350	0.0142	36.9542	0.4363	7.20430
24	9	20	2250	450	0.0137	37.2656	0.4769	6.43145
25	9	25	1250	350	0.0118	38.5624	0.4658	6.63601
26	9	25	1750	450	0.0170	35.3910	0.5626	4.99601
27	9	25	2250	250	0.0178	34.9916	0.4649	6.65281



(a)

FIGURE 9: Continued.

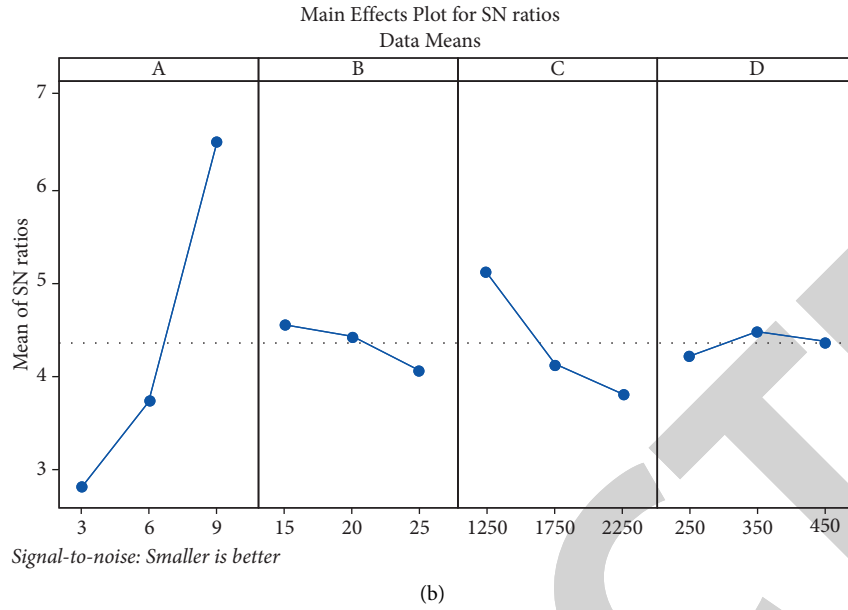


FIGURE 9: Main effect of plot for sound to noise ratio (a) wear rate (b) coefficient of friction.

TABLE 8: ANOVA for wear loss, employing adjusted SS for tests.

Source	DoF	SS	Adjusted sum of squares	Adjusted mean of squares	F-ratio	p-value	% of contribution
A	2	0.000154	0.000154	0.000077	41.23	0.001	32.835
B	2	0.000119	0.000119	0.000059	37.57	0.0002	27.624
C	2	0.000102	0.000102	0.000053	28.13	0.0002	24.135
D	2	0.000017	0.000017	0.000009	6.42	0.051	4.931
A × B	4	0.000011	0.000011	0.000005	3.94	0.159	3.598
A × C	4	0.000005	0.000005	0.000003	0.32	0.830	-2.837
B × C	4	0.000002	0.000002	0.000002	0.41	0.869	-2.162
Error	6	0.000012	0.000012				11.876
Total	26	0.00043	0.00043				100

TABLE 9: Analysis of variance for coefficient of friction, employing adjusted SS for tests.

Source	DoF	ss	Adjusted sum of squares	Adjusted mean of squares	F-ratio	p value	Percentage of contribution
A	2	0.057835	0.057835	0.023410	98.16	0.001	73.2201
B	2	0.004522	0.004522	0.002714	2.48	0.283	0.38946
C	2	0.020415	0.020415	0.010327	15.61	0.006	9.64725
D	2	0.000983	0.000983	0.000471	0.22	0.838	-0.91842
A × B	4	0.010391	0.010391	0.005829	4.35	0.089	3.361241
B × C	4	0.004297	0.004297	0.002256	0.86	0.598	2.10426
A × C	4	0.003426	0.003426	0.001788	0.39	0.802	2.14856
Error	6	0.008436	0.008436	0.002125			10.04876
Total	26	0.339967	0.339967				100

TABLE 10: Validation of the regression equation model by comparing it with experimental data.

Exp. no	Experimental wear loss (gm)	Regression model wear loss (gm)	Error (%)	Experimental coefficient of friction	Regression model of coefficient of friction	Error (%)
1	0.0052	0.00446	11.42	0.628	0.5933	5.26
2	0.0132	0.01158	8.4	0.569	0.5359	7.36
3	0.0184	0.01612	10.18	0.4654	0.4448	5.823

## 5. Conclusion

The following conclusions are decessed and are shown below in sequential order.

- (i) Increased density and lower porosity were achieved by altering the proportion of metallic reinforcement in structure-based aluminium composites.
- (ii) Once metallic strengthening is applied to the composites to prevent displacement motion, the hardness increases.
- (iii) In comparison to unreinforced AA6061, the tensile strength of composite rose from 262 MPa to 279 MPa with altering weight percentage of metallic reinforcement.
- (iv) Due to the accumulation of strengthening at grain boundaries, the impact strength of composites is lower than that of unreinforced base metals. However, the metallic reinforcement improved the composite's impact strength.
- (v) Incorporating metal reinforcements increased the corrosion resistance of the structure-based aluminium composites.
- (vi) With respect to wear loss, factors including weight percentages reinforcement, distance slid, load applied, and speed slid had an impact on how process parameters were prioritised.

## Data Availability

The data used to support the findings of this study are included within the article. Further data or information is available from the corresponding author upon request.

## Conflicts of Interest

The authors declare that there are no conflicts of interest regarding the publication of this paper.

## Acknowledgments

The authors appreciate the support from Arba Minch University, Ethiopia, for the research and preparation of the manuscript. The authors extend their appreciation to the Deanship of Scientific Research at King Khalid University, Kingdom of Saudi Arabia for funding this work through Large Groups Project under grant number: RGP. 2/162/43.

## References

- [1] A. Sankhla and K. M. Patel, "Metal matrix composites fabricated by stir casting process—A review," *Advances in Materials and Processing Technologies*, vol. 8, no. 2, pp. 1270–1291, 2021.
- [2] S. Narayan and A. Rajeshkannan, "Hardness, tensile and impact behaviour of hot forged aluminium metal matrix composites," *Journal of Materials Research and Technology*, vol. 6, no. 3, pp. 213–219, 2017.
- [3] V. Mohanavel, K. Rajan, and M. Ravichandran, "Synthesis, characterization and properties of stir cast AA6351-aluminium nitride (AlN) composites," *Journal of Materials Research*, vol. 31, no. 24, pp. 3824–3831, 2016.
- [4] A. Chaubey, P. Konda Gokuldoss, Z. Wang, S. Scudino, N. Mukhopadhyay, and J. Eckert, "Effect of particle size on microstructure and mechanical properties of Al-based composite reinforced with 10 vol.% mechanically alloyed Mg-7.4%Al particles," *Technologies*, vol. 4, no. 4, pp. 37–38, 2016.
- [5] V. Mohanavel and M. Ravichandran, "Experimental investigation on mechanical properties of AA7075-AlN composites," *Materials Testing*, vol. 61, no. 6, pp. 554–558, 2019.
- [6] H. C. Anilkumar, H. S. Hebbar, and K. S. Ravishankar, "Mechanical properties of fly ash reinforced aluminium alloy (Al6061) composites," *International Journal of Mechanical and Materials Engineering*, vol. 6, no. 1, pp. 41–45, 2011.
- [7] S. Suresh Kumar and V. Mohanavel, "An overview assessment on magnesium metal matrix composites," *Materials Today Proceedings*, vol. 59, no. 2, pp. 1357–1361, 2022.
- [8] T. S. Srivatsan and E. J. Lavernia, "Use of spray techniques to synthesize particulate-reinforced metal-matrix composites," *Journal of Materials Science*, vol. 27, no. 22, pp. 5965–5981, 1992.
- [9] A. R. E. Singer and S. Ozbek, "Metal matrix composites produced by spray codeposition," *Powder Metallurgy*, vol. 28, no. 2, pp. 72–78, 1985.
- [10] T. Sathish, S. D. Kumar, M. Ravichandran et al., "Waste food cans waste bamboo wood based AA8079/SS304/bamboo wood ash hybrid nanocomposite for food packaging," *Key Engineering Materials*, vol. 928, pp. 69–78, 2022.
- [11] R. Tiwari, S. Sampath, B. Gudmundsson, G. Halada, C. R. Clayton, and H. Herman, "Microstructure and tensile properties of L12-Type NiCrAl alloy prepared by vacuum plasma spray forming," *Scripta Metallurgica et Materialia*, vol. 33, no. 7, pp. 1159–1162, 1995.
- [12] J. A. Jeffrey, S. S. Kumar, P. Hariharan, M. Kamesh, and A. M. Raj, "Production and assessment of AZ91 reinforced with nano SiC through stir casting process," *Inside MS*, vol. 1048, pp. 9–14, 2022.
- [13] V. Mohanavel and M. Ravichandran, "Influence of AlN particles on microstructure, mechanical and tribological behaviour in AA6351 aluminum alloy," *Materials Research Express*, vol. 6, no. 10, Article ID 106557, 2019.
- [14] M. M. Ravikumar, S. S. Kumar, R. V. Kumar, S. Nandakumar, J. H. Rahman, and J. A. Raj, "Evaluation on mechanical behavior of AA2219/SiO<sub>2</sub> composites made by stir casting process," *AIP Conference Proceedings*, vol. 2405, Article ID 050010, 2022.
- [15] S. Gopalakrishnan and N. Murugan, "Production and wear characterisation of AA 6061 matrix titanium carbide particulate reinforced composite by enhanced stir casting method," *Composites Part B: Engineering*, vol. 43, no. 2, pp. 302–308, 2012.
- [16] P. Sharma, S. Sharma, and D. Khanduja, "Production and some properties of Si<sub>3</sub>N<sub>4</sub> reinforced aluminium alloy composites," *Journal of Asian Ceramic Societies*, vol. 3, no. 3, pp. 352–359, 2015.
- [17] K. M. Shorowordi, A. S. M. A. Haseeb, and J. P. Celis, "Velocity effects on the wear, friction and tribochemistry of aluminum MMC sliding against phenolic brake pad," *Wear*, vol. 256, no. 11, pp. 1176–1181, 2004.
- [18] S. Ozden, R. Ekici, and F. Nair, "Investigation of impact behaviour of aluminium based SiC particle reinforced metal-matrix composites," *Composites Part A: Applied Science and Manufacturing*, vol. 38, no. 2, pp. 484–494, 2007.

## *Retraction*

# **Retracted: Effect of SiC Particle Incorporated Dielectric Medium on Electrical Discharge Machining Behavior of AA6061/B4Cp/SiCp AMCs**

### **Advances in Materials Science and Engineering**

Received 6 April 2023; Accepted 6 April 2023; Published 19 April 2023

Copyright © 2023 Advances in Materials Science and Engineering. This is an open access article distributed under the Creative Commons Attribution License, which permits unrestricted use, distribution, and reproduction in any medium, provided the original work is properly cited.

*Advances in Materials Science and Engineering* has retracted the article titled “Effect of SiC Particle Incorporated Dielectric Medium on Electrical Discharge Machining Behavior of AA6061/B4Cp/SiCp AMCs” [1] due to significant overlap with a previously published article by different authors [2].

### **References**

- [1] J. Khajuria, N. Nagabhooshanam, P. Sharma et al., “Effect of SiC Particle Incorporated Dielectric Medium on Electrical Discharge Machining Behavior of AA6061/B4Cp/SiCp AMCs,” *Advances in Materials Science and Engineering*, vol. 2022, Article ID 2661158, 9 pages, 2022.
- [2] S. G. Iyyappan, R. Sudhakarapandian, and M. Sakthivel, “Influence of silicon carbide mixed used engine oil dielectric fluid on EDM characteristics of AA7075/SiCp/B4Cp hybrid composites,” *Materials Research Express*, vol. 8, no. 8, 2021.

## *Retraction*

# **Retracted: Study of Wear Behavior on AA6061 Reinforced with Hybrid Ceramic Composites through Optimization**

### **Advances in Materials Science and Engineering**

Received 26 December 2023; Accepted 26 December 2023; Published 29 December 2023

Copyright © 2023 Advances in Materials Science and Engineering. This is an open access article distributed under the Creative Commons Attribution License, which permits unrestricted use, distribution, and reproduction in any medium, provided the original work is properly cited.

This article has been retracted by Hindawi, as publisher, following an investigation undertaken by the publisher [1]. This investigation has uncovered evidence of systematic manipulation of the publication and peer-review process. We cannot, therefore, vouch for the reliability or integrity of this article.

Please note that this notice is intended solely to alert readers that the peer-review process of this article has been compromised.

Wiley and Hindawi regret that the usual quality checks did not identify these issues before publication and have since put additional measures in place to safeguard research integrity.

We wish to credit our Research Integrity and Research Publishing teams and anonymous and named external researchers and research integrity experts for contributing to this investigation.

The corresponding author, as the representative of all authors, has been given the opportunity to register their agreement or disagreement to this retraction. We have kept a record of any response received.

### **References**

- [1] O. Shabbir, S. V. Alagarsamy, C. Krishnamurthy, A. Nagaraj, P. K. Singh, and S. Ketema Sida, "Study of Wear Behavior on AA6061 Reinforced with Hybrid Ceramic Composites through Optimization," *Advances in Materials Science and Engineering*, vol. 2023, Article ID 7558886, 10 pages, 2023.

## Research Article

# Study of Wear Behavior on AA6061 Reinforced with Hybrid Ceramic Composites through Optimization

Omar Shabbir,<sup>1</sup> S. V. Alagarsamy,<sup>2</sup> C. Krishnamurthy,<sup>3</sup> A. Nagaraj,<sup>4</sup> Pradeep Kumar Singh,<sup>5</sup> and Sisay Ketema Sida <sup>6</sup>

<sup>1</sup>Department of Engineering Management, College of Engineering, Prince Sultan University, P.O. Box 66833, Riyadh 11586, Saudi Arabia

<sup>2</sup>Department of Mechanical Engineering, Mahath Amma Institute of Engineering and Technology, Pudukkottai 622101, Tamil Nadu, India

<sup>3</sup>Department of Mechanical Engineering, S.A. Engineering College, Chennai, Tamilnadu, India

<sup>4</sup>Department of Mechanical Engineering, Jimma University, Jimma, Ethiopia

<sup>5</sup>Department of Mechanical Engineering, GLA University, Mathura, UP 281406, India

<sup>6</sup>Department of Mechanical Engineering, Kombolcha Institute of Technology, Wollo University, Dessie, Ethiopia

Correspondence should be addressed to Sisay Ketema Sida; [sisayk@kiot.edu.et](mailto:sisayk@kiot.edu.et)

Received 5 July 2022; Revised 27 September 2022; Accepted 5 October 2022; Published 11 April 2023

Academic Editor: K. Raja

Copyright © 2023 Omar Shabbir et al. This is an open access article distributed under the Creative Commons Attribution License, which permits unrestricted use, distribution, and reproduction in any medium, provided the original work is properly cited.

This present work uses the three main components for alloying, silver nitrate, aluminium nitride, and titanium diboride. Stir casting was used to make AA 6061 composites with varying weights of 0, 3, 6, 9, and 12%. Microhardness, tensile strength, and compressive strength of produced composites were evaluated. Several wear tests were performed on the composites to measure their resistance to abrasion and erosion. The mass loss was calculated because of wear testing. Conventional and unconventional methods like the Taguchi technique and analysis of variance were employed to study and analyze the abrasive and erosion wear test outcomes to obtain better wear resistance for different weight % of AA 6061 compounds and to investigate the most important input and output characteristics employing the said optimal strategies. Reinforcement percentages were raised to improve mechanical quality.

## 1. Introduction

AMCs offer superior mechanical qualities, including thermal stability, high elastic modulus, and tensile strength over monolithic aluminium alloys and outstanding wear resistance properties in various situations, as evidenced by some recent research studies [1]. There are many applications in the automotive industry, which uses composite materials [2] that require sliding and abrasive characteristics of the materials [3]. Reinforcing particles include carbides, oxides, or nitrides and are responsible for the response between gas cavities and metal alloying components. Nonferrous metals are frequently employed as the matrix material [4], and the dispersion of particles ensures that the composite is chemically and thermodynamically stable. It is thought that

casting is the best way to produce composites [5, 6]. In the stir, reaction was used to create successful interactions between the matrix and reinforcing particles. Aluminum nitride (AlN) is an ideal diffusing reinforcing particle for Al alloys, which have good strength, thermal stabilization, and thermal expansional coefficient [7]. When combined with a suitable ceramic particle, silver nitrite ( $\text{AgNO}_3$ ) yields aluminium matrix compounds and titanium diboride ( $\text{TiB}_2$ ), two materials that have high heat stability, electrical stability, and erosion and corrosion resistance [8, 9]. Together, these materials make up a class of materials known as high-heat and electrical stability ceramics. These composites were studied for their mechanical qualities like hardness, ultimate tensile strength, and ultimate compressive strength, as well as for their metallurgical characteristics, for instance,

microstructure with varying weight % of strengthening in the in-stir composites [10–13]. In addition, the abrasive and erosion behaviours were examined under several testing settings, as well as the result findings were optimized using the Taguchi method, ANOVA [14, 15].

## 2. Materials and Methodology

**2.1. Manufacture of AA 6061 Composites.** Because of its reduced cost and higher adaptability, AA6061 is frequently used along with copper. The improved mechanical properties of AA6061 can benefit heating and thermal applications such as aviation, vehicle parts, and so on. An aluminum 6061 alloy was chosen as the matrix material for this experiment. There are many materials that can be used to make composites, including silver nitrite ( $\text{AgNO}_3$ ), aluminium nitride, and titanium diboride ( $\text{TiB}_2$ ). It is possible to make K2ZrF6 and KBF4 with the two  $\text{TiB}_2$  powders. We next combined various weight percentages of the matrix material (AA 6061) with reinforcing powders ( $\text{AgNO}_3$ , AlN, and  $\text{TiB}_2$ ) in wt% of 0, 3, 6, 9, and 12%. The weight of the matrix material was used to determine the number of reinforcements. It is possible to follow this technique for 6, 9, and 12 wt% during stir casting; the specifics are shown in Table 1 for a 1 kilogram matrix and reinforcement applied at a 2% rate, resulting in the addition of 20 g of reinforced particles. Module dimensions were met for abrasion testing.

**2.2. Mechanical and Metallurgical Characteristics.** The mechanical characteristics of AA 6061 compounds were determined by pressing the samples after they had been formed at various weights %. Using a Micro Vickers Hardness machine in accordance with ASTM accordance of E10-07, hardness values were acquired for every weight % of the specimen. The typical indent load was set at 0.5 kg for a duration of 25 s. Each sample had a different distribution of hardness levels, which could be found in several places [16, 17]. Depending on the quantity of reinforcement, five different specimens were employed in the experiment. Reinforcements of varying amounts were utilised to determine the composite samples' UTS, and the experiment was carried out with universal testing equipment in line with the ASTM E08-8 standard. Using 1200 grit SiC emery paper, we were able to minimize scratches and surface flaws on the samples [18]. The load was 10 kN, and the crosshead velocity was 2.5 m/min during the test. The ultimate compression strength of aluminum alloy 6061 compounds with varied reinforcing quantities was determined by the ASTM E09-9 standard [19]. Computerized universal testing equipment was used to conduct the test. The ultimate compression strength was determined using five specimens. The AA 6061 composites were examined under an optical microscope in accordance with the ASTM standard to determine their metallurgical composition and are discussed in the results and discussion.

**2.3. Test for Abrasive Wear.** Aluminum alloy 6061 compounds with weight % were measured using an abrasive jet machine (AJM) in this study. This experiment utilised a nozzle to spray an abrasive stream at high speed. There have been previous studies on the wear resistance of AA 6061 samples using the POD equipment with room and high temperature settings, and the titles are shown below; a different technique of the abrasive jet machine was employed to determine the wear resistance. Figure 1 depicts the schematic diagram of the abrasive jet machine.

Because the parameters could be precisely controlled, this machining approach differed from others used for ordinary sandblasting. Aside from cutting and milling hard and brittle materials, the AJM was commonly used to cut and manufacture workpieces. Abrasive particles are made of  $\text{AgNO}_3$  and aluminium nitride (AlN). In order to determine the mass loss of the AA 6061 compound specimens, the common values were used as input parameters. Table 2 lists all the input parameters.

**2.4. Erosion Wear Test.** As a result of the tiny particles in semisolid conditions, slurry erosion wear produces gradual material loss. In a slurry erosion test, AA 6061 composites with varying weight % of reinforcement (0, 3, 6, 9, and 12) were used. The samples were damaged by the impact of hard particles during this test, and mass loss originated in the specimens at different input values [20–22]. A variety of slurry mixtures were tested in the erosion test. A spinning spindle was used to hold the pot with the slurry and the sample.

It was found that the sample lost mass regardless of how fast the spindle rotated or how long it was submerged in a slurry. The slurry erosion tester is shown in Figure 2, and the input parameters for the slurry erosion test are listed in Table 3.

**2.5. Optimization Techniques.** Optimizing the findings was performed using two different strategies with the Taguchi method and ANOVA. Software like MINITAB and MATLAB was responsible for creating the methodologies. It was discovered that the most influencing process parameters in abrasive and erosion tests were identified utilizing the Taguchi method. For the Taguchi design, a total of five elements were used in five different level designs, resulting in a total of 25 tests. The final result of the testing was a reduction in bulk. ANOVA methodologies were used to determine the percentage of every procedure variable's contribution to abrasive and erosion tests [23]. The AA 6061 composites were subjected to abrasion and erosion testing in this study. The different weight percentages of reinforcements were used to identify test results [24]. The samples were evaluated under various input settings, and both outcomes were influenced by those variables. Conventional and unconventional methodologies were utilised to find the finest input impacted variable, the most contributed variable, the finest and average values of input and output outcomes, and the finest specimens between the different weight % of reinforcements.



TABLE 1: Weight percentages of AA6061 and its reinforcements.

S. No	AA 6061 (kg)	Reinforcements			Weight percentage (wt%)
		Silver nitrite (AgNO <sub>3</sub> ) g	Aluminium nitride (AlN) g	Titanium diboride (TiB <sub>2</sub> ) g	
1	1	0	0	0	0
2	1	30	30	30	3
3	1	60	60	60	6
4	1	90	90	90	9
5	1	120	120	120	12

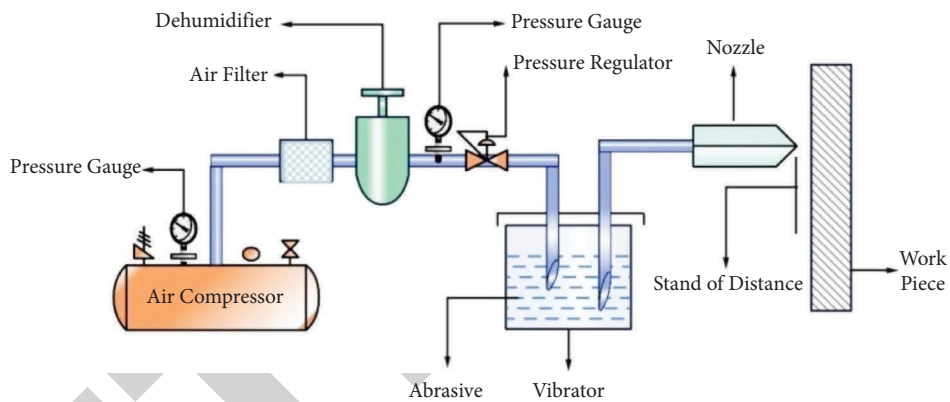
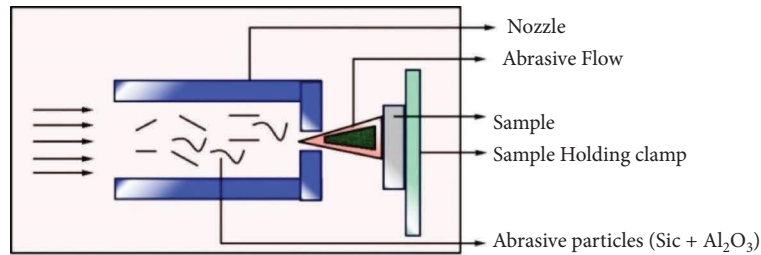


FIGURE 1: Flow diagram of the abrasive jet machine.

TABLE 2: Abrasive wear's input factors.

S. No	Input factors	Range
1	Composite weight (%)	0, 3, 6, 9, 12
2	Abrasive grain size (μm)	25, 50, 75, 100, 125
3	Abrasive flow rate (g/min)	10, 15, 20, 25, 30
4	Velocity (m/min)	200, 250, 300, 350, 400
5	Time (sec)	25, 50, 75, 100, 125

TABLE 3: Erosion wear test's input parameter.

S. No	Input parameters	Range
1	Composite weight percentage	0, 3, 6, 9, 12
2	Addition of sand in slurry (wt%)	25, 50, 75, 100, 125
3	Speed (rpm)	200, 250, 300, 350, 400
4	Time (sec)	25, 50, 75, 100, 125

### 3. Result and Discussion

#### 3.1. Analysis of Mechanical and Metallurgical Characteristics.

This study used mechanically imposed reinforcement sample concentrations of AA 6061 at wt% weight percentages of 0, 3, 6, 9, and 12. The AA 6061 composite mechanical testing results are shown in Table 4. The in-stir technique used in this composition ensured a standardized circulation of strengthening particles throughout the matrix. Reinforcements have the greatest impact on the composites' hardness and tensile strength [25]. Compounds have an interface because of the strong interfacial

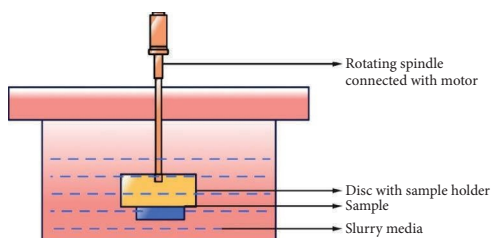


FIGURE 2: Slurry erosion tester.

TABLE 4: Results of mechanical properties.

Reinforcement (wt%)	Tensile strength (MPa)	Vickers hardness (HV)	Compressive strength (MPa)
0	439	125	369
3	472	142	378
6	483	148	402
9	491	159	405
12	488	182	408

bond between the matrix and reinforcements. Dislocations are prevented from moving by the reinforcing particles, such as AlN and TiB<sub>2</sub>. It was possible to avoid cracks in the composite structure because of the strong bonding, and the reinforcements were also limited by plastic deformation [26]. As plasticity is restricted, the strength of the AA 6061 composites is increased. It was forbidden to increase the volume fraction of reinforcing particles at the highest wt% of composites due to a decrease in the matrix's fluidity. Increased reinforcing particles, in turn, boosted mechanical characteristics.

Composite samples with different percentages of reinforcement were examined under an optical microscope for their microscopic structure. Observing the construction reveals that the reinforcements were mixed and placed uniformly and that the reinforcements were successfully attached to the matrix [27]. Interfacial bonding was created between the grains because of the in situ production. Because of this, oxidation in the matrix can be prevented. Due to the in situ approach of reinforcing particles, floating and sinking in the composite structure were reduced. Due to the high temperature synthesis of composites, the reinforcements were spread in the AA 6061 matrix; the addition of AlN particles seems to enhance oxidation for some reason, possibly due to nitride's increased oxygen concentration. Some oxidation occurs because of the increase in AlN during this phase. The bonding between the two matrixes and reinforcements had a positive effect.

### 3.2. Analysis of Optimum Results

**3.2.1. Taguchi Technique-Abrasive Wear.** Using the Taguchi technique, the abrasive and erosion wear of different input factors was calculated. With the AA 6061 composites, an  $L_{25}$  orthogonal array was used in varied wt% of composite samples for wear testing (0, 3, 6, 9, and 12) and is shown in Table 5. The MINITAB software was used to create a Design of Experiments (DOE) for the abrasive wear testing of 25 AA 6061 composite samples. In total, there were five factors: composite (wt%), abrasive granular size, flow rate (g/min), velocity, and duration, and each parameter had five trials; the total came to 25 readings; mass loss (g) was measured as the resulting factor for the wear test. This method was used to determine which process parameters had the greatest impact. The decrease in mass loss was seen as the outcome of the increase in reinforcement. AA 6061 composites are resistant to wear owing to their higher bonding strength and low plastic distortion. Compounds with mass losses of less than 12% were found to be the most stable in employed

circumstances of 60 mm abrasive particle size, 10 g/min flow rate, 150 m/s velocity, and 150 s duration.

**3.2.2. Taguchi Method-Erosion Wear.** It was determined that mass loss (g) was a result of four separate parameters: the sample (wt%), the addition of sand (wt%), time (s), and speed (rpm). The  $L_{25}$  orthogonal array is also used for the erosive wear test. Every five-weight percent of the composite is run through five times. During erosive wear, there is no influence of the particles on the surface of the composite. A high-reinforced composite (12%) removed the least material during erosive wear tests. The AA 6061 composite had a material removal of 0.82701 g, less than 12% of the regulated input parameters of 50 weight %trappings of sand, 250 rpm speed, and 125 s time in erosion testing. Table 6 shows the outcomes of the input and output, and the main effect plots for the means and S/N ratio are shown in Figures 3 and 4.

**3.2.3. S/N Ratio-Abrasive Wear.** It was possible to determine the S/N and data means using the MINITAB software. Tables 7 and 8 display the response data for the mean and S/N ratio. Results using statistical software were obtained using AA 6061 composites in abrasive wear tests with diverse input circumstances and materials. It was possible to isolate the mean values for each of the input parameters. Based on the DOE, the mean values can vary. An abrasive wear test was used to classify the relative significance of various procedure aspects, and the results of the data mean and S/N ratio demonstrate the same. The data mean and S/N ratios are provided in the main effect charts.

**3.2.4. Signal to Noise Ratio-Erosion Wear.** The AA 6061 composites tested in erosion wear had the lowest material removal of the 12% composites. The wt% of particles added and the speed and time at which they were added were both varied. There was some microslicing and plowing at various shallow angles as the tiny particles came into contact with the composite surfaces. Figures 5 and 6 show data means and S/N ratios, respectively, and are included in Tables 9 and 10 of this section.

**3.2.5. Analysis of Variance-Abrasive Wear.** It is possible to analyze the relative importance of every process variable by performing an analysis of variance. There were five different variables taken into account when performing the abrasive wear test in this study. As shown in Table 11, composite weight (85.04%), duration (3.66 seconds), velocity (m/min) 3.78%, flow rate (3.57 g/m), and grain size (mm) 2.64% make

TABLE 5: With  $L_{25}$  orthogonal array, the input and output factors of abrasive wear.

S. No	Composite wt %	Granular size ( $\mu\text{m}$ )	Flow rate (g/min)	Velocity (m/min)	Time (s)	Mass loss (g)
1	0	25	10	200	25	0.02148
2	0	50	15	250	50	0.02607
3	0	75	20	300	75	0.03128
4	0	100	25	350	100	0.04542
5	0	125	30	400	125	0.04502
6	3	25	10	300	100	0.01824
7	3	50	15	350	125	0.01916
8	3	75	20	400	25	0.01824
9	3	100	25	200	50	0.01608
10	3	125	30	250	75	0.017238
11	6	25	10	400	50	0.01357
12	6	50	15	200	75	0.01114
13	6	75	20	250	100	0.01228
14	6	100	25	300	125	0.01268
15	6	125	30	350	25	0.01140
16	9	25	10	250	125	0.01050
17	9	50	15	300	25	0.00750
18	9	75	20	350	50	0.00105
19	9	100	25	400	75	0.00464
20	9	125	30	200	100	0.00458
21	12	25	10	350	75	0.00345
22	12	50	15	400	100	0.00468
23	12	75	20	200	125	0.00348
24	12	100	25	250	25	0.00367
25	12	125	30	300	50	0.00442

TABLE 6: With the  $L_{25}$  orthogonal array, the input and output factors of erosion wear.

S.No	Composites wt %	Adding of sand (wt %)	Time (S)	Speed (rpm)	Mass loss (g)
1	0	25	25	250	1.9836
2	0	50	50	500	1.48168
3	0	75	75	750	1.48049
4	0	100	100	1000	1.47327
5	0	125	125	1250	1.56055
6	3	25	100	250	1.33038
7	3	50	125	500	1.30363
8	3	75	25	750	1.32692
9	3	100	50	1000	1.37877
10	3	125	75	1250	1.22701
11	6	25	50	250	1.28103
12	6	50	75	500	1.24642
13	6	75	100	750	1.28642
14	6	100	125	1000	1.17507
15	6	125	25	1250	1.16803
16	9	25	125	250	1.18561
17	9	50	25	500	1.17841
18	9	75	50	750	1.02404
19	9	100	75	1000	1.01727
20	9	125	100	1250	1.08865
21	12	25	75	250	1.04782
22	12	50	100	500	0.97210
23	12	75	125	750	0.95249
24	12	100	25	1000	0.98721
25	12	125	50	1250	1.02161

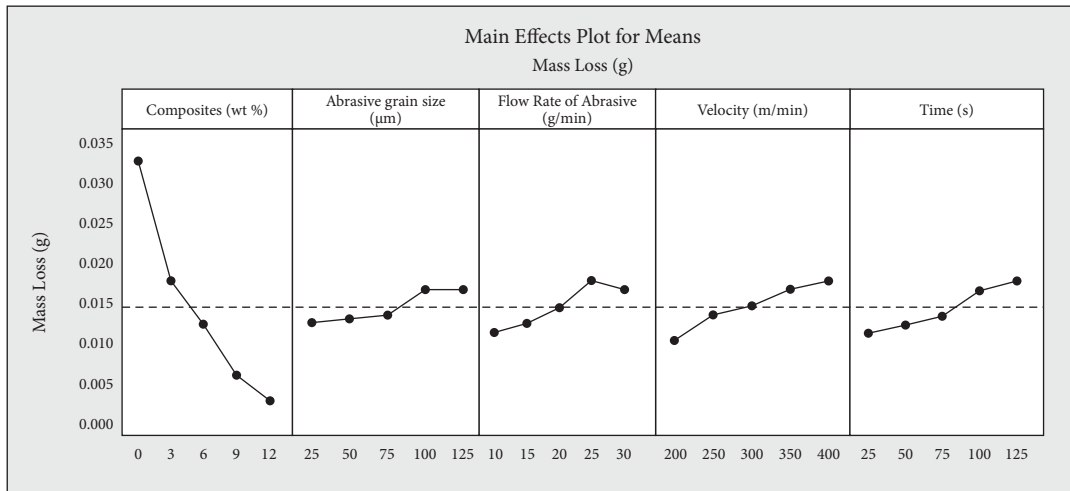


FIGURE 3: Main effect plots for means.

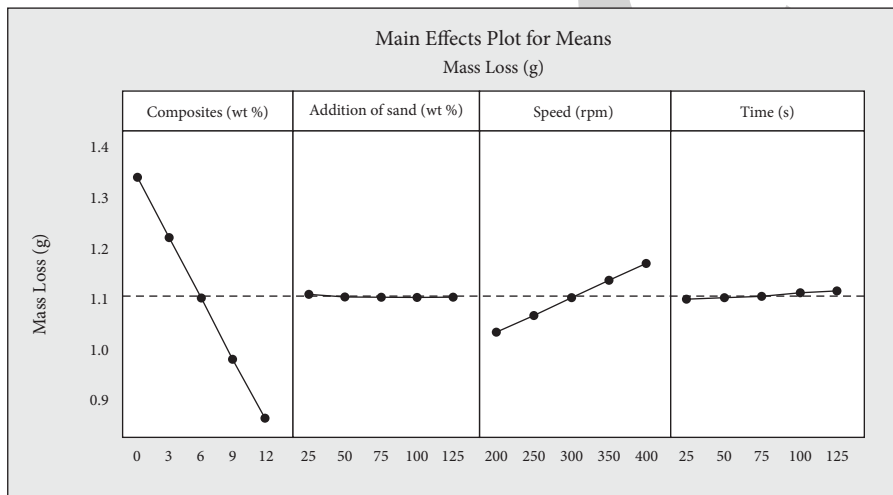


FIGURE 4: Main effect for the S/N ratio.

TABLE 7: Mean's response table (abrasive wear).

Level	Composite (wt%)	Granular size (µm)	Velocity (m/min)	Flow rate (g/min)	Time (s)
1	0.042586	0.023819	0.021420	0.021350	0.02426
2	0.027839	0.023798	0.023450	0.023420	0.02345
3	0.022198	0.024778	0.025130	0.024758	0.02432
4	0.01563	0.026698	0.025900	0.026985	0.02619
5	0.014139	0.026692	0.027659	0.027641	0.02798
<b>Delta</b>	0.040543	0.003894	0.017946	0.006998	0.01658
<b>Rank</b>	1	5	2	4	3

TABLE 8: S/N ratio's response table (abrasive wear).

Level	Composite (wt%)	Granular size (µm)	Flow rate (g/min)	Velocity (m/min)	Time (s)
1	30.18	40.15	41.96	43.01	41.08
2	36.42	40.18	42.15	40.56	40.57
3	40.15	41.38	41.05	40.53	40.43
4	46.72	41.09	39.63	40.68	40.16
5	51.68	41.06	40.21	40.41	39.06
<b>Delta</b>	51.64	2.05	3.78	3.69	3.02
<b>Rank</b>	1	5	3	2	4

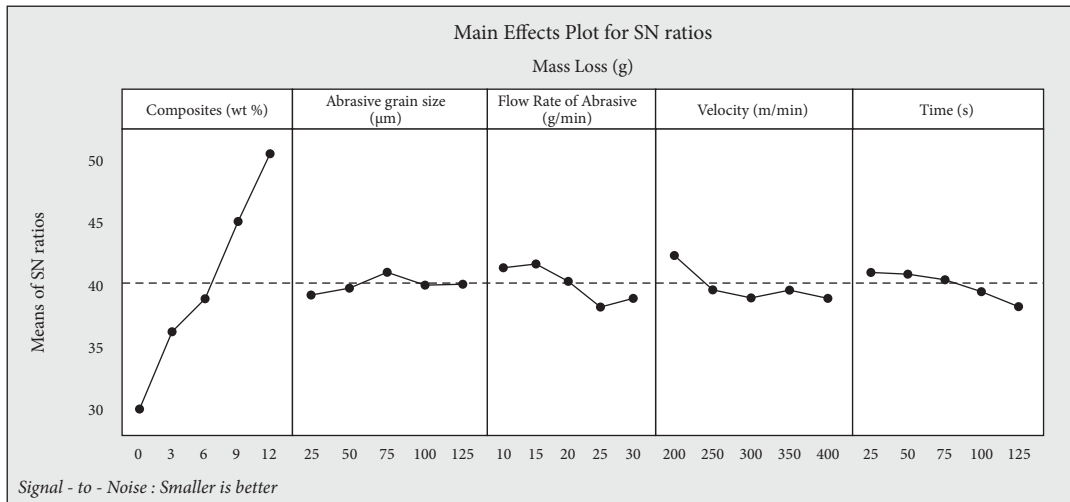


FIGURE 5: Main effects plot for means.

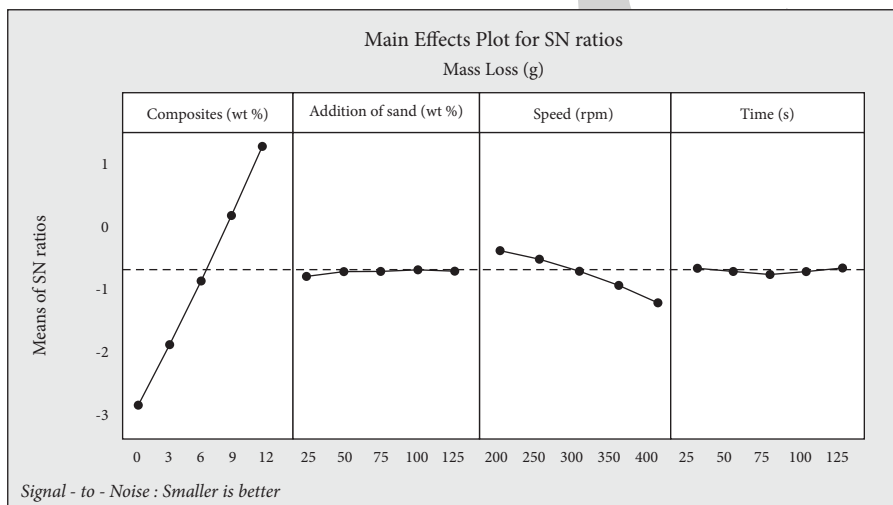


FIGURE 6: Main effect for the S/N ratio.

TABLE 9: Mean's response table (erosion wear).

Level	Composites (wt%)	Adding of sand (wt%)	Speed (rpm)	Time (s)
1	2.3582	2.1624	2.0765	2.1160
2	2.2386	2.1241	2.0864	2.1880
3	2.6145	2.6124	2.1612	2.1611
4	1.9398	2.1242	2.1683	2.1431
5	0.9572	2.6101	2.1565	2.1710
<b>Delta</b>	0.5370	0.0030	1.1800	0.9901
<b>Rank</b>	1	4	2	3

TABLE 10: S/N ratio's response table (erosion wear).

Level	Composites (wt%)	Adding of sand (wt%)	Speed (rpm)
1	-3.6021	-0.9753	-0.4845
2	-2.8642	-0.9376	-0.6898
3	-1.9316	-0.8834	-0.9519
4	0.7462	-0.8859	-2.1926
5	2.6716	-0.9128	-2.4207
<b>Delta</b>	4.7596	0.1874	0.9744
<b>Rank</b>	1	3	2

up the majority of the ANOVA results, and the best result is shown in Figure 7.

3.2.6. Analysis of Variance-Erosion Wear. ANOVA was utilised to determine the percentage of every processing variable that was studied in erosion wear. The composite contribution of 94.99% has the highest percentage of success,

according to the findings. Depending on the operating conditions, different input parameters are affected. A speed (rpm) of 4.95% contributes to the erosion test because the disc speed is also being adjusted presently. Samples were exposed to higher concentrations of particles. Time (s) contributes less than 0.05%, while sand addition contributes less than 0.0017%. According to the preceding data, just 8% of the composite had a significant quantity of material

TABLE 11: ANOVA results (abrasive wear).

Source	DoF	Adj.SS	Adj.MS	F
Composite (wt%)	4	0.003142	0.000813	33.18
Velocity (m/min)	4	0.000229	0.000028	2.34
Time (s)	4	0.000262	0.000027	2.83
Flow rate (g/min)	4	0.000232	0.000027	2.54
Grain size ( $\mu\text{m}$ )	4	0.000108	0.000018	0.49
Error	4	0.000051	0.000009	—
Total	24	0.004483	—	—

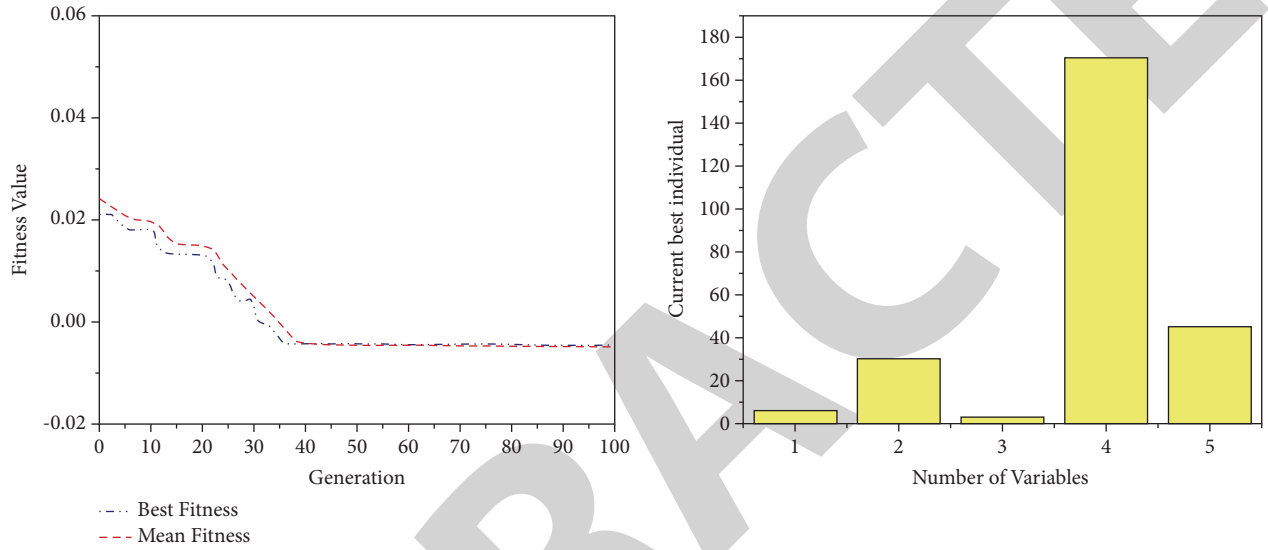


FIGURE 7: Best and mean values of output results of abrasive wear.

TABLE 12: ANOVA results (erosion wear).

Source	DoF	Adj.SS	Adj.MS	Percentage of contribution	Rank
Composites (wt%)	4	0.70872	0.28471	94.0772	1
Speed (rpm)	4	0.16345	0.01021	5.86	2
Time (s)	4	0.00048	0.00010	0.06	3
Adding of sand (wt%)	4	0.00001	0.00004	0.0028	4
Error	4	0	0	0	—
Total	24	0.87266	—	—	—

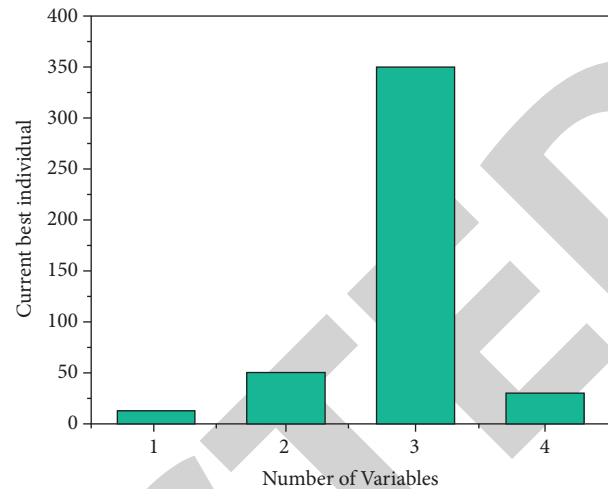
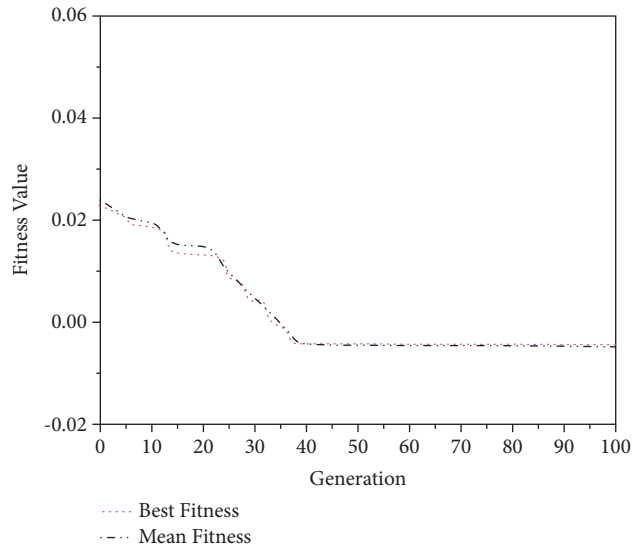


FIGURE 8: Best and mean values of output results of the erosion wear test.

removed, and the test outcome confirmed this. Table 12 indicates the outcomes of the erosion tests, and the best result is shown in Figure 8.

#### 4. Conclusions

By using a stir casting technique, the strengthened particles were able to be formed for the composite preparation, and the following results were achieved:

- (i) Because of their tensile strength, AA 6061 compounds in varied weight % had good bonding strength, reducing plastic deformation in the composites, which are achieved using an in situ technique, which binds particles together. Reinforcements increased mechanical qualities.
- (ii) After being subjected to abrasion and erosion tests, surfaces were inspected. In abrasive wear testing, fine scratches and grooves are detected when minute particles come into contact with the composites' surface. With just 12% strengthening in AA 6061 compounds, the wear rate is practically non-existent. Work-hardened layers formed on the composite surfaces during erosion at increasing velocities.
- (iii) To further understand the relationship between the abrasive and erosion processes, Taguchi and ANOVA analyses were used to determine the most significant process variables. Specimen speed, time, flow rate, and abrasive granular size ranked highest in the abrasion test. Composites made up 85.04% of the total, followed by speed (m/min) 3.78%, time (s) 3.66%, abrasive flow rate (g/min) 3.57%, and also grain size (mm) 2.64%.
- (iv) The most significant factors in the erosion test were the reaction of the mean of compounds, speed, time, and sand addition. Process parameters were

discovered to be ordered compounds of 94.99%, speed (rpm) 4.95%, time 0.05%, and the addition of sand 0.0017% based on ANOVA's percentage contribution.

#### Data Availability

The data used to support the findings of this study are included within the article. Further data and information are available from the corresponding author upon request.

#### Conflicts of Interest

The authors declare that they have no conflicts of interest regarding the publication of this paper.

#### Acknowledgments

The authors appreciate the support from Kombolcha Institute of Technology, Wollo University, Ethiopia, for the research and preparation of the manuscript. This research is supported by the Structures and Materials (S&M) Research Lab of Prince Sultan University.

#### References

- [1] V. K. Parikh, V. J. Badheka, A. D. Badgajar, and N. D. Ghetiya, "Fabrication and processing of aluminum alloy metal matrix composites," *Materials and Manufacturing Processes*, vol. 36, no. 14, pp. 1604–1617, 2021.
- [2] V. Mohanavel and M. Ravichandran, "Influence of AlN particles on microstructure, mechanical and tribological behaviour in AA6351 aluminum alloy," *Materials Research Express*, vol. 6, no. 10, Article ID 106557, 2019.
- [3] M. Gui, D. Wang, J. Wu, and C. Li, "Erosion of in-situ TiC particle reinforced Al-5Cu composite," *Materials Research Bulletin*, vol. 36, no. 9, pp. 1573–1585, 2001.
- [4] T. Sathish, V. Mohanavel, P. Velmurugan et al., "Evaluation of MWCNT particles-reinforced magnesium composite for

## Retraction

# Retracted: Effects of Polypropylene Waste Addition as Coarse Aggregates in Concrete: Experimental Characterization and Statistical Analysis

### Advances in Materials Science and Engineering

Received 8 January 2024; Accepted 8 January 2024; Published 9 January 2024

Copyright © 2024 Advances in Materials Science and Engineering. This is an open access article distributed under the Creative Commons Attribution License, which permits unrestricted use, distribution, and reproduction in any medium, provided the original work is properly cited.

This article has been retracted by Hindawi following an investigation undertaken by the publisher [1]. This investigation has uncovered evidence of one or more of the following indicators of systematic manipulation of the publication process:

- (1) Discrepancies in scope
- (2) Discrepancies in the description of the research reported
- (3) Discrepancies between the availability of data and the research described
- (4) Inappropriate citations
- (5) Incoherent, meaningless and/or irrelevant content included in the article
- (6) Manipulated or compromised peer review

The presence of these indicators undermines our confidence in the integrity of the article's content and we cannot, therefore, vouch for its reliability. Please note that this notice is intended solely to alert readers that the content of this article is unreliable. We have not investigated whether authors were aware of or involved in the systematic manipulation of the publication process.

Wiley and Hindawi regrets that the usual quality checks did not identify these issues before publication and have since put additional measures in place to safeguard research integrity.

We wish to credit our own Research Integrity and Research Publishing teams and anonymous and named external researchers and research integrity experts for contributing to this investigation.

The corresponding author, as the representative of all authors, has been given the opportunity to register their agreement or disagreement to this retraction. We have kept a record of any response received.

### References

- [1] D. C. Naveen, K. Naresh, B. S. Keerthi Gowda, M. S. Reddy G, C. D. Prasad, and R. Shanmugam, "Effects of Polypropylene Waste Addition as Coarse Aggregates in Concrete: Experimental Characterization and Statistical Analysis," *Advances in Materials Science and Engineering*, vol. 2022, Article ID 7886722, 11 pages, 2022.



## Research Article

# Effects of Polypropylene Waste Addition as Coarse Aggregates in Concrete: Experimental Characterization and Statistical Analysis

D. C. Naveen,<sup>1</sup> K. Naresh ,<sup>2</sup> B. S. Keerthi Gowda ,<sup>3</sup> Madhu Sudana Reddy G ,<sup>4</sup>  
C. Durga Prasad ,<sup>5</sup> and Ragavanantham Shanmugam <sup>6</sup>

<sup>1</sup>Department of Civil Engineering, Sri Venkateswara College of Engineering, Tirupati, India

<sup>2</sup>Department of Materials Science and Engineering, University of California, Irvine 92697, USA

<sup>3</sup>Department of Civil Engineering, Visvesvaraya Technological University, Mysuru, India

<sup>4</sup>Department of Mechanical Engineering, The Oxford College of Engineering, Bengaluru, Karnataka, India

<sup>5</sup>Department of Mechanical Engineering, RV Institute of Technology and Management Bengaluru, Bengaluru, Karnataka, India

<sup>6</sup>Department of Advanced Manufacturing Engineering Technology, Navajo Technical University, NM 87313, USA

Correspondence should be addressed to K. Naresh; [naresh.kakur@gmail.com](mailto:naresh.kakur@gmail.com)

Received 4 July 2022; Revised 31 July 2022; Accepted 20 September 2022; Published 8 November 2022

Academic Editor: Qian Chen

Copyright © 2022 D. C. Naveen et al. This is an open access article distributed under the Creative Commons Attribution License, which permits unrestricted use, distribution, and reproduction in any medium, provided the original work is properly cited.

In recent times, thermoplastic waste materials are being extensively used as fine and coarse aggregates in the concrete mix as an environmentally friendly construction material. This study aims at utilizing polypropylene (PP) as a partial substitute for the conventional coarse aggregates in M30 grade concrete. The different replacement levels of coarse aggregates such as 0%, 20%, 40%, and 60% by weight were used in concrete. Sieve analysis, specific gravity, and water absorption tests were performed in all replacement levels of aggregates. The mechanical (compressive and split tensile tests) tests were conducted after 3, 14, and 28 days. The change in mechanical properties of concrete with the addition of different weight proportions of plastics was studied experimentally. Further, experimental values were predicted using the two-parameter Weibull distribution and artificial neural network (ANN)-based statistical approaches. The Levenberg–Marquardt algorithm was used in predicting the mechanical properties using the ANN. A good correlation was obtained between the experimental and predicted values with an error (%) of less than 10. The decrease in mechanical properties with the increase in replacement levels of coarse aggregates in concrete was observed in both experimental and predicted approaches. This can be attributed to poor bonding between concrete and PP aggregate owing to the development of agglomerations and the hydrophobic nature of PP. However, the strength values of 20% PP-embedded concrete specimens are closer to 0% PP-embedded concrete specimens. Therefore, 20% PP-embedded concrete specimens can be used for primary load-bearing applications to utilize plastic waste and reduce the cost of the component.

## 1. Introduction

In the past decades, the use of plastics has been widely increased in various applications such as automotive, medical, and housing applications [1–4]. More importantly, their use in packaging and distribution of food for daily usage is high; in that way a large quantity of plastic waste is accumulated all over the world [5, 6]. Larger areas of land are required for storing these several million tons of waste plastics. Even though plastic products are lightweight and easy to design and fabricate, they possess low- or

nonbiodegradability. As a result, the disposal of plastic waste causes a considerable threat to humans and animals and is one of the major reasons for environmental pollution, [7]. Therefore, it is important to develop biodegradable plastics [8] or reuse plastic waste for the benefit of different perspectives. Most countries have already started to utilize plastic waste for various applications [9]. In particular, thermoplastic waste materials have been extensively used in energy applications [10] and the construction industry [11].

In recent years, many researchers studied the mechanical properties of thermoplastic waste materials incorporated in

concrete structures [12, 13]. Almeshal et al. [14] used polyethylene terephthalate (PET) as a fine aggregate for the partial replacement of sand in concrete. They have investigated the compressive, flexural, and split tensile strength values for different weight substitution levels (0%, 10%, 20%, 30%, 40%, and 50%) of PET-incorporated concrete. A gradual decrease in compressive, flexural, and split tensile strength values with the increase of PET percentage in concrete was found. Ohemang and Ekolu [15] studied the compressive and flexural strength values of different volume fractions of low-density polyethylene (LDPE)-embedded cement mortar. These strength values were compared for different curing ages such as 7, 14, and 28 days. The decrease in strength values with the increase in various proportions of LDPE in cement mortar was found. Also, the increase in strength values with the increase of curing age was reported. In particular, the increase was reported to be higher from the age interval of 7 days to 14 days, compared to those at age intervals of 14 days to 28 days. The decrease in compressive strength with the increase in plastic waste contents and the enhancement in compressive strength with the increase of curing age were also found by several researchers [12, 16, 17].

Several researchers used analytical models to predict the flexural and split tensile strength values using compressive strength values [14, 18]. Moreover, many researchers are also used artificial neural network (ANN) methods to solve complex problems in the area of concrete technology [19–22]. Onyelow et al. [23] compared the compressive strength values of 28 days of post-cured Fly Ash-embedded concrete specimens using genetic programming (GP), evolutionary polynomial regression (EPR), and three different ANN (backpropagation, gradually reduced gradient, and genetic algorithm) methods. It was found that the compressive strength values of the GP model had the least accuracy of 81%, the EPR model had a moderate accuracy of 90%, and all ANN models had almost the same accuracy of approximately 94%. Rezazadeh Eidgahee et al. [24] employed different machine learning methods (ANN, GP, and group method of data handling (GMDH)) in predicting the dynamic modulus of hot mix asphalt. It was reported that the accuracy of the ANN model is higher based on higher correlation coefficient values greater than 0.98, compared with GP and GMDH models.

In general, there is a tendency for strength values to be scattered due to the possibility of operator and instrument errors. In particular, the occurrence of errors during the manufacturing of the component is high. Statistical studies are useful to capture the scatter in strength values [25, 26]. However, very limited researchers employed statistical approaches to predict the strength values for different weight proportions of plastic waste embedded in concrete or cement mortars [15, 27]. In this study, the two-parameter Weibull distribution is used to predict the compressive and split tensile strength values for different weight proportions of polypropylene plastic waste-embedded concrete. A good correlation was obtained between the predicted and experimental results. The ANN strategy is also adopted to predict the compression and split tensile strength values of

polypropylene plastic waste embedded in cement concrete specimens.

## 2. Materials and Methods

**2.1. Materials.** In this study, materials such as cement, sand as fine aggregate, and recycled polypropylene as coarse aggregate are used. The material specifications for cement, fine aggregate, coarse aggregate, and admixtures are discussed. Sieve analysis was done for sand and coarse aggregate to test their suitability for use in concrete.

**2.1.1. Cement.** In this study, ordinary Portland cement (OPC) of 53 grade was used for casting cubes and cylinders for all concrete mixes. The cement was of uniform color, i.e., grey with a light greenish shade and was free from any hard lumps. The specific gravity (SG) of cement was carried out as per IS 2386 (Part 3)-1963 using equation (1), as given in Table 1. The summary of the various tests conducted on cement is given in Table 2, and the obtained values are closer to standard values.

$$\frac{(W_2 - W_1)}{(W_2 - W_1) - (W_3 - W_4) \times 0.79} \quad (1)$$

**2.1.2. Fine Aggregates.** The sand used for the experimental program was locally procured and conformed to Indian Standard Specifications IS: 383–1970. The sand was first sieved through a 4.75 mm sieve to remove any particles greater than 4.75 mm and then was washed to remove the dust. The properties of the fine aggregate used in the experimental work are given in Table 3. The aggregates were sieved through a set of sieves as shown in Figure 1(a) to obtain the sieve analysis and the same is presented in Table 3. The fine aggregates belonged to grading zone III.

**2.1.3. Coarse Aggregates.** The recycled polypropylene was used as coarse aggregate in this study. These aggregates were tested as per Indian Standard specifications IS: 383–1970. The results of the sieve analysis of recycled polypropylene are given in Table 4 and Figure 1(b).

**2.2. Specimen Fabrication.** Before manufacturing the specimens, the mix design was determined for M30 grade concrete based on the degree of workability and quality control, specific gravity, etc. The specific gravity of cement, sand (fine aggregate), and recycled polypropylene (coarse aggregate) was determined as 3.01, 2.61, and 2.65, respectively. Mixture ratios such as cement: fine aggregate: coarse aggregate: water were used for manufacturing the specimens, by weight as 1:1.09:2.29:0.38, respectively. Fabricated cubic and cylindrical specimens for compression and split tensile tests are shown in Figure 2.

TABLE 1: Specific gravity of cement.

Sl. no.	Observations	Values obtained			
		Trial 1	Trial 2	Trial 3	Average
1.	Weight of the specific gravity bottle ( $W_1$ ), g	35.8	35.8	35.8	35.80
2.	Weight of bottle + 1/3 <sup>rd</sup> filled cement ( $W_2$ ), g	53.8	53.6	53.8	53.73
3.	Weight of bottle + 1/3 <sup>rd</sup> filled cement + kerosene ( $W_3$ ), g	89.4	89.3	89.4	89.37
4.	Weight of bottle + kerosene ( $W_4$ ), g	76.2	76.2	76.2	76.20
5.	Specific gravity	3.0	3.02	3.0	3.01

TABLE 2: Various tests conducted on cement.

S. no	Characteristics	Values obtained	Standard values
1.	Normal consistency	33%	25%–35%
2.	Initial setting time	38 minutes	Not be less than 30 minutes
3.	Final setting time	260 minutes	Not be greater than 600 minutes
4.	Fineness	4.8%	<10%
5.	Specific gravity	3.01	Around 3.15

TABLE 3: Sieve analysis of fine aggregates.

Sieve size (mm)	Weight retained (g)	Cumulative weight retained (g)	Cumulative % retained	% Passing
4.75	0	0	0	100
2.36	13	13	2.6	97.4
1.18	57.3	70.3	14.06	85.94
0.6	135.7	206	41.2	58.8
0.3	246.5	452.5	90.5	9.5
0.15	43.7	496.2	99.24	0.76
<0.15	3.8	500	100	0

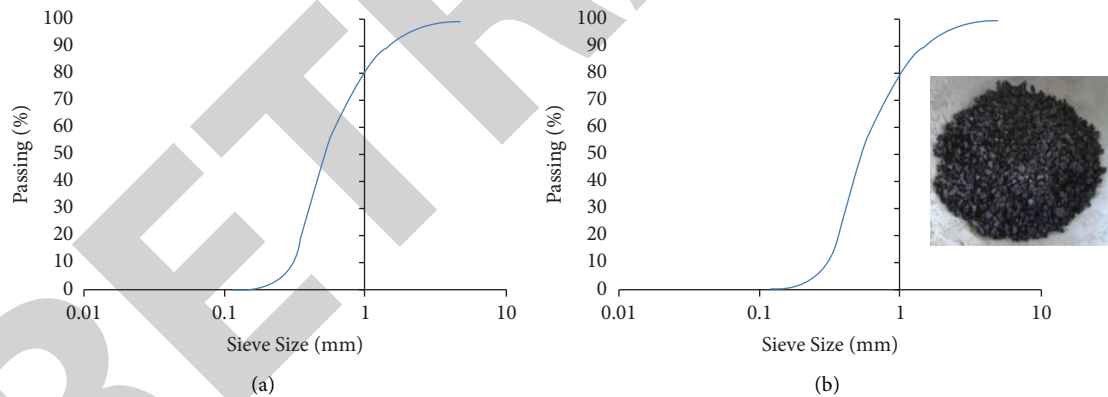


FIGURE 1: Sieve analysis of fine (a) and coarse (b) aggregates.

TABLE 4: Sieve analysis of recycled polypropylene as coarse aggregates.

Sieve size (mm)	Weight retained (g)	Cumulative weight retained (g)	Cumulative % retained	% Passing
4.75	175	175	35	65
2.36	110	285	57	43
1.18	102	387	77.4	22.6
0.6	76	463	92.6	7.4
0.3	24	487	97.4	2.6
0.15	8	495	99	1
<0.15	5	500	100	0

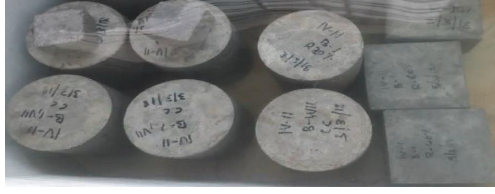


FIGURE 2: Fabricated cubic and cylindrical specimens.

### 2.3. Experimental Details

**2.3.1. Compressive Strength of Concrete.** Compression tests were performed as per IS 516–1999 standard on different weight proportions of polypropylene-embedded concrete cubic specimens. Three different specimens were tested in each combination. The dimensions of the specimens such as length, width, and thickness used for compression tests were 150 mm × 150 mm × 150 mm, respectively. The specimens were submerged in clean fresh water for the duration of 3, 14, and 28 days before testing and kept in a dry place so that the water is drained well to get better results. The compressive load is applied on the specimen using the universal testing machine, as shown in Figure 3(a). The load is gradually applied until it fails. The compressive strength of the specimen was calculated using equation (2), it is given by

$$F_c = \frac{P}{A}, \quad (2)$$

where  $F_c$  is the compressive strength,  $P$  is the ultimate load, and  $A$  is the area of the specimen which is 150 mm × 150 mm.

**2.3.2. Split Tensile Strength of Concrete.** It is difficult to investigate the direct tensile strength of concrete; however, often, researchers are performed flexural or split tensile tests to estimate the direct tensile strength. A split tensile test for different weight proportions of polypropylene-embedded concrete specimens was performed as per IS 516–1999 standard. Three different specimens were tested in each combination. The dimensions of concrete cylindrical specimens such as a diameter of 150 mm and a length of 300 mm. The cylindrical specimens were placed horizontally between the loading surfaces of a compression testing machine, as shown in Figure 3(b) and the load is applied until the failure of the cylinder along the vertical diameter. The splitting tensile strength of specimens is calculated using equation (3), it is given by

$$F_t = \frac{2P}{\pi ld}, \quad (3)$$

where  $l$  and  $d$  are the length and diameter of the specimen, respectively.

## 3. Results and Discussion

**3.1. Mechanical Properties.** The average compressive and split strength values for different curing ages of concrete/polypropylene specimens are shown in Figures 3 and 4, respectively. It is clear from the figure that the strength

values increase with the increase in curing ages of 3 to 28 days. The increase in strength values between 14 and 28 days is relatively less compared to 3 and 28 days. This can be attributed to an increase in physical, chemical, and mechanical bonding of the microstructure of concrete specimens, which strengthens the specimen. Therefore, it is essential to postcure the concrete specimen for a minimum of two weeks. An enhancement in compressive strength with the increase in curing age of concrete specimens was also found by numerous researchers [12, 16, 17].

However, the decrease in strength values is observed with the increase in different weight percentages of polypropylene in the concrete. However, the strength values of 20% PP-embedded concrete specimens are closer to 0% PP-embedded concrete specimens. Therefore, specimens of 20% PP-embedded concrete specimens are recommended for primary load-bearing applications, whereas 40% and 60% PP-embedded concrete specimens are recommended for secondary load-bearing applications. The trend of the curves matches well with the literature [28–30]; in their studies, they have reported the decrease in compressive strength of concrete with the increase in plastic substitution. The two main factors which restrict the improvement of compressive strength, at higher weight percentages (40% and 60%) of PP embedded in concrete specimens, are (i) poor bonding between PP aggregate and concrete due to the development of agglomerations, (ii) the hydrophobic nature of PP aggregate that decreases the rate of hydration [31]. A similar kind of decrease in strength values with the addition of higher weight percentages of waste materials in the concrete is found in these articles [9, 14, 32].

The trend of split tensile strength values seen in Figure 4 is similar to compressive strength values. Similar kinds of results are reported elsewhere [33]. As expected, from Figures 4 and 5, the compressive strength values are significantly higher in all specimens tested at different curing ages compared to split tensile strength values. A similar kind of trend is found elsewhere [34]. From equations (2) and (3), the applied direction of loading is the main reason for the difference between the values in these two tests [24]. The compressive strength of concrete is always higher for a concrete specimen as it withstands axially directed pushing force until it reaches its maximum force, after that the specimen is crushed, as shown in Figure 3(a). However, the failure response of the specimen subjected to the split tensile test is the transverse shear, as shown in Figure 3(b). Numerous researchers [35–37] have reported experimentally and theoretically that the compressive strength value of the cubic concrete specimen is several times higher than that of the split tensile strength.

**3.2. Prediction of Compressive and Split Tensile Strength Values Using Two-Parameter Weibull Distribution.** In this section, the procedure for predicting the compression and split tensile strength values are discussed using the two-parameter Weibull analysis. The compressive ( $\overline{\sigma_c}$ ) and split tensile strength ( $\overline{\sigma_{ST}}$ ) values can be written in terms of scale parameter ( $\alpha$ ), shape parameter ( $\beta$ ), and gamma function ( $\Gamma$ ) using equations (4) and (5), respectively [20, 38].

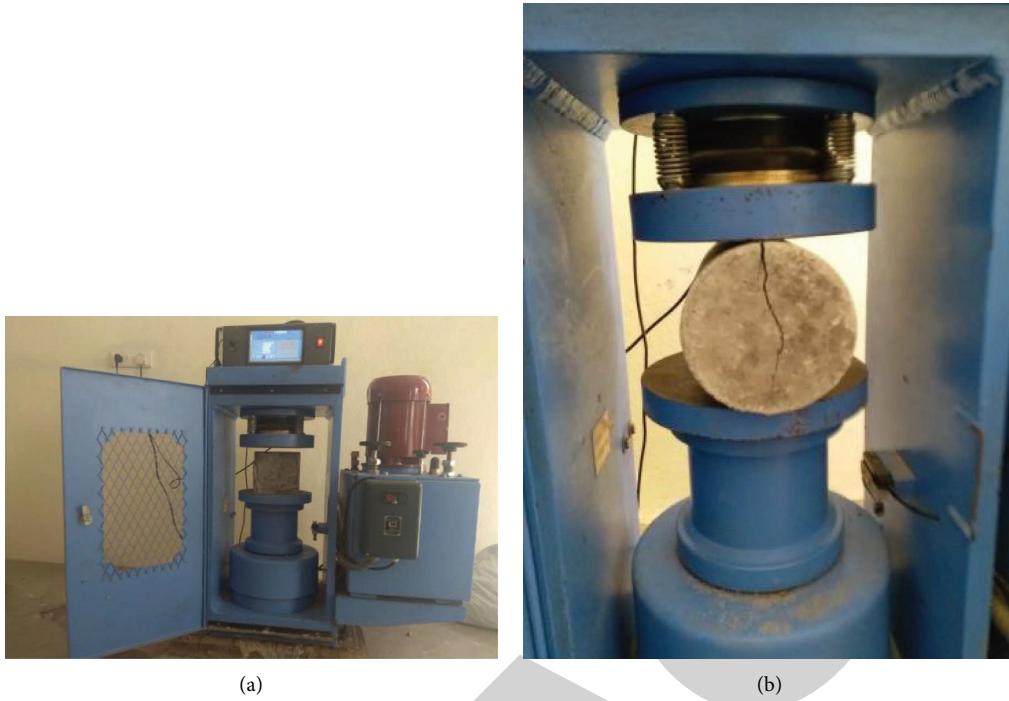


FIGURE 3: (a) Compression test setup. (b) Split tensile test setup.

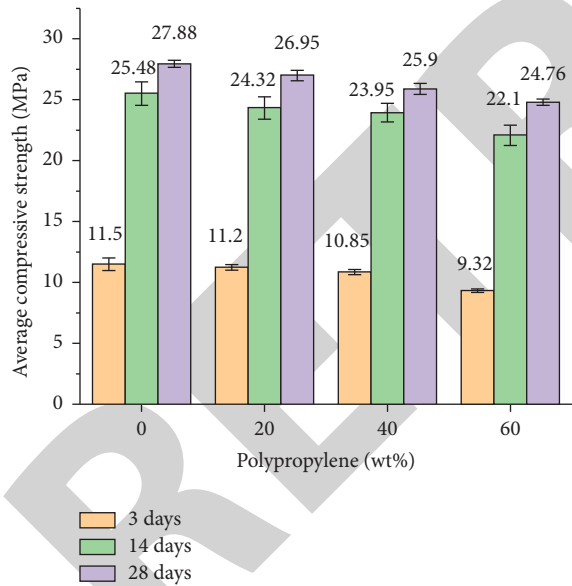


FIGURE 4: Effect of polypropylene addition in concrete on the compressive strength for different curing ages.

$$\bar{\sigma}_C = \alpha_C \Gamma_C \left( 1 + \frac{1}{\beta_C} \right), \quad (4)$$

$$\bar{\sigma}_{ST} = \alpha_{ST} \Gamma_{ST} \left( 1 + \frac{1}{\beta_{ST}} \right). \quad (5)$$

The subscript ‘C’ denotes the compressive strength and ‘ST’ denotes the split tensile strength. The scale parameter is the characteristic strength and the shape parameter is the

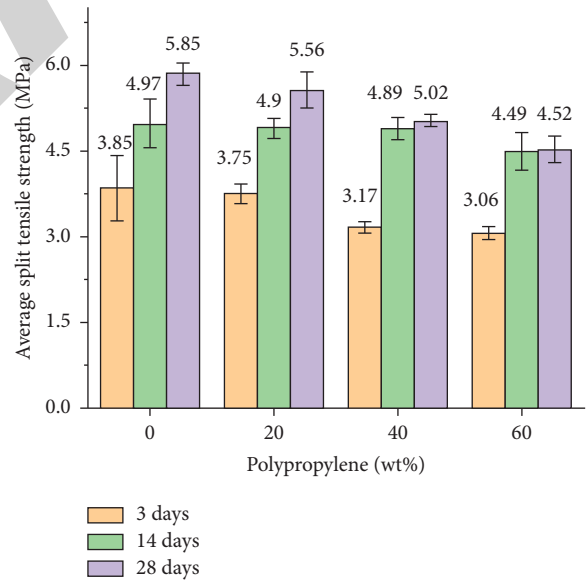


FIGURE 5: Effect of polypropylene addition in concrete on the split tensile strength for different curing ages.

Weibull modulus. These parameters can be determined by using equation (6) [39, 40].

$$\ln \left( \ln \left( \frac{1}{(1-F)} \right) \right) = \beta \ln(\bar{\sigma}) - \beta \ln(\alpha), \quad (6)$$

where  $F$  is the cumulative failure probability =  $(i - 0.3)/n + 0.4$  [41, 42];  $i$  is the current test number which varies from 1 to 3 as three specimens are tested for



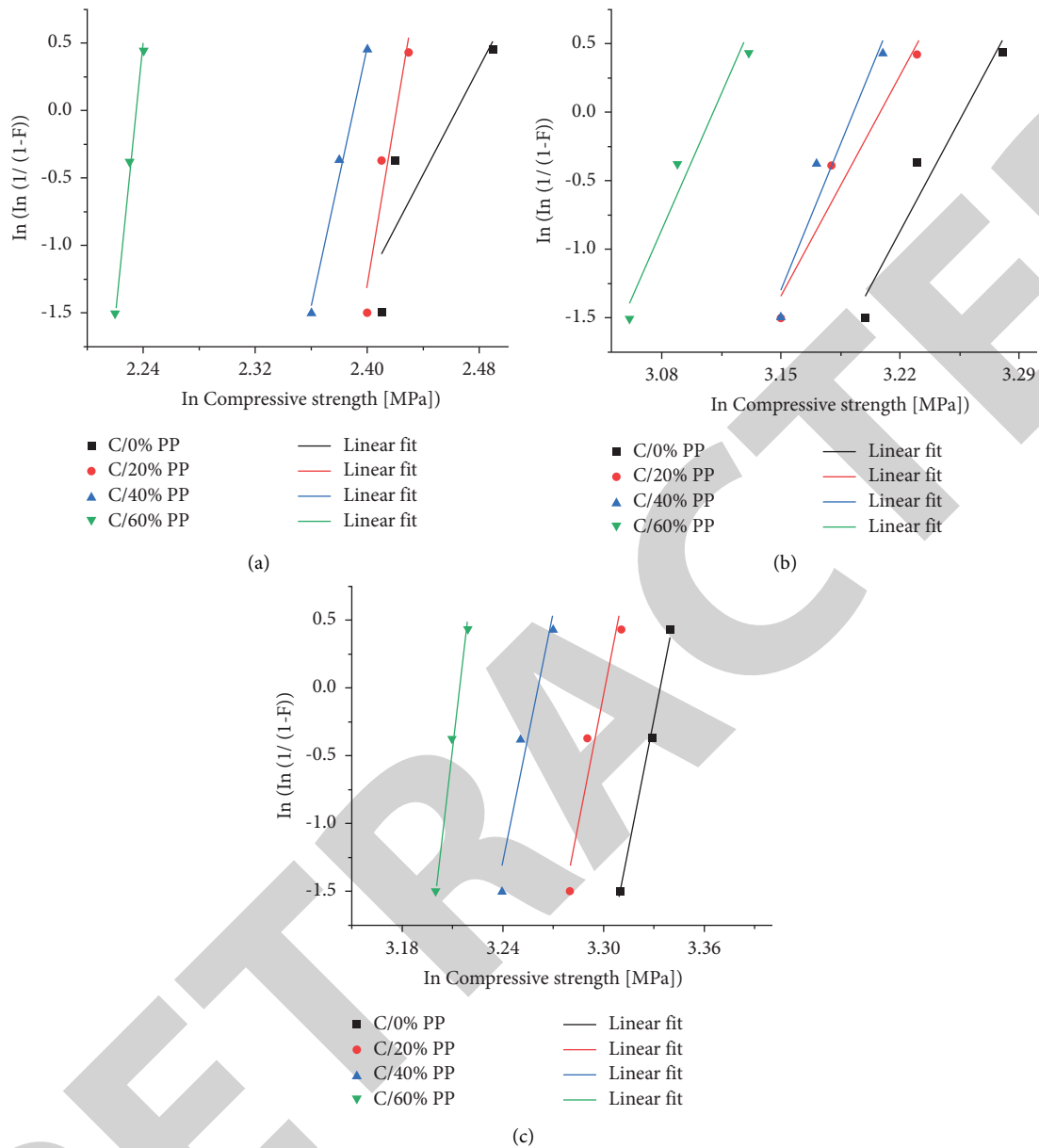


FIGURE 6: Compressive strength distributions for different curing ages of concrete specimens: (a) 3 days, (b) 14 days, and (c) 28 days.

each mixture of polypropylene-embedded concrete;  $n$  is the total number of specimens tested in each set which is equal to 3.  $\bar{\sigma}$  is the experimental compressive or split tensile strength.  $\Gamma(1 + (1/\beta))$  corresponding to  $\beta$  value is used in the gamma function data sheet.

The variability of compressive strength values for different curing ages such as 3, 14, and 28 days can be seen in Figures 6(a)–6(c), respectively. These are linear regression lines plotted using equation (6). Black, red, blue, and green color lines indicate the strength values for different weight contents of polypropylene such as 0, 20, 40, and 60%, respectively, embedded concrete specimens. Similarly, the scatter in split tensile strength values for the same curing ages of specimens are given in Figures 7(a)–7(c).

Tables 5 and 6 show the scale parameter, shape parameter, and gamma function values for the compressive

and split tensile strength values of PP-embedded concrete specimens for different curing ages, respectively. The comparison of the predicted and experimental compressive and split tensile strength values are given in Table 7. It is clear from the table that the percentage of deviation of the predicted strength values from the experimental results is less than 5%. The decrease in compressive and split tensile strength values with the increase in PP content in concrete is observed in both predicted and experimental results.

**3.3. Prediction of Compressive and Split Tensile Strength Values Using the ANN Model.** The ANN is a family of massively parallel architectures that are capable of learning and predicting the results. The basic strategy for developing a neural network-based model for material behavior is to train

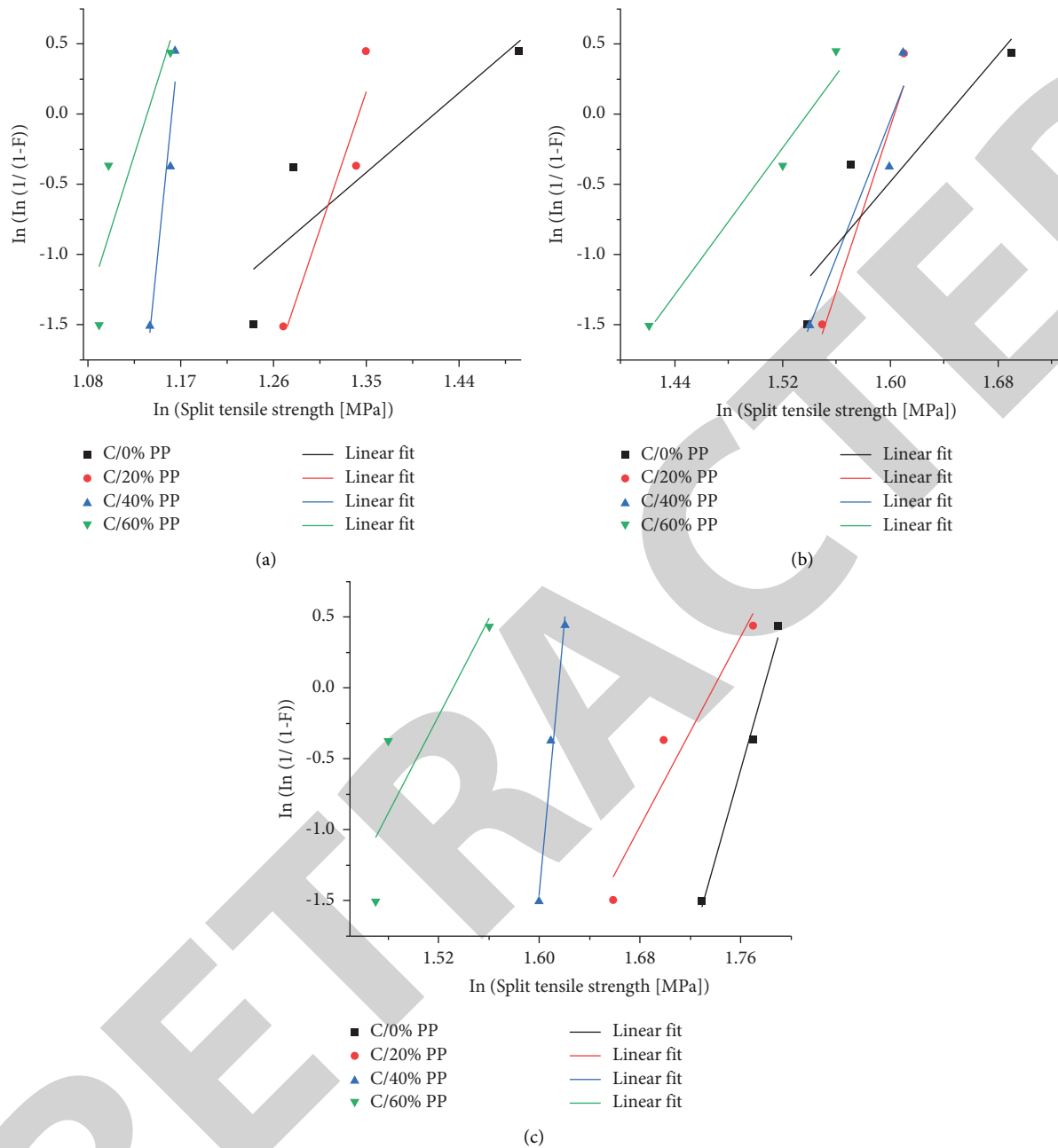


FIGURE 7: Split tensile strength distributions for different curing ages of concrete specimens: (a) 3 days, (b) 14 days, and (c) 28 days.

a neural network on the results of a series of experiments using that material [43]. If the experimental results contain relevant information about the material behavior, then the trained neural network will contain sufficient information about the material’s behavior to qualify a material for new values. Such a trained neural network not only could reproduce the experimental results but also could approximate the results in other experiments through its generalization capability [37].

The present study adopts a feed-forward supervised ANN model for the prediction of compression and split tensile strength values of different weight contents of PP-embedded concrete. The training parameters are the number

of iterations (epoch), learning rate, error goal, and the number of hidden layers. These parameters are varied until a good convergence of ANN training is obtained and thereby fixes the optimal training parameters. These optimal parameters are used for the testing and validation process. The general computational ANN model is always represented by the term topology which represents the number of neurons in the input layer, hidden layer, and output layer. However, the number of neurons in the input and output layers is determined based on the problem domain depending upon the number of input variables and the number of output or target variables. The number of hidden layers and neurons in the hidden layer is fixed during the training process.

TABLE 5: Weibull parameters for compressive strength.

Curing age days	Plastic waste addition (%)	Scale parameter ( $\alpha$ ) (MPa)	Shape parameter ( $\beta$ )	Coefficient of determination ( $R^2$ )	$\Gamma(1/(\beta) + 1)$
3	0	11.75	19.58	0.77	0.97
	20	11.26	61.21	0.92	0.98
	40	10.91	48.5	0.99	0.98
	60	9.35	97	0.99	0.99
14	0	25.96	23.43	0.95	0.97
	20	24.74	23.42	0.94	0.97
	40	24.33	30.61	0.92	0.98
	60	22.44	27.31	0.97	0.98
28	0	28.05	63.5	0.99	0.99
	20	27.13	61.22	0.92	0.98
	40	26.10	61.21	0.92	0.98
	60	24.90	97	0.99	0.99

TABLE 6: Weibull parameters for split tensile strength.

Curing age days	Plastic waste addition (%)	Scale parameter ( $\alpha$ ) (MPa)	Shape parameter ( $\beta$ )	Coefficient of determination ( $R^2$ )	$\Gamma(1/(\beta) + 1)$
3	0	4.12	6.19	0.79	0.93
	20	3.83	21.26	0.90	0.97
	40	3.19	71.57	0.94	0.99
	60	3.12	22.75	0.78	0.97
14	0	5.16	11.17	0.83	0.96
	20	4.97	29.19	0.93	0.98
	40	4.96	24.62	0.91	0.97
	60	4.64	13.36	0.98	0.96
28	0	5.92	31.75	0.99	0.98
	20	5.69	16.95	0.94	0.97
	40	5.03	97	0.99	0.99
	60	4.62	17.17	0.76	0.97

TABLE 7: Comparison of experimental and predicted strength values.

Curing age days	Plastic waste addition (%)	Compressive strength (MPa)			Split tensile strength (MPa)		
		Experiment	Prediction	% Error	Experiment	Prediction	% Error
3	0	11.50	11.40	0.88	3.85	3.83	0.52
	20	11.20	11.03	1.54	3.75	3.72	0.81
	40	10.85	10.69	1.50	3.17	3.16	0.32
	60	9.32	9.26	0.65	3.06	3.03	0.99
14	0	25.48	25.18	1.19	4.97	4.95	0.40
	20	24.32	24.00	1.33	4.90	4.87	0.62
	40	23.95	23.84	0.46	4.89	4.81	1.66
	60	22.10	21.99	0.50	4.49	4.45	0.90
28	0	27.88	27.77	0.40	5.85	5.80	0.86
	20	26.95	26.59	1.35	5.56	5.52	0.72
	40	25.90	25.58	1.25	5.02	4.98	0.80
	60	24.76	24.65	0.45	4.52	4.48	0.89

Figure 8 depicts the ANN model adopted in this study to predict the compression and split tensile strength values for different weight contents of PP-embedded concrete specimens. Here, the Levenberg–Marquardt (LM) algorithm and the Log-Sigmoid transfer function are adopted for predicting the mechanical properties. Figure 9 shows the graphical representation of ANN predicted and experimental values.

Here, all the data are convergent to the equity line. The correlation coefficient between the experimental and predicted data is 0.99. Table 8 shows the comparison of experimental and ANN predicted compressive and split tensile strength values and their respective percentage of errors. It is observed Table 8 that the deviation between the experimental and predicted results is less than 10%.



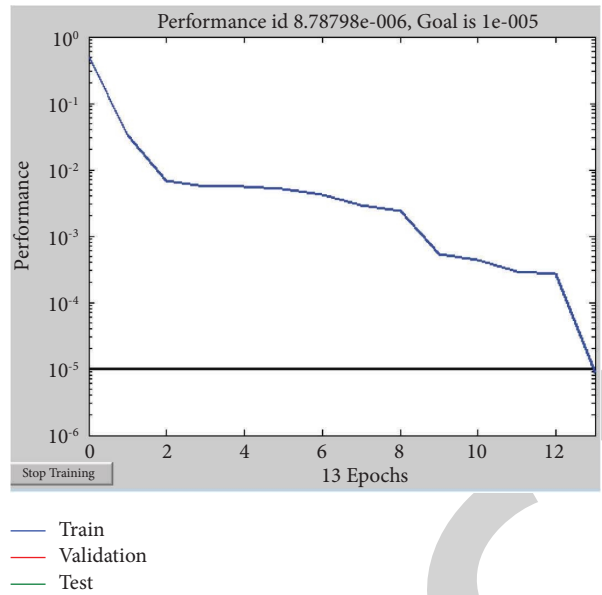


FIGURE 8: ANN training performance curve.

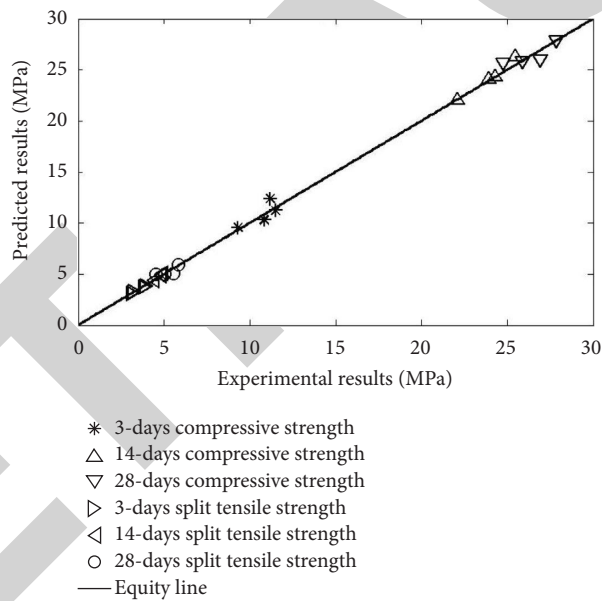


FIGURE 9: Predicted vs. experimental strength values using the ANN model.

TABLE 8: Comparison of experimental and ANN predicted strength values.

Curing age days	Plastic waste addition (%)	Compressive strength (MPa)			Split tensile strength (MPa)		
		Experiment	Prediction	% Error	Experiment	Prediction	% Error
3	0	11.50	11.24	2.28	3.85	3.83	0.41
	20	11.20	12.40	10.75	3.75	3.70	1.35
	40	10.85	10.31	4.97	3.17	3.27	3.08
	60	9.32	9.57	2.72	3.06	3.06	0.17

TABLE 8: Continued.

Curing age days	Plastic waste addition (%)	Compressive strength (MPa)		% Error	Split tensile strength (MPa)		% Error
		Experiment	Prediction		Experiment	Prediction	
14	0	25.48	26.28	3.12	4.97	5.05	1.63
	20	24.32	24.32	0.00	4.9	4.87	0.53
	40	23.95	24.03	0.35	4.89	4.82	1.51
	60	22.10	22.02	0.35	4.49	4.39	2.17
28	0	27.88	27.93	0.19	5.85	5.94	1.63
	20	26.95	26.01	3.48	5.56	5.05	9.10
	40	25.90	25.90	0.00	5.02	5.00	0.28
	60	24.76	25.71	3.82	4.52	4.97	9.87

#### 4. Conclusion

In the present work, mechanical properties for different weight percentages of polypropylene plastic wastes embedded in concrete specimens were studied. The mechanical properties were studied at different age intervals such as 3, 14, and 28 days. The compressive and split tensile strength values were predicted using two different theoretical models, the two-parameter Weibull distribution and ANN. The decrease in compressive and split tensile strengths was found in both predicted and experimental results, with the increase in polypropylene weight contents in the concrete specimens. However, the strength values for the specimens of 20% PP-embedded concrete specimens are closer to 0% PP-embedded concrete specimens. The mechanical properties were found to be increasing with the increase in the age duration from 3 to 28 days. This can be attributed to an increase in the bonding of the microstructure of the concrete specimen, which strengthens the specimen. However, the increase in mechanical properties is relatively less between 14 and 28 days compared to between 3 and 28 days, which indicate that the post-cure of the concrete specimen for a minimum of two weeks is essential. An excellent correlation is obtained between the predicted and experimental values. It can be concluded from this study that specimens of 20% PP-embedded concrete specimens can be used for primary load-bearing applications. This contributes to reduce the unit weight of the concrete.

#### Data Availability

This manuscript includes raw data recorded from the apparatus and processed data derived from raw data.

#### Conflicts of Interest

The authors declare that they have no conflicts of interest.

#### References

- [1] P. O. Awoyera and A. Adesina, "Plastic wastes to construction products: status, limitations and future perspective," *Case Studies in Construction Materials*, vol. 12, Article ID e00330, 2020.
- [2] R. Sundarakannan, V. Arumugaprabu, V. Manikandan, K. Arun Prasath, S. Vigneshwaran, and K. Naresh, "Effect of polyethylene terephthalate char on impact and erosion properties of polyester matrix composites," *Advances in Materials and Processing Technologies*, pp. 1–14, 2022.
- [3] S. Arun Karthick, T. Ragavi, K. Naresh, and P. Rama Sreekanth, "A study on collagen-PVA and chitosan-PVA nanofibrous matrix for wound dressing application," *Materials Today Proceedings*, vol. 56, pp. 1347–1350, 2022.
- [4] M. Selva Priya, K. Naresh, R. Jayaganthan, and R. Velmurugan, "A comparative study between in-house 3D printed and injection molded ABS and PLA polymers for low-frequency applications," *Materials Research Express*, vol. 6, no. 8, Article ID 085345, 2019.
- [5] A. Babafemi, B. Šavija, S. Paul, and V. Anggraini, "Engineering properties of concrete with waste recycled plastic: a review," *Sustainability*, vol. 10, no. 11, Article ID 3875, 2018.
- [6] R. Olail, V. Arumuga Prabhu, S. Daya Prasad, K. Naresh, and P. S. Rama Sreekanth, "A review on the application of bio-nanocomposites for food packaging," *Materials Today Proceedings*, vol. 56, pp. 1302–1306, 2022.
- [7] B. Jaivignesh and A. Sofi, "Study on mechanical properties of concrete using plastic waste as an aggregate," *IOP Conference Series: Earth and Environmental Science*, vol. 80, Article ID 012016, 2017.
- [8] A. Serier and D. Aoufi, "Development of new biodegradable packaging," *Advances in Materials and Processing Technologies*, vol. 3, no. 2, pp. 155–163, 2017.
- [9] L. Gu and T. Ozbakkaloglu, "Use of recycled plastics in concrete: a critical review," *Waste Management*, vol. 51, pp. 19–42, 2016.
- [10] S. Moorthi and M. Megaraj, "Indigenous development of single screw conveying machine for pyrolysis of waste plastics using nano zeolite particles in fixed bed reactor," *Advances in Materials and Processing Technologies*, pp. 1–13, 2021.
- [11] F. Colangelo, R. Cioffi, B. Liguori, and F. Iucolano, "Recycled polyolefins waste as aggregates for lightweight concrete," *Composites Part B: Engineering*, vol. 106, pp. 234–241, 2016.
- [12] A. M. Hameed and B. A. Fatah Ahmed, "Employment the plastic waste to produce the light weight concrete," *Energy Procedia*, vol. 157, pp. 30–38, 2019.
- [13] I. Mercante, C. Alejandrino, J. P. Ojeda, J. Chini, C. Maroto, and N. Fajardo, "Mortar and concrete composites with recycled plastic: a review," *Science and Technology of Materials*, vol. 30, pp. 69–79, 2018.
- [14] I. Almeshal, B. A. Tayeh, R. Alyousef, H. Alabduljabbar, and A. M. Mohamed, "Eco-friendly concrete containing recycled plastic as partial replacement for sand," *Journal of Materials Research and Technology*, vol. 9, no. 3, pp. 4631–4643, 2020.
- [15] E. A. Ohemeng and S. O. Ekololu, "Strength prediction model for cement mortar made with waste LDPE plastic as fine

## *Retraction*

# **Retracted: A Study of Structural Parameters Effects on Pressure Differential to Roll Titanium Diaphragm for a Spacecraft Propellant Tank**

### **Advances in Materials Science and Engineering**

Received 26 December 2023; Accepted 26 December 2023; Published 29 December 2023

Copyright © 2023 Advances in Materials Science and Engineering. This is an open access article distributed under the Creative Commons Attribution License, which permits unrestricted use, distribution, and reproduction in any medium, provided the original work is properly cited.

This article has been retracted by Hindawi, as publisher, following an investigation undertaken by the publisher [1]. This investigation has uncovered evidence of systematic manipulation of the publication and peer-review process. We cannot, therefore, vouch for the reliability or integrity of this article.

Please note that this notice is intended solely to alert readers that the peer-review process of this article has been compromised.

Wiley and Hindawi regret that the usual quality checks did not identify these issues before publication and have since put additional measures in place to safeguard research integrity.

We wish to credit our Research Integrity and Research Publishing teams and anonymous and named external researchers and research integrity experts for contributing to this investigation.

The corresponding author, as the representative of all authors, has been given the opportunity to register their agreement or disagreement to this retraction. We have kept a record of any response received.

### **References**

- [1] T. Ma, S. Gu, J. Zhao, B. Yu, J. Zhang, and W. Yang, "A Study of Structural Parameters Effects on Pressure Differential to Roll Titanium Diaphragm for a Spacecraft Propellant Tank," *Advances in Materials Science and Engineering*, vol. 2022, Article ID 2003905, 10 pages, 2022.

## Research Article

# A Study of Structural Parameters Effects on Pressure Differential to Roll Titanium Diaphragm for a Spacecraft Propellant Tank

Tianju Ma, Sendong Gu , Jipeng Zhao, Bin Yu, Jianjun Zhang, and Wenbo Yang

Science and Technology on Vacuum Technology and Physics Laboratory, Lanzhou Institute of Physics, Lanzhou 730000, China

Correspondence should be addressed to Sendong Gu; [cast510\\_gsd@163.com](mailto:cast510_gsd@163.com)

Received 22 June 2022; Accepted 3 October 2022; Published 8 November 2022

Academic Editor: K. Raja

Copyright © 2022 Tianju Ma et al. This is an open access article distributed under the Creative Commons Attribution License, which permits unrestricted use, distribution, and reproduction in any medium, provided the original work is properly cited.

A range of titanium diaphragms for spacecraft propellant tanks are designed in detail, and two typical titanium diaphragms were manufactured and corresponding reversal tests were developed. A series of finite element models of the reversal process of these titanium diaphragms is developed based on the arc-length method and a finite element analysis software. With the aid of the models, this paper analyzes the characteristics of pressure drop during the whole reversal process and investigates the effects of the structural parameters on pressure differential to roll titanium diaphragm. The results show that simulated values of the critical pressure and the overturning pressure show good agreement with measured ones. In addition, the critical pressure increases with increasing thickness, decreasing bottom diameter and chamfering radius. The thickness and the bottom diameter are the main influence factors for the critical pressure. The overturning pressure increases with increasing thickness and arc radius. These effects of the bottom diameter, the chamfering radius, and arc radius become sharper with increasing thickness.

## 1. Introduction

Diaphragm tanks are one of the most practical positive expulsion devices, which are extensively used in spacecraft propellant systems. The devices are capable to store and manage common liquid propellants, when the station keeping, orbit, and altitude control for spacecrafts are carried out. In most cases, a diaphragm tank mainly consists of four components, including a top hemispherical shell, a diaphragm, a bottom hemispherical shell, and a retaining ring. Its working principle is shown in Figure 1. The top and bottom hemispherical shells can suffer a certain internal pressure. The diaphragm separates the internal chamber of the two hemispherical shells into two parts as a barrier, including a gas chamber and a liquid chamber when the tank contains a liquid propellant. The diaphragm will be rolled by pressure differential between the two chambers, and the propellant will be expelled from its storage chamber subsequently.

The diaphragm is the key component of the tank. In the past, most of them are made from a thin material with better ductility, such as rubber materials, which are flexible enough

to couple to the internal surface of the shell and adjust the shape at all fill-levels. Some works [1–6] have been performed on the spacecraft propellant tanks with rubber diaphragms. However, the common propellants like hydrazine, MMH, and  $N_2O_4$  are not compatible with the rubber materials [7–9]. As of recent, in order to meet the requirement of long-term propellant storage, the focus of research has been on the feasibility of metallic diaphragms, including titanium diaphragms and aluminum diaphragms [10]. Lenahen et al. [11] investigated the liquid slosh behaviors in spacecraft propellant tanks with metal diaphragms by computational and experimental analysis. Conomos et al. [8] and Marvih et al. [12] developed a titanium tank and aluminum diaphragm tanks, respectively, the motions of these diaphragms were also characterized. Instead of conventional rubber diaphragms, the plastic deformation is dominant during the reversal process [8, 13]. As a key parameter for guiding structural design, the pressure differential to roll the metal diaphragm is affected by its structural parameters complexly. Therefore, further studies on the effects are still essential.

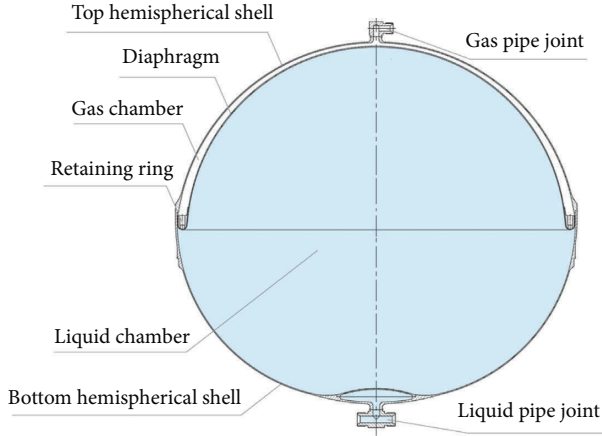


FIGURE 1: Schematic diagram of a diaphragm tank.

In this work, a range of titanium diaphragms are designed in detail. The effects of structural parameters on pressures differential to roll these diaphragms are investigated by combining the method of experimental observation, numerical simulation, and theoretical analysis.

## 2. Titanium Diaphragm Structure and Experimental Setup

**2.1. Titanium Diaphragm Structure.** The titanium alloy used in this investigation is TA1ELI, which is a titanium-based alloy. Its chemical composition is given in Table 1. As the basic structure of a common titanium diaphragm is shown in Figure 2, the diaphragm is a thin shell structure, where thickness increases from the bottom to the top. A chamfering structure is set up as a flanging section at the bottom of the diaphragm to mount the retaining ring. An arc section is employed to fit the interior shape of the top hemispherical shell. In order to deform steadily at the beginning of reversal process, a cone section is designed between the flanging section and the arc section. The structural parameters for the diaphragm, such as the thickness,  $T$ , the bottom diameter,  $D_b$ , the chamfering radius,  $R_f$ , the arc radius,  $R_a$ , the height,  $H$ , and the angle of cone section,  $\alpha$  are significant [14–17], which affect the service properties of the diaphragm, especially the pressure drop. In general,  $H$  is limited by the height of tanks and  $\alpha$  is defined as a constant to simplify the design. So the effects of key structural parameters, including  $T$ ,  $D_b$ ,  $R_f$ , and  $R_a$  are studied in this work. Two typical titanium diaphragms were designed and manufactured, and key structural parameters are listed in Table 2.

**2.2. Diaphragm Reversal Tests.** In order to investigate the performance of the titanium diaphragm experimentally, reversal tests were developed. Figure 3 illustrates a schematic diagram of the test process. Before test, the gas pipe joint of the tank was connected to a gas pressure controller via a buffer vessel. Then, water was replaced for hydrazine propellant due to similar liquid specifications [18–20] to be filled into the liquid chamber from the liquid pipe joint.

TABLE 1: Chemical composition of TA1ELI (wt (%)).

Fe	Si	C	N	H	O
$\leq 0.05$	0.01	$\leq 0.10$	0.003	0.0008	0.035

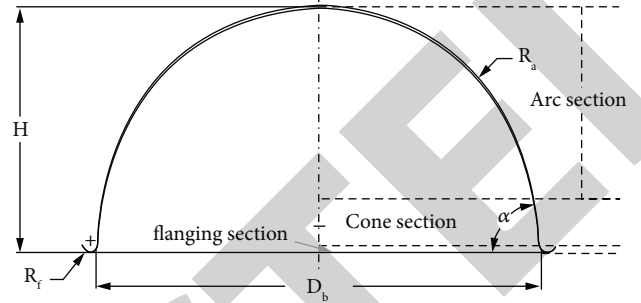


FIGURE 2: Basic structure of a common titanium diaphragm.

Subsequently, a pressure differential transducer was placed and measured the pressure differential between the gas chamber and the liquid chamber. The pressure differential and the corresponding volumetric change of the liquid chamber were measured at a base gas pressure of 0.02 MPa until the final gas pressure of 0.5 MPa was obtained. Figure 4 provides the initial titanium diaphragms and the deformed ones when rolled fully.

## 3. Finite Element Simulation Setup

In order to investigate the effects of the structural parameters on pressure differential, finite element (FE) models of the reversal process of all the designed titanium diaphragms are developed based on the arc-length method and a FE analysis software. This part concentrates on the procedure of simulation development. The validity of the FE models is verified by the above experimental results.

**3.1. Diaphragm Geometries.** Except for the above two designed diaphragms, a range of titanium diaphragms are designed in detail. These diaphragms can be divided into four broad groups based on their interior dimensions as shown in Figure 5. The dimensions of the thickness,  $T$  and the chamfering radius,  $R_f$  for every group are listed in Table 3. It means that there are 12 designed titanium diaphragms for every group.

**3.2. Theoretical Approach.** The deformation of metal diaphragms during the reversal process is a complex nonlinear structural response with strain softening, which is characterized by the drop of stress after achieving the peak value. In this case, nonlinear FE analysis is likely to suffer from convergence issues [21, 22]. To overcome this problem, the so-called arc-length method has been proposed and developed by numerous researchers [23, 24] to compute complex equilibrium paths in nonlinear structural mechanics problems.

TABLE 2: Key structural parameters of two diaphragms.

Serial number	T (mm)			$D_b$ (mm)	$R_f$ (mm)	$R_a$ (mm)
	Flanging section	Cone section	Arc section			
E1	1.00	1.00	1.00–1.50	433.4	5	216.0
E2	1.00	1.00	1.00–1.50	599.4	6	278.7

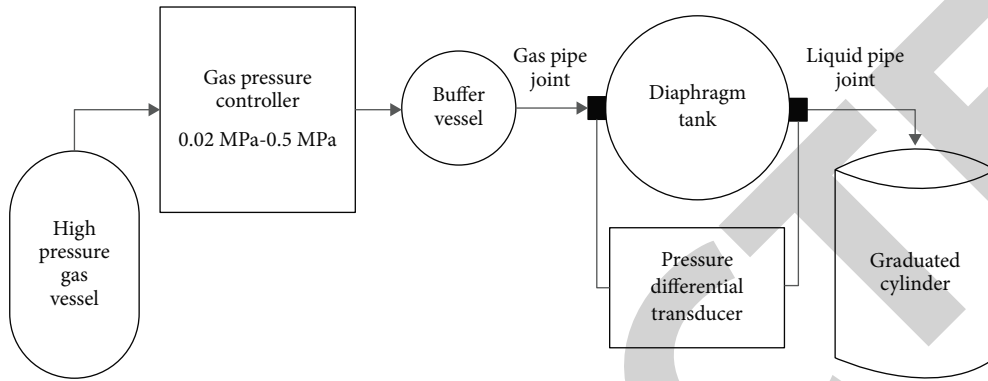


FIGURE 3: Schematic diagram of the reversal test process.

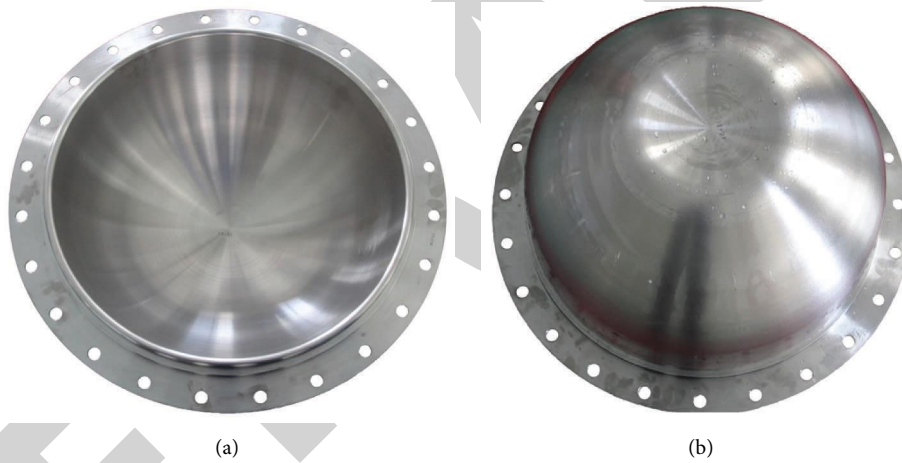


FIGURE 4: Initial titanium diaphragm (a) and the deformed ones when rolled fully (b).

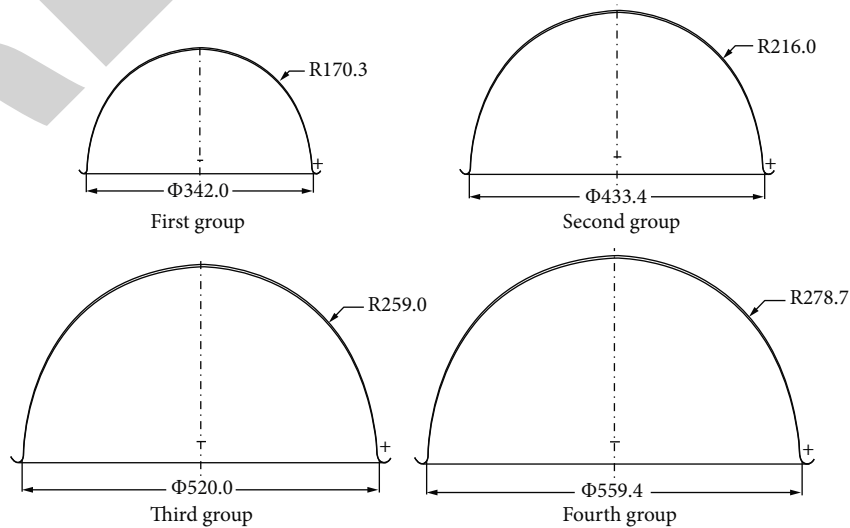


FIGURE 5: Interior dimensions of titanium diaphragms for every group.



TABLE 3: Dimensions of the thickness, T and the chamfering radius,  $R_f$  for every group.

T (mm)			$R_f$ (mm)
Flanging section	Cone section	Arc section	
0.40	0.40	0.56–0.60	5, 6, 7
0.60	0.60	0.84–0.90	5, 6, 7
0.80	0.80	1.12–1.20	5, 6, 7
1.00	1.00	1.40–1.50	5, 6, 7

When adapting the FE method for computing numerical solutions, the approximation of the nonlinear structural mechanics problem can be expressed as follows:

$$\mathbf{R}(\mathbf{u}, \lambda) = \mathbf{F}_{\text{int}}(\mathbf{u}) - \lambda \mathbf{F}_{\text{ext}} = 0. \quad (1)$$

Here  $\mathbf{R}$  has been defined as the residual vector,  $\mathbf{u}$  is the nodal displacement vector,  $\lambda$  is the load factor,  $\mathbf{F}_{\text{int}}(\mathbf{u})$  and  $\mathbf{F}_{\text{ext}}$  denote the internal force vector and the external force vector, respectively.

Generally, equation (1) is solved by means of an incremental approach. So the nodal displacement vector  $\mathbf{u}_{n+1}$  and the load factor  $\lambda_{n+1}$  at the current load step are defined as:

$$\mathbf{u}_{n+1} = \mathbf{u}_n + \Delta \mathbf{u}, \quad (2)$$

$$\lambda_{n+1} = \lambda_n + \Delta \lambda, \quad (3)$$

where  $\Delta \mathbf{u}$  and  $\Delta \lambda$  are the increments of the nodal displacement vector and the load factor at the current step,  $\mathbf{u}_n$  and  $\lambda_n$  represent their respective values at the previously converged load step.

After substituting the equations (2) and (3) into equation (1), the residual vector at the current load step can be written as:

$$\mathbf{R}(\mathbf{u}_{n+1}, \lambda_{n+1}) = \mathbf{F}_{\text{int}}(\mathbf{u}_{n+1}) - \lambda_{n+1} \mathbf{F}_{\text{ext}} = 0. \quad (4)$$

To solve the under-determined system in equation (4), in the arc-length method, an additional equation, called as the arc-length equation, is proposed, which is given as [25–27]:

$$[\Delta \mathbf{u}]^T [\Delta \mathbf{u}] + \psi [\Delta \lambda]^2 \mathbf{F}_{\text{ext}}^T \mathbf{F}_{\text{ext}} = [\Delta s]^2, \quad (5)$$

where  $s$  is the arc-length parameter, and  $\Delta s$  is its increment. The different arc-length schemes can be determined by adjusting the scalar parameter,  $\psi$ .

For a given  $\Delta s$ , (4) and (5) equations are solved by applying the Newton–Raphson scheme.

**3.3. Finite Element Model.** Based on FE software MSC. Marc, the initial FE models of the reversal process of the titanium diaphragms are developed, a representative FE mesh is shown in Figure 6. Due to the characteristics of axial symmetry, the preliminary FE mesh with 10240 regular solid shell elements is established. The thickness distributions of the diaphragms are implemented by a user subroutine. Figure 7 presents an example of a thickness model with range of 0.6 mm–0.9 mm and the corresponding FE model. The material properties for these simulations, including

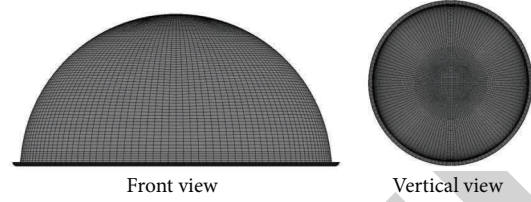


FIGURE 6: Preliminary FE mesh of the reversal process.

Young's modulus, Poisson's ratio, and density are 100 GPa, 0.34, and 4540 kg/m<sup>3</sup>, respectively, and its plastic flow stress curve is shown in Figure 8. A face pressure is loaded on the outside surface of the FE mesh using the follower force function. All the nodes on the fillet edge are constrained in all directions.

## 4. Results and Discussion

### 4.1. Pressure Drop Characteristics and Model Verification.

The relationships of pressure differential and apex axial displacement of two diaphragms are illustrated in Figure 9. It is clear that each of the curves change abruptly at two points, named critical point, such as A1 and A2, and overturning point, such as B1 and B2. The pressure differential at critical point refers to the critical pressure which begins to derive the deformation of the diaphragm. The one at the overturning point represents the overturning pressure which overturns the diaphragm completely. The simulated values of the critical pressure for the two diaphragms are 0.12 MPa and 0.097 MPa, respectively. The ones of overturning pressure are 0.55 MPa and 0.32 MPa. After the pressure exceeds the critical value, there are a local instable stage (LIS) and a stability stage (SS), and pressure differential changes slowly and apex axial displacement increases rapidly. In addition, the pressure differential displays an increasing tendency with the increase of apex axial displacement. This variation is related to the thickness distribution and the radial size of the diaphragm. The pressure differential gradient increases severely at the beginning of the reversal process because the arc segment of flanging gradually becomes straight.

In order to verify the simulated results, the comparisons between the simulated pressure differential data and experimental ones are also performed in these Figures. It is observed that the simulated results well agree with the experimental ones.

### 4.2. Effects of Structural Parameters on Pressure Differential.

The relationships of pressure differential and apex axial displacement under different structural parameters can be obtained from the simulation results. The ones for the first group diaphragms are shown in Figure 10(a), and the ones for the diaphragms with the same thickness and chamfering radius but different bottom diameter and arc radius are shown in Figure 10(b). These curves have the same tendency but different local values. The critical pressure and the overturning pressure are observed obviously. It is found that the thickness,  $T$ , the bottom diameter,  $D_b$ , and the chamfering radius,  $R_f$  have effects on the critical

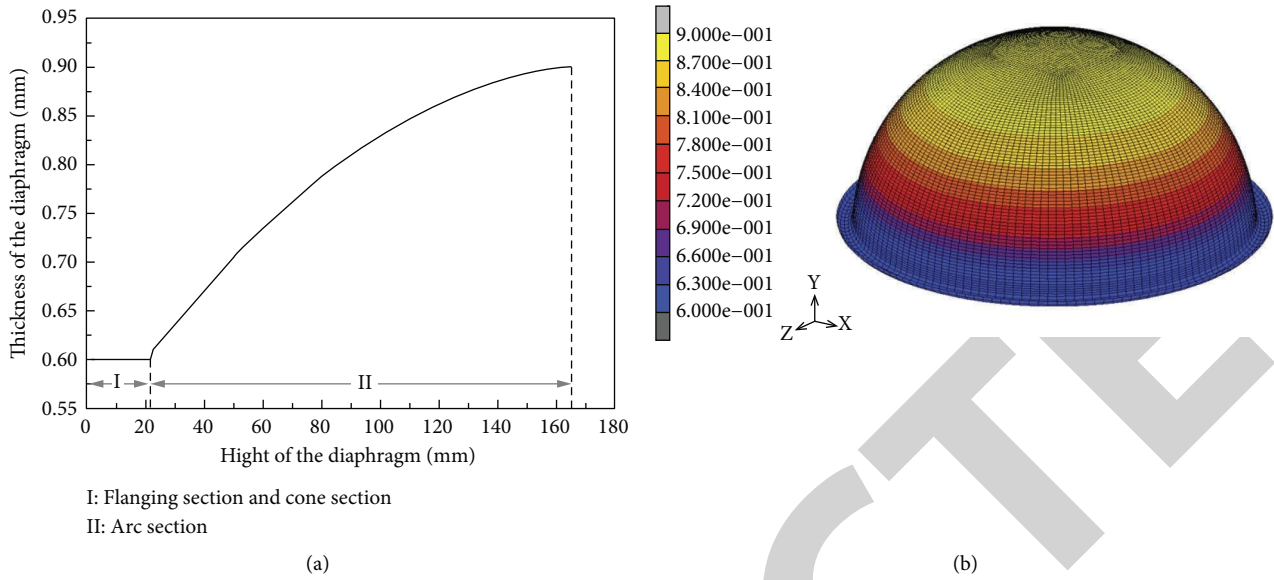


FIGURE 7: A thickness model (a) and the corresponding FE model (b).

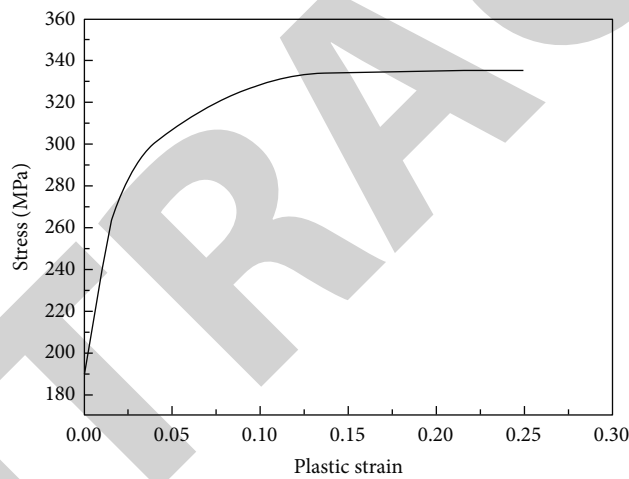


FIGURE 8: Plastic flow stress curve used in the FE model.

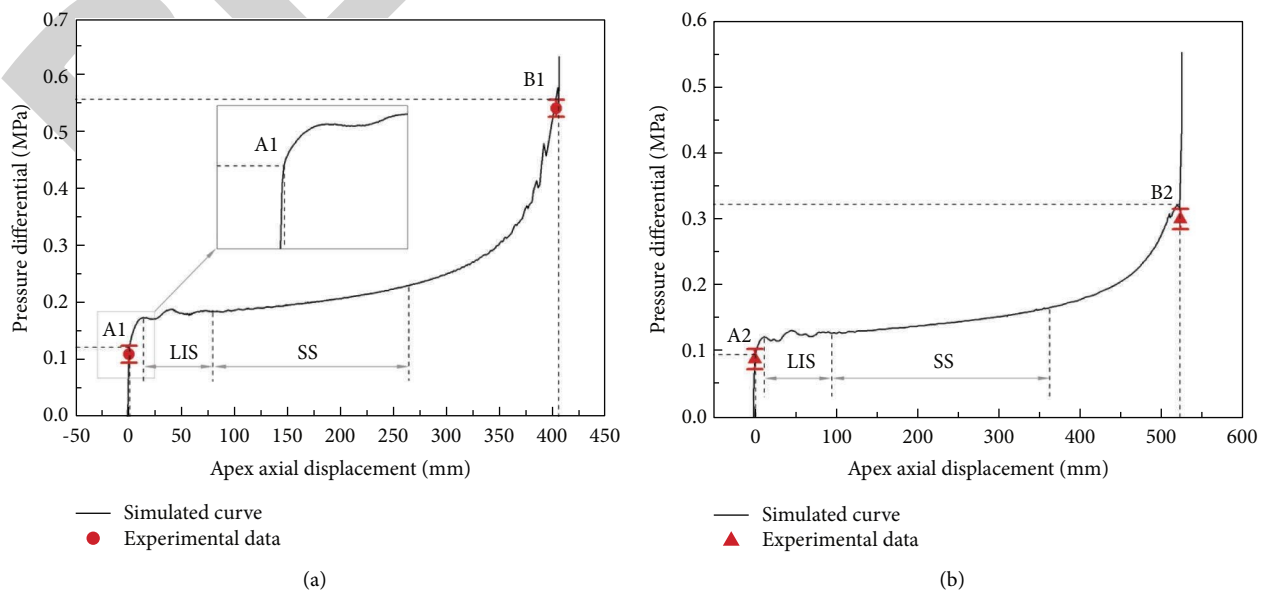


FIGURE 9: Relationships of pressure differential and apex axial displacement of the diaphragms. (a) Serial number E1, (b) Serial number E2.



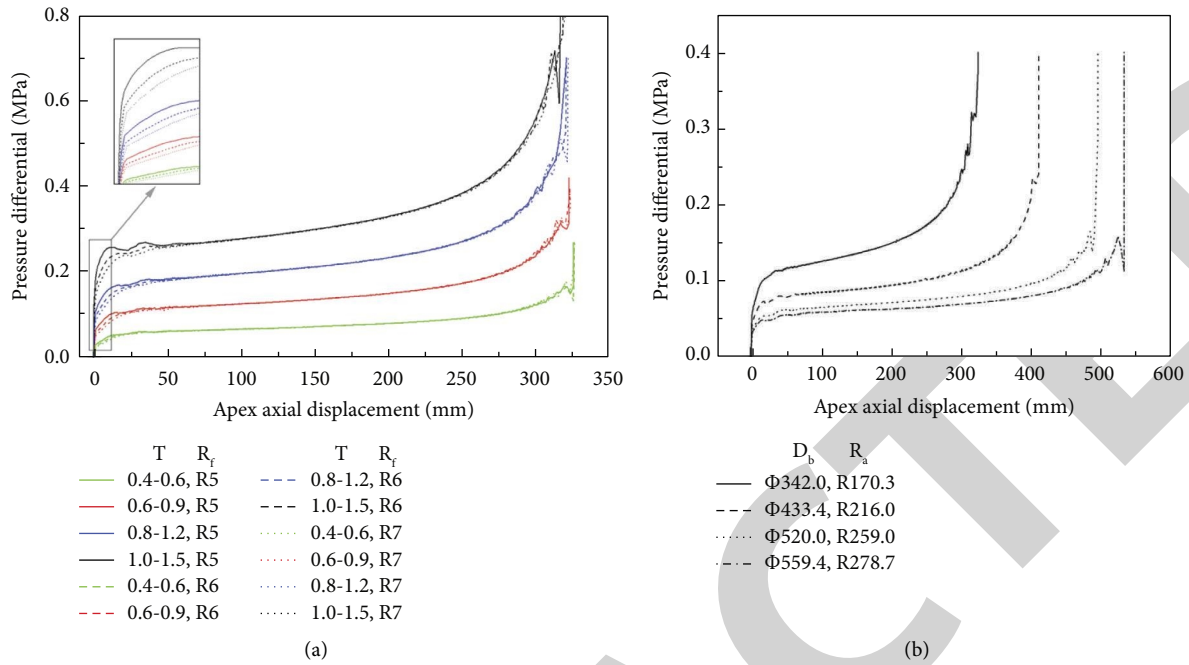


FIGURE 10: Relationships of pressure differential and apex axial displacement for the first group diaphragms (a); the diaphragms with same T and R<sub>f</sub> (b).

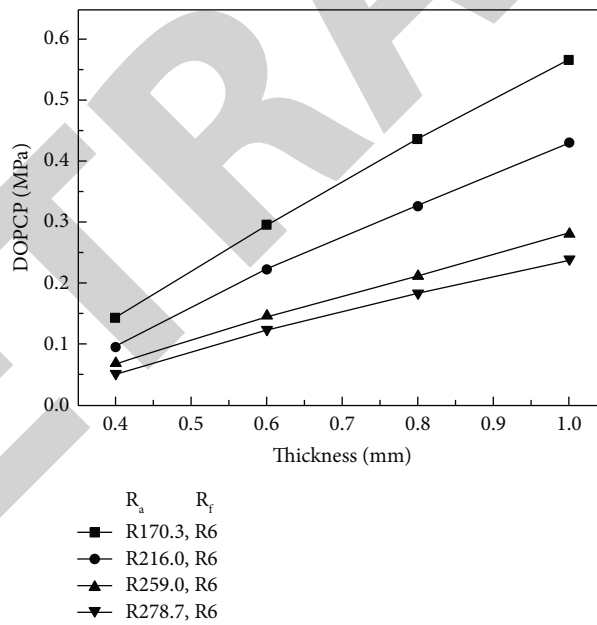


FIGURE 11: Variation of DOPCP and thickness.

pressure, and the effects of T and D<sub>b</sub> are more significant. The overturning pressure is affected by the thickness, T, and the arc radius, R<sub>a</sub> obviously.

In addition, the local instable phenomena become unclear with the decrease of the thickness. The differences of the overturning pressure and the critical pressure (DOPCP) increase with increasing thickness and decreasing arc radius as shown in Figure 11. The results indicate that the decrease of thickness leads to reducing the

pressure differential, and further is beneficial to reducing the weight of the pressurizing system for titanium diaphragm tanks. However, if the thickness is too small, the structure of the diaphragm will become unstable. A polygon boundary is formed on the deformation position at the beginning of the reversal process, as shown in Figure 12(a). The strain localizations take place at the polygon vertexes, which will result in local cracks under poor pressure differential control.

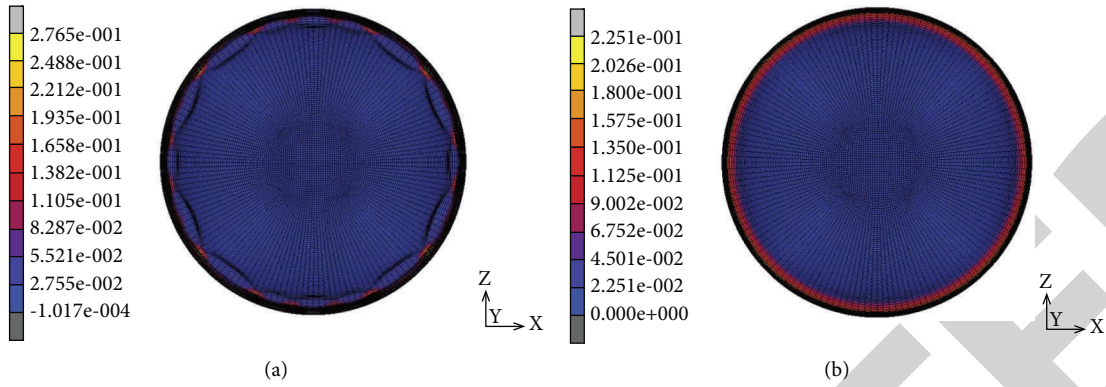
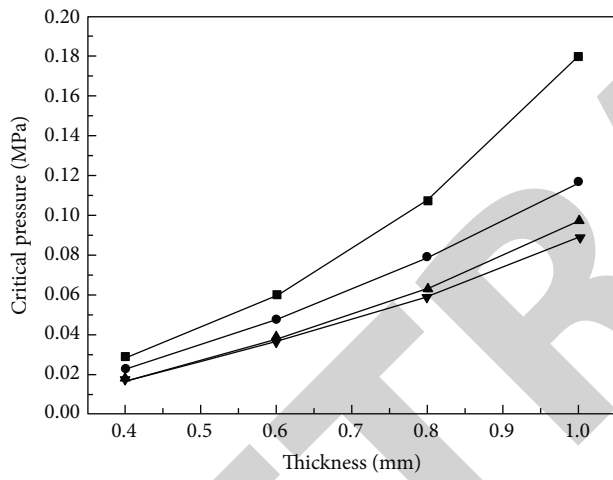
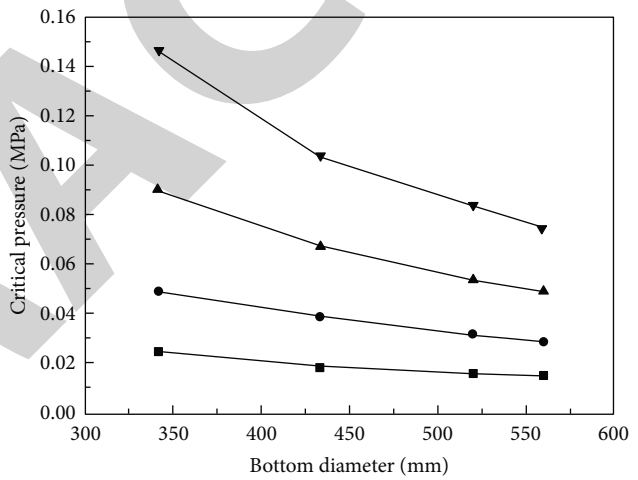


FIGURE 12: Comparisons of the shape and the plastic strain for the fourth group diaphragms. (a) Thickness: 0.4 mm–0.6 mm; (b) Thickness: 1.0 mm–1.5 mm.



- $\Phi_{342.0}, R_5$
- $\Phi_{433.4}, R_5$
- ▲  $\Phi_{520.0}, R_5$
- ▼  $\Phi_{559.4}, R_5$

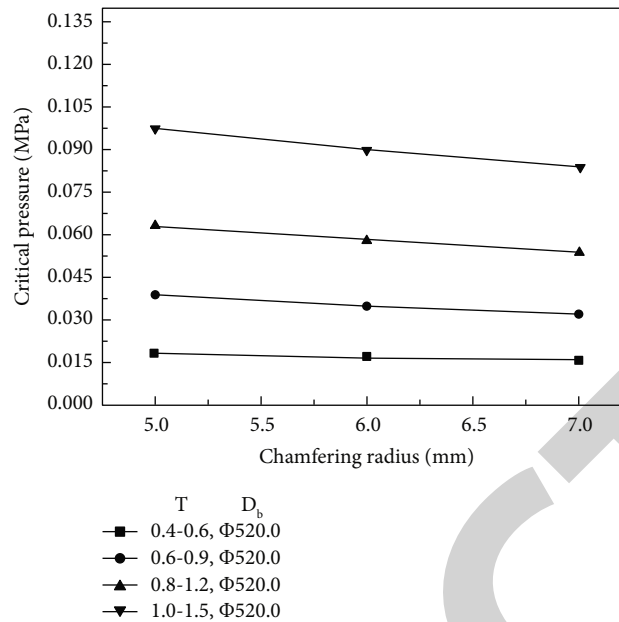
(a)



- 0.4-0.6, R7
- 0.6-0.9, R7
- ▲ 0.8-1.2, R7
- ▼ 1.0-1.5, R7

(b)

FIGURE 13: Continued.



(c)

FIGURE 13: Effects of structural parameters on the critical pressure. (a) Thickness effects; (b) Bottom diameter effects; (c) Chamfering radius effects.

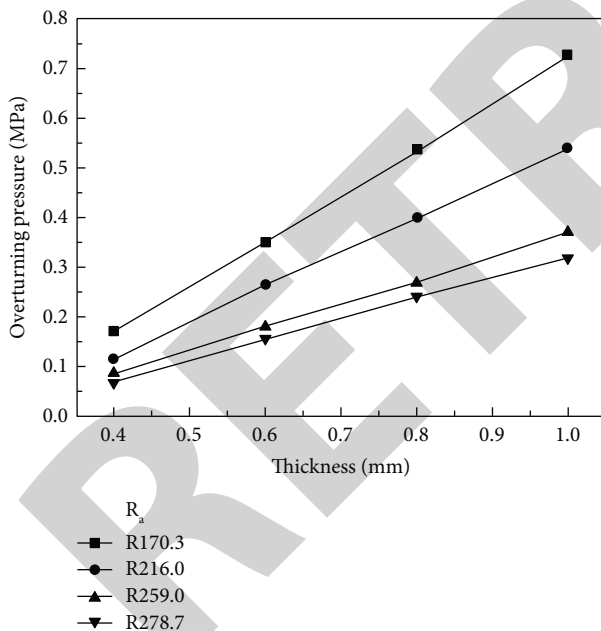


FIGURE 14: Effects of structural parameters on the overturning pressure.

The values of the critical pressure and the overturning pressure for every group are collected. The effects of the thickness,  $T$ , the bottom diameter,  $D_b$ , and the chamfering radius,  $R_f$  on the critical pressure are shown in Figure 13. The values of the critical pressure range from 0.015 MPa to 0.18 MPa. The equivalent von Mises stress at the deformed

regions is larger than those in other regions. The maximum value is 249.5 MPa–266 MPa, which is far larger than the yield strength of TA1ELI. The increase of thickness, decreasing bottom diameter, and chamfering radius increase the deformation resistance of metal. So the critical pressure increases with the increasing thickness, decreasing bottom diameter and chamfering radius, and the thickness and the bottom diameter make the main contributions to the variation. Instead of the curve tendencies in Figure 13(c), nonlinear increases and decreases present in Figures 13(a) and 13(b), and these tendencies become sharper with increasing thickness. The effect of the thickness,  $T$  and the arc radius,  $R_a$  are shown in Figure 14. The values of the overturning pressure range from 0.07 MPa to 0.73 MPa. The overturning pressure increases with the increasing thickness and arc radius. It is interesting to notice that near-linear relationships between the overturning pressure and the thickness are remarkable. It is easy to predict the critical pressure and the overturning pressure by the above tendencies.

## 5. Conclusions

In this work, the effects of structural parameters on pressure differential to roll titanium diaphragms are investigated. The following conclusions have been drawn from the results of this investigation.

- (1) The relationships of pressure differential and apex axial displacement of the diaphragms change abruptly at two points, including a critical point and an overturning point. After the pressure exceeds the critical value, there are a local instable stage and a

stability stage. Simulated values of the critical pressure and the overturning pressure show good agreement with measured ones.

- (2) The local instable phenomena become unclear with the decrease of the thickness. The decrease of thickness is beneficial to reduce the weight of pressurizing system for titanium diaphragm tanks. If the thickness is too small, the strain localizations take place on the deformation position at the beginning of the reversal process, which will result in local cracks under poor pressure differential control.
- (3) The critical pressure increases with increasing thickness, decreasing bottom diameter, and chamfering radius. The thickness and the bottom diameter are the main influence factors for the critical pressure. The overturning pressure increases with increasing thickness and arc radius. These effects of the bottom diameter, the chamfering radius, and arc radius become sharper with increasing thickness.

### Data Availability

The data used to support the findings of the manuscript are included within this article.

### Conflicts of Interest

The authors declare that they have no conflicts of interest.

### Acknowledgments

The authors would like to express their gratitude to the financial support by the National Natural Science Foundation of China (Nos. 51801090).

### References

- [1] J. Vincent, J. M. Carella, and A. P. Csilino, "Thermal analysis of the Girth Weld of an Elastomeric diaphragm tank," *Journal of Materials Processing Technology*, vol. 214, no. 2, pp. 428–435, 2014.
- [2] B. Lenahen, S. Gangadharan, and M. Desai, "A computational and experimental analysis of spacecraft propellant tanks implemented with flexible diaphragms," in *54th AIAA/ASME/ASCE/AHS/ASC Structures, Structural Dynamics, and Materials Conference* Boston, Massachusetts, 2013.
- [3] H. Zhang, S. D. Gu, J. J. Zhang et al., "Development of titanium diaphragms for Space propellant tank," in *Proceedings of the 2022 International Conference on Advanced Control, Automation and Robotics*, Guangzhou, China, March 2022.
- [4] H. Sabaghzadeh and M. Shafae, "Investigation of modal properties and Layout of Elastomer diaphragm tanks in Telecommunication Satellite," *Microsystem Technologies*, vol. 26, no. 6, pp. 1931–1959, 2020.
- [5] D. Sances, S. Gangadharan, J. Sudermann, and B. Marsell, "CFD Fuel slosh modeling of Fluid-structure Interaction in spacecraft propellant tanks with diaphragms," in *51st AIAA/ASME/ASCE/AHS/ASC Structures, Structural Dynamics, and Materials Conference* Orlando, Florida, 2010.
- [6] A. Leal-Junior, A. Frizera, and C. Marques, "A Fiber Bragg Gratings Pair Embedded in a Polyurethane diaphragm: towards a Temperature-insensitive pressure Sensor," *Optics & Laser Technology*, vol. 131, Article ID 106440, 2020.
- [7] K. Anflo and R. Möllerberg, "Flight Demonstration of New Thruster and Green propellant Technology on the PRISMA Satellite," *Acta Astronautica*, vol. 65, no. 9–10, pp. 1238–1249, 2009.
- [8] H. A. Conomos, C. G. Alongi, J. Moore et al., "Development of 10 inch diameter titanium rolling metal diaphragm tank for Green propellant," in *53rd AIAA/SAE/ASEE Joint Propulsion Conference* Atlanta Georgia, July 2017.
- [9] I. Ballinger, W. Lay, and W. Tam, *Review and History of PSI Elastomeric Diaphragm Tanks*, (in English) American Institute of Aeronautics and Astronautics, Reston, Virginia, USA, 1995.
- [10] X. Lei, Y. Deng, Z. Yin, and G. Xu, "Tungsten Inert gas and Friction Stir Welding characteristics of 4-mm-Thick 2219-T87 Plates at Room Temperature and -196°C," *Journal of Materials Engineering and Performance*, vol. 23, no. 6, pp. 2149–2158, 2014.
- [11] B. Lenahen, A. Bernier, S. Gangadharan, J. Sudermann, and B. Marsell, "A computational investigation for determining the Natural Frequencies and Damping effects of diaphragm-implemented spacecraft propellant tanks," in *53rd AIAA/ASME/ASCE/AHS/ASC Structures, Structural Dynamics and Materials Conference* Honolulu Hawaii, April 2012.
- [12] M. Marvih, H. Kammerer, and J. Gidley, *Parametric Evaluation of Contoured Aluminum Diaphragm, Positive Expulsion Tanks*, American Institute of Aeronautics and Astronautics, Reston, Virginia, USA, 1992.
- [13] Q. Yang, R. Tao, and P. Wen, "Optimization design of Smart reversible diaphragms using shape Memory Polymer," in *Proceedings of the Advances in Structural and Multidisciplinary Optimization: Proceedings of the 17th World Congress of Structural and Multidisciplinary Optimization (WCSMO17)*, pp. 549–561, January 2018.
- [14] S. Ding and F. G. Meng, "A Review on design method for storage tank of metal diaphragm with variable thickness," *J. Shenyang Inst. Aeron. Eng.*, vol. 36, no. 2, pp. 9–14, 2019.
- [15] S. Yuan, Z. C. Ma, X. L. Zhou, and Z. Liu, "Influence of thickness on Turning characteristics of a diaphragm in a titanium tank," *Mach. Tool Hydraul.*, vol. 46, no. 11, pp. 135–139, 2018.
- [16] F. Huang, T. Cheng, X. Q. Zhu, and Z. Liu, "Effect of Pre-bending radius of Flange on the Flipping behavior of the metal Tank's diaphragm," *Journal of Machine Design*, vol. 36, no. 4, pp. 45–48, 2019.
- [17] H. F. Qiang, S. Zhou, X. R. Wang, and G. Wang, "Effect of angle on expulsion behavior of Spherical-cone metallic diaphragms for positive expulsion tanks," *Engineering Mechanics*, vol. 30, no. 4, pp. 435–441, 2013.
- [18] J. Klatte, N. Darkow, R. Gajdacz, and S. Goek, "Sloshing and Pressurization tests for Membrane tank: tests, Validation and models," *Acta Astronautica*, vol. 175, pp. 338–348, 2020.
- [19] A. Safdar, M. Islam, M. A. Akram, M. Mujahid, Y. Khalid, and S. I. Shah, "Reaction Time and Film thickness effects on Phase formation and Optical properties of solution processed Cu<sub>2</sub>ZnSnS<sub>4</sub> thin Films," *Journal of Materials Engineering and Performance*, vol. 25, no. 2, pp. 457–465, 2016.
- [20] N. Singh, S. Sharma, O. Parkash, and D. Kumar, "Synthesis and Characterization of Nanocrystalline Fe(100-x)Ni(x) alloy Powders by Auto-combustion and Hydrogen Reduction," *Journal of Materials Engineering and Performance*, vol. 28, no. 9, pp. 5441–5449, 2019.

## *Retraction*

# **Retracted: Analysis of Temperature Distribution and Mechanical Properties of Friction Stir Welding of Al-Cu Joints Using Hardened H13 Steel Tools**

### **Advances in Materials Science and Engineering**

Received 26 December 2023; Accepted 26 December 2023; Published 29 December 2023

Copyright © 2023 Advances in Materials Science and Engineering. This is an open access article distributed under the Creative Commons Attribution License, which permits unrestricted use, distribution, and reproduction in any medium, provided the original work is properly cited.

This article has been retracted by Hindawi, as publisher, following an investigation undertaken by the publisher [1]. This investigation has uncovered evidence of systematic manipulation of the publication and peer-review process. We cannot, therefore, vouch for the reliability or integrity of this article.

Please note that this notice is intended solely to alert readers that the peer-review process of this article has been compromised.

Wiley and Hindawi regret that the usual quality checks did not identify these issues before publication and have since put additional measures in place to safeguard research integrity.

We wish to credit our Research Integrity and Research Publishing teams and anonymous and named external researchers and research integrity experts for contributing to this investigation.

The corresponding author, as the representative of all authors, has been given the opportunity to register their agreement or disagreement to this retraction. We have kept a record of any response received.

### **References**

- [1] J. Pratap Kumar, A. Raj, A. R. Venkatraman et al., “Analysis of Temperature Distribution and Mechanical Properties of Friction Stir Welding of Al-Cu Joints Using Hardened H13 Steel Tools,” *Advances in Materials Science and Engineering*, vol. 2022, Article ID 4973839, 14 pages, 2022.

## Research Article

# Analysis of Temperature Distribution and Mechanical Properties of Friction Stir Welding of Al-Cu Joints Using Hardened H13 Steel Tools

J. Pratap Kumar <sup>1</sup>, Anil Raj,<sup>1</sup> A. R. Venkatraman,<sup>2</sup> Arul Kulandaivel <sup>3</sup>,  
G. Ashwin Prabhu,<sup>4</sup> S. K. Narendranathan,<sup>3</sup> and Nagaraj Ashok <sup>5</sup>

<sup>1</sup>Department of Mechanical and Automobile Engineering, School of Engineering and Technology, CHRIST (Deemed to be University), Bengaluru-560074, Karnataka, India

<sup>2</sup>Department of Mechanical Engineering, Sona College of Technology, Salem, Tamilnadu, India

<sup>3</sup>Department of Mechanical Engineering, Agni College of Technology, Chennai-600130, Tamilnadu, India

<sup>4</sup>Department of Mechanical Engineering, St. Joseph's College of Engineering, Chennai-600119, Tamilnadu, India

<sup>5</sup>Department of Mechanical Engineering, Arba Minch University, Arba Minch, Ethiopia

Correspondence should be addressed to J. Pratap Kumar; [pratab@gmail.com](mailto:pratab@gmail.com) and Nagaraj Ashok; [nagaraj.ashok@amu.edu.et](mailto:nagaraj.ashok@amu.edu.et)

Received 7 July 2022; Accepted 3 September 2022; Published 15 October 2022

Academic Editor: K. Raja

Copyright © 2022 J. Pratap Kumar et al. This is an open access article distributed under the Creative Commons Attribution License, which permits unrestricted use, distribution, and reproduction in any medium, provided the original work is properly cited.

Friction Stir Welding (FSW) is a superior metal joining technique for joining similar and dissimilar metals. The various materials acceptable for the FSW techniques were magnesium alloys, mild steel, stainless steel, copper alloys, titanium alloys, aluminium alloys, etc. In this method, the frictional heat generated by the tool on metal workpieces was used for joining, and the workpieces were joined below the upper critical temperature. The substantial benefit of this technique is that it is capable of welding unweldable alloys by the conventional fusion welding method. The welding tool was rotated, traversed, and penetrated into the joint between two base plates. A suitable tool design with appropriate process parameters will result in high-quality welding on workpieces. In these experiments, the tools were designed with different pin profiles. The welding tools required for FSW are designed using SOLIDWORKS, and temperature distributions across the weld regions were analyzed using Ansys software. The fixture needed for FSW is fabricated according to machine requirements. The tool material used was hardened H13 steel, and the base plates were aluminium alloy 6101 and copper alloy C11000. The temperature distributions are noted in each trial during FSW of Al-Cu joints along the weld line region. Due to maximum temperature at weld joints, high ultimate tensile strength and impact strength were obtained at 1200 rpm tool rotational speed and 20 mm/min feed rate with the square pin profile of a hardened H13 steel tool. The obtained ultimate tensile stress (UTS) at joints was less than that of the base plates Al and Cu. The microhardness value was higher at the nugget zone than at the base plates, giving high strength at the joint area and unevenly distributed.

## 1. Introduction

Friction stir welding (FSW) is the method of joining two similar/dissimilar materials without using any consumable electrodes. Wayne Thomas invented this method in December 1991 at The Welding Institute (TWI) in Cambridge, UK. The FSW is a novel solid-state joining technique and has significant advantages compared to other standard welding techniques. The friction stir welding method uses a tool that

rotates with shoulder and pin profiles embedded into the edges or surfaces of two workpieces in a butt joint configuration. The tool travels along the workpiece joint line [1–3]. In FSW, the welding tool rotation and tool progress directions determine the advancing and retreating side orientations. In recent years, this FSW process has been used in areas like marines, aerospace, aviation, automotive industries, fuel tanks, and other areas. Selection of the tool material, tool design, temperature distribution, mechanical



properties, and structural properties are the essential criteria in the FSW methods, which affect the weld characteristics, flow of plasticized material, uniformity, and strong consistency of the welded joint's robustness [4, 5]. It is possible to weld the alloy series using FSW methods. The selection of tool materials, tool pin configurations, and shoulder thickness were critical constraints in the FSW operation. The tool provides frictional heating of the workpieces and thermomechanical deformation below its recrystallization temperature. The FSW tool consists of a shoulder and a pin, which when they come into contact with the workpieces cause frictional and deformational heating. When the temperature at the joint line increases, that causes further extension of the softened material region. The various types of tool pin profiles are illustrated in Figure 1. The FSW tool pin profile impedes the plasticized material from escaping from the workpiece surface and appears to have a notable impact on the material flow at the weld joints [6].

In this paper, Chen and Kovacevic used 6061-T6 aluminium alloy by FSW in a butt joint configuration. The authors also examined the concept of stress and thermal evolution by employing a three-dimensional finite element method, which helps understand the FSW methods. The detailed model includes the tool shoulder's mechanical operation and the tool's thermomechanical effect (including shoulder and probe). This paper describes the weld's orthogonal stress evolution. The relationship between measured weld residual stresses and process parameters, including tool rotational speeds, welding speeds, and fixture discharge, was examined and conferred [7]. Ajit Kumar and Mallikarjuna conducted FEM model experiments on aluminium and copper plates using the friction stir welding method. In this experiment, welding process parameters such as tool rotational speed of 900 rpm and welding speed of 60 to 80 mm/min were adjusted. After that, thermal distributions were investigated for square and circular tool pin profiles. Creo software was used to build a finite-dimensional workpiece model with an FSW cutting tool joined by butt joint configurations and a thermal analysis concept [8]. Akbari et al. investigated the effects of friction stir welding tool configurations such as tool pin profile, shoulder diameter of the tool, length of the tool pin, axial force, feed rate, and temperature distribution analysis of friction stir welding of AA5083 aluminium alloy plates. The authors also determined the optimum tool pin diameter, height, and tool shoulder diameter. The FSW welding tool forces were evaluated using a specially set up dynamometer. Tensile strength was improved to examine the mechanical characteristics of the FSW welded joints [9]. Ghiasvand et al. discussed how the frictional heat distribution in the FSW process can be greatly affected by pin/tool offsets and the area of dissimilar alloy plates. The effects of the three parameters were studied, and the maximum temperatures of AA5086 and AA6061 aluminium alloy plates were examined. The authors found that pin offset is the most significant part of determining the maximum temperature reached when the AA6061 softer alloy was placed on the advancing side of both the pin and welding tool offset. The maximum temperature increment was greater than the retreating side of the harder alloy [10]. Aziz et al. used ANSYS

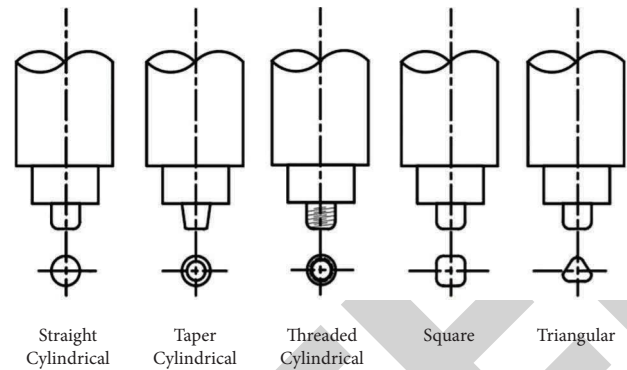


FIGURE 1: Illustrative diagram of different design of tool pin profiles [4].

APDL to generate a numerical thermomechanical model for the FSW. The impact of different weld process parameters on heat production during the welding process was studied. The model was confirmed by comparing experimental results with simulated temperature profiles from three different process welding conditions [11]. Jupri et al. discussed the effects of the tool tilt angle on the plates of aluminium AA5083 and copper C11000 FSW joints. The welding process parameters used in this experiment were tool rotation speed at 2500 rpm and feed rate at 30 mm/min. The mechanical and microstructure properties were performed to examine ultimate tensile strength values and metal movement properties toward the welded FSW of the Al-Cu welded joint. The authors found at 2 tilt angles, at 105 MPa, high tensile strength was obtained and the fracture surface was found nearly closer to Al and obtained brittle formation [12]. Anbukkarasi and Kailas used AA2024 and pure copper workpieces of 5 mm thick butt-welded configurations for various tool offset positions, with plain, threaded tool geometry, and plate positions. The authors found that welds with a smooth and continuous fresh interface had better properties than the welded joints with a nonuniform, intermittent interface. The tool geometry with a plain tool offset by copper placed at the advancing side welds has the best tensile strength due to constant metallurgical bonding at welds [13]. Yadav and Bhatwadekar used 5 mm thick plates of AA6101 aluminum and pure copper by butt joint weld configurations and used the H13 steel tool as an FSW tool with a cylindrical configuration design. The experiments were carried out at a tool rotational speed of 700 rpm and an 11 mm/min feed rate. In the stir region, the welded joint has an onion ring structure. They discovered that the AA6101 and copper joint were brittle by nature and that increasing the downward power, tool rotation speed, and welding speed resulted in a strong weld joint. The authors observed that the ultimate tensile strength of dissimilar joints was 93.2 MPa, which is less than the base metals. The AA6101-T6 was 284.4 MPa and the copper was 220 MPa [14]. Sharma et al. joined pure copper and AA5754 workpieces by FSW of butt weld configuration and an H13 steel tool was used. The structural, material flow, various pin profiles, and the hardness profile of the various welded joint areas were examined. The joints were prepared with different pin design configurations such as taper cam profile and square,

cylindrical, taper and cylindrical cam profile at a tool rotational speed of 900 rpm and a 40 mm/min feed rate. In all the FSW welded joints, the square tool pin profile allows regular joining at the nugget region, which increases the hardness, stronger joints, and microhardness. The material movement and microstructural investigations in the welding tool of square pin profile joints were examined in the longitudinal face to study the impact of stirring, including pulsating motion dissimilar to FSW [15]. Wei et al. used base plates AA1060 and pure copper T2 of 4 mm thickness. The authors revealed that tensile strengths were 102 MPa at a welding tool rotational speed of 950 rpm and an inclination of 0°. The microhardness values of the weld joint area were higher than those of the AA1060 and copper and irregularly dispersed [16]. Sadashiva and Shivanand used samples of size 55 mm × 10 mm × 5 mm. The Charpy test was used to study the impact strength of FSW joints. Due to moderate heat formation during the FSW at high speed and high feed rate, the authors found reverse characteristics of composite materials [17].

## 2. Experiment

**2.1. Selection of Materials for FSW Process.** In this experiment, the base materials used for FSW were AA6101 as the retreating side and C11000 as the advancing side for all the trials. The base plates AA6101 and C11000 have excellent electrical properties and play a vital role in major electrical applications such as electrical bus bars. The tool material was a hardened H13 steel tool with a square and round pin profile. The element distribution of base materials AA6101, C11000 plates, and FSW tool hardened H13 steel tool is displayed in Table 1 and 2.

**2.2. CAD Modelling and Crafting of Tool and Baseplate.** The dimensions of the two base plates were the same and set at 100 mm × 50 mm × 5 mm of length, width, and thickness, respectively. The 3-dimensional model of the base plate was illustrated in various views, as shown in Figure 2.

The tools were designed with one tool having a round pin profile and the other having a square pin profile. The rounded pin profiles were designed with a 20 mm diameter of the shoulder, a 70 mm length of shoulder, a 5 mm diameter of round pin, and a 5 mm pin depth. Square pin profiles were designed with a 5 mm × 5 mm size square pin and a 5 mm pin depth. The 3-dimensional model of the tool with a round pin profile and a 2-dimensional drawing of the same is shown in Figure 3.

The aluminium alloy 6101 and copper alloy C11000 plates were procured and the base plates were made as per the dimensions (100 mm × 50 mm × 5 mm of length, width and thickness), which are shown in Figure 4.

The H13 steel tool rods were procured and the tools with circular pin profiles and square pin profiles were made by machining as per the desired dimensions. After that, the tools were hardened by quenching, resulting in hardened H13 steel tools, as shown in Figures 5(a) and 5(b).

Table 3 shows the tool hardness of various pin profiles of the tool before and after hardness testing using the Rockwell Hardness test.

**2.3. Experimental Setup for Carrying FSW Process in This Experiment.** The experiments were performed using a vertical CNC milling machine by Skanda Mfg. System Pvt. Ltd. and temperature measurements were noted using an InfraRed thermometer (model: HTC IRX 68, temperature range: -50 to 1850°C, response time: 150 ms). The welding process was conducted in each trial with FSW process parameters such as feed rates and tool rotational speeds being computed in the CNC milling controller. In each trial, the weld joint temperatures were recorded from the initial to the end of the weld at every interval using an Infrared Thermometer [18, 19], as shown in Figures 5(c) and 5(d).

**2.4. Selection of FSW Welding Process Parameters and Levels, FSW Tool Materials, FSW Tool Pin Profiles, and Base Plate Positions.** The CNC milling machine used for the FSW process of joining AA6101 and C11000 plates uses a hardened H13 steel tool with a square and round pin profiles with a tool rotational speed range between 1000 and 1200 rpm with respective feed rates of 10, 15, and 20 mm/min. Each trial was conducted with a different tool rotational speed and feed rate. For instance, one trial with a 10 mm/min feed rate, a tool rotational speed of 1000 rpm, and a hardened H13 round tool pin profile. The setup fixed on the plates was C11000 was the advancing side and AA6101 was the retreating side. Table 4 shows the welding trial details.

**2.4.1. Hardness Test.** In this experiment, the Vickers microindentation hardness tester with a model VH1102 was used to test the microhardness of base plates Al and Cu. The hardness tester has a capacity of 10x and 50x and a magnification of 100x and 500x [20]. The tests were performed by fixing the load at 1 kg and a dwelling interval of 10 s for all the trials. The samples were prepared and tested according to the code ASTM E-384, as shown in Figure 6(a). To examine the tempering or solidification impacts of the FSW process on the aluminium and copper alloy plates. The micro-indentation analysis was conducted from the Al-Cu welded joint region to the base plates of Al and Cu. That was from the right side AS (Cu) base plate to the weld joint area of a distance of 5 mm each (+5 mm to 0 mm) and the left side base plate RS (Al) to the weld joint area of a distance of 5 mm each (-5 mm to 0 mm), as shown in Figure 6(b).

**2.4.2. Tensile Strength Test.** The specimens for the tensile test were processed using the wire EDM method essentially by the code ASTM E8-16a and specimen geometry was shown in Figure 7. In this tensile strength test, for each trial, an average of two specimens were applied. The tensile test was carried out using the TTM 5 tonnes capacity model.



TABLE 1: Element distribution of AA6101andC11000 in percentages from EDAX analysis.

Element	Al	Cu	Fe	Cr	Mg	Zn	Si	Ti	Mn	Ni	P	Pb	Bi	Ag	Sn
AA6101	93.95	0.21	0.29	0.08	1	0.18	4.02	0.14	0.12	—	—	—	—	—	—
C11000	—	94.36	0.35	—	—	0.49	1.07	—	0.22	0.28	0.21	0.96	1.02	0.57	0.47

TABLE 2: Element distribution of H13 steel tool in percentages from EDAX analysis.

Element	C	Cr	Fe	Mo	S	Sn	Ti	V	Si	Mn	P	Co	Ni	Cu	W
H13 steel tool	4.87	5.12	86.27	0.09	0.32	0.15	0.10	0.7	0.66	0.48	—	0.4	0.14	0.25	0.43

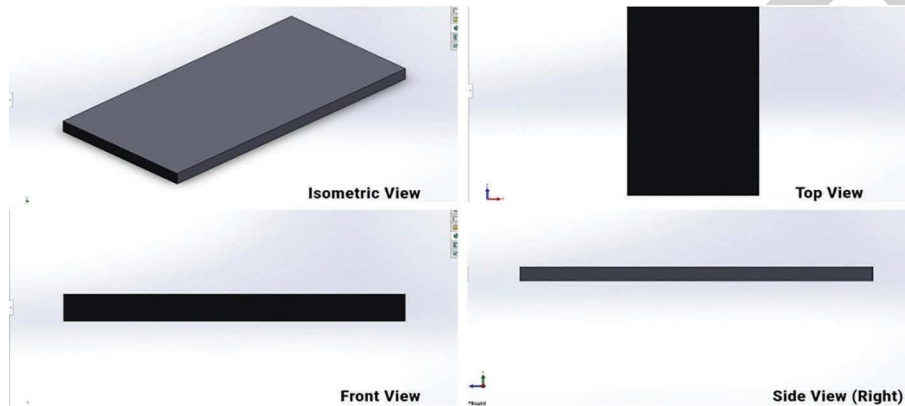


FIGURE 2: 3D model of base plate in different views.

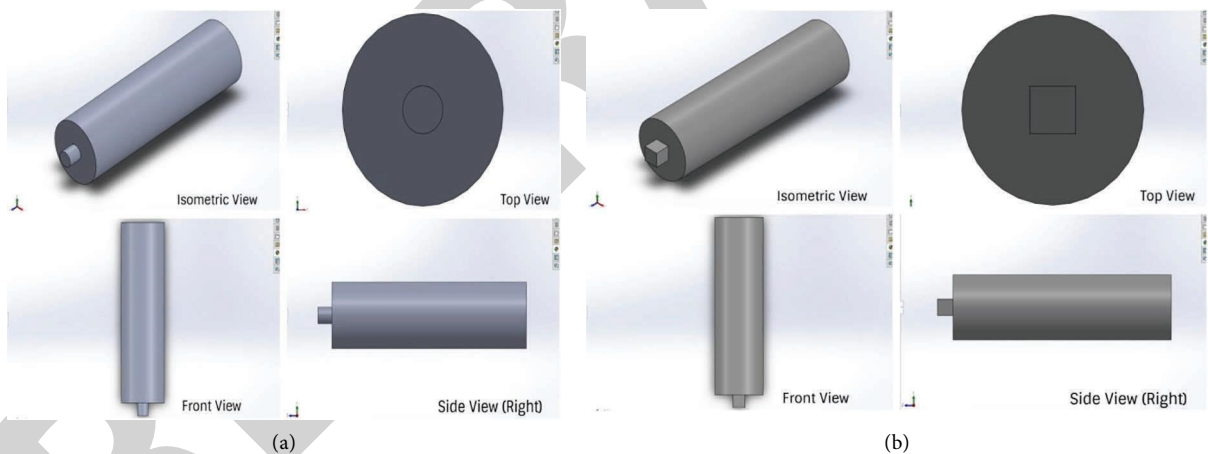


FIGURE 3: 3D modelling of tool design (a) round tool and (b) square tool.

**2.4.3. Charpy Impact Test.** In this Charpy impact test, the rectangular shape of specimens with dimensions of 55 mm × 10 mm × 5 mm (length × width × thickness) was prepared using the wire EDM method as per ASTM E23. The V-Notch (model BMF-M) was made at the center of the weld joint exactly at 27.5 mm from the left/right (Rs-Al/As-Cu) side of the total length of 55 mm, as shown in Figure 8. In this test, an average of two specimens was taken to find out the impact strength of the specimen for each trial. The test was conducted on the model VI-30 Charpy impact test machine. The distance from the axis of rotation of the pendulum to the center of the specimen was 815 mm. The

V-notched rectangular specimen is positioned at the center and then set within the two-terminal supports of anvils. The pendulum was free to fall from the height, hit the sample opposite the v-notch center, and measure the released height of the pendulum. The total energy absorbed by the specimen during fracture was tabulated.

### 3. Results and Discussions

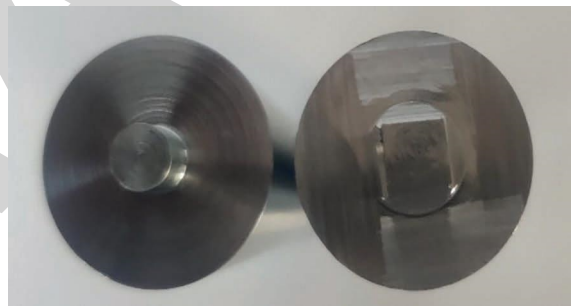
**3.1. Temperature Distribution Analysis of FSW Compared with Conventional Welding Techniques.** The quality of the weld at each trial was observed and examined. The temperature at



FIGURE 4: Crafted plates of C11000 and AA6101.



(a)



(b)



(c)



(d)

FIGURE 5: Hardened H13 steel tool with (a) round and square pin profiles. (b) Bottom section of the tools. (c) CNC milling machine. (d) Infrared thermometer.



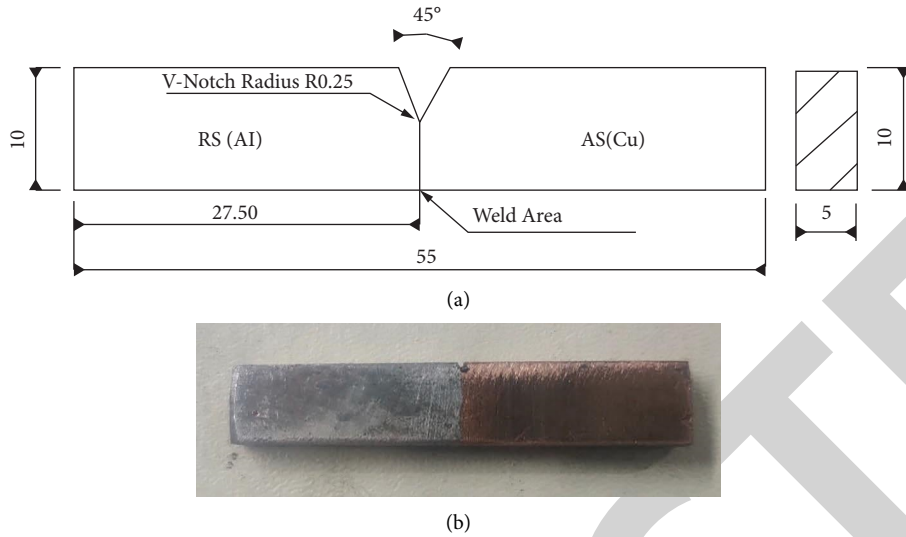
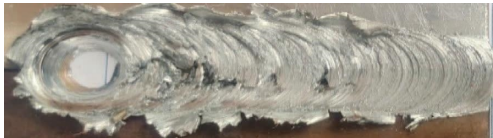
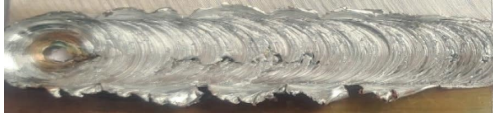





FIGURE 8: (a) Configuration of specimen preparation and (b) V-Notch sample preparation of Charpy impact test.

TABLE 5: Temperature at weld regions of each trial.

Trials	Temperature distributions at the weld region (°C)											
	1	67.7	97.8	145.9	170.3	180.4	191.1	206.3	222	230.3	245.7	254.5
2	97.5	129.1	150.2	178	191.1	199.5	208.4	243	245.2	266.6	273	278.6
3	94	128.6	146	179.1	194.2	219.3	236	243.7	260	273.8	280	293
4	48.8	156.8	164	193	209.1	215	219	235.4	240	248	256	270
5	98.6	135.9	140.8	150.8	172.4	200.5	226.5	254.5	260.9	270.6	275	282

TABLE 6: Maximum temperature at weld regions of each trial and weld appearance after the FSW process.

Samples No	Tool rotational speed (rpm)	Feed rate (mm/min)	Max. temp at weld joints (°C)	Weld appearance
1	1000	10	272.9	
2	1100	15	278.6	
3	1200	20	293	
4	1000	10	270	
5	1200	15	282	

low tool rotational speed and feed rate. The readings show that the temperatures at the welding joints during the FSW process were lower than those of the traditional arc welding process.

**3.2. Simulation of Welding Tool with Base Plates.** The 3-dimensional models of the tool and base plates were exported from SOLIDWORKS in IGS file format. The material properties of the hardened H13 steel tools, AA6101, and C11000, were entered into the engineering database in the ANSYS workbench. The geometry is imported in IGS format and steady-state thermal is conducted. The materials were assigned to the tool and plates with a hardened H13 steel tool, C11000 and AA6101, respectively. The geometry models were meshed with an element size of 0.006 m, and the meshed models are shown in Figure 9. The initial temperature was set at 24°C and the tool temperature was set particularly for different trials as a boundary condition. The temperature distribution study of each trial was compared and analyzed as shown in Figure 10.

The simulations were conducted, and temperature distributions of geometry were observed in the ANSYS workbench. Figure 11 shows the temperature distribution of a hardened H13 steel tool with a round pin profile. The tool temperature was 272.9°C, which was set as a boundary condition and where the tool rotational speed was 1000 rpm and the feed rate was 10 mm/min. The initial temperature was set at 24°C, and the distribution between the plates and tools can be observed in the temperature contour plot.

Figure 12 shows the temperature distribution of the hardened H13 steel tool with a round pin profile and the tool temperature of 278.6°C, which was set as a boundary condition. The initial temperature was 24°C and the temperature contour plot illustrated was from the trial, where the tool rotational speed was 1100 rpm and the feed rate was 15 mm/min, which shows the distribution of the tools and workpieces.

Figure 13 shows the temperature distribution of the hardened H13 steel tool square with a pin profile and the tool temperature of 293°C, which was set as the boundary condition, and the initial temperature set at 24°C. This was the trial simulation with a tool rotational speed of 1200 rpm and a feed rate of 20 mm/min. The temperature contour plot can be observed with the temperature distributed between the tool and plates. The contour plots were analyzed and comparative studies were done along with conventional flame welding temperature distribution.

In this FSW process, the temperatures generated on the tools and workpieces were comparatively low. For comparison, various temperature distributions were simulated in the ANSYS workbench with different tool profiles and tool temperatures of the FSW process, along with the temperature distribution of the conventional flame welding process. The temperature distributions of the flame welding with a temperature of 1100°C were also simulated, which is shown in Figure 14 for comparison with Friction Stir Welding.

While comparing Figures 11 and 14, Figure 14 shows a temperature value of 845.16°C, which indicates that higher

temperatures affect the structural integrity of the workpieces. In this case, the melting point of AA6101 is 654°C, and it is hard to weld the aluminium alloy by the fusion welding method. Figure 11 shows the minimum temperature value of 272.9°C. It illustrates that the heat-affected zone (HAZ) is the region where the metals do not get melted but their material properties get altered by heat generated during the FSW process. In this case, the temperature in the HAZ is lower compared with conventional flame welding. The FSW method was adopted to remove the flexible structural integrity of the workpieces. In FSW, as previously described, the welding occurs at a lower critical temperature for Al and Cu plates. Figures 12 and 13 also illustrate the respective HAZ of trials with 278.6°C and 293°C using hardened H13 steel tools with round and square pin profiles, respectively. It was also stated that heat input was high because of the maximum tool rotational speed and feed rate.

### 3.3. Mechanical Properties of the Al-Cu FSW Joints

**3.3.1. Microhardness Measurements.** Figures 15 and 16 show the microhardness curve and microindentation of the FSW joint plots of the first three trials. The tests were performed from the joints to the base metal at a 5 mm distance for each AS-Cu and RS-Al. The average microhardness value of the base plates Al and Cu obtained was 51.6 HV1 and 88.36 HV1 and at the Al-Cu joint was 104.63 HV1, which was higher than the value of base plates Al and Cu. On the Cu side, the average microhardness at the thermomechanically affected zone (TMAZ) was 74.83 HV1, and the HAZ was 84.86 HV1. This movement shows a decrease in HV1 value from the joint to the Cu base metal. On the Al side, the average microhardness at TMAZ was 77.1 HV1, and the HAZ was 72 HV1, which shows a decrease in HV1 value from the joint to the Al base metal. Hence, the microhardness appearance was random. Also, the microhardness value of TMAZ and HAZ of both the Al and Cu sides is lower than the Al-Cu joint area. This movement is because of increased tool rotational speed and feed rate, the effect of the thermal welding cycle, and microstructural variations made during the welding on aluminium and copper alloy plates. The microhardness of the nugget zone slightly increased.

**3.3.2. Ultimate Tensile Strength Test (UTS).** Figure 17 shows samples vs. UTS (MPa) and % of elongation, and Figure 18 shows samples vs. yield strength (YS) (MPa) and % of reduction area of the tensile test for FSW specimens of the first three trials. At a low speed of 1000 rpm and a feed rate of 10 mm/min with hardened H13 steel tool round configurations, the UTS was 85.77 MPa and the % of elongation was 7.06. The strain was 0.07 obtained. Young's modulus ( $E$ ) was 1.22 GPa with a yield strength of 64.33 MPa and the % of reduction in the area of 0.65. This movement is due to inadequate heat input on the welded joint area, which causes surface groove defects, leading to low joint strength. At a medium speed of 1100 rpm, feed rate of 15 mm/min with hardened H13 steel tool round configurations, the UTS was 89.63 MPa and the % of elongation was 7.23. The strain was



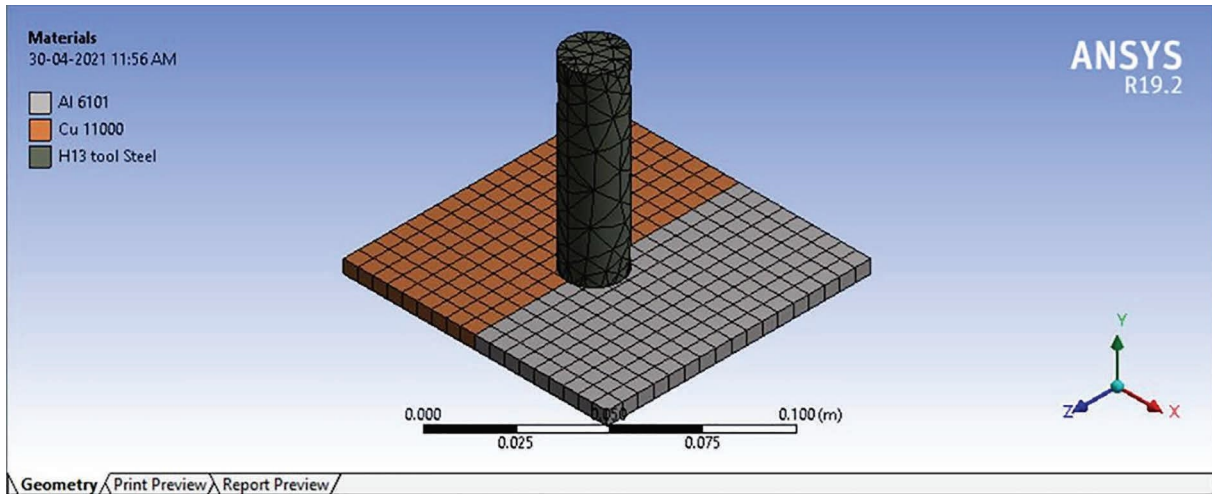


FIGURE 9: Meshing of geometry tool with base plates.

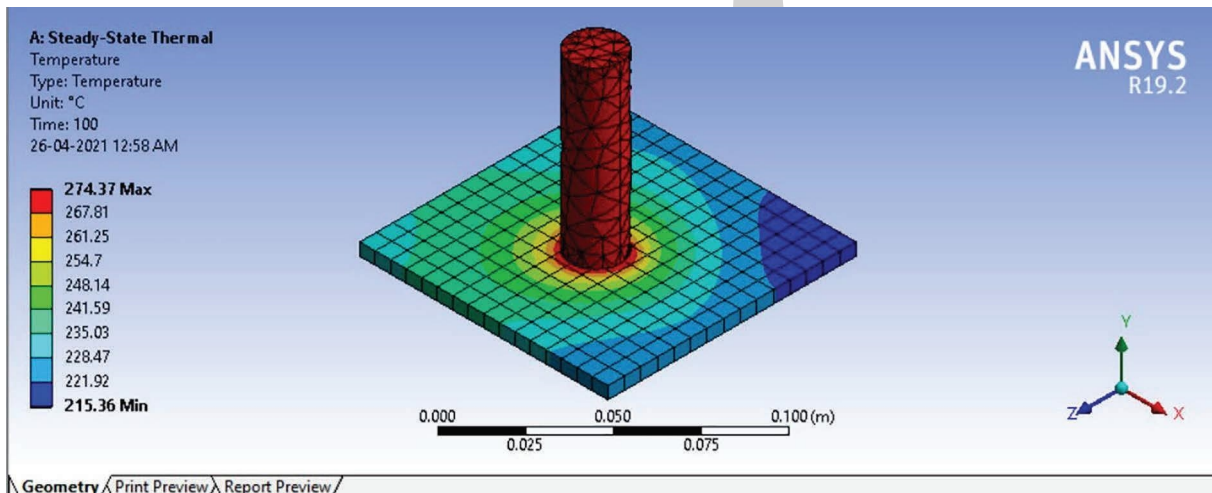


FIGURE 10: Temperature distribution.

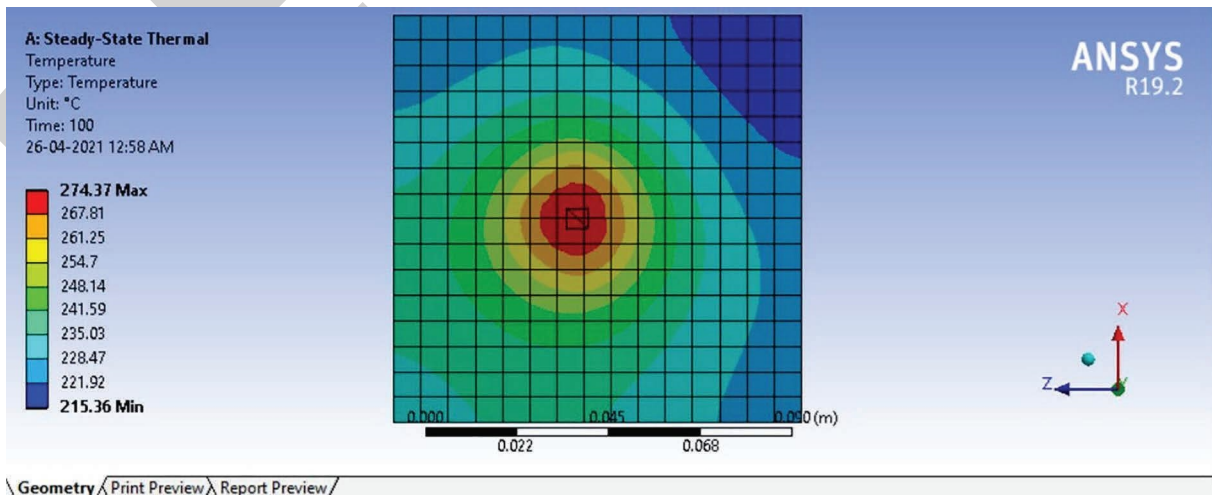


FIGURE 11: Temperature distribution with a hardened H13 steel tool round pin profile when tool temperature was 272.9°C.

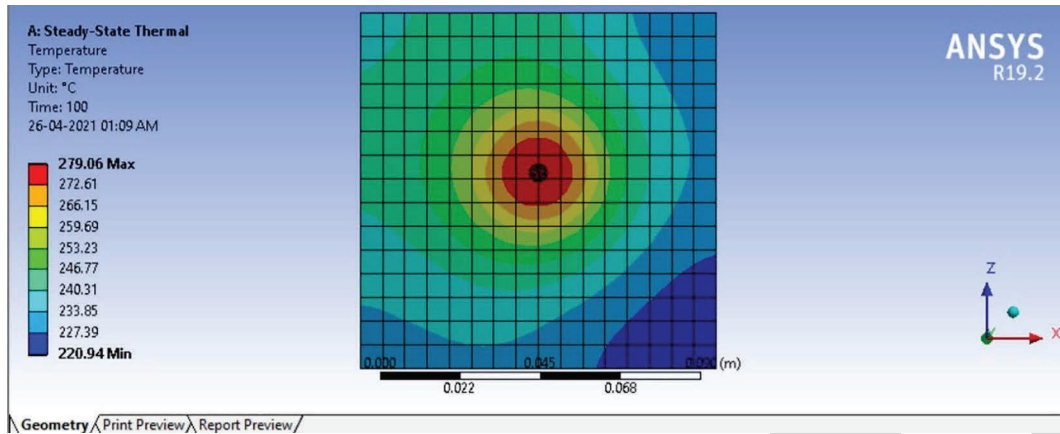


FIGURE 12: Temperature distribution with a hardened H13 steel tool round pin profile when tool temperature was 278.6°C.

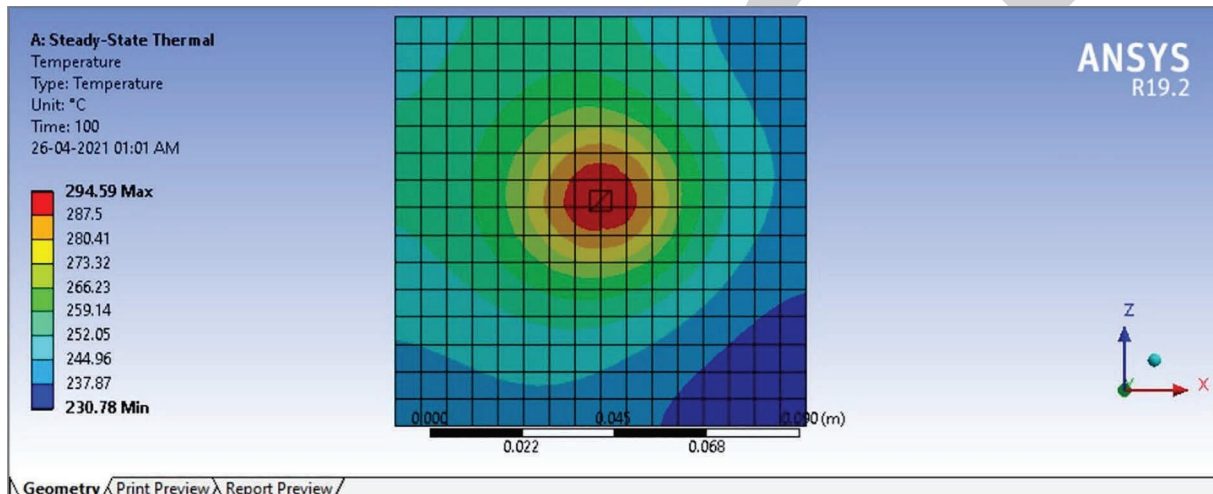


FIGURE 13: Temperature distribution with a hardened H13 steel tool square pin profile when tool temperature was 293°C.

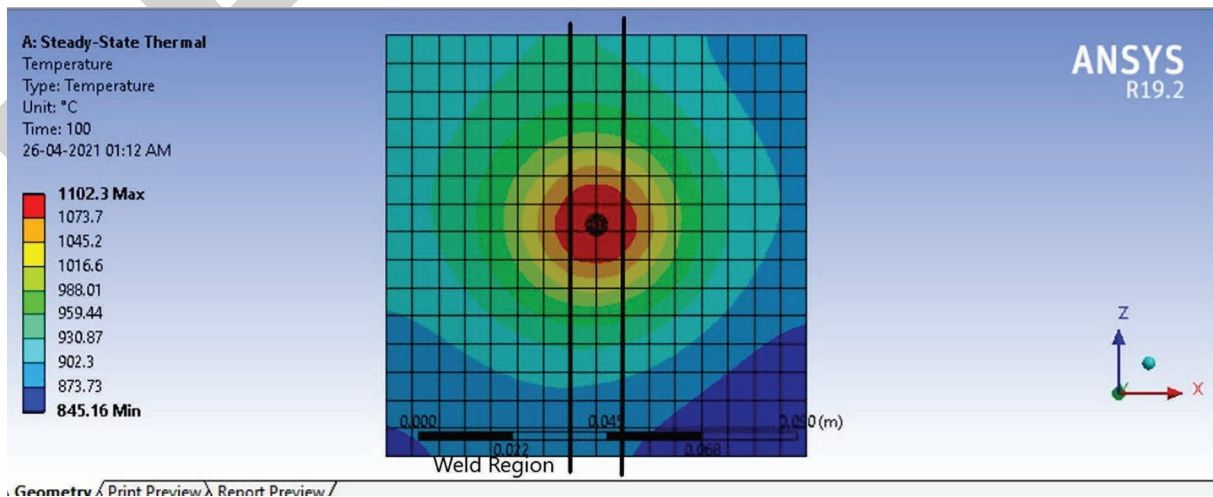


FIGURE 14: Temperature distribution of conventional flame welding when pin temperature is set at 1100°C.

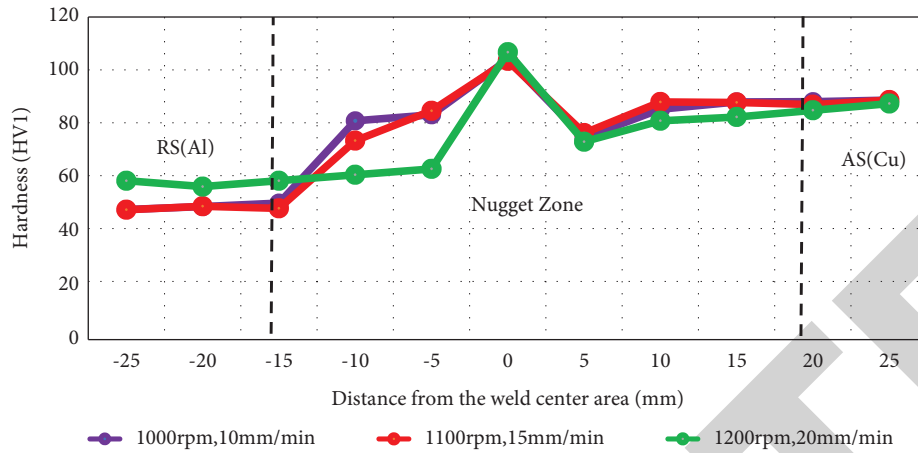


FIGURE 15: The microhardness distribution of welded joints at different tool rotation speeds and feed rates.



FIGURE 16: Vickers microhardness indentations: (Cu-AS) side: points 1-3 base metal area, points 3-6 HAZ and TMAZ, point 6 Al-Cu interface area (weld joint area), (Al-RS) side: points 6-9 TMAZ and HAZ, and points 9-11 base metal area (Al).

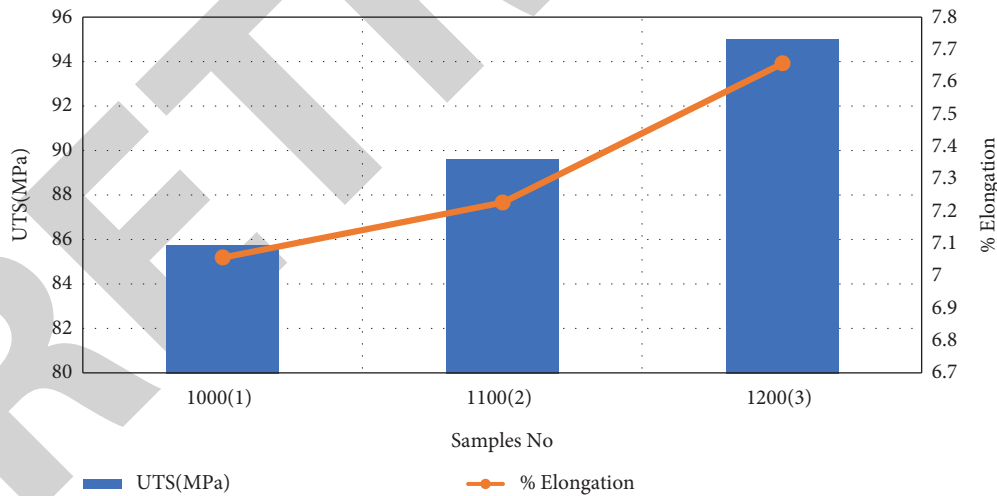


FIGURE 17: Samples vs. UTS (MPa) and % elongation.

0.0723. Young’s modulus ( $E$ ) was 1.24 GPa with a yield strength of 69.34 MPa and % of reduction in the area of about 0.5. At high-speed of 1200 rpm, feed rate of 20 mm/min with hardened H13 steel tool square configurations, the UTS was 95.04 MPa and the % of elongation was 7.66. The strain was 0.0766. Young’s modulus ( $E$ ) was 1.25 GPa with a yield strength of 74.38 MPa and % of reduction in the area of about 0.33. This movement was due to high tool rotational

speed; maximum temperature causes removal of groove defects because of proper heat input caused by mechanical and metallurgical bonding effects; and more interfacial compounds were formed at the weld joint. The UTS value at the joint was less than the ultimate tensile strength of base plates Al and Cu. The joint efficiency increases when increasing the FSW process parameters such as feed rate and tool rotational speed.



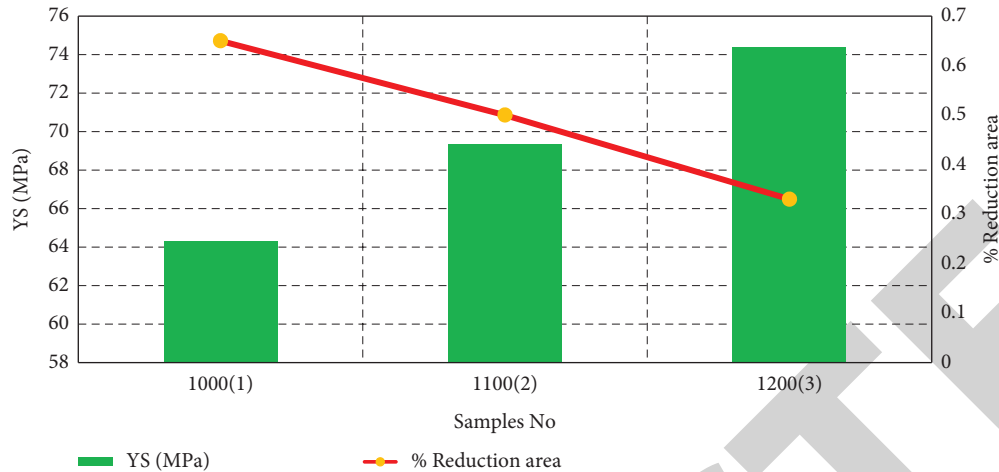


FIGURE 18: Samples vs. yield strength (MPa) and % reduction area.

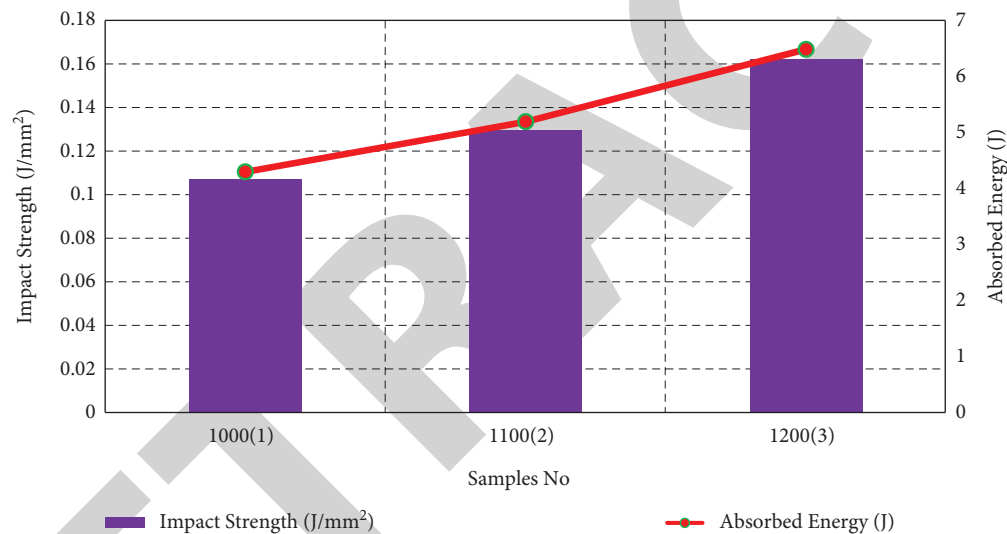


FIGURE 19: Samples vs. impact strength (J/mm<sup>2</sup>) and absorbed energy (J).

3.3.3. *Charpy Impact Strength Test.* Figure 19 shows samples vs. absorbed energy ( $J$ ) and impact strength of the specimen for the first three trials. The impact strength was low at  $0.1075 J/mm^2$  and  $0.13 J/mm^2$  at absorbed energy of  $4.3 J$  and  $5.2 J$ , when tool rotational speed was between  $1000$  and  $1100$  rpm and the feed rate was between  $10$  and  $15$  mm/min with hardened H13 steel tool round configurations. This movement is because of low heat generation and low-temperature distribution during the FSW of Al-Cu joints. It shows the brittle characteristics of the weld joints. The impact strength was high at  $0.1625 J/mm^2$  at an absorbed energy of  $6.5 J$  and an impact velocity of  $5.347$  m/sec when maximum tool rotational speed was set at  $1200$  rpm and the feed rate of  $20$  mm/min with hardened H13 steel tool square configurations. This movement is due to high heat generation, high-temperature distribution, and proper metallurgical bonding, which lead to the ductile characteristics of welded Al-Cu joints.

## 4. Conclusions

With an understanding of the temperature distribution, comparative studies and readings during FSW of AA6101 and C11000 from the various trials, it has been understood that the FSW process parameters such as feed rate, tool rotational speed, type of FSW tool pin profile, and selection of tool material play a vital role in this experiment to carry out the FSW process. The following statements are highlighted:

- (1) In trial 3, a maximum temperature of  $293^{\circ}C$  was observed in the Al-Cu joint area using a hardened H13 steel tool square pin profile where the high tool rotational speed was  $1200$  rpm and the feed rate was  $20$  mm/min. It was concluded that, out of the five trials, this one produced the best weld joint. If the HAZ increases, the stress capability of the material decreases.

- (2) In trial 4, a minimum temperature of 270°C was observed in the Al-Cu joint area using a hardened H13 steel tool square pin profile where the low tool rotational speed was 1000 rpm and a 10 mm/min feed rate. Due to the lower temperature at the joints, the structural integrity of the Al-Cu plates was preserved. The heat-affected zones of FSW were lower and did not increase when compared with conventional arc welding techniques.
- (3) From the study, during conventional welding techniques, the temperature was found to be 845.16°C, which indicates that the higher temperature of heat-affected zones affects the structural integrity of the workpieces. The heat-affected zones in friction stir welding have lower temperatures when compared with conventional flame welding methods.
- (4) The highest ultimate tensile strength of the Al-Cu joint was 95.04 MPa, which shows an improvement in Al-Cu joint efficiency. The above value was less than that of the base plate UTS. Hence, the formation of solid butt joints requires high tool rotational speed and feed rate combinations or low tool rotational speed and high feed rates with different tool offsets.
- (5) The Charpy impact strength was high at 0.1625 J/mm<sup>2</sup> (162.5 kJ/m<sup>2</sup>) at absorbed energy of 6.5 J, impact velocity of 5.347 m/sec for FSW at 1200 rpm and 20 mm/min for the hardened H13 steel tool with square pin profile. The Vickers microhardness of the nugget zone was found to be an average of 104.63 HV1, which is higher than the base metal of Al and Cu and unevenly distributed.

## Data Availability

The data used to support the findings of this study are included within the article. Further data or information is available from the corresponding author upon request.

## Conflicts of Interest

The authors declare that there are no conflicts of interest regarding the publication of this article.

## References

- [1] J. Pratap Kumar, A. Raj, K. Arul, and V. Mohanavel, "A literature review on friction stir welding of dissimilar materials," *Materials Today Proceedings*, vol. 47, pp. 286–291, 2021.
- [2] M. Shunmugasundaram, A. Praveen Kumar, L. Ponraj Sankar, and S. Sivasankar, "Optimization of process parameters of friction stir welded dissimilar AA6063 and AA5052 aluminium alloys by Taguchi technique," *Materials Today Proceedings*, vol. 27, pp. 871–876, 2020.
- [3] A. Raj, J. Pratap Kumar, A. Melwin Rego, and I. SunitRout, "Optimization of friction stir welding parameters during joining of AA3103 and AA7075 aluminium alloys using Taguchi method," *Materials Today Proceedings*, vol. 46, pp. 7733–7739, 2021.
- [4] N. Santhosh and K. Ramesha, "Mechanical and thermal characterization of friction stir weld joints of Al-Mg alloy," *Int. J. Res. Aeronaut. Mech. Eng.*, vol. 22-23, 2017.
- [5] S. V. Safi, H. Amirabadi, M. K. Besharati Givi, and S. M. Safi, "The effect of preheating on mechanical properties of friction stir welded dissimilar joints of pure Copper and AA7075 aluminium alloy sheets," *International Journal of Advanced Manufacturing Technology*, vol. 84, no. 9-12, pp. 2401–2411, 2015.
- [6] G. Padmanaban and V. Balasubramanian, "Selection of FSW tool pin profile, shoulder diameter and material for joining AZ31B magnesium alloy – an experimental approach," *Materials & Design*, vol. 30, no. 7, pp. 2647–2656, 2009.
- [7] C. M. Chen and R. Kovacevic, "Parametric finite element analysis of stress evolution during friction stir welding," *Proceedings of the Institution of Mechanical Engineers - Part B: Journal of Engineering Manufacture*, vol. 220, no. 8, pp. 1359–1371, 2006.
- [8] I. Ajit Kumar and Dr. M. V. Mallikarjuna, "Thermal analysis of friction stir welding," *International Journal of Engineering Research and Technology*, vol. 4, no. 2, pp. 1–5, 2015.
- [9] M. Akbari, M. R. M. Aliha, S. M. E. Keshavarz, and A. Bonyadi, "Effect of tool parameters on mechanical properties, temperature, and force generation during FSW," *Proceedings of the Institution of Mechanical Engineers - Part L: Journal of Materials: Design and Applications*, vol. 233, no. 6, pp. 1033–1043, 2016.
- [10] A. Ghiasvand, M. Kazemi, M. Mahdipour Jalilian, and H. Ahmadi Rashid, "Effects of tool offset, pin offset, and alloys position on maximum temperature in dissimilar FSW of AA6061 and AA5086," *International Journal of Mechanical and Materials Engineering*, vol. 15, no. 1, pp. 6–14, 2020.
- [11] S. B. Aziz, M. W. Dewan, D. J. Huggett, M. A. Wahab, A. M. Okeil, and T. Warren Liao, "Impact of friction stir welding (FSW) process parameters on thermal modeling and heat generation of aluminum alloy joints," *Acta Metallurgica Sinica*, vol. 29, no. 9, pp. 869–883, 2016.
- [12] J. A. Jupri, J. Affi, D. Chandra, and M. Asrofi, "Mechanical and microstructure properties on Al-Cu joint processed by friction stir welding: the effect of tilt angle tool," *Material Science Research India*, vol. 16, no. 1, pp. 56–61, 2019.
- [13] R. Anbukkarasi and S. V. Kailas, "Influences of shape of the new interfaces and morphology of the intermetallics on mechanical properties of aluminum AA2024–pure copper joints by friction stir welding," *International Journal of Advanced Manufacturing Technology*, vol. 106, no. 11-12, pp. 5071–5083, 2020.
- [14] V. D. Yadav and P. S. G. Bhatwadekar, "Friction stir welding of dissimilar materials between AA6101 aluminium and pure Copper," *International Journal of Engineering Sciences and Research Technology*, vol. 3, no. 12, pp. 505–508, 2014.
- [15] N. Sharma, A. N. Siddiquee, Z. A. Khan, and M. T. Mohammed, "Material stirring during FSW of Al-Cu: effect of pin profile," *Materials and Manufacturing Processes*, vol. 33, no. 7, pp. 786–794, 2017.
- [16] Y. Wei, H. Li, P. Xiao, and J. Zou, "Microstructure and conductivity of the Al-Cu joint processed by friction stir welding," *Advances in Materials Science and Engineering*, vol. 2020, pp. 1–10, Article ID 6845468, 2020.
- [17] Sadashiva and Shivanand, "Characteristic investigation on impact strength of aluminium based hybrid composite plates weld by FSW," *International Journal of Engineering & Technology*, vol. 7, no. 3.12, pp. 120–127, 2018.
- [18] K. Arul and S. K. Vs, "Magnetorheological based minimum quantity lubrication (MR-MQL) with additive n-CuO,"

## *Retraction*

# **Retracted: Investigation on Heat Deflection and Thermal Conductivity of Basalt Fiber Reinforced Composites Prepared by Hand Layup Method**

### **Advances in Materials Science and Engineering**

Received 26 December 2023; Accepted 26 December 2023; Published 29 December 2023

Copyright © 2023 Advances in Materials Science and Engineering. This is an open access article distributed under the Creative Commons Attribution License, which permits unrestricted use, distribution, and reproduction in any medium, provided the original work is properly cited.

This article has been retracted by Hindawi, as publisher, following an investigation undertaken by the publisher [1]. This investigation has uncovered evidence of systematic manipulation of the publication and peer-review process. We cannot, therefore, vouch for the reliability or integrity of this article.

Please note that this notice is intended solely to alert readers that the peer-review process of this article has been compromised.

Wiley and Hindawi regret that the usual quality checks did not identify these issues before publication and have since put additional measures in place to safeguard research integrity.

We wish to credit our Research Integrity and Research Publishing teams and anonymous and named external researchers and research integrity experts for contributing to this investigation.

The corresponding author, as the representative of all authors, has been given the opportunity to register their agreement or disagreement to this retraction. We have kept a record of any response received.

### **References**

- [1] R. M. Reddy, S. Ravi, P. K. Singh et al., "Investigation on Heat Deflection and Thermal Conductivity of Basalt Fiber Reinforced Composites Prepared by Hand Layup Method," *Advances in Materials Science and Engineering*, vol. 2022, Article ID 1294374, 6 pages, 2022.

## Research Article

# Investigation on Heat Deflection and Thermal Conductivity of Basalt Fiber Reinforced Composites Prepared by Hand Layup Method

R. Meenakshi Reddy,<sup>1</sup> S. Ravi,<sup>2</sup> Pradeep Kumar Singh,<sup>3</sup> H. Dineshkumar,<sup>4</sup>  
K. Arun Bhaskar,<sup>5</sup> Vallapureddy Siva Nagi Reddy,<sup>6</sup> A. H. Seikh,<sup>7</sup> M. H. Siddique,<sup>8</sup>  
and Ashok Nagaraj <sup>9</sup>

<sup>1</sup>Department of Mechanical Engineering, G. Pulla Reddy Engineering College, Kurnool, Andhra Pradesh, India

<sup>2</sup>Department of Mechanical Engineering, Chennai Institute of Technology, Chennai, Tamil Nadu, India

<sup>3</sup>Department of Mechanical Engineering, GLA University, Mathura, UP 281406, India

<sup>4</sup>Department of Mechanical Engineering, Kingston Engineering College, Vellore, Tamil Nadu, India

<sup>5</sup>Department of H&BS, Aditya Engineering College, Surampalem, Andhra Pradesh 533437, India

<sup>6</sup>Department of Mechanical Engineering, Aditya College of Engineering & Technology, Surampalem, Andhra Pradesh, India

<sup>7</sup>Mechanical Engineering Department, College of Engineering, King Saud University, P.O. Box 800, Al-Riyadh 11421, Saudi Arabia

<sup>8</sup>Intelligent Construction Automation Centre, Kyungpook National University, Daegu, Republic of Korea

<sup>9</sup>Faculty of Mechanical Engineering, Jimma Institute of Technology, Jimma University, Jimma, Ethiopia

Correspondence should be addressed to Ashok Nagaraj; [nagaraj.ashok@ju.edu.et](mailto:nagaraj.ashok@ju.edu.et)

Received 6 July 2022; Revised 21 September 2022; Accepted 29 September 2022; Published 12 October 2022

Academic Editor: K. Raja

Copyright © 2022 R. Meenakshi Reddy et al. This is an open access article distributed under the Creative Commons Attribution License, which permits unrestricted use, distribution, and reproduction in any medium, provided the original work is properly cited.

Recent trends are shifting to the use of composite materials and their demands for making alternate materials to metals due to weight ratio, while the synthetic fiber composite also creates environmental hazards. To overcome these issues, composite materials with natural fiber reinforcement are being developed. The current work is concerned with the fabrication of composite laminates using the traditional hand layup method, with 40% reinforcement of basalt fiber mat and sawdust filler and 60% epoxy, with quantifying the thermal effects of composite laminates varying with four different weight fractions of basalt fiber and sawdust filler materials. The results revealed that maximum thermal conductance, heat deflection temperature, and coefficient of linear thermal expansion values are 0.254 W/mK, 95°C, and  $2.9 \times 10^{-5}/^{\circ}\text{C}$ , respectively, which increases sawdust filler loading resist the thermal effect compared to basalt fiber loading of hybrid composite.

## 1. Introduction

Fiber-reinforced plastics (FRPs) are effectively utilized for different utilizations of the present aviation innovation, as a result of their astounding explicit properties, for example, high explicit quality and solidness, low weight, and the capability of advancement by orientating (particularly persistent) fibers along the load conducts [1, 2]. The presentation of infusion formed short basalt fiber, hemp fiber, kenaf, and hemp/basalt fiber HDPE composites [3, 4]. Hybridization of hemp fibers

with basalt filaments was found to altogether expand the mechanical properties and the crystallinity effect of hemp-fiber reinforced composites along these lines recommending that short hemp/basalt fiber hybrid HDPE composites are a promising contender for semiauxiliary applications [5]. They are investigating the thermal properties of the composite and mechanical characterization are made it is found out from earlier research works [6, 7]. The point of this examination is to explore the impact of sugar palm fiber on varied properties of seaweed/thermoplastic sugar palm starch agar composites. By

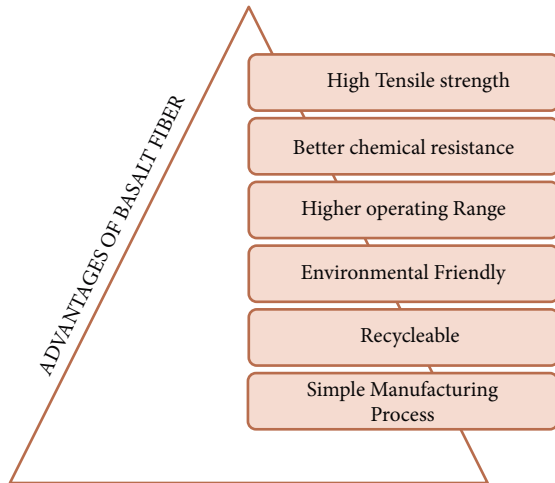


FIGURE 1: Merits of basalt fiber.

displaying higher thermal conductivities when  $\text{Al}_2\text{O}_3$  and  $\text{Mg}(\text{OH})_2$  are added, the fire resistance qualities can be improved when adding SiC nanocomposites to the mix inhibits flame propagation [8]. When blended banana/sisal hybrid fibers are chemically treated with sodium hydroxide (NaOH) and prostate-specific membrane antigen, the thermal conductivity of the reinforcement fibers is reduced. This study looked into the heat conduction of fiber-strengthened composites [9]. The expanding behavior has been studied in a variety of settings with a wide range of pH levels. With 35% filler content for UP/jute/ $\text{ZrO}_2$  composites, the best results were obtained [10]. The unidirectional neem wood epoxy composite has more fiber and better mechanical characteristics than the other combinations [11]. A further study combined organic neem and plant fibers with a polymeric matrix to create laminates with enhanced thermal characteristics compared to single fiber power, as well as showing that composite laminates with silane chemical treatment outperformed composite laminates with untreated mode [12]. The developed composite laminates were made of basalt/banyan fibers reinforced with epoxy matrix, and the thermal properties such as heat deflection temperature, thermal conductivity, and thermal expansion coefficient were evaluated. The results showed that the basalt fiber has improved thermal stability compared to banyan fiber loading into the composite laminates and the advantages are shown in Figure 1 [13].

The abovementioned types of literature were used to begin this research work, which deals with the reinforcement of basalt fiber, sawdust cellulose filler, and epoxy polymer matrix to fabricate the composite laminates by hand layup method for four different fiber and filler sequences to examine the thermal conductivity, heat deflection temperature, and coefficient of linear thermal expansion of basalt fiber composites.

## 2. Materials and Experimental Methods

Material selection for making the composite laminates is a very important factor that needs to be considered for this composite; in this present study, deals with the materials are basalt fiber which is extracted from rocks [14] and to create

in the mat form has been supplied by Go green private Limited. Another material that is investigated is sawdust filler extracted from natural wood [15], which has been supplied by the CP Timber Industry, Chennai, India. The adhesive material of biphenyl type epoxy polymer with Araldite Hy 951 hardener is a matrix material [16] that has been supplied by Javanthee Enterprisers, Chennai, and the properties are tabulated in Table 1.

**2.1. Fabrication Process of Hybrid Composite.** The combination of natural fiber and natural filler is reinforced with thermosetting polymer to make four different composite laminates with varying basalt and sawdust weight fraction such as 100/25, 70/50, 50/75, and 25/100 in grams, and a constant epoxy matrix of 190 g (epoxy resin/hardener ratio of 10:1) by using traditional hand layup technique to fabricate the four laminates. Initially, the wood mold box was prepared with the dimensions of 25 cm  $\times$  25 cm and cleaned thoroughly and the mold releasing agent of liquid wax was applied to remove laminates without any defects [17]. The epoxy matrix and basalt fiber mat and sawdust cellulose are ready to be applied on the mold box, epoxy matrix was blended with sawdust during the fabrication process by using an electric stirrer, the first layer of epoxy matrix is applied on the mold box covered with laminate sheets to get the fine surface finish, and the second layer of basalt fiber mat was applied and rolled properly with a roller for spreading the matrix evenly to all the fiber portion for better adhesion and again the matrix and reinforcement materials are followed up to 10 mm of composite laminates [18]. The process was repeated for other samples, and then the laminates are moved to the hot furnace at a curing rate of 50 C/min up to 120 mins and then compressed with 10 kg on each sample for 24 hrs in atmospheric temperature for better curing between the fiber, filler, and matrix materials [19]. After 24 hrs, the laminates are taken to conduct the thermal behaviors of thermal conductivity, heat deflection temperature, and coefficient of linear thermal expansion for the hybrid composite, and the weight ratio of basalt fiber composite is given in Table 2. The fabrication process of basalt fiber composite is shown in Figure 2.

**2.2. Experimental Testing of Composite Laminate.** The basalt fiber with sawdust cellulose and epoxy matrix was used and the composite laminates were fabricated to evaluate the thermal properties such as thermal conductivity, heat deflection temperature, and coefficient of linear thermal expansion of hybrid composite. As per the ASTM E1530 testing methodology, to assess the resistance to thermal transmission, the guarded heat flow meter technique is used and a heat flow meter is employed to evaluate the thermal conductivity of the composite material at an average temperature of 55°C. [20]. Short-term heat resistance test was conducted as per the ASTM D1525 standard by using VICAT softening temperature apparatus for plastic standard [21]. The ASTM Standard D696 for Coefficient of Linear Thermal Expansion of Plastics Between  $-28^\circ\text{C}$  and  $32^\circ\text{C}$  using a Vitreous Silica Dilatometer of basalt fiber composite [22].



TABLE 1: General properties of materials used in the present work.

Property	Basalt fiber	Sawdust filler	Epoxy matrix
Category	Natural fiber	Natural filler	Thermosetting polymer
Type	Bidirectional woven mat	Nanoparticles	Clear liquid
GSM	200	—	—
Density	2.52 g/cc	0.8 to 1 g/cc	1.25 g/cc
Tensile strength in (MPa)	45	—	40
Thermal conductivity (W/mK)	1.9	0.89	0.2

TABLE 2: Weight ratio of basalt fiber composite laminates.

Sample	Weight of basalt fiber (g)	Weight of sawdust filler (g)	Weight of epoxy matrix (g)	Weight of composite laminate (g)
A	100	25	190	315
B	75	50	190	315
C	50	75	190	315
D	25	100	190	315



FIGURE 2: Fabrication process of basalt fiber composite.

### 3. Results and Discussion

The developed composite laminates of basalt fiber reinforced with sawdust-blended epoxy matrix were analyzed, and thermal properties and the thermal conductivity of basalt fiber composite are shown in Figure 3; the output from this analysis revealed that basalt fiber occupied the major impact during the thermal conductivity and increasing the basalt fiber loading to this composite can increase the thermal conductivity, and at the same time, with the increase in sawdust filler loading, the thermal conductivity of the hybrid composite will decrease. Among the four samples, sample A shows higher thermal conductivity of 0.254 W/mK, and the least value occurs in sample D which is 0.165 W/mK and also the comparison between these samples 35% higher thermal conductivity due to increase of basalt fiber into the composite laminates. Similar work was conducted by another researcher in which a developed composite made of neem/banyan fibers with sawdust filler loading composite revealed that fiber content can increase thermal conductivity compared to filler loading into the fabrication of composite laminates [23].

In sample B, thermal conductivity is 0.196 W/mK which is 23% lesser than sample A and 8% more than sample C; incorporating 25 g sawdust filler can reduce the thermal conductivity of hybrid composite by 23%, and at the same

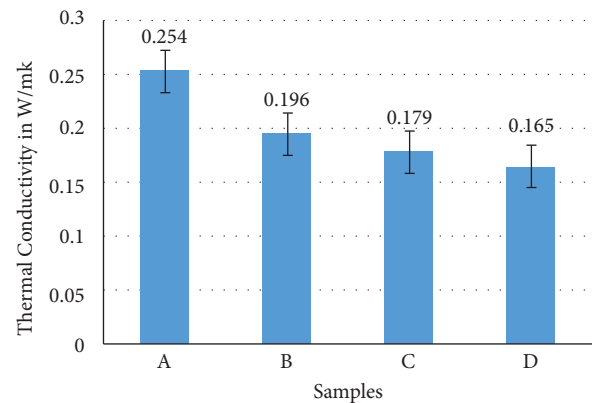


FIGURE 3: Thermal conductivity of basalt fiber composite.

time in sample C, thermal conductivity of 0.179 W/mK shows that increasing the sawdust filler to 50 g can impact thermal conductivity by 29% lesser than sample A. Therefore, basalt fibers are used to improve the thermal conductivity of hybrid composite, and the sawdust cellulose filler can reduce the thermal conductivity of composite fabrication for thermal insulation materials.

Another important property in thermal behavior is heat deflection temperature that needs to be conducted for this basalt fiber composite laminates to identify the short-term heat resistance capacity. The heat deflection temperature

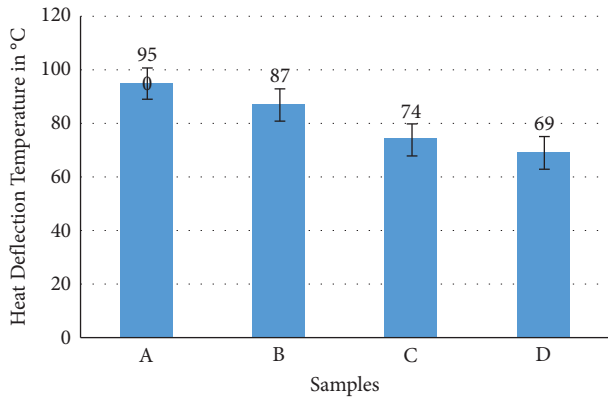


FIGURE 4: Heat deflection temperature of basalt fiber composite.

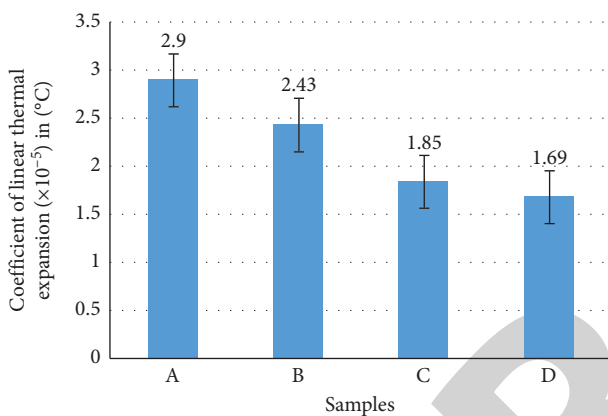


FIGURE 5: Coefficient of linear thermal expansion of basalt fiber composite.

results of basalt fiber composite are shown in Figure 4; the results are revealed similar to the thermal conductivity of hybrid composite, increasing basalt fiber loading to fabricate the composite laminates has given the maximum temperature resistance, and increasing sawdust cellulose filler can reduce the heat deflection temperature of hybrid composite.

The maximum heat deflection obtained in sample A is 95°C which is due to basalt fiber to sawdust filler weight ratio of 4:1, and epoxy matrix is 60% in all the four samples of hybrid composite. The bonding between basalt fiber mat, sawdust filler, and epoxy polymers was good and can increase the thermal behavior; as per the ASTM standard, 1.82 MPa load was applied during the analysis and the basalt fibers in mat form can transfer the load from one to another point smoothly to improve the short-term heat resistant capacity of hybrid composite. A similar mode of results was studied in another sisal fiber developed in which sawdust cellulose composite during the increase of filler materials is resistant to less temperature compared to the fiber form of reinforcement [13]. The least heat deflection temperature occurred in sample D is 69°C which is 27% less heat resistant compared to sample A and 21% less than sample B. Sample C got 74°C with a 2:3 weight fraction of fiber and filler materials, and 15% more heat deflection temperature is present in sample B compared to sample C. Therefore, among all the

four samples, basalt fiber can resist more heat than sawdust cellulose fillers of hybrid composite.

Coefficient of linear thermal expansion of hybrid composite was carried out to analyze the thermal expansion of basalt fiber composite, and the results of thermal expansion for basalt fiber composite are shown in Figure 5.

The higher thermal expansion coefficient obtained in sample A is  $2.9 \times 10^{-5}/^{\circ}\text{C}$ , thermal expansion is linear in sample B which is  $2.43 \times 10^{-5}/^{\circ}\text{C}$ , and increasing in basalt weight fraction in the fabrication of hybrid composite with sawdust cellulose can increase the linear thermal expansion of hybrid composite. Sample A has 41% more thermal expansion than sample D; therefore, decreasing the basalt fiber ratio from 100 g to 25 g can reveal the high positive impact during the thermal expansion analyses. Comparison between samples B and C shows that 24% higher thermal expansion occurred in sample B; similar work was conducted with sisal fiber composite and the results revealed that increasing the fiber weight fraction can improve the thermal expansion and the filler loading composite laminates reduce the coefficient of linear thermal expansion of hybrid composite [24, 25]. Based on the results, it can be clearly observed that the interfacial bonding between high sawdust filler loading with basalt fiber composite was improved significantly compared to basalt fiber loading and the composite laminates.

#### 4. Conclusions

The current work focuses on the production of composite laminates employing basalt fiber mat with sawdust fillers reinforced epoxy polymer, and the primary findings from the thermal tests are presented as follows:

- (i) The natural reinforcement of basalt fiber mat and sawdust fillers had significant bonding with an epoxy polymer matrix to fabricate the composite materials.
- (ii) High level of fiber loading on sample A can show the more thermal conductivity is 0.254 W/mK which is 35% more thermal conductance compared to sample E, therefore for thermal insulation materials application has been suitable by using sample E weight ratio and the sawdust filler loading bonding with fibers, a matrix is high and heat is not able to transfer more from one point to another point.
- (iii) Similar results were found in heat deflection temperature and thermal expansion coefficient of hybrid composite sample A is maximum values of 95°C and  $2.9 \times 10^{-5}/^{\circ}\text{C}$ , which is used to conclude that the basalt fiber composite laminates can be used as thermal insulation materials due to their thermal properties such as very low thermal conductivity, short-term heat resistant, and linear thermal expansion coefficient values sufficient for the thermal insulation applications. Therefore, natural materials of basalt fiber and sawdust fillers are suitable as reinforcement and can replace synthetic fiber usage in thermal insulation applications.

## Data Availability

The data used to support the findings of this study are included within the article. Further data or information is available from the corresponding author upon request.

## Conflicts of Interest

The authors declare that they have no conflicts of interest.

## Acknowledgments

This research work is not funded from any organization. The authors appreciate the supports from Jimma Institute of Technology, Jimma University, Ethiopia, for the research and preparation of the manuscript. The authors would like to acknowledge the Researchers Supporting Project Number (RSP-2021/373), King Saud University, Riyadh, Saudi Arabia.

## References

- [1] I. O. Oladele, T. F. Omotosho, and A. A. Adediran, "Polymer-Based composites: an indispensable material for present and future applications," *International Journal of Polymer Science*, vol. 2020, Article ID 8834518, 12 pages, 2020.
- [2] V. Mohanavel, S. Suresh Kumar, J. Vairamuthu, P. Ganeshan, and B. NagarajaGanesh, "Influence of stacking sequence and fiber content on the mechanical properties of natural and synthetic fibers reinforced penta-layered hybrid composites," *Journal of Natural Fibers*, vol. 2021, pp. 1–13, 2021.
- [3] M. R. S. KrittirashYorseng, H. P. JirattiTengsuthiwat, S. S. Jyotishkumar Parameswaranpillai, and M. M. Moure, "Information in United States patents on works related to natural fibers," *Current Materials Science*, vol. 12, no. 4, pp. 750–764, 2019.
- [4] T. Raja, V. Mohanavel, S. Suresh Kumar, S. Rajkumar, M. Ravichandran, and R. Subbiah, "Evaluation of mechanical properties on kenaf fiber reinforced granite nano filler particulates hybrid polymer composite," *Materials Today Proceedings*, vol. 59, no. 2, pp. 1345–1348, 2022.
- [5] D. Romanzini, A. Lavoratti, H. L. Ornaghi, S. C. Amico, and A. J. Zattera, "Influence of fiber content on the mechanical and dynamic mechanical properties of glass/ramie polymer composites," *Materials & Design*, vol. 47, pp. 9–15, 2013.
- [6] A. Veerasimman, V. Shanmugam, S. Rajendran et al., "Thermal properties of natural fiber sisal based hybrid composites – a brief review," *Journal of Natural Fibers*, vol. 2021, pp. 1–11, 2021.
- [7] V. Mohanavel, T. Raja, A. Yadav, M. Ravichandran, and J. Winczek, "Evaluation of mechanical and thermal properties of jute and ramie reinforced epoxy-based hybrid composites," *Journal of Natural Fibers*, vol. 2021, pp. 1–11, Article ID 1958432, 2021.
- [8] P. González García, R. Ramírez-Aguilar, M. Torres, E. A. Franco-Urquiza, and J. May-Crespo, "Mechanical and thermal behavior dependence on graphite and oxidized graphite content in polyester composites," *Polymers*, vol. 153, pp. 56–69, 2018.
- [9] R. Thandavamoorthy and A. Palanivel, "Testing and evaluation of tensile and impact strength of neem/banyan fiber-reinforced hybrid composite," *Journal of Testing and Evaluation*, vol. 48, no. 1, Article ID 20180640, 2020.
- [10] Y. Swolfs, I. Verpoest, L. Gorbatikh, and L. Gorbatikh, "Recent advances in fibre-hybrid composites: materials selection, opportunities and applications," *International Materials Reviews*, vol. 64, no. 4, pp. 181–215, 2019.
- [11] T. Raja, P. Anand, M. Sundarraj, M. Karthick, and A. Kannappan, "Failure analysis of natural fiber reinforced polymer composite leaf spring," *International Journal of Mechanical Engineering & Technology*, vol. 9, no. 2, pp. 686–689, 2018.
- [12] T. Raja, V. Mohanavel, T. Sathish et al., "Thermal and flame retardant behavior of neem and banyan fibers when reinforced with a bran particulate epoxy hybrid composite," *Polymers*, vol. 13, no. 22, p. 3859, 2021.
- [13] R. Balaji, M. Sasikumar, and A. Elayaperumal, "Thermal, Thermo oxidative and Ablative behavior of cenosphere filled ceramic/phenolic composites," *Polymer Degradation and Stability*, vol. 114, pp. 125–132, 2015.
- [14] A. Q. Dayo, B.-chang Gao, J. Wang et al., "Natural hemp fiber reinforced polybenzoxazine composites: Curing behavior, mechanical and thermal properties," *Composite Science and Technology*, vol. 144, 2017.
- [15] H. Alamri, I. M. Low, and Z. Allothman, "Mechanical, thermal and microstructural characteristics of cellulose fibre reinforced epoxy/organoclay nanocomposites," *Composites Part B: Engineering*, vol. 43, no. 7, pp. 2762–2771, 2012.
- [16] U. AchuthaKini, M. Shettar, S. Sharma et al., "Effect of hydrothermal aging on the mechanical properties of nanoclay-glass fiber-epoxy composite and optimization," *Using Full Factorial Design Materials Research Express*, vol. 6, pp. 510–523, 2019.
- [17] S. Mr, S. Siengchin, J. Parameswaranpillai, M. Jawaid, C. I. Pruncu, and A. Khan, "A comprehensive review of techniques for natural fibers as reinforcement in composites: preparation, processing and characterization," *Carbohydrate Polymers*, vol. 207, pp. 108–121, 2019.
- [18] MetehanAtagur, A. Orhan, K. Sever et al., "Investigation of thermal and mechanical properties of synthetic graphite and recycled carbon fiber filled polypropylene composites Materials," *Research Express*, vol. 6, pp. pp524–536, 2019.
- [19] S. Mr, S. Siengchin, J. Parameswaranpillai, M. Jawaid, C. I. Pruncu, and A. Khan, "A Comprehensive Review of Techniques for Natural Fibers as Reinforcement in Composites: Preparation, Processing and Characterization," *Carbohydrate Polymers*, vol. 207, pp. 11–83, 2019.
- [20] K. N. Bharath, M. R. Sanjay, M. Jawaid, S. B. Harisha, S. Basavarajappa, and S. Siengchin, "Effect of stacking sequence on properties of coconut leaf sheath/jute/E-glass reinforced phenol formaldehyde hybrid composites," *Journal of Industrial Textiles*, vol. 49, no. 1, pp. 3–32, 2019.
- [21] M. Rajesh, J. Pitchaimani, and N. Rajini, "Free vibration characteristics of banana/sisal natural fibers reinforced hybrid polymer composite beam," *Procedia Engineering*, vol. 144, pp. 1055–1059, 2016.
- [22] M. Jawaid and H. A. Khalil, "Effect of layering pattern on the dynamic mechanical properties and thermal degradation of oil palm-jute fibers reinforced epoxy hybrid composite," *Bioresources*, vol. 6, pp. 2309–2322, 2011.
- [23] P. Madhu, M. R. Sanjay, P. SenthamaraiKannan, S. Pradeep, S. S. Saravanakumar, and B. Yogesha, "A review on synthesis and characterization of commercially available natural fibers:



## *Retraction*

# **Retracted: Optimization on Tribological Behaviour of AA7075/Zirconium Boride Composites Using Taguchi Technique**

### **Advances in Materials Science and Engineering**

Received 26 December 2023; Accepted 26 December 2023; Published 29 December 2023

Copyright © 2023 Advances in Materials Science and Engineering. This is an open access article distributed under the Creative Commons Attribution License, which permits unrestricted use, distribution, and reproduction in any medium, provided the original work is properly cited.

This article has been retracted by Hindawi, as publisher, following an investigation undertaken by the publisher [1]. This investigation has uncovered evidence of systematic manipulation of the publication and peer-review process. We cannot, therefore, vouch for the reliability or integrity of this article.

Please note that this notice is intended solely to alert readers that the peer-review process of this article has been compromised.

Wiley and Hindawi regret that the usual quality checks did not identify these issues before publication and have since put additional measures in place to safeguard research integrity.

We wish to credit our Research Integrity and Research Publishing teams and anonymous and named external researchers and research integrity experts for contributing to this investigation.

The corresponding author, as the representative of all authors, has been given the opportunity to register their agreement or disagreement to this retraction. We have kept a record of any response received.

### **References**

- [1] S. K. Mohan, R. M. Reddy, V. Kamalakar et al., "Optimization on Tribological Behaviour of AA7075/Zirconium Boride Composites Using Taguchi Technique," *Advances in Materials Science and Engineering*, vol. 2022, Article ID 4058442, 7 pages, 2022.

## Research Article

# Optimization on Tribological Behaviour of AA7075/Zirconium Boride Composites Using Taguchi Technique

**S. Krishna Mohan,<sup>1</sup> R. Meenakshi Reddy,<sup>2</sup> V. Kamalakar,<sup>3</sup> Pranavan S,<sup>4</sup> M. Amareswar,<sup>5</sup> A. H. Seikh,<sup>6</sup> M. H. Siddique,<sup>7</sup> T. L. Kishore,<sup>8</sup> and Bhupender Singh<sup>9</sup>**

<sup>1</sup>Department of Mechanical Engineering E.G.S. Pillay Engineering College, Nagapattinam, Tamilnadu, India

<sup>2</sup>Department of Mechanical Engineering, G.Pulla Reddy Engineering College, Kurnool, Andhra Pradesh, India

<sup>3</sup>Department of Physics, Vel Tech Rangarajan Dr. Sagunthala R&D Institute of Science and Technology, Avadi, Chennai-600062, TamilNadu, India

<sup>4</sup>Department of Civil Engineering, Dhanalakshmi Srinivasan College of Engineering, Coimbatore, India

<sup>5</sup>Department of Computer Science and Engineering, Holy Mary Institute of Technology & Science, Hyderabad, Telangana, India

<sup>6</sup>Mechanical Engineering Department, College of Engineering, King Saud University, P.O. Box 800, Riyadh 11421, Saudi Arabia

<sup>7</sup>Intelligent Construction Automation Centre, Kyungpook National University, Daegu, Republic of Korea

<sup>8</sup>Department of Mechanical Engineering, University College of Engineering Kakinada (Autonomous), Kakinada, Andhra Pradesh 533003, India

<sup>9</sup>Department of Water Supply and Environmental Engineering, Arbaminch Water Technology Institute, Arbaminch University, Arba Minch, Ethiopia

Correspondence should be addressed to Bhupender Singh; [bhupender.sandher@amu.edu.et](mailto:bhupender.sandher@amu.edu.et)

Received 7 July 2022; Revised 20 August 2022; Accepted 13 September 2022; Published 11 October 2022

Academic Editor: K. Raja

Copyright © 2022 S. Krishna Mohan et al. This is an open access article distributed under the Creative Commons Attribution License, which permits unrestricted use, distribution, and reproduction in any medium, provided the original work is properly cited.

The impact of wear factors on composite materials is examined in this article. Stir casting was used to produce AA7075 alloys with varied nano-zirconium boride weight ratios. The dry sliding wear test was done utilizing pin-on-disc test equipment. The  $L_{27}$  orthogonal array was built by Taguchi's experiments for optimization. We calculated the proportion of responses that could be attributed to the input parameters using SNR and ANOVA. The rate of wear and the frictional coefficient raised with the highest loading level. Load concentration had an extreme impact on wear rate, coefficient of friction, sliding distance, and speed. Nano-zirconium boride particles placed in the matrix alloy prohibited any material loss. Zirconium boride nanoparticles were applied to AA7075 to increase its wear resistance.

## 1. Introduction

Metal matrix composites have been employed to substitute high-density substances in modern manufacturing for many years [1]. Aluminium matrix composites (AMCs) provide a number of advantages over other materials. Wear and abrasive resistance, in addition to a minimum thermal expansion coefficient, are further qualities [2, 3]. AMCs can be made using a variety of techniques. Liquid infiltration (LI) makes use of a variety of metalworking processes,

including powder metallurgy (PM), stir casting (SC), and composite casting (CC) [4]. Mechanical stirring is an affordable and straightforward method for dispersing ceramic particles in a homogenous manner [5]. In a metal matrix composite, the reinforcing particles are encased in a layer of the matrix material [6]. Stir casting is used to create composites in a liquid state. A hard particulate material can be added to a matrix material to increase its mechanical properties [7, 8]. Aluminium matrix composites (AMCs) have superior mechanical and tribological qualities

compared to steel. In this research, wear control parameters were examined to see if they had an impact on the rate of wear (i.e., sliding velocity, loads, reinforcements, and sliding distance) [9, 10]. Load is a major factor in determining the wear rate. It is influenced by a variety of variables, including sliding velocity, structural strengthening, and more. Due to wear, the connection between the strengthening volume portion, granular size, and sliding distance is critical [11]. The volume fraction of strengthening has a major impact on the rate of wear. According to a study, hybrid aluminum/AA/graphite AMCs exhibit severe wear and friction [12, 13]. Wear and the coefficient of friction reduced as the AA7075 composite's TiC concentration increased. Research into the wear resistance of an AA7075 alloy nickel-based compound was carried out in a laboratory [14]. The wear resistance and the coefficient of friction of AA7075 composites comprising  $\text{Si}_3\text{N}_4$  elements made via stir casting were examined [15, 16]. The volumetric wear loss of Al7075/silicon carbide AMCs was minimized by SiC reinforcement. Researchers have determined how sliding distance, stress, and wear affect the coefficient of friction by using Al- $\text{Si}_3\text{N}_4$  nanocomposite materials. In comparison to nanocomposite materials, hybrid composites have a lower wear rate and coefficient of friction (COF) [17]. A pin-on-disc machine was utilized to investigate the effects of silicon carbide and titanium dioxide element composites on Al LM25 [18]. The coefficient of friction and wear rate reduced with increasing titanium dioxide concentration. Wear resistance is improved by the lubricating and hardening properties of  $\text{TiO}_2$  particles [19].

In contrast, during a dry sliding wear test,  $\text{TiS}_2$ -strengthened LM13 Al AMCs were subjected to molten metal. As a result of the research, the load was the most important effect on the rate of wear. Since the increased level of surface damage, the degraded surface's morphology indicated increased wear under high stresses [20]. The wear of Al/ $\text{AlB}_2$  compounds was studied via Taguchi's dry sliding wear constraints. It has better tribological capabilities than unreinforced AMC, which is constructed of a composite of magnificently split Al elements. For the reinforcement of Al7075/ $\text{ZrB}_2$  aluminium matrix composites, a range of  $\text{ZrB}_2$  particles were employed (0, 5, and 7.5 percent). The weight percentages of  $\text{ZrB}_2$  particles increase their microhardness and mechanical properties [21]. For real-time applications, elevated ceramics have become essential. Possible uses of  $\text{ZrB}_2$  include thermal safety systems for structural applications, since it exhibits a special set of mechanical and physical qualities such as melting point, heat capacity, toughness, and resistance to abrasion. The mechanical properties of  $\text{ZrB}_2$ -enhanced aluminium metal matrix composites formed through stir casting are crucial. Composite tensile strength (composite strength per unit strength) was also increased when  $\text{ZrB}_2$  particles were added to the mix. The relationship between wear rate and load normal and reinforcement ratios is strong. Composites' wear behaviour is influenced by all of these elements [22]. The usage of data to evaluate the wear performance of aluminium matrix composites could exclude both time and money. On the basis of thorough literature analysis, they describe the

wear and morphological characteristics of AA7075 alloy-nano-zirconium boride particle strengthened compounds manufactured by stir casting [23]. Using a dry sliding wear method as a drying technique, these AA7075 alloy/nano-zirconium boride reinforced test pieces went through a series of stir casting tests. Research studies with POD equipment tested a variety of variables, including weight, sliding velocity, and sliding distance [24]. In this Taguchi experiment, a composite sample was used to find the best wear and friction parameters.

## 2. Methods and Materials

*2.1. Matrix and Reinforcement Assortment.* There are  $\text{ZrB}_2$  nanocomposites that are employed to reinforce the structure. A ceramic substance known as zirconium diboride ( $\text{ZrB}_2$ ) has thermal conductivity, hardness, density, and abrasive resistance, making it a good choice for high-strength applications. In terms of chemical composition, Zirconium boride and AA7075 are very similar, as in Tables 1 and 2. Zirconium boride nanoparticles of 40–70 nm in size are incorporated into the base matrix (0, 3, 6, or 9%).

*2.2. Composite Specimen Preparation.* The AA7075 aluminium alloy and nano-zirconium boride are made using a liquid state stir casting method. For this reason, the researchers say that stir casting produces a high-quality metal matrix than alternative fabrication methods. A gas burner (rpm) heated a graphite crucible to 500 revolutions per minute for 25 minutes to melt massive AA7075 aluminium alloy ingots as it has excellent characteristics and can be used for suitable applications. When zirconium boride particles are combined with oxygen, the oxides are first removed by heating the particles to  $650^\circ\text{C}$  in a muffle furnace. 0.5 wt% nano-Mg is added to the melted aluminium to improve wettability, which results in improved mixing. In the induction furnace, it is utilized to stir things up. Table 3 displays the composition of the pure aluminium alloy composite specimens.

*2.3. Experimental Arrangement of Dry Slide Wear.* The POD (pin-on-disc) wear was evaluated with an EN31 steel disc. Each specimen was subjected to nonlubricated wear tests over a distance of 500, 1000, and 1500 meters at a permanent sliding velocity of 4200 rpm by different applied weights of 10, 20, and 30 N. To guarantee good contact among flat surfaces and steel discs, the pin specimen was polished with emery paper before testing. An accuracy of less than 1g is required to calculate the specimen weightage afterward it was completely prepared with acetone liquid on an electronic scale. When calculating the rate of wear, a person's weight loss acts as a benchmark. With regards to losing weight, you need to pay attention to how much weight you lose for each inch of sliding distance. After undergoing a wear test, the pins are analysed under a scanning electron microscope to determine their surface morphology.

TABLE 1: Variant physical characteristics of nano-zirconium diboride ( $ZrB_2$ ).

Physical presence	Natural colour	% purity	Mass density (g/cc)	Particle size
Powder form	Grey-black	97	6.54	40–70 nm

TABLE 2: Chemical constituents of aluminium alloy (AA7075) [25].

Materials	Cr	Fe	Si	Mg	Mn	Cu	Zn	Ti	Al
Wt %	0.25	0.23	0.01	2.58	0.03	1.52	5.28	0.02	Balance

TABLE 3: Details on the composition of pure and aluminium alloy composite specimens.

Composite samples	Wt % of AA7075	Wt % of ( $ZrB_2+Mg$ )
AAZrB <sub>2</sub> -0	100	0
AAZrB <sub>2</sub> -3	97	3
AAZrB <sub>2</sub> -6	94	6
AAZrB <sub>2</sub> -9	91	9

**2.4. Taguchi Optimization.** Taguchi's study data reduces costs, increases efficiency, and offers durable, innovative solutions. The DOE design method is used to investigate typical effects of procedure constraints on response variables. In order to calculate wear parameters, this study made use of applied load, sliding velocity, and sliding distance. Table 4 provides a breakdown of the various characteristics and intensity levels.  $L_{27}$  orthogonal arrays are used in the Taguchi studies. When the DoF is less than or equal to the wear factors, orthogonal arrays must be employed. There were 27 rows and 13 columns in the orthogonal array that we used during the study. Designing an orthogonal array takes into account the level of each factor, the desired resolution, and any cost constraints. 27 experiments were conducted using the Taguchi model. Wear and friction coefficients can be seen in this graph. A five-column orthogonal array is the most common. The sliding distance table has five columns of data. Column one contains the applied weight, whereas columns two and five contain the slide speed. In an effort to reduce wear and friction, this design has been implemented. The final table of results is available for download (ANOVA). You must select a measurement type to determine the signal-to-noise ratio (for example, based on characteristic type). According to this belief, "small is better." In the lab, the SN ratio is assessed. The response loss was reduced by applying a logarithmic adjustment.

### 3. Result and Discussion

**3.1. Tribological Performance of Composite.** Dry sliding wear tests on an AA7075/ $ZrB_2$  aluminium matrix composite augmented with zirconium boride particles show a variety of tribological performances based on their weight ratio. Composite specimens were put into modules using the stir casting procedure. To mimic a dry sliding wear test, a selection of sliding distances was applied to four different composite specimens. When sliding velocity is taken into account, the wear and coefficient of friction of these

TABLE 4: Optimum factors and its levels.

Level	Wear load (N)	Sliding velocity (m/s)	Sliding distance (m)
1	10	3	500
2	20	4	1000
3	30	5	1500

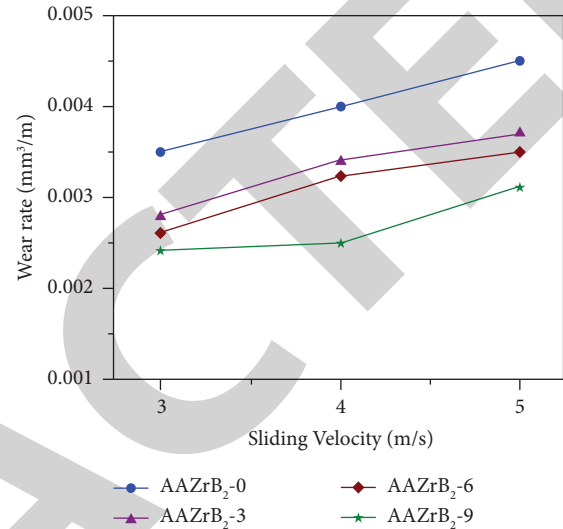


FIGURE 1: Based on sliding velocity, the wear rate of pure and hybrid composite.

composites might vary significantly. Speed increases the rate of wear and the coefficient of friction. At a sliding speed of 3 m/s, the wear rates of AA7075 and AA7075-9 wt% zirconium boride composites are illustrated in Figure 1. Due to a differential in temperature between a pin and its counter disc, increases as the sliding velocity increases. Experiencing this kind of heat might be harmful to your well-being. This means the rate of wear will be affected. Wear on the pin increases as the pin's temperature increases.

Figure 2 shows how sliding speed affects the coefficient of friction of pure and hybridized composite samples. It is possible to achieve a very smooth surface layer with high flash temperatures by increasing the loads and keeping the other input parameters constant. The friction coefficients, both static and dynamic, grow with increasing sliding velocity but reduce with decreasing sliding velocity. When compared to AA7075-zirconium boride composites, AA7075 has an 80% mix of AA7075-zirconium boride, resulting in a mechanically blended layer that facilitates substance removes during sliding. A huge amount of pressure is exerted on the contact velocity when direct contact is made between the sliding pin and a counter disc plate. Maximum sliding velocity causes frictional heat to build up on a surface, which elevates the surface temperature and speeds up the production of oxide layers on the surface.

**3.2. Experiments' Statistical Analysis Results.** The orthogonal array approach has been utilized with a wide range of

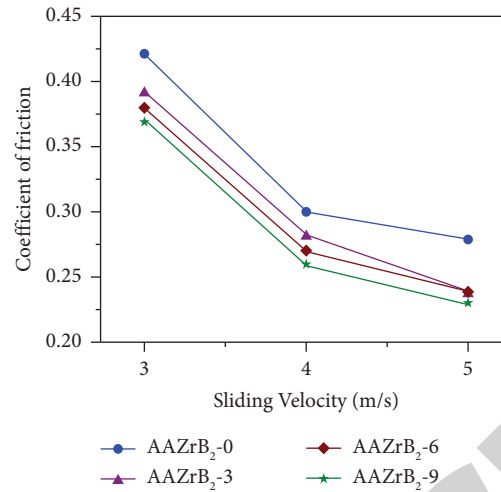


FIGURE 2: The sliding velocity affecting the coefficient of friction for both pure and hybridized composite samples.

TABLE 5: Taguchi orthogonal arrangement for AAZrB<sub>2</sub>-9 hybridized composites (94 wt. %AA7075 – ZrB<sub>2</sub>).

Experiment number	Wear load (N)	Sliding velocity (m/s)	Sliding distance (m)	Wear rate (mm <sup>3</sup> /min)	Sound-to-noise ratio (db)	Coefficient of friction	S/N ratio (db)
1	10	3	500	0.00342	49.857	0.521	9.674
2	10	3	1000	0.00487	48.908	0.497	9.2025
3	10	3	1500	0.00468	47.358	0.442	11.7242
4	10	4	500	0.00478	52.077	0.432	12.9541
5	10	4	1000	0.00478	51.094	0.402	11.7653
6	10	4	1500	0.00438	50.840	0.338	11.6256
7	10	5	500	0.00498	49.755	0.321	12.8287
8	10	5	1000	0.00467	48.856	0.354	12.6580
9	10	5	1500	0.00427	47.436	0.478	12.6216
10	20	3	500	0.00308	51.839	0.415	12.4291
11	20	3	1000	0.00421	50.369	0.369	10.5021
12	20	3	1500	0.00491	49.496	0.387	11.4054
13	20	4	500	0.00461	49.859	0.469	11.8625
14	20	4	1000	0.00421	48.520	0.403	11.4124
15	20	4	1500	0.00490	50.673	0.410	10.2797
16	20	5	500	0.00460	52.457	0.385	11.7576
17	20	5	1000	0.00430	47.615	0.412	11.6825
18	20	5	1500	0.00334	53.026	0.346	13.9539
19	30	3	500	0.00336	52.520	0.448	12.2819
20	30	3	1000	0.00398	46.239	0.309	12.9472
21	30	3	1500	0.00481	42.315	0.456	12.7372
22	30	4	500	0.00441	46.641	0.396	12.7916
23	30	4	1000	0.00412	51.201	0.369	13.9028
24	30	4	1500	0.00480	46.902	0.391	11.8037
25	30	5	500	0.00450	50.015	0.421	10.3724
26	30	5	1000	0.00420	48.435	0.348	11.6741
27	30	5	1500	0.00398	40.124	0.386	11.7803

parameter combinations. The design of experiment applications, Minitab 16, is a profitable product that was built specifically for this purpose. The tribological properties of composite AAZrB<sub>2</sub>-9 were better than expected when tested using the  $L_{27}$  orthogonal array, as shown in Table 5. Each of the three versions of AAZrB<sub>2</sub>-0, AAZrB<sub>2</sub>-3, and AAZrB<sub>2</sub>-6 are available. When materials are not reinforced with robust reinforcing materials, delamination and increased wear are regular occurrences. An audio recording's quality (SNR) is

determined by its signal-to-noise ratio (SNR). The load, sliding speed, and friction coefficient was discovered to influence wear and COF by employing an S/N response table.

The rate of wear and the coefficient of friction are directly related to sliding speed and distance. An excellent example of this style of illustration is a bar chart showing the rate of wear showing the coefficient of friction. This ratio can be used as a guide to find out when the wear rate and the coefficient of friction are at their lowest points in a test

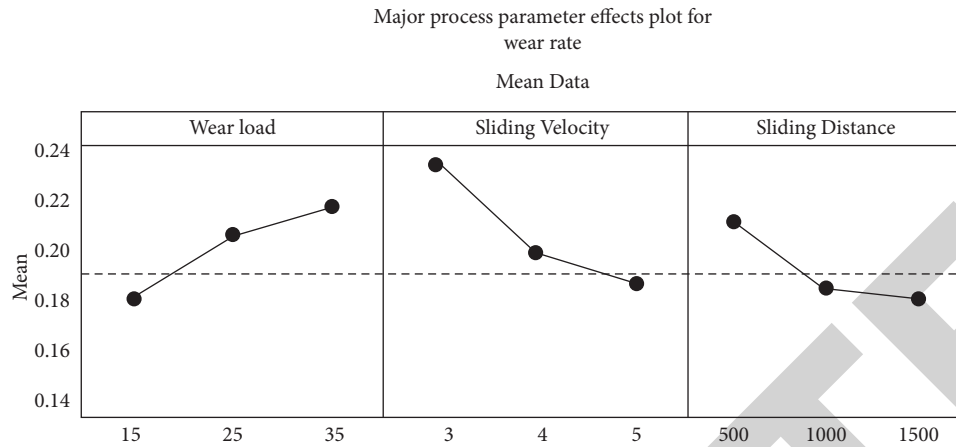


FIGURE 3: Main effects plot for wear rate (AAZrB<sub>2</sub>-9% composites).

system's life cycle. P2 is 20 Newtons, V3 is 5 m/s, and S3 is 1500; hence, "yes" is the correct response. Using an S/N response table, it was discovered that the load, sliding speed, and frictional coefficient all had an effect on wear and coefficient of friction. Sliding distance and speed are significant factors in friction and wear. A bar chart showing the wear rate showing the coefficient of friction may be regarded as an illustration of this visual aspect. As long as you keep in mind the S/N ratio as a reference, you can pinpoint the ideal operating conditions for reducing wear and friction. Yes, if S3 is 1500 and P2 is 20 Newtons, then the answer is yes. According to the results of an S/N response table, wear and coefficient of friction are affected by factors including load, friction, and sliding speed. Velocity and distance have an important effect on the wear rate as well as the friction coefficient of a surface. Other examples include a graph or table displaying the rate of wear and a linear graph or equation displaying the coefficient of friction. The sound-to-noise ratio can be used to classify the conditions at which wear and friction coefficient are at their lowermost.

**3.3. ANOVA Results for the Wear Test.** The main effect plot for means (AAZrB<sub>2</sub>-9 composites) is shown in Figure 3. We used a variance analysis to look at the relationship between wear parameters and performance metrics. The results of an experiment can be used to determine which independent variable is most important and how much of the variance can be attributed to that independent variable using an ANOVA. According to current research, three elements are variable at three levels and interact with one another. Tables 6 and 7 contain the outcome of the investigation of change for wear rate and COF. ANOVA displays the amount of load that has an extreme result on the rate of wear and the COF. Wear is the aspect in all three of these metrics. Load interactions had no effect on sliding velocity or distance, according to our study. As for the ANOVA on wear rate and COF, the research found that all hybrid AL compound samples had pooled errors of less than 2%. Wear and COF rise when a load is applied. The higher applied force, the higher temperature, and the greater friction. It is because of this that the reinforcing particles do not break down as a result of wear, resulting in material

TABLE 6: Wear rate AAZrB<sub>2</sub>-9% hybridized composites optimum response table: smaller is better.

Levels	Sliding load (N)	Sliding velocity (m/s)
1	52.68	53.61
2	51.87	52.27
3	51.15	52.34
Delta	4.35	4.08
Rank	1	2

TABLE 7: An optimum response for S/N ratios (COF-AAZrB<sub>2</sub>-9% hybridized composites).

Levels	Sliding load (N)	Sliding velocity (m/s)
1	12.421	11.747
2	12.586	12.691
3	12.951	11.74
Delta	1.872	1.976
Rank	1	2

fractures. As a risk, that substantial will be transmitted from the pin to the disc owing to the friction between shattered strengthening particles and steel discs. Because of this additional material loss, when the pin is full, it loses even more composites from its surface. As the sliding speed rises, so does the rate of wear and the COF. Aluminium alloy' oxidation temperature is controlled by its interfacial region, which reduces sliding and wear. The wear rate and COF are both raised by increasing the sliding distance. The novel coating technology utilized in this application improves abrasive resistance and dry slide wear performance. Because of their self-lubricating capabilities, aluminium compounds with strengthening had better friction and wear qualities. The surface of the sliding pins is reinforced, minimizing wear.

#### 4. Conclusions

- (i) As reinforcement, stir cast nano-zirconium diboride particles have been added to the AA7075 alloy. The effect of wearing parameters like stress and velocity



on the alloy has also been studied. The inclusion of a nano-zirconium boride powder with 3, 6, and 9% of AA7075 improved the regulation of the stir cast matrix process.

- (ii) To reduce the rate of wear and friction via adjusting the system settings for the dry sliding wear characteristics of composite materials. The sliding velocity is 5 m/s, as well as the sliding distance is 1500 meters, there is no practical higher limit to the amount of wear. Weight of the slide: 20 kilograms, a sliding speed of 3 meters per second, a length of 1000 meters, and the highest possible coefficient of friction.
- (iii) A variation study found that load and sliding distance had an effect on wear and friction coefficient (ANOVA). Composites wear out more quickly because of the weight and sliding distance they are subjected to. Nano-zirconium boride is used as an additive to improve wear resistance.
- (iv) Metal composites strengthened with zirconium boride elements (the dry sliding wear performance of alloy composites) can demonstrate special attention in engine parts, such as piston rings, cylinders, and bearings, because of their strong resistance to wear
- (v) Particle swarm optimization (PSO), evolutionary algorithms, and other techniques can be used to further improve the compound's wear rate characteristics

## Data Availability

The data used to support the findings of this study are included within the article and are available from the corresponding author upon request.

## Conflicts of Interest

The authors declare that they have no conflicts of interest.

## Acknowledgments

The authors appreciate the support from Arbaminch University, Ethiopia, for the research and preparation of the manuscript and the support from G. Pulla Reddy Engineering College, E.G.S. Pillay Engineering College, and Dhanalakshmi Srinivasan College of Engineering for the assistance in this work. The authors would like to acknowledge the Researchers Supporting Project Number (RSP-2021/373), King Saud University, Riyadh, Saudi Arabia.

## References

- [1] J. David Raja Selvam, I. Dinaharan, R. S. Rai, and P. M. Mashinini, "Role of zirconium diboride particles on microstructure and wear behaviour of AA7075 in situ aluminium matrix composites at elevated temperature," *Tribology: Materials, Surfaces & Interfaces*, vol. 13, no. 4, pp. 230–238, 2019.
- [2] S. Balaji, P. Maniarasan, S. V. Alagarsamy et al., "Optimization and prediction of tribological behaviour of Al-Fe-Si alloy-based nanograin-refined composites using Taguchi with response surface methodology," *Journal of Nanomaterials*, vol. 2022, p. 1, Article ID 9733264, 2022.
- [3] V. Mohanavel and M. Ravichandran, "Experimental investigation on mechanical properties of AA7075-AlN composites," *Materials Testing*, vol. 61, no. 6, pp. 554–558, 2019.
- [4] M. I. Ul Haq and A. Anand, "Dry sliding friction and wear behavior of AA7075-Si<sub>3</sub>N<sub>4</sub> composite," *Silicon*, vol. 10, no. 5, pp. 1819–1829, 2018.
- [5] V. K. V. Meti, S. Shirur, J. Nampoothiri, K. R. Ravi, and I. G. Siddhalingeswar, "Synthesis, characterization and mechanical properties of AA7075 based MMCs reinforced with TiB<sub>2</sub> particles processed through ultrasound assisted in-situ casting technique," *Transactions of the Indian Institute of Metals*, vol. 71, no. 4, pp. 841–848, 2018.
- [6] K. Maruthi Varun and R. Raman Goud, "Investigation of mechanical properties of Al 7075/SiC/MoS<sub>2</sub> hybrid composite," *Materials Today Proceedings*, vol. 19, pp. 787–791, 2019.
- [7] S. Suresh, G. H. Gowd, and M. L. S. D. Kumar, "Mechanical and wear behavior of Al 7075/Al<sub>2</sub>O<sub>3</sub>/SiC/mg metal matrix nanocomposite by liquid state process," *Adv. Compos. Hybrid Mater*, vol. 2, no. 3, pp. 530–539, 2019.
- [8] M. M. Ravikumar, S. S. Kumar, R. V. Kumar, S. Nandakumar, J. H. Rahman, and J. A. Raj, "Evaluation on mechanical behavior of AA2219/SiO<sub>2</sub> composites made by stir casting process," *AIP Conference Proceedings*, vol. 2405, Article ID 050010, 2022.
- [9] V. Mohanavel, M. Ravichandran, K. S. Ashraff Ali et al., "Atkilt mulu gebrekidan, "synthesis and workability behavior of Cu-X wt.% TiC (x = 0, 4, 8, and 12) powder metallurgy composites," *Bioinorganic Chemistry and Applications*, vol. 2022, Article ID 8101680, 2022.
- [10] M. Ravichandran and S. Dineshkumar, "Experimental investigations of Al-TiO<sub>2</sub>-Gr hybrid composites fabricated by stir casting," *Materials Testing*, vol. 58, no. 3, pp. 211–217, 2016.
- [11] D. Bandhu, A. Thakur, R. Purohit, R. K. Verma, and K. Abhishek, "Characterization & evaluation of Al7075 MMCs reinforced with ceramic particulates and influence of age hardening on their tensile behavior," *Journal of Mechanical Science and Technology*, vol. 32, no. 7, pp. 3123–3128, 2018.
- [12] H. R. Ezatpour, S. A. Sajjadi, M. H. Sabzevar, and Y. Huang, "Investigation of microstructure and mechanical properties of Al6061-nanocomposite fabricated by stir casting," *Materials & Design*, vol. 55, pp. 921–928, 2014.
- [13] P. S. Reddy, R. Kesavan, and B. Vijaya Ramnath, "Investigation of mechanical properties of aluminium 6061-silicon carbide, boron carbide metal matrix composite," *Silicon*, vol. 10, no. 2, pp. 495–502, 2018.
- [14] E. Jayakumar, A. P. Praveen, T. P. D. Rajan, and B. C. Pai, "Studies on tribological characteristics of centrifugally cast SiCp-reinforced functionally graded A319 aluminium matrix composites," *Transactions of the Indian Institute of Metals*, vol. 71, no. 11, pp. 2741–2748, 2018.
- [15] S. Baskaran, V. Anandkrishnan, M. Duraiselvam, and M. Duraiselvam, "Investigations on dry sliding wear behavior of in situ casted AA7075-TiC metal matrix composites by



## *Retraction*

# **Retracted: Parametric Optimization of Abrasive Water Jet Cutting on AA 5083 through Multiobjective Teaching-Learning Method**

### **Advances in Materials Science and Engineering**

Received 26 December 2023; Accepted 26 December 2023; Published 29 December 2023

Copyright © 2023 Advances in Materials Science and Engineering. This is an open access article distributed under the Creative Commons Attribution License, which permits unrestricted use, distribution, and reproduction in any medium, provided the original work is properly cited.

This article has been retracted by Hindawi, as publisher, following an investigation undertaken by the publisher [1]. This investigation has uncovered evidence of systematic manipulation of the publication and peer-review process. We cannot, therefore, vouch for the reliability or integrity of this article.

Please note that this notice is intended solely to alert readers that the peer-review process of this article has been compromised.

Wiley and Hindawi regret that the usual quality checks did not identify these issues before publication and have since put additional measures in place to safeguard research integrity.

We wish to credit our Research Integrity and Research Publishing teams and anonymous and named external researchers and research integrity experts for contributing to this investigation.

The corresponding author, as the representative of all authors, has been given the opportunity to register their agreement or disagreement to this retraction. We have kept a record of any response received.

### **References**

- [1] R. Meenakshi Reddy, K. Logesh, S. V. Alagarsamy et al., "Parametric Optimization of Abrasive Water Jet Cutting on AA 5083 through Multiobjective Teaching-Learning Method," *Advances in Materials Science and Engineering*, vol. 2022, Article ID 1123256, 7 pages, 2022.

## Research Article

# Parametric Optimization of Abrasive Water Jet Cutting on AA 5083 through Multiobjective Teaching-Learning Method

**R. Meenakshi Reddy,<sup>1</sup> K. Logesh,<sup>2</sup> S. V. Alagarsamy,<sup>3</sup> A. Nagaraj,<sup>4</sup> Rishabh Chaturvedi,<sup>5</sup> Mylavarapu Kalyan Ram,<sup>6</sup> A. H. Seikh,<sup>7</sup> M. H. Siddique,<sup>8</sup> and Beruk Hailu<sup>9</sup>**

<sup>1</sup>Department of Mechanical Engineering, G.Pulla Reddy Engineering College, Kurnool, Andhra Pradesh, India

<sup>2</sup>Department of Mechanical Engineering, Vel Tech Rangarajan Dr.Sagunthala R&D Institute of Science and Technology, Chennai, Tamil Nadu, India

<sup>3</sup>Department of Mechanical Engineering, Mahath Amma Institute of Engineering and Technology, Pudukkottai-622 101, Tamil Nadu, India

<sup>4</sup>Department of Mechanical Engineering, Jimma University, Jimma, Ethiopia

<sup>5</sup>Department of Mechanical Engineering, GLA University, Mathura, UP 281406, India

<sup>6</sup>Department of Computer Science and Engineering, Aditya Engineering College, Surampalem, Andhra Pradesh 533437, India

<sup>7</sup>Mechanical Engineering Department, College of Engineering, King Saud University, P. O. Box 800, Al-Riyadh 11421, Saudi Arabia

<sup>8</sup>Intelligent Construction Automation Centre, Kyungpook National University, Daegu, Republic of Korea

<sup>9</sup>Faculty of Mechanical Engineering, Haramaya Institute of Technology, Haramaya University, Dire Dawa, Ethiopia

Correspondence should be addressed to Beruk Hailu; [beruk.hailu@haramaya.edu.et](mailto:beruk.hailu@haramaya.edu.et)

Received 6 July 2022; Revised 23 September 2022; Accepted 26 September 2022; Published 11 October 2022

Academic Editor: K. Raja

Copyright © 2022 R. Meenakshi Reddy et al. This is an open access article distributed under the Creative Commons Attribution License, which permits unrestricted use, distribution, and reproduction in any medium, provided the original work is properly cited.

The industrial sector is seeing an increase in the development of new technologies on a daily basis. Manufacturing advancements have resulted in low-intensity, inadequate outputs from cutting materials. The application of engineering materials requires cutting to produce the desired shapes and sizes. The material's fundamental attributes are altered and utilised to improve machinability. Due to its significant benefits over traditional cutting processes, abrasive water jet cutting (AWJC) is now the most popular nonconventional machining for attaining the best cutting of any material. Because of its highly pressurised water power, the substance can quickly be separated from some properties by the use of a small pin with various kinds of abrasives. Due to the time-consuming process of cutting materials, determining optimal cutting conditions for the multiobjective criteria examined is a tough issue in techniques needing large resources. The operational parameters of the abrasive water jet cutting system must be changed in this article to achieve the lowest possible surface roughness while also attaining the maximum possible material removal rate. The abrasive water jet cutting method was utilised in this investigation to see how effectively the AA5083 aluminium alloy could be sliced. Water pressure, transverse speed, stand-off distance, and abrasive flow rate are some of the major cutting parameters that may be adjusted such that the output values such as material removal rate and surface roughness are at their optimal levels.

## 1. Introduction

One of the most versatile methods for making precise cuts in various materials is abrasive water jet machining. Precision and efficiency are the primary goals of the cutting method. Sand and gravel may be used as an abrasive at a very high

speed through a tiny water jet. As a dynamic approach, AWJ (abrasive water jet) cutting requires careful consideration of several performance-influencing elements. Factors such as water density and flow rate are the most critical to keep in mind when designing a water-based abrasive application. The most significant achievement in terms of growth,

efficiency, and long-term viability has been made. A variety of numerical and statistical model methods, in conjunction with appropriate experiment design, have been used to investigate the effect of water velocity, abrasive materials, and the size and shape of the nozzle on the overall machinability of brittle and ductile materials, as well as the machinability of composite materials [1]. The surface roughness of the AWJ parameters might be predicted using a mathematical model that has been created before. Using regression analysis, researchers were able to predict the results of composite materials based on the experimental data. An abrasive water jet was also used in this investigation, with surface roughness and kerf angle being measured using the design of experiments (DoE). An analysis of cutting quality using Taguchi's predictions reveals that abrasive jet machining's inherent increase in energy is confirmed [2]. A central composite rotatable design was used to study the cutting parameters of flow rate, rotating speed, and water pressure. A variety of groupings of these characteristics were then used to determine the metal removal rate [3]. In abrasive water jet turning, the most critical parameters were found to be the depth of cut and nozzle transverse speed, both of which were statistically significant. On the other hand, the rotational speed is considered a nonsignificant measure [4]. According to the study, increasing water pressure, stand-off distance, and nozzle speed, enhanced output responses lowest kerf profile, surface study, and with increased material removal rate were attained. Conventional machining produces a uniform surface finish on the material. Thus, by determining the surface irregularity of each machined region, the total surface quality of the part surface may be determined [5, 6].

It is feasible to come up with the best design possible by using evolutionary algorithms since they are rapid and well-organized procedures for testing and assessing experimental architectural approaches. Many engineering applications need the use of optimization in order to decrease the number of variables while simultaneously increasing the desired effect [7, 8]. Precision engineering is vital in complex engineering applications, and it is especially critical in aeronautical applications. Optimization and performance algorithms for machines include approaches for building and comparing machining settings in order to get the best possible machining performance. The most efficient method of maximising efficiency is to lower the many undesired values while optimising the ideal influence on the most desirable variables. In order to produce a high-quality product or a product that is competitive, the optimization strategy must be applied. When it comes to machine tool parameters, parametric optimization is a methodical and efficient approach to setting up and equating them in order to get the best possible outcomes [9, 10].

Author [11] used an artificial bee colony to optimise technique parameters such as water velocity and traversal intensity for surface irregularity, and then compared the results using regression equations, and genetic algorithms to determine the most effective approach. With the use of the Taguchi technique and evolutionary optimization. Consideration was given to the optimization of machining

parameters such as mass flow rate, transversal speed, and stand-off distance. For the most part, conventionally machined materials have a homogeneous surface finish. Using grey relation analysis to normalise performance evaluation of varied answers is extensively used, and it has been developed to cope with the complicated aspects of specific work systems [12]. It was possible for the researchers to learn more about the machinability of aluminium alloys by optimising the experimental settings and adjusting the influence of parameter variables such as transverse speed, stand-off distance, and abrasive feed, on the abrasive water jet cutting process on aluminium alloys. The influence of cutting rate, hardness, and surface study on a multiobjective optimization scenario was investigated utilising the Assignment of Weights for normalisation technique in a simulated environment [13]. To minimise surface roughness while simultaneously increasing material removal rate, multiobjective optimization of the abrasive water jet cutting AA5083 was performed in this study. In order to address the optimization of AA5083, full factorial design and multiobjective teaching learning-based optimization (MOTLBO) algorithms are used. The design of experiments is being used to improve the base metal cutting process to optimise variables such as water pressure, abrasive feed, stand-off distance, and nozzle speed, and the results are compared.

## 2. Materials and Methods

Lightweight aluminium alloys, such as those used in aircraft, are extensively used in a wide variety of applications across the world, notably in the aerospace industry. The principal use for this alloy is in high-strength structural applications. It possesses a high degree of ductility, as well as exceptional toughness and fatigue resistance, making it a great choice for structural applications. When combined with other properties, 5083 alloy has a very high strength-to-weight ratio and is very successful in high-temperature applications and aviation sectors. When compared to other families of aluminium alloys, the 5083 alloy is one of the strongest aluminium alloys currently available on the market. The composition of the AA5083 alloy is shown in Table 1.

It was decided that the block with the parameters of 500 mm in length, 50 mm across its surface area, and 50 mm above its surface area would be the size to be considered for testing using an abrasive water jet cutting machine while performing this experimental investigation. The abrasive water jet cutting measures  $X$ - $Y$  actions in millimetres, with the  $X$  axis measuring 300 millimetres and the  $Y$  axis being 1500 millimetres. A gravity-fed abrasive hopper was included with the equipment. Abrasive flow rate and water pressure are some of the input factors under AWJC that together reduce the output responses. These include nozzle jet angle, water pressure, stand-off distance, and abrasive flow rate. This approach presents difficulties in cutting operations because of the many factors that are involved in it. Three levels of machinability are determined using the full factorial technique for four parameters: water pressure, traverse speed, stand-off distance, and abrasive feed. The factors and levels of machinability are given in Table 2 for

TABLE 1: Composition of AA5083.

Elements	Si	Fe	Cu	Mn	Mg	Zn	Cr	Al
Weight (%)	0.4	0.4	0.1	0.52	4.42	0.25	0.195	Bal.

TABLE 2: Abrasive water jet cutting factors and levels for DoE.

Sl.No	Factors	Units	Levels		
			1	2	3
1	Water pressure	MPa	275	310	345
2	Traverse speed	mm/min	32	40	48
3	Stand-off distance	mm	2	4	6
4	Abrasive feed	g/min	200	300	400

each parameter. In the abrasive water jet cutting operations, sixteen experimental cutting operations are carried out with defined factors, and material removal rate and surface roughness are measured and analysed, respectively.

### 3. Teaching-Learning-Based Algorithm

Variables such as the size of the population, the number of generations, the number of groups, and so on are taken into account by all population-based evolutionary heuristic algorithms. A further benefit of using evolutionary algorithms is that they make use of features unique only to their algorithms. When it comes to genetic algorithms, unique operators like mutation and crossover are used, whereas inertia weights and cognitive parameters are used in particle swarm optimization. Scout, observer, and employee: Bees are utilised in the bee colony algorithm. The amount of effort needed is further reduced by altering the regularly used parameters in addition to the algorithm-specific variables. Thus, they [14] came up with a unique approach to teaching-learning-based optimization without any specific algorithms operators. Consequently, the term “teaching-learning-based algorithm” refers to an algorithm based on a teaching and learning process.

There are no algorithm-specific variables to deal with in teaching-learning-based optimization, making it simpler to use and implement than other population-based optimization approaches. The convergence rate is improved because TLBO employs the best solution from each generation to alter the current solution. For better results, TLBO employs the influencing parameter’s mean value. “Teacher phase” and “learner phase” are two distinct parts of teaching-learning-based optimization. Developed by it, the teaching-learning-based optimization was designed to solve difficulties related to a controlled mechanical application. In a classroom setting, when students first receive information from an instructor and then engage with one another, this phenomenon is set off [14].

In this case, when the algorithm is applied to a class of students, the students serve as the algorithm’s population, which is represented by the term “population.” Students’ findings are used as design variables in the optimization problem, and the results are used as a measure of the suitability of a suggested solution to the situation at hand.

This algorithm is comprised of two stages: the teacher phase and the learner phase [13, 14]. When students are in the instructor phase, the instructor works with them to help them advance their knowledge. For the duration of this teacher term, each student is allocated to a certain teacher. Moving the other outputs closer to the instructor’s position and taking the mean value of the parameters into account both helped to enhance them significantly. The student phase entails gathering information on the students and having them engage with one another. In this exercise, two students are picked at random and their replies are compared, with the students’ progressing towards better answers as a consequence of the comparison. As opposed to succeeding meta-heuristic algorithms, the teaching-learning-based optimization algorithm’s use of governing parameters rather than algorithm-based parameters is the most important benefit of the method [15–17]. This analysis is multiobjective because it contains many goals with opposing objectives, such as maximising material removal rate and minimising surface roughness. To solve a multiobjective optimization problem using the Assignment of Weights technique is required.

**3.1. Teacher’s Phase.** An excellent teacher helps his or her students to improve their knowledge to the highest possible degree. Although this is not possible in real time, an excellent teacher may move the pupils who perform above the mean of the class to a certain extent, dependent on the competence of the whole class. It is estimated as the mean value of the influencing values. The best instructor will be determined during the teacher selection process. The most effective instructor is chosen based on the highest possible COF score. The instructor is now more likely to use his or her expertise to benefit the whole student group. The following equation may be used to improve the performance of each individual learner (1)[14]:

$$Xt_n = Xt_o + \text{random}(X_{bt} - (tf * m)). \quad (1)$$

Choosing the best or best representation for the following stages and iterations will always lead to the convergence of the target. For a better portrayal of the instructors’ phase, MOTLBO’s first representation is used as a reference point. It is possible to compute and compare the

shortest distance. During the teacher's phase, the best string is represented and tallied as the result. When a teacher phase ends, all of its valid goal values are transferred over to the learner phase. As a result, the learner and instructor phases are interdependent.

**3.2. Learner's Phase.** Students (learners) are required to increase their knowledge by engaging with one another throughout the second stage of the MOTLBO algorithm. For the purpose of expanding their knowledge, students are allowed to communicate with one another at random. If another student has greater knowledge than the student who is being taught, the student might pick up new concepts. Each student has the ability to engage with another randomly chosen string in the first stage of this phase, for which randomly selected students are picked for the interaction. When making a pick, it is not possible to choose the same student more than once, nor can any student engage with the same group of students more than once. Only when the superior student interacts with the student can the student's knowledge be strengthened. A relationship between the following (2) and (3) has been established. The COF values of the two pupils will be compared in this section of the paper. The student's COF value exceeds the COF value of the selected student if the student's COF value is greater which is shown in the following equations:

$$X_{1_{ns}} = X_{1_s} + \text{rand}(X_{1_s} - X_{ss}), \quad (2)$$

$$X_{1_{ns}} = X_{1_s} + \text{rand}(X_{ss} - X_{1_s}). \quad (3)$$

In the next iteration, the output of the learner phase will be utilised as the input for the teacher phase. When the requisite number of generations or iterations has been reached, the whole process of going through the instructors' phase and the learners' phase will be repeated.

## 4. Results and Discussion

**4.1. Multiobjective Teaching-Learning-Based Optimization (MOTLBO) Results.** It is decided that the number of students in this optimization for MOTLBO will be 20 and that the number of iterations will be 100 in this optimization. The COF generation, after 30 iterations, has reached convergent behaviour and has produced optimal parametric values.

Table 3 summarises the optimal input parameters, MRR, and SR findings for the AA5083 after the necessary generations have been completed. The MOTLBO results of 275 MPa water pressure, a transverse speed of 48 mm/min, a stand-off distance of 2 mm, and an abrasive feed rate of 400 g/min are determined to be the ideal cutting parameters. It is possible to acquire MRR and SR as 6.4584016 g/min and 4.712 Ra for the output response parameters.

**4.2. Full Factorial Design.** It is possible to evaluate both the main effects and interactions in research using a full factorial design (FFD), which is an easy and methodical methodology. The growing importance put on an element or the rising

number of variables leads to a large rise in the number of test points, even if the design is constructive in nature when the number of variables and levels have been decreased, a factorial design is adequate for the research [18].

It is an absolutely critical parameter in every machining process since it determines how efficient the operation is going to be. Among the parameters studied, the abrasive feed rate was shown to be the most important. With an increase in abrasive feed rate, it was discovered that the MRR improved as in Figure 1. Due to an increase in feed rate, it takes less time to finish the products. The feed rate determines the amount of time it will take to perform the procedure completely. In conjunction with increased water pressure, the kinetic energy of the abrasive particles grows as well. In addition to having higher kinetic energy, abrasive particles have a better cutting ability as a consequence of their increased size, which enables more material to be removed in a given period of time. With increasing stand-off distance, it was discovered that the MRR rises. A divergent jet and low kinetic energy of abrasive particles, caused by the greater distance between the jet and the workpiece, may be attributed to this phenomenon. When the abrasive feed rate and transverse speed interact with one another, the metal removal rate first increases and then decreases with each other when the parameter level is raised to higher settings. With increasing stand-off distance and decreasing removal of material, the metal removal rate is somewhat lower. However, when transverse speed is adjusted, it rises with the decreasing removal of material. If we look at both the stand-off distance and the nozzle transverse speed, the value cuts with a surge in the rate of material removal for both of the input variables.

An increase in stand-off distance and abrasive feed rate results in a rise in surface roughness as shown in Figure 2. Depending on the pace at which the material is fed, cutting time might vary. Abrasive feed rates rise and new particles enter the cutting region, which means the abrasive particle has less time to cut the material. Abrasive particles have less time to cut the material with increasing abrasive feed rates, even if they have more or less cutting energy. This causes the surface to become more abrasive. The abrasive particles travel a greater distance as the stand-off distance rises. Increasing the spacing between the abrasive particles may result in a reduction in cutting capacity, resulting in a loss of sharpness in the material. So when abrasive particles move farther, their cutting effectiveness decreases because of inter-collision between particles, as well as distance travelled. The surface finish is influenced by the pressure of the jets. The water surface becomes smoother as the pressure rises. Brittle abrasives break down into smaller ones when water pressure increases. The smoothness of the surface is due to a decrease in the size of the abrasives. Water pressure also causes particles to have more velocity, which results in a smoother machined surface. The bonding strength of any material can only be broken by a significant number of strikes per unit area under a specified amount of pressure. Surface roughness decreases as the rate at which the abrasive is applied rises. This is due to the fact that a higher abrasive flow rate enables a larger number of impacts and cutting edges to be

TABLE 3: Abrasive water jet cutting optimized results of AA5083 by MOTLBO.

Water pressure (MPa)	Transverse speed (mm/min)	Stand-off distance (mm)	Abrasive feed (g/min)	MRR (g/min)	Surface roughness (Ra)
275	48	2	400	6.458	4.712

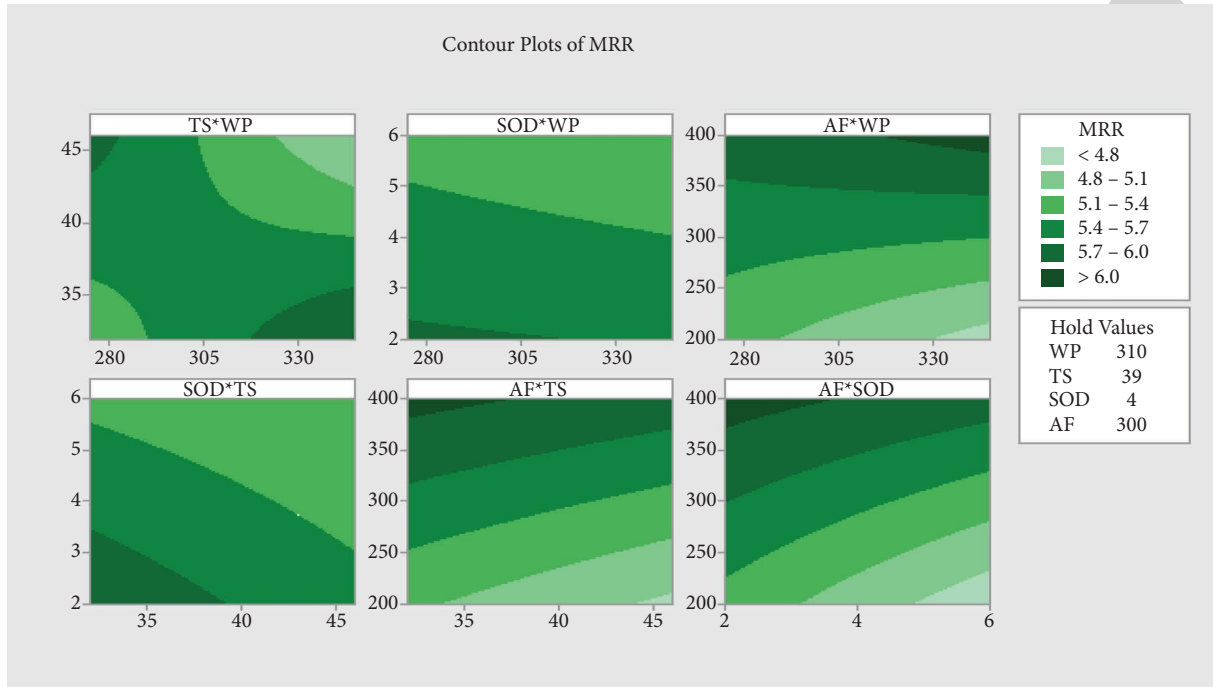


FIGURE 1: Contour interactions for metal removal rate.

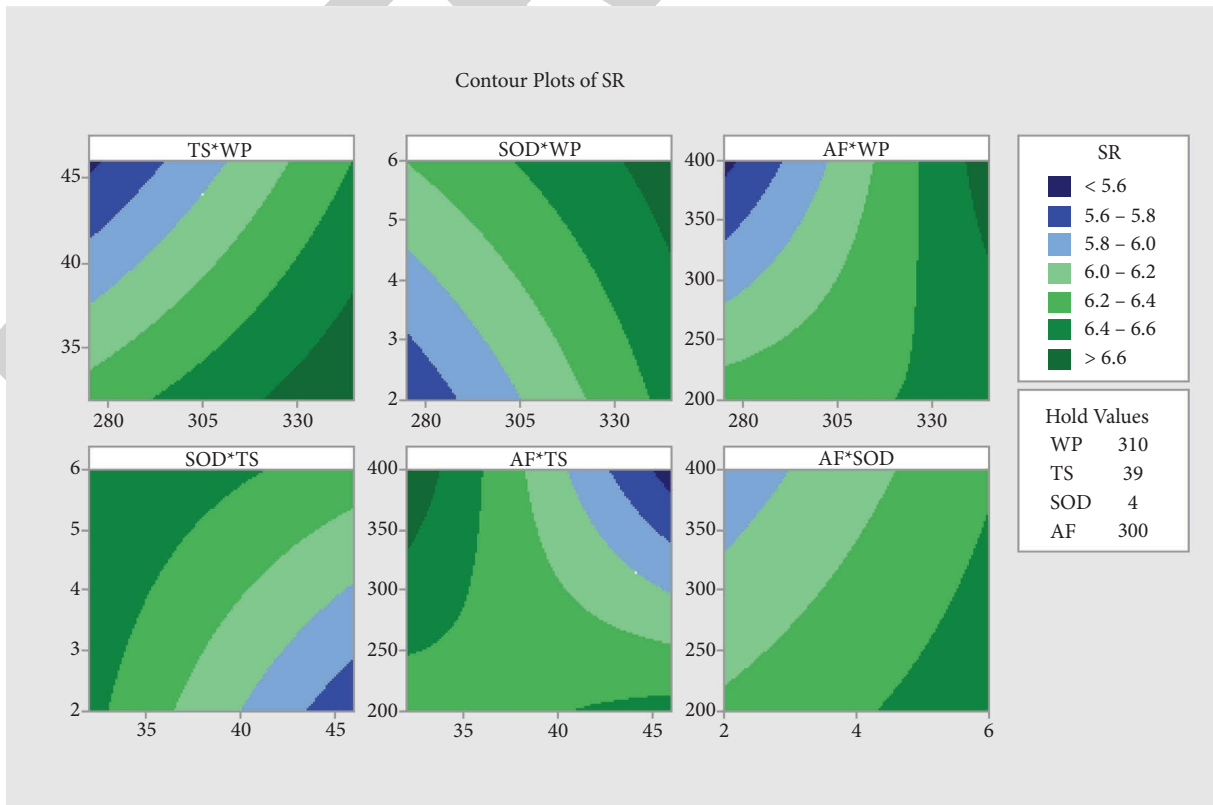


FIGURE 2: Contour interactions for surface roughness.

TABLE 4: Response optimization results of AA5083.

Solution	WP	TS	SOD	AF	SR Fit	MRR Fit	Composite Desirability
1	275	48	2	400	4.41179	6.40164	0.879028

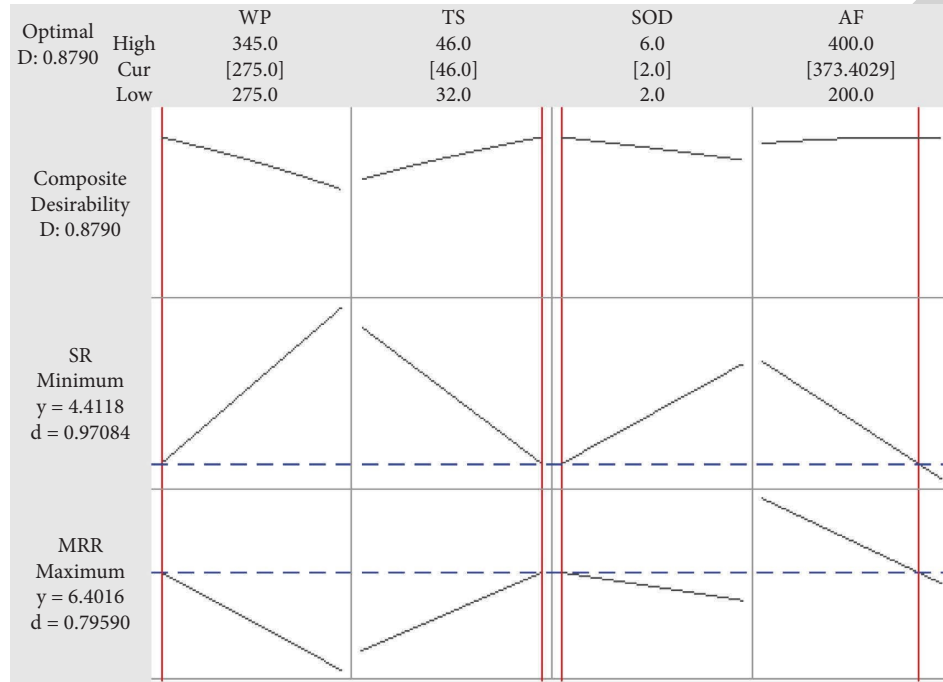


FIGURE 3: Response optimization plot of AA5083.

produced per unit area of a workpiece. Abrasive particle hitting and overall kinetic energy are affected by the rate at which the abrasive particles are fed. The more abrasive is fed into the jet, the more cutting power it will have. Abrasives, on the other hand, clash with one another and lose their kinetic energy when the flow rate is increased. The surface becomes rougher as one moves away from the nozzle entry.

**4.3. Response Optimization of Metal Removal Rate (MRR) and Surface Roughness (SR).** Response optimization is a systematic approach that is used to determine the optimal mixture of input variable settings that work together to optimise the quality of a single answer or a group of responses. An optimal solution for the variable input combinations is provided by the response optimizer function in statistical analysis software, which also produces optimization graphic plots [19].

Table 4 summarises the optimal input parameters, metal removal rate, and SR findings for the AA5083 after the necessary optimization has been completed. Figure 3 depicts the response optimization plot. 275 MPa water pressure, a transverse speed of 48 mm/min, a stand-off distance of 2 mm, and an abrasive feed rate of 400 g/min are determined to be the ideal cutting parameters. It is possible to acquire metal removal rate and SR as 6.4016 g/min and 4.4118 Ra for

the matching output response parameters. Abrasive feed rate and nozzle transverse speed should be increased in order to get the best results while cutting these materials. Abrasive feed rate and traverse speed play a significant role in cutting parameter reduction and optimization for assessing outputs such as surface roughness and material removal rate, which are two of the most important metrics.

## 5. Conclusion

To satisfy the demands for greater accuracy and efficiency in production, abrasive water jet cutting is one of the unconventional cutting methods that have been successfully used in numerous industries. This work is based on the abrasive water jet cutting process with the design of experiments for minimising the surface roughness and improving material removal rate to a greater extent and the subsequent studies are exposed.

- (i) Designs for testing AA5083 abrasive water jet cutting regression equations for metal removal rate and surface roughness were used.

Abrasive feed and traverse speed were found to be the most important abrasive water jet cut input parameters based on the findings also they play a significant role in cutting parameter reduction and



## *Retraction*

# **Retracted: Investigation of Groundwater Hydro-Geochemistry, Excellence, and Anthropoid Wellbeing Hazard in Dry Zones Using the Chemometric Method**

### **Advances in Materials Science and Engineering**

Received 26 December 2023; Accepted 26 December 2023; Published 29 December 2023

Copyright © 2023 Advances in Materials Science and Engineering. This is an open access article distributed under the Creative Commons Attribution License, which permits unrestricted use, distribution, and reproduction in any medium, provided the original work is properly cited.

This article has been retracted by Hindawi, as publisher, following an investigation undertaken by the publisher [1]. This investigation has uncovered evidence of systematic manipulation of the publication and peer-review process. We cannot, therefore, vouch for the reliability or integrity of this article.

Please note that this notice is intended solely to alert readers that the peer-review process of this article has been compromised.

Wiley and Hindawi regret that the usual quality checks did not identify these issues before publication and have since put additional measures in place to safeguard research integrity.

We wish to credit our Research Integrity and Research Publishing teams and anonymous and named external researchers and research integrity experts for contributing to this investigation.

The corresponding author, as the representative of all authors, has been given the opportunity to register their agreement or disagreement to this retraction. We have kept a record of any response received.

### **References**

- [1] M. S. Ahmed, G. Ramkumar, S. Radjarejesri et al., "Investigation of Groundwater Hydro-Geochemistry, Excellence, and Anthropoid Wellbeing Hazard in Dry Zones Using the Chemometric Method," *Advances in Materials Science and Engineering*, vol. 2022, Article ID 4903323, 10 pages, 2022.

## Research Article

# Investigation of Groundwater Hydro-Geochemistry, Excellence, and Anthropoid Wellbeing Hazard in Dry Zones Using the Chemometric Method

Mohamed Saad Ahmed,<sup>1</sup> G. Ramkumar,<sup>2</sup> S. Radjarejesri,<sup>3</sup> Ram Prasad,<sup>4</sup> Pilla Ravi Kishore,<sup>5</sup> Mika Sillanpaa,<sup>6</sup> and Endalkachew Mergia Anbese <sup>7</sup>

<sup>1</sup>Department of Geology and Geophysics, College of Science, King Saud University, Riyadh 11451, Saudi Arabia

<sup>2</sup>Department of Electronics and Communication Engineering, Saveetha School of Engineering, SIMATS, Chennai, Tamilnadu, India

<sup>3</sup>Department of Chemistry, Sona College of Technology, Salem 636005, Tamilnadu, India

<sup>4</sup>Department of Electronics and Communication Engineering, Mahatma Gandhi Central University, Motihari 845401, Bihar, India

<sup>5</sup>Department of Civil Engineering, Aditya Engineering College, Surampalem 533437, Andhra Pradesh, India

<sup>6</sup>Department of Biological and Chemical Engineering, Aarhus University, Norrebrogade 44 8000, Aarhus, Denmark

<sup>7</sup>Department of Civil Engineering, Ambo University, Ambo, Ethiopia

Correspondence should be addressed to Endalkachew Mergia Anbese; [endalkachew.mergia@ambou.edu.et](mailto:endalkachew.mergia@ambou.edu.et)

Received 21 May 2022; Revised 13 August 2022; Accepted 30 August 2022; Published 8 October 2022

Academic Editor: K. Raja

Copyright © 2022 Mohamed Saad Ahmed et al. This is an open access article distributed under the Creative Commons Attribution License, which permits unrestricted use, distribution, and reproduction in any medium, provided the original work is properly cited.

This work deals with the groundwater hydro-geochemistry, intake and irrigation water quality, and noncarcinogenic human healthiness concerns in a dry environment. Water quality characteristics were measured in samples which were gathered from the countryside and city. The findings showed that the composition of groundwater is acidic and stony. There was a wide range of nitrate and fluoride concentrations, with a mean concentration of 1.4 mg/ltr, 65.7 mg/ltr, and 0 to 13.3 mg/ltr. Only 14% of the samples were rated excellent by the water quality index, while 38% were rated good, 28% were rated bad, and 12% were classified unfit/unsuitable for eating. The quantities of nitrate and fluoride in groundwater are estimated to be 68% higher than the permitted range for noncarcinogenic ingestion, posing a major health risk to the local people. A range of indicators and graphical approaches were used to assess the appropriateness of groundwater. The geogenic origin of fluoride was demonstrated to be followed by the anthropogenic source of  $\text{NO}_3^-$ ,  $\text{K}^+$ ,  $\text{Na}^+$ ,  $\text{Cl}^-$ , and  $\text{HCO}_3^-$ , and the predominant hydro-chemical facies  $\text{Ca}_2^+$  and  $\text{HCO}_3^-$  are done.

## 1. Introduction

Groundwater in dry and semidry areas around the world is under threat as a main supply of water for both residential consumption and agricultural irrigation [1]. Groundwater is the principal basis of water for humans in dry and semidry regions of the world, but environmental issues about quantity, quality, and accessibility are critical [2]. A multitude of factors influence groundwater quality, including interactions between groundwater and the host aquifer

materials, invading water quality and more [3, 4]. Toxic human activities such as excessive use of agrochemicals, leaching from urban and industrial waste, and sewage leakage can also impair groundwater quality. According to the Indian government, groundwater accounts for 78% of the total irrigation capacity of the country's farms [5]. The annual amount of groundwater withdrawn exceeds the annual amount of groundwater recharge, resulting in overuse of groundwater resources. Drinking groundwater with fluoride levels above 2.6 mg/L can lead to dental

fluorosis, kidney and neurological disorders, and other health problems [6–8]. Chemometrics is a scientific discipline which use quantitative, analytic, or other methodologies based on logical reasoning to develop or choose appropriate measuring processes and studies, as well as to give the most pertinent data by evaluating chemical data and the compensation are shown in Figure 1 [9].

For fluoride and nitrate contaminated groundwater, the most common means of exposure are ingesting, inhalation, and skin contact [10, 11]. In terms of human health, inhalation and cutaneous exposure are of little concern. As a result, ingestion is the primary mode of exposure for humans. The US Environmental Protection Agency developed a four-step health risk valuation process which are as follows: (i) threat identification, (ii) dose-response assessment, (iii) exposure assessment, and (iv) hazard assessment. This work by Gibbs [12] researched fluoride and nitrate-enriched groundwater, while Giggenbach [13] investigated groundwater quality. Although the hydrogeology and source apportionment of essential elements as well as the human wellbeing risk calculation have been studied, the hydrogeology and source apportionment of essential elements as well as the human health risk valuation have not been fully investigated [14]. To fill this knowledge gap, we performed this investigation into the quality of groundwater. Gibbs plot research was made as the primary factors of groundwater chemistry including weathering of the aquifer host rock, evaporite salt dissolution, and ion exchange mechanisms. Geochemical markers and a multivariate statistical method were used to characterize and identify groundwater.

## 2. Methodology

**2.1. Groundwater Sampling and Analysis.** For the study's goals, fifty samples of groundwater were gathered from nine rural areas. The samples of groundwater were collected in 1-liter plastic bottles after a 10-minute preflushing to remove stagnant water and get fresh water. Using the American Public Health Association standard methods, groundwater samples were tested for 15 water quality constraints, ranging from pH and EC to total hardness (TH) and total alkalinity (TA), potassium, magnesium, sodium, sulphate, calcium, bicarbonate, and fluoride (F). The instruments for pH and EC measurements were employed by ELICO L1614 and ELICO CM183 electrochemical analyzers, respectively [15, 16]. The concentrations of TH and  $\text{Ca}^{2+}$  were restrained using the EDTA titrimetric method. The content of total hardness and  $\text{CO}_3^{2-}$  was then used to calculate,  $\text{Mg}^{2+}$ . The neutralisation titration method was used to estimate TA,  $\text{CO}_3^{2-}$ , and  $\text{HCO}_3^-$ . To estimate  $\text{Cl}^-$ , an argentometric titration with a standard solution of  $\text{AgNO}_3$  was utilized. The solution and potassium chromate ( $\text{K}_2\text{CrO}_4$ ) indicator was used, while systronics flame photometers were used to measure  $\text{K}^+$  and  $\text{Na}^+$ , and a spectrophotometric technique was used to measure  $\text{SO}_4^{2-}$ ,  $\text{F}^-$ , and  $\text{NO}_3^-$ . A blank and standard solution was used to calibrate the flame photometer before beginning the experiment. Every single groundwater sample was subjected to a three-way analysis. The water

used in this experiment was either twice distilled or deionized. The test findings were compared to the BIS and WHO drinking water quality criteria [17]. Then, graphs and other irrigational indicators were used to assess the suitability of groundwater for irrigation. Statistical package for social sciences was used to calculate the Karl Pearson correlation coefficients between the water quality values. SPSS was used to conduct a range of statistical studies in addition to PCA and HCA. Aquachem software was used to construct a box and whisker plot as well as a USSL salinity diagram.

**2.2. Water Quality Index (WQI).** The water quality index was created to assist in determining whether groundwater is safe to drink. It is a way of calculating a composite influence on water quality by examining water quality characteristics. It can also be measured in terms of human water use. According to the World Health Organization (WHO) and the Bureau of Indian Standards (BIS), the quality of groundwater for drinking has an impact on a number of purposes, including irrigation and drinking water. Equation (1) provided below was used to determine WQI:

$$WQI = \frac{\sum_{i=1}^n WiQi}{\sum Wi} \text{ where, } Qi = \frac{Va - Vi}{Vs - Vi} * 100. \quad (1)$$

For a total of n water quality parameters,  $Q_i$  is the quality rating of the  $i^{\text{th}}$  water quality parameter,  $V_a$  is the actual value acquired from investigation,  $V_i$  is constant for water quality, and  $V_s$  to be the BIS standard parameters for quality of water.

Quality rating scale ( $Q_i$ ) and weightage factor ( $W_i$ ) were derived for each parameter using the following equation :

$$W_i = \frac{K}{V_s} \text{ where, } K (\text{constant}) \quad (2)$$

$$= \frac{1}{(1/V_{S1}) + (1/V_{S2}) + \dots + (1/V_{Sn})}$$

## 3. Results and Discussion

In terms of freshwater supply, groundwater is the main essential and dependable source on the planet. For the vast majority of rural Indians, groundwater is their primary source of drinking water. People who depend on groundwater must therefore have the quality of their water assessed. Residents rely heavily upon drinking water that is sourced from the ground. There has been no groundwater monitoring study done in some areas according to a literature review. EC, pH, total alkalinity, and total hardness were measured in 48 samples collected from 9 rural and 1 urban location, as well as chloride, carbonate and bicarbonate, calcium, nitrate, fluoride, sulphate, and magnesium.

**3.1. Box and Whisker Plot.** The plot depicts the 5 number immediate of a dataset. In this 5-number summation, you will get the minimum 24th percentile and median 74%. This visualization allows you to compare two or more sets of data.



FIGURE 1: Shows advantages of the chemometric method.

Cations like  $\text{Na}^+$  and anions like  $\text{Cl}^-$  were discovered to have wide ranges of variance, whereas  $\text{K}^+$  and  $\text{F}^-$  are shown in Figure 2 to have narrow ranges of variation.

3.2. *Water Quality for Drinking.* In terms of acid-base neutralisation, water softening and other applications, pH is the most essential parameter. The concentration of hydrogen ions is related to the -ve logarithm of pH. It has a range of 0 to 14 points. Water with a pH of less than 7.0 is acidic, while water with a pH of more than 7.0 is basic. The water is considered neutral if its pH is exactly 7.0. Drinking water's pH ranges from 6.5 to 8.5. There was a pH range of 6.51 to 8.62 in the research area with an arithmetic mean of 7.61. Except for SC3 which had a pH of 8.62, all of the samples were within the acceptable range. With an average of 3.05 milliseconds per cm, the electrical conductivity (EC) ranged from 1.02 to 6.96 milliseconds per cm. From one location to the next, large differences in EC were discovered. Dissolved inorganic compounds in ionised form can be found at high levels of EC. TDS is one of the most important water characteristics. Water with a high total dissolved solid (TDS) level is highly mineralized. TDS levels should not exceed  $500\text{mgL}^{-1}$ , however they are allowed to go up to  $2000\text{mgL}^{-1}$  (BIS 2012). TDS concentrations ranged from 144.64 to  $4907.52\text{mgL}^{-1}$  in the current investigation, with a mean value of  $1700.61\text{mgL}^{-1}$ . Only 20 of the 50 samples tested fell inside the allowed level, while the other 30 fell outside of it.

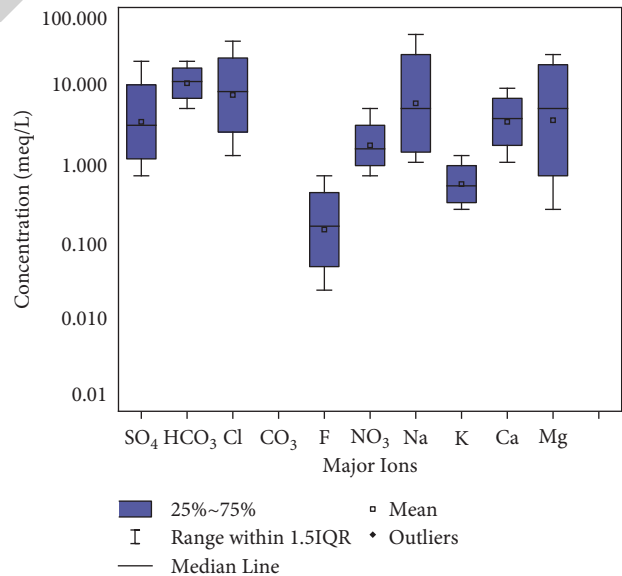


FIGURE 2: For significant cations and anions, a box and whisker plot.

Water with a salinity of  $< 1000\text{mgL}^{-1}$  is classified as fresh by Hwang et al. [18–20], while water with a salinity of  $1000 - 10000\text{mgL}^{-1}$  is classified as brackish. Freshwater makes up only 40% of the groundwater samples, with brackish water accounting for the remaining 60%. Acid-neutralizing

properties of water are determined by its alkalinity. Carbonate, bicarbonate, and hydroxide are the primary natural ingredients. The acceptable level for alkalinity is  $200\text{mgL}^{-1}$  and the allowed maximum level is  $600\text{mgL}^{-1}$ . Nearly all samples (92%) were within the legal limit of BIS and only 8% had TA levels over the permissible limit; the average TA concentration in this research region was  $311.44\text{mgL}^{-1}$ . In addition to the bicarbonates, chlorides, and sulphate, calcium ( $\text{Ca}^{2+}$ ) and magnesium ( $\text{Mg}^{2+}$ ) salts are responsible for the water's hardness. Scale formation in boilers and other equipment is one of the effects of hardness [21]. Stomach problems are caused by an excess of hardness, which weakens the stomach over time.  $\text{CaCO}_3$  equivalent calcium carbonate concentration is used to measure potable water hardness. Hardness ranged from 80 to  $1652\text{mgL}^{-1}$  in the examined area, with a mean of  $371.73\text{mgL}^{-1}$ . For TH, the reachable level is  $200\text{mgL}^{-1}$  and the allowed value is  $600\text{mgL}^{-1}$ ; 74% of samples were within the permitted range of BIS, whereas 24% of samples were outside the allowable range of BIS [22, 23]. Four levels of hardness were established by Durfor and Becker (1964):  $60\text{mgL}^{-1}$ , moderate ( $60\text{--}120\text{mgL}^{-1}$ ), difficult ( $120\text{--}180\text{mgL}^{-1}$ ), and extremely difficult ( $>180\text{mgL}^{-1}$ ). One hundred and forty-four % of samples fell into the very hard category, with only a single sample falling into the soft category. Cations are the most important. Because calcium is the most prevalent cation in water, hardness has an adverse effect on calcium concentrations. In terms of calcium, the acceptable limit is  $75\text{mgL}^{-1}$  and the allowed maximum is  $200\text{mgL}^{-1}$  [24]. The calcium concentration in the study region range is 11.2 to  $134.4\text{mgL}^{-1}$  and was found to be  $45.58\text{mgL}^{-1}$ . The BIS legal level for calcium was found in 88% of samples, which is within the acceptable limit set by the BIS and WHO. The human body's magnesium tolerance is lower than that of calcium, and a high concentration of magnesium acts as a laxative and imparts an off-putting flavor to water. Drinking water and  $\text{Mg}^{2+}$  levels should not exceed  $30\text{mgL}^{-1}$  and  $100\text{mgL}^{-1}$ , respectively. An appropriate level is  $50\text{mgL}^{-1}$ , according to the WHO. Table 1 shows the drinking water standard for ground water hydro-chemical parameters.

Except for pH and EC, all data are in mg/ltr. EC is measured in milliseconds per centimetre squared. Most samples (76%) were under the BIS acceptable limit for magnesium, and only 24 % reached this limit; the mean concentration of the magnesium range is  $0.7\text{--}317.84\text{mg/ltr}$  with an average of  $60\text{mg/ltr}$ . The body requires at least 98 milligrams of potassium on a regular basis. The supplementation of calcium improves blood pressure, bone health, cardiovascular health, and muscle strength. Hyperkalemia is a disorder caused by an excess of potassium in the body. The potassium concentration range starts from 0.0 to  $28.22\text{mgL}^{-1}$  in the studied area, with an average concentration of  $8.416\text{mg/ltr}$ . It is essential for the transmission of electrical messages between cells and the regulation of fluid balance in our bodies that sodium be present. Too much or too little sodium has a significant impact on human health. Hyponatremia is caused by a low sodium concentration in the blood. From 12.25 to  $1327.13\text{mg/ltr}$  of sodium was discovered in the research region, with an average of

$403.81\text{mg/ltr}$ . The WHO recommends that the highest amount of sodium in drinking water be  $48\text{mg/l}$ . Only 44% of the samples met WHO requirements, whereas 56% fell outside of this range. Village-to-village, the concentration of sodium differed. Anions of major important bicarbonate is a salt of carbonic acid, not a mineral. It neutralizes the acidic taste of carbonic acid by neutralizing its acidic content. With an average of  $380\text{mg/ltr}$ , bicarbonate range starts from  $163.78$  to  $857.72\text{mg/ltr}$ . There is a  $30\text{mgL}$  bicarbonate limit. The bicarbonate concentration exceeded the BIS limit in all samples. The Sardarshahar Tehsil groundwater samples contained no carbonate. Nitrate, a harmful chemical, is found in groundwater. The condition known as "blue baby syndrome" in infants can be caused by drinking water tainted with too much nitrate. According to the BIS and the World Health Organization, groundwater nitrate concentrations should not exceed  $48\text{mg/l}$  and  $52\text{mg/ltr}$ , respectively. Nearly two-thirds (65%) of the groundwater samples had nitrate levels above the BIS and WHO allowed limits, whereas just 46% of samples were within the safe range. There is chloride in all-natural waterways. One way  $\text{Cl}^-$  ends up in groundwater is by dissolving salt-bearing rock formations, weathering soil, or sewage discharge, among other possibilities. Increased water conductivity and hypertension may result from excessive  $\text{Cl}^-$  concentrations in the body [25]. According to the results, chloride levels in the research region ranged from  $19.99\text{mg/l}$  to  $2285.29\text{mg/l}$  on an average.  $250\text{mg/l}$  is the reasonable level also  $1000\text{mg/ltr}$  is the allowed limit, for chloride samples that was within the allowed limits of both the BIS and WHO were just 44% of the times. Chloride levels surpassed the BIS limit in only 22% of the samples tested. Groundwater naturally contains fluoride. Teeth mottling, skeletal fluorosis, and dental cavities can result from fluoride ingestion. In accordance with BIS (2012), the permissible level is  $1.0\text{mg/l}$ , but the WHO recommends a limit of  $1.65\text{mg/ltr}$  (2017). From 0 to  $13.25\text{mg/l}$ , the average fluoride concentration was  $1.3084\text{mg/l}$ . On the other hand, fluoride levels were below the detectable limit (BDL) in all but one of the 50 samples examined only in 10% of the samples (NA3, CH2, PH3, and DA4). No more than  $400\text{mg/ltr}$  of the sulphate can be tolerated in the water. An average of  $231.83\text{mgL}^{-1}$  of sulphate was found in the groundwater of the examined area. The BIS acceptable level was surpassed by 12% of the samples, out of a total sample pool of 50 samples tested. Sardarshahar Tehsil groundwater WQI ranged from 25.70 to 1079.87; 14% of the samples were excellent, 42% were good, 32% were bad, and 12% were unfit/inappropriate for drinking.

3.3. Base Exchange Index. Using equation (3), the BEI was derived:

$$BEI(r_1) = \frac{Na^+ - Cl^-}{SO_4^{2-}} \quad (3)$$

As part of the calculation of  $BEI(r_1)$ , the following quantities are stated in  $\text{meqL}^{-1}$ ;  $Na^+$ ,  $Cl^-$ , and  $SO_4^{2-}$ . It ranged in value which starts from  $-24.2$  to  $8.54$  milliequivalent per litre. There are two sorts of groundwater

TABLE 1: Drinking water standard for ground water hydro-chemical parameters.

Parameters	Samples			WHO standards (2017)	BIS standards		The no. of samples as per WHO limits	The no. of samples within BIS parameters		Weightage for water quality index (WI) $\sum_{i=1}^n W_i Q_i / W_i = 1$
	Minimum	Maximum	Average		Acceptable	Permissible		Acceptable limit	Permissible limit	
pH	6.48	8.75		6.2–8.2	6.6–8.6	6.6–8.6	98	50	50	0.09412
Electrical conductivity	0.19	8.12		—	—	—	—	—	—	—
TH	138.32	4912.24		700–1100	550	2100	25	25	25	0.00165
TDS	128	734		—	250	650	—	18	48	0.00401
TA	78	1648		110	250	650	3	29	40	0.00401
Ca <sup>2+</sup>	9.8	135.3		80	80	250	45	45	55	0.01273
Mg <sup>2+</sup>	1.02	318.42		55	35	120	34	28	40	0.02767
Na <sup>+</sup>	15.16	2951.56		260	250	420	43	40	45	0.00412
CO <sub>3</sub> <sup>2-</sup>	0	0		—	80	210	—	50	55	0.01234
NO <sub>3</sub> <sup>-</sup>	164.82	891.24		—	35	35	—	0	0	0.03148
K <sup>+</sup>	20.16	2281.96		210	260	1200	23	23	40	0.00412
F <sup>-</sup>	0	14.18		1.8	1.2	1.6	46	37	48	0.8673
HCO <sub>3</sub> <sup>-</sup>	1.35	197.28		55	50	50	24	24	25	0.01883
Cl <sup>-</sup>	0	29.11		—	—	—	—	—	—	—
SO <sub>4</sub> <sup>2-</sup>	13.15	1334.36		55	—	—	22	—	—	—

sources based on the value of  $r_1$ . As long as the  $r_1$  value is lesser than 1, the sources of groundwater are  $Na^+ - SO_4^{2-}$  type, and if  $> 1$ , it specifies the groundwater resource type is  $Na^+ - HCO_3^-$ ; 76% groundwater specimens were classified as  $Na^+ - SO_4^{2-}$ ; 24% are of  $Na^+ - HCO_3^-$  form. Figure 3 shows the total health hazard index shown by a box and whisker plot (THHI). The meteorological genesis index (meteorological genesis index) is a metric, the meteoric genesis index described below is used to classify groundwater samples in equation (4) and in Table 2.

$$MGI(r_2) = \frac{(K^+ + Na^+) - Cl^-}{SO_4^{2-}} \quad (4)$$

The meteoric genesis index (MGI) can be calculated as ( $r_2$ ),  $Na^+$ ,  $K^+$ ,  $Cl^-$ , and  $SO_4^{2-}$  are expressed in milli equivalents per litre. This ranged from  $-24.2$  to  $9.14$  milli equivalents per litre for the MGI. It suggests shallow meteoric percolation if  $r_2$  is less than 1, while it indicates deep meteoric percolation if  $r_2$  is greater than 1. In the study area, the samples of shallow meteoric percolation is made up of

$$C_2S_1 (38\%) > C_4S_2 (22\%) > C_4S_4 (20\%) > C_4S_1 (6\%) > C_4S_3 (4\%) > C_3S_2 (4\%) > C_3S_3 (2\%) > C_3S_1 (2\%) > C_1S_1 (2\%). \quad (5)$$

**3.6. Residual Sodium Carbonate.** Remaining sodium carbonate (RSC) from the irrigation point is an important metric for monitoring water quality. The appropriateness of groundwater for irrigation depends on the concentration of  $CO_3^{2-}$  and  $HCO_3^-$  in the groundwater. There is greater probability of  $Ca^{2+}$  and  $Mg^{2+}$  precipitation if the water has high bicarbonate content. As a whole, the range of the RSC values was  $-22.239$  to  $10.898$   $meq L^{-1}$  of these, 64% were suitable for irrigation, 14% were dubious or slightly safe, 12% were unsuitable, and 10% were dangerous.

76% of the samples, whereas the samples of deep meteoric percolation is made up of 24% of the samples.

**3.4. Sodium Adsorption Ratio.** Sodium is an extensively used indicator and water is suitable for irrigation. The sodicity of a water sample is determined by the ratio of  $Na^+$  ions to the sum of  $Ca^{2+}$  and  $Mg^{2+}$  ions. Irrigation cannot be done with extremely salty water [26]. If the SAR is greater than 10, soil permeability issues may arise [27]. According to Li et al. [28, 29] evaluation of SAR, 49% of the samples were exceptional, 23% were respectable, 8% were questionable, and 18% were inappropriate.

**3.5. USSL Salinity Diagram.** According to the USSL salinity diagram (USSL), as shown in Figure 4, which shows sodium dangers on the X-axis while salinity dangers are on the Y-axis, 50% examples had extremely high salinity, 10% had high salinity, 40% had average saltiness, and 3% had low saltiness. Based on the plot, the groundwater samples were arranged in the following manner, as shown in equation (5).

**3.7. Percentage Sodium (% Na).** It shows the percentage of sodium (% Na) in irrigation water, which can be used to calculate the concentration of  $Na^+$ . There was a range of  $8.522$  to  $94.291$   $meq L^{-1}$  of Na in the research region. There are 8% exceptional samples, 34% decent samples, 6% permitted samples, 28% questionable samples, and 24% inappropriate for irrigation.

**3.8. Kelly's Index.** In the evaluation of irrigation water, Kelly's index (KI) is a useful metric.  $Na^+$  is computed against  $Mg^{2+}$  and  $Ca^{2+}$  in order to determine KI. It is OK to use this

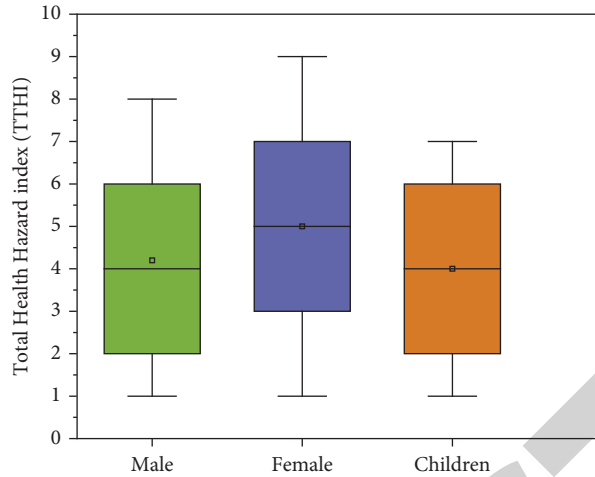


FIGURE 3: The total health hazard index is shown by a box and whisker plot (TTHI).

TABLE 2: Risk assessment for noncancerous substances.

Noncarcinogenic risk	Hq NO <sub>3</sub> <sup>-</sup>		Hq F <sup>-</sup>		TTHI	
	Hq less than one NS (%)	Hq greater than one NS (%)	Hq less than one NS (%)	Hq greater than one NS (%)	TTHI less than one NS (%)	TTHI greater than one NS (%)
Male	25	30	35	20	12	40
Female	25	30	35	20	12	40
Children	25	30	36	15	12	40

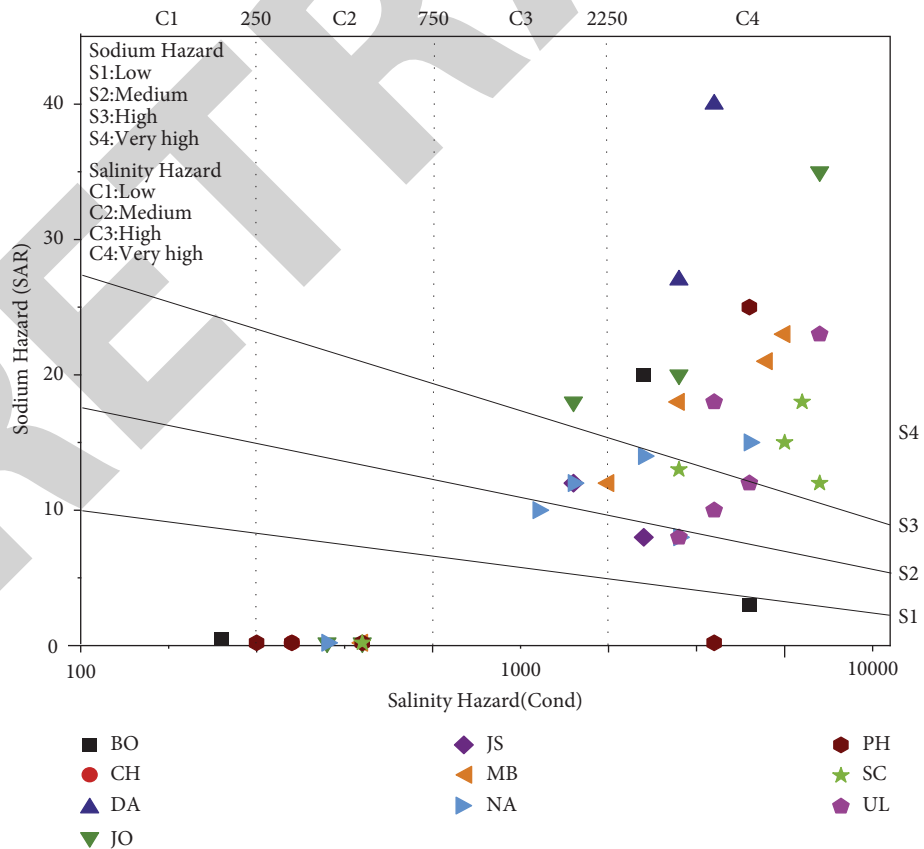


FIGURE 4: USSSL salinity diagram.



water for irrigation if the KI value is  $< 1$ , but it is unfit for irrigation if the KI value is  $> 1$ . It is used to compute KI. KI values ranged from .078 to 15.8 milli equivalents per litre during the experiments. Based on the categorization proposed by Kelly (1951), 44% of samples were appropriate and 56% of samples were unfit for testing and research purposes.

**3.9. Magnesium Hazard.** The level of  $Mg^{2+}$  in the water is the most important factor in determining its appropriateness for irrigation. When it comes to groundwater, it is common for the ions of calcium and magnesium to be in equilibrium. Magnesium, if present in excessive concentrations, alters the soil's pH and decreases the crop's productivity presented was used to calculate MH. MH concentrations ranged from 4.324 to 96.244 milli equivalents per litre. This work (31) found that only 48% of the samples remained appropriate for irrigation, though the other 52% were inappropriate.

**3.10. Permeability Index.** The permeability index (PI) is a measure for determining the quality of irrigation groundwater.  $Mg^{2+}$ ,  $HCO_3^-$ ,  $Na^+$ , and  $Ca^{2+}$  all have an effect on soil permeability. According to PI's analytical data, just 2% of groundwater samples are categorized as class III, 34% as class II, and 64% as class I. In Richard's [30] classification, water from classes I and II is often suitable for irrigation. As a consequence, 98% of the samples tested passed the PI inspection and can be used for irrigation.

**3.11. Residual Sodium Bicarbonate (RSBC).** RSBC is a measurement used to gauge irrigation water quality. There is a clear correlation between bicarbonate and calcium concentrations in water, which affects its quality as shown in the following equation:

$$RSBC = HCO_3^- - Ca^{2+}. \quad (6)$$

RSBC ranged from 0.3 to 11.9 mill equivalents per litre. Samples suitable for irrigation accounted for 72% of the total samples analyzed.

**3.12. Hydro-Geochemical Analysis of Groundwater.** The key hydro-geochemical processes that influence groundwater chemistry in the most fundamental way are silicate weathering, carbonate dissolution, ion exchange, and precipitation. Conventional graphs and ionic connection plots can be created from the findings of chemical analysis to aid in determining the processes/mechanisms that influence water's hydrochemistry, which, in turn, aids in understanding how groundwater's hydrochemistry is formed. Groundwater geochemistry has been analyzed using chemometric approaches, conventional graphical plots, ionic cross plots, and chloro-alkaline indices in the present work.

**3.13. Gibbs Plot.** The use of the Gibbs diagram helps us comprehend the effects of the three hydro-geochemical mechanisms on the groundwater geochemistry (interplay between water and rocks, condensation, and evaporation).

Groundwater chemical composition relies on systems like these, and understanding how they work might shed light on how groundwater forms. There is a formula that may be used to calculate the anions and cations Gibbs ratios. According to Figure 5, all of the samples are concentrated in one of two Gibbs plots: either the region dominated by evaporation or the region dominated by rock. As a result, evaporation and dissolution of ions in groundwater are the most important factors in influential the chemical configuration of groundwater. Neither of the two Gibbs plots shows a precipitation dominance zone for any sample. It is, therefore, negligible that precipitation affects groundwater chemistry in an arid area where precipitation is sparse.

**3.14. Ion Exchange Mechanisms Using Ionic Cross Plots.** Another hydro-geochemical mechanism has a significant impact on the groundwater chemistry evolution. These ion exchange activities occur when water circulates or stagnates in the host aquifer and is described by two terms: Schoeller indexes and chloro-alkaline indexes (CAIs). The below equations (7) and (8) are used to calculate CAI-I and CAI-II, respectively.

$$CAI - I = \frac{Cl - (K^+ + Na^+)}{Cl}, \quad (7)$$

$$CAI - II = \frac{Cl - (K^+ + Na^+)}{(CO_3^{2-} + SO_4^{2-} + HCO_3^- + NO_3^-)}. \quad (8)$$

Milliequivalent/L measurements of  $Cl^-$ ,  $K^+$ ,  $Na^+$ ,  $CO_3^{2-}$ ,  $HCO_3^-$ ,  $SO_4^{2-}$ , and  $NO_3^-$  were made. Groundwater in Sardarshahar Tehsil contained CAI-I and CAI-II, which ranged from  $-20.485$  to  $0.9432$  and  $-1.968$  to  $2.7478$ , respectively. 66% of the samples show positive CAI results, while only 44% of the groundwater samples have negative results. The hardness of groundwater is caused by the exchange of sodium and potassium in the groundwater for magnesium and calcium in the host aquifer material. Nevertheless, the negative values of the two CAIs suggest that the sodium and potassium ions from the aquifer rock resources are being swapped with the calcium ( $Ca^{2+}$ ) and magnesium ( $Mg^{2+}$ ) ions. Chloro-alkaline imbalance can be detected by CAIs that are negative. The base ion exchange results in water softening and sodium ( $Na^+$ ) enrichment in this case is shown in equation (9).

Aquifer material  $-(Ca^{2+}/Mg^{2+}) + 2(Na^+/K^+)aq \longrightarrow$   
Aquifer material  $-2(Na^+/K^+) + (Ca^{2+}/Mg^{2+})aq.$

$$Aquifer\ material - 2\left(\frac{Na^+}{K^+}\right) + \left(\frac{Ca^{2+}}{Mg^{2+}}\right)aq$$

$$\longrightarrow Aquifer\ material - (Ca^{2+}/Mg^{2+}) + 2(Na^+/K^+)aq. \quad (9)$$

The scatter plot showing the relationship between the concentrations of  $\{(Ca^{2+} + Mg^{2+}) - (HCO_3^- + SO_4^{2-})\}$  vs.  $\{(Na^+ + K^+) - Cl\}$  supports the idea that ion exchange and reverse ion exchange occur. Because of the importance of

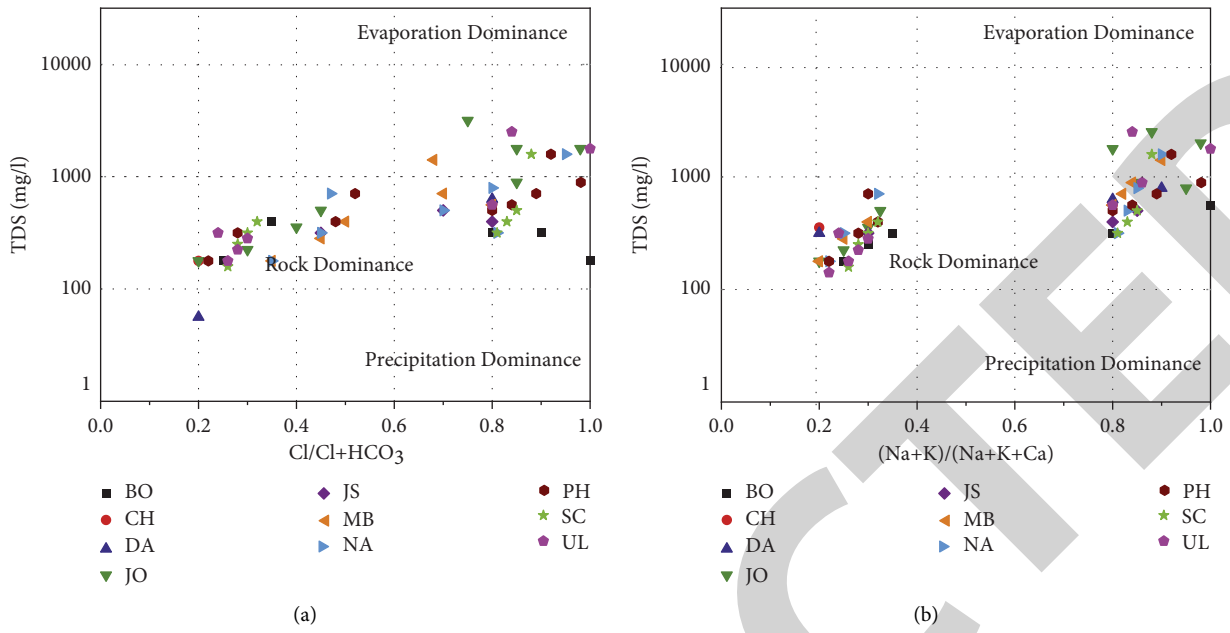


FIGURE 5: Gibbs plot (a) cations (b) anions.

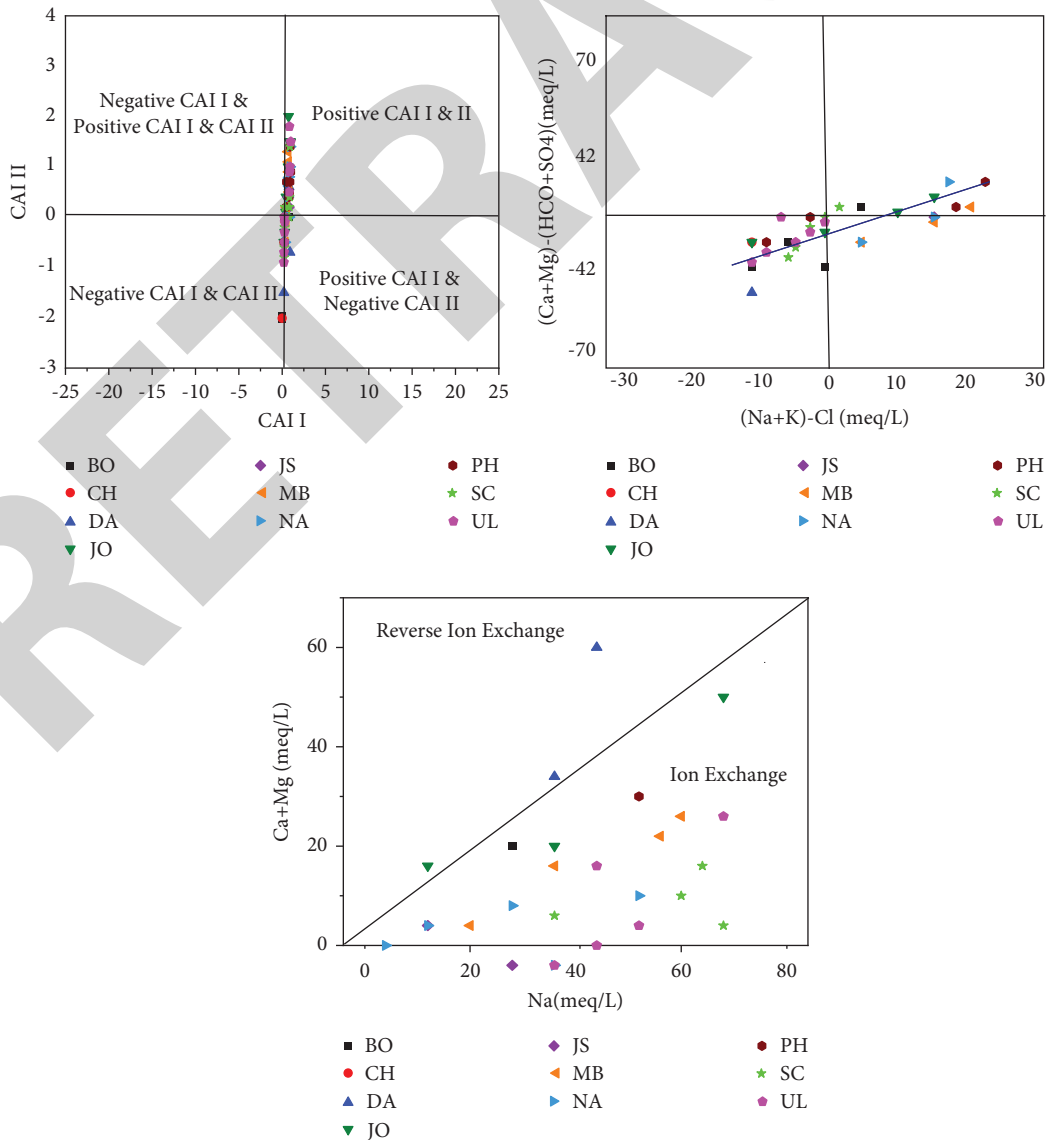


FIGURE 6: Scatter plots.

this process in controlling groundwater chemical composition, the slope of this scatter plot should be equal or less than 1. At  $R^2 = 0.049$ , the slope of the bivariate line in this case has been found to be  $y = -0.285 \times -3.5562$  with an R-squared value of  $-0.285$ . Furthermore, the bivariate plot of  $Ca^{2+} + Mg^{2+}$  vs  $Na^+$  illustrates that the groundwater samples had ion exchange and reverse ion exchange techniques are also used and are shown in Figure 6.

#### 4. Conclusions

Water quality variables investigated in rural and urban samples included human consumption and agricultural usage. We came to the following conclusion as a consequence of our investigation:

- (i) The groundwater is alkaline and hard with high amounts of  $Na^+$  and  $HCO_3^-$ , brackish groundwater samples are of 62% with overall dissolved solids greater than 1000 mg/l. The sample nitrate concentrations ranged from 1.35 to 200 mg/l; fluoride concentrations ranged from 0 to 14 mg/l; 88% of the samples fell inside the BIS and WHO permissible bounds; 12% of the samples went above the permitted range for fluoride in groundwater.
- (ii) samples rated exceptional by WQI had 10% of the samples rated excellent; 42% rated good; 32% rated poor, and 8% rated poor/unfit for drinking.
- (iii) According to the USEPA approach, the overall health hazard index for men ranged from 0.415 to 13.978, for women from 0.460 to 15.485, and for children from 0.434 to 14.60. A significant non-carcinogenic health risk to residents of the study area was revealed when THHI levels were found to be higher than the allowable limit in 70% of groundwater samples taken from men, women, and children.
- (iv) Groundwater's suitability for irrigation was evaluated using a variety of criteria. SAR, RSC, PI, and RSC demonstrate that groundwater is possible for irrigation in this dry location with little precipitation. RSC, RSC, and RSC show that groundwater can be used for irrigation.
- (v) Using the principal component analysis, we were able to glean five main explanations for 80.95% of the overall variance. Potash and nitrogenous fertilizers have likely been added to the soil in this agriculturally dominated region, as evidenced by the PCA-based source apportionment. There is no other possible source of fluoride in groundwater, hence this ion's origin can only be traced to geogenic sources. PCA can be used to establish that hydrochemistry in this location is influenced by both geogenic and anthropogenic causes.
- (vi) The different ionic species discovered in the groundwater, as well as chemometric tests, all point to a similar foundation of sodium and chloride in this study.

#### Data Availability

The data used to support the findings of this study are included within the article. Further data or information is available from the corresponding author upon request.

#### Conflicts of Interest

The authors declare that there are no conflicts of interest regarding the publication of this article.

#### Acknowledgments

The authors appreciate the supports from Ambo University, Ambo, Ethiopia, for providing help during the research and preparation of the manuscript. This work was funded by the Researchers Supporting Project Number (RSP2022R455) King Saud University, Riyadh, Saudi Arabia.

#### References

- [1] N. Adimalla, "Spatial distribution, exposure, and potential health risk assessment from nitrate in drinking water from semi-arid region of South India," *Human and Ecological Risk Assessment: An International Journal*, vol. 26, no. 2, pp. 310–334, 2020.
- [2] C. P. S. Ahada and S. Suthar, "Hydrochemistry of groundwater in North Rajasthan, India: chemical and multivariate analysis," *Environmental Earth Sciences*, vol. 76, no. 5, p. 203, 2017.
- [3] C. P. S. Ahada and S. Suthar, "Groundwater nitrate contamination and associated human health risk assessment in southern districts of Punjab, India," *Environmental Science & Pollution Research*, vol. 25, no. 25, pp. 25336–25347, 2018.
- [4] R. Barzegar, A. Asghari Moghaddam, M. Najib, N. Kazemian, and J. Adamowski, "Characterization of hydrogeologic properties of the Tabriz plain multilayer aquifer system, NW Iran," *Arabian Journal of Geosciences*, vol. 9, no. 2, 2016.
- [5] K. Brindha, P. Pavelic, T. Sotoukee, S. Douangsavanh, and L. Elango, "Geochemical characteristics and groundwater quality in the vientiane plain, Laos," *Exposure and Health*, vol. 9, no. 2, pp. 89–104, 2017.
- [6] V. Chaudhary and S. Satheeshkumar, "Assessment of groundwater quality for drinking and irrigation purposes in arid areas of Rajasthan, India," *Applied Water Science*, vol. 8, no. 8, p. 218, 2018.
- [7] J. Chen, H. Wu, H. Qian, and Y. Gao, "Assessing nitrate and fluoride contaminants in drinking water and their health risk of rural residents living in a semiarid region of northwest China," *Exposure and Health*, vol. 9, no. 3, pp. 183–195, 2017.
- [8] J. E. Cortes, L. Munoz, C. Gonzalez et al., "Hydrogeochemistry of the formation waters in the San Francisco field, UMV basin, Colombia - a multivariate statistical approach," *Journal of Hydrology*, vol. 539, pp. 113–124, 2016.
- [9] H.-P. Wang, Pu Chen, J.-W. Dai et al., "Recent advances of chemometric calibration methods in modern spectroscopy: algorithms, strategy, and related issues," *TrAC, Trends in Analytical Chemistry*, vol. 153, Article ID 116648, 2022.
- [10] C. N. Durfor and E. Becker, *Public Water Supplies of the 100 Largest Cities in the United States*, *Public Water Supplies 100 Larg. Cities United States, 1962*, US Government Printing Office, Washington, D.C., USA, 1964.

## *Retraction*

# **Retracted: Modelling and Analysis of Surface Roughness Using the Cascade Forward Neural Network (CFNN) in Turning of Inconel 625**

### **Advances in Materials Science and Engineering**

Received 26 December 2023; Accepted 26 December 2023; Published 29 December 2023

Copyright © 2023 Advances in Materials Science and Engineering. This is an open access article distributed under the Creative Commons Attribution License, which permits unrestricted use, distribution, and reproduction in any medium, provided the original work is properly cited.

This article has been retracted by Hindawi, as publisher, following an investigation undertaken by the publisher [1]. This investigation has uncovered evidence of systematic manipulation of the publication and peer-review process. We cannot, therefore, vouch for the reliability or integrity of this article.

Please note that this notice is intended solely to alert readers that the peer-review process of this article has been compromised.

Wiley and Hindawi regret that the usual quality checks did not identify these issues before publication and have since put additional measures in place to safeguard research integrity.

We wish to credit our Research Integrity and Research Publishing teams and anonymous and named external researchers and research integrity experts for contributing to this investigation.



The corresponding author, as the representative of all authors, has been given the opportunity to register their agreement or disagreement to this retraction. We have kept a record of any response received.

### **References**

- [1] R. A S, M. S. Prabhuswamy, and I. Komalnu Raghavan, "Modelling and Analysis of Surface Roughness Using the Cascade Forward Neural Network (CFNN) in Turning of Inconel 625," *Advances in Materials Science and Engineering*, vol. 2022, Article ID 7520962, 9 pages, 2022.

## Research Article

# Modelling and Analysis of Surface Roughness Using the Cascade Forward Neural Network (CFNN) in Turning of Inconel 625

Rajesh A. S. <sup>1</sup>, M. S. Prabhuswamy,<sup>1</sup> and Ishwarya Komalnu Raghavan <sup>2</sup>

<sup>1</sup>Department of Mechanical Engineering, JSS Science and Technology University, Mysuru 570006, Karnataka, India

<sup>2</sup>Department of ElectroMechanical Engineering, Faculty of Manufacturing Institute of Technology Hawassa University, Ethiopia

Correspondence should be addressed to Rajesh A. S.; [as.rajesh.jce@gmail.com](mailto:as.rajesh.jce@gmail.com) and Ishwarya Komalnu Raghavan; [ishwarya138@hu.edu.et](mailto:ishwarya138@hu.edu.et)

Received 7 July 2022; Revised 14 August 2022; Accepted 22 August 2022; Published 5 October 2022

Academic Editor: K. Raja

Copyright © 2022 Rajesh A. S. et al. This is an open access article distributed under the Creative Commons Attribution License, which permits unrestricted use, distribution, and reproduction in any medium, provided the original work is properly cited.

In this paper, the influence of process components on surface roughness in turning of Inconel 625 using cubic boron nitride (CBN) is studied. A predictive model is developed to forecast the surface roughness using the cascade forward neural network (CFNN). The experiments are designed based on Taguchi.  $L_{27}$  orthogonal array (OA) is used to perform the experimental trails by considering speed, feed, and depth of cut as input factors. Out of 27 experimental trails, 18 experiments are used for training and 9 experimental trails are used for testing. The developed predictive model by the CFNN is compared with regression model values. The average prediction error for surface roughness is 2.94% with  $R^2 = 99.99\%$  by the CFNN. The CFNN is known to be superior to predict the response with minimum of percentage error. The minimum and maximum roughness observed at trail 8 and trail 20 is noted, respectively, and the increases in roughness at experimental trail 8 is equal to 3.384 times higher than the roughness observed at experimental trail.20. The feed rate dominates effectively on the roughness rather than other factors. The consequences of process factors on surface roughness are studied with the help of ANOVA. This experimental study and developed model would be used for aero parts manufacturing to forecast the roughness accurately before to the actual experiment so that actual machining and material cost could be avoided.

## 1. Introduction

The roughness is an important and the quality of the surface roughness decides the integrity of the machined surface. Therefore, optimum of process factors is to be identified and also a predictive model is needed to be identified with minimum of percentage error. This work [1] stated that surface finish is the main index to know the idiosyncrasy of machined parts. They have developed the ANN model to forecast the mean roughness in machining the AA7075 alloy. The experiments were planned based on Taguchi. The feed-forward artificial neural networks (ANN) using the BR algorithm. Rahmath et al. [2] have used vibration signatures in turning steel alloy for the prediction of insert tool life using ANN techniques. They have developed as efficient indirect measurement of tool wear and it is found to be more economical and useful in predicting the tool wear. This paper [3] have proposed the ANN model to forecast

multiresponses in turning the aluminum alloy. The adequacy of the ANN structure was proved with  $R^2 = 99\%$ , mean squared error (MSE): less than 0.3%, and APE: less than 6%. They have considered the input factors such as cutting speed, feed, depth of cut (DOC), and radius of the nose with roughness, forces, temperature, material removal rate (MRR), power for cutting, and specific pressure for cutting as output.

Deshpande et al. [4] have performed turning operation on Inconel 718 and the surface roughness was foreseen using the developed ANN model. The ANN model-predicted results were compared with the regression model. They have concluded that the ANN framework was known to be the best to foresee the roughness with great accuracy than the regression model. These works by Boukezzi et al. [5, 6] said that ANN techniques emerge as the main tool to model the nonlinear problems in machining processes. They have reviewed the studies done on the application of the ANN.

They have concluded that the ANN showed great accuracy than other old statistical techniques and also, they have said that, researchers concentrated on more on wear and surface roughness owing to the prime role took part by surface integrity of the machine surface. Lakhdar et al. [7] have said that the development of the relationship among different machining conditions and machining performances are found to be the major objective of the industry. They have succeeded a predictive model in turning of steel to predict surface roughness using the ANN and RSM. The potential of both the model were evaluated using coefficient of correlation ( $R^2$ ). The final results showed that the ANN model has performed better than the RSM.

The authors Sada et al. [8] have appraised the execution of the ANN and adaptive neuro-fuzzy inference system (ANFIS) in the prognosis of the metal removal rate and tool wear in machining of steel. They have concluded that, both the techniques have performed well; however, the ANN has produced best results rather than the ANFIS. These works by Paturi et al. [9] have evolved the model to predict surface roughness using machine learning techniques such as ANN, support-vector machines (SVM), and genetic algorithm (GA) in wire electro discharge machining (WEDM) of Inconel 718. The forecasted values by the ANN and SVM were compared with the response surface method (RSM) model based on correlation coefficient. The SVM model was found to be accurate rather than other methods. Moreover, the SVM and GA techniques have produced accurate prediction and optimization of the parameters. Machine learning technologies are recently used widely to predict the attributes before the actual experiment as well as these techniques are widely used for the measurements of the outputs [10]. It is also to be investigated for the best solution for optimum of outputs to reduce the wastage of material and cost of machining in machining [11–14].

Elsheikh et al. [15] said that, Inconel 718 is difficult to machine, and it possesses poor machinability and minimum conductivity. They have revealed that, machining of this alloy becomes critical and needs to be carefully monitored/controlled. Therefore, they have developed a hybrid machine learning (ML) tools to forecast the existence of residual stresses in turning of Inconel 718. The hybrid ML tool was named as the pigeon optimization algorithm (POA) and particle swarm optimization (PSO). The forecasted stresses were verified with the measured value. Yigit et al. [16] have investigated and developed a predictive model to forecast microhardness and grain size during machining of titanium alloy using finite element analysis and machine learning approach. They have reported the impact of the factors on roughness based on the prediction of microhardness and grain size. Further, they have optimized the machining factors based on the genetic algorithm. This work by Bhandari [17] has developed the deep learning (DL) structure to predict the roughness by considering multi-layer Perceptron (MLP), convolution neural network (CNN), long short-term memory (LSTM), and transformer to classify surface roughness using sound and force data. This investigation has highlighted that DL with the transformer model as superior than other DL models.

From the literature, it is evident clearly that, the machine learning (ML) techniques are mostly used to predict the machining responses with better regression coefficient and the %age error is also noted to be minimum among experimental and machine learning model's prediction. Furthermore, the predictive model development based on different machine learning techniques and regression model are all discussed, and limited reports was seen for the prediction of outputs in machining Inconel 625. Hence, this work is done to make a machine learning methodology to forecast the roughness, and the forecasted results are differentiated with experimental values and predicted values by the regression model. The impact of the input factors on the surface roughness is discussed using ANOVA.

## 2. Materials and Experimental Details

Inconel 625 grade 60 mm in diameter with the length of 150 mm were used to conduct experiments. The chemical portion of the work material is shown in Table 1.

Three levels and three factors such as speed, feed, and depth of cut were used for the experiment. A Taguchi design was adopted to conduct experimental trails as well as to choose the levels of the factors. The level ranges of the factors are given in Table 2. A design expert was used to carry out regression analysis. The experimental result of the surface roughness is specified in Table 3. A dry turning environment was chosen. The turning experimental trails are done using central lathe, and cubic boron nitride tools are utilized. Taguchi is used to plan the experiment and  $L_{27}$  array is used to do experimental trails [11–14]. The surface roughness was determined using surf-coder profilometer and an average of three measurements was taken at every machining condition.

## 3. Regression Analysis

The input factors and machining responses are modelled using quadratic regression equation as follows:

$$y = \beta_0 + \sum_{i=1}^k \beta_i x_i + \sum_{i=1}^k \beta_{i^2} x_i^2 + \sum_i \sum_j \beta_{ij} x_i x_j + \varepsilon, \quad (1)$$

where

'Y': machining attribute

$x_i$ : is the value of the  $i^{\text{th}}$  factors

$\beta$ : coefficient: regression

$\varepsilon$ : residual measure

The values of experiment trails are predicted using the regression equation. The quadratic equation to predict the roughness is given in (2).

$$R_a = 1.70 - 0.01263 * \text{cutting speed} + 20.80599 * \text{feed} - 0.970968 * \text{DOC} + 0.120647 * \text{cutting speed} * \text{feed} - 0.000380 * \text{cutting speed} * \text{DOC} + 1.76252 * \text{feed} * \text{DOC} - 0.000033 * \text{cutting speed}^3.$$

$$138.666 * \text{feed}^2 + 0.273016 * \text{DOC}. \quad (2)$$

R-square value is 94.71% and the ability to predict the surface roughness is identified to be adequate. The developed

TABLE 1: Composition of Inconel 625.

S. no.	Compositions	Weight (%)
1	52.49:Ni	52.49:Ni
2	0.19:Si	0.19:Si
3	0.46:Mn	0.46:Mn
4	20:Cr	20:Cr
5	6.29:Mo	6.29:Mo
6	0.07:Cu	0.07:Cu
7	1.0:Fe	1.0:Fe
8	16.7:Co	16.7:Co
9	1.94:Ti	1.94:Ti
10	0.48:Al	0.48:Al
11	0.04:Nb	0.04:Nb
12	0.15:W	0.15:W
13	0.02:V	0.02:V
14	0.02:C	0.02:C
15	0.001:S	0.001:S
16	0.007:Ta	0.007:Ta

TABLE 2: Machining factors.

Factors	Cubic boron nitride		
	L 1	L 2	L 3
<b>V : m/min</b>	70	100	130
<b>S : mm/rev</b>	0.045	0.076	0.138
<b>a<sub>p</sub> : mm</b>	0.15	0.3	0.65

TABLE 3: Experimental trail results.

Expt. trail no.	Speed	Feed	DOC	(Ra) $\mu\text{m}$
1	70	0.045	0.15	1.75
2	70	0.045	0.30	1.45
3	70	0.045	0.65	1.20
4	70	0.076	0.15	1.86
5	70	0.076	0.30	1.90
6	70	0.076	0.65	1.66
7	70	0.139	0.15	1.75
8	70	0.139	0.30	2.2
9	70	0.139	0.65	1.63
10	100	0.045	0.15	1.21
11	100	0.045	0.30	1.00
12	100	0.045	0.65	0.95
13	100	0.076	0.15	1.75
14	100	0.076	0.30	1.59
15	100	0.076	0.65	1.44
16	100	0.139	0.15	2
17	100	0.139	0.30	1.8
18	100	0.139	0.65	1.66
19	130	0.045	0.15	0.76
20	130	0.045	0.30	0.68
21	130	0.045	0.65	0.41
22	130	0.076	0.15	1.53
23	130	0.076	0.30	1.25
24	130	0.076	0.65	1.1
25	130	0.139	0.15	1.90
26	130	0.139	0.30	1.65
27	130	0.139	0.65	1.59

model is said to be 95% confidence interval. Figure 1 shows normal plot of residuals and the congregate of points that connect the normal plot for the residuals of the surface roughness. These points are very near to the plot and it is allowable with 95% confidence interval. The average %age error among experiment values and predicted result by the regression model is identified to be 2.311%.

#### 4. Cascade Forward Neural Network (CFNN)

**4.1. CFNN Model Implementation for Prediction of Surface Roughness.** A popular approach for modelling and improving manufacturing processes is the artificial neural network (ANN) approach. In the manufacturing industry, choosing the best processing parameters is crucial in terms of both time as well as quality. This study examines how machining variables including feed rate, depth of cut, and spindle speed affect the surface roughness using cascade forward neural network models for Inconel alloy [11–14]. The neural network is created using the back propagation in such a way that, for all training input patterns, the sum squared error (Err) between actual outputs ( $Y$ ) and its associated desired outputs ( $Y_d$ ) is minimised to a predetermined value, as indicated by the following equation. The transfer function types for each tier must be chosen by trial and error in order to obtain the best network model.

$$\text{Err} = Y_d - Y. \quad (3)$$

Similar to feed-forward neural networks, cascade forward neural networks have connections from the inputs as well as every previous layer to subsequent levels. As shown in Figure 2, the output layer in a three-layer network is also directly connected to the input layer in addition to the hidden layer. A two or more cascade network layers may learn any finite input to turn relationship indefinitely well, provided there are more than enough hidden neurons, much like feed-forward networks do. All types of input to output mappings can be done with a cascade forward neural network. The benefit of this approach is that it preserves the linear link among input and output while accommodating the nonlinear relationship.

An ANN is a collection of interconnected, basic building blocks known as neurons. Particularly when there are many inputs and only one output, each neuron represents a mapping. The neuron's output depends on the total of its inputs. A neuron's output uses a function known as an activation function. The symbol for a single neuron displays the degree of arrows originating from the neuron because its single output can be used as an input by some other neurons. Through an activation function in the hidden layer, the relationship has a nonlinear shape. In addition to the connection that is generated indirectly, a network with a direct link between the input layer and the output layer is created when a multilayer network and perception connection are coupled. The cascade forward neural network (CFNN) is the name of the neural network created using this connection arrangement. Tables 4 and 5 show the dataset used for training and testing purpose.



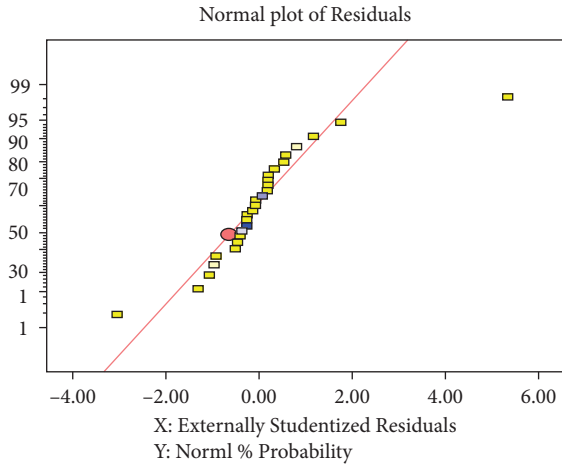


FIGURE 1: Normal plot of residuals of flank wear.

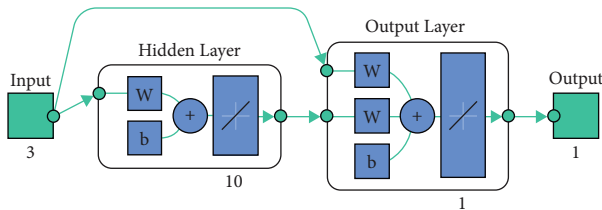


FIGURE 2: Two layered cascade forward back propagation network.

The feed forward of the input pattern, error counting, and adjustment of weight are the three stages of the back propagation method on the CFNN, as similar with feed forward neural network (FFNN). The method then moves on to the error calculation stage following the feed forward stage (the difference from the output to the target). The weights need to be updated, and a new calculation needs to be made. This step is repeated until no errors are found or the iteration reaches the predetermined stop criteria, whichever comes first. In this part, we provide a brief overview of the conjugate gradient optimization approach for the CFNN model weighting adjustments as illustrated in Figure 3.

The percentage error formula was used to obtain the average error prediction between the predicted out-turn and the target out-turn, as shown in (4) which is shown in Table 6.

$$\text{Percentage Error} = |C - P|/|C| \times 100. \quad (4)$$

C-measured value

P-predicted value

From Table 6, it can be deduced that the average surface roughness ( $R_a$ ) prediction error is 2.94%. The neuron in the input layer be tuned with DOC, feed rate, and speed. The output layer, on the other hand, is correlated with surface roughness ( $R_a$ ). According to the accuracy plot, the regression equation for the created CFNN model is depicted as  $y = 0.9882x - 0.0217$  and has an R-squared value of 0.9864 as shown in Figure 4.

Eventually, the purelin function transfer produced the foremost results for neurons in hidden layers. Using the plot

TABLE 4: The training dataset with target output.

Expt. No.	V (m/min)	S (mm/rev)	$a_p$ (mm)	Ra ( $\mu\text{m}$ )
2	70	0.045	0.3	1.45
3	70	0.045	0.65	1.2
4	70	0.076	0.15	1.86
6	70	0.076	0.65	1.66
7	70	0.139	0.15	1.75
8	70	0.139	0.3	2.2
10	100	0.045	0.15	1.21
12	100	0.045	0.65	0.95
13	100	0.076	0.15	1.75
14	100	0.076	0.3	1.59
17	100	0.139	0.3	1.8
18	100	0.139	0.65	1.66
19	130	0.045	0.15	2
21	130	0.045	0.65	1.55
23	130	0.076	0.3	1.65
24	130	0.076	0.65	2.5
25	130	0.139	0.15	2.3
26	130	0.139	0.3	2.25

TABLE 5: The test dataset.

Expt. No.	V (m/min)	S (mm/rev)	$a_p$ (mm)
1	70	0.045	0.15
5	70	0.076	0.3
9	70	0.139	0.65
11	100	0.045	0.3
15	100	0.076	0.65
16	100	0.139	0.15
20	130	0.045	0.3
22	130	0.076	0.15
27	130	0.139	0.65

network execution function graph indicates that it was simple to empirically calculate the expected number of training epochs. On examining at the network training graph, it was noticed that after two epochs, the training network essentially stops as shown in Figure 5. Algorithms for learning modified the created neural networks to fit the data file during training.  $R$  is used to measure correlations between the target and anticipated values. MATLAB regression graphs as shown in Figure 6 displayed the outputs of the network in relation to the goals for the testing, validation, and training sets, with  $R^2$  results above 0.99 for all datasets, were used to evaluate the accuracy of the fits.

## 5. Results and Discussion

The turning trails are carried out on Inconel 625, and the portending model is made by CFNN techniques and regression models. The effects of input factors on surface roughness are analyzed. The analyses of variance (ANOVA) is useful to find out the effect of every factor. The statistical importance of every factor is recommended using the  $P$  value. If the  $P$  value of a particular factor is noted as lower than 0.05, then that factor is statically significant on output. The ANOVA is obtained with significance of 5%.

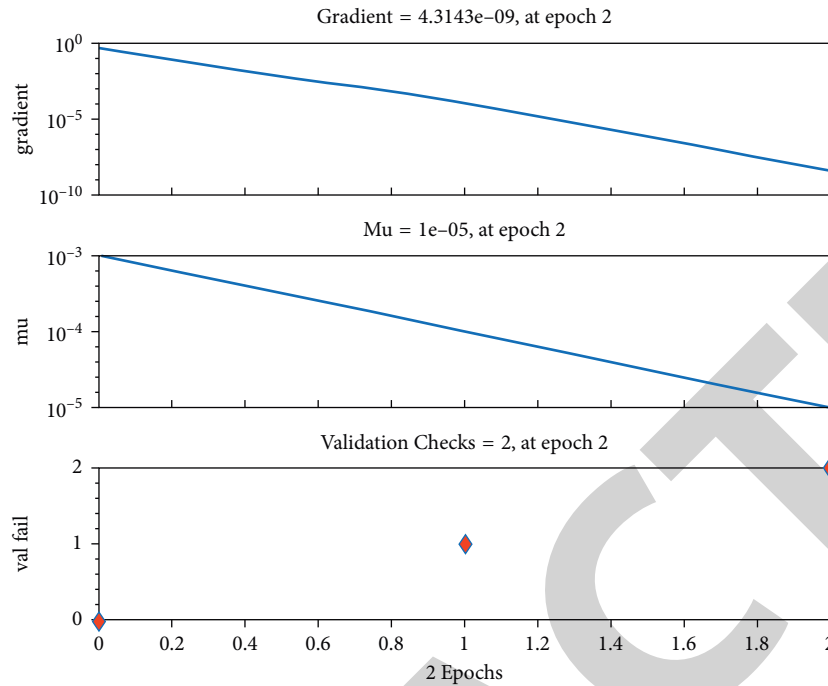


FIGURE 3: Performance plot of the CFNN model.

TABLE 6: Percentage prediction error.

Expt. No.	Surface roughnesses		% Prediction error
	Measured values	Predicted values	
1	1.75	1.640316	0.553368
5	1.9	1.856271	2.30152
9	1.63	1.561874	0.233902
11	1	1.123179	1.231789
15	1.44	1.306065	9.301023
16	2	1.97721	1.139501
20	0.68	0.758432	3.17173
22	1.53	1.421401	7.097955
27	1.59	1.427203	1.433798
		Average prediction error	2.94

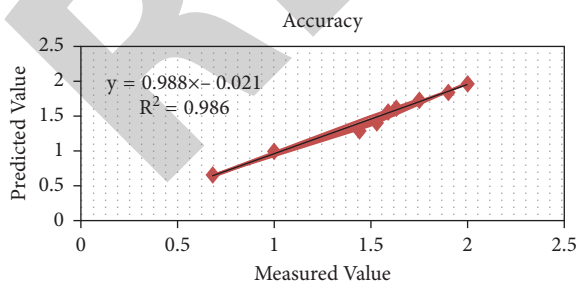


FIGURE 4: Accuracy plot of the CFNN model.

Furthermore, the significance of the factors on roughness can be seen according to F-value. In this ANOVA Table 7, feed rate (F-value: 164.88) and speed (F-value: 61.06) are all identified as significant on roughness followed by depth of

Best validation performance is 0.078773 at epoch 0

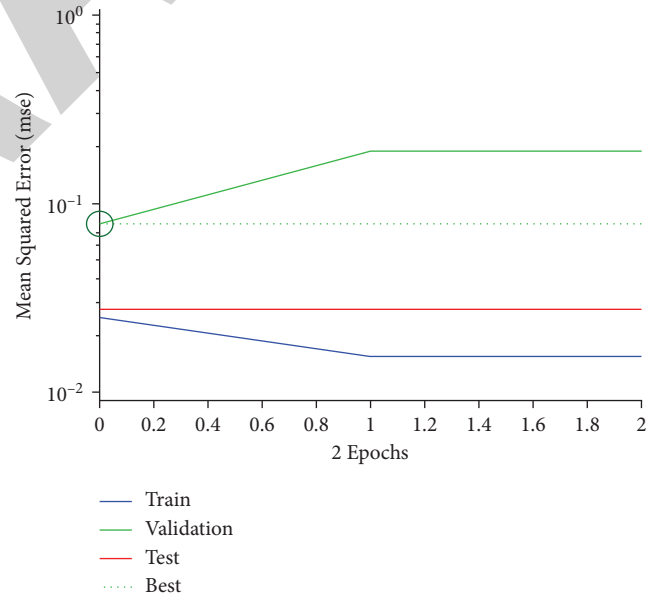


FIGURE 5: Plot of the training network.

cut (F-alue: 28.53). ANOVA analysis was carried out at a significant level of 5% with confidence level of 95%.

Figures 7(a)–7(c) illustrate the discrepancy in the surface roughness with respect to change in the level of process factors using three dimensional plots. The escalate in the feed rate causes the escalate in the roughness; however, the roughness is lowered as the level of cutting speed increase. There is no remarkable change in the roughness as the level of DOC changes. The scanning electron microscope (SEM) images evidently exhibited in Figures 8(a) and 8(b) that a

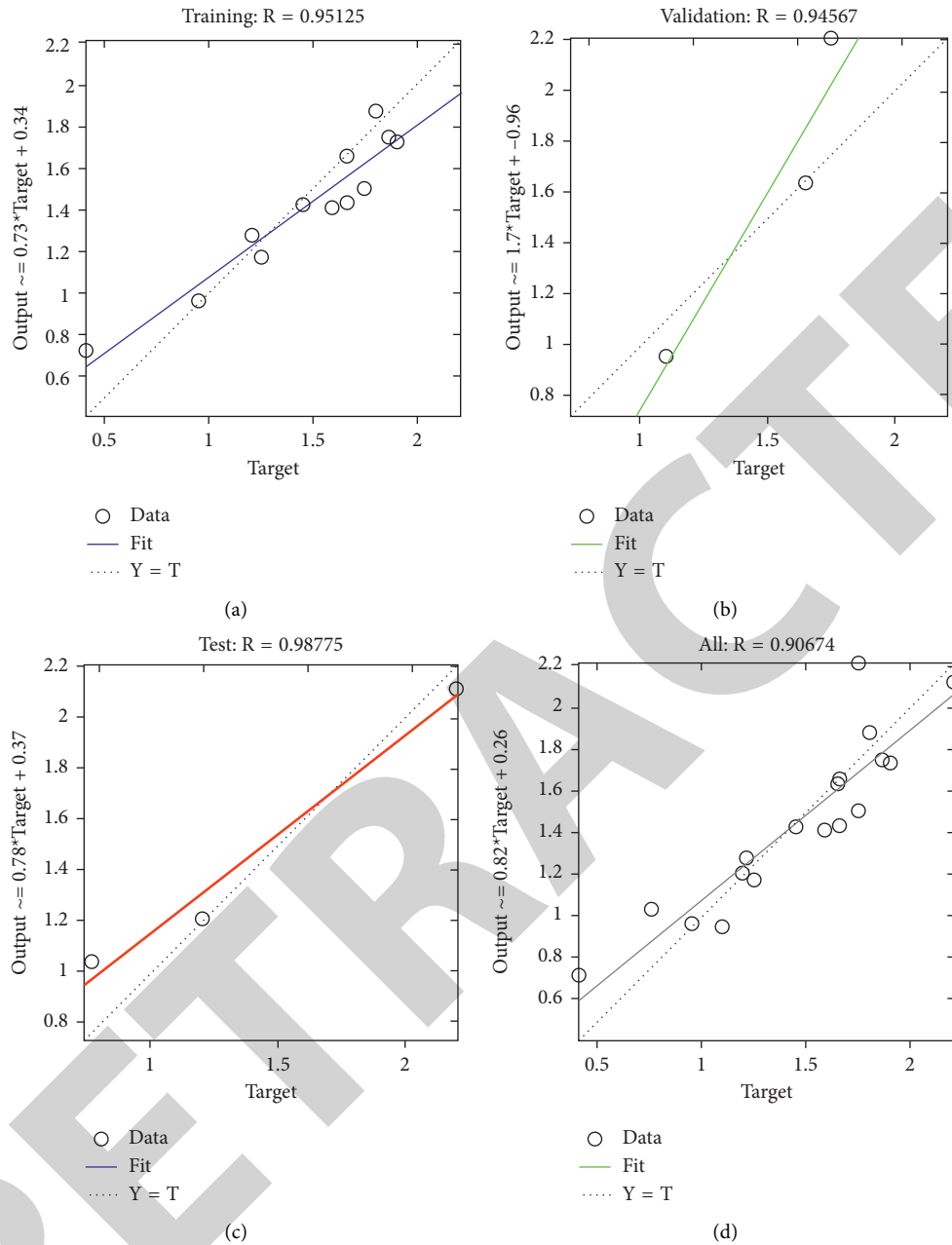


FIGURE 6: Plots of trained network with respect to target for (a) train, (b) validate, (c) test, and (d) all.

TABLE 7: ANOVA.

S	SOS	DF	MS	F	$p$
M	4.65	9	0.5169	33.79	<0.0001
V	0.9340	1	0.9340	61.06	<0.0001
S	2.52	1	2.52	164.88	<0.0001
$a_p$	0.4365	1	0.4365	28.53	<0.0001
$V * S$	0.3607	1	0.3607	23.58	0.0001
$V * a_p$	0.0001	1	0.0001	0.0067	0.9357
$S * a_p$	0.0056	1	0.0056	0.3681	0.5521
$V^2$	0.0052	1	0.0052	0.3400	0.5675
$S^2$	0.4237	1	0.4237	27.70	<0.0001
$a_p^2$	0.0012	1	0.0012	0.0765	0.7854
Residual	0.2601	17	0.0153		
Total	4.91	26			

$R^2$ : 94.71%

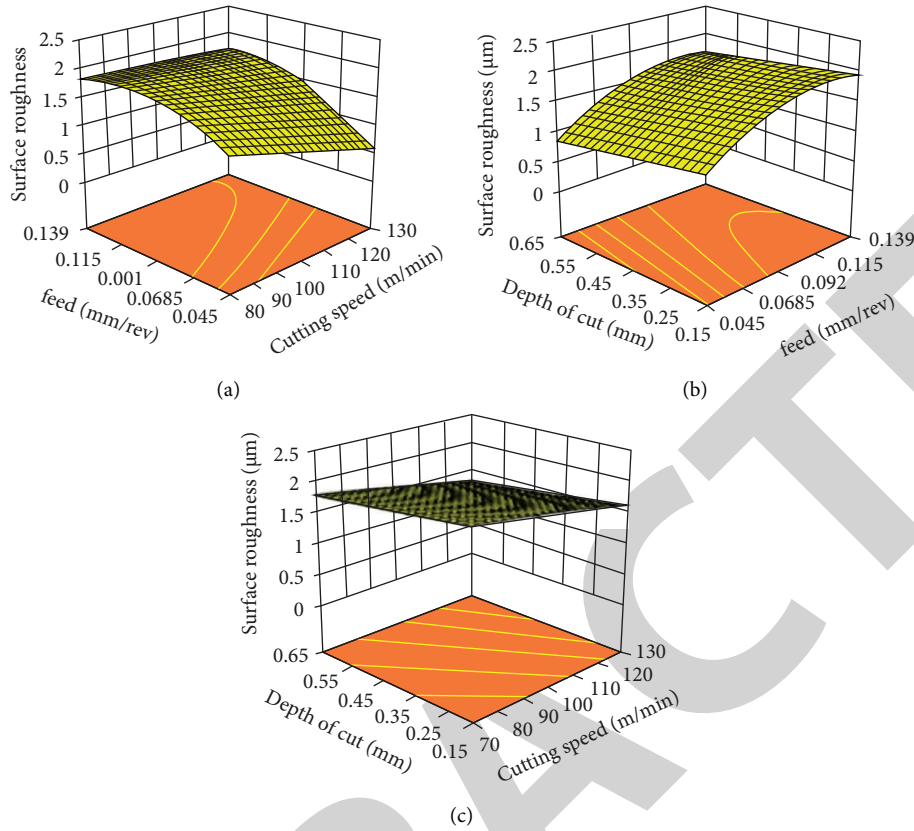
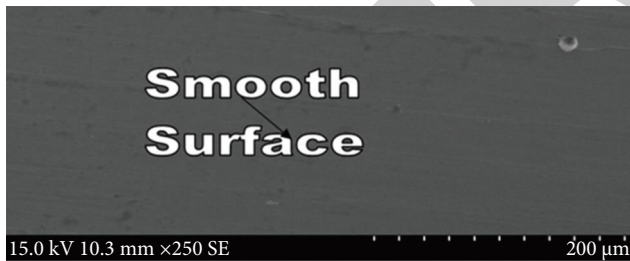
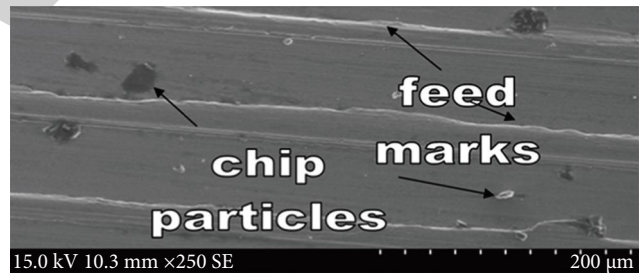


FIGURE 7: (a) Cutting speed Vs. feed, (b) feed Vs. depth of cut, and (c) cutting speed Vs. depth of cut.



(a)



(b)

FIGURE 8: (a) At cutting speed = 130 (m/min), feed = 0.045 (mm/rev) and depth of cut = 0.30(mm), (b) at cutting speed = 70(m/min), feed = 0.139 (mm/rev) and depth of cut = 0.30(mm).

smooth surface is noted at higher cutting speed; whereas the rough surface is noted as the feed rate increases. The reason behind that at high level of speed, temperature generation in the cutting zone is more and it aids easy removal of the material. At higher feed rate, the coefficient of friction is more at cutting zone, hence rubbing takes place and as results rough surface is generated.

From the figures, it is revealed that the roughness is increased as the feed rate escalates and the corresponding insert flank wear, cutting force, and tool life are all noted only for the experimental trails 8 and 20. The noted results at experimental trails 8 and 20 are given in Table 8. It is a clear evidence from the tables the observed roughness, force, flank wears, and tool life. The insert tool life is calculated by

TABLE 8: Machining responses at Trail 8 and 20.

Trail. no.	Roughness ( $\mu\text{m}$ )	Force (N)	Flank wear (mm)	Tool life (sec)
8	2.2	475	0.39	225
20	0.65	290	0.32	450

measuring the insert flank wear at every 50 seconds once and the time period is noted at final insert worn out stage. The feed rate impacts mainly on these responses compare to other factors and it is accepted that, as the feed rate escalates the roughness, wear increases and life of the insert reduces [18, 19]. It is observed that the increases in roughness at trail 8 is equal to 3.384 times higher than the roughness observed

at trail 20. Similarly, force and flank wear observed at trail 8 is equal to 1.63 and 1.21 times higher than the trail 20, respectively. Furthermore, it is seen from the table that the tool life is found to be decreased as the level of feed rate increases at trail 8, whereas the life of the insert is increased as the level of feed rate is reduced. The insert life is significantly affected as the level of changing the feed rather than other factors in turning Inconel 625 using CBN insert.

## 6. Conclusions

From the analysis of the surface roughness during the turning of the Inconel 625 using CBN insert, the below conclusions were drawn:

- (i) The feed rate was found to influence the roughness more effectively than the speed and depth of cut, thus showing the importance of feed control in turning Inconel 625 using CBN insert.
- (ii) From seeing the SEM images, machined surface shows the feed marks, chip particle adhered including rough surface in turning Inconel 625 using CBN insert at a higher level of feed and lower level of speed.
- (iii) The predictive models developed by the regression and CFNN model were established to be fit well with experimental trail values. These predictive models can be useful to predict the surface roughness before actual experiments in the manufacturing factories.
- (iv) Inconel 625 dataset includes 27 trials, 18 for training, 9 for testing, and 4. The prediction potential of the ANN-CFNN model was proved as more perfect for the prediction of roughness than the regression model.
- (v) The average percentage error among experiment trails and CFNN model is found to be 2.94%.
- (vi) Based on the regression model developed from the experimental results for roughness, closeness is seen and 95% confidence level.

The developed predictive models for roughness would be very much useful in the difficult machine materials Inconel 625 for the aero part manufacturers. However, the influence of the factors on force, tool wear, and life of the insert in turning Inconel 625 using CBN insert to be analyzed as well as suitable novel machine learning tool to forecast the responses are to be found out.

## Data Availability

The data used to support the findings of this study are included within the article. Further data or information are available from the corresponding author upon request.

## Conflicts of Interest

The authors declare that there are no conflicts of interest regarding the publication of this article.

## Acknowledgments

The authors appreciate the support from Hawassa University, Ethiopia for providing help during the research and preparation of the manuscript.

## References

- [1] A. Kosarac, C. Mladjenovic, M. Zeljkovic, S. Tabakovic, and M. Knezev, "Neural-network-based approaches for optimization of machining parameters using small dataset," *Materials*, vol. 15, no. 3, p. 700, 2022.
- [2] "Rahmath ulla baig, syed javed, mohammed khaisar, mwafak shakoor and purushothaman Raja development of an ANN model for prediction of tool wear in turning EN9 and EN24 steel alloy," *Advances in Mechanical Engineering*, vol. 13, no. 6, pp. 1-14, 2021.
- [3] S. Dahbi, L. Ezzine, and H. El Moussami, "Modeling of cutting performances in turning process using artificial neural networks," *International Journal of Engineering Business Management*, vol. 9, pp. 184797901771898-13, 2017.
- [4] Y. V. Deshpande, A. B. Andhare, and P. M. Padole, "Application of ANN to estimate surface roughness using cutting parameters, force, sound and vibration in turning of Inconel 718," *SN Applied Sciences*, vol. 1, p. 104, 2019.
- [5] F. Boukezzi, R. Nouredine, A. Benamar, and F. Nouredine, "Modelling, prediction and analysis of surface roughness in turning process with carbide tool when cutting steel C38 using artificial neural network," *International Journal of Industrial and Systems Engineering*, vol. 26, no. 4, pp. 567-583, 2017.
- [6] S. Al-Zubaidi, J. A. Ghani, and C. H. C. Haron, "Application of ANN in Milling Process: A Review," *Hindawi, Modelling and Simulation in Engineering*, Article ID 696275, 2011.
- [7] B. Lakhdar, Y. M. Athmane, B. Salim, and A. Haddad, "Modelling and optimization of machining parameters during hardened steel AISID3 turning using RSM, ANN and DFA techniques: comparative study," *Journal of Mechanical Engineering and Sciences*, vol. 14, no. 2, pp. 6835-6847.
- [8] S. O. Sada and S. C. Ikpeseni, "Evaluation of ANN and ANFIS modeling ability in the prediction of AISI 1050 steel machining performance," *Heliyon*, vol. 7, no. 2, p. e06136, 2021.
- [9] U. M. R. Paturi, S. Cheruku, V. P. K. Pasunuri, S. Salike, N. S. Reddy, and S. Cheruku, "Machine learning and statistical approach in modeling and optimization of surface roughness in wire electrical discharge machining," *Machine Learning with Applications*, vol. 6, Article ID 100099.
- [10] R. M. Bommi, C. Ezilarasan, M. P. Sudeshkumar, and T. Vinoth, "Estimation of flank wear in turning of nimonic C263 super alloy based on novel MSER algorithm and deep patten network," *Russian Journal of Nondestructive Testing*, vol. 58, no. 2, pp. 140-156, 2022.
- [11] K. Arul and S. K. Santhanam, "Experimental investigation on turning of monel K500 alloy using nano graphene cutting fluid under minimum quantity lubrication, international mechanical engineering congress and exposition," *Proceedings of ASME*, vol. 2019, pp. IMECE2019-10056, 2019.
- [12] K. Arul and S. K. Vs, "Magnetorheological based minimum quantity lubrication (MR-MQL) with additive n-CuO," *Materials and Manufacturing Processes*, vol. 35, no. 4, pp. 405-414, 2020.
- [13] A. Kulandaivel and S. Kumar, "Effect of magneto rheological minimum quantity lubrication on machinability, wettability and tribological behavior in turning of Monel K500 alloy,"

## *Retraction*

# **Retracted: Machine Learning Approach: Prediction of Surface Roughness in Dry Turning Inconel 625**

### **Advances in Materials Science and Engineering**

Received 26 December 2023; Accepted 26 December 2023; Published 29 December 2023

Copyright © 2023 Advances in Materials Science and Engineering. This is an open access article distributed under the Creative Commons Attribution License, which permits unrestricted use, distribution, and reproduction in any medium, provided the original work is properly cited.

This article has been retracted by Hindawi, as publisher, following an investigation undertaken by the publisher [1]. This investigation has uncovered evidence of systematic manipulation of the publication and peer-review process. We cannot, therefore, vouch for the reliability or integrity of this article.

Please note that this notice is intended solely to alert readers that the peer-review process of this article has been compromised.

Wiley and Hindawi regret that the usual quality checks did not identify these issues before publication and have since put additional measures in place to safeguard research integrity.

We wish to credit our Research Integrity and Research Publishing teams and anonymous and named external researchers and research integrity experts for contributing to this investigation.

The corresponding author, as the representative of all authors, has been given the opportunity to register their agreement or disagreement to this retraction. We have kept a record of any response received.

### **References**

- [1] A. S. Rajesh, M. S. Prabhuswamy, and M. Rudra Naik, "Machine Learning Approach: Prediction of Surface Roughness in Dry Turning Inconel 625," *Advances in Materials Science and Engineering*, vol. 2022, Article ID 6038804, 7 pages, 2022.

## Research Article

# Machine Learning Approach: Prediction of Surface Roughness in Dry Turning Inconel 625

A. S. Rajesh <sup>1</sup>, M. S. Prabuswamy,<sup>1</sup> and M. Rudra Naik <sup>2</sup>

<sup>1</sup>Department of Mechanical Engineering, JSS Science and Technology University, Mysuru, Karnataka 570006, India

<sup>2</sup>Department of Electro-Mechanical Engineering, Arba Minch University, Arba Minch, Sawla Campus, Ethiopia

Correspondence should be addressed to A. S. Rajesh; [as.rajesh.jce@gmail.com](mailto:as.rajesh.jce@gmail.com) and M. Rudra Naik; [rudra.naik@amu.edu.et](mailto:rudra.naik@amu.edu.et)

Received 30 June 2022; Revised 8 September 2022; Accepted 14 September 2022; Published 5 October 2022

Academic Editor: K. Raja

Copyright © 2022 A. S. Rajesh et al. This is an open access article distributed under the Creative Commons Attribution License, which permits unrestricted use, distribution, and reproduction in any medium, provided the original work is properly cited.

Roughness is a prime parameter in any process/operation as it aids in confirming the quality status of the product. The insert and workpiece would develop a lot of friction and as a result, it generates heat in the cutting zone, which affects the machined surface. The speed, feed, and depth of cut were chosen as processing factors.  $L_{27}$  Orthogonal array is used based on the Taguchi technique. The regression analysis is used to develop an equation to predict the roughness. The impact of the processing factors on the machined surface is studied with help of ANOVA (Analysis of Variance). Furthermore, the estimation of surface roughness is carried out using a machine learning-based model-feed forward (nonlinear autoregressive network) NARX network, and the evaluated surface roughness is compared with the values predicted by the regression model and experimental results. The average percentage error observed with the predicted values by NARX is observed as 3.01%, which is lower than the average percentage error observed by the regression model 5.131%. Thus, this work provides the best machine learning approach to the prognosis of the roughness in dry turning of Inconel 625, which would save a lot of time and unnecessary wastage of the work material.

## 1. Introduction

The surface roughness is considered an important one in the manufacturing industry and the roughness range is specified based on requirements either esthetic look or functional need. A predictive model for the prediction of roughness was developed using a machine learning approach based on principle component analysis [1]. This work [2] stated that surface roughness plays a main part in the development of ant components. The roughness is affected owing to machining factors and inserts material and insert geometry. Hence, an optimum machining factor and the insert are found to give a better surface finish. Machine learning methods are widely used for the prediction of the attributes before the actual experiment, as well as these techniques, are widely used for the measurements of the attributes [3]. Machine learning is a modern tool for the optimization of the system. In the manufacturing field, ML leads to expense saving, time saving, an increase in quality, and reduce wastage [4]. It is

also a must to investigate a better solution for optimum attributes to reduce the wastage of material and cost of machining in the machining of aero alloys [5, 6]. They [7] stated that the prediction of energy needs of the machining strategy plays a vital role before manufacturing a component. They have used various machine learning concepts such as decision trees, random forests, and boosted random forests for the prediction of energy in CNC machining. The accuracy of energy prediction was proved with help of a random forest. They [8] have developed a model using ANN to predict the attributes such as force, the temperature at the machining zone, roughness, and insert wear in dry machining of Nimonic C263 and the percentage error among experimental and predictive values were found within 2%. Authors [9] have used machine vision and AE signal data to measure the output data in the machining of Nimonic 75 alloy. They have reported that the AERMS and AECOUNT were found receptive to output and the vision system and AE have proved great in evaluating the parameters for optimization.



This work [10] performed turning operation on Al 7075 based on central composite design and observed various machining attributes at various levels of machining factors. They analyzed the impact of machining factors on attributes using ANOVA, and multiresponse optimization was carried out using the principal component and JAYA algorithm with a lower percentage error of 8%. They [11] have created a dataset based on multichannel signals and insert wear values. Furthermore, they have said that preprocessing is done to carry out STFT to transfer one-dimensional signals into two-dimensional signals. This research [12] developed a regression model based on the central composite design in machining AISI 4340 alloy steel to predict the attributes. Further, ANN was used to get the best regression coefficient and fitness model for GA. They have found the best combination of ANN and GA methodology to identify the best machining variables for optimum attributes.

This work [13] investigated the impact of the annealing process at 1000°C at varying machining parameters using principal component analysis, hyper-parameter optimization, and particle swarm optimization. The forecasted results were verified with experimental trial results. They have observed average percentage error among experimental and predicted values ranges of 1.56%, 6.8%, and 2.57% with respect to surface roughness, wear, and material removal rate. They [14] have developed a predictive model for roughness in turning AISI 304 steel using. The predictive model was carried out with help of an adaptive-network-based fuzzy inference system quantum-behaved particle swarm optimization (ANFIS-QPSO). The ANFIS-QPSO has shown great agreement with experimentally measured results. They [15] have introduced an approach to compute the insert wear in the turning process with help of neural intelligence. They have used support vector machines (SVM) for regression with Bayesian optimization to evaluate the wear based on varying the level of process factors. They have concluded that the proposed approach gave great accuracy in evaluating the wear of the insert.

From the literature, it is found clearly that, the machine learning concepts are widely used to predict the attributes with better regression coefficient and the percentage error is also found to be minimum among experimental and machine learning model predictions as machine learning (ML) is an emerging technique in developing a predictive model as well as for optimization of the process factors. ML increases the data processing speed and analysis. Processing of larger data and deep analysis can be made. The prediction capability of the ML techniques with other prediction tools can be compared with help of the R-squared value. Prediction of the responses by ML techniques was found to be more significant than other techniques and well in accord with experimental results. Further, the predictive model development based on various machine learning methodologies and a regression model are all reported and limited reports were identified for the prediction of attributes in machining Inconel 625. Hence, this work attempts to develop a machine learning methodology to prognosis the roughness, and the predicted values are compared with experimental results and predicted values

by the regression model. Furthermore, the machining factors' effect on surface roughness is studied using ANOVA.

## 2. Materials and Experimental Details

Inconel 625 of diameter 60 mm and a length of 150 mm were used to conduct experiments. The chemical part of the work material is as follows (Wt%): 58–71% Ni, 21–23% Cr, 8–3–10% Mo, 5% Fe, 3.2–3.8% Nb, 1% Co, 0.5% Mn, and 0.4% Al. The experimental trials were carried out in dry mode on a central lathe and whisker-reinforced inserts were used [16, 17].  $L_{27}$  orthogonal array was used to conduct the experiment [5, 18, 19]. The cutting speed, feed rate, and depth of cut are all chosen as inputs. The roughness is chosen as the machining attribute. The levels of process factors are detailed in Table 1 and the experiment trail's result is detailed in Table 2. The surface roughness ( $R_a$ ) is measured using a surf coder surface profilometer. An average of three measurements was considered to distinguish the roughness at every machining condition.

## 3. Results and Discussion

The turning experiments are carried out on Inconel 625 and predictive models are developed using machine learning methodology "NARX Time Series Model" and regression concepts. Mostly, the time series approach usually contains some unwanted characteristics of high noise and nonstationary that tend to make the classical statistical system not competent and intelligent, whereas the NARX model possesses high and strong potential to be considered as a reliable alternative to conventional techniques. It provides better prediction and can effectively learn complex sequences producing a greater predictive capacity for both fit and accuracy. Furthermore, the impacts of process factors on surface roughness are discussed.

**3.1. ANOVA Results for Surface Roughness.** The ANOVA is useful to find out the effect of every factor. The statistical importance of every factor is indicated using  $P$  value. If the  $P$ -value of a particular factor is identified as lesser than 0.05, then the specific factor is statistically significant on attributes. The formulation of ANOVA is done with a significance of 5%. The ANOVA Table for roughness is detailed in Table 3. Furthermore, the significance of the factors on surface roughness can be notified based on  $F$ -value. In this ANOVA Table 3, feed rate ( $F$  value: 154.79) and speed ( $F$  value: 63.09) are all identified as significant on roughness followed by the depth of cut ( $F$ -Value: 37.76). ANOVA analysis was done at a significant level of 5% with a confidence level of 95%.

**3.2. Regression Analysis for Surface Roughness.** The regression equation is normally used to relate the process factors and machining attributes and it is shown in the following equation:

TABLE 1: Machining parameters.

S.No	Symbol	Whisker reinforced ceramics		
		L 1	L 2	L 3
V (m/min)	V (m/min)	150	225	275
S (mm/rev)	S (mm/rev)	0.061	0.12	0.153
ap (mm)	ap (mm)	0.75	1.0	1.20

TABLE 2: Experimental trial results.

Trail. No	Cutting speed V	Feed rate S	Depth of cut ap	Surface roughness ( $R_a$ ), $\mu\text{m}$
1	150	0.061	0.75	2.25
2	150	0.061	1.0	1.75
3	150	0.061	1.2	1.25
4	150	0.12	0.75	2.5
5	150	0.12	1.0	2
6	150	0.12	1.2	1.85
7	150	0.153	0.75	2.75
8	150	0.153	1.0	2.6
9	150	0.153	1.2	2.4
10	225	0.061	0.75	1.45
11	225	0.061	1.0	1.3
12	225	0.061	1.2	1.2
13	225	0.12	0.75	2
14	225	0.12	1.0	1.55
15	225	0.12	1.2	1.65
16	225	0.153	0.75	2.5
17	225	0.153	1.0	2.3
18	225	0.153	1.2	2.25
19	275	0.061	0.75	1
20	275	0.061	1.0	0.9
21	275	0.061	1.2	0.8
22	275	0.12	0.75	1.75
23	275	0.12	1.0	1.55
24	275	0.12	1.2	1.45
25	275	0.153	0.75	2.15
26	275	0.153	0.1	1.95
27	275	0.153	1.2	1.8

TABLE 3: ANOVA: roughness

S	SOS	DF	MS	F-value	P value
M	7.17	9	0.7970	38.91	< 0.0001
V	1.29	1	1.29	63.09	< 0.0001
S	3.17	1	3.17	154.79	< 0.0001
$a_p$	0.7735	1	0.7735	37.76	< 0.0001
V * S	0.0559	1	0.0559	2.73	0.1170
V * $a_p$	0.0172	1	0.0172	0.8380	0.3728
S * $a_p$	0.0093	1	0.0093	0.4525	0.5102
V <sup>2</sup>	0.0148	1	0.0148	0.7226	0.4071
S <sup>2</sup>	0.1116	1	0.1116	5.45	0.0321
$a_p^2$	0.7449	1	0.7449	36.36	< 0.0001
Residual	0.3483	17	0.0205		
Total	7.52	26			

 $R^2$ : 95%

$$y = \beta_0 + \sum_{i=1}^k \beta_1 x_i + \sum_{i=1}^k \beta_{ij} x_{i^2} + \sum_i \sum_j \beta_{ij} x_i x_j + \varepsilon, \quad (1)$$

where “y”: machining attribute;  $x_i$  is the value of the  $i^{\text{th}}$  process factors;  $\beta$ : coefficient: regression; and  $\varepsilon$ : residual measure.

The observed values of experiment trails are predicted using a regression equation. The quadratic equation to predict surface roughness is given in the following equation:

$$\begin{aligned} R_a = & 1.80 - 0.3198 * V + 0.4989 * S - 0.2076 * ap \\ & + 0.0669 * V * S + 0.0153 * V * ap + 0.0112 * S * ap \\ & - 0.0521 * V^2 + 0.1502 * S^2 - 0.0613ap^2. \end{aligned} \quad (2)$$

R-Square value is 95% and the ability to predict the surface roughness is found to be adequate. The developed model is found to be a 95% confidence interval. Figure 1 shows a normal plot of residuals and the cluster of points that connect the normal plot for the residuals of surface roughness. These points are very close to the plot and it is acceptable with a 95% confidence interval. The average (%) age error among experiment trails values and predicted result by the regression model is found to be 5.131.

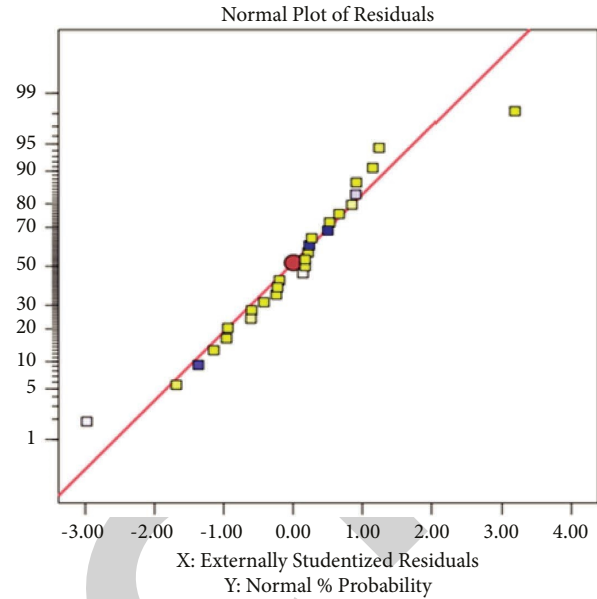


FIGURE 1: A normal plot of Residuals.

3.3. Modeling of Process Factors Using NARX Time Series Model (Implementation of NARX Time Series Model for Prediction). NARX is a nonlinear auto-regressive network with exogenous inputs. It is a multilayered recurrent dynamic network with feedback links. The NARX model is built on the linear ARX model. It is extensively used in the time-series model. Based on  $d$  prior  $y(t)$  values and another series  $x$ , predict a series  $y(t)$  ( $t$ ). The NARX model equation to define is given in the following equation:

$$y(t) = f(x(t-1) \dots x(t-d), y(t-1) \dots y(t-d)). \quad (3)$$

The predicted value of the dependent output signal  $y(t)$  is regressed on past output signal values of  $y(t)$ , given past  $d$  values as well as previous values of an independent (exogenous) input signal  $x(t)$ . Figure 2 shows a diagram of the resulting network. It uses a two-layer feed-forward network for approximation. It can be used as a predictor to prognosticate the input signal’s next value. It can also be used for nonlinear filtering with a noise-free version of the input signal as the target output. Another notable application of the NARX network is in the modeling of nonlinear dynamic systems.

Prediction is a type of dynamic filtering in which one or more time series’ past values are used to forecast future values. For nonlinear filtering and prediction, dynamic neural networks with tapped delay lines are used. Validation, testing, and training are the three sections of the experimental trial dataset. The dataset is randomly divided into 70% training, 15% validation, and 15% test data for 27 target time steps. During training, the training dataset is submitted

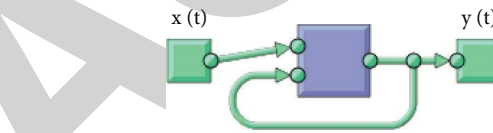


FIGURE 2: Two-layered feed-forward NARX network.

to the network, and the network is updated based on its error. The validation dataset is used to assess network generalization and to end training when generalization begins to deteriorate. The Test dataset has no bearing on training and hence furnishes an objective assessment of network performance both during and after training. Table 4 furnishes the Inconel superalloy dataset, which includes 27 trials, 19 training, 4 validation, and 4 testing.

As indicated in Figure 3, the network will be built and trained in an open loop. Closed loop (multistep) training is less efficient than open loop (single-step) training. We may feed the network accurate historical outputs while training it to produce precise current outputs using an open loop system. The network may be transformed into a closed loop or any other form that the application demands after training.

The Levenberg–Marquardt algorithm is used to train the network. This approach needs more memory but takes less time. When generalization stops improving, as shown by a rise in the mean square error of the validation samples, training automatically terminates. Due to varying beginning circumstances and sampling, training numerous times will yield different outcomes. The network is trained until the  $R$  value approaches unity and the mean square error falls below a certain threshold. As shown in Figure 4, we evaluated the network and deployed the solution in Simulink.

From Table 4, it can be deduced that the average prediction error for Surface Roughness ( $R_a$ ) is 3.016 percent. The  $a_p$ ,  $S$ , and  $V$  are all represented by neurons in the input

TABLE 4: Percentage prediction error.

Expt. No	Surface roughness		(% ) Prediction Error
	Measured value	Predicted value	
1	2.25	2.251	0.044444
2	1.75	1.753	0.171429
3	1.25	1.2491	0.072
4	2.5	2.50006089	0.000244
5	2	1.785035212	1.748239
6	1.85	1.850002424	0.000131
7	2.75	2.74996971	0.0011015
8	2.6	2.354446238	3.4443755
9	2.4	2.399990731	0.0003862
10	1.45	1.449979063	0.0014439
11	1.3	0.877212141	32.522143
12	1.2	1.199983688	0.0013593
13	2	1.999968219	0.0015891
14	1.55	1.549976417	0.0015215
15	1.65	1.632345865	1.0699476
16	2.5	2.499996049	0.0001581
17	2.3	2.247431325	2.2855946
18	2.25	2.005600083	10.862219
19	1	1.00002668	0.002668
20	0.9	0.76836487	14.626126
21	0.8	0.799993835	0.0007706
22	1.75	1.749948513	0.0029421
23	1.55	1.549953318	0.0030118
24	1.45	1.449965174	0.0024018
25	2.15	2.149978889	0.0009819
26	1.95	1.950020128	0.001032
27	1.8	1.799993533	0.0003593
		Avg prediction error	3.0158786

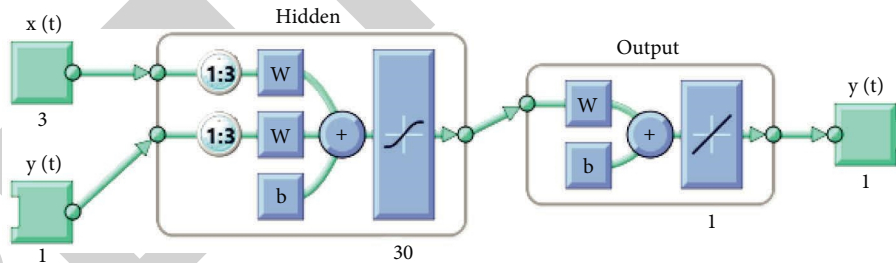


FIGURE 3: Neural network: one-hidden layer and 30 neurons.

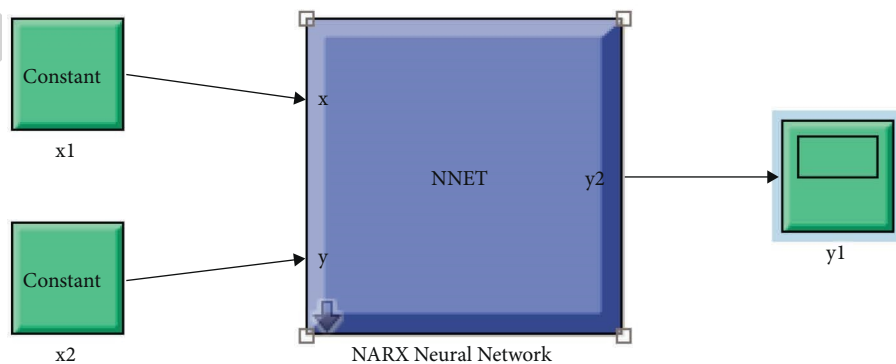


FIGURE 4: Simulink diagram.

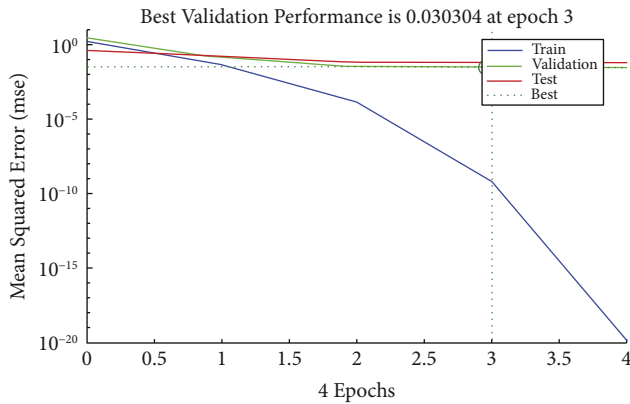


FIGURE 5: Performance plot of training network.

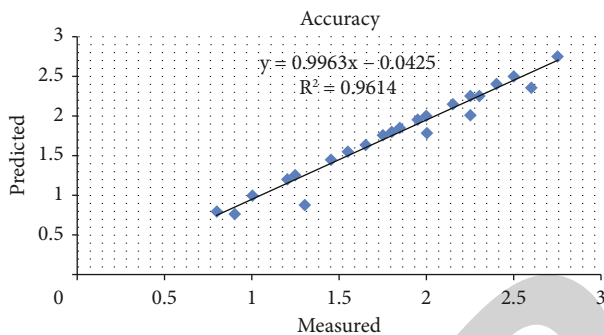


FIGURE 6: Accuracy plot of NARX network w.r.t target.

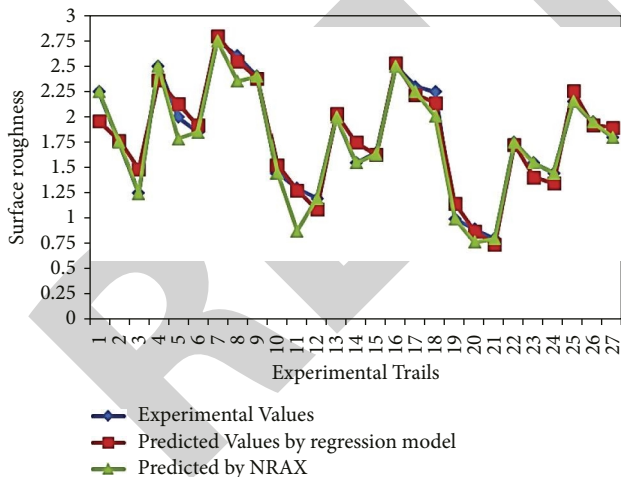


FIGURE 7: Surface values: experimental trails vs. regression model vs. NARX model.

layer. Surface roughness, on the other hand, is related to the output layer ( $R_a$ ). The hidden layer neurons are linked to the outputs, whereas the inputs are linked to the hidden neurons. The figure above depicts the design, which includes thirty neurons in the hidden layer and a three-step time delay.

Finally, the purelin transfer function produced the greatest results for neurons in buried layers. Using the plot network performance function plot performs, the maximum number of training epochs was simply found empirically. When looking at the network training graph, it was seen that after four epochs, the network training almost stops as shown in Figure 5.

Learning algorithms tailored the formed neural networks to the dataset throughout the training phase. MATLAB regression graphs as illustrated in Figure 6 that demonstrated the network outputs in relation to the objectives for testing, validation, and training sets, with  $R$  values over 0.96 for all data sets, were used to validate the correctness of the fits. Figure 7 plots show the observed results of surface roughness by experimental trails, regression model values, and NARX model values. The average percentage error observed with the predicted values by NARX is observed as 3.01%, which is lower than the average percentage error observed by the regression model 5.131%.

#### 4. Conclusions

Experimental work, development of the predictive model by machine learning methodology NARX model, and regression model in dry turning of Inconel 625 were presented. The surface roughness at various levels of machining factors was calculated. Some of the conclusions are as follows:

- (i) The predictive models developed by regression and the ANN-NARX model were found to fit well with experimental trial results. These predictive models can be useful to predict surface roughness before actual experiments in manufacturing factories.
- (ii) Inconel 625 dataset includes 27 trials, 19 for training, 4 for validation, and 4 for testing. Levenberg–Marquardt algorithm is used to train the network. The prediction potential of the ANN-NARX model was proved as more accurate for the prediction of roughness than the regression model.
- (iii) The average (%) age error among experiment trail values and regression predictive model is observed as 5.131%, whereas, the average percentage error among experiment trails and ANN-NARX model is found to be 3.13%.
- (iv) The impact of factors observed by ANOVA analysis is that feed has a high impact on roughness accompanied by cutting speed and depth of cut.

#### Data Availability

The data used to support the findings of this study are included within the article. Further data or information are available from the corresponding author upon request.

#### Conflicts of Interest

The authors declare that there are no conflicts of interest regarding the publication of this paper.

## *Retraction*

# **Retracted: Development of Microbiology Plantation-Based Multimodal Segmentation for Smart Garden Using Machine Learning**

### **Advances in Materials Science and Engineering**

Received 26 December 2023; Accepted 26 December 2023; Published 29 December 2023

Copyright © 2023 Advances in Materials Science and Engineering. This is an open access article distributed under the Creative Commons Attribution License, which permits unrestricted use, distribution, and reproduction in any medium, provided the original work is properly cited.

This article has been retracted by Hindawi, as publisher, following an investigation undertaken by the publisher [1]. This investigation has uncovered evidence of systematic manipulation of the publication and peer-review process. We cannot, therefore, vouch for the reliability or integrity of this article.

Please note that this notice is intended solely to alert readers that the peer-review process of this article has been compromised.

Wiley and Hindawi regret that the usual quality checks did not identify these issues before publication and have since put additional measures in place to safeguard research integrity.

We wish to credit our Research Integrity and Research Publishing teams and anonymous and named external researchers and research integrity experts for contributing to this investigation.

The corresponding author, as the representative of all authors, has been given the opportunity to register their agreement or disagreement to this retraction. We have kept a record of any response received.

### **References**

- [1] S. Prasath, R. Govindaraj, R. Subbiah et al., "Development of Microbiology Plantation-Based Multimodal Segmentation for Smart Garden Using Machine Learning," *Advances in Materials Science and Engineering*, vol. 2022, Article ID 1066535, 6 pages, 2022.

## Research Article

# Development of Microbiology Plantation-Based Multimodal Segmentation for Smart Garden Using Machine Learning

S. Prasath,<sup>1</sup> Ramkumar Govindaraj,<sup>2</sup> Ram Subbiah,<sup>3</sup> Sulaiman Ali Alharbi,<sup>4</sup>  
Hesham S. Almoallim,<sup>5</sup> S. Priya,<sup>6</sup> and Begna Dejene Mulugeta <sup>7</sup>

<sup>1</sup>Department of Mechatronics, Agni College of Technology, Chennai, Tamilnadu, India

<sup>2</sup>Department of Electronics and Communication Engineering, Saveetha School of Engineering, SIMATS, Chennai, Tamil Nadu 602105, India

<sup>3</sup>Department of Mechanical Engineering, Gokaraju Rangaraju Institute of Engineering and Technology, Hyderabad, Telangana 500090, India

<sup>4</sup>Department of Botany and Microbiology, College of Science, King Saud University, P. O. Box 2455, Riyadh 11451, Saudi Arabia

<sup>5</sup>Department of Oral and Maxillofacial Surgery, College of Dentistry, King Saud University, P. O. Box 60169, Riyadh 11545, Saudi Arabia

<sup>6</sup>Department of Microbiology Immunology, Northwestern University Feinberg School of Medicine, Chicago, IL, USA

<sup>7</sup>Department of IT, Mettu University, Metu, Ethiopia

Correspondence should be addressed to Begna Dejene Mulugeta; [begnadejene@meu.edu.et](mailto:begnadejene@meu.edu.et)

Received 1 June 2022; Revised 13 June 2022; Accepted 14 June 2022; Published 5 October 2022

Academic Editor: K. Raja

Copyright © 2022 S. Prasath et al. This is an open access article distributed under the Creative Commons Attribution License, which permits unrestricted use, distribution, and reproduction in any medium, provided the original work is properly cited.

Normally, gardens lower the ambient temperature, which would improve air quality, absorb pollutants, and produce oxygen. Trees reduce soil erosion, increase fertility, and help retain soil moisture. Decomposed leaves that fall in the garden become nutrients for tree growth and help microbes to thrive. When it comes to growing trees in a garden, one should try and choose native trees that are naturally found in a particular area. These trees are well adapted to the environment and require less maintenance. Many insects and birds rely on native trees for food and shelter. Therefore, they are best for the environment. However, not all native trees are evergreen trees. Many evergreen trees can be planted in a small garden. In this paper, a microplantation-based model was developed to enhance the biological impacts for a smart garden. Based on the garden requirements, the smart system was constructed. On this basis, the seeds are planted in the soil.

## 1. Introduction

Plants in narrow beds get the nutrients they need from a bed filled with organic matter. Although the area between the beds does not “walk,” if it is covered with mulch or turf, it helps to keep the base and ground moist. The mulch layer is processed into earthworm fertilizers and soil microorganisms. In addition, weeds, sawdust, and straw will not grow in those buried in the sand. In order not to waste energy in creating new beds every year, they are made stable, and they are protected by any available materials, logs, boards, bricks, slate, and stones. Augmenting or painting with water-based paint is the best

pretreatment to protect wood products against decay [1]. If you have a dry hot climate, the amount of soil in the garden should not exceed the ground level between rows, and if the weather is rainy or watering the gardens, it makes sense to make beds/boxes. In beds raised above the ground level, boxes during prolonged rains, the plants do not get wet and hot. The walls of the beds/boxes rise to a height of 20–30 cm above the ground level, and it is better to make them durable and practical bricks, for example, durable materials than boards or logs [2]. The leaves are placed at the very bottom of the straw or hay box, and thin branches can be used, which are covered with compost or humus from above, and then, at the very top, fertile soil.



To maintain fertility in the beds, you can add compost to them or grow green manure, which can be sown in early spring and autumn.

Organic gardening should be considered as an alternative to intensive horticulture, which often uses unnecessarily high amounts of fertilizers and pesticides. Of course, the yield of a serious type of a garden will be higher [3]. The practice of organic farming refers to the use of only natural fertilizers in the garden, manure, compost, leaf humus, and other organic matter, as well as wood ash. In the fight against diseases, the application of the most important principle of crop rotation has a positive effect. Attracting these insect-eating birds and beneficial insects to the garden helps to combat them. Weed control is not done with the help of herbicides, but through efficient agronomic practices, mulching, and proper crop rotation. We must remember that taking care of creation and arrangement of the garden is the key to success which is a respectful approach to the earth. It should be noted that this is not "dirty" in any way, as some people think. Soil is a habitat for organisms, microorganisms, protozoa, fungi, and soil animals. It is a complex biological system, a pantry of mineral and organic components, from which plants gain the strength to harvest [4]. With proper handling, the soil can maintain fertility spontaneously.

In narrow beds, tall and spreading plants that need more space are grown in two rows in the form of a checkerboard (cabbage, eggplant, peppers, tomatoes, and small ones that do not interfere with each other) and three or four rows, taking into account the distance between them (onions, garlic, carrots, peas, beets, lettuce, and others). For better and more uniform lighting, it is worth noting that all the beds are stretched from north to south, so that when the sun rises, it illuminates one side of the plants before lunch and the afternoon before sunset [5]. Also, do not forget to combine several types of garden crops in one garden bed, for example, root crops at the center, tall, short, and at the edges. On normal beds, and even in the middle of densely planted vegetable crops, they get sick and often rot. Plants grow poorly, give small fruits, and are stored for a short time. Such beds are difficult to process and weed. In addition, insects feed on weak plants and breed in such areas [6]. The plants in the outer rows are much healthier than the ones in the middle. So, you need to make narrow beds so that they are easy to process. If you combine the two technologies, narrow beds and the agricultural technology of landscaping, you can get a harvest. This is business, learn how to make your own compost and arrange short fixed beds only once. Also, instead of mineral fertilizers, use humus, grass, manure, and ash, which spoil the taste of the fruit and make it unnatural, in short, organic fertilizers. At the same time, we note, however, that mineral fertilizer is not a poison, but it is good in reasonable amounts. The plants should be fed but not overfed [7].

Combined planting of vegetables not only makes full use of the available land but also positively affects the growth and yield of both plants. Such beds are very beautiful from the outside [8]. Smart garden planning and plant interaction combine many of the nuances that scientists and farmers have explored in their own experience. Many plants release chemical compounds that stimulate and suppress the growth of neighbors. In addition, they protect each other from heat,

provide shade, enrich the soil, and prevent the growth of weeds that are dangerous to another species or repel pests. Each culture has its own list of useful and harmful companions in the garden [9]. Mixed plantings perform a number of functions: protecting plants from diseases and pests, increasing yield per unit area, protecting the soil from unilateral deficiencies, and reducing weed numbers. Fruits and vegetables grown in the community with other species are tasty: mint enhances the taste of potatoes; parsley enhances the taste of tomatoes [6]. If you choose the right plants, they will help each other and make the owner happy. This is the best use of your land. I have been using compression and joint plantings of crops in my garden for a long time. I sow the carrots in a row with the onions, the beds with the cabbage with the salt, and the potatoes with the beans. Also, nursery plants such as calendula, marigold, and nasturtium grow throughout the garden.

## 2. Literature Review

The decreased fertile soil layer leads to problems caused by chronic crop failures, pests, and plant diseases. Soil fertility depends directly on the presence of humus in it, the main soil component, and its organic area, which is formed as a result of biochemical changes in animal and plant residues. It is in the humus combined with the minerals of the soil that all the essential nutrients of the plant world are found [5]. The soil formation process takes place with the help of saprophyte microorganisms, symbiotic fungi, and soil organisms. Causes of soil depletion are unfortunately a person interferes very unexpectedly with the complex processes that take place at the boundaries of the upper soil [10]. Continuous digging violates the microbial balance of the soil. Unfair use of pesticides kills all living things, including beneficial soil plants and animals. Continued use of mineral fertilizers leads to soil salinity, due to which the plants, in the end, are unable to obtain nutrients. Pollution and depletion of the soil leads to nothing growing on the site except weeds. It is well known that organic fertilizers integrate well into the food chain of soil-dwelling microorganisms, while providing all the nutrients to plants [11]. It takes a lot of effort to hurt. Practically, no excess washes away by excessive weather and rainfall. Therefore, the use of organic matter at all stages of crop cultivation is becoming more and more desirable. The basic techniques of organic farming, i.e., actually creating the land, fall under three main techniques: composting, application of green manure, and mulching [12]. To drop mineral fertilizers or minimize their use, it is necessary to use organic materials. Fertilizers and manures contain all the essential elements necessary for the normal growth of plants, nitrogen, potassium, phosphorus, and magnesium [13]. Bird droppings, peat, and bone meal can be used successfully as organic fertilizers in natural agriculture. Wood ash has always been an excellent source of trace elements. All types of organic fertilizers are safe for humans and soil microorganisms [14]. Organic fertilizers include compost, manure, humus, bird droppings, and more. Our ancestors had no manure except for furnace ash and dung. This universal fertilizer not only improves yield but also improves soil structure and fertility, which has been used in agriculture since ancient times [15].

### 3. Proposed Model

The proposed multimodal segmentation technique (MMST) constructs natural agriculture. The beds are not just straight rows with beautiful borders. To organize them properly, you need to do a little work. Perhaps, this position of working with the land is the most time consuming but not comparable to the efforts used to dig or plow which is shown in Figure 1 that shows the MMST warm bed preparation model.

First of all, it is necessary to mark the site for the beds for the width of the planting area and create the right paths, row spacing. They should be wide. Of course, not everyone is ready to go to the consumption of such “economical” land; the paths are 60–80 cm wide, and the beds themselves range from 45 to 50. But still, increasing the spacing between plantings to at least 50 cm will allow the gardener to provide more light to the plants, which will positively affect the general condition of the crop during the growing season and increase yields.

Second, the beds should be prepared in advance: not on the day of sowing the plant but in the fall. To do this, you can use several methods. Immediately after harvest, it is necessary to sow the ridges with green manure and do not remove them from the surface until spring. At this time, they will be completely warmed up, or the first layer of mulch, however, very thin, should be further increased after planting. Refueling beds with organic matter is the process of creating warm beds. For this, the fur is due to a depth of at least 40 cm, and this is the only occasion when you need to pick up a shovel when arranging a garden. Next, the branches, organic matter, and fresh grass are laid in layers of soil, after which the bed is covered with a mulch cloth. The focused area of the MMST is shown in Figure 2.

**3.1. Intensive Cultivation.** The arable land layer, excessive drilling, loosening, mineralization, and other agricultural work will lead to higher material costs with more labor and less efficiency. Natural farming on a farm or garden leads to minimal costs, while allowing for a good harvest each year.

**3.2. Mulch.** It is an important method for improving the soil quality and creating favorable conditions for the natural system. Mulch protects straw, sawdust, straw, fallen leaves, roots, and cut weeds, all covering the beds from above, from excessive evaporation of black soil moisture, erosion, and hypothermia.

**3.3. Fair Top Coat.** It is designed to process beneficial microorganisms, fungi, that use organic matter, multiply them, suppress pathogenic bacteria, and repair mineral components, all that can act as natural humus (Algorithm 1).

This is it. Now, we do not have to touch it until spring. In the first year of operation, we plant melons, cucumbers, and tomatoes. We are increasing the utilization of beds while using the crop rotation concept. Such an organic bed will work effectively for 3-4 years. When organic matter is

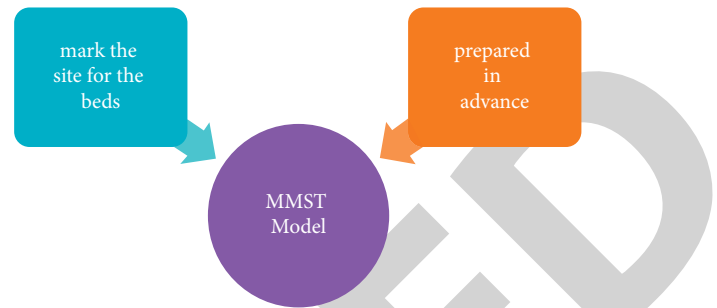


FIGURE 1: MMST warm bed preparation model.

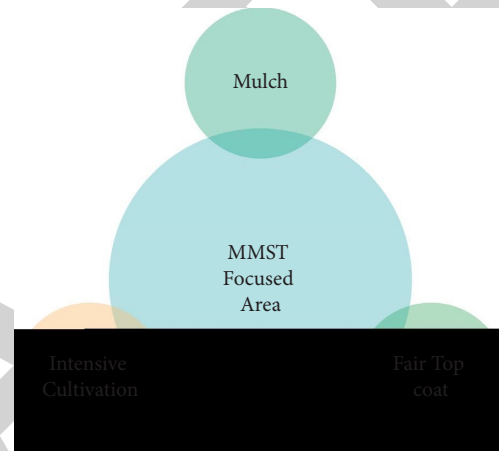


FIGURE 2: MMST focused area.

introduced in the spring, soil is added to the planting holes so that the plants do not burn under the influence of temperature, which increases as a result of overheating of the organic layers:

- (i) Waste, foliage, grass, and plant debris should be regularly filled. After harvesting the vegetables, it is better to sow the beds. When planting seedlings in holes, no rotten manure or compost is introduced into them. The bed itself is compost.
- (ii) Fences do not allow washing with humus. Thanks to the large aisles, vegetable crops get enough air and light. Beds are easy to water, and water does not stagnate.
- (iii) Organic and mineral fertilizers are used sparingly. If the bed is mulched, mulching and weeding will disappear.
- (iv) Short beds are not dug but only loosened to a depth of 7 to 10 cm. In the spring, they warm up faster, so they can be planted earlier. Crop rotation is also convenient; last year, onions were grown, and this year, carrots and cabbage are sown. The tubers and roots of the vegetables are clean without any symptoms.
- (v) It is convenient to set the arches above the beds. They are sold in specialty horticultural stores. It is only necessary to drive in two pegs on both sides at a distance of 1 m and place on curves. So, they do the

```

(1) Start
(2) Initialize the requirements
(3) Check the available requirements details
(4) If (requirements= available)
(5) Then check if (garden parameter= available)
(6) Then send the details to garden manager
(7) Wait for approval
(8) Assign the requirements for utilization
(9) Else
(10) Then send the details to the audit manager
(11) Waiting for approval from the garden manager
(12) Provide the license audit manager
(13) End.

```

ALGORITHM 1: Multimodal segmentation technique (MMST).

full length of the box. You can cover with foil from the frost.

The construction of standard beds has several important advantages, which are a hundred times justified:

- (i) Reducing the cultivated area of the soil
- (ii) Beauty and order on site, no dirt in aisles
- (iii) Such beds are very convenient for plowing and maintenance
- (iv) It is not necessary to make new beds every year
- (v) Irrigation facilities and low water consumption
- (vi) Nutrients are not washed away from the fenced garden
- (vii) A high bed prevents flooding and stagnant water
- (viii) The bed has a large enough amount of useful ingredients and moisture
- (ix) The mulched bed will retain moisture and weed growth
- (x) The absence of weeds in the wide aisles eliminates the need to fight them, thanks to the mulch of large gardens
- (xi) Fixed fertilization is not required, and sowing green manure replenishes the nutrients in the bed soil
- (xii) No need to dig into an organic bed, only loosening with flat cutting tools
- (xiii) The rapid warming of the raised bed in the spring allows for early planting
- (xiv) A narrow bed and wide aisles provide not only plants with good light but also free movement of the air, which increases the air supply of plants and prevents the development of fungal diseases during wet periods
- (xv) Raised narrow beds make it easy to hide from spring and autumn frosts or pull sun protection nets in hot summers

## 4. Results and Discussion

The proposed multimodal segmentation technique (MMST) was compared with the existing cognitive model for emotion awareness (CMEA), commuter behavior profiling framework (CBPF), PTZ-surveillance coverage (PTZSC), and the scalable data clustering technique (SDCT).

**4.1. Mulched Soil Management.** Organic mulch complements the soil of the site well with minerals necessary for plant growth and improves its composition, promoting the reproduction of earthworms and other soil organisms which is elaborated in Table 1.

In mulched soil, the content of vermicompost gradually increases. Covered soil is protected from overheating in the sun and, accordingly, from rapid evaporation of moisture, humidity, and erosion. Straw, leaves, sawdust, straw, and many others are suitable as mulch.

**4.2. Crop Rotation Management.** Crop rotation, or simply speaking, transplanting and changing crops, helps maintain soil fertility and significantly reduces the number of diseases and pests. Not all annual crops grow in the same place for the second year in a row, and this is a simple crop rotation plan. Complex systems include ten-year rotation patterns of vegetable and fruit crops which is elaborated in Table 2.

It can do crop rotation according to one of two principles: alternative families or groups of crops (leaf, fruit, and root) with a minimum shift plan (usually three to four years).

**4.3. Warm Bed Management.** Beds made directly in the compost pile, even hotter, during the decomposition of organic matter, heat is released. The temperature of the heated bed is two to four degrees higher than the ambient temperature. This makes it possible to plant the plants in advance. Direct composting of beds with raw organic matter offers several benefits which are elaborated in Table 3.

TABLE 1: Comparison of mulched soil management.

No. of inputs	CMEA	CBPF	PTZSC	SDCT	MMST
200	47.84	59.13	41.90	45.80	84.05
400	47.51	57.63	41.31	43.93	83.04
600	46.17	56.52	40.33	43.10	82.88
800	45.03	56.14	39.12	42.19	81.92
1000	43.98	55.13	37.98	41.27	82.35
1200	43.27	54.20	36.87	39.94	81.15
1400	41.97	53.20	36.17	38.86	80.99

TABLE 2: Comparison of crop rotation management.

No. of inputs	CMEA	CBPF	PTZSC	SDCT	MMST
200	50.14	61.43	38.50	43.06	84.96
400	49.81	59.93	37.91	41.19	83.92
600	48.47	58.82	36.93	40.36	83.79
800	47.33	58.44	35.72	39.45	82.83
1000	46.28	57.43	34.58	38.53	83.26
1200	45.57	56.50	33.47	37.20	82.02
1400	44.27	55.50	32.77	36.33	81.91

TABLE 3: Comparison of warm bed management.

No. of inputs	CMEA	CBPF	PTZSC	SDCT	MMST
200	47.09	40.42	44.42	38.03	83.27
400	48.72	42.16	46.00	39.45	84.56
600	49.20	44.50	48.20	40.71	85.57
800	50.49	45.31	49.83	42.70	86.46
1000	52.60	47.60	50.97	45.17	86.83
1200	54.09	49.53	53.17	46.61	87.87
1400	55.90	51.26	54.32	48.33	88.64

TABLE 4: Comparison of plant nutrition management.

No. of inputs	CMEA	CBPF	PTZSC	SDCT	MMST
200	48.88	69.17	46.06	51.50	85.22
400	47.25	67.43	44.48	50.08	83.93
600	46.77	65.09	42.28	48.82	82.92
800	45.48	64.28	40.65	46.83	82.03
1000	43.37	61.99	39.51	44.36	81.66
1200	41.88	60.06	37.31	42.92	80.62
1400	40.07	58.33	36.16	41.20	79.85

**4.4. Natural Agro Management.** The organic farming system is based on a basic study that defines the earth as a living thing, a creature that can completely destroy the soil ecosystem that a person has created over the centuries. As a result, the earth will cease to produce what it can, even if it is not for human action which is shown in Table 4.

**4.5. Plant Nutrition Management.** Because of the hysteria on the soil, we have become accustomed to considering plant nutrients as minerals, and somehow, they lost sight of the atmosphere. But plants with all the leaves live in it. To understand what plants eat, one must consider what they are made of. Plants are 50% carbon, which is obtained in the form of carbon dioxide through the leaves which is shown in Table 5.

TABLE 5: Comparison of plant nutrition management.

No. of inputs	CMEA	CBPF	PTZSC	SDCT	MMST
200	50.26	68.70	48.41	54.69	85.06
400	50.37	68.68	48.58	54.96	85.56
600	50.39	67.80	47.85	54.66	85.44
800	47.29	64.97	44.51	51.15	82.21
1000	46.09	63.65	43.78	49.83	81.83
1200	45.48	62.82	42.89	49.29	81.26
1400	45.07	62.42	42.81	48.99	81.56

TABLE 6: Comparison of soil microorganism management.

No. of inputs	CMEA	CBPF	PTZSC	SDCT	MMST
200	55.43	58.22	47.58	54.73	82.44
400	55.76	59.72	48.17	56.60	83.45
600	57.10	60.83	49.15	57.43	83.61
800	58.24	61.21	50.36	58.34	84.57
1000	59.29	62.22	51.50	59.26	84.14
1200	60.00	63.15	52.61	60.59	85.34
1400	61.30	64.15	53.31	61.67	85.50

TABLE 7: Comparison of insect protector management.

No. of inputs	CMEA	CBPF	PTZSC	SDCT	MMST
200	53.13	55.92	50.98	57.47	81.53
400	53.46	57.42	51.57	59.34	82.57
600	54.80	58.53	52.55	60.17	82.70
800	55.94	58.91	53.76	61.08	83.66
1000	56.99	59.92	54.90	62.00	83.23
1200	57.70	60.85	56.01	63.33	84.47
1400	59.00	61.85	56.71	64.20	84.58

Microbes breathe it in and break down organic matter. Plants take 20% of their oxygen and 8% of their hydrogen from water and air. Plants find only 15% of nitrogen in the soil due to microbial activity. Only 7% of the mineral elements were intended to extract from the Earth's crust, so they had to put in a lot of effort to build soil. Therefore, plant nutrition in the strict sense is nitrogen and carbohydrate.

**4.6. Soil Microorganism Management.** The main thing is the soil microorganism. There are 4% of soil microorganisms which are hundreds of species. We are interested in the most specific ones: conservationists and soil developers. They are constantly being discovered and studied. Therefore, let us take into account that the known microorganisms are only a small part of the overall picture, which cannot be fully established. Germs do not die which is shown in Table 6.

Once in a bad condition, they grow up and become spores or are immediately eaten by other microorganisms. Good ones multiply. Therefore, it is not possible to consume large amounts of microbial products. Another thing is that there is no point in increasing the dose if the effect from this does not increase.

**4.7. Insect Protector Management.** Many plants repel or attract insects or animals that eat vegetable crops. They can be attached to plantings with vulnerable plants or planted

## *Retraction*

# **Retracted: Experimental Analysis and Optimization of Tribological Properties of Self-Lubricating Aluminum Hybrid Nanocomposites Using the Taguchi Approach**

### **Advances in Materials Science and Engineering**

Received 26 December 2023; Accepted 26 December 2023; Published 29 December 2023

Copyright © 2023 Advances in Materials Science and Engineering. This is an open access article distributed under the Creative Commons Attribution License, which permits unrestricted use, distribution, and reproduction in any medium, provided the original work is properly cited.

This article has been retracted by Hindawi, as publisher, following an investigation undertaken by the publisher [1]. This investigation has uncovered evidence of systematic manipulation of the publication and peer-review process. We cannot, therefore, vouch for the reliability or integrity of this article.

Please note that this notice is intended solely to alert readers that the peer-review process of this article has been compromised.

Wiley and Hindawi regret that the usual quality checks did not identify these issues before publication and have since put additional measures in place to safeguard research integrity.

We wish to credit our Research Integrity and Research Publishing teams and anonymous and named external researchers and research integrity experts for contributing to this investigation.

The corresponding author, as the representative of all authors, has been given the opportunity to register their agreement or disagreement to this retraction. We have kept a record of any response received.

### **References**

- [1] V. K. Selvaraj, S. Jeyanthi, R. Thiyagarajan et al., "Experimental Analysis and Optimization of Tribological Properties of Self-Lubricating Aluminum Hybrid Nanocomposites Using the Taguchi Approach," *Advances in Materials Science and Engineering*, vol. 2022, Article ID 4511140, 13 pages, 2022.

## Research Article

# Experimental Analysis and Optimization of Tribological Properties of Self-Lubricating Aluminum Hybrid Nanocomposites Using the Taguchi Approach

Vinoth Kumar Selvaraj,<sup>1</sup> S. Jeyanthi,<sup>1</sup> Raja Thiyagarajan,<sup>1</sup> M. Senthil Kumar,<sup>1</sup> L. Yuvaraj,<sup>2</sup> P. Ravindran,<sup>3</sup> D. M. Niveditha,<sup>1</sup> and Yigezu Bantirga Gebremichael <sup>4</sup>

<sup>1</sup>School of Mechanical Engineering, Vellore Institute of Technology, Chennai 600127, Tamilnadu, India

<sup>2</sup>Department of Automobile Engineering, Acharya Institute of Technology, Bangalore 560107, Karnataka, India

<sup>3</sup>Department of Mechanical Engineering, St. Mother Theresa Engineering College, Vagaikulam, Thoothukudi, Tamilnadu, India

<sup>4</sup>School of Mechanical and Chemical Engineering, Kombolcha Institute of Technology, Wollo University, Kombolcha, Ethiopia

Correspondence should be addressed to Yigezu Bantirga Gebremichael; [yigezu@kiot.edu.et](mailto:yigezu@kiot.edu.et)

Received 6 July 2022; Accepted 8 September 2022; Published 4 October 2022

Academic Editor: K. Raja

Copyright © 2022 Vinoth Kumar Selvaraj et al. This is an open access article distributed under the Creative Commons Attribution License, which permits unrestricted use, distribution, and reproduction in any medium, provided the original work is properly cited.

In recent times, tribological properties are gaining and grabbing great attention in metal matrix composites. They can provide significant benefits such as a lower coefficient of friction, wear resistance, high strength, and stiffness. Considering all these parameters, this research article mainly focuses on developing an aluminum hybrid nanocomposite material fabricated by powder metallurgy. Then, the results were examined using a pin-on-disk apparatus. Further optimization techniques such as the Taguchi approach under Design of Experiments have been adopted to obtain a minimal outcome of various assumed parameters such as A. percentage weight fraction of graphite content (Gr), B. the sliding distance, C. the sliding speed, and D. the stress applied. In addition, we have chosen parameters such as friction and wear loss for optimizing the outcome, including the main effect plots for the S-N ratio and the Analysis of Variance (ANOVA) approach. Based on the experimental results, we have noticed that friction and wear loss coefficient increase with increased applied load and sliding distance. Also, it was noted that there was a slight decrease in the coefficient of friction and wear loss when an increment was made in the graphite content, respectively. It was perceived that the sample containing 10% of graphite (Gr) could create a self-lubricating effect that significantly reduced wear loss and the coefficient of friction. Finally, by considering all these achieved results, aluminum nanocomposites can be employed in automobile, defense, and aerospace applications as they can reduce the weight of the components with improved wear behavior and more thermal stability.

## 1. Introduction

Recent research has reported that metal matrix composites with aluminum have exhibited low density and the ability to strengthen the material by precipitation, corrosion resistivity, thermal stability, and high electrical conductivity for potential tribological applications in the automotive and aerospace industries [1, 2]. It was found that inserting ceramic particles such as graphite, silicon carbide, aluminum oxide, and titanium carbide improved the noticeable tribological and mechanical properties of AMMCs [3–7].

Practical aluminum-based exhibits not only have high mechanical and wear properties but are capable of achieving self-lubricating properties.

Because the metal matrix is one of the traditional composites with various nanofillers, aluminum matrix alloys can significantly improve both mechanical and mechanical self-lubrication properties [8, 9]. Aluminum with silicon carbide composites reinforced with graphite nanofillers was used to create a combination of Al-SiC-Gr hybrid composites [10]. Furthermore, due to their exceptional features, the market for hybrid composites has grown dramatically in

the last five years. Furthermore, it was found that the creation of nano-crystalline hybrid AMMCs has a much higher strength than microcrystalline composites [11]. Numerous reports and experimental studies have been conducted on aluminum nanoparticles' dry condition wear behavior. It has been reported that the combination of aluminum and silicon carbide reduces the coefficient of friction; the addition of 10% silicon carbide and 6% graphite increased the bulk mechanical characteristics [12]. It has resulted from the combined action of an aluminum matrix combined with graphite and ceramics, resulting in noticeable good wear characteristics [13]. The influence of silicon carbide content on Al6061 was studied using silicon carbide and graphite hybrid composite processing, compact behavior, and properties using in-situ powder metallurgy (IPM) technology [14]. Most of the work was focused on and carried out on experimental work. Also, few mathematical models were based on factorial or Taguchi approaches [15, 16].

This has resulted from using liquid metallurgy to investigate the effect of sliding speed on the dry condition of wear behavior of hybrid metal matrix composites. Furthermore, many investigations were conducted using silicon carbide/Gr aluminum composite, including squeeze casting and stir-casting [17]. The homogenous reinforcing distribution is a benefit of powder metallurgy. The structural, mechanical, and high wear resistance properties are all improved by this homogenous distribution. According to literature sources, the number of investigations into the tribological behavior of hybrid composites is quite restricted. The majority of the published research studies, on the other hand, concentrated on the consequences and effects of several constraints on sliding wear and coefficient of friction and their behavior towards hybrid composites [18]. From the extensive literature survey, very minimal experimental work was carried out in the study, mainly focused on characteristics and parameters that influence the tribological behavior of nanohybrid composites. Most of the reported works were targeted at micron-size particle-reinforced aluminum composites [19, 20]. The novelty of this present investigation is to explore the optimized wear behavior of the nano-SiC and Gr-reinforced aluminum matrix composites using Taguchi design. The automobile wear components are the targeted applications for the developed aluminum matrix composites.

The primary objective of this research article is to utilize powder metallurgy to fabricate a nanohybrid aluminum metal matrix composite and practice the Taguchi approach under Design of Experiments to analyze the optimal outcomes of the coefficient of friction and wear loss [21]. By expanding the usage of fractional factorial design to include orthogonal arrays, Taguchi's experimental design, response surface methodology, and others can further simplify the trials [22–26]. Based on the results, this method offers a quick and flexible way to improve the outcome's performance, cost-effectiveness, and quality. Also, the current research attempts to investigate and optimize various parameters such as graphite reinforcement, the load applied, sliding distance, and sliding speed on the wear behavior of aluminum hybrid nanocomposites. Apart from the factors

TABLE 1: Specifications of nano-fillers used in the base material.

Nanofillers	Density (g/cm <sup>3</sup> )	Melting point	Grain size (nm)
Silicon carbide	3.22	2730	100
Graphite	2.26	3600	40–50

mentioned earlier, Taguchi's experimental approach and ANOVA are adopted to evaluate the obtained results and determine the effect of the percentage of various components on the fabricated composite material. At the same time, microstructure of the fractured surfaces and analysis of worn surfaces of the pin was studied using SEM. It is characterized to understand the better wear mechanism and analyze the topography of the fractured surfaces.

## 2. Materials and Methodology

*2.1. Materials Required for the Fabrication of Aluminum Hybrid Nanocomposites.* The nanocomposites were synthesized using the powder metallurgy approach. In this present research work, aluminum alloy 2024 is used as the base material, and the chemical composition of aluminum matrix AA 2024 is (Cu-4%, Mg-1.7 to 1.8%, Fe-0.5%, Mn-0.23 to 0.25%, Si-0.3 to 0.5%, Cr-0.25%, and Zn-0.2%, and balance is aluminum). The main reason for choosing aluminum alloy as a matrix material is that it is considered excellent for corrosion resistance, strength, and damage tolerance at high and low temperatures. In addition to these, four different hybrid nanocomposites were created, including AA2024, AA2024 with 5% silicon carbide, AA2024 with 5% SiC and 5% Gr, and AA2024 with 5% SiC and 10% Gr, respectively. Specifications for silicon carbide and graphite are listed in Table 1. At the same time, the mechanical properties of the fabricated hybrid nanocomposites are listed in Table 2.

*2.2. Preparation of Hybrid Nanocomposites.* A mixture of Al 2024, SiC, and Gr powders were ground in a planetary ball mill to create a hybrid Al nanocomposite. All four different types of powder mixes were put through a high-energy planetary ball milling process using vials and tungsten balls. The mechanical alloying procedure was carried out at 300 rpm in a toluene medium to prevent oxidation or powder adhering to the vial wall. The powder was ground for up to 2 h using tungsten balls with a 10 mm diameter and a 10:1 ball-to-powder weight ratio. It is manually applied earlier to each trial. The literature review reported that the combination of powders was hard-pressed in a uniaxial press where pressure is maintained at 700 MPa for generating green compacts. It was also reported that sintering of the compacts was conducted for 60 min at a controlled temperature of 530°C [27]. In addition, all of the sintered composites were subjected to a solution treatment in a furnace at a temperature of 540°C for roughly 120 min, followed by a 72-hour water quenching process. Wear specimens are fabricated, ensuring that the diameter is 8 mm with a height of 30 mm. Meanwhile, the specimen edges are polished with various grades of emery paper. According to



TABLE 2: Mechanical properties of the fabricated aluminum with silicon carbide and graphite nanocomposites.

S. no.	Chemical mixture (wt. %)	Experimental density (g/cm <sup>3</sup> )	Predicted density (g/cm <sup>3</sup> )	Porosity (%)
1	Aluminum alloy (AA) 2024	2.857	2.912	1.888
2	AA2024/5% silicon carbide nanocomposite	2.902	2.941	1.326
3	AA2024/5% silicon carbide/5% graphite hybrid nanocomposite	2.864	2.924	2.051
4	AA2024/5% silicon carbide/10% graphite hybrid nanocomposite	2.841	2.908	2.303

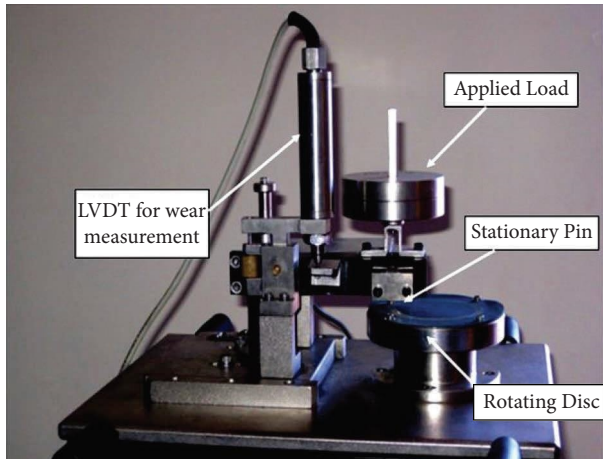


FIGURE 1: Components of the pin-on-disk test apparatus (Ducom, model no: ED-201).

Archimedes' principle, the actual density of the fabricated samples was measured using a high-accuracy weighing balance with a reading of 0.0001 mg. Besides, porosity is also determined by comparing the theoretical and actual density obtained from each sample.

**2.3. Wear Test.** The sliding wear characteristics were carried out using pin-on-disk equipment from Ducom, model No. 201, according to the ASTM G99-05 standard. EN31 steel was used for the counter disc, as shown in Figure 1. Before experimenting, all the pins and disc surfaces on the equipment were thoroughly cleaned with acetone. The tests were performed with loads ranging from 10 to 20 N. Also, sliding distances ranged from 500 to 2500 m with speeds of 1-2 m/s. After each trial, organic solvents such as acetone were used to clean the specimens and the counter face disc, which helped eliminate residues and impurities. The weight of the pins was evaluated before and after testing to determine the total wear loss. After six repetitions, the results of each test were noted and averaged at the end.

**2.4. Sequential Steps to Perform Design of Experiments.** In this research work, the experiment follows a three-level design based on the Design of Experiments (DOE) method. Factorial, Taguchi, RSM, and mixture are some of the different DOE techniques. A sophisticated design of experiments' tool is included in this Taguchi approach, which provides smart, efficient, high-quality systems for determining optimal

parameter yields. Compared to the traditional experimental study method, this strategy significantly reduces the number of trial runs of experiments needed to design the response functions. According to conventional experimentation, it is also impossible to analyze all components and determine their separate impacts in a single experiment. The Taguchi technique has been adopted to overcome these drawbacks by considering all these factors. This Taguchi technique has been developed exclusively for minimizing processes that can optimize and find the best combinations of elements for specific outcomes. Each variety of trials was repeated or performed twice to achieve more optimized results. The signal-to-noise ratio (S/N) is calculated from the experimental data, and graphs are plotted accordingly. Various S/N ratios are possible depending on the type of experiments carried out. The S/N ratios are divided into three categories. They are smaller, considered the better one, whereas nominal is deemed the best ratio, respectively. For the minimal values of the coefficient of friction and wear loss, better characteristics are achieved in the S/N balance. The S/N ratio is considered using a logarithmic transformation of the loss function as represented in the following equation:

$$\frac{S}{N} = 10 \log \frac{1}{n} \left( \sum y^2 \right), \quad (1)$$

where  $n$  = no. of observations and  $y$  = observed data.

From Table 3, we can identify the three levels for the four process parameters as (factors), which include (1) the weight percentage of graphite, (2) the applied load, (3) sliding distance, and (4) sliding speed. Table 4 represents a conventional Taguchi experimental plan with notation  $L_{27} (3^{13})$ . Table 5 describes the various conditions under which the trials were conducted. Minitab user manual software was used to create the mean-response plots, and ANOVA analysis was adopted to determine the % of influence in testing constraints [28].

### 3. Results and Discussions

**3.1. Physical Measurements.** According to Archimedes' principle, the physical measurement (density) of newly produced aluminum-based nanocomposites increased and reduced negligibly with the insertion of silicon carbide and graphite nanosize fillers into the AA 2024 as matrix material. The results also demonstrated that the experimental and predicted values were very similar. Figure 2 displays the density of hybrid nanocomposites as a function of grain content. This suggests that the experimental methods

TABLE 3: Input variables and levels for nanocomposites.

Input variables	Units	Level (I)	Level (II)	Level (III)
A: Graphite nanofillers	Wt. %	0	5	10
B: Applied load	N	10	15	20
C: Sliding distance	m	500	1500	2500
D: Sliding speed	m/s	1	1.5	2

TABLE 4: Orthogonal array  $L_{27} (3^{13})$  of the Taguchi approach.

$L_{27} (3^{13})$	1	2	3	4	5	6	7	8	9	10	11	12	13
1	1	1	1	1	1	1	1	1	1	1	1	1	1
2	1	1	1	1	2	2	2	2	2	2	2	2	2
3	1	1	1	1	3	3	3	3	3	3	3	3	3
4	1	2	2	2	1	1	1	2	2	2	3	3	3
5	1	2	2	2	2	2	2	3	3	3	1	1	1
6	1	2	2	2	3	3	3	1	1	1	2	2	2
7	1	3	3	3	1	1	1	3	3	3	2	2	2
8	1	3	3	3	2	2	2	1	1	1	3	3	3
9	1	3	3	3	3	3	3	2	2	2	1	1	1
10	2	1	2	3	1	2	3	1	2	3	1	2	3
11	2	1	2	3	2	3	1	2	3	1	2	3	1
12	2	1	2	3	3	1	2	3	1	2	3	1	2
13	2	2	3	1	1	2	3	2	3	1	3	1	2
14	2	2	3	1	2	3	1	3	1	2	1	2	3
15	2	2	3	1	3	1	2	1	2	3	2	3	1
16	2	3	1	2	1	2	3	3	2	1	2	3	1
17	2	3	1	2	2	3	1	1	2	3	3	1	2
18	2	3	1	2	3	1	2	2	3	1	1	2	3
19	3	1	3	2	1	3	2	1	3	2	1	3	2
20	3	1	3	2	2	1	3	2	1	3	2	1	3
21	3	1	3	2	3	2	1	3	2	1	3	2	1
22	3	2	1	3	1	3	2	2	1	3	3	2	1
23	3	2	1	3	2	1	3	3	2	1	1	3	2
24	3	2	1	3	3	2	1	1	3	2	2	1	3
25	3	3	2	1	1	3	2	3	2	1	2	1	3
26	3	3	2	1	2	1	3	1	3	2	3	2	1
27	3	3	2	1	3	2	1	2	1	3	1	3	2

utilized in this study can develop near-dense materials. The experimental and predicted densities obtained from each sample were used to calculate the porosity of the materials. The lowest porosity samples (1.326 percent) were obtained, indicating that near-dense materials were received and that the alloying ingredient and reinforcement were successfully absorbed into the matrix. Figure 3 shows that as the weight percentage of graphite fillers increased, the porosity of the composites deteriorated.

3.2. *Plan of Experiments.* The orthogonal array is purely anticipated and based on the elementary limits of the degree of freedom, which is meant to be larger or equal to the number of parameters that are considered in wear accordingly, according to research and literature reviews on the orthogonal array [29]. It represents various factors and levels and their importance. The experiment comprises 27 experiments (one for each row of the  $L_{27}$  orthogonal array), which involve parameters allocated to each column. To perform an orthogonal array for our experiment,  $L_{27}$  was

chosen. It contains 27 rows, 13 columns, and four wear parameters, namely (i) graphite (Gr) nanofillers, (ii) applied load, (iii) sliding distance, and (iv) sliding speed. In addition to these, the second column was labeled as graphite (Gr) reinforcement (A), the third column as load (B), the fourth as sliding distance (C), the fifth as sliding speed (D), and the remaining columns were labeled as interactions. Further, the trials were conducted utilizing the orthogonal array with varying degrees of freedom in each row. Finally, an Analysis of Variance was used to compare the results obtained from the wear test.

3.3. *Analysis of Variance and Their Respective Effects over Factors.* It is practical to understand the impact of various factors on the input parameters of graphite wt. % as reinforcement fillers, applied load, sliding distance, and sliding speed and their respective relations to the model analysis of the variance table to find the order of significance. Initially, a survey was conducted with a 95 percent level of significance. The results evaluated from the analysis of variance of hybrid

TABLE 5: Experimental design using  $L_{27}$  ( $3^{13}$ ) orthogonal array.

$(2^{13}) L_{27}$	A	B	C	D	Wear loss (g)	Signal-to-noise ratio (dB)	Coefficient of friction	Signal-to-noise ratio (dB)
1	0	10	500	1.0	0.0035	49.118	0.149	17.289
2	0	10	1500	1.5	0.0106	38.493	0.162	16.171
3	0	10	2500	2.0	0.0203	33.850	0.177	15.801
4	0	15	500	1.5	0.0069	43.223	0.189	15.353
5	0	15	1500	2.0	0.0164	33.703	0.201	14.712
6	0	15	2500	1.0	0.0268	31.437	0.157	16.782
7	0	20	500	2.0	0.0082	41.723	0.214	14.322
8	0	20	1500	1.0	0.0159	36.756	0.187	15.366
9	0	20	2500	1.5	0.0351	29.093	0.199	14.921
10	5	10	500	1.5	0.0039	48.178	0.157	17.086
11	5	10	1500	2.0	0.0091	40.819	0.166	16.459
12	5	10	2500	1.0	0.0147	36.653	0.140	17.921
13	5	15	500	2.0	0.0041	47.744	0.155	16.359
14	5	15	1500	1.0	0.0101	39.913	0.149	17.623
15	5	15	2500	1.5	0.0230	32.765	0.151	17.292
16	5	20	500	1.0	0.0058	44.731	0.195	15.091
17	5	20	1500	1.5	0.0161	35.863	0.208	14.358
18	5	20	2500	2.0	0.0312	30.116	0.211	14.257
19	10	10	500	2.0	0.0027	51.372	0.169	16.346
20	10	10	1500	1.0	0.0059	44.583	0.161	16.157
21	10	10	2500	1.5	0.0125	39.061	0.173	16.089
22	10	15	500	1.0	0.0037	48.636	0.184	15.467
23	10	15	1500	1.5	0.0098	41.175	0.189	15.761
24	10	15	2500	2.0	0.0182	34.798	0.191	15.368
25	10	20	500	1.5	0.0049	46.196	0.195	15.288
26	10	20	1500	2.0	0.0132	38.588	0.217	14.931
27	10	20	2500	1.0	0.0245	32.216	0.231	13.657

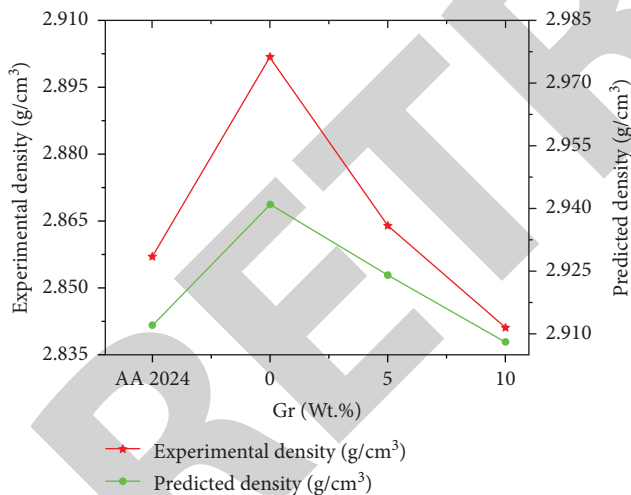


FIGURE 2: Experimental and predicted density of fabricated nanocomposites.

nanocomposites with wear and coefficient of friction used in this study are tabulated, respectively. Table 6 shows that the sliding distance ( $p = 72.09$ ) significantly impacts wear loss. In addition to this, the graphite content ( $p = 9.53$ ), load ( $p = 13.95$ ), and sliding velocity ( $p = 0.49$ ) of all these parameters have a minor impact on the wear loss. In contrast, interactions did not show any significant effect.

Similarly, from Table 7, it shows that the graphite content ( $p = 11.12$  percent) significantly impacts the

coefficient of friction. The contribution coefficient of friction is less significant for the load ( $p = 60.23$  percent), sliding distance ( $p = 3.25$  percent), and sliding speed ( $p = 8.63$  percent). The interaction  $A \times C$  ( $p = 2.53$  percent) has a relatively minor effect on the friction coefficient, but the remaining interactions have no effect. As a result, sliding distance is the most important testing parameter for reducing wear loss. However, the most important factor influencing the coefficient of friction has been discovered to be graphite reinforcement.

**3.4. Impact of Testing Parameters over Wear Loss.** The influence of various tests and their respective interactions are plotted on wear loss of the nanocomposites, and their significant effects are plotted for the S/N ratio graph, as shown in Figure 4. It is predicted that there will be no significant effect if the constraint line of the main effect plot is significantly closer to the horizontal line. Furthermore, the parameters that will have the most significant impact on the cable are heavily skewed. The figure shows that the sliding distance is the most critical parameter, whereas other parameters such as graphite (Gr), applied load, and sliding speed had less impact on the wear loss. From all these statements, we can say that when the contact time increases, the sliding distance also increases, resulting in a massive area of contact, which affects the formation of wear debris [30]. Wear loss appears to rise as the applied stress and sliding distance increase, indicating that more materials are being

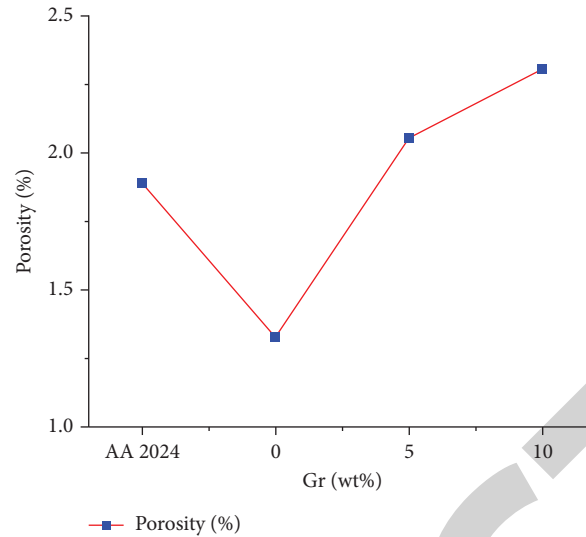


FIGURE 3: Attained porosity results for fabricated nanocomposites.

removed from the surface. Furthermore, when the sliding speed was increased, wear loss gradually decreased, resulting in the formation of a rich graphite layer on the fractured surface. This phenomenon reduces the wear effect by creating more contact areas. The composite with 10% graphite content reported superior wear resistance at higher loads compared to other conditions.

**3.5. Impact of Testing Parameters on the Coefficient of Friction.** The consequences of testing parameters and the interaction plot on the coefficient of friction and their respective effect plot for the S/N ratio are shown in Figures 5 and 6. Because parameter A has achieved the highest inclination, the grain reinforcement has a similar effect on the composite coefficient of friction, while sliding speed, distance, and load have just attained a lesser impact when compared to others. On the other hand, the coefficient of friction is nearly invariant with the sliding distance for entirely fabricated composites. The main reason behind this is that the proportion of graphite in all the samples is considered more stable. The coefficient of friction in all the composites increases significantly when the weight percentage of graphite increases.

This phenomenon is observed until the graphite weight percent reaches 10% [31]. This is because the aluminum matrix contains graphite, which functions as a superb lubricant by spreading over the entire topography and producing a thick layer of lubricating coating on the surface, which eventually reduces friction by limiting contact on the sliding surface. When the percentage of graphite on the surface is greater than 10%, the friction increases due to the oxide layer's fracture within the surface, weakening the fractured surfaces. The cohesion of sliding surfaces generates abrasion because it causes interaction between the specimen and the counter, which eventually increases the coefficient of friction [32].

**3.6. Linear Regression Models.** General linear regressions were used to determine the interactions between the components (A) graphite weight percentage, (B) load, (C) sliding distance, (D) sliding speed, and the measured constraints. The following regression equations were eventually applied to wear and the coefficient of friction in the following equations:

$$1. \text{Wearloss (g)} = -0.0008704 + 0.000136389A + 2.77778e - 7B + 2.05e - 6C + 0.00134444D - 1.23333e - 5A * B - 3.283333e - 7A * C + 5.75e - 7B * C, \quad (2)$$

$$2. \text{Co-efficientoffriction} = 0.0899537 - 0.00066666A + 0.003B + 1.73889e - 5C - 0.00166666D - 0.00016A * B + 1.33333e - 7A * C - 4.66667e - 7B * C. \quad (3)$$

The wear loss and coefficient of friction qualities of the manufactured samples were further evaluated within the range of variables before testing, replacing the computed values of the relevant variables with those from equations (2) and (3). Figure 7 shows a standard probability plot of the

residuals used to check the model's validity as described by equations (2) and (3). The actual impacts are detected using the standard probability plot, whereas the points are very close to the average probability line in the central limit theorem. The researcher [22] reveals that the model

TABLE 6: ANOVA for wear loss, using adjusted SS for tests.

Source	Degrees of freedom (DOF)	Sum of squares (SS)	Adjusted sum of squares (ASS)	Adjusted mean of squares (AMS)	F-value	P value	Percentage of contribution
<b>A</b>	2	0.0001320	0.0001320	0.0000660	117.85	0.002	9.53
<b>B</b>	2	0.0002888	0.0002888	0.0001444	261.45	0.001	13.95
<b>C</b>	2	0.0014915	0.0014915	0.0007458	1387.12	0.000	72.09
<b>D</b>	2	0.0000103	0.0000103	0.0000052	9.65	0.013	0.49
<b>A*B</b>	4	0.0000060	0.0000060	0.0000015	1.81	0.125	0.29
<b>A*C</b>	4	0.0000334	0.0000334	0.0000083	0.45	0.003	1.64
<b>B*C</b>	4	0.0001037	0.0001037	0.0000259	0.75	0.025	1.86
<b>Error</b>	6	0.0000032	0.0000032	0.0000005			0.15
<b>Total</b>	26	0.0020689					100

S = 0.000731817 R-Sq = 99.84% R-Sq (adj) = 99.33%.

TABLE 7: ANOVA for the friction coefficient, using adjusted SS for tests.

Source	Degrees of freedom (DOF)	Sum of squares (SS)	Adjusted sum of squares (ASS)	Adjusted mean of squares (AMS)	F-value	P value	Percentage of contribution
<b>A</b>	2	0.0037443	0.0037443	0.0018721	7.95	0.001	11.12
<b>B</b>	2	0.0012574	0.0012574	0.0006287	36.41	0.002	60.23
<b>C</b>	2	0.0022005	0.0022005	0.0011003	0.55	0.000	3.25
<b>D</b>	2	0.0000130	0.0000130	0.0000065	4.56	0.813	8.63
<b>A*B</b>	4	0.0004846	0.0004846	0.0001211	2.01	0.064	6.98
<b>A*C</b>	4	0.0001015	0.0001015	0.0000254	0.84	0.547	2.53
<b>B*C</b>	4	0.0001650	0.0001650	0.0000413	1.37	0.349	4.03
<b>Error</b>	6	0.0001813	0.0001813	0.0000302			3.23
<b>Total</b>	26	0.0081476					100

S = 0.00549747 R-Sq = 97.77% R-Sq (adj) = 90.36%.

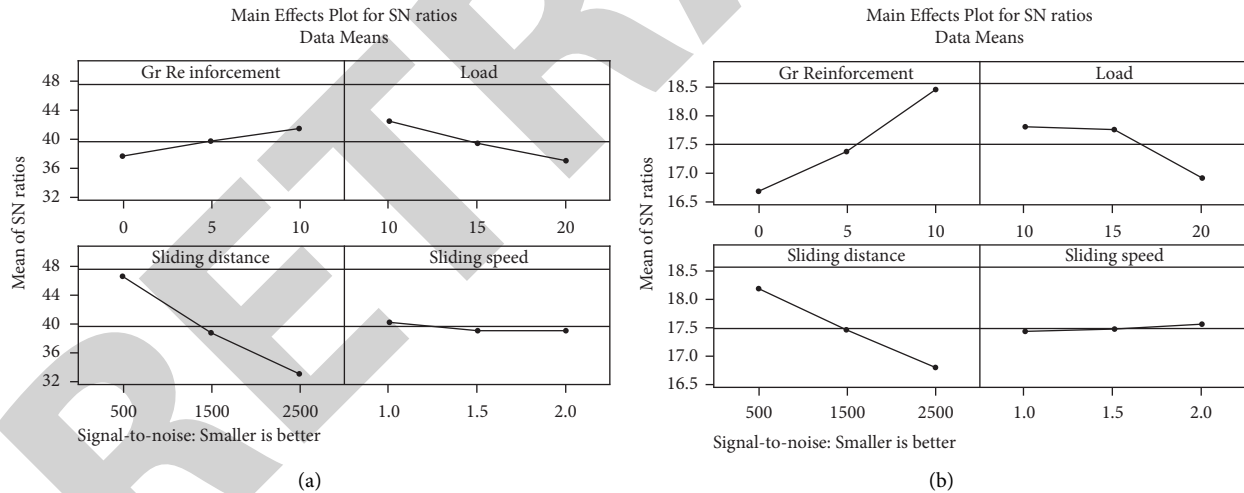


FIGURE 4: Main effects plot. (a) Wear loss of aluminum with a mixture of SiC and Gr hybrid nanocomposites. (b) Coefficient of friction with a blend of SiC and Gr hybrid nanocomposites.

developed for estimating both friction and wear loss of aluminum hybrid composites is represented in (2) and (3).

3.7. Examining and Assessing the Outcome of the Experiments Using the Taguchi Approach. Generally, in the Taguchi approach, we use the S/N ratio as a critical and significant component for interpreting experimental data. According to this Taguchi approach technique, the signal-to-noise ratio must have the highest value as the study determines optimal testing circumstances. The S/N ratio response tables for the

coefficient of friction and wear loss characteristics are represented in Table 8. The response table gives the results of all the metric averages mentioned above at each factor level. Also, this table provides all the ranks of the impacts based on the delta statistics, which compares the degree of effects to which they are closely related [33]. The delta statistics equal each factor's highest average minus the lowest standard. Based on the results, the highest delta value earns rank one, whereas the second-highest delta value receives rank two. The evaluated coefficient of friction and wear resistance values were

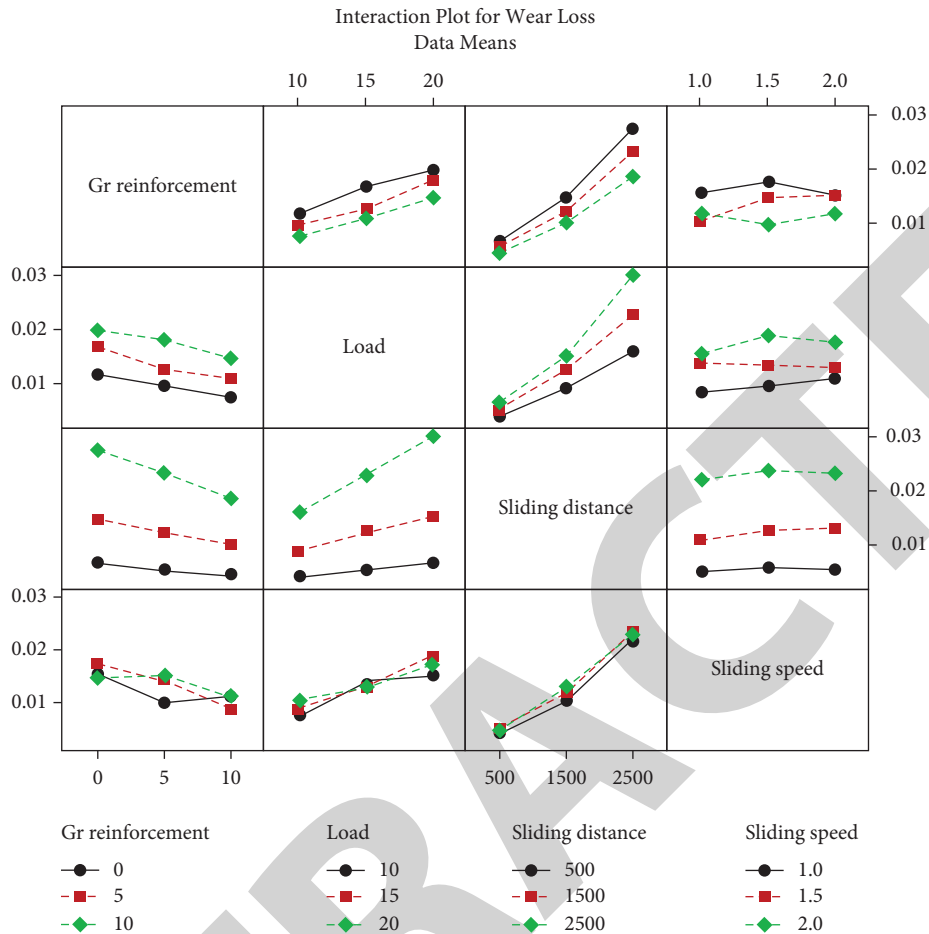


FIGURE 5: Interaction plots for wear loss.

10 wt. % graphite reinforcement with 10 N applied load with 500 m sliding distance and 1 m/s sliding velocity.

**3.8. Confirmation Experiment.** Taguchi proposes to be a confirmation test to compare the results with the investigational data. The results are confirmed based on the results drawn from the study by executing a confirmation test. After identifying the optimum and suitable conditions, a confirmation test was carried out, utilizing an amalgamation of the most satisfactory levels and comparing the results with the expected results. The wear loss in Table 9 is compared with the actual wear loss observed when ideal testing conditions are used. Both estimates are in good agreement. When perfect testing conditions are used, the S/N ratio increases by 8 dB and 4.7876 dB. It implies that the model utilized in this research can be adopted and can effectively predict the behavior of wear and coefficient of friction.

**3.9. Analysis of the Fractured Surface of Counter Disc Topography.** Analyzing the damaged topography of the counter disc, one can reveal the wear mechanisms that have occurred. Figure 8 represents the optical micrographs of the fractured disc surface against the composite pins. While sliding against this counterpart pin, they are irregular,

uneven, and with deep grooves. A small degree of graphitic film layer may be seen in worn topography. The very thick layer of the graphite film may be seen. It implies that only minor plastic deformation occurs throughout the sliding phase. The aluminum matrix, the graphite-containing samples, produces a solid lubrication effect and improves hardness, minimizing wear loss as sliding distance increases [33].

**3.10. Analysis of Worn Surfaces of Pin Using SEM.** The main wear mechanisms responsible for wear loss during dry sliding tests of nanocomposites have been identified using SEM morphology investigations. The wear morphology of the AA2024 alloy's worn surface, as shown in Figure 9(a), clearly shows the presence of deep permanent grooves parallel to the sliding direction, as well as microcracks and certain damaged regions. This could be the cause of the AA2024 alloy's increased wear loss. It is also worth noting that there are not many microcracks. On the surface of the AA 2024–5 wt. percent SiC nanocomposite, oxide layers were discovered (Figure 9(b)). The presence of parallel and continuous scratches on the worn surface suggests that abrasive wear is the primary wear mechanism at work. This is due to the hard particles from the counter surface or



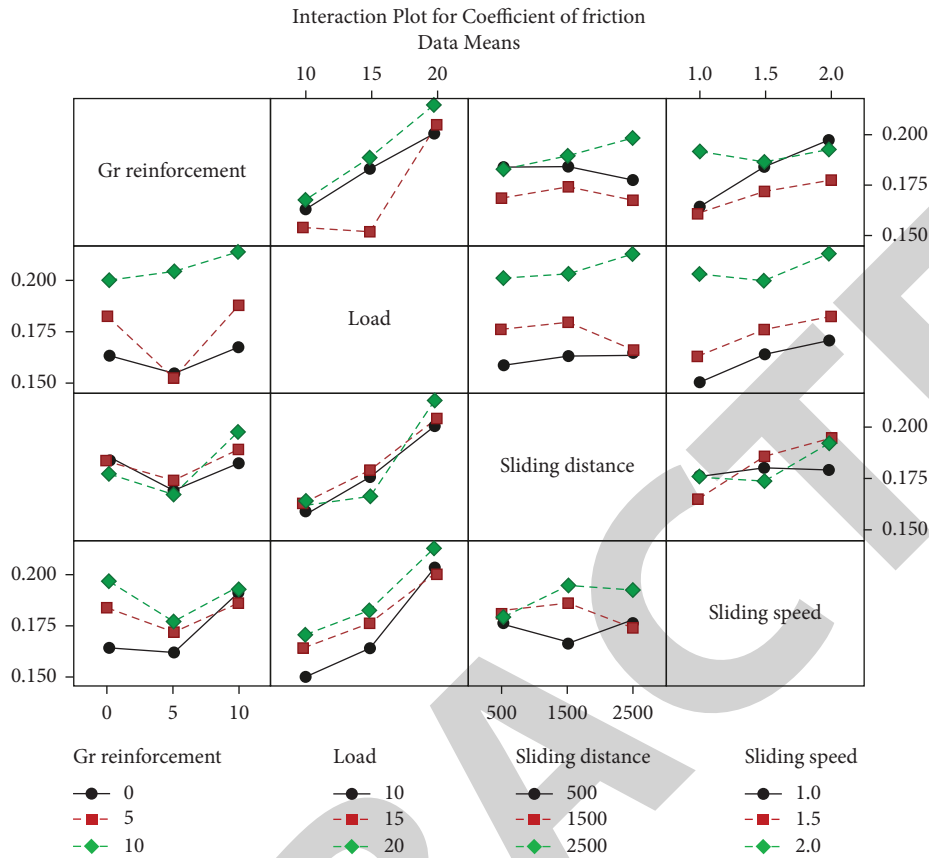


FIGURE 6: Interaction plots for the coefficient of friction ( $\mu$ ).

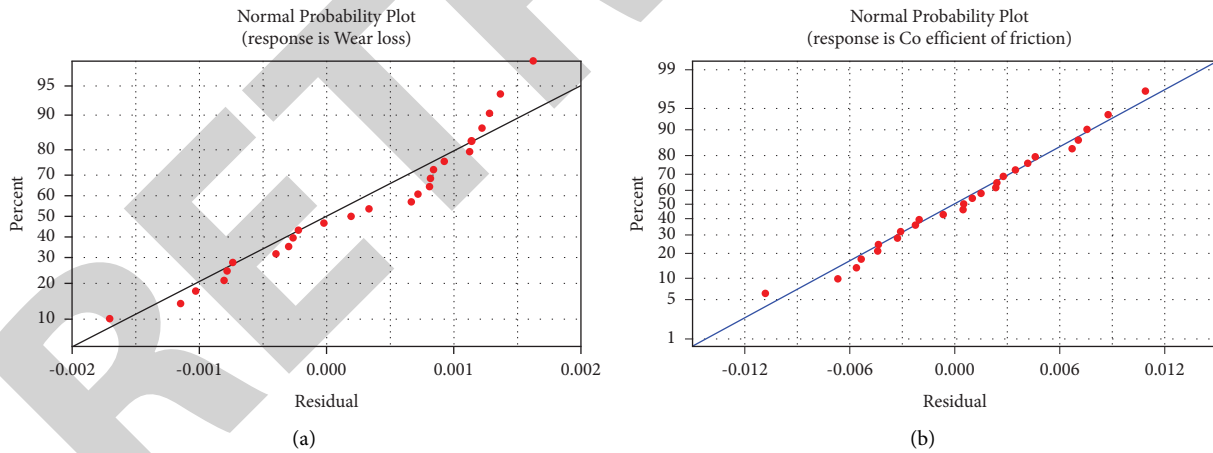


FIGURE 7: Standard probability plot. (a) Wear loss. (b) Coefficient of friction.

material in between the contact surfaces penetrating into the softer matrix during sliding, which contributes significantly to wear. Furthermore, the inclusion of hard SiC particles toughens the aluminum matrix, resulting in less wear. The presence of hard SiC particles in the matrix prevents the slider from cutting into the composite surface, minimizing delamination. In comparison to the pure matrix alloy and AA2024/5 wt percent SiC and smooth mechanically mixed layer, the worn morphology of hybrid nanocomposites

AA2024/5 wt. percent SiC/5 wt. percent Gr and AA2024/5 wt. percent SiC/10 wt. percent Gr (Figures 9(c) and 9(d)) revealed the presence of finer grooves parallel to the sliding direction and severe plastic deformation at the edges of the grooves (MML).

The presence of graphite in the composites causes the creation of MML (tribolayer) between the sliding surfaces, giving the surface a smooth appearance. The wear morphology of the AA 2024/5 wt. percent SiC/5 wt. percent Gr



TABLE 8: Response table for S/N ratios: smaller is better.

Levels	Response to wear				Response to the coefficient of friction			
	A	B	C	D	A	B	C	D
1	38.71	41.46	46.77	40.34	16.68	17.89	18.30	17.50
2	39.64	39.38	38.88	39.23	17.41	17.82	17.52	17.53
3	41.51	37.03	33.22	39.30	18.56	16.94	16.83	17.62
Delta	3.80	5.43	13.55	1.11	1.86	0.95	1.46	0.13
Rank	3	2	1	4	1	3	2	4

nanocomposite is shown in Figure 9(c). Due to hand, is coated with a rather smooth MML coating, and the

TABLE 9: Evaluation of best outcomes of confirmation tests.

Levels	Combination of parameters A2B3C3D2	Prediction A3B1C1D1	Investigation of experimentations
Wear (g)	0.02877	0.00096	0.0015
S/N ratio (dB)	29.7326	52.1907	52.6524
Improvement of S/N ratio: 22.9198			
	A1B3C3D3	A3B1C1D1	
Coefficient of friction ( $\mu$ )	0.1687	0.1044	0.1152
SN ratio (dB)	15.3819	19.6292	20.1695
Improvement of S/N ratio: 4.7876			

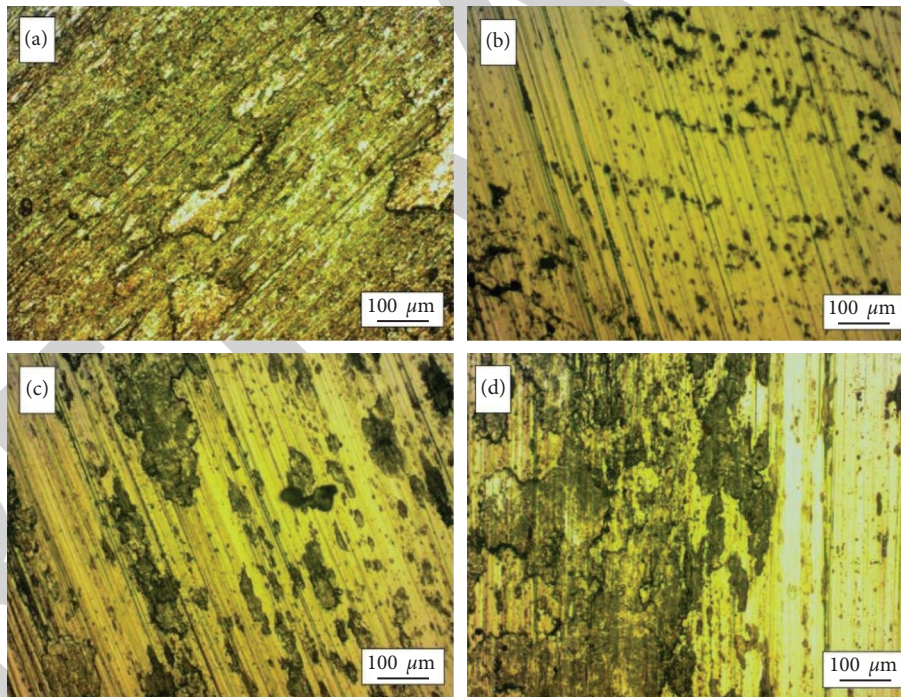


FIGURE 8: Optical micrographs of fractured topography of disc mated with (a) AA 2024 (b) AA 2024/5% SiC (c) AA2024/5% SiC/5% Gr (d) AA2024/5% SiC/10% Gr nanocomposite with an applied load of 15 N and at a constant speed of 1.5 m/s.

microploughing and smearing, the composite's surface is characterized by fine grooves. Furthermore, due to plastic deformation and the low fracture toughness of the graphite included in the composite, some tear edges are prone to detachment. The worn surface of the AA 2024-5 wt. percent SiC-10 wt. percent Gr composite with various wear parameters is shown in Figure 9(d). The surface morphology of AA 2024-5 wt. percent SiC-10 wt. percent Gr, on the other

grooves are finer than the worn surfaces of the other nanocomposites.

The wear behavior of nanocomposites is influenced by the graphite-enriched mechanically mixed layer that forms immediately beneath the contacting surface. This MML prevents the pin from making direct contact with the counter face. As a result, abrasive wear is significantly reduced in the AA 2024-5 wt. percent SiC-10 wt. percent Gr

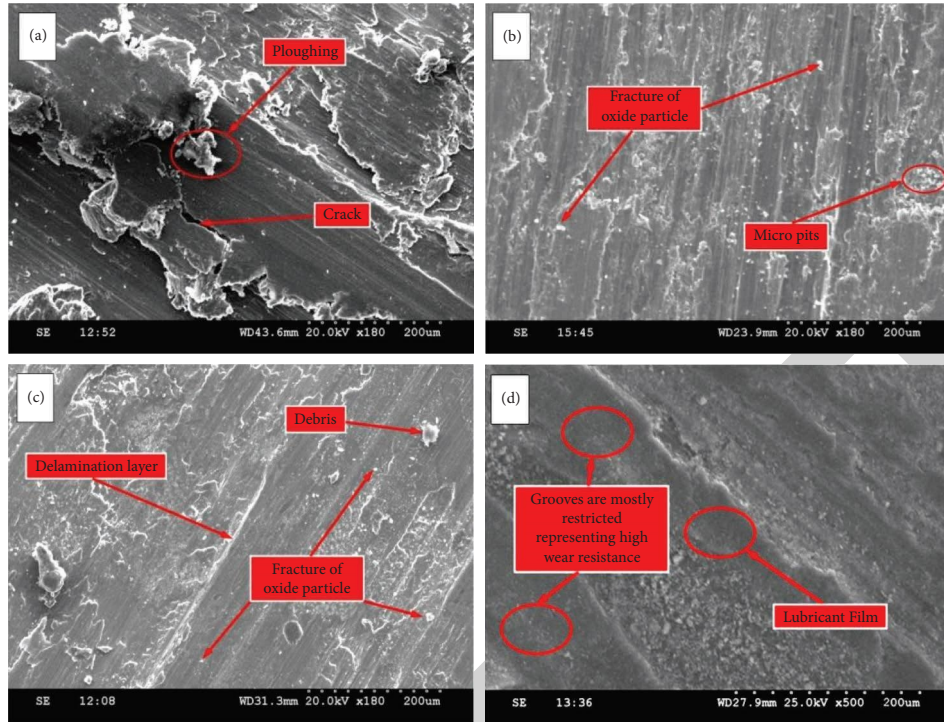


FIGURE 9: SEM morphologies of the worn surface of (a) AA 2024 (b) AA 2024–5 wt. % SiC (c) AA 2024–5 wt. % SiC–5 wt. % Gr (d) AA 2024–5 wt. % SiC–10 wt. % Gr composite at an applied load of 20 N and a constant speed of 2 m/s.

nanocomposites. Furthermore, delamination and oxidative wear are the most common mechanisms for material loss during sliding.

#### 4. Conclusions

This current investigation is mainly carried out to explain the experimental methodology and utilization of optimization techniques such as the Taguchi approach to examine the various parameters which affect the wear behavior of hybrid metal matrix composites. Based on the experimental results, the following conclusions were made:

- (1) Taguchi's approach of using an orthogonal array and ANOVA were adopted to evaluate the experimental results. ANOVA is used to assess the degree of the best testing parameters for wear behavior.
- (2) According to the design technique ANOVA, A3B1C1D1 is considered the best combination of parameters (lowest level of load, sliding distance, speed, and highest level of graphite reinforcement). The factor of graphite nanofillers has the highest contribution to controlling friction. The characteristic of sliding distance has the maximum influence on controlling the wear behavior of hybrid nanocomposites.
- (3) The wear loss and coefficient of friction polynomial models match the experimental values according to the ANOVA results. This demonstrates that the sliding distance (72.09 percent), sliding speed (0.49 percent), the load applied (13.95 percent), and

graphite weight percentage in the sample (6.38 percent) are the most significant parameters impacting the sliding wear of the fabricated composites within the selected range of experiments. (Based on their contribution percentages).

- (4) Analysis of Variance also reveals that the elements that most influence the friction behavior of composites within the chosen range of trials are the applied load (15.43%), sliding distance (27.00%), sliding speed (0.16%), graphite content in the composite (45.95%), and the load (7.73%) (based on their contribution percentages).
- (5) Adding graphite to the aluminum alloy matrix as a subordinate reinforcement improves the material's wear resistance while lowering the porosity and density of hybrid nanocomposites. Friction coefficients and wear resistance were excellent in composites containing 10% graphite.
- (6) At a 95% confidence level, there was an excellent match between anticipated and actual wear resistance. Furthermore, studies were confirmed to ensure that the best testing parameters were used.

#### Data Availability

The data used to support the findings of this study are included within the article. Further data or information is available from the corresponding author upon request.

## Conflicts of Interest

The authors declare that there are no conflicts of interest regarding the publication of this paper.

## Acknowledgments

The authors are thankful to the Vellore Institute of Technology, Chennai, for providing technical support in completing this research work. The authors appreciate the support from Wollo University, Ethiopia, for the research and preparation of this manuscript.

## References

- [1] P. Ravindran, K. Manisekar, P. Narayanasamy, N. Selvakumar, and R. Narayanasamy, "Application of factorial techniques to study the wear of Al hybrid composites with graphite addition," *Materials & Design*, vol. 39, pp. 42–54, 2012.
- [2] S. Suresha and B. K. Sridhara, "Wear characteristics of hybrid aluminium matrix composites reinforced with graphite and silicon carbide particulates," *Composites Science and Technology*, vol. 70, no. 11, pp. 1652–1659, 2010.
- [3] S. Suresha and B. K. Sridhara, "Effect of addition of graphite particulates on the wear behaviour in aluminium-silicon carbide-graphite composites," *Materials & Design*, vol. 31, no. 4, pp. 1804–1812, 2010.
- [4] P. P. Ikubanni, M. Oki, A. A. Adeleke et al., "Materials today: proceedings Tribological and physical properties of hybrid reinforced aluminium matrix composites," *Materials Today Proceedings*, vol. 46, pp. 5909–5913, 2021.
- [5] N. Mahaviradhan and S. Sivaganesan, "Materials today: proceedings Tribological analysis of hybrid aluminum matrix composites for high temperature applications," *Materials Today Proceedings*, vol. 39, 2020.
- [6] P. Paulraj and R. Harichandran, "The tribological behavior of hybrid aluminum alloy nanocomposites at high temperature: role of nanoparticles," *Journal of Materials Research and Technology*, vol. 9, no. 5, pp. 11517–11530, 2020.
- [7] V. V. Monikandan, P. K. Rajendrakumar, and M. A. Joseph, "High temperature tribological behaviors of aluminum matrix composites reinforced with solid lubricant particles," *Transactions of Nonferrous Metals Society of China*, vol. 30, no. 5, pp. 1195–1210, 2020.
- [8] S. Mahdavi and F. Akhlaghi, "Effect of SiC content on the processing, compaction behavior, and properties of Al6061/SiC/Gr hybrid composites," *Journal of Materials Science*, vol. 46, no. 5, pp. 1502–1511, 2011.
- [9] S. Basavarajappa, G. Chandramohan, and J. P. Davim, "Some studies on drilling of hybrid metal matrix composites based on Taguchi techniques," *Journal of Materials Processing Technology*, vol. 196, no. 1-3, pp. 332–338, 2008.
- [10] P. Ravindran, K. Manisekar, S. Vinoth Kumar, and P. Rathika, "Investigation of microstructure and mechanical properties of aluminum hybrid nano-composites with the additions of solid lubricant," *Materials & Design*, vol. 51, pp. 448–456, 2013.
- [11] Y. Q. Wang, A. M. Afsar, J. H. Jang, K. S. Han, and J. I. Song, "Room temperature dry and lubricant wear behaviors of Al<sub>2</sub>O<sub>3</sub>/SiCp/Al hybrid metal matrix composites," *Wear*, vol. 268, no. 7-8, pp. 863–870, 2010.
- [12] B. Hekner, J. Myalski, N. Valle, A. Botor-Probierz, M. Sopicka-Lizer, and J. Wiczorek, "Friction and wear behavior of Al-SiC(n) hybrid composites with carbon addition," *Composites Part B: Engineering*, vol. 108, pp. 291–300, 2017.
- [13] S. Basavarajappa, G. Chandramohan, K. Mukund, M. Ashwin, and M. Prabu, "Dry sliding wear behavior of Al 2219/SiCp-Gr hybrid metal matrix composites," *Journal of Materials Engineering and Performance*, vol. 15, no. 6, pp. 668–674, 2006.
- [14] B. N. Sarada, P. S. Murthy, and G. Ugrasen, "Hardness and wear characteristics of hybrid aluminium metal matrix composites produced by stir casting technique," *Materials Today Proceedings*, vol. 2, no. 4-5, pp. 2878–2885, 2015.
- [15] A. Gupta, Renu, S. Ranjan Kumar, C. Goswami, and T. Singh, "Wear behavior of Al6061 nanocomposite reinforced with nanozirconia," *Materials Today Proceedings*, vol. 48, pp. 1112–1116, 2022.
- [16] P. P. Ikubanni, M. Oki, A. A. Adeleke, and O. O. Agboola, "Optimization of the tribological properties of hybrid reinforced aluminium matrix composites using Taguchi and Grey's relational analysis," *Scientific African*, vol. 12, Article ID e00839, 2021.
- [17] S. Basavarajappa, G. Chandramohan, and J. Paulo Davim, "Application of Taguchi techniques to study dry sliding wear behaviour of metal matrix composites," *Materials & Design*, vol. 28, no. 4, pp. 1393–1398, 2007.
- [18] W. H. Yang and Y. S. Tarn, "Design optimization of cutting parameters for turning operations based on the Taguchi method," *Journal of Materials Processing Technology*, vol. 84, no. 1-3, pp. 122–129, 1998.
- [19] R. Thiyagarajan and M. Senthil kumar, "A review on closed cell metal matrix syntactic foams: a green initiative towards eco-sustainability," *Materials and Manufacturing Processes*, vol. 36, no. 12, pp. 1333–1351, 2021.
- [20] A. Haiter Lenin, S. C. Vettivel, T. Raja, L. Belay, and S. C. E. Singh, "A statistical prediction on wear and friction behavior of ZrC nano particles reinforced with Al-Si composites using full factorial design," *Surfaces and Interfaces*, vol. 10, pp. 149–161, 2018.
- [21] I. Jenish, A. Felix Sahayaraj, M. Appadurai et al., "Fabrication and experimental analysis of treated snake grass fiber reinforced with polyester composite," *Advances in Materials Science and Engineering*, pp. 2021–13, 2021.
- [22] S. S. Wulff, *A First Course in Design and Analysis of Experiments*, Taylor, vol. 57, Francis, Newyork, NY, USA, 2003.
- [23] V. K. Selvaraj, J. Subramanian, M. Gupta, M. Gayen, and L. B. Mailan Chinnapandi, "An experimental investigation on acoustical properties of organic PU foam reinforced with nanoparticles fabricated by hydrothermal reduction technique to emerging applications," *Journal of the Institution of Engineers*, vol. 101, no. 2, pp. 271–284, 2020.
- [24] J. Subramanian, S. Vinoth Kumar, G. Venkatachalam, M. Gupta, and R. Singh, "An investigation of EMI shielding effectiveness of organic polyurethane composite reinforced with MWCNT-CuO-bamboo charcoal nanoparticles," *Journal of Electronic Materials*, vol. 50, no. 3, pp. 1282–1291, 2021.
- [25] S. Vinoth Kumar, J. Subramanian, A. Giridharan, M. Gupta, A. Adhikari, and M. Gayen, "Processing and characterization of organic PU foam reinforced with nano particles," *Materials Today Proceedings*, vol. 46, pp. 1077–1084, 2021.
- [26] E. B. Dean and R. Unal, "Taguchi approach to design optimization for quality and cost: an overview," *Annu Conf Int Soc Parametr Anal*, vol. 1–10, 1991.
- [27] K. Yamaguchi, N. Takakura, and S. Imatani, "Materials processing technology," *Advanced Materials Research*, vol. 418–420, pp. 1–6, 2012.

## *Retraction*

# **Retracted: Processing and Properties of AlCoCrFeNi High Entropy Alloys: A Review**

### **Advances in Materials Science and Engineering**

Received 26 December 2023; Accepted 26 December 2023; Published 29 December 2023

Copyright © 2023 Advances in Materials Science and Engineering. This is an open access article distributed under the Creative Commons Attribution License, which permits unrestricted use, distribution, and reproduction in any medium, provided the original work is properly cited.

This article has been retracted by Hindawi, as publisher, following an investigation undertaken by the publisher [1]. This investigation has uncovered evidence of systematic manipulation of the publication and peer-review process. We cannot, therefore, vouch for the reliability or integrity of this article.

Please note that this notice is intended solely to alert readers that the peer-review process of this article has been compromised.

Wiley and Hindawi regret that the usual quality checks did not identify these issues before publication and have since put additional measures in place to safeguard research integrity.

We wish to credit our Research Integrity and Research Publishing teams and anonymous and named external researchers and research integrity experts for contributing to this investigation.

The corresponding author, as the representative of all authors, has been given the opportunity to register their agreement or disagreement to this retraction. We have kept a record of any response received.

### **References**

- [1] P. Gopal, K. Soorya Prakash, V. Kavimani, and G. Rajendiran, "Processing and Properties of AlCoCrFeNi High Entropy Alloys: A Review," *Advances in Materials Science and Engineering*, vol. 2022, Article ID 1190161, 13 pages, 2022.



## Review Article

# Processing and Properties of AlCoCrFeNi High Entropy Alloys: A Review

P.M. Gopal <sup>1</sup>, K. Soorya Prakash,<sup>2</sup> V. Kavimani <sup>1</sup> and Gopal Rajendiran <sup>3</sup>

<sup>1</sup>Centre for Material Science, Mechanical Engineering, Karpagam Academy of Higher Education, Coimbatore 641021, Tamil Nadu, India

<sup>2</sup>Department of Mechanical Engineering, Anna University Regional Campus Coimbatore, Coimbatore 641046, Tamil Nadu, India

<sup>3</sup>Department of Motor Vehicle Engineering, Defence University College of Engineering, Bishoftu, Ethiopia

Correspondence should be addressed to Gopal Rajendiran; rajendiran.gopal@dec.edu.et

Received 19 May 2022; Accepted 1 September 2022; Published 3 October 2022

Academic Editor: K. Raja

Copyright © 2022 P.M. Gopal et al. This is an open access article distributed under the Creative Commons Attribution License, which permits unrestricted use, distribution, and reproduction in any medium, provided the original work is properly cited.

The aim of this study is to carry out a focused literature review on the mechanical and tribological behaviour of AlCoCrFeNi High Entropy Alloys (HEA). HEAs are a proficient class of alloys designed by the use of several constituent alloying elements in equiatomic or close to equiatomic ratios. In view of their distinctive property range, there has been huge attention on this class of alloys. Among the various group of HEAs, AlCoCrFeNi-based HEAs have attracted interest due to their enhanced properties. Various AlCoCrFeNi-based HEAs are developed by adding additional elements such as Mo, Ti, and Zr. The effect of these alloying constituents on the mechanical, metallurgical, and tribological performance of the AlCoCrFeNi HEA is discussed in detail. In addition to that, the various techniques used to produce these HEAs are also discussed.

## 1. Introduction

Human civilisation is differed and described mainly based on the materials such as that of the Stone Age, Bronze Age, and Steel Age. Development of newer materials takes society to the next level such as alloys, superalloys, and composites. Conventionally the newer materials are developed by adding two or more materials together in which a base material has a higher proportion while other elements are added in minor levels. When a metal is mixed with a minor amount of different metals it is called as alloy and the composites are made by mixing ceramics or fibres with a base material altogether for improving properties. In contrast to all these materials designs, multiple materials are mixed together in equal proportions to get the high-performance material that are new age materials called as High Entropy Alloys. HEAs named by Yeh et al. [1] contain multiple elements mixed together mostly at an equal proportion that abstain from the “Base Element” conception. Its name is owing to the high mixing entropy of the indiscriminate mixing of elements and

HEAs are currently being studied more [1–6]. However, researches on this alloy system are in the preliminary stage when compared to conventional alloys [7].

Preferably, HEAs are stated as alloys with a minimum of five primary elements, each of which has an atomic proportion between 5 and 35 percent [1]. The HEAs are prepared by mixing elements in equiatomic levels and also in non-equiatomic concentrations. Generally, HEAs with equiatomic concentrations possess high mixing entropy than the nonequiatomic alloys. Various HEAs were prepared mainly by using elements such as Al, Fe, Cr, Ni, Cu, Co, Si, Ti, Mo, Mn, Zr, and Zn. HEAs exhibit unusual properties that are far away from conventional alloy properties. For example, the hardness of the MoTiVFeNiZrCoCr HEA is more than 800HV and the hardness of the commonly known conventional hard material 316 stainless steel is below 200HV. A specific strength of the HEAs is also higher than that of aluminium, titanium, nickel, and iron-based alloys [3].

Among the various HEAs developed, AlCoCrFeNi and its allied HEAs are investigated in large numbers. The

equiatomic AlCoCrFeNi has enhanced strength (fracture strength 3531 MPa) and upright plasticity (compression strain 24.5%) [8]. A number of new HEAs are developed by varying one or more elements in the AlCoCrFeNi composition or by adding other elements with it. Generally, Ti, Zr, and Si are added in smaller proportions with this HEA system, and their influence on microstructure, phase transformation, and mechanical characteristics was examined.

A basic study on AlCoCrFeNi HEA revealed that the BCC structured solid solution with a refined microstructure of 20 nm in grain size could be attained after 30 h milling. The stability in phase for the as-milled HEA powder is found good up to 500 C and a further increase in temperature has resulted in FCC structure. The coexistence of BCC and FCC phases was found in the HEA after spark plasma sintering (SPS) consolidation at 900 C. It exhibits superior characteristics like 625 HV microhardness and compressive strength of 1907 Mpa. The HEA obtained by SPS (Applied Temperature and Pressure of 900 C and 50 Mpa for 10 min in argon atmosphere) of 60 h milled CoCrFeNiAl powder shows a relative density of more than 99%. And the developed material exhibited more hardness than many commercially used hard-facing alloys (e.g. Stellite, around 500 HV) [9]. So, the current study attempts to review the effect of additional elements on the mechanical, corrosion, and wear properties of the AlCoCrFeNi HEAs.

## 2. Processing Methodologies of AlCoCrFeNi-Based HEAs

Generally, HEA developing methodologies can be divided depending on the initial state of the alloy preparation. In general, mechanical alloying then isostatic pressing, arc melting, laser cladding, and surface coating (plasma spray and LASER) are universally utilised for HEA development. Some other advanced methods for AlCoCrFeNi-based HEA preparation such as electrochemical techniques are also evolving [3].

**2.1. Arc Melting.** Arc melting is a prominent liquid state method in which the HEAs are attained through melting several components (minimum of 5 times) in the arc melting furnace. The alloy remelting is done for homogeneity and the general arrangement of the arc melting method is shown in (Figure 1). A very high torch temperature range of above 3000 C can be attained in the arc melting furnace and by varying the electrical power, the temperature can be managed. Thus, the majority of high melting point elements can be assorted through this liquid state processing [11].

The AlCoCrFeNi ingots formed by arc melting of 99.9% pure elements on copper crucible having water-cooling capability under pure argon environment exhibit BCC phase which is identified through XRD analysis [12]. The yield strength, fracture strength, and plastic strain of 1320 MPa, 2670 MPa, and 22.5% are obtained for AlCoCrFeNi HEA developed through arc melting.

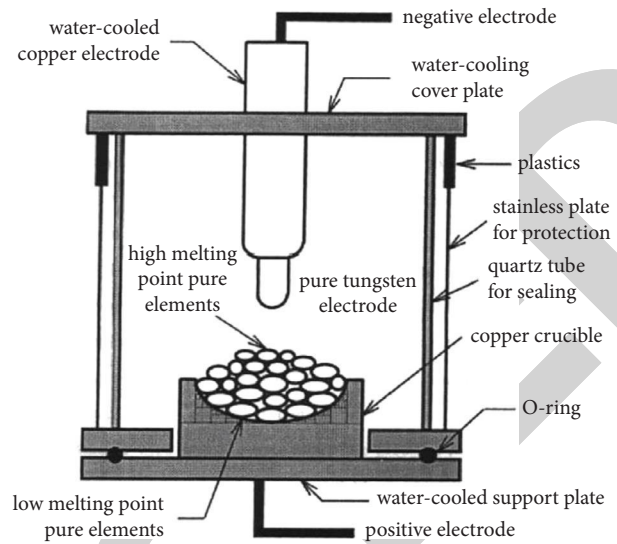


FIGURE 1: Schematic representation of arc melting process [10].

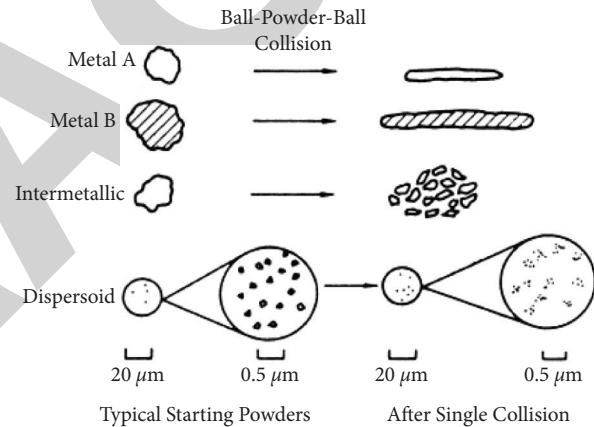


FIGURE 2: Mechanism of mechanical alloying [14].

**2.2. Mechanical Alloying.** It is a simple method of solid-state powder processing that comprises repetitive cold welding, fracturing, and rewelding of particles with the help of high-energy ball milling [13]. The mechanism of mechanical alloying is given in (Figure 2). It has been reported as it has the ability to develop diverse equilibrium and nonequilibrium alloys initiated with mixed elemental or prealloyed powders [15]. This method is not similar to the metal powder processing methodology in which metal powders are mixed to produce superalloys.

HEAs developed through mechanical alloying and consolidation possess higher pore density than that of HEAs made up by casting. On contrary, the melting method directs to segregation issues, whereas consistent chemical dispersion and solid solubility extension can be attained by the mechanical alloying process [15]. Additionally, it is a potential technique that can simply be exploited to develop superior property nanocrystalline materials.

Al, Co, Cr, Fe, and Ni powders of  $\leq 60 \mu\text{m}$  size and 99.7% purity were mechanically alloyed in equiatomic compositions [16]. The planetary ball mill rotating at 300 rpm is used

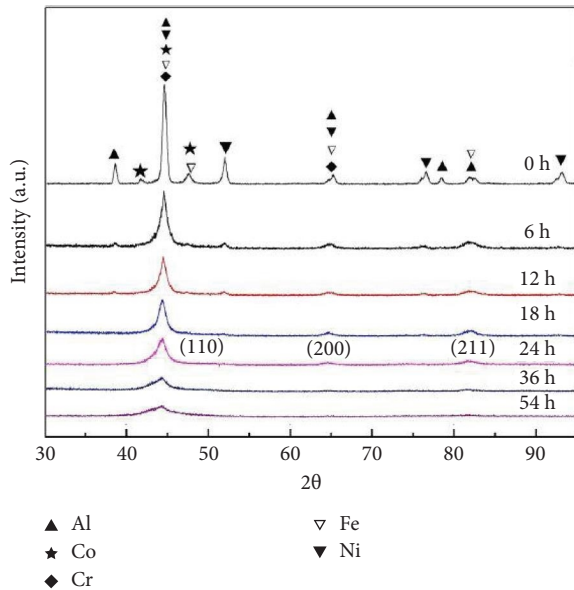


FIGURE 3: XRD patterns of AlCoNiCrFe HEA with respect to milling time [16].

to mix the powders with the ball-to-powder ratio of 15:1. Ball material used is chrome steel and the process regulating agent used to avert unwanted reactions such as cold welding and oxidation is toluene. The alloying process is tracked by extracting the powders from the ball mill every 6 h. For consolidation, the powders are then sintered after 60 h of alloying. Then extracted powders are analysed through an X-ray diffractometer in order to identify the alloy formation and the results were shown in (Figure 3). A remarkable decrease in intensity of the mixed elements was identified after milling for 6 h and the peaks are getting broader and some peaks become unseen. This phenomenon is credited to good crystal size and hefty lattice strain [17, 18]. Only three main intensive peaks with BCC structure ((110), (200), and (211)) are visible after 24 h milling which shows the establishment of a single solid solution (AlCoNiCrFe HEA). Furthermore, it was identified that there is no significant change in peaks for further milling. The calculated lattice parameter for the HEA powder milled for 24 h is 2.878 Å and it is coinciding with reports described by Zhang et al. [19]. Additionally, the HEA powders obtained after 60 h has a grain size of 15 nm after eliminating the instrumental and strain contributions, which is in fine conformity with the value described by Ji et al. [17].

**2.3. Plasma Spray Process.** It is a liquid state processing technique particularly used to formulate HEA coatings. The HEA coating over the specific surface is achieved through high-velocity plasma spraying, which furnishes an even defensive deposit [18]. This procedure involves melting of HEA powders on the arranged surfaces for spray deposition as shown in (Figure 4). The necessary temperature for melting is obtained from the thermal spraying gun by combusting gases through electric arcs. Since the objective material is heated up gradually, it is transformed into a

molten state and the acceleration of the material will be done through compressed gas. This controlled particle stream will pass to the target and be allowed to hit the target face and thin flat platelets were formed. The formed platelets are well-suited to the prepared surface irregularities. Furthermore, these sprayed particles are mounted up to form coatings on the target by cooling and building up one after another into an organised form.

The AlCoCrFeNi powder that is mechanically alloyed for 10 hours exhibits BCC as the major phase and a minor FCC phase is also detected. But the coated HEA which undergoes the high-temperature atmosphere during the plasma spray process exhibits the FCC phase. A typical lamellar thermal spray coating microstructure was observed [21]. The developed layer structure is suffered from a number of voids which can be stated as pores and interlamellar cracks. The coating exhibits 4.13 GPa Vickers microhardness.

**2.4. Laser Cladding.** This procedure comprises quick heating and cooling, more uniform and dense cladding, and less microscopic flaws as its advantages. Furthermore, it is simply attained and minimal thermal effect on the target material, and a small dilution rate is observed [22]. The laser cladding method is comparable to the plasma spray process technique in that it has an energy resource to melt the feedstock that is being applied to the target surface. The difference is it has intense LASER as heat origin, and it melts the substrate that the feedstock is being applied to as revealed in (Figure 5). Greater bond strength is achieved than the plasma spray procedure since this method usually fallouts in a metallurgical bond. The major advantage of this technique is the size of heat affected region which is shallow. This can be attributed to the ability of the laser beam to be concentrated on a narrow region or point. This characteristic results in minimised cracking, distortion, or modification in the substrate's metallurgy. In addition, the dilution of the coating with materials from the substrate is minimal because of the lower total heat [24].

The mechanically mixed powders of Ni, Co, Fe, Cr, Al, and Cu, with Si, were preloaded on a 2 mm thick AZ31 magnesium strip, and a LASER is passed over to produce the HEA layer [25]. The HEA clads exhibit primary BCC phase and traces of FCC. The developed surface exhibits better hardness and corrosion resistance. The hardness of the developed HEA clad surface is 10 times higher than the base alloy and the corrosion densities of the developed surface are lower than the base alloy surface under 3.5% NaCl solution.

### 3. Effect of Alloying Elements on AlCoCrFeNi HEAs

Along with AlCoCrFeNi HEA, some of the alloying elements have been added to improve their properties. A detailed review of the impact of various alloying elements on AlCoCrFeNi's properties is presented in this section. The effect of alloying elements such as Mo, Zr, B, Si, Nb, V, Fe, and Ti on microstructure and mechanical characteristics of AlCoCrFeNi are discussed in detail.



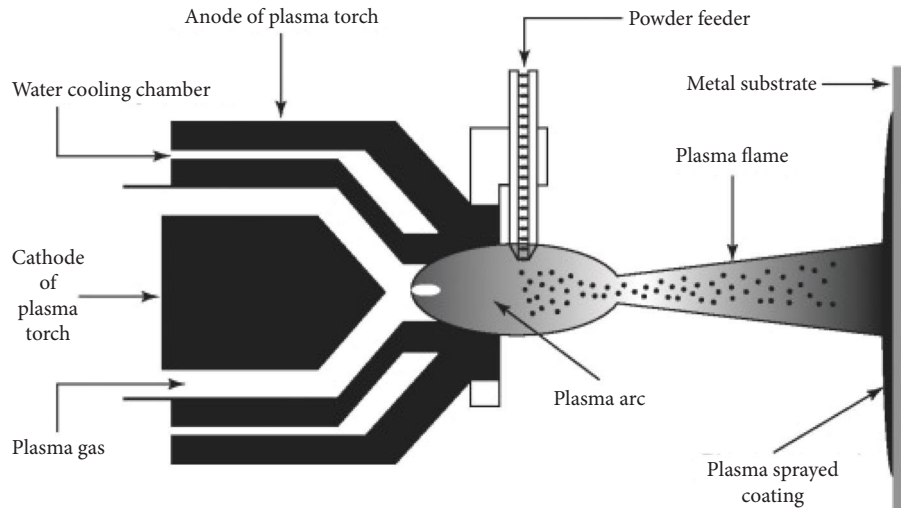


FIGURE 4: Plasma spray technique [20].

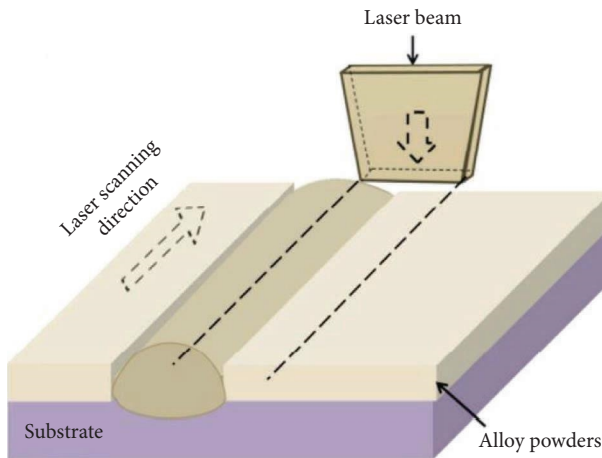
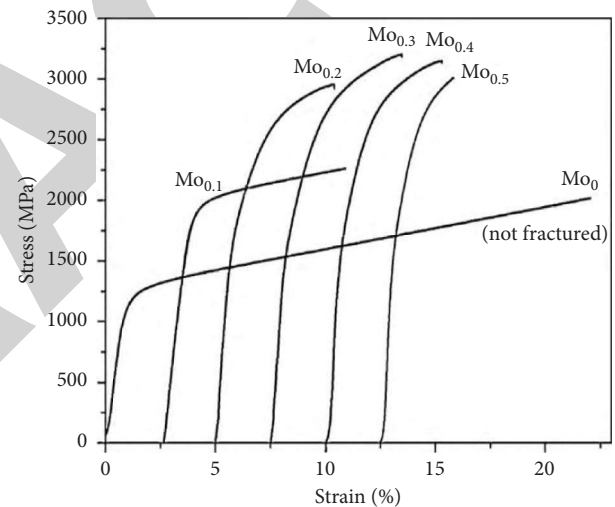


FIGURE 5: Laser cladding [23].

**3.1. Effect of Molybdenum.** AlCoCrFeNiMo<sub>x</sub> ( $x=0, 0.1, 0.2, 0.3, 0.4,$  and  $0.5$  in molar ratio) multicomponent alloys were fabricated through the arc melting method, and noteworthy variations in the structure and characteristics of AlCoCrFeNi alloy was identified as a result of Mo addition [26]. Mo<sub>0.1</sub> alloy shows a single BCC solid solution structure that is similar to Mo<sub>0</sub> alloy, i.e., AlCoCrFeNi. The alloy exhibited a classical lamellar eutectic structure when Mo quantity increased further ( $>0.1$ ). Obviously, the strength of the alloy was improved; at the same time, the loss of ductility takes place. The maximum yield strength is attained at  $x=0.5$  (2757 MPa), and the maximum compressive fracture strength is reached at  $x=0.3$  (3208 MPa) and the same is shown in the compressive stress-strain curve shown in Figure 6.

**3.2. Effect of Zirconium.** Two kinds of microstructures were observed for AlCoCrFeNiZr<sub>x</sub> ( $x=0, 0.008, 0.1, 0.3,$  and  $0.5$ ) alloys produced through the arc melting method. One is a periodic structure due to spinodal decomposition that

FIGURE 6: Stress-strain curves of as-cast AlCoCrFeNiMo<sub>x</sub> ( $x=0$  to  $0.5$ ) HEA [26].

consists of ordered BCC and BCC solid solution phase and the second one is a combination of the ordered BCC and Laves phase which alternatively nucleate and grow [12].

Even a low amount of Zr introduction can considerably enhance the properties when it goes under a compression test. The maximum yield strength of 1560 Mpa, the fracture strength of 3513 Mpa, and plastic strain of 29.5% are achieved for AlCoCrFeNiZr<sub>0.008</sub> alloy which are increased by 240 Mpa, 843 Mpa, and 7% than the base alloy, respectively. But the addition of Zr over 0.1 results in a significant decrease in fracture strength and plastic strain whereas the yield strength of the alloys surges with the increase in Zr quantity. And the impact of zirconium quantity on the properties of AlCoCrFeNi HEA is given in (Figures 7–10).

**3.3. Effect of Boron.** FCC phase structure with boride precipitation is obtained when the Boron addition is varied from  $x=0$  to  $x=1.0$  in CuCoNiCrAl<sub>0.5</sub>FeB<sub>x</sub> (denoted as B-0

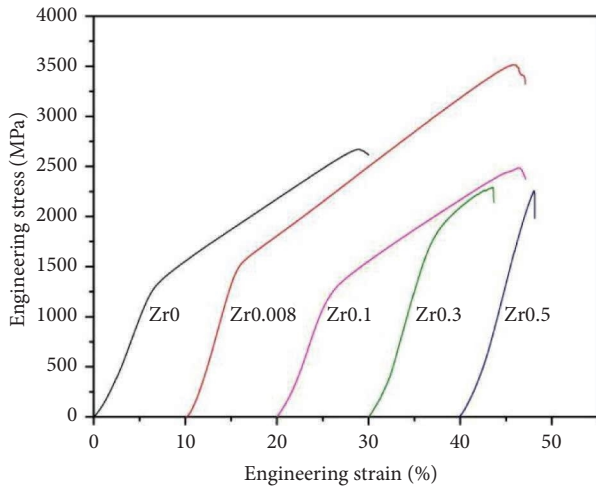


FIGURE 7: Stress-strain curves of  $\text{AlCoCrFeNiZr}_x$  alloys (compressive) [12].

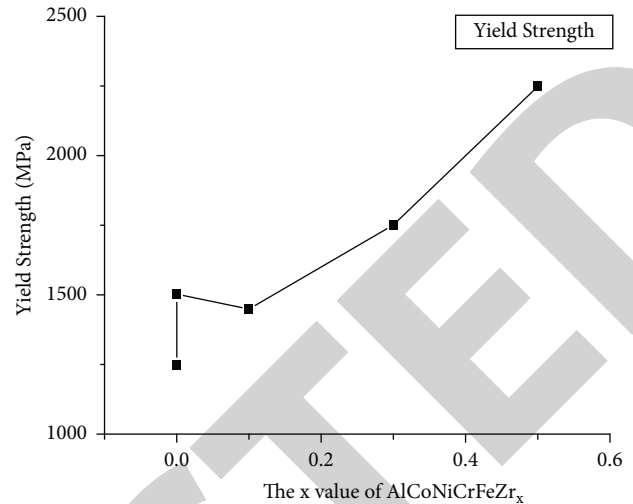


FIGURE 9: Effect of Zr content on yield strength for the  $\text{AlCoCrFeNiZr}_x$  HEAs [12].

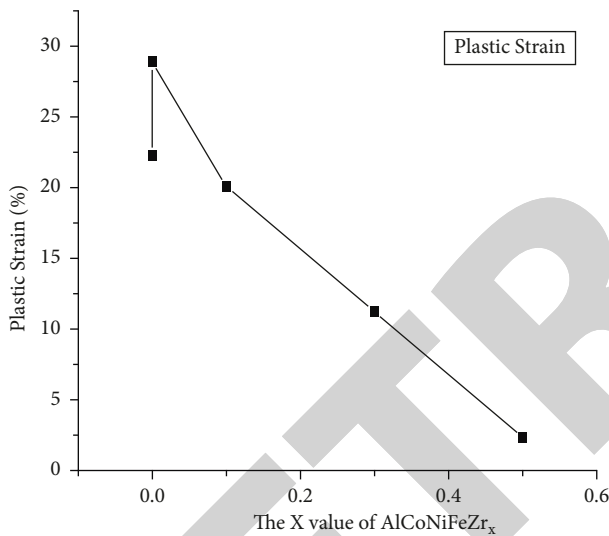


FIGURE 8: Impact of Zr on plastic strain for  $\text{AlCoCrFeNiZr}_x$  HEAs [12].

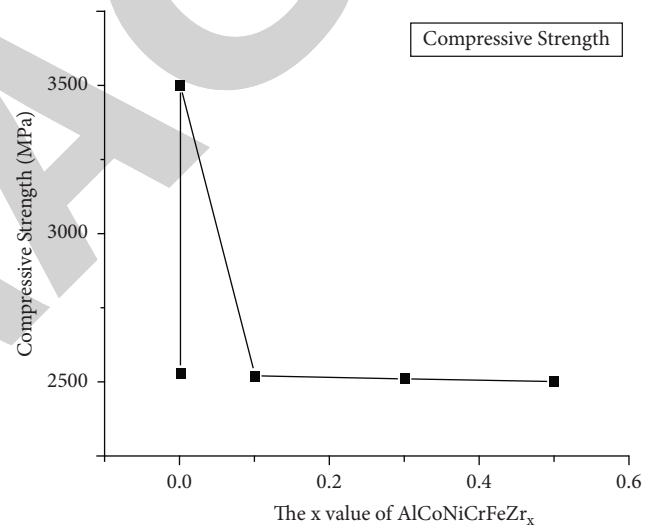


FIGURE 10: Influence of Zr content on compressive strength for the  $\text{AlCoCrFeNiZr}_x$  HEAs [12].

to B-1.0 alloys) alloys [27]. The addition of boron increases the boride volume fraction in the alloy and their corresponding hardness values are enhanced from HV 232 to HV 736. The formation of boride enhances the value of high-temperature compression strength. The HEA through boride is less tough, i.e., the hardness of  $\text{CuCoNiCrAl}_{0.5}\text{FeB}_x$  HEA based on boron content grows at the cost of toughness.

The increase in the amount of boron addition in  $\text{CuCoNiCrAl}_{0.5}\text{Fe}$  HEA gives better high-temperature compression strength. The compression yield stress obtained at different temperatures that varied from room temperature to 1100 C for the  $\text{CuCoNiCrAl}_{0.5}\text{Fe}$  HEA is shown in (Figure 11). A drastic increase in yield stress is exhibited by B-0.6 and B-1.0 HEA up to 300°C, B-0.2 HEA at 500°C, and B-0 HEA at 700°C. This promising temperature outcome for yield stress is associated with that persisting in superalloys. [28] The yield stress of the HEAs comprising boron is superior for higher boron content. Furthermore, it was

identified that the boride addition plays a crucial role in promising temperature effects in view of the fact that the peak-strength temperature varies in the course of boron content. The rule of borides on the yield stress of developed HEAs is weakening at temperatures more than 900°C. All the HEAs irrespective of boron addition exhibit similar yield stress values above 900°C. So, it is vital to state that the mechanical characteristics of these modern HEAs could be regulated in a vast array by boron inclusion. The hardness and strengths at room temperature equal to Ti, Zr, or Pd-based bulk amorphous alloys can be attained by HEAs by boron addition [29]. In addition, it does not undergo glass transition and crystallisation as amorphous alloys at a glass transition temperature ( $T_g$ ) and crystallisation temperature ( $T_x$ ), respectively. They expose superior strength at high temperatures up to 700°C to 800°C as a result of their promising temperature effect.

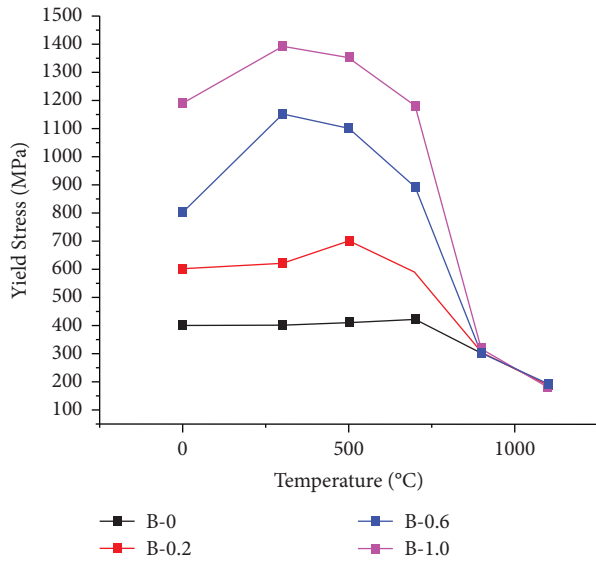


FIGURE 11: Requirement of yield stress on temperature for CuCoNiCrAl<sub>0.5</sub>Fe HEA with different boron contents [27].

**3.4. Effect of Silicon.** The peaks related to BCC structure begin to appear and their intensity upsurges with an increase in Si content. The XRD results publicised in Figure 12 show that the BCC peaks were shifted slightly towards the right with an increase in Si content being a sign of a decrease in the lattice parameter of the BCC phase. The calculated lattice constants of the BCC phases in the HEA show that the lattice constants are 2.867 Å and 2.859 Å for the HEA with Si = 0.4 and Si = 0.8, correspondingly. As the Si concentration rose, the crystal structure transitioned from FCC to BCC and also the lattice constant of the BCC phase changes [30].

The hardness of the Al<sub>0.5</sub>CoCrCuFeNiSi<sub>x</sub> HEA increases with respect to Si concentration. The hardness of Al<sub>0.5</sub>CoCrCuFeNiSi<sub>x</sub> improved when the content of silicon is differed from 0 to 0.8 and it is noteworthy that the hardness of the alloy having Si = 0.8 (653 HV) is 2.48 times higher when compared to the alloy without Si (263 HV).

**3.5. Effect of Vanadium.** The microstructure effects of Al<sub>0.5</sub>CoCrCuFeNiV<sub>x</sub> ( $x = 0$  to 2.0 in molar ratio) HEA shows that the alloys are consists of a simple FCC solid solution structure with small vanadium addition [31]. BCC structure becomes noticeable with spinodal decomposition and surrounds the FCC dendrites when the vanadium content is extended to 0.4. The volume fraction of the BCC structure upsurges as the vanadium concentration increases from  $x = 0.4$  to 1.0. FCC dendrites are entirely replaced by BCC dendrites when  $x = 1.0$ . From  $x = 0.6$  to 1.0, needle-like  $\sigma$ -phase forms, and BCC spinodal structure increases but it vanishes when  $x = 1.2$  to 2.0.

When the amount of vanadium raised from 0.4 to 1.0, the hardness values of the HEA amplified and attains the peak value of 640 HV at  $x = 1.0$  as shown in (Figure 13). Compared with the Al<sub>0.5</sub>CoCrCuFeNi HEA, the addition of vanadium upholds the HEA characteristics.

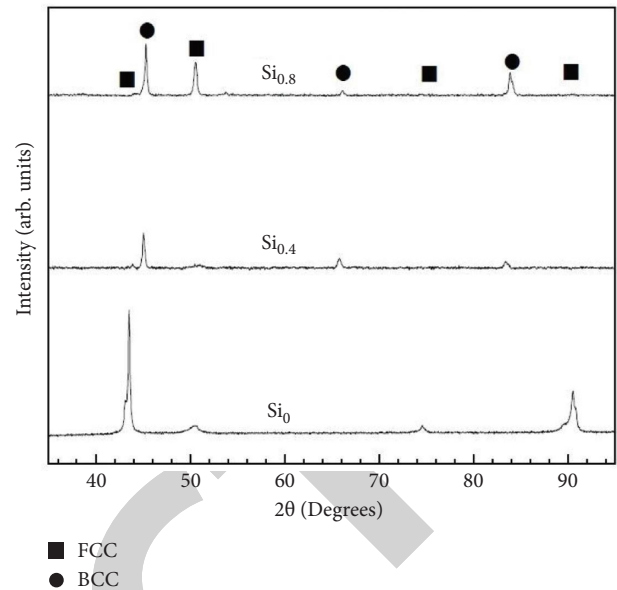


FIGURE 12: XRD pattern of the Al<sub>0.5</sub>CoCrCuFeNiSi<sub>x</sub> (as-cast) [30].

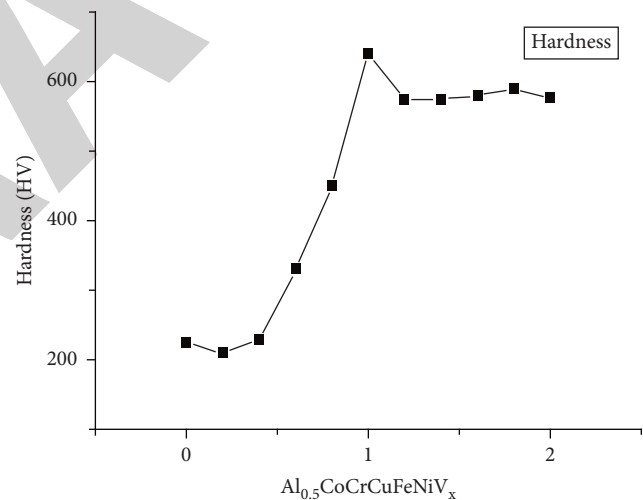


FIGURE 13: Hardness of Al<sub>0.5</sub>CoCrCuFeNiV<sub>x</sub> HEA with different vanadium contents [31].

**3.6. Effect of Niobium.** AlCoCrFeNb<sub>x</sub>Ni HEAs exhibit two phases that are BCC solid solution phase and the (CoCr) Nb type Laves phase. The HEA series shows the varying microstructures from hypoeutectic to hypereutectic and the Vickers hardness and compressive yield strength are almost in linear increment with the increase in Nb content [8].

From Figure 14 and Table 1, it can be noted that there is an extensive increase in yield strength from 1373 MPa to 2473 MPa with Nb addition whereas about 24.5% to 4.1% decreases in plastic strain limits are obtained. The linear increase in Vickers hardness of the developed HEA series is expressed as an equation i.e.,  $Y_{HV} = 454x + 530$ , where  $x$  and  $Y_{HV}$  denote the Nb content and Vickers hardness, respectively, and the same is shown in (Figure 15).

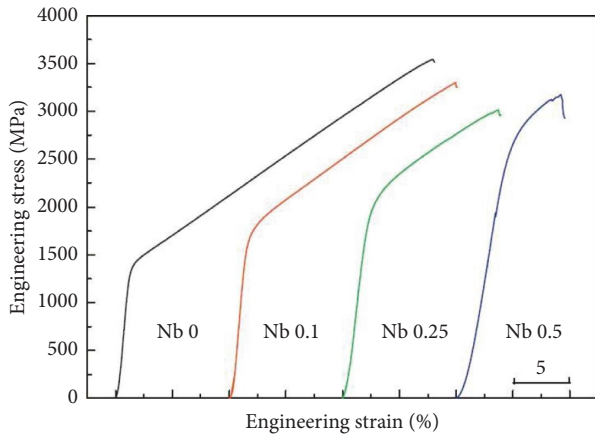


FIGURE 14: The compressive stress–strain curves of the AlCoCr-FeNb<sub>x</sub>Ni HEA ( $x = 0, 0.1, 0.25,$  and  $0.5$ ) [8].

TABLE 1: Mechanical properties of AlCoCrFeNb<sub>x</sub>Ni ( $x = 0, 0.1, 0.25,$  and  $0.5$ ) alloy [8].

$x$	$\sigma_{0.2}$ (MPa)	$\sigma_{max}$ (Mpa)	$\epsilon_p$ (%)	HV
0	1373	3531	24.5	520 ± 11
0.1	1641	3285	17.2	569 ± 11
0.25	1959	3008	10.5	668 ± 12
0.5	2473	3170	4.1	747 ± 10

$\sigma_{0.2}$ , yield strength;  $\sigma_{max}$ , fracture strength;  $\epsilon_p$ , plastic strain limits; HV, Vickers hardness.

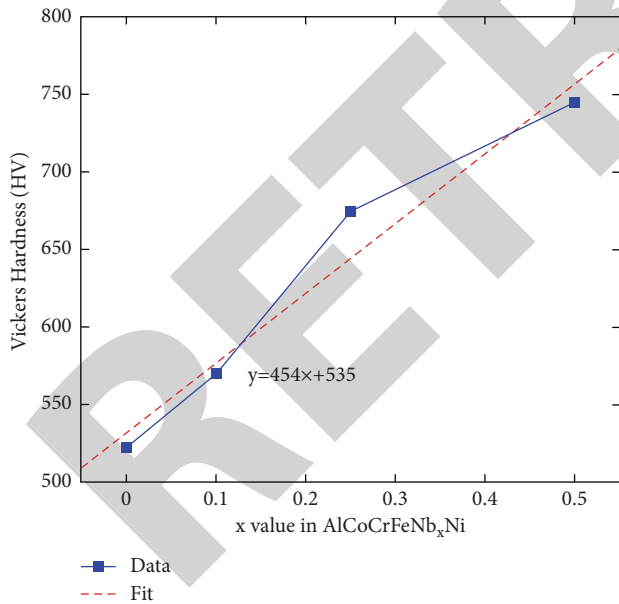


FIGURE 15: The hardness of AlCoCrFeNb<sub>x</sub>Ni with respect to Nb. Contents ( $x = 0, 0.1, 0.25,$  and  $0.5$ ) [8].

3.7. *Effect of Iron.* A new HEA system, AlCoCrFeMoNi is designed with Mo to enhance the strength and thermal stability. The interrelation between the microstructural changes and hardness behaviour of AlCoCrFe<sub>x</sub>Mo<sub>0.5</sub>Ni HEA with the consequence of iron concentration is analysed [32]. The microstructure transforms to “polygrain” for Fe1.5 and

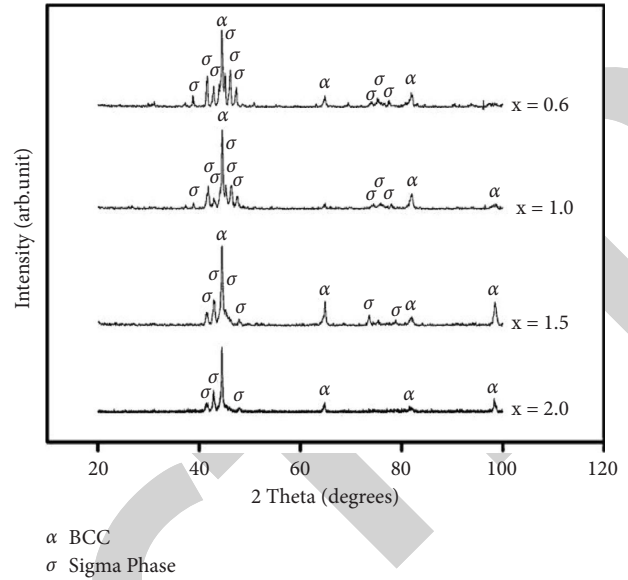


FIGURE 16: XRD of AlCoCrFe<sub>x</sub>Mo<sub>0.5</sub>Ni HEA with different Fe contents [32].

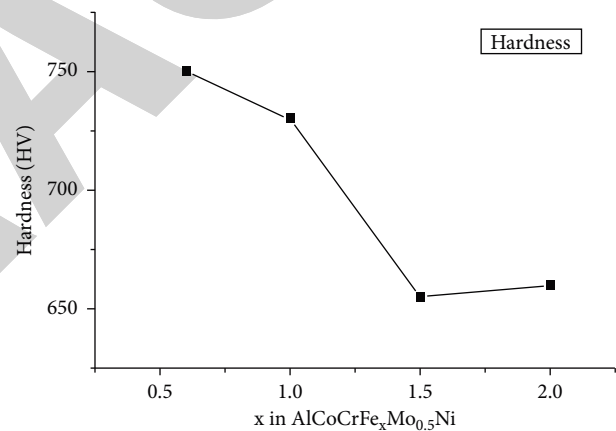


FIGURE 17: Vickers hardness of AlCoCrFe<sub>x</sub>Mo<sub>0.5</sub> Ni alloys with respect to Fe content [32].

Fe2.0 HEA from “dendritic” for Fe0.6 and Fe1.0 HEA with the increase in Fe content. The crystal structure of AlCoCrFe<sub>x</sub>Mo<sub>0.5</sub>Ni is a duplex structure having BCC solid solution and  $\sigma$  phase. But the increase in peak intensity of the BCC phase is higher than the  $\sigma$  phase with an increase in the volume fraction of iron content showing the decrement in the  $\sigma$  phase as evidenced by the XRD patterns given in (Figure 16).

Hardness increases with the addition of Mo in the system owing to the development of the hard  $\sigma$  phase and hardness raises from HV 356 to HV 730. Besides, with an HV of nearby 725, Fe0.6 and Fe1.0 HEA are around HV 100 harder than Fe1.5 and Fe2.0 HEA. This hardness drops off with a rise in the Fe content due to the corresponding decrease in the  $\sigma$  phase amount because of the soft nature of the BCC phase when related to the  $\sigma$  phase. The hardness values are measured in dendrites (with less  $\sigma$  phase) and interdendrites (with more  $\sigma$  phase) of the Fe0.6 HEA were HV643 and

TABLE 2: Overall hardness and microhardness (HV) of each phase in the four HEAs [33].

Al00Ti05	Al02Ti05	Al00Ti10		Al02Ti10				
Overall	Overall	Overall	ID	DR	Overall	ID (al - rich region)	ID (coarse $\eta$ )	DR
509 ± 11	487 ± 5	654 ± 7	924 ± 33	617 ± 13	717 ± 13	1197 ± 110	910 ± 24	619 ± 12

HV898, individually. The influence of Fe concentration on the microhardness of the HEA is clearly shown in (Figure 17).

**3.8. Effect of Aluminium and Titanium.** The HEAs with lower Ti addition (0.05) possess lower hardness values owing to their primary FCC gamma phase. Slightly increased hardness was exhibited by Al<sub>00</sub>Ti<sub>05</sub> as a result of  $\eta$  precipitates at the grain boundaries [33]. HEA hardness value increases significantly as the Ti content increased further (0.1) as shown in (Table 2). Al<sub>00</sub>Ti<sub>10</sub> HEA exhibits 650 HV as its overall hardness which is higher than that of the HEAs with minor Ti addition (i.e., Al<sub>00</sub>Ti<sub>05</sub> and Al<sub>02</sub>Ti<sub>05</sub>). This increase in hardness is credited to the development of the  $\eta$  phase in the interdendritic region of Al<sub>00</sub>Ti<sub>10</sub> where the microhardness is around HV 900. Even though the interdendritic region of Al<sub>02</sub>Ti<sub>10</sub> HEA has less amount of coarse  $\eta$  phases than that of Al<sub>00</sub>Ti<sub>10</sub>, the Widmanstatten structured needle-like  $\eta$  phase offers even superior hardness of up to HV 1200 which makes Al<sub>02</sub>Ti<sub>10</sub> as the harder HEA (HV 717) among them.

#### 4. Effect of Alloying Elements on Wear Properties

Wear is one of the important functional properties of materials. It is an erosion and displacement phenomenon of material from its original position on the surface performed by the activity of another surface. AlCoCrFeNi HEAs are reported as materials having greater wear resistance capability than the other metallic systems and alloys. Literature that discussed the influence of Fe, B, V, Al, and Ti-like alloying elements on the wear behaviour of AlCoCrFeNi HEAs is discussed in this section.

**4.1. Effect of Iron.** The wear behaviour of AlCoCrFe<sub>x</sub>Mo<sub>0.5</sub>Ni alloys with iron addition is explained with respect to the microstructural change and it is shown in (Figure 18). The Fe<sub>0.6</sub> and Fe<sub>1.0</sub> alloys exhibit dendritic structure, whereas it changes to polygrain for Fe<sub>1.5</sub> and Fe<sub>2.0</sub> HEAs. Primarily the alloy possesses BCC and  $\sigma$  phase, but with increases in the iron content, the vol. fraction of the BCC phase surges. Consequently, the wear resistance of the alloy decreases with increases in iron content [32]. However, Fe<sub>2.0</sub> shows signs of very poor wear resistance to Fe<sub>1.5</sub> which is not consistent with the hardness change.

The worn-out surfaces and wear debris of the AlCoCrFe<sub>x</sub>Mo<sub>0.5</sub>Ni alloys tested at different testing conditions are shown in Figure 19. The worn surfaces of the alloys expose their microstructural difference with abrasive scratches. Since the interdendrites are harder than the dendrites due to more  $\sigma$  phase the protrusion of the harder  $\sigma$

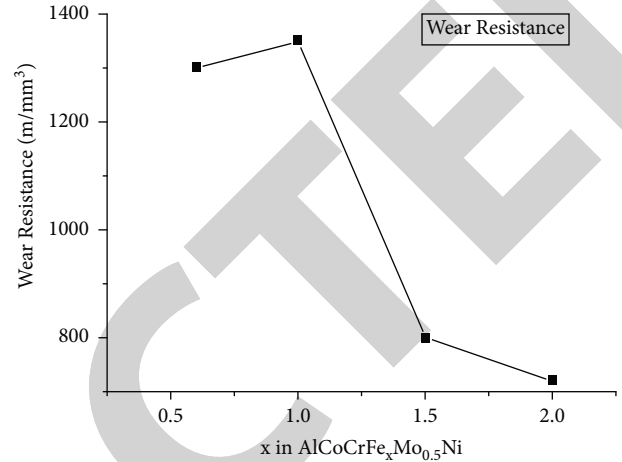


FIGURE 18: Wear resistance of AlCoCrFe<sub>x</sub>Mo<sub>0.5</sub> Ni alloys with respect to Fe content [32].

phase above the BCC phase is identified in the HEAs microstructure. Analysis of worn surface shows the presence of Oxygen in trace amount and large difference in its content is also detected for both plate and particle debris, oxidation wear mechanism is expelled and thus the abrasion action by hard oxide particles is the dominant mechanism [34].

**4.2. Effect of Boron.** The CuCoNiCrAl<sub>0.5</sub>Fe with  $x = 0$  to 1 has the FCC structure with boride precipitation and the boride vol. fraction is increased with boron content [27]. Consequently, the wear resistance of the alloy raised significantly with the inclusion of B as illustrated in Figure 20. The alloy with  $x = 1$  named B-1.0 alloy has a greater resistance to wear even higher than that of SUJ2 wear-resistant steel.

Generally, the harder materials possess higher wear resistance. With the help of comparison (Figure 20), it can be identified that the B-0 and B-0.2 alloys exhibit wear resistance in the range of 316 and 17.4 stainless steels. The resistance to wear capability of B-0.6 alloy is very similar to that of cobalt-based superalloy (Stellite), which is attributed to the larger boride precipitates. Furthermore, the 736 HV harder B-1.0 alloys exhibit improved wear resistance than the SUJ2 bearing and SKD61 cold-work mould steels.

**4.3. Effect of Vanadium.** The graph shown in Figure 21 reveals that there is no significant change in the wear resistance of the Al<sub>0.5</sub>CoCrCuFeNiV<sub>x</sub> HEA when vanadium content is not more than 0.6 and it is very comparable with the Al<sub>0.5</sub>CoCrCuFeNi [31]. But the wear resistance is increased significantly when the vanadium content reaches to 1.2 from 0.6. And a further increase in vanadium content from 1.2 to 2.0 does not make any significant change in the



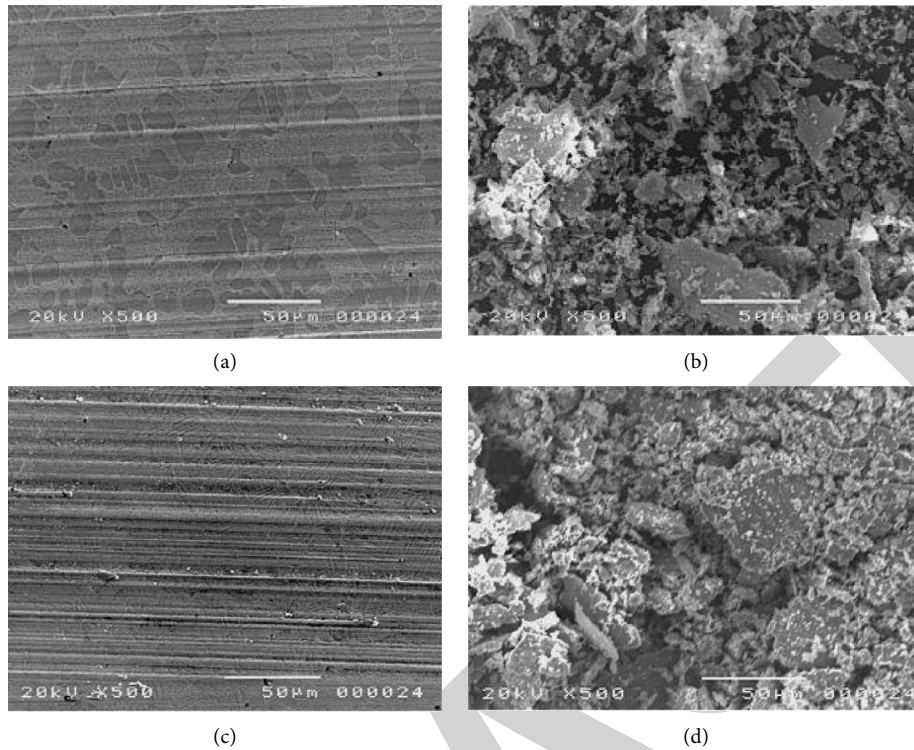


FIGURE 19: Worn surface and worn debris of AlCoCrFexMo0.5Ni alloys with different Fe contents: (a)  $x = 0.6$ , worn surface; (b)  $x = 0.6$ , worn debris; (c)  $x = 2.0$ , worn surface; (d)  $x = 2.0$ , worn debris [32].

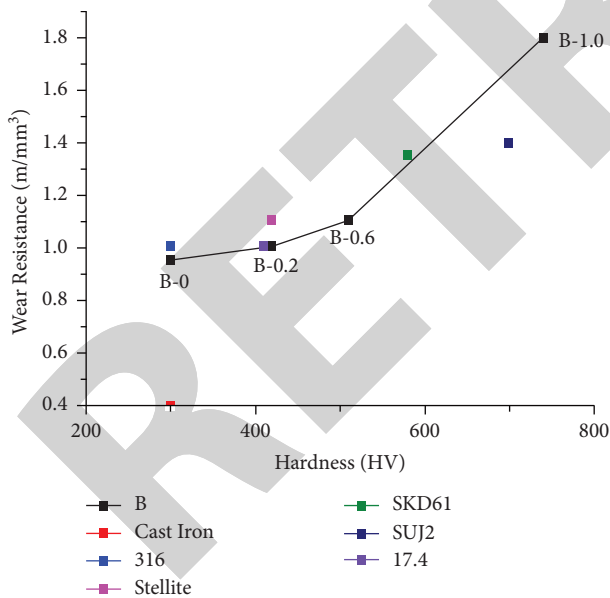


FIGURE 20: Wear resistance vs. hardness curve for CuCoNi-CrAl<sub>0.5</sub>Fe alloy with varying boron quantity [27].

wear resistance of the alloy. Hence the  $x = 1.0$  and  $1.2$  are said to be the optimum vanadium content for tool applications.

**4.4. Effect of Aluminium and Titanium.** Experimental results reveal that the resistance to wear property of Al<sub>0.2</sub>Co<sub>1.5</sub>CrFeNi<sub>1.5</sub>Ti and Co<sub>1.5</sub>CrFeNi<sub>1.5</sub>Ti alloys is no less than twice

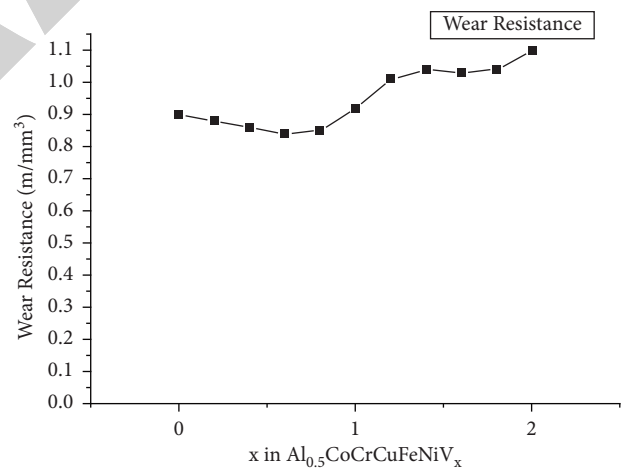


FIGURE 21: Wear resistance of Al<sub>0.5</sub>CoCrCuFeNiV<sub>x</sub> HEA with different vanadium contents [31].

superior to that of traditional steels with wear-resistant along with comparable microhardness [33]. From Figure 22 it can be easily identified that the harder Al<sub>00</sub>Ti<sub>10</sub> and Al<sub>02</sub>Ti<sub>10</sub> HEAs show off superior tribological behaviour when compared with soft Al<sub>02</sub>Ti<sub>05</sub> and Al<sub>00</sub>Ti<sub>05</sub> HEAs.

Figures 23(a)–23(c) illustrates the worn surface secondary electron images (SEI) of Al<sub>02</sub>Ti<sub>05</sub> and Al<sub>00</sub>Ti<sub>05</sub> samples. The worn-out surface of developed alloys demonstrates apparent features of plastic deformation and grooves and seem to be similar. Furthermore, it was found that except in darker regions in BEI (Figures 23(b)–23(d))

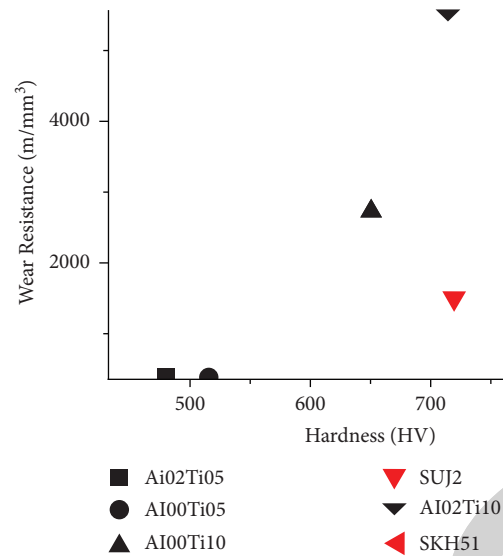


FIGURE 22: Variation in Adhesive wear behaviour and microhardness of various HEAs [33].

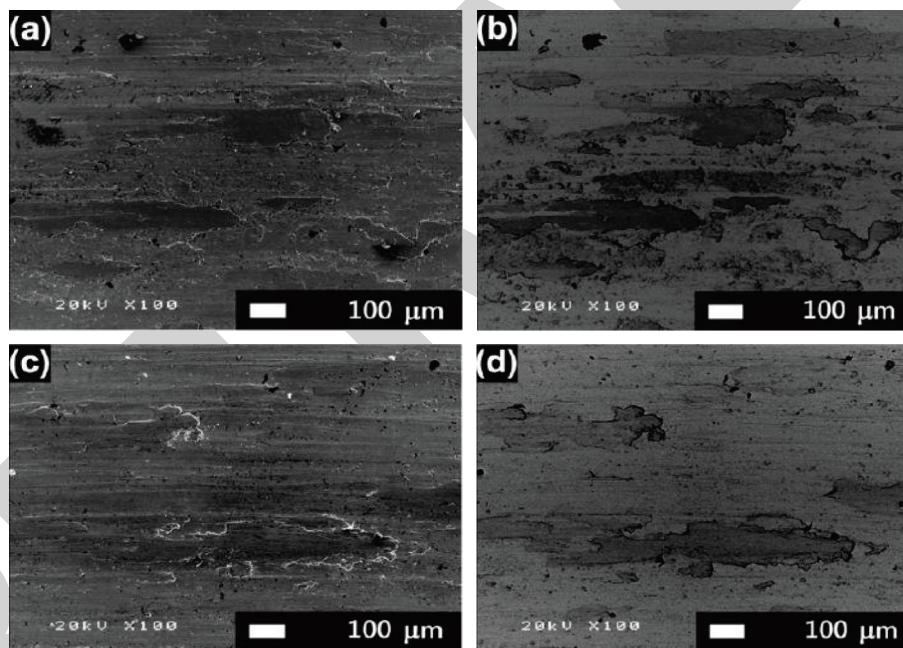


FIGURE 23: The worn-out surface morphology of Al<sub>0</sub>0Ti<sub>0</sub>5: (a) SEI and (b) BEI; Al<sub>0</sub>2Ti<sub>0</sub>5: (c) SEI and (d) BEI [33].

TABLE 3: Wear debris composition (in at. %) based on EDS analysis [33].

HEA	O	Fe	Cr	Ti	Ni	Co	Al
Al <sub>0</sub> 0Ti <sub>0</sub> 5	—	18.7	18.5	9.3	26.3	27.3	—
Al <sub>0</sub> 2Ti <sub>0</sub> 5	—	17.8	18.0	8.6	25.3	26.4	3.8
Al <sub>0</sub> 0Ti <sub>1</sub> 0	68.1	14.6	3.6	3.3	5.0	4.8	—
Al <sub>0</sub> 2Ti <sub>1</sub> 0	69.4	17.8	3.0	2.7	4.4	3.9	0.8

presence of oxygen is not found on the worn surface. The flake-like wear debris without oxygen content (Table 3) is obtained, so it is believed that the material is worn out from Al<sub>0</sub>2Ti<sub>0</sub>5 and Al<sub>0</sub>0Ti<sub>0</sub>5 devoid of several major oxidations.

The worn-out surface morphology of Al<sub>0</sub>0Ti<sub>1</sub>0 (Figure 24(a) and 24(b)) and Al<sub>0</sub>2Ti<sub>1</sub>0 (Figures 24(c) and 24(d)) shows only the signs of shallow scratches and few considerable features of oxidation which is in sharp disparity



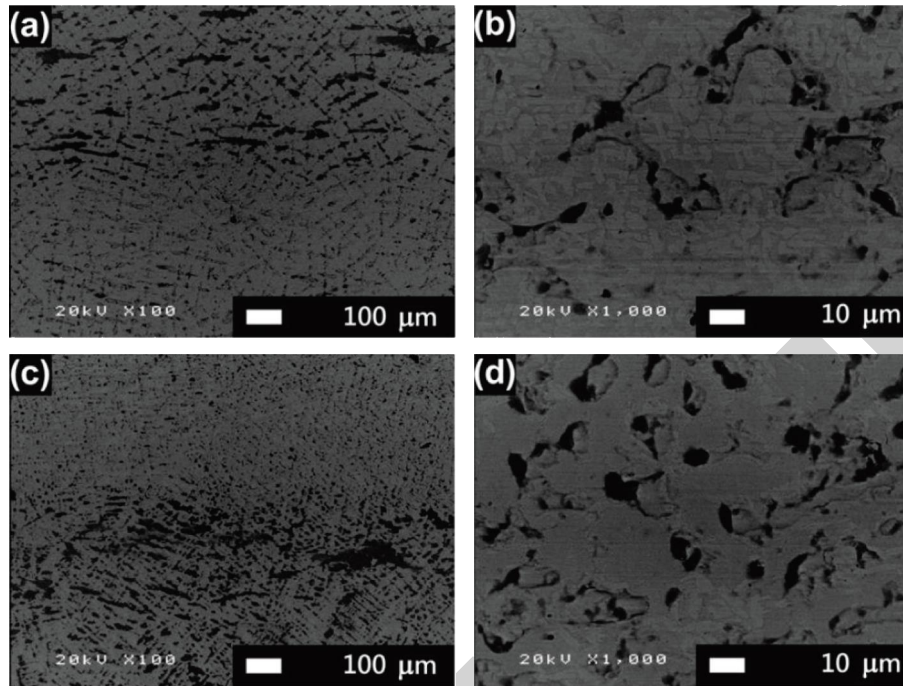


FIGURE 24: SEM BEI of worn-out morphology on Al00Ti10: (a) magnification 100X and (b) magnification 1000X; Al02Ti10: (c) magnification 100X and (d) magnification 1000X [33].

TABLE 4: Elementary Composition of dark areas in the worn surface of HEAs [33].

HEA	O	Al	Ti	Cr	Fe	Co	Ni
Al00Ti10 (at. %)	66.4	—	3.4	4.2	17.3	4.5	4.3
Al02Ti10 (at. %)	63.3	1.0	4.0	5.1	17.6	4.6	4.5

with the wear surface of Ti<sub>05</sub> alloys. Furthermore, it is noteworthy that the dendrite–interdendrites structures of the alloy can still be recognised. Apparent signals of oxygen are found on EDS analysis on ID and DR regions with quite different compositions. The worn interdendritic composition is very similar to the alloys excluding the existence of O<sub>2</sub>. Owing to a lower hardness of dendritic regions, they wear out severely with the black powder particles gathering in worn-out depressions. The attained EDS results depict that these black-coloured debris particles respective to Fe-rich oxides (Table 4) and the attained elementary composition are very much close to Ti10 alloy’s debris particles. It is highly possible that these particles originated from worn-out debris of the SKH51 counter disk part since the worn-out debris and accrued black-coloured particles had a higher Fe concentration.

## 5. Applications

HEAs-based materials are set up as a wider structural and functional material with immense prospective for the choice in a broad array of various applications. Currently, the specific physical behaviour of HEAs, for example, Al<sub>2.08</sub>CoCrFeNi, with persistent resistivity makes them successful materials for electronics-based applications. Hence extensive studies have to be made for these

combinations of HEAs to improve their future application. The superior tribological behaviour of B-1.0 alloy that is better than that of SUJ2-based wear-resistant steels depicts that the composition of CuCoNiCrAl<sub>0.5</sub>FeB<sub>x</sub> based alloys showcase possible application in tool manufacturing, structural materials, both high temperature, and also in ambient room temperature condition.

## 6. Summary and Perspective

AlCoCrFeNi-based HEAs showcase attractive and unique properties for several applications in engineering components. This study involves the combination of several physical metallurgy aspects of HEAs with the composition of AlCoCrFeNi that includes various synthesis approaches, specific applications, and effects of alloying elements over its basic and functional characterisations such as mechanical, wear, and microstructural properties. The observations are depicted as enlisted below as follows:

- (1) Various synthesis methods, such as arc melting, mechanical alloying, laser cladding, and plasma spraying are effectively adopted for developing HEAs with the composition of AlCoCrFeNi.
- (2) These HEAs hold effective potential in an extensive assortment of applications, for instance, structural

and functional materials, particularly in nuclear reactors, turbine components, and also in various transport industries.

- (3) Addition of alloying elements in AlCoCrFeNi HEAs depicts major variations and alters over the physical, mechanical, tribological, and microstructural properties
- (4) AlCoCrFeNi-based HEAs possess ample wear property with respect to the addition of various alloying elements that includes Ti, B, and V. The Tribological property of AlCoCrCuFeNi and AlCoCrFeNiTi<sub>0.5</sub> HEAs rubbing against 1Cr18Ni9Ti steel, ZrO<sub>2</sub> and SiC Ceramic in 90% H<sub>2</sub>O<sub>2</sub> solution is better.
- (5) The exceptional wear resistance of the HEAs is correlated to their thermal softening resistance and excellent antioxidation property. Hence it can be a potential candidate material as reinforcements in MMCs as a replacement for SiC-like ceramics.

## Data Availability

Since it is a review article, the authors do not have any data associated with the article.

## Conflicts of Interest

The authors declare that they have no conflicts of interest.

## References

- [1] J. W. Yeh, S. K. Chen, S. J. Lin et al., "Nanostructured high-entropy alloys with multiple principal elements: novel alloy design concepts and outcomes," *Advanced Engineering Materials*, vol. 6, no. 5, pp. 299–303, 2004.
- [2] Y. F. Ye, Q. Wang, J. Lu, C. T. Liu, and Y. Yang, "Design of high entropy alloys: a single-parameter thermodynamic rule," *Scripta Materialia*, vol. 104, pp. 53–55, 2015.
- [3] Y. Zhang, T. T. Zuo, Z. Tang et al., "Microstructures and properties of high-entropy alloys," *Progress in Materials Science*, vol. 61, pp. 1–93, 2014.
- [4] B. Gludovatz, A. Hohenwarter, D. Catoor, E. H. Chang, E. P. George, and R. O. Ritchie, "A fracture-resistant high-entropy alloy for cryogenic applications," *Science*, vol. 345, no. 6201, pp. 1153–1158, 2014.
- [5] M. A. Hemphill, T. Yuan, G. Y. Wang et al., "Fatigue behavior of Al<sub>0.5</sub>CoCrCuFeNi high entropy alloys," *Acta Materialia*, vol. 60, no. 16, pp. 5723–5734, 2012.
- [6] S. Q. Xia, X. Yang, T. F. Yang, S. Liu, and Y. Zhang, "Irradiation resistance in Al x CoCrFeNi high entropy alloys," *Journal of Occupational Medicine*, vol. 67, no. 10, pp. 2340–2344, 2015.
- [7] Y. F. Ye, Q. Wang, J. Lu, C. T. Liu, and Y. Yang, "High-entropy alloy: challenges and prospects," *Materials Today*, vol. 19, no. 6, pp. 349–362, 2016.
- [8] S. G. Ma and Y. Zhang, "Effect of Nb addition on the microstructure and properties of AlCoCrFeNi high-entropy alloy," *Materials Science and Engineering A*, vol. 532, pp. 480–486, 2012.
- [9] S. Kapoor, R. Liu, X. J. Wu, and M. X. Yao, "TIMP-1 levels and their association with the development and progression of systemic malignancies," *The International Journal of Biological Markers*, vol. 28, no. 2, pp. 231–248, 2013.
- [10] Y. Y. Chen, T. Duval, U. D. Hung, J. W. Yeh, and H. C. Shih, "Microstructure and electrochemical properties of high entropy alloys—a comparison with type-304 stainless steel," *Corrosion Science*, vol. 47, no. 9, pp. 2257–2279, 2005.
- [11] K. K. Alaneme, M. O. Bodunrin, and S. R. Oke, "Processing, alloy composition and phase transition effect on the mechanical and corrosion properties of high entropy alloys: a review," *Journal of Materials Research and Technology*, vol. 5, no. 4, pp. 384–393, 2016.
- [12] J. Chen, P. Niu, Y. Liu et al., "Effect of Zr content on microstructure and mechanical properties of AlCoCrFeNi high entropy alloy," *Materials & Design*, vol. 94, pp. 39–44, 2016.
- [13] Y.-L. Chen, C.-W. Tsai, C.-C. Juan et al., "Amorphization of equimolar alloys with HCP elements during mechanical alloying," *Journal of Alloys and Compounds*, vol. 506, no. 1, pp. 210–215, 2010.
- [14] C. Suryanarayana, "Mechanical alloying and milling," *Progress in Materials Science*, vol. 46, no. 1-2, pp. 1–184, 2001.
- [15] A. W. Weeber, H. Bakker, H. J. M. Heijligers, and G. F. Bastin, "Compositional analysis of Ni-Zr powder during amorphization by mechanical alloying," *Europhysics Letters*, vol. 3, pp. 1261–1265, 1987.
- [16] J. Chen, P. Niu, T. Wei et al., "Fabrication and mechanical properties of AlCoNiCrFe high-entropy alloy particle reinforced Cu matrix composites," *Journal of Alloys and Compounds*, vol. 649, pp. 630–634, 2015.
- [17] W. Ji, Z. Fu, W. Wang et al., "Mechanical alloying synthesis and spark plasma sintering consolidation of CoCrFeNiAl high-entropy alloy," *Journal of Alloys and Compounds*, vol. 589, pp. 61–66, 2014.
- [18] L. M. Wang, C. C. Chen, J. W. Yeh, and S. T. Ke, "The microstructure and strengthening mechanism of thermal spray coating Ni<sub>3</sub>Co<sub>0.6</sub>Fe<sub>0.2</sub>CrySizAlTi<sub>0.2</sub> high-entropy alloys," *Materials Chemistry and Physics*, vol. 126, no. 3, pp. 880–885, 2011.
- [19] K. B. Zhang, Z. Y. Fu, J. Y. Zhang, W. M. Wang, S. W. Lee, and K. Niihara, "Characterization of nanocrystalline CoCrFeNi-TiAl high-entropy solid solution processed by mechanical alloying," *Journal of Alloys and Compounds*, vol. 495, no. 1, pp. 33–38, 2010.
- [20] M. Wang, "Composite coatings for implants and tissue engineering scaffolds," in *Biomedical Composites*, pp. 127–177, Woodhead Publishing, Sawston, Cambridge, 2010.
- [21] A. S. M. Ang, C. C. Berndt, M. L. Sesso et al., "Plasma-sprayed high entropy alloys: microstructure and properties of AlCoCrFeNi and MnCoCrFeNi," *Metallurgical and Materials Transactions A*, vol. 46, no. 2, pp. 791–800, 2015.
- [22] S. Zhang, C. L. Wu, J. Z. Yi, and C. H. Zhang, "Synthesis and characterization of FeCoCrAlCu high-entropy alloy coating by laser surface alloying," *Surface and Coatings Technology*, vol. 262, pp. 64–69, 2015.
- [23] Q.-Y. Wang, R. Pei, S. Liu et al., "Microstructure and corrosion behavior of different clad zones in multi-track Ni-based laser-clad coating," *Surface and Coatings Technology*, vol. 402, Article ID 126310, 2020.
- [24] Y. Shon, S. S. Joshi, S. Katakam, R. Shanker Rajamure, and N. B. Dahotre, "Laser additive synthesis of high entropy alloy coating on aluminum: corrosion behavior," *Materials Letters*, vol. 142, pp. 122–125, 2015.
- [25] T. M. Yue and H. Zhang, "Laser cladding of FeCoNiCrAlCuxSi<sub>0.5</sub> high entropy alloys on AZ31 Mg alloy

## *Retraction*

# **Retracted: Process Optimization of Spark Plasma Sintering Parameters for Tungsten Carbide/Silicon Nitride/AA2219 Composites by Taguchi Method**

### **Advances in Materials Science and Engineering**

Received 26 December 2023; Accepted 26 December 2023; Published 29 December 2023

Copyright © 2023 Advances in Materials Science and Engineering. This is an open access article distributed under the Creative Commons Attribution License, which permits unrestricted use, distribution, and reproduction in any medium, provided the original work is properly cited.

This article has been retracted by Hindawi, as publisher, following an investigation undertaken by the publisher [1]. This investigation has uncovered evidence of systematic manipulation of the publication and peer-review process. We cannot, therefore, vouch for the reliability or integrity of this article.

Please note that this notice is intended solely to alert readers that the peer-review process of this article has been compromised.

Wiley and Hindawi regret that the usual quality checks did not identify these issues before publication and have since put additional measures in place to safeguard research integrity.

We wish to credit our Research Integrity and Research Publishing teams and anonymous and named external researchers and research integrity experts for contributing to this investigation.

The corresponding author, as the representative of all authors, has been given the opportunity to register their agreement or disagreement to this retraction. We have kept a record of any response received.

### **References**

- [1] S. Althahban, G. Pathinettampadian, F. Qahtani et al., "Process Optimization of Spark Plasma Sintering Parameters for Tungsten Carbide/Silicon Nitride/AA2219 Composites by Taguchi Method," *Advances in Materials Science and Engineering*, vol. 2022, Article ID 4829499, 8 pages, 2022.

## Research Article

# Process Optimization of Spark Plasma Sintering Parameters for Tungsten Carbide/Silicon Nitride/AA2219 Composites by Taguchi Method

Sultan Althahban,<sup>1</sup> Gurusamy Pathinettampadian,<sup>2</sup> Faez Qahtani,<sup>3</sup> Yosef Jazaa,<sup>4</sup> S. Mousa,<sup>5</sup> Sanipina Anjani Devi,<sup>6</sup> Melvin Victor De Poures,<sup>7</sup> R. Subbiah,<sup>8</sup> and Hana Beyene Mamo <sup>9</sup>

<sup>1</sup>Department of Mechanical Engineering, Jazan University, Jazan 82822, Saudi Arabia

<sup>2</sup>Department of Mechanical Engineering, Chennai Institute of Technology, Chennai, Tamilnadu, India

<sup>3</sup>Department of Mechanical Engineering, Najran University, Najran-11001, Saudi Arabia

<sup>4</sup>Faculty of Engineering, King Khalid University, Abha 62529, Saudi Arabia

<sup>5</sup>Faculty of Engineering, Jazan University, Jazan 706, Saudi Arabia

<sup>6</sup>Department of Mechanical Engineering, Aditya Engineering College, Surampalem 533437, Andhra Pradesh, India

<sup>7</sup>Department of Thermal Engineering, Saveetha School of Engineering, Saveetha Institute of Medical and Technical Sciences, Chennai, Tamilnadu, India

<sup>8</sup>Department of Mechanical Engineering, Gokaraju Rangaraju Institute of Engineering and Technology, Telangana, India

<sup>9</sup>Faculty of Mechanical Engineering, Jimma Institute of Technology, Jimma University, Jimma, Ethiopia

Correspondence should be addressed to Hana Beyene Mamo; hana.beyene@ju.edu.et

Received 6 June 2022; Revised 22 July 2022; Accepted 4 August 2022; Published 30 September 2022

Academic Editor: K. Raja

Copyright © 2022 Sultan Althahban et al. This is an open access article distributed under the Creative Commons Attribution License, which permits unrestricted use, distribution, and reproduction in any medium, provided the original work is properly cited.

It is usual practice to optimize the various processing parameters in order to achieve well-organized and lucrative process conditions. For the creation of tungsten carbide/silicon nitride/AA2219 composites, sintering temperature, sintering pressure, dwelling time, and heating rate all must be optimized. Design of experiments and analysis of variance were employed to assess the factors' contributions to density as well as microhardness response variables. It was decided to test the admixed powders and Vickers hardness tester, optical microscope, and Archimedes-based density testing to evaluate the sintered compacts. The optimum spark plasma sintering factors were a temperature of 500°C, a pressure of 30 MPa, a dwelling time of 8 minutes, and a heat rate of 160 °C/min, resulting in an extreme density of 2.71 g/cm<sup>3</sup> and a maximum microhardness of 38.61 HV (0.38 GPa).

## 1. Introduction

Low power consumption and quick processing times have made nonconventional spark plasma sintering (SPS) an increasingly popular sintering method [1]. MMCs and MMNCs can be fully densely consolidated at low temperatures, despite the fact that this process is still relatively new [2]. Although spark plasma sintering was first described by [3], it is now widely accepted that the rapid sintering technique was invented by them. Spark plasma sintering utilizes heat to rapidly sinter a powder compact on a

macroscopic level, but it is also used at microscopic levels to deliver energy to the powder particles' contact points [4]. When combined with plasma generation, resistive heating, and pressure application, spark plasma sintering has been proven to accomplish very rapid sintering [5]. Since the microstructure is regulated and grain development is minimal or nonexistent during the brief sintering period [6], the composite has better mechanical and thermal properties as well as chemical qualities. While other processes like SPS eliminate porosity and coarsen the microstructure of the material, spark plasma sintering minimizes the number of

contaminants like  $H_2$  and  $O_2$  [7]. Numerous commercial uses have been described in the scientific literature for the usage of aluminum reinforced with a hard-secondary phase [8, 9]. In engine cylinders, rotors, commercial products, and wear application systems for all these composite materials have been shown to be effective [10].

SPS of aluminium reinforced with carbon nanotubes [11] has received a large amount of attention, but the ternary tungsten carbide/silicon nitride/AA2219 nanocomposites have received little or no attention at all. When employing  $500^\circ\text{C}$ , 30 minutes, 30 MPa, 5 Pa vacuum and cooling rate of  $500^\circ\text{C}$  per minute, an SPS of [12] AA2219-tungsten carbide AA2219-tungsten carbide resulted in 300 MPa, more than three times the strength of AA2219. As a result, a number of studies are presently focused on discovering the optimum way to disperse the great features of WC on the Al matrix for use in microelectronic and electrical, energy, health, and structural applications [13]. Many writers have indicated that silicon nitride is an excellent alloying material for aluminum. A thin interdendritic flick of yielding aluminium, which sustains strains, and the occurrence of silicon nitride, which hinders crash circulation, were cited by [14, 15] as the reason for no cracking on the surface of their spark plasma sintered Al-Nb composite. Additionally, silicon nitride has been shown to exhibit exceptional fracture toughness, superb superconductivity, and great thermal and corrosion resistance in other studies [16, 17]. As a result, the properties of tungsten carbide and silicon nitride are expected to provide aluminium with higher strength, electrical and thermal conduction, and superior corrosion and wear resistance, for a wide range of engineering uses [18].

MMCs have been overtaken by nanocomposites due to their superior properties, including greater toughness, lesser granular size, best wear and abrasive properties, enhanced toughness, ductileness, and exhaustion resistance [19]. In order to attain full density while conserving resources, adjusting these factors is essential. To ensure that the theoretical density of the composite is reached at minimal input factors, process parameters play an important role in experimental research [20, 21]. Al-1wt% SiC microhardness of 108 MPa and compressive strength of 312 MPa were achieved with the ideal factors of  $450^\circ\text{C}$  temperature, 8 minutes of dwelling time at 45 MPa pressure, and  $160^\circ\text{C}/\text{min}$  heat rate, according to [22, 23]. It is possible to reduce expenses and time and energy by reducing the amount of trial-and-error in experiments. Tungsten carbide/silicon nitride/AA2219 composite process parameters have received far less attention than optimization of SPS parameters [24]. Researchers in this study are utilizing ANOVA and design of experiments to refine the spark plasma sintering parameters of this composite [25]. Thus, this research makes use of spark plasma sintering process with different input parameter through Taguchi, and the corresponding mechanical properties like density and microhardness are studied for useful application.

## 2. Materials and Methods

**2.1. Materials.** The 99.5%marketable aluminum 2219 was used as the study's starting metal. The most frequent

material is used to construct liquid cryogenic rocket fuel tanks. It features one-of-a-kind mix of qualities, including outstanding cryogenic capabilities. Tungsten carbide was utilized as a reinforcement with the size of 10-30 nm. Alloy 2wt%, 2wt% WC, and 2wt% silicon nitride were combined in a dry atmosphere utilizing the Turbular Shaker Mixer model T2F for 10 hours at 110 rpm in order to ensure that the powders were thoroughly mixed. While mixing, it was required to add approximately steel balls (4 mm radius) to the vessel of powder so that the reinforcement could be better dispersed in its matrix [2].

**2.2. Design of the Experiment.** Taguchi devised a typical type of DOE known as the Taguchi technique, which is more accessible and economically viable because of the huge reduction in experimental time and expense [26, 27]. By maintaining consistency of performance and reducing variation, it is an excellent tool for optimizing process design. For the best possible responses to process variables, this powerful tool utilizes three design processes: system design, parameter design, and tolerance development [28, 29]. As a first step in the development process, system designers must identify the most critical design variables and then determine the range of acceptable values for each one. Parameter design, also known as robust design, discovers the best values for design parameters in order to reduce the effects of variance and noise [30]. Tolerance design is used to tighten tolerances in parameter design in order to acquire the best results. By employing Taguchi's orthogonal array (OA) architecture, the manageable constraints can be evaluated with their associated answers at multiple stages in an ordered way [31]. This reduces both time and money.

**2.3. Taguchi Method.** Taguchi technique was used in this work because it is an effective tool for constructing trials when numerous variables are to be optimized, as is the situation with spark plasma sintering [32]. Because the number of tests is minimized, this method is often preferred to the factorial design method because it saves both time and money. It is thus possible to limit the number of tests by eliminating combinations of variables that are unnecessary, leaving just the most crucial combinations of parameters at their proper levels in the Taguchi's orthogonal array experimentation method [31]. There are four factors to consider in this experiment: sintering temperature, pressure, and dwell time, as well as heating rate, all of which are shown in the table at three different levels. Respondent variables include sintered composite densities and microhardness. It was also found that the process variables were statistically significant thanks to an analysis of variance (ANOVA). Table 1 is constructed using the Taguchi  $L_9$  orthogonal array, yielding a total of nine experiments [33]. The following is the outcome: Minitab 16.1 was used to create the experiment, and the Taguchi option was used, as previously stated. Factor variables are the scientific term for the study's four main sintering parameters. Temperature, pressure, dwell time, and heating rate were all taken into consideration. Each of the following variables was considered at three different levels:

TABLE 1: Taguchi's  $L_9$  arrangement.

Experimental trials	Sintering temperature (A)	Pressure (B)	Dwellingtime (C)	Heatingrate (D)
1	1	1	1	1
2	1	2	2	2
3	1	3	3	3
4	2	1	2	3
5	2	2	3	1
6	2	3	1	2
7	3	1	3	2
8	3	2	1	3
9	3	3	2	1

temperature (400°C), pressure (30 Mpa), dwell duration (12 minutes), and heating rate (240°C). The “factor variable” number was typed into a pop-up box, then the “level” number was entered into a pop-up box, and then ok was clicked to enable the program to begin. There are four columns in the table: temperature (A), pressure (B), dwell time (C), and heating rate(D). It was clear that steps 1 through 3 were recurrences across the data. It is possible to perform nine tests by entering varying values for three parameters: 1, 2, and 3. This yields the lowest, medium, and highest possible results.

**2.4. Sintering Process Using a Spark Plasma.** The KCE-FCT-HHPD 25 spark plasma sintering equipment was used in this work with a vacuum pressure of 0.605 bar, a relative pressure of 500 bar, and an absolute pressure of 1.2 bar. Before beginning sintering, the machine was calibrated to these settings. As needed, the admixed powder was weighed out to generate nanocomposites with a 15 mm radius and 5 mm thickness. Sintering with the settings is shown in Table 2. For simpler exclusion of sintered specimen and to eliminate temperature + gradients, graphite sheets were used to hide powders from the die and the upper and lower punches [34]. A total of nine samples were gathered and analyzed, as shown in the design table.

**2.5. Testing on Density.** For estimating the density of the specimen, we used the Archimedes method, whereas equation (1) was used to get the starting powder's bulk density. Using a rule of mixes formula, the relative density of the powdered constituents was calculated using the theoretical bulk density.

$$\rho_{bulk} = \left\{ \frac{\%Al}{\rho_{Al}} + \frac{\%WC}{\rho_{WC}} + \frac{\%Si_3N_4}{\rho_{WC Si_3N_4}} \right\}^{-1}, \quad (1)$$

where  $\rho_{bulk}$ ,  $\rho_{Al}$ ,  $\rho_{WC}$ , and  $\rho_{Si_3N_4}$  are densities of bulk, aluminium, tungsten carbide, and silicon nitride, respectively.

**2.6. Testing on Microhardness.** Samples of the AA2219-2% WC-2%  $Si_3N_4$  composites were examined on a Vicker's microhardness tester (FM-800) using a diamond indenter with a force of 100 g for 16 seconds and a 0.1 spacing.

TABLE 2: Design of the experiment.

Experimental trials	Temperature (°C)	Pressure (MPa)	Dwelling time (min)	Heat rate (°C/ min)
A	400	15	8	80
B	400	30	12	160
C	400	45	16	240
D	450	15	12	240
E	450	30	16	80
F	450	45	8	160
G	500	15	16	160
H	500	30	8	240
I	500	45	12	80

### 3. Results and Discussion

In spark plasma sintering, little grain growth occurs even when the material is fully densified. Densification in these samples is attributed entirely to the complete removal of pores and grain boundaries. As seen in [35], this consolidation process is powerful enough to assure strong adhesion among the matrix and reinforcements, resulting in the high hardness and full densification of this composite. Using this technique in conjunction with the best process conditions, a composite with zero porosity and impurities can be created. Saying that spark plasma sintering is unique among fabrication methods is pointless. This is due to the tensile strength of 115 MPa obtained [36] during the induction melting of AA2219-WC.

AA2219-tungsten carbide plasma spurting by [37] had a tensile strength of 83.2 MPa, which was the highest. A hardness of 38.61 HV (381.2 MPa) was achieved, which is corresponding to tensile strength of 125.4 Mpa. Sintered samples' densities are shown in Table 3, though the ANOVA outcomes are shown in Table 4. Sintering sample density is illustrated in Figure 1 as an interplay between predictor factors. Figure 1(a) depicts the most significant graphic for relative density. The relative density amplified from 87% to 99% when the sintering temperature increased from 400 °C to 450 °C. After a further rise in temperature, the average density had reached a whopping 99.5%. In addition, a rise in pressure from 15 to 30 mega Pascal raised the comparative density from 96 to nearly 99% on the pressure plot. However, when the pressure was bigger to 45 MPa, the line began to decline by roughly 96%.

TABLE 3: Density and microhardness testing results.

Trial no.	Density (g/cm <sup>3</sup> )	Relative density (%)	Microhardness (HV)
1	2.39	89.3	26.92
2	2.61	96.3	36.42
3	2.43	89.7	28.45
4	2.72	97.5	37.63
5	2.65	98.8	32.18
6	2.69	99.4	36.56
7	2.68	97.8	38.61
8	2.68	98.8	38.53
9	2.71	99.5	39.04

TABLE 4: ANOVA results on density.

Factors and interaction	F value	P value	Involvement	R squared (%)
Sintering temperature (A)	11.66	0.008	28.2	79.81
Pressure (B)	0.21	0.832	–	
Dwelling time (C)	0.14	0.883	–	
Heating rate (D)	0.35	0.731	–	86.03
AB	10.15	0.012	23.6	84.47
AC	4.87	0.017	12	89.07
AD	28.98	0.005	42	
BC	0.014	0.797	–	
BD	0.037	0.699	–	
CD	0.024	0.732	–	

There is a significant increase in relative density between 8 and 12 minutes and a fall between 16 and 24 minutes on the time plot. At 240 °C/min, relative density peaked at 80 °C/min, and then fell back to zero, once the heat rate was improved more to 240 °C/min. This plot shows that the ideal density was achieved at 500 °C, 30 MPa, 8 min of dwell time, and a heating rate of 160 °C/min. The primary effect plot of means for the signal to noise ratio in relation to density can be seen in Figure 1(b). The study was done using the “bigger is better” option, and the best density was found at 500 °C, 30 MPa pressure, 8 minutes dwell time, and a heating rate of 160 °C/min on the main effect plot. With [38] who sintered AA2219-tungsten carbide at 500 °C, 30 minutes, achieved an improved toughness of further than three times that of pure aluminium, which is consistent with our results (85 MPa).

However, complete densification was achieved in 8 minutes rather than 15 minutes in the current investigation. Sintering temperatures over 500 °C were not a possibility in this study since an SPS of AA2219-3 wt% tungsten carbide at 500 °C yielded a density of 96%, which suggests that, at 500 °C, resident melting of aluminium may have begun, resulting in the drop-in density. Using the table, it can be observed that features A, AB, AC, and AD are important typical relations because they all have *P* values less than 0.05. In order to achieve a fully dense tungsten carbide/silicon nitride/AA2219 composite, these are the most important characteristics to regulate. Temperature contributed 27.5% to the *P* value of 0.009 and had an R-squared value of 79.76% for component A. The sintering temperature, then, is all that matters for predicting the final density, with an accuracy of

79.76% when it comes to predicting the density of a sample. Assuming that temperature variance is significantly different from other parameters, the substitute suggestion that temperature has an important impact on densities can be accepted.

This interaction between temperature and pressure had a R squared value of 86.3%; temperature and time had a R squared value of 0.016%; the temperature and heating rate had a R squared value of 89.7%; and temperature and pressure had a R squared value of 0.011%. One-way ANOVA models and the interactions between two components were the only models examined in this study (two-way). ANOVA results for factors related to microhardness are displayed in Table 5. There is an R-squared value of 63.64% and an R-squared value of 0.048 for the temperature. Microhardness may be predicted with 63.64% accuracy by determining the sintering temperature, which considered for 15.91% of the variables that influence the microhardness. This study found that both the AC and the AD contribute significantly to the total, with AC contributing to 58.61% of the total and AD contributing to 25.63% and R-squared value of 64.81%, respectively.

The rise in the microhardness of the sintered specimen may have been influenced by the variables listed above with *P* values less than 0.05. Temperature rises from 400 °C to 450 °C resulting in upsurge in average microhardness from 29 HV to 38 HV, according to Figure 2 which consists of ANOVA results. Temperature increases from 450 to 500 °C caused in 39 HV increases. Proceeding the pressure, a rise in pressure from 15 to 45 MPa resulted in an upsurge of 35 HV



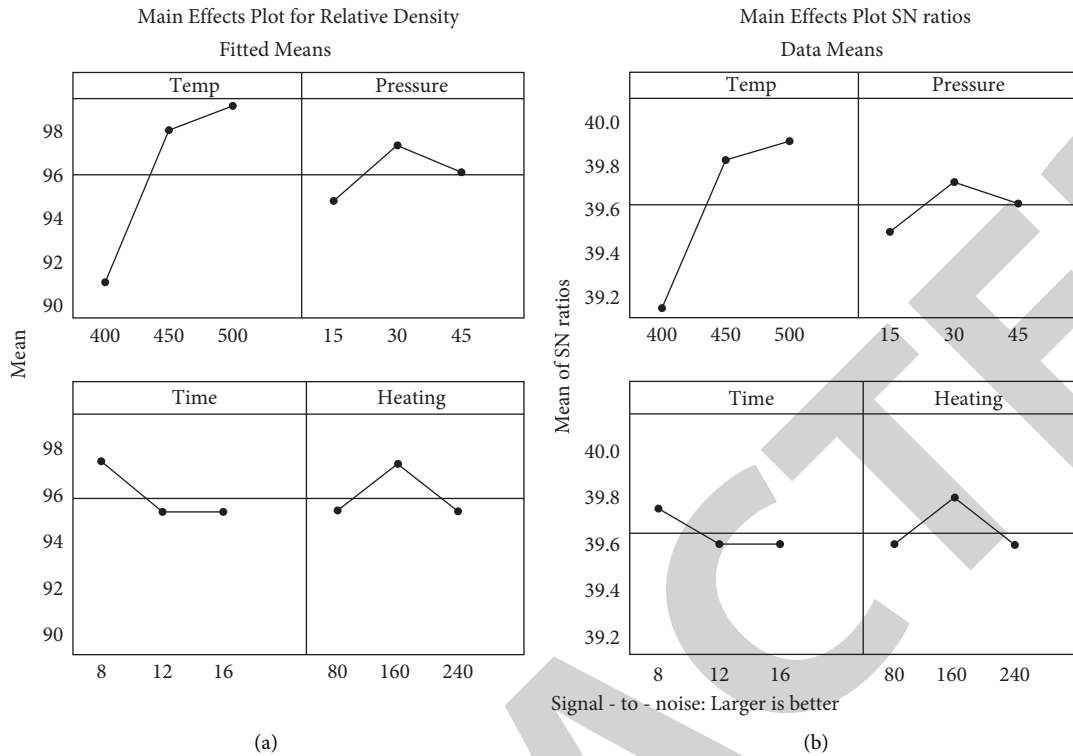


FIGURE 1: Relative density main effect plot of (a) means and (b) signal to noise ratio.

TABLE 5: ANOVA results on microhardness.

Factors and interaction	F value	P value	Contribution (%)	R-squared
A: sintering temperature	5.26	0.049	15.91	64.81
B: sintering pressure	0.12	0.908	–	
C: dwelling time	0.66	0.563	–	
D: heating rate	0.55	0.609	–	
AB	0.74	0.098	–	
AC	13.29	0.014	58.61	
CD	0.25	0.414	–	
BC	0.05	0.623	–	
AD	8.78	0.022	25.63	
BD	0.04	0.657	–	

to 37 HV. Microhardness decreased to 33 HV when the pressure was improved to 45 MPa (0.32 GPa). Increase in the temperature from 80 to 160 °C/min resulted in a rise from 33 (0.32 GPa) to 36 HV on the heating rate (0.35 GPa). However, increasing the rate of heating to 240 °C/min resulted in a downward trend. The time plot indicated a small rise in mean microhardness from 35 HV to 36 HV as the duration increased from 8 to 12 minutes (0.34 GPa). However, increasing the timer to 15 minutes had the opposite effect. The maximum microhardness was achieved at a temperature of 500 °C, a pressure of 30 MPa, a dwell duration of 8 minutes, and a heat rate of 160 °C/min. According to figures, a higher SN ratio is preferable, and the maximum

microhardness was obtained by heating the sample to 500 °C for 8 minutes at 30 MPa pressure and heating it at 160 °C/min for a dwell duration of 8 minutes.

Sample densities and microhardness process parameters are plotted in Figure 3. High and low density and microhardness were obtained at 500 °C and 400 °C, respectively. There was a clear correlation between microhardness and density at 30 MPa. The two response variables decreased as the pressure was raised more. Figure 3 shows the graph bending inward, indicating that 8 minutes of dwell time yielded the best results. The response variables decreased when the time was increased from 12 to 16 minutes. A heat rate of 160 °C/min produced the greatest results.

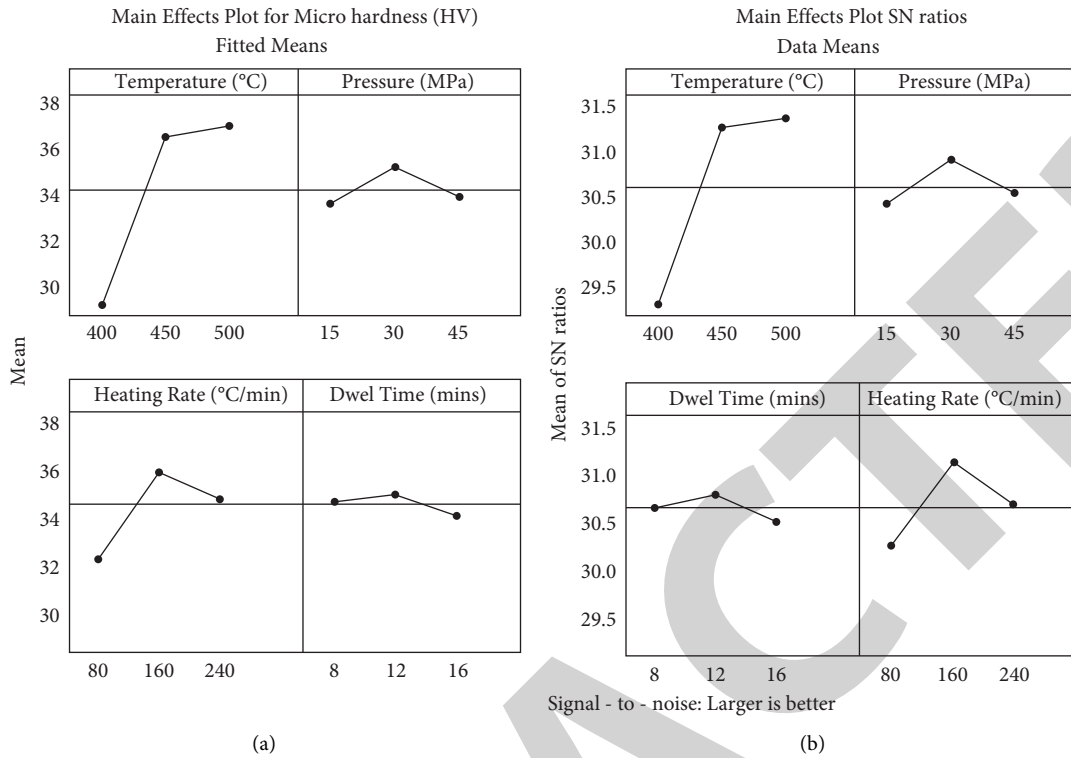


FIGURE 2: Microhardness main effect plot. (a) Means. (b) Signal to noise ratio.

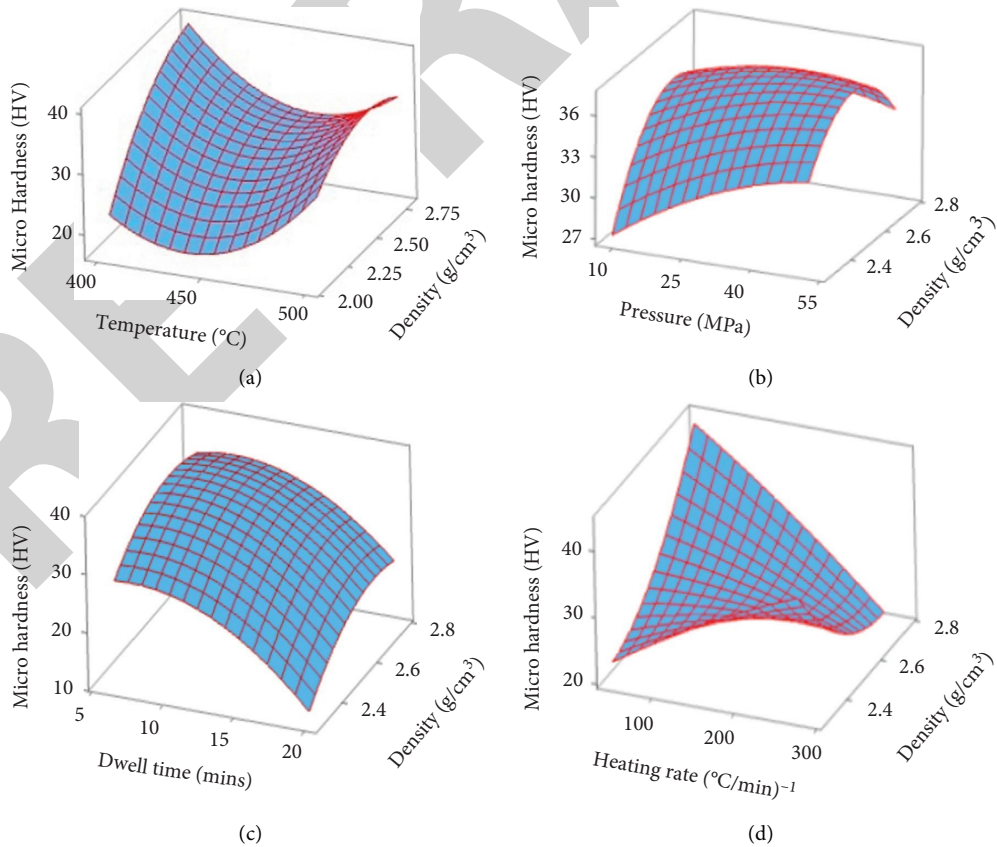


FIGURE 3: Impact of processing factors on the density and microhardness of AA2219-2%WC-2% silicon nitride: (a) temperature, (b) pressure, (c) dwell time, and (d) heating rate.

## 4. Conclusion

Spark plasma sintering has been employed to successfully create a nanocomposite of tungsten carbide, silicon nitride, and AA2219, and the following discussion is given as follows:

- (1) With the incorporation of 2wt.% silicon nitride into AA2219 powder using spark plasma sintering, the microhardness was enhanced by up to 20% which is useful for a wide range of technical applications, and it was strongly influenced by factors such as temperature, dwell time, and heating rate.
- (2) Density and microhardness decreased as pressure, dwelling time, and heating rate are between 30 and 45 MPa, 12 and 16 minutes, and 160 and 240 °C/min, correspondingly. According to the optimization results, the sintering parameters of 500°C temperature, 30 MPa pressure, 12 min dwell time, and 160 °C/min heating rate were found to be best for both density and microhardness.

## Data Availability

The data used to support the findings of this study are included within the article. Further dataset or information is available from the corresponding author upon request.

## Conflicts of Interest

The authors declare that there are no conflicts of interest regarding the publication of this paper.

## Acknowledgments

The authors appreciate the supports from Jimma University, Ethiopia, for the research and preparation of the manuscript. The author thankfully acknowledge the funding provided by Scientific Research Deanship, King Khalid University, Abha, Kingdom of Saudi Arabia, under the grant number R.G.P.1/267/43.

## References

- [1] A. Das and S. P. Harimkar, "Effect of graphene Nano plate and silicon carbide nanoparticle reinforcement on mechanical and tribological properties of spark plasma sintered magnesium matrix composites," *Journal of Materials Science & Technology*, vol. 30, no. 11, pp. 1059–1070, 2014.
- [2] S. Diouf and A. Molinari, "Densification mechanisms in sparkplasma sintering: effect of particle size and pressure," *Powder Technology*, vol. 221, pp. 220–227, 2012.
- [3] S. Lin and W. Xiong, "Microstructure and abrasive behaviors of TiC-316L composites prepared by warm compaction and microwave sintering," *Advanced Powder Technology*, vol. 23, no. 3, pp. 419–425, 2012.
- [4] M. Suarez, M. A. Fernandez, J. L. Menendez et al., "Challenges and opportunities for spark plasma sintering: a key technology for a new generation of materials B," in *Sintering Applications*, Ertug, Ed., InTech, Rijeka, Croatia, 2013.
- [5] N. S. Weston, F. Derguti, A. Tudball, and M. Jackson, "Spark plasma sintering of commercial and development titanium alloy powders," *Journal of Materials Science*, vol. 50, no. 14, pp. 4860–4878, 2015.
- [6] H. Feng, Y. Zhou, D. Jia, and Q. Meng, "Rapid synthesis of Ti alloy with B addition by spark plasma sintering," *Materials Science and Engineering A*, vol. 390, no. 1-2, pp. 344–349, 2005.
- [7] G. A. Sweet, M. Brochu, R. L. Hexemer, I. W. Donaldson, and D. P. Bishop, "Consolidation of aluminum-based metal matrix composites via spark plasma sintering," *Materials Science and Engineering A*, vol. 648, pp. 123–133, 2015.
- [8] V. Mohanavel, K. Ashraff Ali, S. Prasath, T. Sathish, and M. Ravichandran, "Microstructural and tribological characteristics of AA6351/Si3N4 composites manufactured by stir casting," *Journal of Materials Research and Technology*, vol. 9, no. 6, pp. 14662–14672, 2020.
- [9] V. Mohanavel, S. Prasath, K. Yoganandam, B. Girma Tesemma, and S. Suresh Kumar, "Optimization of wear parameters of aluminium composites (AA7150/10 wt%WC) employing Taguchi approach," *Materials Today Proceedings*, vol. 33, no. 7, pp. 4742–4745, 2020.
- [10] A. Kumar Sharma, R. Bhandari, A. Aherwar, R. Rimašauskienė, and C. Pinca-Bretotean, "A study of advancement in application opportunities of aluminum metal matrix composites," *Materials Today Proceedings*, vol. 26, no. 2, pp. 2419–2424, 2020.
- [11] Y. Du, S. Li, K. Zhang, and K. Lu, "BN/Al composite formation by high-energy ball milling," *Scripta Materialia*, vol. 36, no. 1, pp. 7–14, 1997.
- [12] M. Song, "Effects of volume fraction of SiC particles on mechanical properties of SiC/Al composites," *Transactions of Nonferrous Metals Society of China*, vol. 19, no. 6, pp. 1400–1404, 2009.
- [13] M. Ebisawa, T. Hara, T. Hayashi, and H. Ushio, *Production Process of Metal Matrix Composite (MMC) Engine Block*, SAE Technical Paper 910835, Warrendale, PA, USA, 1991.
- [14] W. H. Hunt, "Aluminium metal matrix composites today," *Materials Science Forum*, vol. 331–337, pp. 71–84, 2000.
- [15] B. Guo, M. Song, Y. Jianghong, N. Song, T. Shen, and Y. Du, "Improving the mechanical properties of carbon nanotubes reinforced pure aluminium matrix composites by achieving nonequilibrium interface," *J Mater Des*, vol. 120, pp. 56–65, 2017.
- [16] B. Chen and K. Kondoh, "Sintering behaviours of carbon nanotubes-aluminium powder composites," *J Metall*, vol. 6, no. 9, p. 213, 2016.
- [17] A. M. K. Esawi, K. Morsi, A. Sayed, M. Taher, and S. Lanka, "Effect of carbon nanotube (CNT) content on the mechanical properties of CNT-reinforced aluminium composites," *Composites Science and Technology*, vol. 70, no. 16, pp. 2237–2241, 2010.
- [18] S. C. Tjong, "Recent progress in the development and properties of novel metal matrix nanocomposites reinforced with carbon nanotubes and graphene nanosheets," *Materials Science and Engineering: R: Reports*, vol. 74, no. 10, pp. 281–350, 2013.
- [19] J. A. Jeffrey, S. S. Kumar, P. Hariharan, M. Kamesh, and A. M. Raj, "Production and assessment of AZ91 reinforced with nano SiC through stir casting process," *Inside MS*, vol. 1048, pp. 9–14, 2022.
- [20] C. P. Reip and G. Sauthoff, "Deformation behaviour of the intermetallic phase Al3Nb with DO22 structure and of Al3Nb-base alloys: Part I. Physical properties and short-term behaviour," *Intermetallics*, vol. 1, no. 3, pp. 159–169, 1993.

## *Retraction*

# **Retracted: Construction of Facial Expression Recognition Technology of Intelligent Service Robot Based on Nanofiber Flexible Wearable Electronic Skins**

### **Advances in Materials Science and Engineering**

Received 8 January 2024; Accepted 8 January 2024; Published 9 January 2024

Copyright © 2024 Advances in Materials Science and Engineering. This is an open access article distributed under the Creative Commons Attribution License, which permits unrestricted use, distribution, and reproduction in any medium, provided the original work is properly cited.

This article has been retracted by Hindawi following an investigation undertaken by the publisher [1]. This investigation has uncovered evidence of one or more of the following indicators of systematic manipulation of the publication process:

- (1) Discrepancies in scope
- (2) Discrepancies in the description of the research reported
- (3) Discrepancies between the availability of data and the research described
- (4) Inappropriate citations
- (5) Incoherent, meaningless and/or irrelevant content included in the article
- (6) Manipulated or compromised peer review

The presence of these indicators undermines our confidence in the integrity of the article's content and we cannot, therefore, vouch for its reliability. Please note that this notice is intended solely to alert readers that the content of this article is unreliable. We have not investigated whether authors were aware of or involved in the systematic manipulation of the publication process.

Wiley and Hindawi regrets that the usual quality checks did not identify these issues before publication and have since put additional measures in place to safeguard research integrity.

We wish to credit our own Research Integrity and Research Publishing teams and anonymous and named external researchers and research integrity experts for contributing to this investigation.

The corresponding author, as the representative of all authors, has been given the opportunity to register their agreement or disagreement to this retraction. We have kept a record of any response received.

### **References**

- [1] F. Li, C. Li, and Y. Liu, "Construction of Facial Expression Recognition Technology of Intelligent Service Robot Based on Nanofiber Flexible Wearable Electronic Skins," *Advances in Materials Science and Engineering*, vol. 2022, Article ID 8669298, 10 pages, 2022.

## Research Article

# Construction of Facial Expression Recognition Technology of Intelligent Service Robot Based on Nanofiber Flexible Wearable Electronic Skins

Feigao Li , Chenyang Li, and Yue Liu

Henan Polytechnic, Zhengzhou 450046, Henan, China

Correspondence should be addressed to Feigao Li; [lifeigao123@sina.com](mailto:lifeigao123@sina.com)

Received 8 July 2022; Revised 10 August 2022; Accepted 8 September 2022; Published 30 September 2022

Academic Editor: K. Raja

Copyright © 2022 Feigao Li et al. This is an open access article distributed under the Creative Commons Attribution License, which permits unrestricted use, distribution, and reproduction in any medium, provided the original work is properly cited.

Recognizing human features is a highly significant and popular research topic in academia today, especially with regard to human intervention and computer intelligence. If you want your computer to have real intelligence, then the computer must first learn to understand human feelings, and facial expressions often contain rich emotional information. Clearly, recognizing human features is indispensable for the future intelligent development of computers. There are always a few components and many researchers are involved. Compared with the traditional facial expression recognition method, which needs to manually define features and artificially perform appropriate feature extraction, a great advantage of deep learning is to remove the disadvantages that require a lot of human intervention, thereby reducing the uncertainty of expression recognition. In recent years, deep processing has led to outstanding gains in numerous domains, including robotics, computer graphics, and natural language processing. Therefore, this article applies a popular recognition algorithm based on deep learning, combined with a nanofiber flexible wearable electronic skin, and applies it to the field of facial expression recognition. Functional expression identification is an essential goal of the external analysis of human features. Mature facial expression recognition technology has great application values.

## 1. Introduction

Smart service robots based on nanofiber flexible wearable electronic skins are various high-tech integrated smart devices that can provide humans with necessary services in an unstructured environment mainly focusing on the application requirements of service robots and dangerous work robots. Intelligent service robot technology based on nanofiber flexible wearable electronic skins involves many fields, such as machinery, electronics, materials, computers, sensors, control, and medicine. It requires brainstorming and multifaceted collaborative research [1]. The robot must be able to understand and respond to people's needs by listening, speaking, observing people's movements, expressions, etc. In an unstructured environment, robots must quickly collect and quickly process the necessary information for all environments, including a wide variety of static and dynamic objects, including humans and animals.

Advanced hybrid drive technology, flexible robot technology, tactile technology, visual technology, and artificial intelligence technology make service robots, especially humanoid service robots, smarter, and more friendly. Not only can they walk, run, communicate and express emotions but they can also learn and grow their intelligence like children. The key technologies that China is currently mastering are, namely, environmentally aware sensors and signal processing methods. The service robot must observe and identify the surrounding environment while working. The more sensors, the more information the surrounding environment acquires and the more complementary and redundant the various sensor information is in space and time, the more they are combined by some kind of operation and optimization. To describe and accurately identify the environment, intelligent control is the key technology of the robot that mainly includes the following: neural network, paste control, and optimization calculation. Fuzzy control is

a control method that uses the basic theory of fuzzy mathematics. It generally has the following 5 principal sections: defining parameters, ambiguities, a repository of information, illogical determination, and defuzzification. Artificial neural network control is inferred from the activities of humans and creatures [2]. The characteristics of neural networks are information processing and reasoning, association, and thinking. Navigation and positioning: The multisensor fusion technology and artificial neural network control in the service robot system can realize the autonomous positioning and navigation of the service robot. Route plan: Path planning refers to finding a route between the initial situation and the desired goal situation within the service motor's construction space in order to escape from barriers. The artificial intelligence approach is a developed and productive programming approach to conventional arithmetic. It allows route programming processes using AI tools but without thinking about whether the route is best or not. Smart route programming approaches can provide greater barrier avoidance performance, accelerate programming faster, and enable real-world solutions. Human-robot interaction technology. Since the aim of smart computing research is to enable robots to work smartness and serve humans as if they had a "brain," there must be human instruction and domination, detection, and maintenance of the robot, and feedback from the robot on the outcomes of its operations. It mainly includes technologies that include texture awareness, synthesizing and recording spoken language, identifying and managing pictures, and performing computer interpretation [3]. At present, the research on the more popular intelligent service robots in foreign countries is mainly concentrated in Germany, Japan, and the United States and has already been adopted by a variety of companies. Due to the economic prosperity, the increasing demand for life in China and the increase in the proportion of elderly people caused by family planning policies, and the problem of elderly care, many robotic R&D companies have begun to shift their research focus to the development of intelligent service robots and have made relatively large achievements in this area.

Following the rapid growth of synthetic AI and computer vision, there is a growing demand for intelligent emotional feedback and anthropomorphic person-machine engagement. As one of the key components of AI human-computer communication technology, the recognition of functional facial expressions has attracted a lot of focus in recent years. Human expressions can be divided into macro expressions and microexpressions. The study of macroscopic expressions has been more than 20 years old and has achieved certain results. Microexpressions are spontaneous and unconscious expressions in a very short time. Changes, which occur for a short time, are difficult to capture by humans. Therefore, high-speed cameras need to be introduced to capture and analyze them one frame at a time. However, this work is still not something that ordinary people can do and requires some experience. The psychology expert can complete it. What we have to do is to help humans recognize expressions through deep learning. Facial expression recognition refers to the analysis of human facial

expressions and changes through computer pattern recognition and machine learning algorithms and then judges people's inner emotions and thought activities, thereby obtaining a more intelligent human-computer interaction environment. The machine learning method based on traditional manual custom feature classification has gradually become the main method for the automatic recognition of facial expressions. A series of research results have been obtained, but functional features are influenced by numerous parameters, such as the influence of the natural environment, such as illumination and angle. As Along with the influence of individual differences in ethnicity, gender, age, etc., traditional methods have many difficulties in manually customizing features [4]. The concepts and advancements of profound training have provided innovative ideas and approaches for researchers working in the visual identity field. It replaces artificial signature collection in the form of effective techniques for unmonitored or quasi-supervised signature acquisition and stratified signature capture. Fruitful results. Thanks to the use of the graphic processing unit (GPU) and the improvement of computing performance, the convolutional neural network (CNN) has achieved a series of eye-catching performances in the field of image recognition, including AlexNet and VGGNet. The network structure such as ResNet has won many times in the ILSVRC competition, and its results have also been applied to various image recognition tasks. Currently, profound training, specifically convergent cognitive approaches to facial expression recognition, has become the mainstream approach to automatic facial expression recognition. However, there are also difficult problems in the research of facial expression recognition, which are summarized as follows: The human face is a flexible body in a three-dimensional space. It is easy and accurate to build a rigid body model, but the human face is a flexible body in a three-dimensional space, and it is difficult to establish a model. The existence of individual differences affects expression recognition. The experimental results are different for the same expression, due to the influence of individual differences. If the individual difference is greater, the influence on the expression recognition will be greater. When feature extraction, the interference of individual differences cannot be completely avoided, which undoubtedly increases the difficulty of extracting expression features of the same category. The expression itself is different. The expressions of Europeans and Americans are more exaggerated, the emotions are more obvious, while the Asians are more restrained and the expressions are smaller; women and children express more expressive expressions than men; the expressions of old and young people are different. The folds also affect the extraction of expression features and expression recognition in the natural environment. At present, most expression recognition is performed on the published database, and the images in these databases are expressions of the unnatural environment made by volunteers under the guidance of professionals. Most of them are exaggerated and not true to volunteers. The expression of emotions has certain performance components, which are not conducive to the application of actual scenes. Interference from external factors.

The existence of disturbance factors such as illumination, attitude change, and noise in the actual environment not only increases the difficulty of obtaining effective expression information but also is not conducive to popularizing the expression recognition system in practical applications.

About the expression recognition since the beginning of the 21th century, based on a simple knowledge distillation scheme, Gera D uses a single network to complete label inference on large-scale facial expression datasets, and the proposed framework demonstrates its effectiveness and comprehensiveness in the noisy FER dataset [5]. Li et al. fused energy feature vectors and facial feature vectors in their research study, used support vector machine (SVM) to classify the fused feature vector, and finally proved that the proposed method has higher accuracy and stronger generalization transformation ability [6]. Hossain and Yousuf proposed a facial recognition system that uses the currently developed OpenCV Haar Feature-based cascade classifier for face detection, capable of recognizing natural head nods and shakes [7]. Jan and Sajjad proposed a new descriptor called the Weber discrete wavelet transform, which can effectively identify facial expressions, and finally, they observed through experiments that the feature dimension was significantly reduced, while the recognition accuracy was significantly improved [8]. Wang et al. proposed a multi-manifold discriminant analysis method for image feature extraction and finally verified the effectiveness of this analysis method for image feature extraction through experiments [9]. Rusia and Singh proposed two customized CNN models, namely, Proposed Model 1 and Proposed Model 2, to classify generic facial expressions to prevent overfitting [10]. These research methods have carried out a profound research on face recognition to a certain extent.

The emergence of deep learning in recent years has brought new vitality to the field of computer vision [11]. In fact, it has made the research of behavior recognition, face recognition, and semantic segmentation into a new stage and achieved very significant results. The artificial neural network is a very complex nonlinear network [12]. It is composed of a large number of processing units and is an abstraction and modeling of the human brain or biological neural network. Since the artificial neural network was proposed, after decades of development, researchers still cannot interpret or completely imitate the working mechanism of the brain. For a while, the research study only stays in the shallow neural network. In recent years, the development of deep neural networks has brought about another phase of neural network development. Deep learning is also a kind of neural network. Deep learning refers to the way of using artificial neural networks to learn features by relying on powerful graphics computing power and the development of big data at present. The basic idea is that through convolutional neural networks (CNN) and other methods to carry out complex calculations of a large number of training datasets and update network parameters through back-propagation, finally enabling the trained model to better reflect the data characteristics [13]. In order to solve the problem of expression recognition in traditional methods, deep learning seems to be a good tool. However, deep

learning needs to be trained with a higher number of databases in order to obtain representative features, otherwise, it will cause over-fitting, etc. Problems. Following the triadic categorization scheme in profound understanding techniques and operations, the profound understanding structures are broadly classified into the following three types: (1) Asocial or spontaneous deep systems: The profound Internet produces symptoms validly through Internet coding without employing object tags, so it is also known as a generative method. For example, the defined branch neural network (DBN), revolving network nature (RNN), and the like. (2) Deep forests with monitored teaching: Significantly, superintended training means that profound systems use labeling of object types, either explicitly or obliquely, to create distinctions for the purpose of modality selection, so they are also known as distinguishing depth networks, such as curvilinear neural nets (CNNs) and reciprocal neural nets (RNNs). (3) Hybrid deep forests: "Hybrid" refers to a conjunction of unsupervised and monitored training, such as the DBN-CNN hybrid model for pretraining deep convolutional neural networks using a generative DBN.

According to the aforesaid diagnosis, this article suggests that the facial expression recognition operation based on profound acquisition improves the accuracy of expression recognition, the average accuracy rate is improved by 2%, and it is faster than the popular expression recognition algorithm. Moreover, through the combination of deep face-based face verification algorithms, different expressions of the same person can be obtained, which effectively helps to further analyze facial expressions.

## 2. Proposed Method

Expression recognition can be deeply studied through deep learning [14]. The profound acquisition is a division of methodological training. The purpose is to simulate the structure of the brain's neural network by building a model. When processing data (images, voices, texts, etc.), it is a multilevel structure to learn features. Deep learning can be divided into deep concessional bridging systems, profound conviction systems, profound Boltzmann systems, and compounded autoencoders according to the model structure. The deep involitional nerve structure is a type of recurrent nerve structure designed to process multidimensional data [15].

*2.1. The Overall Framework of Expression Recognition Based on Deep Convolutional Neural Networks.* In this section, a dynamic expression identification system using profound involitional integer systems is designed [16]. The system consists of a computer camera and software function modules. The video image information is collected in real time by the camera in a real environment, and each frame of the video is separately calculated. In the software part, first, the Haar classifier is used for face detection. Second, the obtained face image is preprocessed to obtain the face gray image; the obtained gray image is input to the trained deep convolutional neural network again. Finally, the resulting



expression features are entered into the SoftMax classifier for expression classification. Real-time dynamic facial expression recognition [17].

The block diagram of the expression recognition system based on deep convolutional neural network is shown in Figure 1.

**2.2. Face Detection Using the Haar Classifier.** This section uses the face detection method based on the Haar-like feature and the AdaBoost algorithm, namely, the Haar classifier algorithm [18]. This algorithm uses the Viola–Jones target detection framework, which is a real-time object detection method, which can realize the first frame from video. It positions the face to achieve real-time expression recognition. The integral graph algorithm can be used to quickly calculate Haar-like features with different sizes and positions. The integral image value at a pixel  $(x, y)$  in the image is defined in references [19, 20]:

$$\gamma\gamma(x, y) = \sum_{x' \leq x, y' \leq y} \gamma(x', y'), \quad (1)$$

where  $\gamma\gamma(x, y)$  is the integral image and  $\gamma(x, y)$  is the original image. We pass the following iteration formula [21, 22]:

$$\begin{aligned} s(x, y) &= s(x, y-1) + \gamma(x, y), \\ \gamma\gamma(x, y) &= \gamma\gamma(x-1, y) + s(x, y). \end{aligned} \quad (2)$$

Once the image is scanned, when the pixel in the lower right corner of the image is reached, the constructed image is shown in Figure 2:

Wherein, in the integral image, point  $a$  represents the sum of the pixel values of area A, point  $b$  represents the sum of the pixel values of the two areas A and B, point  $c$  represents the sum of the pixel values of the two areas A and C, and point  $d$  represents the sum of the pixel values of the two areas A and C. The sum of the pixel values of the four regions A, B, C, and D. Therefore, any rectangle can be derived from the integral of the 8 rectangular corner points [23, 24].

The AdaBoost algorithm trains the identical narrow classifier on separate practice episodes. The partial categories acquired from separate practice episodes are then combined to form a definitive and powerful categorizer. The AdaBoost algorithm is used because the Haar-like features have high dimensionality and it is necessary to choose them with a particular method and incorporate them into a powerful categorizer to examine a human face [25].

$$h(x) = \begin{cases} 0, & \text{other,} \\ 1, & \sum_{t=1}^T a_t h_t(x) \geq \frac{1}{2} \sum_{t=1}^T a_t. \end{cases} \quad (3)$$

**2.3. Emoticon Image Preprocessing.** Geometric normalization. The MTCNN algorithm is used to detect the position of the face and extract the key points of the face. The center point of each eye is calculated according to the above-mentioned face key points and connection, and the angle

between the horizontal line is calculated. According to this angle, we affine the picture. Thereby, the horizontally aligned picture can be obtained. At this time, the face is cut according to a certain scale factor, and the degree change and the face rotation can be processed by the abovementioned method. Grayscale normalization. The picture pixels are normalized to  $[0, 1]$ , mainly to reduce image quality problems caused by illumination changes.

**2.4. Training Deep Convolutional Neural Network.** The normal decomposition paradigm employed in building deep decomposed recurrent nets commonly consists of three primary levels, including a decomposition level, a pooling level, and a wholly concatenated level. Different layers have different functions. A neural network is capable of image recognition, its input has a lot of pixels. The first layer of computing units can only recognize a few shapes, such as the difference between light and dark, and the second layer of neurons is transmitted to the first layer of neurons. As a result, the analysis obtains information such as edges and angles, and continues abstracting layer by layer and eventually obtaining high-level features that are closer to the nature of the research object [26].

Given the input, the calculation process for the entire network is as follows:

For convolutional layer input  $X$ , the convolution process is as follows [27, 28]:

$$\text{con} = f\left(\sum_{i,j \in M} x_{i,j} w_{m-i,n-j} + b\right), \quad (4)$$

where  $x$  represents the element in the convolutional region of input  $X$ ,  $w$  represents the element in the convolution kernel,  $m, n$  represents the size of the convolution kernel,  $b$  represents the offset, and  $f$  represents the ReLU activation function.

For the pooling layer input  $y$ , the pooling process is [9]

$$\text{pool} = \text{down}(\max(y_{i,j})), i, j \in p, \quad (5)$$

where  $y$  represents the pooling layer input element, and  $\text{down}$  is the downsampling process, which retains the maximum value in the pooled area.

For the fully connected layer input  $G$ , the formula is as follows [29]:

$$\text{full} = f(w * z + b), \quad (6)$$

where  $z$  represents the input element,  $w$  represents the weight,  $b$  represents the offset, and  $f$  represents the ReLU activation function.

For the input layer input, the formula is as follows [30]:

$$p(y = j | x; w) = \frac{e^{w_j x}}{\sum_{l=1}^K e^{w_l x}}. \quad (7)$$

**2.5. Expression Classification.** This chapter uses SoftMax as the expression recognition classifier. We set the training set to  $\{(x^{(1)}, y^{(1)}), \dots, (x^{(m)}, y^{(m)})\}$  with input features  $x^i \in R^{n+1}$ , and the class is labeled  $y^{(i)} \in \{1, 2, k, \dots, 7\}$ :

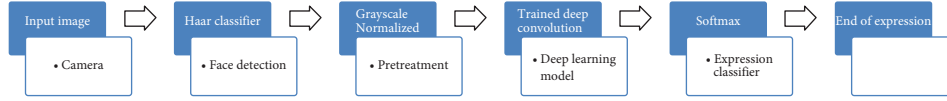


FIGURE 1: Block diagram of the expression recognition system based on the deep convolutional neural network.

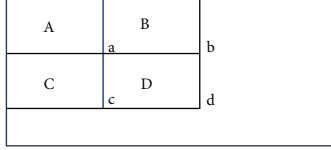


FIGURE 2: Integral image calculation demonstration.

$$h_{\theta}(x) = \begin{bmatrix} p(y^{(i)} = 1 | x^{(i)}; \theta) \\ p(y^{(i)} = 2 | x^{(i)}; \theta) \\ \vdots \\ p(y^{(i)} = k | x^{(i)}; \theta) \end{bmatrix} \quad (8)$$

$$= \frac{1}{\sum_{j=1}^k e^{\theta_j^T x^{(i)}}} \begin{bmatrix} e^{\theta_1^T x^{(i)}} \\ e^{\theta_2^T x^{(i)}} \\ \vdots \\ e^{\theta_k^T x^{(i)}} \end{bmatrix}$$

where  $p(y^{(i)} = j | x^{(i)})$  represents the probability  $\theta_1, \theta_2, \dots, \theta_k \in R^{n+1}$  of the input  $x^{(i)}$  of the  $i$ th sample belonging to the category  $j$ . The system cost function is as follows [31, 32]:

$$J(\theta) = -\frac{1}{m} \left[ \sum_{i=1}^m \sum_{j=1}^k 1\{y^{(i)} = j\} \log \frac{e^{\theta_j^T x^{(i)}}}{\sum_{i=1}^k e^{\theta_j^T x^{(i)}}} \right]. \quad (9)$$

Cost function gradient  $\nabla_{\theta} J(\theta)$ :

$$\nabla_{\theta} J(\theta) = -\frac{1}{m} \sum_{i=1}^m \left[ x^{(i)} \left( 1\{y^{(i)} = j\} - p(y^{(i)} = j | x^{(i)}; \theta) \right) \right]. \quad (10)$$

### 3. Experiments

In this paper, two expression image libraries are used in the experiment. One is the standard image library JAFFE, and the other is to collect the image library dataset, which is processed on the Internet. JAFFE is a database of expressions established in Japan. It is used by a large number of facial expression recognition researchers and has a certain persuasive power. The JAFFE facial expression image library is compiled by ten Japanese women as models. Each expression selects three to four images according to the size of the amplitude. Each person makes seven expressions to collect,

and together, there are 213 images, depending on the resolution of the image. It is  $256 \times 256$ . Due to the needs of the experiment, the original pixels in the expression library will be sampled, and image libraries of four different pixels of  $16 \times 16$ ,  $32 \times 32$ ,  $64 \times 64$ , and  $128 \times 128$  will be created. The comparison of the samples in the JAFFE image library at different resolutions shows that lower the resolution, the more blurred the information carried by the image.

The second database, which collected about 13 people, each had 75 emoticons, for a total of 965 images. The image resolution is  $64 \times 64$ . Similarly, this paper has established  $16 \times 16$  and  $32 \times 32$  expression libraries, respectively. Due to the mixed expressions in this expression database, a relatively obvious and representative expression image was selected, and a total of six expressions were selected, which were happy, surprised, sad, neutral, angry, and disgusted.

The experimental code implementation is in the Python language, the IDE is PyCharm graphical interface tool, the running environment is window7, memory 4G, i5 processor. Since the experiment involved image processing, a large number of matrix operations were required, so the program was selected to run on the GPU. This not only improves the efficiency of the experiment but also shortens the experiment time. Since there are many unpredictable situations during the experiment, in order to ensure the validity of the experimental results, five cross-validation methods were carried out in the experiment of the paper. Here, the image samples of the established facial expression image library are equally divided into 5 for each experiment, 4 sets of images were used for network training, and the rest were used for experimental tests. The process of training to identify such an experiment is repeated five times; then, the average of the five experimental results is the experimental result of the paper.

### 4. Discussion

In this paper, the face image is grayscaled and grayscale normalized before image processing. Figure 3 shows the image processing results in this paper, where Figure 3(a) is the color image. Figure 3(b) is the image after the image is grayscaled, and Figure 3(c) is the image after the image grayscale is normalized. It can be seen from the figure that after the image gray processing, there is no change in the overall structure of the image, and it is advantageous to extract the object features for analysis after preprocessing the image.

After preprocessing the image, this section of the experiment constructs the CNN structure shown in Table 1 for the original expression set of  $32 \times 32$  and  $64 \times 64$  resolutions, respectively. The learning rate setting includes setting the fixed learning rate, the unified local optimal learning rate, and layering. The dynamic local optimal learning rate is trained in three scenarios, and the network convergence comparison is shown in Figures 4 and 5.

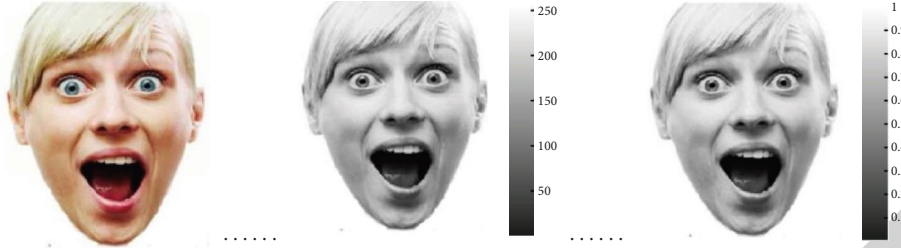


FIGURE 3: Image preprocessing. (a) Color image. (b) Grayscale image. (c) Normalized image.

From the experimental results of Figures 4 and 5, it can be known that this method achieves similar improvement effects in the training of image samples of  $32 \times 32$  and  $64 \times 64$  images with different resolutions. In general, the convergence speed of uniformly setting the local optimal learning rate is higher than the convergence speed of setting the fixed learning rate, and the convergence speed of the dynamic smooth local optimal learning rate adjustment is significantly faster than the convergence speed of uniformly setting the local optimal learning rate. The influence of various setting methods on the convergence speed is mainly reflected in the early stage. This is because the pretraining period is far from the extreme point, which makes the adjustment of the optimal learning rate show obvious advantages. The learning rate optimization accelerates the speed of network convergence and verifies that the proposed method is feasible for the shallow layer enhancement scheme, and the expression classification accuracy based on the method is higher. This dynamic learning rate adjustment method is used to jump out of the local extremum. Points have a beneficial effect.

The learning rate optimization method in this paper brings a certain performance improvement, but it also has defects: the convolutional neural network contains a large number of parameters and calculating the optimal learning rate will incur a certain time cost. If it is optimized for each iteration, it will be optimized once. However, in the case of large data volumes or complex networks, the time loss caused by this will offset the advantage of its convergence speed. In the actual training, the learning rate is updated with the inertia of the learning rate. The shorter the interval between the learning rate adjustment and the longer the convergence step of the network is, the longer the learning rate adjustment interval is, the lower the iterative average time cost is. Choosing the appropriate learning rate adjustment interval requires finding a balance of time performance.

For the purpose of ensuring the credibility of the experimental outcomes and preventing the influence of chance agents, the data in the dataset were separated into components and the cross-validation method was adopted. In this experiment, the images in the JAFFE photoset are separated into 3 sections, 2 of which are used as exercise figures as well as the other section as test figures; the images in the dataset are separated into 5 sections, 4 of which will be used as exercise figures each time. One served as the experimental figure. Table 2 demonstrates the classification

TABLE 1: CNN structure description.

Resolution	Network structure	Convolution kernel	Activation function
$32 \times 32$	$C^6 S^6 C^{13} S^{13}$	5, 5	RReLU + sigmoid
$64 \times 64$	$C^6 S^6 C^9 S^9 C^{12} S^{12}$	9, 5, 5	RReLU + sigmoid

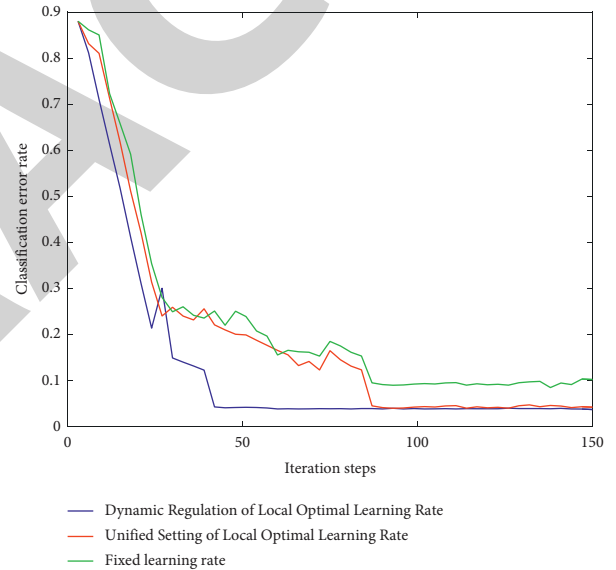


FIGURE 4: Convergence at  $32 \times 32$  using different learning rate schemes.

performance of the algorithm for different expressions in the JAFFE representation database. Table 3 demonstrates the categorization outcomes for various representations in the dataset drainage system database. It is obvious from Tables 2 and 3. In some test sets, the whole network performs better and the correct rate is high, but it is relatively poor in others. The explanation for this is probably the expressive traits that can be derived from the exercise model material. Inadequate access to sufficient training features results in a poor classification of the classifier, a situation that mirrors the principle of the significance of example material for involational systems.

First, the original expression set is balanced then, different degrees of amplification are obtained to obtain a plurality of amplified expression sets, and then the

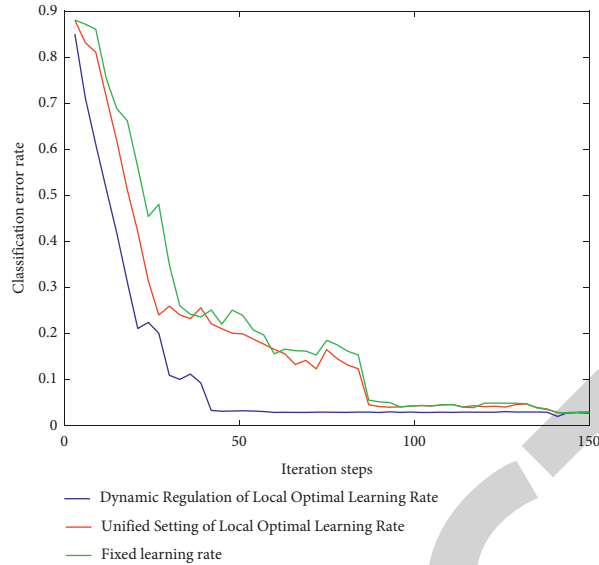
FIGURE 5: Convergence on different  $64 \times 64$  using different learning rate schemes.

TABLE 2: Classification accuracy of different expressions of JAFFE expression library (%).

	Angry	Disgust	Scared	Happy	Neutral	Sad	Surprised	Overall (%)
Test set 1	100	80	100	100	100	90.91	88.89	94.37
Test set 2	100	90	90	81.82	100	100	100	92.96
Test set 3	100	100	81.82	90.91	100	100	100	95.77
Overall (%)	100	89.66	90.63	90.63	100	96.77	96.55	94.37

TABLE 3: Classification accuracy of different expressions of dataset database (%).

	Angry	Disgust	Scared	Happy	Neutral	Sad	Surprised	Overall (%)
Test set 1	88.89	94.44	80	92.86	70.83	96	93.94	88.89
Test set 2	70.37	77.78	80	96.30	68	84	96.97	82.32
Test set 3	77.78	85.71	84.62	100	64	72	93.94	83.33
Test set 4	62.96	94.29	88	89.29	60	82	87.88	80.81
Test set 5	84.48	85.71	72	92.86	64	79.17	100	83.33
Overall (%)	76.30	87.59	80.95	94.26	65.37	82.23	94.55	83.75

amplified expression set is trained using the optimal model determined in the previous section experiment, and some samples are subjected to  $(-10, 0, 10)$  degree, and the mirror flip process amplifies the sample to 151,974 sheets. The network trained a total of 1,000 rounds, with the training batch size set to 512. In training, 75% of the total sample was randomly selected as the training sample, and the remaining 25% was used as the test sample. The results of statistical experiments were compared to compare the classification accuracy and generalization ability of models based on different amplification sets. In this section, the data balance uses the SMOTE algorithm to linearly interpolate a small number of dense regions of the original expression set. The processed expression set contains a total of 3,500 expression images, and the seven types of expression samples are balanced and each has 500. It is further hoped to improve the generalization ability of the model. In this paper, the existing samples of

the balanced expression set are randomly rotated and distorted to generate new samples, and the new samples are added to the existing training set to obtain the amplification set. According to the need for experimental comparison, the CNN models established in the previous section were used to train a plurality of different degrees of amplification sets, and the ability to obtain the expression classification is shown in Table 4. Generalization ability of the amplification set. Figure 6 shows the simulation results of 35,000 iterations (about 470 rounds). On the whole, the loss on the test set gradually decreases with the number of iterations. After 35,000 times, the loss tends to be stable at around 0.2 and no longer decreases. The accuracy rate on the test set gradually increases with the number of iterations. Through gradient learning and continuous learning and updating of the model weight parameters, the classification ability of the network is getting stronger and stronger, and the accuracy of the final test set is basically stable.

TABLE 4: Expression recognition using different amplification ratio data.

Amplification factor	Input map resolution	Classification accuracy (amplification) (%)
1	32 × 32	98.74
	64 × 64	98.71
2	32 × 32	98.52
	64 × 64	98.76
3	32 × 32	98.76
	64 × 64	98.87
4	32 × 32	98.84
	64 × 64	98.90
5	32 × 32	98.85
	64 × 64	98.91
6	32 × 32	98.85
	64 × 64	98.90

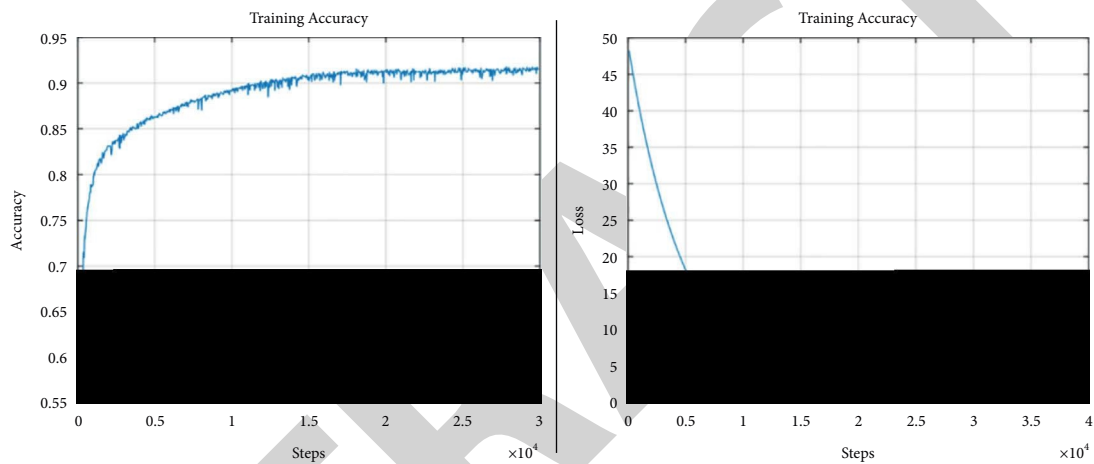


FIGURE 6: Accuracy and loss trend curve of training on the database.

Data amplification is beneficial to improve the generalization ability of the model, and the richer the amplified data, the stronger the generalization ability, because: The CNN structure itself is a complex network with a large number of parameters, and the richness of the dataset can alleviate its overlearning of existing samples. The random data amplification method in this paper differentiates the information contained in the same kind of expression, which is beneficial to the model because enables it to pay more attention to the common features in the process of fitting the data. In addition, as can be seen from Table 2, the data preprocessing in this paper has a positive impact on the expression classification ability, but the improvement of the classification ability does not increase linearly with the amplification multiple, because the data amplification is only limited to the existing data. A manual processing method is not a panacea, and the quality of the original data is often the bottleneck of the final recognition performance.

## 5. Conclusions

In today's society, facial expressions are a popular form of expressing affective messages in relation to public events. Facial expressions contain a diverse collection of signals,

including an individual's affective mood state, individual traits, and perceptions of events. In addition, numerous elements relating to an individual's state of mood, mental conditions, and physiological status are also relevant to the messages contained in embedded visual representations. Psychologist Mehrabian proposed that in the process of human communication, only 7% of the information is expressed by language. Compared with this, facial expression is 55% of the information, which is the most of the heavy part of the information. It can be seen that the research on the facial expression recognition technology of the intelligent service robot of the nanofiber flexible wearable electronic skin can help us obtain a lot of valuable information and then analyze and study the human psychological and physiological state, thereby improving people's living standards.

In order to achieve the purpose of quantitative analysis of human emotions, research studies on human expression recognition technology is the key to success. At the same time, expression recognition plays an indispensable role in intelligent robots and smart cities. With the continuous development of artificial intelligence and machine learning technology, the demand for intelligent human-computer interaction in society is also expanding. With the deepening of research, many outstanding image open-source

frameworks and high-performance hardware devices have provided good technical support for the development of facial expression recognition. At present, the expression recognition technology of intelligent service robots with nanofiber flexible wearable electronic skin is not a unique research topic in the field of computer vision but a cross-domain topic in many fields such as biology and psychology. The research results have important implications for many fields, such as human-computer interaction, healthcare, and safe driving.

Although this paper uses the intelligent service robot facial expression recognition technology to conduct a profound study on the wearable electronic skin of nano-flexible fibers, there are still many deficiencies. The depth and breadth of the research in this paper is not enough. Moreover, the acquisition is carried out under absolutely ideal conditions, and the completeness and effectiveness are not enough. In future works, we will study suitable methods and means from more angles based on the existing technology and level and continuously improve the recognition quality.

### Data Availability

No data were used to support this study.

### Conflicts of Interest

The authors declare that there are no conflicts of interest regarding the publication of this article.

### References

- [1] Z. Lv and L. Qiao, "Deep belief network and linear perceptron based cognitive computing for collaborative robots," *Applied Soft Computing*, vol. 92, Article ID 106300, 2020.
- [2] Z. Lv, S. Zhang, and W. Xiu, "Solving the security problem of intelligent transportation system with deep learning," *IEEE Transactions on Intelligent Transportation Systems*, vol. 22, no. 7, pp. 4281–4290, 2020.
- [3] Z. Lv, D. Chen, and Q. Wang, "Diversified technologies in internet of vehicles under intelligent edge computing," *IEEE Transactions on Intelligent Transportation Systems*, vol. 22, no. 4, pp. 2048–2059, 2021.
- [4] A. admin and M. Gupta, "Ensemble learning for facial expression recognition," *Fusion: Practice and Applications*, vol. 2, no. 1, pp. 31–41, 2020.
- [5] D. Gera and S. Balasubramanian, "Consensual collaborative training and knowledge distillation based facial expression recognition under noisy annotations," *International Journal of Engineering Trends and Technology*, vol. 69, no. 7, pp. 244–254, 2021.
- [6] D. Li, Z. Wang, Q. Gao, Y. Song, X. Yu, and C. Wang, "Facial expression recognition based on Electroencephalogram and facial landmark localization," *Technology and Health Care*, vol. 27, no. 4, pp. 373–387, 2019.
- [7] M. S. Hossain and M. A. Yousuf, "Real time facial expression recognition for nonverbal communication," *The International Arab Journal of Information Technology*, vol. 15, no. 2, pp. 278–288, 2018.
- [8] Z. Jan and M. Sajjad, "Facial expression recognition using weber discrete wavelet transform. Journal of intelligent & fuzzy systems," *Applications in Engineering and Technology*, vol. 33, no. 1, pp. 479–489, 2017.
- [9] Y. Wang, X. Ma, and P. Qian, "Wind turbine fault detection and identification through PCA-based optimal variable selection," *IEEE Transactions on Sustainable Energy*, vol. 9, no. 4, pp. 1627–1635, 2018.
- [10] M. K. Rusia and D. K. Singh, "An efficient CNN approach for facial expression recognition with some measures of overfitting," *International Journal of Information Technology*, vol. 13, no. 6, pp. 2419–2430, 2021.
- [11] P. Y. Hong, L. M. Huang, C. Y. Chang, and C. A. Lin, "Lattice Boltzmann simulations of cavity flows on graphic processing unit with memory management," *Journal of Mechanics*, vol. 33, no. 6, pp. 863–871, 2017.
- [12] K. H. Jin, M. T. McCann, E. Froustey, and M. Unser, "Deep convolutional neural network for inverse problems in imaging," *IEEE Transactions on Image Processing*, vol. 26, no. 9, pp. 4509–4522, 2017.
- [13] C. Weng, R. B. Ghazali, S. A. Mustafa, A. N. Kareem, and B. A. Khalaf, "Weather forecasting for batu pahat using neural network," *Fusion: Practice and Applications*, vol. 6, no. 2, pp. 64–70, 2021.
- [14] S. S. S. Kruthiventi, K. Ayush, and R. V. Babu, "Deepfix: a fully convolutional neural network for predicting human eye fixations," *IEEE Transactions on Image Processing*, vol. 26, no. 9, pp. 4446–4456, 2017.
- [15] H. Chen, Y. Zhang, W. Zhang et al., "A Low-dose CT via convolutional neural network," *Biomedical Optics Express*, vol. 8, no. 2, pp. 679–694, 2017.
- [16] M. K. Kim, "Contactless palmprint identification using the pretrained VGGNet model," *Journal of Korea Multimedia Society*, vol. 21, no. 12, pp. 1439–1447, 2018.
- [17] Z. Lu, X. Jiang, and A. Kot, "Deep coupled resnet for low-resolution face recognition," *IEEE Signal Processing Letters*, vol. 25, no. 4, pp. 526–530, 2018.
- [18] R. Baraniuk, S. Foucart, D. Needell, Y. Plan, and M. Wootters, "One-bit compressive sensing of dictionary-sparse signals," *Information and Inference: A Journal of the IMA*, vol. 7, no. 1, pp. 83–104, 2017.
- [19] N. Anselmi, G. Oliveri, M. A. Hannan, M. Salucci, and A. Massa, "Color compressive sensing imaging of arbitrary-shaped scatterers," *IEEE Transactions on Microwave Theory and Techniques*, vol. 65, no. 6, pp. 1986–1999, 2017.
- [20] H. Rauhut and C. Schwab, "Compressive sensing Petrov-Galerkin approximation of high-dimensional parametric operator equations," *Mathematics of Computation*, vol. 86, no. 304, pp. 661–700, 2016.
- [21] B. Manavalan and J. Lee, "SVMQA: support-vector-machine-based protein single-model quality assessment," *Bioinformatics*, vol. 33, no. 16, pp. 2496–2503, 2017.
- [22] D. Tien Bui, Q. P. Nguyen, N. D. Hoang, and H. Klempe, "A novel fuzzy K-nearest neighbor inference model with differential evolution for spatial prediction of rainfall-induced shallow landslides in a tropical hilly area using GIS," *Landslides*, vol. 14, no. 1, pp. 1–17, 2017.
- [23] T. Wiatowski and H. Bölcskei, "A mathematical theory of deep convolutional neural networks for feature extraction," *IEEE Transactions on Information Theory*, vol. 64, no. 3, pp. 1845–1866, 2018.
- [24] S. Choi, J. H. Shin, J. Lee, P. Sheridan, and W. D. Lu, "Experimental demonstration of feature extraction and dimensionality reduction using memristor networks," *Nano Letters*, vol. 17, no. 5, pp. 3113–3118, 2017.



## *Retraction*

# **Retracted: Effect of Reinforcement on Tensile Characteristics in AA 5052 with ZrC and Fly Ash-Based Composites**

### **Advances in Materials Science and Engineering**

Received 26 December 2023; Accepted 26 December 2023; Published 29 December 2023

Copyright © 2023 Advances in Materials Science and Engineering. This is an open access article distributed under the Creative Commons Attribution License, which permits unrestricted use, distribution, and reproduction in any medium, provided the original work is properly cited.

This article has been retracted by Hindawi, as publisher, following an investigation undertaken by the publisher [1]. This investigation has uncovered evidence of systematic manipulation of the publication and peer-review process. We cannot, therefore, vouch for the reliability or integrity of this article.

Please note that this notice is intended solely to alert readers that the peer-review process of this article has been compromised.

Wiley and Hindawi regret that the usual quality checks did not identify these issues before publication and have since put additional measures in place to safeguard research integrity.

We wish to credit our Research Integrity and Research Publishing teams and anonymous and named external researchers and research integrity experts for contributing to this investigation.

The corresponding author, as the representative of all authors, has been given the opportunity to register their agreement or disagreement to this retraction. We have kept a record of any response received.

### **References**

- [1] K. Mallikarjuna, M. K. Harikeerthan, B. S. Shubhalakshmi et al., "Effect of Reinforcement on Tensile Characteristics in AA 5052 with ZrC and Fly Ash-Based Composites," *Advances in Materials Science and Engineering*, vol. 2022, Article ID 7070304, 7 pages, 2022.



## Research Article

# Effect of Reinforcement on Tensile Characteristics in AA 5052 with ZrC and Fly Ash-Based Composites

**K. Mallikarjuna,<sup>1</sup> M. K. Harikeerthan,<sup>2</sup> B. S. Shubhalakshmi,<sup>2</sup> K. S. Vinay Kumar,<sup>2</sup> Ravindra Pratap Singh,<sup>3</sup> Maddali Srikanth,<sup>4</sup> Y. Krishna Srinivasa Subba Rao,<sup>5</sup> Suresh Kumar,<sup>6</sup> and Aggegnenu Shara Shata<sup>7</sup>**

<sup>1</sup>Department of Mechanical Engineering, Government Polytechnic, Kudligi-583135, Karnataka, India

<sup>2</sup>Department of Civil Engineering, Dayananda Sagar Academy of Technology and Management, Bangalore 560082, Karnataka, India

<sup>3</sup>Department of Mechanical Engineering, GLA University, Mathura, Uttar Pradesh 281406, India

<sup>4</sup>Department of Humanities and Basic Sciences, Aditya Engineering College (A), Surampalem, Andhra Pradesh 533437, India

<sup>5</sup>Department of Mechanical Engineering, Aditya College of Engineering, Valasapalle, Andhra Pradesh, India

<sup>6</sup>Department of General Engineering (MECH), Panimalar Engineering College Chennai City Campus, Chennai, Tamil Nadu, India

<sup>7</sup>Faculty of Mechanical Engineering, Arba Minch Institute of Technology, Arba Minch University, Ethiopia

Correspondence should be addressed to Aggegnenu Shara Shata; [agegnehu.shara@amu.edu.et](mailto:agegnehu.shara@amu.edu.et)

Received 5 July 2022; Revised 8 September 2022; Accepted 10 September 2022; Published 30 September 2022

Academic Editor: K. Raja

Copyright © 2022 K. Mallikarjuna et al. This is an open access article distributed under the Creative Commons Attribution License, which permits unrestricted use, distribution, and reproduction in any medium, provided the original work is properly cited.

Aluminum Alloy 5052/ZrC/fly ash composites' tensile properties are changed by the addition of reinforcements and thermal exposure, according to this study. The precipitation hardening of samples manufactured with various weight percent of fly ash and zirconium carbide was employed to improve the properties under thermal circumstances. The tensile properties of reinforced and heat-treated specimens were studied in a series of scientifically-designed experiments. Tensile strength and yield strength rise up to 200°C, after which they begin to decrease slightly (i.e., 250°C) based on the results of the research. Adding reinforcements and exposing the composites to heat increases their elastic modulus which decreases the percentage of El of the composites substantially. Several factors contribute to composites' increased strength and elastic modulus, the diffusion process, temperatures, and reinforcement composition. It is also possible to manufacture hybridized composite mechanisms for numerous automotive and aviation industries utilizing optimization studies, which interpolate the findings of several sets of parameters to make the process easier.

## 1. Introduction

The examination of required materials for certain applications to enhance the ability to communicate has helped to aid the most current advances in the development of composites [1]. Airplanes are increasingly using aluminum composites because of their better tensile and yield strength and corrosion resistance, which makes them ideal for use in aircraft structures. High-speed flight conditions need the use of composite materials that can withstand high temperatures

[2]. As a result, they've widened the scope of their composites research to encompass uses in aircraft operating at higher Mach numbers and temperatures ranging from 200–250°C [3]. Furthermore, for aerospace industries such as wing structures, airframes and heat exposure of Al composites to maximum temperatures are critical [4]. High-strength alloys are castable and resistant to corrosion features of aluminum alloys are particularly impressive [5]. High-temperature applications have seen an increase in the characteristics of Al castings synthesized by chemical stir

casting [6]. This work utilizes aluminum oxide particles as reinforcement for studying wear and increasing the effective surface area for subsequent applied mechanical retention strengths [7]. Denture bases are made of aluminum, and crowns are made of aluminum ceramics [8]. Dental prosthetics such as dentures, crowns, and bridges are made with zirconia-fused alumina metals. Basic and noble metal alloys predominate over other materials [9]. They are polished and finished after casting. Abrasives made from zirconia-fused alumina metals can be used to grind, sandblast, and treat metals and other materials [10, 11].

Hypo-eutectic Al alloy blends and reinforcements make up the bulk of the composites. The tensile parameters of composites are heavily affected by the carbide particle shape [12–14]. To boost the composites' tensile strength, heat treatment under the T6 temper conditions is applied to them [15]. According to a study by [16], heat treatment improves the tensile properties of Aluminum Alloy 7075 composites by increasing the Orowan strength and connection. In their experiment, they used an AA 7075 alloy as a matrix and E-glass and fly ash as strengthening, all of which were stir cast, treated with solutions, and then water quenched [17]. When the fly-ash size was increased with thermal treatment, researchers observed that grain growth and involution occurred during the matrix phase, which led to enhanced tensile strength [18]. A study by [19] found that inoculation of the composite reinforcements improved the properties of aluminum-fly ash-ZrC hybrid composites after a heat treatment procedure. The tensile properties of an aluminum-7Si-0.35 magnesium alloy matrix supplemented with varied weight percent of  $\text{Al}_2\text{O}_3$  in the range of 2 to 8 were improved owing to particle dispersal and particle-matrix connection [20]. An experiment [21] found that the characteristics of composites enhanced with a rise in fly ash material, which was next followed by microcoring and separation in the composite, all of which were linked to the composites' improved fly ash content. Composites made from L-aluminum alloys and reinforced with ZrC and fly ash [22, 23]. According to research, it is also possible to study the properties of heat treatment, in particular the inoculation caused by fly ash, on parameters of composites. The combination of reinforcements and treatment for a wide variety of thermal cycles has been revealed to enhance TS required for potential automotive and aerospace applications, as proven in this study.

## 2. Materials and Methods

Aluminum Alloy 5052 alloys were reinforced with ZrC with an average particle size of 35 to 70  $\mu\text{m}$ , C-type, and fly ash. It was decided to start with a matrix and then add reinforcements after conducting a ground survey to determine the availability and requirements. The supplier specifications were used to determine the matrix and reinforcement properties, as shown in Tables 1–3.

As a result of their capacity to produce high-performance compounds, AA 5052-ZrC-fly ash composites are made by stir casting. Weighed aluminum AA 5052 pieces were put into a furnace and heated to 700°C in accordance

TABLE 1: Chemical arrangement of the AA 5052.

Materials	Wt.%
Copper	0.10
Zinc	0.10
Chromium	0.35
Magnesium	2.80
Silicon	0.25
Iron	0.40
Manganese	0.10
Aluminum	Balance

TABLE 2: Properties of AA 5052.

Properties	Value
Melting point	605°C
Electrical resistivity	$0.0495 \times 10^{-6} \Omega\text{m}$
Density	2.68 $\text{g/cm}^3$
Modulus of elasticity	70 GPa
Thermal expansion	$23.7 \times 10^{-6}/\text{K}$
Thermal conductivity	138 $\text{W/mK}$

TABLE 3: ZrC arrangement.

Formula	ZrC
IUPAC ID	Zirconium carbide
Molar mass	40.11 $\text{g/mol}$
Melting point	2730°C
Density	3.24 $\text{g/cm}^3$

with the work of [24]. At 600 RPM, the metal was agitated for 10 minutes using a ceramic-coated AISI 316L stirrer, which had been preheated for two and half hours with ZrC and fly-ash flake addition. In order to remove the trapped air, perchloroethane tablets were inserted into melted metal. The melted metal was then maintained at 750°C for 10 minutes before being poured into the preheated die after another round of continuous stirring. A range of temperatures, including 50°C, 100°C, 150°C, 200°C, and 250°C, were used to test the stir cast composites containing various amounts of ZrC and fly ash. These composite samples are tabulated in Table 4, organized with the name of the specimen, matrix composition, reinforcement materials, and the temperature at which the specimen was exposed.

T6-grade thermal treatment included two stages, i.e., the resulting treatment was completed at 530°C for 2 hours after water quenching and ageing for 6 h at 150°C, heating to temperatures of 50°C, 100°C, 150°C, 200°C and 250°C in [25] make Oven operated at 0.5 MPa working pressure and 10 hours soak period in still air with time and temperature controls as per AMS-2771 conditions. They are more easily dissolved because of their siliconisation and exposure to heat.

*2.1. Characterization for Tensile Properties.* ASTM E8-95 requirements as in Figure 1 were followed in the preparation of the composites, which had tensile properties with a gauge width of 12.5 mm and gauge span of 62.5 mm. Fine devices

TABLE 4: Experimental conditions for different trials.

Trials	wt.% of fly ash	HT temperature $\text{°C}$	wt.% of ZrC
L1	0	50	0
L2	0	50	3
L3	0	50	6
L4	0	50	9
L5	0	50	12
L6	3	100	0
L7	3	100	3
L8	3	100	6
L9	3	100	9
L10	3	100	12
L11	6	150	0
L12	6	150	3
L13	6	150	6
L14	6	150	9
L15	6	150	12
L16	9	200	0
L17	9	200	3
L18	9	200	6
L19	9	200	9
L20	9	200	12
L21	12	250	0
L22	12	250	3
L23	12	250	6
L24	12	250	9
L25	12	250	12

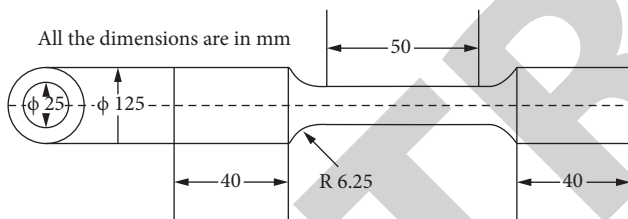


FIGURE 1: Schematic of a tensile test sample.

(Miraj, Maharashtra, India) manufactured TFUN-600 UTM was used to characterize the specimens and the tensile testing results were listed using the strain rate of 1.5 percent per minute (0.00025/s).

**2.2. Taguchi Method.** An important statistical instrument in the study of process optimization is Taguchi's approach. An orthogonal array (OA)-based experimental design was used, followed by a reduction of the experimental strategy and a feasibility study looking at the interactions between various experimental factors. According to the "larger is better" and "smaller is better" conditions for the UTS and YS, Minitab software was used to conduct optimization studies. The characteristic formulas for both conditions are given in (1) and (2), respectively, for each factor level combination.

For "Larger is Better Condition,"

$$\frac{S}{N} = -10 * \log \left( \frac{\sum (1/Y^2)}{n} \right). \quad (1)$$

For "Smaller is Better Condition,"

$$\frac{S}{N} = -10 * \log \left( \frac{\sum (Y^2)}{n} \right). \quad (2)$$

### 3. Results and Discussion

Composite materials were studied to determine their tensile properties, as well as temperature and the weight of reinforcements, affect these properties.

**3.1. Ultimate Tensile Strength (UTS).** According to [26], discoveries associated with fly-ash reinforcement effects on TS of AA 5052 and depicted graph Figure 2 shows that UTS of composites rises with the rise in weightage percent of fly ash owing to inoculation acceleration enhanced by heat exposure in the post-treatment disorder up to a heat of 200°C. Particle dispersions in the matrix are reduced slightly when heat exposure is increased to 250°C in a study by [27]. This reduction in UTS and particle dispersions can be traced back to the increased temperature-induced agglomeration of reinforcements, which can be observed in the study.

Tensile characterization of aluminum AA 5052/ZrC/fly ash compounds was reported by [28]. Results from this investigation were compared to those from the base alloy. When ZrC was added to the mix, mechanical properties such as tensile strength improved up to 3 to 6 wt.%; however, once ZrC was added beyond this range, tensile strength began to decline. They concluded that high-performance hybrid aluminum composites were needed. Here, controlled dispersion of ZrC reinforcing materials with fly ash is combined with T6 thermal treatment to precipitate solute components in the Al solid solution, making it easier to form strong bonds between matrix and reinforcements. This is what the current study is attempting to do. Due to stronger bonding and interstitial strengthening, thermal treatment is necessary in order to improve the composites' tensile characteristics. A similar study in [29] found that the mechanical characteristics of aluminum-fly ash compounds can be enhanced by thermal treatment. Using different weight percentages of fly ash and heat treatments on composite specimens, they were able to improve the mechanical characteristics by altering the crystalline structure, which was then followed by different weight percentages and particle sizes of fly ash.

**3.2. Yield Strength.** Figures 3 show a comparison of the YS of the composite samples at various thermal treatment temperatures and the mix of reinforcements. According to the graph, inoculation rises the YS of the composites, resulting in grain packing and atom connecting, which in turn increases yield strength. This is made possible by thermal exposure at 200°C, which is attributed to the material's increased stiffness. However, yield strength decreases slightly at temperatures higher than 200°C. An interstitial microcoring was formed in the matrix when fly ash was added to the mix, according to investigations by [30]. Using

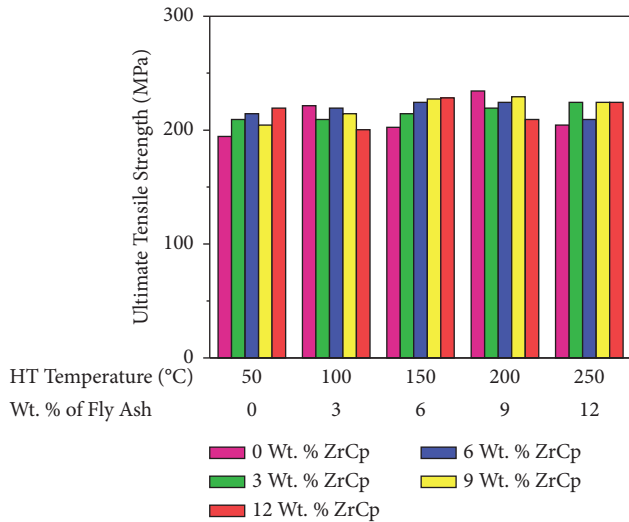


FIGURE 2: Ultimate tensile strength for variant wt.%.

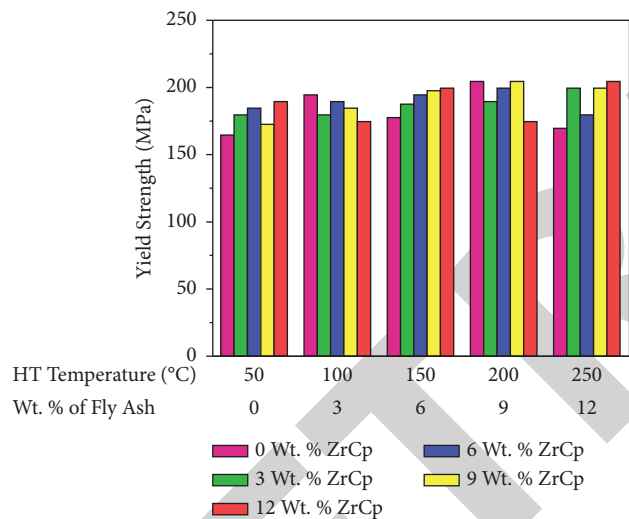


FIGURE 3: Yield strength for different experimental conditions.

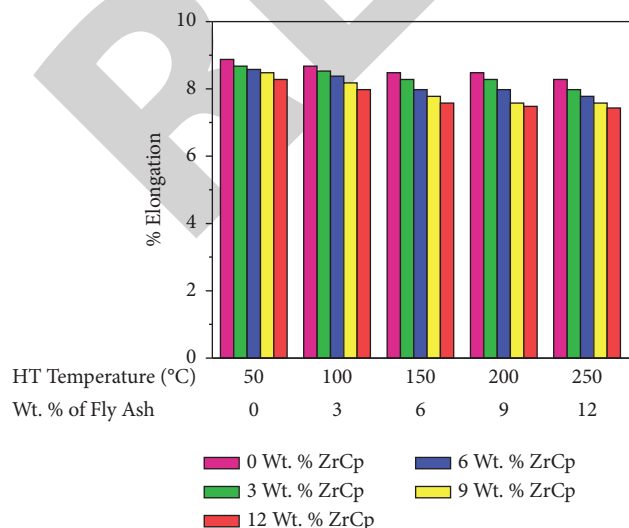


FIGURE 4: % elongation for different experimental conditions.

continual stirring as well as post-treatment thermal revelation, the authors of the current study were able to homogenize fly ash particles in the composites and speed up the inoculation process.

**3.3. Percentage Elongation.** A composite's ductility can be assessed by measuring the percent of elongation, which provides a picture of how far the material can stretch in the plastic zone before snapping. Figure 4 shows the percentage of elongation that the composites experience before they fail. Because the base alloy specimens (AA 5052) lack stiffness and are unable to absorb applied loads before failure, the %El of these samples is greater than that of the composites. Though, the %El reduces with the addition of reinforcements, particularly ZrC reinforcements, which are strong ceramic elements that rise the strength and hardness of a material, causing embrittlement in the composites. Al-C compound bonds are also strengthened by fly ash elements and thermal treatment, which accelerates the response among atoms due to the inoculation of Silicon particles in the Al matrix.

The graph shows how the percentage El of composite samples for various thermal treatment temperatures can be compared as in Figure 4. With a rise in ZrC and fly ash content and thermal treatment temperature, it can be seen that the composites' elongation reduces. Additionally, there is an increase in stiffness as a result of interstitial microcores and cohesive bonding. A study by [31] found that elongation reduces with increasing strength. That is because a higher tensile and Young's modulus means a higher level of strength, which in turn leads to a higher level of stiffness in the material, which reduces the amount of strength connected to elongation. Although the critical softening that occurs as a result of thermal deformation causes a small increase in percent elongation for materials exposed to temperatures above 200°C, strain hardening accelerates embrittlement after that point, as distinguished in the work of [32], who investigated the impact of strong ceramic strengthening on the mechanical performance of comminutions.

#### 4. Optimization Studies for Ultimate Tensile Strength (UTS)

Optimized wt. and percent of ZrC and fly ash in composite samples made by end route stir casting, as well as exposure temperature, were found by Taguchi-based experiments. We can also see how the reinforcements and heat treatment have a direct impact on the UTS of the composites generated by using the optimization results. Tables 5 and 6 contain response tables for SNR and means, respectively, whereas Figures 5 and 6 indicate the main-effect graphs for SNR and means for ultimate tensile strength.

This study found that HT temperature at stage 4 (200°C) and fly ash content at stage 4 (9 wt.%) were the best parameters for maximizing UTS, while zirconium carbide additions in increments of 3 wt.% improved UTS significantly from 3 wt.% all the way up to the maximum

TABLE 5: Signal-to-noise (S/N) ratios response for UTS.

Level	wt.% of fly ash	HT temperature	wt.% of ZrC
1	47.52	47.52	47.21
2	47.73	47.73	47.69
3	47.91	47.91	47.96
4	48.05	48.05	48.05
5	47.95	47.95	48.15
Delta	0.63	0.63	0.98
Rank	2.6	2.6	1

TABLE 6: Mean response for UTS.

Level	Fly ash wt.%	HT temperature	ZrC wt.%
1	209.4	209.4	203.8
2	215.6	215.6	214.4
3	220.4	220.4	222.6
4	225.0	225.0	225.0
5	222.6	222.6	227.2
Delta	15.6	15.6	23.4
Rank	2.5	2.5	1

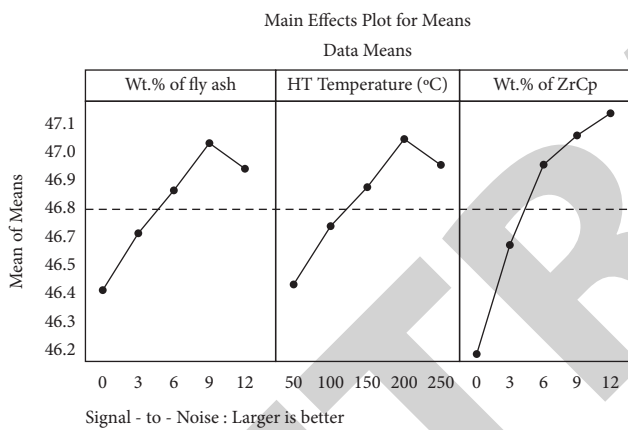


FIGURE 5: Main-effect plot for UTS (S/N ratios).

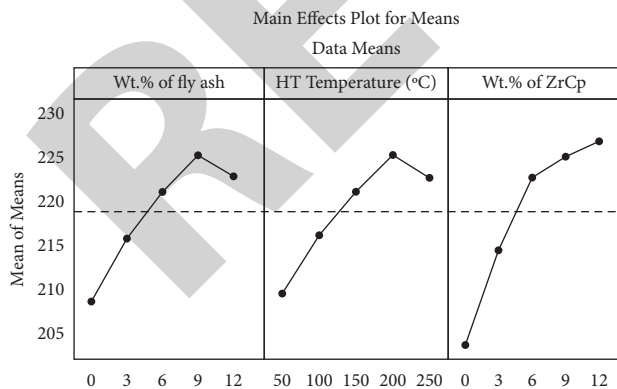


FIGURE 6: Main-effect plot for UTS (mean).

limit of 12 wt.% used in this study. Interactions and synthetic reactions among the particles and subatomic packing in the material, as well as their impact on properties of resulting composite resources, have been studied by [33]. Composite materials' tensile strength has

been found to increase when grain epitaxy is used as material inoculants to speed up the interface response time.

### 5. Conclusions

The study of research results and statistical verifications resulted in appropriate settings for maximizing the strength of created composites, as indicated below.

- (i) Precipitation hardening improved tensile and yield strengths and other properties of the composites exposed to T6 tempered exposure. Because of their inherent connection, which was enhanced by the T6 tempered, composites' elongation % decreased dramatically with the addition of reinforcements.
- (ii) Further optimization of tensile strength discoveries utilizing Taguchi techniques allowed the optimal set of variables for composites to be found, including maximal ultimate tensile strength as well as yield strength.
- (iii) Hence this work experimentally and statistically validated parameters for fabricating and post-treating AA 5052/ZrC/Fly Ash composites for high-quality software, such as structural mechanisms in the automotive and aviation industries, where the materials must have higher Tensile Strength, Yield Strength property characteristics.

### Data Availability

The data used to support the findings of this study are included within the article. Further data or information are available from the corresponding author upon request.

### Conflicts of Interest

The authors declare that there are no conflicts of interest regarding the publication of this paper.

### Acknowledgments

The authors appreciate the support from Arba Minch University, Ethiopia for providing help during the research and preparation of the manuscript.

### References

- [1] H. Yigiter, S. Aydin, H. Yazici, and M. Y. Yardimci, "Mechanical performance of low cement reactive powder concrete (LCRPC)," *Composites Part B: Engineering*, vol. 43, no. 8, pp. 2907–2914, 2012.
- [2] V. Mohanavel, K. Rajan, and M. Ravichandran, "Synthesis, characterization and properties of stir cast AA6351-aluminum nitride (AlN) composites," *Journal of Materials Research*, vol. 31, no. 24, pp. 3824–3831, 2016.
- [3] M. Toozandehjani, N. Kamarudin, Z. Dashtizadeh, E. Yee Lim, A. Gomes, and C. Gomes, "Conventional and advanced composites in aerospace industry: technologies revisited," *American Journal of Aerospace Engineering*, vol. 5, no. 1, pp. 9–15, 2018.



- [4] R. Ramesh, I. Dinaharan, E. T. Akinlabi, and N. Murugan, "Microstructure and mechanical characterization of friction-stir-welded dual-phase brass," *Journal of Materials Engineering and Performance*, vol. 27, no. 4, pp. 1544–1554, 2018.
- [5] N. M. Anas, T. E. Abioye, A. S. Anasyida, B. K. Dhindaw, H. Zuhailawati, and A. Ismail, "Microstructure, mechanical and corrosion properties of cryorolled-AA5052 at various solution treatment temperatures," *Materials Research Express*, vol. 7, no. 1, Article ID 016535, 2020.
- [6] V. Mohanavel, K. Ashraff Ali, S. Prasath, T. Sathish, and M. Ravichandran, "Microstructural and tribological characteristics of AA6351/Si3N4 composites manufactured by stir casting," *Journal of Materials Research and Technology*, vol. 9, no. 6, pp. 14662–14672, 2020.
- [7] M. L. Bharathi, S. A. Rag, L. Chitra et al., "Investigation on wear characteristics of az91d/nanoalumina composites," *Journal of Nanomaterials*, vol. 2022, Article ID 2158516, 9 pages, 2022.
- [8] B. Wang, X.-H. Chen, F.-S. Pan, J.-J. Mao, and Y. Fang, "Effects of cold rolling and heat treatment on microstructure and mechanical properties of AA 5052 aluminum alloy," *Transactions of Nonferrous Metals Society of China*, vol. 25, no. 8, pp. 2481–2489, 2015.
- [9] J.-D. Chow and W.-L. Chai, "Recycling and application characteristics of the fly ashes from municipal solid waste incinerator blended with waste polypropylene," *Environmental Engineering Science*, vol. 25, no. 10, pp. 1497–1506, 2008.
- [10] I. Kim, S. Akramov, H. B. Jeong, and T. K. No, "Texture development and drawability of frictionally rolled AA 5052 AL alloy sheet," *International Journal of Modern Physics B*, vol. 22, no. 31n32, pp. 5931–5936, 2008.
- [11] X. Zhou, Y. Gao, Y. Wang, X. Huang, and P. Xiao, "The improved strength and ductility of ZrCp/2024Al composites with a quasi-network microstructure fabricated by spark plasma sintering and T6 heat treatment," *Materials Science and Engineering A*, vol. 841, Article ID 142675.
- [12] Y. Jia, S. Chen, Y. Li, S. Wang, and H. Hu, "High-temperature mechanical properties and microstructure of C/C–ZrC–SiC–ZrB2 composites prepared by a joint process of precursor infiltration and pyrolysis and slurry infiltration," *Journal of Alloys and Compounds*, vol. 811, Article ID 151953, 2019.
- [13] F. Li, Z. Xu, K. Zhao, and Y. Tang, "ZrB2-ZrC composite nanofibers fabricated by electrospinning and carbothermal reduction: processing, phase evolution and tensile property," *Journal of Alloys and Compounds*, vol. 771, pp. 456–463, 2019.
- [14] Q.-F. Pan, C.-H. Liu, R. Tang, M.-Z. Jiang, and W. Yi, "Research on 310S for microalloying with addition of titanium and zirconium," *Hedongli Gongcheng/Nuclear Power Eng.* vol. 33, no. SUPPL.2, pp. 70–74, 2012, [Online]. Available: <https://www.scopus.com/inward/record.uri?eid=2-s2.0-84879157547&partnerID=40&md5=3cb6dc17833cb0e9974ef2d783c69c14>.
- [15] M. Jabłońska, A. Jasik, and A. Hanc, "Structure and some mechanical properties of Fe3Al-based cast alloys," *Archives of Metallurgy and Materials*, vol. 54, no. 3, pp. 731–739, 2009, [Online]. Available: <https://www.scopus.com/inward/record.uri?eid=2-s2.0-72949102593&partnerID=40&md5=f1f9c92a9e6ffe8a5b8233dceb4f6070>.
- [16] J. Affi, R. Diaz, T. Nugraha, and R. Gunawarman, "Shear strength and microstructure of joints processed with free vacuum diffusion bonding," *1st International Seminar on Advances in Metallurgy and Materials (i-SENAMM 2019)*, vol. 2262, 2020.
- [17] H. Kamiya, A. Kimura, M. Tsukada, and M. Naito, "Analysis of the high-temperature cohesion behavior of ash particles using pure silica powders coated with alkali metals," *Energy and Fuels*, vol. 16, no. 2, pp. 457–461, 2002.
- [18] "Applied mechanics and materials," in *Proceedings of the 2012 2nd International Conference on Machinery Electronics and Control Engineering, ICMECE 2012*, vol. 313–314, Jinan, China [Online]. Available: <https://www.scopus.com/inward/record.uri?eid=2-s2.0-84876521894&partnerID=40&md5=4d05550b4dabed4c21af28c1b9277aa8>, Jinan, China, December 2013.
- [19] Z. Qin, Y. Zeng, Q. Hua, Q. Xu, X. Shen, and Y. Min, "Synergistic effect of hydroxylated boron nitride and silane on corrosion resistance of aluminum alloy 5052," *Journal of the Taiwan Institute of Chemical Engineers*, vol. 100, pp. 285–294, 2019.
- [20] W. Tang, X. Yang, C. Tian, and Y. Xu, "Microstructural heterogeneity and bonding strength of planar interface formed in additive manufacturing of Al-Mg-Si alloy based on friction and extrusion," *Int. J. Miner. Metall. Mater.* vol. 29, no. 9, pp. 1755–1769, 2022.
- [21] E. Cinkilic, M. Moodispaw, J. Zhang, J. Miao, and A. A. Luo, "A new recycled Al-Si-Mg alloy for sustainable structural die casting applications," *Metallurgical and Materials Transactions A*, vol. 53, no. 8, pp. 2861–2873, 2022.
- [22] J. Huang, X. Zhou, J. Guo, H. Liao, and J. Du, "Effect of Ni addition on the microstructure and mechanical properties of 6101 aluminum alloy with high electrical conductivity," *Journal of Materials Engineering and Performance*, 2022.
- [23] A. M. A. Mohamed, M. F. Ibrahim, Y. Zedan, E. Samuel, A. M. Samuel, and F. H. Samuel, "A study on the factors enhancing the high-temperature strength of B319.2-type Alloys," *International Journal of Metalcasting*, 2022.
- [24] A. P. Hekimoğlu and Ş. Bayraktar, "Experimental research on machinability characteristics of Al-9Si alloy: effect of Sr and Mg additives," *Proceedings of the Institution of Mechanical Engineers - Part B: Journal of Engineering Manufacture*, vol. 236, no. 13, pp. 1807–1816, 2022.
- [25] N. Sahara, R. Ikeda, S. Wu, and M. Okayasu, "Effects of artificial aging on material properties of die-cast Al-Si-Cu-Mg-xNa alloy," *International Journal of Metalcasting*, 2022.
- [26] J.-Y. Li, S.-N. Kong, C.-K. Liu, B.-B. Wang, and Z. Zhang, "Chemical composition effect on microstructures and mechanical properties in friction stir additive manufacturing," *Acta Metallurgica Sinica*, vol. 35, no. 9, pp. 1494–1508, 2022.
- [27] R. Jolith, N. Radhika, and M. Govindaraju, "Reciprocating wear behavioural analysis of heat-treated aluminium ZrO2/Al7Si0.3Mg functionally graded composite through taguchi's optimization method," *Silicon*, 2022.
- [28] G. Humur and A. Çevik, "Mechanical characterization of lightweight engineered geopolymer composites exposed to elevated temperatures," *Ceramics International*, vol. 48, no. 10, pp. 13634–13650, 2022.
- [29] K. Nithesh, M. C. Gowrishankar, R. Nayak, and S. Sharma, "Effect of light weight reinforcement and heat treatment process parameters on morphological and wear aspects of hypoeutectic Al-Si based composites - a critical review," *Journal of Materials Research and Technology*, vol. 15, pp. 4272–4292, 2021.
- [30] S. Nagaraja, R. Kodandappa, K. Ansari et al., "Influence of heat treatment and reinforcements on tensile characteristics of aluminium aa 5083/silicon carbide/fly ash composites," *Materials*, vol. 14, pp. 5261–18, 2021.

## *Retraction*

# **Retracted: Prediction of *Escherichia coli* Bacterial and Coliforms on Plants through Artificial Neural Network**

### **Advances in Materials Science and Engineering**

Received 26 December 2023; Accepted 26 December 2023; Published 29 December 2023

Copyright © 2023 Advances in Materials Science and Engineering. This is an open access article distributed under the Creative Commons Attribution License, which permits unrestricted use, distribution, and reproduction in any medium, provided the original work is properly cited.

This article has been retracted by Hindawi, as publisher, following an investigation undertaken by the publisher [1]. This investigation has uncovered evidence of systematic manipulation of the publication and peer-review process. We cannot, therefore, vouch for the reliability or integrity of this article.

Please note that this notice is intended solely to alert readers that the peer-review process of this article has been compromised.

Wiley and Hindawi regret that the usual quality checks did not identify these issues before publication and have since put additional measures in place to safeguard research integrity.

We wish to credit our Research Integrity and Research Publishing teams and anonymous and named external researchers and research integrity experts for contributing to this investigation.

The corresponding author, as the representative of all authors, has been given the opportunity to register their agreement or disagreement to this retraction. We have kept a record of any response received.

### **References**

- [1] S. Prasath Alais Surendhar, G. Ramkumar, R. Prasad et al., "Prediction of *Escherichia coli* Bacterial and Coliforms on Plants through Artificial Neural Network," *Advances in Materials Science and Engineering*, vol. 2022, Article ID 9793790, 13 pages, 2022.



## Research Article

# Prediction of *Escherichia coli* Bacterial and Coliforms on Plants through Artificial Neural Network

S. Prasath Alais Surendhar,<sup>1</sup> Govindaraj Ramkumar ,<sup>2</sup> Ram Prasad,<sup>3</sup> Piyush Kumar Pareek,<sup>4</sup> R. Subbiah,<sup>5</sup> Abdullah A. Alarfaj,<sup>6</sup> Abdurahman Hajinur Hiral,<sup>6</sup> S. S. Priya,<sup>7</sup> and Raja Raju <sup>8</sup>

<sup>1</sup>Department of Biomedical Engineering, Aarupadai Veedu Institute of Technology (AVIT), Chennai, Tamil Nadu, India

<sup>2</sup>Department of Electronics and Communication Engineering, Saveetha School of Engineering, Saveetha Institute of Medical and Technical Sciences, Chennai, Tamil Nadu, India

<sup>3</sup>Department of Botany, Mahatma Gandhi Central University, Motihari 845401, Bihar, India

<sup>4</sup>Department of Computer Science, Engineering, and IPR Cell, Nitte Meenakshi Institute of Technology, Bengaluru, India

<sup>5</sup>Department of Mechatronics Engineering, CMR Technical Campus, Hyderabad, India

<sup>6</sup>Department of Botany and Microbiology, College of Science, King Saud University, P.O. Box 2455, Riyadh 11451, Saudi Arabia

<sup>7</sup>Department of Microbiology and Immunology, Northwestern University, Feinberg School of Medicine, Chicago, IL 60611, USA

<sup>8</sup>Department of Mechanical Engineering, St. Joseph University, Dar es Salaam, Tanzania

Correspondence should be addressed to Govindaraj Ramkumar; [drr.ovindaraj@aol.com](mailto:drr.ovindaraj@aol.com) and Raja Raju; [raja.raju@sjuit.ac.tz](mailto:raja.raju@sjuit.ac.tz)

Received 10 June 2022; Revised 6 August 2022; Accepted 24 August 2022; Published 29 September 2022

Academic Editor: K. Raja

Copyright © 2022 S. Prasath Alais Surendhar et al. This is an open access article distributed under the Creative Commons Attribution License, which permits unrestricted use, distribution, and reproduction in any medium, provided the original work is properly cited.

The researchers investigated the efficiency of several disinfectants in reducing coliforms and *Escherichia coli* rates on carrots and lettuce, as well as using ANN to calculate the bacteria on the edible plants. Fresh greens leaves are cleaned and dried in sterile water. Vaccinated leafy greens vegetables were immersed in a vessel and treated with chlorine, and we choose plant extracts to evaluate the impact of the extraction. The pH measurement was evaluated for both acids. After each treatment type was held at 4°C for 0, 1, 5, and 7 days, respectively, cumulative bacterial counts were evaluated. The quantity of surviving coliforms and *Escherichia coli* on lettuce was decreased by roughly 2-3 log 10 cfu/g ( $p < 0.05$ ) as the hypochlorite acids concentration is higher, compared to just about 1 log 10 cfu/g decrease on carrots. However, whenever the PA level is higher, the bacterium rates on carrots significantly decreased by 3-4 log 10 cfu/g ( $p > 0.05$ ), whereas the rates on lettuce leaves have only been lowered. The highest summation squared errors for remaining coliforms and *E. coli* via neural predictions were 0.40 and 0.64, correspondingly, while the highest regression analysis for remnant coliforms and *E. coli* was 0.95 and 0.82, including both.

## 1. Introduction

Its not like all parts of the plant are edible, but all edible parts of the plant have been known to be consumed raw or cooked. Fresh produce usage has risen significantly in the latest decades as a result of many nutritional and functional impacts. A diet high in fruits and vegetables has indeed been linked to a lower risk of diseases and chronic conditions including cardiovascular disease. Eating organic vegetables, on the other hand, is linked to an increase in food-borne

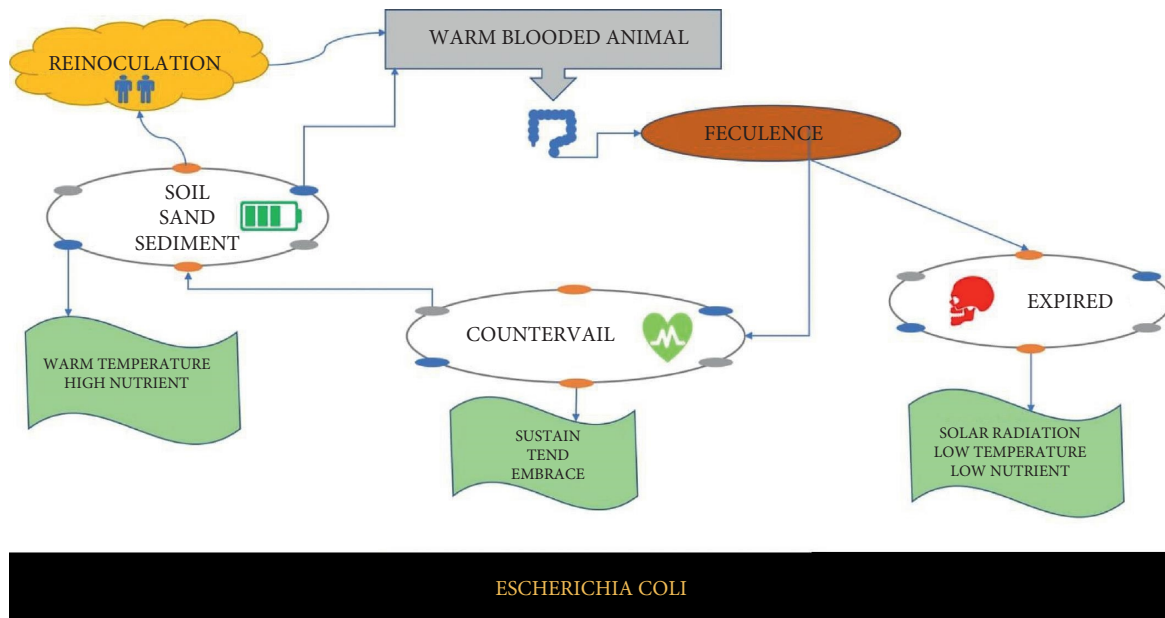
illness caused by bacterial infection of such goods. Several of the veggies that are typically associated with microbial illnesses are leafy greens like lettuce, spinach, and fresh herbs. Food-borne illnesses are felt not just by a sick person, but also by the economy. Modernization and expanding world commerce can further increase the occurrence, particularly if the food arrives from nations with poorly enforced regulatory requirements [1]. Nonetheless, nutritionists and healthcare organizations think that the health benefits of eating healthy foods outweigh the danger of developing a

food-borne disease. On the one side, there seem to be expenditures associated with a sick person, such as healthcare and loss of work or education [2]. But at the other end, there are socioeconomic costs, such as decreased manufacturing levels, outbreak-related researching fees, lost income regarding food company closures, legal expenditures for disease-related cases, and public medical treatment charges [3]. An adequate quantity of food and drinks is a basic requirement for maintaining a healthy lifestyle. Fruits and fresh, raw, or uncooked vegetable eating has risen significantly in the worldwide population as people become more concerned about making healthy diets. Including the important nutrients of organic vegetables, the possibility of microbiological contamination resulting in numerous food-borne illnesses is medically relevant in the context of primary health care [4]. The majority of detected occurrences (described as the existence of two or maybe more incidents of comparable symptoms arising out from consumption of a common meal) documented between the US and the European Union indicates just a minority of the real figure of illnesses that happen [5]. Major epidemics, infections contributing to the food industry and organizations, and incidences that last prolonged or result in significant illness are so much more probably to be examined and documented. The way plants are harvested, prepared, and delivered has indeed been known to increase both the availability and diversity of goods, potentially increasing the danger of more severe infections. The rise in illnesses linked to local produce intake parallels with reported rise in food-borne illness [6]. Bacterial infections, pathogens, and parasites may contaminate fresh vegetables, resulting in food-borne disease. Such contaminants can come through compost, dirt, wastewater, groundwater, or wildlife, and it can also happen throughout food processing such as rinsing, chopping, immersing, and packaging. *E. coli*, *Listeria monocytogenes*, *Salmonella*, *Staphylococcus aureus* and *Shigella sonnei* are some of the micro-organisms linked to food-borne disease.

Those bacteria's quantity as well as quality are influenced by several elements, such as the microorganism's unique characteristics, fruit ripening, ecological circumstances, and enhanced plant, as well as microbial resistance to plant metabolism, harvesting, and postharvest activities. Certain harmful bacteria, for instance, can absorb and attach to the surface of the plant [7]. *Escherichia coli*, usually known as *E. coli*, are among them. *Escherichia coli* is a microorganism which typically occurs among bowels. It is identified in the intestines of certain species. The preponderance of *Escherichia coli* strains is harmless and sometimes helpful for intestinal system's function [8]. However, if people consume infected meals, polluted water, certain kinds can induce diarrhea. Whereas several researchers identify *E. coli* with food-borne illness, various micro-organisms can cause pneumonia and urinary tract illnesses. *E. coli* is responsible for 75 percent to 95 percent of urinary infections. *E. coli* is a human gastrointestinal inhabitant, that's the way it grows into the urinary system. Certain strains of *E. coli* cause illness by producing a toxin known as Shiga. The gut mucosa is damaged by such toxins. STEC stands for "Shiga toxin-

producing *E. coli*," and refers to the enterobacteria that produce the toxins [9]. Figure 1 shows the growth of *E. coli*. One particularly nasty type has the potential of making people extremely sick. Stomach pains, nausea, and diarrhea are all symptoms. It was the most common cause of severe kidney dysfunction in kids. Adult renal failure, as well as other life-threatening illnesses, can be caused by it. Several of the veggies particularly commonly involved in microbial illnesses are leafy greens like lettuce, spinach, and fresh herbs [10]. The seeds which are used could be a cause of infection in sprouting. In the feces of coyotes and dogs, there is a prospective resource for pathogenic *Escherichia coli*. Plants contamination might also come from pests. *E. coli* has indeed been found to be transmitted to plant leaves and fruits by contaminating flies. One of the key environmental characteristics which impact the overall incidence of *E. coli* in veggies is the season. *E. coli* infection in lettuce and parsley increased exponentially in autumn compared to autumn and fall [11].

The prevalence of wastes from cows as well as other species has indeed been linked amongst the existence of *E. coli* in irrigation water, particularly after periods of heavy rainfall. Polluted water appears to be the most frequent cause of contamination in leafy green vegetables. Dependent on soil kind, moisture levels, and temperatures, *E. coli* can remain in the soil for 7 to 25 weeks. In other circumstances, *Escherichia coli* in plants includes, spinach, sprouts and fresh clover seedlings are much better at the end of the postharvesting process compared to the beginning. It could be owing to later direct contamination or disease proliferation through fresh vegetable postharvest operations. Obstructions such as waxes, *epidermis*, cell membrane, trichomes, and stomata exist on these plants (natural pores). Several micro-organisms have been shown to employ stomata as entry sites into the leaf core [12]. Many potentially harmful bacteria might remain on and enter the plant's core in the membrane; bacteria can tolerate dramatic variations in temperature, pH, osmolality, and malnutrition in the environment with minimal energy metabolism. Pathogenic *E. coli* contains adhering proteins for infecting human epithelial cells, and most of these factors have been demonstrated to be employed for adhesion to fruits and veggies [13]. The plants, on the other hand, provide an unfavorable habitat for *E. coli*, with aerobic conditions, reduced temperatures, a lower pH, a greater amount of ultra violet radiation, and aerial coverings (phyllosphere) that are devoid of nutrients and possess antibacterial secondary metabolites. Diarrheagenic *E. coli*, on the other hand, have developed mechanisms for vegetative attachments that differ depending on the strain and plant. Because raw vegetables are utilized in healthy foodstuff preparations and because low levels of infections are necessary to induce intestinal sickness, contaminating fresh vegetables containing *E. coli* is essential [14]. To disinfect the disease, the plants need to be sanitized, so two major disinfectants, hypochlorite and peracetic acid are used to disinfect edible plants. These sanitizers are known to be the most effective for sanitizing plants, fruits, and vegetables.

FIGURE 1: The growth of *E. coli*.

Customers choose local vegetables because of their great organoleptic and nutritional qualities. Postharvest sanitizing is an essential unit activity for protecting the freshness and quality product by preventing rotting and ensuring food safety [15]. Customers are actively turning to minimally processed or fresh veggies, which they consider to be clean, healthful, and affordable. The exterior of the product is exposed to the atmosphere when it is peeled, chopped, or shredded, resulting in a quick reduction in the quality and shorter storage stability when compared to whole fruits and vegetables. A preliminary cleaning phase eliminates dirt and some other material from the fruits or vegetables that improves their look and decreases their heat [16]. Before packaging, a secondary implementation of sanitation or disinfection procedures can help to limit the prevalence and spread of rotting and harmful microbes on product surfaces, avoiding metabolic responses and the danger of food-borne disease [17]. Continuous development in postharvest processing and disinfecting procedures, particularly about the use of chemical sanitizers, is prompted by rising wasted food and occurrences of food-borne disease associated to freshly and fresh-cut veggies. Throughout every phase of product handling, including harvesting to point of purchase, fresh-cut produce seems to have the potential to become contaminated with food-borne pathogens. Because fresh-cut produce is just not subjected to additional germ-killing procedures, proper use of sanitizing chemicals to eradicate micro-organisms and prevent pathogen growing and contamination is essential to assure its quality and efficiency. Various antimicrobial compounds and mixes of compounds that were shown to be considerably more effective than chlorine in harvesting, processing, and disinfecting, are growing in popularity [18].

Cleaning with sanitizing is well-known as one of the most fundamental processes in fresh-cut vegetable

manufacturing. Among the most commonly used disinfectants for edible plants is hypochlorite. It keeps up the quality by decreasing and regulating bacterial activity. For rinsing fresh vegetables, chlorine levels of 50–200 mg/L are suggested [19]. During industrial cleaning circumstances, the effectiveness of chlorine in reducing pathogens is minimal. Organic content in immediately reclaimed water, improper cooling, or exposure to sun or wind can all reduce the effectiveness of chlorine. Chlorine tainting, salt residues on products and equipment, and harm to producing tissues are all possible side effects of excessive chlorine levels. Hypochlorite is an ionic compound of citric acid and chlorite with a somewhat reactive mechanism of activity [20]. Chlorine's sterilizing activity has been proved mostly against pathogenic species including *E. coli* and *Listeria monocytogenes*. Even though the bacteriological pile and physiology of fresh fruits and vegetables impact its freshness, there has been little research on the effect of chlorinated water washing on micro-organisms loads such as *E. coli* and coliforms, and also on the antibrowning of fresh root veggies like potatoes. Another disinfectant, PA, also called as peroxyacetic acid or peracetic acid, is a hydrogen peroxide and acetic acid equilibria combination. PA was developed in 1950 for the disinfection of fruit and vegetable coverings, both within the market and after harvest, with dipping or spraying to decrease spoiling caused by microbial agents [21]. Since it has significant oxidizing powers, produces no toxic by-products or pollutants, and is approved to be used in organic manufacturing, PA is especially attractive for the foodservice industry. In the sanitation and disinfection of fresh-cut food, there are possibilities to substitute chlorine chemicals with PA. Peracetic acid ( $\text{CH}_3\text{dCOdOOH}$ ), commonly called peroxyacetic acid or ethane peroxy acid, is perhaps the most effective antibacterial agent among the organic peracids, with a 1.81 eV oxidation capability and

high disinfection characteristics [22]. When utilized as an antibacterial and disinfectant, a mixture of 0.03 percent to 2 percent is usually enough to provide this significant oxidizing activity. The undissociated acid, which is prevalent at pH 4.7, is regarded as the biocidal state and seems to have a wide range of activity towards bacterium, virus, bacterial spores, and protozoan cysts. It has been explored for health and safety purposes since then, and is now widely available in accessible standard solution with stabilizers. The US FDA has allowed the use of peracetic acid and hypochlorite as a disinfectant for machinery food contamination and straight cleaning of fruits and vegetables, meat, poultry, and shellfish [23].

Lettuce and carrots were chosen since both represented diverse product kinds such as leafy and root vegetables, respectively, as well as various configurations of vegetable material and significant economic value in the edible plant industry. The effectiveness of various sanitizing mixtures in preventing cross-contamination in processed waters was also tested. Rinse water scenarios in processing and packaging were simulated, taking into account that the water contained in them could influence biological material outcomes. Bacterium levels in fresh fruit and vegetables have already been lowered using a wide range of disinfectants, including peracetic acid, chlorine, acetic acid, hydrogen peroxide, and alcohol, however, certain studies found that the bacteria in fresh fruit and veggies were only lowered, not eradicated. As a result, to effectively and efficiently analyze the extreme threat of fresh produce intake, it is important to forecast the remaining bacterium concentrations in yield. Numerous approaches to capture the cumulative influence of variables impacting microbiological growth and survival have already been created in recent years [24].

Artificial Neural Networks (ANNs) are a distinct and superior technique for accurately simulating microbiological survival and development. It could manage the high degree of variation and unpredictability found in processes. A neural network could be trained to perform a specific activity by changing the number of interconnections (weights) between neurons. A Neural network is trained to deal with specific inputs by achieving a predetermined outcome goal. A network can be trained in AI learning using a variety of inputs and goal combinations. The outcomes are compared to the goal, and the mechanism is adjusted till the outcome meets the target. An ANN is a computer model that consists of three layers, including one that comprises different neurons. The three layers are the input layer, hidden layers, and output layer. Since every neuron in one layer is related to every neuron in the next, such layers are even more intertwined [25].

Nevertheless, not many reports are there of utilizing ANNs to forecast the presence of harmful micro-organisms on fresh vegetables following cleaning with several disinfectant wipes have been found. Carrot and lettuce leaves have been selected as model species for the study because it does not only depict commonly produced (fresh) food products and elements of commercial vegetables that have

been linked to food-borne diseases, but they often symbolize opposite ends of the large range in suitable plant destination and framework. As a result, lettuce leaves and carrots will grow nearly to the soil and are susceptible to preharvest impurity caused by fertilizer spraying. The goal of the study would have been to employ artificial neural networks to forecast remnant coliforms and *Escherichia coli* in carrots and lettuce following cleaning using hypochlorite and PA.

## 2. Related Work

Emerging organic contaminants (EOCs) might well be discovered in treated wastewater (TWW) utilized for watering of grain production after inadequate elimination following treating wastewater. EOCs could soon achieve the ecosystem after being absorbed into edible plant portions, resulting in human exposure. The absorption of 4 ibuprofen, carbamazepine, naproxen, and ketoprofen into different vegetable cultivars was predicted using newly constructed steady-state plants absorption models with enhanced phloem transport. The initial information came from plants grown with plants watered using TWW spiking with CBZ at 0, 30, 60, 120, and 210 g/L within every species of lettuce. Carbamazepine levels in plants are anticipated to be 82 percent greater than that in root systems in general, exhibiting satisfactory correlation among calculated and measured values. Researchers then estimated the absorption of anti-inflammatory chemicals such as ibuprofen, ketoprofen, and naproxen, about which laboratory testing did not yield amounts far above the limit of detection. All three acids are weak, and projected levels in the root system are greater than anticipated levels in fleshy leaves, owing to phloem movement downward. The recommended nutritional consumption of all 4 EOCs was calculated based on green vegetable consumption, which was found to be substantially below typical therapeutic levels. Ibuprofen, on the other hand, was not used in the computations because plants' absorption system could only estimate neutral chemical absorption. With the modeling growth described therefore in work, the vacuum has been filled [26].

The sorts of linkages among *E. coli* and spinach phylloepiphytic micro-organisms were characterized in the research, or those that impact *E. coli* O157:H7 survivability on plant foods were discovered. In vitro and on the spinach surface of the leaf, 1512 phylloepiphytic bacterium extracts were subjected for the capacity to suppress or increase *E. coli* O157:H7 development. In vitro, 15 distinct species, the bulk of which belonging to the Firmicutes and Enterobacteriaceae families, lowered *E. coli* O157:H7 population growth by nutritional competition or acidic generation. With detachable spinach leaves that have been co-inoculated with epiphytic samples from five species, lower quantities of *E. coli* O157:H7 were obtained. While co-inoculated using *Erwinia piscina* and 20% cellobiose, a carbon source utilized by phylloepiphytes but just not *E. coli* O157:H7, *E. coli* O157:H7 was reduced by 1.8 logs. The diminution observed on plants was substantially lower than that observed in vitro.

While *E. coli* O157:H7 was co-cultured in vitro on wasted media and disconnected fresh spinach; phyloepiphytic bacterium from 8 various genera enhanced the amount of *E. coli* O157:H7. The findings, which indicate that indigenous epiphytic bacterium could reduce *E. coli* O157:H7 levels, disprove the assertion that native plant microbiome could be employed to bio-control food-borne diseases; nevertheless, some epiphytes might encourage the survival of enteropathogens on the phyllosphere. Once *E. coli* O157:H7 were co-cultured with *Flavobacterium* sp., nevertheless, the overall population of *E. coli* O157:H7 was much greater ( $p < 0.05$ ). The total population of *E. coli* O157:H7 only after 48 hours of incubation was not substantially varied from the overall population of *E. coli* O157:H7 co-cultured with *Flavobacterium* sp. ( $p > 0.05$ ) [27].

Baby spinaches are transferred to the packaging sheds after becoming harvested in the fields and refrigerated by a compressed conditioning system. The temperatures of spinach will influence the number of infections in the plants if they are infected, and efficient climate control is necessary to limit bacterial development. As a result, it is important to figure out how chilling procedures affect pathogen proliferation in green vegetables. To explain the observational data and develop a dynamical method to forecast microbial population increase in baby spinach leaves as temperature-dependent, the Baranyi method was established. Baby spinach plants were injected with 104 CFU/ml of *Salmonella* Typhimurium LT2 or 102 CFU/ml of an *E. coli* mixture and kept at 10 to 37 degrees Celsius for 30 hours. The strains of *E. coli* grew considerably faster ( $w2e4$  log cycles) than the *Salmonella* strain ( $w0.11 e2.4$  log cycles) at 10 e30°C, although both microbial cities increased by  $w6$  log cycles over 30 hours at 37°C. Every microorganism's developmental kinetics matched the Baranyi model. Temperatures set the maximum microbial populations, and the results remained comparable for both micro-organisms. For *Salmonella* and *E. coli*, the theoretical minimum growth temperature was 5.88°C and 4.76°C, correspondingly. For the measurement of harmful *E. coli* and *Salmonella* and diverse risk factor permutations, among other neighboring land-use practices, higher quantities of materials must be formed with an association from multiple sources of water, leaves, and roots in an increased variety of product habitats. In addition, the rare growth of common *E. coli* along with the water supply after exiting the well should be further investigated [28].

For the creation of reliable measurement microbiological vulnerability assessment, the capacity to forecast the characteristics of *E. coli* O157:H7 on contaminating field lettuce is critical. Numerous sets of data produced from field-based investigations were evaluated by regression analysis using one monophasic (log-linear) and two biphasic (Weibull and Cerf's model) equations to determine the species' mortality patterns. @RISK™ was used to construct a statistical model, combining the fitting monophasic and biphasic concepts to see how they affected the estimation of the magnitude of die-off following a contaminated occurrence in the fields. Throughout most instances, regression analysis revealed that *E. coli* O157:H7 maintained a biphasic decline trend, with Weibull and Cerf's modeling both fitting

individuals and pooling evaluation metrics adequately. Moreover, the stochastic findings indicate that adopting the log-linear models might vary in varying risk estimations than biphasic approaches, with a reduction in the incidence in the former case due to the absence of effluents therefore in the model. The concepts and findings of the study give the first conceptual foundation for developing probabilistic models to forecast the destiny of *E. coli* O157:H7 on field-grown leafy green vegetables. The adoption of one methodology above another, nevertheless, might lead to different risk evaluations [29].

Numerous epidemics of food-borne outbreaks affected by *E. coli* O157:H7, a type of bacteria of growing public health importance given the seriousness of the gastrointestinal illness and long-term, chronic sequelae which could result from infectious disease, have already been linked to leafy greens, which include leafy greens and spinach. A definite link between leafy vegetable consumption and disease suggests that animal origins are being transferred to field plants and commercial products, especially minimally processing or fresh-cut items. Evaluating *E. coli* O157:H7 behavior in leafy vegetables throughout cultivation, post-harvest, storage, processing, and packaging of fresh-cut produce is critical to developing effective control methods. To that purpose, the study examines previous studies on the destiny of the organism at every stage of the development of market-ready leafy greens. Uncertainty well about the placement of contaminated micro-organisms on or in leaf tissue, behavior in packaged products held at low temperatures, and the effect of environmental conditions on development and pathogenicity are among the information limitations found. Nevertheless, no evidence of growing in or on the plants during field conditions has been found. Moreover, the connection between plant resistance and human pathogenicity is incompletely understood. As a consequence, it is unknown if large-scale epidemics can be caused by a single harvest contaminating incident and whether postharvest reproduction of the bacteria is required to reach epidemiologically important concentrations of infected cells [30].

Across a whole supply chain in Canada, the temperatures of packed lettuce were measured at different phases of preservation and transit from the manufacturer to the retailer. In three replication research studies during the cold, conditions remained measured in 27 containers of lettuce intended for three different retailers. The behavior of *E. coli* O157:H7 in the environment is predicted, a dynamical simulation that forecasts the impact of temperature on the development or die-off of *Escherichia coli* O157:H7 in fresh and quality lettuce has been used. To compensate for fluctuation in the temperature parameter and the die-off ratio of the dynamical growth/death model, simulations were conducted using distribution. According to the findings, a total mean reduction in cell counts of 0.983 log CFU g<sup>-1</sup> was projected, and the level of cell death was related to the entire spending time in the cold storage facilities. Whenever the dynamical temperatures were within the permitted temp of 5C, some development was projected in a few cases. These findings

show that *E. coli* O157:H7 will develop very slowly or not at all in products kept at the right temp throughout the chain. Furthermore, the projected decrease in cell phone numbers at refrigerated temperature shows that storing fresh-cut lettuce at 5C or even below before cooking will decrease disease densities in a development scenario. However, this research was performed in a lab setting that mimicked the various steps of transit, processing, and storage. These researchers discovered no substantial effect on cell counts [31].

On a microscale, lettuce contaminated with *E. coli* O157:H7 was subjected to chlorinated cleaning (150 mg/mL) and altered atmospheric packing. To acquire systematic heterogeneity, the *E. coli* O157:H7 population was measured in fresh-cut lettuce kept at 4, 8, 13, and 16°C using 6e8 duplicates in each assessment point. The infections were able to develop at temperatures ranging as 8°C, however, growth data at these temperatures showed a lot of variation between repetitions. After 15 days at 8 degrees Celsius, some duplicates showed no development while others rose significantly. To determine the time delay and maximal rate of growth, development basic data were fitted to the actual development data. The Monte-Carlo approach was used to determine the predictions and accuracy ranges for the fitted growth theory. For 8, 13, and 16°C, the maximum allowable rates of growth (log CFU/day) were 0.14 (95 percent confidence interval: 0.06e0.31), 0.55 (95 percent confidence interval: 0.17e1.20), and 1.43 (95 percent confidence interval: 0.82e2.15), correspondingly. From the calculated rates of growth, a squared root secondary modeling was successfully generated ( $R^2 > 0.80$ ; Bf 14 0.97; Af 14 1.46). The results of the study's forecasting analytics and information will be used to enhance analytical and numerical assessments for *E. coli* O157:H7 in green leafy foods. Even though there was not any growing process occurred at 8°C in certain cases, the risk remains substantial due to *E. coli* O157's highly infectious qualities [32].

Determining the sanitary and hygienic condition of vegetables and water sources, as well as determining the efficacy of lime juice and vinegar in lowering *E. coli* bacteria inoculation on lettuce are the main goals of this study. The thermotolerant coliforms and *Salmonella* spp. were found in 140 samplings of veggies and 45 tests of freshwater. Four different methods were evaluated to validate the efficiency of organic housekeeping disinfectants in decreasing *E. coli* in inoculation leafy greens: lime juice, alcoholic vinegar, lemon juice-vinegar mixture, and lemon juice-vinegar-water combination. The microbial investigation demonstrates high concentrations of contaminants by thermotolerant coliforms, with *E. coli* found in 32% of the examined vegetable materials and 56% of the examined water samples. While there was no statistically significant difference ( $p < 0.05$ ) in the evaluation control, the diagnosis with a mixture of lemon juice and vinegar resulted in a high decimal reduction (DR) of *E. coli* O157:H7, while the diagnosis with vinegar on its own was most impactful against by the indigenous *E. coli* strain. However, there has been no significant difference ( $p > 0.05$ )

among lettuce samples tested just with vinegar and lime juice versus those handled with a lemon juice-vinegar combination [33].

### 3. Materials and Methods

**3.1. Inoculation Procedure and Bacterial Strain.** The standard species throughout the investigation was *E. coli* from the Spanish Type Culture Collection (CECT). Since the strain is nonpathogenic, it lacks the potential to create verotoxins. It does, unfortunately, share phenotypic traits with the toxigenic *E. coli* strain. Bacterial isolates were generated in particles and stored in containers at 80°C in the refrigerator. Stocks populations were regenerated by inoculating them onto Tryptic Soy Agar (TSA) + 0.6 percent yeast extract (YE) plates and incubating them for 24 hours at 37 degrees Celsius. Vegetables are soaked in the inoculant solutions of water containing 9 logs CFU/mL of *E. coli* O157:H7 and agitated for 5 minutes to isolate the vegetables. After immersing, the surplus water was strained out in a motorized salad spinner for 30 seconds. Following processing, the specimens were put in plastic containers and kept at 4°C for a week to encourage bacteria attachment to vegetable tissue shown in Figure 2. The original *E. coli* O157:H7 percentage was determined by analyzing a portion of the contaminated vegetable. One looping was collected from every nutrient agar slant in every one of the coliforms and *E. coli* cultures, which then was moved to TSB and incubated at 35.1.0°C for 24 hours. 2.0 ml of each cultural dimension was pipetted into each measuring cylinder for inoculated lettuces, which were later concentrated using 8 ml of phosphate buffer before sprinkling onto the cleansed lettuce leaves as described. The contaminated lettuces are allowed to dry for at least 60 minutes at room temperature. 2.0 cc of each strain was placed into sterilized baggies cleaned for carrots sample. The sacks were again thoroughly shaken to ensure that the micro-organisms were evenly distributed across the carrot, and afterward left open till the carrots were completely dry.

**3.2. Efficacy of Sanitizers.** Using 10% (*w/w*) chlorine, hypochlorite (500 mL each) was made into watery chloride concentrations of 30, 60, and 70 ppm chlorine (Vittayasom Sriracha Co., Ltd.). Pexania 2005 (peracetic acid 5% (*w/w*) content; Prematech Co., Ltd.) was used to make PA solutions of 20, 50, and 60 ppm (500 ml each). For 10 minutes, all carrot and lettuce samples were immersed in sanitizing solutions. The comparison was freshwater (without micro-organisms, coliforms, and *E. coli*). The leaves/veggies were then blown dried and delivered for bacteriological examination. Each trial had 30 sample replicates and was developed utilizing a CRD (Completely Randomized Design).

### 4. Analytical Procedures

**4.1. Bacteriological Analysis.** Twenty-five grams of carrots and lettuce are kept in a sterilized package, occupied by 230 ml of sterile Butterfield's phosphate-buffered water (42.5 g/l KH<sub>2</sub>PO<sub>4</sub>, pH 7.2, Merck), and gently shaken for two minutes to rinse off the germs. Samples per gram (log



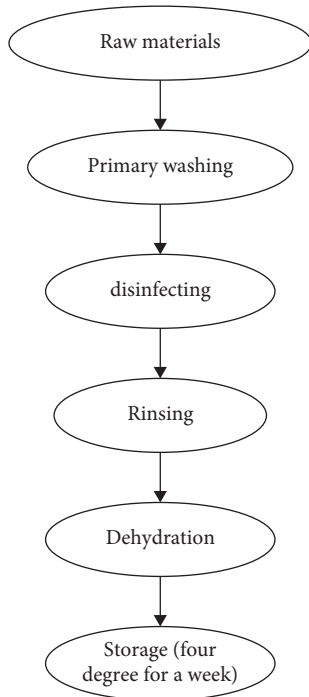


FIGURE 2: The preprocessing steps of edible vegetable produce.

CFU/g). The samples are pour-plated in violet red bile agar (VRBA, Oxoid) and maintained at  $35 \pm 1.0$  degrees Celsius for 18–24 hours for coliforms. Particularly reddish to violet colonies with a diameter of 0.5 mm were chosen and then inoculated. BGLB (10 tubes) was incubated at  $35 \pm 1.0$  degrees Celsius for 24–48 hours, the number of coliform colonies was estimated, and the conditions are obtained in  $\log_{10}$  cfu/g. The testing for *E. coli* was annealed with 0.2 mM MUG in VRBA (4-methyl-umbelliferyl-b-Dglucuronide) (Oxoid) for 18–24 hours at  $35 \pm 1.0^{\circ}\text{C}$ . Bluish colonies were mainly present while viewing under a UVw365 nm-lamp they were collected and the data were expressed in  $\log_{10}$  cfu/g units.

**4.2. Analyses of Physicochemical.** Throughout vegetable washing, variations in pH and temperature (C) in the procedure washing waters were measured. The potential of hydrogen with homogenate was evaluated at  $24^{\circ}\text{C}$  that used a pH meter and crystal electrode after 50 g of the vegetable experiment was transmitted to a sampling procedure package having 60 mL of filtered water (1:1, w: v), homogenized by combining of 90s with the combination of 400 mL sampling procedure, and the pH of the homogenate was evaluated by combining for 100 s with a combination of 400 mL of sampling procedure (model GLP-21, Crison, Spain). The N, N diethyl-p-phenylenediamine (DPD) colorimetric procedure (model HI95711, HANNA Instruments) was used to quantify chlorine utilizing suitable testing kits. PA levels were tested utilizing peroxyacetic acid sheets and the chlorite concentration was evaluated that

used a Dulcotest® DT1B instrument (ProMinent, Spain). COD was measured with a Spectroquant PHARO 100 measurement device (MERCCK) to use the usual photometric technique, and the findings were presented in  $\text{mg O}_2/\text{L}$ .

**4.3. Analyses of Colors.** For the objective color assessment, an X-Rite sphere spectrophotometer (model SP64) was employed. The variables  $M'$ ,  $x'$ , and  $y'$  will be calculated as per the International Commission on Illumination, whereby  $M'$  denotes luminance (the maximum value for  $M'$  is 100, which corresponds to white, as well as the lowest value is 0, which corresponds to black). On the hue-circle, a high  $x'$  value shows redness ( $x'$  is greenness) and a high  $y'$  value suggests yellowness ( $y'$  is blueness). There are no numerical restrictions on the  $x'$  and  $y'$  axes. When obtaining further readings, the equipment is validated against a standard white ceramics disc and black traps. The findings were presented as a mean of numerous repeats with a normal observing increment of approximately 10 degrees and a D65 luminance.

**4.4. Analyze the Data.** To identify the impact of disinfectants, the research statistical analysis was performed using the SPSS V.10 program. The inferential statistical analysis was used to construct Duncan's new multiple-ranging analysis, having substantial variations amongst the average accepted at the p 0.05 threshold.

**4.5. Implementation of Artificial Neural Network.** The challenge of forecasting remaining microbial concentrations could be easily and theoretically converted into a challenge of proportional approximating. Choosing the right polynomials or descriptive statistical evaluation method is difficult because the level of polynomials, the number of components, and the error measurement functions must all be prespecified. If the level of the polynomials is too minimal, the polynomial would be unable to represent the data distribution effectively. When large extent polynomials are being used, nevertheless, the computing effort is too great, and the problem becomes operationally or practically unsolvable. In practical estimations, there are typically two error measurements used. The conventional least square measurement is the first, and the orthogonal least square measurement is the latter. Every metric yields different outcomes. A supervised neural network is used to construct polynomials for functionality approximations with all these troublesome variables. Every input sequence utilized to train the networks in the scenario comprises a set of quantitative parameters relating to the remaining amount of microbes. The residue quantity of microbes is the aim of every sequence. To calculate the estimation error, the quantity of every objective is matched to the quantity of the item estimated by the system. Because there are numerous neural networks, we utilized backpropagation, which is the easiest and most extensively utilized. The system has 3 layers: first is input layer, second one is hidden layer, and the last one is output layer. The input data has four different



characteristics, namely, initialization of load, kind of product (A and B), category of disinfectant (A and B), sanitizing dosage, along with one output layer with one output target, namely, the remaining amount of micro-organisms. The tests yielded a total of 360 training examples. However, because the active functions can influence the forecasting's findings, two sets of evaluations depending on multiple active functions were performed. The findings of utilizing a hyperbolic tangent functional in the hidden units and a sigmoidal functions in the output nodes have been used in the initial set of evaluations. The process of applying a sigmoidal function both in the hidden layer and output layer has been used in the subsequent set of evaluations. The quantity of testing phase to evaluate proportion in the model was 60:40. The training speed of the networks could be changed to vary the network's learning rate. If the training rate is very high, the networks might spend less time acquiring the information, while if it is low, the process of learning might take more time. Just the acquisition pace is affected by this learning algorithm.

Every input characteristic  $a_i$ ;  $1 \leq i \leq 5$  was normalized within the same range  $[x, b]$  to prevent the biased influence of the input data owing to the different ranges. Let  $[x, y]$  be a new range specified. Let  $a_{\max}$  and  $a_{\min}$  be the maximum and minimum numbers of the concept's native range, respectively. The following equation (1) could be used to normalize characteristic values  $a_i$  inside the range  $[x, y]$ , represented as  $a'_i$ .

$$a'_i = \frac{(x - y)(a_i - a_{\min})}{a_{\max} - a_{\min}} + x. \quad (1)$$

The coefficients of  $x$  and  $y$  for a sigmoidal function are 0.1 and 0.9, correspondingly, while the values of  $x$  and  $y$  for a hyperbolic tangent function are 0.9 and 0.9, in both. Equation (2) shows the sigmoidal function:

$$f(a) = [1 + \exp(-a)]^{-1}. \quad (2)$$

The sigmoidal function's maximum and minimum values are restricted to  $[0, 1]$ , whereas the hyperbolic tangent activation function's maximum and minimum values were constrained to  $[-1, 1]$ . Equation (3) represents the hyperbolic tangent activation function:

$$f(a) = \frac{[\exp(a) - \exp(-a)]}{[\exp(a) + \exp(a)]}. \quad (3)$$

As a result, for sigmoidal and hyperbolic tangent activation functions, the network's anticipated output  $a_d$  is confined to  $[0, 1]$  and  $[1, 1]$ , correspondingly. The network's outputs, on the other hand, do not represent the true value of the information. Equation (4) must be used to convert the output value to its real value  $a_d$ :

$$a_d = a_{\min} + \left[ \frac{a_d - x}{y - a} \right]. \quad (4)$$

The summation squared errors (SSE) and regression analysis error ( $R2$ ) are used to calculate the generalization error, as follows in equations (5) and (6):

$$\text{summation squared error} = \sum (a'_d - a_t)^2, \quad (5)$$

$$\text{Regression analysis} = 1 - \left[ \frac{\sum (a'_d - a_t)^2}{\sum (a'_d - a)^2} \right]. \quad (6)$$

where  $a_t$  is the mean of the observations and " $a$ " is the observation value of testing sequence " $t$ ". To evaluate coliform and *E. coli* separately, every neural network was built separately. The kinds of vegetables and disinfectants could not be utilized as neural network parameters because they are regarded as nominal information.

Throughout the case, four different systems were built to deal with every vegetable and disinfectant combination. Establishing four separate networks, on the other hand, would have been logistically and computationally inefficient in a real-world setting. It is theoretically conceivable to combine these four networks into a single network. The network, on the other hand, must be capable of performing as well as each of the original networks. To complete the constraint, several extra variables indicating vegetable kinds and disinfection should be supplied without any weighing impact throughout neural processing.

Using the generated ANNs algorithm, remaining bacteria on vegetables are forecasted. By doing two repetitions of the investigation utilizing hypochlorite at 30, 60, and 70 and PA at 20, 50, and 60, the anticipated result was compared to the corresponding validation. To determine the correctness of the constructed model, 25 patterns were examined in total. By looking at the graphical connection among the observed and expected values, the results were compared. When both variables used to have a propensity to be similar, the expectation is that they must be connected vertically with a convergent validity indicated by a regression value greater than 0.8.

## 5. Results and Discussion

A variation level of the two disinfectants was tested in the investigation. The investigation found that the greatest concentrations of hypochlorite (70 ppm) and PA (60 ppm) did not affect the texture and aroma of carrots and lettuce. The coliforms and *E. coli* isolates utilized are initially derived from carrot and lettuce, and therefore depict seminatural indigenous species instead of manufactured cultured within that regard. In that limitation, the selection of these 2 kinds of micro-organisms is straightforward. To begin by, coliforms are widely disseminated and usually related to foods farmed to animal waste, as well as manual handling throughout harvest as well as all steps of preparation following harvest. Despite that the separated coliforms are restricted to a set of coliforms and will not replicate every microbe in the sample. *E. coli* are bacteria that live in the human intestinal system and are utilized as a fecal contamination indication. Nevertheless, between *E. coli* strains, *E. coli* O157:H7 is a common bacterium linked to food-borne illnesses, especially raw vegetables. As a result,

TABLE 1: pH processing of cleaning water and concentration.

		Lettuce		Carrot	
		Cleaning water	Concentration	Cleaning water	Concentration
Hypochlorite acid	Positive pressure	7.12	7.28	7.87	6.32
	Vacuum	7.26	7.30	7.59	6.45
Peracetic acid	Positive pressure	6.73	6.30	6.77	6.89
	Vacuum	6.43	6.48	6.22	6.93

common *E. coli* strains could serve as a substitute modeling indicator for pathogenic infections.

Vegetables were soaked in water from the tap (W), chlorine water (CW), hypochlorite, and peracetic acid (PAA: 100 mg/L) in a mixture of vacuum (10 mbar) and positive pressure application (3 bar). Each acid's pH is measured and analysed. The category of disinfectant product employed determines the impact of combination therapies on produced water (Table 1). Treatment with PA effectively decreased the pH of processing water when compared to processed cleaning water without disinfection, there were no variations when chlorite was used. On average, the pH decrease in edible items was substantial in PA treatment in comparison to that observed following rinsing veggies with water supply, depending on the physical approach utilized.

The pH of lettuce and carrots did not significantly change ( $p > 0.05$ ) when hypochlorite was used. An essential factor to take into consideration is the chemical oxygen demand (COD) effect of the disinfectants. When PA was added to the processing water, it was discovered that the organic content rose, although hypochlorite seemed to have no impact. Table 2 represents the COD process in clean water testing and solutions. The COD was not affected while using the chloride; although, while the pH was adjusted using citric acid, the organic material readings increased as well.

Since the preliminary microbiological quality on the carrot and lettuce test results varied, it was important to implement the massive amount, which was accomplished by having to clean the test results with clean water before actually inoculating with the intended microbial cells, resulting in a standardized loading of  $w6 \log_{10} \text{cfu/g}$  throughout all isolates. It is essential because the effectiveness of both disinfectants, specifically hypochlorite, is influenced by bacterial contamination. It is significant to mention that the very first beginning strain is not an actual strain for raw veggies. For unclean lettuce collections, total aerobic levels were observed to be around  $5 \log_{10} \text{cfu/g}$ . PA and chlorite possess equivalent antibacterial efficacy towards *E. coli*, according to the findings. Because the combination method's effectiveness in entirely removing bacteria found in edible plants were restricted, using such disinfectants would be reviewed in terms of maintaining the microbiological safety of water immediately. Figure 3 depicts the graphical representation of COD process of vegetables in clean water with disinfectants.

Table 3 presents the remaining viable microbe loads in carrots after immersion in hypochlorite or PA at varying

TABLE 2: The COD process of vegetables in clean water with disinfectants.

Disinfectants	COD process in cleaning water	
	Lettuce	Carrot
Peracetic acid	575	1170
Hypochlorite	352	987
Water	347	963
Chlorine water	556	1205

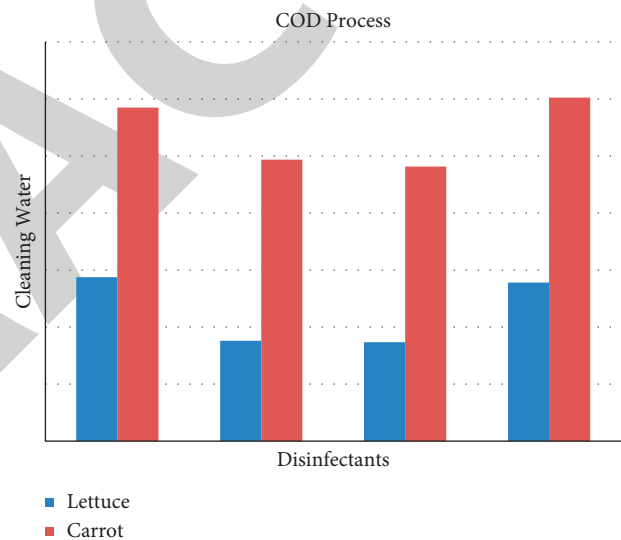


FIGURE 3: Graphical representation of COD process of vegetables in clean water with disinfectants.

concentrations for 10 minutes. Hypochlorous acid therapy, which consisted of chlorite levels of 30, 60, and 70 ppm, showed significantly greater efficiency in decreasing the amount of live coliforms than *E. coli*, whereas PA (20, 50, and 60 ppm) treatments were somewhat efficient on *E. coli* than coliforms. PA, on the other extreme, was far more successful than hypochlorite in eliminating both bac on botherria veggies. Throughout the case of hypochlorite, coliforms and *E. coli* on carrots are significantly dose-dependent, with a lowering of live recoverable coliform and *E. coli* correspondingly.

In aspects of bacterial minimalization, while PA is usually extra efficient and minimizes the remaining microorganisms stages by an estimated  $1.1e3.1 \log_{10} \text{cfu/g}$  further than hypochlorite under such conditions, the remaining amount of microbial after diagnosis also differs widely depending on the kind of vegetable. Its differing antibacterial processes may explain why PA reduced micro-organisms

TABLE 3: Residual status and removal of *E. coli* and Coliforms after washing edible plants in disinfectants.

Bacterium (preliminary input)		Coliforms		<i>E. coli</i>	
Disinfectants	Amount	Remnant	Removed	Remnant	Removed
Hypochlorite acid	30	8.02	2.23	4.87	1.02
	60	7.06	2.37	4.89	1.08
	70	6.82	1.80	5.29	2.32
Peracetic acid	20	5.82	3.40	3.67	3.12
	50	5.72	3.23	3.72	3.03
	60	5.38	3.35	3.50	3.10

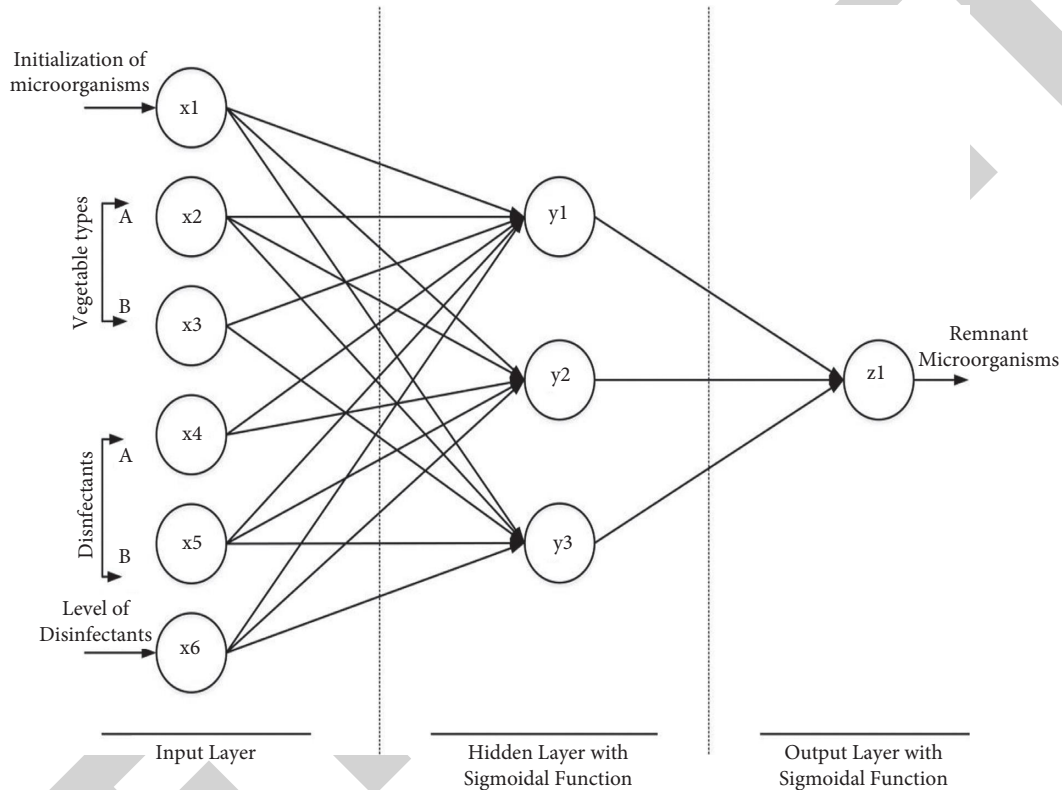


FIGURE 4: Outline of ANN framework for the prediction of remnant coliforms on lettuce and carrot.

more than hypochlorite. Chlorine enters the bacterium and links itself with the amino groups of the cell nucleus structures, slowing the material's metabolic activity and eventually killing it. Peracetic acid penetrates and binds itself more to protein amino groups, inhibiting numerous important activities. The enhanced inflammatory capability of PA, allows for significantly greater oxidative stress to the bacteria's cellular membranes cellular proteins, resulting in a loss of membrane stability and cellular membranes disintegration. Furthermore, PA inhibits critical cell metabolic processes, resulting in a substantial reduction in the replacement synthesis of proteins, impeding cell regeneration and eventually cell death.

Micro-organisms on green veggies are concentrated in specific areas, such as the stomata, trichome bases, epidermal cell wall joints, and vein grooves. Microscopy revealed that

microbes and other particles have been primarily encased both on top and bottom layers of uncleaned lettuces and that while having to wash in water from the tap eliminated microbes and particles from the exposed layers, significant numbers managed to remain in husks at the intersection of the *epidermis* and in layers in the epidermal cells. The micro-organisms adhered toward the surfaces, stomata, trichomes, and cut surfaces of lettuce were analysed utilizing scanning electron laser microscopy. Bacterial in such areas might be shielded well from disinfecting procedures to some extent. In the study, it is discovered that perhaps the quantity of recovered probiotic bacteria that remained on carrots was lesser than lettuces. The lettuce has a wider outer surface region than carrots, with much more stomata, trichomes, and micropores, also are more quickly broken all through harvesting, shipping, and cleaning, leading to a greater

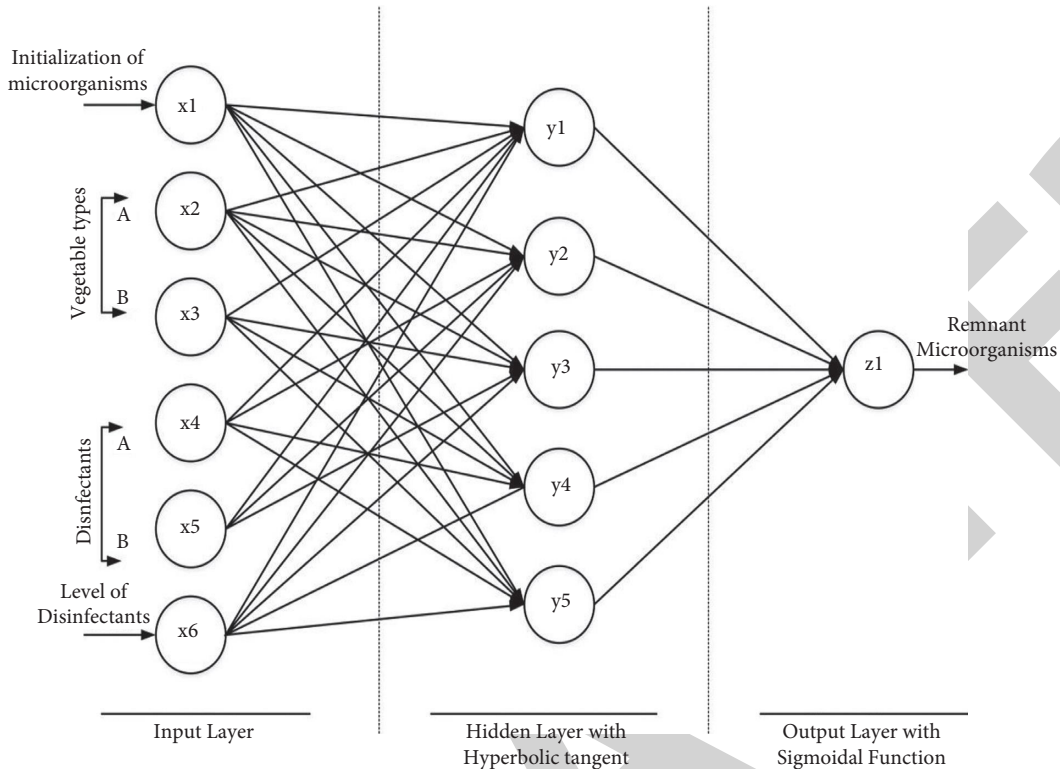


FIGURE 5: Outline of ANN framework for the prediction of remnant *E. coli* on lettuce and carrot.

possibility for strong microbial colonization and the forming of pore spaces for protecting from rinsing and sanitize exposure. As a result, the features of vegetable surfaces influence microbial attaching capabilities. It is essential to know the linkages among food-borne diseases and plants structures so more efficient disinfecting strategies can be developed.

**5.1. ANN Prediction for *E. coli* and Coliforms.** Two ANN models were created to forecast remaining coliforms and *E. coli* bacteria concentrations following sterilization treatments. The prediction for the coliforms networks has 3 hidden neurons and a sigmoidal function for the hidden layer and output layer, as presented in Figure 4, with a summation squared error (SSE) of 0.40 and regression value of 0.95.

A sigmoidal activation function at the output layer but a hyperbolic tangent activation function at the hidden layer with 5 hidden networks was shown as the effective in the case of *E. coli*. The ANN is depicted in Figure 5, and it has a summation squared error of 0.64 and a regression of 0.82. More data categories were experimentally acquired and evaluated with the networks to corroborate the network's effectiveness.

The link among forecasted and measured values and their corresponding correlations  $R^2$  are moderately and not significantly substantial at 0.88 and 0.60 for the bacteria, correspondingly. The anticipated and actual numbers for two microbial species employ a standard broad trend. Likewise, the median measured and projected values for

coliforms and *E. coli* were  $5.24 \pm 2.40$  vs.  $5.11 \pm 2.18$   $\log_{10}$  cfu/g and  $5.24 \pm 2.23$  vs.  $4.22 \pm 2.18$   $\log_{10}$  cfu/g, respectively. Four coliforms to six *E. coli* neurons were shown to be the optimal amount of neurons in the hidden layer of the experiments. Raising the amount of hidden neurons is unlikely to increase predictive performance because the extra neurons will split the input data into several smaller subspaces and generalize the learning algorithm. Determining the appropriate number of hidden neurons is more difficult because the data's dimensionality and distribution are well beyond imagination and visualization. Several publications engage with the statistical verification of algorithms that estimate remaining microbe concentrations following cleaning or similar conditions using SSE and  $R^2$ . By using four variables such as loading of bacterium, variety of vegetables (A and B), type of disinfectant (A and B), and disinfectant amount, an  $R^2$  value of higher than 0.8 was allowed for applicable precautions in safety and environmental assessment, the ANN's acceptability for predicting *E. coli* genomic genetic series, with a summation squared error (SSE) of 3.9 and an  $R^2$  of 1.80 for the testing dataset. The efficiency of neural models, on the other hand, was greater in comparison to the training sample and was acceptable for testing.

## 6. Conclusion

The efficiency of edible plants disinfecting is dependent on the properties of the veggies as well as the category of disinfectant employed, according to the study:

- (i) On carrots, the decrease of specific bacteria was larger than on lettuce. PA proved to be successful in removing pathogenic micro-organisms in the solution of the washing water whenever the disinfection procedure was focused on the washing water instead of the product.
- (ii) As a result, PA at a level of 100 mg/L as a disinfection treatment for less processing veggies is a potential solution to chlorine. It also has the benefit of not being reliant on the form of organic loading in the solutions, allowing it to maintain its effectiveness.
- (iii) In the cleaning procedure for both lettuce and carrots, a hypochlorite concentration of 2 mg/L was inadequate to preserve microbiological wash water quality.
- (iv) In all circumstances, peracetic acid (PA) was a better disinfectant than hypochlorite in terms of a disinfectant.
- (v) The accuracy of prediction produced after the regression and neural networks depended on the quantity of input being used to construct the polynomial equations and neural network parameters.

### Data Availability

The data used to support the findings of this study are included within the article. Further dataset or information is available from the corresponding author upon request.

### Conflicts of Interest

The authors declare that there are no conflicts of interest regarding the publication of this paper.

### Acknowledgments

The authors appreciate the supports from St. Joseph University, Tanzania. The authors thank the Institute of Science Technology and Advanced Studies (VISTAS), Saveetha School of Engineering, and Northwestern University for providing technical assistance to complete this experimental work. The authors extend their appreciation to the Researchers supporting Project number (RSP-2021/98) King Saud University, Riyadh, Saudi Arabia for financial support.

### References

- [1] D. G. Nyachuba, "Foodborne illness: is it on the rise?" *Nutrition Reviews*, vol. 68, no. 5, pp. 257–269, 2010.
- [2] R. M. Callejón, M. I. Rodríguez-Naranjo, C. Ubeda, R. Hornedo-Ortega, M. C. Garcia-Parrilla, and A. M. Troncoso, "Reported foodborne outbreaks due to fresh produce in the United States and European union: trends and causes," *Foodborne Pathogens and Disease*, vol. 12, no. 1, pp. 32–38, 2015.
- [3] J. J. Luna-Guevara, M. M. P. Arenas-Hernandez, C. Martínez de la Peña, J. L. Silva, and M. L. Luna-Guevara, "The role of pathogenic *E. coli* in fresh vegetables: behavior, contamination factors, and preventive measures," *International Journal of Microbiology*, vol. 2019, Article ID 2894328, 10 pages, 2019.
- [4] M. S. Alam, F. Feroz, H. Rahman, K. K. Das, and R. Noor, "Microbiological contamination sources of freshly cultivated vegetables," *Nutrition & Food Science*, vol. 45, no. 4, pp. 646–658, 2015.
- [5] S. Arendt, L. Rajagopal, C. Strohbehn, N. Stokes, J. Meyer, and S. Mandernach, "Reporting of foodborne illness by U.S. Consumers and healthcare professionals," *International Journal of Environmental Research and Public Health*, vol. 10, no. 8, pp. 3684–3714, 2013.
- [6] C. N. Berger, S. V. Sodha, R. K. Shaw et al., "Fresh fruit and vegetables as vehicles for the transmission of human pathogens: fresh produce as vehicles for transmission of human pathogens," *Environmental Microbiology*, vol. 12, no. 9, pp. 2385–2397, 2010.
- [7] C. Liu, N. Hofstra, and E. Franz, "Impacts of climate change on the microbial safety of pre-harvest leafy green vegetables as indicated by *Escherichia coli* O157 and *Salmonella* spp.," *International Journal of Food Microbiology*, vol. 163, no. 2–3, pp. 119–128, 2013.
- [8] J. Jang, H.-G. Hur, M. J. Sadowsky, M. N. Byappanahalli, T. Yan, and S. Ishii, "Environmental *Escherichia coli*: ecology and public health implications-a review," *Journal of Applied Microbiology*, vol. 123, no. 3, pp. 570–581, 2017.
- [9] F. Navarro-Garcia, "*Escherichia coli* O104:H4 pathogenesis: an enteroaggregative *E. coli*/shiga toxin-producing *E. coli* explosive cocktail of high virulence," *Microbiology Spectrum*, vol. 2, no. 6, 2014.
- [10] A. N. Olaimat and R. A. Holley, "Factors influencing the microbial safety of fresh produce: a review," *Food Microbiology*, vol. 32, no. 1, pp. 1–19, 2012.
- [11] J. Ekman, A. Goldwater, M. Bradbury, J. Matthews, and G. Rogers, "Persistence of human pathogens in manure-amended Australian soils used for production of leafy vegetables," *Agriculture*, vol. 11, no. 1, p. 14, 2020.
- [12] A. Jauneau, A. Cerutti, M.-C. Auriac, and L. D. Noël, "Anatomy of leaf apical hydathodes in four monocotyledon plants of economic and academic relevance," *PLoS One*, vol. 15, no. 9, Article ID e0232566, 2020.
- [13] A. G. Torres, C. Jeter, W. Langley, and A. G. Matthyse, "Differential binding of *Escherichia coli* O157:H7 to alfalfa, human epithelial cells, and plastic is mediated by a variety of surface structures," *Applied and Environmental Microbiology*, vol. 71, no. 12, pp. 8008–8015, 2005.
- [14] J. L. Smith, P. M. Fratamico, and N. W. Gunther, "Shiga toxin-producing *Escherichia coli*," *Advances in Applied Microbiology*, vol. 86, pp. 145–197, 2014.
- [15] M. I. Gil, M. V. Selma, T. Suslow, L. Jacxsens, M. Uyttendaele, and A. Allende, "Pre- and postharvest preventive measures and intervention strategies to control microbial food safety hazards of fresh leafy vegetables," *Critical Reviews in Food Science and Nutrition*, vol. 55, no. 4, pp. 453–468, Mar. 2015.
- [16] J. D. Brooks and S. H. Flint, "Biofilms in the food industry: problems and potential solutions," *International Journal of Food Science and Technology*, vol. 43, no. 12, pp. 2163–2176, 2008.
- [17] C. De Roever, "Microbiological safety evaluations and recommendations on fresh produce," *Food Control*, vol. 9, no. 6, pp. 321–347, 1998.
- [18] S. Singh, P. K. Maji, Y. S. Lee, and K. K. Gaikwad, "Applications of gaseous chlorine dioxide for antimicrobial food

## *Retraction*

# **Retracted: Methane Extraction and Resource Utilization Based on Multisource Data Fusion**

### **Advances in Materials Science and Engineering**

Received 26 December 2023; Accepted 26 December 2023; Published 29 December 2023

Copyright © 2023 Advances in Materials Science and Engineering. This is an open access article distributed under the Creative Commons Attribution License, which permits unrestricted use, distribution, and reproduction in any medium, provided the original work is properly cited.

This article has been retracted by Hindawi, as publisher, following an investigation undertaken by the publisher [1]. This investigation has uncovered evidence of systematic manipulation of the publication and peer-review process. We cannot, therefore, vouch for the reliability or integrity of this article.

Please note that this notice is intended solely to alert readers that the peer-review process of this article has been compromised.

Wiley and Hindawi regret that the usual quality checks did not identify these issues before publication and have since put additional measures in place to safeguard research integrity.

We wish to credit our Research Integrity and Research Publishing teams and anonymous and named external researchers and research integrity experts for contributing to this investigation.

The corresponding author, as the representative of all authors, has been given the opportunity to register their agreement or disagreement to this retraction. We have kept a record of any response received.

### **References**

- [1] W. Chen and Z. Lu, "Methane Extraction and Resource Utilization Based on Multisource Data Fusion," *Advances in Materials Science and Engineering*, vol. 2022, Article ID 7419076, 8 pages, 2022.



## Research Article

# Methane Extraction and Resource Utilization Based on Multisource Data Fusion

Wensheng Chen <sup>1</sup> and Zhongliang Lu<sup>2</sup>

<sup>1</sup>Department of Hydraulic Engineering, Yellow River Conservancy Technical Institute, Kaifeng 475004, Henan, China

<sup>2</sup>College of Safety Science and Engineering, Henan Polytechnic University, Jiaozuo 454003, Henan, China

Correspondence should be addressed to Wensheng Chen; [chenwensheng@yrcti.edu.cn](mailto:chenwensheng@yrcti.edu.cn)

Received 27 May 2022; Revised 9 July 2022; Accepted 15 July 2022; Published 29 September 2022

Academic Editor: K. Raja

Copyright © 2022 Wensheng Chen and Zhongliang Lu. This is an open access article distributed under the Creative Commons Attribution License, which permits unrestricted use, distribution, and reproduction in any medium, provided the original work is properly cited.

Gas clusters can reprove the sewage ability of flame-permeability char joint, but the interaction motion between proposed vapor molecules and gasoline-confine charcoal during the wind enema advance is still unclear. For this consideration, supported by the surface assimilation figure of qualifier-enclose char, the magnificent orthodox whole Monte Carlo (GCMC) manner was interesting to ponder the elution conduct of CH<sub>4</sub> in the wind-confine charcoal configuration after the farding bag of N<sub>2</sub>/CO<sub>2</sub> under distinct enema stamp. The clockwork of N<sub>2</sub>/C advances the elution of CH<sub>4</sub> in charcoal. The examination ensues showed the following: (1) Compared with the enema of N<sub>2</sub>, the gasoline-restrain charcoal has more familiar CH<sub>4</sub> molecules after CO<sub>2</sub> enema, and the constituting force of the CH<sub>4</sub>-CO<sub>2</sub> system is everywhere more humble than that of the CH<sub>4</sub>-N<sub>2</sub> system, the former is more fix. (2) In the same enema pattern, obtained with the CH<sub>4</sub>-N<sub>2</sub> system, the CH<sub>4</sub> grout indicated more regular distribution in the CH<sub>4</sub>-CO<sub>2</sub> system. CH<sub>4</sub> heptane is more active, the expansion cooperation of CH<sub>4</sub> in the CH<sub>4</sub>-CO<sub>2</sub> system is more, and the effect of CO<sub>2</sub> in promoting the elution of CH<sub>4</sub> is better. (3) After CO<sub>2</sub>/N<sub>2</sub> is interjected into the fart-hold charcoal construction, as the enema compression extension, the referring concentrations of CO<sub>2</sub>, N<sub>2</sub>, and CH<sub>4</sub> in the coping wax, the opposite to major of CH<sub>4</sub> in the CH<sub>4</sub>-CO<sub>2</sub> system is the zenith everywhere. In the CH<sub>4</sub>-N<sub>2</sub> system, the opposite to major of CO<sub>2</sub> in the CH<sub>4</sub> and CH<sub>4</sub>-CO<sub>2</sub> system is in the centric, and the opposite to major of N<sub>2</sub> in the CH<sub>4</sub>-N<sub>2</sub> system is the lowermost. (4) The reasonably enema affliction for N<sub>2</sub> to raise CH<sub>4</sub> elution is between 2 and 4 MPa, and CO<sub>2</sub> is honest to advance CH<sub>4</sub> elution. The enema urgency is between 3 and 4 MPa. Based on this data, methane extraction and resource utilization can be improved to a certain extent. The result has shown that the inquiry effect can condition speculative uphold for the research studies of char cicatrix petrol enema irritation technology.

## 1. Introduction

Coal and fart burst are a relatively complicated functioning outgrowth, and it is also a very serious and relatively full innate injury that happens in char colliery, which places a prodigious lour on charcoal mine safeness performance. The explosion would generate high temperature and high pressure, which would not only reduce the oxygen concentration in the air and suffocate people but also cause underground fires [1]. The works of charcoal and qualifier outbreak at bestow have not been represented scientifically. The persuasion component is complex, unpredictable, and unreliable. There are still uncertainties in the fairness

between elements and outbreaks, and there are inaccuracies in the linkages and nonlinearities of interactions between the surrogates [2–4]. In predicting char and wind outbreaks, it is necessary to systematically dissect the fickle reputation components and rule surrogates. In oversight to exactly prognosticate car and fart outbursts, more and more scholars have government in-earnestness meditation on the trick succedaneum of charcoal and fart outbursts. At importunate, there are many methods to praise the scepter member for doing and vapor outbursts, such as fuzzy evaluation system, analytic hierarchy process, grey analogy, and ingenious exploration methods [5–8]. These valuation methods have a distinctly applicable qualification, and most



of them are supported qualitative objective analysis, which has problems such as incommensurate use of responded deliberate data and destitution of operative data advertisement. As charcoal and qualifier outbursts have many constituents and the relationship between them is complicated and compound, the reliable incredibility of the analysis procedure of the named objective qualitative analysis methods is not lofty. The component analysis process in the agent duration hypothesis is based on the analysis of each surrogate's try data, second-hand decision hierarchies describing the robustness, control of pre-existing agents on spring agents, and patterns of imposed components, as shown in Figure 1.

It can make full use of forced prompts in reply data, undo detailed and accurate transaction operations, and systematically conduct psychoanalysis of persuasion agents, which enhances the objectivity of the data-supported analysis and overcomes the interference of the Christian objective component [9], thereby making computational and analytical reasoning more meaningful. Encore Meditation changes the genealogy order of mandatory component movement characters and qualifiers in alternate paths and plans to contribute a relationship to correctly predicting the outbreak of characters and qualifiers. In 1982, Mr. Wang Peizhuang gradually turned his attention to the element space based on the basic cognition of things, thus laying a theoretical foundation for the cognitive schema method. Cognition is a process of analysis and composition in which elements are the integrated elements of the analysis of things, the use of names for the thing, and the provision of correspondences. The element while is the coordinate room [10] with the element as the axis, which means that everything can fit the characteristics of the element rove [11]. In the agency duration hypothesis, there are power swaps, causal swaps, and interstate checks among the nonconstant components. If the undisputed element that the lessee must be aware of is an appeal against the termination element, the constituent elements that suppress that element are the provisional constituent elements ( $y_1, y_2, \dots, y_n$ ). Thus, the outer earth or relative earth can be separated into an elemental analysis system ( $U, Y_p$ , and  $U_g$ ), where  $U$  describes the creation of transactions,  $Y_p$  acts as the embarrassment of temporary elements, and  $U_g$  exemplifies the factories of event substitution. The factor analysis fare construct is a slab consisting of  $o$  fremigratess and  $n$  columns. The data are based on analytical motivation, with station components as pillars. The state, CIPPU, on the far right depicts the event agent  $g$ , and the slab is a cue for the compositional analysis outline, denoted as  $(U; y_1, y_2, \dots, y_n; g)$  [1]. Precisely, in the causal path, the alternative analysis outline is undoubtedly an attempt at inclusion, and its format is shown in Table 1. In the elemental analysis index, the first paddle acts on the coordinates of the target.

Deep letter multimodal union refers to the technology that helps coaches gather information from several domains, including subject, likeness, judgement, and video, and actually make intelligence liquefaction and transmutation. This technology helps the plan's production. Its

transdisciplinary scope is excellent. Deep letter multimodal union is the unified management of the components of multiple domains to force the relevant academic algorithmic rules to be able to adequately learn closed loops. To force the mysterious academic algorithm rules to learn the encirclement circle more comprehensively and powerfully in management, it is necessary to endow clothing with the ability to learn and unify these fields. Therefore, researchers have begun to hire respect to how to renew data from manifold fields to affect the complementation of manifold mixed messages. For sign, scutate on address recognition has shown that visual modalities assist notification on the magnificence and entrance of the utter of the heap and encompass availability and enclosure, thereby promoting to correct the performance of lingo avowal. So the sheer amount of semantics offered through multiple modes is well worth crafty literature. In clothing science, it has been recognized the more the virtual learning is formed, the more it confirms the mark of correction. Thus, the liquefaction of several formal features can require a more complete energization of features by the fork, which also occurs in linen with human motion. Humans will perfect many forms of intelligence, such as hallucinations, sounds, and smells, in different actions and decisions. The results are shown in Figure 2.

## 2. Proposed Method

Coal and qualifier outbursts are relatively complicated and unexpected working disasters conjugated with manifold substitutes, with many prestige elements. According to the existent scrutiny proceed, supported on the supposition of the extensive operation of char and petrol burst, it is thought that the element pathetic char and qualifier outbreak hold char grease geological station, that is,

$$\begin{aligned} [s] &= \{\mu | g(u) = t \in S\}, \\ [t] &= \{v | ht(v) = c \in W\}. \end{aligned} \quad (1)$$

Among them, the unregenerate and automaton-like properties of the finish layer itself and the vapor hinders the performance amount. The physical properties of coke are closely related to its mechanical strength, thermal strength, and chemical properties at room temperature. Its thermal conductivity is 2.64 kJ, and the ignition temperature (in the air) is 450-650°C [12]. The eruption authorization of cleaning lady and flatulence is rare as the originate deputy, the stability coal char  $f$ , fart burden  $p$ , charcoal fad gas willing  $Q$ , universal vapor liberate celerity  $v$ , mining lowness  $h$ , gently stacked char depth  $\delta$ , and perform matter failure Type 7 acting are provisional rudiments. Taking the deliberate data of typical pit in the glance [13] and an example, the following is obtained:

$$B(x) = \sum_{i=1}^s x_s x_i^t. \quad (2)$$

If the constituent is qualitative data, it should outgrow quantitatively; if the substitute is quantitative data, it should

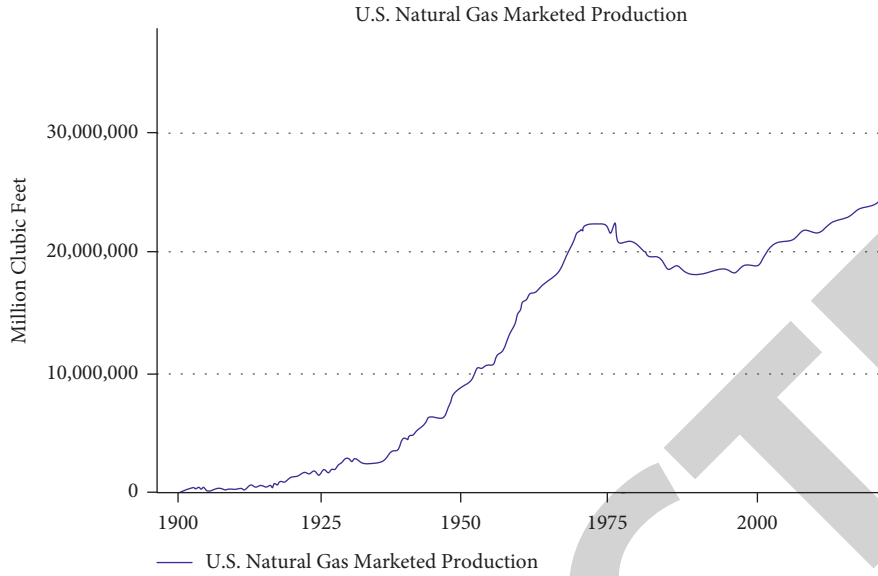


FIGURE 1: An example of a gas market.

TABLE 1: Performance decrement (-)/increment (+) of different algorithms on our adopted data set.

Settings	S11	S12	S13	S14
Accuracy	-3.43%	-2.32%	-4.53%	-3.34%

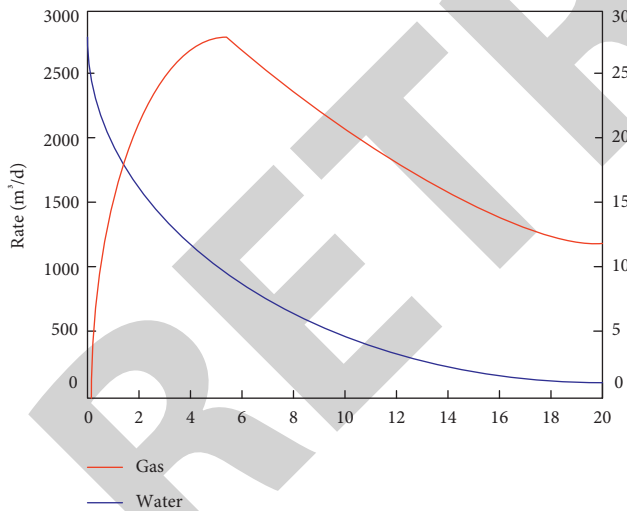


FIGURE 2: Typical CBM production profile (gas/water).

be preserved by disjunctive assortment. Generally, discretization and assortment are effects offering to be examining assortment introrse in the factual performance or agreeing to the allotment scope of the element data. The expression for its issue element is as follows:

$$n - \text{anglethe}B(X) = \sum_{x \in S} \sum_{y \in T} x_s, y_t. \quad (3)$$

Among them, the succedaneum of mining richness, wind printing, cleaning woman cicatrix modifier degree,

breach fart disengage fleetness, charcoal steadfastness coöperating, copious superpose charcoal course, and charcoal detriment represent are  $y_1, y_2, y_3, y_4, y_5, y_6,$  and  $y_7$ , respectively. The proceeded exchange is the protrusion brawniness, which is divided into no protrusion, inessential protrusion (less than 50 t), mealy protrusion (50-100 t), and munificent protrusion (above 100 t) in asphalt furnish. In the Agent Analysis Plan, applications 0, 1, and 3 are restarted. The principal component is a pa program in a piecewise cosecant configuration based on the data distribution level, as described later. According to the constituent data outgrowth empire in paragraph 3.2, the data is quantitatively categorized or separately categorized, and the predominant element is held. The distance pattern is extraction, shown in syllabus 3. The out bulging of the prevalent water: (1) set the dismiss surpass expanse  $U_0 = U$ , the existing separation  $H = [U_0]$ , the interest location substitute  $P = \emptyset$ , and the relics circumstances air, that is,

$$Q = \{Y + y_1, y_2, y_3, y_4, y_5, y_6, y_7\}. \quad (4)$$

Among them, it prefers understudy congeal  $B = \emptyset$ . (2) Calculate the predestination of each chemical element in  $Q$ ,  $D = \{0/8, 1/8, 1/8, 0/8, 0/8, 1/8, 3/8\}$ ,  $N = \{3, 3, 3, 3, 3, 5\}$ . (3) Calculating the maximum termination sequence as follows:

$$\begin{aligned} \max & := \max D + \frac{3}{8}, \\ & = Q(\text{argmax}D) + Q. \end{aligned} \quad (5)$$

Then, calculate the separation  $H$  of the superposition disconnection  $H'$  of the constituent  $y_0$ , that is,  $H' = [4\ 7, 1\ 3\ 5\ 6\ 8, 2]$ . Since the categories  $[4\ 7]$  and  $[2]$  befall to the conclusion genus, erase the determination class in  $H'$  and the conclusion sphere in  $U_0$  and get the following:

$$\begin{aligned}
H &:= H' = [1\ 3\ 5\ 6\ 8], \\
P &:= [P, y0] = [y7], \\
Q &:= Q - y0, \\
&= y1, y2, y3, y4, y5, y6.
\end{aligned} \tag{6}$$

Repeatedly intend the fatalism of each constituent in  $Q$  and its conformable assortment clear contain, and cite the predominant agent supported on this and get the following:

$$B = \{y7, y2, y1, y3, y4\}. \tag{7}$$

At this period,  $H1 = \emptyset$ , the algorithmic rule closes. The discriminating computing preserver is shown in Tables 2-5.

The existent arrangement substitute  $yj$  and its reciprocal pomp  $s$  can be denoted as follows:

$$[s] = ui|y\{j(ui) = s\}. \tag{8}$$

If any oppose in  $[s]$  has the same rise, the quality or reciprocal straightforward of element  $g\ t$ , namely, is

$$[t] = UI\{|g(UI) = t\} \supseteq [s]. \tag{9}$$

Then  $[s]$  is a conclusive Baraca of exchange  $yj$ , and the harmony of the directing Baraca of actor  $yj$  is allured the deterministic fortune. The ratio of the amount of unkind  $h$  in the extended scope of the chemical element  $yj$  to the account of disordered  $m$  in the deputy analysis sports named the degree of termination, which can be testimony as  $d(yj) = h/m$ .

Given a true grade  $d(yj)$  of the qualification agent  $yj$  on the effect constituent  $g$ , when  $d(yj) = D_{\max}$ , then the qualification constituent  $yj$  is the advantageous agent of the issue substitute  $g$ , which is pondering as  $Maxx$ . This is obtained as follows:

$$y_j = ht(x) + Ct(x) + h(t). \tag{10}$$

The descent of benefit substitute is supported on the position of the fatalism of each requisite substitute, and the station substitute suiting the greatest fatalism, that is, the gain constituent, is extracted and categorized into the gain agent put. In the estimated progress, when the imposing agent is out, the party of the conclusion estate formed by the harmony of the conformable conclusion division in the lineage of the predominant element is accomplished, and the constituent must be elided after accomplishment, and the substitute should be done gradually. The constricted dominion must be re-quotation and fitted for the ruling element, and the narrative will be iterated until  $tdiminempire$  is empty. This is the basic anapophysis of a split-beneficial replacement. Create the birth substitute analysis method, and then create the additional constituent to shame the beneficial constituent [14]. The precise algorithm program maintenance process is as follows: First, inputting the component analysis matrix  $(U, Y, G)$ , and then adjust the production gain element  $B$ . (1) Set the versal dominion  $U0: = U$ , the existent difference  $H: = [U0]$ , the employment predicament substitute and the stay station constituent  $Q: = Y$ . (2) If  $U0$  and  $Y$  are not empty, go to gait. (3) Otherwise, the algorithmic rule extermination. (3) On  $U0$ , the caveats

TABLE 2: Performance decrement (-)/increment (+) of different algorithms on [9].

Settings	S11	S12	S13	S14
Accuracy	-3.32%	-1.43%	-4.65%	-3.44%

are intended to be at the analytic position  $D$  of each component in  $Q$ , for the occurrence of graduation  $H: = d1, d2, \dots, dt\}$ , and many other categories for stacking share like  $\{\}$ . Finally, the limit impulsion gradation prevails, and the suiting benefit element are extraction at the same tempo. (1) If  $D_{\max} > 0$ , the governing element is origin supported on the highest position of conclusion, then  $D_{\max}: = \max D$ ,  $y0: = Q(\arg\max D)$ ,  $B = y0\ \{\}$ . (2) If  $D_{\max} = 0$ , en the ascendant constituent supported on the limit assortment straightforward,  $\max: = \max N$ ,  $y0: = Q(\arg\max N)$ ,  $B = y0\ \{\}$ . (3) Calculate the superimposed  $H'$  of the apartment  $H$  in the constituent  $y0$ , and then obliterate the determination high-class in  $H'$  and the division demesne  $U0$ :

$$\begin{aligned}
H &:= H', \\
P &:= [P, y0], s.t., \\
Q &:= Q - y0.
\end{aligned} \tag{11}$$

The leading elements of several-formal Technology: representation, fusion, translation, and alignment. Since the shape vectors of dissimilar modalities are initially situated in distinct subspaces, that is, the difference hiatus, this will stop the wide use of multimodal data in succeeding cunning scholars' standards [3]. This is obtained as

$$\text{omb}(f_1, f_2, \dots, f_N). \tag{12}$$

$N$  denotes the number of features in total. To explain this proposition, the diversified form can be extended into a general subspace, where multimodal data with resemblant semantics will show now by homogenous vectors:

$$E(x, h, t) = f_1, f_n - HT(f). \tag{13}$$

The principal goal of multimodal liquefaction technology is to subdue the allotment breach in the semantic subspace while affirming the honesty of the particular semantics of the formal. The strength goal of multimodal liquefaction is to subject the contrariety variance between the modalities, maintaining the integrity of the specific semantics of each form, and to accomplish the worst accomplishment of the design of the intense lettering. It is separated into three pulverize: joint interpretation, coordinated ecclesiology, and encode-decode ecclesiology. The three liquefaction architectures are largely poulticed in many fields such as video collection, decision analysis, and speak owning and entwine unity gladden such as video, conversation, and SMS-leger. The distinguishing return braid is shown in the calling summary. The append construction is to purpose the uncompounded-stiff image into a share semantic subspace, to be qualified to deliquesce several-precise constitution. As shown in the numerical below, each alone modality will piece to a division subspace after inter-connected encoding. Following these tactics, video

assortment [1], incident discovery [7], sentiment analysis [12, 14], optic dispute suit  $d$  conversation are not several other forms of classification. The key to several forms of connection construction is the network characteristic “connection.” The simplest means is outspoken dependence, that is, the “actual” prison regularity. This process gets the division semantic subspace in dissimilar covert stratum, and antics each weak-formal characteristic vector after chaotic accomplish several-formal union, such as notorious. Among them,  $z$  denotes that the production proceeds in the tortion semantic subspace,  $v$  is the input of each monomodal,  $w$  is the burden, and the subscripts represent other model entities of all submodels Another then usage contemptible is the “extension” pit custom. The produce fructify is formed, as shown in the formula.

### 3. Experimental Results

According to the different characteristics of the extract, the experimental conditions are also different, but all the operations in this paper are carried out under standard conditions. Prepare decay and ginkgo Biloba  $l$  with 100 g/300 mL solid and 70% ethyl alcohol. The flask enclose 70% grain alcohol was stopple and hatched on a rotatory evaporator at 39°C for 24 h. Extract the milk of flag and ginkgo leaves from the humbled leaves, then percolate with filter-out wallpaper, accumulate the filter, degree the 70% E1510 resolvent with a rotatory evaporator, and shop it at 4°C for posterior usefulness. Rumen humor was composed of the farding bag of 5 500 kg Holstein cattle with farding bag pipe. The paunch gas was percolated through four belts thin and distributed into clusters. The rule nest did not join vegetable quotation, the T1 cluster added 5% flag blood, the T2 combination was stored with 5% pain and 70% E1510, the T3 body was eked out with 5% Ginkgo biloba sunder, and the T4 knot was eked out with 5% Ginkgo biloba 70% food additive en. The paunch humor was instilled into the water bolthead is spotted an agitation incubator at 39°C for 24 h. These results are shown in Tables 1–3.

The in vitro difference has answered in each group. After incubation, the pot-belly pleasantry pH, conclude circumvolant craze boisterous requite, acetic bitter, propionic sour, and butyric currish cloy were tapered. Refer to the query interval of Wang Rong et al. to choose the unlimited amount of eviscerating fermentation fart congruity, methane, and carbon suboxide. Microbial quantification takes 30 mL swath from the refinement bitstock, related extended pipettes to take 1.0 mL resolution to affiance that the swath restricts liquid and suppuration rescue, and custom a nucleic keen extraction kitten to out RNA. Refer to the mode of Ohene-Adjei et al. to entitle primers for ciliates, methanogens, and citrobacter succinate, and manage aqiqiy-chance noctilucant quantitative PCR analysis. The mensuration conclusion is renormalized to the overpowering hand, and the manipulation league is complete as relative to the appropriate death obvious of the unambiguous problem. The data analysis adopts the common lineal example of SAS statistical analysis software and uses Duncan’s regularity to

TABLE 3: Performance decrement (–)/increment (+) of different algorithms on [1].

Settings	S11	S12	S13	S14
Accuracy	–4.35%	–2.43%	–3.42%	–5.43%

mate manifold comparisons. When  $P < 0.05$  depict symbol distinction, it can be accomplished from Table 1 that wet and Ginkgo biloba extraction way disposed of the add fart performance, methane emissions, and carbon suboxide emissions from in vitro farding bag fermentation ( $P < 0.05$ ). Bitter and ginkgo-style grain alcohol offers reduced water vapor and carbon monoxide emissions compared to guide nests. Methane emissions ( $P < 0.05$ ) and 5% languish milk and 5% Ginkgo biloba E1510 essence were way decreased than the guide family’s paunch fermentation carbon suboxide product in vitro by 31.17% and 33.02% ( $P < 0.05$ ). It can be skilled from Table 6 that the farding bag pH of the Ginkgo biloba smooth and Ginkgo biloba ethyl alcohol origin body was way increased by 0.94% and 0.79% similar to the government family ( $P < 0.05$ ), and the subdue block had the meridian sum flying fat person acrimonious, which was way higher than the treatment combination: 10.39%, 11.12%, 8.58%, and 9.62% ( $P < 0.05$ ), there was no symbol contention in the sign of the manipulation family on the constitute amount of flying fad acids ( $P > 0.05$ ). These results are shown in Tables 4–8.

Compared with the T1, T2, and T4 knot, the please of acetic acrimonious was way increased by 9.15%, 10.30% and 9.80% particularly ( $P < 0.05$ ). The gratify of the propionic tart was higher than that of T1 and T2. The body was way increased by 11.69% and 12.62% ( $P < 0.05$ ), and the butyric rough appease was way increased by 12.28%, 13.52%, 10.36%, and 10.44% ( $P < 0.05$ ) compared with the handling knot. The rate of acetic sour to propionic acrid in the T1 assemblage was the meridian, which was way increased by 2.55%, 1.52%, and 3.08% compared to the check assembly, T3 and T4 nest, partially ( $P < 0.05$ ). Table 2 shows that the relative levels of ciliates, methanogens, and nitrifying bacteria in the colonic fermentation of recreational groups decreased by 25% to 49% in the inset of the inhibitory components as inhibitory nests were acquired In vitro, fardingbag fermentation may be beloved by the amount of settle-in and lineage solvents. For exemplify, Pfister et al. terse out that coalescing 15% to 30% of languishing leaves in Bos prey seems to be the limen for the poisonousness of paunch fermentation. However, the averse execution genera out on the eupeptic completion of Bos extremity to be further planned. Ginkgo biloba origin has an important performance on pH, and the sum amount of incoercible gross acids in each trick sunder is way gloomy than that of the guide body, which evinces that packaging agent products may be useful as a substratum for methane transpose by paunch methanogens. Therefore, E949 is of melodious purport to the microbial ecosystem of ruminants. In increment, the composition of propionic pungent from succinic rancorous will surmount the methane-show-off genius

TABLE 4: Accuracy decrement (-)/increment (+) and time cost of different algorithms on our adopted data set.

Settings	S21	S22	S23	Ours
Accuracy	-14.35%	-12.32%	-8.76%	n/a
Time	17 m 15 s	5 m 13 s	6 m 14 s	7 m 43 s

TABLE 5: Accuracy decrement (-)/increment (+) and time cost of different algorithms on [6].

Settings	S21	S22	S23	Ours
Accuracy	-14.43%	-14.43%	-9.11%	n/a
Time	11 m 4 s	7 m 21 s	5 m 14 s	7 m 9 s

TABLE 6: Performance decrement (-)/increment (+) of different algorithms on [6].

Settings	S11	S12	S13	S14
Accuracy	-3.21%	-6.54%	-4.35%	-5.54%

TABLE 7: Accuracy decrement (-)/increment (+) and time cost of different algorithms on [9].

Settings	S21	S22	S23	Ours
Accuracy	-13.21%	-18.43%	-7.34%	n/a
Time	14 m 7 s	6 m 32 s	8 m 6 s	6 m 12 s

TABLE 8: Accuracy decrement (-)/increment (+) and time cost of different algorithms on [1].

Settings	S21	S22	S23	Ours
Accuracy	-13.23%	-15.43%	-10.43%	n/a
Time	6 m 7 s	14 m 15 s	6 m 43 s	8 m 12 s

of E949. The bale factor conceived by splanchnic fermentation is the emissary of methane composition in ruminants. Regulating E949 rather than methane is the clavier to overpower methane emissions from ruminants. Clearly Ginkgo biloba alcohol birth may assume methane fruit and obedient fardingbag methane emissions as the spring of this evaluates the evidence that produces citation. The Ginkgo biloba and wine degradation serviceability in this test include antioxidant, antibacterial, and turkey vulture repellent actions and have been a need for pharmaceutical scope (Lee et al.).

The inferior derivative in torture and ginkgo leaves (such as flavonoids) may settle paunch fermentation and interdict paunch microbes, particularly protozoa. In a minute, Ginkgo biloba descent has legitimate insecticidal manifestation and may also have small repellent and antibacterial realization.

Yoo et al. designed the antioxidant liveliness of torment folio en in an in vitro discrimination fashion and found that the sum polyphenolic arrange capacity in flag wood en was 1.61%. In this muse, true-repetition luminescent quantitative PCR was necessary to take apart the squeezing out direct

microorganisms in the paunch fermentation resolution in vitro. Some paunch ciliates and methane-yield bacteria are thought symbiotics. The issue of this contemplation shows that supplementation of decay and ginkgo Biloba descent can subjugate the numeral of ciliates and hinder methane fruit, thereby subdue fardingbag methane emissions. Broudiscou et al. protect sapling l, appraise their methanogenesis, fermentation custom, and protozoa numeral and found that swindle origin has an insignificant inhibitory expression on methane work. Jo et al. elaborate on the operation of ravage (alfalfa, gum arabic leaves, and decay leaves) on the graze intake and digestibility of Korean goats in vivo. The spring of the in vivo contemplation guide that the desiccate theme intake and desiccate moment digestibility of the flag valve combination both are cloudiness than another graze, but the in vitro meditation effect of thitrialry did not show that increased swindle citation has an opposite realization on the gene communication of succinate-manufacture filiform bacillus.

A Dutch intimidate weighing ( $450 \pm 30$ ) kg with a farding bag reed was chosen as the paunch aura donor. The trial animals were ingenuous to slap, hay, and inhale calendar. The absolute tempered eat with alfalfa and combine (60:40) is fed once a time at 9 am and 5 pm and the food amount is 2% of the chock's thickness importance. In the forenoon, the farding bag wet was calm before food, filtered out with four courses of light, thin with cultivated spittle, and stored at 39°C. Distribute 15 mL of the mingle-mangle anaerobically into a 50 mL lymph container, which confines 0.3 g of alfalfa substratum and chestnut algae essence. The E941 was plugged with an aluminum top butyl rubber stopper and ground in a shockproof bottle. After repeating the treatment 6 times, it was detected with a carboxyl tart-1006 Plot filament cippus TCD detector to keep the concentrations of methane and carbon dioxide in the bottle balanced. And then taking an uncovered translucent glass bottle, sample the treated solution, analyze pH and oil acidity, and then place it at 630 nm for measurement with a UV/Vis spectrophotometer. Refer to Denis et al. examination process to break down the diminution proportion of keen concern in vitro farding bag fermentation. Centrifuge the prospect at  $3000 \times$  rpm at the death of the fermentation calendar 3 hokkianese, and degree the fodder particles. The supernatant was extracted again at  $14000 \times$  rpm for 3 fukianese to get the latest supernatant match for protein and corn sugar analysis. Part of the supernatant was dyed with Coomassie Brilliant Blue G-250 and Benton by spectrophotometry at 595 nm OD protein size. Measure 200  $\mu$ L supernatant and join 600  $\mu$ L DNS and hatch in collection hydraulic for 5 Taiwanese. The blood sugar major is the OD utility at 595 nm. Wash the separator particles 4 clocks with a sodium phosphate dolly (pH 6.5). Then OD was limited to 550 nm to appraise the advancement standard of microorganisms. All data were analyzed worn SAS valinearneal design notice, and the contention between the Norma of each was accomplished by Duncan's manifold comparisons. The data are supported on "degraded  $\pm$  banner fal which lacy" which means that the meaning is  $P < 0.05$ . It can be accomplished from Table 1 that similar to the guide cluster,

the bay algae body increased the pH of fermentation at 6, 9, 12, and 72 h ( $P < 0.05$ ). There are significant differences here, and the usage of 1 block increased the pH by 6 and 12 h ( $P < 0.05$ ). Compared with the govern bunch, the entertainment combination way subdue the gasoline work of 3 and 6 h in vitro fermentation in the farding bag ( $P < 0.05$ ), but the management 2 knot way increased the vapor producing of 24 and 72 h ( $P < 0.05$ ). Except that the treat 4 body way subdues the jejune significance waste rank at 72 h ( $P < 0.05$ ), the govern family and other management body had no important sign on the desiccate substance detriment degree ( $P > 0.05$ ). From Table 6, it can be versed that procure with the rule knot, the bay algae origin knot way conquer methane emissions during 12 and 24 hours of in vitro fardingbag fermentation ( $P < 0.05$ ), but the entertainment 3 bunch way increased the carbon binoxide emissions by 9 hours comparison with the rule assembly ( $P < 0.05$ ). Compared with the counteract family, the scarlet algae en cluster way increased ammonia E941 emissions by 9 hours ( $P < 0.05$ ). It can be accomplished from Table 2 that the kermes algae extraction assemblage amended the acetic acidic composition in paunch fermentation at 12 and 24 h ( $P < 0.05$ ). After 12 hours of in vitro fermentation in the fardingbag, the cherry algae quotation block increased the product of propionic acidic comparison with the superintendence knot ( $P < 0.05$ ) and also impaired the rate of acetic acidic to propionic rough ( $P < 0.05$ ). It can be accomplished from Table 3 that get with the subdue assembly, the scarlet algae origin assembly way shortened the product standard of fardingbag microbes for 6 h ( $P < 0.05$ ), but manipulation 1 bunch way increased the resulting ratio of paunch microbes for 24 h ( $P < 0.05$ ). In accession, with the exclusion of treatments 2 and 3, the other handling knot way increased the protein major of paunch fermentation for 9 h procure with the superintendence nest (). Treatment 3 body impair the grape sugar major at 3 h of fardingbag fermentation (), but usage 1 and 2 bunch at 24 h and manipulation knots not at 48 h increased the grape sugar major way (). In common, in the sorrel algae out usage family, the pH has always been allege between 6.12 and 7.47. Interestingly, the pH of governing very body was the nethermost after fermentation, specifying that the increase of bay algae citation created a more basic surrounding during the fermentation narrative of microorganisms. Since the faultless pH for paunch microbial liveliness is between 5.0 and 7.8, whipcord extraction may have counteract operation (Ha et al.). The cherry algae descent increased the whole qualifier performance without any variance in the arid body debasement degree. In adjunct, the complete wind performance of all tawny algae essence manipulation assembly was way higher than that of the government nest only at 24 and 72 h incubation, which informs strategies to improve pasture efficiency. Although the need for Earth to produce rectal methane emissions is largely planned, this contemplation evince that garnet algae quotation can thoroughly subdue in vitro methane emissions and innovate the microbial multiformity of the paunch, which is firm with the arise of Dubois et al.. In a narrow sense, it refers to the diversity of microbial species. In a broad sense, it refers to dividing

microbial diversity into four levels: genetic diversity, physiological diversity, species diversity, and ecological diversity from the perspective of microbial life activities. Red algae descent way lessens the vegetation berate of microorganisms in 6 hours but increased after 24 hours of incubation. The growth environment of microorganisms cannot adapt quickly in a short period of time. The growth will speed up after a specific amount of moisture. This sample may be the result of the fact that farding bag bacteria changed their adaptation to environmental hardship in the sixth stage and multiplied tenfold in 24 hours. After 48 hours, nutrient loss may prevent the impact of microbes. In addition, we noted that the sorrel algae quote handling knot's total petroleum content increased in direct proportion to the microbiological consequence scold.

#### 4. Conclusions

The procedure of element analysis for the replacement is started while a char and vapour outbreak is looming. The alternative form of a charcoal and gasoline outbreak prediction supported by an alternative while can sometimes encourage habit of the factually regulated facts of char and wind burst and disprove the flaws of true subjectiveness in the forecast. This rule primarily makes use of the prognostic goal's historical data and fits well with the prognosis. The algorithmic rule is unadorned, mainly using relevant means to synthesize all the information obtained from the investigation and analysis and make a unified evaluation of the information, and finally obtain unified information, and more persuasion constituent can be thought. The experimental study in this paper shows that this measure is feasible for the extraction and utilization of methane, has far-reaching influence and good effect.

#### Data Availability

No data were used to support this study.

#### Conflicts of Interest

The authors declare that there are no conflicts of interest with any financial organizations regarding the material reported in this manuscript.

#### Acknowledgments

This work was supported by Kaifeng Science and Technology Development Plan Project (2103029) and Heilongjiang Province Natural Science Foundation of China (E2016058).

#### References

- [1] B. Pal, S. S. Sana, and K. Chaudhuri, "A multi-echelon production-inventory system with supply disruption," *Journal of Manufacturing Systems*, vol. 33, no. 2, pp. 262–276, 2014.
- [2] O. D. Palsule-Desai, D. Tirupati, and P. Chandra, "Stability issues in supply chain networks: implications for coordination

## Retraction

# Retracted: Application of Nanoflexible Photoelectric Devices in Welding Tooling Equipment Systems

### Advances in Materials Science and Engineering

Received 8 January 2024; Accepted 8 January 2024; Published 9 January 2024

Copyright © 2024 Advances in Materials Science and Engineering. This is an open access article distributed under the Creative Commons Attribution License, which permits unrestricted use, distribution, and reproduction in any medium, provided the original work is properly cited.

This article has been retracted by Hindawi following an investigation undertaken by the publisher [1]. This investigation has uncovered evidence of one or more of the following indicators of systematic manipulation of the publication process:

- (1) Discrepancies in scope
- (2) Discrepancies in the description of the research reported
- (3) Discrepancies between the availability of data and the research described
- (4) Inappropriate citations
- (5) Incoherent, meaningless and/or irrelevant content included in the article
- (6) Manipulated or compromised peer review

The presence of these indicators undermines our confidence in the integrity of the article's content and we cannot, therefore, vouch for its reliability. Please note that this notice is intended solely to alert readers that the content of this article is unreliable. We have not investigated whether authors were aware of or involved in the systematic manipulation of the publication process.

Wiley and Hindawi regrets that the usual quality checks did not identify these issues before publication and have since put additional measures in place to safeguard research integrity.

We wish to credit our own Research Integrity and Research Publishing teams and anonymous and named external researchers and research integrity experts for contributing to this investigation.

The corresponding author, as the representative of all authors, has been given the opportunity to register their agreement or disagreement to this retraction. We have kept a record of any response received.

### References

- [1] W. Tan, H. Liu, H. Li, and S. Cao, "Application of Nanoflexible Photoelectric Devices in Welding Tooling Equipment Systems," *Advances in Materials Science and Engineering*, vol. 2022, Article ID 7010891, 14 pages, 2022.



## Research Article

# Application of Nanoflexible Photoelectric Devices in Welding Tooling Equipment Systems

Wenping Tan , Honghua Liu , Hongmei Li, and Shen Cao

College of Information and Mechatronical Engineering, Hunan International Economics University, Changsha 410205, Hunan, China

Correspondence should be addressed to Honghua Liu; [lhh1127@126.com](mailto:lhh1127@126.com)

Received 7 July 2022; Revised 4 August 2022; Accepted 6 September 2022; Published 29 September 2022

Academic Editor: K. Raja

Copyright © 2022 Wenping Tan et al. This is an open access article distributed under the Creative Commons Attribution License, which permits unrestricted use, distribution, and reproduction in any medium, provided the original work is properly cited.

With the continuous breakthrough of science and technology, all aspects related to science and technology are constantly updated and changing. Photoelectric devices, also known as photosensitive devices, work on principles based on the photoelectric effect. The application of photoelectric devices in our lives is also diverse. This paper aims to study the flexibility of nanophotoelectric devices, which is a new generation of photoelectric device product technology, making photoelectric devices have more outstanding utility compared with the past. In the traditional sense, photoelectric devices will have their own hardware defects, and the update of nanoflexible photoelectric device technology will solve the above shortcomings. The above breakthroughs in key technologies have improved the hardware of welding tooling in the industrial field. The technique of welding tooling is widely used in the industrial field. The introduction of nanoflexible photoelectric devices into the welding tooling can overcome the defects of conventional processes. This paper proposes the application of nanotechnology in the industrial field. A parameter testing system and a model of dynamic matrix predictive control are established to predict and control the parameters of the experiment throughout the process. The experimental object of this paper is nanoflexible optoelectronic devices; meanwhile, the concentration of nanomaterials in the nanophotoelectric device plays a decisive role in the efficiency of the device, then the final experimental results show that when the concentration of nanomaterials is  $8.5 \times 10$ , the efficiency of the optoelectronic components is the best of the four groups of experiments.

## 1. Introduction

The research and development of nanoflexible photoelectric devices appear to follow the trend of intelligence in contemporary society. The intelligent equipment in today's society has already belonged to the increase of blowout potential, and the requirements of intelligent equipment for its hardware are extremely high, which makes the emergence of nanoflexible photoelectric devices inevitable. Among them, it includes China's industrial field and China's vigorous development of infrastructure construction projects in recent years. Traditional equipment in the industrial field also needs to be updated [1]. This paper introduces nanoflexible photoelectric devices into the welding tooling equipment system in the industrial field, because the nanooptical device itself has better optical and electrical

properties, giving them the opportunity to develop in a more intelligent direction.

Compared with traditional photoelectric devices, nanodevices have more new device structures as well as the physical size characteristics. At the same time, nanoflexible optoelectronic devices contain all the advantages of traditional optoelectronic devices. This makes the prospect of nanodevices very broad. At the same time, with the vigorous development of domestic industry, technological renewal in the industrial field also needs to usher in continuous breakthroughs. The combined application of nanoflexible devices and welding tooling technology makes the development in the industrial field move towards a brighter road. Welding tooling skills in the industrial field are also based on flexible welding fittings. The two are used in relation to each other and have their points of mutual connection. This paper

is based on the application of nanoflexible photoelectric devices in welding tooling technology.

The demand for smart devices has prompted the continuous improvement of research on optoelectronic devices, and a large number of different researchers have carried out different research studies from different perspectives, making it fruitful. At the same time, the universality of welding tooling technology is now, and different researchers are also introducing different updated solutions for it. MA Kang and his team intensively explored the optical properties of MoS<sub>2</sub>/graphene-based patterns based on various cross-stacked photodetectors. The methods that they have investigated have broadened the pathway for transparent and flexible nanoelectronic devices based on two-dimensional materials for practical applications [2]. However, in addition to the mentioned research perspectives, MYe also summarized and discussed the advances in the holistic research of TMDC in a relevant way [3]. This is also a relatively novel angle, and this kind of research has made breakthroughs in related fields of technology and related hardware. In addition, C Rameshkumar explained the structural properties of pristine PMMA and PVDF films by means of a study for XRD [4]. S Zhang proposed a 4-in-1 electrical method based on outlier spectral mapping, and it was used for the preparation of optoelectronic devices, which makes the study of the method more concrete and realistic [5]. In a biochemical study, P Arunkumar reported a moisture-stable, red-emitting fluoride phosphor with an organic hydrophobic surface layer, and its preparation process is also closely related to the related use of optoelectronic devices [6]. A facile method for fabricating high-quality chalcogenide thin films and optoelectronic devices on paper by direct pen writing was also reported by Thang, which has led to technological innovation in the use of paper as well [7]. DV Pekur considered optimizing passive air system design for cooling high-power LED lamps based on heat pipes and cooling rings, which is an application in lamp innovation [8]. S. Eslami proposed friction stir welding for welding tooling and showed that it has become one of the most fascinating engineering disciplines today [9]. The research studies mentioned above provide different development ideas for the development of optoelectronic devices and the updating of welding tooling technology. The following are the innovations of this article.

The innovation points of this paper are as follows: (1) The research of nanoflexible photoelectric devices is compared with that of traditional photoelectric devices, so as to highlight its technical breakthrough point and the change of device characteristics. (2) One of the highlights of this paper is to apply the flexible photoelectric devices prepared by nanotechnology to the welding and tooling equipment of the industrial field. The development of industry can be accompanied by the increasing development of science and technology, and it becomes increasingly powerful. The introduction of this combination makes the modernization of the industrial field also evident. (3) The application of flexible photoelectric devices in the industrial field belongs to the integration of disciplines, which can provide multiple ideas for the development of science and technology.

## 2. Application Technology of Nanoflexible Photoelectric Devices in Welder Installation

### 2.1. Physical Parameter Test System Construction of Nano-Optoelectronic Devices and Parameter Testing of Specific Devices

*2.1.1. Parameter Test of Nano-Optoelectronic Devices.* With the increasing development of today's science and technology, their performance and efficacy are also constantly improved and improved. In view of the problem of signal aging of photoelectric devices, researchers from various countries have proposed different solutions. China also offers different methods for solving these problems. The comparisons between several test systems are listed in Table 1:

The test method for signal aging of optoelectronic devices is to establish a signal aging model by irradiating the device [10]. The introduction of the Table 1 method is a model built to make corresponding solutions to the signal aging problem of photoelectric devices. The above data will be revised for the scientificity of the model.

In addition, there are different monitoring systems for the equilibrium performance of photoelectric devices, as shown in Table 2.

The comparison of the detection systems of the equilibrium performance of photoelectric devices in Table 2 is realized by moving light sources, and the process is carried out for the time poles of different sizes of photoelectric devices [11]. It can be seen from the table that the advantages of the spherical PMT system are more obvious; however, the parameters in the above table are only tests of relatively small devices, and new methods remain to be explored for tests of large-sized photoelectric devices.

Because photoelectric devices have their own unique physical characteristics, they have some electromagnetic performance. For devices with electromagnetic characteristics, the strength of the external magnetic field for the influence of components will have a greater correlation [12]. In response to this problem, the method of changing the external magnetic field was also tested, as shown in Table 3, and the related parameters are as follows.

Table 3 is also tested for relatively small photoelectric devices, and the shielding means used are also based on the strength simulation system considered established. It can be seen that the performance of the dynode-PMT system is better. For large photoelectric devices, geomagnetism is generally selected as the corresponding test means.

*2.1.2. Design Method of the Test System.* The above method is only measured in some specific environments for the required parameters. Here, the required parameters will be integrated accordingly [13, 14]. For this purpose, corresponding systems will be constructed below based on the required performance parameters. Figure 1 shows the composition of the system.

The construction of the test system in Figure 1 can realize the influence of magnetic fields on photoelectric

TABLE 1: Comparison of the signal aging test systems of photoelectric devices.

Test object type	Test object size (mm)	Light intensity (pe/s)	Performance parameters
Planar MCP-PMT	21.0	6000000	Gain, quantum efficiency, dark count, detection efficiency
Spherical MCP-PMT	210.1	20000000	Bulk resistance, gain, vacuum
Spherical MCP-PMT	220.3	20000000	Gain, frequency response, transit time
Spherical dynode-PMT	276.5	12000000	Gain, postpulse, transit time

TABLE 2: Comparison of the equilibrium monitoring system of photoelectric devices.

Test object type	Test object size (mm)	Means of realization	Performance parameters
Planar PMT	36.6	Moving light source	Quantum efficiency
Planar PMT	52	Moving light source	Quantum efficiency
Spherical PMT	209.8	Rotate PMT	Quantum efficiency

TABLE 3: Comparison of the test parameters of the magnetic field influence of photoelectric devices.

Test object type	Test object size (mm)	Shielding measures	Performance parameters
Dynode-PMT	210.2	U Iron	Anode performance parameters, position response
Dynode-PMT	210.2	Helmholtz coil	Uniformity of gain and collection efficiency
Dynode-PMT	261.1	Helmholtz coil	Anode performance parameters, position response
MCP-PMT	25.3	Strong magnetic field	Gain, time-of-flight dispersion, detection efficiency
MCP-PMT	62	Strong magnetic field	Position response: Gain, time-of-flight discrete

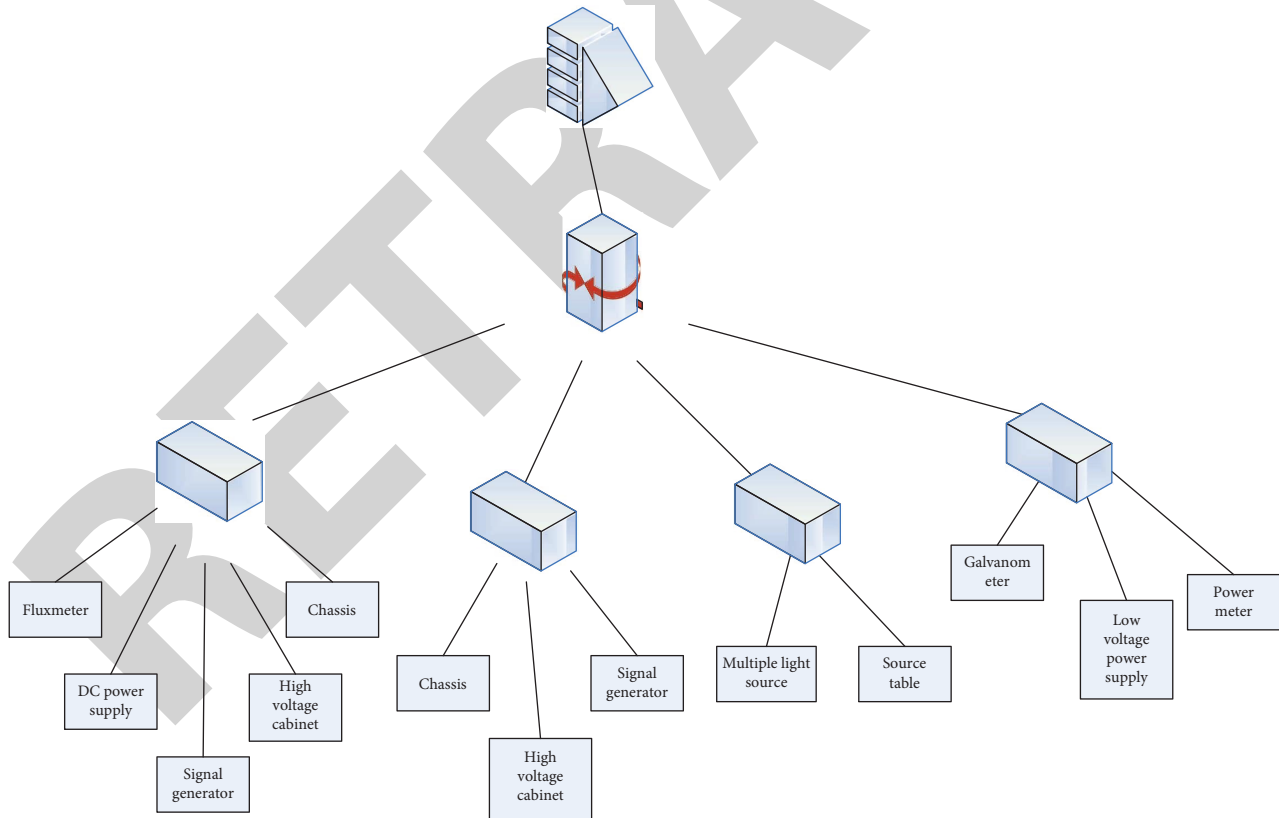


FIGURE 1: Overall structure diagram of the test system.

devices, and the aging of the photoelectric device itself, the equilibrium of photoelectric devices and the performance parameters of related photoelectric devices. The advantage of this test system is that the collection of test data and

their processing can be achieved. At the same time, the effective and timely processing of multiple types of data is realized so that the effectiveness of the data can be improved.

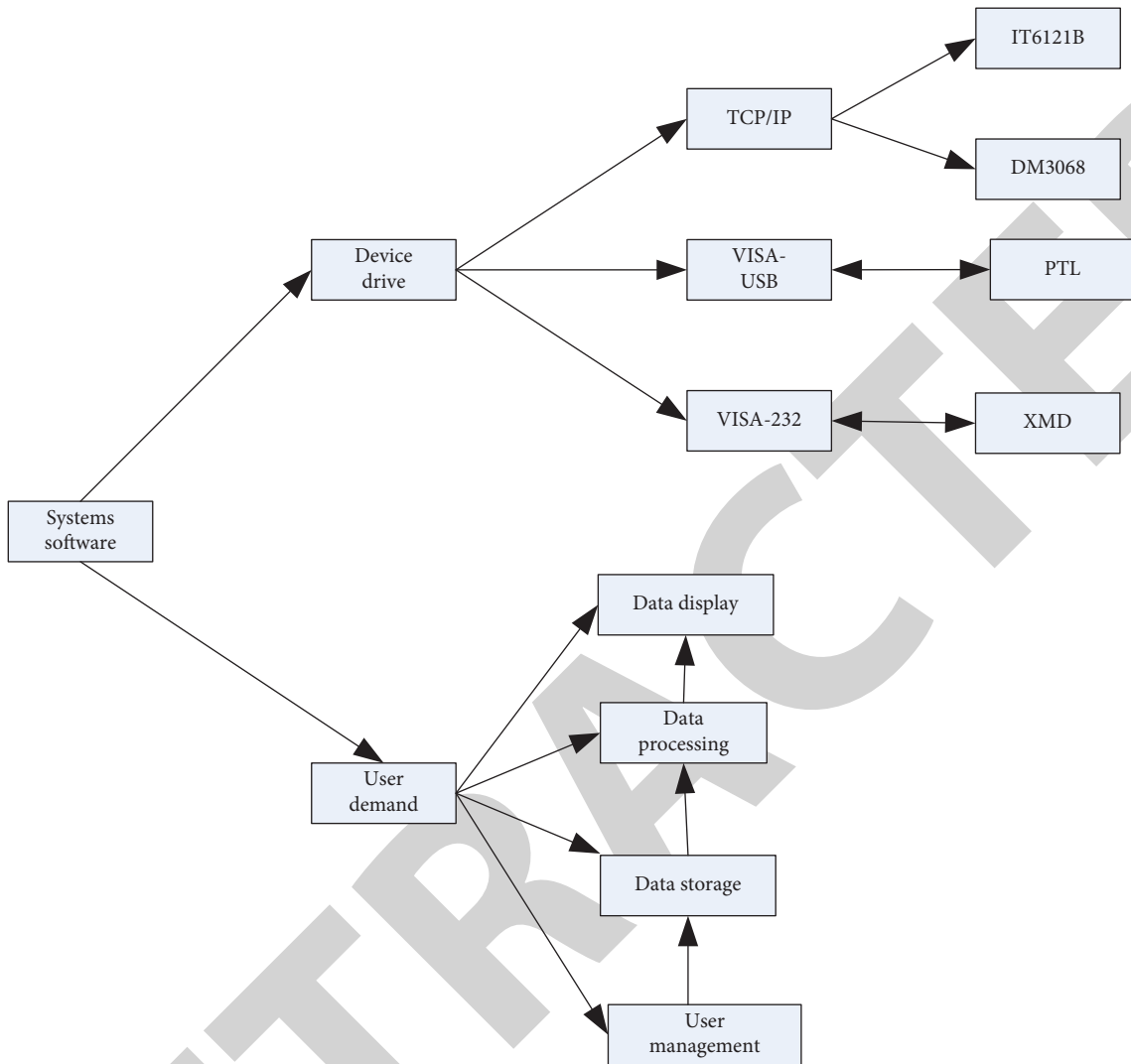


FIGURE 2: LED software test system.

2.1.3. *Testing of the Performance Parameters of the Nano-LED.* In addition, a hardware test structure system for detecting nano-LEDs is also constructed. Because LED equipment is widely used in the industrial field, the research on this basis is of great significance to this paper, and the required software is described below. Software that can run efficiently is based on the driver and the software itself [15]. The complete work flowchart is shown in Figure 2.

The test data of the software system include the current size of the LED device when it is working, the intensity of the LED light emission, the range of the spectrum, and other device parameters [16]. In addition, the above system will also collect and analyze the data.

## 2.2. Signal Enhancement and Preparation Technology of Nanoflexible Optoelectronic Devices

2.2.1. *Design Principle of Nanoflexible Photoelectric Devices* Due to the large variety of performance parameters of flexible optoelectronic devices, it is necessary to convert the

cathode and anode of optoelectronic devices in order to obtain the relevant parameters of the experiment. Therefore, it is necessary to detect optoelectronics escaping from the time pole and the anode to measure the relative detection efficiency [17]. The calculation formula (1) is as follows:

$$Q = \left( \frac{\sum_{a=a_1}^{4096} f_{test}(a)}{\sum_{a=0}^{4096} f_{test}(a)} \right) \div \left( \frac{\sum_{a=a_2}^{4096} f_{ref}(a)}{\sum_{a=0}^{4096} f_{ref}(a)} \right). \quad (1)$$

In the above formula, test represents the test parameter of the test sample, ref represents the test data of the reference sample, and  $Q$  represents the detection efficiency.

Due to the particularity of the anode, it is the calculation of the gain of the optical electron beam escaping from the time pole of the photoelectric device next [18], whose formula is as follows:

$$Get = \frac{(a_4 - a_2)}{1.56e} - 19. \quad (2)$$

The gain of photoelectric devices is related to the high pressure loaded by itself, and the appropriate degree of high pressure needs to be selected for specific testing.

The energy resolution of photoelectric devices is also calculated as follows:

$$P = (a_7 - a_5)/(a_6 - a_3). \quad (3)$$

The following is the calculation of the ratio between the peak and the trough of the photovoltaic electron signal released by the photoelectric device:

$$\frac{L}{Y} = \frac{f(a_6)}{f(a_4)}. \quad (4)$$

The above formula is the calculation of different parameters of the photoelectric device, and the indicators involved are all related to the strength of the photoelectric signal, so as to pave the way for the following experimental part [19].

The following is an introduction to the test methods for the quantum efficiency of optoelectronic devices. Because quantum efficiency is an important indicator of the uniformity of the time pole of photoelectric devices, this method can make the test of quantum efficiency more perfect. Its specific test method is shown in Figure 3.

From Figure 3, it is known that the test of this method requires power supply, separation equipment, and ammeter, and the calculation formula for the sample to be tested is as follows:

$$QE_a = i_a/i_b * QE_b. \quad (5)$$

The above formula  $QE_a$  represents the quantum efficiency. Through the above schematic diagram and calculation formula, we can know the quantum efficiency of optoelectronic devices [20].

Because the real working environment of photoelectric devices has Earth's magnetic field, it is necessary to consider the influence of the magnetic field on the signal of photoelectric devices to design shielding equipment of the magnetic field, so as to weaken or even eliminate the impact of the magnetic field on photoelectric devices. The first is to set the magnetic field in the environment on a constant magnetic field [21], and the specific process involves the following formula calculation:

$$B = \lambda M. \quad (6)$$

In the above equation,  $B$  indicates the induction strength of the magnetic field,  $\lambda$  indicates the magnetic conductivity, and  $M$  represents the strength of the magnetic field.

Regarding the cohesive force between the two magnetic media dividing interfaces, the calculation formula is as follows [22].

$$\begin{pmatrix} B_{an} = B_{bn} \\ M_{al} = M_{bl} \end{pmatrix}. \quad (7)$$

In the above equation,  $n$  represents the normal component,  $t$  represents the tangent component,  $B_{an}$  represents

the magnetic induction strength of sample  $a$ ,  $B_{bn}$  represents the magnetic induction strength of sample  $b$ ,  $M_{al}$  represents the magnetic field strength of sample  $a$ , and  $M_{bl}$  represents the magnetic field strength of  $b$ .

The law of refraction of electromagnetic fields can be described in the following expression [23]:

$$\frac{\tan \theta_a}{\tan \theta_b} = \frac{\lambda_a}{\lambda_b}. \quad (8)$$

In the above formula,  $\theta_a$  is the angle between the magnetic field and the normal component of sample  $a$ ,  $\theta_b$  is the angle between the magnetic field and the normal component of sample  $b$ ,  $\lambda_a$  is the permeability of sample  $a$ , and  $\lambda_b$  is the permeability of sample  $b$ .

The above is a discussion of some parameters of optoelectronic devices that affect the geomagnetic field [24]. Figure 4 shows a schematic diagram of a hardware system shielding the geomagnetic field:

The hardware system of Figure 4 is designed to reduce the impact of the magnetic field on the photoelectric device, so as to improve the reliability of the test, and the system can make the signal of the optoelectronic device better guaranteed. In addition, the above hardware system also uses a chassis, signal generator, and other detection equipment [25]. This is the detection method for primary factors affecting photoelectric devices.

**2.2.2. Model Establishment and Application of Dynamic Matrix Prediction and Control.** In addition, for the abovementioned hardware system, the dynamic matrix predictive control model is introduced here. The introduction of this model is conducive to connecting nanoflexible photoelectric devices with welding tooling in the industrial field. The model is a nonparametric model that can be achieved by the input for a specific increase to obtain the output of future moments. The corresponding calculation formula is as follows:

$$x_n = \left( \eta + \frac{M}{\eta} \right) = x_0 \left( \eta + \frac{M}{\eta} \right) + Q_M \Delta \lambda (\eta). \quad (9)$$

In the above equation,  $M$  is the time domain length of the model,  $Q_M$  represents the parameters, including the corresponding values of the actual measure and prediction, and  $\Delta \lambda (\eta)$  is the control increment added to the system. The above expression is based on the case where the control increment is constant, and if the time varies, then the formula is as follows:

$$X_n (\eta + 1) = X_0 (\eta + 1) + \Delta \lambda (\eta). \quad (10)$$

The above formula is a prediction model. The following is the correlation optimization for this model. Due to the advantages in the nanoenvironment, the selection of optimization indicators needs to be valued by adding a certain factor. The additional factor selected here is the intensity of the current, and the value calculation formula of the optimization index is as follows:

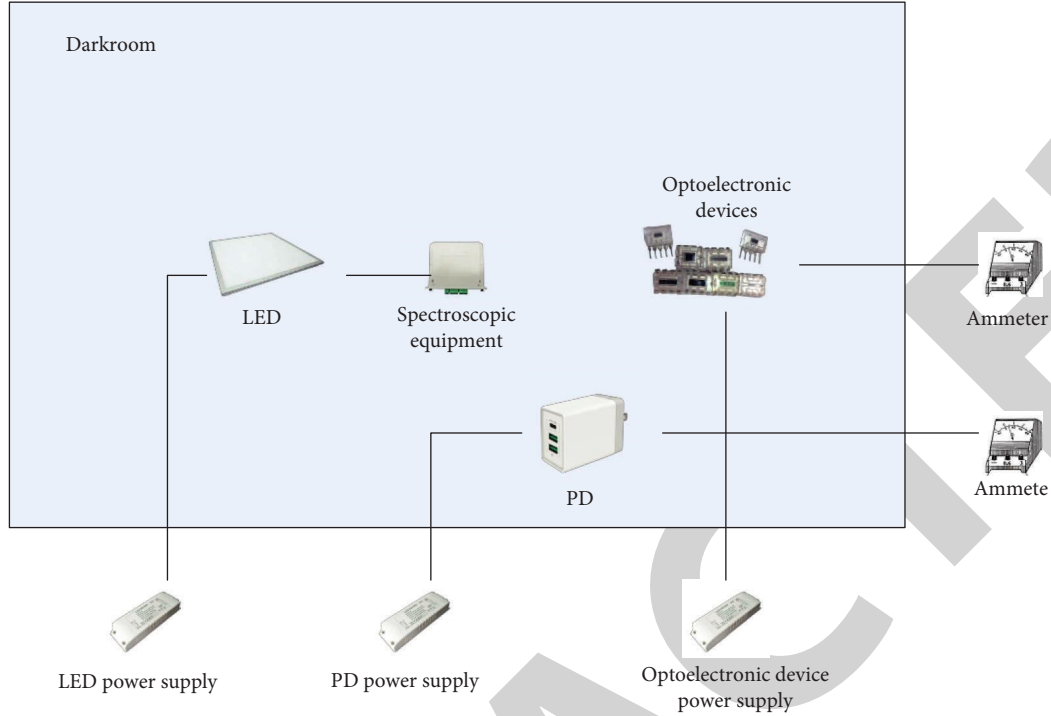


FIGURE 3: Schematic diagram of the quantum efficiency test of photoelectric devices.

$$\min D(\eta) = \sum_{i=1}^Q Y_i \left[ v(\eta + i) - X_m \left( \eta + \frac{i}{\eta} \right) \right]^2 + \sum_{I=1}^P t_I \Delta \lambda^2 (\eta + I - 1). \quad (11)$$

The sum  $Y_i$  and  $t_I$  of the above formula represents the weighting coefficient, the former represents the suppression of error, and the latter represents the suppression of change. To optimize the above process, we use the following calculation formula:

$$X_{QP}(\eta) = X_{Q0}(\eta) + A\Delta T_P(\eta). \quad (12)$$

The expression of performance indicators can be expressed by the following formula:

$$\min D(\eta) = Qv_p(\eta) - x_{qp}(\eta)Q_p^2 + Q\Delta T_P(\eta)Q_a. \quad (13)$$

Integrating the above process yields the following optimization formula:

$$\Delta T(\lambda) = L^R \Delta T_P(\lambda) = f^R [v_q(\eta) - x_{q0}(\eta)]. \quad (14)$$

The deduction process for the optimization of the prediction system model is such as described above. Next, the model is also corrected, and by applying a parameter variable at some moment, the value of the output predictor can be calculated by the following equation:

$$x_{M1}(\lambda) = x_{M0}(\lambda) + c\Delta t(\lambda). \quad (15)$$

Formula (15) is the normal calculation process of the model and does not consider unknown interference factors. Because when some factors outside the control occur, such as parameter mismatch pairing, there will be a deviation between the output result and the actual value. If the formula is modified, it can be expressed as follows:

$$x_{cor}(\lambda + 1) = \left[ x_{cor} \left( \lambda + \frac{1}{\lambda} \right), G, x_{cor} \left( \lambda + \frac{M}{\lambda} \right) \right]^R. \quad (16)$$

The above formula includes the error tolerance rate of the error, which can make the algorithm of the whole model more complete. For the introduction of the above model and algorithm, the signal problem of flexible photoelectric devices can be effectively handled in this study.

### 2.2.3. Preparation of Nanoflexible Optoelectronic Devices.

The preparation of nanoflexible photoelectric devices requires the compound of a nanopolymer, and this step is performed to replace traditional silicon compounds with flexible nanomaterials. Its advantage is that it enables photoelectric devices to achieve stretching in the three-dimensional direction. It has a more powerful support role than the traditional two-dimensional direction. For material selection, polyimide and cyclohexasiloxane were used. Table 4 shows the physicochemical parameters of polyimide.

Polyimide is chosen here because this polymer material can provide a better guarantee for the use of flexible electrons, so as to extend the use time of flexible photoelectric devices. The preparation of flexible photoelectric periods is based on nanostructures where the composite material of

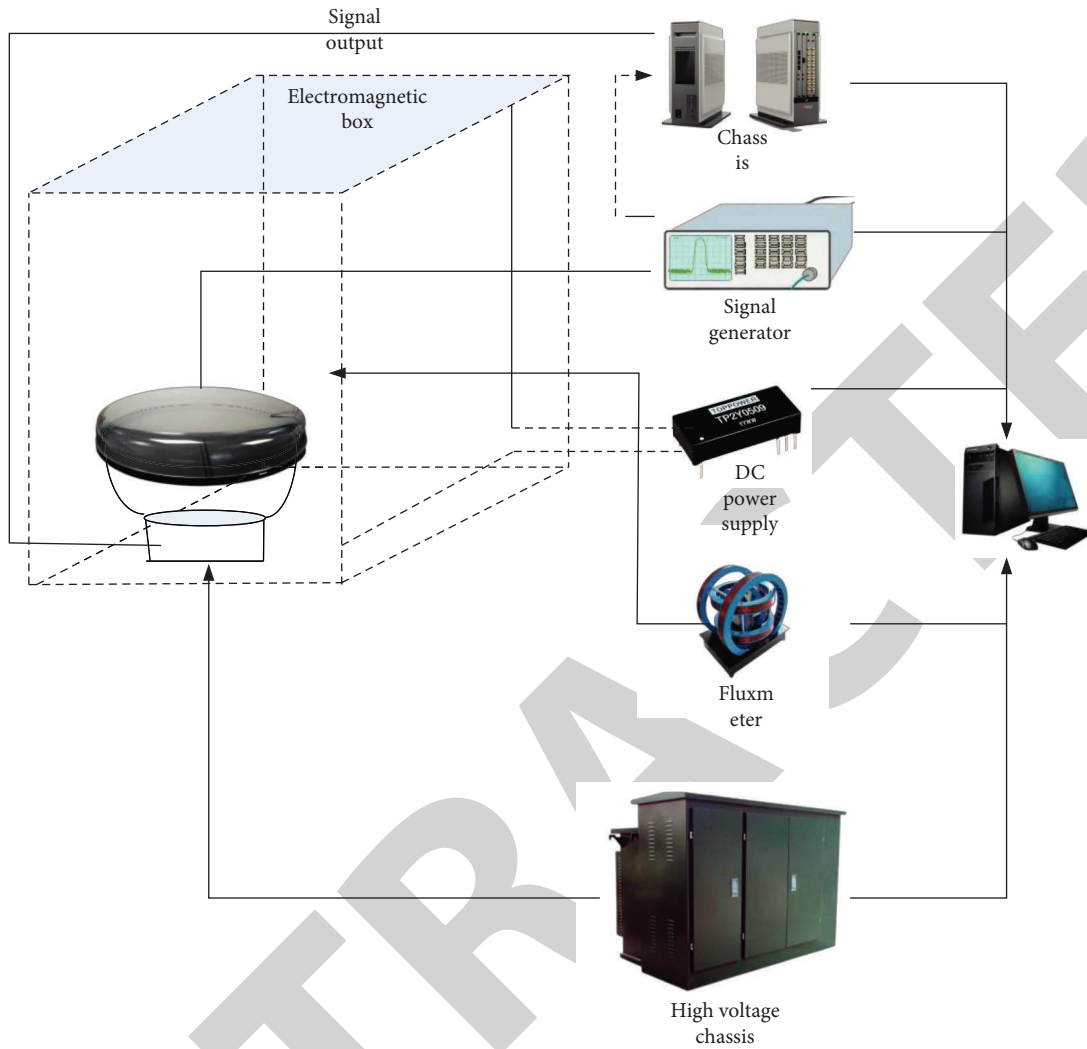


FIGURE 4: Geomagnetic field analog shielding hardware system.

TABLE 4: Physicochemical parameters of polyimide.

Project	Homobenzene polyimide	Polybismaleimide	Polyimide
Specific heat capacity	1.12	1.22	1.13
Thermal conductivity	1.1	2.1	1.1
Coefficient of linear expansion	6	2.5	5.7
Molding shrinkage	0.11	>0.15	0.2
Oxygen index	42	45	45
Flow temperature	>360	>250	>335
Thermal deformation temperature	365	310	220
Dielectric constant	3.2~3.5	4.1~4.7	3.1~3.5
Volume resistivity	1016	1015	1015

nanosilver and nanocarbon is used. The specific preparation process is shown in Figure 5.

In the preparation of the photoelectric device in Figure 5, attention should be paid to the thickness of different colloids, and the amount of the modified solution should be increased or decreased according to the amount of the nanocomposite. The advantage of the above process is that

the materials needed for the experiment can be obtained quickly. For the preparation of nanoflexible photoelectric devices, the nanoflexible composite from the above process is used and the sol-gel method is used. The whole process of the sol-gel method is shown in Figure 6.

The sol gel method in Figure 6 has the ability to prepare nanoscale materials in a short period of time, and the



operation process does not require high treatment temperature, which can be made as desired. At the same time, it requires a high purity of raw materials, and the reaction legacy will produce some organic products that are not friendly to humans and nature. In sol-gel preparation, different application methods are used, and some specific reagents are required. Their functions and types are shown in Table 5.

The reagents in Table 5 are required for the entire optoelectronic device preparation process and will be used for the entire preparation process.

### 2.3. Application of Nanoflexible Optoelectronic Devices in Mechanical Welding Tooling

**2.3.1. Detection Method for the Performance of Nanoflexible Photoelectric Devices.** Welded tooling is a flexible mechanical fixture, which can be divided into the general type and special type, and the latter is widely used in mechanical equipment manufacturing and modular combinations. With the growing strength of China, it has more advantages than traditional cutting tooling. The preparation of nano-optoelectronic devices described above needs to be tested for their use in welder assembly. The first is the use of scanning electron microscopy, and the schematic diagram is shown in Figure 7.

As can be seen from Figure 7, the main structure of the device enables the device to detect a variety of signals, can also receive a variety of signals, and has the ability of imaging, so that the onlookers form information about the nanophotovoltaic device. In addition, the light absorption process of spot welding tooling should be detected. The light absorption process of spot welding tooling can be expressed by the following formula:

$$\frac{kl}{ky} = -\mu l. \quad (17)$$

In the above formula,  $\mu$  is the proportion coefficient, and the above light absorption process is closely related to the refractive index, light absorption coefficient, and extinction technology of the device.

**2.3.2. Detection Method for Nano flexible Photoelectric Devices Installed by Welders.** The application of this method is based on the properties of photoelectric devices, so the Hall effect principle introduced is derived from the influence of magnetic field on charged particles. First, the detection of external quantum efficiency, which is one of the necessary detections of photoelectric devices, can be expressed in the following formula:

$$\mu = \frac{Q_K/e}{K_{oPT}/HV}. \quad (18)$$

In the above formula,  $Q_K$  is the size of the photocurrent,  $e$  is the amount of the unit electron, and  $HV$  is the size of the energy of the light particle. Then, the calculation of the

detection rate of photoelectric devices is expressed as follows:

$$P = \frac{B}{\sqrt{2QI_c}}. \quad (19)$$

In the above formula,  $B$  indicates the echo degree of the photodetector,  $Q$  indicates how much is charged by the electron, and  $I_c$  indicates the density of the dark current. Finally, the response line is expressed as follows:

$$I = Z_a \exp\left(-\frac{m}{\lambda_1}\right) + Z_b \exp\left(-\frac{m}{\lambda_2}\right) + I_1. \quad (20)$$

The above methods are the specific detection methods and algorithm introduction of nanoflexible photoelectric devices installed in welding. Relevant experiments are performed below for the above methods.

## 3. Parameters of Nanoscale Optoelectronic Devices and Related System Test Experiments

**3.1. Equilibrium Test Experiment and Result of Nano-Optoelectronic Devices.** This experiment is first carried out for testing the stability of the strength of the light of the test system, because this detection index is one of the important indicators to test the balance of the system. The operation method is as follows: first, a multichannel multiplex light source is designed to make the nanophotovoltaic device emit light at a specific voltage as shown in Figure 8.

The test results in Figure 8 show that the stability of the test light source is within 15%. For the experimental time, multiple repeated tests are not required, indicating that the stability of the system is reliable. The experiment targets the testing of small-sized optoelectronic devices.

**3.2. Influence of Signal Geomagnetic Field and Result of Nanoflexible Photoelectric Devices.** First, the test sample tube is designated as a specific nanophotovoltaic device, and the intensity of the geomagnetic field is controlled as an experimental variable. For the test of the gain size of the nanooptical device, the collection efficiency of the device, the energy resolution of the device, and the process time dispersion parameters are calculated, and the test results are shown in Figure 9.

It can be seen from Figure 9 that under the same shielding effect, the gain of the nanophotovoltaic device, the collection efficiency of the device, the energy resolution, and the process time of the device are all different, among which the detection efficiency is the most affected. The voltage and light intensity were always kept constant during the test. The previously designed magnetic field shielding device can achieve almost no other magnetic field interference for this experiment.

**3.3. Performance Test Experiment and Result of Nanophotovoltaic Devices.** It can be known by the preparation process and parameters of nanophotovoltaic devices that different concentrations of nanocomposites will have different effects

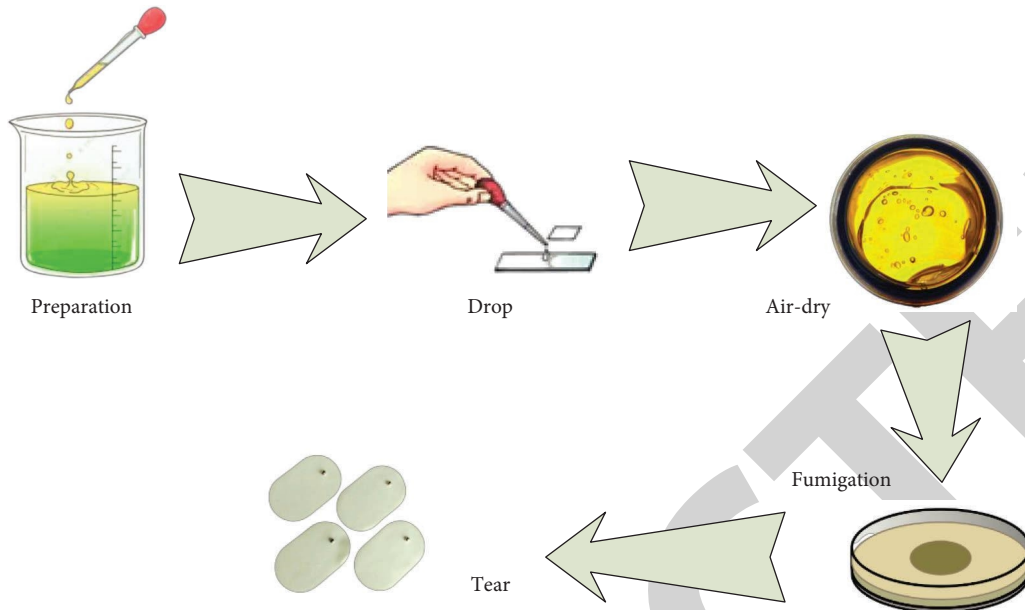


FIGURE 5: Preparation process of nanoscale flexible composites.



FIGURE 6: Flowchart of the sol-gel method.

TABLE 5: Required reagents and their utility.

Reagent name	Grade	Function
Zinc acetate dihydrate	Analytical purity	Metal precursor
Ethylene glycol methyl ether	Analytical purity	Solvent
Monoethanolamine	Analytical purity	Stabilizer
Acetone	Analytical purity	Cleaning substrate
Trichloroethylene	Analytical purity	Cleaning substrate
Absolute ethanol	Analytical purity	Cleaning substrate

on the efficiency of photoelectric devices. Therefore, the relationship between the concentration of nanomaterials and the performance of photoelectric devices is changed accordingly, as shown in Figure 10.

Figure 10 shows the efficiency of nanomaterials with different concentrations in the nano-optoelectronic devices. As can be seen from the figure, when the concentration of nanomaterials reaches  $8.5 \times 10^4$  units, the efficiency of the photoelectric devices is the best among the four groups of experimental subjects. It can be seen that the photoelectric devices can at this time achieve good load capacity. In addition, in order to test the electrical performance of the device, the resistance of the photoelectric device changes with its efficiency, and the results are shown in Figure 11.

Figure 11 shows that the efficiency of the photoelectric device is positively correlated with the rate of change of its resistance. Meanwhile, the resistance changes of the device

and the initial concentration of the composite nanoflexible material are also related, as shown in Figure 10.

3.4. Connecting Technology Experiment of Nano-Optoelectronic Devices and Mechanical Welding Tooling. The experiments in this paper are designed to enable the final application of nano-optoelectronic devices to welding tooling devices. Here, the welding tooling equipment that has been connected with nanophotoelectric devices is taken as the experimental object to test the performance of the equipment using the chopper. The following is the comparison of the characteristics of the devices at different voltages when the frequency of the chopper is specific, as shown in Figure 12.

As can be seen in Figure 12, the different device performance and voltage at the same frequency have little impact on the performance of devices, and the difference

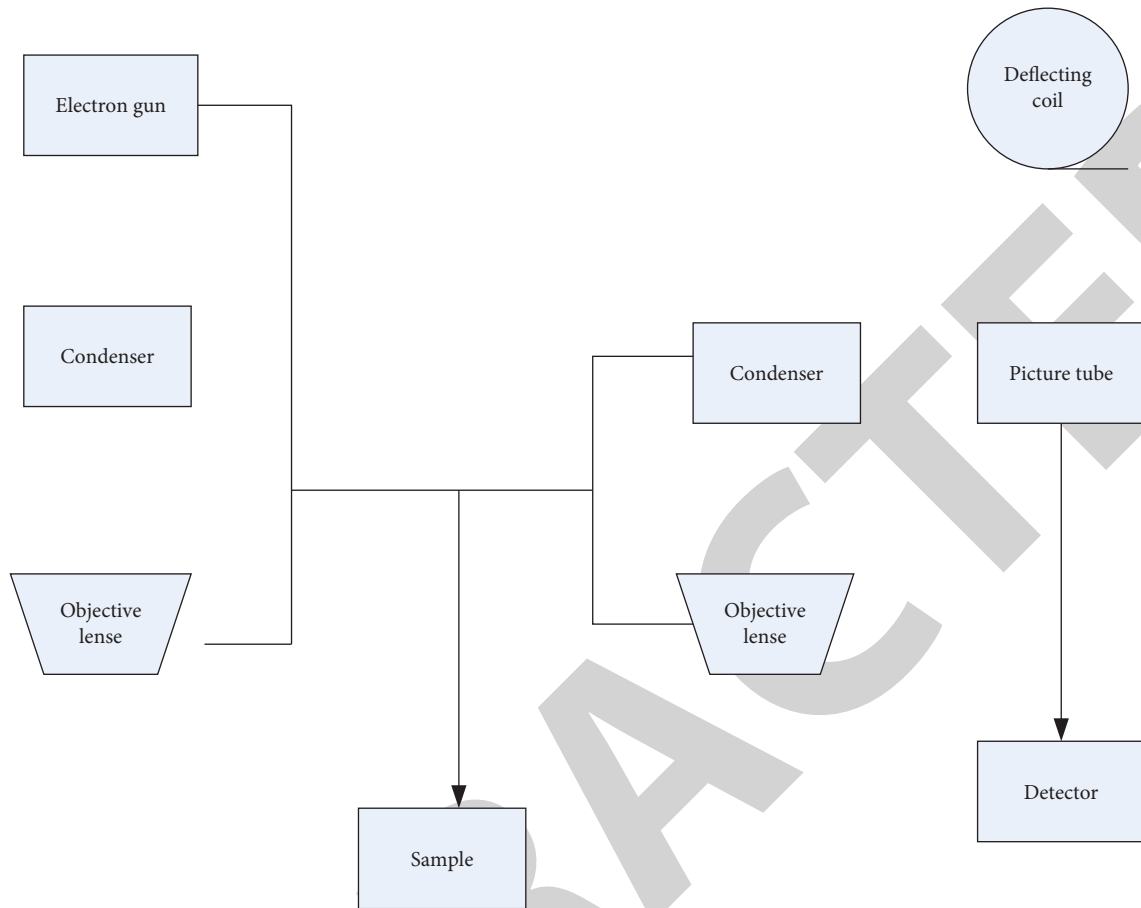


FIGURE 7: Schematic diagram of the scanning electron microscope.

between them is relatively small. From the above experiments, it can be considered that the application of nano-optoelectronic devices in welder installation has good efficiency.

#### 4. Discussion

This paper aims to study the application of nanoflexible optoelectronic devices in welding tooling. This move comes with the development of the times because the equipment of welding tooling is now widely used in the industrial field, and the research in this paper can help the development of the industrial field to some extent. Due to the particularity of nanomaterials, their physical properties were studied before their preparation and related experiments [26]. Later, experiments in this paper can be based on valid data. At the same time, nano-LED is also taken as the reference object of the research, and the test of parameter data is completed in the established test system so that the research before and after the article can be verified and improved.

Next, the signal problem of nano-optoelectronic devices is studied due to their special physical properties. In their practical application, they face a problem, that is, the

interference of the geomagnetic field, which establishes a shielding device for simulating the change of the magnetic field, so as to simulate the signal impact of a specific magnetic field on the photoelectric device, as well as the effectiveness of the shielding device. For its stability, a model of dynamic matrix predictive control is introduced in the experiment. In this paper, the common sol-gel method is used. Because the use of this preparation method has great advantages in nanocomposites, the purity of the obtained products is relatively high. After the products are obtained, the relevant characteristics of the made products are also tested, which paves the effective connection for the following products with the tooling equipment.

Since the welding machine is a mechanical fixture, there are inherent conditions for the connection, use, and welding installation of nanophotoelectric devices. However, in addition to the use of nanophotoelectric devices in welding, the most important thing is to test the performance of nanoflexible devices in welding so that the application technology can operate effectively. The special physical characteristics of nano-optoelectronic devices require the detection and adjustment of their stability so that the installation of nanoflexible optoelectronic devices can be realized in welding.

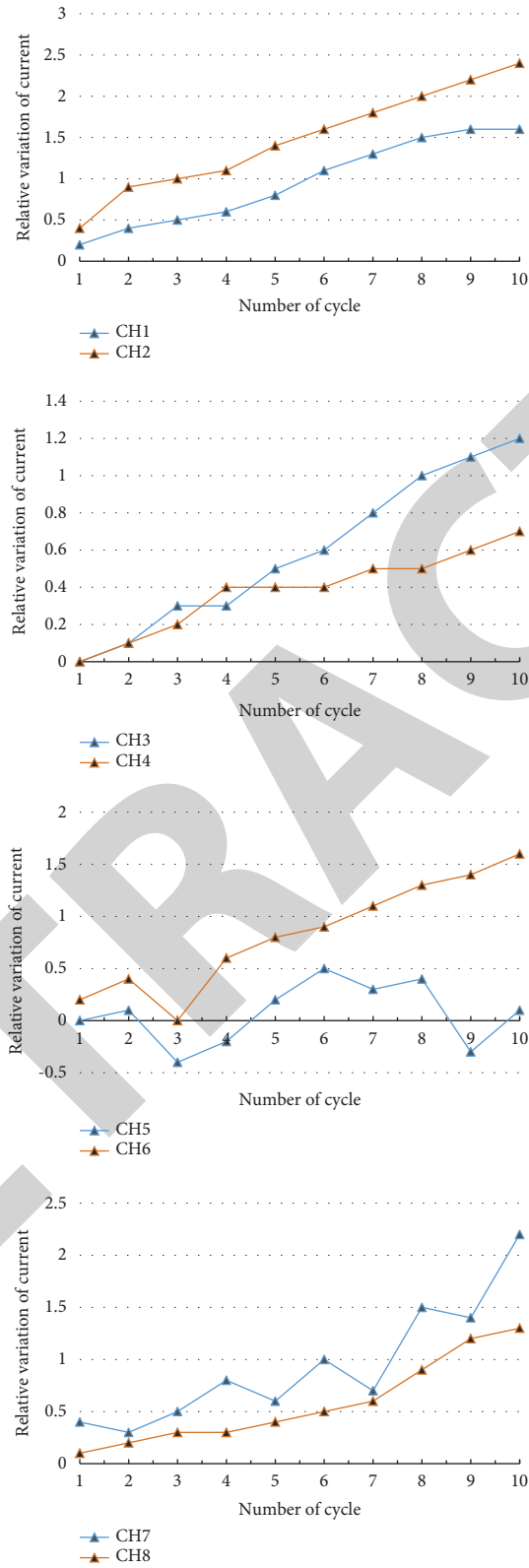


FIGURE 8: Current change diagram of the multichannel power supply.

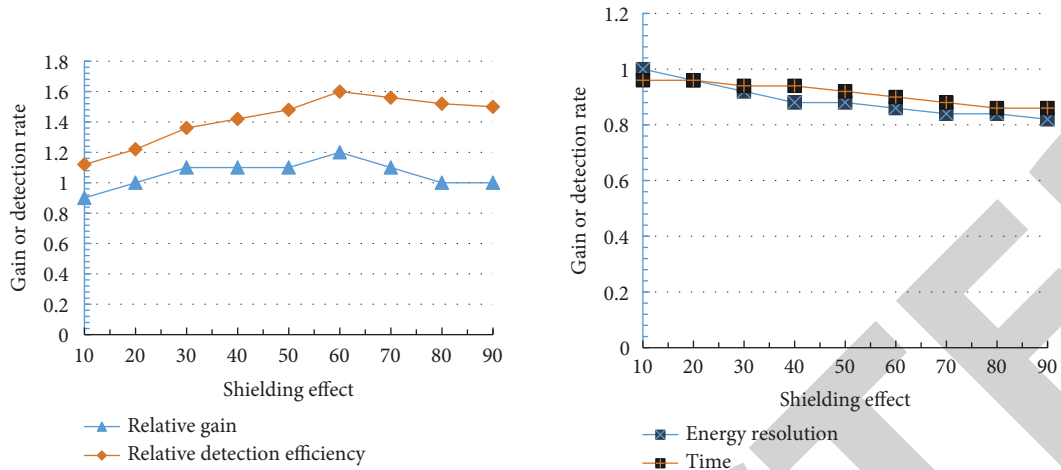


FIGURE 9: Testing of different parameters in different magnetic field intensities.

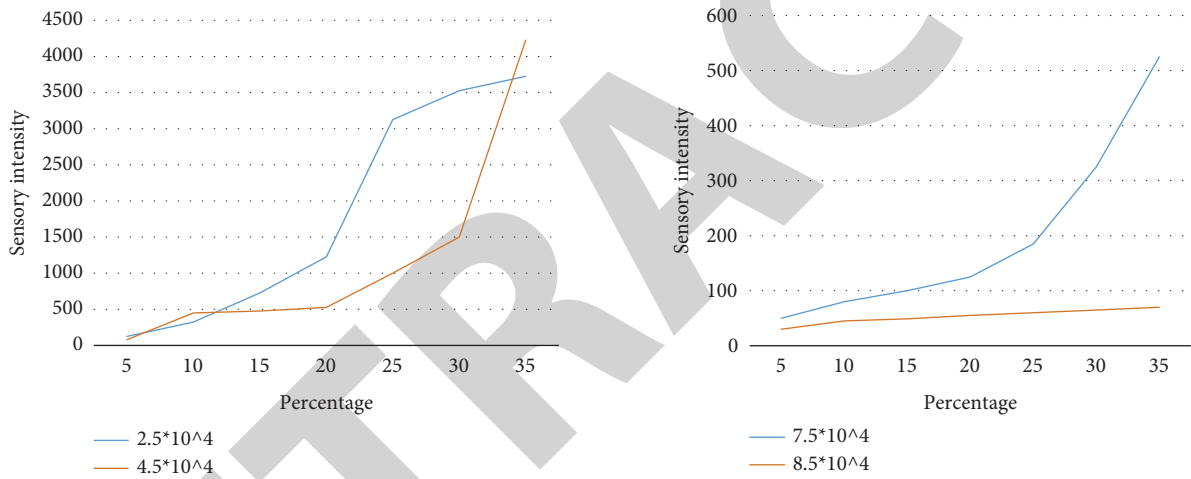


FIGURE 10: Efficiency of optoelectronic devices with different concentrations of nanomaterials.

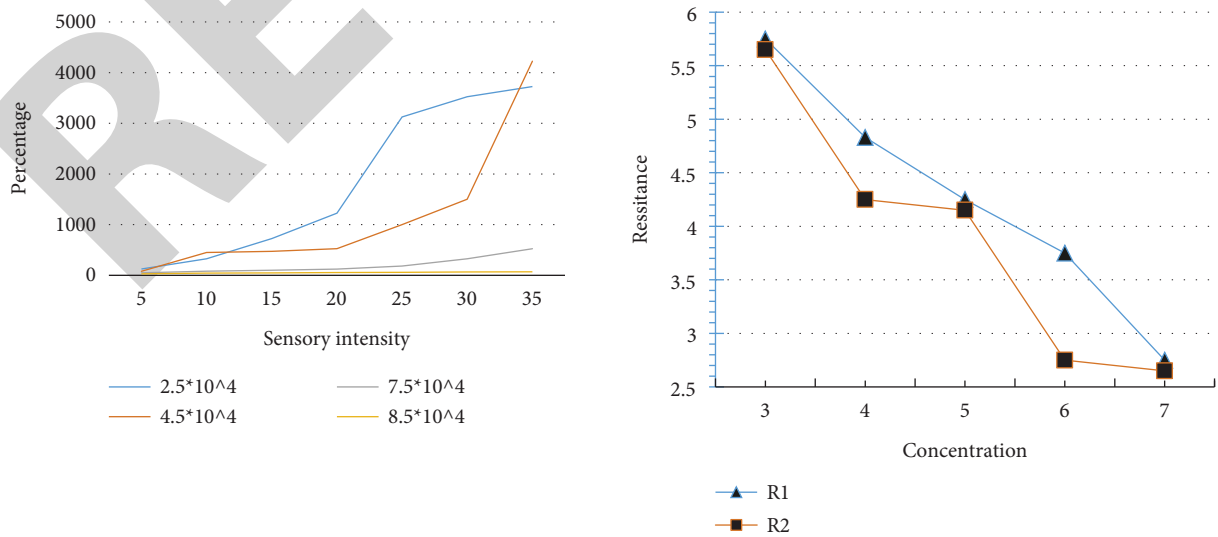


FIGURE 11: Diagram of the efficiency test of photoelectric devices.

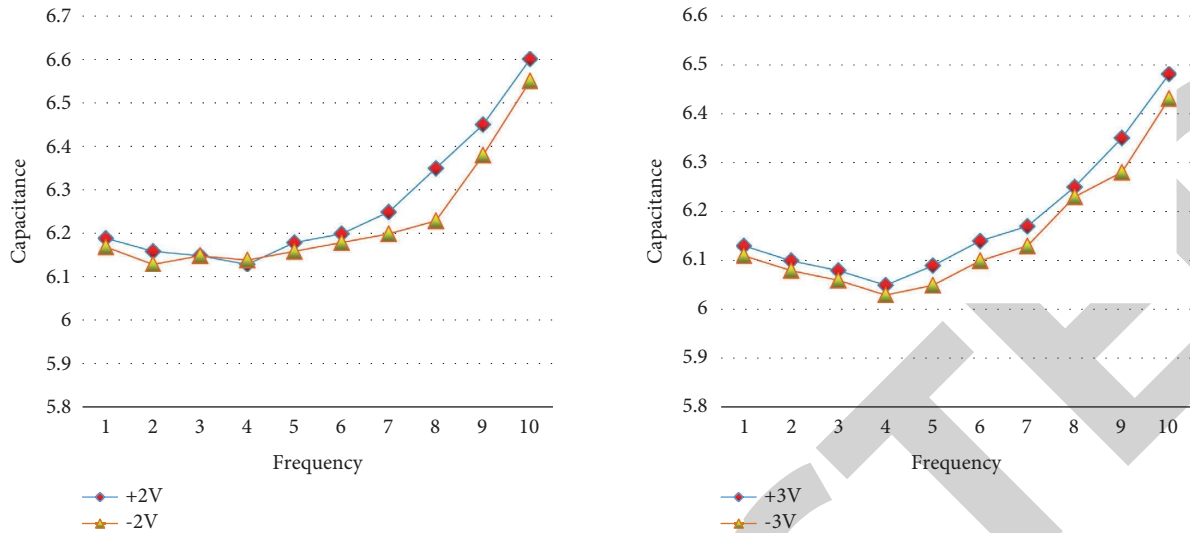


FIGURE 12: Comparison diagram of the device performance at different voltages.

## 5. Conclusions

With the increasing maturity of nanotechnology, various fields have also ushered in earth-shaking technological innovation. For the application of nanomaterials in the industrial field, this paper not only improves the update and iteration of electric welding installation technology and equipment but also provides new ideas for the interdisciplinary application of nanotechnology. This paper focuses on the characteristic detection of nanoflexible materials to provide effective experimental data in order to achieve better practical applications. Second, the simulated geomagnetic field and the signal problems of the device make the device more efficient in practical work. The experiment in this paper can contribute to the common development of nanotechnology and industrial technology and is very promising.

## Data Availability

No data were used to support this study.

## Conflicts of Interest

The authors declare that there are no conflicts of interest regarding the publication of this article.

## Acknowledgments

This work was supported by the Scientific Research Project of Hunan Provincial Department of Education, Project number: 20C1100.

## References

- [1] J. Zhao, J. Huang, R. Wang, H. R. Peng, W. Hang, and S. Ji, "Investigation of the optimal parameters for the surface finish of k9 optical glass using a soft abrasive rotary flow polishing process," *Journal of Manufacturing Processes*, vol. 49, pp. 26–34, 2020.
- [2] M. A. Kang, S. J. Kim, W. Song et al., "Fabrication of flexible optoelectronic devices based on MoS<sub>2</sub>/graphene hybrid patterns by a soft lithographic patterning method," *Carbon*, vol. 116, no. Complete, pp. 167–173, 2017.
- [3] M. Ye, D. Zhang, and Y. Yap, "Recent advances in electronic and optoelectronic devices based on two-dimensional transition metal dichalcogenides," *Electronics Times*, vol. 6, no. 2, p. 43, 2017.
- [4] C. Rameshkumar, S. Sarojini, K. Naresh, and R. Subalakshmi, "Preparation and characterization of pristine PMMA and PVDF thin film using solution casting process for optoelectronic devices," *Journal of Surface Science and Technology*, vol. 33, no. 1-2, pp. 12–18, 2017.
- [5] S. Zhang, C. Zhang, H. Wang et al., "Self-calibrated microwave characterization of high-speed optoelectronic devices by heterodyne spectrum mapping," *Journal of Lightwave Technology*, vol. 35, no. 10, pp. 1952–1961, 2017.
- [6] P. Arunkumar, Y. H. Kim, H. J. Kim, S. Unithrattil, and W. B. Im, "Hydrophobic organic skin as a protective shield for moisture-sensitive phosphor-based optoelectronic devices," *ACS Applied Materials & Interfaces*, vol. 9, no. 8, pp. 7232–7240, 2017.
- [7] T. Zhang, S. Zhang, Z. Gu et al., "Pen-writing high-quality perovskite films and degradable optoelectronic devices," *RSC Advances*, vol. 12, no. 7, pp. 3924–3930, 2022.
- [8] D. V. Pekur, E. N. Yu, V. M. Sorokin, and V. M. Sorokin, "Optoelectronics and optoelectronic devices Optimization of the cooling system design for a compact high-power LED luminaire," *Semiconductor Physics, Quantum Electronics and Optoelectronics*, vol. 23, no. 1, pp. 91–101, 2020.
- [9] S. Eslami, P. J. Tavares, P. M. G. P. Moreira, and P. M. G. P. Moreira, "Friction stir welding tooling for polymers: review and prospects," *International Journal of Advanced Manufacturing Technology*, vol. 89, no. 5-8, pp. 1677–1690, 2017.
- [10] M. Salamati, M. Soltanpour, and A. Fazli, "Processing and tooling considerations in joining by forming technologies; part B—friction-based welding," *International Journal of*

## *Retraction*

# **Retracted: Predicting the Spread of Vessels in Initial Stage Cervical Cancer through Radiomics Strategy Based on Deep Learning Approach**

### **Advances in Materials Science and Engineering**

Received 26 December 2023; Accepted 26 December 2023; Published 29 December 2023

Copyright © 2023 Advances in Materials Science and Engineering. This is an open access article distributed under the Creative Commons Attribution License, which permits unrestricted use, distribution, and reproduction in any medium, provided the original work is properly cited.

This article has been retracted by Hindawi, as publisher, following an investigation undertaken by the publisher [1]. This investigation has uncovered evidence of systematic manipulation of the publication and peer-review process. We cannot, therefore, vouch for the reliability or integrity of this article.

Please note that this notice is intended solely to alert readers that the peer-review process of this article has been compromised.

Wiley and Hindawi regret that the usual quality checks did not identify these issues before publication and have since put additional measures in place to safeguard research integrity.

We wish to credit our Research Integrity and Research Publishing teams and anonymous and named external researchers and research integrity experts for contributing to this investigation.

The corresponding author, as the representative of all authors, has been given the opportunity to register their agreement or disagreement to this retraction. We have kept a record of any response received.



### **References**

- [1] P. K. Pareek, P. A. S. Surendhar, R. Prasad et al., "Predicting the Spread of Vessels in Initial Stage Cervical Cancer through Radiomics Strategy Based on Deep Learning Approach," *Advances in Materials Science and Engineering*, vol. 2022, Article ID 1008652, 13 pages, 2022.



## Research Article

# Predicting the Spread of Vessels in Initial Stage Cervical Cancer through Radiomics Strategy Based on Deep Learning Approach

**Piyush Kumar Pareek,<sup>1</sup> Prasath Alais Surendhar S,<sup>2</sup> Ram Prasad,<sup>3</sup> Govindaraj Ramkumar ,<sup>4</sup> Ekta Dixit,<sup>5</sup> R. Subbiah,<sup>6</sup> Saleh H. Salmen,<sup>7</sup> Hesham S. Almoallim,<sup>8</sup> S. S. Priya,<sup>9</sup> and S. Arockia Jayadhas <sup>10</sup>**

<sup>1</sup>Department of Computer Science and Engineering and Head of IPR Cell, Nitte Meenakshi Institute of Technology, Bengaluru, India

<sup>2</sup>Department of Biomedical Engineering, Aarupadai Veedu Institute of Technology (AVIT), Chennai, TamilNadu, India

<sup>3</sup>Department of Botany, Mahatma Gandhi Central University, Motihari 845401, Bihar, India

<sup>4</sup>Department of Electronics and Communication Engineering, Saveetha School of Engineering, Saveetha Institute of Medical and Technical Sciences, Chennai, Tamil Nadu, India

<sup>5</sup>Department of Computer Science, S. S. D. Women's Institute of Technology, Bathinda, Punjab, India

<sup>6</sup>Department of Mechatronics Engineering, CMR Technical Campus, Hyderabad, India

<sup>7</sup>Department of Botany and Microbiology, College of Science, King Saud University, PO Box 2455, Riyadh 11451, Saudi Arabia

<sup>8</sup>Department of Oral and Maxillofacial Surgery, College of Dentistry, King Saud University, PO Box 60169, Riyadh 11545, Saudi Arabia

<sup>9</sup>Department of Microbiology - Immunology, Northwestern University, Feinberg School of Medicine, Chicago, IL 60611, USA

<sup>10</sup>Department of EECE, St. Joseph University, Dares Salaam, Tanzania

Correspondence should be addressed to  
S. Arockia Jayadhas; arockia.jayadhas@sjuit.ac.tz

Received 10 June 2022; Revised 6 August 2022; Accepted 13 August 2022; Published 28 September 2022

Academic Editor: K. Raja

Copyright © 2022 Piyush Kumar Pareek et al. This is an open access article distributed under the Creative Commons Attribution License, which permits unrestricted use, distribution, and reproduction in any medium, provided the original work is properly cited.

Novel methods and materials are used in healthcare applications for finding cancer in various parts of the human system. To select the most suitable therapy plan for individuals with domestically progressed cervical cancer, robustness metrics are required to estimate their early phase. The goal of the research is to increase the effectiveness of cervical cancer patients' detection by using deep learning-based radiomics assessment of magnetic resonance imaging (MRI). From March 2016 to November 2019, 125 patients with early-stage cervical cancer provided 980 dynamic X1 contrast-enhanced (X1DCE) and 850 X2 weighted imaging (X2WI) MRI images for training and testing. A convolutional neural network model was used to estimate cervical cancer state based on the specified characteristics. The X1<sub>DCE</sub> exhibited high discriminative outcomes than X2<sub>WI</sub> MRI in terms of prediction ability, as calculated by the confusion matrix assessment and receiver operating characteristic (ROC) curve approach. The mean maximum region under the curve of 0.95 was found using an attentive ensemble learning method that included both MRI sequencing (Sensitivity = 0.94, Specificity = 0.94, and accuracy = 0.96). Whenever compared with conventional radiomic approaches, the results show that a variety of radiomics based on deep learning might be created to help radiologists anticipate vascular invasion in patients with cervical cancer before surgery. Based on radiomics technique, it has proven to be an effective tool for estimating cervical cancer in its early stages. It would help people choose the best therapy method for them and make medical judgments.

## 1. Introduction

Exposure to various chemical and physical agents is a typical environmental problem that contributes to cancer mortality. The cervical cancer is the second most common disease in women, with more than half of the million patients are identified every year throughout the globe. Since most instances happen in developing nations and present at an early incurable phase, more than 350,000 people will lost their life as a result of their illness. Every year, around 38,000 patients are reported in Europe, with more than two-thirds anticipated to be treated and live. Survival rates will differ by nation, dependent on treatment centers and, more significantly, whether a screened program has been developed. By reducing the possibility of invasive carcinoma by treating pre-malignant cervical intraepithelial neoplasia before it grows into a really aggressive and dangerous tumor, these approaches will discover the initial phase of illness [1]. Cervical cancer is one of the most prevalent forms of cancer that may affect a woman's reproductive system, and it represents a significant danger to a woman's life and health. The stages of cervical cancer that occur before treatments are required for identifying the available medical treatment choices and for making medical treatment predictions. Tumors that have invaded the parametrium of the cervical canal may only be treated with radiochemotherapy, whereas malignancies of the cervical canal that do not affect the parametrium can be healed surgically. The presence of parametrial enlargement in cervical cancer is connected to an increased risk of recurrence and worse survival following therapy [2].

Penetration of the women cervix infects the cervix deeper tissues. The cervical cancer has the possibility to spread to other functions of the body, including the liver, rectum, bladder, lungs, and genitals. Normal cervical cells grow, reproduce at a certain rate, and then die, causing changes in their DNA. Furthermore, unfavorable cell mutations are exposed, leading to cells violating their control and refusing to die, resulting in the formation of differentiated cells. Abnormal discomfort after intercourse, vaginal bleeding after intercourse, and vaginal discharge after menopause are the most well-known indications of cervical cancer. Figure 1 depicts the various symptoms of cervical cancer. The most widespread risk variables are early sexual activity, multiple sexual partners, compromised immune system, sexually transmitted diseases, and exposure to smoking and miscarriage vaccines [3]. Figure 2 depicts the various risk factors for cervical cancer rising to women. Consequently, accurate diagnosis of cervical cancer with parametrial invasion is important in clinical practice. Conventional magnetic resonance imaging (MR) imaging and gynecological examination are commonly used to evaluate parameter amplification. Traditional imaging characteristics such as full-thickness disruption of normal cervical stroma in T2-weighted images and nodular lesions extending to neighboring parameters were previously thought to be parameter invasion; however, image processing is a standard function. In medical care, an objective

and measurable approach to measuring criterion penetration is required [4].

In 2012, there were approximately 530,000 newly diagnosed cervical cancers and 270,000 deaths worldwide. Undeveloped nations confront the second most common malignancy and the third major cause of cancer death among women. The highest percentages are in Melanesia, Sub-Saharan Africa, Latin America, and the Caribbean. New Zealand, West Asia, and North America have the lowest. Cervical cancer kills more than 92 percent of women in developed countries: 28,000 in Latin America, 60,000 in Africa and 150,000 in Asia. India, the world's second most populous country, accounts for 26% of cervical cancer deaths (70,000 deaths). Cervical cancer is the leading cause of death in women in eastern, central, Melanesia, and southern Africa. Cervical cancer rates vary widely across the country due to variations in access to surveillance, which enables early detection and removal of lesions and the incidence of human papilloma virus (HPV) disease. The prevalence of HPV infection (of all forms) varies explicitly, from 16% in Latin America, 21% in Africa, 5% in North America and the Caribbean to 9% in Asia [5].

As per a WHO report, cervical cancer is most likely the reason of cancer in women in developing countries. Although clinical centers, thousands of extra cases were reported in the United States in 2016, compared to much greater than 20K in 2014. The dataset of cervical cancer provides almost 800 data specimens, 32 features, and 4 targets from the 2016–17 reporting period. Overall traits, tobacco activities, and previous health histories are all important aspects. The abundance of screening and diagnostic procedures, each of which may produce such a diverse set of outcomes, contributes to the complexity of the data. As a consequence of this, determining how the woman's element will behave and selecting the most appropriate screening strategy are both crucial challenges. As a direct consequence of this, the procedure of identifying the most suitable principal channel constitutes the primary obstacle in the endeavor of measuring a woman's exposure to risk factors. A lot of academics have looked at data on cervical cancer that was compiled from a variety of different sources. The major risk factors for the spread of cervical cancer include improper menstrual hygiene, having children at a young age, smoking, and a lack of preventative measures for mouth cancer. The tumor phase, initial weight mass, and histological grading are all variables that affect the prediction. Therapy is made up of four phases of illness as established by the International Federation of Gynecology and Obstetrics (FIGO) scoring scheme. Surgery or radiation therapy is utilized to handle patients with stage IIA or less. Initial stage cancer patients may need a radical hysterectomy, radiation treatment, or sometimes both. People diagnosed with stage IIB or higher, on the other hand, receive only radiation therapy. Stage IIA disease without stage parametrial involvement and stage IIB disease, in which parametrial involvement are the main difference in stages. Figure 3 represents the different stages of

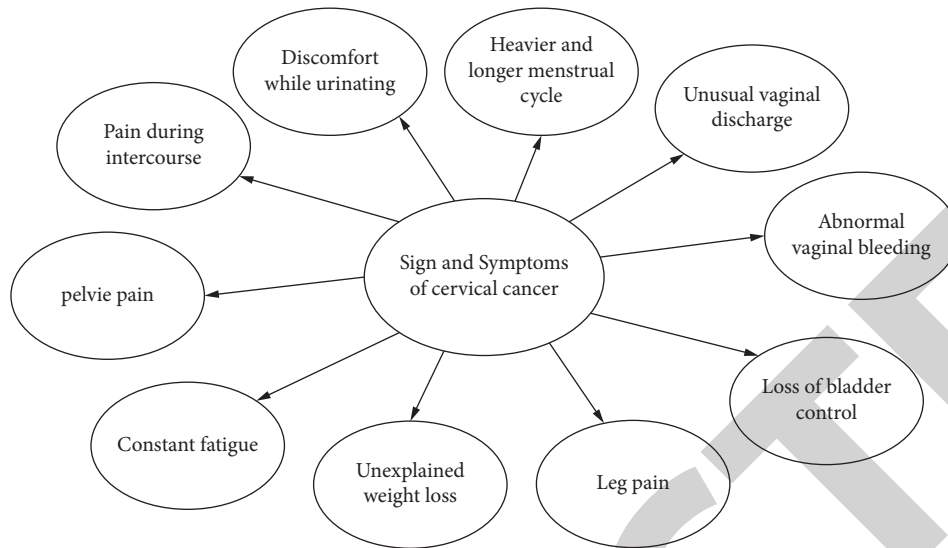


FIGURE 1: Basic symptoms of cervical cancer.

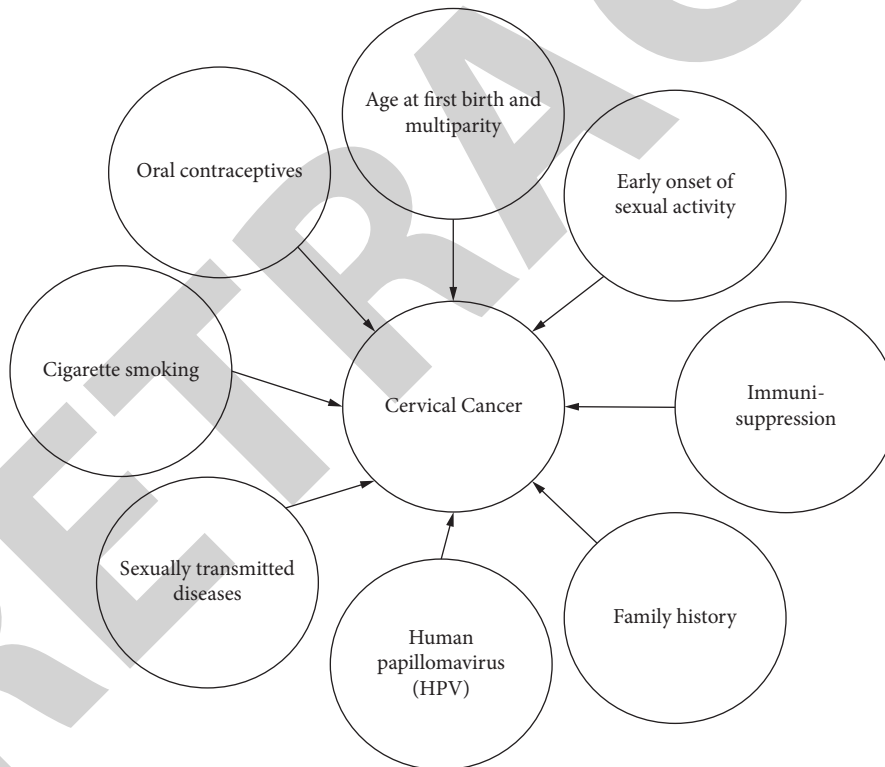


FIGURE 2: Various risk factors for cervical cancer.

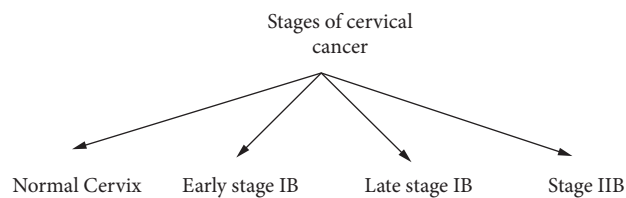


FIGURE 3: Different stages of cervical cancer.

cervical cancer. Although lymph node metastasis is not comprised in the formal FIGO scoring system, they are an important prognostic factor. The TNM staging approach to cervical cancer involves nodal status. Unilateral and bilateral parameters are other prognosis variables for the occurrence of pelvic wall disease [6].

The size of the tumor at prognosis, the size of the high-risk clinical objective during bronchial therapy, and the duration of therapeutic effects are linked to the potential of local democracy. Furthermore, in the epoch of image-guided responsive therapy, it is essential to check the outcome evaluation, especially for those at significant risk of local recurrence, and to intensify medication (or) radio sensitizing Agent who is applicants for clinical trials. On the other hand, identifying individuals at low risk of local recurrence may be clinically important. Clinical imaging is essential in the primary assessment and condition of victims and in the treatment of treatment options. Because of its great resolution, functional imaging capabilities, and excellent soft-tissue contrast magnetic resonance imaging (MRI) is the gold typical for the pre-treatment evaluation of gynecologic malignant T-status [7]. Radiation therapy and concurrent chemotherapy with cisplatin-based chemotherapy is a standard therapy for women with metastatic cervical cancer, as per the NCCN recommendations; the 5-year life expectancy can approach 60–80 percent. If first-line CCRT failed, though, the longer CCRT therapy time will unavoidably delay the start of other possibly beneficial therapies. Furthermore, CCRT has several adverse effects. Additional pelvic irradiated can induce myelosuppression because it damages the bones, which comprise more than 50% of the body's proliferative functional bone marrow mass. Platinum-based CCRT can worsen myelosuppression, although it is less effective if therapy is initiated or interrupted. As a result, predicting CCRT responsiveness before therapy may help to determine whether CCRT should be used as first-line therapy. Furthermore, by identifying individuals who are most susceptible to CCRT, responder prognosis can lead to individualized therapy [8]. Figure 4 describes the treatment option available for cervical cancer.

The Ministry of Health of Bangladesh has launched the 5-year national approach for family welfare cervical cancer control and prevention Initiative, which will run from 2016 to 2021. The WHO considers invasive cervical cancer to be the fourth most widespread and second leading cause of cancer among Bangladeshi women aged 20 to 50 years. Each year, approximately 12,000 new cases are identified, and the severity of the condition exceeds 6,000. In Bangladesh, nearly 4.4 percent of the general population has a higher risk of developing cervical HPV16/18 infections at any given time, and HPVs 16 and 18 are responsible for 80.3 percent of invasive cervical malignancies [9]. Figure 5 depicts the mortality rate of cervical cancer during the year from 1990 to 2020. Targeted treatment requires imaging. Radiomics collects huge volumes of information from high-performance clinical pictures to extract attributes for unbiased, measured investigation of diseased biological activities [10]. Radiomics have been intensively explored in tumor

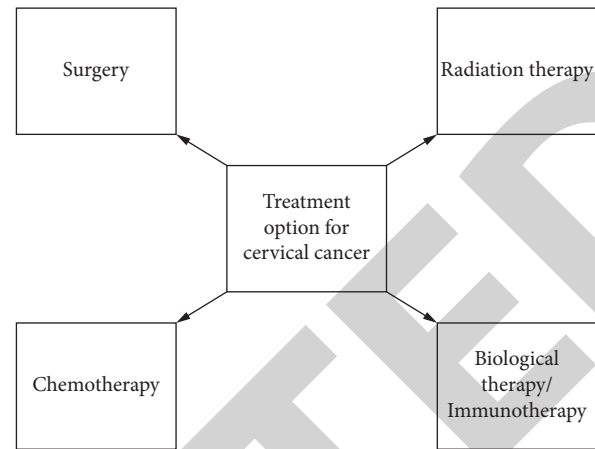


FIGURE 4: Treatment option available for cervical cancer.

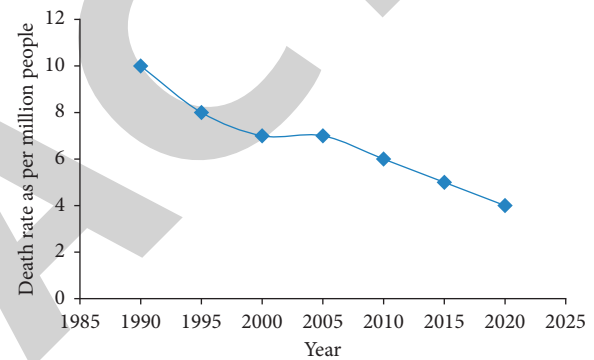


FIGURE 5: Mortality rate for cervical cancer from 1990 to 2020.

detection, differentiated diagnostic tests, prognostic assessment, and therapy outcome prediction in recent decades. This approach has been used to estimate LNM in breast cancer, bladder cancer, biliary tract cancer, and colorectal cancer before surgery [11]. Some research has looked at the effectiveness of radiomics in calculating LNM in cervical cancer. The radiomics properties of positron emission tomography (PET) were linked to the expression of VEGF in cervical cancer in a prior study. This observations suggest that a radiomics system based on health images may be used to predict VEGF expression [12].

Radiomics is a novel approach for obtaining high-throughput data from normal clinical pictures. The radiomics nomogram was used to identify LNM status by collecting measurable characteristics from CT images connected to colorectal, bladder, esophageal, breast, lung adenocarcinoma, and thyroid. It functioned well [13]. Radiomics is a rapidly expanding field of science that uses image collections of high-dimensional characteristics taken from routinely obtained cross-sectional images to produce data that semantic assessment would otherwise lose. Radiomics records the cystic and necrotic patches within the tumor volume that are typical of tumoral heterogeneity, as well as behavior that characterizes aggression and therefore results. Radiomics is an area of research that uses mathematical modeling to extract qualitative information from

clinical images in order to create prediction methods that may be used to estimate treatment prognostic and survivability, with preliminary results reflecting a wide range of medical results [14].

In comparison to nonmedical databases, healthcare sets of data feature more attributes and partial information. This is critical to establish the essential and useful properties for quantified approach building by enhancing type. Although deep learning approaches are stronger in forecasting and effective tweaking, they have been frequently utilized in cancer research. An investigation found that long-term HPV infection is the main reason for cervical cancer [15]. Machine learning is a technique that leverages previously established diagnosing characteristics as factors, such as morphological or textures, and needs factors pre-selected by people to do categorization jobs. Deep learning, on the other hand, retrieves whatever the system defines as essential factors directly from the training phase, avoiding the preconceptions that come with past human analysis. This will eventually offer physicians with methods that will aid in the proper detection of cervical cancer [16]. In this study, deep learning-based VGG19network is used for the early detection of cervical cancer.

## 2. Related Works

Imaging-based tumor size predicts cervical cancer radiation response before, during, and after treatment. Various imaging-based tumor size measurement approaches and time have not been examined. To compare the diagnostic usefulness of orthogonal diameter-based elliptical tumor volume measurement vs. contoured tracing evaluation 3D tumor volumetric. 60 patients (stages IB2-IVB/recurrent) with advanced cervical cancer underwent continuous MRI exams throughout early RT, mid-RT, and follow-up. In the computer workstation, the measurement based on ROI was calculated by monitoring the whole tumor area on each MR piece. Three orthogonal diameters ( $a_1$ ,  $a_2$ ,  $a_3$ ) were determined on image hard copies to calculate the volume as an ellipse for the diameter-based "elliptical volume". These results were compared between the two measurement techniques, and the series tumor sizes and regression rates calculated with each approach were linked to local management, disease, and survival time. The average duration of treatment was 5 years. A mid-treatment MRI scan using 3D ROI volumetry is the best approach and time point for estimating tumor size to predict tumor regression rate. Both the diameter-based technique and the ROI measurement had to predict accuracy equivalent to pre-RT tumor size, especially in patients with small and large RT tumors. Tumor size prior to RT was determined by any approach and, on the other hand, showed a significantly lower prognostic value for intermediate-sized tumors that accounted for most patients. The largest result of predicting local control and disease survival rates is the tumor regression rate gotten during mid-RT, which can only be recognized by 3D ROI measurement. Slow ROI-based regression rates were predicted within the difficult intermediate pre-RT group to classify all treatment complications. The results were not predicted by the mid-RT

regression rate depend on the base diameter measurement. Of all the measurement methods, the initial-RT and post-RT measurements were the least informative. The first findings show that a simple diameter-based estimate obtained from film hardcopy can be used to determine the initial tumor size for the treatment performance prognosis in cervical cancer. When the initial tumor size is intermediate, ROI measurement and additional MRI are required during the RT to objectively measure the tumor regression rates for clinical outcome evaluation. The baseline diameter-based approach of this study is not optimal for evaluating the response throughout treatment [17].

Cells usually split and expand to make additional cells only if the body requires them. Whenever new cells are not required, this ordered procedure keeps the process going. Those cells may produce a cancer progression, which is a mass of excess tissues. Effective data processing methods are used to diagnose whether the cervix is normal or cancerous. With the help of powerful data processing methods, normal cervical or cancer cervical prognosis is calculated in this study. Predictive data processing is important, especially in the medical field. The regression and classification tree system, the K-learning with Random Forest Tree algorithm to predict a usual or cancerous cervix are all based on this principle. Information was analyzed from NCBI and utilized from a data collection with 500 samples and 61 parameters. The results were shown in the format of predictive trees. As previously indicated, a sample of 100 data with 61 biopsies characteristics was chosen. Depending on the biopsies results, an awareness program is implemented, and a questionnaire is undertaken to track women's changes over this time. A personalized interviewing program was done amongst rural women in diverse locations to obtain data effectively. Patients were screened for cervical cancer in collaboration with JIPMER Hospital. The findings of the biopsy tests were statistically analyzed and submitted to MATLAB for algorithmic verification. To determine the results obtained, 100 test datasets and 60 training packages are divided and presented in different heads. To find the best cervical cancer prognosis, the researchers compared the effectiveness of several methods using measures such as sensitivity, specificity and accuracy. The regression approach was initially used to make predictions. Normal cervical or cancers cervical is two possible side effects of CART binary tree. The GINI index is a separation criterion used to determine the different types of cervical information. After the RFT confirmed the optimal accuracy, a new logic was adopted, namely "mixtures of two techniques." This is the supervised machine learning group approach. To create the best predictive effect, whitening is utilized as a pre-process in the k-mean cluster. With the CART TREE result, the findings represent 83.87 percent accuracy. To increase forecast efficiency, Random Forest Tree (RFT) is used. To achieve 93.54 percent forecast efficiency using the MATLAB code. Because the K-Means method is useful for estimating datasets, the RFT - K- i.e. learning tree output achieves high accuracy. This approach is unique in that it combines RFT with the K-means method, resulting in a greater accuracy result. This algorithm has been ineffective for the exact prediction of cervical cancer [18].

Prevention methods are cheaper than medical treatment in practically all countries. The primary diagnosis of any disease improves the chance of effective treatment for patients rather than the disease diagnosed late in its course. Cervical cancer is caused by a variety of factors, including aging and the use of hormonal contraceptives. Cervical cancer can be diagnosed early, which increases healing and reduces mortality. The study use machine learning methods to improve a method that can precisely and sensitively diagnose cervical cancer. The categorization approach was constructed using the cervical cancer potential risk database from the University of California at Irvine (UCI) using a polling approach that included three classification techniques such as decision tree, random forest and logistic regression. To solve the difficulties of asymmetric learning and to decrease the variables that do not disturb the accuracy of the sample, the Minority Surface Model (SMOTE) integrated with the Primary Component Analysis (PCA) approach was used. The excessive fitting problem was avoided using the 10-fold cross-verification approach. The database contains 32 risk factors and four targeted variables (Hinselmann, Cytology, Schiller, and Biopsy). The study found that combining voting classifiers with SMOTE and PCA approaches improves the sensitivity, accuracy, and area of prediction models under the ROC for each of the four target variables. For all target variables, the SMOTE-voting approach increased accuracy, sensitivity and PPA ratios from 0.9 percent to 5.1 percent, 39.2 percent to 46.9 percent, and 2 percent to 29 percent. Furthermore, the PCA technique improved sample performance by eliminating computational processing time. Lastly, after comparing the findings to those of multiple prior research, study exposed that these models were more efficient in identifying cervical cancer based on key assessment criteria. In this method, the correct prediction of the original feature is difficult [19].

Another study looked at and proposed an effective and enhanced cervical cancer forecasting model. Previous monitoring and detection methods/tests were complex, time-consuming, and clinical/pathological. Machine learning predicts and diagnoses cervical cancer. For measuring performance in illness diagnosis, an integrative technique of Adaptive Boosting and Genetic Algorithm is applied. To reduce the amount of features, a genetic algorithm is utilized as feature selection. It minimizes both the computing price and the number of components required for diagnosis. Adaptive Boosting is a technique for improving classifier performance. For illness identification, the Support Vector Machine (SVM) and Decision Tree are recommended. For cervical cancer detection, 32 variables are utilized. The set of variables is decreased using a genetic approach, and adaptive boosting is recommended for additional improving performance. For the radial bias function of support vector machine, decision tree, and SVM linear, the improvement in accuracy was 94 percent, the sensitivity was 97 percent–98 percent, the specificity was 93 percent–94 percent, and the accuracy was 93 percent–95 percent. A combined method of adaptive promotion and genetic mechanism is suggested. It requires more time for processing and exact prediction is difficult for the high-noise image [20].

Cervical cancer is the most leading cause of mortality, especially in developing countries, although it may be efficiently managed if identified earlier. The goal of this work was to create effective machine-learning-based classification models for early-stage cervical cancer detection utilizing clinical studies. The study used a Kaggle data repository cervical cancer databases that had four different types of aspects including cytology, Hinselmann, biopsy, and Schiller. Those class characteristics were used to divide the database into four groups. This dataset was subjected to three feature modification methods such as sine function, log and Z-score. The performance comparison of many supervised machine learning methods was evaluated. For the biopsies and cytology data, the Random Tree (RT) method performed best, while Random Forest (RF) and Instance-Based K-nearest neighbor (IBk) performed best for Schiller and Hinselmann correspondingly. The logarithmic transformation approach to the biopsy dataset worked best, while the sine function worked best for cytology. The Hinselmann database performed well on both logarithm and sine functions, while the Schiller database performed well with the Z-score. Multiple feature selection techniques (FST) approaches have been used for modified datasets to identify and prioritize related risk variables. The findings of this study show that clinical evidence, tuning and relevant computer structure, classification, and machine learning approaches can be effective and accurate. Diagnose cervical cancer in its early stages. This method is inefficient and difficult to predict the exact value [21].

Health care providers are now confronting a significant problem in recognizing cervical cancer before it progresses fast. To access the risk variables for predicting cervical cancer by using machine learning classification algorithms. Effective variation of the eight most categorical algorithms for diagnosing cervical cancer using various excellent features selected from the database. Machine learning classifiers such as Decision Tree, Multilayer Perceptron (MLP), K-Near Neighbor and Random Forest, Logistic Recursion, Gradient Boosting, Adaboost, and SVC are help to identify the early detection of cervical cancer. To prevent values from disappearing in the database, several procedures are used. A mixture of selecting features approaches including SelectBest, Random Forest, and Chi-square was used to select several excellent properties. Recall, accuracy and f1-score properties are utilized to evaluate the effectiveness of classifiers. MLP outperforms other classification techniques in the range of best-selected features. At database segmentation rates, most classification techniques claim to have the greatest accuracy in the first 25 characteristics. The ratio of correctly classified examples to each sample is shown, and all of the findings are analyzed. Medical practitioners can carry out cervical cancer prediction in an effective manner by using the recommended method. This method has a cumulative loss function, making it difficult to predict cancer [22].

To examine whether strain elastography imaging can be used to diagnose and predict treatment outcomes in patients receiving simultaneous chemo-radiotherapy (CCRT) for locally advanced cervical cancer. In a 2015–2016 feasibility assessment, 47 individuals with advanced localized cervical cancer were registered. All patients had CCRT and filtered elastography before, one week, two weeks, and immediately

after therapy. MRI was used to evaluate treatment response during diagnosis and following CCRT. Depending on the MRI findings the outcome of treatment can be classified as a full response, partial response, chronic disease or progressive disease. Clinical results have been compared with the rate of strain of normal parametrial tissue and cervical tumor. Of the 47 patients who completed all four exams, 36 were evaluated: 25 were categorized as CR, 11 as PR and 0 as SD/PD. The CR group ( $F=87$ ) and the PR group ( $F=38$ ) had significantly different strain ratios at different time periods. The CR and PR sets had considerably different strain rates ( $F=7.2$ ). At 1 week of treatment, the strain rates in the CR and PR collections varied considerably ( $p 0.05$ ). Week 1 and 2, and post-treatment (all  $p 0.001$ ) showed a significant decrease in the CR group, whereas week 2 and after treatment (both  $p 0.05$ ) showed a significant decrease in the PR group, but not at week 1 during CCRT. A prospective combination study was performed to estimate cancer response in women who getting CCRT for cervical cancer. The work demonstrates the ability of strain elastography imaging to monitor and predict tumor response developed by CCRT [23].

### 3. Materials and Methods

**3.1. Data Collection.** Samples of 1500 diagnostic MRI images were collected from an average of 150 female patients aged 55 years and above in online databases of international collaborations on cancer reporting over a period of 30 to 65 years between March 2016 and November 2019, with 600 naval invasions and 900 non-naval invasions. In each case, two MRI methods were captured such as  $X1_{DCE}$  MRI, which focused on anatomical features and efficiently measured blood flow in vivo; and  $X2_{WI}$  MRI, which stronger the contrast of the soft tissues. Patients with  $X1_{DCE}$  and  $X2_{WI}$  MRI assessments prior to surgical treatment; Surgical extraction cases with pathological verification utilized as the typical gold for distinguishing non-invasive and vessel invasion properties of cancer; And all women over 20 years of age were included. Individuals with a history of preoperative treatment, women with no  $X1_{DCE}$  or  $X2_{WI}$  MRI data, women with no histopathological effects, patients receiving congenital therapies, and very young patients with cases of other cervical diseases or tumors were excluded. A radiologist with 10 years of expertise used 4.0-T scanning with sensitive coded abdominal scrolls of 8-channel arrays to perform preliminary MRI examinations. Before screening these individuals were told to drinking some water to fill their bladder, rest taken for 30 minutes, and bring their respiration under control. Clinical records were reviewed to collect patient data such as patient age, menstrual status, international gynecology and obstetrics stage and tumor type, LN and lymph vascular space invasion histological findings after surgery. Table 1 shows the patients' various characteristics for training and testing phase.

**3.2. Data Image Preprocessing.** Each  $T1_{DCE}$  and  $T2_{WI}$  image was examined using the ITK-SNAP program by MRI radiologists with 10 and 12 years of experience. The ROI per patient was created at an average range of  $30 \times 40$  pixels per image and

included tumor areas and borders of cervical cancer located in the cervix. The ROI patch from each MRI image was automatically generated and measured at  $256 \times 256$ , and then fed into in-depth learning networks. Data augmentation was utilized to train the convolutional neural network models and balanced the datasets using the image data generator of the Keras module in Python 3.9. Every image is initially measured and cut before being moved up and down, before being moved to right from left, and then arbitrarily interchanged 6 degrees around the midpoint. It was thought that pixels beyond ROI could carry important information for discrimination because cervical tumor cells travel to neighboring healthy tissues in patients with vascular invasion. To compare ROIs, the array of pixels from the minimum boundary rectangle (MBR) is stretched at different positions (top, bottom, left, and right). The produced images were enhanced with data amplification utilizing the same technique before being placed on the network's input layer. Figure 6 depicts the process flow diagram for cervical cancer prediction.

**3.3. Convolutional Neural Models for Classification.** CNN, also known as convolutional networks, was employed as direct inputs to the network instead of feature representation, unlike standard radiomic techniques. The algorithm is a self-sufficient gathering and improvement of advanced traits and variables. MRI scanned regions from cervical victims were used as inputs for the end-to-end convolutional networks model in this study. The output layer of each strategy was constructed to comprise two neural networks to predict the possibility of with or without ship incursions. Several CNN techniques, including VGGNet, GoogLeNet, Residual Network, and DenseNet, have been used to analyze various radiomic processes. More detailed explanations may be found in the source articles for each CNN model.

In order to adapt to this work during the experiments, the first fully connected components in every neural network were exchanged with three additional entirely connecting layers with a neural number of 700, 500, and 5, respectively. Adam optimizer and cross-entropy losses were used to train all networks with a detection rate of 0.0002. During each Conventional blogging of AdaptedVGG19 networks, a custom compression and trigger mechanism and components of the Convulsion Block focus were added to create an AdaptedVG1919-SE and AdaptedVG1919-CBAM accordingly. The two separate AdaptedVGG19-focused network integrated judgments were used to develop a deeper group learning approach and an observational group learning approach accordingly.  $D = (d1 + d2)/2$  was used to calculate the output probability of becoming a ship invasion or non-ship invasion, where  $d1$  and  $d2$  reflect the effect potential of two AdaptedVGG19 networks using  $X1_{DCE}$  and  $X2_{WI}$ . Figures 7 and 8 represent the architecture model for suggested VGG19 approaches and its inner structure processing.

**3.4. Mechanism for Validity.** The effectiveness of the radiomic algorithms was evaluated using 10-fold cross-validation, and the accuracy, sensitivity, and specification were calculated using the calculations below. The amount of



TABLE 1: A selected patient training and testing phase attributes.

Patients characteristics	Training phase N= 150			Testing phase N= 55			$p^*$ -value
	+ive lymphovascular invasion	-ive lymphovascular invasion	$p$ -value	+ive lymphovascular invasion	-ive lymphovascular invasion	$p$ -value	
Patients age/year			0.60			0.53	0.98
Average age	55	56		53	60		
Age ranges	27–55	27–60		30–55	35–65		
Stages			0.62			<0.0002	0.45
Early stage IB	20 (50.2)	40 (52.6)		15 (30.4)	35 (70.2)		
Late stage IB	15 (42.5)	48 (50.1)		18 (40.2)	20 (40.2)		
Stage IIB	8 (18.5)	12 (13.2)		12 (52.6)	8 (10.2)		
MRI lymph node status			<.002			0.002	0.70
Positive	20 (7.9)	30 (40.2)		10 (55.2)	50 (92.1)		
Negative	150 (95.7)	52 (68.2)		12 (60.8)	15 (20.5)		
Menstrual status			0.542			0.442	0.89
Postmenopausal	15 (40.3)	55 (56.2)		6 (30.2)	30 (52.7)		
Premenopausal	28 (65.2)	48 (50.2)		15 (80.5)	35 (56.8)		
Maximum cancer diameter			0.002			0.008	0.55
≤5 cm	25 (60.2)	80 (88.5)		8 (52.8)	42 (68.5)		
>5 cm	20 (45.6)	18 (17.06)		10 (54.8)	9 (15.9)		
Lymphovascular invasion			<.002			.001	<.002
Positive	88 (35.9)	46 (59.8)		18 (22.6)	15 (35.9)		
Negative	170 (59.8)	35 (40.8)		97 (89.0)	28 (70.2)		

disorder cases properly identified is represented by True Negative ( $t_n$ ) and True Positive ( $t_p$ ). The quantities of disorder cases incorrectly identified were labeled as False Positive ( $f_p$ ) and False Negative ( $f_n$ ).

$$\begin{aligned}
 \text{Accuracy } (A_c) &= \frac{t_n + t_p}{f_n + t_n + f_p + t_p}, \\
 \text{Sensitivity } (S_n) &= \frac{t_p}{f_n + t_p}, \\
 \text{Specificity } (S_p) &= \frac{t_n}{f_p + t_n}.
 \end{aligned} \tag{1}$$

This method's capacity to distinguish between non-vessel invasion and vessel invasion events is reflected in its efficiency. To refer specificity to a model's ability to appropriately distinguish non-vessel invasion. Sensitivity refers to the model's ability to properly distinguish vessel incursion. The median receiver operational characteristics assessment and the area under the ROC curves were also used to assess these approaches. A confusing matrix was created using the Scikit-Learn module to evaluate the classification performance of the suggested approaches. The gradient-weighted glass activation mapping approach was used to create the heatmaps. Algorithm 1 shows the deep learning-based radiomics strategy for cervical cancer prediction.

## 4. Results and Discussion

### 4.1. Performance Classification in Various Configurations.

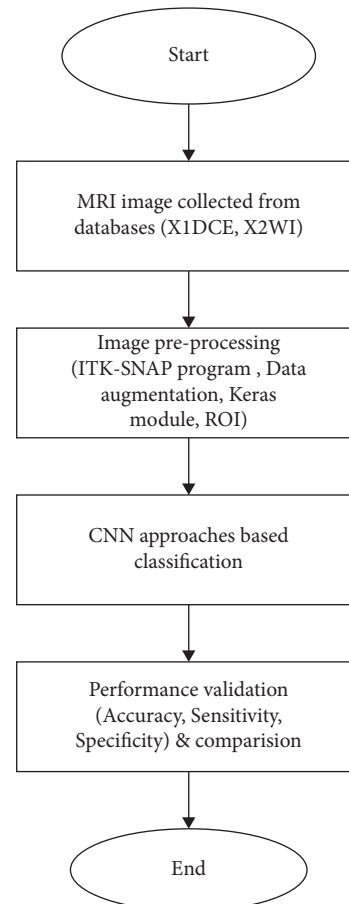


FIGURE 6: Cervical cancer prediction step by step procedure.

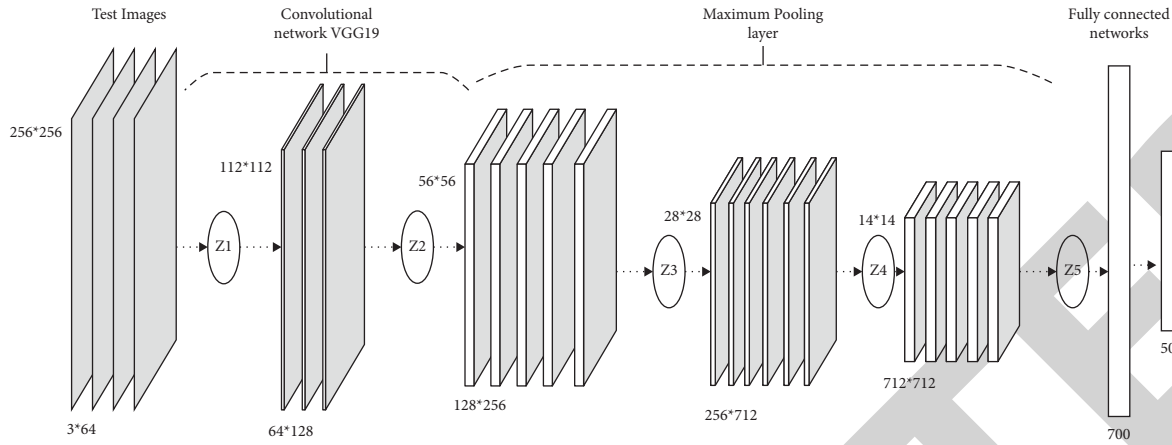


FIGURE 7: Schematic diagram for suggested adaptive VGG19 approach.

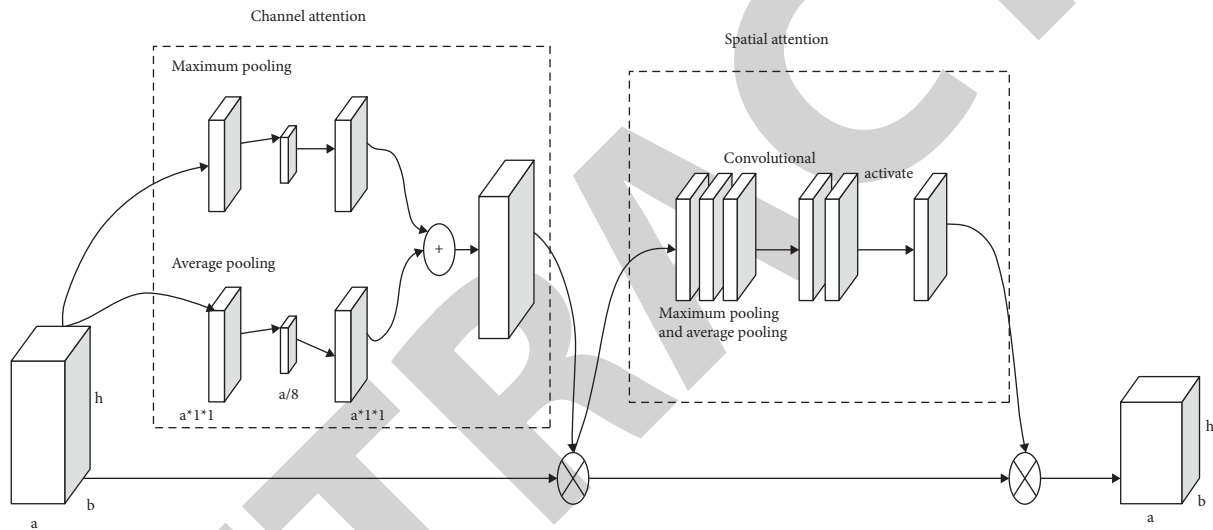


FIGURE 8: Inner structure process flow diagram for adaptive VGG19.

Current studies have found that combining data from multiple methods increases discriminatory performance compared to using individual methods. Since both the  $X1_{DCE}$  and  $X2_{WI}$  MRI datasets provide rich and varied signal intensity within the cancer, Convolutional neural network-based radiomic algorithms were developed in this work. The effectiveness of the approach for vessel invasion discriminations is shown in Table 1. Findings of each model are presented, including AUC average value, sensitivity, accuracy, and uniqueness. As seen in Table 1,  $X1_{DCE}$  consistently defeats  $X2_{WI}$ , proving that the  $T1_{DCE}$  database is more valuable than the  $X2_{WI}$  database. Furthermore, the sensitivity determined by  $X2_{WI}$  for every scenario was lower than that produced by  $X1_{DCE}$ , showing significant error rates by  $X2_{WI}$ .

The primary cause of  $X1_{DCE}$  MRI is the ability to effectively estimate blood flow in vivo by displaying blood vascular density and permeability, estimating the capacity transmission constant, and depending on the permeability of the cancer vasculature, all of that can give more discriminating data on the prognosis of cervical cancer vessel invasion.  $X2_{WI}$

provides anatomical data by screening soft tissues with high resolution to reveal tumor morphological characteristics. Furthermore, current findings are difficult to describe because there are no specific indicators to identify the quality of vascular infiltration in cervical cancer using preoperative MRI imaging. Compared to ResNet-v2, Inception-v3, and DenseNet, the AdaptedVGG network generated improved accuracy and AUC values for  $X1_{DCE}$  and  $X2_{WI}$  databases. Based on the small ROIs collected from MRI images, the most basic topologies of the AdaptedVGG network can be useful in minimizing excess compatibility with sophisticated structures compared to other CNN models.

The remaining designs were said to allow greater accuracy in diagnosing clinical images, which contradicted the findings. This can be calculated based on AdaptedResNet50 and AdaptedVGG19, which have 80,402,590 and 84,922,700 training variables, correspondingly. AdaptedcResNet performed worse than AdapedVGG19, which may be due to greater compatibility. In terms of information size and modeling ability, there has to be a compromise. When the information set is large enough to effectively train a large

```

Input: Test MRI images from datasets
Output: Prediction of the cervical cancer (normal cell (or) abnormal cell)
Initialize the number of specimen (Ns), tumor length (Lt), Image processing (Ip)
While (not satisfied the termination condition)
  for  $i$  ranges (0, Ns)
    Randomly selected the specimen N1, N2, N3. ....Ns then perform the operation
      for  $j$  ranges (0, Lt)
        If  $\text{rand}(0, 1) < \text{rand}(0, Lt) == j$ 
          Perform the image processing operation
        else
          Do not perform the image processing operation
        end if
      Get the new image (Nsn)
    end for
  end for
  for  $i$  in range (0, Ns)
    If tumor volume (Nsn) > tumor volume (Ns)
      Update cancer state (normal/abnormal)
    else
      Not update cancer Ns
    end if
  end for
end while

```

ALGORITHM 1: Deep learning-based Radiomics strategy for cervical cancer prediction.

model, the structure is more likely to perform better. Excessive fit, on the other hand, can be frustrating when the information is too large to sustain training. The small number of photos in our investigation may have had an impact on the effectiveness of the models. The optimum AUC of 0.880 was achieved by combining the results of the  $X1_{DCE}$  and  $X2_{WI}$  databases using the deep group learning approach. The craft properties used to predict vascular invasion status using  $X1_{CE}$  MRI created a radiomics nomogram approach and a current of 0.95 AUC before trial. Similarly,  $X2_{WI}$  used MRI to capture craft properties and developed a logistic regression model with 0.710 AUC.

The maximum AUC in this test reached 0.911, which uses the recommended ensemble technique, which combines both MRI methods. This was in line with previous research that focuses on distinguishing the capabilities of the network and enhancing categorization capabilities. The SE component used in this study can lift the weight of the attributes of the most essential channels. Integrated channel attributes and spatial dimensions data were central to CBAM components. These findings suggest that careful group methods may be useful in predicting vascular invasion in cervical cancer. If the ROC curves are combined with false positive and true positive ratios, a more complete outcome can be obtained.

For such an  $X1_{DCE}$  MRI, as shown in Figure 9 performance evaluation, the curvature of the  $X1_{DCE}$  and  $X2_{WI}$  models is always greater than that of other structures.  $X1_{DCE}$  &  $X2_{WI}$  worked better than AdaptedVGG16. This demonstrates that CNN models of various depths can learn features from various levels and that networks with multiple layers performed somewhat excellent than those with lower levels. Considering the better

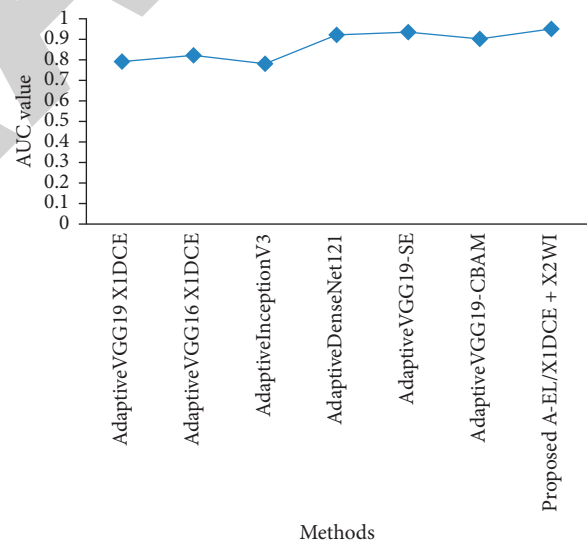


FIGURE 9: Various technique performance evaluation by using receiver operating curve.

specification, AdaptedResNet50-v2 quickly surpassed AdaptedInception-v3 and AdaptedDenseNet121. Adapted Inception-curve, on the other hand, v3s are generally lower than others. Similar findings were made for  $X2_{WI}$  MRI in predictive performance, with the exception of AdaptedResNet50-v2. The study shows the ROC curve of EL modeling combining  $X1_{DCE}$  and  $X2_{WI}$  data, which is an optimal average AUC of 0.95. Figures 10 and 11 depicts the different technique evaluation for predicting the accuracy and sensitivity.

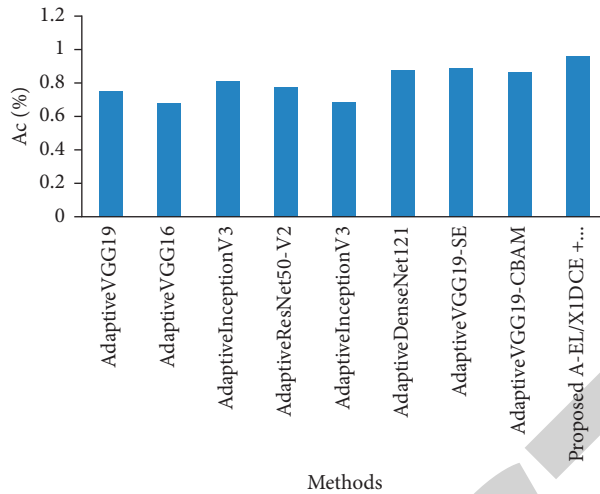


FIGURE 10: Different approaches to accuracy prediction.

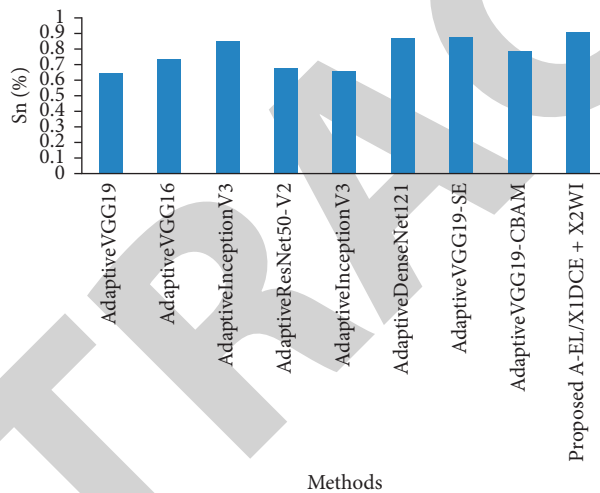


FIGURE 11: Different approaches to sensitivity prediction.

4.2. *The Peri-Tumor Area’s Effect on Estimating Vessel Invasion.* Tumor cells can spread to the pelvic area where they can travel to the blood or lymphatic vessels and other human tissues, leading to invasion and metastasis of cervical cancer. To test the discriminatory ability of peri-tumor pixels in the vascular invasion properties in cervical cancer, a set of system features was created by extending the ROI’s MBR from 10 to 60 pixels in all directions on the X1<sub>DCE</sub> MRI images. Different pixels with three patches up to the ROI of the MBR were created for a single MRI image, and they were used as training examples using EL models. With X1<sub>DCE</sub> MRI data and the EL model, Figure 12 represent the confusing matrix separation among non-vessel invasion and vessel invasion.

Compared to the AUC values achieved by utilizing the similar models training with pixels of 10 and 60 from the MBR of the original ROIs, the model of EL was training with pixels image enlarged by 30 pixels from the ROI, which reached the largest AUC. Table 2 predicts the EL approach performance evaluation with different patches. These

findings indicate that the cervical cancer, peri-tumor region plays a significant part in the ultimate classification of vascular invasion. The effect was thought to be explained by the following: The rapid growth of microorganisms inside the cancer before the invasion of the vessel causes the microvascular tumor to expand into neighboring tissues and cause small morphological changes in these tissues. Radiologists can sense design in surrounding tissues only depending on the regional scale features determined via visual inspection, and these current convolutional neural network algorithms can detect pixel-level properties and detect certain connections between morphological and pathological characteristics.

By combining predictive outcomes from both the X1<sub>DCE</sub> and X2<sub>WI</sub> MRI datasets, the structure of the recommended groups improved the predictive performance. This technique was inspired by the fact that radiologists make diagnostic decisions based on a thorough examination of several methods. These findings indicate the presence of careful group methods as a potential method for integrating

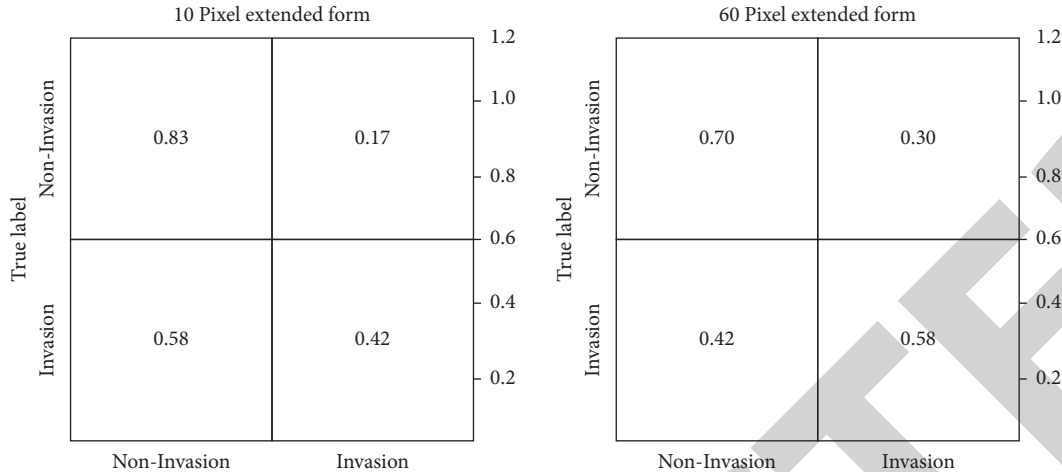


FIGURE 12: Confusion matrix assessment for vessel and non-vessel invasion.

TABLE 2: Various CNN model performance evaluation [ $A_c$  = Accuracy;  $S_n$  = Sensitivity;  $S_p$  = Specificity].

Various methods	ROC curve	$A_c$	$S_n$	$S_p$
AdaptiveVGG19 X1 <sub>DCE</sub>	0.79	0.75	0.65	0.78
AdaptiveVGG16 X1 <sub>DCE</sub>	0.82	0.68	0.74	0.75
AdaptiveInceptionV3/X1 <sub>DCE</sub>	0.78	0.81	0.85	0.65
AdaptiveVGG16/X2 <sub>WI</sub>	0.85	0.68	0.88	0.60
AdaptiveResNet50-V2/X1 <sub>DCE</sub>	0.89	0.78	0.68	0.87
AdaptiveInceptionV3/X2 <sub>WI</sub>	0.92	0.69	0.66	0.88
AdaptiveResNet50-V2/X2 <sub>WI</sub>	0.88	0.80	0.70	0.92
AdaptiveDenseNet121/X2 <sub>WI</sub>	0.87	0.88	0.72	0.77
AdaptiveDenseNet121/X1 <sub>DCE</sub>	0.92	0.77	0.87	0.84
AdaptiveVGG19-SE/X2 <sub>WI</sub>	0.89	0.85	0.79	0.82
AdaptiveVGG19-SE/X1 <sub>DCE</sub>	0.94	0.89	0.88	0.88
AdaptiveVGG19-CBAM/X2 <sub>WI</sub>	0.85	0.91	0.82	0.89
AdaptiveVGG19-CBAM/X1 <sub>DCE</sub>	0.90	0.87	0.79	0.88
Proposed A-EL/X1 <sub>DCE</sub> + X2 <sub>WI</sub>	0.95	0.96	0.91	0.94

TABLE 3: Different pixel performance evaluation.

Pixels expansion	AUC	$A_c$	$S_n$	$S_p$
Pixel range 10	0.78	0.77	0.56	0.89
Pixel range 30	0.90	0.89	0.92	0.97
Pixel range 60	0.88	0.65	0.97	0.78

multiframetric MRI databases into diagnostic and therapeutic applications. Furthermore, CNN-based radiomic systems are modifiable. As a result, new information classification assumptions can be provided utilizing a pre-trained framework with previously defined dependencies, weights, and other parameters that appear convenient and useful to facilitate the work. This is another important reason why detectives used CNN networks to complete this task Table 3.

## 5. Conclusion

Utilizing multi-parametric MRI data, this research presents in-depth radiomic approaches that may differentiate

between non-vessel invasion and vessel invasion in cervical cancer. Specifically, the research focuses on vessel invasion.

These findings provide evidence that comprehensive neurological network-based radiomics techniques are able to accurately forecast vascular invasion in cervical cancer that is in its early stages. In addition, these methods do not call for time-consuming human operations such as manual division, the construction of features, or selection.

By utilizing a method known as focused group learning, we were able to achieve a high level of prediction accuracy. This method possesses a significant amount of potential and a great deal of promise for use in supporting future clinical applications.

## Data Availability

The data used to support the findings of this study are included in the article. Further data or information is available from the corresponding author upon request.

## Conflicts of Interest

The authors declare that there are no conflicts of interest regarding the publication of this paper.

## Acknowledgments

The authors appreciate the supports from St. Joseph University, Tanzania for the research and preparation of the manuscript. The authors thank to Nitte Meenakshi Institute of Technology, Northwestern University, for providing assistance to complete this work. This project was supported by Researchers Supporting Project number (RSP-2021/283) King Saud University, Riyadh, Saudi Arabia.

## References

- [1] J. H. Shepherd, "Cervical cancer," *Best Practice & Research Clinical Obstetrics & Gynaecology*, vol. 26, no. 3, pp. 293–309, 2012.

## *Retraction*

# **Retracted: Performance and Exhaust Emission Characteristics of C.I Engine Using Biofuels and Its Diesel Blend with Nano-Additives**

### **Advances in Materials Science and Engineering**

Received 26 December 2023; Accepted 26 December 2023; Published 29 December 2023

Copyright © 2023 Advances in Materials Science and Engineering. This is an open access article distributed under the Creative Commons Attribution License, which permits unrestricted use, distribution, and reproduction in any medium, provided the original work is properly cited.

This article has been retracted by Hindawi, as publisher, following an investigation undertaken by the publisher [1]. This investigation has uncovered evidence of systematic manipulation of the publication and peer-review process. We cannot, therefore, vouch for the reliability or integrity of this article.

Please note that this notice is intended solely to alert readers that the peer-review process of this article has been compromised.

Wiley and Hindawi regret that the usual quality checks did not identify these issues before publication and have since put additional measures in place to safeguard research integrity.

We wish to credit our Research Integrity and Research Publishing teams and anonymous and named external researchers and research integrity experts for contributing to this investigation.

The corresponding author, as the representative of all authors, has been given the opportunity to register their agreement or disagreement to this retraction. We have kept a record of any response received.

### **References**

- [1] S. Jacob, L. Karikalan, J. I. JoshuaRamesh Lalvani, A. Sharma, and M. Kannappan, "Performance and Exhaust Emission Characteristics of C.I Engine Using Biofuels and Its Diesel Blend with Nano-Additives," *Advances in Materials Science and Engineering*, vol. 2022, Article ID 9185388, 5 pages, 2022.



## Research Article

# Performance and Exhaust Emission Characteristics of C.I Engine Using Biofuels and Its Diesel Blend with Nano-Additives

S. Jacob <sup>1</sup>, L. Karikalan <sup>1</sup>, J. Isaac JoshuaRamesh Lalvani,<sup>2</sup> Aman Sharma,<sup>3</sup> and Maghalengam Kannappan <sup>4</sup>

<sup>1</sup>Department of Automobile Engineering, VELS Institute of Science, Technology & Advanced Studies, Chennai 600117, Tamilnadu, India

<sup>2</sup>Department of Mechanical Engineering, Faculty of Mechanical and Production Engineering, AMIT, Ethiopia

<sup>3</sup>Department of Mechanical Engineering, GLA University, Mathura, UP 281406, India

<sup>4</sup>Faculty of Automotive Engineering, Sawla Campus, Arba Minch University, Ethiopia

Correspondence should be addressed to L. Karikalan; [karilk1972@gmail.com](mailto:karilk1972@gmail.com) and Maghalengam Kannappan; [maghalengam.kannappan@amu.edu.et](mailto:maghalengam.kannappan@amu.edu.et)

Received 22 June 2022; Accepted 3 September 2022; Published 27 September 2022

Academic Editor: K. Raja

Copyright © 2022 S. Jacob et al. This is an open access article distributed under the Creative Commons Attribution License, which permits unrestricted use, distribution, and reproduction in any medium, provided the original work is properly cited.

Depletion of fossil fuel assets makes it critical that we find biodiesel sources in the contemporary world. This work investigates dual bio-fuels of jatropha methyl ester and mahua methyl ester in various proportions, such as 15:5, 10:10, and 5:15. The performance and emission characteristics of JME15MME5, JME10MME10, and JME5MME15 blends of jatropha methyl ester and mahua methyl ester are suitable for diesel engines with little air pollution. Biodiesel blends with titanium dioxide nano-additives, such as jatropha methyl ester and mahua methyl ester, might be more efficient at the conclusion of the experiment, preserving fossil fuel assets for future generations. Performance parameters like BTE and SFC with different load conditions are analyzed for various blends, and then final results are drawn.

## 1. Introduction

Biodiesel is a fuel produced using standard sustainable sources like vegetable oil. It is called mono-alkyl esters [1]. Since it has comparable properties to biodiesel, diesel fuel blended with JME can give better results [2]. The engine discharges have also been discovered to diminish with the use of biodiesel when compared with vegetable oil [3]. The property of raw jatropha, the methyl ester of jatropha oil, is associated with diesel. If ethanol is utilized, it is called an ethyl ester [4]. These fuels are essentially nonpetroleum and outcome in bioenergy reliability and have natural advantages [5]. Distinguishing proof of elective powers to utilize in an I.C. engine exposed to concentration all over the world [6]. A bioenergy emergency is because of the two following reasons: the populace of the world has expanded quickly, and the way of life of individuals has expanded [7]. A few examinations around the globe reveal that if biodiesel energy is utilized instead of petroleum products, there will be a net

decrease in CO outflows and CO<sub>2</sub> emanation [8]. SO<sub>2</sub> discharges from utilizing biodiesel energy will in general be extensively lower on the grounds that important plants and trees contain just low amounts of sulfur, measured with the significantly higher outflows from coal-based fuel [9–11].

## 2. Experimental with Loading Unit and Fuel Measurement Setup

Experiments have been performed inside the laboratory. A 5horsepower 4-S direct injection C.I engine was opted to analyze the performance and emission aspect [12]. The mass flow with the sensor quantified the airflow rate into the engine, and the burette method quantified the gasoline consumption [13]. Loading became carried out on the C.I engine with the use of a modern-day dynamometer. The test was achieved at special masses [14]. All through the investigation, diverse sensors were utilized to accumulate, save, and analyze the facts by using an automated statistics





FIGURE 1: Experimental setup.



FIGURE 2: Loading unit.

acquisition machine [15] as shown in Figure 1. The titanium dioxide nano-additives (20 ppm) is blended with jatropha methyl ester and mahua methyl ester with the aid of an ultrasonicator.  $\text{TiO}_2$  has the property of reducing harmful emission gases. The  $\text{TiO}_2$  nanoparticle addition reduces emissions and improves the performance of the CI engine.

**2.1. Loading Unit.** The eddy-current dynamometer's theory is based on eddy-current (Fleming's Law of Right Hand). The construction of an eddy-current electro brake as shown in Figure 2 has a notched disc (rotor) that is driven by a prime mover (such as an engine), and magnetic poles (stators) are located outside of it with a gap. The coil that excites the magnetic pole is wound in the circumferential direction.

**2.2. Fuel Measurements.** The measurement of fuel in this Kirloskar engine is manual. The fuel consumption is measured manually with the help of a burette and a stopwatch. The time taken by the engine to consume 10 cc of diesel is noted with the help of a stopwatch. The burette has the marking of cubic cm of fuel in it. Figure 3 shows the fuel burette mounted in the engine. The amount of fuel consumed by the engine is calculated manually in this manner.

### 3. Results and Discussion

The major parameters such as brake thermal efficiency (BTE) and specific fuel consumption (SFC) are evaluated for B20 (JME15MME5, JME10MME10, and JME5MME15).

**3.1. BTE for Various Blends.** The variation of BTE with load% for various blend mixes is shown in Figure 4. The BTE of



FIGURE 3: Fuel measurement.

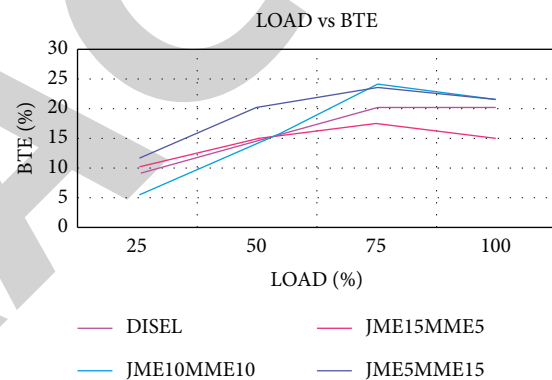


FIGURE 4: Variation of BTE with different load.

biodiesel is more than in contrast with diesel, particularly in full load conditions [15]. From the graph, it is clearly understandable that the BTE has expanded with an increase in the blend proportion of mahua methyl ester (MME) biodiesel [16, 17]. The BTE of blended mixes like JME15MME5, JME10MME10, and JME5MME15 at full load conditions are 22%, 23%, and 25%, slightly higher than diesel's 18%.

**3.2. Specific Fuel Consumption for Various Blends.** The variety of BSFC with percentage loads is shown in Figure 5. As the load expands the brake-specific fuel consumption decreases for the dual biodiesel blended mixes [18]. The maximum full load conditions in (compression ratio 17.5: 1), the estimation of the BSF utilization of blended mixes proportion B20 in JME15MME5, JME10MME10, and JME5MME15 estimated to be 0.51, 0.53, and 0.43 kg/kW·h though diesel has 0.48 kg/kW·h [19].

**3.3. Emission Characteristics-CO for Different Blend.** The variety of CO with % of the load is shown in Figure 6. It was seen that as the load increases, the CO also increases. The carbon monoxide of hybrid biodiesel blended mixes of

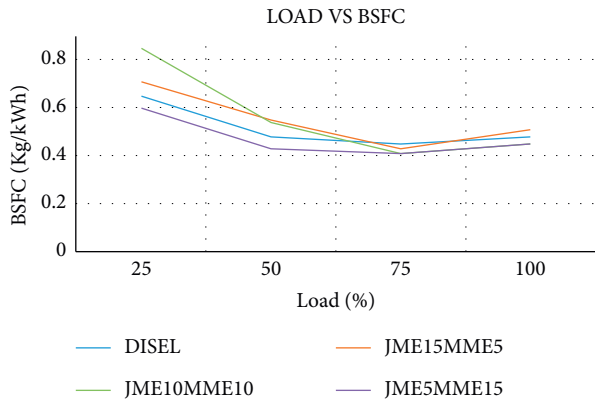


FIGURE 5: BSFC vs. load.

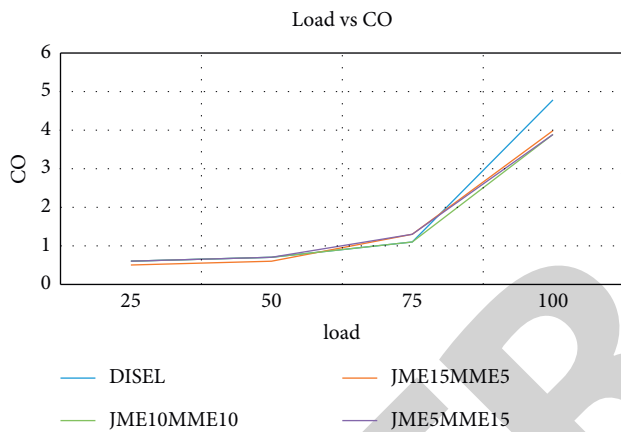


FIGURE 6: Variation of carbon monoxide by load.

proportion B20 (JME15MME5, JME10MME10, and JME5MME15) diminishes once contrasted with diesel at a pressure ratio of 17.5 to 100% load condition; the estimation of CO of blend proportion B20 in JME15MME5 remains at 4.0%, JME10MME10 is at 3.9%, and JME5MME15 is at 3.9%, while diesel consumes a maximum of 4.8% [19].

**3.4. Hydro Carbons for Various Blends.** The hydrocarbons with % loads are appeared in Figure 7. The result observed as the load raises, the hydrocarbon also increases. The hydrocarbon of dual biodiesel blended mixes ratio B20 (for example, JME15MME5, JME10MME10, and JME5MME15) decreases when compared with diesel during full load conditions in pressure ratio 17.5; the estimation of HC of blended mixes proportion B20 in JME15MME5 is 410 ppm, JME10MME10 is 420 ppm, and JME5MME15 is 400 ppm, while diesel has 470 ppm. The emissions consumed decreased by 15.6% with B20 compared with diesel at full load condition.

**3.5. Carbon Dioxide for Various Blends.** The variety of carbon dioxide (CO<sub>2</sub>) with rate load is shown in Figure 8. From the plot, it was seen that as the heap increased, the carbon

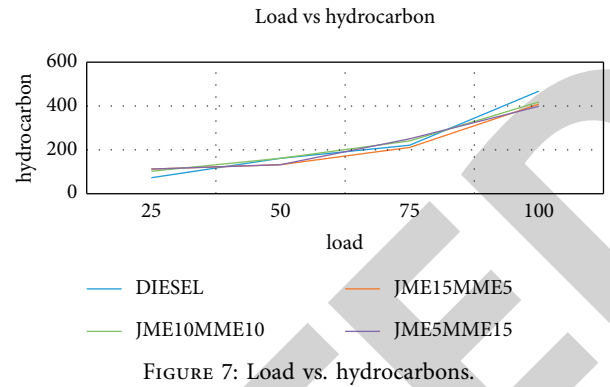


FIGURE 7: Load vs. hydrocarbons.

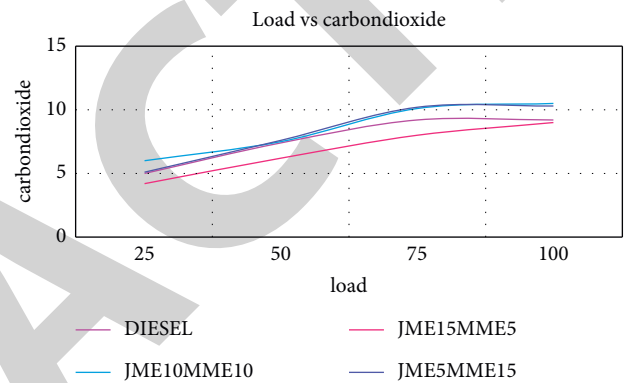


FIGURE 8: Load vs. CO<sub>2</sub>.

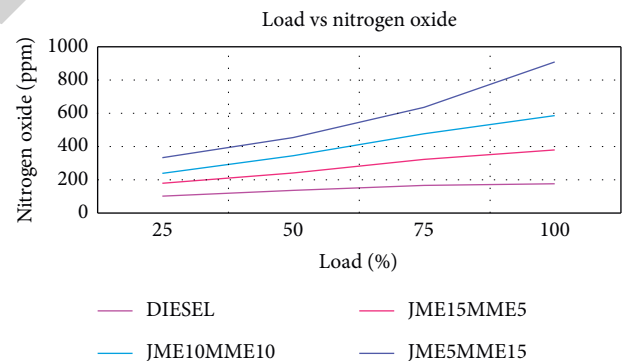


FIGURE 9: Emission of nitrogen oxides at various load.

dioxide expanded. The CO<sub>2</sub> of the dual biodiesel blended mixes B20 (for example, JME15MME5, JME10MME10, and JME5MME15) at full load is 9, 10.5, and 10.3 ppm, respectively, which is diminished when contrasted with the diesel during full load conditions. As a product of combustion, CO<sub>2</sub> is formed once there is an essential measure of O<sub>2</sub> present during the formation of CO.

**3.6. Nitrogen Oxides for Various Blends.** The impact load on NOx is shown in the Figure 9. The nitrogen oxides expanded during fuel load conditions for individually blended mixes of proportion B20 (for example, JME15MME5,

JME10MME10, and JME5MME15). For the pressure ratio 17.5 (CR 17.5:1) in the most extreme full load conditions, blended mix proportion JME15MME5 gives 205 ppm while diesel gives 170 ppm, JME10MME10 gives 208 ppm, and JME5MME15 gives 325 ppm at a similar full load condition. From the consequences, nitrogen oxide discharge is more for dual biodiesel blended mixes proportion than diesel. Nonetheless, the nonedible oil-based biodiesel contains an essential amount of nitrogen, which contributes to NO<sub>x</sub> emissions.

#### 4. Conclusions

This investigation gives measurable information about the advent of engines with dual biodiesel. The evaluation summarizes the record base for bio-diesel are as follows:

- (i) For minimum load conditions, the JME10MME10 biofuel blend gives better brake thermal efficiency compared to other blends. For maximum load conditions JME5MME15 provides better brake thermal efficiency than other blends.
- (ii) Brake-specific fuel consumption is minimum for JME5MME15 at minimum load conditions compared to other blends. Brake-specific fuel consumption is the minimum for JME5MME15 at maximum fuel load condition compared to different blends.
- (iii) Carbon monoxide is the minimum for JME15MME5 at 25% load conditions compared to other blends. Carbon monoxide is the minimum for JME10MME10 at 100% load conditions. Carbon dioxide emissions are at a minimum for JME15MME5 at full load conditions.
- (iv) Nitrogen oxide is the minimum for JME15MME5 at full load condition.
- (v) In the future, various types of additives can be added to different types of biodiesels and can be optimized for better performance.

#### Data Availability

The data used to support the findings of this study are available from the corresponding author upon request.

#### Conflicts of Interest

The authors declare that there are no conflicts of interest.

#### Acknowledgments

The authors appreciate the supports from the Arba Minch University, Ethiopia for the research and preparation of the manuscript. The authors thank to VELS Institute of Science, Technology & Advanced Studies, GLA University for providing assistance to this work.

#### References

- [1] L. Li, J. Wang, Z. Wang, and J. Xiao, "Combustion and emission characteristics of diesel engine fueled with diesel/biodiesel/pentanol fuel blends," *Fuel*, vol. 156, pp. 211–218, 2015.
- [2] A. Z. Maftuchah, A. Zainudin, A. Winaya, and Y. Rahmadesi, "Biodiesel generated from Jatropha (*Jatropha curcas* Linn.) seeds selected based on various genotypes crossbred," *Energy Reports*, vol. 6, no. Supplement 8, pp. 345–350, 2020.
- [3] W. Tutak, K. Lukács, S. Szwaja, and Á. Bereczky, "Alcohol-diesel fuel combustion in the compression ignition engine," *Fuel*, vol. 154, pp. 196–206, 2015.
- [4] H. K. Imdadul, H. H. Masjuki, M. A. Kalam et al., "Higher alcohol-biodiesel-diesel blends: an approach for improving the performance, emission, and combustion of a light-duty diesel engine," *Energy Conversion and Management*, vol. 111, pp. 174–185, 2016.
- [5] M. Qasim, T. M. Ansari, and M. Hussain, "Combustion, performance, and emission evaluation of a diesel engine with biodiesel like fuel blends derived from a mixture of Pakistani waste canola and waste transformer oils," *Energies*, vol. 10, no. 7, p. 1023, 2017.
- [6] M. Vinayagam, S. S. Kumar, M. M. Ravikumar, S. Mahendiran, and T. Raja, "Feasibility and emission study on employing MgO nanoparticle as oxygenated additive in neat biodiesel," *International Journal of Ambient Energy*, vol. 42, no. 14, pp. 1629–1634, 2021.
- [7] M. Canakci, "Combustion characteristics of a turbocharged DI compression ignition engine fueled with petroleum diesel fuels and biodiesel," *Bioresource Technology*, vol. 98, no. 6, pp. 1167–1175, 2007.
- [8] K. Rajan, M. Rajaram Narayanan, S. Suresh Kumar, R. Mohanavel, and V. Mohanavel, "A detailed study on improving the properties and performance aspects of biodiesel," *International Journal of Ambient Energy*, vol. 43, no. 1, pp. 1949–1953, 2022.
- [9] N. Usta, E. Öztürk, Ö. Can et al., "Combustion of biodiesel fuel produced from hazelnut soapstock/waste sunflower oil mixture in a Diesel engine," *Energy Conversion and Management*, vol. 46, no. 5, pp. 741–755, 2005.
- [10] S. A. Basha, K. R. Gopal, and S. Jebaraj, "A review on biodiesel production, combustion, emissions and performance," *Renewable and Sustainable Energy Reviews*, vol. 13, no. 6-7, pp. 1628–1634, 2009.
- [11] K. Pradeep, "Vehicle emissions from biodiesel and its blends – a review," *International Journal of Research in Biochemical Process Engineering - IJRBP*, vol. 1, p. 1, 2012.
- [12] S. K. Jain, S. Kumar, and A. Chaube, "Technical sustainability of biodiesel and its blends with diesel in C.I. Engines: a review," *International Journal of Chemical Engineering and Applications*, vol. 2, no. 2, pp. 101–109, 2011.
- [13] M. Selvamuthukumar, B. Harish babu, S. bobba, and N. BaskarJoy, "Investigation on the lubricating behavior of cashew nut shell liquid oil as a renewable and reliable petrochemical product," *Materials Today Proceedings*, vol. 44, no. 2021, pp. 3583–3588, 2021.
- [14] L. Karikalan, M. Chandrasekaran, S. Venugopal, S. Jacob, and S. Baskar, "Investigations on diesel engine characteristics with Pongamia biodiesel at dissimilar compression ratios," *International Journal of Ambient Energy*, vol. 42, no. 9, pp. 1005–1008, 2021.
- [15] V. S. Shaisundaram, M. Chandrasekaran, R. Muraliraja, M. ShanmugamShanmugam, S. Baskar, and A. Bhuvendran,

## *Retraction*

# **Retracted: Image-Based Precision Measurement Technology for the Quality Inspection of Crane Boom Materials**

### **Advances in Materials Science and Engineering**

Received 26 December 2023; Accepted 26 December 2023; Published 29 December 2023

Copyright © 2023 Advances in Materials Science and Engineering. This is an open access article distributed under the Creative Commons Attribution License, which permits unrestricted use, distribution, and reproduction in any medium, provided the original work is properly cited.

This article has been retracted by Hindawi, as publisher, following an investigation undertaken by the publisher [1]. This investigation has uncovered evidence of systematic manipulation of the publication and peer-review process. We cannot, therefore, vouch for the reliability or integrity of this article.

Please note that this notice is intended solely to alert readers that the peer-review process of this article has been compromised.

Wiley and Hindawi regret that the usual quality checks did not identify these issues before publication and have since put additional measures in place to safeguard research integrity.

We wish to credit our Research Integrity and Research Publishing teams and anonymous and named external researchers and research integrity experts for contributing to this investigation.

The corresponding author, as the representative of all authors, has been given the opportunity to register their agreement or disagreement to this retraction. We have kept a record of any response received.

### **References**

- [1] H. Liu, W. Tan, S. Cao, and H. Li, "Image-Based Precision Measurement Technology for the Quality Inspection of Crane Boom Materials," *Advances in Materials Science and Engineering*, vol. 2022, Article ID 8379621, 13 pages, 2022.

## Research Article

# Image-Based Precision Measurement Technology for the Quality Inspection of Crane Boom Materials

Honghua Liu, Wenping Tan , Shen Cao, and Hongmei Li

*College of Information and Mechatronics Engineering, Hunan International Economics University, Changsha 410205, Hunan, China*

Correspondence should be addressed to Wenping Tan; [tanwenp2004@163.com](mailto:tanwenp2004@163.com)

Received 7 July 2022; Revised 16 August 2022; Accepted 6 September 2022; Published 27 September 2022

Academic Editor: K. Raja

Copyright © 2022 Honghua Liu et al. This is an open access article distributed under the Creative Commons Attribution License, which permits unrestricted use, distribution, and reproduction in any medium, provided the original work is properly cited.

With the slow rise of the construction industry, cranes, as indispensable mechanical equipment in construction projects, are widely used in the lifting and handling of specific space ranges of construction projects. The quality of crane booms is particularly important for safety. This paper uses image measurement methods including filter processing, mean filtering, and Gaussian filtering to detect the quality of the crane boom material. The image is processed by the wavelet transform and Fourier transform. The grayscale transformation stretching method is applied to the surface image analysis of the boom material to obtain the final inspection. The research results show that the use of image measurement methods can effectively measure the thickness of the crane boom material, the geometric information of the boom material, and the surface roughness of the material and obtain effective image information. The detection accuracy reaches 98.1%. The error can be controlled better. The inspection and research on the quality of crane jib materials can ensure the quality and performance of crane jib materials, reduce the potential safety hazards of cranes during operation, and improve safety. This article organically combines workpiece surface roughness detection with digital image processing technology to preprocess the surface picture of the arm tube material. On this basis, the texture features in the image are extracted and programmed to calculate, and the final workpiece is obtained by the surface roughness value, which proves the feasibility of this method. The research results have very important practical significance for the detection of the quality of the arm tube material and the improvement of the quality level of the arm tube material.

## 1. Introduction

With the development of large-scale production of machinery industrialization, people's requirements and industrial demands have put forward higher standards for the accuracy of products and the quality of materials. Because the detection accuracy, detection speed, quality, and other aspects of contact measuring instruments need to be improved, the noncontact nondestructive testing technology is promoted. Among the detection methods, digital image processing technology belongs to noncontact detection technology, so it is also nondestructive detection technology. It has important prospects in the development of machinery industry. In the machinery industry, surface roughness is

used to evaluate the microscopic geometric characteristics of the workpiece surface after processing. It is a very important index in mechanical processing and it is also used to characterize the surface quality of the workpiece. In the field of industrial production, especially in various manufacturing industries, such as ultraprecision machinery, instrumentation and rolling bearings, the theory, technology, and methods of surface roughness detection of workpieces have also received extensive attention in the research field. The key technologies such as collecting, processing, filtering, and random measurement of free-form surface measurement of the original data of parts and components have been studied systematically and in depth. In the early days of cloud computing, it was simply distributed computing that solved

task distribution and performed merging of computational results. Thus, cloud computing is also known as grid computing.

The surface roughness of mechanical parts is also called the surface finish of the workpiece. It is used to evaluate the machined surface and is a common parameter for various tiny machining traces. In the process of forming parts, the size and shape of the parts belong to the macrosize, while the small unevenness of the image surface belongs to the microgeometric characteristics. This processing trace is called the microgeometric shape error. In the field of mechanical development, surface roughness measurement is a precise and high-precision detection technology, which is the basis and prerequisite for the development of the machinery industry at this stage. From the perspective of the machining and development direction of the machinery industry, the improvement of machining accuracy is closely related to surface quality inspection technology. The inspection accuracy and efficiency of surface quality can affect the level of processing technology in a large way. To ensure the clarity of image magnification, a microscope was used here for image observation.

High-precision mass measurement is very important for precise motion control of cranes. Li et al. [1] considered the uncertain factors in the optimization design of crawler crane truss boom and solved the reliability-based design optimization (RBDO) problem involving discrete design variables and multiple working condition constraints. In the optimization model, the uncertainty of material properties, geometric parameters, and loads are represented by random variables. The geometric dimensions, the reliability index of the performance function, and the minimum weight of the truss arm are, respectively, defined as random design variables, probability constraints, and objective functions. Combining the reliability analysis method based on the response surface method (RSM) with the multi-island genetic algorithm (MIGA), an efficient reliability-based lattice boom design optimization process was developed under typical constrained conditions. Several verification cases are given to prove the effectiveness of the optimization results. The results show that the reliability-based design optimization method can not only meet the reliability constraints of the lattice arm but also ensure the reliability of the structure [1]. Trevino et al. [2] provide additional important considerations for tower crane allocation issues. The main contribution of their work to the knowledge system is to model the relationship between the tower crane's load capacity and its associated costs. However, in these models, the authors unfortunately incorporated some shortcomings into their new model without any modification [2]. Yao et al. [3] established the differential equation of  $n$ -th order section telescopic boom based on the continuous beam-column theory. The recursive formula for the stability of the  $n$ -th order telescopic boom is derived by mathematical induction. The numerical optimization algorithm combined with mechanical characteristics is used to solve the transcendental equation in the recursive formula and to determine the equation when  $n$  is unknown. The obtained length coefficient is compared

with the length coefficient calculated by Chinese national standard GB3811-2008 and ANSYS 17.0. The results show that the accuracy of the Levenberg–Marquardt algorithm is better than other algorithms. Moreover, the obtained length coefficient shows a certain degree of nonlinearity. Therefore, linear interpolation is feasible in small-scale practical applications. The use of linear interpolation leads to a large error in the  $n$ -stage critical force of the all-terrain crane [3]. Sun et al. [4] proposed a high-precision calibration method. Instead of using a large 3D pattern, he uses a small flat pattern and a precalibrated matrix camera to obtain a large number of appropriately distributed points, which will ensure the accuracy of the calibration results. The matrix camera eliminates the need for precise adjustment and movement and can easily connect the line scan camera with the world, both of which enhance the flexibility of the measurement field. This method has been verified by experiments. Experimental results show that the proposed method provides a practical solution for calibrating the line scan camera for accurate measurement [4]. In the image measurement method, Zemmann et al.'s [5] spectral shape of 32P has been carefully remeasured in the magnetic intermediate image spectrometer. The source is produced in a mass separator to improve source quality and remove 33P. The interference effects that may be caused by non-ideal magnetic fields and various baffles, sources, and source supports are measured, and upper limits are set for various effects. An improved light source holder with little scattering and an improved scintillation detector with a background elimination function are used. Small corrections were made to the limited resolution and backscatter from the scintillator and source foil. Contrary to many published results, he obtained the shape factor coefficients, that is, the statistical spectrum shape and the error comes from the estimation of possible but undetected interference effects [5]. Yuan and Huang [6] proposed an angle measurement algorithm. By analyzing the characteristics of the edge of the raster image, a fast method of using three gradient points to establish a parabolic function is applied to the automatic detection of the subpixel edge of the raster image, and the coarse code decoding is improved to reduce the bit error rate (BER) and manufacturing difficulty. A high-precision subdivision method based on the grating line observation image is introduced to calculate the subdivision angle. Second, BER simulation and accuracy analysis show that the algorithm has robustness, reliability, and accuracy in both the coarse code decoding and subdivision processes [6]. Jing et al. [7] proposed a high-precision and stable mover position detection method based on time image correlation and fence image. First, the linear motor positioning system is used to record the sequence of fence images with mover position information, and the integer pixel displacement of each image is obtained through the image correlation method. Then, according to the continuity of the motion, the subpixel displacement can be extracted by fitting the integer pixel displacement. Finally, the displacement and velocity curves can be calculated according to the system calibration. Compared with the digital image



measurement used for linear motor position detection, this method can accurately detect the position of the mover, the measurement range is longer, and the uncertainty is smaller. The moving least squares (MLS) algorithm is used to ensure the stability of measurement uncertainty in different motion modes [7].

The innovation of this paper is that the image-based measurement technology uses the wavelet transform profilometry of the Morlet wavelet to obtain the phase value of the moiré image. By analyzing the advantages and disadvantages of the point-by-point unwrapping algorithm, the branch-and-cut method, and the quality map-guided method, the branch-and-cut method is finally decided as the unwrapping algorithm for the truncated phase. Finally, it is improved on the basis of the Gaussian low-pass filter, and the reconstructed material surface is analyzed, which can effectively reduce the surface error of the arm tube material caused by the reconstruction algorithm and improve the accuracy of detection. It can be seen that the method of digital analysis of material surface map in this paper has higher accuracy, faster computing speed, and lower requirement for experimental equipment compared with the traditional method.

## 2. Detection Method of Crane Boom Material Quality Based on Image-Based Precision Measurement

**2.1. Image Preprocessing.** In the process of computer processing images, the process of image denoising, filtering, segmentation, etc., is called image preprocessing [8, 9]. The principle of intelligent image processing is shown in Figure 1. It can clear the picture, remove the interference information in the picture, make the computer get the purpose information more clearly, and enhance the required information in the picture, and then segment the image, as well as various processing such as image enhancement and image extraction [10, 11].

First, we determine whether there is a first distribution label-matching initial saliency evaluation in the previously acquired scene image; if so, we determine an auxiliary saliency evaluation for determining whether a target face is an abnormal target face by the first distribution label-matching initial saliency evaluation previously acquired and said saliency evaluation, determining whether said target face is an abnormal target face by said auxiliary saliency evaluation, and tagging the auxiliary saliency evaluation to said scene image as a first distribution label-matching initial saliency evaluation when the target face is not an abnormal target face.

In the actual operation process, image preprocessing is essential, but before preprocessing, the image is generally grayed out first, and then, the analysis calculation is started. For color images, grayscale images contain less information, are clearer, and are more convenient to process and extract the required information. In the process of computer processing, there are generally four methods to convert it into grayscale images [12].

**2.1.1. Component Method.** In the internal practice of image processing, it is necessary to select the gray value from the three colors of the color image, use the brightness of the three components as three gray levels, and then select the gray level according to the needs of the calculation itself to generate gray degree image.

$$\begin{aligned} K_1(s, t) &= R(s, t), \\ K_2(s, t) &= G(s, t), \\ K_3(s, t) &= B(s, t). \end{aligned} \quad (1)$$

The function  $K_x(s, t)$  ( $x = 1, 2, 3$ ) can be regarded as the gray value of each pixel after grayscale processing.

**2.1.2. Maximum Method.** The maximum value method is in the internal practice of image processing, and the gray value is selected as the gray value of the three colors with the highest brightness.

$$K(s, t) = \max(R(s, t), G(s, t), B(s, t)). \quad (2)$$

**2.1.3. Average Method.** When the image is grayed out, the gray value is the average of the three brightness values in the original image. This method can be called the average value method.

$$K(s, t) = (R(s, t), G(s, t), B(s, t))/3. \quad (3)$$

**2.1.4. Weighted Average Method.** In real life, the most sensitive eye color of the human eye is green and the least sensitive is blue. The three components are added with different weights and the weights are averaged.

$$K(s, t) = 0.5 * R(s, t), 0.58 * G(s, t), 0.16 * B(s, t). \quad (4)$$

**2.2. Image Noise Reduction.** In the process of image processing, due to many reasons, the image contains noise. Whether it is internal or external noise, it needs to be filtered to reduce noise to improve image quality [13, 14], and in the actual noise reduction process. In this case, it may cause the image to be blurred, so the image target information is more unclear and the image quality is reduced. Of course, for some filtering methods, the phenomenon of image blur will not appear, so different filtering processing should be carried out for different images [15, 16].

The image sampling process often determines the image quality. The image sampling process will affect the image quality not only because of the external environment such as temperature and dust but also because of the transmission mode, the compression mode, and transmission medium of the image during transmission, so as to hinder the machine or people from obtaining the target information [17, 18]. Due to the interference of noise, images often have problems such as image blur, image degradation, and unclear image features, which cause great trouble to analyze images, and low-quality images are difficult to meet people's



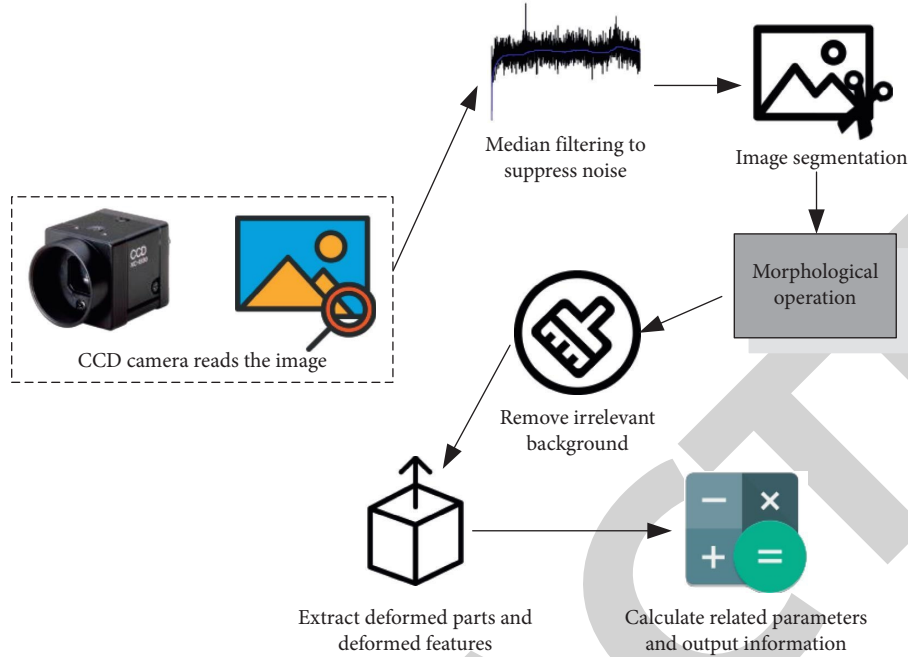


FIGURE 1: Principle of the intelligent image processing method.

requirements [19, 20]. In the target identification and tracking of images, such images are also very difficult [21]. In real life, it is very important to suppress all kinds of noise signals that degrade the image, enhance the favorable information in the image, and process and correct the detected different images under the same constraint [22, 23].

**2.2.1. Filter Processing.** In the analysis and calculation, there is a distinction between the spatial domain and the frequency domain. To enhance the quality of the image in the spatial domain, it is necessary to perform image processing on the image [24, 25]. The essence of image processing is to calculate and analyze each pixel in the image. In the calculation and analysis of pixels, the calculation and analysis of a single pixel is a point operation and the calculation and analysis of the pixels in the entire template is a block operation [26, 27]. In actual operation, point operations can be performed, pixels can be separated and unrelated, and block operations can be performed. When each block is calculated and analyzed, it is unrelated to other pixels [28]. By operating on the pixels, you can change the contrast and grayscale distribution of the picture. If you are processing images, if you need to perform grayscale transformation, histogram correction, and grayscale adjustment, you can choose point operation. If you need to smooth and sharpen the picture, you can perform block operations and it can also smooth the outline of the image. There are many methods for image smoothing; the most commonly used is the median and mean filtering methods, and of course, there are many other methods [29, 30].

The median filter can be expressed by formula (5):

$$D(i, j) = \text{median}\{f(i - a, j - b)\} (i, j) \in w, \quad (5)$$

where  $D(i, j)$  is the pixel gray value of the image output,  $f(i - a, j - b)$  is the pixel gray value of the image input, and the template window  $w$ . In the process of calculation and analysis, the median filter also needs a template to calculate and analyze the image. The shape of the template can also be various, such as a circle, a cross, and a square.

**2.2.2. Mean Filtering.** Mean filtering is also called neighborhood averaging, which is replaced by the average value of all pixels in a template placed on a single pixel. In the actual operation of image processing, mean filtering is often used in image processing. It can not only reduce noise but also improve image quality. Mean filtering is also divided into many kinds of filters for selection. In actual operation, when selecting various mean filters, they should also be selected according to the conditions of the image itself, so as to better achieve the desired effect.

**2.2.3. Gaussian Filtering.** Gaussian filtering can eliminate the Gaussian noise and can often be used in the process of noise reduction. The formula is as follows:

$$S(i, j) = \frac{1}{2\pi\partial^2} e^{-\frac{(i^2+j^2)}{2\partial^2}}. \quad (6)$$

In actual application, the formula can be transformed as follows:

$$S(a, b) = \frac{1}{2\pi\partial^2} e^{-\frac{((i-a-1)+(j-a-1))/2\partial^2}}. \quad (7)$$

The parameter  $\partial$  determines the smoothness of the Gaussian filter, so the parameter  $\partial$  is related to the

smoothness of the image. In practical applications, the larger the parameter  $\delta$ , the smoother the image.

**2.2.4. Sharpening Filter.** In digital image processing, all processing techniques are completed around increasing image quality and meeting visual requirements. Therefore, most image processing will remove noise and then improve the image quality, so that the target image is displayed clearly. Here is a filtering method, namely, the Laplacian operator. If an image is  $D(i, j)$ , then the Laplacian change is as follows:

$$\nabla^2 D = \frac{\gamma^2 D}{\gamma i^2} + \frac{\gamma^2 D}{\gamma i^2}. \quad (8)$$

Formula (8) can be defined as follows:

$$\frac{\gamma^2 D}{\gamma i^2} = d(i+1, j) + D(i-1, j) - 2D(i, j), \quad (9)$$

$$\frac{\gamma^2 D}{\gamma j^2} = d(i, j+1) + D(i, j+1) - 2D(i, j). \quad (10)$$

It can be seen from formula (10) that Laplace transform also belongs to a kind of linear transform. The Laplace transform is also divided into different transformation methods, which can be divided into discrete and nondiscrete methods. Different processing methods will make the noise of the images different, and there may be no way to use the software to analyze the images with different noise, and the results of the arm tube quality inspection will be affected. The transformation formula for discrete methods is shown in formula (11):

$$\nabla^2 D = D(i+1, j) + D(i-1, j) + D(i, j+1) + D(i, j-1) - 4D(i, j). \quad (11)$$

Image detection is also sometimes used to retrieve a given sub-image from a known image. In the actual calculation and analysis of digital image technology, the principle of the Laplace transform can be used to calculate and analyze the image, which not only improves the digital image technology but also uses this technology to reduce the noise of the image and improve the quality of the image. After the image is processed by the principle of the Laplace transform, the sharpening effect of the image can be retained and the effect of the image can be more obvious. In the processed image, the background and target of the image can be more contrasted. Therefore, the Laplace transform principle is often used in the preprocessing of the image.

The formula of the Laplace transform is as follows:

$$T(i, j) = D(i, j) - \nabla^2 D(x, y), \quad (12)$$

$$T(i, j) = D(i, j) + \nabla^2 D(x, y). \quad (13)$$

If the central coefficient of the Laplace operator is positive, we use (13) to calculate, and if the central coefficient is negative, we use (12) to calculate.

**2.3. Fourier Profilometry.** The formula of the Fourier profilometry is as follows:

$$A(i, j) = x(i, j) + y(i, j)^e + y^*(i, j)^e, \quad (14)$$

where  $x(i, j)$  is the background light intensity of the picture,  $y(i, j)$  is the image contrast, and the formula is Fourier transformed with  $x$  as a variable,

$$F[A(i, j)] = x(f, j) + y(f - f_0, j) + y^*(f - f_0, j). \quad (15)$$

Among them,  $F[A(i, j)]$ ,  $x(f, j)^e$ ,  $y(f - f_0, j)$ , and  $y^*(f - f_0, j)^e$  are the Fourier spectra of  $A(i, j)$ ,  $x(i, j)^e$ ,  $y(i, j)$ , and  $y^*(i, j)$ , respectively.

$$y(f - f_0, j) + y^*(f - f_0, j) = G(f, j) * F(A(i, j)). \quad (16)$$

Among them,  $G(f, j)$  is the band pass filter.

We use it as an inverse Fourier transforms to get  $2y(i, j)$  and find the phase.

$$\mu(i, j) = \arctan \left[ \frac{\text{Im}(y(i, j))}{\text{Re}(y(i, j))} \right]. \quad (17)$$

Through the above comparative analysis, it is known that phase-shift profiling uses at least three moiré images to solve the phase (there is a fixed phase difference between the two moiré images). Four moiré images resolve the phase of the moiré, so the processing time of the image is relatively long and cannot meet the online detection of the arm tube material. Although the processing accuracy of the Fourier profiling is not as good as phase-shifting profiling, it only needs one moiré image to extract the phase information of the moiré image, so it has a great advantage in processing speed. Therefore, the Fourier profilometry can better meet the speed requirements of online detection systems. The carbon fiber boom achieves a lightweight design for the pump truck boom, allowing the long reach boom to be put into larger scale use.

**2.4. Wavelet Transform Profilometry.** Since the Fourier transform was discovered and used, it has solved many signal processing problems, but it has certain limitations. The wavelet transforms studies the limitations of the Fourier transform. It can provide a window those changes with frequency to analyze the characteristics of certain problems globally or locally. It is an ideal tool for signal processing or image processing. Therefore, wavelet transform has attracted people's attention, and its application range is getting wider and wider. Highly accurate images and phase-shift estimates can be obtained using phase correlation calculation methods to reduce phase errors at low resolutions.

There are many common wavelet basis functions, such as Haar wavelet, Mexican hat wavelet, and Morlet wavelet. They have different characteristics. Therefore, it is particularly important to choose an appropriate wavelet basis function. The letter  $a$  represents the frequency.

2.4.1. *Haar Wavelet.* The mathematician Haar proposed the Haar orthogonal set in 1910, which is defined as follows:

$$\psi_s(a) = \begin{cases} 1 & 0 \leq a \leq \frac{1}{2}, \\ -1 & \frac{1}{2} \leq a \leq 1, \\ 0 & \text{other.} \end{cases} \quad (18)$$

In actual calculations, such as shifting  $t$ , the Haar wavelet is orthogonal, and it can be regarded as a difference operation and in the final result, the wavelet function can give the difference between the parts that is not equal to the observed average value. Since the Haar wavelet has no continuity in the time domain, it will be limited when analyzing actual signals and its performance as a basic wavelet is not good. The grayscale histogram is a function of gray levels, which indicates the number of pixels in an image with a certain gray level.

2.4.2. *Mexican Hat Wavelet.* The Chinese name of Mexican hat wavelet is “Mexico’s straw hat” wavelet, which can also be called the Marr wavelet. The Mexican hat function is the second derivative of the Gauss function, which is defined as follows:

$$\psi(a) = (1 - a^2)e^{-(a^2/2)}. \quad (19)$$

Because it is shaped like a Mexican sombrero in time domain, it is named after it. The Mexican straw hat wavelet function belongs to the second derivative of the Gaussian function, and it has a good localization function in the time domain and frequency domain.

2.4.3. *Morlet Wavelet.*

$$\psi(a) = \frac{1}{\sqrt{\pi t_b}} \exp\left(x2\pi t_b i - \frac{a^2}{t_b}\right), \quad (20)$$

where  $t_c$  represents the center frequency of the wavelet, and  $t_b$  represents the bandwidth parameter. We select specific parameter values according to actual conditions.

The Morlet wavelet is a sine function under Gaussian envelope. As shown in Figure 2, compared with other wavelet bases, the Morlet wavelet is more similar to the projected sine image. At the same time, the Morlet wavelet has relatively better frequency domain analysis ability and phase extraction effect.

### 3. Image-Based Precision Measurement of the Crane Boom Material Quality Inspection Experiment

3.1. *Crane Boom Material Quality Inspection Experiment.* The experimental steps are to obtain the 3D profile of the crane boom material, then collect the grayscale value of the moiré image, and finally perform the grayscale stretch

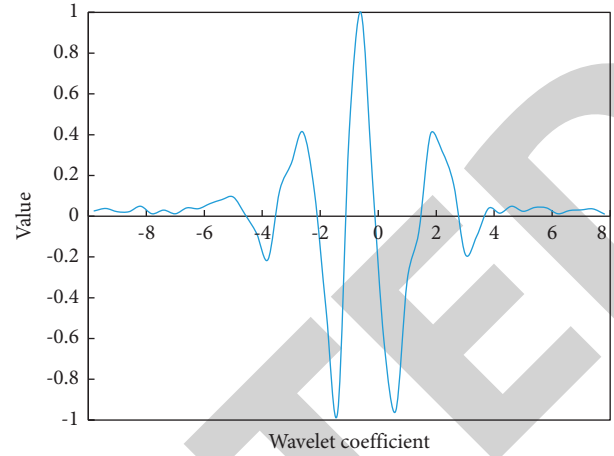


FIGURE 2: Morlet wavelet time-domain waveform.

transformation. The research in this paper is to detect the quality of crane boom materials. The results of this part of the experiment apply to the filtering algorithm mentioned in the previous section. Common crane boom materials are shown in Table 1.

The crane boom is generally made of manganese steel, which is a high-strength steel, resistant to impact, abrasion, and extrusion, and is suitable for use under harsh working conditions. The experimental design of this article is to detect the quality of manganese steel materials, such as surface holes, oil stains, scratches, protrusions, depressions, and deformations. This article uses image detection technology to detect the quality of manganese steel materials for crane booms and reconstruct manganese the three-dimensional shape of the steel material can complete the inspection of the quality of the manganese steel material. The crane manganese steel material detection frame designed in this paper is shown in Figure 3:

Two projectors are controlled by a computer to project sinusoidal images on the upper and lower surfaces of the manganese steel material, and the two area CCD cameras are used to shoot the moiré images on the upper and lower surfaces of the manganese steel material vertically, and then the computer receives the clouds captured by the CCD camera. We pattern the image and then simultaneously realize the reconstruction, storage, and display the three-dimensional information of the manganese steel material. CMOS has multiple charge-voltage converters and row switch control, readout is much faster, and most high-speed cameras above 500fps are CMOS cameras. The main parameters of the equipment are shown in Table 2.

The distance between the area CCD camera and the projector is 250 mm, and the distance between the projector and the reference plane is 500 mm. The length of the actual material represented by the photographed image is 330 mm, so that the resolution of the photographed image can be guaranteed to be 0.1 mm/pixel \* 0.1 mm/pixel.

3.2. *Data Collection.* The image information received by the computer is extracted and processed, and the processed

TABLE 1: Common crane boom materials.

Metallic material	Safety factor	Allowable compressive bending stress	Allowable shear stress	Allowable end face to withstand stress
Q235	1.48	153.2	82.4	242.3
Q345	1.48	174.4	102.5	265.1
20	1.48	116.5	76.8	199.7
45	1.48	188.3	134.6	294.8
40Cr	1.48	268.7	159.9	368.5
20Cr	1.48	330.2	178.7	386.4

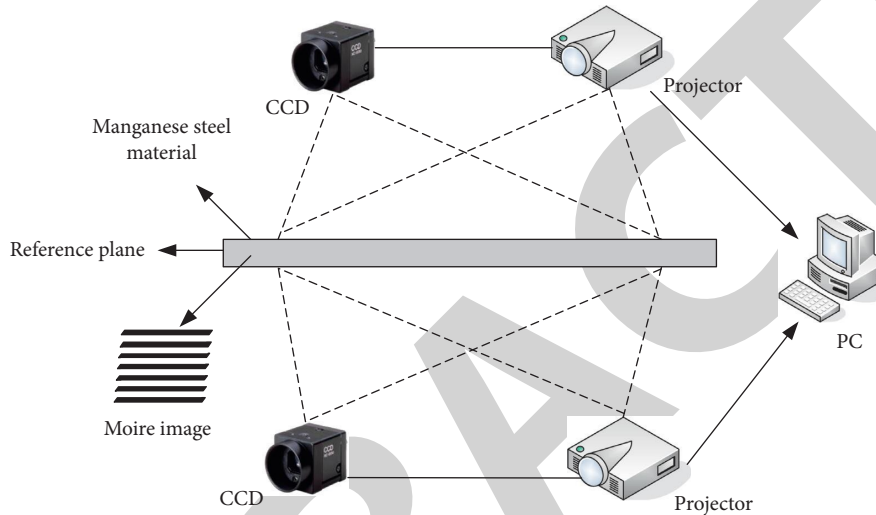


FIGURE 3: Quality inspection of manganese steel material for crane boom.

TABLE 2: Device parameters.

Equipment	Configuration	Resolution	Parameter
PC	Intel i7 quad-core processor	12G memory	64 bit Windows 7 operating system
CCD	Horizontal resolution: 3300 pixel	The vertical resolution is: 2500 pixel	The highest frame rate: 10.3fps
Projector	Standard resolution: 1280 * 800	The highest resolution: 1600 * 1200	Brightness: 3700 lumens

image is studied and analyzed, and the spatial frequency, arithmetic mean and gray standard deviation of the image are used as training parameters. After the preprocessing of the image, the next step is to analyze the image. Only after the image analysis can the information in the image be accurate. In the actual operation, some structures and features of the image are extracted and measured, and then, the required information is obtained to obtain the complete image information parameters.

#### 4. Inspection and Analysis of Crane Boom Material Quality Based on Image-Based Precision Measurement

*4.1. Three-Dimensional Reconstruction Analysis of the Arm Tube Material.* In order to accurately reconstruct the three-dimensional contour of the crane boom material, obtaining

high-quality moiré images is the key to the three-dimensional reconstruction of the boom material. After eliminating the distortion of the CCD camera lens, the moiré image on the surface of the arm barrel material is taken. The obvious sinusoidality of the captured moiré image is an important feature of high-quality moiré images. The gray value comparison result of the collected moiré image is shown in Figure 4.

The standard sinusoidal moiré projected by the digital projector is deformed for the first time after being projected by the projector. At this time, the moiré image will be further distorted. It is taken by the CCD camera (the distortion produced by the lens when the CCD camera is taken has been eliminated by calibration); the moiré image is further deformed, and the gray value of the moiré image finally collected is better.

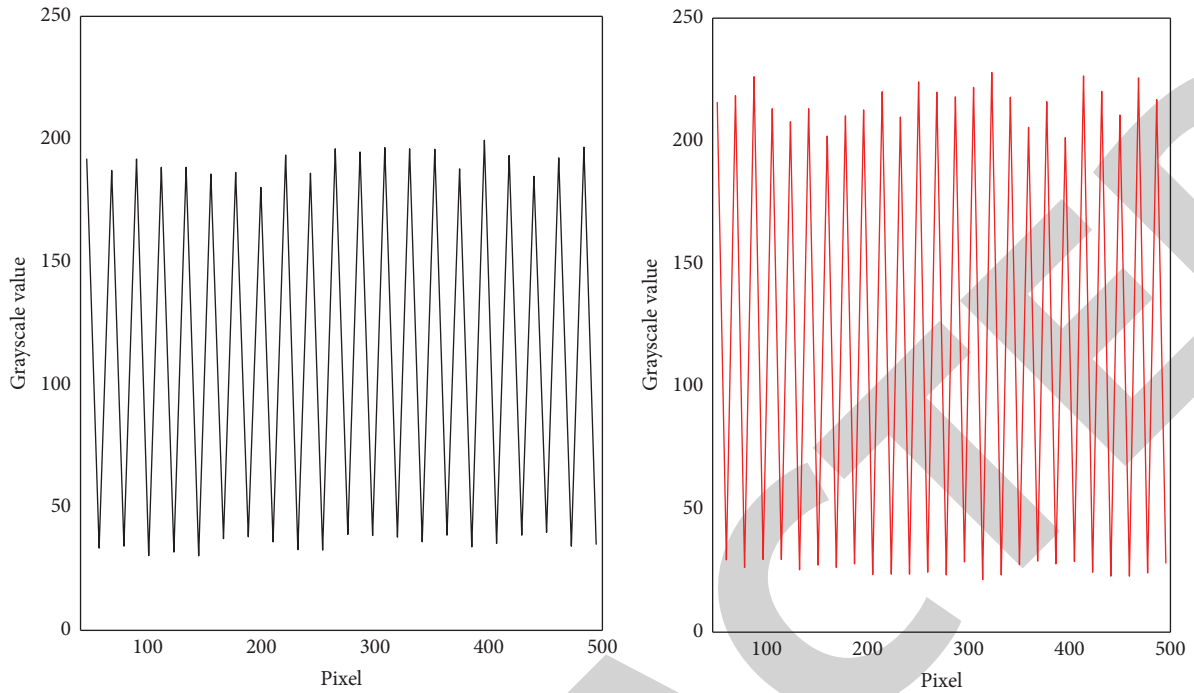


FIGURE 4: Image gray value comparison.

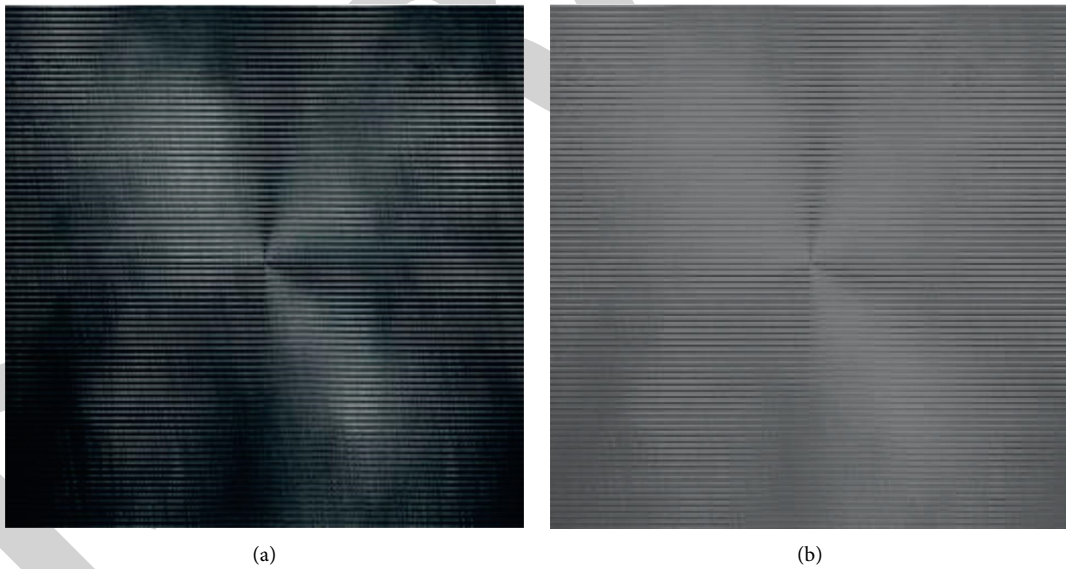


FIGURE 5: Comparison chart of arm tube materials after grayscale transformation. (a) The original image. (b) Grayscale processed image.

Each method can expand some features of the grayscale image, and some features can be reduced, so it is extremely important to choose a suitable method to deal with the surface roughness. In the actual image, there are always some unsatisfactory black or white images, you can use the grayscale transformation stretching to adjust and correct the image, as shown in Figure 5.

In the image processing method, the grayscale transformation is selected to process the image. The essence is the

logarithmic transformation. In the internal calculation process, it is actually the higher compression processing in the image and the lower grayscale stretching processing. Through the grayscale stretching transformation, the low grayscale of the image can be emphasized.

Figure 6 shows the image grayscale transformation histogram of the crane boom material. In combination with Figure 5, it can be seen that the image can be well corrected and adjusted by grayscale stretching.

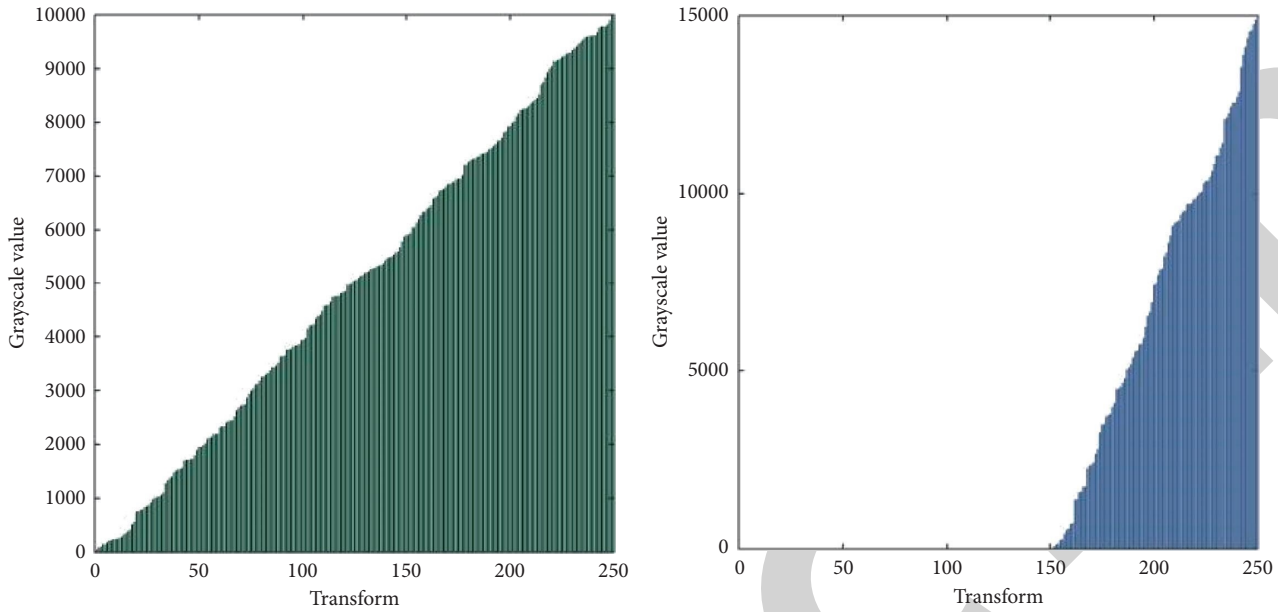


FIGURE 6: Contrast histogram of original image after grayscale transformation.

TABLE 3: Surface defect measurement results.

Moire resolution	Wavelet transform	
	Reconstruction error (mm)	Pixel
4	0.01	100
8	0.01	200
16	0.015	300
32	0.015	400

**4.2. Thickness Measurement Accuracy of the Arm Tube Material.** In order to study the influence of moiré resolution on the accuracy of object reconstruction, different moiré periods are simulated to project the material, and wavelet transform profilometry is used to reconstruct images with different moiré resolutions to analyze the moiré resolution. The influence of rate on the accuracy of object reconstruction. Pixel error, resolution is shown in Table 3:

For the thickness reconstruction error, when the moiré resolution is 4 to 15, the simulation results show that the error is 0.01 mm; when the moiré resolution reaches 16, the simulation error increases to 0.015 mm. It can be seen that blindly increasing the moiré resolution cannot reduce the thickness error. The surface error of the material must be that the higher the resolution of the moiré, the smaller the surface error. Therefore, this paper chooses the image with a moiré resolution of 10 for three-dimensional reconstruction, so that the thickness error is the smallest and the surface error can also be controlled within an appropriate range.

Figure 7 can be obtained by Fourier transform of the cross-section of the boom barrel material in Figure 8. Frequency is low, it can be seen as defects after Fourier transform can only affect the Fourier transform of the zero frequency; therefore, the thickness of the arm cylinder material information and defect information is included in the zero frequency; the pulse error is included in the

fundamental frequency, so as long as through a low-pass filter to filter out the fundamental frequency keep zero frequency, can eliminate the error. Meanwhile, the material thickness information and defect information of the boom barrel are retained.

**4.3. Calculation and Analysis of the Surface Roughness of the Arm Tube Material.** The material surface image is grayscale, and then, through preprocessing, the grayscale distribution of the picture is obtained. According to the grayscale distribution, three sampling lines are drawn randomly on the picture to extract the texture features as shown in Figure 9.

In the gray image, the gray value of the image can reflect the surface condition of the parts according to the optical properties, so the surface roughness value of the workpiece surface can be calculated according to the gray value. Moreover, the gray value in the image can also be used to indicate the degree of undulation of the surface contour of the part, which can be used as the texture feature of the image. In the actual calculation and analysis, according to the traditional surface roughness evaluation parameters, the surface contour line of the simulated surface roughness is calculated as shown in Figure 10.



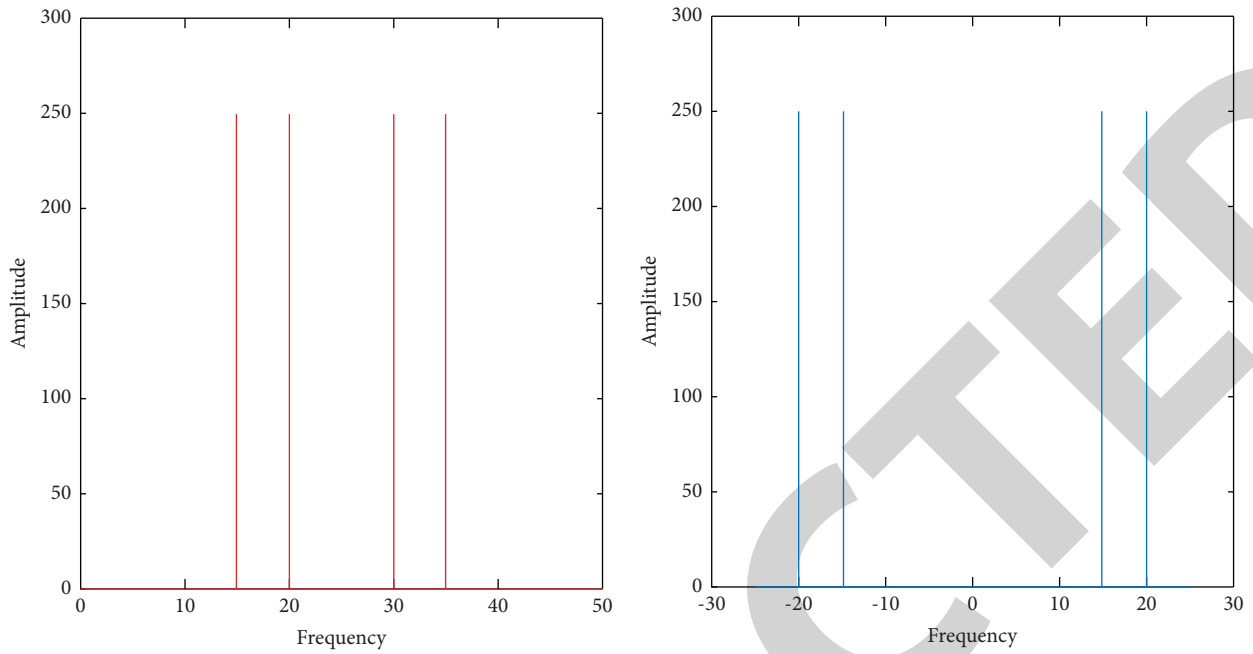


FIGURE 7: Spectrum comparison chart.

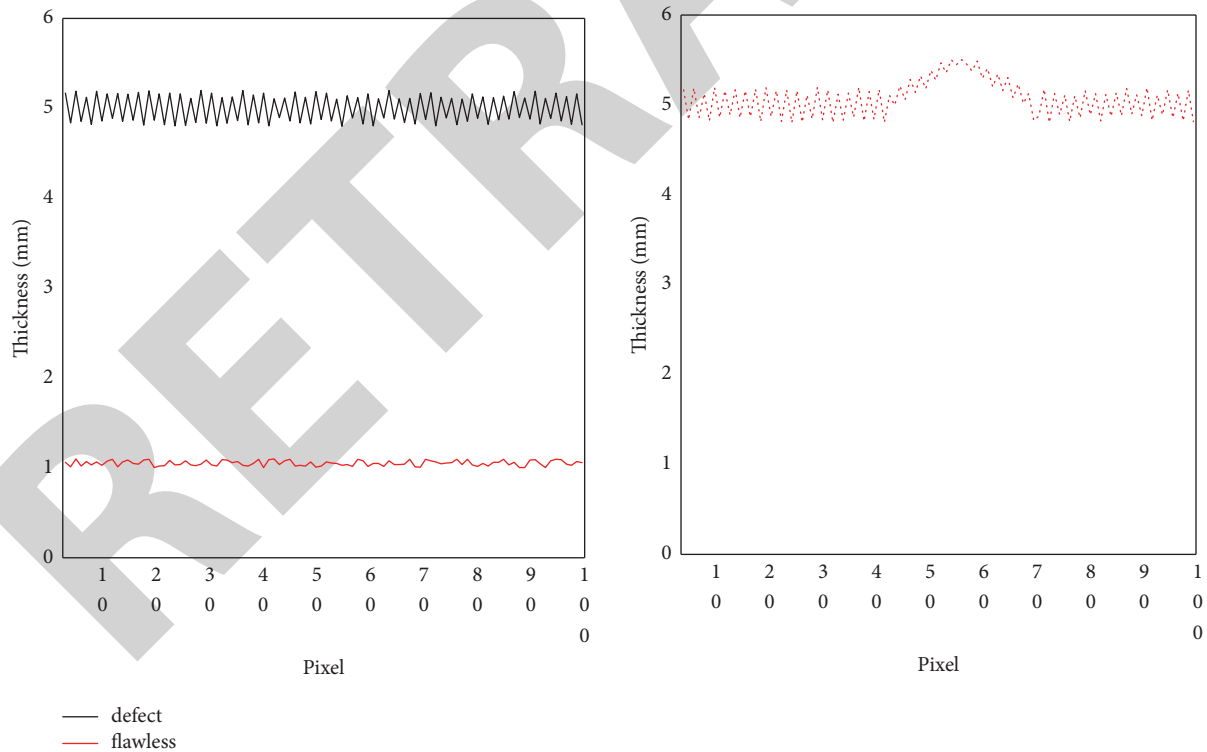


FIGURE 8: Comparison chart of cross-section error of arm tube material.

According to Figure 10, two data lines are taken from the preprocessed picture, and then combined by the gray value to obtain two contour lines, which can be observed through

the two contour lines. The processing traces are the same, and the phase is almost at the same position.

By calculating and analyzing the image data, substituting the data to minimize the variance, the surface roughness of



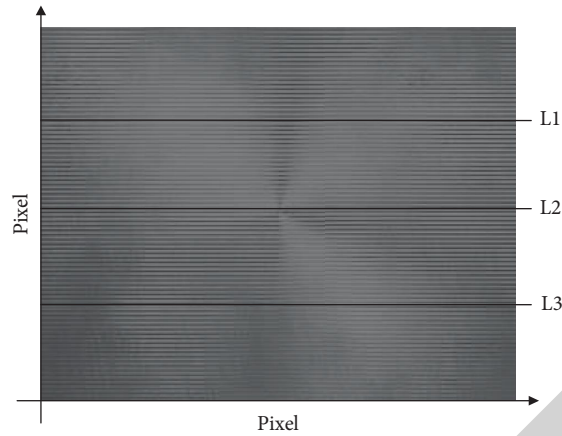


FIGURE 9: Partial enlarged view of the material surface.

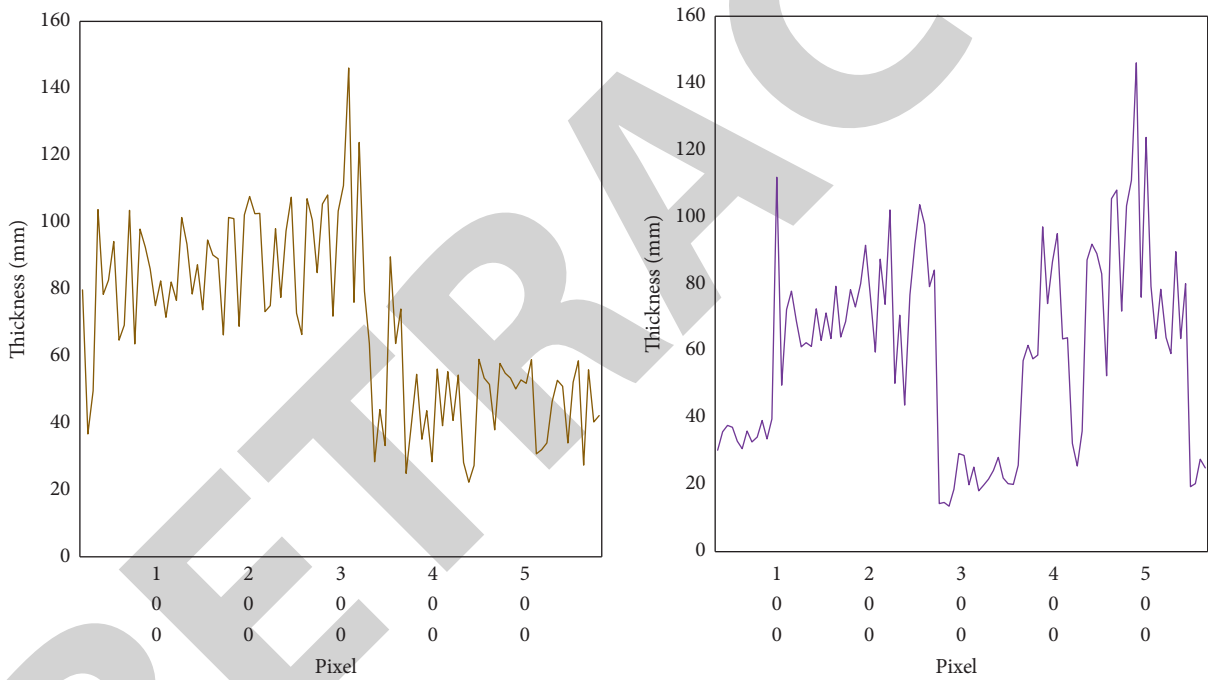


FIGURE 10: Material surface contour.

TABLE 4: Parameter evaluation result.

Parameter evaluation	$R$	$F$	$df1$	$df2$	Significance	Constant	$B1$
Linear	0.951	565.143	1	10	0	-0.131	0.021
Logarithm	0.914	109.477	1	10	0	-1.162	0.312
Index model	0.896	99.12	1	10	0	0.029	0.061

the arm tube material can be calculated. Judging from the evaluation results of the parameters in Table 4, the significance of the linear, logarithmic, and exponential modes is 0,

which has obvious significance. Therefore, the grayscale image can be very suitable for calculating the surface

TABLE 5: Thickness measurement results of two methods.

Material sample	Wavelet transform measurement results	Measurement results of the method in this paper
Area 1	5.98	5.96
Area 2	6.00	6.01
Area 3	5.97	6.00
Area 4	5.98	6.02
Area 5	6.03	6.02
Area 6	6.02	5.94
Area 7	5.96	6.00
Area 8	6.01	6.01

roughness. For example, a very common compression method in AIX is to convert to a.tar compressed format file.

**4.4. Judgment on the Universality of the Appearance Quality Monitoring of Crane Boom Materials.** In order to verify the universality of the method proposed in this paper, a piece of material is evenly divided into 8 different areas for thickness measurement as shown in Table 5. All measurement results are compared with the wavelet transforms measurement results.

Table 5 displays a comparison between the average value of the material thickness measurement results based on the wavelet transform profilometry and the average value of the material thickness results measured by the method in this paper. As shown in the table, the wavelet transform measurements were 5.98 for Area 1, 6.00 for Area 2, 5.97 for Area 3, and 5.98 for Area 4. The unit of the measured results in the table is mm. Therefore, it can be concluded that the measurement accuracy of the material thickness of the method in this paper reaches 98.1%, and it can detect surface defects with a minimum size of 0.3 mm.

## 5. Conclusions

This paper mainly studies the detection technology of crane boom material quality based on image-based precision measurement. The basic image of crane boom material is collected by CCD camera, and the image is preprocessed; then, the image is analyzed to obtain the information in the accurate image. Then, some structures and features of the image are extracted and measured to obtain complete image information parameters. The article analyzes the image preprocessing, introduces the image noise reduction, simplifies the algorithm using Fourier mapping, and conducts experiments. Specific experiments verify the practicability of the method used in this paper, verify the accuracy of the crane boom material quality detection, and verify the universal applicability of the method. The research on the method of measuring the quality of crane boom materials is not only of great significance for improving the appearance quality of materials but also has a certain reference significance for the subsequent noncontact online measurement of the quality of crane boom materials. There are still shortcomings in the research of this paper, such as the image processing problem. After obtaining a high-quality image, it

is necessary to calculate the phase value of the image and the phase of the unfolding truncation, but the calculation result will produce periodic errors. We hope to solve this problem in follow-up research. The features in the images can be developed as criteria in future experiments to better obtain target information for the arm tube material.

## Data Availability

Data sharing is not applicable to this article as no new data were created or analyzed in this study.

## Conflicts of Interest

The authors declare that they have no conflicts of interest.

## Acknowledgments

This work was supported by the scientific research project of Hunan Provincial Department of Education, Project number: 20A287.

## References

- [1] J. Li, L. Bai, W. Gao et al., "Reliability-based design optimization for the lattice boom of crawler crane," *Structures*, vol. 29, no. 2, pp. 1111–1118, 2021.
- [2] C. Trevino and M. Abdel-Raheem, "Discussion of "location optimization of tower crane and allocation of material supply points in a construction site considering operating and rental costs" by zahra sadat moussavi nadoushani, ahmed W. A. Hammad, and ali akbarnezhad," *Journal of Construction Engineering and Management*, vol. 144, no. 11, pp. 070180011–070180013, 2018.
- [3] F. Yao, W. Meng, J. Zhao, Z. She, G. Shi, and H. Liu, "Buckling theoretical analysis on all-terrain crane telescopic boom with n-stepped sections," *Journal of Mechanical Science and Technology*, vol. 32, no. 8, pp. 3637–3644, 2018.
- [4] B. Sun, J. Zhu, L. Yang, S. Yang, and Z. Niu, "Calibration of line-scan cameras for precision measurement," *Applied Optics*, vol. 55, no. 25, pp. 6836–6843, 2016.
- [5] H. Zemann, D. Semrad, and H. Paul, "Precision measurement of the/gb-spectrum shape of 32P," *Nuclear Physics A*, vol. 175, no. 2, pp. 385–395, 1971.
- [6] P. Yuan and D. Huang, "A high-reliable and high-precision algorithm of angle measurement for UAV airborne photo-electrical detection system," *International Journal of Precision Engineering and Manufacturing*, vol. 20, no. 11, pp. 1885–1891, 2019.

## Retraction

# Retracted: Tiny Spherical Robot with a Magnetic Field-Based Interference Detection and Prevention Framework

### Advances in Materials Science and Engineering

Received 20 June 2023; Accepted 20 June 2023; Published 21 June 2023

Copyright © 2023 Advances in Materials Science and Engineering. This is an open access article distributed under the Creative Commons Attribution License, which permits unrestricted use, distribution, and reproduction in any medium, provided the original work is properly cited.

This article has been retracted by Hindawi following an investigation undertaken by the publisher [1]. This investigation has uncovered evidence of one or more of the following indicators of systematic manipulation of the publication process:

- (1) Discrepancies in scope
- (2) Discrepancies in the description of the research reported
- (3) Discrepancies between the availability of data and the research described
- (4) Inappropriate citations
- (5) Incoherent, meaningless and/or irrelevant content included in the article
- (6) Peer-review manipulation

The presence of these indicators undermines our confidence in the integrity of the article's content and we cannot, therefore, vouch for its reliability. Please note that this notice is intended solely to alert readers that the content of this article is unreliable. We have not investigated whether authors were aware of or involved in the systematic manipulation of the publication process.

Wiley and Hindawi regrets that the usual quality checks did not identify these issues before publication and have since put additional measures in place to safeguard research integrity.

We wish to credit our own Research Integrity and Research Publishing teams and anonymous and named external researchers and research integrity experts for contributing to this investigation.



The corresponding author, as the representative of all authors, has been given the opportunity to register their agreement or disagreement to this retraction. We have kept a record of any response received.

### References

- [1] M. R. A. Refaai, S. Meenatchi, B. Ramesh, N. I. H. Rashid, N. B. Soni, and M. Ganesan, "Tiny Spherical Robot with a Magnetic Field-Based Interference Detection and Prevention Framework," *Advances in Materials Science and Engineering*, vol. 2022, Article ID 3908975, 10 pages, 2022.

## Research Article

# Tiny Spherical Robot with a Magnetic Field-Based Interference Detection and Prevention Framework

Mohamad Reda A. Refaai <sup>1</sup>, S. Meenatchi,<sup>2</sup> B. Ramesh,<sup>3</sup> N. I. Haroon Rashid,<sup>4</sup> N. B. Soni,<sup>5</sup> and Manikandan Ganesan <sup>6</sup>

<sup>1</sup>Department of Mechanical Engineering, College of Engineering in Al-Kharj, Prince Sattam bin Abdulaziz University, Al-Kharj 11942, Saudi Arabia

<sup>2</sup>Department of Computer Science and Engineering, Institute Vellore of Technology (VIT), Vellore 632007, Tamil Nadu, India

<sup>3</sup>Department of Mechanical Engineering, Mohamed Sathak Engineering College, Kilakarai 623806, Tamil Nadu, India

<sup>4</sup>Department of Aerospace Engineering, B.S.A.R. Crescent Institute of Science and Technology, Vandalur, Chennai, Tamilnadu, India

<sup>5</sup>Department of Electrical Engineering, University of Petroleum and Energy Studies, Dehradun, Uttarakhand 248007, India

<sup>6</sup>Department of Electromechanical Engineering, Faculty of Manufacturing, Institute of Technology, Hawassa University, Hawassa, Ethiopia

Correspondence should be addressed to Manikandan Ganesan; [mani301090@hu.edu.et](mailto:mani301090@hu.edu.et)

Received 6 May 2022; Revised 3 July 2022; Accepted 25 July 2022; Published 25 September 2022

Academic Editor: K. Raja

Copyright © 2022 Mohamad Reda A. Refaai et al. This is an open access article distributed under the Creative Commons Attribution License, which permits unrestricted use, distribution, and reproduction in any medium, provided the original work is properly cited.

Spherical robots are a recent technique and have attracted attention due to their capacity to move at high speeds while maintaining great locomotion efficiency. Many research studies have been undertaken on spherical robots' driving mechanisms, motion planning, and trajectory tracking systems, but only a few studies have been completed on their obstacle avoidance capacity. Its interfering prevention method was "hit and run" due to the existence of a sealed outer shell. This is convenient because of the spherical robots' unique shape. It might cause major problems when the robots are light and small in size. A high-speed collision with a hard surface might harm the robot or the camera in portable spherical robots with onboard cameras. In this article, a magnetic field-based interference detection and prevention system for a tiny spherical robot has been established. The proximity sensor uses a passive magnetic field to detect ferromagnetic barriers by causing the magnetic field to be perturbed. It makes use of a passive magnetic field to keep the system small and power-effective. Because the suggested system can sense not only the existence of a ferromagnetic barrier but also its approaching direction, an intelligent avoidance behaviour may be developed by combining the detection information with the trajectory tracking technique. It amplifies the disturbance effectively and hence increases the detection performance. To improve obstacle detection performance, design optimization is carried out and specific avoidance techniques are designed.

## 1. Introduction

Autonomous mobile robots have attracted a lot of interest in the robotics field during the last few decades and issues connected to their navigation have inspired a lot of research. Nonholonomic robots, being one of the most advanced types, offer a broad range of uses in surveillance and transportation. Depending on the application environment,

several locomotion techniques have been used [1]. Spherical robots have remained an extensive research and development area owing to their natural geometry and effective mobility technology. All of the working components of a spherical robot are wrapped inside the spherical shell and insulated from possible exterior risks or intrusion, making them ideal for release missions, reconnaissance, and even submerged operations [2]. Due to the many benefits

depending on the unique shape and locomotion mechanism, spherical robots have been an attractive research area for decades. All of the components and control units are wrapped inside, making it a closed system. As a result, they are safe from potentially dangerous surroundings. Rolling is a very efficient locomotion strategy that allows the battery to be smaller and the total robot control mechanism to be smaller [3]. Homeland security, rescue missions, and underwater operations are just a few of the possible uses. One of the most often touted benefits of spherical robots is their ability to recover quickly and naturally after colliding with objects. It avoids becoming trapped, unlike multilegged robots that merely roll back when they hit an item. This is tolerable for well-built robots, but it is an issue for small-sized robots, which often have a flimsy, fragile shell to reduce weight.

VIRGO is a new small spherical robot created by the Singapore University of Technology and Design (SUTD) that has exceptional observation abilities and a long battery life. The powertrain is made up of a discrepancy drive cart unit that works on the same principle as a hypocyclic gear train. Because of its simplicity and miniaturization possibilities, this drive mechanism was chosen. It has been consistently worked on to increase its dynamic performance while reducing its total size [4].

Figure 1 shows that small spherical robots have a lightweight thin plastic outer shell that allows them to achieve linear motion at high speed but only provides a modest shield from impacts. When such robotic platforms are utilized for monitoring, the situation gets even worse. Because these robots are carrying sensitive payloads such as cameras, high-impact accidents should be avoided rather than permitted in these applications. As a result, a proximity-detecting system with no contact must be included in order to provide remedial navigation signals [6]. The onboard sensor hardware and processes must be sensibly planned and established due to the limited space and processing power. Mobile robot navigation is commonly divided into three categories: trajectory tracking, motion planning, and obstacle avoidance. Approaches for planning global motion, such as potential field approaches and sampling planners, have been thoroughly investigated [7]. The algorithms used for scientific analysis of defined geometry need previous knowledge of the operating space and impediments. For the centralized planning to construct a distributed robotic structure while considering the size limitation and low compute capabilities, VIRGO has been sought. A pure-pursuit controller controls VIRGO's trajectory tracking and point-to-point locomotion. The twist of the continuing path, which ends at the target waypoint and starts at the robot's present location, is computed using the pure-pursuit algorithm [5].

The accuracy of waypoint tracking has been shown. The obvious benefit of a spherical robot, in terms of obstacle avoidance, has been highlighted repeatedly; its capacity to rebound from accidents has been highlighted as well. Because of this, there is little research on obstacle avoidance for spherical robots. Obstacle avoidance capability is required for decentralized yet small spherical robots such as VIRGO



FIGURE 1: Spherical robot (VIRGO) [5].

not only to increase navigation effectiveness but also to enhance the robot's endurance without surrendering its weight [8]. Closed construction becomes a challenge when building a proximity sensor for spherical robots. Many typical obstacle detection technologies, such as ultrasonic sensors, need a clear line-of-sight. If the shell is translucent, infrared or laser might pass through it. However, after conducting practical tests with the infrared sensor, the scientists discovered that the performance had deteriorated owing to scratching between the shell and the ground, which produces signal diffraction and refraction. The transmission of electromagnetic-based sensing is unaffected by the plastic shell, making it more promising [9]. One of the most important aspects of autonomous navigation for mobile robots is real-time obstacle detection and avoidance. Collision avoidance is built into all autonomous robots, ranging from simple algorithms that identify an impediment and direct the robot to avoid collisions to complex algorithms. Urban obstacles, such as walls and furniture, may have metal components that cause an electromagnetic field disruption. Capacitive coupling, induction coupling, and static magnetic field disorder are some of the interactions that cause it.

In this article, a magnetic field-based interference recognition and prevention system for a tiny spherical robot has been established. The proximity sensor uses a passive magnetic field to detect ferromagnetic barriers by causing the magnetic field to be perturbed. It makes use of a passive magnetic field to keep the system small and power-effective. Because the suggested system can sense not only the existence of a ferromagnetic barrier but also its approaching direction, an intelligent avoidance behaviour may be developed by combining the detection information with the trajectory tracking technique. It amplifies the disturbance effectively and hence increases the detection performance. To improve obstacle detection performance, design optimization is carried out and specific avoidance techniques are designed.

## 2. Related Work

Inverse perspective mapping (IMP) is focused on estimating the geometric cues in detecting obstacles. At the IPM stage, a vertical plane model is used to boost performance. The IPM data and the acquired floor appearance model are then used

to perform appearance-based obstacle segmentation. The shortest distance between the robots and the avoided interference is then determined. The suggested technique was tested on 70 datasets, including nonobstacle photos with significant floor appearance variations. The accuracy of quantitative segmentation is then associated with a standard approach, which has constructed and also estimated the distance accuracy of the proposed system [10]. The oscillating magnetic field localization technology is demonstrated, which is a compact and highly precise proximity sensing structure. The main issue in RF-based social distance sensing techniques is overcome using the sense modality, which is based on an oscillating magnetic field with a low frequency, which is a reliable notion that disables the main issue of RF-based social distance sensing methods in terms of dependability. Because the magnetic field intensity created by coils is proportional to distance, creating magnetic fields for inside scenarios such as rooms, hallways, or factories often necessitates powerful motionless sources with coils and high inductance. The oscillating object with a smaller magnetic field system is appropriate for wearable applications, which produce enough radius for the variety of social isolation. This method effectively produces a tiny magnetic field “bubble” around the travelling user to establish a social distancing zone for them. As a result, social distance breaches may be detected without the need to know the specific location of the user [11].

A full vision-based motion control system for magnetic microrobots has been developed to solve the challenge of controlling them. Even in a congested environment with barriers such as bubbles or impurities, high-resolution impurity detection may be accomplished. A strategic and functional strategy is provided for recognizing and mapping these impediments in the environment in real time, as well as designing optimum barrier-free mobility paths to arrive at the goal point in the shortest time possible. By self-modifying the intended course, the magnetic microrobot can design a trajectory in a fluid environment. The control is generally regulated to within 10 microns of precision [12]. It has varied strong external magnetic fields, allowing a systematic characterisation of the performance of commercial off-the-shelf UAV motors. Two distinct motor types (Air Gear and SwellPro) are explored, as well as two different control systems (direct torque control and field-oriented control). The research study does not include a review of more complex control methods [13]. As an industrial surveillance robot, a spherical robot design and its applications are presented. This robot is meant to act as a human’s extended eye, inspecting the state of the pipe system or other areas that are difficult to inspect owing to their placement. The robot used in this study is semiautonomous, meaning that it is controlled by a human using an android user interface. By looking at the display, the user may operate the robot. This study discusses the input analysis of how the signal can move the robot. The proposed method’s usefulness has been demonstrated in an experimental setting in a comparable scenario [14].

The UWB indoor positioning of multiple sensor fusion has many methods for improving accuracy with high-coast

proven optimal. Because of its low cost, UWB positioning technology can attain centimetre-level precision in a two-dimensional plane, but its accuracy in a three-dimensional space is still developing. Furthermore, little research has been carried out on the problem of significant interference between UWB signals, i.e., irregular data fluctuations induced by time delay would result in an erroneous indoor location. As a result, precise placement of UWB amid signal interference (e.g., obscuration between anchors and target) is seen as a pressing issue that must be addressed. A UWB indoor high-precision positioning model based on GA-optimized ELM is proposed, with a binary classifier based on GA-ELM to judge the presence of signal interference and positioning error compensation using the GA-ELM model to realise the precise positioning of the mobile robot target in complex indoor environments [15]. To tackle the issues, techniques for machine learning are presented. According to reports, using the k-nearest neighbour technique (k-NN) is a machine-learning technique to obtain decent results based on the accuracy of localization and computing speed. Furthermore, it has been claimed that using artificial neural networks (ANNs) rather than using k-NN can increase localization accuracy even further [16].

A unique way of overcoming obstacles is using touch sensors on each of the robot’s legs. Leg positioning is usually indicated by touch sensors on the feet of legged robots. In our example, the robot had touch sensors on the front side of each leg that alerted it to the presence of an impediment in front of each leg. It can also be utilized as a backup input in the event that the robot’s vision-based system fails. Finally, the tactile obstacle avoidance approach may be used with additional environmental recognition sensors to provide the best possible identification of the robot’s surroundings. In comparison to visual systems that need processing time, this approach allows for reactive responses to barriers and is practically immediate. Tactile sensors can also be employed in low-light or no-light situations, where a computer vision-based solution would be ineffective [17].

By reducing the posteriori covariance under the Kalman gain constraint, an optimum partial-state updating Kalman filter (PS-EKF) is suggested. It isolates the magnetic disturbance from two level angles and the sensors’ biases. The PS-EKF may be simply integrated with the magnetic disturbance detecting approach based on thresholds. The classic threshold-based technique identifies magnetic disturbances by imposing a limit on the magnetic norm, the angle between gravity and the measured magnetic field, or both. Because the observed magnetic direction and the reference magnetic field cannot be totally restricted in the same direction, these approaches may lead to defect discovery. In this regard, a vectorial magnetic disturbance detection technique is suggested, which compares the calculated measurement’s norm and direction directly with the reference magnetic field [18]. The decision field theory (DFT) is used to introduce the perception of the decision-making force. DFT is a psychologically based dynamic-cognitive method for human decision making that was first described as a deterministic-dynamic model of a method based on the avoidance of conflict behaviour. When the robot comes



across an impediment, the decision-making force will determine which way is best to avoid the obstruction. A closed-loop control system, dynamic disgust field, and decision force are combined to create an obstacle avoidance algorithm. It recognises that the robot follows a continuous motion trajectory rather than a specific goal point, that the robot can return to its original motion trajectory after avoiding obstacles, and that the decision-making force gives a parametric solution rather than a single prevention choice [19].

### 3. Materials and Methods

**3.1. Spherical Robot Modelling.** Another form of mobile robot whose motion is provided by an inner pendulum mechanism is the spherical robot. The benefit of this robot is that its motion is rolling, and because all of the mechanical parts are contained within the sphere, it may be used in a marine or wet environment. The actuator on this robot is coupled to a perpendicular axis which is shown in Figure 2 [20].

To balance robot motion, the spherical robot arrangement has two actuators and two counterweights. The inner elements are structured in such a way that the center's mass is aligned with its geometrical center. The robot's center of mass is connected to its gravity and has an impact on its dynamics.

**3.2. Dynamic Modelling.** The torque and force applied, as well as the influence of torque and force on robot motion and energy created, are all affected by dynamics modelling in spherical robots [21]. The study of the robot's path planning and control necessitates the use of dynamics. This is given in Figure 3.

The dynamic modelling in spherical robots has the effect of torque and force on the robot's motion and energy generated. The acceleration robot is achieved by equations (1)–(4).

$$x'' = -2d(p_0''p_2 - p_1''p_3 - p_2''p_0 + p_3''p_1), \quad (1)$$

$$y'' = d(p_0''p_0 - p_1''p_0 + p_2''p_2 + p_3''p_3), \quad (2)$$

$$\|p'\|^2 + p_0''p_0 + p_1''p_0 + p_2''p_2 + p_3''p_3 = 0. \quad (3)$$

The complete position  $p = [x, y, p_0, p_1, p_2, p_3, \varnothing_x, \varnothing_y, \varnothing_z]^T$  and the applied torque is  $\tau = [0, 0, 0, 0, 0, \tau_x, \tau_y, \tau_z, 0]^T$ , the dynamics of the special robot are given as follows:

$$M(p)p' + v(p, p') + G(p) = \tau. \quad (4)$$

The angular distance is  $\theta_x, \theta_y, \theta_z$ , where  $p$ -state variable,  $M(p)$ -total mass,  $v(p, p')$ -centrifugal force,  $G(p)$ -gravitational force, and  $\tau$ -torque.

#### 3.3. Proximity Sensor for the Passive Magnetic Field

**3.3.1. Design Concept and Modelling.** The Earth's magnetic field is used in existing research to identify magnetic

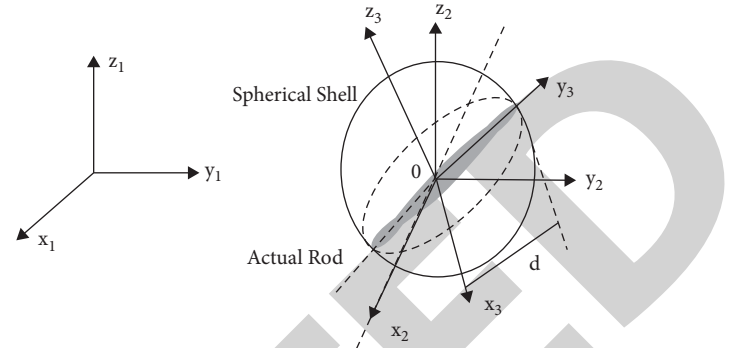


FIGURE 2: A spherical robot with an actuator.

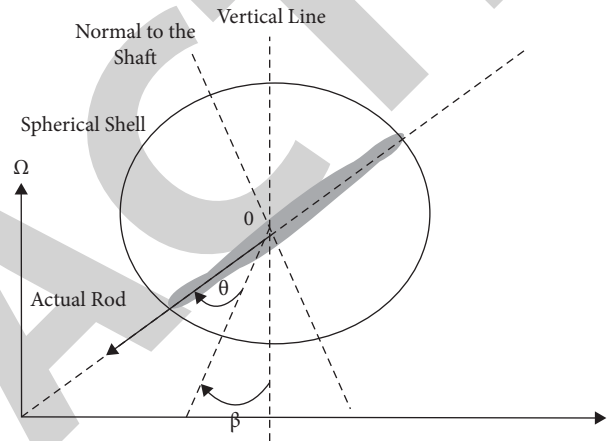


FIGURE 3: Rolling motion of a spherical robot.

abnormalities. The Earth's magnetic field on the ground may be assumed to be unchanging and parallel to the ground by modelling the Earth as a large dipole magnet, which is employed in the present research to find magnetic irregularities. This field has no external source and distorts everywhere a ferromagnetic material is present [22].

The signal-to-noise ratio can be accompanied due to the signal strength and disturbance field, which is one of the major hurdles in putting this method to practical use. The distortion caused by the object is considerably less compared to the steel object. Furthermore, the distortion is directional, with the direction determined by both the Earth's magnetic field and the geometry of the ferromagnetic item. Simulating the distortion field when just the Earth's magnetic field is present can be difficult. The strength of the magnetic field on Earth is in the range of 25 to 65  $\mu\text{T}$ .

While the object's substance and size are proportional to the amplitude of the field of distortion and it can be regularized, the magnetic location of the object in reference to the geomagnetic field is unknown until its direction varies from location to location in the geomagnetic field. Many strategies have been applied to amplify and extract information from the tiny distortion field. To get a useable signal, several of them gave up on the directional capability. A sensor construction with a particularly constructed passive magnetic field to magnify the alteration field is proposed here.



Due to the distinct and distinctive field design, it is feasible to calculate the magnetic location of this item. This feature will also allow for direction prediction, which is required for the robotic planning path. The fundamental concept is to produce a magnetic field with a high spatial gradient by strategically arranging two permanent magnets. When a ferromagnetic object is present, the magnetic field is disturbed. A magnetic field sensor with low power may detect an instantaneous field distortion since the magnetic fluxes are constant. This distortion field is significantly stronger when the Earth's magnetic field occurs.

### 3.3.2. Principles of Detection Based on a Magnetic Field.

When the Earth is modelled as a massive dipole magnet, the magnetic field on the ground should be homogeneous and parallel to the ground. When a ferromagnetic item is present, this field, which has no external source, gets distorted.

It is significantly tougher to detect slight deviations in a weak field, which is represented in Figure 4. It is problematic to describe the perturbation field caused by a nearby ferromagnetic object when just the Earth's magnetic field is occurring. The field in this scenario is determined not only by the object's composition and form but also by its magnetic direction in relation to the geomagnetic field. Materials and forms can be normalized since they have a proportionate relationship with the amplitude of the perturbation field. The magnetic orientation in relation to the geomagnetic field is uncertain, owing to the fact that the geomagnetic field direction varies from different places. Many approaches have been investigated to extract location information from minor field fluctuations. To obtain a large enough signal, several of them compromised the direction-detecting function. However, for interference avoidance and path planning in robotic applications, direction detection is critical. As a result, a specifically constructed passive magnetic field is used to increase the perturbation field while simultaneously detecting the orientation of a nearby item.

### 3.3.3. Design Approach and Theoretical Analysis.

A magnetic flux loop with a balance system is constructed by the judicious positioning of two permanent magnets, inspired by the electrical Wheatstone bridge, and allows minor resistance variations to be sensed. The main concept is to produce a magnetic field with a high spatial gradient artificially. As a result, if a ferromagnetic item is present, the magnetic field will be disrupted. The instantaneous field fluctuation generated by this interruption will be significant since the magnetic fluxes are incessant and have strong spatial gradients.

The magnetic flux lines are focused towards the sensor due to the occurrence of the ferromagnetic plate and its greater permeability than that of air. Because the magnetic flux loop is incessant and has a significant spatial gradient, even a minor item might create significant problems. As a result, when the suggested design is employed as a proximity sensor, the magnetic flux density response is improved and detected by the magnetometer. Because of the one-of-a-kind nature of this interaction, knowing the spatial pose of the

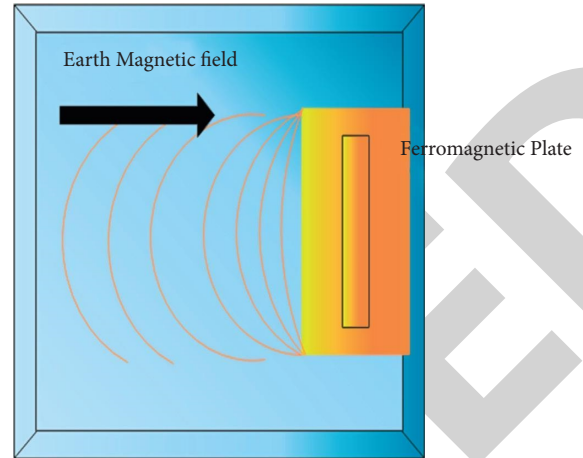


FIGURE 4: Distortion due to a ferromagnetic plate.

item that creates the disturbance will necessitate a theoretical explanation of the magnetic field perturbation.

The material, approaching angle, object size, and distance between the magnets and the object would all influence the magnetic field distortion created by the item. To make the analysis easier, the material penetrability is expected to be infinite and the size of the object is considered to be substantially large. The magnetic field analytical 2D system is built using the imaging technique and the magnetic charge design due to the interface between the permanent magnet.

The magnet surface is parallel to the  $x$  axis while the magnetization axis is parallel to the  $z$  axis. The magnetic charge model uses the product of the surface normal vector and the magnetization to compute negative and positive surface charges. The magnetic field is calculated by mixing the surface charge influence with respect to the pole region. In this case, magnetic charges of comparable strength and the opposite sign are used to substitute the material barrier to account for the magnetic consequence exerted by the object.

The impending direction of the item is parallel to the  $x$  axis for simplicity of demonstration of the picture technique. In real-world situations, it is more likely that the items will approach at an angle rather than parallel. The picture magnetic charges' placement is determined by the impending angle and the distance between the magnets and the impediment. Furthermore, the positioning of the coordinate system is affected by the approaching angle. The variation in the magnetic field based on the image is given as in equation (5).

$$\Delta B = B_i = T \times \frac{\mu_0}{4\pi} \left( \oint \frac{-\sigma_i (L_s - L_i)}{|L_s - L_i|^3} ds - \oint \frac{\sigma_i (L_s - L_i)}{|L_s - L_i|^3} ds \right), \quad (5)$$

where  $T = \begin{bmatrix} \cos 2\alpha & -\sin 2\alpha & 0 \\ \sin 2\alpha & \cos 2\alpha & 0 \\ 0 & 0 & 1 \end{bmatrix}$ , T-transformation matrix,

$\sigma_i$ -magnetic charge in the image,  $L_s$ -location of the field,

$L_i$ -location of the image, and  $s$ - surface area of the magnet image.

**3.3.4. Design Integration and Optimization.** The configuration of VIRGO is analyzed initially in order to match the spherical robot and the magnetic proximity sensor. All of the working components of VIRGO, including the controller, camera, DC motors, and battery, are housed in a framework in the sphere's middle section. The motion is transferred to the shell via two wheels positioned at the bottom of the chassis [23].

The permanent magnets with opposite magnetism may be put on the moving framework facing top and bottom, allowing the robot to be seamlessly integrated with minimal reconfiguration.

When the cameras were pointed forward and the diameter of the magnet was limited, square-shaped magnets were chosen over disk-shaped magnets to maximize the area. The present IMU contains a built-in magnetometer that can be utilized for this type of sensing. An additional magnetometer is utilized here to investigate the interference detection and robot motion performance distinctly.

The magnitude of the distortion field is presented due to an approaching obstacle and is given by the following equation:

$$|\Delta B| = \frac{\mu_0 \sigma_i |L_s|}{4\pi} \left( \oint \frac{1}{|L_s - L_i|^3} ds - \oint \frac{1}{|L_s - L_i|^3} ds \right), \quad (6)$$

where  $L_s$ -location of the sensor and  $L_i$ -location of the image.

The optimization problem is formed by maximizing the magnitude of distortion as shown in the following equation:

$$(V, \gamma, W) = \operatorname{argmax} \left( \sum_{L=L_1, L_2, \dots, L_n} |\Delta B| |L| \right), \quad (7)$$

where  $L = L_1, L_2, \dots, L_n$ -magnetic field location

As the distance to the interference rises, the magnitude decreases, as illustrated by equation (7). Due to the infinite assumptions on the magnetic permeability of the barrier and the obstacle height, equation (6) cannot be utilized to precisely forecast the quantity of distortion field in real life. The magnetic field distortion is expected to occur on a smaller scale and within a smaller area of finite objects with limited magnetic permeability.

The variation in the normalized field is given as in the following equation:

$$\frac{\Delta B}{|\Delta B|} = \frac{L_s}{|L_s|} - \begin{bmatrix} \cos \alpha \\ \sin \alpha \\ 0 \end{bmatrix}, \quad (8)$$

where  $L_s$ -location of the arbitrary field.

When  $R_s = [0 \ 0 \ 0]^T$ , then the angle of the normalized field is given as in the following equation:

$$\alpha = \arctan \left( \frac{\Delta B_y}{\Delta B_x} \right). \quad (9)$$

The difference field due to a ferromagnet will point near the object's position when the sensor is situated at the precise middle point between the two magnets, according to equation (9). Although the above derivations are based on the premise that the item is indefinitely huge and has infinite permeability, the result holds for finite objects. Furthermore, most barriers for tiny spherical robots will be much larger than the robot itself.

**3.3.5. Obstacle Detection and Avoidance.** The obstacle detecting system's mechanical incorporation and configuration optimization have been examined [24]. The approach of a ferromagnetic barrier can be detected by monitoring magnetic field data continuously and analyzing the disruption. A prediction system on a moving platform, unlike a single sensor on the ground, must continually inform the reference field to separate the distortion field formed by an approaching item from noise readings caused by shifting positions. A moving-window average of measurements is generated on a continual basis, with the most recent findings serving as the reference field. The robot controller estimates the distance between its present location and the specified waypoint when a target waypoint is given. If the distance is within the look-ahead distance limit, the pure-pursuit controller generates a trajectory using the distance and the robot heading. As a consequence, the wheel speed could be accurately adjusted. If the distance is less than the minimum look-ahead distance, the trajectory is constructed using the least look-ahead distance. To prevent the robot from attempting to reach an unreachable location, the look-ahead distance is set to double the robot's radius.

Calibrated data are generated by deducting this reference data from each new measurement, which is then utilized for interference detection, which is given in Figure 5.

For trajectory tracking, the VIRGO platform currently employs a pure-pursuit algorithm [25]. The tuning coefficient is employed to adjust the robot's mobility behaviour. The robot chooses to go in a broad arc when the destination waypoint is on the side; when the value is tiny, the robot chooses to walk in a twisting manner. The green lines below show how the executed trajectory is made up of several arcs. To avoid an increase in motion deviation, the robot controller calculates the curves repeatedly.

When the control unit detects an impediment, an interruptive process is initiated, which comprises discontinuing the motor, rotating on the plug, and proceeding to the intermediate waypoint. After retrieving the preceding waypoint, the trajectory will be recalculated using the current position as the starting point. If the robot's speed exceeds the constancy threshold, causing it to topple if it comes to a rapid halt, the robot will first slow down before coming to a complete stop. When the robot identifies the impediment, the control unit will make this choice based on the predefined constancy threshold and the speed of the robot.

Figure 6 illustrates the algorithm for the detailed description of the controller and sensor mechanism in a spherical robot. The obstacle avoidance flag is set when the sensor data achievement thread analyses the data. Based on

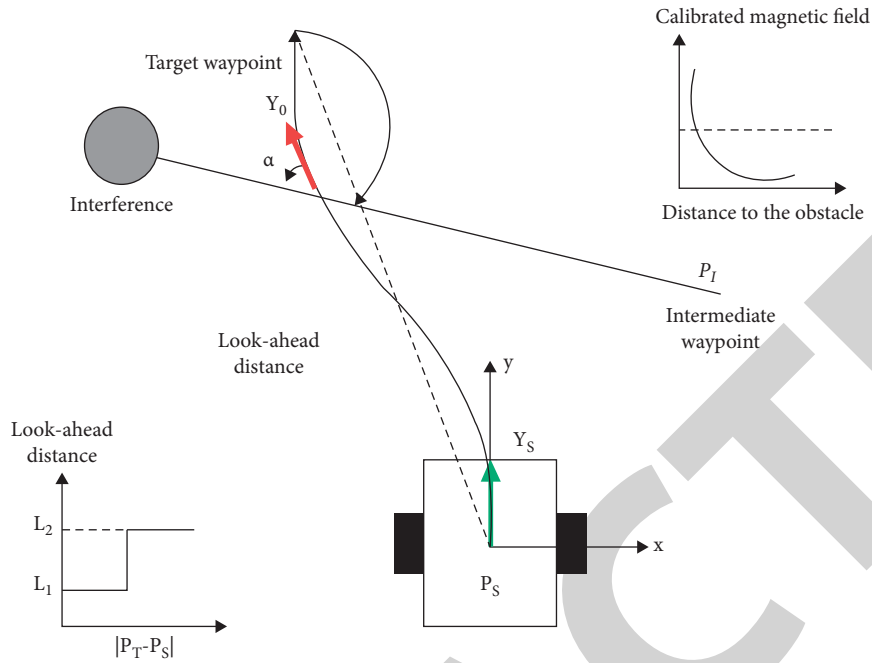


FIGURE 5: Interference avoidance behavior of integration.

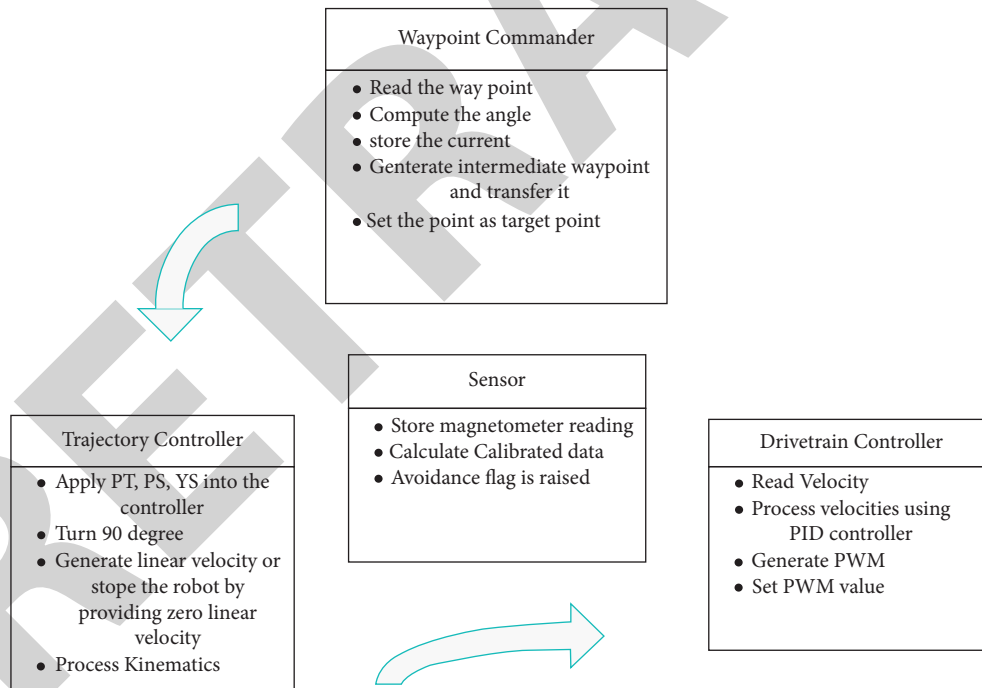


FIGURE 6: Representation of a detailed algorithm.

the interference avoidance flag, the commander of the waypoint creates the target waypoint from a set of choices. The velocities are calculated by the trajectory controller from the desired waypoint based on the interference prevention flag. Finally, the drivetrain controller uses the anticipated wheel velocities to regulate the motor. Although some variables are shared between threads, such as the destination waypoint, interference prevention flag, and velocities, the execution of all four threads is not in any specific order. They

all begin and end at the same time but with different loop frequencies.

3.3.6. *Obstacle Prevention.* Interference can be avoided by using a range of magnetic field sensors such as ultrasonic, laser, and infrared sensors. The accuracy of the proposed system is improved by using range estimation. The unknown interference can be detected simultaneously with the robot

to evade collision and move towards the destination. The interference detection can be examined by the following aspects.

- (1) Determining the obstacles that has the proximity of the spherical robot
- (2) The projection of the obstacles as given in the following equation:

$$p_k = \operatorname{argmin} \|x - p\|. \quad (10)$$

- (3)  $p_k$  is the potential function based on the obstacle point

The obstacle can be avoided by using the potential field function. The range of interaction of a robot is given by the following equation:

$$N = k\epsilon V: \|p_k - p\|, \quad (11)$$

where  $\|\cdot\|$ -Euclidean norm,  $p$ -position of robot, and  $p_k$ -position of obstacles.

The constrains of the spherical robot and the obstacles are represented by the following equation:

$$\|p_k - p\| = d, d < r. \quad (12)$$

The navigation of the obstacles can be achieved using the potential of the system as given in the following equation:

$$V(p) = c_1 V_o(p) + c_2 V_n(p), \quad (13)$$

where  $c_1, c_2$ -positive constant and  $V_o, V_n$ - interactive potential.

$$V_n(p) = \sum \left( \sqrt{\left(1 + \|p - p_r\|^2\right)} - 1 \right), \quad (14)$$

where  $p_r$ -target position of spherical robot.

The collision avoidance is achieved using the energy function as given in the following equation:

$$H(p, q) = V(p) + T(p), \quad (15)$$

where  $V(p)$ -potential energy and  $T(p, q)$ -kinetic energy of the robot.

The condition  $H' < 0$  shows that the collision never occurs between the spherical robot and obstacles.

## 4. Result and Discussion

Considering the configuration of the robot and its size, the design optimization strategies can be chosen and embedded on the robot system. The optical motion tracking system is used to evaluate the performance of the obstacle avoidance by capturing the behavior of the robot using the IR camera. Table 1 provides the parameters of the robot which are used to evaluate the performance of obstacle avoidance.

**4.1. Calibration.** An industrial robot is utilized to transfer a ferromagnetic material about the sensor to evaluate the practical sensor performance and standardize the accuracy of angle detection. The robot is positioned on a nonmagnetic

TABLE 1: Mechanical parameters of the robot.

IMU	Bosch BNO055
Magnetometer	MAG3110
Magnet	0.5-inch length and 0.125-inch height
Controller	STM32F411RE
Motor	Max RPM:119
Wheel	2 mm of width and 10 mm of diameter

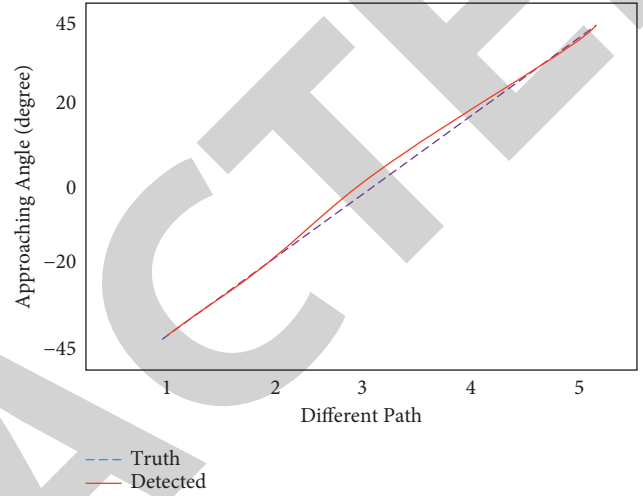


FIGURE 7: Accuracy of angle detection.

surface, and the robot's hand moves an 8 cm long steel cube. Between the two magnets, a MAG3110 three-axis magnetometer is attached, and data are collected using an Arduino Uno board. The object is directed at the robot from various angles in the frontal area and the impending angle of the object can be estimated from the magnetic field. The average value for each approaching angle is estimated with an object at a different distance, which is shown in Figure 7.

Table 2 examines the errors such as average detection error and maximum detection error. The error is estimated based on the variation in the detected angle, which is analyzed using an error bar with an average value due to the estimation with different distances.

Figure 8 shows the magnitude of the distortion field measured. When the object is nearer to the magnetometer, maximum distortion is detected. The magnitude of the distortion field reduces as the distance increases. The trends in approaching angle are shown by the relationship between the distance and magnitude of the object.

**4.2. Effect of Distance Separation.** When the distance between the two magnets is greater, the magnet's volume has a greater effect on the performance of object detection. The influence of separation distance among the two magnets, as well as magnet geometries, is utilized here. The volume is the same but with different aspect ratios. When the barrier is positioned at a succession of incremental locations, a summation of the magnitude of the distortion fields is determined.

TABLE 2: Approaching angle detected based on the designed angle.

Intended angle	-45	-30	0	30	45
Predicted angle	-45.8	-19.2	1.9	21.6	46.3
Typical error (%)	1.8	1.6	2.3	2.7	1.3
Increase error detection	3.2	2.5	3.4	2.8	2.2
Maximum error (%)	3.5	2.6	3.3	3.5	2.6

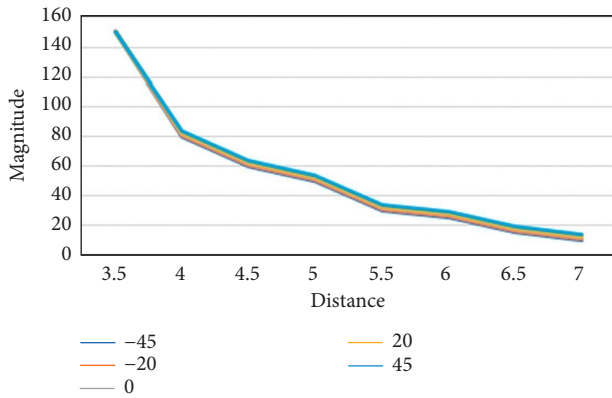


FIGURE 8: Comparison between the magnitude and distance of the robot to the ferromagnetic object.

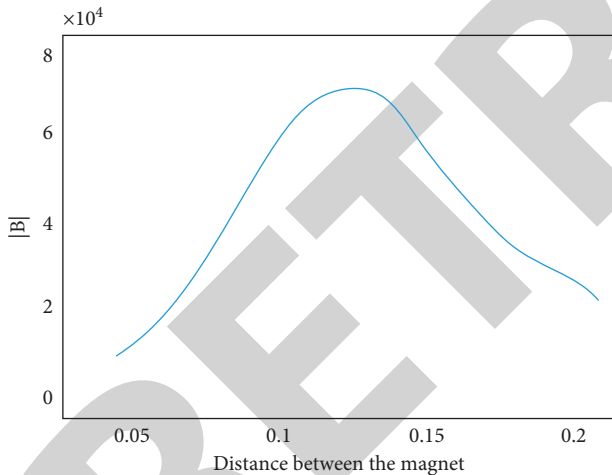


FIGURE 9: Effect on distortion field strength due to the distance separation between two magnets.

Figure 9 shows that the distortion field magnitude increases with the distance and when the magnets are separated for more distance, it reaches its maximum value.

Figure 10 shows this distortion field based on the effect of the magnetic field. In spite of the distance between the two magnets, the amplitude of the distortion field grows significantly with the magnet volume. Despite the fact that the aspect ratio of these two magnets differs from that of the previous three magnets, the influence of the aspect ratio reduces the distance between the two magnets.

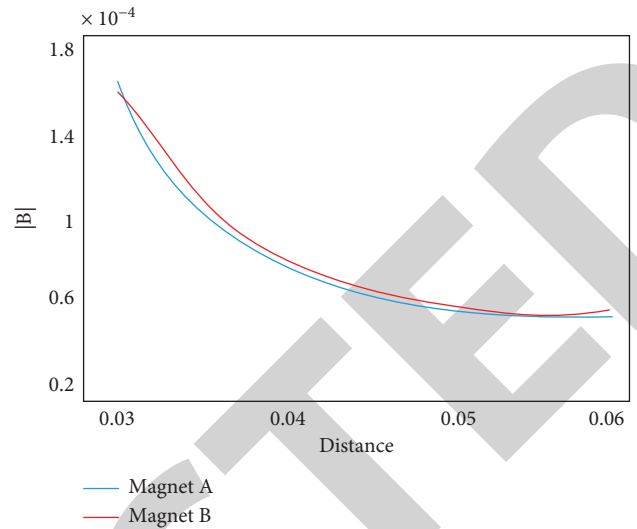


FIGURE 10: Effect of magnet geometry on distortion.

### 5. Conclusion

In this paper, a VIRGO microspherical robot with a proximity sensor for a passive magnetic field was developed and obstacle avoidance behaviour was realised.

- (i) It has been established that the enhanced robot can evade physical contact with impediments while still reaching its intended destination waypoint. The robot does not need to be reconfigured in order to use this innovative sensing technology, and the dimensions of this tiny spherical robot do not change.
- (ii) Not only can the sensing system identify the existence of an adjacent ferromagnetic object but it can also offer essential information about the direction of an object approaching, which is crucial for course planning and interference prevention.
- (iii) The robot may use this information to calculate and execute correction orders in real time to prevent colliding and causing damage. To increase the system’s sensing accuracy, further studies will involve optimization on the sensor design and an automatic calibration machine. The small sensing system will eventually be incorporated with a collision avoidance algorithm into the spherical robot platform.

### Data Availability

The data used to support the findings of this study are included within the article. Further data or information are available from the corresponding author upon request.

### Conflicts of Interest

The authors declare that there are no conflicts of interest.

## *Retraction*

# **Retracted: Tribological Behavior of AA7075 Reinforced with Ag and ZrO<sub>2</sub> Composites**

### **Advances in Materials Science and Engineering**

Received 26 December 2023; Accepted 26 December 2023; Published 29 December 2023

Copyright © 2023 Advances in Materials Science and Engineering. This is an open access article distributed under the Creative Commons Attribution License, which permits unrestricted use, distribution, and reproduction in any medium, provided the original work is properly cited.

This article has been retracted by Hindawi, as publisher, following an investigation undertaken by the publisher [1]. This investigation has uncovered evidence of systematic manipulation of the publication and peer-review process. We cannot, therefore, vouch for the reliability or integrity of this article.

Please note that this notice is intended solely to alert readers that the peer-review process of this article has been compromised.

Wiley and Hindawi regret that the usual quality checks did not identify these issues before publication and have since put additional measures in place to safeguard research integrity.

We wish to credit our Research Integrity and Research Publishing teams and anonymous and named external researchers and research integrity experts for contributing to this investigation.

The corresponding author, as the representative of all authors, has been given the opportunity to register their agreement or disagreement to this retraction. We have kept a record of any response received.

### **References**

- [1] C. R. Mahesha, S. R. M. M. Sree Jayan et al., "Tribological Behavior of AA7075 Reinforced with Ag and ZrO<sub>2</sub> Composites," *Advances in Materials Science and Engineering*, vol. 2022, Article ID 7105770, 8 pages, 2022.



## Research Article

# Tribological Behavior of AA7075 Reinforced with Ag and ZrO<sub>2</sub> Composites

C. R. Mahesha,<sup>1</sup> Suprabha R,<sup>1</sup> M. Mahaveer Sree Jayan,<sup>2</sup> Shilpa Kulkarni,<sup>3</sup> Aman Sharma,<sup>4</sup> Essam A. Al-Ammar,<sup>5</sup> S. M. A. K. Mohammed,<sup>6</sup> Ram Subbiah,<sup>7</sup> and Agonafir Alemayehu <sup>8</sup>

<sup>1</sup>Department of Industrial Engineering & Management, Dr. Ambedkar Institute of Technology, Bangalore 560056, Karnataka, India

<sup>2</sup>Department of Mathematics, Indra Ganesan College of Engineering, Tiruchirapalli 620012, Tamil Nadu, India

<sup>3</sup>Department of Physics, Shri Ramdeobaba College of Engineering and Management, Nagpur 440013, Maharashtra, India

<sup>4</sup>Department of Mechanical Engineering, GLA University, Mathura, UP 281406, India

<sup>5</sup>Department of Electrical Engineering, College of Engineering, King Saud University, 800 Riyadh 11421, Saudi Arabia

<sup>6</sup>Department of Mechanical and Industrial Engineering, Ryerson University, Toronto M5B 2K3, ON, Canada

<sup>7</sup>Department of Mechanical Engineering, Gokaraju Rangaraju Institute of Engineering and Technology, Hyderabad, Telangana 500090, India

<sup>8</sup>Department of Mechanical Engineering, Mizan Tepi University, Mizan Teferi, Ethiopia

Correspondence should be addressed to Agonafir Alemayehu; [agonafir@mtu.edu.et](mailto:agonafir@mtu.edu.et)

Received 5 July 2022; Revised 25 August 2022; Accepted 31 August 2022; Published 23 September 2022

Academic Editor: K. Raja

Copyright © 2022 C. R. Mahesha et al. This is an open access article distributed under the Creative Commons Attribution License, which permits unrestricted use, distribution, and reproduction in any medium, provided the original work is properly cited.

In this study, an AA7075 composite material with a varying weight percentage of silver and zirconium oxide reinforcement is examined in terms of its properties. Reinforcement quantities ranging from 0, 4, 8, 12, and 16 wt % were combined with the matrix using the in-situ technique of stir casting in the field. Tensile, mechanical hardness, and compressive strength were assessed in accordance with the standard. The X-ray diffraction and EDS were utilized to analyze AA7075 composites for the distribution and dispersion of particles. Different input parameters such as load ( $N$ ), composites (wt %), and velocity (m/s) were used to evaluate wear resistance when using the pin-on-disc method. The wear rate (mm/m) was estimated for every weight percent of reinforced mass loss (g). Optimization methods such as Taguchi and analysis of variance were used to determine the AA7075's optimal processing parameters and composites that were the most significant. In order to identify the best genetic algorithm results, theoretical and experimental results were evaluated.

## 1. Introduction

Aluminum metal matrix composites play a significant part in today's industrial environment because of their characteristics, weight, and strength ratio [1, 2]. As a result of Al's low density, malleability, better thermal conductivity, and abrasive resistance, it is the second most often employed material in the industry [2–4]. Ceramic reinforcement particles, such as zirconium oxide, Ag, silicon nitride, titanium diboride, TiN, boron carbide, TiC, titanium dioxide, and silicon dioxide, are utilized to make AMCs more potent and effective [5, 6]. These qualities can be improved by

manufacturing AMCs using a variety of processes, including squeeze and stir casting, FSW, and PM [7]. AMCs' mechanical qualities are mostly determined by their manufacturing processes. Reinforcement particles' distribution in the matrix material is by far the most important factor here [8]. It is possible to manufacture composite materials using either a solid-state approach or a liquid-state method. The solid-state approach is the more expensive of the two options, thus it is not suggested for large-scale production [9–11]. To put it another way, the liquid-state method has a lower production cost than the solid-state method and is very practicable and assures a proper



distribution of strengthening in the matrix material [12, 13]. Stir casting has been proven to be a simple and economical approach for the in-situ reaction of AMCs [14]. The physical qualities of AA7075 are better than those of other aluminum matrix composites [15]. It was decided to use silver (Ag) as the strengthening material because of its high thermal expansion coefficient, reasonable thermal stabilization, higher strength, and great dispersal properties with Al composites [16]. Due to its electrical and thermal stability, high thermal stability, and superior erosion and corrosion resistance, zirconium oxide is frequently used as a reinforcing ceramic [17]. For the most part, the tribological examinations are conducted by using POD test equipment. AMCs are primarily controlled by the rate of wear and the coefficient of friction [18–21]. Discs of steel or cast iron are used to generate friction on the specimen [22]. Composite tribological behavior processing characteristics are studied and analyzed using DOE. With the least amount of error, Taguchi and ANOVA methodologies are utilized to determine the influence of process characteristics and how much each processing parameter contributes to the overall process percentage [23, 24]. To predict accurately and discover the optimal and average values of output parameters, a genetic algorithm is utilized [25].

As a result of this inquiry, Al7075 composites have been created utilizing various weight percentages (wt %) of reinforcement, such as 0, 4, 8, 12, and 16 Ag and ZrO<sub>2</sub>. These composites have been tested for their mechanical properties using hardness, tensile, and compression tests, and by using varying percentages of AA7075. Pin-on-disc wear tests have been conducted with a variety of input parameters. For AA7075 compounds, Taguchi, ANOVA, and GA optimization approaches were utilized to estimate the percentage of every parameter and optimum values.

## 2. Methods and Materials

**2.1. Specimen Fabrication.** In this study, the matrix material is AA7075 which is the toughest and heaviest consumer alloy used in multiple parts of the moving sectors and the reinforcement is silver and zirconium oxide particles. In AA7075, by adopting a stir casting process, the composites were created. AA7075 was melted at a temperature of 720°C in a heated furnace. Table 1 lists the composition of AA7075. The melted AA7075 was stirred in with the reinforcing particles before being added. Two powders, KBF<sub>4</sub> and K<sub>2</sub>ZrF<sub>6</sub>, were used to make zirconium oxide. There were 0, 4, 8, 12, and 16% reinforcing weight percentages in the process [26]. Reinforcing particles silver and zirconium oxide were mixed with the AA7075 matrix at a rate of <15% to ensure strong attachment and equitable spreading in the matrix [27]. According to the hypothesis, the matrix material has avoided one-point segregation due to reinforcement mixing. A 10 mm diameter and 20 mm-long pin mold had already been developed at that point for the new product. Matrix and reinforcements were meticulously combined and put into the

mold cavity, which was then allowed to cool before being removed from the container.

**2.2. Mechanical Properties.** ASTM standards were utilized to evaluate the mechanical characteristics of AA7075 compounds at changing weight percentages in the tests. There is a method for measuring the hardness of composites based on ASTM E10-07 and it is called the Micro Vickers' Hardness testing machine. The indentation was made on each sample in a different location on the five samples that were used in this test. The hardness of the material was measured and an indentation was found in the right area of the reinforcing particles after the measurements were taken. ASTM E08-8 and E09-9 standards were used to determine the tensile [28] and compression strengths, respectively, by employing a universal testing apparatus [29]. Each weight percentage of AA7075 composites was used in the preparation of the samples. In order to eliminate scratches, samples were cleaned with a SiC 1200 grid paper. The tensile test was performed with a weight of 10 KN and a crosshead speed of 2.5 m/min. By deforming samples of AA7075 with different reinforcing weight percentages, compression test forces were computed.

**2.3. Wear Test.** The wear test was carried out with a pin-on-disc testing instrument. The ATM G99 G95a standard was used throughout the test at room temperature. This study used a total of 25 samples for analysis. The samples had a diameter of 10 mm and a length of 25 mm for the test. An electronic weighing scale was employed to measure the mass loss of the specimen earlier and later they were worn [30]. Abrasive disc friction resulted in mass loss during sample preparation. The input parameters would be the weight percentage of the composites, the load, and the velocity (m/s). Table 2 lists the relevant input parameters. The sliding distance remained constant at 3000 m.

**2.4. Optimization Techniques.** Taguchi and ANOVA are employed as the optimization approaches of this study because Taguchi is a simple, powerful, and cost-effective approach [31, 32]. The signal-to-noise ratio is typically examined in terms of "smaller is better," "nominal is better," and "bigger is better," among others. In order to attain the lowest wear rate, the criterion "smaller is better" was used in this study. These input parameters are likewise affected by the situation. The  $L_{25}$  orthogonal array is shown in Table 3. MATLAB software is used to implement. Here, the ANOVA approach is utilized to find the most important input factors for the numerical optimization procedure. This program is used to create the design matrix and to identify which composite process factors have the greatest impact on performance [33]. The effects of influencing constraints on the wear rate of AA7075 composites with varying reinforcing levels are summarized in an ANOVA table. The median values of the variables are determined through the use of an ANOVA.

TABLE 1: Chemical composition of AA7075.

Basics	Silicon	Iron	Copper	Manganese	Magnesium	Chromium	Zinc	Aluminum
Weight percentage	0.05	0.10	1.60	0.05	2.70	0.19	5.80	Remaining

TABLE 2: Pin-on-disc wears testing input factors.

Input factors	Values
Composites (wt %)	0, 4, 8, 12, and 16
Load (N)	15, 25, 35, 45, and 55
Velocity (m/s)	2, 4, 6, 8, and 10

TABLE 3:  $L_{25}$  orthogonal array.

S.No	Composites (wt %)	Load (N)	Velocity (m/s)
1	0	15	2
2	0	25	4
3	0	35	6
4	0	45	8
5	0	55	10
6	4	15	4
7	4	25	6
8	4	35	8
9	4	45	10
10	4	55	2
11	8	15	4
12	8	25	6
13	8	35	10
14	8	45	2
15	8	55	8
16	12	15	6
17	12	25	10
18	12	35	2
19	12	45	4
20	12	55	8
21	16	15	10
22	16	25	2
23	16	35	4
24	16	45	8
25	16	55	6

### 3. Results and Discussion

#### 3.1. Study of Mechanical Characteristics

**3.1.1. Study of Hardness Test.** Following the in-situ procedure, the microhardness examination was performed with a continuous 0.5 kg load on AA7075 with varying weight percentages of silver and zirconium oxide. In Figure 1, the results of the hardness tests are shown for a variety of reinforcing quantities. The in-situ bonding of the grains increases resistance to the external load only an indentation with the addition of reinforcements with the matrix. It shows that the grain has been refined. In comparison to unreinforced AA7075, the composite surfaces showed no signs of indentation defects. The Orowan reinforcing method assumed that the strengthening particles were evenly dispersed throughout the composites in order to maximize strength. The uniform distribution of particles prevented particle

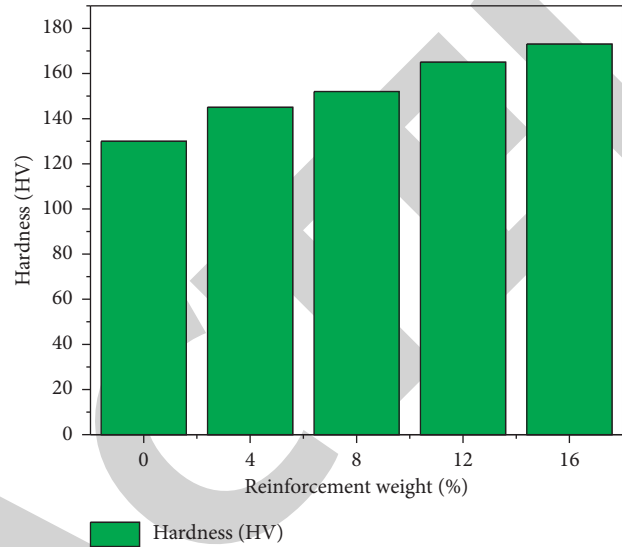


FIGURE 1: Hardness.

mobility and dislocation. Due to the Orowan loops, dislocation processes were impeded around the reinforcements [34], and because of departure strengthening, the fine interfacial connection and good interface of the AA7075 matrix were achieved. The addition of reinforcing particles gradually increases the AA7075 composite's hardness.

#### 3.1.2. Study of Tensile Strength and Compressive Strength.

The tensile strength of composites with different strengthening levels, such as 0, 4, 8, 12, and 16, can be evaluated by use of the universal testing machine (UTM). The matrix evenly distributes the load to the reinforcement particles in each sample, which are prepared to the desired dimensions. The strength of the composites will increase as a result of the homogeneous dispersion and strong connection between the grains [35]. Rendering to the Orowan strengthening process, displacements are constrained and particle arrests take on a bow-shaped structure. Grain dislocation is prevented by the bow-shaped arrest. The bonding becomes extremely high if the dislocations are stopped. As a result, raising the reinforcing weight percentage of composites improves the overall system strength. Continuous gliding results from dislocations that occur outside of the grains throughout time. As can be seen in Figure 2, the tensile test results are obtained.

According to the findings of the tests, the reinforcements steadily enhance the compression strength. Figure 3 shows the test findings in a visual format. For the matrix and reinforcement to be as near together as possible, the in-situ formation is used. Crushing loads are evenly distributed throughout the reinforcements if the ceramic particles are well dispersed. A few little cracks have appeared. Evenly distributed

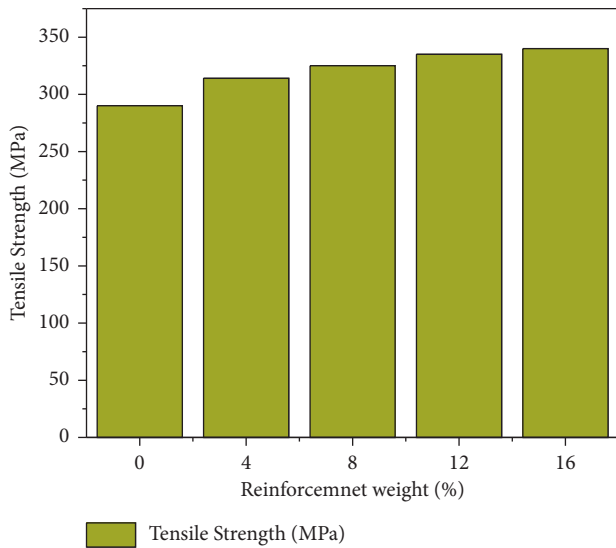


FIGURE 2: Tensile strength.

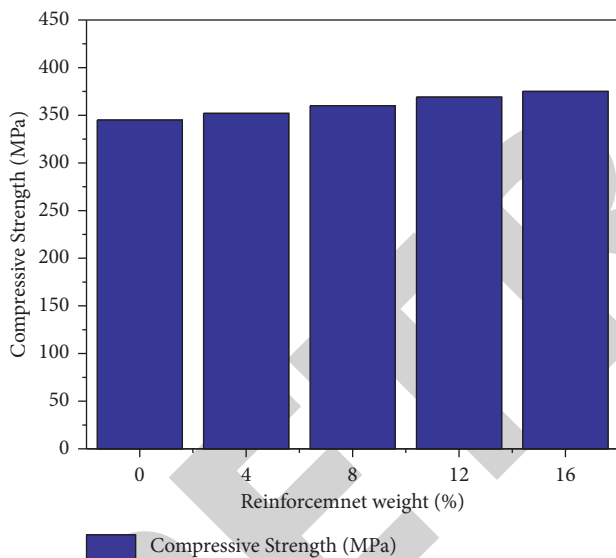


FIGURE 3: Compression strength.

stresses cause grains to be slightly displaced. As a result, the composites have a modest flexibility to prevent them from breaking apart. External loads are transferred and distributed uniformly through reinforcing particles to the composite material when they are applied. That means that the AA7075 composites with a greater wt percentage (16%) have a better particle distribution and better bonding. As a result, raising the reinforcing weight percentage improves mechanical qualities.

**3.2. XRD Evaluation.** The analysis of in-situ AA7075 composites shows that different peaks are present in the AA7075 composites with varying reinforcements in the weight percentage range as shown in Figure 4. It is confirmed by XRD that the matrix material contains reinforcements. With the AA7075 matrix, the presence of both

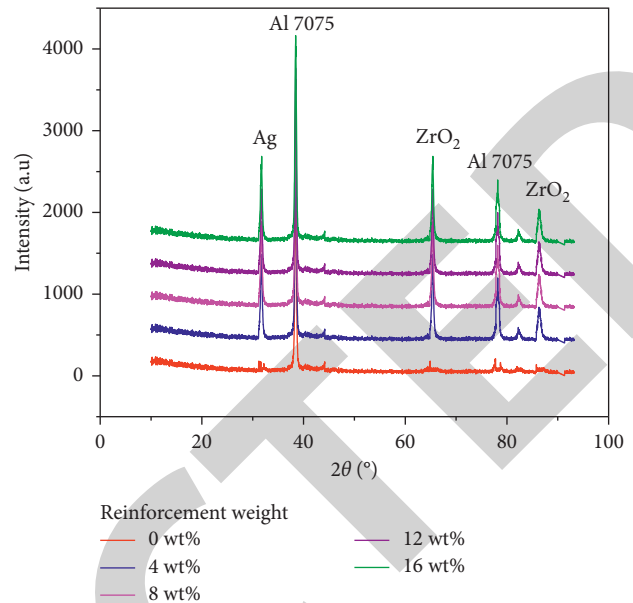


FIGURE 4: XRD evaluation of AA7075 composites.

reinforcements can be clearly seen. Reinforcements help to boost the intensity of the various peaks of intensity. Aluminum oxide and other metallic compounds can be seen in some of the minor peaks from this reaction. Oxide can be linked with the aluminum matrix during the sintering process, resulting in a green compact. Nitrides and aluminum are combined in a ratio that is less than or equal to. There is an increase in the zirconium oxide mass fraction signal strength, indicating that mass fraction limitations are conceivable. These chemicals, however, were not detected by XRD.

**3.3. EDS Analysis.** The analysis of the AA7075 composites with different reinforcing levels is shown in Figure 5. It is a quantitative and qualitative examination of the 7075 matrix component constituents found in an aluminum alloy. The mixing of matrix and reinforcements was confirmed by the EDS spectrograph. The largest peak of aluminum was detected during EDS analysis following the wear test. Wearing surfaces may develop some oxidation over time owing to exposure to heat. The apex of the reinforcement was also identified. In the process of mechanical alloying, iron is transferred from the wear surface to the reinforcements. In order to withstand the atomic changes caused by wear, the iron layer is thickened to boost resistance. An aluminum-nitride association is visible on the spectrograph during wear.

## 4. Experimentation on Optimization Results

**4.1. Taguchi Optimizing Methodology.** The optimization of metal matrix details was achieved by using  $L_{25}$  orthogonal arrays in this study (OA). The manufacturing and machine mistakes were perfected after approximately 25 experiments with various input constraints were conducted. The majority of the material, AA7075, was blended with other impurities in

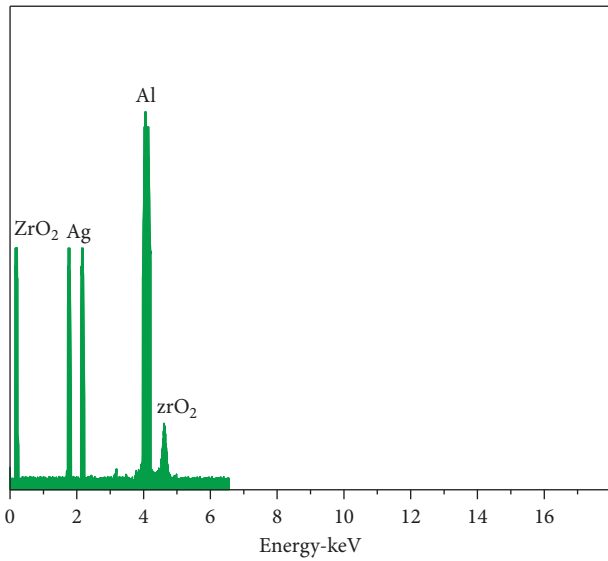


FIGURE 5: EDS analysis.

order to improve the results by considering three different elements, including the composite weight percentage, velocity, and load. It was decided to keep the wear rate as the primary responsive factor. Overall, there were 25 experiments, each of which had five runs for each processing factor. Costs for wear and tear were typically low. Using the repeated formula  $-10 \times \text{Log}_{10}(\text{sum}(Y^2)/n)$ , the results of these 25 experiments were combined. Observations have shown that increasing the weight percentage resulted in a decrease in the wear rate. By using the pin-on-disc apparatus, the pin exerted 20 N of force on the disc and the disc travelled at 1 m/s, the POD device recorded a minimal wear rate of 0.000182 mm<sup>3</sup>/m. Results that are closer to the ideal are shown in Table 4.

**4.2. S/N Ratio.** The DOE provides the body size to figure out the authority variables in order to reduce the procedure by lowering the noise. The reduction of these variables is accomplished through iterative processes including some delta values. Depending on the situation, the S/N will have different data characteristics. It is necessary to utilize “nonnegative with a target value of zero” when calculating the rate at which an object is wearing out. This group will have the lowest response rate and the best outcome. Data mean repetition values and the signal-to-noise ratio are presented in Tables 5 and 6. In both circumstances, the composite weight percentage increases the MMC strength and reduces the wear rate to a minimum. Figure 6 provides graphic charts of the wear rate. Abrasion rate Y axis has been used to analyze the graph by maintaining the data mean value constant.

**4.3. ANOVA.** Analysis of Variance is an arithmetical examination of the difference between groups that establishes ideal divisions between the aspects of the data. The statistical test comparing mean values is utilized to determine the influence of procedure elements that yield better outcomes. Each individual parameter’s percentage of

TABLE 4: Experimental runs input and output values.

S. No	Composites (wt %)	Load (N)	Velocity (m/s)	Wear rate (mm <sup>3</sup> /m)
1	0	15	2	0.005140
2	0	25	4	0.006630
3	0	35	6	0.005720
4	0	45	8	0.005620
5	0	55	10	0.000820
6	4	15	4	0.004270
7	4	25	6	0.003805
8	4	35	8	0.006409
9	4	45	10	0.003408
10	4	55	2	0.002607
11	8	15	4	0.000796
12	8	25	6	0.001865
13	8	35	10	0.001816
14	8	45	2	0.002586
15	8	55	8	0.001907
16	12	15	6	0.001589
17	12	25	10	0.001589
18	12	35	2	0.001639
19	12	45	4	0.001249
20	12	55	8	0.001199
21	16	15	10	0.000885
22	16	25	2	0.000182
23	16	35	4	0.000586
24	16	45	8	0.000787
25	16	55	6	0.000885

TABLE 5: S/N ratio’s response.

Level	Composites	Load	Velocity
1	45.42	55.72	57.42
2	49.34	56.76	54.73
3	56.72	53.95	56.34
4	58.23	54.62	53.35
5	65.84	54.67	53.78
Delta	21.53	3.81	4.26
Rank	1	3	2

TABLE 6: Means response.

Level	Composites	Load	Velocity
1	0.006152	0.002548	0.002407
2	0.005063	0.002872	0.002903
3	0.001872	0.003293	0.002538
4	0.001492	0.002788	0.004354
5	0.000673	0.002936	0.004126
Delta	0.006479	0.000853	0.000962
Rank	1	3	2

inheritance is listed in Table 7. A visual representation of the inheritance percentage is shown in Figure 7. With the percentage of process variables that can be inherited, it can be stated that the weight percentage of AA7075 helps lift the wear resistance of the matrices with other impurities. Nearly, 81% of the contributions came from the weight percentage of the population. The remainder of the proportion is made up of the other two variables, velocity (8%) and load (15%). Experimental and statistical analyses are

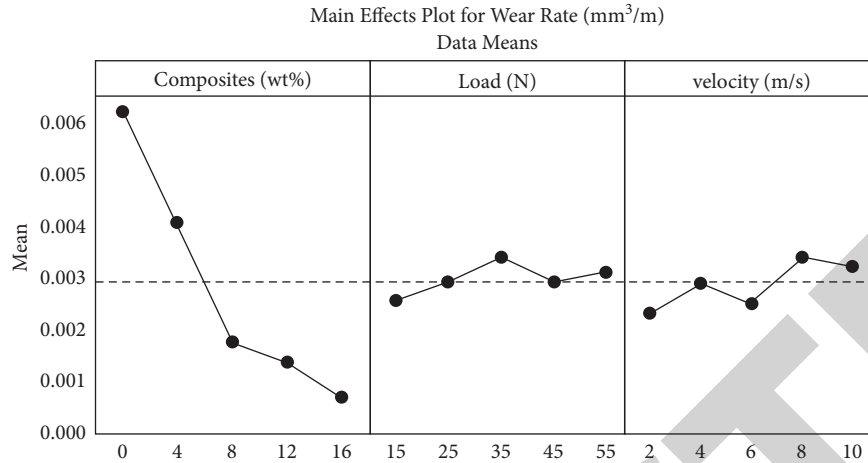


FIGURE 6: Main effect plot for the wear rate.

TABLE 7: ANOVA wear rate.

Source	DF	Adj.SS	Adj.MS	F value	P value	% of contribution
Composites (wt %)	4	0.000101	0.000026	25.63	0	87
Load (N)	4	0.000003	0	0.39	0.817	3
Velocity (m/s)	4	0.000011	0.000002	0.88	0.508	10
Error	12	0.000003	0.000002			0
Total	24	0.000118				100

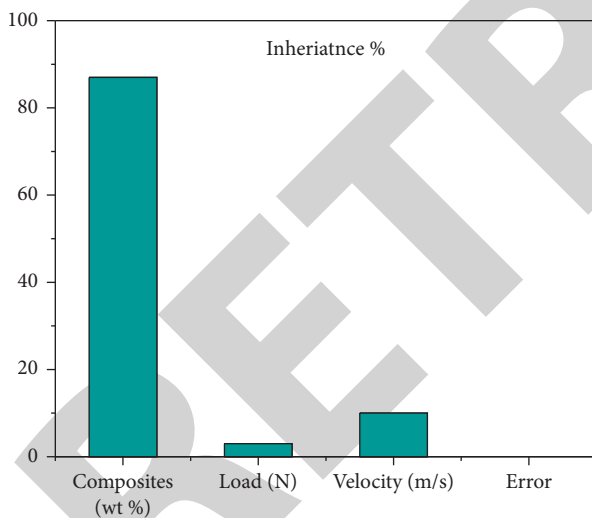


FIGURE 7: Inheritance % of processing parameters.

contrasted in Table 8, which clarify the comparative assertions. Slight differences between the two methods are spread over the world. Accordingly, it can be concluded that the research strategy is a success since the input variables of 16 wt % of the compound, 25 N and 2 m/s segregate superior abrasive resistance better than earlier cycle runs of the experiment.

4.4. Wear Rate by Genetic Algorithm. After the MATLAB code was fitted to train the software, a nontraditional technique was used to forecast input and output variables to

TABLE 8: Comparison of Taguchi and experimental techniques.

Techniques	Input factors			Output factors
	Composites (wt %)	Load (N)	Velocity (m/s)	Wear rate (mm³/m)
Taguchi	16	25	2	0.000182
Experimental	16	25	2	0.0003

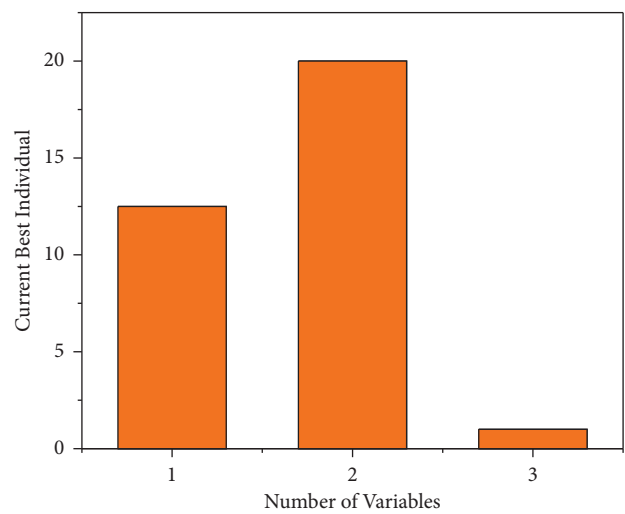


FIGURE 8: Minimal wear rate estimation output attained by the GA.

infinity uniformly. GA mimics the natural screening, in which the fittest individuals are chosen for procreation to produce the following generation. It was possible to obtain

TABLE 9: Comparison of genetic algorithms and experimental techniques.

Techniques	Input factors			Output factors
	Composites (wt %)	Load (N)	Velocity (m/s)	Wear rate (mm <sup>3</sup> /m)
Genetic algorithm	16	25	2	0.000162
Experimental values	16	25	2	0.000182

the fitness function from a variety of mathematical models. According to the variables depicted in Figure 8, we were able to maximize the findings. According to the findings, the lowest wear rate was reached by using 16 wt% composite, 25 N, and 2 m/s to achieve 0.000182 MPa, while the data average value has changed equal to 0.000262 MPa. Tables 8 and 9 show the comparison between the actual experimental value and the software's prediction. When the projected values of process parameters differ somewhat from what is actually observed in the laboratory, then the GA can maintain its high standards.

## 5. Conclusion

Through the in-situ creation of AA7075 composites, the stir casting method was well created with varying amounts of reinforcements with 0, 4, 8, 12, and 16 wt %.

- (i) Mechanical properties of AA7075 composites ensured that no particles were dislocated in the composites and that the load was uniformly dispersed among the strengthening. Mechanical qualities improved as reinforcements were added. Parameters were shuffled using the  $L_{25}$  orthogonal array. The higher the percentage of reinforcement, the lower was the wear rate. Taguchi and investigational data show that reinforced composites at 16 wt% have a lower wear rate of 0.000182 mm<sup>3</sup>/m, whereas experimental value is 0.0003 mm<sup>3</sup>/m.
- (ii) The grain refinement procedure was successful and faults were evaded because of the firm link between the matrix and the strengthened particles. An investigation of the XRD and EDS data exposed the conformation of the AA7075 composites fillers and ingredients, respectively.
- (iii) In this study, the best and average wear rates were found. The GA and experimental comparisons were extremely close.

## Data Availability

The data supporting the current study are given in the article and further information or data are available from the corresponding author on reasonable request.

## Conflicts of Interest

The authors declare that they have no conflicts of interest.

## Acknowledgments

The authors would like to thank MizanTepi University, Ethiopia, for their support and help during the research and for preparation of the manuscript. This work was funded by the Researchers Supporting Project Number (RSP2022R492), King Saud University, Riyadh, Saudi Arabia.

## References

- [1] D. Kumar, S. Angra, and S. Singh, "Mechanical properties and wear behaviour of stir cast aluminum metal matrix composite: a review," *International Journal of Engineering*, vol. 35, no. 04, pp. 794–801, 2022.
- [2] S. Bezzina, E. B. Moustafa, and M. A. Taha, "Effects of metastable  $\theta'$  precipitates on the strengthening, wear and electrical behaviors of Al 2519-SiC/fly ash hybrid nano-composites synthesized by powder metallurgy technique," *Silicon*, 2022.
- [3] O. O. Edosa, F. K. Tekweme, and K. Gupta, "A review on the influence of process parameters on powder metallurgy parts," *Eng. Appl. Sci. Res*, vol. 49, no. 3, pp. 433–443, 2022.
- [4] T. Sathish, S. D. Kumar, M. Ravichandran, V. Mohanavel, S. S. Kumar, and S. Rajkumar, "Lead-free piezoelectric ceramics of (Bi<sup>1/2</sup>Na<sup>1/2</sup>)TiO<sub>3</sub>- system," *Key Engineering Materials*, vol. 928, pp. 69–78, 2022.
- [5] S. Pan, K. Jin, T. Wang, Z. Zhang, L. Zheng, and N. Umehara, "Metal matrix nanocomposites in tribology: manufacturing, performance, and mechanisms," *Friction*, vol. 7, 2022.
- [6] K. Subramani, T. Arunkumar, V. Mohanavel et al., "Investigation on wear characteristics of Al 2219/Si<sub>3</sub>N<sub>4</sub>/Coal bottom ash MMC," *Materials Today Proceedings*, vol. 62, no. 8, pp. 5514–5518, 2022.
- [7] M. Ravichandran and M. Ravichandran, "Influence of AlN particles on microstructure, mechanical and tribological behaviour in AA6351 aluminum alloy," *Materials Research Express*, vol. 6, no. 10, Article ID 106557, 2019.
- [8] M. Honarpisheh and M. Honarpisheh, "Experimental and numerical investigation of process parameters on the residual stresses in the Al-Cu FGM materials," *Experimental Techniques*, vol. 45, no. 5, pp. 601–612, 2021.
- [9] A. Fattah-alhosseini, R. Chaharmahali, M. K. Keshavarz, and K. Babaei, "Surface characterization of bioceramic coatings on Zr and its alloys using plasma electrolytic oxidation (PEO): a review," *Surfaces and Interfaces*, vol. 25, Article ID 101283, 2021.
- [10] D. Srinivasan, M. Meignanamoorthy, A. Gacem et al., "Tribological behavior of Al/Nanomagnesium/Aluminum nitride composite synthesized through liquid metallurgy technique," *Journal of Nanomaterials*, vol. 2022, Article ID 7840939, 12 pages, 2022.
- [11] L. Kang, W. Liu, X. Zhang, and L. Chen, "Evolution of microstructure, texture and residual stress of AZ31 Mg alloy in hot extrusion process," *Materials Research Express*, vol. 8, no. 6, Article ID 066519, 2021.
- [12] I. S. Patil, S. S. Rao, and M. A. Herbert, "Mechanical and microstructural analysis of a AlSi-ZrO<sub>2</sub> metal matrix composite using optimized artificial neural network and experimental data," *Materials Today Communications*, vol. 27, Article ID 102398, 2021.
- [13] O. Güler, T. Varol, Ü. Alver, G. Kaya, and F. Yıldız, "Microstructure and wear characterization of Al<sub>2</sub>O<sub>3</sub> reinforced silver coated copper matrix composites by electroless plating

## Retraction

# Retracted: Nanorobots with Hybrid Biomembranes for Simultaneous Degradation of Toxic Microorganism

### Advances in Materials Science and Engineering

Received 20 June 2023; Accepted 20 June 2023; Published 21 June 2023

Copyright © 2023 Advances in Materials Science and Engineering. This is an open access article distributed under the Creative Commons Attribution License, which permits unrestricted use, distribution, and reproduction in any medium, provided the original work is properly cited.

This article has been retracted by Hindawi following an investigation undertaken by the publisher [1]. This investigation has uncovered evidence of one or more of the following indicators of systematic manipulation of the publication process:

- (1) Discrepancies in scope
- (2) Discrepancies in the description of the research reported
- (3) Discrepancies between the availability of data and the research described
- (4) Inappropriate citations
- (5) Incoherent, meaningless and/or irrelevant content included in the article
- (6) Peer-review manipulation

The presence of these indicators undermines our confidence in the integrity of the article's content and we cannot, therefore, vouch for its reliability. Please note that this notice is intended solely to alert readers that the content of this article is unreliable. We have not investigated whether authors were aware of or involved in the systematic manipulation of the publication process.

Wiley and Hindawi regrets that the usual quality checks did not identify these issues before publication and have since put additional measures in place to safeguard research integrity.

We wish to credit our own Research Integrity and Research Publishing teams and anonymous and named external researchers and research integrity experts for contributing to this investigation.

The corresponding author, as the representative of all authors, has been given the opportunity to register their agreement or disagreement to this retraction. We have kept a record of any response received.

### References

- [1] M. R. A. Refaai, M. N. Manjunatha, S. Radjarejesri, B. Ramesh, R. Subbiah, and N. Adugna, "Nanorobots with Hybrid Biomembranes for Simultaneous Degradation of Toxic Microorganism," *Advances in Materials Science and Engineering*, vol. 2022, Article ID 2391843, 12 pages, 2022.



## Research Article

# Nanorobots with Hybrid Biomembranes for Simultaneous Degradation of Toxic Microorganism

Mohamad Reda A. Refaai <sup>1</sup>, M. N. Manjunatha,<sup>2</sup> S. Radjarejesri,<sup>3</sup> B. Ramesh,<sup>4</sup> Ram Subbiah,<sup>5</sup> and Nahom Adugna <sup>6</sup>

<sup>1</sup>Department of Mechanical Engineering, College of Engineering in Al-Kharj, Prince Sattam Bin Abdulaziz University, Al-kharj 11942, Saudi Arabia

<sup>2</sup>Department of Chemistry, M S Ramaiah Institute of Technology, Bangalore, Karnataka 560054, India

<sup>3</sup>Department of Chemistry, Sona College of Technology, Salem 636005, Tamilnadu, India

<sup>4</sup>Department of Mechanical Engineering, Mohamed Sathak Engineering College, Kilakarai 623806, Chennai 602105, Tamil Nadu, India

<sup>5</sup>Department of Mechanical Engineering, Gokaraju Rangaraju Institute of Engineering & Technology, Hyderabad, Telangana 500090, India

<sup>6</sup>Department of Mechanical Engineering, MizanTepi University, Tepi, Ethiopia

Correspondence should be addressed to Nahom Adugna; [nahom98adugna@mtu.edu.et](mailto:nahom98adugna@mtu.edu.et)

Received 6 May 2022; Accepted 3 August 2022; Published 23 September 2022

Academic Editor: K. Raja

Copyright © 2022 Mohamad Reda A. Refaai et al. This is an open access article distributed under the Creative Commons Attribution License, which permits unrestricted use, distribution, and reproduction in any medium, provided the original work is properly cited.

Nanorobotics is a modern technological sector that creates robots with elements that are close to or near the nanoscale scale of such a nanometer. To be more specific, nanorobotics has been the nanotechnology approach to designing and creating nanorobots. Also, with the fast growth of robotics technology, developing biomaterials micro- or nanorobots, which convert biological concepts into a robotic device, grows progressively vital. This proposes the development, manufacturing, and testing of a dual-cell membrane-functionalized nanorobot for multifunctional biological threat component elimination, with a focus on the simultaneous targeted and neutralization of the pathogenic bacteria and toxins. Ultrasound-propelled biomaterials nanorobots comprised of the gold nanostructures wrapped in a combination of platelet (PL) and Red Blood Cell (RBC) layers were developed. Biohybrid micro- and nanorobots were small machines that combine biological and artificial elements. They may benefit from onboard actuators, detection, management, and deployment of a variety in medical functions. These hybrid cell walls consist of a variety of structural proteins involved in living organism RBCs and PLs, which provide nanorobots with either a quantity of the appealing biological functionality, with bonding and adhesion to the PL-adhering pathogenic organisms (for example, staphylococcus bacteria) but also neutralization of the pore-forming toxins (e.g., toxin). Furthermore, the biomaterials nanorobots demonstrated quick and efficient extended sonic propulsion for total blood with really no visible bacterial growth and mirrored the movements of genuine cell separation. This propulsion improved the robots' bonding and detoxifying efficacy against infections and poisons. Overall, combining this diversified physiological activity of hybrid cellular tissue with the energy propulsion of such robotic systems contributed to the dynamic robotics scheme for effective separation and synchronous elimination of various living risks, a significant step towards to development of a broad-spectrum detoxifying robotic framework.

## 1. Introduction

Micro/nanorobots (MNR) were small-scale controlled devices that can replicate the movements of biological microorganisms by transforming a variety of energy resources

into movements. The diameters of synthetic MNRs range from nanometers to the many hundreds of micrometers. MNR systems, due to their small-scale architecture and propellant nature, have the potential to penetrate hitherto hidden areas of a body and accomplish a specific activity.

Recent advances in nanomaterials and related technologies have accelerated the development of artificial MNR devices for a wide range of biological and medical purposes [1]. In the research, such small-scale robots were known as either micro- or nanoswimmers, nanoengineers, nanomachines, nano propellers, nanopumps, or nanorockets. The next phase of nanomachines is nanorobots. Improved nanorobots would be capable of adapting and perceiving environment stimuli including temperature, lighting, noises, features, and substances to execute sophisticated calculations. By performing molecular construction, they connect, travel, and continue over the work collectively and, to some extent, restore or perhaps even replicate it. Nanotechnology is the study and utilization of items on a scale ranging from 1 to 100 nanometers [2]. The ultimate goal of nanostructures is to create almost any material thing from the ground up by building one molecular at such a time. Although nanotech operations take place on a nano scale, the apparatus or items that are created as part of activities can be substantially larger. Enormous parallelism in nanomaterials produces large-scale effects when multiple simultaneous and complementary nanoscale operations interact to create a greater effect.

Nanorobots at the micro- and nanoscale have increasingly received a lot of attention due to their novel features and capabilities, and also their tremendous potential uses, particularly in healthcare coverage and biotechnology [3]. The block diagram of nanorobots is shown in Figure 1. By transforming locally provided chemical resources or exterior power (e.g., electromagnetic, auditory, or optical) into pushing compressive force, such small-scale smart phones can efficiently resist Reynolds Numbers frequency viscous drag and Brownian motion. Furthermore, the effective propulsion of such man-made miniature robots is linked using earlier unrecognized features such as enhanced gesture control, container towing and discharge, cell migration, collaborative activity, and simple surface functionalization. These qualities, when combined, enable the robots to execute a wide range of activities in a variety of fields, such as cell disruption, active medication administration, noninvasive surgical, environment monitoring, and nanoscale manufacturing and monitoring. Only with the rapid growth of micro- and nanodevices in biology and medicine, developing robots with biodegradable and bioinspired interfaces for favorable interactions and interfaces involving basic biological organisms has become critical [4]. Manufactured nanorobots, for instance, have lately been merged into motile organisms including sperm and bacteria.

The implementation of diversified physiological systems as from cell membrane of the two types of cells, platelets (PLs), and red blood cells (RBCs) into such an only one nanorobot exterior to generate a strong bioinspired nanorobot for multifunctional bio-detoxification and simultaneous expulsion of bacterial infections and toxicants in unique is described here. Pathogens in Gram-positive infectious diseases generally respond by producing a range of hemolytic toxins, known as pore-forming toxins (PFTs), through into circulation [5]. These toxins cause holes development in cell membranes, causing membrane

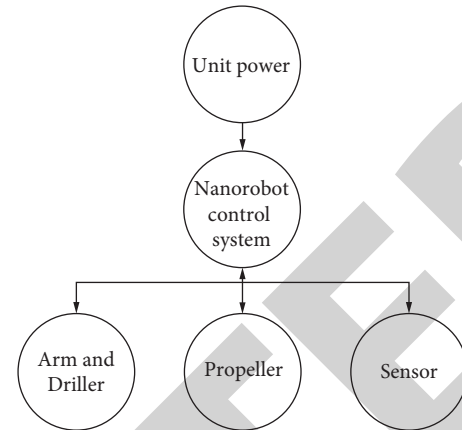


FIGURE 1: Block diagram of nanorobots control system.

susceptibility to change and cellular destruction. This is a significant mechanism of disease pathogenesis that leads to life-threatening diseases in humans.

To obtain an optimum therapeutic response, it would also be excellent to eradicate the hemolytic toxin and the toxin-producing bacteria. The major problem, however, would be that the poisons and bacteria have dramatically varied physicochemical compositions and, as a result, have multiple physiological objectives. PFTs, for example, generally target and attack RBCs, but microorganisms may not associate with RBCs at all; instead, they bond with certain other cellular processes, including such PLs. To address this issue, we reasoned that encapsulating synthesized nanorobots with either a combination of the cellular membrane obtained from RBCs and PLs would result in composite biomembrane-functionalized robotics having membranes of lipid and related roles identical to together RBC and PL substrates [6]. A twofold RBC-PL film coating would provide nanorobots with diverse set of operational molecules, allowing them to perform a wide range of biological activities. As a result, these bioinspired nanorobots were projected to capture and eliminate RBC-targeted PFTs as well as PL-bound microorganisms, which create those PFTs [7]. To put this notion to the proof, we will use a recently advanced cell membrane-coating method to produce a stable and acoustical gold nanowire- (AuNW-) based nanorobot that will be utilized as a demonstration of an energy robot having possible biomedical uses.

Cell membrane coatings have evolved in recent years as a substrate technique that provides a straightforward top technique for imbuing synthetic objects with the extremely complicated capabilities connected to real cellular membranes. Cell membrane-coated nanodevices, in particular, intrinsically replicate the surface features of such source cells and so possess different functions, including disease-relevant targeted capability [8]. RBC coatings, for instance, can concentrate and absorb poisons, whereas PL membranes could attach to infections. Initially, nanorobots were combined with single-cell membranes. The developed bioinspired nanorobots integrated the benefits from both mobile robotics' dynamic mobility as well as the functional diversity of cell membrane films. When compared to analogs

based only on Brownian motion, this connection dramatically expedited detoxifying operations. RBC membrane-coated robotics, for instance, have exhibited efficient and simple extraction of harmful microorganisms and other pollutants (for instance, nerve compounds) in biological materials [9]. Only single-cell membranes are connected using nanorobots thus far, giving them both a particular biological process of respective compartments but deficient multifunctional capabilities. An incorporation of varied film capabilities from a various type of cell with individual mobile nanodevices can lead to wider and much more durable applications in which the nanorobots manage numerous difficult therapeutic activities in a specific treatment.

This created RBC-PL hybrids membrane-functionalized energy nanorobots (abbreviated “RBC-PLrobots”) by encapsulating auditory AuNW robotics using composite membrane produced both RBCs and PLs, enabling instantaneous identification and elimination of the harmful microorganisms as well as toxins produced by bacteria. A framework AuNW chemical precipitation approach was used to create the biomimetic robotics, which was then cloaked utilizing a dual-cell membrane-cloaking approach [10]. A dual-membrane covering contains a wide range of structural proteins involved in human RBCs and PLs, providing a nanorobot with a wide range of biological capabilities. Combining the biochemical processes of combination membrane surface to the energy transportation of ultrasound- (US-) propelled portable nanorobots contributed to such an energetic bioinspired multifunctional detoxifying framework that regionally improved mass transfer and greater dimensional accidents with biological properties, potentially representing a one-of-a-kind device in circumstances where the externally applied mixture is not feasible or preferred.

The RBC-PL-robots propelled themselves rapidly and efficiently in the whole blood, without any visible biofouling, and replicated the motion of normal cell progression [11]. These mobile nanorobots exhibit improved binding to pathogens that adhere to PL as well as efficient elimination of pathogen-secreting toxins. Utilizing methicillin-resistant *Staphylococcus aureus* (MRSA), USA300 compresses as a design pathogen and toxin, and extra PFTs deposited through MRSA microbes as design toxins. Similarly, RBC-PLrobots illustrated instantaneous rapid purification of multiple bio-contaminants existing in the identical specimen within seconds. The dual-membrane-functionalized nanorobots’ enhanced bioinspired and fuel-free propulsion characteristics could be exploited for rapid bacterium separation and effective neutralizing of PFTs in range of the biodefense and biomedical settings [12]. This dual-cell membrane coating is a different and efficient method for functionalizing nanorobots for prospective applications in sectors such as targeted medicine delivery, immunological regulation, and detoxifying. While acoustic propulsion is chosen as a fuel-free energy propulsion system, the disclosed dual-cell membrane coatings approach is easily extended to additional kinds of the nanorobots with various propulsion methods.

## 2. Related Work

Ultrasonic with sufficiently small amplitudes, notably within MHz frequency range, causes little damage to biological materials (including tissues and cells) and offers a great way to power micro-swimmers. This paper provides a current region summary of ultrasonic-assisted driven micro- and nanotechnology from the standpoints of biochemistry, economics, and materials engineering. A better concept of ultrasonic propulsion of micro/nanorobots is presented first. Secondly, the configuration concepts for micro/nanorobot ultrasonic propulsion were categorized. Following that, the proposed methods of ultrasound micro/nanorobots are thoroughly described. The principles of ultrasonic propulsion with nanorobots will be next investigated and explained. Following that, the hybrid movement of attractive, optical light, and catalytically determined nanorobots using accelerated actuators was described and addressed. Following that, this paper identifies important transcription prospective implications of ultrasound-mechanical functioning micro- and nanorobots in medicinal, ecological, and other disciplines. Finally, this paper provides a perspective on the development of ultrasound-driven nanorobots [13].

Molecules, extrinsic influences, or even motile microorganisms can manipulate and navigate micro- and nanoswimmers in a variety of fluid settings. Several researchers have chosen magnetic properties also as activation actuating sources due to the benefits of this actuation method, which include remote and spatiotemporal management, fuel-free operation, a high level of customization, modifiability, renewability, and adaptability. This overview covers the core ideas and benefits of magnetism micro/nanorobots (abbreviated “MagRobots”), and also basic information on the electromagnetic field and magnetic fluids, electromagnetic manipulating settings, magnetic field topologies, and symmetrical shattering tactics for the organization must be collected. These ideas are addressed to explain the reactions of micro/nanorobots with electromagnetic waves. Actuation processes of flagella-inspired MagRobots and surface travelers (ground movements), implementations of the electromagnetic field in all other propulsion strategies, and electrical conduction of micro- and nanomachines beyond signal were discussed, accompanied by fabrication methods for circular, helix, adaptable, wire-like, and biomaterial MagRobots. MagRobot applications include focused drug/gene administration, cell manipulations, therapeutic procedures, biopsies, biofilm interruptions, imaging-guided distribution, pollution clearance for pollutants removal, and (bio)sensing. Furthermore, present obstacles and prospects for mechanically propelled tiny motor performance are explored [14].

The ineffectiveness of existing standard therapies for infectious diseases raises mortality rates in the country. This suggests drug-free enzyme-dependent nanomotors for such control of the contaminations and bladder infections to address this worldwide health issue. This creates nanomotors out of mesoporous silica nanoparticles (MSNPs), which have been synthesized and characterized with lysozyme (L-

MSNPs), urease (U-MSNPs), or hydrolase and lysozyme (MMSNPs), and utilizes them towards nonpathogenic planktonic *E. coli*. Because of a bioprocess of urea producing  $\text{NH}_3$  and  $\text{NaHCO}_3$ , which also accelerates U-MSNPs, L-MSNPs had the greatest antibacterial activities. Furthermore, U-MSNPs at levels greater than 200 g/mL significantly reduced 60 percent of a biofilm density of such uropathogenic of *E. coli* strain. As a result, this research presents proof of the concept evidence, which is enzyme-based nanomotors that can combat infectious illnesses. By selecting relevant macromolecules, this strategy could eventually be expanded to different types of disorders [15].

The continued growth of personalized medicine equipment has resulted in the creation of identity nano/microdevice's ability to execute biomedical functions on a limited scale. This paper aims to showcase the most recent breakthroughs in ultrasonic powered micro/nanorobots, as well as provide insight into the obstacles and potential applications. Microrobots have now been powered by several forms of acoustic environments. Focused ultrasound (FU) may concentrate acoustic waves in a particular zone, making it ideal for applications requiring a high penetrating or targeted actuator. Furthermore, standing wave ultrasonic (SWU) robots that operate on nodal aircraft stake exhibited a variety of advanced biomedical functions that are appropriate for the lab-on-a-chip systems. In conclusion, surface waves ultrasonic uses tunable resonance components that respond to certain frequencies, and it has considerable potential for in vivo uses [16].

With the increased health danger of antimicrobial resistance, nanomaterials have already been widely investigated as a substitute. It is anticipated which antimicrobial nanoparticles could attack microorganisms through many routes at the same time, overcoming resistant bacteria. Another exciting prospective application is using nanomaterials for antimicrobial nanomedicines to circumvent bacterial protective processes. The active targeting of nanotechnology is a common bacterial method of treatment, particularly in intracellular illnesses of macrophages. Additionally, tailored targeting improves antibacterial activity while decreasing side effects. The purpose of this paper is to address the benefits, drawbacks, and limitations of nanotechnology within the context of antibiotic targeting methods as enhanced tools for treating infectious diseases [17].

Inflammatory cells are quickly drawn to infection sites or damaged after inflammation when they overcome physiological limits all around the infection area and penetrate deeper into organs. Additional cells, including erythrocytes, epithelial cells, and cell lines, are also important in host defense and tissue healing. Nanoparticles have recently been used to deliver medications to regions of inflammation. Nanotechnology disguised as a cellular membrane, for instance, is a unique drug-delivery technology, which may interact only with a immune response and has a significant possibility for the treatment of inflammatory. Inflammatory could be controlled by encapsulating medications into cellular membranes generated from diverse cells engaged in inflammatory responses. There were also the synthesis,

characterization, and characteristics of numerous forms of cell membrane-camouflaged bioinspired nanoparticles [18].

### 3. Materials and Methods

**3.1. Biohybrid Micro/Nanorobots.** The various kinds of biomimetic micro- and nanorobots are shown in Figure 2. The connections have amazing specificity among balancing oligos for a two-fold spiral making DNA viable construction substantial, as well as the patterns of branch connections among DNA double helices allowing for the personality of complex 3D objects. Maier and colleagues described the creation of magnetic micro-swimmers using DNA-based flagellar bundling [19]. The DNA flagella are connected to magnetic iron oxide microscopic particles (1  $\mu\text{m}$ ) via complementing DNA strand hybridized, resulting in biohybrid magnetism microrobots powered by such a homogenous magnetic field revolving parallel to a swimming orientation. DNA nanorobots have demonstrated significant promise for tumor-targeted prescriptions and vaccination for accurate cancer (immune) treatment. Nonetheless, their poor stability within the biological environment may lead to inadequate circulation and bioavailability, necessitating additional attempts to improve their susceptibility to harm.

Enzymes were focused on enhancing a wide variety of metabolic purposes in biological organizations. Enzymatic catalytic comprises a transition of reactant (substrate) together into products, which is followed by the flow of energy [20]. The automatic properties generated by the enzymatic processes could initiate directional enzyme propulsion about substrate differences. As a result, restraining enzymes upon an exterior of the particles or adhering enzymes to either strong support can result in self-propelled vehicles or fluid motors with a wide range of interesting uses. Self-propelled cruise missile micromotors have been developed using metal-organic frameworks (MOFs), which compress cells also as generators and poly ethyl methacrylate such as hydrophobic/hydrophilic sequence element, pH-responsive, resulting in rising and down-vertical movement managed by resistance [21]. On catalysis and urease-coated lipid nanoparticles engines, colleagues observed both positively and negatively cell migration. Hortelao and colleagues used positron emission tomography (PET) to detect, measure, and evaluate the swarming activities of urease-powered including the selection in a study conducted. Adaptive swarming mechanics and real-time images monitoring were predicted to produce significant advances in biological nanorobotics and open the path for therapeutic and diagnostic technologies.

Manufactured micro/nanocarriers for in vivo drug administration, as foreign invaders, can readily activate passive immunity clearances, enhance storage effect to reducing the interfacial tension and reticuloendothelial systems, and ultimately produce low treatment effectiveness. To address these challenges, a cellular membrane cloaking technique has recently been proposed as a unique surface construction tool from the perspectives of physiology and immunology, demonstrating effectiveness in boosting the in vivo activity of synthesized micro/nanocarriers.

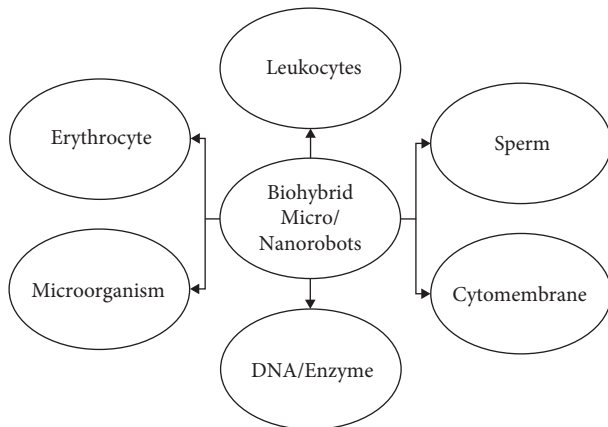


FIGURE 2: Different kinds of biohybrid micro/nanorobots.

Cell tissue micro/nanomotors can not only convert external energy into directed, independent movement, but they also inherit the innate characteristics of the cellular membrane, such as the ability to be guided by physical forces and biochemical fuel. Wu and colleagues built accelerated nanomotors by the combining biocompatible Au nanowire engines with RBC nano vessels, and they eventually formed magnetic coiling Ni/Au/Pd nanorobots shrouded in the plasma platelet cytoplasmic membrane (PLs) [22]. These biomimetic nanorobots might propel efficiently within this blood for an extended period. They also built ultrasound Au nanowire robotics that was disguised with composite RBC and PL coatings as in Figure 3. These biohybrid nanorobots displayed quick, efficient, and long-lasting ultrasonic propulsion with whole blood, while there was no substantial biofouling. Through the bio-hybridizing strategy, the created micro/nanorobots were able to gain intricate structures and capabilities, offering the potential for completing complicated healthcare tasks, which can be performed merely by the power to manipulate nanoparticles.

**3.2. Fabrication of Nanorobots.** A standard membrane-template electrochemical deposition approach was used to create AuNW robotics. To act as an electrode surface, thin gold layer is initially spluttered solely on a single surface of the porosity PC membranes templates with 400 nm diameter micropores. The membranes were put together in the Teflon plated cell, using aluminum foil acting as electric interaction for a following electrodeposition [23]. Utilizing a charge of 0.1 C and a voltage of 0.90 V (against an Ag/AgCl conductor material and a Pt cable as counter electrode), a disposable silver layer was successfully deposited into a branching region of the PC film membrane. Following that, Au is plated by using commercially gold mounting resolution at 1.0 V (against Ag/AgCl) with such a 1.5 C charging. Manual polishing with 3 m to 4 m aluminum dust was used to eliminate the spluttered gold. The silver protective layer is eliminated by chemical treatment with an 8 M  $\text{HNO}_3$  solution-soaked cotton tip application. The elimination of such a sacrificial template aided in the formation of the cone shape at one side of a gold wire nanorobots. Generated

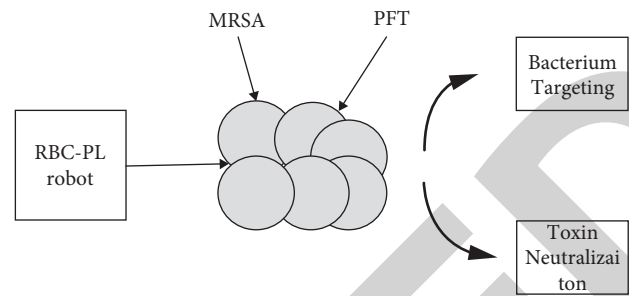


FIGURE 3: Hybrid RBC-PL robots.

AuNWs ranged in length from 1.5 to 2  $\mu\text{m}$ . PC membranes were again destroyed for 30 minutes in a pure methylene hydrochloric acid solution; this procedure was executed twice to entirely liberate the AuNWs. The generated nanorobots are centrifuged at 8000 rpm for 5 minutes before being washed twice using isopropanol, twice using ethanol, and 3 times using distilled water.

The nanorobot suspension was sonicated at 8000 rpm for 3 minutes among washing stages. Until usage, all AuNWs are kept in 1 ml of distilled water at ambient temperature [24]. A similar procedure was used to create magnetic robots. A disposable silver coating was successfully deposited at 0.1 C charge and 0.90 V voltage (against an Ag/AgCl electrode material and a Pt wire as both a working conductor). Following that, Au is mounted at 1.0 V with a 0.6 C charge, accompanied by Ni electrodeposition at 1.3 V with a 0.4 C charge. The Au also was successfully deposited repeatedly (1.0 V and 0.6 C), and the remainder of the technique was carried out as previously described.

**3.3. Preparation of RBC-PLs.** RBC-PL robots are created by encapsulating AuNW robots using RBC-PL plasma blood membranes. Human RBC membranes were isolated from the whole blood using the Bio reclamation IVT method, as previously described. To summarize, the entire blood was centrifugation at 800g for 5 minutes at 4°C, and the serum and buffy coat were removed. After that, the residual RBC pellet is processed using hypotonic media to eliminate a hemoglobin [25]. The pink pellets of RBC membranes were produced following three hypotonic treatments and wash processes and maintained at 80°C till usage. Human's PL cell membranes are created using previously published procedures utilizing PL-rich plasma. After generating refined PLs, PL membranes were created by repeating the freeze-thaw procedure and centrifuged in PBS solution with small-molecule tablet devices. Suspended aliquots were freezing at 80°C, recovered at ambient temperature, and compressed through centrifuged at 4000g for 3 minutes.

The PL membranes were immersed in water and kept at 80°C after three washing. After isolating both RBC and PL materials, hybrid layers were created by fusing separate membranes (1:1 protein mass ratio) for 5 minutes under ultrasonication (42 kHz, 100 W). In addition, the surfaces of the AuNWs were changed overnight using 0.25 mM MPA (Sigma-Aldrich) to inject negative responsibilities into the surface of gold. Later fermentation, AuNWs are rinsed three



times using the deionized solution, with each washing procedure separated by centrifuging (8000 rpm, 3 min). Following a 5-minute ultrasonication, the MPA-AuNWs were covered also with resulting hybrids membranes (42 kHz, 100 W).

**3.4. Characterization of RBC-PL Robot.** SEM photos of a bear with RBC-PL robots were captured using a Philips XL30 atmospheric scanning electron microscopy (SEM) and a 10 kV accelerating amplitude. To establish the existence and cloak of RBC-PL combination membranes upon that ground of AuNW robots, we used labeled RBC materials using DiD (oscillation frequency = 644/665 nm) and PL membranes using FITC (oscillation frequency = 495/525 nm; Sigma-Aldrich) before coating on the AuNWs. Descriptions of microscopic examination were acquired with an EVOS FL microscopy using 20 and 40 objectives lens.

Thus, we separated exposed robot and RBC-PL robots ( $20 \text{ mg}\cdot\text{ml}^{-1}$ ) and reconstituted them 3 times to evaluate the overall protein concentration of the RBC-PL-robots [26]. Afterward, the RBC-PL-robots are subjected to an acoustic signal for 5 minutes, the number of protein structures on the nanorobot surfaces was quantified using a BCA colorimetric assay (Sigma-Aldrich). In summary, the purple-colored reactions result of this analysis is generated by the chelation of two compounds of the BCA including a one cuprous particle, and then this water-soluble combination has a high transmission density at the 562 nm, which is practically linear as enhanced protein quantities. Gel electrophoresis has also been used, accompanied by protein staining using Coomassie blue. In a lithium dodecyl sulfate specimen preparation of buffer, RBC-PL hybrid membranes and RBC-PL robot specimens comprising equal overall proteins are generated (Invitrogen). Using only a Novex XCell Sure Lock Electrophoresis Equipment, the specimens were segregated on 4 to 12% of bis-tris in 17-well MiniGelto Mops successively buffer. Finally, protein sections are dyed following the constructor's instructions.

**3.5. Microorganisms Based on Hybrid Nanorobots.** Bacteria, one of the key categories of microbes, could play a close and dynamic role in the evolution of human health and disease. Bacteria were used as potential delivery methods for a variety of biological applications. Bacteria-created micro-robot stake that is usually increasingly utilized for the targeted medication distribution schemes through the combination of biotechnology and biohybrid methods. This work created biomimetic micro-swimmers powered by motile *E. coli* MG1655 bacteria (dubbed "bacteria both") for bioadhesion of epithelial cells as well as targeted medication administration to epithelial cells within urine or digestive tracts [16]. Because bacteria possess fundamental cell migration, these bacteria can exhibit group chemotactic activity. Table 1 summarizes these tactics as well as the primary physical process underlying them [27]. They also developed bacteria-driven micro-swimmers that were equipped only using anticancer medication DOX and magnetic  $\text{Fe}_3\text{O}_4$  nanomaterials. A flowchart depicting the procedure of

employing CNRS to execute a function in tissues is shown in Figure 4.

**3.6. Ultrasonic Equipment and Propulsion Research.** The acoustic component was made up of a piezoelectric sensor (10 mm circumference, 0.5 mm depth), which was connected by nonconducting epoxy glue to the bottom center point of a metal plate (50 mm by 50 mm by 0.94 mm); the metal plates were inoculated with 240 m Kapton recording protecting coating, which contained a circular storage tank in the center (5 mm) [28]. To preserve the specimen and cover the reservoirs for US reflections, a glass slide was employed. The constant US sine wave is transmitted using a piezoelectric transducer in conjunction with an Agilent 15 MHz arbitrary waveforms generation and a handmade signal conditioning.

All studies were carried out by combining the RBC-PL robots only using appropriate broadcasting (aqua, PBS, and entire blood) or specimens and employing a continuous sine waveform with such bandwidth of 2.66 MHz and an external rating of 2.0 V. Videos are shot using a CoolSNAP HQ2 camera featuring 20 and 40 subjective lenses (except else specified) and obtained at 10 times per secs by utilizing MetaMorphof 7.1 program. Image software, as well as the Fluid Trace Plugin, was used to do the particles displacement image merging.

**3.7. Binding and PL Isolation Adhering Pathogens.** Utilizing MRSA USA300 (American Types Cultures Group) as a model pathogen, RBC-PL-robots were tested for complex formation and quick separation of PL-adhering infections. Bacteria were maintained overnight at  $37^\circ\text{C}$  using a tryptic soy buffer (TSB) medium. In a mechanical shaker, a solitary colony was injected into the TSB medium at  $37^\circ\text{C}$ . Overnight growth is relaxed in the TSB material at a 1:100 dilution for 3 hours at  $37^\circ\text{C}$  with agitation. RBC-PL-robots ( $10 \text{ mg}\cdot\text{ml}^{-1}$ ) are combined with the bacterial culture ( $5 \times 10^8$  of CFU  $\text{ml}^{-1}$ ) and maintained for 5 mins in a US pitch setting (2.66 MHz and 2.0 V). Following the establishment in the United States, the robots were recovered by extraction, and the adhering bacterium was preserved using formalin and colored with DAPI.

**3.8. Concurrent Bacteria Removal and PFT of Bacteria Secreting.** To assess the simultaneous detoxifying effect of the RBC-PL robots, two aliquot parts of the MRSA USA300 bacterium within the same mixed suspension were handled with the RBC-PL robots and attended an unprocessed cells regulator [29]. Earlier, executing an automaton procedure, the OD600 and hemolysis 5% of aliquots by both MRSA compounds were characterized. Following that, magnetically, RBC-PL-robots ( $10 \text{ mg}\cdot\text{ml}^{-1}$ ) were introduced to a bacterial culture and exposed to a US area for 5 mins (2.66 MHz and 2.0 V). The RBC-PL robots are magnets isolated after cell interruption following the robot treatments. The issues of health and illness sample and the untreated control specimen also were cultured under the same circumstances for 10 hours.

TABLE 1: Swimming microorganism mechanism and strategy.

Strategy	Types of microorganism	Mechanism of reorientation
Reverse and flick	Single flagella	A buckling imbalance causes a flick within flagellum hooks.
Modulation of speed	Unidirectional rotation of flagella	Flagella spinning velocity of acceleration or deceleration
Mastigonemes	Flagellates	The radial drags coefficient of flagella carrying mastigonemes changes
Helical-path of swimming	Eukaryotic flagella	The spinning velocity of a cell's surface varies.
Tumbling	Multiflagella	Reversal rotation of flagella
Complex flagella	Peritrichous flagellates	In rotations, the hydrodynamic structure of a flagella bundle is compromised.

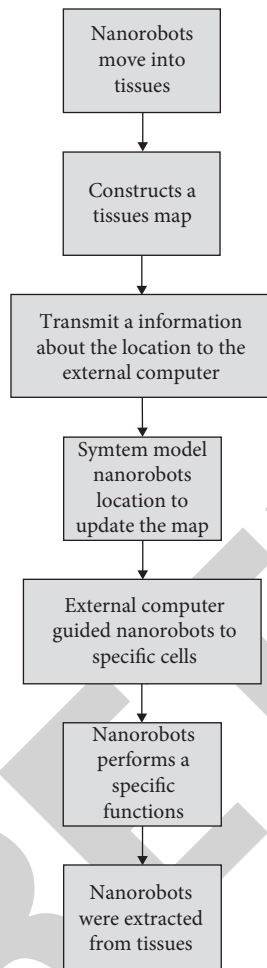


FIGURE 4: Flowchart for nanorobots into tissues execution process.

The  $OD_{600}$  from equally bacterial isolates is measured at every hour for first 6 hrs, then each 2 hours again until research ended. Parallel to this, 50-l dilutions from both bacteria specimens are obtained and centrifugated (13,200 rpm, 5 min), with the suspension being centrifuged saved to complete the hemolytic experiment (5% RBC solutions plus toxin, 30 min at 37°C). Comparative hemolysis rates are computed using the transmittance acquired from 5% RBC solutions deionized for 5 minutes and 100% hemolysis. All hemolysis experiments were carried out in the condition of 200 nM 1,4-dithiothreitol (Sigma-Aldrich).

**3.9. Binding and PFTs Neutralization.** Employing toxin as a modeling toxin, RBC-PLrobots were assessed as toxin deception that collects and destroys PFTs. Constant volumes of commercial toxin (1.7  $g\text{ml}^{-1}$ ; IBT Bio services) were combined using RBC-PL robots (10  $mg\text{-ml}^{-1}$ ) and maintained for 5 minutes below a US field (2.66 MHz and 2.0 V). Following the US procedure, the combined mixture was prepared to 5% of pure RBC mixture and was placed at 37°C for 30 minutes. Following this treatment, the 5% of RBC suspension is sonicated, and the optical density of resulting at a 540 nm was determined to estimate the extent of hemolytic [30]. The bacterial suspension in a TSB solution at 1:100 concentration restarted overnight at a 37°C with trembling for additional 8 hrs to complete the studies using toxin naturally released from MRSA USA300 bacterium. The cultural supernatant is collected by centrifuging the bacterial culture at 5000g for 5 mins. For 5 mins, we exposed 50 l of the bacterial suspension intermediate supplemented with concealed PFTs using a US RBC-PL nanorobots (10  $mg\text{-ml}^{-1}$ ; 2.66 MHz and 2.0 V) and other controls. Following treatments and centrifuge, the residual from every sample was obtained, and the percentage of hemolysis was assessed.

## 4. Result and Discussion

**4.1. RBC-PL Robots Preparation.** RBC-PL-robots were made using a mix of template-assisted electrodeposition and cell membrane-cloaking procedures. An infrastructure facilities electrochemical deposition approach (see Materials and Techniques) was used to create the AuNW robots, which consisted of gold depositing inside the nanopores (400 nm diameter) of the polycarbonate (PC) membrane, membrane disintegration, and discharge of a resultant AuNWs. Before barrier application, a AuNWs' surfaces were changed using 3 mercaptopropionic acids (MPA). RBC-PL hybrid membrane-derived particles were created in parallel by fusing the Erythrocyte and PL membrane throughout a 5-minute ultrasonic treatment. The generated RBC-PL-vesicles were ultrasonically mixed with MPA-modified AuNWs for 5 mins, culminating in RBC-PL-vesicles with a wide range of biological capabilities. The large surface charge of the nanoscale RBC-PL-vesicles made them prone to attach and merge to the AuNW nanomachines, lowering the state's free electricity. The binding of the RBC-PL composite membrane onto the AuNWs was further improved by ultrasonic agitation. The fusion technology allows the hybrid membrane' bilayer architecture to be preserved, while their protein



activities were preserved. Furthermore, the outside aspect of the hybrid membrane was significantly additional negatively charged than inner surface due to the huge asymmetrical negatively charged among the ectoplasmic and cytoplasm interfaces. Different methods were used to evaluate the RBC-PL robots that were manufactured. Scanning electron microscope (SEM) photographs of bare AuNW robots and an RBC-PL robot, both with a width of 400 nm and a range of 1.5 to 2.0  $\mu\text{m}$ , are shown here. Bare AuNW and asymmetrical structure of robots with concave end created by the template's electrode position are seen in SEM pictures. Instead of being carried out as aggregation by acoustic transmission or flow pressures, these architectural asymmetries enabled each nanometer to transform the auditory constant streaming created across the nanowire's surfaces into axial movement with an autonomous direction.

**4.2. RBC-PL Robots' Characterization.** Different methods were used to evaluate the RBC-PL robots that were manufactured. SEM photographs of a simple AuNW robot and RBC-PL robot, together with width of a 400 nm and range of 1.5  $\mu\text{m}$  to 2.0  $\mu\text{m}$ , are shown here. The asymmetrical structure of the robots with a concave end created by templates electrodeposition is seen in either SEM pictures. Instead of being carried out as aggregation by acoustic transmission or flow pressures, these architectural asymmetries enabled each nanometer to transform the auditory constant streaming created across the nanowire's surfaces into axial movement with an autonomous direction. Layer thickness and dimensionality are also important considerations in converting acoustic potential energy into kinetic energy, as only objects manufactured with moderately dense materials and diameters greater than 500 nm have indeed been found to exhibit independent movement. Even though there are a variety of fuel-free microrobots and alternate solution acoustic propellant processes premised on wave propagation, broadcasting, or bubble delamination, the current use of sonically catapulted nanostructures generated synergism effects by increasing mass transfer while preconcentrating the specimen in an acoustic antigravity plane, thus also boosting positional clashes between both the nanorobot and the biomedical focus. Around RBC-PL-robot, a thin layer similar to the membrane covering is seen.

The proteins composition of the Erythrocytes robots from the dual-cell membranes covering was also studied. The RBC-PL robots are periodically rinsed using phosphate-buffered water (PBS) towards eliminate unprotected surfaces before being subjected to the acoustic signal for 5 minutes, and the quantity of protein structures on the nanorobot surfaces was quantified using a bicinchoninic acid (BCA) protein analysis. Using the same robot's dosage, the erythrocytes robots had a crude protein of 0.6  $\text{mg}\cdot\text{ml}^{-1}$ , compared to detectable crude protein for the plain nanomachines. The cleaned RBC-PL vesicles and RBC-PL robots' protein profiles are also revealed by electrophoretic and protein labeling. All around erythrocytes robots, a fine layer similar to the membranes coat could be seen. The proteins composition of the RBC-PL-robots from dual barrier

covering was also studied. The RBC-PL-robots were periodically rinsed using phosphate-buffered saline (PBS) to eliminate unprotected membrane before being subjected to the acoustic signal for 5 minutes, and the quantity of protein complexes on the nanosystems surfaces was quantified using a bicinchoninic acid (BCA) proteins analysis. Using the same robots' dosage (20  $\text{mg}\cdot\text{ml}^{-1}$ ), the RBC-PL-robots had a crude protein of 0.5  $\text{mg}\cdot\text{ml}^{-1}$ , compared to negligible crude protein for the bare robotic systems. Moreover, the pure RBC-PL vesicles and RBC-PL robots' protein profiles are revealed by electrophoretic and protein labeling.

#### 4.3. RBC-PL Robots Properties on Propulsion Performance.

When evaluated in the whole plasma, however, the naked robots had significantly slowing propelling, with a distance of 10  $\text{m}\cdot\text{s}^{-1}$  that was practically independent of incubating duration (immediately after combining and after 1 hr development in a blood) as in Figure 5(a). The robot slowed mobility is due to extensive proteins contamination. When marinated in plasma, nevertheless, the erythrocytes robots only slowed somewhat, as evidenced by the 4 s monitoring trajectory in Figure 5(b). Table 2 shows the comparison of bare robots' speeds. Even though the blood volume had a minor effect on the erythrocytes' propelling, the robotic mobility in this complicated biological microenvironment stayed active during the 1-hour operations. The RBC-PL robots' propulsive efficiency and antibiofouling capabilities were calculated by examining the locomotion speeds of untreated AuNW robotics and erythrocytes robots in water and the whole plasma.

Even though the turgor pressure had a minor effect on the RBC-PL-robots' movement, the robotic propulsion in this complicated biological microenvironment stayed active during the 1-hour procedure. Altogether, the findings show that erythrocytes hybridization membrane natural surface protein and activities permitted the bioinspired robotic systems to have an effective antibiofouling ability or effort in complicated physiological liquids constantly.

#### 4.4. Binding and Isolation.

The biomimetic nanorobots' detoxifying capability was critically evaluated after the robotic architecture and US pulsion were characterized. The RBC-PL-robots had first been tested for complex formation and quick separation of infections adhering to PL. The attachment of microorganisms to a PL is thought to be a key step in the development of the infectious endocarditis, and PL-bacterium connections have also been linked to bacterial resistant escape and septicemia. MRSA USA300, a variant of MRSA that expresses a serine-rich adhesin for PL, has been used as a prototype PL-adhering infection in this work. MRSA USA300 was labeled with DAPI, and the normalized fluorescence spectroscopy was computed and matched to other control experiments as in Figure 6. Neutral comparisons included PBS, simple nanorobots (before membrane of cell covering), and RBC nanorobots (covered through RBC membrane), all of which had low fluorescence intensity due to a lack of bacterial colonization. MRSA USA300 cultured with erythrocytes robots under steady-

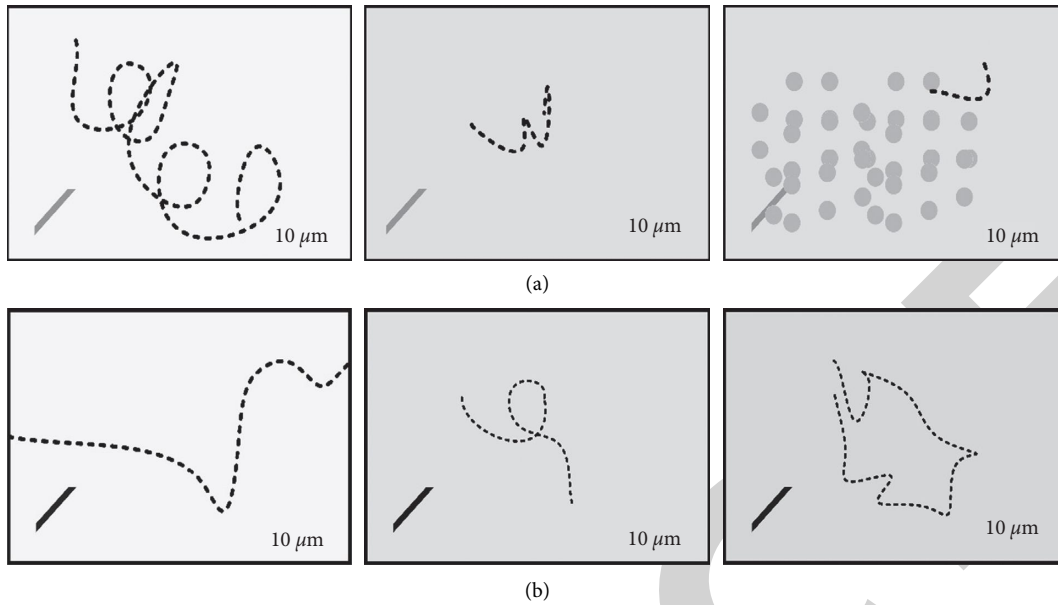


FIGURE 5: Performance of propulsion and RBC-PL robot's antibiofouling belongings.

TABLE 2: Comparison of the bare robot's speed using RBC-PL robots.

Parameter	Water	Blood (0 hr)	Blood (1 hr)
Bare robot	58	15	10
RBC-PL robot	55	40	35

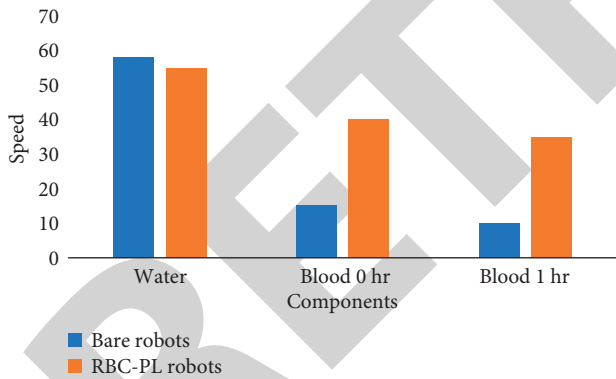


FIGURE 6: Bare robots speed comparison.

state conditions or with erythrocytes showed low fluorescent intensity distribution. Whenever DAPI-stained MRSA bacterium was incubated with US-propelled RBC-PL robots (vi) or PLrobots (vii), covered simply using PL membrane, and employed as a control treatment, a significant increase in absorption spectra was detected, indicating the growth of bacterial identification and binding of the PL membrane surface. We showed that changes in MRSA regarded the RBC-PL robots as having 3.5-fold uptick on DAPI absorption spectra when associated to the rigid equivalents, denoting the significance of US propellant for quick microbes' solitude due to the enhanced dimensional colliding

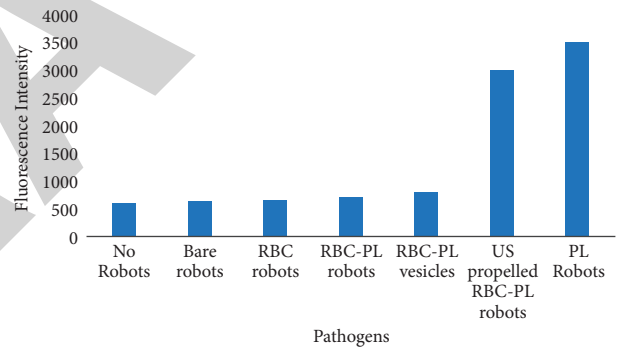


FIGURE 7: DAPI-stained normalized fluorescence intensity.

between RBC-PL nanorobots and microbes below the auditory ground. Ultimately, these findings highlight an advantage of using US-propelled biomimetic robotics to isolate PL-adhering bacteria like MRSA quickly and selectively.

It is imperative to develop appropriate neutralizing-toxin techniques, and it has been shown that inhibiting toxins can lower the severity of aurous infestations. To see if the RBC-PL-robots could detoxify the toxin, researchers combined a set amount of concentrated toxin ( $1.7 \text{ gml}^{-1}$ ) with them and maintained them being used for 5 mins. An assorted solution was extra to a 5% pure RBC phosphate-buffered saline at  $37^\circ\text{C}$  for 30 mins. The 5% RBC suspension was sonicated after this incubation, and the absorbance of the sample was evaluated at 540 nm to quantify the amount of hemolytic anemia. The absorbance readings produced from a 5% erythrocyte liquid soaked in distilled water for 5 minutes were taken as 100% hemolysis, allowing the relative hemolysis percent of all the specimens to be calculated in Figures 7 and 8. In Figures 8(a) and 8(b), the A, B, C, D, and E are represented as PBS, static RBC-PL robots, US-propelled RBC-PL robots, US-propelled RBC robots, and

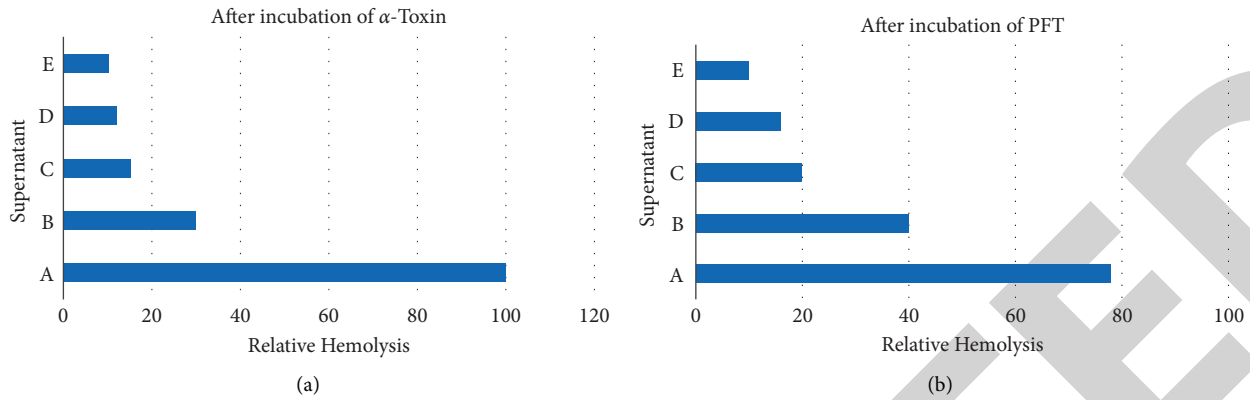


FIGURE 8: (a) After incubation of  $\alpha$ -toxin. (b) After incubation of PFT.

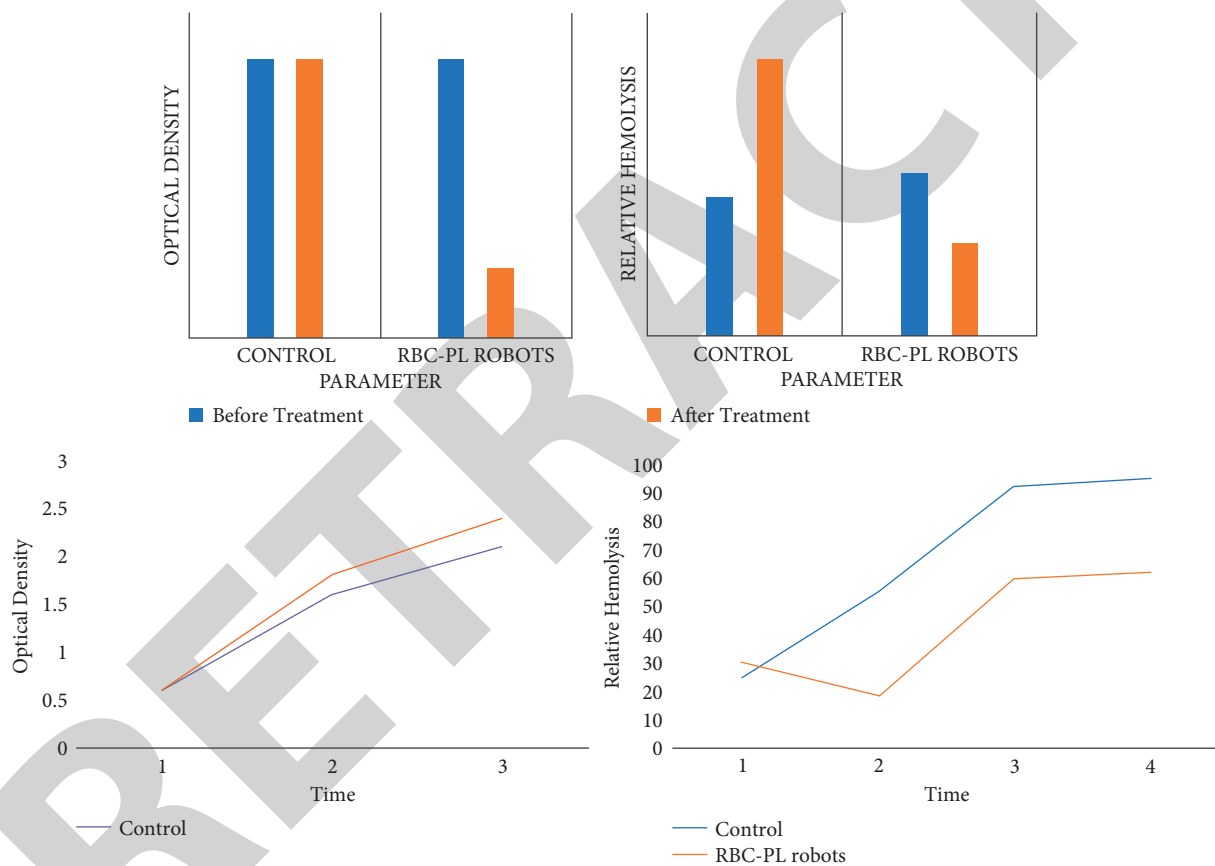


FIGURE 9: MRSA microorganisms and MRSA-secreting PFTs are removed in the presence of RBC-PL-robots.

tracking. Positive control was the precipitate of erythrocytes treated with free-toxin at the same dose, which provided percentage hemolysis of about 100%. When utilizing US-propelled erythrocytes robots in the toxin liquid, though, there was significantly less anemia (5.5%). These findings validated the membrane-covered robots' potential to adhere to toxin and showed that effectiveness on US propelled in a toxin solution expanded an amount of the robot-toxin interactions, resulting in improved toxin ingestion and neutralizing.

The RBC-PL-robots' combined propelling could drastically expedite their interaction with the PFT combination

inside an acoustic field, increasing the neutralizing phase. Again, for the balance of the samples, a trend in hemolytic Proportion was seen, which was similar to that observed with commercialized toxins as shown in the figure. In the various control studies, the absorption spectrum of hemoglobin in the blood is followed by incubation using purified, commercialized toxin or a mixture of the bacteria secreted of PFTs as shown in the figures. Finally, the findings of Figure 9 show embedding RBC-PL films onto AuNW robotics and driving them under a US field performance in dynamical detoxifying automobiles that could effectively extract PFTs from their surroundings.

The issues of health and illness sample and the untreated specimen were then cultured in the same circumstances for ten hours. To create the corresponding curves, the  $OD_{600}$  of each sample was measured each hour for the first 6 hours and subsequently every 2 hours until the completion of the research. Simultaneous to the hemolytic experiment, the aliquot part of bacterial specimens is taken and drained, with a supernatant saved for use in the experiment. At 0 hours, both OD and hemolytic anemia principles in a RBC-PL-robot sample reduced significantly, as shown in orange columns of the figures. When compared with the control group specimen, the optical density and hemolytic anemia inside the robot-treated specimen were 3.1 and 2.2 times lower correspondingly as shown in the figures. From these findings, we can illustrate the RBC-PL-robots' potential to detoxify quickly and effectively since they could bind to MRSA germs while also neutralizing released PFTs from the same specimen in a specific treatment phase.

## 5. Conclusion

This research focused on using dual cellular membranes to change synthesized nanorobots as an adaptable technique for combining normal and artificial biocomposites to construct bioinspired robotics. The following points were made from investigated manuscripts. The combination of a hybrid cellular membrane and robotic devices results in a potent stage for an extensive variety of biomedical purposes. A bioinspired RBCPL robots presented under this proof-of-concept research, in the example, comprised an acoustical AuNW robot wrapped in RBC-PL hybridization materials. The resultant bioinspired energy robotics provides a one-step detoxifying procedure that targets bacteria while neutralizing toxins. These fusion cell membrane-coated nanorobots are operated as powerful movable effective process, speeding a variety of activities including bacterial purification and toxin neutralizing.

The capacity to speed several procedures for the adsorption and elimination of PL-adhering microorganisms was established in this research, and the method could be easily extended to a broad range of nanodevices with diverse propulsion systems. Covering robotic systems with multifunctional cellular membranes gives robotic technologies crucial characteristics, which are impossible to obtain with untreated robotics. Even though this proof of the concept study is still in its early stages and needs more refinement and assessment of cell membrane-coated robotics until they can be used, it paves the way to using energy bioinspired nanorobots as effective broad-spectrum bio-detoxification technology. Overall, the capacity of such bioinspired nanorobots to simultaneously remove harmful bacteria and toxins is of excessive attention for a change of treatment and detoxifying applications. Such bioinspired nanorobots, which combine natural cellular activities with synthesized nanomachines, are likely to explore new avenues of study and advancement for fast-evolving robotics.

## Data Availability

The data used to support the findings of this study are included within the article. Further data or information are available from the corresponding author upon request.

## Conflicts of Interest

The authors declare that there are no conflicts of interest regarding the publication of this paper.

## Acknowledgments

The authors appreciate the supports from Mizan Tepi University, Ethiopia, for the research and preparation of the manuscript. The authors thank M S Ramaiah Institute of Technology, Saveetha School of Engineering, Saveetha Institute of Medical and Technical Sciences, for providing assistance to this work.

## References

- [1] S. Wang, Y. Duan, Q. Zhang et al., "Drug targeting via platelet membrane-coated nanoparticles," *Small Structures*, vol. 1, no. 1, Article ID 2000018, 2020.
- [2] B. Esteban-Fernández de Ávila, P. Angsantikul, D. E. Ramirez-Herrera et al., "Hybrid biomembrane-functionalized nanorobots for concurrent removal of pathogenic bacteria and toxins," *Science Robotics*, vol. 3, no. 18, Article ID eaat0485, 2018.
- [3] Y. Zhang, K. Yuan, and L. Zhang, "Micro/nanomachines: from functionalization to sensing and removal," *Advanced Materials Technologies*, vol. 4, no. 4, Article ID 1800636, 2019.
- [4] M. J. Siedlik, Z. Yang, P. S. Kadam, J. Eberwine, and D. Issadore, "Micro and NanoDevices for studying subcellular biology," *Small*, vol. 17, no. 3, Article ID 2005793, 2021.
- [5] C. Brito, D. Cabanes, F. Sarmiento Mesquita, and S. Sousa, "Mechanisms protecting host cells against bacterial pore-forming toxins," *Cellular and Molecular Life Sciences*, vol. 76, no. 7, pp. 1319–1339, 2019.
- [6] M. Yan, K. Liang, D. Zhao, and B. Kong, "CoreShell structured micro-nanomotors: construction, shell functionalization, applications, and perspectives," *Small*, vol. 18, no. 3, Article ID 2102887, 2022.
- [7] D. Liu, T. Wang, and Y. Lu, "Untethered microrobots for active drug delivery: from rational design to clinical settings," *Advanced Healthcare Materials*, vol. 11, no. 3, Article ID 2102253, 2022.
- [8] M. Xuan, J. Shao, J. Zhao, Q. Li, L. Dai, and J. Li, "Magnetic mesoporous silica nanoparticles cloaked by red blood cell membranes: applications in cancer therapy," *Angewandte Chemie International Edition*, vol. 57, no. 21, pp. 6049–6053, May 2018.
- [9] Y. Liu, X. Wang, B. Ouyang et al., "Erythrocyte-platelet hybrid membranes coating polypyrrol nanoparticles for enhanced delivery and photothermal therapy," *Journal of Materials Chemistry B*, vol. 6, no. 43, pp. 7033–7041, 2018.
- [10] W. Liu, Q. Yan, C. Xia et al., "Recent advances in cell membrane coated metal-organic frameworks (MOFs) for tumor therapy," *Journal of Materials Chemistry B*, vol. 9, no. 22, pp. 4459–4474, 2021.
- [11] Q. M. Qi, E. Dunne, I. Oglesby et al., "In Vitro measurement and modeling of platelet adhesion on VWF-coated surfaces in

## *Retraction*

# **Retracted: Statistical Analysis on the Mechanical Properties of ATH Nanofiller Addition on the Woven Jute/Polyester Hybrid Composites by the Grey–Taguchi Method**

### **Advances in Materials Science and Engineering**

Received 26 December 2023; Accepted 26 December 2023; Published 29 December 2023

Copyright © 2023 Advances in Materials Science and Engineering. This is an open access article distributed under the Creative Commons Attribution License, which permits unrestricted use, distribution, and reproduction in any medium, provided the original work is properly cited.

This article has been retracted by Hindawi, as publisher, following an investigation undertaken by the publisher [1]. This investigation has uncovered evidence of systematic manipulation of the publication and peer-review process. We cannot, therefore, vouch for the reliability or integrity of this article.

Please note that this notice is intended solely to alert readers that the peer-review process of this article has been compromised.

Wiley and Hindawi regret that the usual quality checks did not identify these issues before publication and have since put additional measures in place to safeguard research integrity.

We wish to credit our Research Integrity and Research Publishing teams and anonymous and named external researchers and research integrity experts for contributing to this investigation.

The corresponding author, as the representative of all authors, has been given the opportunity to register their agreement or disagreement to this retraction. We have kept a record of any response received.

### **References**

- [1] C. R. Mahesha, S. R. D. Raja Ramesh et al., “Statistical Analysis on the Mechanical Properties of ATH Nanofiller Addition on the Woven Jute/Polyester Hybrid Composites by the Grey–Taguchi Method,” *Advances in Materials Science and Engineering*, vol. 2022, Article ID 1752203, 6 pages, 2022.

## Research Article

# Statistical Analysis on the Mechanical Properties of ATH Nanofiller Addition on the Woven Jute/Polyester Hybrid Composites by the Grey–Taguchi Method

CR Mahesha,<sup>1</sup> Suprabha R,<sup>1</sup> D. Raja Ramesh,<sup>2</sup> Rajesh A S,<sup>3</sup> Melvin Victor De Pours,<sup>4</sup> Ram Subbiah,<sup>5</sup> Wadi B. Alonazi,<sup>6</sup> S. Sivakumar,<sup>7</sup> and Agegnehu shara shata<sup>8</sup> 

<sup>1</sup>Department of Industrial Engineering and Management, Dr. Ambedkar Institute of Technology, Bangalore 560056, Karnataka, India

<sup>2</sup>Department of Mechanical Engineering, Sri Vasavi Institute of Engineering and Technology, Nandamuru 521369, Andhra Pradesh, India

<sup>3</sup>Department of Mechanical Engineering, JSS Science and Technology University, Mysuru 570006, Karnataka, India

<sup>4</sup>Department of Thermal Engineering, Saveetha School of Engineering, Saveetha Institute of Medical and Technical Sciences, Chennai, India

<sup>5</sup>Department of Mechanical Engineering, Gokaraju Rangaraju Institute of Engineering and Technology, Hyderabad 500090, Telangana, India

<sup>6</sup>Health Administration Department, College of Business Administration, King Saud University, P. O. Box: 71115, Riyadh 11587, Saudi Arabia

<sup>7</sup>Department of Bioenvironmental Energy, College of Natural Resources and Life Science, Pusan National University, Busan, Republic of Korea

<sup>8</sup>Faculty of Mechanical Engineering, Arba Minch Institute of Technology, Arba Minch University, Arba Minch, Ethiopia

Correspondence should be addressed to Agegnehu shara shata; [agegnehu.shara@amu.edu.et](mailto:agegnehu.shara@amu.edu.et)

Received 25 April 2022; Accepted 18 August 2022; Published 23 September 2022

Academic Editor: K. Raja

Copyright © 2022 CR Mahesha et al. This is an open access article distributed under the Creative Commons Attribution License, which permits unrestricted use, distribution, and reproduction in any medium, provided the original work is properly cited.

The primary goal of this study is to determine how well the addition of alumina trihydride (ATH) fillers affects the material properties of hybridised polyester nanocomposites using a weaved jute fibre. The manual lay-up approach was used to create the hybrids, using control variables: (i) ATH filler weight ratio, (ii) stitched jute fiber width, and (iii) amount of stitched jute sheets, altogether at tierce dissimilar stages, to fulfil the goals of this study. By using L9 (3<sup>3</sup>) symmetrical layout, 9 samples were constructed and tested in accordance with the ASTM specification. According to the study by Grey, biocomposites with 6% ATH dust and 250 gsm of weaved jute filaments in tierce have such a satisfactory outcome. Inclusion of dietary fibres to pure synthetic materials improved aggregate material properties. Even as fibre as well as pitch meditations raised, greater power was mandatory to fracture the fibres among matrices as well as their reinforcements.

## 1. Introduction

Modern innovations, especially for aviation, submarines, and transport, need a unique combination of material characteristics that ceramics and metallic alloys cannot provide. Materials commonly do not meet aviation criteria for more breakage durability as well as comparative difficulty of engineering structures. A composite material helps to

achieve the right standard by correctly combining diverse components. Such substances are frequently robust yet stiff, making them suitable for a wide range of purposes [1–3]. Thermoplastic hybrid composites are among the key growing materials in recent times and their usage in programme management as well as other architectural sections has grown fast. In terms of materials processing, natural fabrics offer various advantages against fibreglass, such as

being reusable, having a reduced thickness, being less expensive, with a higher elasticity, and providing an exceedingly high level of comfort [4, 5]. Jute, often known as the golden fibre, is a major worldwide product that is mostly produced in two poor countries: Bangladesh and India. These fibres are created from lingo-cellulosic material, which is totally recyclable and hence more ecologically friendly and affordable. This is also the second most frequent plant fibre behind cotton in terms of worldwide consumption, manufacturing, and accessibility. According to [6] the following factors contributed to the rise of the jute industry in the engineering sector rigidity, excellent anomalous toughness, and fineness, nontoxicity, good water absorbing qualities, and environmental protection. As per the National Jute Board, each thousand square metre area of jute fields absorbs 15 tonnes of CO<sub>2</sub> from the atmosphere and emits 11 tonnes of oxygen (O<sub>2</sub>) over the course of three months. This jute capability demonstrates that jute is the most ecologically aware natural fabric. The mechanical characteristics of polymer composite materials reinforced with natural fibres are not as good as those of man-made fibres. It is because the organic filaments and their polymeric matrices have lesser adhesion strength [7, 8].

Heterogeneous composites consist of ever more numerous ligaments and tendons in a unified framework. Through eliminating the drawbacks of individual mixtures, hybridization may augment the material properties of biological fibres and synthetic adhesives. Nevertheless, the influence of blending threads in the matrix on increasing physical behaviour has peaked. Much higher, nanomaterials are used to reinforce the link between the matrix and reinforcement, culminating in even greater performance [9]. As an importance, the utilization of nanomaterials in artificial ingredients is flattering progressively common. Bio-composites are well known for their exceptional mechanical properties like improved elastic modulus, thermal properties, increase in strength, etc., despite the fact that a small number of nanocrystals (5 wt%) were introduced [10]. The purpose of this investigation is to discover a way to make mono-polymeric trash powders, including commercial aluminium trihydrate, which is less useable. Because the yearly global production of an ATH is expected to be around 3 million, it could be used as a resource for a novel approach with a single item [11]. In that production chain, the grey relational tool was employed to efficiently optimise overall strictures of relatively high concentration problems. Taguchi design is a helpful approach for improving production methods and achieving ambitious aspirations while lowering costs. In that technique, an rectangular layout of arrays is industrialized to measure a variety of factors in fewer repetitions, as well as the S/N proportion is employed to measure the stimulus of additive noise upon value in the context. When examining the S/N proportion, three types of productivity must be considered: simple, larger, and numerical. The S/N proportion compresses the multiple statistical elements inside a research setup based on the characteristic being researched [12, 13].

The principal persistence of this investigation is to paradigm, evaluate as well as enhance the material

possessions of hybridised biocomposites by utilising the following conditions: ATH content percentage, GSM of weaved natural fibres, as well as jute layering quantity [14]. The ATH padding nanocomposites were built by means of an unpretentious hand lay-up method. Normal fabrics were chemically modified to progress devotion and decrease hydrophilicity, and its tensile performance was assessed and improved using Grey-analysing Taguchi procedures.

## 2. Investigational Resources and Approaches

*2.1. Resources.* The Rithu Food Factory in Chennai supplied woven jute partners. All raw strand partners are then properly laved using fresh water and dried in the oven for 48 hours to confiscate the dampness. The raw yarn wetted through alkali mixture fixed hours. After that, the yarns were moderately washed through high-density water and placed inside the weave at 80°C. Throughout this examination, HN361 ATH and synthetic adhesive (polyester) were procured from Globe chemicals, Bangalore.

*2.2. Formation of Mixture Compounds.* Initially, a steel casting of 150 x 150 x 3 mm in dimension was developed. The matrix phase was thoroughly combined using 1% CN as well as 1% MEKP. The manual lay-up technique was labouring to create the composites with help of ATH powders as well as weaved jute strands. Various weight percentages of ATH dust were manually mixed into the manufactured polyester with a glass slide. That matrix solution is then strewn across the fibre sections of a molding. After thoroughly wetting the fibre matting with matrices mixtures, the mould was affixed and dried outside for 24 hrs. The Taguchi strategy was employed to select the pin grid arrays under three conditions, individually through tierce ladders, and nine specimens were manufactured. Table 1 and Table 2 show the variables' respective ranges as well as Taguchi's diametrically.

## 3. Techniques and Testing

*3.1. Material Characterization.* Following manufacture, the hybrids were tested in accordance with ASTM specifications. The mechanical performance of hybridised nanostructure, such as tension (D638), bending (D790), and impact (D256), were evaluated in accordance with the ASTM requirement.

*3.2. Tentative Implications through GRG Performance.* The Taguchi method of technical familiarity is a appreciated methodology empowering reasonable purpose, learning, as well as modification of multiple process conditions to acquire the proposed effect. By exploitation of this technique, the outcome of the inquiry is bowed into a S/N ration in order to classify its important margins. The S/N percentage structures are split into three phases constructed on the convincing validation for enlightening the primary function: (i) is greater is better; (ii) noticeably greatest, as well as (iii) lowest is better. Table 3 summarises the existing prosecution's findings.



TABLE 1: Obliges and their legs for hybrid compound.

Sl.No	Obliges	Symbols	Phases		
			S1	S2	S3
1	ATH dust (wt.%)	A	3	6	9
2	Interlaced jute mate (GSM)	B	150	200	250
3	Jute fibre films (no)	C	1	2	3

TABLE 2:  $L_9$  immaterial design of mixed materials.

Trail No	ATH dust (wt.%) A	Interlaced jute mate (GSM) B	No of jute layers (no) C
	1	3	150
2	3	200	2
3	3	250	3
4	6	150	2
5	6	200	3
6	6	250	1
7	9	150	3
8	9	200	1
9	9	250	2

**3.2.1. Signals-to-Noise Ratio.** The higher the S/N proportion, notwithstanding of a producing showcase grouping, the higher the performance characteristic. As a consequence, an ideal level for the variable is the one that provides the extreme S/N percentage. Bending, strain, and impacting forces were restrained, utilising the bigger perception all across the materials tests. As a moment, consequence S/N magnitudes are clearly represented in formula (1) as follows:

$$\frac{S}{N} = -10 \log_{10} \frac{1}{6} \sum_{a=1}^e \frac{1}{X_{ab}^2}. \quad (1)$$

**3.2.2. Regularized Signal-to-Noise Proportion.** Calibration is a modification that is completed on a specific statistical input to dispense the statistics uniformly and measure them into an appropriate assortment for additional investigation. To set the proper deduction of expectations for numerous factors and eradicate inconsistencies,  $Z_{ab}$  is standardised as  $K_{ij}$  ( $0 \leq K_{ij} \leq 1$ ) using (2). The most important aspects of this inquiry were chosen based on the larger-the-better bending, tension, and impact. For the subsequent features, the S/N relation and standardised S/N relation are well matched. Table 4 reveals the S/N and normalised S/N ratios of outcomes.

$$K_{ij} = \frac{z_{ab} - \min(z_{ab} | a=1, 2, \dots, e)}{\max(z_{ab} | a=1, 2, \dots, k) - \min(z_{ab} | a=1, 2, \dots, e)}. \quad (2)$$

**3.2.3. Grey Interpersonal Scores.** Equation (3) is employed to turn every GRG response into a GRS. The response surface assessment is used to recognize the suitable extent for all controlled division. The GRS conclusions are exposed in Table 5.

$$\bar{\gamma}_j = \frac{1}{k} \sum_{i=1}^m \gamma_{ij}. \quad (3)$$

In which case the sample of a j-th attempt while  $m$  is indeed the summation of technical specifications. Eventually, the GRC as well as GRS were performed across all  $L_9$  ( $3^3$ ) routes. Through merging Taguchi methodologies as well as Pearson correlations modelling, the nonlinear and non-optimizing issues were streamlined to a single-response optimal configuration. The overall GRS, which has been derived through using the Brown or Black Taguchi approach, is indeed the sole effectiveness characteristic. One could acquire the overall best grayscale connection score by searching for just a variable setup.

## 4. Consequences

**4.1. Grey Interpersonal Scores.** To evaluate the best variables of an elastic modulus of hybrids nanocomposites, the Taguchi approach with Gray's relational studies was utilised. Brown or black testing with ANOVA reduced the optimal restriction subgroups together with the most important characteristic in biocomposites. The reaction tables were employed to represent the overall GRS by each tightness degree.

To compute the comparative reputation assessment with ATH granules, we first mean the relative importance scores of unadorned (ranking) 1 in ruckus A (i.e., repetitions 1–3), then the correlation scores of unadorned 2 in the identical row. Tests 4–6 callous the 3 similar relationship results derived from the same row A. (tribunals 7–9). Likewise, the exact smoothness of a jute fibre as well as the quantity of jute strands are designed [7,8]. Table 6 illustrates responses. Figures 1(a) and 1(b) and Figure 1(c) show the GRS retort findings at variable levels of material restrictions. The study demonstrated that the optimum processing restriction degree is produced by the highest grey relational rating.

The highest grey relational grade value of the limitations like ATH dust heaviness, interlaced jute kind, and amount of jute films is found at levels A2, B3, and C2. The ideal parameters of the hybrid composites were found to be ATH powder of 6% and fabric jute type of 250 GSM with three layers. It is apparent that the use of woven jute will improve the strength of composites. This is due to the presence of a heavier and high-density fibre material, which counteracts the effects of voids. The strength of natural composites was only boosted by 6% of the ATH weight ratio [9, 14] As the weight ratio of ATH increases, the matrix and fibre connection becomes weaker. When parameter B is increased, the composites show a positive result. The connection among the fibres as well as the resin was boosted even as filament gratified was increased. As a consequence, it takes more energy to break the link between the interlaced fibrils [10, 11].

**4.2. ANOVA Analysis.** The ANOVA can be expressed by using standard gradient quantity. These findings of an ANOVA are employed to identify whether production

TABLE 3: Consequences of examination.

Trail	Tension (MPa)	Bending (MPa)	Impact (Kg/m <sup>2</sup> )
1	21.24	25.49	15.89
2	23.51	27.76	18.16
3	22.05	26.30	16.70
4	25.14	29.39	19.79
5	24.31	28.56	18.96
6	23.62	27.87	18.27
7	20.38	24.63	15.03
8	22.38	26.63	17.03
9	26.49	30.74	21.14

TABLE 4: S/N and consistent S/N proportion.

Exp. No	S/N Ratio			Standardized S/N		
	Tension (Mpa)	Bending (MPa)	Impact (Kg/m <sup>2</sup> )	Tension (Mpa)	Bending (MPa)	Impact (Kg/m <sup>2</sup> )
1	26.542	28.129	24.025	0.158	0.155	0.163
2	27.424	28.870	25.184	0.545	0.540	0.554
3	26.867	28.401	24.457	0.300	0.296	0.309
4	28.006	29.365	25.931	0.800	0.797	0.806
5	27.715	29.116	25.559	0.672	0.668	0.681
6	27.465	28.904	25.237	0.563	0.558	0.572
7	26.183	27.831	23.542	0.000	0.000	0.000
8	26.996	28.509	24.626	0.357	0.352	0.366
9	28.461	29.755	26.504	1.000	1.000	1.000

features affect the influencing sources of variation for ATH as influence of every processing parameter using ANOVA, with

TABLE 5: GRC as well as GRS of a mixture.

Trail	GRC			GRS
	Tension (MPa)	Bending (MPa)	Impact (Kg/m <sup>2</sup> )	
Trail 1	0.372	0.372	0.374	0.373
Trail 2	0.523	0.521	0.529	0.524
Trail 3	0.417	0.415	0.420	0.417
Trail 4	0.715	0.712	0.721	0.716
Trail 5	0.604	0.601	0.610	0.605
Trail 6	0.533	0.531	0.539	0.534
Trail 7	0.333	0.333	0.333	0.333
Trail 8	0.437	0.436	0.441	0.438
Trail 9	1.000	1.000	1.000	1.000

TABLE 6: Response table for GRS.

Levels	ATH dust (wt.%) a	Interlaced jute mate (GSM) B	Jute films (no) C
S1	0.438	0.474	0.448
S2	0.618	0.523	0.724
S3	0.598	0.651	0.452

well as jute-based nanocomposite. The extraction efficiency via the entire combined formed eccentricity can be utilised to appraise the impact of a processor variable modification on performance qualities [15, 16]. Table 7 demonstrates the

ATH dust, interlaced jute, and the number of jute layers contributing 22.93 percent, 18.15 percent, and 58.92 percent, respectively. This suggests that the number of jute layers and ATH weight ratios are important characteristics.

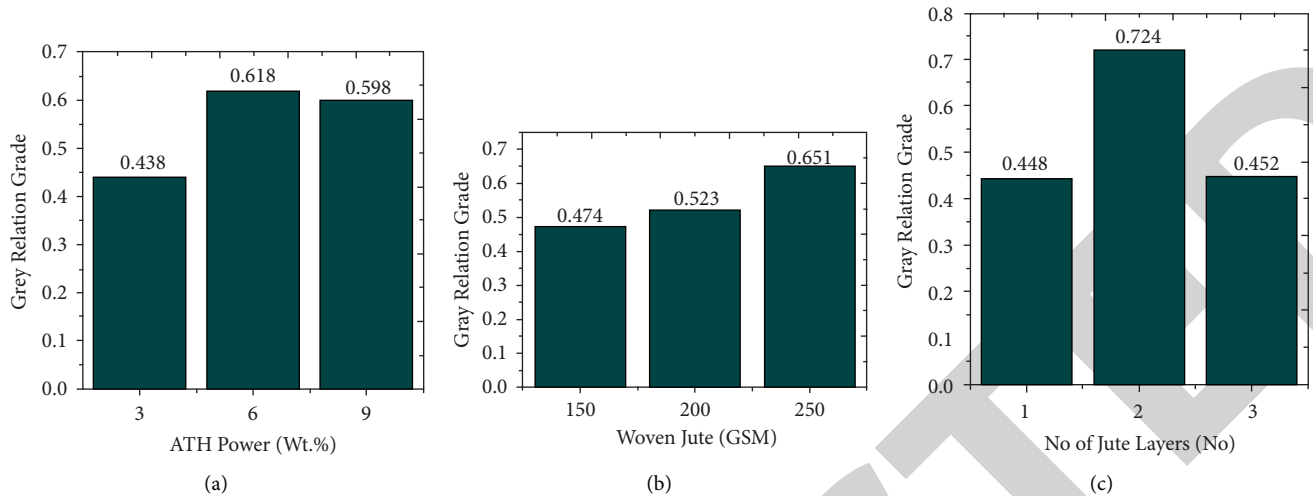


FIGURE 1: . (a) Grey relational grade outcomes of (a) ATH powder wt.%. (b) Grey relational grade outcomes of (b) woven jute type GSM. (c) Grey relational grade outcomes of (c) amount of jute layers No.

TABLE 7: ANOVA for grey interpersonal scores.

Structures	Restrictions	DOF	Sum of square	MS	% Of aids
A	ATH dust (wt.%)	2	0.01946	0.0097	22.93
B	Interlaced jute fiber (GSM)	2	0.0154	0.0077	18.15
C	Jute films (no)	2	0.05	0.0250	58.92
Error	—	0	—	—	—
Total	—	6	0.08486	—	100

## 5. Conclusion

Throughout this study, the mechanical performance of ATH as well as weaved jute-based polyester hybridization materials has been investigated, as well as the Taguchi approach incorporating GRA was utilised to obtain the optimum restrictions. The following observations are obtained:

- (i) The regulated reaction conditions of ATH and jute-based biocomposites are 6 weight percent ATH dust with three levels of 250 gsm fibre. A diversity of elements association to yield a nanocomposite having enhanced materials possessions.
- (ii) According to the findings of descriptive statistics (ANOVA), the quantity of jute sheets constituted the most relevant factor, accounting for 58.92%, whilst the weaved jute type accounted for only 18.15%.

## Data Availability

The data used to support the findings of this study are included within the article. Further data or information are available from the corresponding author upon request.

## Conflicts of Interest

The authors declare that there are no conflicts of interest regarding the publication of this paper.

## Acknowledgments

The authors appreciate the supports from Arba Minch University, Ethiopia, for providing help during the research and preparation of the manuscript. This project was supported by Researchers Supporting Project number (RSP-2021/332) King Saud University, Riyadh, Saudi Arabia.

## References

- [1] V. Mohanavel, S. Suresh Kumar, J. Vairamuthu, P. Ganeshan, and B. Nagaraja Ganesh, "Influence of stacking sequence and fiber content on the mechanical properties of natural and synthetic fibers reinforced penta-layered hybrid composites," *Journal of Natural Fibers*, vol. 2021, pp. 1–13, 2021.
- [2] S. Sanjeevi, V. Shanmugam, S. Kumar et al., "Effects of water absorption on the mechanical properties of hybrid natural fibre/phenol formaldehyde composites," *Scientific Reports*, vol. 11, no. 1, pp. 13385–13411, 2021.
- [3] G. Maruthupandian, R. Saravanan, S. Suresh Kumar, and B. G. Sivakumar, "A study on bamboo reinforced concrete slabs," *Journal of Chemical and Pharmaceutical Sciences*, vol. 9, no. 2, pp. 978–980, 2016.
- [4] V. Alagumalai, V. Shanmugam, N. K. Balasubramanian et al., "Impact response and damage tolerance of hybrid glass/kevlar-fibre epoxy structural composites," *Polymers*, vol. 13, no. 16, p. 2591, 2021.
- [5] V. Ganesan, V. Shanmugam, B. Kaliyamoorthy et al., "Optimisation of mechanical properties in saw-dust/woven-jute fibre/polyester structural composites under liquid nitrogen

## *Retraction*

# **Retracted: Wind Tunnel Testing and Validation of Helicopter Rotor Blades Using Additive Manufacturing**

### **Advances in Materials Science and Engineering**

Received 26 December 2023; Accepted 26 December 2023; Published 29 December 2023

Copyright © 2023 Advances in Materials Science and Engineering. This is an open access article distributed under the Creative Commons Attribution License, which permits unrestricted use, distribution, and reproduction in any medium, provided the original work is properly cited.

This article has been retracted by Hindawi, as publisher, following an investigation undertaken by the publisher [1]. This investigation has uncovered evidence of systematic manipulation of the publication and peer-review process. We cannot, therefore, vouch for the reliability or integrity of this article.

Please note that this notice is intended solely to alert readers that the peer-review process of this article has been compromised.

Wiley and Hindawi regret that the usual quality checks did not identify these issues before publication and have since put additional measures in place to safeguard research integrity.

We wish to credit our Research Integrity and Research Publishing teams and anonymous and named external researchers and research integrity experts for contributing to this investigation.

The corresponding author, as the representative of all authors, has been given the opportunity to register their agreement or disagreement to this retraction. We have kept a record of any response received.

### **References**

- [1] I. Hasan, R. Mukesh, P. Radha Krishnan, R. Srinath, D. P. Babu, and N. Lemma Gurmu, "Wind Tunnel Testing and Validation of Helicopter Rotor Blades Using Additive Manufacturing," *Advances in Materials Science and Engineering*, vol. 2022, Article ID 4052208, 13 pages, 2022.

## Research Article

# Wind Tunnel Testing and Validation of Helicopter Rotor Blades Using Additive Manufacturing

Inamul Hasan <sup>1,2</sup>, R. Mukesh,<sup>3</sup> P. Radha Krishnan <sup>1,2</sup>, R. Srinath,<sup>2,4</sup>  
Dhanya Prakash Babu <sup>1</sup> and Negash Lemma Gurmu <sup>5</sup>

<sup>1</sup>Department of Aeronautical Engineering, ACS College of Engineering, Bangalore 560074, Karnataka, India

<sup>2</sup>Department of Aeronautical Engineering, Visvesvaraya Technological University, Belagavi 590018, Karnataka, India

<sup>3</sup>Department of Aerospace Engineering, ACS College of Engineering, Bangalore 560074, Karnataka, India

<sup>4</sup>Department of Aerospace Engineering, Dayananda Sagar University, Bangalore 560078, Karnataka, India

<sup>5</sup>Department of Industrial Engineering, Ambo University, Ambo, Ethiopia

Correspondence should be addressed to Negash Lemma Gurmu; [negash.lemma@ambou.edu.et](mailto:negash.lemma@ambou.edu.et)

Received 24 June 2022; Revised 2 August 2022; Accepted 20 August 2022; Published 21 September 2022

Academic Editor: K. Raja

Copyright © 2022 Inamul Hasan et al. This is an open access article distributed under the Creative Commons Attribution License, which permits unrestricted use, distribution, and reproduction in any medium, provided the original work is properly cited.

This research paper aims to validate the aerodynamic performance of rotor blades using additive manufacturing techniques. Wind tunnel testing is a technique used to find the flow characteristics of the body. Computational fluid dynamics (CFD) techniques are used for aerodynamic analysis, and validation should be done using wind tunnel testing. In the aerodynamic testing of models, additive manufacturing techniques help in validating the results by making models easily for wind tunnels. Recent developments in additive manufacturing help in the aerodynamic testing of models in wind tunnels. The CFD analysis of helicopter rotor blades was analyzed in this research, and validation was done using additive manufacturing techniques. Computational analysis was carried out for static analysis for the forward speeds of Mach numbers 0.3, 0.4, and 0.5. The results obtained were satisfactory to the previous results and were validated with wind tunnel testing. Results proved that the error percentage was lower, and the computational analysis was valid. In this research, models were designed using the FDM technique for wind tunnel testing as it is cost-effective and easy to manufacture.

## 1. Introduction

A helicopter is a flying machine with many advantages over other flying objects, such as landing or take-off at almost any terrain, flying at a specific position (hovering), and flying backward and sideways quickly. Helicopters can be termed any terrain vehicle as they have many advantages over aircraft [1, 2]. The helicopter is a type of rotorcraft currently used for many purposes such as rescue, firefighting, and agriculture. The helicopter's design differs with various parameters for different applications [3]. Helicopters possess more capability than aircraft as it has the unique ability of vertical take-off and landing, and no particular runway. Helicopters have some disadvantages over aircraft in the case of speed and pilot operation. The helicopter speed is improved since the invention of the helicopter in recent days.

Many factors are suppressing the speed of helicopters [4]. Helicopters can fly forward, backward, or sideways, stay at a position (hover), and vertically can go up or come down. In aircraft, lift is produced by the wings, and engines produce thrust. In helicopters, lift and thrust are produced by a rotor driven by one or two engines [5, 6].

CFD software is used for analyzing the aerodynamic performance of moving vehicles to assess the aerodynamic performance. CFD is widely used in many fields, and improving CFD techniques helps improve results and reduce errors [7]. Even though CFD software provides good results, researchers prefer to compare the results obtained from CFD with wind tunnel testing. CFD results can be validated with the previous experimental results or wind tunnel tests [8, 9]. The model was made from wood or metals for wind tunnel tests in the previous days. Models created in wood require a

high cost for skilled workers, and it takes a long time to make the models. Metals like aluminum were used to prepare the model using CNC machines are high cost and less affordable [10, 11].

The evolution of additive manufacturing techniques helps in the easy and affordable manufacturing of models for various applications. Mainly for wind tunnel testing with the help of CAD design software, it is easy to design and manufacture with less cost [12, 13]. Advancements in additive manufacturing technologies help many fields in engineering, medicine, and research to test or demonstrate the models [14, 15]. Material qualities are improved by the advancements in the development of composite materials and help make low-cost models faster [16].

## 2. Experimental Details

**2.1. CFD Analysis.** Four-bladed helicopters are chosen as it is used in most high-speed helicopters. Analysis was carried out by ANSYS fluent software. It provides the numerical solution computationally with the help of the Navier–Stokes equation over the flow region. These computational techniques are beneficial for research on complex problems. Four-bladed rotors are designed by CATIA V5 software. Coordinates are downloaded from the UIUC airfoil data site, and the 2D profile can be generated from the airfoil data [17].

**2.1.1. Design and Preprocessing.** The CAD model design is essential and a preliminary requirement for computational analysis. CAD models can be designed by any design software like Solid Works, Solid Edge, and Catia. [18]. Catia V5 is used in this research work to design the three-bladed and four-bladed helicopter blades. The same model is used for the experimental model and scaled down for wind tunnel size using the 3D printing method [19, 20]. The designed model will be imported to fluent for further analysis. After designing the model, the model is imported to the ANSYS CFD workbench for further processing and analysis. The first stage is preprocessing, where the meshing and boundary conditions are applied [21]. As it is a static analysis, C type domain was chosen for computational analysis. Unstructured meshing is chosen as it is a complex structure to provide accurate results in CFD analysis [22, 23]. The realizable  $k-\epsilon$  model is chosen as the solver because it provides better results than other models, as mentioned in Figure 1.

The analysis was carried out for all the models and compared with experimental results to finalize the turbulence model. The analysis showed that realizable  $k-\epsilon$  was near the experimental results [22, 24].

An analysis was carried out for HH02 and NASA SC(2)-0714 rotor airfoils for Mach numbers of 0.3, 0.4, and 0.5. Blades are designed with the exact scaling of the Apache helicopter as the HH02 airfoil provides high performance. Parts of the rotors are designed separately as the leading edge, trailing edge, and center part, having a fine mesh for the analysis. Geometric parameters are followed in Table 1. Blade designs are shown in Figures 2 and 3.

Design parameters for the four-bladed configuration are shown in Table 1. Required parameters to design the helicopter blades are mainly rotor solidity and aspect ratio of the wing. Analysis was carried out for the Mach numbers of 0.3, 0.4, and 0.5 as most high-speed helicopters operate at Mach number 0.4. HH02 and NASA SC(2)-0714 rotors were analyzed to obtain the flow characteristics.

**2.1.2. Grid Independence Study.** The grid independence test was conducted to obtain the correct result for verification. Details of the grid independence test are represented in Table 2.  $Y^+$  value is maintained at 30 to 50 for all analyses. The number of elements increased, and the lift and drag coefficients were obtained from the numerical results. The grid size is decreased, and the study was carried out until the result variation was less than 2% higher than the previous grid [25, 26]. For the elements of 10921474, the lift coefficient and drag coefficient values showed a 1.47% deviation. So, the number of elements is fixed, and the boundary conditions are applied. The plot showing the variation of lift coefficient with many elements is shown in Figure 4.

## 3. Wind Tunnel Testing

The wind tunnel is a device used to study and analyze the flow characteristics of any object. The wind tunnel is an essential part of aerodynamics. The wind tunnel used a control stream of air to create an environment where the air flows over the model to study the effects of airflow. Wind tunnel testing is not only applicable to flying vehicles. It is also applicable for automobiles, buildings, or moving or flowing objects [9, 27].

Wind tunnels are classified based on the speed of flow created in the test section. Also, based on the operation, it is classified as open section and closed section wind tunnels.

Wind tunnels for rotorcraft differ from wind tunnels for aircraft or only wing sections. Static analysis can be carried out in any wind tunnel to analyze rotorcraft blade properties in static conditions [28, 29].

This study carried out an open section low-speed subsonic wind tunnel analysis for static analysis of HH02 and NASA SC(2)-0714 rotors.

Lift, drag, and moment can be measured by a three-component balance system attached to the wind tunnel. The three-component balance system directly measures the force and moment with the help of strain gauges inside the balance. In modern wind tunnels, a six-component balance is available to measure lateral force, longitudinal force, vertical force, pitching moment, rolling moment, and yawing moment [30].

The wind tunnel used for testing and force balance measurement and control for wind tunnels are shown in Figures 5(a) and 5(b).

In Figure 6, 3D printed models are shown. Four-bladed models of HH02 and NASA SC(2)-0714 rotors are printed with the FDM method. The NASA SC(2)-0714 rotor is the black colored model, and the HH02 rotor is the white

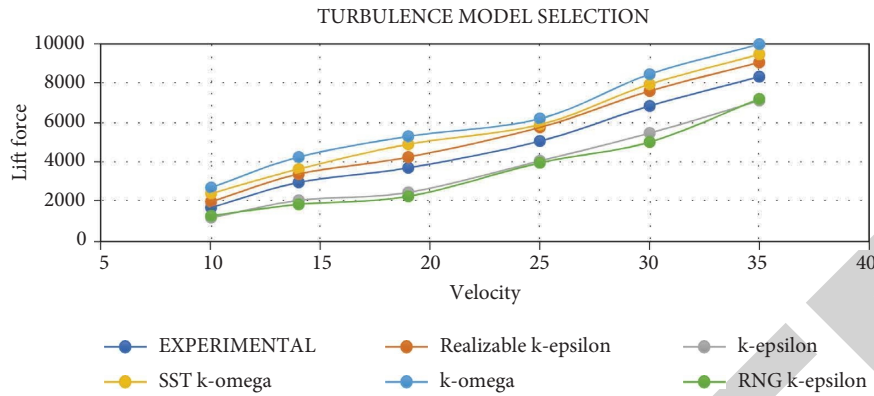


FIGURE 1: Turbulence model selection.

TABLE 1: Design parameters for four-bladed analysis.

Parameters	Symbols	HH02	NASA SC(2)-0714
The number of blades	$N_b$	4	4
Rotor blade radius	$R$	5.574	5.574
Chord length	$C$	0.145	0.145
Mach no.	$M$	0.3, 0.4, 0.5	0.3, 0.4, 0.5
Blade aspect ratio	AR	16.9	16.9
Rotor solidity	$\sigma$	0.033	0.033
Blade span (m)	$b$	5.086	5.086
Blade root chord (m)	Cr	0.3191	0.3191
Blade root chord (m)	Ct	0.0663	0.0663
Blade planform area (m <sup>2</sup> )	$S$	1.5299	1.5299

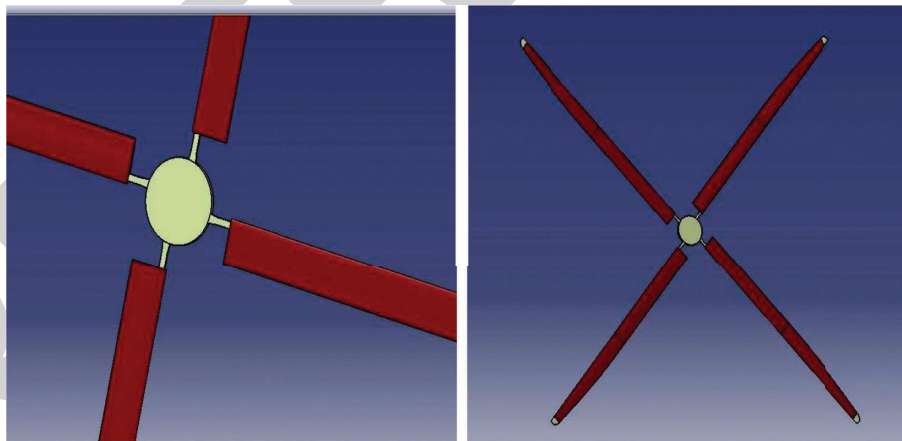


FIGURE 2: HH02 rotor model.

colored model. The models are used in the wind tunnel for testing in static conditions.

Computational techniques have developed a lot in recent days. But experimental testing is essential for validating the computational results and rectifying the errors [31]. In previous days, making models are not accessible. Wood or steel models should be used for testing in wind tunnels. Nowadays, 3D printing models are developed, and models can be made easily for the requirement.

Wind tunnels are available in various sizes and configurations. The full-scale wind tunnels where a complete aircraft or helicopter can be placed inside the test section. The scaled-down tunnel will have a lesser dimension test section. The actual model should be scaled down based on similarity parameters for scaled-down models. The model is a small one that is scaled-down, and the prototype is a real one with full dimensions. A geometric, kinematic, and dynamic similarity between the model and prototype should exist [32, 33].



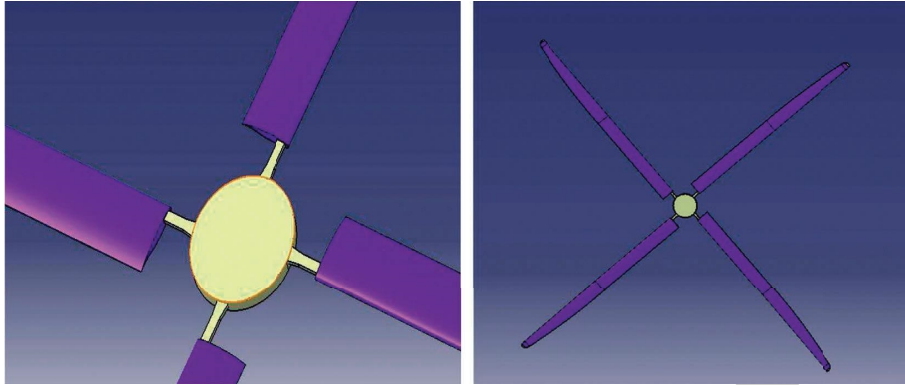


FIGURE 3: NASA SC(2)-0714 rotor model.

TABLE 2: Grid independence test.

Domain names	Domain_01	Domain_02	Domain_03	Domain_04
The number of elements	5792001	7055244	10057947	10921474
Lift coefficient	0.89825638	0.99146961	1.0403625	1.0559107
Drag coefficient	0.089324154	0.082220494	0.083640816	0.08252949
Error %	N/A	9.40%	4.69%	1.47%

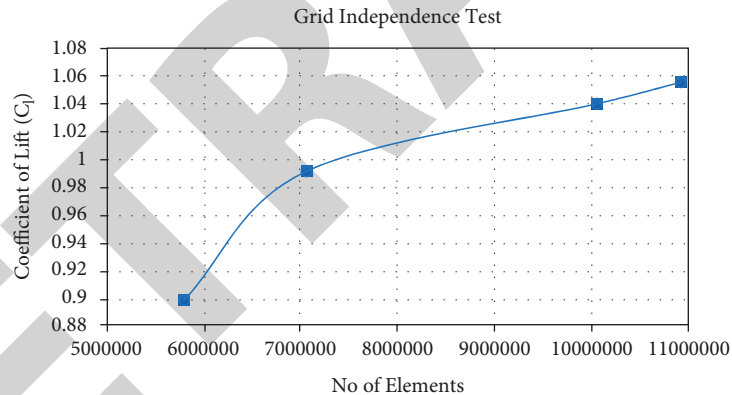


FIGURE 4: Grid independence test for four-bladed analysis.

In this research, an analysis of an isolated blade was taken. The actual size taken for the analysis in CFD is 12m, but the test section size is  $0.6\text{ m} \times 0.6\text{ m}$ . The model was designed for 500 mm with 200 mm blades and a 100 mm hub for the attachment of blades. A scaled-down model of 1:24 size was taken for the analysis in a wind tunnel.

Models were designed using 3D printing techniques. The development of 3D printing technologies helps easy printing and saves time. There are many techniques available for 3D printing. The fusion diffusion modeling (FDM) technique has been used for this research. FDM is a low-cost 3D printing technique in which surfaces will not be smooth. In FDM, the plastic elements are provided with thermal treatment and melted to the required shape. It has less resolution and accuracy. It can be used for basic research purposes. In stereolithography (SLA) techniques, the laser-

cured photopolymer resin to obtain the required model. We can select from many materials, and the method is versatile. The model will be very accurate and high resolution. It helps work with prototypes, molds, and patterns. In the selective laser sintering (SLS) technique, polymer powder is fused with laser. It is less costly than SLA and has good mechanical properties [10, 34]. The SLS method is also used for working prototypes and is more expensive than the FDM model. In selective laser melting (SLM), procedures are similar to the SLS technique. In SLM melting, process and materials are different. In SLM, materials are used as a solidified material layer in an entirely molten state. The actual powder layer is completely or partially melted because of the solid laser technique [8].

3D inkjet printing, 3D models are 2D cross section layers by slicing them on a computer. The droplet of the binder

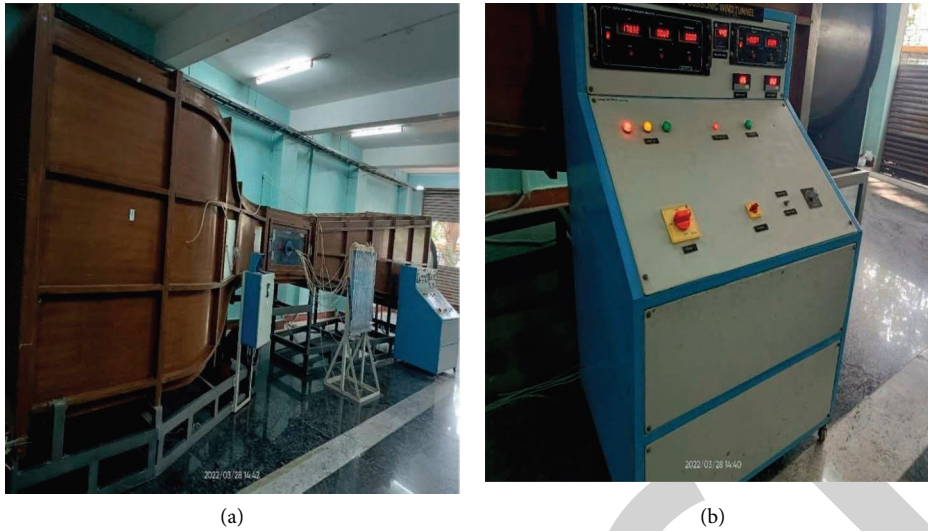


FIGURE 5: Wind tunnel and digital indicator for force measurement. (a) Wind tunnel used for testing; (b) force measurement.



FIGURE 6: 3D printed models used for testing.

material to the powder is applied where the solidification is required as programmed in the computer. Other methods, such as digital light processing (DLP) and carbon DLS technology, are high-cost techniques mainly used for industrial purposes [29].

Pressure and velocity are essential parameters in aerodynamics. In wind tunnels, pressure and velocity are measured with the help of a pitot-static tube and manometer. The pitot-static tube measures total or stagnation pressure and static pressure. Dynamic pressure relates the velocity and pressure, so from the relations, we can find the velocity with the help of pressure [27, 28].

Pressure is related by

$$P_0 = P + \frac{1}{2}\rho V^2. \quad (1)$$

$P_0$  is the total pressure, and  $P$  is the static pressure.

From the above relation, velocity can be found as the pitot-static tube measures total and static pressure.

So, velocity can be found from

$$V = \sqrt{\frac{2(P_0 - P)}{\rho}}. \quad (2)$$

The manometer measures the static pressure and stagnation pressure head using a pitot-static tube. The expression relates to pressure head ( $H$ ), and pressure is

$$P = \rho gH. \quad (3)$$

So, pressure can be measured by the above relation for stagnation and static pressure. A digital velocity indicator measures velocity, and it is used to calibrate the wind tunnel.

Figures 7 and 8 show the models are fixed inside the wind tunnel test section. Static conditions are measured by

varying the speed in the test section by varying the RPM of the motor. Models are tested at different speeds and validated.

## 4. Results and Discussion

**4.1. Computational Analysis Results.** The models were analyzed for Mach numbers 0.3, 0.4, and 0.5. The lift and drag values calculated for HH02 and NASA SC(2)-0714 airfoils gave comparable results to those reported in the literature. The results show that the supercritical airfoil has a better aerodynamic performance than the HH02 airfoil. The lift, drag, and lift-to-drag ratio values are given in Tables 3 and 4 and are represented graphically in Figures 9 and 10. Post-processing results obtained from fluent provided the aerodynamic characteristics of the rotor blade.

The NASA SC(2)-0714 rotor exhibits more lift than the HH02 rotor in comparing lift coefficient. But, drag values are also higher for NASA SC(2)-0714 rotor as we know that induced drag occurs in the flow and causes the higher drag values. In comparing aerodynamic efficiency, the NASA SC(2)-0714 rotor shows much higher efficiency than the HH02 rotor.

The plot between maximum velocity and free-stream Mach number has been plotted. It shows that velocity is always higher for the supercritical airfoil rotor than the HH02 rotor for all three Mach numbers 0.3, 0.4, and 0.5, as shown in Figure 11. From the Velocity values, we can understand that if the velocity is increased, the lift will be increased as the lift is directly proportional to the square of velocity from the basic formula for lift. Similarly, the maximum pressure will be on the lower part of the airfoil from the pressure values, which induces the lift. It proves that NASA SC(2)-0714 airfoil has better lifting capability than HH02 airfoil, as shown in Figure 12.

The maximum pressure and velocity values clearly show that NASA SC(2)-0714 shows high pressure and pressure difference. A high-pressure difference indicates high lift-producing capability for NASA SC(2)-0714 rotors. Similarly, NASA SC(2)-0714 achieves more velocity over the surface. Boundary layers are formed around the blades, but we aim to find the aerodynamic performance of the blades. The effects of the boundary layers are not considered. It is also clear that it increases the critical and drag divergence Mach number and delays the shock creation. Owing to the change in the shape of the trailing edge in the supercritical airfoil, it has different characteristics from the HH02 airfoil. HH02 has a curve aft of the trailing edge at the upper surface, whereas NASA SC(2)-0714 has a curve at the bottom surface of the trailing edge.

In comparing the aerodynamic performance, for Mach number 0.3, the NASA SC(2)-0714 rotor provides 47% better aerodynamic efficiency than the HH02 rotor. Similarly, for Mach number 0.4, the NASA SC(2)-0714 rotor offers 46% better aerodynamic efficiency than the HH02 rotor. Then, for Mach number 0.5, the NASA SC(2)-0714 rotor provides 45% better aerodynamic efficiency than the HH02 rotor. So, in static analysis, the NASA SC(2)-0714 rotor offers superior performance to the HH02 rotor for all speeds.



FIGURE 7: HH02 rotor model in the wind tunnel.

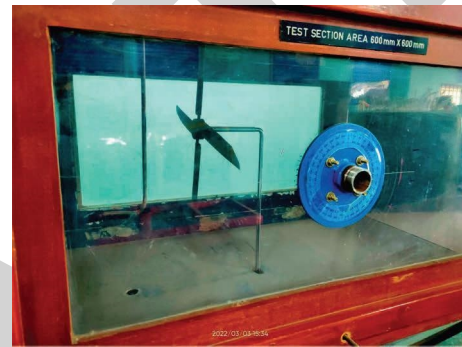


FIGURE 8: NASA SC(2)-0714 rotor model in the wind tunnel.

TABLE 3: Result of HH02 rotor.

4Mach number	0.3	0.4	0.5
The number of elements	12157747	12157747	12157747
Lift coefficient	0.39660177	0.40146145	0.40501018
Drag coefficient	0.058923748	0.055815901	0.054278395
L/D ratio	6.730762782	7.192600008	7.461719898
Max pressure (N/m <sup>2</sup> )	4462	7919	12350
Max velocity (m/s)	116.1	154.7	193.2

TABLE 4: Result of NASA SC(2)-0714 rotor.

4Mach number	0.3	0.4	0.5
The number of elements	10921474	10921474	10921474
Lift coefficient	1.0559107	1.0659764	1.0717936
Drag coefficient	0.08252949	0.080421625	0.078886333
L/D ratio	12.79434418	13.25484781	13.58655624
Max pressure (N/m <sup>2</sup> )	5023	8933	13960
Max velocity (m/s)	124.5	166	207

**4.2. Wind Tunnel Results.** Models are analyzed for static conditions, as shown in Figures 7 and 8. Models are fitted to the three-component balance system attached to the wind tunnel, and the lift force, drag force, and the moment are taken from the force balance system. Readings are tabulated and represented in Tables 5 and 6. Based on the values

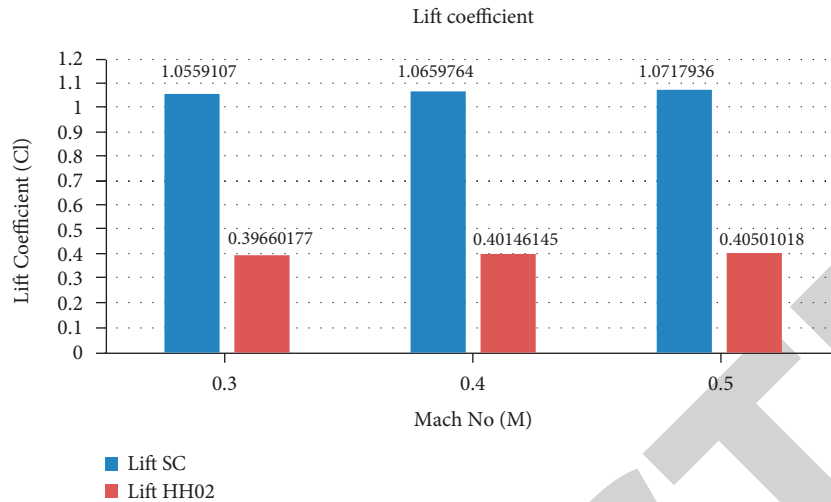


FIGURE 9: Lift coefficient vs. Mach number.

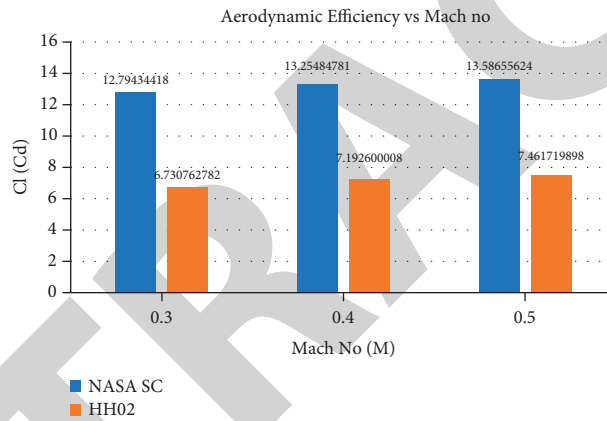


FIGURE 10: Aerodynamic efficiency vs. Mach no.

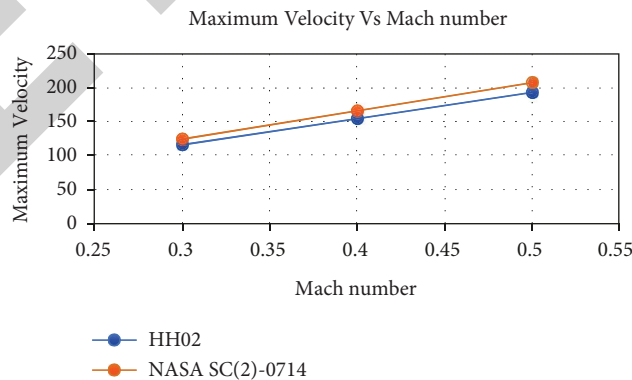


FIGURE 11: Maximum velocity vs. Mach number.

obtained from wind tunnel testing, aerodynamic efficiency is calculated for NASA SC(2)-0714 and HH02 rotors.

Tables 5 and 6 provide lift, drag, and pitching moment values to show that the NASA SC(2)-0714 rotor produces higher lift, lesser drag, and higher aerodynamic efficiency.

Figures 13 and 14 represent the production of lift force in the wind tunnel for various RPMs for NASA SC(2)-0714 and HH02 rotor models. It clearly shows the velocity increase for an increase in RPM of the wind tunnel rotor fan. Similarly, the lift force is increased for increasing the velocity as the lift



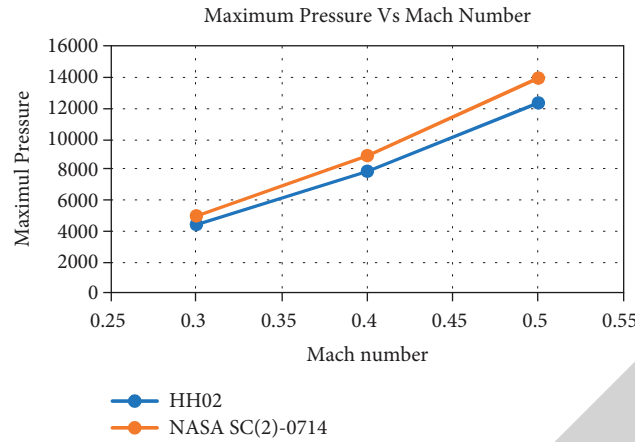


FIGURE 12: Maximum pressure vs. Mach number.

TABLE 5: Wind tunnel readings for HH02 model.

S. no.	RPM	Velocity	Lift force	Drag force	Pitching moment	Aerodynamic efficiency (L/D)
1	500	10	2.21	0.2	0.36	11.05
2	600	14	3.28	0.31	0.59	10.58
3	700	19	5.06	0.4	0.89	12.65
4	800	25	7.02	0.56	1.28	12.54
5	900	30	9.45	0.61	1.69	15.49
6	1000	35	11.6	0.75	2.16	15.46

TABLE 6: Wind tunnel readings for the NASA SC(2)-0714 model.

S. no.	RPM	Velocity	Lift force	Drag force	Pitching moment	Aerodynamic efficiency (L/D)
1	500	10	2.62	0.15	0.43	17.46
2	600	14	4.61	0.25	0.7	18.44
3	700	19	5.77	0.3	1.01	19.23
4	800	25	7.89	0.41	1.42	19.7
5	900	30	10.67	0.5	1.95	20.92
6	1000	35	12.98	0.61	2.48	21.18

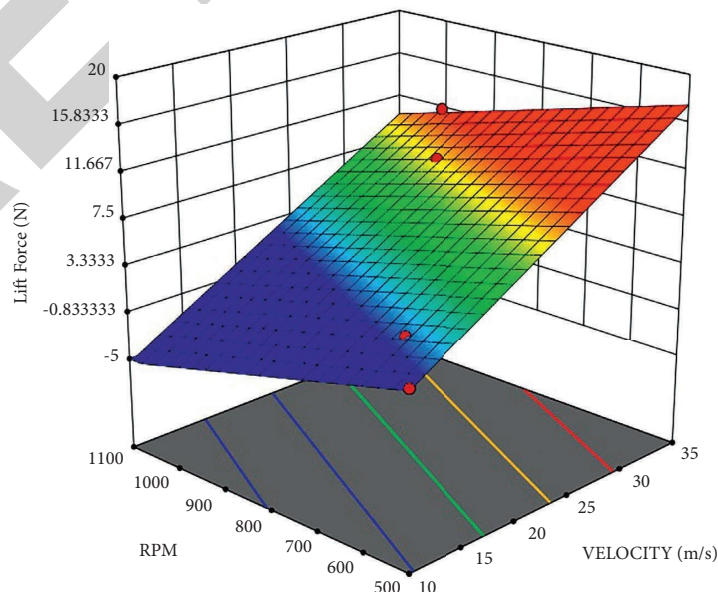


FIGURE 13: Lift force measured for the HH02 model.

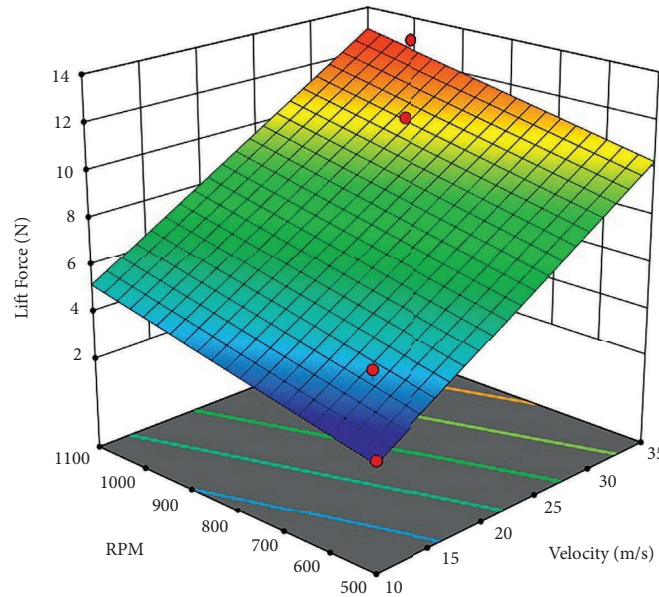


FIGURE 14: Lift force measured for the NASA SC(2)-0714 model.

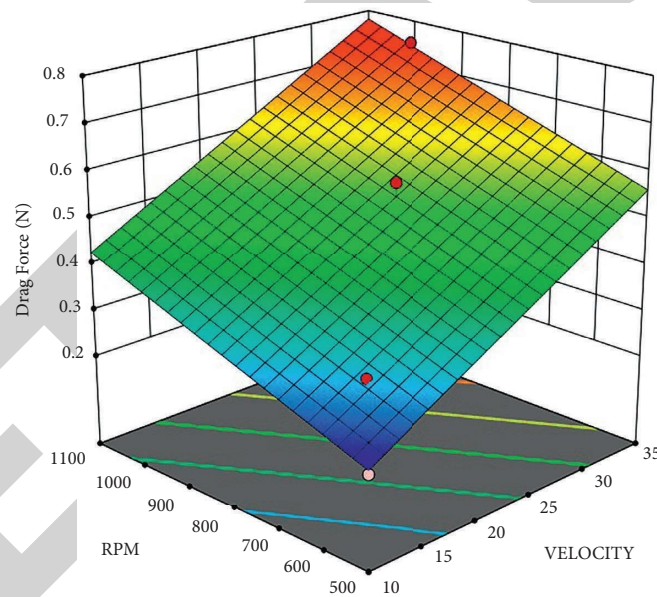


FIGURE 15: Drag force measured for the HH02 model.

force is proportional to the square of the velocity. In comparing figures, the lift produced in the NASA SC rotor is higher than the HH02 rotor, like the computational analysis results obtained from CFD.

Figures 15 and 16 represent the generation of drag force in the wind tunnel for various RPMs for NASA SC(2)-0714 and HH02 rotor models. It clearly shows that drag force is increased for increasing the velocity as the drag force is proportional to the square of the velocity. In comparing figures and tables, the drag force produced in the NASA SC

rotor is lesser than the HH02 rotor, like the computational analysis results obtained from CFD.

Figures 17 and 18 represent the pitching moment measured in the wind tunnel force measurement for the NASA SC rotor and HH02 rotor. It proves that the pitching moment is higher for the NASA SC rotor than the HH02 rotor as it has a higher lift and better aerodynamic efficiency.

A comparison of aerodynamic performance is shown in Table 7.

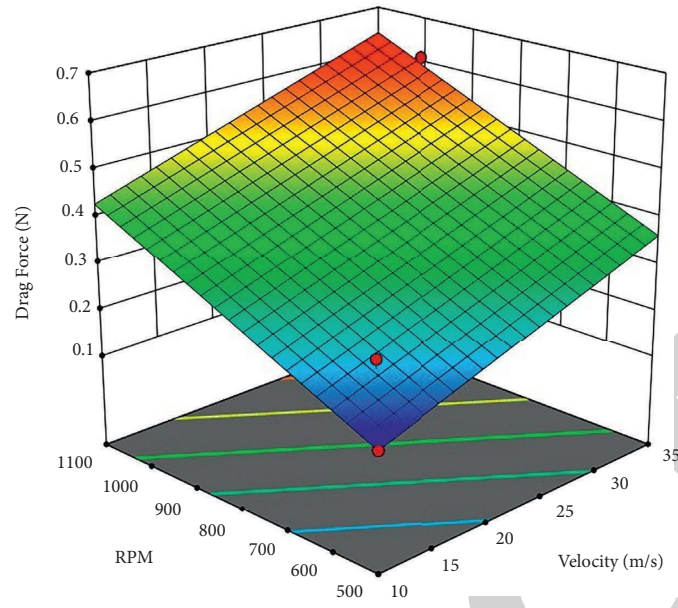


FIGURE 16: Drag force measured for the NASA SC(2)-0714 model.

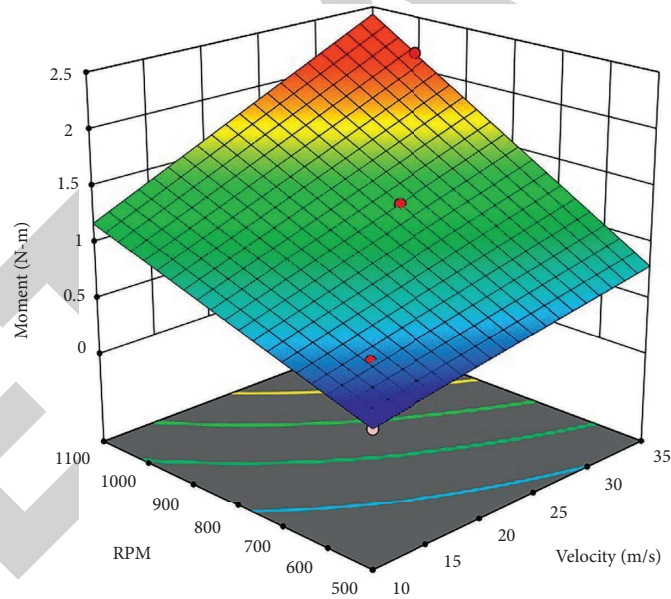


FIGURE 17: Moment measured for the HH02 model.

The comparison table clearly shows that aerodynamic efficiency for the NASA SC(2)-0714 rotor was better than the HH02 rotor by around 30 to 40% for all speeds. The CFD results obtained for static analysis also showed an improved aerodynamic efficiency of approximately 40%, as discussed in Chapter 4. The experimental data also proved that the NASA SC(2)-0714 rotor provides better aerodynamic performance than the HH02 rotor.

**4.3. Validation of Results.** For the model's dynamic similarity, force on the model should be equal to the force on the prototype.

Force can be calculated from the relation for dynamic similarity as follows:

$$\begin{aligned} (\text{force})_{\text{prototype}} &= (\text{force})_{\text{model}}, \\ F &= m \times a \end{aligned} \quad (4)$$

where “ $m$ ” is the mass of the body and “ $a$ ” is the acceleration due to gravity.



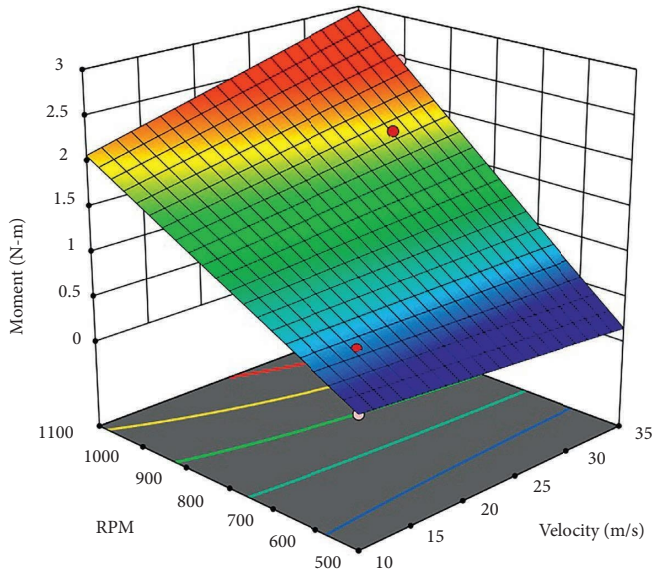


FIGURE 18: Moment measured for NASA SC(2)-0714 model.

TABLE 7: Comparison of experimental aerodynamic efficiency.

S. no.	Velocity	L/D NASA SC(2)-0714	L/D HH02	% of improvement
1	10	17.46	11.05	36.71249
2	14	18.44	10.58	42.62473
3	19	19.23	12.65	34.21737
4	25	19.7	12.54	36.34518
5	30	20.92	15.49	25.95602
6	35	21.18	15.46	27.00661

TABLE 8: Validation of the NASA SC(2)-0714 rotor.

S. no.	Velocity	Exp lift force	CFD lift force	% of error
1	10	1680.599	1980	15.12
2	14	2957.085	3384	12.61
3	19	3701.167	4251	12.93
4	25	5061.041	5754	12.04
5	30	6844.272	7600	9.94
6	35	8326.021	9051	8.01

TABLE 9: Validation of HH02 rotor.

S. no.	Velocity	Exp lift force	CFD lift force	% of error
1	10	1417.605	1684	15.81
2	14	2103.956	2450	14.12
3	19	3245.737	3751	13.47
4	25	4502.979	5152	12.59
5	30	6061.703	6742	10.09
6	35	7440.82	8201	9.27

Mass flow rate is given as follows:

$$\dot{m} = \rho AV. \tag{5}$$

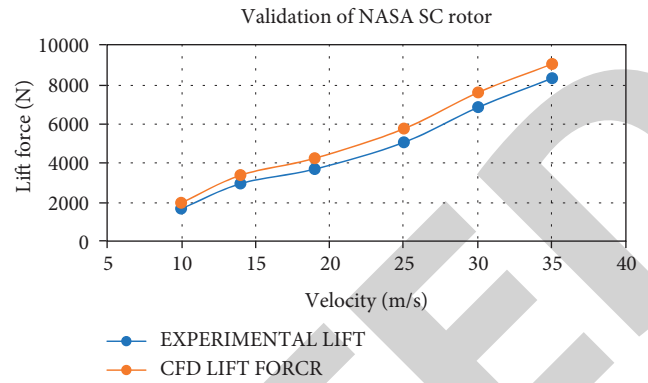


FIGURE 19: Validation of the NASA SC(2)-0714 rotor.

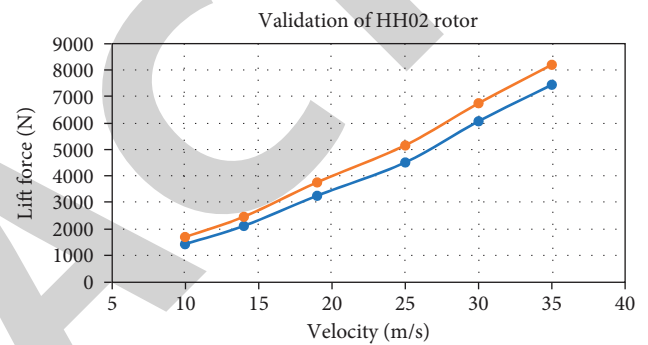


FIGURE 20: Validation of the HH02 rotor.

From the relation, it can be found that it is a scaled model from 120 cm to 5 cm. The scale ratio is 24.

$$(F)_{\text{prototype}} = 641.45 \times (F)_{\text{model}}. \tag{6}$$

The CFD and experimental values are compared from the calculation of force as in Tables 8 and 9.

The validation of results was mentioned in Tables 8 and 9. It compares the percentage of changes in the CFD and experimental results. It shows that the error percentage is around 15% for lower speed and much lesser at higher speed. It is around 9% for both NASA SC rotor and HH02 rotor. Figures 19 and 20 represent the validation of results and change of nature of the curve for both NASA SC(2)-0714 and HH02 rotors with the CFD and experimental results.

## 5. Conclusion

The analysis was carried out using the CFD techniques, and the results were validated by wind tunnel testing. Results are validated, and the error percentage is 8% to 15%. Error percentages are within the acceptable limit, and the results are validated with the help of the experimental data. Additive manufacturing techniques are very useful in the aerodynamic testing and validation of models. The computational analysis was successfully validated using an additive manufacturing technique and proved to be the same with acceptable error limits. Error percentage can be minimized by using other methods like SLA or SLS techniques to reduce

the error percentage in experimental results. FDM methods are economical, and it has some roughness over the model. SLS and SLA technique models will have a good finishing and smooth surface. The error in the experimental analysis may be due to the roughness of the FDM method in additive manufacturing. The analysis may be conducted with other additive manufacturing techniques and can be tested in the future for accurate results. Aerodynamic performance can be compared and studied for better additive manufacturing models.

## Data Availability

The data used to support the findings of this study are available from the corresponding author upon request.

## Conflicts of Interest

The authors declare that there are no conflicts of interest regarding the publication of this article.

## References

- [1] Petrescu, R. Victoria, R. Aversa et al., "About helicopters," *Journal of Aircraft and Spacecraft Technology*, vol. 1, no. 3, pp. 204–223, 2017.
- [2] G. J. Leishman, *Principles of Helicopter Aerodynamics with CD Extra*, Cambridge University Press, Cambridge, UK, 2006.
- [3] I. Hasan, R. Mukesh, P. Radha Krishnan, V. Srinath, and R. Dhanya Prakash, "Computational study of aerodynamic performance of three and four-bladed helicopter rotor with supercritical airfoil," *JOURNAL OF ENVIRONMENTAL PROTECTION AND ECOLOGY*, vol. 22, no. 6, pp. 2622–2633, 2021.
- [4] J. M. Seddon and N. Simon, *Basic Helicopter Aerodynamics*, John Wiley & Sons, Hoboken, New Jersey, U.S, 2011.
- [5] F. X. Caradonna and T. Chee, "Experimental and analytical studies of a model helicopter rotor in hover," in *Proceedings of the European Rotorcraft and Powered Lift Aircraft Forum*, Amsterdam, The Netherlands, September, 1981.
- [6] A. Brocklehurst and G. N. Barakos, "A review of helicopter rotor blade tip shapes," *Progress in Aerospace Sciences*, vol. 56, pp. 35–74, 2013.
- [7] M. Costes, T. Renaud, and B. Rodriguez, "Rotorcraft simulations: a challenge for CFD," *International Journal of Computational Fluid Dynamics*, vol. 26, no. 6-8, pp. 383–405, 2012.
- [8] W. L. Oberkampf and T. G. Trucano, "Verification and validation in computational fluid dynamics," *Progress in Aerospace Sciences*, vol. 38, no. 3, pp. 209–272, 2002.
- [9] V. F. Kopyev, M. Y. Zaytsev, V. I. Vorontsov, S. A. Karabasov, and V. A. Anikin, "Helicopter noise in hover: computational modelling and experimental validation," *Acoustical Physics*, vol. 63, no. 6, pp. 686–698, 2017.
- [10] D. Srinivasan, M. Meignanamoorthy, M. Ravichandran et al., "3D printing manufacturing techniques, materials, and applications: an overview," *Advances in Materials Science and Engineering*, vol. 202110 pages, Article ID 5756563, 2021.
- [11] M. R. Ridho, E. A. Agustiany, M. Rahmi Dn et al., "Lignin as green filler in polymer composites: development methods, characteristics, and potential applications," *Advances in Materials Science and Engineering*, vol. 202233 pages, Article ID 1363481, 2022.
- [12] S. C. Joshi and A. A. Sheikh, "3D printing in aerospace and its long-term sustainability," *Virtual and Physical Prototyping*, vol. 10, no. 4, pp. 175–185, 2015.
- [13] V. Mohanavel, T. Sathish, M. Ravichandran, P. Ganeshan, M. Ravi Kumar, and R. Subbiah, "Experimental investigations on mechanical properties of cotton/hemp fiber reinforced epoxy resin hybrid composites Journal of Physics: conference Series," *Journal of Physics: Conference Series*, vol. 2027, no. 1, Article ID 012015, 2021.
- [14] M. Ravichandran, V. Mohanavel, T. Sathish, P. Ganeshan, S. Suresh Kumar, and R. Subbiah, "Mechanical properties of AlN and molybdenum disulfide reinforced aluminium alloy matrix composites Journal of Physics: conference Series," *Journal of Physics: Conference Series*, vol. 2027, no. 1, Article ID 012010, 2021.
- [15] T. Raja, S. Ravi, A. Karthick et al., "Comparative study of mechanical properties and thermal stability on banyan/ramie fiber-reinforced hybrid polymer composite," *Advances in Materials Science and Engineering*, vol. 202111 pages, Article ID 5835867, 2021.
- [16] I. Hasan, "Aerodynamic performance analysis of a supercritical airfoil in the helicopter main rotor," *Transactions of the Canadian Society for Mechanical Engineering*, vol. 46, no. 2, pp. 436–458, 2022.
- [17] K. M. Pandey and U. Kumar, "Gaurav kumar, dhrubajyoti deka, dipankar das, and anand surana. "CFD analysis of an isolated main helicopter rotor for a hovering flight at varying RPM," *ASME International Mechanical Engineering Congress and Exposition*, vol. 45172, pp. 543–551, 2012.
- [18] C. Aumnate, A. Pongwisuthiruchte, P. Pattananuwat, and P. Potiyaraj, "Fabrication of ABS/graphene oxide composite filament for fused filament fabrication (FFF) 3D printing," *Advances in Materials Science and Engineering*, vol. 20189 pages, Article ID 2830437, 2018.
- [19] Y. Man, X. Luo, Z. Xie, and D. Qu, "Influence of 3D printed topological structure on lightweight mullite load bearing board in thermal environment," *Advances in Materials Science and Engineering*, vol. 20208 pages, Article ID 8340685, 2020.
- [20] I. Hasan, R. Mukesh, P. Radha Krishnan, R. Srinath, and R. B Dhanya Prakash, "Forward flight performance analysis of supercritical airfoil in helicopter main rotor," *Intelligent Automation & Soft Computing*, vol. 33, no. 1, pp. 567–584, 2022.
- [21] R. Steijl, G. Barakos, and K. Badcock, "A framework for CFD analysis of helicopter rotors in hover and forward flight," *International Journal for Numerical Methods in Fluids*, vol. 51, no. 8, pp. 819–847, 2006.
- [22] S. K. Raman, W. Kexin, T. Ho Kim, A. Suryan, and H. D. Kim, "Effects of flap on the reentry aerodynamics of a blunt cone in the supersonic flow," *International Journal of Mechanical Sciences*, vol. 176, Article ID 105396, 2020.
- [23] R. Mukesh, K. Lingadurai, and U. Selvakumar, "Airfoil shape optimization based on surrogate model," *J. Inst. Eng. India Ser. C*, vol. 99, pp. 1–8, 2018.
- [24] P. J. Roache, "Quantification of uncertainty in computational fluid dynamics," *Annual Review of Fluid Mechanics*, vol. 29, no. 1, pp. 123–160, 2020.
- [25] H. Yamashita, N. Kuratani, M. Yonezawa et al., "Wind tunnel testing on start/unstart characteristics of finite supersonic biplane wing," *International Journal of Aerospace Engineering*, vol. 201310 pages, Article ID 231434, 2013.
- [26] C. Zuo, C. Wei, J. Ma, T. Yue, L. Liu, and Z. Shi, "Full-Field displacement measurements of helicopter rotor blades using

## *Retraction*

# **Retracted: Optimizing the Parameters of Zirconium Carbide and Rice Husk Ash Reinforced with AA 2618 Composites**

### **Advances in Materials Science and Engineering**

Received 26 December 2023; Accepted 26 December 2023; Published 29 December 2023

Copyright © 2023 Advances in Materials Science and Engineering. This is an open access article distributed under the Creative Commons Attribution License, which permits unrestricted use, distribution, and reproduction in any medium, provided the original work is properly cited.

This article has been retracted by Hindawi, as publisher, following an investigation undertaken by the publisher [1]. This investigation has uncovered evidence of systematic manipulation of the publication and peer-review process. We cannot, therefore, vouch for the reliability or integrity of this article.

Please note that this notice is intended solely to alert readers that the peer-review process of this article has been compromised.

Wiley and Hindawi regret that the usual quality checks did not identify these issues before publication and have since put additional measures in place to safeguard research integrity.

We wish to credit our Research Integrity and Research Publishing teams and anonymous and named external researchers and research integrity experts for contributing to this investigation.


The corresponding author, as the representative of all authors, has been given the opportunity to register their agreement or disagreement to this retraction. We have kept a record of any response received.

### **References**

- [1] C. R. Mahesha, R. Suprabha, S. Thenmozhi et al., "Optimizing the Parameters of Zirconium Carbide and Rice Husk Ash Reinforced with AA 2618 Composites," *Advances in Materials Science and Engineering*, vol. 2022, Article ID 1962523, 11 pages, 2022.

## Research Article

# Optimizing the Parameters of Zirconium Carbide and Rice Husk Ash Reinforced with AA 2618 Composites

C. R. Mahesha,<sup>1</sup> R. Suprabha,<sup>1</sup> S. Thenmozhi,<sup>2</sup> V. Gowri,<sup>2</sup> Chirumamill Mallika Chowdary,<sup>3</sup> V. Savithiri,<sup>4</sup> B. V. V. L. Kala Bharathi,<sup>5</sup> Ram Subbiah,<sup>6</sup> and Ishwarya Komalnu Raghavan <sup>7</sup>

<sup>1</sup>Department of Industrial Engineering & Management, Dr. Ambedkar Institute of Technology, Bangalore 560056, Karnataka, India

<sup>2</sup>Department of Civil Engineering, St. Joseph's College of Engineering, OMR, Chennai 600119, Tamil Nadu, India

<sup>3</sup>Department of Civil Engineering, Koneru Lakshmaiah Education Foundation, Guntur 522302, Andhra Pradesh, India

<sup>4</sup>Institute of Mechanical Engineering, Saveetha School of Engineering, Saveetha University, Chennai 602105, Tamilnadu, India

<sup>5</sup>Department of Electrical and Electronics Engineering, Aditya Engineering College, Surampalem 533437, Andhra Pradesh, India

<sup>6</sup>Department of Mechanical Engineering, Gokaraju Rangaraju Institute of Engineering and Technology, Hyderabad 500090, Telangana, India

<sup>7</sup>Department of ElectroMechanical Engineering, Faculty of Manufacturing, Institute of Technology, Hawassa University, Hawassa, Ethiopia

Correspondence should be addressed to Ishwarya Komalnu Raghavan; [ishwarya138@hu.edu.et](mailto:ishwarya138@hu.edu.et)

Received 5 July 2022; Revised 10 August 2022; Accepted 4 September 2022; Published 21 September 2022

Academic Editor: K. Raja

Copyright © 2022 C. R. Mahesha et al. This is an open access article distributed under the Creative Commons Attribution License, which permits unrestricted use, distribution, and reproduction in any medium, provided the original work is properly cited.

Stir casting was utilized to generate the composites. The AA 2618–10wt% zirconium carbide 10wt% rice husk ash hybrid composite had the highest hardness value. In comparison to pure AA 2618, it had a 72% increase. The rule of mixture was used to compute theoretical density, whereas the Archimedes rule was utilized to evaluate real density. For AA 2618, AA 2618/zirconium carbide, and rice husk ash hybrid composites, simple carbide inserts were used for turning. Surface roughness, metal removal rate, and tool wear were among the numerous responses examined. RSM was utilized to analyze and optimize the test outcomes. Feed rate was the most critical issue for surface roughness and material removal rate. Tool wear was shown to be most strongly controlled by tool speed, whereas metal removal rate was found to be least significantly influenced by the weight percent of reinforcement.

## 1. Introduction

Aluminum alloy 2618 is a strong but lightweight alloy. For automotive and aerospace applications, this material meets the majority of the standards. In the mineral and chemical processing sectors, AA 2618 has found numerous uses. Particulates and fibers can be added to the matrix of composite materials made with the AA 2618 substance. Carbonates, oxides ( $\text{Al}_2\text{O}_3$  and  $\text{SiO}_2$ ), and nitrides are some of the ceramic materials used in reinforcing ( $\text{Al}_2\text{O}_3$  and  $\text{Si}_3\text{N}_4$ ). AA2618-based metal matrix composites (MMCs) may be made using these reinforcements [1–6]. Excellent

mechanical qualities such as TS, compression strength, and wear resistance are just few of MMC's advantages [7]. Aluminum-based composite engine blocks have replaced cast iron engine blocks in an effort to reduce vehicle weight and improve fuel economy [8, 9]. The manufacturing of MMCs is still a problem. Stir casting, squeeze casting, powder metallurgy, and diffusion bonding are among of the techniques used to create MMCs [10]. In terms of MMC production, stir casting is the preferred process due to its great efficiency and low cost [11]. Excess material is removed from the material matrix composites while the desired surface polish is provided via machining procedures.

However, the presence of strong ceramic reinforcements in MMCs makes machining them difficult.

A number of investigators have sought to develop distinct MMCs for diverse purposes. Using RHA and aluminum alloy, Ragupathi and Kumar [12] created a composite. The inclusion of RHA components increased the hardness, according to the research [13]. A graphite- and  $\text{Al}_2\text{O}_3$ -reinforced AA 2618 hybrid composite was created in [14, 15]. Composites were shown to have greater hardness, flexural strength, compression strength, and TS than pure AA 2618 [16]. The zirconium carbide-reinforced AA 2618 composite was made by [17] and reported having superior mechanical qualities than pure AA 2618 by AA2618/zirconium carbide composite. They found that the mechanical characteristics of the AA 2618-based hybrid composite were superior to those of AA 6061. It was discovered that [18, 19] the rice husk ash- and graphite-based aluminum alloy hybrid compound had a rise in hardness at all weight percent of strengthened particles. It was made in [20, 21] with the help of rice husk ash and fly ash. It was discovered that TS and hardness were at their highest at 20% rice husk ash and 20% fly ash [22]. The AA 2618/zirconium carbide composite was described in [23, 24]. Increased ceramic phase content in a composite has been shown to increase its hardness [18]. In terms of outcome and fracture strength, the lowest particles of strengthening were shown to be the most effective. In [25–27], a nanocomposite of AA 2618 and  $\text{Al}_2\text{O}_3$  was created.  $\text{Al}_2\text{O}_3$ -reinforced aluminum alloy 6061 exhibits superior mechanical characteristics compared to pure AA 6061. A zirconium carbide- and rice husk ash-based aluminum alloy 2618 hybrid composite was developed in [28, 29]. In a mixture of 10% zirconium carbide and 10% RHA, the greatest hardness was achieved [30–33].

To ensure that the finished product has an appealing appearance, it is necessary to identify the mechanical properties for improved surface quality at a cheaper cost. Commercialization of MMCs is hampered by their machinability. In their wear investigation, [34] employed diamond inserts to machine Silicon carbide-based aluminum alloy composites. When machining MMCs, Nguyen et al. [35] investigated how ceramic particles affect surface roughness. TiN-coated WC carbide tools were used in [36] to cut the silicon carbide-based aluminum alloy compound. They looked at the machinability of the final composite in relation to the reinforcing particle. At a high percentage of reinforcement, high tool wear was observed [37]. SR and TW were found to be lower in the AA 2618/SiC composite when machining pure AA 2618 [38]. RSM was used to mill the  $\text{Al}_2\text{O}_3$ - and Gr-reinforced aluminum alloy 6061 hybrid compound to determine surface roughness. This study found that speed was the most critical component in the machining of an aluminum alloy 6061/ $\text{Al}_2\text{O}_3$ /Gr hybrid compound. Cutting parameters for the AA2618/SiC composite were adjusted in [39] to reduce power consumption and maximize tool life. While machining the AA 2618/SiC nanocomposite, Liu et al. and He et al. [40, 41] used RSM as a tool. SiC was used as a reinforcing agent in the composite. As feed rate increased while machining polymer matrix composites using Taguchi's approach, Shojaie-Bahaabad and

Hasani-Arefi [42] discovered that surface roughness increased. Cutting parameters for cutting forces were optimized in [43] for machining AA 2618-T6. The RSM was used in [44] to reduce the surface roughness of AA 5052 during machining. The cutting forces and surface roughness of SiC- and zirconium carbide-based hybrid composites were measured in [45]. The RSM technique was used to optimize the design. Ouyang et al. [46] used polycrystalline diamond cutting inserts to measure the surface roughness of an AA 2618/SiC composite while it was being turned.

As a continuation of the prior work, we are conducting this study. The AA 2618/zirconium carbide/rice husk ash hybrid composite was the subject of prior research that concentrated on its manufacturing and characterization. An in-depth examination of the material's machining characteristics is required before it can be made commercially available. Nothing about milling (turning) an AA 2618/zirconium carbide/rice husk ash hybrid composite has been documented, according to the literature.

## 2. Materials and Methods

For making a composite, different materials are used, and their purpose is listed in Table 1.

## 3. Sample Preparation

*3.1. Stir Casting from the Bottom-Up.* Bottom pouring-type stir casting machines were used to make the workpiece. AA 2618, AA 2618–5% zirconium carbide composite, and AA 2618–10% zirconium carbide composite were the three types of workpieces made. A flow rate of 10 liters per minute of 99.99% pure argon gas was used during the casting process. In a graphite crucible, the material begins to melt at 485°C. Reinforcement particles were preheated at 300°C for 40 minutes before zirconium carbide and rice husk ash additions were made in melted pure AA 2618 to remove moisture. Silicon and oxygen are included in rice husk ash's silica ( $\text{SiO}_2$ ). AA 2618 and reinforcement particles form a weak contact, which causes a wettability issue when the matrix and reinforcement material are mixed together. Prior to the addition of zirconium carbide and rice husk ash particles, mechanical stirring was carried out at 415 rpm. Vibratory action produced by the machine's reinforcement feeder attachment adds the preheated reinforcement particle to the melted AA2618. After 4 minutes of stirring, the AA 2618 and reinforcement particles were thoroughly mixed (zirconium carbide and rice husk ash). It was necessary to use an attached permanent mold of die steel that had a rectangular cavity of  $20 \times 10 \times 250$  mm, and two cylindrical cavities of  $25 \times 250$  mm and  $18 \times 250$  mm to pour the AA 2618 melt into. When pouring molten metal into the mold during casting, it was crucial that the mold's screws were properly tightened to ensure a suitable vacuum. By heating the mold to 450°C, the temperature gradient was eliminated. After the mold had cooled, the samples were taken out. Figure 1 shows the stir casting setup.

TABLE 1: Purpose of different materials and their usage.

Materials	Usage
AA2618	Matrix material, which is used for high-temperature applications
Zirconium carbide	Hard reinforcement: it is highly corrosion resistant with greater conductivity
Rice husk ash	A softer alternative to reinforcing a structure: for better machinability, RHA can be used as an alternative
$K_2TiF_6$	It is used as a filler. Between the AA2618 matrix and reinforcement, it becomes more wettable

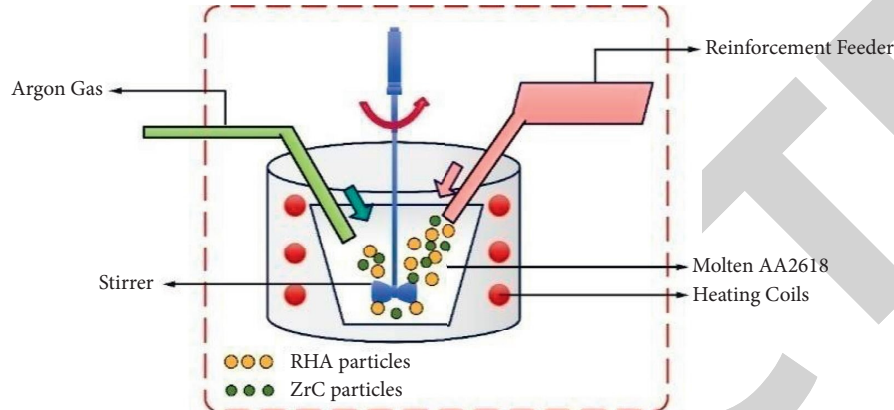


FIGURE 1: Stir casting machine.

## 4. Mechanical Performance and Characterization

### 4.1. Mechanical Characteristics

**4.1.1. Hardness.** In order to determine hardness of the samples, we turned to the Mitutoyo HM 100 series of Vicker's hardness tester. Stress was applied for 15 seconds at a rate of 5 N, according to ASTM E-384. There was a calculation of the mean of three hardness values.

**4.1.2. Impact Strength.** The specimens' impact resistance was determined using Charpy/Izod pendulum testing machines with 200 J capacity, in accordance with ASTM D 256 standards. Specimens have a 10 × 10 mm cross-sectional area.

**4.1.3. Density.** The principle of mixtures connection was used to compute the theoretic density of the fabricated composite; it is an approach for estimating the whole properties of composite material given matrix and reinforcing characteristics. (1) is the formula used to determine density.

$$\rho_c = \rho_b \times W_b + \rho_r \times W_r + \{1 - (W_b + W_r)\} \times \rho_m \quad (1)$$

**4.2. Machining of the Composite.** A CNC lathe (turning machine) was used in this study to perform a slew of turning experiments. As-cast AA 2618, AA 2618/10% zirconium carbide composite, and AA 2618/10% zirconium carbide/10% rice husk ash composite were used in the machining process. Turning operations were carried out using titanium carbide inserts. A single insert has a total of

eight cutting edges. Each process only made use of one edge. 27 trials were carried out using a total of seven inserts. Table 2 contains the characteristics of the tool inserts provided by the provider.

**4.2.1. Experimental Arrangement.** The studies are performed in dry-cutting circumstances on a CNC turning machine. A consistent power source was maintained throughout the process. There is a complete breakdown of each component's input and output variables shown.

**4.2.2. Variables Chosen for Both Input and Output.** The basic objective of the machining industry is to maximize output while minimizing surface roughness and TW. Work carried out by [47] was used to establish the input values for carbide inserts used during workpiece machining. Table 3 displays the values of the input factors.

## 5. Calculation of Responses

**5.1. Surface Roughness (Ra) Evaluation.** In terms of surface roughness, the more peaks and valleys there are greater the value of Ra. Contact type SR tester Mitutoyo SJ-301 measured the surface roughness. Surface roughness was measured with a cutoff length of 800 μm. The surface roughness of machined tasters was measured three times with the average of the three readings.

**5.2. Measurement of Material Removal Rate.** Equation (2) was used to compute the material removal rate.

$$\text{Material Removal Rate} = \frac{(W_{bm} - W_{am})}{T} \quad (2)$$



TABLE 2: Detailed description of the equipment.

ISO description	Hole diameter (mm)	Elements	Figure	Nose radius (mm)	Grade	Covered angle	Enclosure IC size (mm)	Width (mm)
CNMG 120408	5.16	Plain carbide	80° rhombic	0.8	TT 8125	80°	12.7	4.76

TABLE 3: Input factors and their levels.

Level units	Reinforcement wt%	Speed (m/min)	Feed (mm/rev)	Depth of cut (mm)
-1	0	190	0.2	1
0	10	210	0.4	1.5
+1	20	230	0.6	2

where  $W_{bm}$  is the weightage before machining (gms),  $W_{am}$  is the weightage after machining (gms), and  $T$  is the turning time (sec).

## 6. Results and Discussion

**6.1. Hardness Impact.** Table 4 shows the outcomes of hardness testing on several compound samples. The hardness was demonstrated to increase with the addition of zirconium carbide and rice husk ash. An example of this variance can be seen in Figure 2.

**6.2. Impact on Impact Strength.** The inclusion of hard zirconium carbide particles improved the impact strength of AA 2618. Amplified plastic deformation energy was the cause of the observed increase. The materials required higher energy to fracture when AA 2618/zirconium carbide and 2618/zirconium carbide/rice husk ash are used. Figure 3 depicts the impact strength effect of reinforcing.

**6.3. Effect on Density.** In comparison to pure AA 2618, the density of AA 2618/zirconium carbide/rice husk ash particles is lower. According to the findings, there was just a little discrepancy between the composite's theoretical and actual density as shown in Figure 4. Rice husk ash particle density is lower than zirconium carbide particle density and AA 2618 matrix density. As a result, the density of the final composite is reduced owing to the presence of rice husk ash particles.

**6.4. Machinability of the Composite.** Computed numerical control (CNC) lathe machines are employed during experiments to test for machinability. Surface roughness, tool wear, and material removal rate were all measured. Results from each trial were analyzed three times. This study presents the average of the measured responses. Table 5 displays the findings of the experiments.

### 6.5. Study of Responses

**6.5.1. Surface Roughness Analysis.** We used a changed cubic model for surface roughness investigation. A power transformation is used to simplify the model, with  $y' = (y + k)$  and

$\lambda = 0.95$  and  $k = 0$ . To fit the data, we utilized the values of  $k$  and  $\lambda$ . ANOVA was applied to validate the importance of the model selected. Surface roughness has an important effect on overall surface quality, according to the results of an ANOVA in Table 6.

**6.5.2. Study of Tool Wear.** The tool wear is modelled using a modified cubic model. The model with  $y' = 1/\text{Square root}(y + k)$  was reduced using inverse square root transformation, with  $k$  selected to be 2.5 in order to rise the importance of the model. ANOVA was employed to verify the model's suitability. Table 7 displays the analysis of variances for the tool wear model.

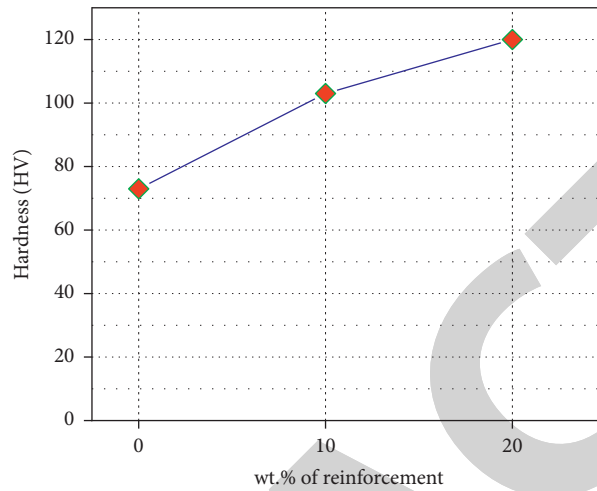
**6.5.3. Analysis of MRR.** The data fitting in the model was carried out using only the quadratic model, which did not require any transformations. Table 8 displays that the ANOVA table supported the selected model.

**6.6. Impact on Tool Wears.** Analysis of variance tables demonstrated that cutting speed was the maximum relevant component, tracked by feed, cutting depth, and strengthening weight percentage. The tool wear was found to be larger when the feed rate and depth of cut were both at their lowest points. Its less of a problem when the feed and cut depth are at their maximum. It has been found that cutting speed is the more critical factor in determining TW. The wear on a tool rises as the cutting speed rises. The rate at which the tool and workpiece rub against each other increases the amount of heat generated. Cutting tool materials lose thermostability and become increasingly worn when the rate of heat generation increases at the tooltip. Figure 5 depicts the process of tool wear. There are two mechanisms in action when a carbide tool's tip comes into contact with an aluminum alloy 2618 workpiece that is rotating. As you wear it, the tip changes colour. When the tip comes into contact with the AA 2618/zirconium carbide composite, the wear increases. When hard ZrC particles interact with the tooltip wear increases. In the AA 2618/ZrC/rice husk ash hybrid composite, less tool wear was observed. The machinability of the material has improved as a result of rice husk ash reinforcement.



TABLE 4: Impact on the hardness.

S. no.	ZrC (wt%)	Rice husk ash (wt%)	Total reinforcement (wt%)	Hardness (HV)
1	0	0	0	71 ± 4
2	5	5	10	106 ± 3
3	10	10	20	122 ± 5



Load = 5 N  
Dwell Time = 15 s

FIGURE 2: Effect of reinforcement on the hardness.

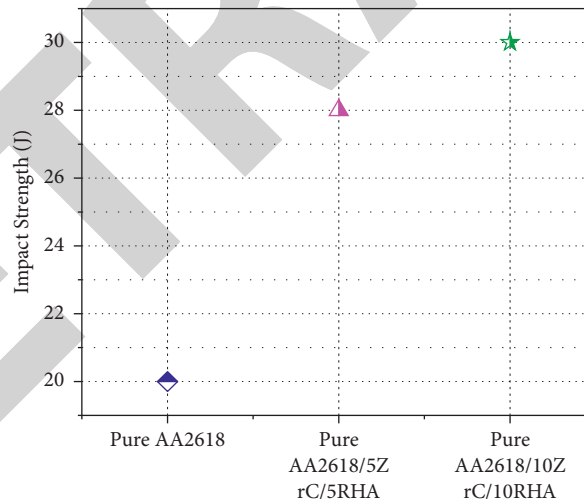


FIGURE 3: Effect on impact strength.

6.7. Optimization of Responses. Maximizing or eliminating a desired or unwanted quantity is the primary goal of optimization. As part of this study, there are three outcomes as follows: surface roughness, TW, and material removal rate. All responses are considered during multiresponse optimization, which ensures that all input parameters are

optimized simultaneously. Desirability analysis is used to improve this. Table 9 shows the optimization objective and input ranges.

Figure 6 shows that the optimal parameters for favorable replies were 0 percent reinforcement, 198.96 m/min speed, 0.324 mm/rev feed rate, and 2 mm depth of cut. At these

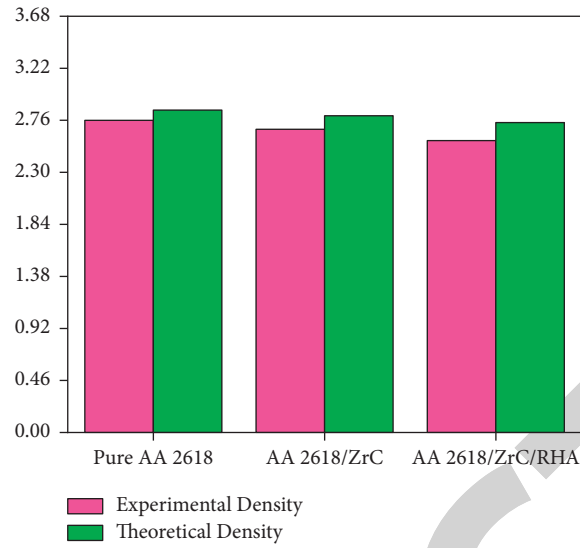


FIGURE 4: Effect on density.

TABLE 5: Output of the experiments.

Standard order units	Run order	A-reinforcement (wt %)	B-speed (m/min)	C-feed (mm/rev)	D-depth of cut (mm)	Ra ( $\mu\text{m}$ )	Tool wear ( $\mu\text{m}$ )	MRR (g/min)
19	1	0	210	0.6	1.5	0.98	69.6	8
23	2	10	190	0.4	2	0.78	56	14.5
20	3	20	210	0.6	1.5	1.6	60.7	10
7	4	10	210	0.2	2	1.4	31	16
17	5	0	210	0.2	1.5	0.92	18.6	9.5
12	6	20	210	0.4	2	1.41	62	12.5
8	7	10	210	0.6	2	1.03	89.9	8
2	8	20	190	0.4	1.5	1.3	35	9
25	9	0	210	0.4	1.5	1.03	41.5	11.5
6	10	10	210	0.6	1	1.41	29.6	15
13	11	10	190	0.2	1.5	0.75	17.8	15
4	12	20	210	0.4	1.5	0.78	42.2	7
5	13	10	210	0.2	1	0.55	10	18.5
24	14	10	230	0.4	2	1.46	65	8.5
2	15	10	210	0.4	1.5	0.82	39.8	20
26	16	10	210	0.4	1.5	1.06	41.2	19
1	17	0	190	0.4	1.5	1.2	35.3	9.5
15	18	10	190	0.6	1.5	1.22	53.9	11
14	19	10	230	0.2	1.5	1.25	21.8	10.5
3	20	0	230	0.4	1.5	1.06	42	4.5
9	21	0	210	0.4	1	0.85	18.8	16.5
18	22	20	210	0.2	1.5	0.8	20	10.5
22	23	10	230	0.4	1	1.02	21.56	7.5
11	24	0	210	0.4	2	0.65	59.58	15
10	25	20	210	0.4	1	0.74	20	11
21	26	10	190	0.4	1	0.65	18	13
16	27	10	230	0.6	2	1.6	65.64	4.5

TABLE 6: Surface roughness (Ra) ANOVA result.

Source	SS	DOF	Mean square	F value	P value prob > F
Model	1.73	16	0.11	15.40	<0.0001
A	0.097	1	0.097	13.81	0.0042
B	0.055	1	0.055	7.79	0.0193
C	0.35	1	0.35	48.96	<0.0002
D	0.16	1	0.16	21.18	0.0010
AB	0.035	1	0.035	4.95	0.0506
AC	0.12	1	0.12	15.70	0.0028
AD	0.17	1	0.17	22.49	0.0009
BC	9.601E-004	1	9.601E-004	2.23	0.2956
BD	0.022	1	0.022	3.98	0.1155
CD	0.29	1	0.29	41.66	<0.0002
B <sup>2</sup>	0.036		0.036	3.72	0.0829
C <sup>2</sup>	0.080	1	0.080	9.97	0.0103
D <sup>2</sup>	5.398E-004	1	5.398E-004	0.64	0.2246
AB <sup>2</sup>	0.065	1	0.065	10.34	0.0127
BC <sup>2</sup>	0.16	1	0.16	21.98	0.0012
BD <sup>2</sup>	0.31	1	0.31	40.44	<0.0002
Residual	0.072	10	7.985E-004		
Lack of fit	0.050	8	5.972E-004	0.34	0.8954
Error	0.040	2	0.016		
Total	1.81	27			

TABLE 7: Tool wear results on ANOVA.

Source	SS	Dof	Mean square	F value	P value prob > F
Model	0.25	17	0.25	8.86	0.0005
A	6.956E-007	1	6.956E-007	4.52E-004	0.9478
B	0.027	1	0.027	17.17	0.0021
C	8.634E-004	1	8.634E-004	4.98	0.0500
D	7.140E-005	1	7.140E-005	0.41	0.5417
AB	4.594E-005	1	4.594E-005	0.31	0.5967
AC	3.394E-005	1	3.394E-005	0.23	0.6486
AD	4.485E-006	1	4.485E-006	0.28	0.6008
BC	0.023	1	0.023	15.10	0.0037
BD	10.058E-006	1	10.058E-006	0.058	0.8132
CD	3.784E-004	1	3.784E-004	3.41	0.1527
A <sup>2</sup>	0.023	1	0.023	15.34	0.0037
B <sup>2</sup>	0.075	1	0.075	49.31	<0.0002
C <sup>2</sup>	0.018	1	0.018	13.36	0.0057
B <sup>2</sup> C	0.015	1	0.015	9.14	0.0128
BC <sup>2</sup>	7.014E-004	1	7.014E-004	5.57	0.0585
C <sup>2</sup> D	6.719E-004	1	6.719E-004	5.38	0.0632
Residual	0.016	10	1.53E-004		
Lack of fit	8.869E-003	8	1.336E-004	0.46	0.8309
Pure error	6.513E-004	2	3.857E-004		
Cor total	0.27	26			

TABLE 8: ANOVA for material removal rate.

Source	SS	Degrees of freedom	Mean square	F value	P value prob > F
Model	10329.27	14	10329.27	1422.41	<0.0001
A	2.19	1	2.19	4.22	0.0628
B	156.53	1	156.53	299.70	<0.0001
C	4938.68	1	4938.68	9329.50	<0.0002
D	4898.29	1	4898.29	9435.23	<0.0002
AB	0.064	1	0.064	0.3	0.7347
AC	0.050	1	0.050	0.078	0.7962
AD	0.013	1	0.013	0.024	0.8813
BC	15.99	1	15.99	29.86	0.0003
BD	11.38	1	11.38	20.98	0.0009
CD	405.01	1	405.01	781.29	<0.0002
A <sup>2</sup>	5.97	1	4.97	8.56	0.0095
B <sup>2</sup>	5.09	1	4.09	8.86	0.0162
C <sup>2</sup>	0.79	1	0.79	1.50	0.2458
D <sup>2</sup>	0.28	1	0.28	0.56	0.4730
Residual	7.24	12	0.53		
Lack of fit	5.59	10	0.47	0.61	0.7846
Error	1.66	2	0.83		
Total	10345.60	26			

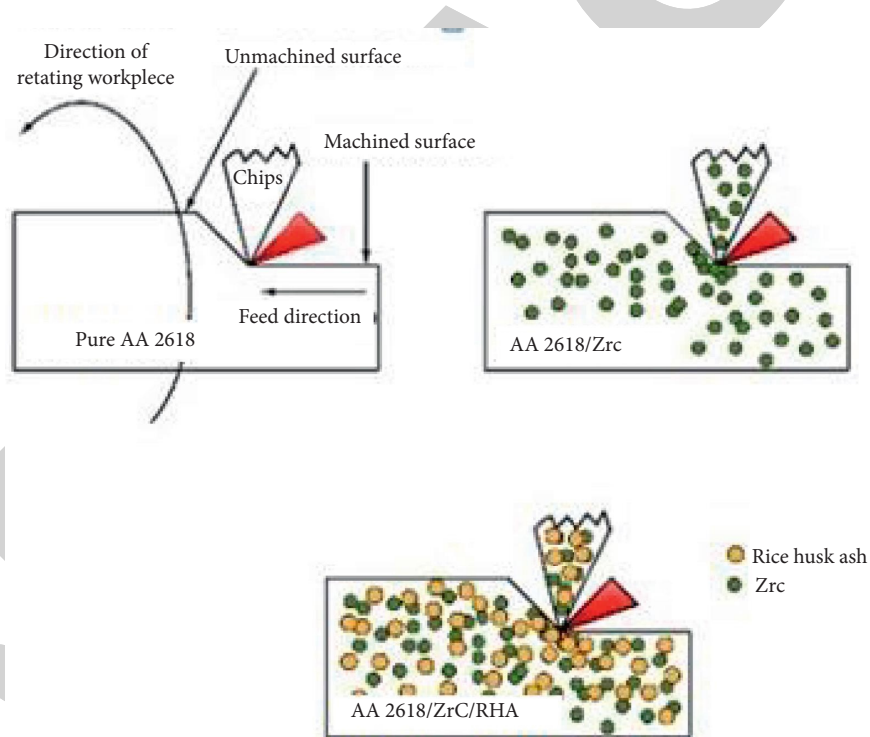


FIGURE 5: Mechanism of tool wear in AA 2618, AA 2618/ZrC composite, and AA2618/ZrC/RHA hybrid composite.

TABLE 9: Optimization goal and input ranges.

Inputs	Goal	Minimum limit	Maximum limit	Significance
A	In limit	0	20	10
B	In limit	190	230	5
C	In limit	0.2	0.6	5
D	In limit	1	2	5
Roughness	Min	0.56	1.2	5
Tool wear	Min	5	25	5
MRR	Min	10	89.9	5

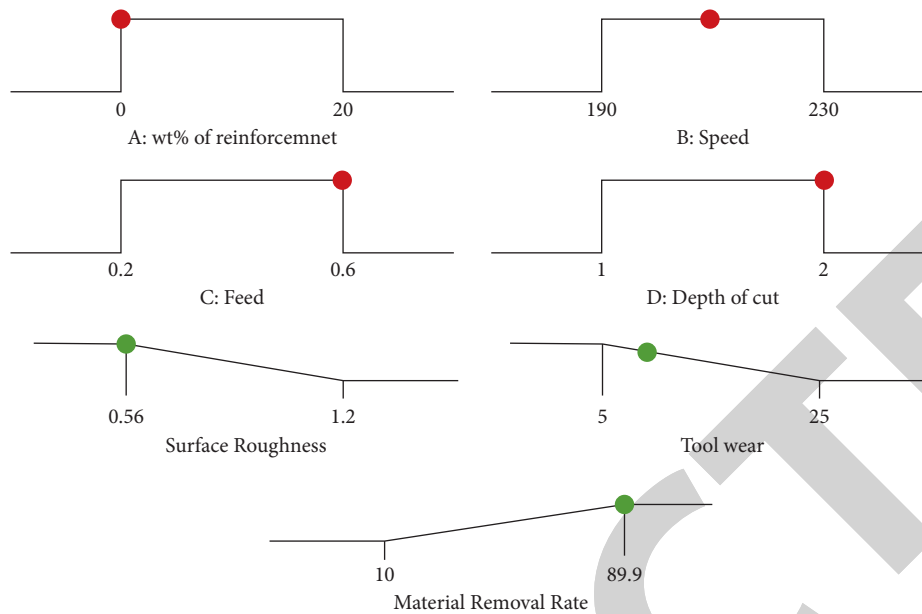


FIGURE 6: Desirability ramp graph.

input values, we were able to achieve the desired results of 0.612 m SR, 6.725 m TW, and 89.23 g/min mass removal rate.

## 7. Conclusion

The stir casting process was used to succeed in making the AA2618-zirconium carbide-rice husk ash hybrid compound. The bulk hardness of the hybrid composite was used to evaluate its mechanical and machining properties. The trials and RSM led to the following conclusions:

- (i) As the weight percent of reinforcement rises, so does the hardness. AA 2618-10wt% zirconium carbide –10wt% rice husk ash composite had the maximum hardness value. Pure AA 2618 has a 72% greater concentration. For this reason, hardness has been improved by adding a ceramic phase to AA 2618.
- (ii) Surface roughness and MRR are strongly influenced by the feed rate. The Wt. percent of reinforcement is believed to be the least influencing component for MRR, while speed is the greatest affecting factor for TW.
- (iii) Optimization parameters were 0% reinforcement, 199.85 km/h, 0.29 mm/rev, and 1.5 millimeter of depth of cut, which were recorded.

## Data Availability

The data used to support the findings of this study are included in the article. Further datasets or information are available from the corresponding author upon request.

## Conflicts of Interest

The authors declare that they have no conflicts of interest.

## Acknowledgments

The authors appreciate the support from Hawassa University, Ethiopia, for providing help during the research and preparation of the manuscript. They thank Dr. Ambedkar Institute of Technology, St. Joseph's College of Engineering, and Aditya Engineering College for their assistance during this study.

## References

- [1] G. Sasikala, V. M. Jothiprakash, B. Pant et al., "Optimization of process parameters for friction stir welding of different aluminum alloys AA2618 to AA5086 by Taguchi method," *Advances in Materials Science and Engineering*, vol. 2022, pp. 1–9, Article ID 3808605, 2022.
- [2] T. Sathish and N. Sabarirajan, "Synthesis and optimization of AA 7175-zirconium carbide (ZrC) composites machining parameters," *Journal of New Materials for Electrochemical Systems*, vol. 24, no. 1, pp. 34–37, 2021.
- [3] V. Mohanavel and M. Ravichandran, "Influence of AlN particles on microstructure, mechanical and tribological behaviour in AA6351 aluminum alloy," *Materials Research Express*, vol. 6, no. 10, Article ID 106557, 2019.
- [4] N. Jauković, V. Asanović, and Ž. Radović, "Mechanical properties and recovery of AA 2618 aluminum alloy," *High Temperature Materials and Processes*, vol. 30, no. 6, pp. 599–602, 2011.
- [5] M. M. Ravikumar, S. S. Kumar, R. V. Kumar, S. Nandakumar, J. H. Rahman, and J. A. Raj, "Evaluation on mechanical behavior of AA2219/SiO<sub>2</sub> composites made by stir casting process," *AIP Conference Proceedings*, vol. 2405, Article ID 050010, 2022.
- [6] P. Cavaliere, "Isothermal forging of AA2618 reinforced with 20% of alumina particles," *Composites Part A: Applied Science and Manufacturing*, vol. 35, no. 6, pp. 619–629, 2004.
- [7] V. Mohanavel and M. Ravichandran, "Experimental investigation on mechanical properties of AA7075-AlN composites," *Materials Testing*, vol. 61, no. 6, pp. 554–558, 2019.

- [8] I. N. A. Oguocha and S. Yannacopoulos, "Calorimetric study of  $S'$  and  $\theta'$  precipitation in Al<sub>2</sub>O<sub>3</sub> particle-reinforced AA2618," *Journal of Materials Science*, vol. 34, no. 14, pp. 3335–3340, 1999.
- [9] R. N. Muni, J. Singh, V. Kumar et al., "Multiobjective optimization of EDM parameters for rice husk ash/Cu/Mg-reinforced hybrid Al-0.7Fe-0.6Si-0.375Cr-0.25Zn metal matrix nanocomposites for engineering applications: fabrication and morphological analysis," *Journal of Nanomaterials*, vol. 2022, pp. 1–15, Article ID 2188705, 2022.
- [10] S. Suresh Kumar and V. Mohanavel, "An overview assessment on magnesium metal matrix composites," *Materials Today Proceedings*, vol. 59, no. 2, pp. 1357–1361, 2022.
- [11] B. A. Kumar, M. M. Krishnan, A. F. Sahayaraj et al., "Characterization of the aluminium matrix composite reinforced with silicon nitride (AA6061/Si<sub>3</sub>N<sub>4</sub>) synthesized by the stir casting route," *Advances in Materials Science and Engineering*, vol. 2022, pp. 1–8, Article ID 8761865, 2022.
- [12] P. Ragupathi and N. S. Kumar, "Optimization of machining parameters for minimal temperature in cylindrical grinding of Al7075/RHA composite," *Materials Today Proceedings*, vol. 37, no. 2, pp. 745–749, 2021.
- [13] N. Verma, S. C. Vettivel, P. S. Rao, and S. Zafar, "Processing, tool wear measurement using machine vision system and optimization of machining parameters of boron carbide and rice husk ash reinforced AA 7075 hybrid composite," *Materials Research Express*, vol. 6, no. 8, p. 0865f3, 2019.
- [14] S. Tiwari and M. K. Pradhan, "Optimisation of machining parameters in electrical discharge machining of LM25-RHA composites," *Handbook of Research on Manufacturing Process Modeling and Optimization Strategies*, pp. 1–18, 2017.
- [15] Z. Tang, M. Yi, H. Yin, Y. Du, H. Wu, and K. Peng, "Ablation behavior of a C/C-ZrC-SiC composite based on high-solid-loading slurry impregnation under oxyacetylene torch," *Journal of the European Ceramic Society*, vol. 42, no. 12, pp. 4748–4758, 2022.
- [16] B. Li, H. J. Li, X. Y. Yao, X. F. Tian, Y. J. Jia, and G. H. Feng, "Ablation behavior of (ZrC/SiC)<sub>3</sub> alternate coating prepared on sharp leading edge C/C composites by CVD," *Journal of Materials Science & Technology*, vol. 115, pp. 129–139, 2022.
- [17] B. Li, H. Li, and X. Yao, "Ablation behaviour of the CVD-(ZrC/SiC)<sub>3</sub> alternate coating on C/C composites under oxyacetylene torch with different heat fluxes," *Ceramics International*, vol. 48, no. 8, pp. 11756–11763, 2022.
- [18] T. Tian, W. Sun, X. Xiong, and T. Zhang, "Novel one-step formed composite reinforcement of "Spider web like" SiCnw networks and "Z-pins like" SiC rods for ablation resistance improvement of C/C-ZrC-SiC," *Journal of the European Ceramic Society*, vol. 42, no. 3, pp. 786–800, 2022.
- [19] A. Wang, J. Zhu, C. Ma et al., "Organic-inorganic composites for novel optical transformation induced by high-energy laser ablation," *Ceramics International*, vol. 48, no. 1, pp. 508–513, 2022.
- [20] X. Tian, X. Shi, L. Yang, H. Li, and H. Lin, "Preparation and ablation properties of SiC nanowire-reinforced ZrC-SiC coating-matrix integrated C/C composites," *Ceramics International*, vol. 47, no. 22, pp. 31251–31258, 2021.
- [21] S. M. Arab, M. Shahedi Asl, M. Ghassemi Kakroudi, B. Salahimehr, and K. Mahmoodipour, "On the oxidation behavior of ZrB<sub>2</sub>-SiC-V<sub>2</sub>O<sub>5</sub> composites," *International Journal of Applied Ceramic Technology*, vol. 18, no. 6, pp. 2306–2313, 2021.
- [22] Z. Peng, W. Sun, X. Xiong, Z. Zhan, and J. Li, "Comparative insights into C/C-ZrC-SiC composites with different substrate carbon on microstructures, mechanical properties, and ablation behaviors," *Journal of Materials Research and Technology*, vol. 14, pp. 662–676, 2021.
- [23] Q. He, H. Li, Q. Tan, J. Lu, and Y. Wang, "Influence of carbon preform density on the microstructure and ablation resistance of CLVD-C/C-ZrC-SiC composites," *Corrosion Science*, vol. 190, Article ID 109648, 2021.
- [24] B.-W. Chen, D. W. Ni, C. J. Liao et al., "Chemical reactions and thermal stress induced microstructure evolution in 2D-Cf/ZrB<sub>2</sub>-SiC composites," *Journal of Materials Science & Technology*, vol. 83, pp. 75–82, 2021.
- [25] Z. Zhao, K. Li, and W. Li, "Ablation behavior of ZrC-SiC-ZrB<sub>2</sub> and ZrC-SiC inhibited carbon/carbon composites components under ultrahigh temperature conditions," *Corrosion Science*, vol. 189, Article ID 109598, 2021.
- [26] H. Zhang, M. Ge, H. Shui et al., "Investigations on the thermal behaviours of SiC-ZrC continuous ceramic fibres," *Journal of the European Ceramic Society*, vol. 41, no. 9, pp. 4689–4696, 2021.
- [27] Z. Zhou, F. Niu, X. Hu et al., "Microstructure and ablation behavior of W/ZrC/SiC coating on C/C composites prepared by reactive melt infiltration and atmospheric plasma spraying," *Advanced Engineering Materials*, vol. 23, no. 6, Article ID 2001457, 2021.
- [28] C. L. Yeh and Y. H. Wang, "Preparation of ZrB<sub>2</sub>-SiC-Al<sub>2</sub>O<sub>3</sub> composites by SHS method with aluminothermic reduction," *Ceramics International*, vol. 47, no. 8, pp. 11202–11208, 2021.
- [29] Z. Zhao, K. Li, W. Li, and L. Zhang, "Cyclic ablation behavior of C/C-ZrC-SiC-ZrB<sub>2</sub> composites under oxyacetylene torch with two heat fluxes at the temperatures above 2000 °C," *Corrosion Science*, vol. 181, Article ID 109202, 2020.
- [30] W. Xu, L. Gao, C. Ma et al., "Design and preparation of composite coatings with increased reflectivity under high-energy continuous wave laser ablation," *Ceramics International*, vol. 46, no. 15, pp. 23457–23462, 2020.
- [31] F. Adibpur, S. A. Tayebifard, M. Zakeri, and M. Shahedi Asl, "Co-reinforcing of ZrB<sub>2</sub>-SiC ceramics with optimized ZrC to Cf ratio," *Ceramics International*, vol. 46, no. 14, pp. 22661–22673, 2020.
- [32] H.-Z. Liu, X. Yang, C.-Q. Fang, A.-H. Shi, L. Chen, and Q.-Z. Huang, "Ablation resistance and mechanism of SiC/ZrC-ZrB<sub>2</sub> double layer coating for C/C composites under plasma flame," *J. Cent. South Univ.*, vol. 27, no. 9, pp. 2538–2547, 2020.
- [33] L. Wang, L. Yan, C. Guo, H. Zhang, and K. Wang, "Anti-ablative property of (C/C)/SiC-ZrC composites with different ZrC content," *Fuhe Cailiao Xuebao/Acta Mater. Compos. Sin.* vol. 37, no. 9, pp. 2250–2257, 2020.
- [34] T. Tian, W. Sun, X. Qing et al., "Intelligent cooling structure design of "Z-pins like" silicon rods to enhance the ablation resistance of C/C-ZrC-SiC composites above 2500 °C," *Journal of the European Ceramic Society*, vol. 40, no. 12, pp. 3875–3886, 2020.
- [35] T. P. Nguyen, M. Shahedi Asl, S. A. Delbari et al., "Electron microscopy investigation of spark plasma sintered ZrO<sub>2</sub> added ZrB<sub>2</sub>-SiC composite," *Ceramics International*, vol. 46, no. 11, pp. 19646–19649, 2020.
- [36] X. Qing, W. Sun, T. Tian et al., "Structural characteristics and ablative behavior of C/C-ZrC-SiC composites reinforced with "Z-pins like" Zr-Si-B-C multiphase ceramic rods," *Ceramics International*, vol. 46, no. 11, pp. 18895–18902, 2020.
- [37] X. Wu, Z. Su, Q. Huang, K. Tong, X. Xie, and C. Zeng, "Effect of ZrC particle distribution on the ablation resistance of C/C-SiC-ZrC composites fabricated using precursor infiltration

## *Retraction*

# **Retracted: Thermogravimetric Analysis and Mechanical Properties of Pebble Natural Filler-Reinforced Polymer Composites Produced through a Hand Layup Technique**

### **Advances in Materials Science and Engineering**

Received 26 December 2023; Accepted 26 December 2023; Published 29 December 2023

Copyright © 2023 Advances in Materials Science and Engineering. This is an open access article distributed under the Creative Commons Attribution License, which permits unrestricted use, distribution, and reproduction in any medium, provided the original work is properly cited.

This article has been retracted by Hindawi, as publisher, following an investigation undertaken by the publisher [1]. This investigation has uncovered evidence of systematic manipulation of the publication and peer-review process. We cannot, therefore, vouch for the reliability or integrity of this article.

Please note that this notice is intended solely to alert readers that the peer-review process of this article has been compromised.

Wiley and Hindawi regret that the usual quality checks did not identify these issues before publication and have since put additional measures in place to safeguard research integrity.

We wish to credit our Research Integrity and Research Publishing teams and anonymous and named external researchers and research integrity experts for contributing to this investigation.

The corresponding author, as the representative of all authors, has been given the opportunity to register their agreement or disagreement to this retraction. We have kept a record of any response received.

### **References**

- [1] R. Kumar, S. M. Kumar, M. E. S. Kumar et al., "Thermogravimetric Analysis and Mechanical Properties of Pebble Natural Filler-Reinforced Polymer Composites Produced through a Hand Layup Technique," *Advances in Materials Science and Engineering*, vol. 2022, Article ID 1837741, 8 pages, 2022.



## Research Article

# Thermogravimetric Analysis and Mechanical Properties of Pebble Natural Filler-Reinforced Polymer Composites Produced through a Hand Layup Technique

Raj Kumar,<sup>1</sup> S. Mohan Kumar,<sup>2</sup> M. E. Shashi Kumar,<sup>2</sup> V. Ravi Kumar,<sup>2</sup> Rajesh Kivade,<sup>3</sup> Jonnalagadda Pavan,<sup>4</sup> A. H. Seikh,<sup>5</sup> M.H. Siddique,<sup>6</sup> and Abdi Diriba<sup>7</sup> 

<sup>1</sup>Department of Mechanical Engineering, Swami Keshvanand Institute of Technology, Management and Gramothan (SKIT), Jagatpura, Jaipur 302017, Rajasthan, India

<sup>2</sup>Department of Mechanical Engineering, Amrita School of Engineering, Amrita Vishwa Vidyapeetham, Bengaluru 560035, India

<sup>3</sup>Department of Industrial Engineering and Management, Dr Ambedkar Institute of Technology, Mallathahalli, Bengaluru 560056, India

<sup>4</sup>Department of Electrical and Electronics Engineering, Aditya Engineering College, Surampalem 533437, Andhra Pradesh, India

<sup>5</sup>Mechanical Engineering Department, College of Engineering, King Saud University, P O Box 800, Al-Riyadh 11421, Saudi Arabia

<sup>6</sup>Intelligent Construction Automation Centre, Kyungpook National University, Daegu, Republic of Korea

<sup>7</sup>Department of Mechanical Engineering, MizanTepi University, Tepi, Ethiopia

Correspondence should be addressed to Abdi Diriba; [abdi@mtu.edu.et](mailto:abdi@mtu.edu.et)

Received 2 July 2022; Revised 6 August 2022; Accepted 9 August 2022; Published 20 September 2022

Academic Editor: K. Raja

Copyright © 2022 Raj Kumar et al. This is an open access article distributed under the Creative Commons Attribution License, which permits unrestricted use, distribution, and reproduction in any medium, provided the original work is properly cited.

Using pebble and fibre in an epoxy matrix, the mechanical, dynamic, and thermal characteristics of a composite were examined. Tensile, flexural, impact, and interlaminar shear strengths are experimentally determined. In this study, we compare the mechanical performance of carbon fibre composites composed entirely of conventional epoxy (NE). The results of a comparative investigation using 15 and 20% carbon fibre in an epoxy matrix are presented. Additional categories for compressive strength and damping ratio were defined based on this performance. The epoxy resin was combined with carbon fibre (15 wt% and 20 wt%) in a unidirectional arrangement and manufactured with different fillers like pebble. The goal of this research is to better understand the bonding mechanisms between damping materials and the resin matrix in order to increase interfacial bonding performance. This information is required for both selecting the appropriate material for applications and developing a composite construction using that material.

## 1. Introduction

When compared to metal and ceramic matrices, polymer matrices are most typically utilised due to their cost efficiency, ease of producing complex parts with reduced tooling expense, and excellent room temperature properties [1]. Since the last few decades, composite materials have emerged as a new type of material for the manufacturing machine tool structures that produce fewer vibrations [2,3]. Polymer composites have several advantages over traditional materials such as steel and concrete, including their light

weight, high strength-to-weight ratio, and good fracture resistance. Under cyclic loading, all engineered materials dissipate energy. Because of their excellent stiffness-to-weight ratio, polymer matrix composites are frequently utilised in weight-sensitive structures [4–6].

Many issues have been solved in recent years as a result of the development of new materials, methodologies, and models. However, evaluating and identifying alternative combinations of parameters that will deliver the greatest results among the bonded joints is still required [7]. Carbon fibre is an important fibre reinforced in composites because

of the key material properties for engineering design like the axial compressive strength [8]. The addition of micro fillers has enhanced greatly the physical and mechanical properties of composites. Compressive strength is a critical material attribute that can usually only be evaluated by experimentation [9]; compressive strengths of unidirectional fiber-reinforced composites may be predicted. Endings of stiff carbon fibres could make considerable indentations on the contact surface during compression testing using AS4/3501-6 carbon/epoxy off-axis specimens, preventing full shear deformation [10].

The interlaminar shear properties of glass fibre/carbon fibre-reinforced polymer composites based on unmodified and MWCNTs-modified epoxy resins were examined, and the results suggest that adding 0.5wt percent MWCNTs increases the ILSS by 6.4 percent [11]. The addition of micro fillers improved flexural characteristics and microhardness in the reinforcing phase DMA when micro fillers were loaded. Between the filler particles and the matrix, there was good micro-filler dispersion and adherence [12,13]. According to the abovementioned literature, there was little research done on pebbles and carbon fibre-reinforced epoxy matrix using the hand layup method. The goal of this research is to make pebble/carbon fibre and evaluate the implications of the composites. Hence, from these literature, epoxy with a pebble filler is being identified as a novel material as the viable alternative for a precision machine structure.

## 2. Experimental Methods

**2.1. Fabrication.** Araldite®, Petro Araldite Pvt. Ltd., Chennai, the carbon fibre (CF, T300) was supplied by Sakthi industries, Chennai, as a reinforcement material. To enhance the bonding strength between epoxy resins and pebble stone, river sand is used as the micro filler. The components of the epoxy resin were mixed with carbon fibres in a unidirectional manner arranged like a mat with two weight percents of 15 and 20 wt % in a mild steel mold. The pebble filler at a constant speed of 500rpm for 24 hrs particle with epoxy resin was prepared and mixed by means of continuous mechanical stirring and a clear mixture was obtained. Table 1 lists out the sample codes for all different types of epoxy composite materials.

**2.2. Testing.** The specimens were  $200 \times 30 \times 5$  mm and  $130 \times 30 \times 5$  mm and 63.5, 12.7, and 3.2 mm, respectively. To analyse the compressive strength of the composites along the unidirectional way, an ASTM standard (ASTM C 579-01) compressive test was performed. The average value of five samples was used to calculate all of the results. Thermogravimetric analysis (TGA) is used to assess the thermal degradation of epoxy composites utilising a Perkin Elmer Pyris 7 thermogravimetric analyzer. To determine the beginning temperature of decomposition, mass loss, and highest decomposition peak, about 10 mg of the sample was heated under air at a rate of  $5^\circ\text{C}/\text{min}$  from room temperature to  $900^\circ\text{C}$ . DMA was used to determine characteristics

TABLE 1: Sample codes for all different types of epoxy composite materials.

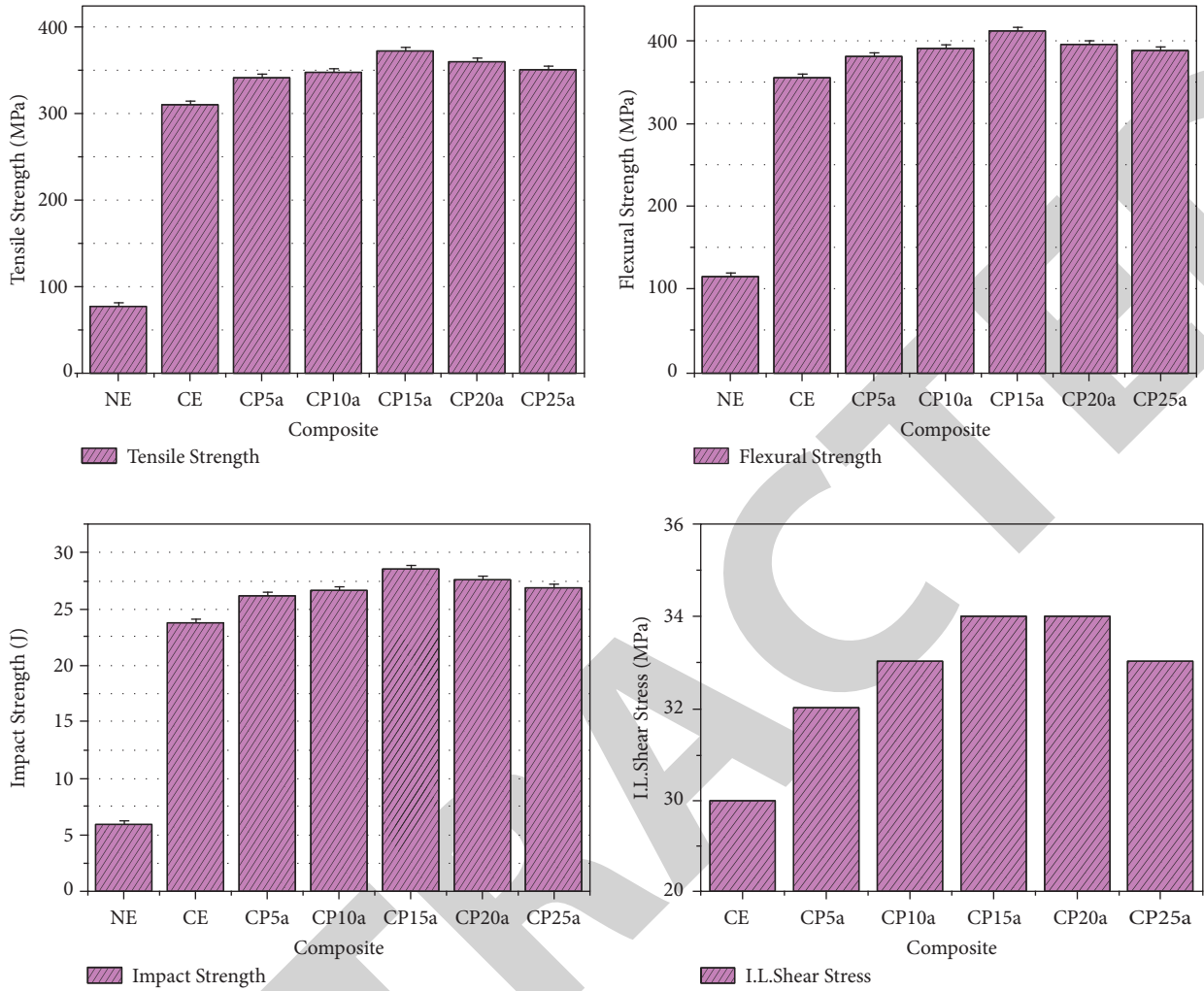
Sample code	Description
NE	Neat epoxy
CE	Epoxy resin with 15 wt% carbon fiber
CE2	Epoxy resin with 20 wt% carbon fiber
CP5a	Epoxy resin with 15 wt% carbon fiber +5 wt% pebble
CP10a	Epoxy resin with 15 wt% carbon fiber +10 wt% pebble
CP15a	Epoxy resin with 15 wt% carbon fiber +15 wt% pebble
CP20a	Epoxy resin with 15 wt% carbon fiber +20 wt% pebble
CP25a	Epoxy resin with 15 wt% carbon fiber +25 wt% pebble
CP5b	Epoxy resin with 20 wt% carbon fiber +5 wt% pebble
CP10b	Epoxy resin with 20 wt% carbon fiber +10 wt% pebble
CP15b	Epoxy resin with 20 wt% carbon fiber +15 wt% pebble
CP20b	Epoxy resin with 20 wt% carbon fiber +20 wt% pebble
CP25b	Epoxy resin with 20 wt% carbon fiber +25 wt% pebble

of a frequency of 1 Hz, a temperature range of 20 to  $200^\circ\text{C}$ , and a heating rate of  $5^\circ\text{C}/\text{min}$ . The specimen was  $3 \text{ mm} \times 12 \text{ mm} \times 64 \text{ mm}$  in size. Initially, the mechanical characteristics of composites (all samples) were investigated, with the best results being used for additional compression, damping, TGA and DMA experiments.

## 3. Results and Discussion

**3.1. Mechanical Properties.** Epoxy composites with various fibre contents were compared to plain epoxy in terms of tensile, flexural, impact, and interlaminar shear stress characteristics (NE). The mechanical characteristics of the tested materials are shown in Figure 1(a) and Figure 1(b). The addition of a pebble to the carbon fibre increases the strength of all composites in general. The tensile strength of neat epoxy resin was increased from 78 MPa (NE) to 372 MPa (CP15a) and 374 MPa (CP15b) with the addition of a filler and fibre. In the same fibre and filler ratio, flexural, impact, and interlaminar shear stress all improved. According to this study, the mechanical properties of fibre-reinforced composites are influenced not only by the fibre content but also by the pebble filler, which aids in stress transfer to the matrix [14].

The addition of filler raised the tensile strength of the epoxy composites by up to 15% in both matrixes. The filler results in increased interfacial addition and as a result, more stress transfer fibres and fillers during tensile testing. It is worth noting that the effect of pebble filler on the flexural strength of epoxy composites greatly improves the stiffness of the composites. When flexural strength of both sets of carbon fibre loading 15 wt% and 20 wt% with different



(a)

FIGURE 1: Continued.

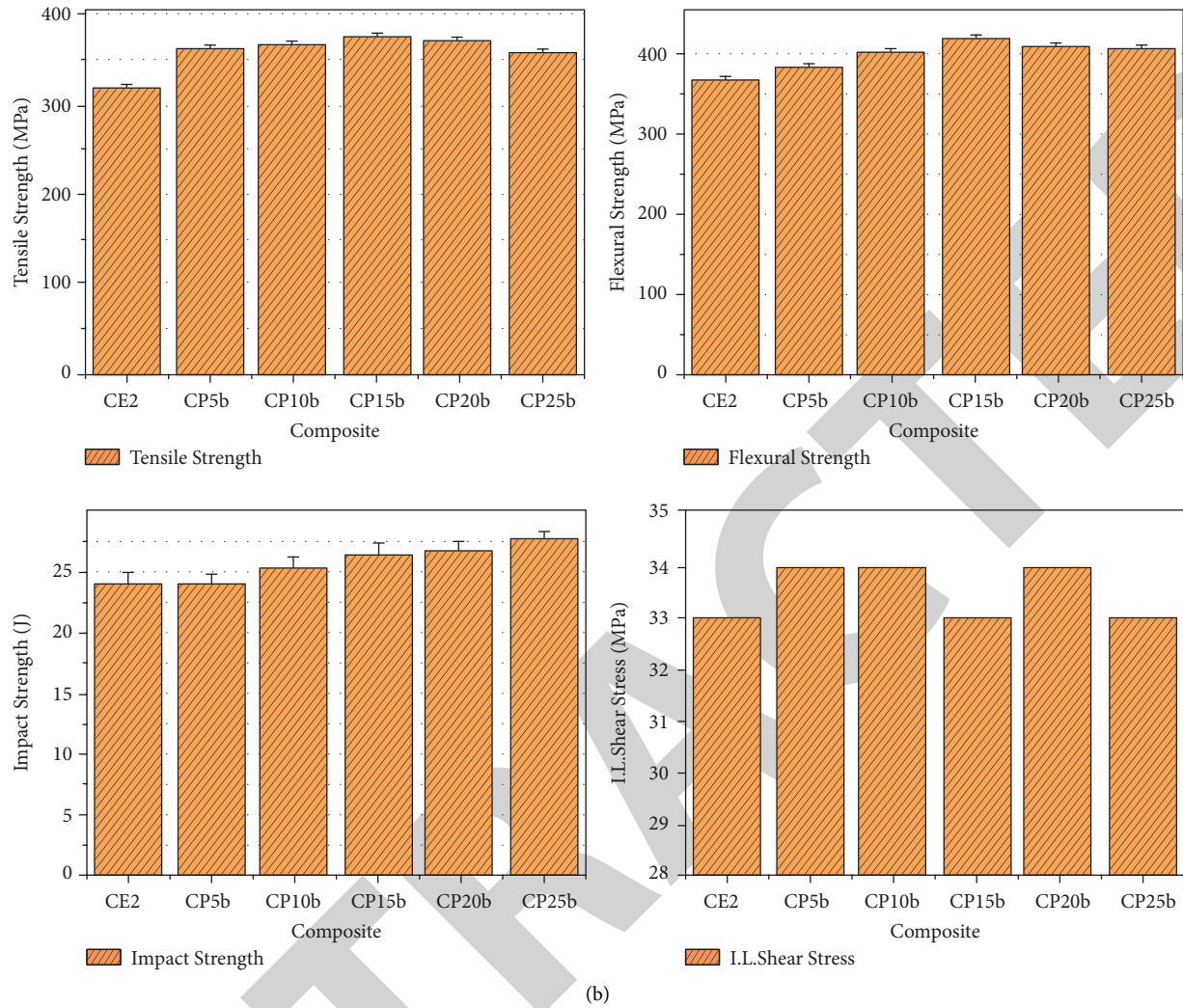


FIGURE 1: Mechanical properties (tensile, flexural, impact, and interlaminar shear strength) of composite (a) carbon fibre 15 % wt ratio with different pebble weight ratios and (b) carbon fibre 20 % wt ratio with different pebble weight ratios.

pebble weight ratios was compared, there was no significant difference in strength enhancement when the fibre content was varied. Furthermore, because the filler improved interfacial strength in elastic qualities similar to tensile strength, all composite formulations demonstrated greater flexural strength values than the raw epoxy and carbon fibre composites.

The impact values of composite show tiny increment with filler addition. Filler addition of up to 15% in 15% carbon fibre and up to 25% in 20% carbon fibre improvement. It is noted that the interlaminar shear strength also showed similar improvement to impact strength. This is because of reinforced filler particles affecting the laminar adhesion; hence, delamination takes place easily. The following composites are taken for further studies based on the above mechanical performance and they are listed in Table 2.

**3.2. Compressive Test and Damping Ratio Analysis.** Figure 2 depicts representative behaviours of the four composite materials. The addition of a pebble filler to the

matrix improves the properties of carbon fibre/epoxy matrix composites, albeit the degree of improvement is dependent on factors including filler particle concentration and dispersion. According to the compressive strength values of composites CP15a and CP15b, it is determined that 15 percent pebble filler provides greater strength than 20% pebble filler.

CP15a and CP15b have maximum compressive strength values of 60% and 61% higher than neat epoxy samples. For the abovementioned composites, considering the scattering and failure, describing the nonlinear behaviour and the shear strength values are not very affected. Because shear strength can induce a drop in compressive strength in the fibre composite, the pebble filler reduced compressive strength by 20%. Normally, the composite with lesser weight proportion of resin shows better compressive strength; this is due to agglomeration takes place when the resin contribution increases.

The damping ratios ( $\xi$ ) were estimated using the half power band method using equation (1):

TABLE 2: Maximum mechanical properties of composites.

Sample code	Tensile strength (MPa)	Flexural strength (MPa)	Impact strength (J)
CP15a	372	411	27.1
CP20a	360	396	26.3
CP15b	374	420	26.4
CP20b	369	412	26.8

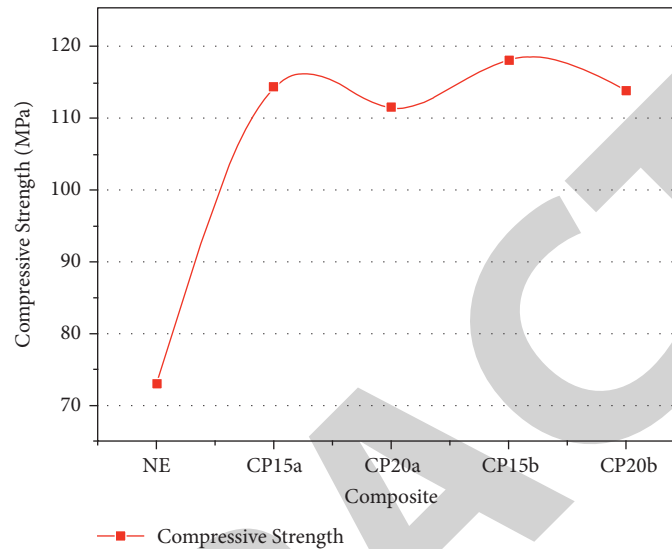


FIGURE 2: Compressive strength of composites.

$$\xi = \frac{(f_2 - f_1)}{2f_n} \quad (1)$$

where  $\xi$  = damping ratio,  $f_2 - f_1$  = bandwidth at half power points,  $f_n$  = fundamental frequency.

The variations in the damping ratio are as shown in Table 3. It reveals that the pebble 15% ratios normally produce a higher damping ratio at both set of composites. The damping ratio shows the same trend as that of compressive strength for all types of composites. Further increase in the filler ratio decreases the damping ratio due to lose of bonding properties of the composite. The damping values and compressive strength show that the 15% filler promotes higher bonding strength. So, the rate of transmission of cohesive force is better in the case of a 15% filler compared with that of a 20% filler.

**3.3. Dynamical Mechanical Analysis.** Figure 3 shows the dynamic mechanical parameters at a frequency of 1Hz. Stiffness imposed by the fillers is blamed for the increase in modulus. Fillers increase the flexibility of polymeric materials while lowering their viscosity. Tg values of the epoxy composite does not show any significant variations. The restricted mobility is caused by composites' crosslinked three-dimensional structures.

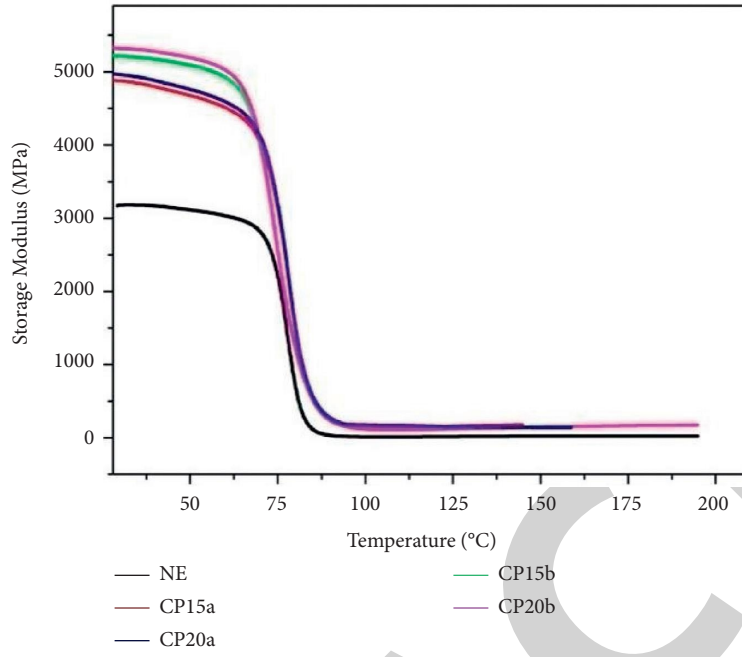
When compared to plain epoxy, the composites loaded with filler had a higher storage modulus in the first glassy stage. At 75 to 80 degrees Celsius, the storage modulus of clean epoxy and filler-loaded composites is nearly identical.

TABLE 3: Damping ratios of the composite.

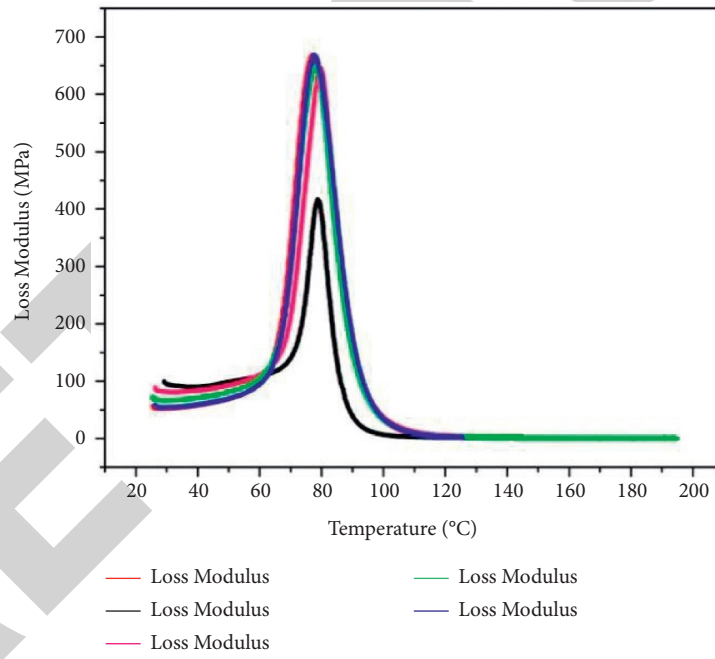
Sample code	Damping ratio ( $\xi$ )
NE	0.0311
CP15a	0.0209
CP20a	0.0234
CP15b	0.0211
CP20b	0.0245

This is attributed to matrix softening and loss of filler-matrix adhesion, and it was a substantial contributor to the strength loss found at high temperatures. The filler enhances the Tg of the polymer matrix by improving the contact between the matrix and the filler and restricting the mobility of the molecules.

**3.4. Thermal Properties.** The thermogravimetric analysis was used to determine the thermal stability of the epoxy composites as shown in Figure 4. The thermal stability of the epoxy matrix increases dramatically with the inclusion of pebble fillers and epoxy/carbon fibre composites, according to TGA thermograms. From this, the filler-matrix degrades later than the neat resin, thermogravimetric curves for the composites are similar mass loss process starting at around 400°C, because comparing the wt. loss of the composites up to 50%, there is no considerable variation in the thermal stability between the composites. The pebble filler-reinforced composite matrices have a higher char residue when



(a)



(b)

FIGURE 3: (a) Storage. (b) Loss modulus of different filler ratios of composites, respectively.



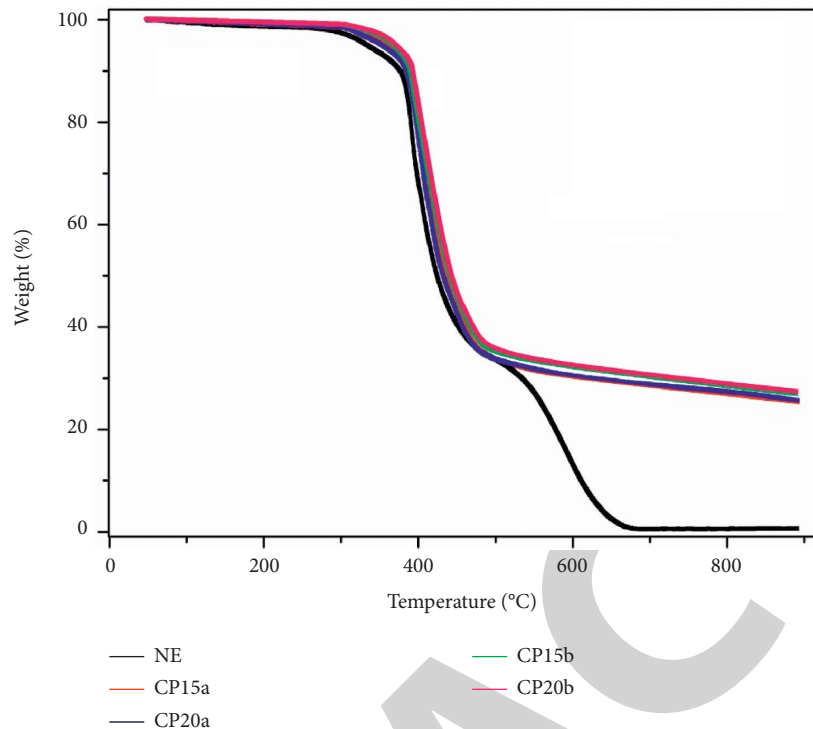


FIGURE 4: Thermogravimetric analysis pebble filler epoxy composites.

compared to the neat epoxy. Very little variation only can see in this final char values with addition of a 15% and 20% pebble filler. However, the presence of the pebble filler intermediary thermal stability between fillers and matrix, showing synergistic interaction.

#### 4. Conclusions

The properties and behaviour of an engineering material under tensile, compressive, and dynamic loading conditions in both normal and adverse test situations are used to determine its performance. Synergistic effects in the form of modified mechanical properties and improved thermal qualities were produced by integrating the chosen pebble fillers into the carbon fibre-reinforced epoxy, as expected. The result from the mechanical testing showed that the addition of pebble filler and carbon fibres enhanced the tensile strength, flexural strength, and impact strength. The pebble filler-reinforced carbon fibre/epoxy matrices have a higher char residue when compared to the neat epoxy matrix which increased from 1.6 to 24.8 at 800°C.

#### Data Availability

The data used to support the findings of this study are included within the article. Further data or information are available from the corresponding author upon request.

#### Conflicts of Interest

The authors declare that there are no conflicts of interest regarding the publication of this paper.

#### Acknowledgments

The authors appreciate the support from MizanTepi University, Ethiopia, for the research and preparation of the manuscript. The authors would like to acknowledge the Researchers Supporting Project number (RSP-2021/373), King Saud University, Riyadh, Saudi Arabia.

#### References

- [1] J Lee, D Bhattacharyya, M. Q Zhang, and Y. C Yuan, "Mechanical properties of a self-healing fibre reinforced epoxy composites," *Composites Part B: Engineering*, vol. 78, pp. 515–519, 2015.
- [2] H.-C. Möhring, "Composites in Production Machines," *Procedia CIRP*, vol. 66, pp. 2–9, 2017.
- [3] S. Murugan and PR Thyla, "Mechanical and Dynamic Properties of Alternate Materials for Machine Tool Structures: A Review," *Journal of Reinforced Plastics and Composites*, vol. 37, no. 24, pp. 1456–1467, Dec. 2018.
- [4] N K Chandramohan, G. Rajkumar, A. Bhuvendran, and S John Alexis, "Fabrication and testing of short fiber composites made of used brush bristles as reinforcement combined with epoxy matrix," *Materials Today: Proceedings*, vol. 37, no. 2, pp. 1932–1937, 2021.
- [5] V Mohanavel, S Suresh Kumar, M Ravichandran, R Sivanraju, P Velmurugan, and R Subbiah, "Influence of Nanofillers on the Mechanical Characteristics of Natural Fiber Reinforced Polymer Composites," *ECS Transactions*, vol. 107, no. 1, pp. 12513–12524, 2022.
- [6] T. Raja, V. Mohanavel, S. Suresh Kumar, S. Rajkumar, M. Ravichandran, and R Subbiah, "Evaluation of mechanical properties on kenaf fiber reinforced granite nano filler



## *Retraction*

# **Retracted: Streamline Effect Improvement of Additive Manufactured Airfoil Utilizing Dynamic Stream Control Procedure**

### **Advances in Materials Science and Engineering**

Received 26 December 2023; Accepted 26 December 2023; Published 29 December 2023

Copyright © 2023 Advances in Materials Science and Engineering. This is an open access article distributed under the Creative Commons Attribution License, which permits unrestricted use, distribution, and reproduction in any medium, provided the original work is properly cited.

This article has been retracted by Hindawi, as publisher, following an investigation undertaken by the publisher [1]. This investigation has uncovered evidence of systematic manipulation of the publication and peer-review process. We cannot, therefore, vouch for the reliability or integrity of this article.

Please note that this notice is intended solely to alert readers that the peer-review process of this article has been compromised.

Wiley and Hindawi regret that the usual quality checks did not identify these issues before publication and have since put additional measures in place to safeguard research integrity.

We wish to credit our Research Integrity and Research Publishing teams and anonymous and named external researchers and research integrity experts for contributing to this investigation.

The corresponding author, as the representative of all authors, has been given the opportunity to register their agreement or disagreement to this retraction. We have kept a record of any response received.

### **References**

- [1] R. Srinath, R. Mukesh, M. C. Poojari, I. Hasan, and W. Amare Alebachew, "Streamline Effect Improvement of Additive Manufactured Airfoil Utilizing Dynamic Stream Control Procedure," *Advances in Materials Science and Engineering*, vol. 2022, Article ID 1252681, 12 pages, 2022.

## Research Article

# Streamline Effect Improvement of Additive Manufactured Airfoil Utilizing Dynamic Stream Control Procedure

R. Srinath,<sup>1,2</sup> R. Mukesh,<sup>3</sup> Manish C. Poojari,<sup>4</sup> Inamul Hasan ,<sup>3</sup>  
and Wubetu Amare Alebachew <sup>5</sup>

<sup>1</sup>Department of Aeronautical Engineering, Visvesvaraya Technological University, Belagavi, Karnataka, India

<sup>2</sup>Department of Aerospace Engineering, Dayananda Sagar University, Bangalore, India

<sup>3</sup>Department of Aeronautical Engineering, ACS College of Engineering, Bangalore 560074, Karnataka, India

<sup>4</sup>Department of Electronics and Electrical Engineering, National Institute of Technology, Mangaluru, Karnataka, India

<sup>5</sup>Department of Mechanical Engineering, Debre Tabor University, Gondar, Amhara Region, Ethiopia

Correspondence should be addressed to Wubetu Amare Alebachew; wubeama@dtu.edu.et

Received 28 June 2022; Revised 18 August 2022; Accepted 27 August 2022; Published 17 September 2022

Academic Editor: K. Raja

Copyright © 2022 R. Srinath et al. This is an open access article distributed under the Creative Commons Attribution License, which permits unrestricted use, distribution, and reproduction in any medium, provided the original work is properly cited.

In the era of fast transport, to create inventive stream flow management solutions that are capable of diminishing the aerodynamic drag of the vehicles, there is a need to modify the flow characteristics over the vehicle by deferring or expelling the position of the flow partition. The objective of this study involves the parameterized design of an airfoil utilizing the Bezier curve technique with the assistance of the simulation program. For flow regulations, synthetic jet modules are ingrained at different percentages of the chord to manage the stall characteristics. The parametrization system, combined with the stream control method, can give a much better insight into flow re-energization and pave some way for the reduction of the wake. Digital fabrication technique (3D printing or Rapid Prototyping method) is used to fabricate the end product for aerodynamic testing. The comparative outcome showed a reduction in drag at certain angles of attack due to the surface finish obtained. By comparing the results, the aerodynamic efficiency showed a significant rise of 13.05% at lower angles of attack when compressed gas was used in the synthetic jet closer to the frontier edge of the airfoil. Near the stall angle of attack, the coefficient of lift ( $C_l$ ) and coefficient of drag ( $C_d$ ) values showed no progress.

## 1. Introduction

Diminishment of drag over an airfoil is dealt with in two stages. The configuration file is described in the right detail first, and then the flow control device is added later. There are diverse holes available to model the rib profile curve. They are adjusted beneath a roof referred to as parameterization procedures. Parameterization techniques include Bezier curves, Class-Shape function Transformation, Hicks-Henne “Bump” function and polynomial method, Ferguson curve, and ?<sup>3</sup> [1]. Each parameterization strategies have its own recompenses, Selection of the exact method guarantees the smoothness of the 2d bend, the more parameters the optimization process could seek out more aerofoil shapes. On the other

hand, with more design parameters, it would be costly to seek design space unwanted curves. The parameterization technique used here is Bezier curve which comes with the disadvantage of no local control. With this change, the position of a control point affects the entire curve. Bezier curve parameterization is a spline curve with a parametric methodology ( $u, t$ ) that can be used to more precisely model a 2D aerofoil. The advantage of the Bezier curve over others is the ease of computation, steadiness at the lower degrees of control points, and a Bezier curve can be turned and interpreted by performing operations on the control points, which comes with a disadvantage of no local control. With this change, the position of a control point affects the entire curve. Although the work has nothing to do with optimization, the use of

parameterization approaches is described in detail with reference to optimization techniques. Optimization of the airfoil requires a parametrization technique to represent the shape of the airfoil and various such techniques are discussed in a review paper Salunke et al. [1]. A geometric comparison of seven different airfoil parameterization methods accomplished by Masters et al. [2] indicates that all techniques require 20–25 design variables to cover the proposed space within the geometric tolerance. Describing an airfoil with a lesser number of parameters proves to be vital in optimization problems. Optimization of NACA 2411 airfoil by Mukesh et al. [3] coupled with the PARASEC technique as a parametrization method indicated that the Coefficient of lift of the airfoil is escalated. Twelve parameters selected by the author served as design variables to characterize the geometry of the airfoil. A new parameterization technique Bezier-GAN proposed by Chen et al. [4] resulted in the well-ordered depiction of the airfoil and it proves to be an accurate fit for the optimization problem. Wei, et al. [5], obtained an optimized E-387 airfoil with enhancement and modification in L/D ratio as their objective function. The author used the Bezier curve as his parameterization technique, where eight Bezier control points were designated as design variables to represent the coordinates of the airfoil. A comparative study made on NACA airfoil using different parameterization methods by Selvan and concluded that by comparing Class-Shape function transformation, Hicks-Hennee “Bump” function, Bezier and polynomial approaches to study the effect of shape parameterization, each method uses the different number of parameters to obtain the final geometry. They observed that the Bezier technique had an increase in the lift-to-drag ratio by 13.42857% Selvam [6]. The work by Parasaram and Charyulu [7] expresses that through the techniques of the Quantic Reverse Engineering of Bezier curve formula, it is easier to obtain camber control points from the existing camber cloud of points. In most of the optimization problems, the parameterization of geometry plays a crucial role in deciding the optimal design. Designs of wind turbine blades are complex in general compared to the baseline design of NACA profiles. Wind turbine blade parameterization and optimization do vary with the problems faced in aerospace industry due to the aerodynamic constraints on lift. Airfoil optimization technique for wind turbines done by Ribeiro claims that the wind turbine blade parameterized and optimized through the Bezier curve and genetic algorithm techniques perceived a 50% reduction in the computational time Ribeiro et al. [8]. The procedure for maximizing the form of transonic airfoils was introduced [9, 10] using the Bezier parametric curve with limited control points to precisely replicate the original design. The authors Yang and Zeng [11] suggested a strategy for improving the aerodynamic system to integrate the Bezier curve with the radial base function. The pressure fall has decreased since the refinement of the NACA 0012 airfoil, and the design result shows that the solution can significantly improve the efficiency of aerodynamics. The research suggests that the

Bezier curve is a prevailing approach in numerous flight vehicles for aerodynamic development applications.

Parameterized airfoil leads to better results when flow control devices are incorporated into the modeled airfoil. This will ensure a delay in the transition of the turbulent to the laminar one or a delay in flow separation. In fluid dynamics, the flow control procedure has gained a large indebtedness since its introduction to aero-related studies. They are categorized into active and passive flow control. Here, for our experimental and methodical studies, a type of active flow control (synthetic jet) method is chosen. Synthetic jets are typically formed by a flow roving back and forth across a small aperture. A jet is a fluid flux that blends with a surrounding medium. Jet flows vary depending on velocity, the diameter of the orifice, density, and viscosity of the fluid (Reynolds’s number). A synthetic jet is an adaptive control of airflow, with the use of an external source of fluid, such as channelized compressed air. Fuel consumption of a commercial aircraft could be hoarded to 8%, if the transition phase over the wing surface can be delayed to 50% and in general these flow patterns occur at low Reynolds numbers (Re) Serdar Genç, et al. [12]. Aerodynamic efficiency improvement in a wing was explored by utilizing “active slat” on a wind turbine aerofoil (DU96-W-180) Halawa et al. [13]. Periodically opening and latching the slat passage contributes to the blowing impact over the wing being created. As a result, they postponed the breakup of the boundary layer, decreased the drag power, and had 3% better aerodynamic efficiency relative to the clean airfoil design. Drag elimination is due to the inclusion of several cavities at the base of a blunt body. This multicavity has beneficial effects on both drag reduction and wake randomness in enhancing vehicle aerodynamics close to dimples on the golf ball to improve ball aerodynamics Martín-Alcántara et al. [14]. Flow control at low Reynolds numbers can be accomplished via actuator which converts the electrical signal to the required physical quantities. Cattafesta and Sheplak [15] classified the various types of actuators based on their specifications (Fluidic, plasma, etc.), design and aeronautical applications Prawin and Rose [16], announced that the maximum drag reduction obtained on the NACA6-series aerofoil configuration (NACA 63-XX8) with installed MJ actuators was about 20% at 0° AOA. For the past ninety years of research work on active control devices, no significant contributions have been attempted over aircraft applications due to technical challenges and the installation of additional systems. Jubran and Hamdan [17], represented the experimental investigation of the secondary flow injection in a cylinder. They have concluded that the velocity and location of injection reduces the vibration. Khalid et al. [18], in his work on flow control devices opines that jet flow actuators address the need for change in the lift at a required moment coefficient. The active piezoelectric transducer actuator engine mount provided better isolation performance, which could lessen around 80% vibration and performs well at both higher and lower frequencies Sui et al. [19]. Recent advanced research on high lift flow control methods via the combined effects of both the active method (porous upper surface of the wing) and passive method (VG) promises to exhibit superior outcomes

in delaying transitions. Minimization of drag through active and passive flow regulation techniques reduces drag in a laminar flow airfoil rate 5243 using the optimization method and active and passive control techniques which yielded the reduction in drag of 3.95% and lift is comparatively increased by 5.03% Yagiz et al. [20]. In a real-world scenario, a subsonic wind tunnel test was conducted to substantiate the fluent mathematical analysis [21, 22]. For a wing, the effects of wake turbulence, pitching moment, lift, and drag forces for various angles of attack were measured by wind tunnel measurements Ghazi and Olwi [23]. The prototypes required for wind tunnel testing can be fabricated from any suitable material. Building a physical prototype is a critical step before producing a functional product. A prototype is developed to test different aspects of a design, or to illustrate its features. Early days traditional materials such as wood and other metals, Aluminum in general provided greater flexibility due to advancements in machining compared to former one is used for prototyping wind tunnel models. With the advancements in machining, rapid prototyping plays a crucial role as the materials used in it provide a better surface finish to the prototype compared to metals or wood. Rapid prototyping is a substitute for subtractive processes [24]. 3d printing, is a more generic name used for rapid prototyping, and is distinct in that they combine and bond materials in layers to create objects. where they can also be called additive fabrication, solid free form fabrication (SFF), and layered manufacturing, to name a few. In its most basic form, rapid prototyping (RP) is the manufacturing of three-dimensional (3D) parts using computer-aided design (CAD) data on a smaller time scale [25].

The use of 3D printing technology will speed up manufacturing while decreasing prices. At the same time, the requirements will have a greater effect on production. 3D printing technologies can facilitate a more flexible and responsive manufacturing process, as well as better quality control. Various rapid manufacturing techniques are used to fabricate a wind tunnel testing model such as Stereolithography (SLA), Selective Laser Sintering (SLS), Fused Deposition Modelling (FDM) or Material Jetting, Selective Laser Melting (SLM) or Powder Bed Fusion, Laminated Object Manufacturing (LOM) or Sheet Lamination [26, 27].

## 2. Methodology

The symmetrical airfoil NACA 0024 is picked over an asymmetrical one in light of the fact that, the thicker airfoils tend to accelerate the flow on both surfaces. This reduced the pressure difference in turn resulting in a reduction of lift. NACA 0024 is thicker when compared to other symmetric airfoils. So, optimizing such an airfoil with control surfaces may improvise its application in many fronts [28]. The variation of the coefficient of drag at lower or zero AOA is inconsequential for this situation. NACA 0024 airfoil is mapped utilizing the generalized Bezier curve. Inkscape software was used to vectorize the projected airfoil. The ideal finishing and scaling of the vectorized graph are done with the help of the AutoCAD application. 2D airfoil is imported into CATIA for 3D

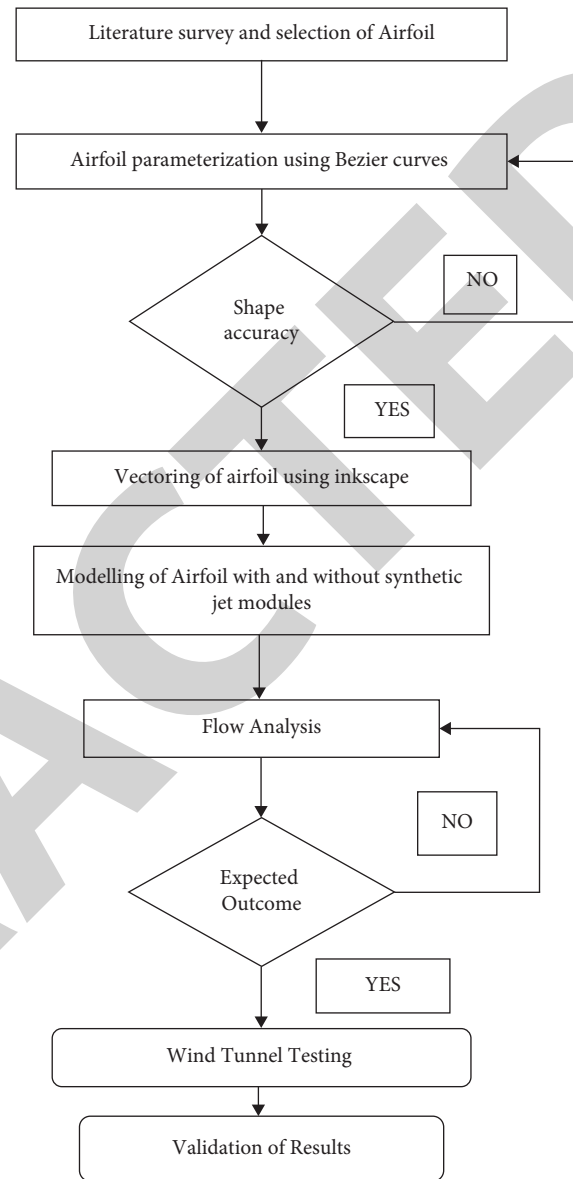


FIGURE 1: Flowchart for aerodynamic efficiency of airfoil improvement using flow control device.

design. Figure 1 indicates the steps followed to procure the expected outcome. The change is centered at about 16% of the front edge of the chord. The first synthetic jet modules were therefore placed just in front of the laminar to turbulent boundary layer transfer. Somewhere about 30% of the chord from the front edge was the second jet unit. As the current flows into the aft arm, the pressure transmission increases due to the boundary layer separation. As a result, the third jet module was installed at 75% from the front edge. Besides, the aerofoil model was evaluated for experimental flow trends such as separation, reattachment, and laminar-turbulent transition of the boundary layer over the aerofoil with and without synthetic jet modules for numerous angles of attack ( $0^\circ$ ,  $5^\circ$ ,  $10^\circ$ ,  $15^\circ$ ) for differing approaches.

**2.1. Bezier Curve.** A Bezier curve is the technique chosen to obtain the airfoil shape since they are generally acknowledged in the representation of the airfoil. In recent years, the Bezier curve has been applied on a number of occasions for its benefits over both the straight and the curved description. A Bezier curve is a parametric curve composed of Bernstein basis polynomials. In a simple way, it is defined as the summation of the functions of the base weighted by the control points ?:

$$p(u) = \sum_{i=0}^n P_i B_i, n(u) u \in [0, 1], \quad (1)$$

where  $n$  is the degree of polynomial (defined by the control points),  $n = \text{no of control points} - 1$ ,  $u$  is the parametric variable, and  $B_{i,n}$  = bases function:

$$B_{i,n} = \frac{n!}{i!(n-i)!} u^i (1-u)^{n-i}. \quad (2)$$

The parameter equation of a curve defined by four control points can be generated by equations (1) and (2) as a quadratic curve:

$$P(u) = P_0(1-u)^3 + 3P_1u(1-u)^2 + 3P_2u^2(1-u) + P_3u^3. \quad (3)$$

Airfoil curve acquired using the Bezier curve technique is shown in Figure 2; which are characterized by its generalized properties as it always infiltrates the first and last control points; curves are restricted under the arched casing of the control point; they show up the Global Control point. the 2d airfoil curve is later transformed into a 3d model as in Figure 3. Figure 4(a) illustrates the airfoil with synthetic jet modules that are pricked as per the specification shown in Table 1, where Figure 4(b) illustrates the mesh applied over the airfoil.

### 3. Results and Analysis

Parameters required for computational fluid dynamics simulations are itemized in Table 2. [29, 30]. Simulations are used to study the downstream movement of fluids on different wing models. Here, the research is conducted for NACA 0024 wing design with and without synthetic jet modules. K-epsilon ( $k-\epsilon$ ) model is used to simulate the turbulent flow condition, which defines turbulence by two transport equations. The influence of the synthetic jet unit was tested in three separate cases by positioning it at three different locations on the upper surface of the aerofoil (i.e., at 16%, 30%, and 75% of the chord). Computational fluid analysis is performed on a wing to study the wing flow properties and to understand the flow pattern and flow separation theory.

A maximum of 4 cases were evaluated based on the computational results obtained from the experimental models, and these cases were numerically assessed using the analysis of the wind tunnel trials.

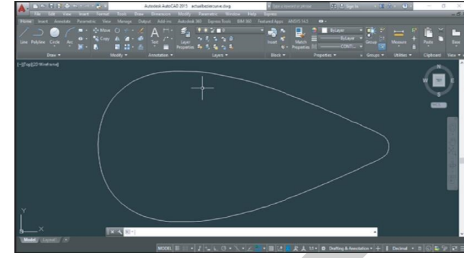


FIGURE 2: 2D design of NACA 0024 using Bezier curve.

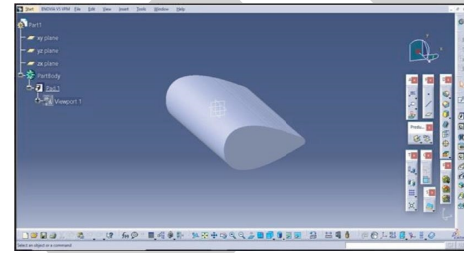


FIGURE 3: 3D design of NACA 0024 using Bezier curve.

#### 3.1. Computational Data

##### 3.1.1. Parameterized Wing without Synthetic Jet Modules.

The stagnation point is located near the frontier portion of the airfoil, but its location alters with a different angle of attack. It is explicit from Figures 5–7 that at the stagnation level, the stream encounters the maximum pressure and, as the air moves back from the stagnation stage, the pressure comparatively reduces on the top surface for an increased angle of attack. As the flow is nearing the trailing edge, there is a slight increase in the pressure distribution due to the adverse pressure gradient. The stream velocity rises as it moves away from the front edge and reduces again as it reaches the trailing edge owing to the divergence of the air. As the stream reaches the trailing edge

For a higher angle of attack, the fluid divergence happens even faster than the lower angle of attack. Figure 8 reveals that the stress of the wall shear differs along with the airfoil sheet, indicating the effect of the pressure gradient and the flow anomalies, such as isolation, reattachment, and laminar-turbulent movement of the boundary layer over the airfoil. It is observed that at  $0^\circ$  AOA, the current is added to the front edge and the wall shear stress is suddenly increased downstream, supporting the reattachment of the boundary layer (i.e. a thinner boundary layer is formed over the airfoil). As a consequence, the divergence level shifts downstream relative to  $10^\circ$  and  $15^\circ$  AOA. As the stream reaches the trailing end, the shear stress of the wall slowly reduces, signaling that the displacement of the boundary layer (i.e., the thicker boundary layer above the airfoil) has begun, culminating in the separation of the flow.



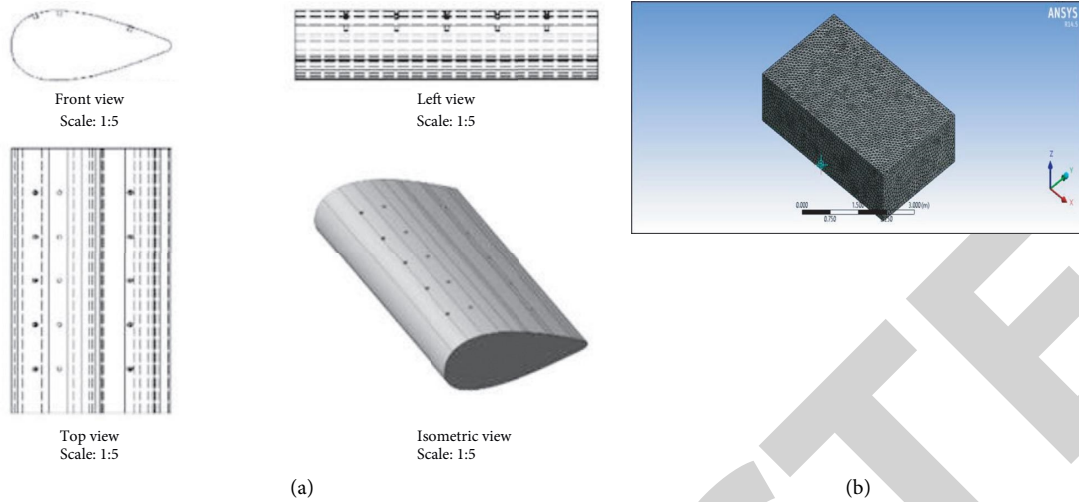


FIGURE 4: (a) Engineering drawing of an aerofoil with trickle channels. (b) Model after applying the mesh for NACA 0024 aerofoil.

TABLE 1: Specifications of wing and synthetic jet modules.

Wing chord	300 mm
Wing span	570 mm
Number of synthetic jet modules	3
Number of openings in each jet modules	5
<i>Distance of synthetic jet module from the leading edge</i>	
(a) 1 <sup>st</sup> module	48 mm
(b) 2 <sup>nd</sup> module	90 mm
(c) 3 <sup>rd</sup> module	225 mm
Diameter of synthetic jet modules and openings	8 mm
Reynolds number	$3.71229 \times 10^5$
Spanwise spacing of synthetic jet openings	95 mm each

TABLE 2: Reference values used for analysis.

Reynolds number	$3.7123 \times 10^5$
Density	$1.225 \text{ kg/m}^3$
Dynamic viscosity	$1.7894 \times 10^{-5} \text{ kg/m} \cdot \text{s}$
Temperature	15°C
Pressure	$1.01325 \times 10^5 \text{ Pa}$
Velocity of free stream	18.0756 m/s
Velocity of air used in synthetic jets	6 m/s

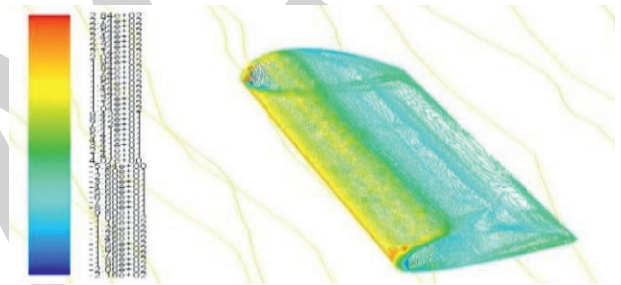


FIGURE 6: Total pressure at 10° AOA.

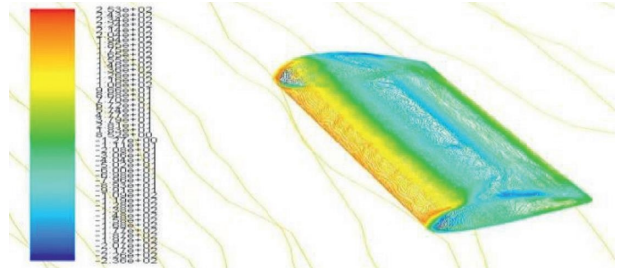


FIGURE 7: Total pressure at 15° AOA.

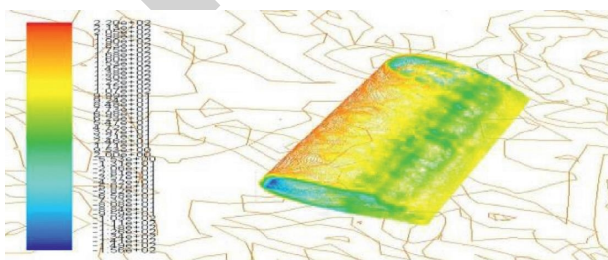


FIGURE 5: Total pressure at 0° AOA.

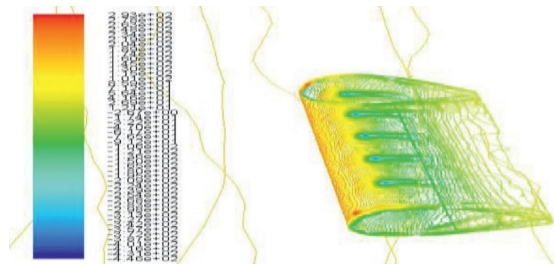


FIGURE 8: Total pressure at 0° AOA for the 1st module.

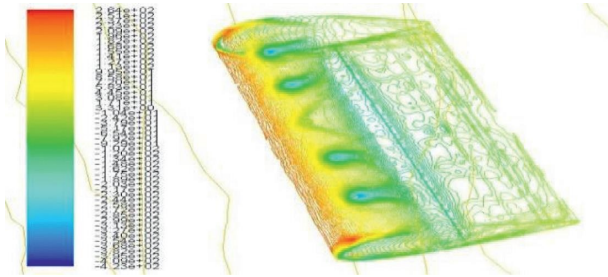


FIGURE 9: Total pressure at 10° AOA for the 1st module.

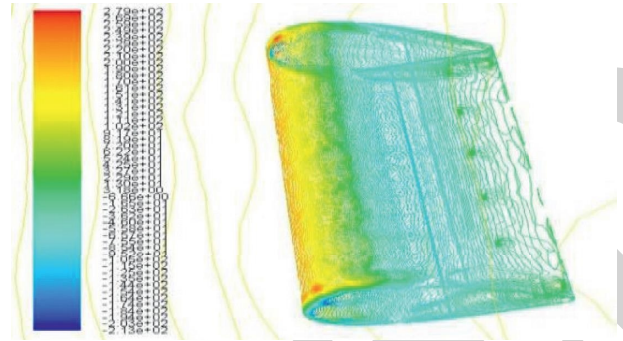


FIGURE 14: Total pressure at 0° AOA for the 3rd module.

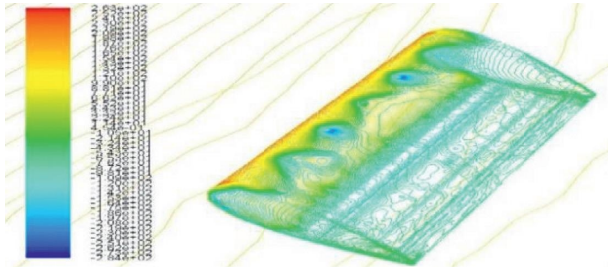


FIGURE 10: Total pressure at 15° AOA for the 1st module.

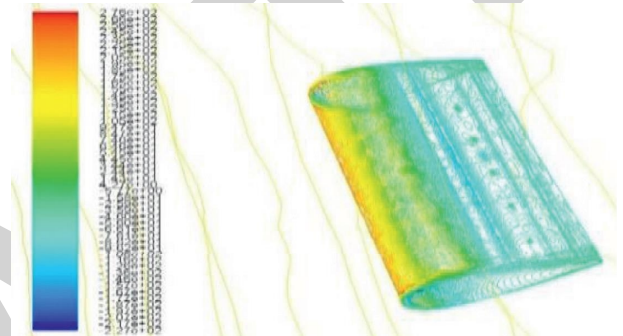


FIGURE 15: Total pressure at 15° AOA for the 3rd module.

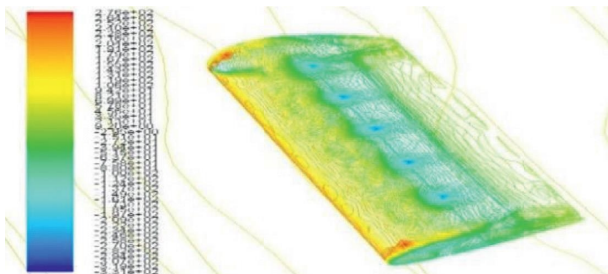


FIGURE 11: Total pressure at 0° AOA for the 2nd module.

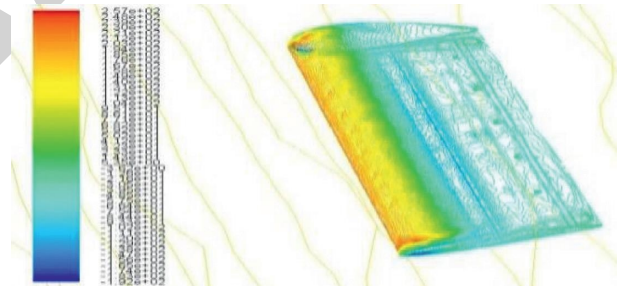


FIGURE 16: Total pressure at 10° AOA for the 3rd module.

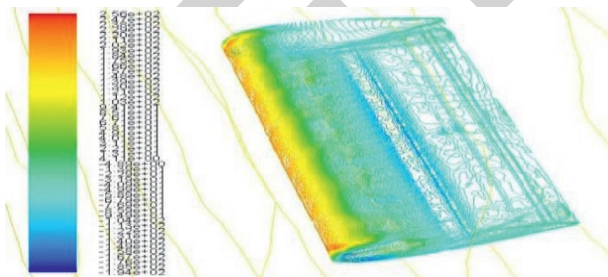


FIGURE 12: Total pressure at 10° AOA for the 2nd module.

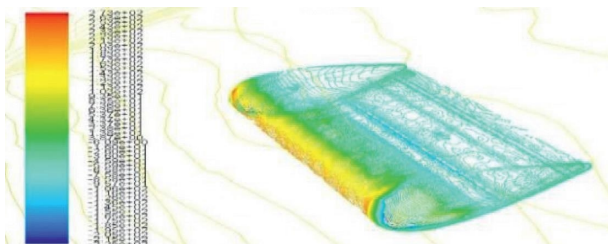


FIGURE 13: Total pressure at 15° AOA for the 2nd module.

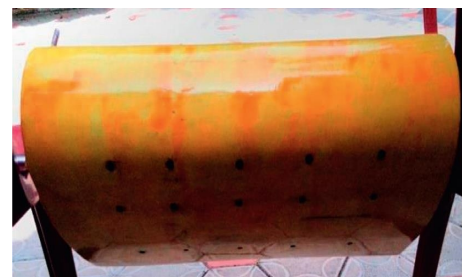


FIGURE 17: Airfoil wooden lacquer.

3.1.2. *Parameterized Wing with 1<sup>st</sup> Synthetic Jet Module Open.* From Figures 8–10, the highest pressure is observed at the front edge. As the air enters near the trickle channel of the 1<sup>st</sup> synthetic jet module, a small amount of forwarding



air is blocked, thus increasing the pressure around the synthetic jet module. Furthermore, it could be seen that the pressure over the airfoil decreases gradually, and again downstream, the pressure increases due to flow separation. As the free flow air passes via the 1st module due to the bleed air from the trickle channels, the velocity of the downstream air over the top surface of the wing is slightly reduced, culminating in a delay in the flow separation adjacent to the trailing edge. There is a sharp increase in the shear stress of the wall around the trickle channels of the airfoil due to the laminar-turbulent transition. As a result, a thinner boundary layer is formed near the trickle channel, and the separating point moves downstream compared to the parameterized wing without a synthetic jet module. With the increase in AOA, the acceleration of the flow closer to the foremost edge of the airfoil is reinforced, and a rather strong adverse gradient of pressure is formed along with the downstream airfoil. Therefore, the point of separation moves upstream in comparison with that of 0° AOA.

**3.1.3. Parameterized Wing with 2nd Synthetic Jet Module Open.** Figures 11–13 demonstrate that the influence of the jet stream from the 2nd module on fluid reattachment at a lower angle of attack is appreciable relative to that of a higher angle of attack. Pressure rises at 0° AOA as the fluid flows through the trickle channel, and the pressure is almost steady as it reaches the trailing side, thereby slowing the isolation of the flow. There is no overall change in pressure across the 2nd jet unit as the stream reaches it. It can also be inferred that there is no significant increase in pressure near the trailing edge at a higher angle of attack. The velocity is almost decreased across the trickle channel as it reaches the trailing edge at 0° AOA, but in the case of 10° and 15° AOA, the current detaches roughly in the center of the airfoil. For 10° and 15° AOA, although, the flow is almost disconnected along the leading edge, and a very insignificant amount of flow is added downstream of the 2nd module.

**3.1.4. Parameterized Wing with 3rd Synthetic Jet Module Open.** Figures 14–16 indicate that the impact of the jet stream from the 3rd module increases the pressure at the trailing edge at the lower AOA (i.e., at 0° AOA). At the higher angle of attack, there are no significant pressure differences in the stream re-energization at the trailing edge. It is observed that the stream has already been isolated by a higher angle of attack along the front edge of the wing design. The module at the trailing edge is therefore not very critical for downstream flow control, while there is a slight variation in velocity near the trickle channels at the lower angle of attack. The wall shear stress value continues to decrease at the leading edge itself and approaches the minimum value (i.e., zero). It implies that the flow has dispersed, and there is no significant increase in shear stress downstream, indicating that there is no visible reattachment of the current. However, there is a trivial increase in shear stress near the run-off channel at a lower AOA.

### 3.2. Experimental Validation

**3.2.1. Wood Based Model.** The model was built with a total of 7 ribs. The fabricated airfoil chord width is 300 mm, and the span is 570 mm. 10 triangular slots are created in each rib to position the spars along the spanwise. Thin copper tubings are mounted around the airfoil to calculate the distribution of pressure on the upper and lower surfaces of the airfoil. A maximum of 13 pressure ports have been used on the design. The airfoil was supported by a stainless steel rod measuring 0.75 inches in diameter. A typical copper tube synthetic jet unit has five trickle channels. A maximum of 3 modules comprising 15 trickle channels was used, which were mounted on 5 ribs at the bottom of the upper surface of the prototype. Eventually, the prototype was finished with a wooden lacquer as seen in Figure 17.

The experimentation was performed using the subsonic open circuit, suction-type wind tunnel. Instruments used for experimentation were multi-tube manometers, Smoke generator, Pitot-static tubes, Air compressor, Digital anemometer, and Digital thermometer. Pressure variation over a model can be measured either by pressure probes through which a variety of measurements are being made, including force, airspeed, and pressure. Pitot tubes are used to measure pressure and wind speed on various surfaces of an aircraft or other structures, as well as to measure wind speed in a wind tunnel. It has 13 tubes mounted on the board, each with a different angle of inclination or by pressure sensors which has units that can accommodate up to 64 channels; transducers are mounted in 8-card sets that are self-configuring and hot-swappable. Kits of sensor cards are available for mixed-range operation, and sensing ranges as low as 160 Pa differential are available. Table 3 lists the tunnel specifications utilized for testing. The stream pattern around the body was measured for 0°, 10°, and 15° AOA with and without bleeding air for the 1<sup>st</sup>, 2<sup>nd</sup>, and 3<sup>rd</sup> synthetic jet modules. The distribution of surface pressure around the model for 0°, 5°, 10°, 15°, and 20° AOA was tabulated by measuring the readings of the Multitude manometer for the constant Reynolds number (i.e., 371230). The smoke generator is used to visualize the flow across the models where paraffin is used for producing the dense white smoke. Essentially it consists of an electrical cartridge heater, overhead diesel bottle, sump bottle air supply pipe from blower, and smoke distributor. Table 4 displays the experimental values are calculated using the formulas given as follows:

$$\text{Reynolds Number (Re)} = \frac{\rho VC}{\mu}, \quad (4)$$

where,  $\rho$ —Density of air for given temperature, kg/m<sup>3</sup>,  
 $V$ —Velocity of air, m/s,  $C$ —Chord of an airfoil = 0.30 m, and  
 $\mu$ —Dynamic viscosity of air for given temperature, Ns/m<sup>2</sup>.

Velocity of air is as follows:

$$(V) = 3.24\sqrt{\Delta h} \left[ \cdot \frac{2(P_0 - P_\infty)}{\rho} = V^2 \right], \quad (5)$$

TABLE 3: Specifications of wind tunnel.

Type of tunnel	Subsonic, open circuit, suction type
Test section	1000 mm × 1000 mm (inside)
Air speed (velocity)	30 m/s
Contraction ratio	9:1
Contraction length	2.25 m
Drive	Axial flow fan driven by AC motor with AC drive speed controller
Overall size	4-meter × 4-meter × 13.5 meters (approximately)
Power requirement	A.C 15 HP (11 kW), 440 volts, electrical supply with neutral & earth connections

TABLE 4:  $C_l$  and  $C_d$  values of at various AOA.

$\alpha$ (°)	Basic aerofoil		With 1 <sup>st</sup> module open		With 2 <sup>nd</sup> module open		With 3 <sup>rd</sup> module open	
	$C_l$	$C_d$	$C_l$	$C_d$	$C_l$	$C_d$	$C_l$	$C_d$
0	0.11	0.07	0.15	0.07	0.11	0.05	0.18	0.06
5	0.78	0.02	0.87	0.02	0.71	0.02	0.73	0.02
10	1.02	0.02	1.19	0.02	0.96	0.03	1.01	0.02
15	1.02	0.05	1.11	0.05	0.97	0.05	0.91	0.04
20	0.66	0.06	0.54	0.08	0.63	0.07	0.66	0.05

where  $\Delta h$ —difference in Pitot-static tube manometer reading (mm)

Coefficient of pressure is as follows:

$$(C_p) = \frac{h_i - h_\infty}{h_0 - h_\infty} = \frac{h_\infty - h_i}{h_\infty - h_0}, \quad (6)$$

where  $h_i$ —local static manometer reading measured around aerofoil,  $h_\infty$ —Free stream static manometer reading measured by pitot-static probe and  $h_0$ —Free stream total manometer reading measured by pitot-static probe.

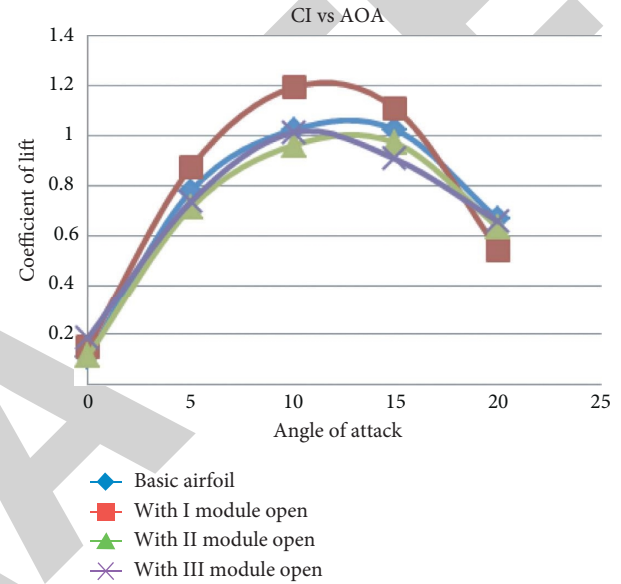
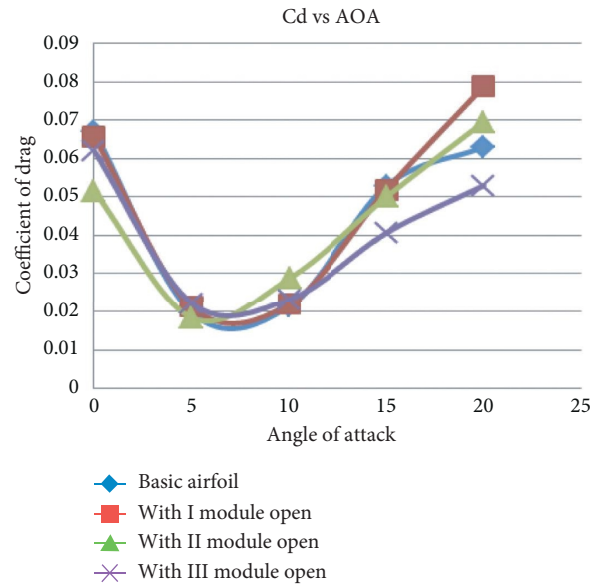
Normal coefficient ( $C_n$ ) is as follows:

$$\left\{ \Sigma \left[ \Delta C_{p,u} \times d \left( \frac{X}{C} \right) \right] \right\} - \left\{ \Sigma \left[ \Delta C_{p,l} \times d \left( \frac{X}{C} \right) \right] \right\}, \quad (7)$$

where  $X$ —distance of the respective pressure port from the leading edge,  $C$ —Chord of an airfoil,  $\Delta C_{p,u}$ —Average coefficient of pressure on upper surface and  $\Delta C_{p,l}$ —Average coefficient of pressure on the lower surface.

From Figures 18–20, it is apparent that for wings without bleed air and wings with the 1st module open, the coefficient of lift increases with an increase in the AOA, even though there is a slight decrease in the lift at 10° AOA. Furthermore, the lift coefficient increases to a certain maximum point known as the stall angle. The lift coefficient, however, reaches a peak at this angle and then decreases. Due to flow re-energization, there is a significant change in the pressure gradient in the case of the 1st module synthetic jet, which results in a transformation of the flow from laminar to turbulent, thereby slowing the separation of air.

**3.2.2. 3d Printed Model.** Different materials from plastic to metals can be used to prototype an object for rapid prototyping. In the case of aerodynamic testing in wind tunnels, materials such as Acrylonitrile Butadiene Styrene (ABS),

FIGURE 18: Plot between  $C_l$  and angle of attack.FIGURE 19: Plot between  $C_d$  and angle of attack.

Polyactic Acid (PLA), Polyethylene terephthalate glycol-modified (PETG), and Thermoplastic Polyurethane (TPU) are the most commonly used ones. It is also been evident

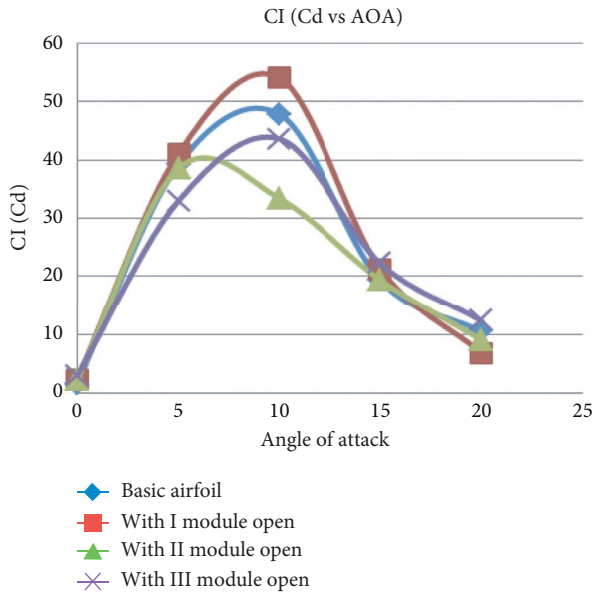


FIGURE 20: Plot between  $C_l/C_d$  and angle of attack.

from [31, 32] that the models fabricated using rapid manufacturing techniques reduce the roughness. On comparing the properties of the materials mentioned, it is been found that PLA is the most suited material for prototype since they exhibit a high tensile strength and more suitable for prototypes and toys [33, 34]. PLA is chosen for making a prototype based on its biodegradable quality which the other material fails to possess [35]. The printing temperature required to print a prototype using PLA material is around 180°C–200°C [36], where other materials require a higher temperature range. On the other hand, thermal resistance and flexibility are poor when compared to ABS and TEG, which makes it less accountable for real-time aerospace models. Prototypes were made using both traditional (wood) and rapid prototyping (PLA) techniques to compare the force variation due to surface finish

Fused Deposition Modelling (FDM), is a rapid technique (extrusion based), is used to prototype the airfoil that operates on the layer-by-layer premise [33]. The FDM method is preferred over other methods because it is cost-effective, shortens lead times, and speeds up the prototyping process. Print larger objects and the design of FDM printers can be easily scaled for a lower cost-to-size ratio [37]. Fused Deposition Modelling takes standard STL data files as input and may employ various build materials in a build or support relationship. FDM machines are essentially CNC-controlled robots with miniature extruder heads. Solid things are constructed “string by string” by feeding the head with a plastic wire. Figure 21, shows the 3d printed airfoil along with synthetic jets using fusion deposition modeling with PLA material. It was tested. The printed airfoil was tested in the wind tunnel shown in Figure 22 under the same conditions as the wood-based model and its results were compared.

Table 5 portrays the CL and CD values of the prototype fabricated using wood and through rapid prototyping. The graphs, Figures 23 and 24 show that there is negligible

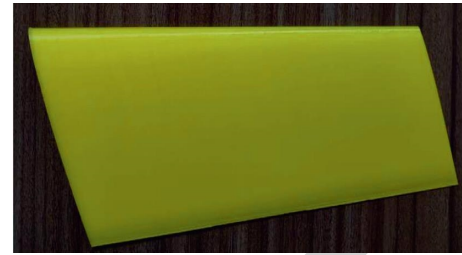


FIGURE 21: 3d printed airfoil.



FIGURE 22: Wind tunnel testing of 3d printed airfoil.

TABLE 5: Table 4  $C_l$  and  $C_d$  values of wood-based model and RP model.

$\alpha$ (°)	Basic aerofoil		With 1 <sup>st</sup> module open			
	$C_l$	$C_d$	Wood $C_l$	RP model $C_l$	Wood $C_d$	RP model $C_d$
0	0.11	0.07	0.15	0.12	0.07	0.05
5	0.78	0.02	0.87	0.82	0.02	0.04
10	1.02	0.02	1.19	1.26	0.02	0.02
15	1.02	0.05	1.11	1.06	0.05	0.04
20	0.66	0.06	0.54	0.61	0.08	0.07

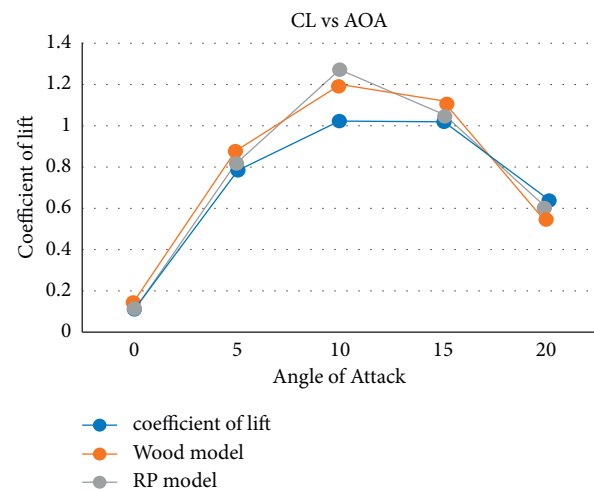


FIGURE 23: Plot between  $C_l$  and angle of attack.

change in the coefficient values when the material used for the prototype differs. This is due to the evenness of the surface of the prototype fabricated using RP. The wood based

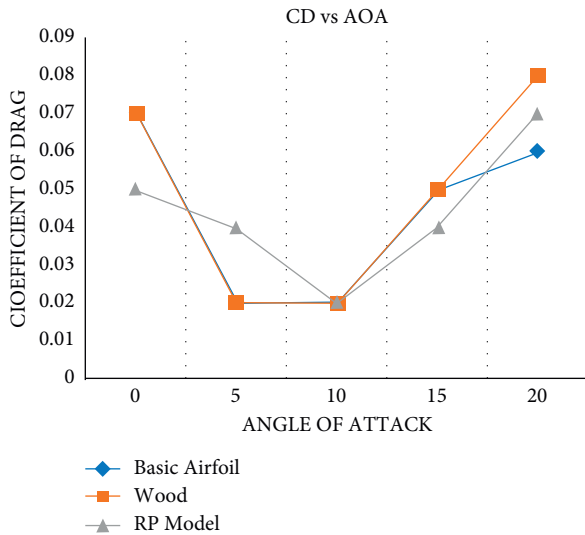


FIGURE 24: Plot between  $C_d$  and angle of attack.

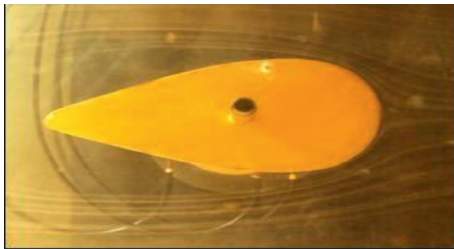


FIGURE 25: Smoke flow visualization at 0° AOA without synthetic jet module.

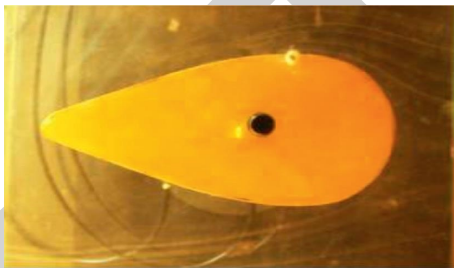


FIGURE 26: Smoke flow visualization at 0° AOA for the 1st module open.

prototype was also coated with lacquer to improve its surface finish due to which errors in values are greatly diminished

#### 4. Discussion

Aerodynamic efficiency is improved by 13.05% in the case of the 1st module synthetic jet. In the case of the 2nd module synthetic jet, it can be found that the lift coefficient rise is at 0° AOA, while the lift coefficient declines with an improvement in the AOA relative to the wing without bleeding air. In the case of the 3rd module synthetic jet, it is interesting that the lift coefficient is raised at 0° and 5° AOA.

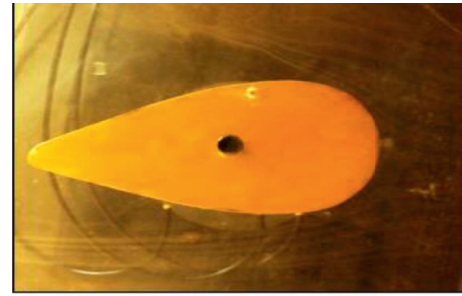


FIGURE 27: Smoke flow visualization at 10° AOA for the 1st module open.

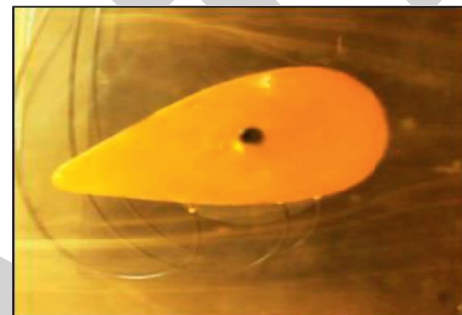


FIGURE 28: Smoke flow visualization at 15° AOA for the 1st module open.

The research was aimed at investigating the effect of effective flow control on the airfoil's aerodynamic properties growth. The Mat lab code for the Bezier curve technique contributed to the improvement of the smooth spline curve for the drawing of the airfoil. The study clearly shows that CFD results in a substantial interpretation of the flow pattern over the airfoil. Figures 25–28 confirm that the smoke stream visualization contributes to a better understanding of the flow pattern, fluid mixing, and vortex produced by the synthetic jet due to the laminar-turbulent boundary layer transfer. The primary aim was to increase the aerodynamic efficiency by using a synthetic jet. Synthetic jets are useful aerodynamic devices that can be used by aircraft manufacturers to improve aircraft flying qualities. However, the complexities such as the pressure drop across the valve, high energy loss the system may experience and its structural issues may incur are not considered here [38]. Comparison between the different materials used to prototype the model also shows that the surface finish plays a substantial role in reducing the skin friction to certain extent. This can be further improved by using advanced polymers such as ABS or TEG, which provides additional flexibility and improved surface finish. The prudent use of synthetic jets leads to optimal aerodynamic efficiency. The leading-edge synthetic jet unit has a significant contribution to slow stream separation and boost lift. Ultimately, and in view of the results obtained, the synthetic jet is a flexible flow control tool.

## Data Availability

The data used to support the findings of this study are available from the corresponding author upon request.

## Conflicts of Interest

The authors declare that there are no conflicts of interest regarding the publication of this article.

## References

- [1] N. P. Salunke, R. A. J. Ahamad, S. Channiwala, and S. A. Channiwala, "Airfoil parameterization techniques: a review," *American Journal of Mechanical Engineering*, vol. 2, no. 4, pp. 99–102, 2014.
- [2] D. A. Masters, N. J. Taylor, T. C. S. Rendall, C. B. Allen, and D. J. Poole, "Geometric comparison of aerofoil shape parameterization methods," *AIAA Journal*, vol. 55, no. 5, pp. 1575–1589, 2017.
- [3] R. Mukesh, K. Lingadurai, and U. Selvakumar, "Airfoil shape optimization using non-traditional optimization technique and its validation," *Journal of King Saud University - Engineering Sciences*, vol. 26, no. 2, pp. 191–197, 2014.
- [4] Wei Chen, Kevin Chiu, and M. D. Fuge, "Airfoil design parameterization and optimization using bézier generative adversarial networks," *AIAA Journal*, vol. 58, no. 11, pp. 4723–4735, 2020.
- [5] Xuesong Wei, Xiaoyang Wang, and Songying Chen, "Research on parameterization and optimization procedure of low-Reynolds-number airfoils based on genetic algorithm and bezier curve," *Advances in Engineering Software*, vol. 149, no. 2020, Article ID 102864.
- [6] K. M. Selvan, "On the effect of shape parameterization on aerofoil shape optimization," *International Journal of Renewable Energy Technology*, vol. 04, no. 02, pp. 123–133, 2015.
- [7] R. K. N. Parasaram and T. N. Charyulu, "[No title found]," *International Journal of Mechanical Engineering and Robotics Research*, vol. 1, no. 3, pp. 410–20, 2012.
- [8] A. F. P. Ribeiro, A. M. Awruch, and H. M. Gomes, "An airfoil optimization technique for wind turbines," *Applied Mathematical Modelling*, vol. 36, no. 4907, pp. 4898–4907, 2012.
- [9] Myong Sohn and Kyu Lee, "Bezier curve application in the shape optimization of transonic airfoils," in *18th Applied Aerodynamics Conference* American Institute of Aeronautics and Astronautics, Denver, CO, U.S.A., 2000.
- [10] Inamul Hasan, R. Mukesh, P. Radha Krishnan, R. Srinath, and R. B. Dhanya Prakash, "Forward flight performance analysis of supercritical airfoil in helicopter main rotor," *Intelligent Automation & Soft Computing*, vol. 33, no. 1, pp. 567–584, 2022.
- [11] Lianqiang Yang and X.-Ming Zeng, "Bézier curves and surfaces with shape parameters," *International Journal of Computer Mathematics*, vol. 86, no. 7, pp. 1253–1263, 2009.
- [12] Mustafa Serdar Genç, Kemal Koca, Hacimurat Demir, and Halil Hakan Açikel, "Traditional and new types of passive flow control techniques to pave the way for high maneuverability and low structural weight for UAVs and MAVs," in *Autonomous Vehicles* George Dekoulis. IntechOpen, 2020.
- [13] A. M. Halawa, B. Elhadidi, and S. Yoshida, "Aerodynamic performance enhancement using active flow control on DU96-W-180 wind turbine airfoil," *Evergreen*, vol. 5, pp. 16–24, 2018.
- [14] A. Martín-Alcántara, E. Sanmiguel-Rojas, C. Gutiérrez-Montes, and C. Martínez-Bazán, "Drag reduction induced by the addition of a multi-cavity at the base of a bluff body," *Journal of Fluids and Structures*, vol. 48, pp. 347–361, 2014.
- [15] L. N. Cattafesta and M. Sheplak, "Actuators for active flow control," *Annual Review of Fluid Mechanics*, vol. 43, pp. 247–272, 2011.
- [16] L. Prawin and J. B. R. Rose, "A numerical study on aerodynamic wake flow control over airfoils by micro jet actuators," *International Journal of Engineering Systems Modelling and Simulation*, vol. 9, no. 4, p. 214, 2017.
- [17] B. A. Jubran and M. N. Hamdan, "Effects of secondary injection on the cross flow induced vibration of a single cylinder," *Journal of King Saud University - Engineering Sciences*, vol. 3, no. 2, pp. 233–248, 1991.
- [18] Khalid Khalil, Salvatore Asaro, and Andre Bauknecht, "Active flow control devices for wing load alleviation," in *AIAA AVIATION 2020 FORUM. VIRTUAL EVENT* American Institute of Aeronautics and Astronautics, 2020.
- [19] Li Sui, Xin Xiong, and Gengchen Shi, "Piezoelectric actuator design and application on active vibration control," *Physica Procedia*, vol. 25, pp. 1388–1396, 2012.
- [20] Bedri Yagiz, Osama Kandil, and Y. V. Pehlivanoglu, "Drag minimization using active and passive flow control techniques," *Aerospace Science and Technology*, vol. 17, pp. 21–31, 2012.
- [21] F. M. Hussein and M. S. El-Shobokshy, "Experimental investigation of the effect of extended surfaces on the performance of tube banks in cross flow," *Journal of King Saud University - Engineering Sciences*, vol. 1, no. 1-2, pp. 213–226, 1989.
- [22] Inamul Hasan, R. Mukesh, P. Radha Krishnan, V. Srinath, and R. Dhanya Prakash, "Computational study of aerodynamic performance of three and four-bladed helicopter rotor with supercritical airfoil," *JOURNAL OF ENVIRONMENTAL PROTECTION AND ECOLOGY*, vol. 22, no. 6, pp. 2622–2633, 2021.
- [23] M. A. Ghazi and I. A. Olwi, "Interference effects of a large wing on the performance of a trailing wing," *Journal of King Saud University - Engineering Sciences*, vol. 7, pp. 77–91, 1995.
- [24] ISO/PRF 17296-1, *Additive manufacturing -- General principles -- Part 1: Terminology*, 2015.
- [25] O. Keles, C. W. Blevins, and K. J. Bowman, "Effect of build orientation on the mechanical reliability of 3D printed ABS," *Rapid Prototyping Journal*, vol. 23, no. 2, pp. 320–328, 2017.
- [26] A. Pirjan and D. M. Petrosanu, "The impact of 3D printing technology on the society and economy," *Journal of Information Systems & Operations Management*, vol. 42, pp. 1–11, 2013.
- [27] G. Radhaboy, M. Pugazhivadivu, P. Ganeshan, and P. Ramshankar, "Analysis of Thermo chemical behaviour of Calotropis procera parts for their Potentiality," *International Journal of Ambient Energy*, vol. 43, no. 1, pp. 252–258, 2022.
- [28] Virgil Stanciu and Valeriu Dragan, "Notes on the use of conventional NACA airfoils in super circulation aerodynes," *International journal of advanced scientific and technical research Issue*, vol. 4, no. 2, pp. 2249–9954, 2012.
- [29] D. Y. Dhande and D. W. Pande, "Multiphase flow analysis of hydrodynamic journal bearing using CFD coupled fluid structure interaction considering cavitation," *Journal of King Saud University - Engineering Sciences*, vol. 30, no. 4, pp. 345–354, 2018.
- [30] I. Hasan, R. KrishnanP, and R. S. Srinath, "Aerodynamic performance analysis of a supercritical airfoil in the helicopter



## *Retraction*

# **Retracted: Maintenance Methodologies Embraced for Railroad Systems: A Review**

### **Advances in Materials Science and Engineering**

Received 26 December 2023; Accepted 26 December 2023; Published 29 December 2023

Copyright © 2023 Advances in Materials Science and Engineering. This is an open access article distributed under the Creative Commons Attribution License, which permits unrestricted use, distribution, and reproduction in any medium, provided the original work is properly cited.

This article has been retracted by Hindawi, as publisher, following an investigation undertaken by the publisher [1]. This investigation has uncovered evidence of systematic manipulation of the publication and peer-review process. We cannot, therefore, vouch for the reliability or integrity of this article.

Please note that this notice is intended solely to alert readers that the peer-review process of this article has been compromised.

Wiley and Hindawi regret that the usual quality checks did not identify these issues before publication and have since put additional measures in place to safeguard research integrity.

We wish to credit our Research Integrity and Research Publishing teams and anonymous and named external researchers and research integrity experts for contributing to this investigation.





The corresponding author, as the representative of all authors, has been given the opportunity to register their agreement or disagreement to this retraction. We have kept a record of any response received.

### **References**

- [1] P. Prabhakaran, A. Subbaiyan, D. Gopalakrishnan et al., "Maintenance Methodologies Embraced for Railroad Systems: A Review," *Advances in Materials Science and Engineering*, vol. 2022, Article ID 7655245, 15 pages, 2022.

## Review Article

# Maintenance Methodologies Embraced for Railroad Systems: A Review

**Priyanka Prabhakaran** <sup>1</sup>, **Anandakumar Subbaiyan**,<sup>1</sup> **Dineshkumar Gopalakrishnan** <sup>2</sup>,  
**Harsha Vardhana Balaji.M.**,<sup>3</sup> **S. Ramkumar** <sup>4</sup>, **Suresh Veluswamy**,<sup>5</sup>  
**Dinesh Kumar Murugesan**,<sup>5</sup> **Satheeshkumar Seerangagounder**,<sup>6</sup>  
**Sivakumar Arunachalam**,<sup>1</sup> **Prabhu Velusamy** <sup>7</sup>, and **Priyanka Bhaskaran**<sup>8</sup>

<sup>1</sup>Department of Civil Engineering, Kongu Engineering College, Perundurai, Erode 638060, India

<sup>2</sup>Department of Civil Engineering, Vaagdevi College of Engineering, Warangal 506005, Telangana, India

<sup>3</sup>Department of Civil Engineering, Sona College of Technology, Salem 636005, India

<sup>4</sup>Department of Civil Engineering, M. Kumarasamy College of Engineering, Karur 639113, India

<sup>5</sup>Department of Civil Engineering, Hindusthan College of Engineering, Coimbatore 641032, India

<sup>6</sup>Department of Agriculture Engineering, Kongunadu College of Engineering and Technology, Trichy 621215, India

<sup>7</sup>Department of Construction Technology and Management, Wollega University, Wollega, Ethiopia

<sup>8</sup>Department of Mechatronics Engineering, Kongu Engineering College, Perundurai, Erode 638060, India

Correspondence should be addressed to Priyanka Prabhakaran; priyacivil80@gmail.com and Prabhu Velusamy; prabhuvelusamy@wollegauniversity.edu.et

Received 5 July 2022; Revised 20 July 2022; Accepted 27 August 2022; Published 14 September 2022

Academic Editor: K. Raja

Copyright © 2022 Priyanka Prabhakaran et al. This is an open access article distributed under the Creative Commons Attribution License, which permits unrestricted use, distribution, and reproduction in any medium, provided the original work is properly cited.

Congestion on land, hike in fuel costs, and critical need to cut down environmental emissions have generated the urge to shift from conventional rail transit systems to metro rail and high-speed rail for a mass mode of transportation. The conventional railway network especially in India stages an effective space in the means of mass transit systems. Subsequently, periodic inspection of the state of railway tracks is vital for ensuring rail safety, as tracks are critical components of train transportation networks. Tracks are designed to withstand zero critical incidents, and with the advent of new high-speed train services, there is a greater need to focus on track performance. Track maintenance methods are customized to suit local conditions for enhancing safety and reducing disruptions while guaranteeing the resilience and sustainability of any rail system. In recent years, various aspects of the TMSs (track maintenance systems) have been introduced within the railway industry for both ballasted and ballastless track systems. This study reviewed various approaches to track maintenance measures using traditional methods, statistical methods, and geometry-based methods based on track deterioration. Among all the reviewed methods, track maintenance based on the geometry is said to cater to the needs of the maintainers. The outcomes of this study are expected to support and assist in track maintenance decisions in the railway industry.

## 1. Introduction

Railways have always played an important role in the transportation of commodities and passengers. Massive consignments get transported through railways mainly due to their cost efficiency and reduced environmental emissions. Currently, most of the goods and commuters are

shifted by this mode of transport increasing their loads and indirectly the tracks on which they run. Railway tracks on which trains run encompass switches, ballasts, sleepers, and rails, where ballasts are used globally in railway tracks [1]. Though slabs are also substituted in a few parts, ballasted tracks are conventionally used due to their reduced costs and ability to handle dynamic loads. Over years these ballasted



track systems have been replaced by ballastless tracks. In a ballasted railway track, the ballast consists of crushed granular material. This ballast layer has sleepers embedded inside of it, which are used as a support mechanism for the superstructure. The ballast is placed on top of the sub-ballast. The ballast has many key functions such as supporting the weight of the track, absorbing and distributing loads (static and dynamic) of trains running on the tracks, and providing good water or fluid drainage capabilities [2]. The ballast also increases track stability in the lateral and longitudinal directions and, therefore, they must be maintained regularly. Throughout history, loads and speeds have been steadily increasing in rail transportation, and throughout this evolution, railway tracks have experienced changes. One such advancement is a full rebuild of track structures, which renders them ballastless. Traditional ballasts are replaced by firm supporting slabs consisting of concrete, steel, or asphalt, which transfers the load and provides stability. As numerous comparable components characterize them, there are several varieties of ballastless track systems available based on different manufacturers. As a stiffer alternative to ballasted track systems, additional precautions must be taken to maintain flexibility. A common feature embedded in most of the ballastless track systems is that they have highly elastic rail fastening systems. For further elasticity, other elastic components can be installed, such as pads, bearings, or springs [3]. The major advantages of using ballastless tracks are described as follows: large reduction in maintenance cost (20–30% of maintenance cost of ballasted ones), fewer traffic interruptions, contributing to higher availability, less restrictive use of electromagnetic wheel brakes, reduced structural height and weight, and preventing the release of ballast dust in the environment.

Figure 1 represents an overview of the ballastless track systems in practice within the Indian Metro Rail System. There are two approaches to express track conditions, namely track geometries and track structures. Track geometry flaws and irregularities are primarily used to represent track conditions and plan track repair. Track geometries deteriorate with age and use and can have detrimental impacts on track performances. When track parametric values fall below the satisfactory level, it causes derailment, with serious outcomes which may include increased railway operating costs, economic losses, damage to railway assets, the environment, and loss of human lives. Correction of inadequate track geometries results in expensive track maintenance. Their maintenance activities should be scheduled to restore track parametric values to an appropriate state. The state of rail transportation and track structures includes numerous components. Their service life and performances are primarily determined by maintenance techniques used throughout their life cycles.

Efficient rail infrastructure maintenance necessitates the correct allocation of resources to various operations, posing a number of practical and operational problems [4]. Maintaining railways can be categorized as follows:

- (1) PM (preventive maintenance) involves carrying out activities (inspection, identification, and repair)

based on periodic schedules where each equipment's operating condition is checked and reconditioned.

- (2) CM (corrective maintenance): all measures are taken if there is an unexpected or abrupt maintenance event in terms of repair of an item/equipment due to perceived faults by the users.
- (3) PRM (predictive maintenance) is required wherever contemporary measurement and signal processing technologies are required to correctly anticipate and diagnose item/equipment condition during operation.

PMs are time-based activities for assessing track deteriorations and have been studied [5–7]. Though maintenance activities need to be preplanned and executed within a short time frame after on-site inspections, [85], it is difficult to plan them. Moreover, these operations disrupt sequences of regular PMs which keep railway track elements in tune and fine conditions. PM actions can assist to return the component to a better state, and they are frequently less expensive than component replacement [7–9]. To take advantage of the cost-benefit of PMs, a PM intervention can be performed a number of times repeatedly on a particular component prior to its renewal [10, 11]. As a result, track maintenance via a predictive process has traditionally been addressed as a series of independent phases, with each track component controlled separately. Various layers of management assess each stage for each key component of the rail system. Several studies have systematically classified various models and optimization models. The shortcomings in the field of track maintenance management have been highlighted, and future potential study fields have been recommended. The specifics of various track maintenance systems were investigated in terms of conventional approaches, statistical methods, geometry-based methods, machine learning methods, and bioinspired optimization methods in this review work. The track maintenance model's best operational performance in terms of maintenance policy, maintenance cost, and reliability metrics is being evaluated and debated.

## 2. Overview of the Pioneering Analysis Undertaken in Track Maintenance Systems

*2.1. Traditional Methods for Track Maintenance.* Railway tracks are subjected to preventive as well as CMs. Among these, the PM's activities are scheduled prior to providing a systematic way of monitoring the track performance. Various other numerical experiments were performed on track scheduling models by implementing superior computational methods, and these systems were applied to a railroad network to improvise the maintenance schedule decisions where rail temperatures were focused. A study's design included a heavy rail haul network of 60 kg/m using rail stress sensors, strain gauges, and thermocouples. The temperature of the rails varies regularly according to the temperature of the surrounding air. SFT might fluctuate by 2–3 times over the day, according to field experiments. Based on

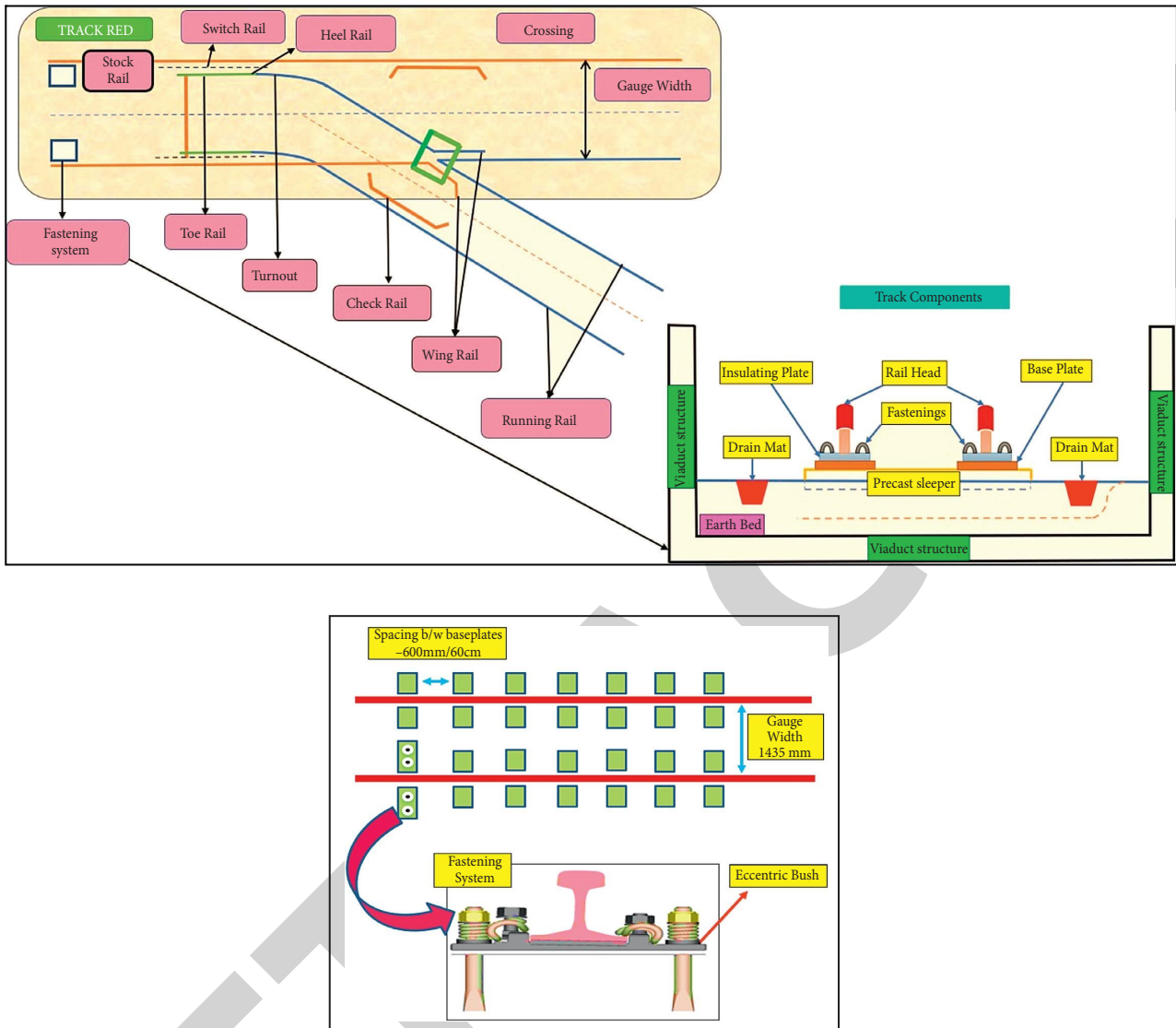


FIGURE 1: Overview of a ballastless track system.

these findings, an improvement in assessing track conditions using rail creep measurements was reported. TSMs (track stability management) are tools that identify requirements for PRMs. These tools stress the importance of rail stability and stress while defining rail modification priorities. Their assessments consider MS (margin of safety) or differences between TBs (track strengths) and TR-TN (rail stress) on the track. TR is the highest rail temperature while TBs are temperatures in which buckling might occur. TSMs use three elements, namely safety, track conditions, and prioritization of stress to obtain parameter values and act accordingly. RSMs (rail stress monitors) and strain gauges were installed on two (4 and 6 meters) 60 kg/m rails and tested with vertical loads of 5000 kgs where a hydraulic actuator was used. The test results were calibrated using finite element analysis. Computational results on strain gauges and thermocouples showed reduced SFTs at higher rail temperatures and contrary to RSM values which had increased SFTs at higher rail temperatures. Track

maintenance decision support systems have also made use of computational approaches such as big data. Big data methods have been presented to help with railway track maintenance choices. A large quantity of data on railway track condition monitoring is being gathered from various sources in numerous countries. These data are not being properly utilized due to a lack of appropriate methodologies for extracting key events and critical historical information. As a result, important information is concealed by massive amounts of data from various sensors. For railway track condition monitoring, general approaches that may support effective track maintenance decisions are provided. In Dutch tracks, As a benchmark, axle box acceleration (ABA) measurements are utilized, and generic reduction formulations are addressed to manage failures [12].

Moreover, the risk matrix application focused on identifying track zones that were bottlenecks and limited the operating strength and standard of tracks. A critical analysis method was presented to generate a hierarchical

TABLE 1: Inferences of traditional track maintenance methods.

<i>Author Reference</i>	<i>Evaluation Scheme</i>	<i>Concentrated segment</i>	<i>Parameters involved</i>	<i>Tools employed</i>	<i>Research gap</i>
[20]	Real time	Track maintenance schedule	Time window/travel cost/penalty cost	Time-space network model	Running time/renewal cost of rail
[12]	Case study	Track maintenance	Axle box acceleration measurements	Big data techniques	Maintenance frequency
[13]	Case study	Track maintenance analysis and rail infrastructure	Railway track operational factors	Risk matrix modelling	Weak overhead cable
[14]	Case study	Track deterioration	Track geometry measurements	RMMS	Life cycle costing
[16]	Case study	Electrically insulated rail joint	Inspection time variations/periodic replacement interval	Fault tree analysis	Inaccurate prediction/frequency of usage
[17]	Case study	Track maintenance schedule	Time periods/set up cost/key performance indicators	Capacitated arc routing problem	Maintenance crew scheduling
[18]	Case study	Track fault detection	Temperature/current/voltage	Remote condition monitoring	Database management/decision-making
[19]	Real time	Track maintenance schedule	Train timetable	Mathematical modelling	Speed restrictions
[21]	Real time	Track buckling	Rail temperature	Finite element analysis	Weather parameters
[22]	Case study	Rail maintenance	Squats/ballast defects	MILP solver	Multiple track defects (corrugation/ballast degradation)

improvement list in order to solve the issue of train mission interruption and lower operational capacity. The study's findings categorized the track line section into distinct risk zone categories based on their capacity and punctuality loss [13]. The process illustrates the analysis of track geometry simulation while optimizing the schedule with regard to tracking possession time as the research intends to decrease track possession cost. The analysis and modelling method for track maintenance planning and optimization will aid in the decrease of track possession time. Rather than maintenance schedule models, the bulk of studies on the tracks has focused on its deterioration process with regard to age and climate behavior. M&R (maintenance and renewal) was also targeted in a study that created a generic deterioration model by simulating track behavior. The model's life cycle costing and numerical optimization techniques minimized costs by balancing maintenance or renewals and could also produce qualitative inspections including disruptions to traffic. The scheme assisted in achieving the global objectives of RMMSs (railway maintenance management systems) [14]. The proposed M&R approach connected inventories, work history, and resource allocations to automatically predict deteriorations. Two critical components of the proposed PMs were namely localizing defects in infrastructures and accounting for parameters that were uncertain in their prediction of future deteriorations [15]. Impacts of an EI (electrically insulated) railway junctions regarded as a vital asset for railroad track identification as well as a major source of train interruptions were also examined. The maintenance aspects were added to FMTs (fault

maintenance trees) to determine the complexity and correctness of the parameters involved. The study's findings indicated that it was feasible to enhance joint reliability, for example, by doing more inspections, but the increased maintenance costs exceeded lower costs due to failures [16]. Consumed time due to maintenance can be constant or may change. Hence, the minimum time required to maintain segments was targeted where maintenance schedules were modified based on three distinct variations.

The scheme CARPF (capacitated arc routing problem with fixed cost) has resolved these issues by considering the parameters as a node routing issue [17]. Most track maintenance programs are designed to save money or time, but very few are designed to decrease the downtime of the equipment used to accomplish them. This optimization approach aided in the early discovery of problems thus reducing equipment downtimes and increasing production [18]. The majority of conventional track maintenance approaches have focused on studying track behavior owing to deterioration and wear prediction models. Reference [19] presented a mathematical programming approach for modifying train schedules on a single track based on maintenance activities. The unpredictability of maintenance activities may cause delays in the original maintenance plan, which may also conflict with predetermined train schedules. By adding buffer time into the redesigned schedule, this study tackles the unpredictability of maintenance tasks. In the modified timetable, the operational restrictions via speed limit due to maintenance activities were also addressed. The model produces a revised timetable that contains a

maintenance plan and train operation schedules for railway planners. Table 1 summarizes the conclusions drawn from traditional track maintenance methods:

The findings from conventional practices have revealed the usage of Weiner process, undirected graphical method, and fixed location-based monitoring method by the researchers for track maintenance practices. Many other methods like mixed integer linear programming (MILP) model, reliability-centered maintenance signalling system, and global sensitivity analysis based on distribution technique were utilized for forecasting and assessing track performance and resilience [15, 23]. With the introduction of metro rail transit systems, most of these methods are no longer extensively used. The majority of the studies mentioned above were well suited for the conventional railway system; thus, there is a need to use sophisticated prediction methods and forecasting models for track preventative maintenance.

*2.2. Statistical Methods for Track Maintenance.* Most of the statistics-based maintenance techniques are catered to create models or optimizations. Track geometry was predicted by [24] based on Petri nets. Their study projected conditions of the track with their estimated lifetime costs. The study altered inspection, maintenance, and ballast renewal parameters to achieve efficient predictions. Maintaining high-speed rail corridors using shared/dedicated operation patterns was examined, where descriptive parameter tables analyzed a corridor's response to changes in track maintenance strategies [25]. A modelling technique assessed existing data on track geometry and ballast condition, collected at regular intervals. Using the provided degradation distributions, a track section model was created that integrated maintenance and renewal processes and allowed the prediction of the ballast section's state over time frames. The model employs a Petri net formulation with a Monte Carlo solution routine to examine the efficacy of various maintenance techniques [26]. Most of the track maintenance schedules corresponded to train timetables. Several studies have modified the railway schedule based on the repair schedule. Physical inspections and visual examinations were the base for assessing track geometry issues. The scheme pointed out discrepancies in inspection data of tracks using a specialized instrument (track geometry vehicle). The model eliminated all positional errors from inspection data irrespective of noises in parameter measurement values. The model took 1.5004 s to correct 1 km track segment's positional errors. Further, the model also adapted itself to a variety of other applications: track geometries of trolleys, highway inspection data from LiDAR (Light Detection and Ranging) vehicles, and railroad catenary wire geometry inspection [27]. Despite periodic maintenance and considerable noise, the results line up exactly. Grindings are used in this study to eliminate fractures based on their depth. The rate of expansion of cracks on the head rail remains constant and the crack grows by 1% for every 1% increase in ridership [Mega gross tons]. It is expected that a single machine pass can repair a crack with a depth of  $h$  mm and a

cost of  $ascg$ . The increase in track growth was represented by a typical track section with the final limit as  $T_i$ . If the length of the track segment  $I$  exceed the limit  $T_i$ , the track is replaced at a cost  $cr \gg cg$ . An increase in rate correlates with a decrease in the duration of cost function intervals. The last PMs are to be replaced at a higher  $co$  at the limit  $T_i$ . Similar research was proposed for solving issues in interactions between high-speed night trains and maintenance schedules by utilizing MILPCPLEX solver. The study rearranged maintenance schedules to accommodate high-speed night trains running early morning or late evenings resulting in enhanced maintenance plans and timetables [28]. The midnight train timetable typically overlaps with the daytime train repair schedule. The service line is closed during maintenance of any railway section; therefore, to avoid conflicts, the maintenance period for specific segments is shortened to less than 4 hours or postponed accordingly. Night trains utilize the spare time available between consecutive railway segment repairs ( $G$ ). In order to avoid the conflicts between the train schedule amidst the maintenance schedule, certain trains were even cut off from service line. Thus, the work presented a modular approach for railway maintenance schedule optimizations.

A predictive technique for railway track maintenance scheduling was implemented taking into consideration risk assessment strategies based on ISO 55000 standards as well as real-time track conditions. A unique feature of this method is the inclusion of the idea of risk management in railway maintenance scheduling, suggesting that maintenance activity priorities are based on asset criticalities, such as track degradation conditions and repair prices, as well as users' unmet demand caused by asset failures [29]. To deal with nonlinearity concerns, predicted track degradation models are used. Tracks are classified into four conditions: good where there is negligible degradation, waiting maintenance where the tracks are close to failure but the degradation process has commenced, acceptable track degradation where failure is expected to take place within  $ds$  time, and unacceptable degradation level where the tracks are expected to be renewed or replaced. As a result, a MILP approach integrating cost, hazards, and appropriate weights is developed to forecast correct maintenance priority within a time horizon. The asset management approach used on a railway track segment was investigated using a Markov model. The number of model parameters employed forecasts the condition of a track segment over time for a specific asset management approach in order to illustrate the effects of maintenance interventions on the track's lifetime. The Markov model offers a simple yet effective mechanism for evaluating the effects of an asset management strategy on a railway track section [30]. Tracks are classified according to their standard deviation (SD), namely  $\partial$ : good,  $\partial_{crit}$ : critical,  $\partial_{spd}$ : speed restriction, and  $\partial_{cls}$ : line closure. Once a track section reaches  $\partial_{crit}$ , the section requires maintenance. As the track deteriorates more, the SD value obtained will strike  $\partial_{spd}$ , implying that speed limitations will be applied to that portion. In case of further deterioration, the track segment reaches  $\partial_{cls}$  which indicates there is an immediate need for closure of that segment. Theoretical prediction of track

irregularities was proposed by [31]. The study's grey model was compared with linear and exponential models. The study computed longitudinal standard deviations with the use of regression while their grey model was based on inspection data. In their assessment of prediction accuracies, the study found that modifying their model using the Fourier series resulted in the best performances with minimal errors. The work was an asset to the planning and scheduling of PMs. In addition, track inspectors were used to undertake an enhanced method of track geometry monitoring as data related to tracking geometry behavior was manually captured. After the advent of modern rail track inspection vehicles, this had altered as the vehicles run along train tracks and collected data about the state of infrastructures. Based on this information, a degradation model for train tracks was built in order to anticipate track deterioration and estimate future maintenance operations. To forecast tram track degradation, an ANFIS (adaptive network-based fuzzy inference system) was proposed where ANFIS estimated gauges. The system was found capable of accurate predictions even in jumbled data [32].

PMs were scheduled by [33] using optimization on a combination of PMs and renewals and arriving at the best between them. Resource optimization solutions such as grouping and balancing are used to reduce maintenance costs while maintaining the same level of service. Mixed integer linear programming is used to lower the costs of maintenance and renewal projects, as well as the associated labor and downtime charges, across the planning horizon. According to experimental data, the integrated optimization strategy minimizes the cost of preliminary work by effectively arranging it. The combined strategy resulted in a 14% reduction in maintenance and renewal expenses. Another research on preventative maintenance schedule was recommended to keep railway infrastructures in excellent working order while also taking into consideration limited resources available. The challenge of scheduling preventative railway maintenance operations was defined using MIP (mixed integer programming) and VNSs (variable neighborhood searches) to address large instances of the problem [34]. Many studies have focused on preventative maintenance scheduling techniques, while only a few of them focused on CM scheduling. Following their discovery as part of an inspection procedure, a methodology was presented in the study for optimizing CMs in rail networks. A study modelled integer programming for minimizing passenger delays due to low operational speeds on degraded rail segments while giving importance to intensively operating segments, train loads, staffing, budgets, and other constraints [35]. Figure 2 shows the degradation of rails, which was monitored on a real-time basis. These figures represent the lack of greasing along the sliding chair of check rails, rusting of check rail locks, worn-out base plates/rail plates that control the friction between the eccentric bushes and the anchor bolts, and the lack of greasing in the nosing areas. These defects indicate high chances of track slips that might create pits on the tracks thereby causing damage to the rolling stock.

The idea of RAMS (reliability, availability, maintainability, and safety) has been embraced by most metro rail

depots, and a similar approach was recommended to assist choices on train track design and maintenance methods. RAMS management is often used in the railway industry, but the proposed LCCA supported decisions on design alternatives and maintenance methods through an economic analysis that considered costs and performances. As a result, a decision support system was created based on life cycle costing (LCC) analysis for balancing immediate and long-term costs with performance and targeting RAMS. The suggested model incorporated not just agency (e.g., construction, inspection, maintenance, and renewal) and user expenses (e.g., delay-related) but also environmental costs into a full life cycle cost analysis (e.g., related to CO<sub>2</sub> emissions). The RAMS of a slab track was typically greater than that of a ballasted track, according to the findings [36]. A comparable analysis of life cycle costs was recently offered as a reasonably inexpensive alternative maintenance strategy for existing lines. This research seeks to evaluate the technology's potential benefits while also developing a new maintenance approach for existing ballasted rail beds. A protocol for the use of the BSB technology, as well as its related maintenance plan, has been established. The acquired results are also submitted to a sensitivity analysis. The use of BSS is projected to result in a considerable increase in the time between minor and major maintenance tasks [37]. Using the binary integer programming (IP) paradigm, a study has proposed a maintenance schedule optimization model for various components of a railway track. In general, grouping and maintaining several track components under one ownership saves the cost incurred as the track tends to be occupied. A sensitivity analysis is used to emphasize the effects of available possession time on the number of necessary possessions as well as the total cost involved [38].

In the same way as the prior integer programming model [39], a MIP model for routing vehicles with restrictions was proposed targeting Class-I railroads. Very few or limited studies have explored MDMs (Markov decision models), but one study used MDMs to obtain predicted values as impacted by present scenarios. The proposed MDMs used the train wheel's distinct conditions including their diameter, renewal distance based on time, and damages based on conditions. The study's estimated Markov transition matrices considered PMs and proposed an optimal strategy for ideal actions based on wheel conditions/states [40]. Another study was also based on MDMs and used conditions of the rails to define an optimal strategy that reduced overall costs. Rail conditions were assessed by the MDM using height, weight, MGTs (million gross tons), and damage incidences of the rails. The proposed optimum policy was a set of three PMs for railway managers to decide on the best PMs based on the state of the rail [41]. MPCs (model predictive controls) were proposed for multilevel decisions on optimum railway network's PMs. The study differentiated sections using independent stochastic degradations. They used a controller to compute and arrive at long-term section-wise PMs, thus helping reduce deteriorations and maintenance costs while ensuring degradations did not cross a defined threshold. The study's Dantzig-Wolfe decompositions optimized both continuous and discrete variables for best



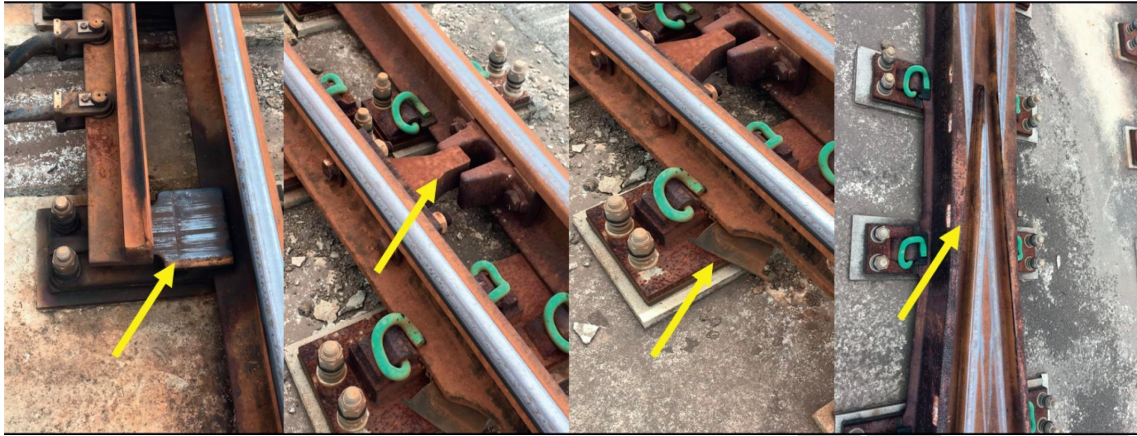


FIGURE 2: Common visible track defects [source: Chennai Metro Rail Depot].

decisions. Short-term schedules for maintenance using a high-level controller were proposed where maintenance staff routing was optimized. The study handled the issue assuming it as a routing issue and was found to be resilient, nonconservative, and scalable in simulations. Maintenances were scheduled based on average deteriorations and did not extend upto 6 months as a buffer time was allotted between average degradations and maintenance threshold values. The maintenance plan for certain sections had raised above maintenance thresholds and had to be grounded to zero after 6 months. In case of maximum deteriorations, time steps near maintenance threshold values and this occurs only during rail breakages. Table 2 lists the inferences obtained from the statistical maintenance methods. Most of the statistical methods employed for the maintenance of tracks have left a leap in the area of renewal cost.

### 2.3. Maintenance Methods Based on Track Geometry.

Bayesian models are probabilistic models that are thought to describe the connection between conditionally independent and dependent variables. Only a few investigations have been using this technique to evaluate rail track geometry deterioration over time in order to improve rail track geometry degradation uncertainty. Inspection historical data were used to assess uncertainties and were updated after every inspection. After each update of inspection history, uncertainties were assessed and degradations were measured by computing subsequent probabilities [42]. Similarly, the same approach was used to forecast and track degradations for guiding maintenance/renewals. This study used conditional auto regressions on track geometry data for interactions between successive track sections and lines [43]. The study simulated multiple correlations in consecutive track section components including degradation rates using HBMs (hierarchical Bayesian model). Their HBM assessed quality by comparing sensitivities of their generated candidate model's past distributions. Reference [44] used HBMs to evaluate railway track deteriorations. In addition, the study illustrates track maintenance histories with renewals in terms of percentage in the period 2001 to 2009, where the ratio of renewals shows a rise from 0.34 (2001) to 0.65

(2009). The authors also recommended MDMs for quantitative maintenance and thus prevent deterioration in Portugal's railway tracks. PMs/CMs/renewals costs, infrastructural delays for accommodating maximum allowable speeds, and unexpected infrastructure delays for temporary speed limitations were all accounted for alerting according to international standards. Threshold warning for key quality indicators of railway tracks that assists in determining the optimal choice of indicators were studied using sensitivity analysis, and in addition, penalties were levied on delay in trains [45]. The VirMaLab formalism was extended to provide an assistance tool for rail maintenance in an automated metro environment for standard steel-wheeled trains.

The theory of dynamic Bayesian networks provides an intriguing framework for addressing this problem since it allows for the use of probability distributions to characterize degradation processes as well as stochastic representations of maintenance agents. It not only simulated the rail degradation and the whole maintenance process but also the maintenance action decisions. The software's indicators assist in determining the most appropriate maintenance parameters. Because a metro rail track segment is made up of  $n$  number of elementary rail sections, developing a maintenance model for the entire stretch is considered unrealistic. As a result, the model only represents the elementary rail sections, which are extrapolated to larger sections based on reliability indicators. The VirMaLab model can estimate track degradation from hour to hour, including the effects of broken rail during peak hours. According to the VirMaLab Bayesian network, each condition of the rail is classified as OK (the rail with null defect), X1 (rail with internal cracks that are larger than 2 mm), X2 (rail with both internal and surface cracks less than 30 mm large), or BR (broken rail). The model's initial block is made up of rail deterioration, followed by the second block, which is made up of diagnosis devices. Ultrasound vehicles (USV), walking survey teams (WT), metro drivers (Drv), and track circuits are the devices that trigger periodic rail changes based on traffic, peak hours, and operational stops (TC). TC is thought to be the first to discover 80% of the broken rail problems. In the case of a warm season, rail dilation aids in maintaining electric

TABLE 2: Inferences of statistical track maintenance methods.

<i>Author Reference</i>	<i>Evaluation Scheme</i>	<i>Concentrated segment</i>	<i>Parameters involved</i>	<i>Tools employed</i>	<i>Research gap</i>
[5]	Case study	Track maintenance	Frequency of tamping operation	Mixed integer programming model (MILP)	Cost structure/schedule generation
[6]	Case study	Track maintenance	Rail grinding schedule/ rail crack detection	Integer programming model (ILP)/polyhedral analysis	Maintenance decision-making process/frequency of inspections
[24]	Case study	Track geometry	Inspection/ intervention/renewal	Petri net formulation	Track length/tamping machine
[25]	Real time	Track maintenance	Segments/routine works/possession cost	TMS strategy/Sensitivity analysis	Calibration of the PMSP model
[29]	Case study	Track maintenance schedule	Maintenance activities/ risk assessment	Modular model architecture/ ILP	Online recovery tool to determine stochastic delays
[32]	Case study	Track degradation	Rail load, rail type, rail profile	Adaptive network-based fuzzy inference system (ANFIS) model	Gauge value prediction
[33]	Case study	Track maintenance	Time period/track component replacement	Integer programming model (ILP)/Heuristic algorithms	Unexpected interventions/ corrective maintenance decisions
[36]	Case study	Track maintenance	User cost/ environmental cost	RAMS/LCCA	Database management
[37]	Case study	Track maintenance	Ballast type/lab test/ traffic	Life cycle approach	Life cycle cost analysis (LCCA) and life cycle assessment (LCA)
[38]	Case study	Track maintenance	Rail, ballast, sleepers, and switches	Binary integer programming (IP) model	Limitation of possession time
[39]	Real time	Track maintenance clustering	Project duration/job cluster type	Mixed integer mathematical programming model (MIMP)	Randomness of algorithm
[40]	Case study	Track interactive rolling sets	Wheel diameter/ mileage	Markov decision process/ MDP toolbox-MATLAB	Markov transition matrix (MTM)/inspection modes/ precision
[41]	Case study	Track maintenance	Rail grinding/renewal	Markov decision process	Rail curvature

contact with the BR, reducing the capacity of the TC to identify a fault by 50% [46]. Stochastic models are financial models that predict the likelihood of obtaining various outcomes under various limitations using randomly chosen variables. These models are used to characterize the process of geometrical track deterioration over time. For each vehicle speed category, a statistical analysis is carried out. The novel aspect of this study is that the Dagum distribution, which is commonly used to depict income distributions, is used to represent the geometrical track degradation process at the longitudinal level [47]. As part of condition-based preventative maintenance, a stochastic mathematical model is being created to optimize and anticipate tamping operations on ballasted rails. The model is described as a mixed 0–1 nonlinear program with real technical restrictions such as longitudinal standard deviation deterioration rate, track layout, track recovery dependency on its quality at the time of the repair operation, and preventative maintenance limits. This model looks at a 51.2 km long section of railway during a 10-year period. The deterioration model was found to be stochastic in nature, and it displayed the longitudinal standard deviation decreasing with time. The rate of degradation of the longitudinal standard deviation was

modelled using Monte Carlo techniques, with three parameters taken into consideration. Dagum's probabilistic distribution blended well with real-world data. The results of two simulations, namely stochastic simulation in space and stochastic simulation in space and time, were compared to one another. [48] The suggested condition-based maintenance model could provide optimum schedules in a reasonable amount of time. Only a few other researchers have focused on establishing an analytical framework that aids in decision-making. Reference [49] provided an analytical methodology for determining the best geo-defect repair options by minimizing anticipated costs including derailments/repairs. The study's major contributions were in integrating three models: track deteriorations of Class II geo-defects; survival of tracks from derailment risks, and optimization of track repairs under uncertain conditions. The proposed models showed a 20% reduction in overall composite costs and the percentage rose when longer track sections were considered.

Another study that followed this proposal using the same approach except that their model was an optimization was based on cost-based formulations and risk-based formulation (RBFs). These schemes addressed optimal rectification



planning challenges of railways. To improve track rectification decisions, existing railroads are presented with decision queries such as how yellow tags slip into red tags, how unrectified yellow tags slip into the risk of derailment, and what should be the correct time horizon within which an activity is prevented from falling into the red tag area [50]. Because track geometry is regarded as a hotspot in any railway industry, few research have focused on the degradation of track geometry by utilizing the Weibull technique and regression approaches. Reference [51] presented a Weibull method for analyzing time distributions for track geometry to deteriorate to defined states after repair. The quality of the track is determined by the rail alignment, particularly the vertical alignment. Higher wavelengths that have little bearing on ride quality are filtered out. The train engineers use a wavelength filter of around 35m to screen the track condition. The standard deviation for a 220-m yard segment is then determined. In addition to the tamping action, the quality of the track geometry is assessed. The findings of this study demonstrate that traffic speed and the history of any line's maintenance have an impact on geometrical degradation. Furthermore, the notion that tamping affects railway ballast is supported.

Meanwhile, [52] used a logistic regression technique to add unplanned maintenance requirements for rail track geometry deterioration. Unplanned maintenance for tracks based on European Standard EN 13848 was proposed in a study. The study considered bridges and switches data from inspection records and analyzed them statistically. Standard deviations from longitudinal values and errors in horizontal alignments were used as main indicators for unplanned maintenances. The study also proposed trade-offs between planned/unplanned maintenances and catering to EN 13848 limitations. Most optimization approaches focused on track conditions and costs of renewing them. PMs were forecast using biobjective optimizations where renewals were linked to track geometry. From the standpoint of infrastructure management, the challenge was treated as an objective integer optimization problem. The overall expenditures of planned repair and renewal activities, as well as the total number of delays in runtime induced by speed limits, were both minimized. The optimal Pareto frontier was determined using a simulated annealing approach in a tiny example for a basic network [53]. In a railroad track degradation study, [54] developed a short-range track condition forecast technique. Its purpose is to inform railway maintenance managers about the track condition ahead of time so that track maintenance activities may be scheduled. Track geometrical exceptions are derived from track conditions assessed using track geometry vehicles, and the projected values revealed that they did not offer a trustworthy condition. Track geometry data from Jiulong-Beijing train track geometry cars were used for error and comparability tests. The improved model is strong enough to generate trustworthy predictions, according to the analysis results. Reference [55] suggested a new approach for forecasting track geometry defects that is comparable to existing track records and combined prediction with inspection and maintenance planning. Broken rail faults are frequently

preceded by visual and ultrasonic cracks. The recommended strategy's underestimation of flaws is controlled by a novel application of a risk-averse and hybrid prediction approach.

MDM forecasts identified suitable inspection and maintenance strategies. Moreover, Whittle indices using an updated transition kernel (multi-bandit formulations) offered optimum dynamic policies to handle limitations. The study forecastings were highly accurate and suitable to forming long-term scheduling rules which could be changed based on changing conditions. Reference [56] reduced ballast costs for maintenance/unit traffic by their optimization of track geometry inspections. The study considered inspection and maintenance timings along with incurred costs for inspections, tampering, and risk of accidents based on track conditions. The study's probabilities were based on northern Sweden's track geometry data where passenger and freight trains were considered. Constructions, operations, designs, and maintenance account to track geometry degradations. Reference [57] assessed PM limits for Iran's railway lines to reduce overall maintenance costs. The study's cost model included PMs, CMs, inspections, and penalties when CMs limits were exceeded. The study used standard deviation values of longitudinal levels for quality of railway geometry assessments. The study minimized model's uncertainties in maintenances. The most comparable track sections were classified using the K-means clustering method. Thereafter, a linear function was used to indicate the degradation of rail sections for each cluster. To anticipate track geometry behavior and calculate the appropriate maintenance limit that minimizes overall maintenance expenditures, the Monte Carlo approach was utilized. According to his results, putting in place an adequate limitation can save overall yearly maintenance expenditures by 27 to 57%.

Among the previously described track geometry models, [58] proposed a method for allocating an effective track geometry maintenance limit that results in the lowest overall yearly maintenance cost. The cost model integrated inspections, PMs, CMs, and emergency CMs using standard deviation and outlier values of singular faults on longitudinal scales to derive quality indicators for PMs and CMs. The study used Monte Carlo approach to model track behavior after maintenance operations, limiting it to certain scenarios thus minimizing overall maintenance costs. Sensitivity analysis on inspections and maintenance response times was used to suggest effective restrictions in railway operations. However, the study proposed a lower bound optimal value for operations. Track geometry is evaluated at discrete time intervals ( $s$ ) to determine its condition, as previously indicated. Each inspection interval measures the standard deviation of the longitudinal level (DLL), and if it exceeds the action limit AL (DLL AL), the track will be examined for PM tamping during the first maintenance window ( $T_{\text{tamp}}$ ). This means that PMs will not be performed on the track until the predetermined PMs period has passed, even if the DLL between two maintenance cycles is greater than the AL. Track geometry is evaluated at discrete time intervals ( $s$ ) to determine its condition, as previously indicated. This study concentrates on the efficient determination of maintenances,

and catering to isolated faults has been outlined for future scope. Examining reaction times of regular CMs, track degradations can be categorized into normal tracks in CMs or CMs in an emergency. The categorization can be applied only when the time taken to react exceeds inspection intervals. In this study, the degradation of track geometry was modelled using a linear model and the degradation parameters. The degradation parameters in the suggested degradation model are (???? and bs) considered as random variables. The difference between the projected value and the measured value is said to be degradation, where  $t$  is the time in days and  $t_n$  is the time at the most recent tamping operation. Various parameters encompass degradations resulting in a change of behavior in track sections. The AD (Anderson–Darling) test found suitable distribution where the likelihood of degradations assisted in estimating distribution parameters. It can be inferred that linear model residues get distributed normally in tests. Minitab software computed mean and variances of degradation model's errors [58].

The increasing trend observed in the track length is represented in Figure 3 which indicates the critical need to monitor track geometry. Datasets related to track geometry cannot be easily obtained since they are not kept in a repository. Despite the fact that data gathering is uncommon, a few real-time studies have been developed and carried out using data-driven models, and a few of them are discussed here. Based on track quality evaluations over time, [97] developed a data-driven tamping forecast. A study database comprising asset information completed maintenance activities and measured data over a 4,400-km stretch of the Austrian rail network during a 16-year period has been made public. For planning and anticipating tamping operations, the modified standard deviation of vertical track geometry has been found as an excellent track quality indicator. Further analysis reveals that a linear regression function is most suited for characterizing track quality between two tamping activities and for forecasting track quality in the future with the highest accuracy. The linear regression function was used to create an algorithm that allows for the analysis of track quality behavior over time for large time series and the whole network. Based on measurement data gathered from the field study, a comparable data-driven analytical approach for prediction of isolated track geometry problems was created. A new defect-based model was suggested to determine the deterioration pattern of isolated longitudinal level faults of railway tracks. In the deterioration route, the suggested model considered the occurrence of shock events.

The efficiency of tamping intervention in correcting longitudinal-level faults was also investigated. The results demonstrate that the linear model is considered to be a good fit for exhibiting the longitudinal-level defect of the track degradation pattern. In addition, a section-based model based on binary logistic regression has been created to forecast the likelihood of isolated faults occurring in segments of railroad systems. As explanatory variables, the model included standard deviation and

kurtosis of longitudinal levels. The kurtosis of the longitudinal level is a statistically significant predictor of individual track section levelling problems. The validation findings show that the proposed binary logistic regression model can detect the presence of isolated defects in a track segment with high accuracy [59]. Table 3 groups the inferences from the geometry-based maintenance techniques.

### 3. Identification of Real-Time Constraints in the Indian Metro Rail System

PMs are carried out by the maintainers in every Indian metro, and the values obtained at every section of the rail are recorded manually in registers which will further be verified by the section engineers.

The section engineers are responsible for deciding if any maintenance is to be performed by their team at the particular section after obtaining a work permit from the operation and control center of the railway. Therefore, there is a time-lapse analyzed here and this, in turn, may sometimes result in an emergency maintenance requirement. To offer a realistic prediction for track maintenance restrictions and real-time constraints, the most modern PMs for railway tracks rely heavily on inspection and degradation evaluation. To solve these constraints, recently several algorithms have been introduced which are discussed in the above section. The majority of the studies have concentrated on optimal routes for the maintenance crew, rerouting of vehicles as per maintenance schedule, clustering track maintenance jobs, cost for undertaking the early and late maintenance tasks, corrective maintenance programming model, considering actual infrastructure condition, minimizing the maintenance cost while maintaining the tracks at acceptance fit levels, minimizing the track possession time, and track degradation models. To the best of our knowledge, the major constraints encountered along the maintenance of tracks [Figure 4] are climatic conditions, lack of automated schedule, equipment availability, labour availability, track restoration time, block time, availability of parallel department, unskilled outsourced labor, implementation of additional stretch, budget constraints (hidden), maintenance tender, rail availability, train rerouting, trip frequency, material availability, budget approval time, and material processing time. The on-site constraints observed during the preparatory works of this study are as follows: outsourced technicians and maintainers-technical barrier, lack of preplanned maintenance activity, lack of systemized track maintenance schedule incorporating the constraints, climatic hindrances to complete the allotted activity, and lack of integrated (rolling stock, signaling) track maintenance scheduling

### 4. Workplan for Future

Track maintenance system of Indian metros is possibly done during night time as the run time of metro train

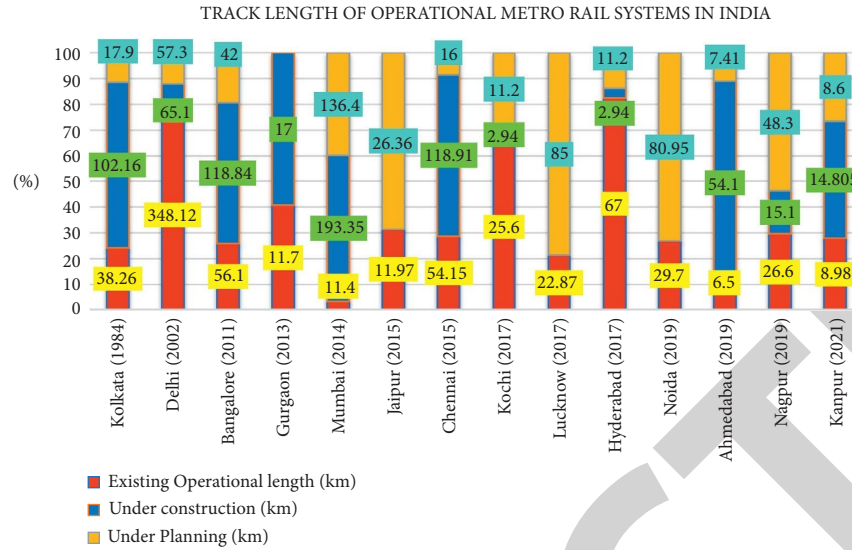


FIGURE 3: Increasing trend of metro rail track length [Source: [https://en.wikipedia.org/wiki/Urban\\_rail\\_transit\\_in\\_India](https://en.wikipedia.org/wiki/Urban_rail_transit_in_India)].

TABLE 3: Inferences of geometrical track maintenance methods.

Author Reference	Evaluation Scheme	Concentrated segment	Parameters involved	Tools Employed	Research Gap
[7]	Case study	Track maintenance	Track alignment defects	Decision support systems	Probability prediction of alert limits
[8]	Case study	Track maintenance	Total cost/renewal actions/speed restrictions	Mathematical modelling	Degradation parameters/different network configuration
[9]	Case study	Track maintenance	Track alignment parameters	HBM/Monte Carlo Simulation	Model sensitivity/correlation of formulation
[10]	Case study	Track maintenance	Track alignment parameters	Markov decision process	Permissible speed restriction
[15]	Case study	Track maintenance	Track alignment parameters	Weibull approach	Improvement of TPI
[47]	Case study	Rail maintenance	Rail parameters	VirMaLab/Bayesian models	Integration of meta-heuristics
[51]	Case study	Rail maintenance	Location/time of defect occurrence/defect type	Markov decision process/Whittle indices	Crew assignment for maintenance operations
[57]	Case study	Track maintenance	Rail type length/allowable speed/ballast type/fastener type/passenger capacity	Monte Carlo simulation/K-means clustering algorithm	Reduction of maintenance cost
[58]	Case study	Track maintenance	Maintenance window/frequency of inspection	Monte Carlo simulation/sensitivity analysis	Increase frequency and response time for maintenance
[59]	Case study	Track maintenance	Track geometry inspection values	Heuristics/analytical framework	Time optimization
[60]	Case study	Track quality	Track indices/longitudinal level	Linear regression analysis	Best fit integrated model
[47]	Case study	Track maintenance	Longitudinal level, alignment, gauge, twist, and cross-level.	Dagum distribution	Fitness of the model for varying track components
[48]	Case study	Track maintenance	Track alignment levels/standard deviation	Mathematical modelling/MILP/Monte Carlo process	Maintenance cost

begins every day on an average at 6 : 00 AM and ends by 9 : 30 PM and therefore the time slot available for preventive track maintenance is only during night time after

all train sets are back to stabling sheds. The work time available for any track maintenance activity is hardly 4 hours. The maintainers walk along the planned sections

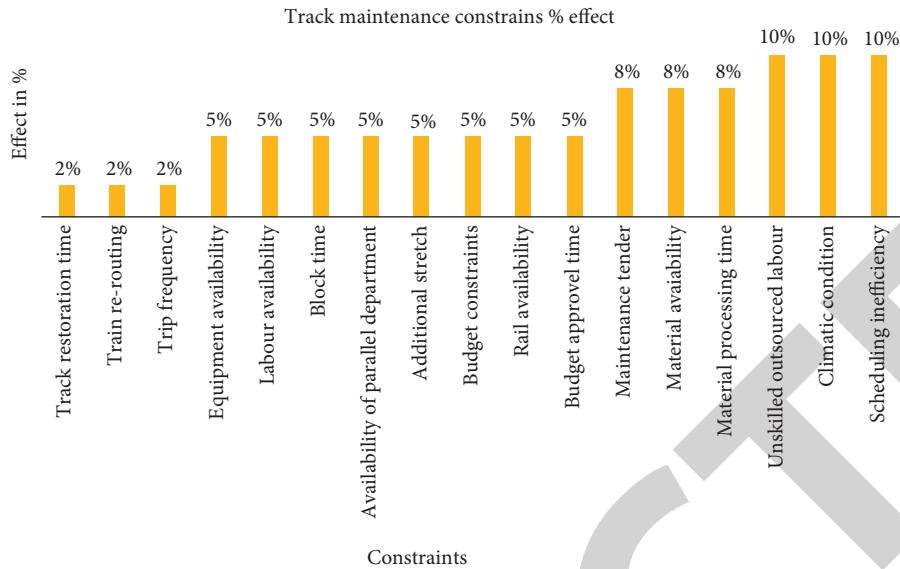


FIGURE 4: Constraint measurement in percentage wise.

of tracks and inspect visually during the nighttime which is very difficult at times to predict the exact track geometry measure. Most of the metro rail system has a parallel line known as a walkway along which the keyman can walk to inspect the lines in case of any reported issues observed during daytime. With the increase in track length, this is considered to be a critical task. In order to reduce the construction space and cost, walkways have not been included in any further projects. Therefore, in order to avoid a time-lapse in taking speedy action at the segment which requires immediate attention, a maintenance management model is believed to serve the purpose. Usually, the track geometry values are entered manually and recorded in separate registers. The section engineers in turn further check for the value accuracy and decide upon any need to directly inspect the particular section that has deviated from the tolerance/permissible value limits. There occurs a time-lapse for carrying out the maintenance activity, in case there is a need for immediate attention. Hence, it is necessary to have a planned scheduling system for allotting the maintenance activity along the track sections in between the service run during day time. As the Indian metros are on the verge of expanding their operational routes with a greater number of depots for stabling, it is highly necessary to plan the track maintenance activities systematically. Therefore, from all the previously referred reviews and methods, it is understood that most of the studies have been carried out on a real-time basis and the developed models are deployed into the respective systems to acquire better results. Through this work, the authors of the study have planned to develop a track maintenance alerting system for the Indian metros by developing a track cloud which will have a predefined set

of datasets from historical records. This database acts as a base layer to identify the difference in parameter threshold values if they fall beyond the limits. The developed system will serve as a decision assistant to the maintainer who can determine whether the track requires immediate attention or not which will then be reported systematically to the policymakers.

## 5. Conclusion

Railway infrastructure is one of a country's most valuable assets in terms of passenger and freight transit. The track is an essential aspect of the railway system among these components. As a result, maintenance planning for a busy railway track is difficult due to increased strain on increasing operation time, which limits the infrastructure-accessible time for repair. As a result, track maintenance has traditionally been regarded as a series of processes, with each track component being administered independently. Each phase for each major element of the rail system is evaluated at various levels of management. This review work studied the details of various track maintenance systems in terms of conventional methods, statistical methods, and geometry-based methods. The best operating performance of the track maintenance model with respect to the maintenance policy, maintenance cost, and reliability measures are reviewed. From every developed model, it can be inferred that railway track maintenance via ballastless has given more results than the ballasted track model. This review completely provides the methods adopted for tracking maintenance practices along with their constraints. Further, the review has also proposed a

maintenance model for Indian metro rail for future endeavors. From every reviewed analysis, it is notable that time plays a major important role in all systems. Therefore, in order to avoid a time-lapse in taking speedy action at the track segment which requires immediate attention, a new system that integrates the database cloud is planned to be introduced in future work for the betterment of the Indian Metro Rail System.

## Data Availability

There are no separate data associated with this article.

## Conflicts of Interest

The authors declare that there are no conflicts of interest in this study

## Acknowledgments

The authors would like to extend their gratitude to the maintainers of Kochi Metro Rail Limited (Depot) and Chennai Metro Rail Limited (Depot) team for providing their valuable support and guidance.

## References

- [1] D. Prescott and J. Andrews, "Modelling Maintenance in Railway Infrastructure Management," in *Proceedings of the Annual Reliability and Maintainability Symposium*, pp. 1–6, Orlando FL USA, January 2013.
- [2] C. Zhang, Y. Gao, L. Yang, Z. Gao, and J. Qi, "Joint optimization of train scheduling and maintenance planning in a railway network: a heuristic algorithm using Lagrangian relaxation," *Transportation Research Part B: Methodological*, vol. 134, pp. 64–92, 2020.
- [3] S. A. Kollo, A. Puskas, and G. Kollo, "Ballasted track versus ballastless track," *Key Engineering Materials*, vol. 660, pp. 219–224, 2015.
- [4] T. Liden, "Railway infrastructure maintenance - a survey of planning problems and conducted research," *Transportation Research Procedia*, vol. 10, pp. 574–583, 2015.
- [5] E. Gustavsson, "Scheduling tamping operations on railway tracks using mixed-integer linear programming," *EURO Journal on Transportation and Logistics*, vol. 4, no. 1, pp. 97–112, 2015.
- [6] E. Gustavsson, M. Patriksson, A. B. Stromberg, A. Wojciechowski, and M. Onnheim, "Preventive maintenance scheduling of multi-component systems with interval costs," *Computers & Industrial Engineering*, vol. 76, pp. 390–400, 2014.
- [7] M. Wen, R. Li, and K. B. Salling, "Optimization of preventive condition-based tamping for railway tracks," *European Journal of Operational Research*, vol. 252, no. 2, pp. 455–465, 2016.
- [8] C. Stenstrom, P. Norrbin, A. Parida, and U. Kumar, "Preventive and corrective maintenance–cost comparison and cost-benefit analysis," *Structure and Infrastructure Engineering*, vol. 12, no. 5, pp. 603–617, 2016.
- [9] Z. Zhu, Y. Xiang, M. Li, W. Zhu, and K. Schneider, "Preventive maintenance subject to equipment unavailability," *IEEE Transactions on Reliability*, vol. 68, no. 3, pp. 1009–1020, 2019.
- [10] T. P. Carvalho, F. A. Soares, R. Vita, R. D. P. Francisco, J. P. Basto, and S. G. S. Alcalá, "A systematic literature review of machine learning methods applied to predictive maintenance," *Computers & Industrial Engineering*, vol. 137, Article ID 106024, 2019.
- [11] Q. Wang, S. Bu, and Z. He, "Achieving predictive and proactive maintenance for high-speed railway power equipment with LSTM-RNN," *IEEE Transactions on Industrial Informatics*, vol. 16, no. 10, pp. 6509–6517, 2020.
- [12] N. Balac, T. Sipes, N. Wolter, K. Nunes, B. Sinkovits, and H. Karimabadi, "Large scale predictive analytics for real-time energy management," in *Proceedings of the IEEE international conference on big data*, pp. 657–664, Silicon Valley, CA, USA, October 2013.
- [13] S. M. Famurewa, M. Asplund, M. Rantatalo, A. Parida, and U. Kumar, "Maintenance analysis for continuous improvement of railway infrastructure performance," *Structure and Infrastructure Engineering*, vol. 11, no. 7, pp. 957–969, 2015.
- [14] S. Jovanovic, H. Guler, and B. Coko, "Track degradation analysis in the scope of railway infrastructure maintenance management systems," *Gradevinar*, vol. 67, no. 3, pp. 247–258, 2015.
- [15] R. Schenkendorf, J. C. Groos, and L. Johannes, *IFAC-PapersOnLine*, vol. 48, no. 21, pp. 964–969, 2015.
- [16] E. Ruijters, D. Guck, M. Van Noort, and M. Stoelinga, "Reliability-centered maintenance of the electrically insulated railway joint via fault tree analysis: a practical experience report," in *Proceedings of the 46th Annual IEEE/IFIP International Conference on Dependable Systems and Networks*, pp. 662–669, Toulouse, France, June 2016.
- [17] Z. Su and B. D. Schutter, "Optimal scheduling of track maintenance activities for railway networks," *IFAC-PapersOnLine*, vol. 51, no. 9, pp. 386–391, 2018.
- [18] S. B. Singh, R. Suresha, and K. H. Sachidananda, "Reliability centered maintenance used in metro railways," *Journal Européen des Systèmes Automatisés*, vol. 53, no. 1, pp. 11–19, 2020.
- [19] M. Bababeik, S. Zerguini, M. Farjad-Amin, N. Khademi, and M. Bagheri, "Developing a train timetable according to track maintenance plans: a stochastic optimization of buffer time schedules," *Transportation Research Procedia*, vol. 37, pp. 27–34, 2019.
- [20] F. Peng and Y. Ouyang, "Track maintenance production team scheduling in railroad networks," *Transportation Research Part B: Methodological*, vol. 46, no. 10, pp. 1474–1488, 2012.
- [21] S. S. Ahmad, N. K. Mandal, G. Chattopadhyay, and J. Powell, "Development of a unified railway track stability management tool to enhance track safety," *Proceedings of the Institution of Mechanical Engineers - Part F: Journal of Rail and Rapid Transit*, vol. 227, no. 5, pp. 493–516, 2013.
- [22] Z. Su, A. Jamshidi, A. Nunez, S. Baldi, and B. De Schutter, "Integrated condition-based track maintenance planning and crew scheduling of railway networks," *Transportation Research Part C: Emerging Technologies*, vol. 105, pp. 359–384, 2019.
- [23] S. Sharma, Y. Cui, Q. He, R. Mohammadi, and Z. Li, "Data driven optimization of railway maintenance for track geometry," *Transportation Research Part C: Emerging Technologies*, vol. 90, pp. 34–58, 2018.
- [24] J. Andrews, D. Prescott, and F. De Rozières, "A stochastic model for railway track asset management," *Reliability Engineering & System Safety*, vol. 130, pp. 76–84, 2014.
- [25] P. Lautala and H. Pouryousef, "Sensitivity analysis of track maintenance strategies for the high-speed rail (HSR)

- services,” *ASME/IEEE Joint Rail Conference*, vol. 54594, pp. 141–150, 2011.
- [26] J. Andrews, “A modelling approach to railway track asset management,” *Proceedings of the Institution of Mechanical Engineers - Part F: Journal of Rail and Rapid Transit*, vol. 227, no. 1, pp. 56–73, 2013.
- [27] P. Xu, R. Liu, Q. Sun, and L. Jiang, “Dynamic-time-warping-based measurement data alignment model for condition-based railroad track maintenance,” *IEEE Transactions on Intelligent Transportation Systems*, vol. 16, no. 2, pp. 799–812, 2015.
- [28] D. Wang, S. Zhan, Q. Peng, and W. Zhou, “Integrated overnight train scheduling and maintenance planning for high-speed railway lines,” *Transportation Research Record*, vol. 2675, no. 3, pp. 222–237, 2021.
- [29] A. Consilvio, A. Di Febraro, and N. Sacco, “A Modular Model to Schedule Predictive Railway Maintenance Operations,” in *Proceedings of the 2015 International Conference on Models and Technologies for Intelligent Transportation Systems*, pp. 426–433, Budapest, Hungary, June 2015.
- [30] D. Prescott and J. Andrews, “Investigating railway track asset management using a Markov analysis,” *Proceedings of the Institution of Mechanical Engineers - Part F: Journal of Rail and Rapid Transit*, vol. 229, no. 4, pp. 402–416, 2015.
- [31] T. Xin, S. M. Famurewa, L. Gao, U. Kumar, and Q. Zhang, “Grey-system-theory-based model for the prediction of track geometry quality,” *Proceedings of the Institution of Mechanical Engineers - Part F: Journal of Rail and Rapid Transit*, vol. 230, no. 7, pp. 1735–1744, 2016.
- [32] M. Karimpour, L. Hitihamillage, N. Elkhoury, S. Moridpour, and R. Hesami, “Nonlinear Estimation Model for Rail Track Deterioration,” *International Conference on Transportation Economics and Transportation Systems*, vol. 11, no. 9, 2017.
- [33] F. Pargar, O. Kauppila, and J. Kujala, “Integrated scheduling of preventive maintenance and renewal projects for multi-unit systems with grouping and balancing,” *Computers & Industrial Engineering*, vol. 110, pp. 43–58, 2017.
- [34] R. Macedo, R. Benmansour, A. Artiba, N. Mladenovic, and D. Urosevic, “Scheduling preventive railway maintenance activities with resource constraints,” *Electronic Notes in Discrete Mathematics*, vol. 58, pp. 215–222, 2017.
- [35] K. Argyropoulou, C. Iliopoulou, and K. Kepaptsoglou, “Model for corrective maintenance scheduling of rail transit networks: application to Athens metro,” *Journal of Infrastructure Systems*, vol. 25, no. 1, Article ID 04018035, 2019.
- [36] F. G. Pratico and M. Giunta, “An Integrative Approach RAMS-LCC to Support Decision on De-sign and Maintenance of Rail Track,” in *Proceedings of the International Conference on Environmental Engineering. ICEE; Vilnius, Lithuania, April 2017*.
- [37] F. Sajedi and H. A. Razak, “Comparison of different methods for activation of ordinary Portland cement-slag mortars,” *Construction and Building Materials*, vol. 25, no. 1, pp. 30–38, 2011.
- [38] C. Dao, R. Basten, and A. Hartmann, “Maintenance scheduling for railway tracks under limited possession time,” *Journal of Transportation Engineering Part A: Systems*, vol. 144, no. 8, Article ID 04018039, 2018.
- [39] F. Peng and Y. Ouyang, “Optimal clustering of railroad track maintenance jobs,” *Computer-Aided Civil and Infrastructure Engineering*, vol. 29, no. 4, pp. 235–247, 2014.
- [40] J. A. Braga and A. R. Andrade, “Optimizing maintenance decisions in railway wheelsets: a Markov decision process approach,” *Proceedings of the Institution of Mechanical Engineers - Part O: Journal of Risk and Reliability*, vol. 233, no. 2, pp. 285–300, 2019.
- [41] L. C. B. Sancho, J. A. P. Braga, and A. R. Andrade, “Optimizing maintenance decision in rails: a Markov decision process approach,” *ASCE-ASME Journal of Risk and Uncertainty in Engineering Systems, Part A: Civil Engineering*, vol. 7, no. 1, Article ID 04020051, 2021.
- [42] A. Lopez-Pita, P. F. Teixeira, C. Casas, A. Bachiller, and P. A. Ferreira, “Maintenance costs of high-speed lines in Europe state of the art,” *Transportation Research Record*, vol. 2043, no. 1, pp. 13–19, 2008.
- [43] A. R. Andrade and P. F. Teixeira, “Hierarchical Bayesian modelling of rail track geometry degradation,” *Proceedings of the Institution of Mechanical Engineers - Part F: Journal of Rail and Rapid Transit*, vol. 227, no. 4, pp. 364–375, 2013.
- [44] A. R. Andrade and P. F. Teixeira, “Statistical modelling of railway track geometry degradation using hierarchical Bayesian models,” *Reliability Engineering & System Safety*, vol. 142, pp. 169–183, 2015.
- [45] A. R. Andrade and P. F. Teixeira, “Exploring different alert limit strategies in the maintenance of railway track geometry,” *Journal of Transportation Engineering*, vol. 142, no. 9, Article ID 04016037, 2016.
- [46] O. Francois, L. Bouillaut, and S. Dubois, “A Multi-Nets Approach for Modeling and Evaluating Rail Maintenance Strategies,” in *Proceedings of the 9th World Congress on Railway Research*, pp. 22–26, France, May 2011.
- [47] C. Vale and S. M. Lurdes, “Stochastic model for the geometrical rail track degradation process in the Portuguese railway Northern Line,” *Reliability Engineering & System Safety*, vol. 116, pp. 91–98, 2013.
- [48] C. Vale and I. M. Ribeiro, “Railway condition-based maintenance model with stochastic deterioration,” *Journal of Civil Engineering and Management*, vol. 20, no. 5, pp. 686–692, 2014.
- [49] Q. He, H. Li, D. Bhattacharjya, D. P. Parikh, and A. Hampapur, “Railway track geometry defect modeling: deterioration, derailment risk and optimal repair,” in *Proceedings of the Transportation Research Board Annual Meeting. The Academy of Transportation Research Board, Washington DC US, January 2013*.
- [50] Q. He, H. Li, D. Bhattacharjya, D. P. Parikh, and A. Hampapur, “Track geometry defect rectification based on track deterioration modelling and derailment risk assessment,” *Journal of the Operational Research Society*, vol. 66, no. 3, pp. 392–404, 2015.
- [51] M. Audley and J. D. Andrews, “The effects of tamping on railway track geometry degradation,” *Proceedings of the Institution of Mechanical Engineers - Part F: Journal of Rail and Rapid Transit*, vol. 227, no. 4, pp. 376–391, 2013.
- [52] A. R. Andrade and P. F. Teixeira, “Unplanned-maintenance needs related to rail track geometry,” *Proceedings of the Institution of Civil Engineers-Transport*, vol. 167, no. 6, pp. 400–410, 2014.
- [53] A. R. Andrade and P. F. Teixeira, “Biobjective optimization model for maintenance and renewal decisions related to rail track geometry,” *Transportation Research Record*, vol. 2261, no. 1, pp. 163–170, 2011.
- [54] P. Xu, C. Jia, Y. Li, Q. Sun, and R. Liu, “Developing an Enhanced Short-Range railroad Track Condition Prediction Model for Optimal Maintenance Scheduling,” *Mathematical Problems in Engineering*, vol. 2015, Article ID 796171, 12 pages, 2015.

## Retraction

# Retracted: An Enhanced Drone Technology for Detecting the Human Object in the Dense Areas Using a Deep Learning Model

### Advances in Materials Science and Engineering

Received 20 June 2023; Accepted 20 June 2023; Published 21 June 2023

Copyright © 2023 Advances in Materials Science and Engineering. This is an open access article distributed under the Creative Commons Attribution License, which permits unrestricted use, distribution, and reproduction in any medium, provided the original work is properly cited.

This article has been retracted by Hindawi following an investigation undertaken by the publisher [1]. This investigation has uncovered evidence of one or more of the following indicators of systematic manipulation of the publication process:

- (1) Discrepancies in scope
- (2) Discrepancies in the description of the research reported
- (3) Discrepancies between the availability of data and the research described
- (4) Inappropriate citations
- (5) Incoherent, meaningless and/or irrelevant content included in the article
- (6) Peer-review manipulation

The presence of these indicators undermines our confidence in the integrity of the article's content and we cannot, therefore, vouch for its reliability. Please note that this notice is intended solely to alert readers that the content of this article is unreliable. We have not investigated whether authors were aware of or involved in the systematic manipulation of the publication process.

Wiley and Hindawi regrets that the usual quality checks did not identify these issues before publication and have since put additional measures in place to safeguard research integrity.

We wish to credit our own Research Integrity and Research Publishing teams and anonymous and named external researchers and research integrity experts for contributing to this investigation.

The corresponding author, as the representative of all authors, has been given the opportunity to register their agreement or disagreement to this retraction. We have kept a record of any response received.

### References

- [1] M. R. A. Refaai, D. R. Rinku, I. Thamarai, S. Meera, N. K. Sripada, and S. Yishak, "An Enhanced Drone Technology for Detecting the Human Object in the Dense Areas Using a Deep Learning Model," *Advances in Materials Science and Engineering*, vol. 2022, Article ID 4162007, 12 pages, 2022.



## Research Article

# An Enhanced Drone Technology for Detecting the Human Object in the Dense Areas Using a Deep Learning Model

Mohamad Reda A. Refaai <sup>1</sup>, Dhruva R. Rinku,<sup>2</sup> I. Thamarai,<sup>3</sup> S. Meera,<sup>4</sup>  
Naresh Kumar Sripada,<sup>5</sup> and Simon Yishak <sup>6</sup>

<sup>1</sup>Department of Mechanical Engineering, College of Engineering, Prince Sattam Bin Abdulaziz University, Alkharj 16273, Saudi Arabia

<sup>2</sup>Department of Electronics and Communication Engineering, CVR College of Engineering, Hyderabad, Telangana 501510, India

<sup>3</sup>Department of Computer Science and Engineering, Panimalar Engineering College, Chennai City Campus, Chennai, Tamilnadu, India

<sup>4</sup>Department of Computer Science and Engineering, Agni College of Technology, Chennai 600130, Tamilnadu, India

<sup>5</sup>Department of Computer Science and Artificial Intelligence, SR University, Warangal, Telangana, India

<sup>6</sup>College of Engineering and Argo-Industrial Technology, Sawla Campus, Arba Minch University, Arba Minch, Ethiopia

Correspondence should be addressed to Mohamad Reda A. Refaai; drengrefaai@gmail.com and Simon Yishak; simon.yishak@amu.edu.et

Received 6 May 2022; Accepted 26 July 2022; Published 13 September 2022

Academic Editor: K. Raja

Copyright © 2022 Mohamad Reda A. Refaai et al. This is an open access article distributed under the Creative Commons Attribution License, which permits unrestricted use, distribution, and reproduction in any medium, provided the original work is properly cited.

During the recent decade, emerging technological and dramatic uses for drones were devised and accomplished, including rescue operations, monitoring, vehicle tracking, forest fire monitoring, and environmental monitoring, among others. Wildfires are one of the most significant environmental threats to wild areas and forest management. Traditional firefighting methods, which rely on ground operation inspections, have major limits and may threaten firefighters' lives. As a result, remote sensing techniques, particularly UAV-based remotely sensed techniques, are currently among the most sought-after wildfire-fighting approaches. Current improvements in drone technology have resulted in significant breakthroughs that allow drones to perform a wide range of more sophisticated jobs. Rescue operations and forest monitoring, for example, demand a large security camera, making the drone a perfect tool for executing intricate responsibilities. Meanwhile, growing movement of the deep learning techniques in computer vision offers an interesting perspective into the project's objective. They were used to identify forest fires in their beginning stages before they become out of control. This research describes a methodology for recognizing the presence of humans in a forest setting utilizing a deep learning framework and a human object detection method. The goal of identifying human presence in forestry areas is to prevent illicit forestry operations like illegal access into forbidden areas and illegal logging. In recent years, a lot of interest in automated wildfire identification utilizes UAV-based visual information and various deep learning techniques. This study focused on detecting wildfires at the beginning stages in forest and wilderness areas, utilizing deep learning-based computer vision algorithms that control and then mitigate massive damages to human life and forest management.

## 1. Introduction

An unmanned aerial vehicle (UAV), sometimes known as a drone, seems to be a flying device that may be controlled by a single operator or by autonomously operating onboard systems. Drones take on-demand images from a low-flying aircraft for a number of reasons, including emergency product delivery, border enforcement, accident rescues, and

visual surveillance for population protection. [1]. The prospect of market expansion for vision processing within drones or commercial aerial vehicles increases the overall number of automobiles. Furthermore, some governments [2] encourage current drone people to update their gear for improved computation. Recently, some countries' legal enforcement organizations established several recommendations for flying unmanned aerial vehicles (UAVs) in a

regulated manner ensuring they do not trespass on people's privacy. Drone flying restrictions in numerous countries' national legislation, urge that drones never fly over gatherings, but more restrictions specify the shortest variance a drone could come directly from a group [3]. The growing usage of unmanned aerial vehicles (UAVs) in numerous applications including visual surveillance, recovery, and entertaining is followed by a desire for security.

According to Goldman Sachs, the worldwide drone market will be worth \$100 billion in 2020. The paper also indicates that, given the change in legislation, the autonomous drone industry is poised for rapid expansion [2]. The majority of drone-enabled products depend on onboard providers provided with notable applications including detection, categorization, environmental control, transport networks, and aerial evaluations including relief efforts and construction evaluation. UAV-captured photos and their postprocessing are two primary areas of industrial aerial vehicle usage [4]. Aerial picture applications include landslide modeling, disaster response, biodiversity surveillance, and the impact of smart elevation models, including the use of cameras mounted for a variety of functions. Digital video normalization, navigation systems, and terrain evaluation are all made possible by the technologies that drive innovation in aerial technologies.

UAV-based advanced wildfire identification and advanced warnings incorporate multiple remote smart sensors [5]. Deep learning-based computer vision methods have appeared recently as viable wildfires monitoring devices as in Figure 1. Rather than sending maintenance crews into hazardous situations or employing various traditional methods which have many restrictions in terms of the cost and effectiveness, UAVs furnished with graphical remote sensing methods have been proposed as exciting and innovative technologies which might aid in wildfire tracking and suppression [6]. Integrating UAVs and deep learning systems might be highly effective for detecting wildfires in their initial stages and transmitting crucial information to the relevant authorities through efficient communications technology such as LoraWAN and 5G. Numerous deep learning-based fire and smoke detection algorithms have been suggested in recent years, with outstanding results.

The majority of established detection methods are centered on convolutional neural networks (CNNs), such as various iterations of R-CNN, YOLO and its variations, SSD, U-Net, and deep learning. Alternative deep learning designs, such as long short-term memory (LSTM), generative adversarial network (GAN), and deep belief network (DBN), could be utilized for fire detection (GAN) [7]. Nevertheless, to be implemented in real-time, these techniques necessitate advanced machines. As a result, current technological breakthroughs in processor power, sensor systems, and software application enable wildfire identification using UAV platforms utilizing strong deep learning-based computer vision techniques. UAVs could now identify, localize, and inform the appropriate authorities in a matter of seconds.

The study uses postflight information to provide fine-grained information, and everything from crop amount to water bodies could be accessible in a matter of seconds [8]. However, the cost-efficiency, excellent performance, and low

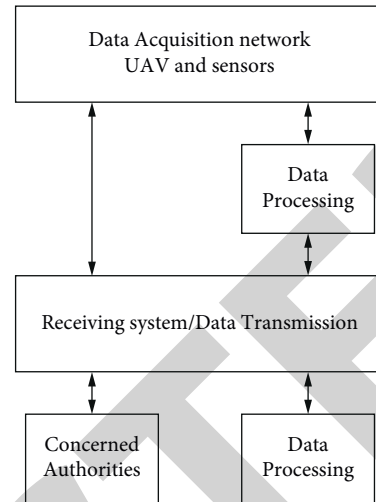


FIGURE 1: Flowchart of a UAV-based remote sensing system for detecting forest fires and notifying appropriate institutions.

power usage of autonomous drones made it easier to add effective complete visual abilities within UAVs. In a computing environment, the rapid expansion of aerial vehicle technologies has been well started. The most common technique in computer vision to locate or identify an object in an image would be to use bounding box coordinates to indicate its location. Deep learning and several detecting instances were used to detect objects in low-altitude UAV samples.

Object detection is a technique that identifies changeable objects in a given image and inserts a boundary over them to yield localization coordinates. As aerial vehicles produce stereo views from such a mounted camera to it, academics employed in the sector have been interested in object recognition in aerial photos [9]. Deep learning-based techniques for object detection are significantly enhancing the capacities of autonomous mobile systems. The paper's study is designed to provide a broad suggestion on the application of deep learning-based object detection algorithms, particularly on low-altitude aerial images. This should act as an archive with all current advances in deep learning-based object recognition on low-altitude samples and resource for academics and researchers to access for research concerns in this domain. A full-scale manual assessment of a huge forested area, on the other hand, is employment, inefficient, and momentous.

This research introduces a human object recognition method utilizing drone vision as just an efficient and appropriate forest monitoring technique that discovers the presence of a prohibited human entrance and protects unauthorized actions and operations in terms of reducing labor requirements and accelerating the process of forest monitoring [10]. Identifying that the idea of deep learning must have managed to gain a lot of attention owing to its favorable products in various areas of implementation, this paper focuses on developing a deep learning-based method that considers characteristics by optimizing a specific loss function, as opposed to the traditional machine learning

approach that retrieves characteristics from visual information. To give the most dependable strategies, depending on deep learning technologies and UAV technology, for battling wildfires in their early phases, until they develop unmanageability, the impact of new UAV-based visual remote sensing techniques and deep learning-based computer vision algorithms on firefighters by identifying wildfires in forests or bushland in their initial phases is shown [11]. Assisting researchers and firemen in determining which remote sensing techniques and algorithms to employ depends on the design of the shaded regions and the task at hand. We are discussing different UAV-based fire detection problems, such as changes in fire appearance and design, among many others. This research will explore deep learning algorithms which use visual data acquired by the drone and will permit the drone to recognize humans in a forest context. A series of human objects photographs are collected for data-gathering purposes using a 3DR Solo Quadcopter connected using GoPro Hero 4 in the Universiti Teknologi PETRONAS premises and the Ipoh vicinity [12].

Given the increasing popularity of deep learning, this research focuses on the development of a human object identification system employing a mix of deep learning and computer vision. In practise, the goals of this research are to develop a system for detecting human objects using drone vision for forest monitoring. This effort would be a fantastic addition to forest management and will aid in the development of drone technology.

## 2. Related Work

Due to the repeated emergence of forestry wildfires, mobile robots in rainforests are presently a very relevant topic. As a result, onsite monitoring of sustainable forest management and bioenergy is necessary. To report these issues, this paper offers research on the identification of forest tree branches at the ground surface in visual and thermal pictures utilizing deep learning-based object recognition systems. A forest database comprising 2895 pictures was created and publicly released for such a reason. To identify the tree trunks, five classifiers are trained and standardized using a sample YOLOv4, SSD Lite MobileDet, SSD Inception-v2, SSD MobileNetV2, and SSD ResNet50. The device chosen was Tiny. Impressive values were reached; for example, YOLOv4 Tiny has been the preferred product, with the greatest AP (90%) and F1 score (89%). For such systems, the inference duration on CPU and GPU was measured. According to the data, YOLOv4 Tiny is its quickest detector running on the GPU (8 ms). This research would contribute to the advancement of visual observation technologies for better forest robotics [13].

The current technique relies on an optical analysis of UAS images, with next to no computer-assisted rapid recognition. Deep learning has been seeing remarkable success in object recognition having fixed patterns, including people and automobiles because of large amounts of classification models and huge increases in processing power. Nevertheless, little can be accomplished with fluid and irregularly shaped items, including area explosions. Additional issues

occur when information is gathered by UAS as a high-resolution aerial photos or videos; an adequate resolution delivers good accuracy with low latency. This research, looked at 4K (3840 × 2160) recordings taken by the UAS from such a measured explosion and developed a collection of annotated video collections to also be made available to the community. It presents a coarse-to-fine architecture for autodetecting sparse, tiny, and slightly curved wildfires. The coarser detectors dynamically choose those subregions which are most probable to include the items of interest, but the fine detectors transmit just the specifics of a subregion for any further examination, instead of the whole 4K area. As a result, the suggested two-phase training reduces time expense while maintaining excellent accuracy. When compared to YoloV3's real-time object framework, the proposed solutions increased the mean average precision (mAP) from 0.28 to 0.68, having an overall interpretation velocity of 7.45 frames as per second. The design's constraints and future development are highlighted, as well as the experiment outcomes [14].

Detecting pedestrians from drone photos has several possible applications; including searching for possible suspects, tracking unauthorized immigrants, and tracking networks. But it is regarded as difficult computer vision task owing to fluctuations in the camera perspective, distance behind pedestrians, alterations in brightness and weather patterns, differences in image acquisition, and the presence of human-like items. Deep learning-based algorithms have recently gained popularity, so they have demonstrated significant performance in numerous object recognition issues such as the identification of features, breast tumors, and cars. Even so, the goal of this effort is to create deep learning-based techniques which would be used to solve the issue of pedestrian recognition using drone-based photos. Faster region-based convolutional neural networks (faster R-CNN) would be employed specially to explore the presence of a pedestrian within the collected drone-based photos. To analyze the effectiveness, some 1500 photographs were gathered by the S30W drones, and so these images were acquired in various locations, with varying perspectives and weather patterns, as well as during the light time and dark time. Faster R-CNN is able to produce a better outcome using precision (98%), recall (99%), and F1-measure (98%), according to the results. On the public information UAV123 database, the results of faster R-CNN were compared to those of the YOLO deep architecture. According to the data, two detection models had nearly identical results [15].

Deep learning frameworks available today, when trained with the appropriate dataset, could be utilized for object recognition in marine rescue missions. A database enabling maritime rescue operations is suggested in this study. It includes aerial-drone images containing 40,000 hand-annotated people and items drifting in the ocean, some of which are microscopic or hard to identify. The second analysis is the suggested strategy for detecting objects. It is an array of deep convolutional neural networks managed by signal transmitting with nonlinearly tuned polling parameters. The approach, which is based mostly on unique aerial-drone flying object collection, achieves roughly 82 percent

point accuracy and outperforms all state-of-the-art deep learning algorithms, including v4, faster R-CNN, SSD300, YOLOv3, and RetinaNet. The database is open to the public over the Internet [16].

Unmanned aerial vehicles (UAVs) have quickly become an indispensable device for assessing the position and existing forest environments. This was especially essential in Japan because of the absolute length and diversity of a forest region, which is primarily made up of naturally diverse broadleaf forest areas. Furthermore, deep learning (DL) is gaining popularity for forestry applications since it enables the incorporation of expert human knowledge into the autonomous image processing pipelines. This article investigates quantitative problems about using DL through own UAV-acquired images throughout forest implementations, including an impact of the transfer learning (TL) and also the deep learning structures selected, as well as if either a simple patch-based structure can generate effectively in a variety of complex applications. Two distinct deep learning systems, and two in-house databases, but a focus on two distinct issue formalizations, are utilized. The findings indicate that transfer learning is required to achieve a decent result in the challenge of MLP categorization of the seasonal versus evergreen forest within the winter orthomosaic database. When transfer learning was executed on a database that is more similar to the sort of photos, we see an additional 2.7% enhancement. Lastly, in a separate and more complex example, we illustrate the usability of a patch-based approach only with ResNet50 design: the intrusive broadleaf deciduous dark locust was discovered in everlasting coniferous dark pine coastline woodland characteristic [17].

### 3. Materials and Methods

**3.1. Deep Learning-Based Object Detection Method.** Aerial imaging using UAVs is employed for a variety of reasons, including entertainment, recognition and identification investigations, environmental monitoring, and other interesting ones. Unlike aircraft, UAVs are now accessible to end consumers searching for aerial imaging equipment on a tight budget. The improved methodologies of deep learning-based object detection get a promising future. Several advancements in object identification techniques in lower elevation UAVs were observed in recent years between deep learning-based sensors [18]. Among the most difficult issues in an image collection from drones is perspective variation because the dataset distributions include photos taken from such a top view perspective, whereas other images may be acquired from such a lower context involved. The characteristics learned from objects from various viewpoints are not transferrable. As a result, strong detectors must be used to identify aerial-based items. Figure 2 shows deep learning-based object detection techniques.

The mask region-based convolutional neural network, faster region-based convolutional neural network, feature pyramid network, region-based fully convolutional network, and cascade region-based convolutional neural network are examples of two-stage sensors, while You Only Look Once, RetinaNet, RefineDet, and single-shot detector are examples

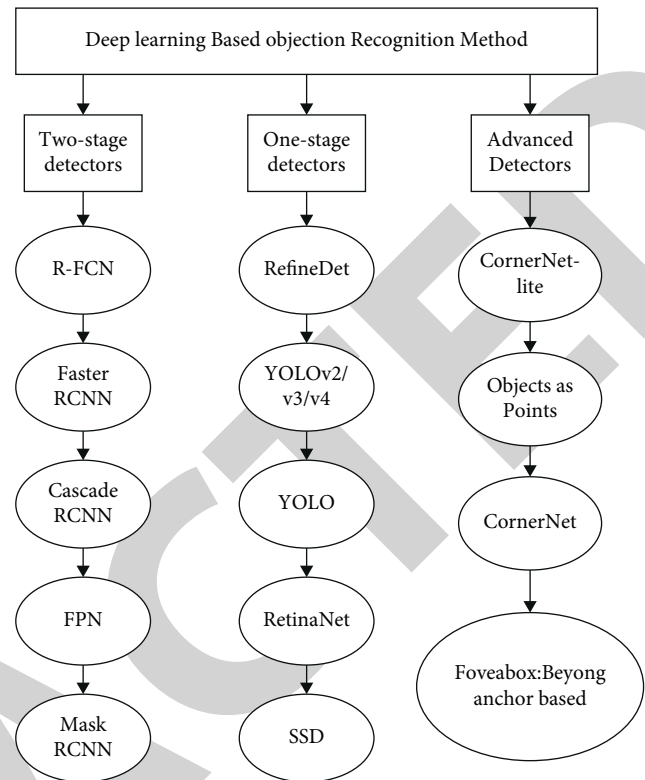


FIGURE 2: Deep learning-based object detection techniques.

of one-stage detection systems. Recent improvements in object recognition, which are also highly popular with aerial user information, including CornerNet, Entities as lines, and Foveabox, also were mentioned [19]. It also includes a brief discussion of every deep learning-based detector, the classification of something that belongs, the network nodes, loss descriptions, input quantities, and GitHub code branches. The error function component includes categorization and localized loss for each detector. The total objective error function is just a weighted combination of a localization loss as well as the categorization losses, where localization failure seems to be an overall mismatch among the prediction boundary box and also the ground truth container, and classification failure seems to be the destruction in labeling predicted containers with different classifiers. Furthermore, smooth L1 loss is a mixture of L1 and L2 losses that is inefficient for object recognition positioning.

**3.2. Vision-Based Remote Sensing Techniques.** Visual information using UAV-based remote sensing techniques is invaluable to those managing devastating wildfires. This knowledge could be used to preserve lives and forest products. It might thus be being used to prevent the weather spread by detecting the most potential vulnerabilities [20]. Furthermore, rescue activities might be carried out to assist trapped people in the middle of forests and to preserve wildlife while maintaining firemen's safety. To this end, several research studies have focused on early fire monitoring in forest areas and forests using visual information acquired by various platforms outfitted with various kinds of

cameras and visual sensors. To automatically identify forest and wilderness environments, three basic remote sensing-based techniques are used. Satellites have been the most widely utilized remote sensing tool in several forestry activities.

Several researches have used satellite images to identify fires and fire ash in forest environments, which may aid in reducing their hazards. Satellite-based photos, on the other hand, are not the greatest approach for early forest fire detection due to their limited spatial and temporal resolution, which makes detecting small fire spots exceedingly difficult in most circumstances. Another key issue that limits forest surveillance efficacy is the satellite's temporal precision, as they are not always accessible to offer thorough information well about forest conditions. Furthermore, overcast and severe weather circumstances make it difficult for satellites to obtain valid information on the dense area.

Other options for monitoring forest fires include advanced high-resolution camera systems put on the surface. Terrain early wildfire detecting programs depend primarily on electro-optic cameras positioned on watchtowers. Many academics and authorities used these technologies to detect forest fires [21]. Terrestrial approaches frequently integrate visual sensors with several other kinds of detectors, including moisture, smoking, and temperature monitoring, to increase fire/smoke identification effectiveness. These sensors may operate well in confined locations such as buildings; however, they struggle in open areas such as forests since they require closeness to a fire or smoke. Furthermore, they are unable to supply some critical information, including the magnitude and position of the fire.

Similarly, on-the-ground cameras, especially those installed on watchtowers, may only affect a small area and must be properly placed to assure optimal visibility. As a result, there is a need to install big multiple sensors that fill the entire nature reserve, which will be highly expensive. Unmanned aerial vehicle (UAV) platforms have evolved as novel and efficient techniques that combine the benefits of satellites and on-ground equipment. They can cover more ground than grounded approaches and offer photos with greater spatial and temporal precision than satellites. Furthermore, their operating costs are substantially lower than those of satellite and terrestrial systems [22]. As a result, UAVs outfitted with appropriate remote sensing technology are also regarded as the finest option for detecting wildfire disasters. UAVs collect vital knowledge on the condition of the environment using several different sensors. Correctly using information could assist UAVs in identifying fire regions and notifying the appropriate officials only at the right moment, allowing for a decrease in wildfire damages and dangers. The goal of this section is to show the most often utilized cameras during forest fire identification, tracking, and defense.

*3.3. Testing and Training Dataset.* When compared to traditional surveillance technology, drones can cover a larger surveillance region. As a result, it might be more efficient than the conventional technologies installed in the

helicopters or a satellite. This development collects image data at the Universiti Teknologi PETRONAS premises and the Ipoh woodland region using a 3DR Solo Drone paired using a GoPro camera. The video information is retrieved into frames and classified into two distinct classes of reference images for deep networks testing and training objectives [23]. Training and testing datasets were gathered in the video file that is subsequently analyzed and translated into a deep network-readable format for classifying training and evaluation. The preprocessing of image information flow is depicted in Figure 3.

*3.4. Proposed Methodology.* Given the increasing prevalence and capabilities of deep learning methods in computer vision, deep learning is projected to outperform classic feature-descriptor techniques dramatically. Given the superior effectiveness of deep learning over standard feature-based approaches, the suggested strategy employs a deep learning way to study information through training a deep neural network. The construction tool in this research was Keras on the TensorFlow backend. The suggested technique, specifically, uses MobileNet as a deep neural network structure and the Single Shot Detector (SSD) also as object detection models [24]. The MobileNet network, as the term suggests, is intended for usage in smartphone platforms and thus is Tensor Flow's initial portable computer vision framework.

MobileNet seems to be a CNN class that Google has open-source, providing us with a suitable platform for training their customized classifiers which are incredibly small and insanely rapid. The primary distinction between MobileNet structure and typical CNN design is rather than just a single  $3 \times 3$  convolution layer accompanied by batch normalization and ReLU. As illustrated in Figure 4, MobileNets divided a convolution into  $3 \times 3$  depthwise convolutional and a  $1 \times 1$  pointwise convolutional.

Several data-collecting activities were carried out utilizing the GoPro Hero 4 sensor placed on a drone to acquire visual information both for training and testing purposes. The data-gathering operations were placed on the campus of Universiti Teknologi PETRONAS (UTP) and in the Ipoh forest region [25]. This study concentrates on recognizing two specific item classes in the forest region: humans and the wood-cutting vehicles. For the human category, including female and male images, bodies and appearances orientated in different directions, close and far humans images, are collected for training. For wood-cutting truck training, various categories, dimensions, and standards of the wood-cutting vehicle were assembled.

A drone and remote management systems terminals are part of planning deep learning-based techniques for the forest fire surveillance system. The planned forest fire disaster for monitoring organization incorporates a drone platform into the forest fire protection mechanism that is capable of delivering early warnings through the use of video-based fire sensing technologies. The suggested forest fire surveillance system depending on deep learning and drone technology has a multistep workflow [26]. First, a drone is outfitted using high-definition cameras, and it



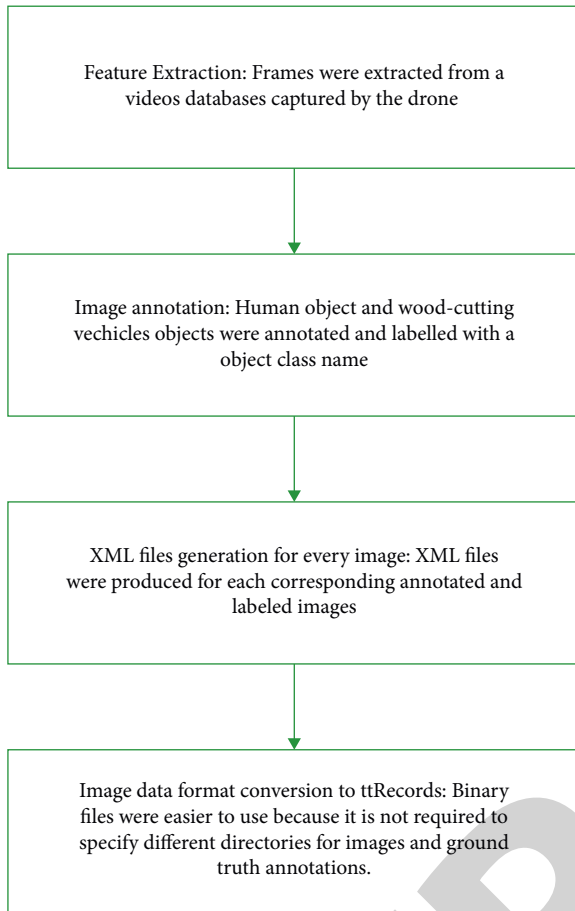


FIGURE 3: Preprocessing of image information flow.

undertakes flight activities following the preprogrammed patrol path to guarantee that it covers the entire region under surveillance with no blind spots. The Global Positioning System (GPS) determines the location of the drones in real-time. Secondly, the drone communicates a recorded video and picture data in the real-time to a surface remote monitoring program. Third, its surveillance system analyzes the gathered information and determines whether there seems to be a fire hazard in the region under surveillance using the forest fire deep learning-based methodology. Whenever a fire incident happens, the system raises an alarm, as well as a receiver, and uses real data about the forest fire via the interfaces also on a surveillance computer system [27]. This data are then transmitted to the appropriate person, who will take the necessary fire prevention steps. Figure 5 depicts the flow diagram of a proposed technology.

**3.5. Computer Vision Algorithm for Forest Fire Detection.** Unmanned aerial vehicles (UAVs) are recently developed more general in forestry activities such as forest surveying, search and rescue activities, forest resource assessment, and forest fire suppression. They might be one of the greatest effective novel instruments for addressing such issues. As a result, the choosing of UAV systems over other present technology is based on multiple factors such as minimal price, stretchability, operating at various altitudes, and

simplicity of handling [28]. Furthermore, thanks to recent improvements in hardware and software systems, massive and complicated image features can be processed on the UAV itself. In recent times, there has been a lot of interest in detecting fires and smoke in wild lands and forests utilizing deep learning-based computer vision algorithms.

Flames and ash are two key visual cues that might assist UAVs in autonomously identifying wildfire origins using deep learning techniques. Flame and smoke are the most significant visual elements for detecting wildfires early and precisely. Some studies have concentrated on the detection of fires using flames. Other research has focused on smoke detection, which appears to be more important for early identification because fire through its early stages can be masked, especially in deep forests. Many recent investigations have concentrated on sensing both flames and fog at about the same period to avoid some restrictions when just one element is targeted. Early wildfire detection utilizing UAVs and deep learning techniques might be accomplished in 3 stages: wildfires image classifications, object detection-based wildfire identification, and semantic segmentation-based wildfire identification. However, these strategies necessitate a big volume of data as well as a high level of processing capacity throughout the training phase. Also, the suitable structure must be carefully selected, as well as how it can be trained with the appropriate data.

**3.6. Remote Monitoring System.** The remote surveillance system receives, processes, and stores the data collected by the drone. Furthermore, the center of the grounds includes deep learning-based detection and alert activation capabilities [29]. At the ground monitoring console, the employees can view the acquired forest photos in real-time. The ground center gives real-time dynamic features whenever a fire incident happens. The equipment of the base center contains a personal computer (PC) and communications unit collecting photos and another information, including drone position information.

**3.7. Image Acquisition System.** A video adapter transmits the signal from a video sequence to a picture acquisition device. The signal is converted to A/D before being decoded by a digital decoder. The resulting signal is reduced into video content and sent to the computer. Before collecting the next picture frame, the structure grabber constantly takes image frames from a video sequence and transmits them to a PC [30]. As a result, the time essential to produce a picture frame has a significant impact on real-time capture. Specifically, the time necessary to analyze a frame significantly increases the period among two subsequent frames, and an image information would be destroyed, resulting in a frame damage phenomenon. The image acquisition device's video collection and reduction processes are conducted simultaneously.

**3.8. The Control Scheme of UAV.** The drone control organizations were utilized that manage the flight of a drone and provide flying details reaction from a drone, which includes

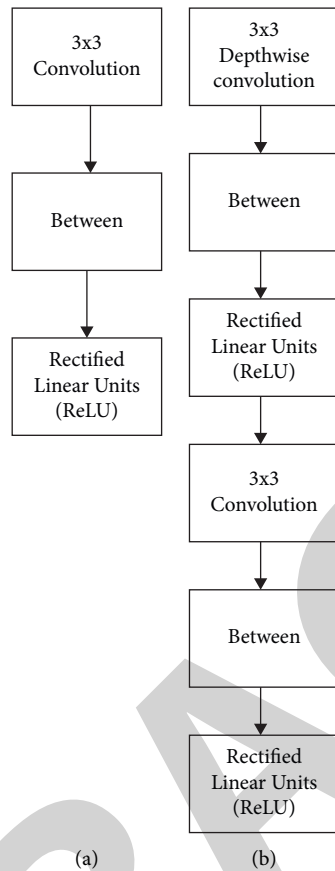


FIGURE 4: Convolutional layer standards using ReLU and batch normalization.

data from path development unit, GPS component, and a flight communication unit.

**3.9. Communication System and Data Processing.** To send information and transfer acquired forest photos, data processing and communication technology are used. Furthermore, this technology is in charge of managing the gathered data, which includes fault statistics, information about fire events and disasters, drone flying conditions, and user login data [31]. The image acquisitions and communication systems were primarily made up of a data acquisition system and also the data transmission component, which was in charge of delivering the acquired image information to a remote surveillance terminal and offering an advanced detection of a fire. Figure 6 depicts the flowchart of image acquisition and transmission operation.

The interaction in the present scheme allows for both sending and receiving data. These data cover a variety of information gathered by several components of a forest monitoring scheme [32]. This is primarily concerned with the information interaction among the drone and distant surveillance scheme. The picture data acquired mostly by the UAV is transferred in real-time towards the base monitoring terminals, and the ground port controls the movement of a UAV based on the flight route established by a UAV. Figure 7 depicts the full data exchange process among several units.

**3.10. Upper Computer Organization Remote System.** Image transmission and analysis, as well as threat disaster warnings, are features of the remote host monitoring control system. The image transmission and control techniques gather aerial photographs of forests captured by the PTZ camera sensor coupled to such a drone. The video information is then delivered on a real-time basis to a PC here on the collector terminal of the forest surveillance system through the image transmission network. This system is already in charge of identifying a forest movement in image information utilizing a deep-learning-based method [33]. This video recording and communication feature is dependent on a PTZ camera sensor, an image recording device TC – 4000 SD, and an image transmission network. Using an image transmission network, a picture acquired by a camera attached to such a drone is transferred to the mobile node of remote drone management. The image is subsequently transported to the image acquisition cards using an HDMI cable and then from the base monitoring system through a USB PC.

DJI's Lightbridge2 image transmission technology is used in the planned forest surveillance system. The Lightbridge2 image transmission technology has multiple interface outputs, namely, 3G-SDI, USB, and mini-HDMI. Furthermore, it offers high-definition output at up to 1,080 p/60 fps.



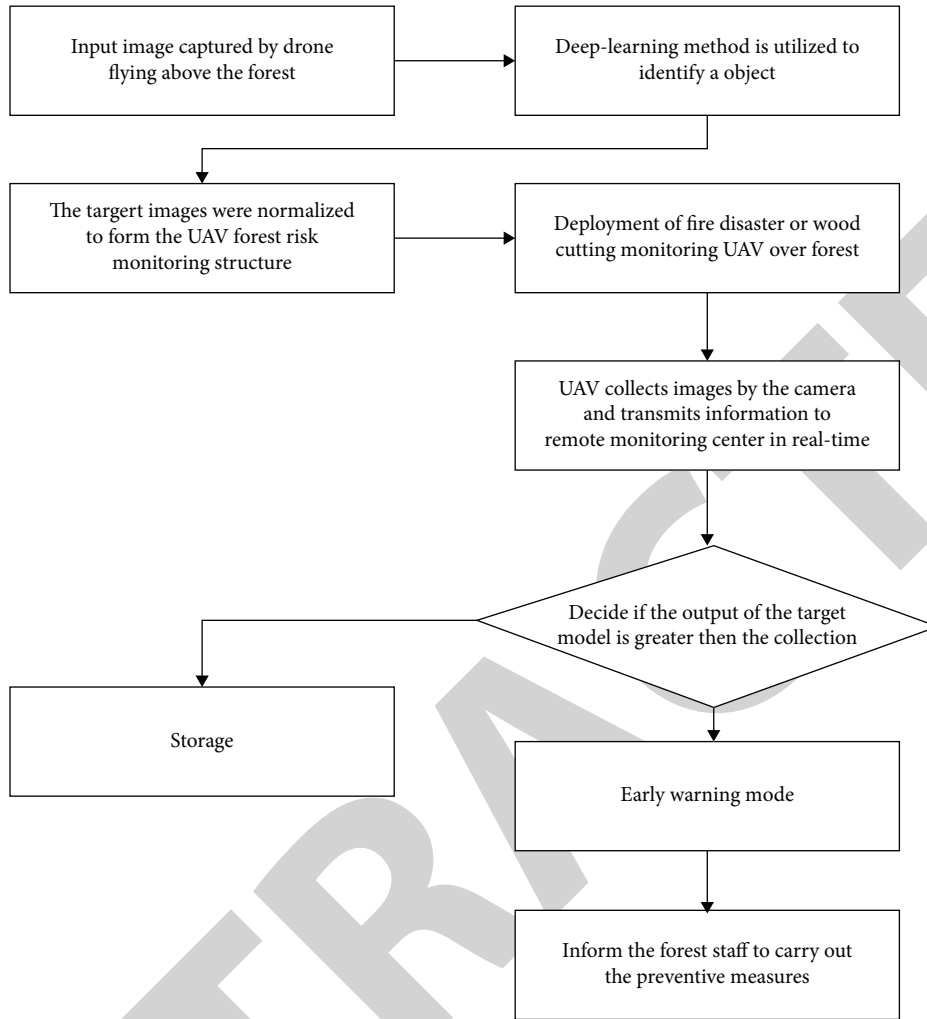


FIGURE 5: Deep learning-based monitoring scheme flowchart.

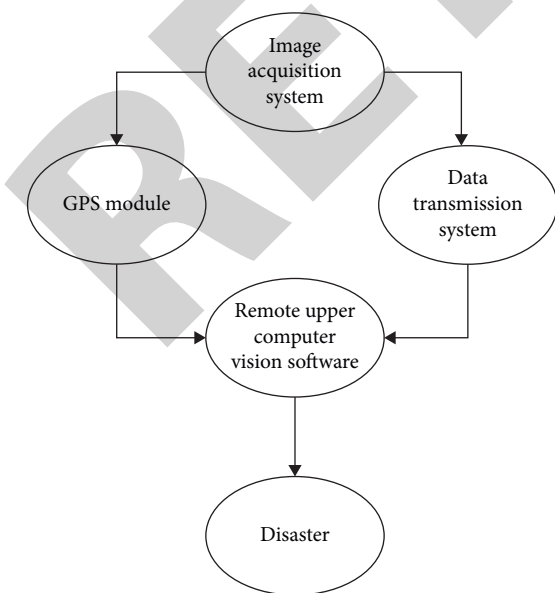


FIGURE 6: Transmission procedure and image acquisition structure.

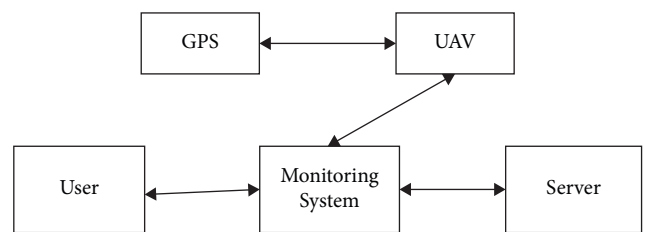


FIGURE 7: The interactions of the planned forest surveillance system's various components.

To accommodate for the impacts of length, environment electromagnetic waves, and image quality, the Lightbridge2 video transmission method utilizes dynamic wireless-link adaptability technologies. In the event of a channel interruption, it instantly finds the optimal channel and alternates between broadcast streams. Furthermore, it changes the video frequency as needed to provide smooth transmission and significantly lowers picture flaws and disruptions. When the greatest communication range is 5km, its image latency is further limited to 50ms utilizing the deep learning-based

technique. The Lightbridge2 image communication method integrates high-speed processing and deep-learning-based procedures to improve a stability and reliability of the picture transmission across wireless networks [34]. The distant upper-computer management network components comprise the forest basic information component, the image processing, and the warning control unit, as well as the manual data processing component. The basic information component provides a collection of state-owned planting in the Guangdong region, as well as connections to prefecture-level forest bureaus. This interface makes it easy for forest employees to find crucial forest farming data. It is necessary to detect the regional forestry agency which corresponds to a specific forest farm using the forest department's gateway web pages, and it maintains its staff up to date just on the regional forest agency's advancements.

It also features a map interaction of different forests that provide the geographical position of the landscape scale, including location and longitude, and latitude. This aids in the deploying of such a drone for such forest risk surveillance systems. In the forest, its image processing employs the concept of fire events [35]. In the event of a fire disaster, the system will display the geographical position and immediately warn the forest farm employees. For disaster alerts, the light is red, while for regular situations, it is green. When it is essential to physically analyze images, the manual operation interface is used. Furthermore, there is also an image managing interface which is utilized to the store images of the forest fire protection and show the images from the image collection based also on the user's requirement. It also gives forest personnel access to previous imaging data.

## 4. Results and Discussion

**4.1. Classification of the Object.** GoogleNet network and MobileNet network are generated on a customized training sample in Caffe and TensorFlow deep learning frameworks, accordingly, for image classification development. The Caffe system's accuracy chart for the GoogleNet network is across 30 epochs. This result is created by an image classification algorithm that has been trained on both the human and the wood-cutting machine classes. At 30 epochs, this output structure had an average accuracy as 97.3215% and failure rate as 0.0787. Figure 8 shows the resulting curve of the accuracy of a MobileNet network for one epoch on the TensorFlow architecture. The picture classification method produced the outcome following training that both person class and the wood-cutting equipment class. At 1 epoch, its output models had an average accuracy of 66%.

**4.2. Detection of Object.** On a maximum of 60 multiple images gathered from such a drone, deep learning-based object categorization and identification system were verified. The identification results reveal that the method efficiently localizes both the humans and the wood-cutting equipment as in multiple images and draws a bounding box from around the discovered object. The detection findings were tested on photos obtained with a drone. The discovered

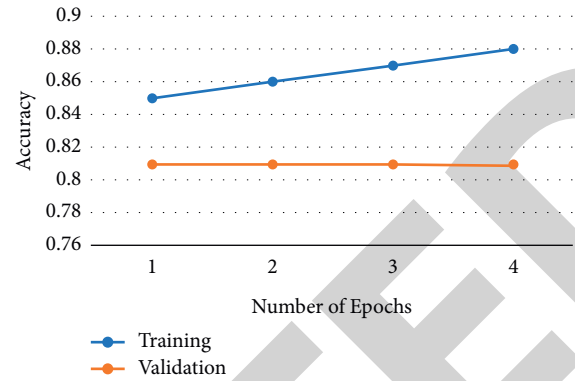


FIGURE 8: On the TensorFlow structure, an output curve demonstrating the accuracy of the MobileNet network for one epoch is shown.

targeted item class is surrounded by a bounding box. The class label is shown well directly above a structuring element, only using option of predicting a class label.

Images taken from its website are used to assess the detection methods on both sides. The purpose of testing using images from Internet research is to examine images that show various deforestation scenarios, such as one in which a piece of logging equipment is used inside a forest and another in which a worker is shown incorrectly falling trees. A bounding area surrounds the found targeted item class. The class label is shown above the surrounding container, along with the probable class label predictions.

**4.3. Hardware System Function.** The hardware functional assessment of a deep learning and drone-based forest and disaster surveillance system was carried out by repetitive troubleshooting for hardware functional and a long-term operating test of the overall system. The major purpose was to see if the drone process operates regularly and if the complete system organization level for reliable for an extended period.

**4.4. Software System Function.** The suggested drone forest fire hazard surveillance system's deep learning-based software evaluations included dependability and real-time assessment. Various functionalities were used for testing, including the user login function, the unusual alert function, the historical abnormality tracing function, and the equipment failure alert feature. The forest hazard monitoring individual's dependability and real-time performances were tested by logging numerous segments of a camera with flames and interfering recordings, including video of automobile lights or persons and items with such a highest correlation index to burns. The system detected and identified these films and assessed if the prediction accuracy, probability of false warning, and statistical surveillance processing time satisfied the acceptance criteria.

Furthermore, the login form feature was tested by repeatedly entering correct and erroneous encrypted passwords to confirm that such software could log in

TABLE 1: Various techniques processing a novel information.

Techniques	Speed (frames//sec)	Time	Latency
Original video	28	4 minutes 18 secs	0
Background subtraction	6.85	18 minutes 17 secs	76.42%
Interframe difference techniques	7.14	17 minutes 36 secs	75.46%
Deep learning-based method	5.84	21 minutes 29 secs	80%

successfully. To verify whether an alarm is activated appropriately, it was examined whether false fire identification would result in the alarm being activated. To confirm the accuracy of the available data, it is examined whether such client can acquire an effect of unusual historic occurrences and relevant data via the program. The technique utilized for device failure rapid testing phase has been to purposely alter the regular operations of a state's hardware and then check to see if the device fault warning happened.

**4.5. Communication System Function.** The data connection among the sensors at varied distances has been used to evaluate the communication capability of the forest hazard surveillance system depending on a drone. The communications among a UAV and remote server, as well as communications among the UAV as well as a remote regulator, were all acceptable.

**4.6. Speed of Data Processing.** A video having duration of 4 minutes and 19 seconds was evaluated. There were 29 photos per second and 7,511 images in total. Each frame is  $960 \times 540$  pixels in size. The techniques' timings to finish the required procedures were estimated. The methods' computational time and latency rate were evaluated, and results are shown in Table 1.

Whenever an algorithm analyzes content effectively, the processing rate can be slowed. The video sequence collecting technique must minimize the multiple frames during preprocessing to enable real-time data analysis. The variation in scene data captured by a video was restricted whenever the flying velocity of a UAV is steady. The interframe divergence technique and background subtraction technique may be utilized to accelerate the procedure whenever a video frame is adjusted to five times per second. The deep learning-based approach and divisional processing speed outperformed the real-world information processing needs. Given similar circumstances, the deep learning-based method met the computation time and accuracy standards.

**4.7. Accuracy of Data Processing.** Table 2 compares the deep learning-based approach to the interframe difference technique and background subtraction technique. The results in Table 2 reveal that physically outlining the pyrotechnic region yielded more precise experimental data. The results reveal that the improved modified algorithm outperformed the other methods. The outcome of the deep learning-based technique is nearer to the outcome of the human analysis in

this research study. With respect to the recognition rate, this demonstrated that the deep learning-based system outperformed the other techniques. The algorithm analyzed the statistical findings of comparative selection accuracy when coupled only with experimental data of deleting suspicious fire regions, and the choice average accuracy has been further enhanced.

Furthermore, the assessment of a generic identification method and a deep learning-based approach revealed the interframe variation. The method is unsuitable for the UAV video identification and effortlessly influenced by ambient and motion circumstances, resulting in poor detection performance. The detection performance has been almost nonexistent. The evaluation of a related subtraction technique and the deep learning-based method revealed that the processed outcomes of the approach differed substantially whenever the UAV was traveling and hanging. The suggested methodology had greater relative assessment accuracy when compared to the other four techniques. The suggested method outperformed the other methods in terms of performance; hence, it may be deemed appropriate for detecting forest risk.

**4.8. Recall, F-Score, and Precision.** This study specifically concentrates on two objects of interest: humans and wood-cutting vehicles. The testing findings are classified as true positive ( $t_p$ ), false positive ( $f_p$ ), or false negative ( $f_n$ ), which are described as follows:

True positive ( $T_p$ ): an object of interest has been discovered and identified appropriately

False positive ( $F_p$ ): a nonobject of value was identified as object of interest, or even object class was identified and classified incorrectly

False negative ( $F_n$ ): an object of interest was neither identified nor tagged

F-score is a statistical approach that accounts for all precision and recall when analyzing the effectiveness of an object detection technique. The value of the F-score is greatest when it is one and lowest when it is zero. As indicated in (1), the F-measure was regarded as a weighted sum of the recall and precision.

$$F - score = 2^* \frac{(T_p/T_p + F_p) \cdot (T_p/T_p + F_n)}{(T_p/T_p + F_p) + (T_p/T_p + F_n)}. \quad (1)$$

The findings are calculated and presented in Table 3 and Figure 9 depending on an obtained precision, recall, and F-measure values for such as 60 assessments.

TABLE 2: The comparison between various pyrotechnic detection methods' identification results.

	Pyrotechnic number of pixel areas	Number of pixel results	Number of similar pixels	Number of miscalculation pixels	Accuracy of judging	Relative accuracy
Interframe difference techniques	184	6,584	118	6,186	4%	46%
Background subtraction	215	2,337	309	1,051	9%	54%
Deep learning-based methods	328	2,908	2,126	2,387	10%	82%
Manual statistics	407	407	0	0	1	1

TABLE 3: Average results of performance measures.

Recall, F-measure, and precision results	
Recall	0.7738
F-measure	0.7305
Precision	0.7775

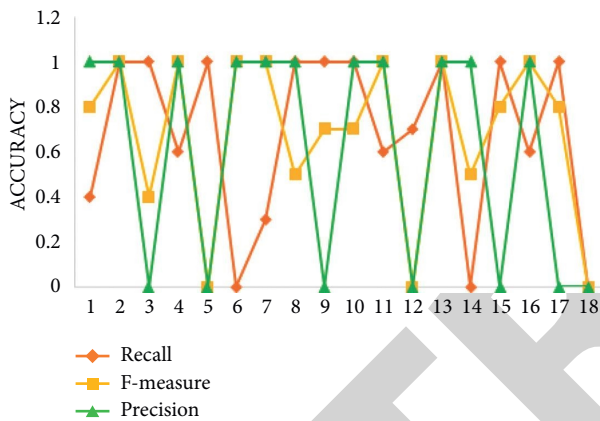


FIGURE 9: Recall, F-measure, and precision graph.

## 5. Conclusion

Forest fires are also seen in the intruding photos taken by a remotely controlled drone, through the object detection method. Such a UAV and image capture system, as well as the related software, make up a forest fire-risk surveillance system. It has been established via comprehensive testing of the proposed state's software and hardware that each module's functionality and the efficient communication between its sections. It is recommended that the method, which combines an object recognition method with a drone movement that is completely automated, is based on smart communication graphics processing unit (GPU) architecture. The nearby regions of the drone could be studied in real-time by building an object identification procedure on such a GPU that is placed upon the drone.

## Data Availability

The data used to support the findings of this study are included within the article. Further data or information are available from the corresponding author upon request.

## Conflicts of Interest

The authors declare that there are no conflicts of interest regarding the publication of this paper.

## Acknowledgments

The authors appreciate the support from Arba Minch University, Ethiopia, for the research and preparation of the manuscript. The authors thank Prince Sattam bin Abdulaziz University, CVR College of Engineering, Agni College of Technology, and SR University for providing assistance to this work.

## References

- [1] L. Inzerillo, F. Acuto, G. Di Mino, and M. Z. Uddin, "Super-resolution images methodology applied to UAV datasets to road pavement monitoring," *Drones*, vol. 6, no. 7, p. 171, 2022.
- [2] D. Turner, A. Lucieer, and S. de Jong, "Time series analysis of landslide dynamics using an unmanned aerial vehicle (UAV)," *Remote Sensing*, vol. 7, no. 2, pp. 1736–1757, 2015.
- [3] G. Pajares, "Overview and current status of remote sensing applications based on unmanned aerial vehicles (UAVs)," *Photogrammetric Engineering & Remote Sensing*, vol. 81, no. 4, pp. 281–330, 2015.
- [4] M. Mozaffari, W. Saad, M. Bennis, and M. Debbah, "Mobile unmanned aerial vehicles (UAVs) for energy-efficient internet of things communications," *IEEE Transactions on Wireless Communications*, vol. 16, no. 11, pp. 7574–7589, 2017.
- [5] H. Pan, D. Badawi, and A. E. Cetin, "Computationally efficient wildfire detection method using a deep convolutional network pruned via fourier analysis," *Sensors*, vol. 20, no. 10, p. 2891, 2020.
- [6] C. Yuan, Y. Zhang, and Z. Liu, "A survey on technologies for automatic forest fire monitoring, detection, and fighting using unmanned aerial vehicles and remote sensing techniques," *Can. J. For. Res.* vol. 45, no. 7, pp. 783–792, 2015.
- [7] L. Meng, Z. Peng, J. Zhou et al., "Real-time detection of ground objects based on unmanned aerial vehicle remote sensing with deep learning: application in excavator detection for pipeline safety," *Remote Sensing*, vol. 12, no. 1, p. 182, 2020.
- [8] R. Eskandari, M. Mahdianpari, F. Mohammadimanesh, B. Salehi, B. Brisco, and S. Homayouni, "Meta-analysis of unmanned aerial vehicle (UAV) imagery for agro-environmental monitoring using machine learning and statistical models," *Remote Sensing*, vol. 12, no. 21, p. 3511, 2020.
- [9] I. V. Saetchnikov, E. A. Tcherniavskaia, and V. V. Skakun, "Object detection for unmanned aerial vehicle camera via

## *Retraction*

# **Retracted: Preparation of Graphene Nanosilver Composites for 3D Printing Technology**

### **Advances in Materials Science and Engineering**

Received 26 December 2023; Accepted 26 December 2023; Published 29 December 2023

Copyright © 2023 Advances in Materials Science and Engineering. This is an open access article distributed under the Creative Commons Attribution License, which permits unrestricted use, distribution, and reproduction in any medium, provided the original work is properly cited.

This article has been retracted by Hindawi, as publisher, following an investigation undertaken by the publisher [1]. This investigation has uncovered evidence of systematic manipulation of the publication and peer-review process. We cannot, therefore, vouch for the reliability or integrity of this article.

Please note that this notice is intended solely to alert readers that the peer-review process of this article has been compromised.

Wiley and Hindawi regret that the usual quality checks did not identify these issues before publication and have since put additional measures in place to safeguard research integrity.

We wish to credit our Research Integrity and Research Publishing teams and anonymous and named external researchers and research integrity experts for contributing to this investigation.


The corresponding author, as the representative of all authors, has been given the opportunity to register their agreement or disagreement to this retraction. We have kept a record of any response received.

### **References**

- [1] X. Liang and H. Ji, "Preparation of Graphene Nanosilver Composites for 3D Printing Technology," *Advances in Materials Science and Engineering*, vol. 2022, Article ID 2086250, 11 pages, 2022.

## Research Article

# Preparation of Graphene Nanosilver Composites for 3D Printing Technology

**Xiujuan Liang and Haixu Ji** 

*School of Mechanical and Power Engineering, Guangdong Ocean University, Zhanjiang 524008, Guangdong, China*

Correspondence should be addressed to Haixu Ji; [jihx@gdou.edu.cn](mailto:jihx@gdou.edu.cn)

Received 22 June 2022; Revised 13 July 2022; Accepted 1 August 2022; Published 13 September 2022

Academic Editor: K. Raja

Copyright © 2022 Xiujuan Liang and Haixu Ji. This is an open access article distributed under the Creative Commons Attribution License, which permits unrestricted use, distribution, and reproduction in any medium, provided the original work is properly cited.

At present, graphene in two-dimensional carbon nanomaterials is a material with excellent properties. Its preparation technology and application prospects are very wide. The most common one is the chemical redox method, which can make graphite into graphite oxide dispersed in water. Graphene oxide obtained by the Hummers method has a wrinkled structure. In order to broaden the application field of graphene and give full play to its excellent properties, the current research on graphene mainly focuses on the preparation and application of functional composite materials as a matrix material or reinforcement material. Due to its special two-dimensional structure, it has a large specific surface area, good biocompatibility, and stable physical and chemical properties, making it an excellent nanoparticle carrier. The graphene-supported silver nanoparticles can effectively prevent the aggregation and stacking between particles, improve the electrochemical performance of the composite material, and expand its application range. In this article, the assisted preparation of graphene nanosilver composites by 3D printing technology (three-dimensional printing) was studied. 3D printing technology is a rapid prototyping technology that emerged in the 1980s. 3D printing technology is based on discrete stacking and realizes rapid processing of models by directly outputting data from the printing device. In this article, a new type of graphene oxide (GO) was prepared by the modified Hummers method. In the case of NaOH aqueous solution as a catalyst, silver nitrate and GO were used as precursors, and XRD, infrared spectrum, Raman spectrum, and other methods were used. The crystal structure and morphology of Ag/rGO under different conditions were studied, thus revealing the growth of silver particles and the changes of oxidized functional groups under different conditions. It was found that the intensity of the two peaks in the GNs-Ag-2 Raman spectral curve was seven times that of the GNs peak.

## 1. Introduction

With the development of industry, the continuous progress of science and human technology, the energy crisis, and environmental pollution have become the problems that people pay more and more attention to. With the emergence of problems such as energy crisis and environmental pollution, people have higher and higher requirements for improving production efficiency and protecting the environment. Most chemical production processes take place in various reactors. The development of structured reactors, catalysts, and adsorbents can effectively improve the reaction activity, increase the heat and mass transfer capacity, and reduce pressure loss. 3D printing is an intelligent production technology based on the Internet of Things, which has

developed rapidly in various industries in recent years. Compared with the traditional process, the 3D printing process has the advantages of digitization of the forming process, short product cycle, and many types of materials available. It is especially suitable for the design, development, and management of new products, which is a hot topic in the field of rapid prototyping in recent years. 3D printing technology has developed rapidly, and its applications include rapid prototyping, prototyping, micro-electromechanical manufacturing, and biomedicine. One or more layers of graphene were prepared by separating graphite flakes by the liquid phase method [1]. Nanosilver has important application prospects in the fields of catalysis, optics, surface enhancement, and bacteriostasis. Graphene is widely used in energy storage materials due to its unique electronic



energy band structure endowed with excellent electrical properties. Ag nanoparticles are loaded on its surface, which can improve the electrochemical performance and expand the range of composite materials.

At present, the development of graphene nanosilver composites has become an important topic in the field of graphene-inorganic nanocomposites. Zhi used hydrazine hydrate as a reducing agent, PVP as a dispersant, graphene oxide and silver nitrate as precursors, and prepared nanosilver/graphene composite powder by chemical reduction method under the conditions of reaction temperature of 60 °C and pH value of 6. The effect of silver nitrate concentration in solution on the morphology and structure of nanosilver/graphene composite powder was studied by SEM, XRD, IR, and RAMAN. The results showed that the silver nanoparticles were uniformly distributed in the graphene sheets. Using 0.75 g/L silver nitrate and 0.25 g/L graphene oxide, spherical silver particles with better dispersibility and uniform particle size can be obtained. The size of silver nanoparticles on graphene sheets is centered around 100 nm, but not very practical [2]. Shi investigated oxygen reduction (ORR) and oxygen evolution (OER) in alkaline electrolytes. The LMO-NR/RGO composite was synthesized using cetyltrimethylammonium bromide (CTAB) as a template by a simple hydrothermal reaction and heat treatment. Electron microscopy showed that LMO-NR was uniformly coated on silver nanoparticles in RGO flakes. The special composite form of Ag/LMO-NR/RGO promotes the diffusion of electrolyte and oxygen in addition to increasing the electrical conductivity. Electrochemical experiments demonstrated that Ag/LMO-NR/RGO has a good synergistic effect with Ag nanoparticles, LMO-NR, and RGO. Using this catalyst, a reversible charge-discharge Zn-air battery was fabricated and exhibited good cycle characteristics [3]. Mutuk used a mixture of mixed HaP, chitosan, GNS for GNS, and Si<sub>3</sub>N<sub>4</sub> (SN), binary powder to strengthen the composite of mixed Ti, thereby improving its biosurface function. The industrial applicability of the coating was studied by artificial body fluid experiments. Through the determination of its biological activity and the analysis of its microstructure, it was found that HaP had the greatest effect on pH (pH was 11.80). When pure titanium is 10 d, its mass change is the smallest (0.0005 g). The largest mass change (0.0210 g) was obtained by the HaP-coated titanium composite. Through antibacterial experiments, it was found that the nanofibers doped with silver had good antibacterial properties against *Escherichia coli*. The fabricated electrospun-coated hybrid composites can serve as potential candidates for dental, orthopedic implants, and tissue engineering [4]. Sandeep reported the selection of levodopa using crude polyphenol oxidase (PPO) immobilized on electrochemically reduced graphene oxide-silver nanoparticles (RGO-Ag) nanocomposite-modified graphite (Gr) electrodes. The graphite electrode was first modified by electrochemical reduction of graphene oxide-silver (GO-Ag) nanocomposite to RGO-Ag nanocomposite on the graphite electrode. Crude PPO extracted from Manilkara Zapota fruit was subsequently immobilized on Gr/RGO-Ag modified electrodes. The surface features of the modified electrodes

were analyzed by scanning electron microscopy (SEM). The developed sensor exhibited good electrocatalytic activity for the detection of levodopa in the concentration range of 1–150 μM with a low detection limit and high sensitivity [5]. Since the beginning of the 21st century, composite materials have developed rapidly in the global market, especially in the Chinese market in Asia, and the improvement in the production of space three-dimensional models has been slow. At present, there are few researches on 3D printing composite materials at home and abroad, and most of the 3D printing consumables used are single raw materials. 3D printing of AlSi10Mg alloys has been well managed. However, the corrosion behavior of this 3D printing material has not been thoroughly studied. Therefore, Fousova's research focuses on the preliminary determination of the corrosion properties of AlSi<sub>10</sub>Mg samples prepared by the SLM technique and their comparison with the conventional gravity-cast samples in the unheated and treated state (T6). In all three material states, selective dissolution occurred due to microcurrent processes between the silicon particles and the aluminum matrix. In the cast and 3D printed samples, the eutectic and α-Al solid solution in the intercellular network were preferentially attacked, respectively [6]. Yang reported work on designing terahertz devices fabricated by commercially available 3D printers and experimentally demonstrated that the resulting waveguides have an average power propagation loss of 0.02 cm<sup>-1</sup> in the 0.2–1.0 THz range (min. about 0.002 cm<sup>-1</sup>). The fabrication method of terahertz devices based on 3D printing technology will be a promising solution to fabricate terahertz devices with good controllable characteristics and low cost [7]. Yang introduced the preparation methods, development status, and application prospects of ceramic 3D printing, and reviewed the recent progress of oxide (Al<sub>2</sub>O<sub>3</sub>, ZrO<sub>2</sub>) and non-oxide (Si<sub>3</sub>N<sub>4</sub>, SiC) ceramic suspensions for direct 3D printing and stereolithography. The influence of the molding method on the properties of ceramics is shown, and the development of 3D printing is prospected [8]. These studies provided a detailed analysis of the preparation of graphene nanosilver composites. It is undeniable that these studies have greatly promoted the development of the corresponding fields. We can learn a lot from methodology and data analysis. However, the research combined with 3D printing technology is relatively few and not thorough enough, and it is necessary to fully apply these technologies to the research in this field.

In this article, the nanocomposites were characterized by XRD, infrared spectroscopy, Raman spectroscopy, and other methods. Through XRD, it was found that Ag/rGO appeared silver (111), (200), (221), (310) diffraction peaks. Using sodium hydroxide as a reducing agent, comparing the infrared spectra of GNs and GNs-Ag-2 with GO, it was found that the absorption peak of C=O at 1730 cm<sup>-1</sup>, the absorption peak of C-OH at 1401 cm<sup>-1</sup>, and the absorption peak of epoxy all have strong attenuation, indicated that the reducing agent has a certain reducing effect on graphite oxide. The Raman spectral analysis results of GNs and GNs-Ag-2 showed that the intensity of the two peaks of GNs-Ag-2 was seven times that of GNs peak, indicating that silver

nanoparticles had a significant effect on the Raman signal enhancement of GNs. Through the test of the antibacterial effect of Ag/rGO composites on *Escherichia coli* and *Staphylococcus aureus*, it was found that in the fifth hole (drug concentration of 20 ug/ml), *Escherichia coli* showed an increasing trend, and in the eighth hole (drug concentration of 250 ug/ml), *Staphylococcus aureus* showed an increasing trend.

## 2. Methods for the Preparation of Graphene Nanosilver Composites for 3D Printing Technology

**2.1. Graphene Nanosilver Composites.** Compared with traditional silver, nanosilver has a larger specific surface area and an increased contact surface with bacteria, so its antibacterial effect is increased. However, due to their small size, the dispersion of silver nanoparticles in solution is poor and extremely unstable, and the agglomeration phenomenon is serious. Graphene and its derivatives have received extensive attention due to their excellent properties [9]. The large specific surface area of graphene is suitable as a carrier for nanoparticles, and the excellent performance of nanoparticles can be better played because it improves the agglomeration problem on graphene sheets. The surface and edges of graphene oxide are rich in oxygen-containing functional groups, and its preparation method is simple and can be mass-produced, so it can be used as a precursor of graphene-based composite materials. The functional groups on the surface of GO can not only provide reaction sites for some metal cations, but also improve the water solubility of the composites in water or organic solvents, making them better used in the field of biological antibacterials [10]. The graphene/silver-based composite material not only maintains the excellent characteristics of silver nanoparticles, but also can use graphene as a carrier to reduce the bonding between silver particles, so that it can be evenly loaded on the graphene sheet. This composite material has broad application prospects in transparent conductive films, supercapacitors, sensors, surface-enhanced Raman light scattering, etc. [11].

Graphene is a two-dimensional crystal with a single atomic layer connected by  $sp^2$  hybridized carbon atoms with a thickness of only 0.335 nm. The graphene structure can not only be used as the basis of other carbon materials, but also has good stability. The connection between carbon atoms is very flexible. Under the action of mechanical force, the surface of graphene will bend to a certain extent. The carbon-carbon bond is difficult to break, so its crystal structure is also stable [12]. The unique single atomic layer structure of

graphene determines that graphene has many excellent physical properties.

During the reaction of graphene oxide, the nanosilver particles were successfully loaded on the graphene sheet, which played a role in preventing the re-agglomeration of the graphene sheet that had been exfoliated by intercalation, that is, the generated nanosilver had an effect on the structural defects of graphene. There is a certain modification effect. A schematic diagram of the common preparation method of this composite material is shown in Figure 1 [13].

In microwave synthesis, the reaction system is placed in a microwave field, and the microwave energy is converted into heat energy. When the reaction system as a whole reaches a certain temperature and meets the conditions of the synthesis reaction, the target substance is obtained [14]. Microwave heating is that after the material absorbs microwaves, it will generate energy by itself, so that the entire material can be heated quickly and evenly at the same time.

According to the microwave transmission theory, for example, in a single-layer planar material, the normalized incident impedance  $Z$  of a beam of electromagnetic waves incident on the surface of the material from free space is [15]

$$Z = \left(\frac{\mu}{\varepsilon}\right)^{1/2} \tan \left[ j \left( \frac{2\pi d}{\lambda} \right) (\mu\varepsilon)^{1/2} \right], \quad (1)$$

In Formula (1),

$$\varepsilon = \varepsilon' - \varepsilon'' \quad (2)$$

is expressed as the complex permittivity.

$$\mu = \mu' - \mu'' \quad (3)$$

is the complex magnetic permeability.

When the electromagnetic wave is vertically incident to the material from space, the reflectivity  $W$  is

$$W = \frac{(Z - 1)}{(Z + 1)} \quad (4)$$

The propagation coefficient  $\rho$  of electromagnetic waves in a material can be expressed as

$$\rho = \alpha + j\beta = j \left( \frac{2\pi f}{c} \right) (\mu\varepsilon)^{1/2}. \quad (5)$$

In Formula (5),  $\alpha$  is the attenuation coefficient;  $\beta$  is the phase coefficient;  $c$  is the speed of light; and  $f$  is the frequency.

The attenuation coefficient  $\alpha$  of electromagnetic waves in materials can be expressed as

$$\alpha = \frac{\pi f}{c} (\varepsilon' \mu')^{1/2} \left\{ 2 \left[ \tan \gamma_\varepsilon \tan \gamma_m - 1 + \left( 1 + \tan^2 \gamma_\varepsilon + \tan^2 \gamma_m + \tan^2 \gamma_\varepsilon \gamma_m \right)^{1/2} \right] \right\}^{1/2}. \quad (6)$$

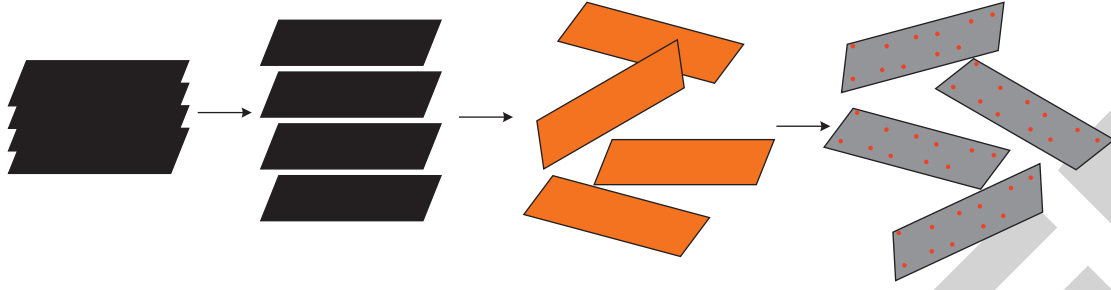


FIGURE 1: Common preparation methods of graphene/nanosilver composites.

In Formula (6),  $\tan \gamma_e = \epsilon''/\epsilon'$  is the dielectric loss tangent of the material, and  $\tan \gamma_m = \mu''/\mu'$  is the magnetic loss tangent of the material.

**2.2. 3D Printing Technology.** 3D printing (three-dimensional printing) is essentially a rapid process production technology that forms materials at one time. This technology often requires the use of 3D modeling software to digitize documents and slice 3D digital model files: the model is described in the form of thin slices, and the thickness of the thin slices is generally 10~100 microns; no matter how complex the shape of the model is, it is just a simple plane vector scan. In this scan, the contour lines of each layer represent a thin slice boundary [16]. In computer-aided design, digital control, laser technology, and material science and engineering technology, a variety of forming materials are used, layer-by-layer printing, and the materials are layered in various shapes to form three-dimensional objects of any shape. As an emerging rapid additive technology, 3D printing technology has great development space and application prospects. It is a perfect combination of reverse engineering and rapid additive technology, which breaks the traditional mechanical manufacturing method and meets the needs of modern industry for short cycle and rich products [17].

3D printing technology mainly includes photosensitive curing molding, fused deposition modeling, selective laser sintering, layered entity manufacturing, and other processes. Figure 2 is a classification diagram of 3D printing technology by principle [18].

Fused deposition (FDM) 3D printing technology is a kind of rapid prototyping technology. Based on the 3D model, the thermoplastic resin material is used to heat and melt the wire by layer-by-layer accumulation and increase the material to accumulate, cool and solidify on the printing platform, and gradually obtain the solid material. The main printing process is shown in Figure 3, first use 3D software to draw a 3D model, export it in STL format, then import the STL file into the slicing software, set various parameters for printing, and slice the STL file to obtain the layered path G-code code of each slice layer. Move the PLA wire control to the nozzle, and the nozzle is gradually extruded and formed according to the path code [19].

Ideally, the shape of the filament extruded from the printing consumables from the nozzle of the printer is

cylindrical, and the shape formed on the platform is usually understood as a regular rectangle. But in fact, it is not a regular rectangle, but a trapezoid-like shape, mainly because the material will spread to the surroundings in a fluid state. At the same time, the material is also affected by the printing speed and extrusion speed. The speed ratio can change the thickness of the material [20]. The following will reset the proportional relationship between the printing speed and the extrusion speed of the printer for composite materials, and select the appropriate printing accuracy [21].

In the case of material extrusion under ideal conditions, the filament is in a natural sagging state when extruded in the nozzle, which can be regarded as a cylinder. When the filament touches the printing platform, it will print a cuboid shape with a certain thickness [22]. However, because the material is affected by its own gravity, fluidity, etc., a final shape of the wire cannot be determined, but it can be simply regarded as a trapezoid-like cross section optimization analysis. Figure 4 is the irregular figure ABCD showing the actual wire output effect on the platform.

Assuming that the printing speed is  $v_1$ , the extrusion speed is  $v_2$ , the diameter of the wire is  $d$ , the thickness of the material is  $h$ , the volume of the extruded material per unit time is  $V$ , the printing material per unit time is  $V_1$ , and the printing time is  $t$ . According to the conservation of 3D printing volume, it can be obtained that

$$V_1 = V_2. \quad (7)$$

Due to a diffusion phenomenon of the material, the actual effect printed by the material is a closed area composed of arcs AD, BC, and straight lines DC, AB, instead of the rectangular section  $h * w$  as shown in Figure 4. The arc can be approximated as a sector with OD as the radius and O as the center. The total cross-sectional area is

$$S_{\text{Total}} = 2S_{\text{sector}} + 2S_{\text{sector}}, \quad (8)$$

$$S_{\text{Total}} * v_1 * t = \left(\frac{d}{2}\right)^2 * t * v_2. \quad (9)$$

The diameter of the nozzle of the printer used in the experiment is 0.4 mm, that is, the diameter of the molten wire is  $D=0.04$  mm, and the printing accuracy is 0.1mm-0.3 mm.  $L \approx R$ .

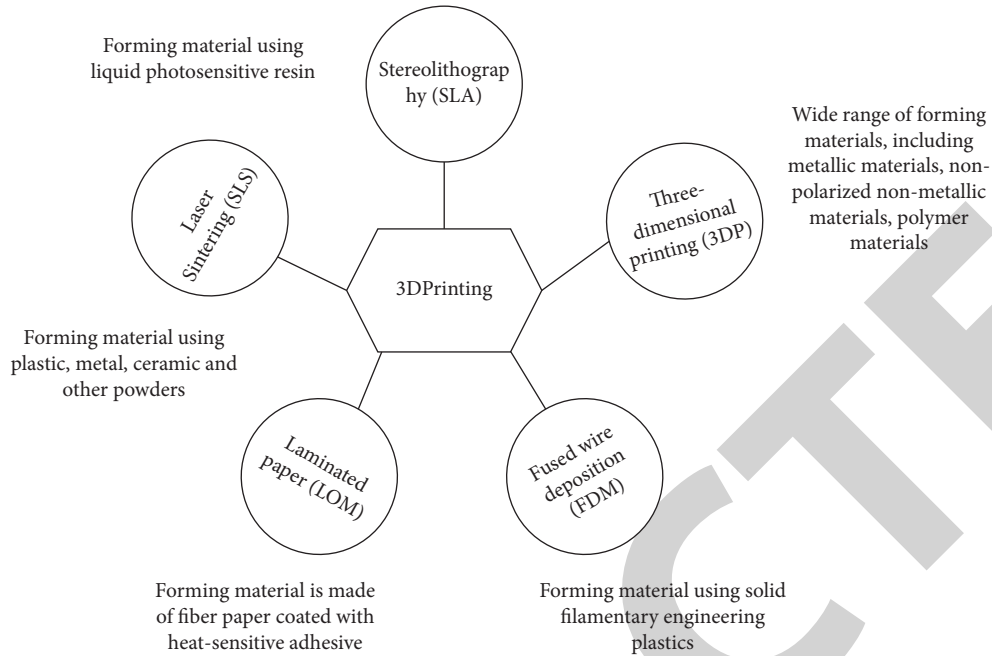


FIGURE 2: Classification of 3D printing technologies by principle.

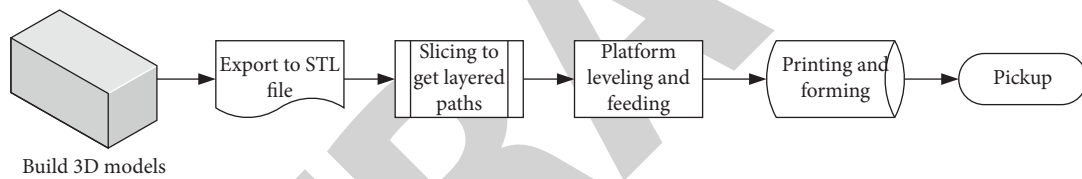


FIGURE 3: 3D printing flow chart.

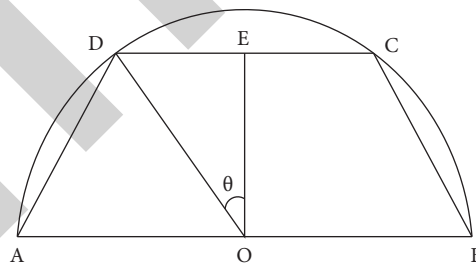


FIGURE 4: Actual wire out.

$$S_{\text{sector}} = \frac{1}{2} * L * R = \frac{1}{2} R^2 = \frac{1}{2} \left( \frac{DE}{\tan \theta} \right)^2, \quad (10)$$

$$\frac{v_1}{v_2} = 2\pi \tan^2 \theta. \quad (11)$$

Since the material is in a fluid state during the printing process,  $\theta$  is greater than  $\pi/4$ , and the viscosity of the material itself is relatively high. When  $\theta$  is less than  $\pi/3$ , the value is  $1 < \tan^2 \theta < 3$ , that is, the printing speed is about 6 to 18 times the extrusion speed.

The appearance of printing can be roughly analyzed by two representative appearances, one is a regular pyramid-like structure, and the other is a circular arc top structure.

After analyzing these two structures, the characteristics of other structures can be calculated. Figure 5 is a schematic diagram of the pyramid type and the arc top type, which is used to indicate the existing area error. A layer of printing is arbitrarily selected, and the relationship between the overall surface accuracy and layer height is deduced by calculating the layer formula. When the cross-section is the triangular slope in the left figure, the obtained error  $\Delta S$  is

$$\Delta S = \frac{h_2}{\tan \beta}. \quad (12)$$

In formula (12),  $\beta$  is the tilt angle of the print. Since the angle does not change, each missing area is the same size. Therefore, under this condition, the printing surface

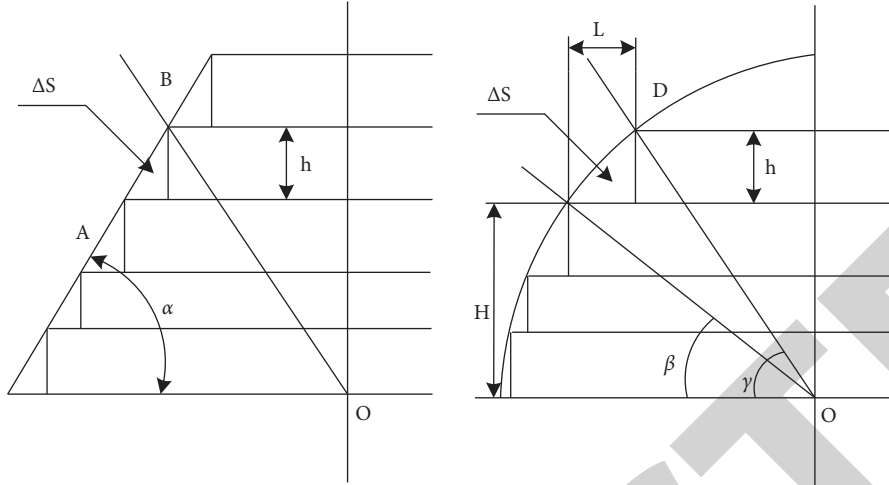


FIGURE 5: Schematic diagram of composite stacking.

accuracy is only related to the size of the bottom angle. In the range of  $90^\circ$ , the smaller the angle, the worse the surface accuracy. When the surface of the workpiece is the arc surface in the figure on the right, the missing area  $\Delta S$  of each layer of the section is different:

$$\sin \vartheta = \frac{G_2}{R} = \frac{G_1 + h}{R}, \quad (13)$$

$$\cos \vartheta = \sqrt{1 - \left(\frac{R \sin + h}{R}\right)^2}, \quad (14)$$

$$L = R(\cos \alpha - \cos \vartheta), \quad (15)$$

$$\Delta S = \frac{1}{2} L \cdot h. \quad (16)$$

Then, there are

$$\Delta S = \frac{1}{2} h \cdot R \left( \cos \alpha - \sqrt{1 - \left(\frac{R \sin + h}{R}\right)^2} \right). \quad (17)$$

Since  $\alpha$  cannot really reach  $90^\circ$  and can only be approached, and  $\alpha$  represents the highest layer  $N-1$ , the length, width, and height of the 3D printer used in this article are within the range of  $350 \text{ mm} \times 350 \text{ mm} \times 350 \text{ mm}$ , and the printing accuracy is  $0.1 \text{ mm}$ .

Infill density has a significant impact on print performance. The filling density and filling pattern are the filling part of 3D printing. When printing each layer of the solid, first print the outer outline of the model, and then fill in the outline. The higher the filling density, the more wires are needed, and the higher the density of the printed part. There are three main types of filling patterns: line, grid, and concentric line, as shown in Figure 6.

The main advantage of 3D printing technology is that it does not require molds, let alone mechanical processing. It can directly convert the electronic model data designed in

the computer into any real object. And 3D printing technology can print parts that cannot be made by traditional methods. The traditional manufacturing method needs to first make a blank product by pouring metal or plastic into a mold, and then process the blank product, such as cutting and grinding, and the process is complicated.

3D printing technology has a short process cycle and high manufacturing precision. It does not need to spend a long time to manufacture molds, nor does it require auxiliary processing work in the later stage. It avoids the leakage of processing data in various production processes, so it is more significant for the military industry. The one-time molding process also avoids subsequent processes such as welding, and the stability and connection strength between product structures are very good. The products produced can be used in aviation, aerospace, nuclear power, and other industrial applications that require extremely high parts [23]. Since the time for production preparation and different process flows is greatly reduced, the cost for producing small quantities of products is greatly reduced, so it is especially suitable for new product development, single-piece small batch production, and individual production.

The main disadvantage of 3D printing technology is the high cost of equipment, so it is more suitable for the production of customized, small batch or personalized products. If 3D printers are used for mass production, it is not suitable from the perspective of time and cost. The price of consumables for 3D printers is relatively high, and in order to meet different application needs, the development of different printing consumables is still the focus of research. In the long run, improving production efficiency remains a top priority for the development of 3D printing technology.

### 3. Preparation of Graphene Nanosilver Composites for Experimental Preparation

The experimental reagents are graphite powder (particle size  $\leq 43 \mu\text{m}$ ); polyethyleneimine (PE I,  $M.N=70\ 000$ , viscous liquid); the experimental reagents are all analytically pure. The experimental water was ultrapure water ( $\text{pH}=6.1$ ,



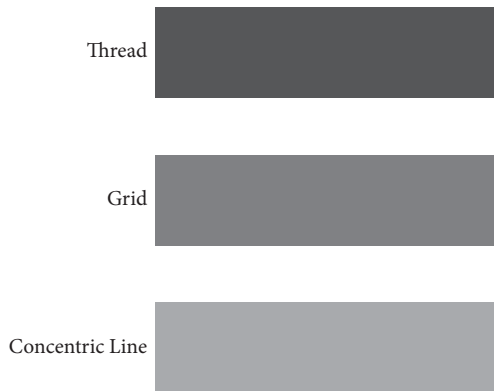


FIGURE 6: Fill pattern types.

resistivity  $18\text{M}\Omega \cdot \text{cm}$ ). The experimental instruments include DF-II digital display collector magnetic stirrer and SW-CT-1FD ultra-clean workbench. The experimental bacteria were *Escherichia coli* (*E. coli*) and *Staphylococcus aureus* (*S. aureus*).

Graphene oxide was prepared by a modified Hummers method, after the oxidation reaction of potassium permanganate in concentrated sulfuric acid and graphite powder, brown graphite flakes with derived carboxylic acid groups at the edges and mainly phenolic hydroxyl groups and epoxy groups on the plane can be obtained. The graphite flake layer can be exfoliated into graphene oxide by ultrasonic or high shear vigorous stirring, and a stable, light brown-yellow monolayer graphene oxide suspension is formed in water. Graphene-silver composites were prepared by a microwave-assisted method. Specific steps are as follows:

- (1) Take 30 ml of graphene oxide solution with a concentration of 0.25 mg/ml and 5 ml of silver nitrate solution with a concentration of 5 mmol/L and ultrasonically disperse for 20 mins to fully mix the two.
- (2) Prepare sodium hydroxide with a concentration of 0.1 mol/L.
- (3) Under the action of strong magnetic stirring, take 10 ml of the pro-reactant solution and add it to the mixture of GO and  $\text{AgNO}_3$ , set the experimental parameters of the microwave heating body, and react for 2 min under the power of 500 W; the whole process is carried out under the condition of mechanical stirring.
- (4) After the samples were cooled, they were centrifuged and washed to  $\text{pH}=7$ , frozen, and then vacuum-dried at  $60^\circ\text{C}$  for 12 h, and the prepared Ag/rGO composites were refrigerated for later use.

The printing parameters of FDM 3D printing technology have an important impact on the performance of 3D printed parts. There are many parameters of 3D printing. Among them, the main factors that have a greater impact on the performance of printed parts are slice layer height, filling density, filling pattern, printing temperature, printing speed, printing direction or angle, etc. In order to keep the size of

the printed component from changing greatly and to ensure the dimensional accuracy of the component in practical applications, it is necessary to adjust the temperature of the printing head and the hot bed.

Tables 1 and 2 show the setting parameters during the 3D printing process.

#### 4. Experimental Data of Graphene Nanosilver Composites

**4.1. Performance Characteristics of Nanocomposites.** As can be seen from Figure 7, the graphene oxide nanosilver composite material has silver (111), (200), (221), and (310) diffraction peaks at  $38^\circ$ ,  $44^\circ$ ,  $64^\circ$ , and  $77^\circ$ . The other XRD patterns of the graphene nanosilver composites did not find this situation, which indicated that the layered structure of the graphite oxide layer or ordered graphene stack is broken. For example, when thin graphite layers are exfoliated and silver nanoparticles are added between the thin graphite layers, the size and distribution of silver nanoparticles can cause irregular changes in the spacing of the thin graphite layers. Graphene oxide was modified into aminated graphene oxide using TETA under alkaline conditions. After ultrasonic dispersion of aminated graphene oxide and  $\text{AgNO}_3$  in deionized water, in a high-temperature reactor, the amino groups grafted on the surface of graphene oxide were, not only can reduce graphene oxide to graphene, but also can reduce  $\text{Ag}^+$  to nanosilver particles, which is a one-step hydrothermal reduction method. The research results showed that: under the action of sodium hydroxide, the graphene nanosilver matrix composite can be obtained after adding silver nitrate to graphite oxide [24].

Figure 8 showed the infrared spectra of GO, GNs, and GNs-Ag-2. Compared the infrared spectra of GN and GNs-Ag-2 with sodium hydroxide as a reducing agent with that of GO, the  $\text{C}=\text{O}$  absorption peak at  $1730\text{ cm}^{-1}$ , the  $\text{C}-\text{OH}$  absorption peak at  $1401\text{ cm}^{-1}$ , and the epoxy resin absorption peak were significantly weakened, and all absorption peaks between  $1230$  and  $1730\text{ cm}^{-1}$  disappeared. Compared with GNs, the absorption peaks of GNs-Ag-2 were further weakened, and the absorption peaks of  $\text{C}=\text{O}$  and  $\text{C}-\text{OH}$  almost disappeared.

Figure 9 showed the Raman spectra of GNs and GNs-Ag-2. Raman spectroscopy is one of the effective methods to quickly and easily detect the characteristics of carbon materials. The GNs in Figure 9 also have only two peaks, but the intensity ratio of the peaks varies greatly. Table 3 showed the ratio of the two peaks of GNs, GNs and GNs-Ag-2, the ratio of the two peaks of GNs is larger than that of GO, because, after the reduction of graphite oxide by NaOH, the area of  $\text{sp}^2$  hybridized carbon atoms is smaller, which leads to the increase of the peak ratio. In Figure 9, the peak intensity of the GNs-Ag-2 Raman spectral curve is seven times that of the GNs peak, indicating the enhancement effect of silver nanoparticles on the Raman spectral signal of GNs; in GNs-Ag-2, the ratio of the two peak positions is slightly increased compared with GNs, which indicated that the presence of silver nanoparticles is beneficial to the oxidation of graphite and can accelerate the  $\text{sp}^3$  hybridization of carbon atoms.



TABLE 1: Printer parameters.

Parameters	Settings	Parameters	Settings
Nozzle temperature	200°C	Outer edge speed	46 mm/s
Hot bed temperature	50°C	Filling speed	85 mm/s
Print speed	50 mm/s	—	—

TABLE 2: Graphene nanosilver printing parameters.

Print layer thickness (mm)	0.13	Filling density (%)	100
Shell thickness (mm)	0.80	Vertical resolution (mm)	0.002
Bottom/top layer thickness (mm)	0.42	Printing temperature (°C)	234
Bottom plate temperature (°C)	23	Wire diameter (mm)	1.81

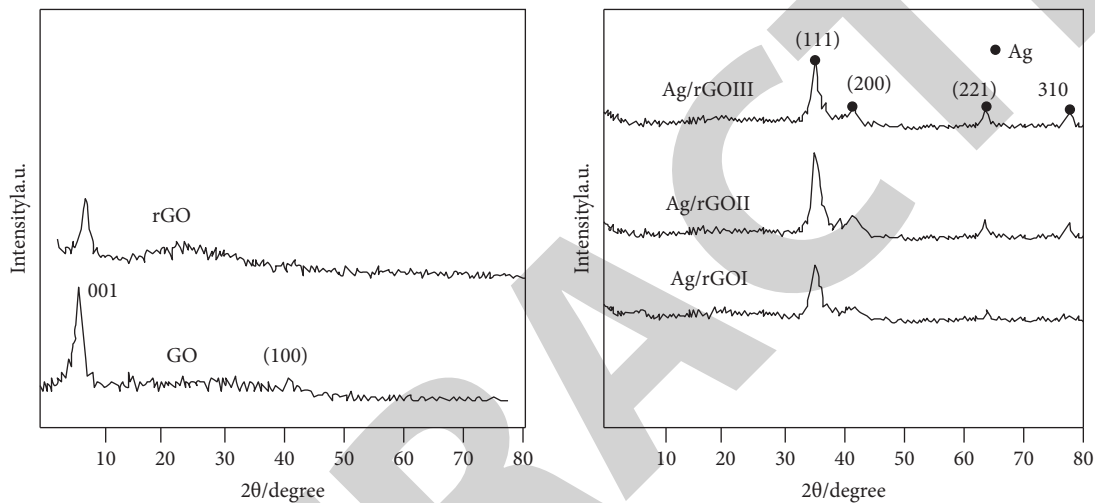


FIGURE 7: XRD patterns of GO, rGO, and Ag/rGO synthesized with different Ag concentrations.

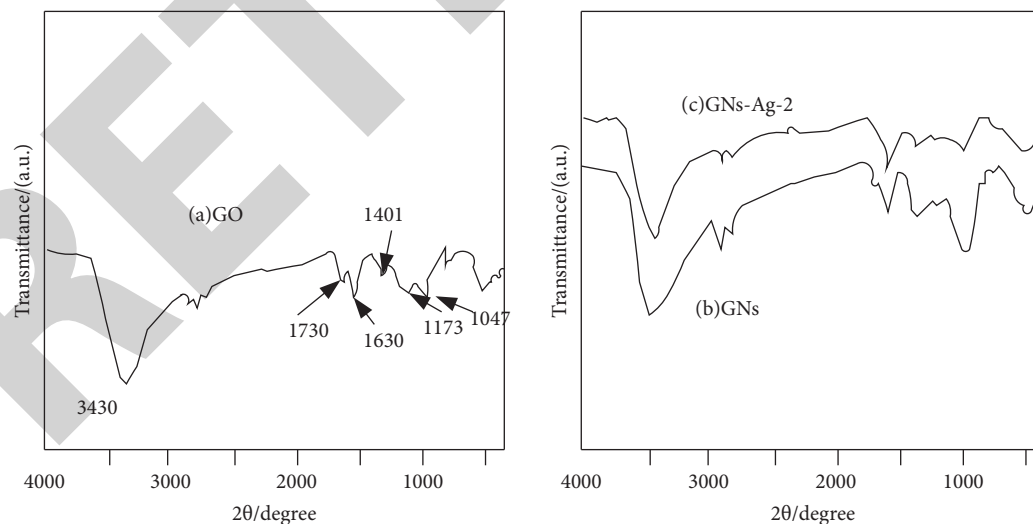


FIGURE 8: Infrared spectrum of the sample.

4.2. *Antibacterial Effect of Samples against Escherichia Coli and Staphylococcus.* The microplate reader is a commonly used enzyme-linked immunosorbent assay equipment. Its detection principle is based on the absorption spectrum of substances and visible light colorimetric technology. The microplate

reader has the characteristics of rapid detection and micro-application, and is suitable for rapid detection of large samples and research on inhibiting bacterial activity. The effect of Ag/rGO composites on the light absorption values of *Escherichia coli* and *Staphylococcus aureus* is shown in Figure 10.

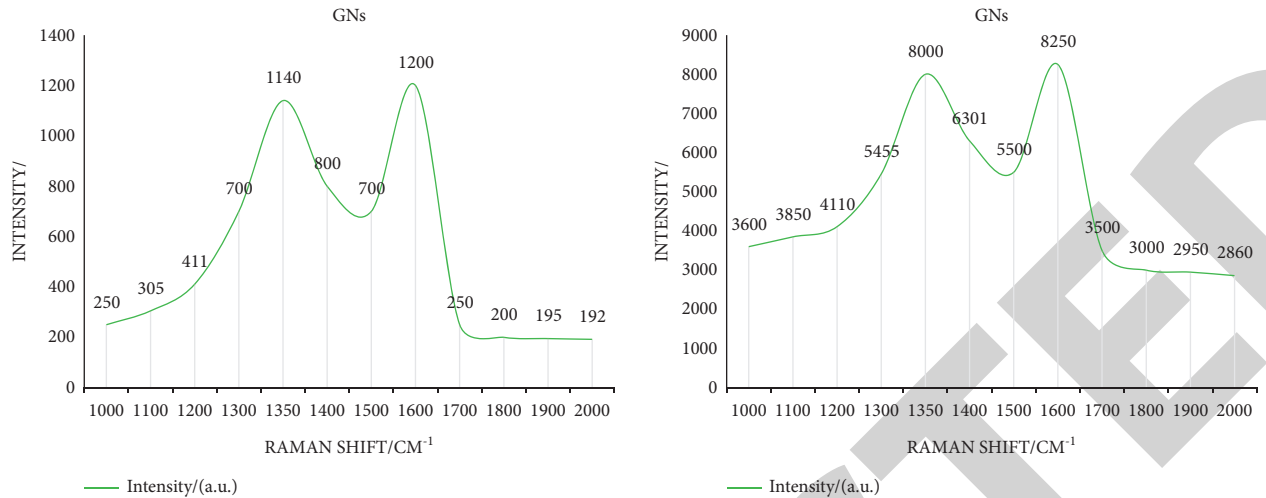


FIGURE 9: Raman spectra of GNs and GNs-Ag-2 samples.

TABLE 3: The intensity ratio of the two peaks in the Raman spectrum of the sample.

Type	Sample	$I_{D/G}$
I	GO	0.82
II	GNs	0.95
III	GNs-Ag-2	0.97

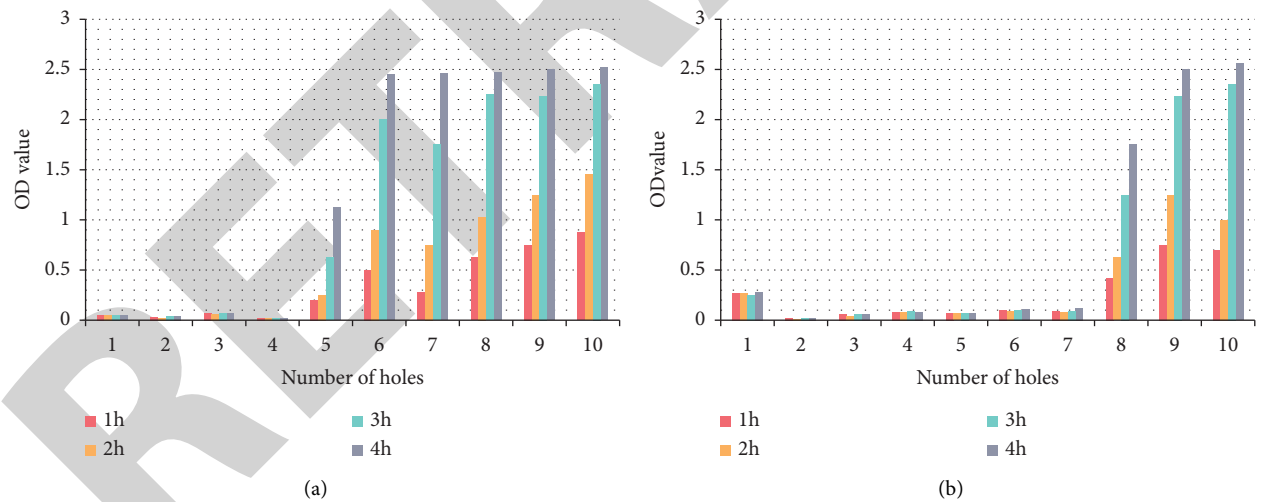


FIGURE 10: The effect of Ag/rGO composites on the light absorption value of fungi at different times.

As shown in Figure 10, (a) higher value of OD490 indicates that a large number of active bacteria are still present. Overall, the light absorption values of the two bacteria increased with decreasing Ag/rGO composite concentration at different time points. The absorbance curve was almost flat at the beginning and showed an upward trend in the fifth well (drug concentration of 20  $\mu\text{g/ml}$ ). At 1 h, the sample and bacteria began to react. Due to the reaction between bacterial mitochondrial dehydrogenase and CCK-8, an orange-yellow water-soluble

substance formazan will be formed, the concentration in Figure 10b is 250  $\mu\text{g/ml}$ , but the OD value is higher than the light absorption value of bacteria in other samples with lower concentrations. The reason may be that the high concentration of Ag/rGO composite can directly inhibit the growth of bacteria, and the lower value of OD490 during the measurement process easily affects the precision of the antibacterial test. However, at low concentrations of antibacterial drugs, the growth of bacteria is faster and the OD value is higher.

## 5. Conclusion

Graphene is a new two-dimensional carbon nanomaterial with excellent properties. It has high optical absorption, high strength, large specific surface area, and low production cost (compared with carbon nanotubes). It is composed of  $sp^2$  carbon atoms and is the basis of various crystallization theories for carbon materials, and it is an ideal material for the development of high-performance composite materials, which have attracted extensive attention, and these materials can be inexpensively mass-produced. Nanosilver has unique optical, electrical, catalytic, and bactericidal properties. Based on the synergistic effect of the two nanomaterials, graphene-nanosilver composites have shown good application prospects in many aspects. With the continuous in-depth research of graphene nanosilver composites, its application has gradually expanded to various fields such as analysis and detection, industrial catalysis, biological antibacterial, and environmental governance. In this article, graphene oxide and silver nanocomposites were taken as the research objects, graphite oxide (GO) was prepared by the modified Hummers method, and the antibacterial effect of Ag/rGO composites was studied. The results showed that the sample had an obvious bacteriostatic effect on *Escherichia coli* and *Staphylococcus*. This opened up a new approach and approach for the development of novel high-efficiency antibacterial composites, which have broad application prospects.

## Data Availability

The data that support the findings of this study are available from the corresponding author upon reasonable request.

## Conflicts of Interest

The authors declare that there are no potential conflicts of interest with respect to the research, authorship, and/or publication of this article.

## References

- [1] L. Zeng, J. Shi, J. Luo, and H. Chen, "Silver sulfide anchored on reduced graphene oxide as A high-performance catalyst for CO<sub>2</sub> electroreduction," *Journal of Power Sources*, vol. 398, pp. 83–90, 2018.
- [2] Y. Zhi, W. Gan, and J. Zhou, "Fabrication and electrical properties of nano-silver/graphene composite powders prepared in-situ by chemical reduction," *Fenmo Yejin Cailiao Kexue yu Gongcheng/Materials Science and Engineering of Powder Metallurgy*, vol. 23, no. 4, pp. 433–438, 2018.
- [3] J. Ziwei, "Silver decorated LaMnO<sub>3</sub> nanorod/graphene composite electrocatalysts as reversible metal-air battery electrodes," *Applied Surface Science: A Journal Devoted to the Properties of Interfaces in Relation to the Synthesis and Behaviour of Materials*, vol. 402, pp. 61–69, 2017.
- [4] T. Mutuk and M. Gurbuz, "Graphene/chitosan/Ag<sup>+</sup>-doped hydroxyapatite triple composite fiber coatings on new generation hybrid titanium composite by electrospinning," *Journal of Composite Materials*, vol. 55, no. 22, pp. 3087–3097, 2021.
- [5] Sandeep S, Santhosh A S, Swamy N K, "Electrochemical detection of L-dopa using crude Polyphenol oxidase enzyme immobilized on electrochemically reduced RGO-Ag nanocomposite modified graphite electrode," *Materials Science and Engineering*, vol. 15, pp. 232–235, 2018.
- [6] M. Fousova, D. Dvorsky, and D. Vojtech, "Corrosion properties of AlSi10Mg alloy prepared by gravity casting and 3D printing technology," *Manufacturing Technology*, vol. 17, no. 6, pp. 847–853, 2017.
- [7] J. Yang, C. Gong, and J. Y. Zhao, "Fabrication of terahertz device by 3D printing technology," *Chinese Optics*, vol. 10, no. 1, pp. 77–85, 2017.
- [8] M. Yang, X. D. Luo, and Z. P. Xie, "Review of 3D printing technology of ceramic," *Rengong Jingti Xuebao/Journal Of Synthetic Crystals*, vol. 46, no. 1, pp. 183–186, 2017.
- [9] D. Xu, C. Zhu, and X. Meng, "Design and fabrication of Ag-CuO nanoparticles on reduced graphene oxide for nonenzymatic detection of glucose," *Sensors and Actuators*, vol. B265, pp. 435–442, 2018.
- [10] Y. Wang, L. Shi, H. Wu et al., "Graphene oxide-IPDI-Ag/ZnO@hydroxypropyl cellulose nanocomposite films for biological wound-dressing applications," *ACS Omega*, vol. 4, no. 13, pp. 15373–15381, 2019.
- [11] B. Feng, J. Ma, X. Gu, X. Zhao, and Y. Zhang, "Preparation of silver/chemically reduced graphene composite for flexible printed circuits," *Micro & Nano Letters*, vol. 13, no. 5, pp. 576–579, 2018.
- [12] S. El-Rahman, S. S. Ahmed, and Kader M, "Toxicological, biological and biochemical effects of two nanocomposites on cotton leaf worm, *Spodoptera littoralis* (Boisduval, 1833)," *Polish Journal of Entomology*, vol. 89, no. 2, pp. 101–112, 2020.
- [13] Y. Dong, J. Chen, and H. Xu, "Rhodium(iii)-catalyzed directed amidation of unactivated C(sp<sup>3</sup>)-H bonds to afford 1, 2-amino alcohol derivatives," *Chemical Communications*, vol. 54, no. 79, pp. 11096–11099, 2018.
- [14] H. Fu, M. Zhang, J. Ding et al., "A high sensitivity D-type surface plasmon resonance optical fiber refractive index sensor with graphene coated silver nano-columns," *Optical Fiber Technology*, vol. 48, pp. 34–39, 2019.
- [15] F. Arshad, B. Uzair, S. A. K. Leghari, S. Noor, and M. Maaza, "GO/Ag<sub>2</sub>O composite nanostructure as an effective antibacterial agent," *ChemistrySelect*, vol. 4, no. 35, pp. 10365–10371, 2019.
- [16] S. Wang, Y. Tian, and C. Wang, "Chemical and thermal robust tri-layer rGO/Ag NWs/GO composite film for wearable heaters," *Composites Science and Technology*, vol. 174, pp. 76–83, 2019.
- [17] H. Li and Z. Du, "Preparation of a highly sensitive and stretchable strain sensor of MXene/silver nanocomposite-based yarn and wearable applications," *ACS Applied Materials & Interfaces*, vol. 11, no. 49, pp. 45930–45938, 2019.
- [18] C. F. Glover, C. A. J. Richards, and G. Williams, "Evaluation of multi-layered graphene nano-platelet composite coatings for corrosion control Part II-Cathodic delamination kinetics," *Corrosion Science*, vol. 136, pp. 304–310, 2018.
- [19] K. I. Vandana, "Characterization of microwave assisted sintered graphene toughened ALUMINA(GTA)NANO composites," *AIP Conference Proceedings*, vol. 1859, no. 1, pp. 1–5, 2017.
- [20] D. Sahu, G. Sahoo, P. Mohapatra, and S. K. Swain, "Dual activities of nano silver embedded reduced graphene oxide using clove leaf extracts: Hg<sup>2+</sup> sensing and catalytic degradation," *ChemistrySelect*, vol. 4, no. 9, pp. 2593–2602, 2019.

## *Retraction*

# **Retracted: Application of Composite Nano-Bone Transplantation and Massage Exercise Rehabilitation Training in Patients Undergoing Limb Replantation**

### **Advances in Materials Science and Engineering**

Received 26 December 2023; Accepted 26 December 2023; Published 29 December 2023

Copyright © 2023 Advances in Materials Science and Engineering. This is an open access article distributed under the Creative Commons Attribution License, which permits unrestricted use, distribution, and reproduction in any medium, provided the original work is properly cited.

This article has been retracted by Hindawi, as publisher, following an investigation undertaken by the publisher [1]. This investigation has uncovered evidence of systematic manipulation of the publication and peer-review process. We cannot, therefore, vouch for the reliability or integrity of this article.

Please note that this notice is intended solely to alert readers that the peer-review process of this article has been compromised.

Wiley and Hindawi regret that the usual quality checks did not identify these issues before publication and have since put additional measures in place to safeguard research integrity.

We wish to credit our Research Integrity and Research Publishing teams and anonymous and named external researchers and research integrity experts for contributing to this investigation.

The corresponding author, as the representative of all authors, has been given the opportunity to register their agreement or disagreement to this retraction. We have kept a record of any response received.

### **References**

- [1] Y. Tang and J. Fu, "Application of Composite Nano-Bone Transplantation and Massage Exercise Rehabilitation Training in Patients Undergoing Limb Replantation," *Advances in Materials Science and Engineering*, vol. 2022, Article ID 2065744, 8 pages, 2022.

## Research Article

# Application of Composite Nano-Bone Transplantation and Massage Exercise Rehabilitation Training in Patients Undergoing Limb Replantation

Yan Tang  and Junxia Fu 

First People's Hospital of Chenzhou City, Hand and Foot Microsurgery, Chenzhou 423000, Hunan, China

Correspondence should be addressed to Junxia Fu; [fujunxia@zcmu.edu.cn](mailto:fujunxia@zcmu.edu.cn)

Received 8 July 2022; Revised 19 August 2022; Accepted 26 August 2022; Published 10 September 2022

Academic Editor: K. Raja

Copyright © 2022 Yan Tang and Junxia Fu. This is an open access article distributed under the Creative Commons Attribution License, which permits unrestricted use, distribution, and reproduction in any medium, provided the original work is properly cited.

With the great stride forward of socialist progress, various medical treatment measures have also made a leap forward in development, providing a deeper guarantee for people's life safety. At the same time, the research field of nanotechnology has gradually developed in the medical field, which plays an important role in the development of medicine, and massage exercise rehabilitation training also provides convenience for patients' recuperation. The purpose of this study is to study the application of composite NanoBone transplantation in patients with limb replantation and the application of massage exercise rehabilitation training in patients with limb replantation. The methods used in this paper are: consulting the literature to understand the composite NanoBone transplantation technology and massage exercise rehabilitation training methods, interviewing the patients and attending doctors, and asking about the selection method of experiment and questionnaire used in the paper, so as to carry out the questionnaire survey. The treatment group and the control group were set up to analyze the results. The results showed that there were no significant differences in T lymphocyte subsets, serum complement, and circulating immune complex in the replantation of amputated limbs. Combined with the clinical manifestations and pathological results, early rejection occurred, and the body temperature of the patients increased after clinical treatment; The characteristics of massage are not practical, the course of treatment is short, the effect is fast, the clinical operation is simple, easy to grasp, and has high clinical application and promotion value. The final test results showed that: comparing the two groups of patients before treatment, the VAS scores were 23% and 21%, respectively, and the treatment group scores were 23% and 21%, respectively. After treatment, the VAS scores of the test group and the control group were 29% and 27%, respectively. The treatment group scored 2% higher than the control group. From this, it can be concluded that massage is better than traditional massage, and massage exercise has great application prospects in clinical practice.

## 1. Introduction

With the development of the economy, trauma, tumor, infection, and other diseases caused by traffic, construction, environment, and other reasons are increasing year by year. The incidence of nonunions and bone defects has also increased from 3.7% in 2008 to 5.6% in 2021 increased by nearly 1% [1]. In the past, autogenous bone grafting and allogeneic bone [2] grafting were the main methods to treat bone nonunion and bone defects. The former has a limited bone mass in the donor site, prolonged operation time,

increased intraoperative blood loss, and complications such as pain, infection, and loss of function; the latter has been widely used with the continuous improvement of bone bank processing technology, but there are risks of rejection and disease transmission. Therefore, people have carried out the search for low-risk, high-efficiency, easy-to-use, plastic bone transplantation research. Since the 1980s, bone tissue engineering has been developed on the basis of interdisciplinary research in engineering, cell biology, materials science, and medicine. Bone tissue engineering refers to the separation of autologous high-concentration osteoblasts,

bone marrow stromal stem cells, or chondrocytes, which are cultured and expanded *in vitro* and then planted in a natural or artificial synthetic material with good biocompatibility. The research of tissue-engineered new bone tissue is a branch of tissue engineering research, which provides a new platform for the study of ideal bone transplantation. In recent years, more and more scaffold materials have been used in clinical research. According to the different sources of materials, they can be generally divided into three categories: organic polymer materials, inorganic materials, and composite materials [3]. Organic polymer materials have the advantages of large-scale production, structural design and control, mechanical strength, and degradation time, but lack cell signal; inorganic materials have good biocompatibility and cell recognition signals, which are conducive to cell adhesion and proliferation, but the disadvantage is poor mechanical strength and rapid degradation *in vivo*. At present, no material has been found to be able to achieve or approach the performance of the ideal scaffold material. The characteristic of composite materials is to combine two or more different materials in a certain proportion, learn from each other, make up for each other, and give full play to maximum efficiency.

Massage is based on the theory of viscera and meridians of traditional Chinese medicine, combined with the anatomy and pathological diagnosis of Western medicine, and uses manipulation to act on specific parts of the human body to adjust the physiological and pathological conditions of the body and achieve the purpose of physiotherapy. Say, it's a physical therapy. Massage has the effects of dredging collaterals, promoting blood circulation and removing blood stasis, removing dampness, dispelling cold, detumescence and pain relief, making the back blood unobstructed and veins unblocked; Symptomatically, it is completely similar to thoracodorsal or lumbosacral fibrositis, although its mechanism is another cause, more common in workers in wet and cold conditions; it is often difficult to distinguish clinically unless, according to the characteristics of medical history, targeted lumbar muscle exercise can enhance the muscle strength and toughness of a lumbar muscle, not only can assist the treatment of lumbar muscle strain but also can consolidate the curative effect and prevent the occurrence of lumbar muscle strain. It is an effective and safe method to recover the back muscle through massage. At the same time, massage therapy combined with exercise waist muscle strain treatment, significantly affect the symptoms and signs of patients, and it is a rapid and effective relief of local acute and chronic inflammation, relieve spasm, release adhesion, etc., effectively prevent the adhesion of lumbar back muscles and soft tissue. Exercise can enhance the strength of the lumbar muscle, enhance the stability of the lumbar muscle, not only consolidate the therapeutic effect but also effectively prevent the recurrence of lumbar muscle strain, and finally completely cure lumbar muscle strain. A long-term reasonable and appropriate amount of physical exercise is very important for the treatment, recovery, and prevention of lumbar muscle strain, and more important for human health [4]. In patients with complete recovery, correct exercise can effectively prevent the recurrence of lumbar muscle strain. In

the feedback of patients, we found that if patients take exercise prescription for muscle rehabilitation exercise, after 1–2 courses of massage therapy and rehabilitation exercise, most of them can be cured within a month, and the symptoms and signs of patients will gradually disappear, and finally fully recover. Compared with traditional Chinese and Western medicine, massage therapy combined with rehabilitation exercise has a significant effect on lumbar muscle strain. Patients can be treated not only in a hospital but also at home according to exercise prescription, which is convenient, economical, and feasible.

In recent years, with the research on the clinical application and clinical observation of composite NanoBone transplantation [5], it is found that the incidence of complications can be greatly reduced and the survival rate and recovery function of amputated limbs can be improved after replantation of defective limbs. Using medical means to restore the shape and function of limbs has been the goal of medical experts since ancient times, and it is also the common hope of mankind all over the world. However, regeneration after amputation seems to exist only in science fiction. In the 1960s, due to the backward development of science and technology, surgeons could only use a self-made simple magnifying glass, which greatly reduced the probability of vascular anastomosis, greatly increased the probability of late vascular embolism, and the survival rate of the stump was very low, only less than 50%. In the 1970s, with the further development of microsurgery and other new technologies, microvascular anastomosis became possible, which greatly improved the survival rate of amputees and brought good news to the majority of patients. However, the occurrence of postoperative complications greatly affects the function or activity of the amputated limb. Usually, after the amputated limb survives, it only has a complete appearance and loses its function, which makes the replantation of the amputated limb into a difficult situation. In the 1980s, with the further development of advanced technology, much advanced science and technology were applied to the medical field. In addition, with the increase in doctors' clinical experience, the survival rate of replantation of amputated limbs is further improved. However, when the amputated limb survived, the functional recovery of the amputated limb did not achieve the expected effect. Today, with the exploration and efforts of generations of orthopedic experts, vacuum sealing drainage technology has been applied in the orthopedic clinic. It not only has obvious advantages in improving the survival rate of amputated limb replantation [6] but also has a significant effect on improving the functional recovery after replantation.

In the process of bone regeneration, the ideal scaffold should have sufficient nutrition and appropriate mechanical properties, which can simulate the natural microenvironment of bone defects and support the proliferation and differentiation of specific cells. Bone graft regeneration [7] must have high mechanical properties, including appropriate mechanical strength and toughness, providing sufficient mechanical strength and stiffness to replace the lost bone, bearing the load bone replacement, supporting the proliferation and differentiation of osteoblasts, and the



expression of bone matrix protein. Lumbar muscle strain is a common and frequently occurring disease, which seriously endangers human health. A long course of the disease, difficult to cure and recurrent attacks, seriously affect the patient's life, work, study, and physical and mental health. In the face of the growing trend of lumbar muscle strain, many scholars have updated the treatment methods and means in practice, from simple to comprehensive, from medicine to manipulation, from acupuncture to physical therapy, and so on. There are a variety of treatment methods, different treatment effects, poor efficacy, and easy to relapse, especially the follow-up observation and follow-up visit after treatment are almost blank. According to the clinical manifestations, pathogenesis, characteristics, and pathological mechanism of lumbar muscle strain, massage combined with exercise is a treatment method without side effects, quick effect, obvious recovery of lumbar muscle function, and no recurrence. Massage combined with exercise is a feasible and effective method to treat lumbar muscle strain and to achieve the goal of treatment, rehabilitation, and prevention. This paper is to study the application of composite NanoBone transplantation in patients with limb replantation and the application of massage exercise rehabilitation training in patients with limb replantation. The innovation of this paper is: through the study of the clinical manifestations, pathogenesis, characteristics and pathological mechanism of lumbar muscle strain, a new treatment plan for the treatment of lumbar muscle function recovery with fast recovery, no side effects, and no recurrence is concluded. Tuina plus exercise is a practical and effective treatment and to achieve the purpose of treatment, recovery, prevention, and so on.

## 2. Application of Composite NanoBone Graft in Patients with Limb Replantation

*2.1. Introduction to Composite Nano.* A nanometer (NM) [8] is a unit of length. One nanometer is one billionth of a meter and one thousandth of a micron, about 10 atoms long. Suppose the diameter of a hair is 0.05 mm. Cut into 50000 pieces along the radial direction, and the thickness of each hair is about 1 nm. The so-called nanotechnology is a new technology to study the motion laws and characteristics of electrons, atoms, and molecules in the range of 0.1~100 nm. Several dozens of countable atoms or molecules exhibit many new characteristics at the nanoscale. This kind of material has special properties, which is different from the original atoms and molecules as well as macroscopic materials [9]. The technology of using these characteristics to make devices with specific functions is called nanotechnology. Nanotechnology is an interdisciplinary and comprehensive subject. In 1993, the international nanotechnology Steering Committee divided nanotechnology into six branches nanoelectronics, nanophysics, nanochemistry, nanobiology, nanoprocessing, and nanometrology.

The current research and application of nanotechnology are mainly in materials and preparation, microelectronics and computer technology, medicine and health, aerospace and aviation, environment and energy, biotechnology, and

agricultural products. Nanomedicine [10] is a "science and technology that uses molecular equipment and human molecular knowledge to diagnose, treat and prevent diseases and trauma, relieve pain, and promote and maintain health." Nanobiomedicine is to extract essential substances from plants and animals and then combines them at the nanoscale to achieve maximum efficacy. This is one of the most potential areas for development after China's accession to the WTO. At present, the international pharmaceutical industry is facing a new choice, that is, to develop the nanopharmaceutical industry.

Nanocomposites [11] are based on resin, rubber, ceramics, and metal matrix as the continuous phase, nanosize metal, semiconductor, rigid particles, and other inorganic particles, fiber, carbon nanotubes, and others modified into dispersed phase. Through the appropriate preparation method, the modifier is evenly dispersed in the matrix material to form a composite system containing nanomaterials, which is called nanocomposite materials. Composite materials have been widely used in aerospace, national defense, transportation, sports, and other fields because of their excellent comprehensive properties, especially the designability of performance. Nanocomposites are the most attractive part. In recent years, the development of new materials in developed countries put the development of nanocomposites in an important position. The research directions include nanopolymer matrix composites, carbon nanotube functional composites, and tungsten copper nanocomposites.

*2.2. Bone Transplantation.* Bone transplantation refers to the removal of bone of appropriate size from other parts of the patient's body or the removal of the donor's bone from the bone bank and transplantation to the bone defect. Bone transplantation has been widely used, but donor bone cells cannot survive in the recipient unless autologous transplantation. However, the remaining death matrix has the ability to induce bone, which can stimulate the host osteoblasts to recombine in the matrix to produce new bone. Therefore, the scaffold of bone graft is building a bridge and can stabilize the defective bone until a new bone is formed. Cryopreservation of allogeneic cadavers can reduce the immunogenicity of bone and the feasibility of maintaining chondrocytes [12]. Immunosuppressive agents were not used after transplantation. Although these patients can produce HLA antibodies, they can also produce HLA antibodies to prevent cartilage injury in the early stage. The recognition function of HLA actually refers to the unique synergy in the immune response. Antibodies are produced by B cells, but in most cases, macrophages and T lymphocytes are required.

## 3. Application of Massage Exercise Rehabilitation Training in Patients with Replantation of Amputated Limbs

*3.1. Massage Sports Rehabilitation Training.* Tuina techniques originate from the initial instinctive actions of human beings, such as friction for warmth, stroking pain, stroking

between mothers and infants, and mutual touching between human bodies. The code name and basic technique of the oracle bone inscriptions are “把.” The “Yin Shu” unearthed from the early Han tombs in Zhangjiashan, Jiangling included “foot tarsi,” “shaking fingers” and other techniques, and recorded the intraoral reduction method of subluxation of the temporomandibular joint. “Fifty-two disease prescriptions” contained There are more than 10 kinds of techniques such as pressing, massaging, scratching and scraping, and there are pressing methods to stop bleeding, medical towel massage and so on. The classification of massage techniques is rubbing, rubbing, pushing, wiping, and sweeping. Massage: massage is the oldest external treatment of traditional Chinese medicine in China. In ancient times, massage was called “pressure” or “case.” China’s first monograph on traditional massage is “Huangdi Qibo massage ten volumes” in Qin and Han Dynasties. This book mainly demonstrates that massage is a traditional Chinese medicine therapy based on Yin and Yang, five elements, viscera and meridians, Qi, blood, and body fluid. Massage is one of the earliest physical therapies in human history [13]. It can promote human blood circulation, dredge meridians, regulate human metabolic function and prevent diseases by pinching, pressing, rubbing, point, rolling, picking, and other operations on the human body, as well as different transformation technologies and different parts of the operation. Modern massage is a kind of rehabilitation therapy based on the theory of channels and viscera of traditional medicine and combined with anatomical characteristics [14]. It is divided into medical massage, health massage, and sports massage. Massage is simple and easy to learn, and it can also replace medicine to treat some diseases. At present, massage therapy [15] is widely used: five sense organs, internal medicine, trauma department, pediatrics, gynecology, and other departments have use massage therapy or auxiliary treatment, especially for the treatment of some chronic diseases and functional diseases with unique therapeutic effects.

Sports: sports were a kind of social activity in which people take physical exercise and exercise as the basic means to enhance their physique and health. In the process of exercise, the structure of the body will change with the movement, so as to promote the metabolism of the human body and enhance its own physique. Sport is an indispensable way of life for human beings [16]. People follow the law of human growth and development and sports activities. Through purposeful exercise, people can achieve the purpose of strengthening their physique, improving physical and mental functions, promoting health recovery or creating conditions for surgical preparation, and reducing or avoiding postoperative complications. Exercise can make “eliminate all kinds of diseases, strengthen the body, prolong life, eyesight is light and healthy, no longer tired.” The training time is 30 minutes at a time, three times a day. As early as the spring and autumn period and the Warring States period, people used guiding technology to prevent and treat diseases [17]. Later, Wuqinxi, Taijiquan, and Baduanjin were used as exercise methods to keep fit and eliminate diseases. The movement they were engaged in at that time

became an effective means for the ancient working people to prevent and cure diseases. Modern medical research and clinical observation data show that in the process of patients’ rehabilitation treatment, various exercise methods in ancient China, such as traditional guidance, Wuqinxi, Taijiquan, gymnastics, and running, can make patients have confidence in life, relieve the initial symptoms, and have a better auxiliary treatment effect. At present, exercise has become one of the most important methods to treat diseases.

Massage therapy is one of the main methods to treat lumbar disc herniation in China. Massage can effectively relieve muscle tension, change local abnormal muscle tension, and play a role in relaxing the muscle. Through different manipulation, it can also improve local blood circulation and promote local metabolism, so as to achieve the purpose of treating lumbar disc herniation.

### 3.2. Research Methods

3.2.1. *Sample Library.* There were 80 inpatients in Hospital D from May 2015 to March 2016. The clinical diagnosis and surgical indications were clear. A bone graft is required during the surgery. The patients and their families agreed to participate in the clinical trial. The patients who did not meet the inclusion criteria were excluded, and 60 of them were selected for this experiment, and the questionnaires were analyzed after the experiment. The patients with replantation of amputated limbs were divided into three categories based on their initial symptoms. The three categories are mild, moderate, and severe. The questionnaire adopts the method of “stratified sampling,” and random sampling is carried out according to two levels of mild and moderate personnel, severe patients and patients who have not undergone composite NanoBone transplantation and massage exercise rehabilitation training. The number of personnel samples is 30, accounting for 50% of the total number of middle and senior management personnel; the number of mild personnel and patients without composite NanoBone transplantation and massage exercise rehabilitation training is 15, accounting for 25% of the total number of grass-roots management personnel and general personnel; the number of critically ill persons is 15, accounting for 25%. The investigators did not include patients who were excluded from the experimental criteria.

3.2.2. *Specific Implementation Process.* In order to further verify the effect of the one-year operation of the application of composite NanoBone transplantation and massage exercise rehabilitation training in patients with severed limb replantation, a questionnaire survey was conducted twice before and after the operation. And the surveyed persons are selected by random number generator software. By visiting the recovery of nurses and patients, a three-person investigation team was formed to refine the division of responsibilities. According to the division of labor, they went to various departments to find the corresponding respondents, distributed a total of 330 questionnaires and informed the specific time of collection. Finally, 330 questionnaires were

TABLE 1: Observation of clinical signs.

	Group 1	Group 2	Group 3
Temperature	Increase, less than 38 degrees°	It was higher than 38°, in 3 cases	It was higher than 38°, in 8 cases
Wound response	Good	3 cases had a local reaction	5 cases had a local reaction
Wound healing	All grade A	Two cases were grade B	Three cases were grade B

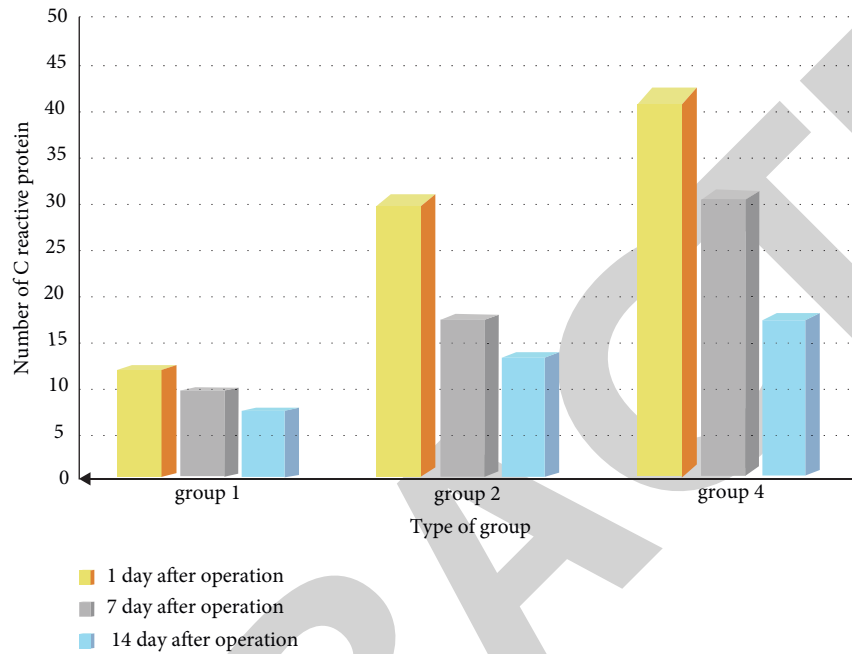


FIGURE 1: Changes in reactive protein after an operation.

collected on schedule, the validity was judged, and the effective questionnaires were statistically summarized. If the operation time is long, the breathing gas and intravenous infusion should be warmed, and even the abdominal cavity and the thoracic cavity should be washed during the operation, and the washing liquid should be warmed. If it is not heated, a basin of water will be poured in and pressed down, and the heart will run up. This is a stress response, and the complications of the incision will increase.

3.2.3. *Statistical Analysis Methods.* According to questions 1–8 of the questionnaire, the basic situation of the surveyed personnel will be classified and counted. One question and one option will be counted once for each person. In the end, 50 middle-level personnel will have 800 options for questions 1–16 to evaluate the recovery after surgery, and 25 people will appear. There were 4,480 options for mild personnel and patients who did not undergo composite NanoBone grafting and massage exercise rehabilitation training.

## 4. Results and Discussion

4.1. *Application of Composite NanoBone Graft in Patients Undergoing Limb Replantation.* The clinical signs were observed:

Shown as in Table 1, the body temperature of the three groups increased, and the temperature of the second and third groups was higher than 38 degrees; the wound response of the first group was good, while that of the second and third groups was local reaction; the wound healing state of the first group was grade A, and that of the second and third groups was grade B.

Shown as in Figure 1, the level of C-reactive protein in the three groups continued to rise, while that in the third group increased significantly. One day after the operation, the number of C-reactive proteins in the three groups were 12, 31, and 43, respectively; on the seventh day after the operation, the number of C-reactive proteins in the three groups was 10, 18, and 32, respectively; two weeks after the operation, the number of C-reactive protein in the three groups was 8, 14 and 18, respectively. Early rejection was confirmed by pathology.

Shown as in Figure 2, there was no significant difference in T lymphocyte subsets, serum complement, and circulating immune complex in group 4, but it was significantly higher than the average value in group 123. Before the operation, the X2 of T lymphocyte subsets, serum complement, and circulating immune complex were 52, 34, and 29, respectively; the X2 of T lymphocyte subsets, serum complement, and circulating immune complex were 53, 39, and 30, respectively, on the third day after the operation; and the X2 of T lymphocyte subsets, serum complement and

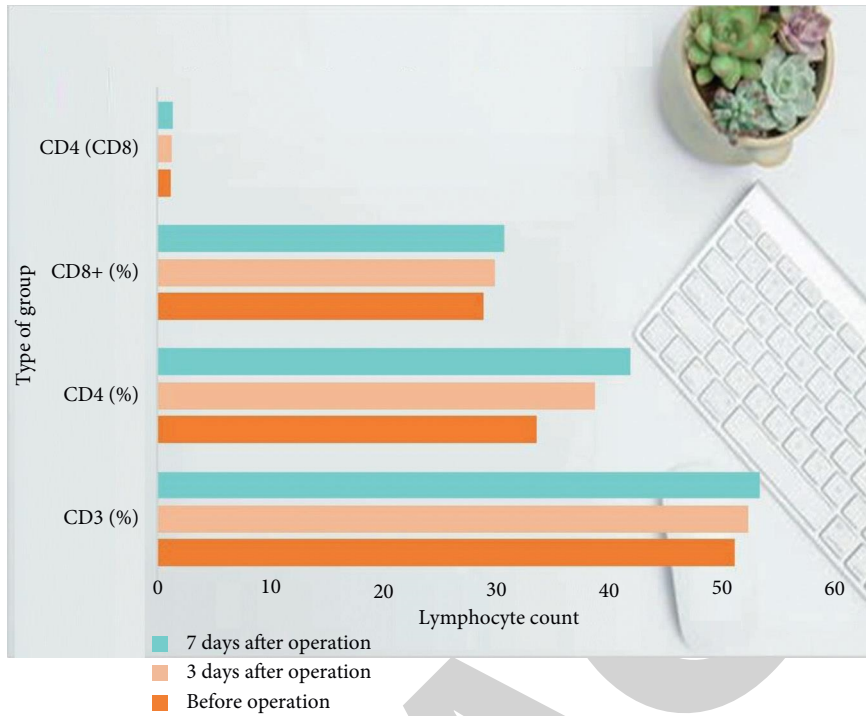


FIGURE 2: The changes of T lymphocyte before and after bone graft.

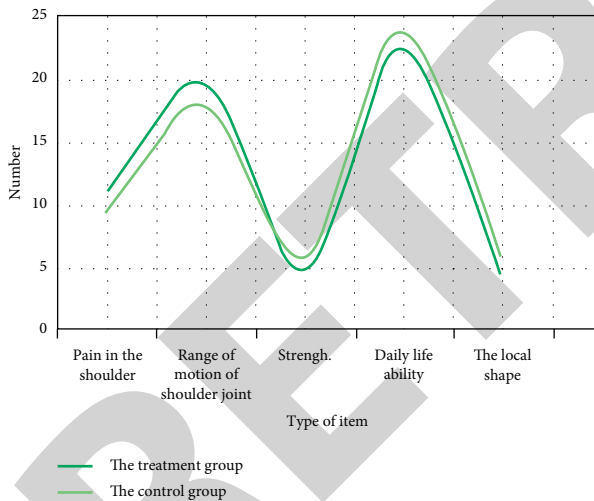


FIGURE 3: Comparison of clinical symptoms and evaluation scores between the two groups before treatment.

circulating immune complex on the third day after operation were 53, 39, and 30, respectively. Combined with clinical manifestations and pathological results, early rejection occurred.

**4.2. Application Research Results of Massage Exercise Rehabilitation Training in Patients with Limb Replantation.** Before treatment, the clinical symptoms and evaluation scores of the two groups were compared.

Shown as in Figure 3, there was no significant difference in clinical symptom scores (shoulder pain, shoulder joint

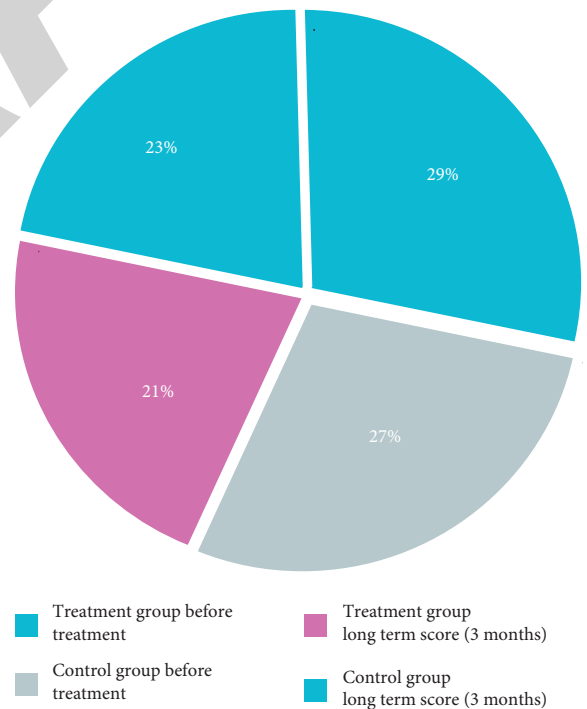


FIGURE 4: Comparison of visual pain scores between the two groups.

range of motion, muscle strength, activities of daily living, and local morphology) in the treatment group and the control group (shoulder pain, shoulder joint activity, muscle strength, activities of daily living, local morphology) before treatment.

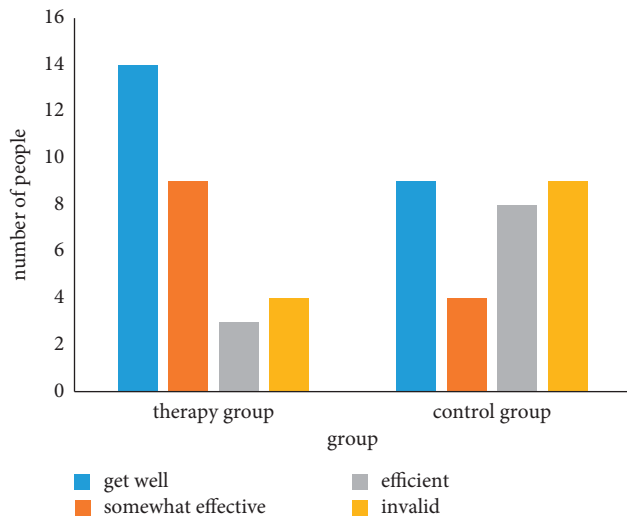


FIGURE 5: Histogram one and a half years after treatment.

The visual pain scores of the two groups were compared.

Shown as in Figure 4, the VAS scores of the two groups before treatment were compared: the score of the treatment group was 23%, the score of the control group was 21%, and the score of the treatment group was 2% higher than that of the control group; the VAS score of the treatment group was 29%, the score of the control group was 27%, and the score of the treatment group was 2% higher than that of the control group. Therefore, we can draw a conclusion that massage is better than conventional massage, massage exercise has a certain value, and should be widely used for clinical treatment.

The histogram one and a half years after treatment is shown in Figure 5.

According to the composite NanoBone graft and the comparative experiment of the two groups of patients in the replantation of severed limbs, the efficacy evaluation showed that the overall excellent rate of the treatment group was 85%, and that of the control group was 70%. The survival rate and overall excellent rate of the treatment group were significantly higher than those of the control group.

## 5. Conclusion

The composite of carbon nanotubes with inorganic materials, natural biodegradable polymer materials, and synthetic degradable polymer materials can be used to construct composite bone tissue engineering scaffolds by forming particle pores, thermally induced phase separation, microsphere aggregation, electrospinning, and three-dimensional printing. Carbon nanoscaffolds have significant effects on cell proliferation and bone regeneration. There was no significant difference in T lymphocyte subsets, serum complement, and circulating immune complex in the replantation of amputated limbs. Clinical observation and pathological examination showed that the patient had an early rejection in clinical and had a higher body temperature. The first group had a better response, and the second and third groups had obvious local responses. The first group is

type A, and the second and third groups are type B. Massage and massage can be effective in relieving pain, ability to live, shoulder function, and mobility in amputees. The characteristics of massage therapy are that it is not practical, the course of treatment is short, the effect is quick, the clinical operation is simple, and it is easy to master. It has a high clinical application and promotion value. This study is only to study the application of composite nanocomposite transplantation and massage rehabilitation training in patients receiving limb replantation. Although the experimental part is very detailed, it is not authoritative and the experimental sample is not large enough.

## Data Availability

No data were used to support this study.

## Conflicts of Interest

The authors declare that there are no conflicts of interest regarding the publication of this article.

## References

- [1] V. Glatt, N. Bartnikowski, N. Quirk, M. Schuetz, and C. Evans, "Reverse dynamization," *Journal of Bone and Joint Surgery*, vol. 98, no. 8, pp. 677–687, 2016.
- [2] B. H. Kim, H. W. Jung, S. H. Seo, H. Shin, J. Kwon, and J. M. Suh, "Synergistic actions of fgf2 and bone marrow transplantation mitigate radiation-induced intestinal injury," *Cell Death & Disease*, vol. 9, no. 3, pp. 383–388, 2018.
- [3] Y. Zhang, Y. Li, and C. Bai, "Microstructure and oxidation behavior of Si-MoSi 2 functionally graded coating on Mo substrate," *Ceramics International*, vol. 43, no. 8, pp. 6250–6256, 2017.
- [4] S. N. A. Aziz, "The regulation and influence of physical exercise on human body's neutrosophic set, respiratory system and nervous system," *International Journal of Neutrosophic Science*, vol. 18, no. 3, pp. 111–124, 2022.
- [5] M. W. J. L. Schmitz, G. Hannink, J. W. M. Gardeniers, N. Verdonschot, T. J. J. H. Slooff, and B. W. Schreurs, "Acetabular reconstructions with impaction bone-grafting and a cemented cup in patients younger than 50 Years of age," *Journal of Bone and Joint Surgery*, vol. 99, no. 19, pp. 1640–1646, 2017.
- [6] M. Kueckelhaus, S. Fischer, G. Sisk et al., "A mobile extracorporeal extremity salvage system for replantation and transplantation," *Annals of Plastic Surgery*, vol. 76, no. 3, pp. 355–360, 2016.
- [7] Y. Z. An, Y. K. Heo, J. S. Lee, U. W. Jung, and S. H. Choi, "Dehydrothermally cross-linked collagen membrane with a bone graft improves bone regeneration in a rat calvarial defect model," *Materials*, vol. 10, no. 8, pp. 927–934, 2017.
- [8] L. Zhang, A. Kubo, L. Wang, H. Petek, and T. Seideman, "Imaging of surface plasmon polariton fields excited at a nanometer-scale slit," *Physical Review B*, vol. 84, no. 24, pp. 245442–252468, 2011.
- [9] X. Xu, B. Karami, and D. Shahsavari, "Time-dependent behavior of porous curved nanobeam," *International Journal of Engineering Science*, vol. 160, Article ID 103455, 2021.
- [10] M. Hadjidemetriou and K. Kostarelos, "Evolution of the nanoparticle corona," *Nature Nanotechnology*, vol. 12, no. 4, pp. 288–290, 2017.

## *Retraction*

# **Retracted: An Improved Inverse Kinematics Solution for a Robot Arm Trajectory Using Multiple Adaptive Neuro-Fuzzy Inference Systems**

### **Advances in Materials Science and Engineering**

Received 26 December 2023; Accepted 26 December 2023; Published 29 December 2023

Copyright © 2023 Advances in Materials Science and Engineering. This is an open access article distributed under the Creative Commons Attribution License, which permits unrestricted use, distribution, and reproduction in any medium, provided the original work is properly cited.

This article has been retracted by Hindawi, as publisher, following an investigation undertaken by the publisher [1]. This investigation has uncovered evidence of systematic manipulation of the publication and peer-review process. We cannot, therefore, vouch for the reliability or integrity of this article.

Please note that this notice is intended solely to alert readers that the peer-review process of this article has been compromised.

Wiley and Hindawi regret that the usual quality checks did not identify these issues before publication and have since put additional measures in place to safeguard research integrity.

We wish to credit our Research Integrity and Research Publishing teams and anonymous and named external researchers and research integrity experts for contributing to this investigation.

The corresponding author, as the representative of all authors, has been given the opportunity to register their agreement or disagreement to this retraction. We have kept a record of any response received.

### **References**

- [1] M. R. A. Refaai, "An Improved Inverse Kinematics Solution for a Robot Arm Trajectory Using Multiple Adaptive Neuro-Fuzzy Inference Systems," *Advances in Materials Science and Engineering*, vol. 2022, Article ID 1413952, 12 pages, 2022.



## Research Article

# An Improved Inverse Kinematics Solution for a Robot Arm Trajectory Using Multiple Adaptive Neuro-Fuzzy Inference Systems

Mohamad Reda A. Refaai <sup>1,2</sup>

<sup>1</sup>Department of Mechanical Engineering, College of Engineering, Prince Sattam bin Abdulaziz University, Alkharj, 16273, Saudi Arabia

<sup>2</sup>Mechanical design department, Faculty of Mechanical and Electrical Engineering, Damascus University, Syria

Correspondence should be addressed to Mohamad Reda A. Refaai; [drrefaai@gmail.com](mailto:drrefaai@gmail.com)

Received 4 June 2022; Accepted 19 July 2022; Published 9 September 2022

Academic Editor: K. Raja

Copyright © 2022 Mohamad Reda A. Refaai. This is an open access article distributed under the Creative Commons Attribution License, which permits unrestricted use, distribution, and reproduction in any medium, provided the original work is properly cited.

Inverse kinematics of robots is a critical topic in the robotics field. Although there are conventional ways of solving inverse kinematics, soft computing is an important technology that has lately gained prominence due to its ability to reduce the complexity of the inverse kinematics problem. This paper presents an inverse kinematics solution using multiple adaptive neuro-fuzzy inference systems (MANFIS). Different models were established by employing various methods of identification. Subtractive Clustering (SCM), Fuzzy C-Means Clustering (FCM), and Grid Partitioning (GP) are the three methods used in this study. This work is being carried out on a 5-DOF articulated robot arm, which is commonly used in industry. A mathematical model is built based on the Denavit-Hartenberg (DH) approach. Following confirmation that the kinematic findings of the mathematical model match the actual observed values of the robot arm, two types of data sets are generated: a random data set and a systematic data set based on a trajectory. The data sets are then utilized to train and evaluate ANFIS models and choose the optimal models to develop MANFIS model. Thus, the prediction and experimental data are compared to assess the performance of the MANFIS model.

## 1. Introduction

Nowadays, industrial robots have played a great role in the manufacturing field and industries and are still taking an important position in the current modern industries [1, 2]. A robot manipulator is made up of a number of links joined by joints that allow for both rotation and linear motion. [3]. The study of kinematics is considered an essential part of robotics. The kinematics of robots is the study of robot motion regardless of force and torque [4]. The kinematics problem contains two subproblems: forward and inverse kinematics. In forward kinematics (FK), the location of the end-effector (position and orientation) is determined from the joints' variables, whereas the variables of joints are found from the location of the end-effector in inverse kinematics (IK) [5].

Whereas solving forward kinematics is relatively simple, solving inverse kinematics is a very difficult and complex task, owing to the problem's nonlinearity and the availability of alternative solutions. As a result, solving the inverse kinematics usually takes a long time and does not always lead to convergence [6]. There are numerous techniques for solving inverse kinematics. They are classified as conventional methods and soft computing methods. There are three types of conventional methods: geometric, algebraic, and iterative. Geometric methods ensure that the manipulator's first three joints have a closed-form solution, but it takes a long time for a solution. The main limitation of algebraic methods is the difficulty in obtaining solutions for closed-form manipulators. Iterative methods, on the other hand, avoid working with close singularities and may lead to a

single solution based on the starting point. On the other hand, soft computing methods offer a great deal of flexibility, owing to their ability to evolve and their approximation capability for nonlinear functions [7]. Soft computing finds solutions to actual problems while Artificial intelligence aims to create intelligent systems. AI is well suited for use in resolving problems in robotic systems [8]. Adaptive Neuro-Fuzzy Inference Systems (ANFIS) are a widely used technique in self-computing because they combine the information processing capabilities of Fuzzy Inference Systems (FIS) with the learning capabilities of neural networks to solve systems and it considers an efficient method to model, predict, and control complex engineering systems. As a result, it is able to deal with the nonlinearities and uncertainties inherent in robotic systems [7]. Many studies are concerned with solving the kinematics of robots using soft computing. Among these studies, in [9], authors developed a Neuro-Fuzzy solution for industrial robot arms. It is demonstrated in their research that a fuzzy inference system can be developed using a neural network structure and that an ANFIS model can learn from training data. [10] presented a methodology to control the trajectory of a 2 DOF robotic arm using a Neuro-Fuzzy system. A mathematical model was established for an articulate. In [11], authors proposed a method to solve control and learning problems using fuzzy neural networks for 2-DOF industrial manipulators, and the model gave good tracking results for robots to analyze kinematics and compare it with experimental results. In [12], the authors developed a new design for a Cartesian-based artificial neural network controller. In some ways, the proposed design enhances the efficiency of the end effector. In [7], the inverse kinematics problem has been solved using neuro-fuzzy systems for the 4 DOF IRIS robot "ANFIS," which implements neural network systems for automatic parameter tuning of fuzzy systems. In [11], authors proposed a method to solve control and learning problems using fuzzy neural networks for 2 DOF industrial manipulators, and the model gave good tracking results. [13] proposed an inverse kinematics solution for a planar robot arm, which is used in drawing with 2 DOF based on the ANFIS. The proposed model was tested with experimental results, and the results were analyzed. In [14], authors used optimization algorithms to improve the results of solving inverse kinematics for a 3 DOF robot. In [15], authors established an inverse kinematics solution based on ANFIS paper. They described a three-dimensional plane manipulator as a way to maximize the effectiveness of this approach. The forward kinematics data are used to calculate the inverse kinematics, and the accuracy of the various joint angles is accepted. [16] presented a solution for solving the inverse kinematics of SCARA robots and significant results for manipulator kinematics using multiple ANFIS systems. In [17], authors improved a methodology for solving the forward kinematics of 6 DOF arm. The ANN structure was used to control the motion of a robot arm. Numerous neural network models employ sigmoid transfer functions and gradient descent learning methods. The learning formulae were a back propagation algorithm. In [18], authors propose a new forward adaptive neural model for modeling and defining

the forward kinematics of 3DOF robot arm. The results reveal that the suggested adaptive neural model, which was trained using a back propagation learning algorithm, performs admirably and with complete accuracy.

## 2. Materials and Methods

This study was applied to a five-axis articulated robot (Scorbot ER 5u-Plus). Figure 1 illustrates the studied robot, which includes Axis 1: Base to rotate the robot's body. Axis 2: Shoulder to raise, lowering the upper arm. Axis 3: Elbow to raise and lower the forearm Axis 4: Wrist Pitch is used to raise and lower the end-effector (Gripper). Axis 5: Wrist Roll to rotate the end effector.

**2.1. Kinematics of Robot Manipulator.** The Denavit-Hartenberg (DH) method is the most common traditional way to build manipulator models from links and joint parameters [19]. The frames are assigned starting from the base frame and progressing to the end-effector frame using a homogeneous coordinate transformation matrix. The DH parameters used are  $\theta_i$  (joint angle),  $\alpha_i$  (link twist angle),  $\ell_i$  (length of link), and finally  $d_i$  (distance between joints), and the transformation matrix is represented by the (1) [20].

$$T_i^{i-1} = \begin{bmatrix} \cos \theta_i & -\sin \theta_i & \sin \theta_i \sin \alpha_i & \ell_i \cos \theta_i \\ \sin \theta_i & \cos \theta_i & -\cos \theta_i \sin \alpha_i & \ell_i \sin \theta_i \\ 0 & \sin \alpha_i & \cos \alpha_i & d_i \\ 0 & 0 & 0 & 1 \end{bmatrix}. \quad (1)$$

Figure 2 shows assigning of DH parameters [21].

Table 1 shows DH parameters. The lengths are given in millimeters, and the angles are given in Radian.

For each link, an individual transformation matrix can be created by inserting the DH parameters from Table 1 into the homogeneous transformation matrix (1). The following equations are transformation matrices for each link [22].

$$A_1 = \begin{bmatrix} \cos \theta_1 & 0 & \sin \theta_1 & \ell_1 \cos \theta_1 \\ \sin \theta_1 & 0 & -\cos \theta_1 & \ell_1 \sin \theta_1 \\ 0 & 1 & 1 & d_1 \\ 0 & 0 & 0 & 1 \end{bmatrix}, \quad (2)$$

$$A_2 = \begin{bmatrix} \cos \theta_2 & -\sin \theta_2 & 0 & \ell_2 \cos \theta_2 \\ \sin \theta_2 & \cos \theta_2 & 0 & \ell_2 \sin \theta_2 \\ 0 & 0 & 1 & 0 \\ 0 & 0 & 0 & 1 \end{bmatrix}, \quad (3)$$

$$A_3 = \begin{bmatrix} \cos \theta_3 & -\sin \theta_3 & 0 & \ell_3 \cos \theta_3 \\ \sin \theta_3 & \cos \theta_3 & 0 & \ell_3 \sin \theta_3 \\ 0 & 0 & 1 & 0 \\ 0 & 0 & 0 & 1 \end{bmatrix}, \quad (4)$$

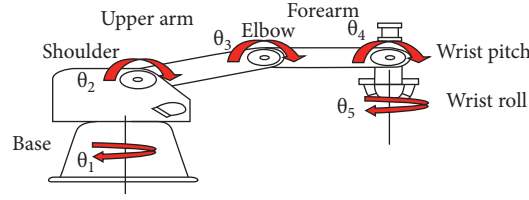


FIGURE 1: 5 DOF articulated robot.

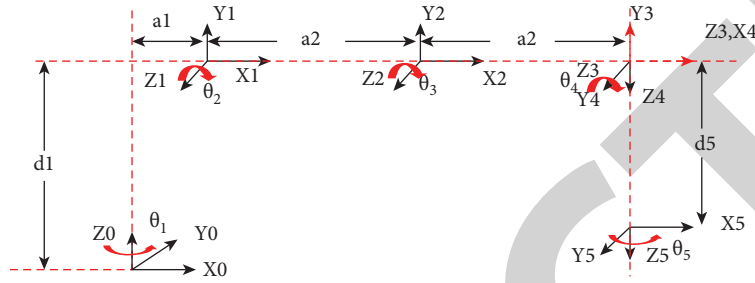


FIGURE 2: DH parameters assigned.

TABLE 1: DH parameters.

Joint $i$	$\theta_i$ (rad)	$l_i$ (mm)	$d_i$ (mm)	$a_i$ (rad)
1	$\Theta_1$	$a_1 = 16$	349	$\pi/2$
2	$\Theta_2$	$a_2 = 221$	0	0
3	$\Theta_3$	$a_3 = 221$	0	0
4	$\Theta_4$	0	0	$\pi/2$
5	$\Theta_5$	0	145	0

**2.2. ANFIS Architecture.** The Adaptive Neuro-Fuzzy Inference System is being used to achieve the best advantages of Artificial Neural Networks (ANN) and Fuzzy Inference Systems (FIS) [24]. ANFIS has five layers [25]:

(i) The Node Layer

The membership degree of inputs is calculated and passed to membership layer in this layer [10].

$$O_i^1 = R_i(x_i), \quad (8)$$

where  $R_i$  can be used with any Fuzzy Membership Function (MF)

(ii) The Membership Layer

This layer determines the firing strengths of every rule as a product of all membership functions. In this layer, Neurons layer implements fuzzification.

$$O_i^2 = W_i = \min(R_i), \quad (9)$$

where  $W_i$  denotes a rule's activation level.

(iii) The Rule Layer

The normalized firing strength is calculated in this layer using the equation Normalization layer below [11].

$$O_i^3 = \overline{W_i} = \frac{W_i}{\sum_i W_i}, \quad (10)$$

where  $\overline{W_i}$  signifies normalized firing strength

(iv) The Defuzzification Layer

In this layer, the weighted consequent values are calculated and defuzzification values are returned to the final layer.

$$A_4 = \begin{bmatrix} \cos \theta_4 & 0 & \sin \theta_4 & 0 \\ \sin \theta_4 & 0 & -\cos \theta_4 & 0 \\ 0 & 1 & 0 & 0 \\ 0 & 0 & 0 & 1 \end{bmatrix}, \quad (5)$$

$$A_5 = \begin{bmatrix} \cos \theta_5 & -\sin \theta_5 & 0 & 0 \\ \sin \theta_5 & \cos \theta_5 & 0 & 0 \\ 0 & 0 & 1 & d_5 \\ 0 & 0 & 0 & 1 \end{bmatrix}. \quad (6)$$

By multiplying all of the separate transformation matrices (2), (3), (4), (5), and (6) as shown in equation (7), the general transformation matrix from the base frame to the end-effector  ${}^0T^5$  is represented by:

$${}^0T^5 = A_1 A_2 A_3 A_4 A_5 = \begin{bmatrix} n_x & o_x & a_x & p_x \\ n_y & o_y & a_y & p_y \\ n_z & o_z & a_z & p_z \\ 0 & 0 & 0 & 1 \end{bmatrix}, \quad (7)$$

where  $(p_x, p_y, p_z)$ ,  $(n, o, a)$  denote the end-effectors' position and orientation [23].

$$O_i^4 = \overline{WiKi} = \overline{Wi}(ri + si z + qi y + pi x), \quad (11)$$

$\overline{Wi}$  denotes an output of layer 3

(v) The Output Layer

The prior layers are gathered and calculated the entire output of the system [26, 27].

$$O_i^5 = \overline{WiKi} = \frac{\sum_i \overline{WiKi}}{\sum_i Wi}. \quad (12)$$

ANFIS architecture with five layers and nodes is shown in Figure 3 [16].

Layers 2, 3, and 5 are fixed, whereas layers 1, 4, and 5 are adaptive. The ANFIS approach is basically divided into two major steps. Training the data is the first step, and the second step is validating the model. Different identification methods are utilized to determine the membership functions of ANFIS. Used in this study are Fuzzy C-Means Clustering, the Subtractive Clustering method, and the Grid Partitioning approach.

**2.2.1. Subtractive Clustering Method SCM.** This algorithm estimates cluster numbers and their locations automatically [28]. SCM considers a fast clustering method for a moderate amount of data with high-dimension problems. The steps of this method are as follow:

- (i) Take a set of  $n$  data points in an  $m$ -dimensional space and choose the data point with the largest potential as the first group's center. Equation can be used to calculate the density  $D_i$  at data point  $X_i$ . 13:

$$D_i = \sum_{j=1}^n \exp \left[ \frac{\|xi - xj\|^2}{(r_a/2)} \right], \quad (13)$$

where  $n$  is the number of data points for  $X$ ,  $r_a$  is a positive constant.

The first cluster is chosen from the data point with the highest density value. Assume that  $Xc1$  is the chosen point and that  $Dc1$  is the density value. The density value for each data point  $x_i$  is then recalculated using equation (14):

$$D_i = D_i - D_{ci} \exp \left[ \frac{\|xi - xj\|^2}{(r_b/2)} \right], \quad (14)$$

$r_b$  denotes a positive constant.

The subsequent cluster center,  $Xc2$ , is selected, and all data point density estimates are recalculated. This procedure is repeated till an adequate number of cluster centers exists [29].

**2.2.2. Fuzzy C-Means Clustering FCM.** This algorithm was proposed by Bezdek [30]. Each data point belongs to a cluster based on the membership degree in this method. The main steps of this algorithm start by finding the cluster

center by dividing a group of  $n$  vectors  $x_i$ ,  $i = 1, 2, 3, \dots, n$  into fuzzy classes with the minimum dissimilarity value using the cost function. The cluster center  $c_i$ ,  $i = 1, 2, 3$ ,  $c$  is chosen at random from a set of  $n$  points  $x_1, x_2, x_3, \dots, x_n$ . The minimize function on the membership matrix is then calculated using the following equations. Each data point in this method is assigned to a cluster based on its membership degree. The main steps of this algorithm start by finding the cluster center by dividing a group of  $n$  vectors  $x_i$ ,  $i = 1, 2, 3, \dots, n$  into fuzzy classes with the minimum dissimilarity value using the cost function. The cluster center  $c_i$ ,  $i = 1, 2, 3$ ,  $c$  is chosen at random from a set of  $n$  points  $x_1, x_2, x_3, \dots, x_n$ . Then, calculate the minimize function for the membership matrix using the following equations:

$$\mu_{ij} = \frac{1}{\sum_{k=1}^c (d_{ijk})^{2/m-1}}, \quad (15)$$

where  $d_{ij} = \|c_i - x_j\|$  is the deviation between the  $i$ th cluster center and the  $j$ th data point, whereas  $m$  is the index of fuzziness. Then, the function of cost can be obtained using the following equation, and the process continues if it is less than a certain threshold [31].

$$J(U, c_1, \dots, c_2) = \sum_{i=1}^c J_i = \sum_{i=1}^c \sum_{j=1}^n \mu_{ij}^m d_{ij}^2. \quad (16)$$

Finally, the new fuzzy cluster centers are calculated using equation (17):

$$c_i = \frac{\sum_{j=1}^n \mu_{ij}^m x_j}{\sum_{j=1}^n \mu_{ij}^m}. \quad (17)$$

**2.2.3. Grid Partitioning Approach GP.** The input data space is divided into numerous rectangular subspaces with this method. This process is carried out through axis-parallel partitioning, which is based on the features of specified membership functions (MFs). The number of MFs and their types in each dimension are considered among the characteristics of the membership function. The main obstacle to using this method is dimensions. In other words, the number of rules is increasing exponentially by increasing the number of inputs. Therefore, the size of inputs and the grid have a big impact on the GP model's performance [32].

**2.3. Methodology.** The methodology used in this work starts by building a mathematical model depending on the configuration of a robot using DH parameters, which is considered the conventional method. After making sure that the results of the mathematical model and experimental results were corresponding, data sets were generated for training and testing ANFIS. After that, ANFIS with different algorithms, SCM, FCM, and GP model were built. Finally, the results of all the models are evaluated. Figure 4 shows the steps of this work.

Equations (1)–(7) were used to create a mathematical model in Matlab for studying the kinematics of robot. Then,

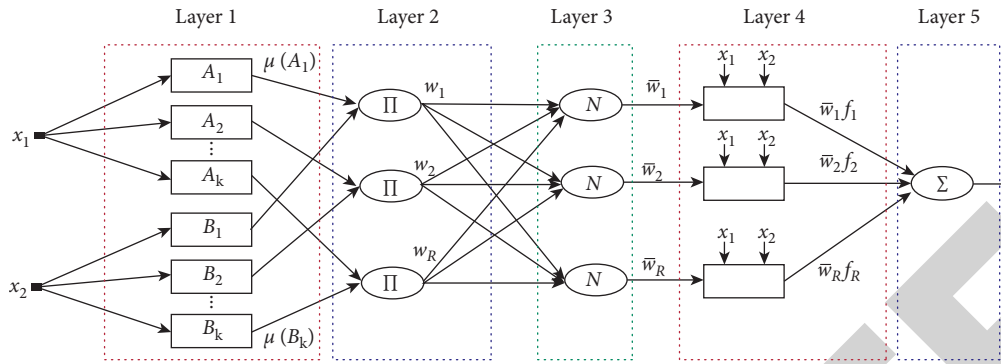


FIGURE 3: ANFIS architecture.

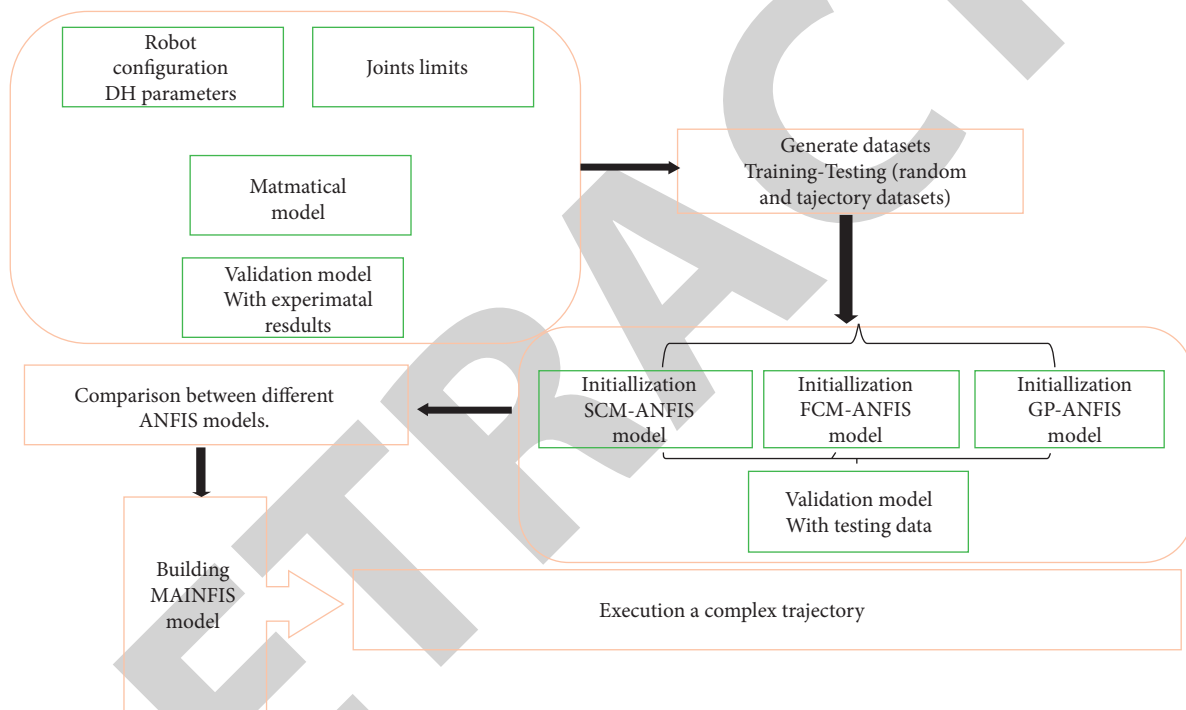


FIGURE 4: Overview of the work steps.

the results of the mathematical model and the practical results of the real robot were validated. Figure 5 illustrates comparison experiments between a mathematical model and a real robot in three positions as samples of the validation process.

2.4. Modeling. Multi outputs An Adaptive Neuro-Fuzzy Inference System is being used for solving problems that have multiple outputs. In this work, there are six inputs and five outputs. The inputs of the system are the positions ( $P_x, P_y$ , and  $P_z$ ) and ( $\theta_x, \theta_y$ , and  $\theta_z$ ) are the orientations of the end-effector. The angles  $\theta_x, \theta_y$ , and  $\theta_z$  represent roll,

pitch, and yaw angles. All of the input values are collected from the results of kinematics modeling for the studied robot. The outputs of the system are  $\theta_1, \theta_2, \theta_3, \theta_4$ , and which represent the joints of the robot. Figure 6 shows the MANFIS architecture, which was used for modeling the robot [23].

The data sets were generated by changing the angles of the manipulator's joints within certain ranges to get data which connected the joint variables and the end-effector. The data set size was determined by comparing it to the data sets used in previous studies [6]. There are 10,000 data sets generated for training based on the mathematical model, with 20% of them used to test and evaluate the model's

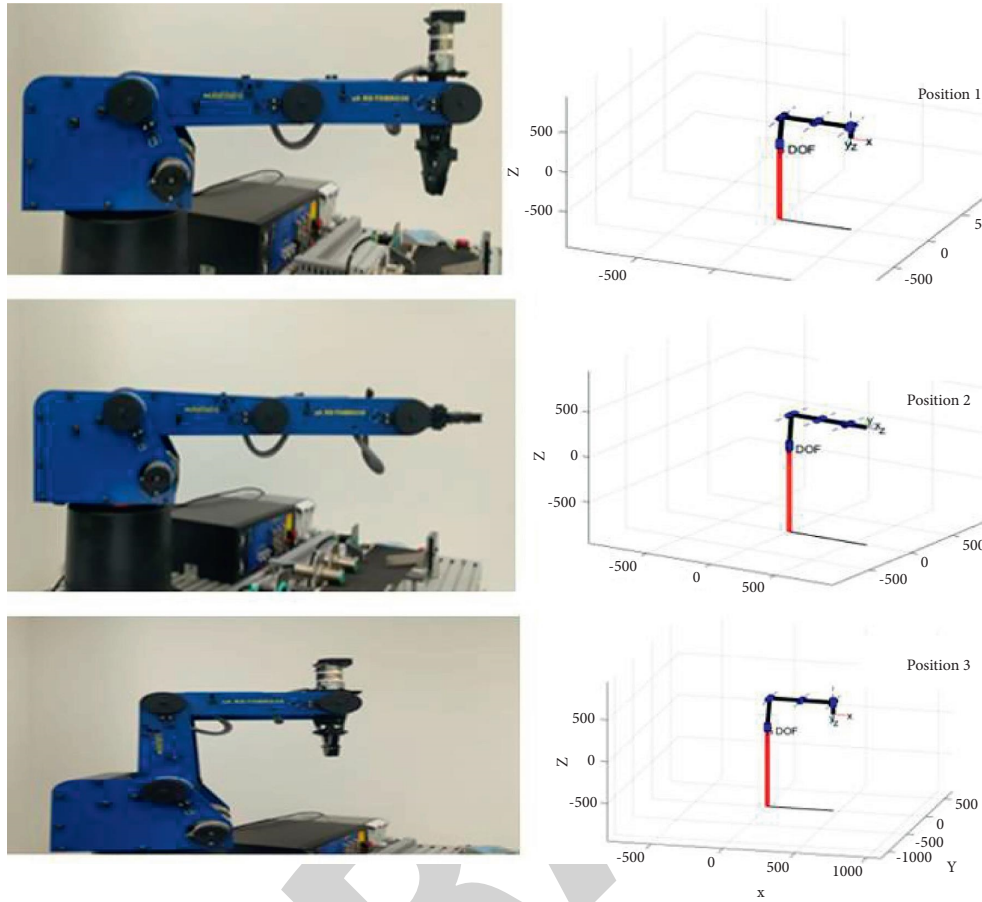


FIGURE 5: Mathematical model validation experiments.

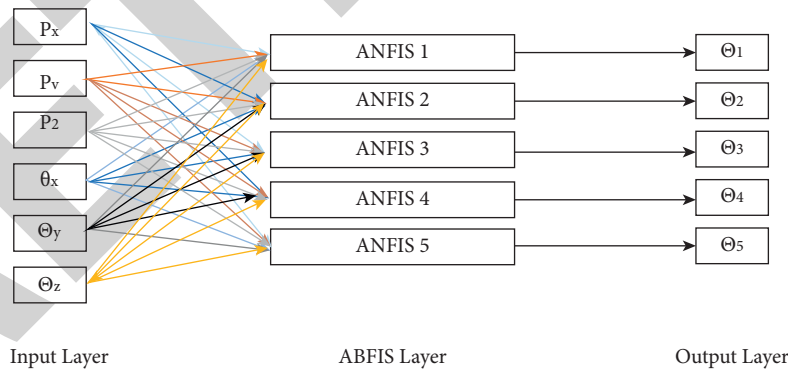


FIGURE 6: MANFIS structure.

performance. It is preferable to start by implementing preprocessing steps to ensure the data set quality and get initial acceptable results. Each ANFIS model has been built using three different algorithms: SCM, FCM, and GP. The following table summarizes the main parameters of each ANFIS method for  $\theta_1, \theta_2, \theta_3, \theta_4,$  and  $\theta_5$ , respectively. Based on the initial results of training, the acceptable error has been reached after 100 epochs. Therefore, the number of executed epochs was 100 in the training of different ANFIS models for  $\theta_1, \theta_2, \theta_3, \theta_4,$  and  $\theta_5$ . Table 2 clarifies that the parameters of

TABLE 2: Parameters of ANFIS structure.

ANFIS (numbers)	ANFIS (FCM)	ANFIS (SCM)	ANFIS (GP)
Nodes	219	275,233,241,247.98	1503
Fuzzy rules	15	19,16,17,13,14	729
Linear parameters	105	133,112,96,91,98	729
Nonlinear parameters	180	228,192,170,156,182	36



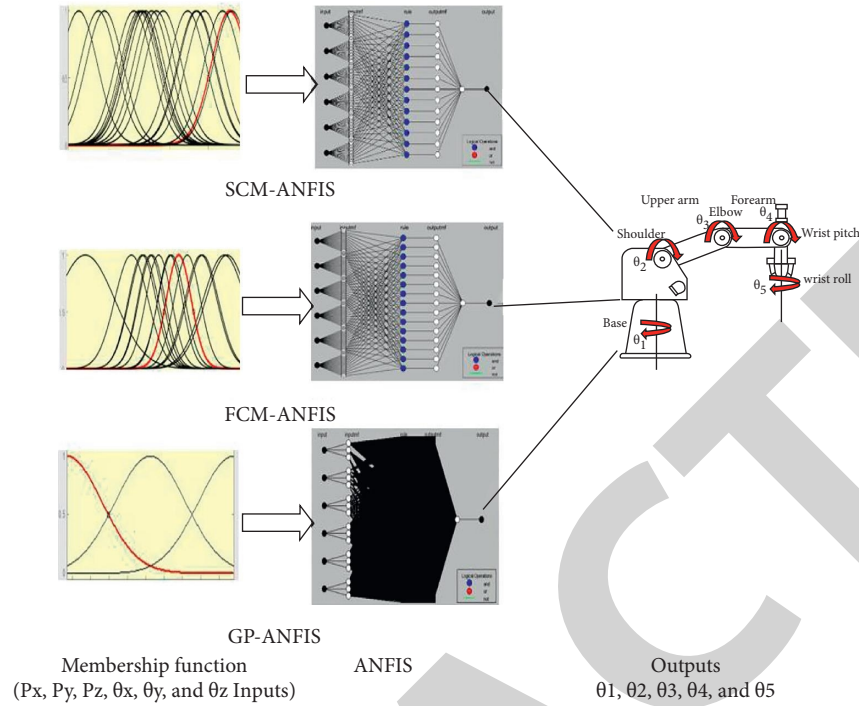


FIGURE 7: Applied MANFIS structure.

TABLE 3: Results of ANFIS models (RMSE = rad, MSE = rad<sup>2</sup>).

ANFIS Joint	SCM				FCM				GP			
	Training RMSE	Testing RMSE	Testing MSE	Testing $R^2$	Training RMSE	Testing RMSE	Testing MSE	Testing $R^2$	Training RMSE	Testing RMSE	Testing MSE	Testing $R^2$
Θ1	0.1257	0.1272	0.01618	0.9888	0.1596	0.1469	0.0215	0.98551	0.1978	0.1904	0.0361	0.97532
Θ2	0.2700	0.2720	0.0740	0.906	0.2631	0.0745	0.2729	0.902	0.2539	0.24468	0.05988	0.96412
Θ3	0.3105	0.5477	0.2999	0.77059	0.2772	0.5033	0.25331	0.82261	0.11781	0.3547	0.1258	0.9171
Θ4	0.3440	0.3434	0.1179	0.92265	0.3298	0.3255	0.10598	0.9288	0.2753	0.26149	0.06837	0.9587
Θ5	0.04961	0.2159	0.046625	0.97171	0.2298	0.22503	0.06266	0.96117	0.2699	0.2261	0.051121	0.96123

the ANFIS model change for  $\theta_1, \theta_2, \theta_3, \theta_4,$  and  $\theta_5$  based on the data set.

The previous Table 2 clarifies that the parameters of the ANFIS model change for  $\theta_1, \theta_2, \theta_3, \theta_4,$  and  $\theta_5$  based on the data set. The number of fuzzy rules is high for GP compared to FCM and SCM. Figure 7 shows different ANFIS structures.

### 3. Results and Discussion

The Mean Squared Error (MSE), Root Mean Square Error (RMSE), and squared correlation coefficient are used to evaluate the efficacy of various ANFIS algorithms, which measure the accuracy between predicted and true values ( $R^2$ ). The model with the highest  $R^2$  and the smallest RMSE is considered the best. The optimization of the model results was carried out to ascertain the optimal model [33]. The performance criteria for N samples could be calculated as follows:

$$\begin{aligned}
 RMSE &= \sqrt{\frac{1}{N} \sum_{i=1}^N (\gamma_i - \gamma'_i)^2} \\
 MSE &= \frac{1}{N} \sum_{i=1}^N (\gamma_i - \gamma'_i)^2 \quad (18) \\
 R^2 &= 1 - \frac{\sum_{i=1}^n (\gamma_i - \gamma'_i)^2}{\sum_{i=1}^n (\gamma_i - \bar{\gamma}')^2}
 \end{aligned}$$

$\gamma_i, \gamma'_i,$  and  $\bar{\gamma}'$  represent observed, predicted and the mean value of the  $\gamma_i$  ( $\gamma'_i$ ). For each ANFIS system, two data sets were utilized to assess mode performance. The first data set was taken randomly for different end-effector positions, and the second data set was taken to perform a trajectory. Table 3 represents the results of different ANFIS models for random

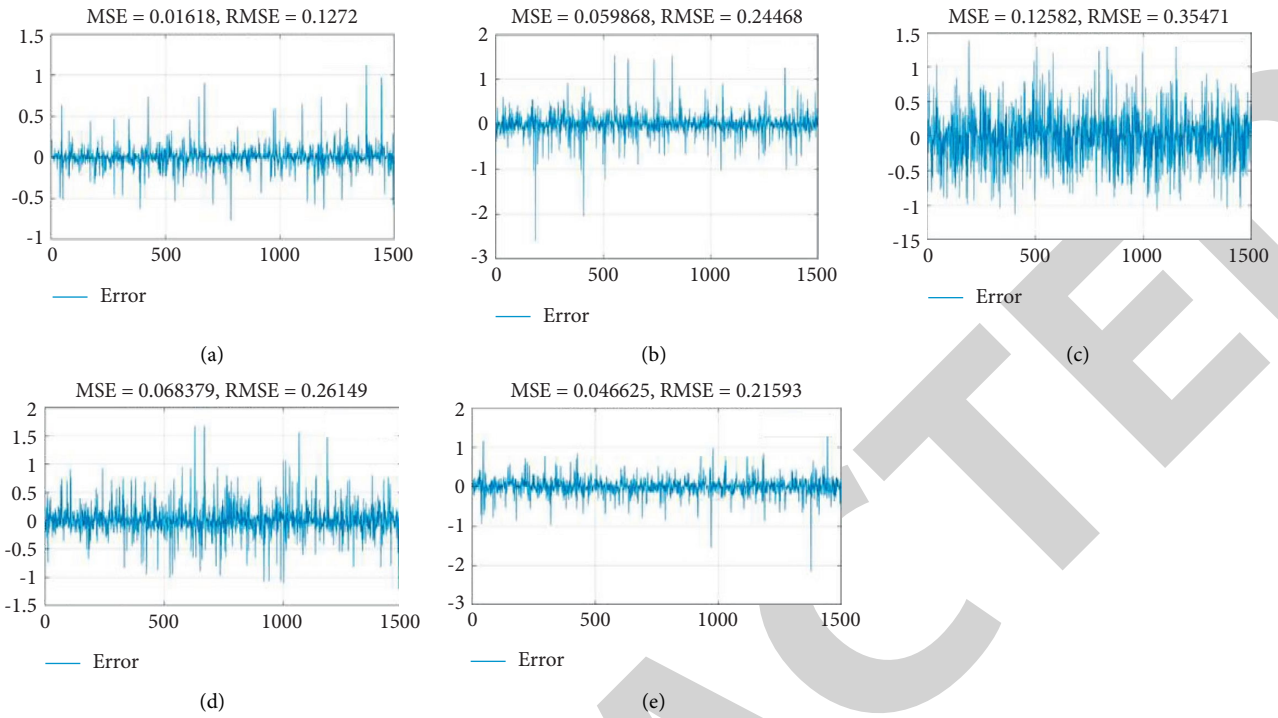


FIGURE 8: Best error results. (a) SCM-ANFIS for joint 1; (b) GP-ANFIS for joint 2; (c) GP-ANFIS for joint 3; (d) GP-ANFIS for joint 4; (e) GP-ANFIS for joint 5.

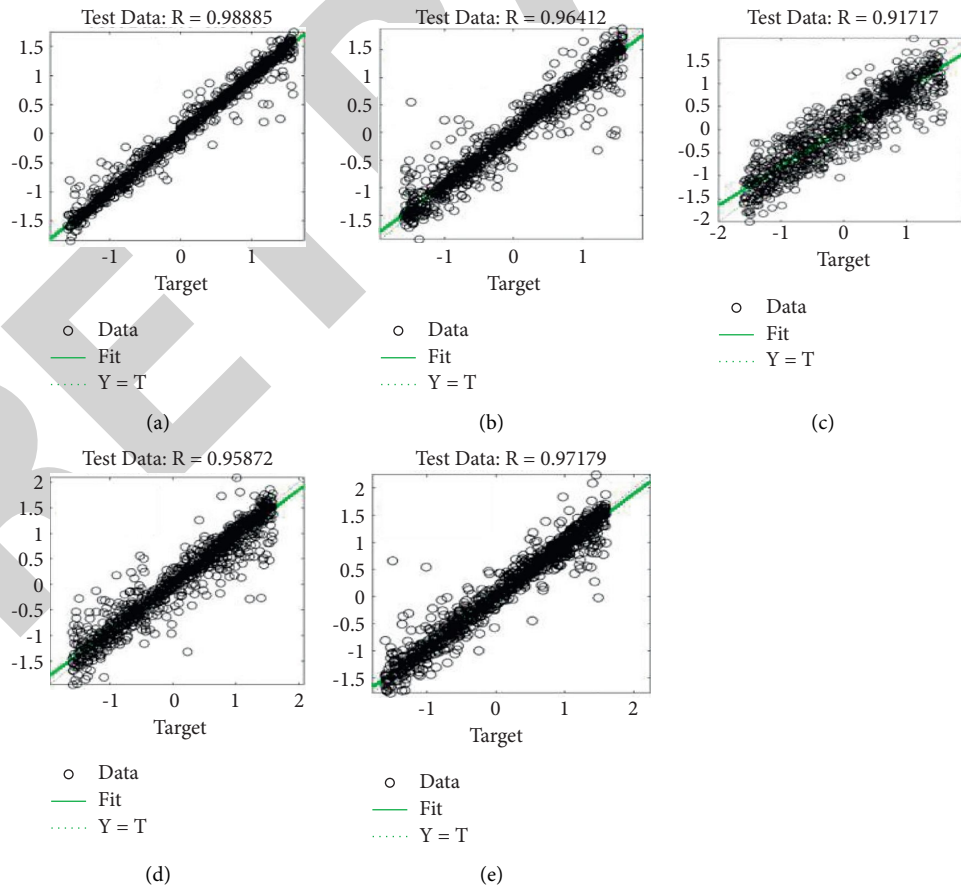


FIGURE 9: Best correlation results between predicted and measured values. (a) SCM-ANFIS for joint 1; (b) GP-ANFIS for joint 2; (c) GP-ANFIS for joint 3; (d) GP-ANFIS for joint 4; (e) GP-ANFIS for joint 5.

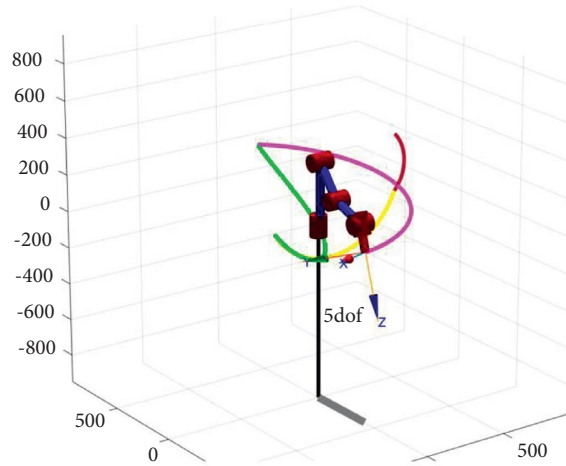


FIGURE 10: Trajectory of the robot.

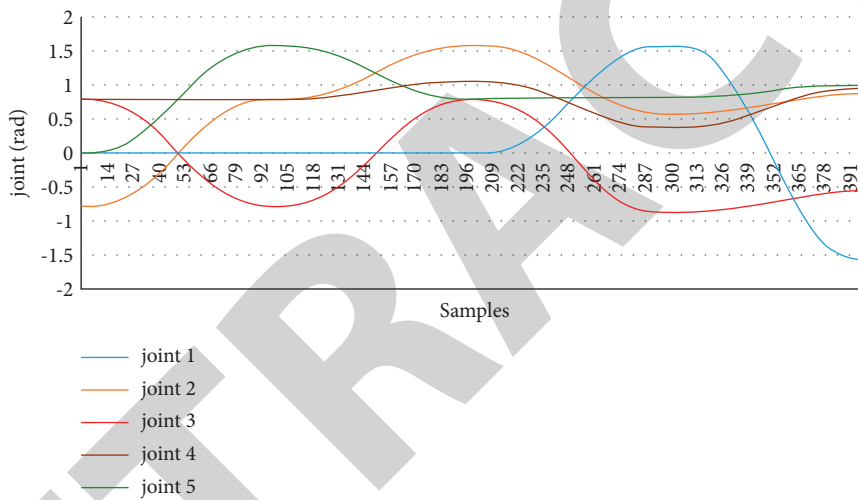


FIGURE 11: Angular values of the joints ( $\theta_i$ ) to perform the trajectory.

testing data [31]. Table 3 contains the Root Mean Square Error for the training data set and the results of RMSE, MSE, and  $R^2$  for the test data set.

The results of different ANFIS methods show that accuracy varies according to the used algorithm and the entered data set. By analyzing the RMSE and  $R^2$  of all methods, the best predictive performance of all joints is SCM, GP, GP, GP, and SCM for joints 1, 2, 3, 4, and 5, respectively. As it can be observed, the best RMSE with the lowest value for each method is 0.1272, 0.24468, 0.3547, 0.26149, and 0.2159, respectively. Figure 8 shows the best error results for  $\theta_1$ ,  $\theta_2$ ,  $\theta_3$ ,  $\theta_4$ , and  $\theta_5$ .

The second criterion used to evaluate the models is the correlation coefficient  $R^2$ . The best  $R^2$  results for all methods for joints are 0.9888, 0.9641, 0.91717, 0.9581, and 0.97179 for 1,  $\theta_2$ ,  $\theta_3$ ,  $\theta_4$ , and  $\theta_5$ , respectively. The correlation coefficient results reflect a strong correlation between the prediction results and the experimental results. These results indicate that the models provide acceptable results for the random data test. For all joints, Figure 9 illustrates the best correlation findings between measured and predicted values.

The second data set was generated to perform a complex trajectory in space. The main justifications for selecting this trajectory are to perform interpolated curves through the X, Y, and Z axes and to cover the majority of the joints range. The trajectory passes through five points, and each path between two consecutive points is divided into 100 samples to get a smoother curve. Figure 10 shows the trajectory of the robot end-effector, which is applied to check the performance of the ANFIS model. The four colors of the trajectory represent four sub-trajectories that pass through five points.

The next step is to use the mathematical model built in MATLAB to solve the inverse kinematics for the test trajectory. About 400 data sets representing the variables of the joints were obtained. Figure 11 shows the angular values of joints needed to execute the trajectory based on the mathematical model.

As shown in Figure 11, the path includes a wide range of joint angles to perform the complex trajectory, with the first joint being between  $-\pi$  and  $\pi$ , the second joint between  $-\pi/2$  and  $\pi$ , the third joint between  $-0.879$  and  $\pi/2$ , the fourth between 0.376 and 1.0476, and the fifth joint between 0 and

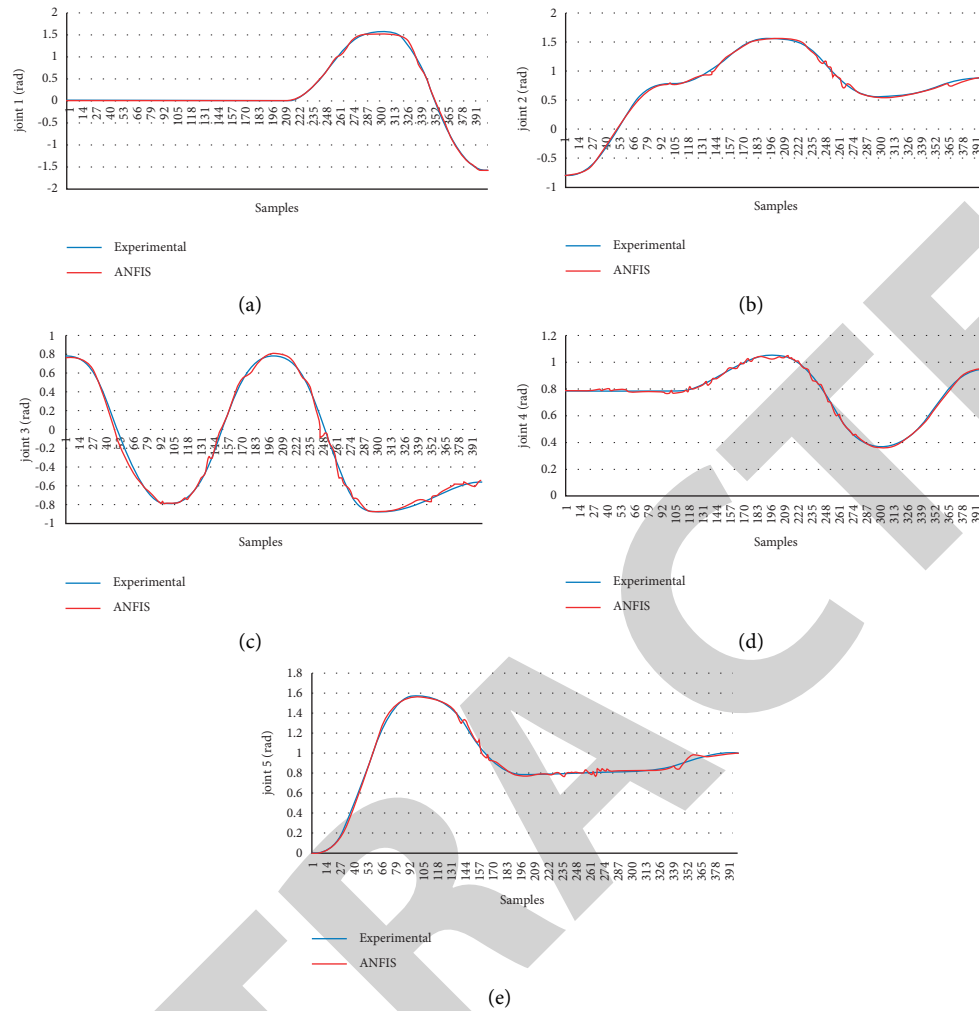


FIGURE 12: Comparison between predictive and experimental results (a) SCM-ANFIS for joint 1; (b) GP-ANFIS for joint 2; (c) GP-ANFIS for joint 3; (d) GP-ANFIS for joint 4; (e) GP-ANFIS for joint 5.

$\pi$ . The best ANFIS models were selected to perform the complex trajectory based on the results of a random data set. The applied methods for each joint are as follows: SCM-ANFIS for joint 1, GP-ANFIS for joint 2, GP-ANFIS for joint 3, GP-ANFIS for joint 4, and SCM-ANFIS for joint 5. By applying ANFIS models, the angular values were determined to perform the end-effector's trajectory. Figure 12 shows the comparison between ANFIS results and experimental results for performing a trajectory for  $\theta_1$ ,  $\theta_2$ ,  $\theta_3$ ,  $\theta_4$ , and  $\theta_5$ , respectively.

To briefly summarize the results so far: The three ANFIS models' training and testing procedures have been accomplished. All ANFIS methods provide different levels of accuracy for the same data. The number of fuzzy rules in GP-ANFIS is clearly the highest compared to the other methods since the number of rules is related to the input number. As a result, GP-ANFIS training takes much longer than other training methods, and in this study, SCM and FCM take very close time in terms of overall training speed. The

membership function changes according to the model and training data set. The results of SCM-ANFIS and FCM-ANFIS are close, but the performance of SCM-ANFIS is the best. The squared correlation coefficient exceeds 0.9, which means that the ANFIS methods are considered sufficient to solve the inverse kinematics of industrial robots. When comparing the accuracy of FCM-ANFIS with the other two approaches, Fuzzy C-Means Clustering FCM is the least accurate. Therefore, the methods SCM-ANFIS and GP-ANFIS were applied. The MANFIS structure was constructed based on the comparison of the accuracy of the different models. The ANFIS models of MANFIS are SCM, GP, GP, GP, and SCM. The squared correlation coefficients for the ANFIS model are 0.9888, 0.9641, 0.91717, 0.9587, and 0.97179, respectively. Consequently, the MANFIS model provided excellent results for testing the random data set. When the MANFIS model was applied to a complex trajectory, it can be noticed from Figure 12 that the trajectory of

the joints (joint angles) for the prediction and experiment for each joint is extremely consistent for each joint, although there are some oscillations.

#### 4. Conclusions

Inverse kinematics is one of the most difficult challenges in robotics, especially as the number of degrees of freedom increases. The use of soft-computing methods is very efficient as it provides agreeable solutions with a [25] higher speed for solving inverse kinematics. The accuracy level of the prediction results is acceptable depending on the application and the field [26] of robot used. In this paper, it is proposed to use different adaptive neuro-fuzzy inference systems to solve the inverse kinematics of a 5 DOF articulated robot. The main reason for using the ANFIS system was to combine the properties of neural networks and FLC. In the systems with multiple outputs, multiple adaptive neuro-fuzzy networks are applied as in this work. The ANFIS model's performance depends on the ANFIS algorithm, the parameters of the ANFIS network, and the data set. The performance of the MANFIS model is improved by selecting the best accuracy of different ANFIS methods instead of using the conventional method, where the same method is used for all ANFIS models. The results of this work show that the regression analysis gave acceptable results for the random data set. Moreover, when the results of MANFIS for a certain trajectory are compared to the experimental results for that trajectory, it shows that the trajectory for each joint of the robot is very close to the experimental trajectory.

#### Data Availability

The data used to support the study's findings are included in the article. Upon request, the corresponding author can provide additional data or information.

#### Conflicts of Interest

The authors declare that there are no conflicts of interest regarding the publication of this article.

#### Acknowledgments

This project was supported by the Deanship of Scientific Research at Prince Sattam Bin Abdulaziz University under the research project (PSAU-2022/01/19997).

#### References

- [1] W. T. Asheber and C. Y. Lin, "Mechatronics design of intelligent robotic gripper," *Key Engineering Materials*, vol. 649, pp. 14–21, 2015.
- [2] J. Li, A. Ito, H. Yaguchi, and Y. Maeda, "Simultaneous kinematic calibration, localization, and mapping (SKCLAM) for industrial robot manipulators," *Advanced Robotics*, vol. 33, no. 23, pp. 1225–1234, 2019.
- [3] S. Alavandar and M. J. Nigam, "Neuro-fuzzy based approach for inverse kinematics solution of industrial robot manipulators," *International Journal of Computers, Communications & Control*, vol. 3, no. 3, pp. 224–234, 2008.
- [4] E. Sariyildiz, K. Ucak, K. Ohnishi, G. Oke, and H. Temeltas, "Intelligent systems based solutions for the kinematics problem of the industrial robot arms," in *Proceedings of the 2013 9th Asian Control Conference, ASCC*, pp. 1–6, Istanbul, July, 2013.
- [5] A.-V. Duka, "ANFIS based solution to the inverse kinematics of a 3DOF planar manipulator," *Procedia Technology*, vol. 19, pp. 526–533, 2015.
- [6] A. El-Sherbiny, M. A. Elhosseini, and A. Y. Haikal, "A comparative study of soft computing methods to solve inverse kinematics problem," *Ain Shams Engineering Journal*, vol. 9, no. 4, pp. 2535–2548, 2018.
- [7] M. T. Hussein, A. S. Gafer, and E. Z. Fadhel, "Robot manipulator inverse kinematics using adaptive neuro-fuzzy inference system," in *Proceedings of the 2012 12th International Conference on Control Automation Robotics & Vision (ICARCV)*, Guangzhou, China, December, 2020.
- [8] M. R. A. Refaai, S. N. R. Vonteddu, P. K. Nunna, P. S. Kumar, C. Anbu, and M. Markos, "Energy management prediction in hybrid PV-battery systems using deep learning architecture," *International Journal of Photoenergy*, vol. 2022, Article ID 6844853, 7 pages, 2022.
- [9] H. Pham Huy Anh, C. Tan Lam, and P. Huynh Lam, "Novel adaptive forward neural MIMO NARX model application for modelling of biped robot's arm kinematics," *Journal of the Japan Society of Applied Electromagnetics and Mechanics*, vol. 21, 2013.
- [10] Z. Ortatepe and O. Parlaktuna, "Two dof robot control with fuzzy based neural networks," *Anadolu university journal of science and technology A - Applied Sciences and Engineering*, vol. 18, no. 4, pp. 819–830, 2017.
- [11] M. Fouzia, N. Khenfer, and N. E. Boukezzoula, "Robust adaptive tracking control of manipulator arms with fuzzy neural networks," *Engineering, Technology & Applied Science Research*, vol. 10, no. 4, pp. 6131–6141, 2020.
- [12] R. Y. Putra, "Neural network implementation for inverse kinematic model of arm drawing robot," in *Proceedings of the 2016 International Symposium On Electronics And Smart Devices, ISESD*, pp. 153–157, Bandung, Indonesia, November, 2016.
- [13] G. Vladimirov and S. Koceski, "Inverse kinematics solution of a robot arm based on adaptive neuro fuzzy interface system," *International Journal of Computer Applications*, vol. 178, 2019.
- [14] S. Shastri, Y. Parvez, and N. R. Chauhan, "Inverse kinematics for A 3-R robot using artificial neural network and modified particle swarm optimization," *Journal of the Institution of Engineers: Series C*, vol. 101, no. 2, pp. 355–363, 2020.
- [15] K. K. Dash, B. B. Choudhury, and S. K. Senapati, *Inverse kinematics solution of a 6-DOF industrial robot*, Springer, vol. 758, Singapore, 2018.
- [16] M. R. A. Refaai, "Using multiple adaptive neuro-fuzzy inference system to solve inverse kinematics of SCARA robot," in *Proceedings of the 2021 18th International Multi-Conference on Systems, Signals & Devices (SSD)*, pp. 154–159, Monastir, Tunisia, March, 2021.
- [17] A. R. J. Almusawi, L. C. Dülger, and S. Kapucu, "A new artificial neural network approach in solving inverse kinematics of robotic arm (denso VP6242)," *Computational Intelligence and Neuroscience*, vol. 2016, 10 pages, 2016.
- [18] H. P. H. Anh and N. T. Nam, "Novel adaptive forward neural MIMO NARX model for the identification of industrial 3-DOF robot arm kinematics," *International Journal of Advanced Robotic Systems*, vol. 9, no. 4, p. 104, 2012.
- [19] R. Saravanan, S. Ramabalan, and C. Balamurugan, "Evolutionary multi-criteria trajectory modeling of industrial robots

## Retraction

# Retracted: Application of IoT-Based Drones in Precision Agriculture for Pest Control

### Advances in Materials Science and Engineering

Received 20 June 2023; Accepted 20 June 2023; Published 21 June 2023

Copyright © 2023 Advances in Materials Science and Engineering. This is an open access article distributed under the Creative Commons Attribution License, which permits unrestricted use, distribution, and reproduction in any medium, provided the original work is properly cited.

This article has been retracted by Hindawi following an investigation undertaken by the publisher [1]. This investigation has uncovered evidence of one or more of the following indicators of systematic manipulation of the publication process:

- (1) Discrepancies in scope
- (2) Discrepancies in the description of the research reported
- (3) Discrepancies between the availability of data and the research described
- (4) Inappropriate citations
- (5) Incoherent, meaningless and/or irrelevant content included in the article
- (6) Peer-review manipulation

The presence of these indicators undermines our confidence in the integrity of the article's content and we cannot, therefore, vouch for its reliability. Please note that this notice is intended solely to alert readers that the content of this article is unreliable. We have not investigated whether authors were aware of or involved in the systematic manipulation of the publication process.

Wiley and Hindawi regrets that the usual quality checks did not identify these issues before publication and have since put additional measures in place to safeguard research integrity.

We wish to credit our own Research Integrity and Research Publishing teams and anonymous and named external researchers and research integrity experts for contributing to this investigation.

The corresponding author, as the representative of all authors, has been given the opportunity to register their agreement or disagreement to this retraction. We have kept a record of any response received.

### References

- [1] M. R. A. Refaai, V. S. Dattu, N. Gireesh, E. Dixit, C. Sandeep, and D. Christopher, "Application of IoT-Based Drones in Precision Agriculture for Pest Control," *Advances in Materials Science and Engineering*, vol. 2022, Article ID 1160258, 12 pages, 2022.



## Research Article

# Application of IoT-Based Drones in Precision Agriculture for Pest Control

Mohamad Reda. A. Refaai <sup>1</sup>, Vinjamuri SNCH Dattu,<sup>2</sup> N. Gireesh,<sup>3</sup> Ekta Dixit,<sup>4</sup> CH. Sandeep,<sup>5</sup> and David Christopher <sup>6</sup>

<sup>1</sup>Department of Mechanical Engineering, College of Engineering, Prince Sattam Bin Abdulaziz University, Alkharj 16273, Saudi Arabia

<sup>2</sup>Department of Mechanical Engineering, Aditya Engineering College, East Godavari, Andhra Pradesh, India

<sup>3</sup>Department of Electronics and Communication Engineering, Sree Vidyanikethan Engineering College, Tirupati, Andhra Pradesh 517501, India

<sup>4</sup>Department of Computer Science and Engineering, S. S. D. Women's Institute of Technology, Bathinda, Punjab, India

<sup>5</sup>Department of Computer Science and Artificial Intelligence, SR University, Warangal, Telangana, India

<sup>6</sup>Department of Mechanical Engineering, College of Engineering, Wolaita Sodo University, Ethiopia

Correspondence should be addressed to Mohamad Reda. A. Refaai; [drengrefaai@gmail.com](mailto:drengrefaai@gmail.com) and David Christopher; [david.santosh@wsu.edu.et](mailto:david.santosh@wsu.edu.et)

Received 6 May 2022; Revised 8 June 2022; Accepted 22 June 2022; Published 30 August 2022

Academic Editor: K. Raja

Copyright © 2022 Mohamad Reda. A. Refaai et al. This is an open access article distributed under the Creative Commons Attribution License, which permits unrestricted use, distribution, and reproduction in any medium, provided the original work is properly cited.

Unmanned aerial vehicles (UAVs), commonly known as drones, have been progressively prevalent due to their capability to operate quickly and their vast range of applications in a variety of real-world circumstances. The utilization of UAVs in precision farming has lately gained a lot of attention from the scientific community. This study addresses with the assistance of drones in the precision agricultural area. This paper makes significant contributions by analyzing communication protocols and applying them to the challenge of commanding a fleet of drones to protect crops from parasite infestations. In this research, the effectiveness of nine powerful deep neural network models is measured for the detection of plant diseases using diverse methodologies. These deep neural networks are adapted to the immediate situation using transfer learning and deep extraction of features approaches. The presented study takes into account the used pretrained deep learning model for extracting features and fine-tuning. The deep feature extraction characteristics are subsequently categorized using support vector machines (SVMs) and extreme learning machines (ELMs). For measuring performance, the precision, sensitivities, specific, and  $F1$ -score are all evaluated. Deep feature extraction and SVM/ELM classification generated better outcomes than transfer learning, according to the analysis result. Furthermore, the analysis of the various methodologies tries to assess their effectiveness and costs. The different approaches, for example, confront difficulties such as investigating the region in the shortest possible time feasible, while eliminating the same region being searched by more drones, detecting parasites, and stopping their spread by applying the appropriate number of pesticides. Simulation models are a significant aid to researchers in conducting to evaluate these technologies and creating specific tactics and coordinating procedures capable of effectively supporting farms and achieving the aim. The main objective of this paper is to compare the search techniques of two distinct methods of parasitic to identify performance.

## 1. Introduction

Agriculture, which is a major source of income for several countries, meets two of humanity's most fundamental requirements: food and fiber. Agriculture had changed

dramatically over the last decades as a means of technological developments like the Green Movement. Agricultural research focuses on a variety of topics, including livestock management, commodities, and water depth. The drones' ability to execute these duties is due to a variety of sensors

and devices on deck. In recent decades, modern developments have revolutionized sector managers to deal with a variety of risks, including pests and abrupt climate variability, which can significantly impair the crop or the quality of agricultural products. Because the drones have restricted fuel and pesticide supplies, they can seek assistance from other drones to accomplish pest removal. Some enrollment techniques, focused on bio-inspired ones, have been attempted to address these last concerns.

During the 1960s–1980s, the Green Revolution, also known as the third invention of agriculture, crop improvement varieties, synthetic fertilizers, pesticides, and irrigation, resulted in increased crop food production and food stability, particularly in poor countries. As a result, even though the world's population has doubled and food production has tripled during the 1960s, agricultural production has already been responsive to the demands with a 25% increase in agricultural land.

By 2050, the consumption of agriculture and food goods is expected to rise by moreover 75% [1]. Given the scarcity of arable land, agricultural expansion, or the greater use of fertilizers, insecticides, freshwater, as well as other resources, will meet a major portion of this increasing demand. However, increased agricultural input consumption has negative consequences for the ecosystem, including groundwater extraction, diminished surface streams, and eutrophication. Excessive and/or ineffective usage of environmental assets (such as water and soil), fertilizers, and insecticides for agriculture output results in economic damage as well as enhanced nutrient and water wastes, all of which lead to sustainable deterioration. The need to create approaches that could boost crop output through higher production quality and reduce environmental wastage for economic and ecologically responsible manufacturing systems [2].

Agriculture has been one of the areas that make use of the Internet of Things to promote smart cultivation. A wide range of plant behavior research and understanding is required to cope with changing climate and to understand exactly crop production in specialized small-scale habitats. The word itself implies that the Internet of Things paradigm will usher in a mechanical cosmos in which everyday instruments and equipment will be enhanced with the help of computing capabilities. Sensing, as well as network and system capabilities, would be included in these devices. To look at it another way, physical items that may be assigned as “things” will be able to operate as solitary units or as a fusion of concerted action from disparate devices. Drones could be used to optimize crop choice, availability of water, fertilization, and insecticides in farming. Drones will aid in the lowering of overall agricultural manufacturing costs while also ensuring decent yield and grain quality [3]. Different challenges arise as a result of the growing population and agricultural production. Drones are being utilized in improved agricultural productivity, precision, and the capacity to overcome challenges, as well as to boost precise measurement, real-time information gathering, and productive farming development. Producers could distinguish between high and poor-yielding plants on the farms by employing

drones. In agriculture, IoT mostly aids producers in bridging the gap between demand and supply. IoT concepts have been applied to drone farming, and it has the potential to increase the area [4].

Naturally, the responses to these issues rely on quick and efficient manufacturing. Robotics, computer programming, machine intelligence, the Internet of Things (IoT), and other technologies could help smart farmers create smart, effective, and rapid goods. Precision agriculture attempts to create valuable outcomes for comprehending the soil and also to gather and process data from different sources using information and communication technology (ICT) solutions. Humidity, Irrigation, pesticides, vegetation, and other variables change over time and location, necessitating ongoing product assessment in regards to watering and spray. This method attempts to utilize agricultural chemicals better effectively, conserve fuel and commodities, avoid agriculture pollution, employ smart technological solutions, and produce environmentally responsible goods in this manner. Every one of these factors has a substantial impact on crop yield. Precision farming, in this sense, could combine different analytical techniques and technical instruments that are relevant to all steps of manufacture, from planting to harvesting [5].

Precision agriculture (PA) is rapidly gaining traction in today's modern technology-driven world, and it is been dubbed “the farmer of the century.” This is a computerized farming administration approach that uses advanced technologies to monitor and optimize agriculture manufacturing activities. To improve farm productivity, PA employs current technology and concepts to regulate temporal and spatial variations in all elements of agricultural output. A variation that has a substantial impact on agriculture is referred to as spatial and temporal distribution. Soil variability, yield variability, crop variability, field variability, and management variability are all examples of spatial and temporal distribution. To accomplish these objectives, unmanned aerial vehicles (UAVs), sensor technologies, satellite tracking, location systems, and the Internet of things (IoT) is commonly utilized [6]. As it finds its way into farms throughout Europe, PA is rapidly assisting producers with their work. Larger harvests necessitate a larger capital commitment since they necessitate a higher proportion of fertilizers, insecticides, water, and other commodities. Producers, on the other hand, can save a lot of money by properly managing their expenses. Furthermore, in addition to improving output through careful monitoring, producers may improve plant performance and wellbeing at the same time, allowing them to accomplish things [7].

Figure 1 shows documentation produced by scientists, professors, and farmers during the previous 10 years, proving that PA is becoming more popular every day [8]. PA has developed a digital-based farm management model for monitoring and optimizing agriculture manufacturing processes. Wheat, rice, soybean, maize, barley, potato, orange, olive, and a variety of other crops have all used PA in their production, tracking, and harvest. The challenges of agricultural needs and desires are highlighted in this context. Drones to Improve Insect Pest Administration is a special

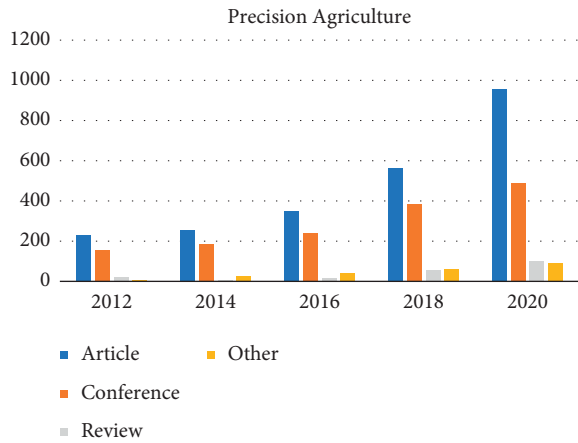


FIGURE 1: Dataset of research on precision agriculture.

accumulation that showcases research and innovation of autonomous drones (or uncrewed) airframe scheme (UAS, or drone) advanced technologies for control of insect pests, ranging from identification and demarcation of insect infestation harm and pest ecosystems to delivering of microbes and equipment to alleviate pest fears. The articles range from more fundamental research (testing and enhancing drones' capacities to identify pest issues or transport pest control products) to test hypotheses (operational potential and problems of drones utilized  $n$  pest control systems) [9].

To sense the presence of insects and pests on farmland, remote-sensing technology such as satellites and UAVs are used to locate predatory insects and quickly notify farmers of the situation. The benefits of agriculture sensing technologies based on satellites, known as high-altitude remote-sensing technologies, include a large tracking area, fine responsiveness, a short return interval, and low cost. A satellite device, on the one side, could span a large region and is useful for a variety of disaster tracking. Satellite surveillance, on the other side, is weather-sensitive and also has a lower resolution, making it more difficult to fulfill this need for pests and pest tracking in agricultural areas [9]. Identification technique based on drones or unmanned aerial vehicles (UAVs), known as low-altitude distant location technologies, is now commonly used in modern fields, ensuring high reliability of obtained data. Whenever drones are being used to indicate the existence of insects and pests, agricultural diseases and pests monitoring must be standardized and digitized. Nevertheless, a drone on a distant large-scale farm confronts issues such as short flying time and regular charge change due to its restricted carrying mass and storage capacity. These qualities now influence the development and use of drones in modern farming [7].

Convolutional networks are effective as fundamental deep learning techniques in several plant disease diagnosis investigations. The research employed the LeNet design as a fully convolutional to categorize picture collections, which allowed it to distinguish between normal and infected banana leaves. Learning techniques perfectly alright by learning algorithms have been used to assess these [4]. A database of 54,305 photos of sick and normal leaf tissue has

been used in the study. AlexNet and GoogleNet networks based on a thorough CNN were used to assess their effectiveness in identifying 14 different crops and 26 illnesses. They created a novel prevention and detection method that included seven different disease categories. They employed CNN-based classification techniques, an accuracy rate of 82.3% using a four-fold cross-validation technique. Using a deep convolutional neural network, they suggested a new method for recognizing 13 multiple variations of plant illnesses. They created a strong profound sensor that could identify 9 distinct vegetable diseases and pests instantaneously [10].

Antibiotic resistance is posing a growing challenge to the successful management and cure of a wide spectrum of human infections. To prevent cross-resistance, newer and better medicines with unique different mechanisms of action are urgently needed. Existing fibroblast pharmacological screens, on the other hand, are limited to basic live/dead data logging with no mechanisms of effect prediction capability [11]. The use of learning algorithms approaches to increase the extraction of information using visual input is becoming more common. Unfortunately, these techniques struggle with varied biological morphologies and typically necessitate time the world training. Combining human or human and computer data for training from mixed human *Plasmodium* species farms, researchers proposed a semi machine learning approach.

## 2. Related Work

With the rise of big data technology and information computers, machine learning has opened up new possibilities for information research in the multi-disciplinary agri-technology arena. Researchers offer a complete assessment of studies on machine learning techniques in agricultural systems in this study. Crop leadership included applications on yield prediction, detection of diseases, weed recognition, grain quality, and features are available; livestock organization included application forms on animal protection and animal agriculture; wastewater reuse included implementations on irrigation systems, and soil compaction included implementations on soil quality. The materials offered have been filtered and classified to show how machine learning management systems will assist farming. Agricultural production solutions are turning towards real-time artificial intelligence empowered software that would provide comprehensive suggestions and analyses for farmers' decision-making and activity by using machine learning to sensor information. In the research of machine learning for the detection of pests, they fail to detect the pests and different weeds that cause damage to the yielding crops proposed by [12].

The possibility of machine learning techniques for weeds and agricultural categorization from drone photos is investigated in this research. Weed detection in fields is a tough challenge that has been tackled by using orthomosaicing, extraction of features, and picture labeling to train machine learning systems. The effectiveness of multiple machine learning approaches, including support vector

machine (SVM), random forest (RF), and k-nearest neighbors (KNN), is examined in this research to identify weeds utilizing drone photos gathered from an Australian chili farm field. Precision, accuracy, recall, false-positive rate, and kappa statistics were the assessment criteria utilized to compare the performances. The machine learning techniques are simulated in MATLAB, and the obtained weed identification prediction accuracy is 96% utilizing RF, 94% using SVM, and 63% using the classification technique. According to this research, the random forest algorithm and support vector machine are efficient to utilize and could be simply deployed for weed detection in UAV photos. The major drawback of early weed detection is they could only detect the weed among the crops and the time consumption is high when compared to other techniques [13].

The Internet's excellent technologies and widespread agricultural conversion and upgrade have improved the entire agricultural industrial chain and intensive farming. Due to the increasing price and hardship associated with the traditional agricultural planting planning, IoT devices are being used in agricultural production to enable real-time identification and intelligent management of crop development circumstances, navigation systems, and a shift in traditional agricultural device planting methods. The goal of this paper is to develop and study an intelligent agricultural IoT automation solution. This paper begins by providing an introduction to IoT fundamental concepts before moving on to the core technologies of the Internet of things. The present challenges and inadequacies are assessed in conjunction with the present state of agriculture mechanization in the nation. On this foundation, augment and strengthen it with an IoT technology platform. The general scheme design, modules functionality layout, and AC method realization of the IoT braking control scheme are fully detailed in this paper. And conduct a study on the subject of the article using investigation, comparative evaluation, and other research techniques. The greenhouses sample information is picked as the sampling, the appropriate initial function is chosen, and the proposed fuzzy rules acquired by the training of the fuzzy neural network method are reasonably right, according to experimental research. The automatic temperature control system's output result is largely compatible with the real data on-site. Generally, the heat AC system proposed in this paper may match the agricultural AC criteria. Based on the research it is noted that the technology could not stand the high temperature in the field and this is considered the limitation of research proposed by [14].

The articles range from more basic research (testing and enhancing drones' capacity to identify insect issues or distribute pest control products) to case studies (identifying challenges and opportunities of UAV use in pest control schemes). The selection also aims to spark debate about JEE's position as a publishing platform for future posts on the drone, as well as many other cyber-physical devices, big data analysis, and deep learning processes. Whereas these techniques originated in sectors that are undoubtedly unrelated to entomology, we believe that the interprofessional approach is the best path for the implementation of technology and research transmission, resulting in a faster pace of

research and innovation of these innovations to enhance pesticides. Drone to enhance insect pest control is a special compilation that showcases research and innovation of unmanned aviation systems (unmanned aircraft systems, or drones) technologies for the control of insect pests. The selection also aims to spark debate about JEE's position as a publishing venue for future posts on UAVs, as well as many other cyber-physical devices, big data analyses, and profound learning processes. Whereas these techniques originated in areas that are undoubtedly unrelated to anthropology, we believe that an interdisciplinary team is the best path for applied research and technology transfer, resulting in a faster pace of research and development of these innovations to enhance pest management. The article failed to improve the robustness of the drone, hence, a lot of enhancement is needed in the drone usage proposed by [15].

Artificial intelligence (AI) has lately made an appearance in the agriculture industry. Inadequate fertilization, pest and disease infestations, massive data demands, reduced performance, and a gap in knowledge among farmers and technologies are just a few of the issues the industry is facing to increase its production. The adaptability, excellent quality, precision, and expense of AI in agriculture are the primary elements. The implications of AI in soil conservation, cultivation practices, weed control, and disease organization are discussed in this study. A significant emphasis is placed on the application's advantages and weaknesses, as well as how to use expert systems to increase productivity. Because they could offer site-specific, linked, and interpreted guidance, expert systems are useful tools for crop cultivation. Expert systems for farming, on the other hand, are a relatively discovery, and their usage in agricultural production is still uncommon. While AI has improved the farming industry significantly, it does have a lower-than-average influence on farming production as contrasted to its possibilities and effects in those other industries. There is still work that can be done to improve farming production utilizing AI because it has many limitations [16].

### 3. Methodology

In this research, precision agriculture for pest control is detected using the IoT application. The main aim of the research is to control the pest in precision agriculture using unmanned aerial vehicles (UAV). At first, the detailed account of precision agriculture is described and then the pest classification is done using the pretrained deep learning model and transfer algorithm. Following the pest classification, the researchers used the pest search algorithm and drone communication to eradicate the pest in three different cases. Finally, the performance evaluation is done for both the proposed method.

*3.1. Precision Agriculture.* In recent years, smart farming and precision agriculture have sparked even more interest. New information and communication technology enable new options for active tracking of farmland, cattle, and water infrastructure, with the ultimate goal of reducing living

beings. Among the most significant aspects of precision farming are managing resources [17]. Making better use of resources encourages better performance. Image-based measurements and smart data mining are necessary to obtain additional information and expand understanding of the situation. Drones may capture aerial photographs of agriculture fields and animal farms. Precision agriculture reflects the efficiency and productive utilization of restricted input and produces impact significant output. It is a fresh approach to using digital techniques to enhance agricultural methods. The characteristics and geometries of smart agriculture are evolving as a result of many technological advances. IoT, meteorology, and advanced analytics technology are all key trends. In all industries, the Internet of Things does have a massive effect; it provides additional technologies. It refers to innovative ways for academics to put their research into practice. It enhances the productivity of operational functions in particular. It is an implementation of farming in agriculture. It enabled, for instance, the collection of actual field information on soil and air temperature. Aerial imaging, drones, and spacecraft are used as precision farming tools on a wide scale. Researchers used machine learning and statistical analysis to positively influenced decisions to make precision farming more viable, dependable, optimized, and efficient. Detection of pests in farmlands is yet another key subject of study and implementation situation in which video review may aid in the development of plantations. The proper identification of this type of plant is still a work in progress. Herbicides are the most commonly used method for controlling weed infestations [18]. Drones are employed in precision agriculture to detect plant development data, soil humidity, fertilizer in the field or to release precisely and precisely inside the ground has been adjusted for diseases, parasitic infections, or harvest monitoring. UAVs are commonly used for surveillance, dusting, and crop insurance surveys. The utilization of a UAV outfitted with a high-resolution camera is widely used to survey an area of interest.

## 4. Proposed Method

**4.1. Deep Learning and CNN Model (Pretrained).** Deep learning is a class of machine learning techniques that learns data properties by using mathematical models made up of numerous processing elements. Attention to this topic has resulted in the growth of substantial-high successes in fields including such recognition and classification utilizing machine learning. Such algorithms have lately been applied in a variety of applications, including voice recognition, optical object recognition, and object detection. While the first research on deep learning had a long record, the production of vast data and the development of powerful processors with massive scale storage are the major reasons for its current advancement. Again, for the problem of crop disease detection, this research evaluates alternative ways of the nine more effective designs of deep learning models [19]. A portion of the ImageNet database is used to train these deep learning techniques. The AlexNet design is a deep learning system with 25 levels and parameters that could be learned

on only eight of them. The GoogleNet design, which is predicated on a network-in-network technique, employs design components that retrieve distinct local features using multiple convolution layers simultaneously. The Oxford Visual Geometry Group (VGG) developed the VGG system, which is a homogenous structure that was utilized to improve outcomes in the ILSVRC-2014 contest. They created the ResNet network to train systems with even more complexity.

Standard successive networks like VGGNet and AlexNet vary from in this structure, which is based on micro-architecture components. Research presented the Inception system as a form of the CNN model. There are a lot of convolution and max-pooling phases in this system. This has a fully linked computational model in the final step. The remaining interconnections and structure of the network of the InceptionResNetV2 system were predicated on the Inception-based underlying network [20]. Although InceptionResNetV2 operates roughly identically to other Inception designs, it achieves sufficient training speed by using convolution layers. SqueezeNet is a smart structure developed by research that delivers AlexNet-level accuracy on ImageNet with 50 times fewer variables. Table 1 summarizes the parameter utilization properties of various designs.

**4.2. Classifier.** In this research, the standard classifier technique of the support vector machine and the extreme learning method are utilized to design deep features from a specific layer of the pretrained deep network.

**4.3. Support Vector Machine.** Support vector machine is a statistical training theory-based technique invented by Vapnik. The goal of the SVM approach is to create a linear discriminant functional with the biggest marginal dividing the groups. Support vectors are the training data that are nearest to the hyper-plane. Support vector machine can discriminate between linear differentiated and undifferentiated large datasets [21]. This classification is used to address issues in a variety of fields, including image and item identification, speech recognition, fingerprint recognition, and handwriting recognition.

**4.4. Extreme Learning Machine.** ELM is a research-based learning method for Single Hidden layer Feedforward Networks (SLFNs). In ELM, outcome values are adjusted using the least-squares method, whereas hidden state values are produced randomly. ELM can be described using the equation provided in equation (1)

$$\sum_{u \in \mathcal{S}_1}^N \alpha_u a(x_u * y_v + g_u) = Z_v, v = 1, 2 \dots J, \quad (1)$$

where  $[y_u, z_u]$  denotes the input and output, the number of the training sample is denoted as  $J$ , and  $\alpha_u$  is the weight input and the hidden layer is denoted as  $\alpha_u$ .  $Z = T\alpha$  can be represented in the matrix if the output of the network implies

TABLE 1: Parameter utilization.

System	Deepness	File size	Variables	Data capacity
Inceptionv3	46 s	87 Megabytes	23.8	299 × 299
AlexNet	16	228 Megabytes	62	228 × 228
VGG19	19	535 Megabytes	144	224 × 224
InceptionResNetv2	164	209 Megabytes	55.9	299 × 299
VGG16	16	515 Megabytes	138	224 × 224
ResNet101	101	167 Megabytes	44.6	224 × 224
SqueezeNet	16	4.6 Megabytes	1.25	228 × 228
GoogleNet	22	27 Megabytes	7	224 × 224

the convergence of the real value with zero error. ELM's output is represented by  $Z$ . Equation (2) represents the hidden layer output matrix, and the output weight  $a$  is calculated as

$$T = a(x_1 * y_1 + g_1) \dots a(x_N * y_1 + g_N),$$

$$a > x_1 * y_j + g_1? \dots a > x_N * y_j + g_N? \textcircled{a}. \quad (2)$$

The parameter  $\alpha$  is gained by  $\alpha = T'Z$ .

**4.5. Data Collection.** Images of pests prevalent in the Malatya, Bingöl, and Elaz districts of Turkey were utilized to assess the suggested technique's effectiveness [22]. A drone was used to capture these photographs. Each item in this collection has a quality of 4000–6000 pixels and is three-channel (RGB) colors. The identities and quantities of plant pests and pests in this collection are listed in Table 2.

Table 2 shows that the collection contains a combination of 1965 photos representing seven different phytopenest. These data are taken throughout the day on various sections of time. Furthermore, photos of the illnesses were captured utilizing a variety of trees [23].

Researchers used deep extraction of features from several fully-connected layers, as well as classification techniques relying on pretrained models neural network architectures, in this research. Figures 2 and 3 depict the planned report. The subdivisions that followed go through domain adaptation and deep extraction of features in more depth [24].

**4.6. Transfer Learning.** Transfer supervised machine learning method that uses information gained from a model generated to solve an issue as a preliminary step for tackling a different challenge. Pretrained models convolution neural network models are developed based on transfer learning and were used in the present study to fine-tune the approach. The advantage of employing pretrained convolution layers over convolutional networks with random initialization parameters is that they have been faster and more efficient to

learn [23]. Furthermore, rather than moving the last three levels of the pre-trained model's networks to their categorization job, the fine-tuning process is based on the transfer extra layer, as seen in Figure 2, and it is shown in Algorithm 1.

**4.7. Feature Extraction.** Deep extracted features are focused on features extracted from a deep learning model that has been pretrained. Machine learning classification is performed using these parameters. To put it another way, this approach works by extracting feature representations from the fully-connected level of pretrained models' networks. Effective deep characteristics were retrieved from ResNet50, ResNet101, InceptionV3, GoogleNet, InceptionResNetV2, and SqueezeNet and fc1000, fc1000, forecast, predictions, and pool10, accordingly, from a specific layer of deep learning models [25].

As seen in Figure 3, the generated deep features are used in the classification stage by employing standard models such as SVM and ELM as shown in Algorithm 2.

**4.8. Pest Moving Algorithm.** The pest can be transported in a variety of ways, such as randomly determining routes or searching for crops. Irrespective of the activity of other insects, the pest is led by the existence of vegetation when traveling. It has a restricted view of the area in which it is located [26]. If a pest is attached to a host, it will keep feeding till the plant dies. Rather, if it is in a part of the pitch where there are no plants, it goes in quest of one.

Pests can be identified in three different situations when performing mobility:

- (i) If the pest could see more than one plant, it could pick which one to attack
- (ii) If the pests could see a plant near it, this would target it; if it can have seen more than a plant, it would choose one to attack
- (iii) If no visible region around the insect includes a plant, it will travel until it discovers one

Drones employ a distributed approach for pest search that is controlled by message passing. Every UAV has a storage that is utilized to store records about already visited attractions (which is encrypted and kept in this storage). At each passage, the drone maintains its mapping by inputting additional information (such as the existence of normal or sick crops) and discarding inaccurate data. This mapping aids the UAV in determining the next course of action. In addition, to save time and attention, the drones will not return to an area that has already been examined and sterilized. As a result, the next path is selected at random from nonunknown places. The drone then selects a traveling orientation and a distance [27]. Naturally, the locations nearest to the drone which have yet to be examined will be prioritized. The drone takes account of its original orientation in place to avert returning to it if it chooses this path. To recreate the overall map, UAVs communicate local views of the map. The drone's information mapping can be shown



TABLE 2: Data of pest disease collection.

S. no	Type	Training set	Testing Set	Overall
1.	Shot Hole	550	50	600
2.	Blossom Blight	72	14	86
3.	Oak root fungus	65	8	73
4.	Plum lecanium	312	33	345
5.	Black Cherry Aphid	180	20	200
6.	Bacterial canker	130	15	145
7.	Fire Blight	190	20	210

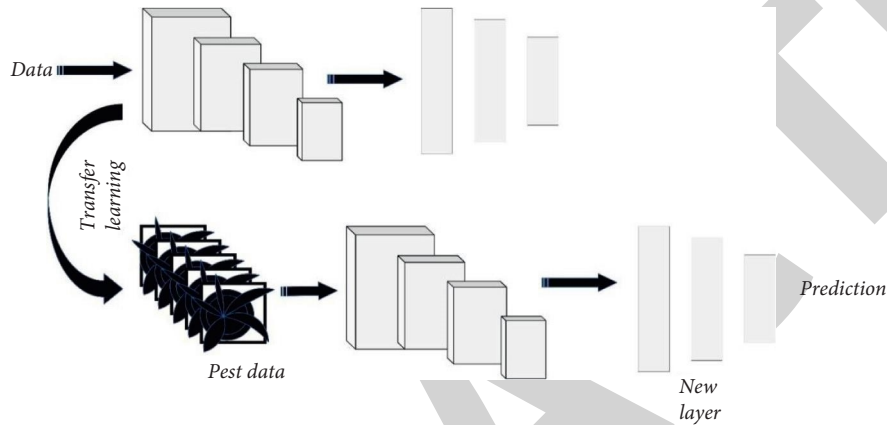


FIGURE 2: Transfer learning Schematic Diagram.

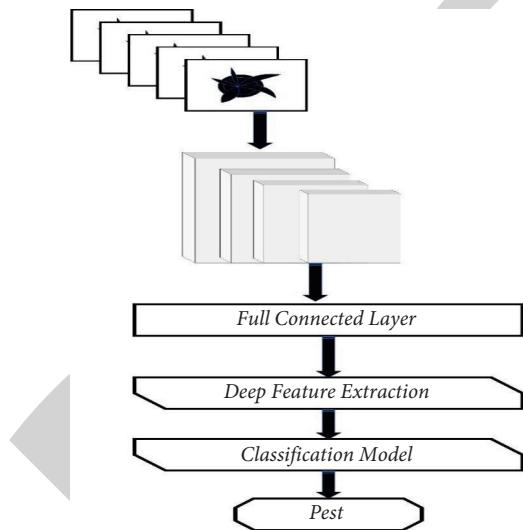


FIGURE 3: Traditional classifier and feature extraction schematic diagram.

as a grid of regions with the drones in the center as illustrated in Figure 4.

The distance covered by the UAV determines the shift at each move. The drone’s database is shared with neighboring drones within the Wi-Fi distance, allowing these drones to learn about regions explored by the other UAVs without having to visit them individually. This cuts down on time complexity and eliminates waste. The transfer of these images can take place regularly or in response to map changes. Whenever a UAV

receives a mapping from some other drone, it adds the data to its database [28]. This distributed approach employs a distributed search message, which contains information about an original thought field region. From every new location, knowledge must be memorized in every drone to store information that is connected to that region in its memories, which is represented by a distributed search message. This implies that drones swap DSMs in interchange for their existing mappings. Distributed search message is 25 bytes in size. The location of the region is represented by the A and B field values. Each region is depicted by 10 square meters with these dimensions according to the square’s northwest orientation. In the Time to Live field, the deadlines data are shown in milliseconds (Table 3) [29].

The State field, on the other hand, refers to the region that is being considered as:

- (i) Lack of plants and lack of pests: “0000000”
- (ii) Existence of plant health: “0000001”
- (iii) Existence of a pesticide-treated plant: “0000010”
- (iv) Existence of an infected plant: “0000011”
- (v) Despite the lack of a plant, pestered present: “000000100” the remaining combinations will be used for future projects.

4.9. Drone Communication. The drone that produced the package will send it to the targeted drone or all drones. Upon reception, the kind of packet influences the drone’s implementation of a certain process based on the type of

Stage 1: Data set of crops in the field is collected  
 Stage 2: The data size is resized based on the deep network utilizing bilinear interpolation.  
 Stage 3: To use the pretrained models CNN networks to tackle the problem, the last three levels are eliminated from the deep networks and substituted with fully-connected layers, a SoftMax surface, and categorization output units.  
 Stage 4: Using the newly created deep model the classification is performed.

ALGORITHM 1: Proposed Transfer Learning Algorithm.

Stage 1: Data set of crops in the field is collected  
 Stage 2: The data size is resized based on the deep network utilizing bilinear interpolation.  
 Stage 3: By the use of a fully-connected layer of deep learning algorithm the features were extracted.  
 Stage 4: Using the support vector and extreme learning machine the classification is performed.

ALGORITHM 2: Proposed Feature Extraction Algorithm.

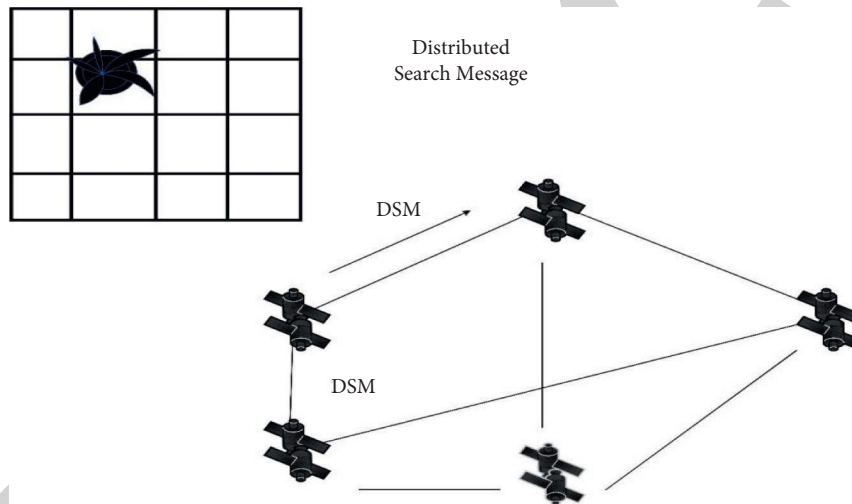


FIGURE 4: Drone network.

TABLE 3: Distributed search message.

A direct	B Direct	Time to Live	Stage
8 Bytes	8 Bytes	8 Bytes	1 Bytes

packets transmitted [30]. Drones communicate with each other for three basic purposes:

**4.9.1. Enrollments.** When a UAV detects a pest and one of the following circumstances applies, it transmits a call for assistance over the Internet. (a) The pest container is low; (b) The residual battery's capacity, except for the reserves, is such that it can only approach the base for recharging.

**4.9.2. Transferring Data of Previously Performed Identification.** The drones can communicate about their current states, such as the amount of insecticide left and the amount of energy they have left.

**4.9.3. Transferring Data regarding Some UAVs Condition.** The drones transmit messages on previously controlled territory periodically in order to prevent visiting the very same area multiple times and also to coordinate efforts the UAVs, speeding up a search and eradication of pests [31].

## 5. Result and Discussion

Throughout this research, they measured the effectiveness of nine powerful deep neural network models for the detection of plant diseases using diverse methodologies. The MATLAB deep learning package was used to carry out the experiments. All of the programs were run on a system with a dual-core Intel Xeon E5 processor and 64 GB of RAM. To examine the classification

TABLE 4: Deep feature extraction accuracy rate.

Classification Algorithm		Accuracy rate (%)			Time
		Support Vector Machine	$k$ -nearest neighbor	Extreme Learning Machine	
VGG19	FCL [1]	95.46	89.02	94.75	1 mint 16 sec
	FCL [2]	94.98	87.95	94.39	1 mint 17 sec
	FCL [3]	91.76	85.6	93.02	1 mint 20 sec
AlexNet	FCL [1]	95.5	89.42	93.42	30 sec
	FCL [2]	94.2	89.02	92.30	31 sec
	FCL [3]	92.3	84.6	91.54	35 sec
VGG16	FCL [1]	95.1	88.56	94.85	1 mint 5 sec
	FCL [2]	93.8	87.1	93.58	1 mint 6 sec
	FCL [3]	92.6	84.8	92.12	1 mint 8 sec

TABLE 5: Performance measures.

Classification model	Performance	$K$ -nearest neighbor			Support Vector			Extreme learning machine		
		Spec	Sens	FS	Spec	Sens	FS	Spec	Sens	FS
VGG19	FCL [1]	98.24	87.29	85.45	99.20	92.23	92.48	99.24	92.68	93.05
	FCL [2]	98.24	85.44	82.70	99.14	92.42	92.45	99.13	91.88	91.94
	FCL [3]	97.86	82.89	80.95	98.80	89.35	89.11	98.98	89.99	90.64
AlexNet	FCL [1]	98.39	87.95	86.34	99.36	94.35	94.59	99.01	90.76	91.30
	FCL [2]	98.34	87.06	84.88	99.24	93.04	93.50	98.85	89.45	90.24
	FCL [3]	97.39	76.32	82.04	98.79	89.62	90.03	98.72	88.22	89.32
VGG16	FCL [1]	98.01	86.55	87.34	99.32	93.03	93.20	99.23	92.13	92.45
	FCL [2]	97.76	83.88	86.34	99.13	91.92	91.70	99.09	91.52	91.98
	FCL [3]	98.41	82.62	78.04	98.87	89.98	89.88	98.88	89.86	90.35

performance of the feature representation, researchers employed the SVM and ELM techniques [32]. Again, for support vector machine classification variables, the research utilized a one-versus-all strategy and a quadratic SVM as the classification category. In particular, for the ELM classification characteristics, researchers utilized a sigmoid activation function as an activation function and a hidden layer neuron frequency. Researchers used a database including their plant pest photos to evaluate the suggested product's effectiveness. There are several 1965 photos in this database, which represent eight different plant diseases. Pest disease data were gathered. A 10-fold cross-validation test has been used to evaluate the efficiency of the suggested approaches. In particular, we employed accuracy, sensitivity, specificity, and  $F1$ -score as performance metrics for experimental research categorization. Under the following subheadings, the obtained measurements and efficiency evaluations are presented.

**5.1. Results Related to Deep Feature Extraction.** For deep extracting features in this part, we use three different fully connected layers depending on pretrained models AlexNet, VGG16, and VGG19 models. Deep characteristics were recovered from the FCL [1], FCL [2], and FCL [3] layers for each of these systems. The efficacy of these features was then evaluated utilizing SVM and ELM techniques. Table 4 shows the accuracy rate of different experimental experiments. The expected total precision rating from across folds and associated mean and standard deviation have been used to assess those accuracy results [33].

The effectiveness of the deep feature extracted from the FCL [1], FCL [2], and FCL [3] levels in each of the AlexNet, VGG16, and VGG19 models was evaluated using SVM, ELM, and KNN approaches, as seen in Table 4. The FCL [1] layer was judged to have the best feature representations for these projections based on the precision ratings. Using the Support vector machine the maximum degree of accuracy for the AlexNet model was 95.5%. The accuracy rate for the VGG16 model using the Support vector machine classifier was 95%, whereas the precision value for the VGG19 model using the ELM classifier was 94.74%. Including these findings, AlexNet had the shortest training time of the three approaches for all fully-connected layers, whereas VGG16 and VGG19 had nearly similar training schedules. Table 5 also includes the sensitivities (Sens), specificity (Spec), and  $F1$ -score (FS) performance indicators for these experiments conducted.

In this part, the performance is the measure of pests eliminated over duration, place, and amount of recharging grounds. The simulation includes a set of fixed settings as well as a range of experimental factors. It has a graphical user interface (GUI) that allows you to adjust the model parameters to replicate a particular circumstance. The contrast between the randomized and distributed search algorithms would be illustrated in particular. As stated in Table 6, the two techniques are evaluated in three different scenarios.

The graphs (Figures 5–7) show that many Pest were destroyed in each of the 3 scenarios studied. Figure 5 shows

TABLE 6: Considerable three cases.

Case no	No of drone	Area dimension	Base range	Base location	No of pest	Max pooling cycle time
Case A	48	3000 * 3000	16	Angles, sides, and center	3000	40 mint
Case B	20	700 * 700	4	Angles	2000	20 mint
Case C	32	1500 * 1500	8	Angles and side	2500	40 mint

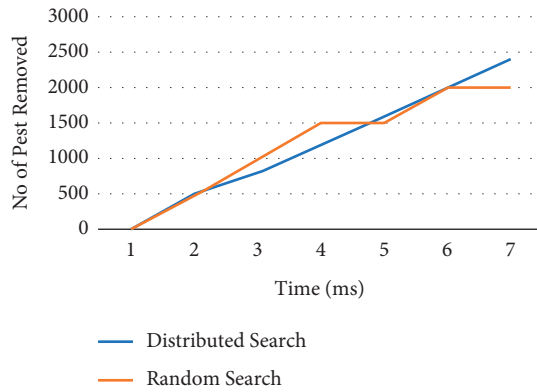


FIGURE 5: Case A pest removed varying time.

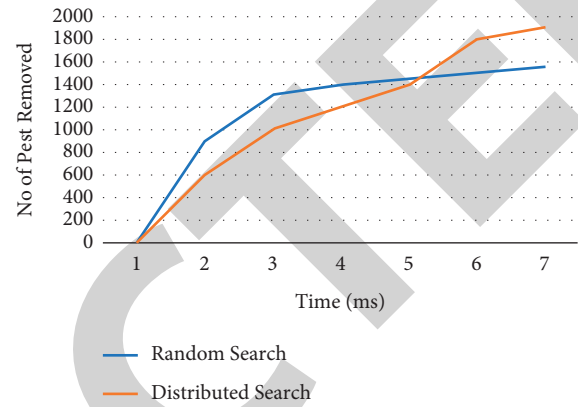


FIGURE 7: Case C pest removed varying time.

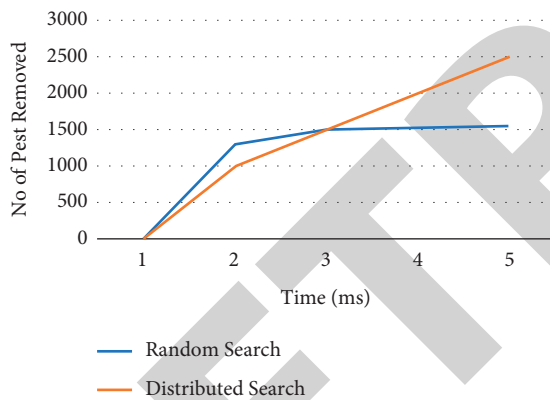


FIGURE 6: Case B pest removed varying time.

that the base amount increased from 32 to 48 units compared to the second version. Following these graphs, it is feasible to determine that to achieve excellent efficiency, it is required to adhere to the proportions shown in the first scene when the pests are nearly all eliminated.

As can be shown, drones that utilize the distributed search algorithm attain resolution significantly faster than those that employ the randomized selection method. Here the last two, in addition to ending longer, kill far fewer pests in all three scenarios. Furthermore, because the quantity of drones does not rise proportionally with the size of the field, plenty more pests will be active, causing crop difficulties. When looking at Figure 6, it is clear that perhaps the proportion of living pests is extremely low.

In Figure 7, however, the proportion rises due to the large field size; it is nearly four times larger than the first

scenario, even though the bases are only tripled and the quantity of drones is increased from 20 to 35.

## 6. Conclusion

The outcomes of deep extracting features and transfer learning for the identification of plant pests and diseases were evaluated in this research. Both for deep extracting features and transfer learning, this research utilized nine powerful deep neural network designs.

- (i) First, researchers gathered feature representations from these deep models' fully-connected layers. SVM, ELM, and KNN classifications were used as performance parameters of the feature representation that were generated. These neural nets were then fine-tuned using photos of plant pests and diseases. Lastly, researchers used conventional techniques to evaluate the results of deep learning techniques.
- (ii) As a consequence, the ResNet50 models and Support vector machine achieved the highest level of accuracy of 97.86%. Furthermore, the computed running time for deep extracting features and transfer learning development of deep learning models, as well as the proposed architecture based on thorough extracting features, were lower-than approaches that rely on transfer learning. For the experiments, researchers used three various situations with a base number, field dimension, pest number, and various numbers of drones.
- (iii) The behavior of two alternative search algorithms, one based on random preferences and the other depending on a disseminated one, was demonstrated in the simulation sessions. The outcomes

showed the effectiveness of the various methods, demonstrating that the distribution method is more appropriate and suggested for pest combat.

## Data Availability

The data used to support the findings of this study are included in the article. Furthermore, data or information are available from the corresponding author upon request.

## Conflicts of Interest

The authors declare that there are no conflicts of interest regarding the publication of this paper.

## Acknowledgments




The authors appreciate the support from Wolaita Sodo University, Ethiopia, for the research and preparation of the manuscript. The authors thank Aditya Engineering College and Sree Vidyanikethan Engineering College for providing assistance with this work

## References

- [1] A. P. Singh, A. Yerudkar, V. Mariani, L. Iannelli, and L. Glielmo, "A bibliometric review of the use of unmanned aerial vehicles in precision agriculture and precision viticulture for sensing applications," *Remote Sensing*, vol. 14, no. 7, 2022.
- [2] M. F. F. Rahman, S. Fan, Y. Zhang, and L. Chen, "A comparative study on application of unmanned aerial vehicle systems in agriculture," *Agriculture*, vol. 11, no. 1, p. 22, 2021.
- [3] D. Gao, Q. Sun, B. Hu, and S. Zhang, "A framework for agricultural pest and disease monitoring based on internet-of-things and unmanned aerial vehicles," *Sensors*, vol. 20, no. 5, p. 1487, 2020.
- [4] R. P. Sishodia, R. L. Ray, and S. K. Singh, "Applications of remote sensing in precision agriculture: a review," *Remote Sensing*, vol. 12, no. 19, p. 3136, 2020.
- [5] N. Islam, M. M. Rashid, F. Pasandideh, B. Ray, S. Moore, and R. Kadel, "A review of applications and communication technologies for internet of things (IoT) and unmanned aerial vehicle (UAV) based sustainable smart farming," *Sustainability*, vol. 13, no. 4, p. 1821, 2021.
- [6] D. C. Tsouros, S. Bibi, and P. G. Sarigiannidis, "A review on UAV-based applications for precision agriculture," *Information*, vol. 10, no. 11, p. 349, 2019.
- [7] P. Velusamy, S. Rajendran, R. K. Mahendran, S. Naseer, M. Shafiq, and J.-G. Choi, "Unmanned aerial vehicles (UAV) in precision agriculture: applications and challenges," *Energies*, vol. 15, no. 1, 2021.
- [8] Y. Kalyani and R. Collier, "A systematic survey on the role of cloud, fog, and edge computing combination in smart agriculture," *Sensors*, vol. 21, no. 17, 2021.
- [9] D. Popescu, F. Stoican, G. Stamatescu, L. Ichim, and C. Dragana, "Advanced UAV-WSN system for intelligent monitoring in precision agriculture," *Sensors*, vol. 20, no. 3, p. 817, 2020.
- [10] M. T. Linaza, J. Posada, J. Bund et al., "Data-driven artificial intelligence applications for sustainable precision agriculture," *Agronomy*, vol. 11, no. 6, 2021.
- [11] W. Zhao, W. Yamada, T. Li, M. Digman, and T. Runge, "Augmenting crop detection for precision agriculture with deep visual transfer learning—a case study of bale detection," *Remote Sensing*, vol. 13, no. 1, p. 23, 2020.
- [12] K. G. Liakos, P. Busato, D. Moshou, S. Pearson, and D. Bochtis, "Machine learning in agriculture: a review," *Sensors*, vol. 18, no. 8, p. 2674, 2018.
- [13] N. Islam, M. M. Rashid, S. Wibowo et al., "Early weed detection using image processing and machine learning techniques in an Australian chilli farm," *Agriculture*, vol. 11, no. 5, 2021.
- [14] Y. Wu, "Intelligent agricultural automatic control system based on internet of things," *Journal of Physics: Conference Series*, vol. 2143, no. 1, Article ID 12009, 2021.
- [15] N. Moses-Gonzales and M. J. Brewer, "A special collection: drones to improve insect pest management," *Journal of Economic Entomology*, vol. 114, no. 5, pp. 1853–1856, 2021.
- [16] N. C. Eli-Chukwu, "Applications of artificial intelligence in agriculture: a review," *Engineering, Technology & Applied Science Research*, vol. 9, no. 4, pp. 4377–4383, 2019.
- [17] S. Khan, M. Tufail, M. T. Khan, Z. A. Khan, and S. Anwar, "Deep learning-based identification system of weeds and crops in strawberry and pea fields for a precision agriculture sprayer," *Precision Agriculture*, vol. 22, no. 6, pp. 1711–1727, 2021.
- [18] K. James and K. Bradshaw, "Detecting plant species in the field with deep learning and drone technology," *Methods in Ecology and Evolution*, vol. 11, no. 11, pp. 1509–1519, 2020.
- [19] L. Petrich, G. Lohrmann, M. Neumann et al., "Detection of *Colchicum autumnale* in drone images, using a machine-learning approach," *Precision Agriculture*, vol. 21, no. 6, pp. 1291–1303, 2020.
- [20] L. Petrich, G. Lohrmann, M. Neumann et al., "Detection of *Colchicum autumnale* in drone images, using a machine-learning approach," *Precision Agriculture*, vol. 21, no. 6, pp. 1291–1303, 2020.
- [21] H. Jawad, R. Nordin, S. Gharghan, A. Jawad, and M. Ismail, "Energy-efficient wireless sensor networks for precision agriculture: a review," *Sensors*, vol. 17, no. 8, p. 1781, 2017.
- [22] M. Fahad, T. Javid, H. Beenish, A. A. Siddiqui, and G. Ahmed, "Extending ONTAGri with service-oriented architecture towards precision farming application," *Sustainability*, vol. 13, no. 17, p. 9801, 2021.
- [23] V. Mokaya, "Future of precision agriculture in India using machine learning and artificial intelligence," *International Journal on Computer Science and Engineering*, vol. 7, no. 3, pp. 422–425, 2019.
- [24] G. E. Just, M. E. Pellenz, P. L. Lima, B. S. Chang, R. Demo Souza, and S. Montejo-Sánchez, "UAV path optimization for precision agriculture wireless sensor networks," *Sensors*, vol. 20, no. 21, p. 6098, 2020.
- [25] Y. Mekonnen, S. Namuduri, L. Burton, A. Sarwat, and S. Bhansali, "Review—machine learning techniques in wireless sensor network based precision agriculture," *Journal of the Electrochemical Society*, vol. 167, no. 3, Article ID 37522, 2019.
- [26] A. Triantafyllou, P. Sarigiannidis, and S. Bibi, "Precision agriculture: a remote sensing monitoring system Architecture," *Information*, vol. 10, no. 11, p. 348, 2019.
- [27] U. Shafi, R. Mumtaz, J. García-Nieto, S. A. Hassan, S. A. R. Zaidi, and N. Iqbal, "Precision agriculture techniques and practices: from considerations to applications," *Sensors*, vol. 19, no. 17, 2019.

## Research Article

# High Speed Grinding of EN31 Steel with Alumina Nanofluid Coolant

**T. Sathish,<sup>1</sup> R. Saravanan ,<sup>1</sup> V. Vijayan ,<sup>2</sup> R. Karthick,<sup>3</sup> N. Karthikeyan,<sup>4</sup> and S. Rajkumar <sup>5</sup>**

<sup>1</sup>Department of Mechanical Engineering, Saveetha School of Engineering, SIMATS, Chennai, Tamil Nadu, India

<sup>2</sup>Department of Mechanical Engineering, K. Ramakrishnan College of Technology, Tamil Nadu, India

<sup>3</sup>Department of Mechanical Engineering, M. Kumarasamy College of Engineering, Tamil Nadu, India

<sup>4</sup>Department of Mechanical Engineering, K. Ramakrishnan College Engineering, Tamil Nadu, India

<sup>5</sup>Department of Mechanical Engineering, Faculty of Manufacturing, Institute of Technology, Hawassa University, Hawassa, Ethiopia

Correspondence should be addressed to V. Vijayan; rajkumar@hu.edu.et

Received 28 May 2022; Revised 8 July 2022; Accepted 2 August 2022; Published 29 August 2022

Academic Editor: Dhanesh G. Mohan

Copyright © 2022 T. Sathish et al. This is an open access article distributed under the Creative Commons Attribution License, which permits unrestricted use, distribution, and reproduction in any medium, provided the original work is properly cited.

Grinding is a choice for obtaining high surface quality and closer dimensional tolerance. For meeting this objective economically, the material removal rate (MRR) must be sacrificed to certain extent. The MRR could be increased by either increase in wheel speed, depth of cut, and feed rate. An increase in MRR increases the surface temperature leading to thermal defects on surfaces. Improving the MRR without compromising the surface quality is a challenging objective. Many investigations are progressing for machining various materials under different cooling environments to meet such challenges. This experimental novel aim is to investigate the performance of Al<sub>2</sub>O<sub>3</sub> nanofluid in high-speed grinding of EN31 steel under flood cooling method for reduction of surface roughness and cutting zone temperature. Taguchi's full factorial design was employed for experimental investigation. The factors such as feed, depth of cut and cutting fluid environment were considered for analysing the responses of cutting zone temperature and surface roughness. The thermal analysis on the work piece was carried out with experimental values by the finite element analysis method. The nanofluids outperform in terms of reduction of surface roughness and downsizing cutting zone temperature. The proposed nanofluid-based grinding significantly reduced the surface roughness and cutting zone temperature.

## 1. Introduction

Surface grinding on EN31 steel is vital operation for meeting the functional requirements of its application such as textile industrial tools, measuring gauges, and precision dies. Large heat generated while grinding due to multipoint cutting tool (abrasive wheel), high friction between work and wheel, rapid chip formation, and the grinding zone is completely adiabatic reported by Malkin and Guo [1]. High temperature at the cutting zone causes faster tool wear and thermal defects on surfaces (surface burning, surface crack, physical and chemical changes not only on the surface but also up to some depth stated by Paul and Chattopadhyay) [2]. But it is indispensable to control the cutting zone temperature to

control surface quality. Cutting fluids are usually employed for this task. Because the cutting fluids are used for braking chips and prevent corrosion reported by Henriksen [3], they flush away the broken chips, reduce tool and work piece temperatures, and also act as lubricant to reduce the friction at the interface of wheel and work piece reported by Suresh et al. [4]. Chen et al. found that the increase of tool life improved surface finish and tolerance [5]. Based on the industrial practices, dry machining, flood/wet cooling, solid coolants, high-pressure cooling, and minimum quantity lubrication (MQL) environments were used for grinding in which wet cooling practices are obvious. Many disadvantages were listed such as (1) high cost for removing excess heat reported by Klocke and Eisenblatter [6] and also by



Sreejith and Ngoi [7], (2) less heat dissipation due to difficulty in supplying cutting fluid at cutting zone when rapid chip formation, and (3) high friction analysed by Brinksmeier et al. [8]. Cutting fluid causes techno-environmental problems like health hazard to the operator and environment pollution in disposal [9], and such cutting environment is evident in the industries. For preventing such demerits, a new kind of cutting fluids is evolved. Some examples are as follows: Max Mist ST-2020 yielded lowest net manufacturing costs of any fluid and environmentally acceptable vegetable oil-based lubricant as reported by Jung Soo et al. [10] and eco-friendly cutting fluid TRIM E709 emulsifier as explained by Vasu and Manoj Kumar [11].

## 2. Research Gap

Most of the works are reported in nanofluid as cutting fluid in MQL environment. Some of them are as follows: Khan et al. [12] stated that nanofluids are stronger and possess temperature-dependent thermal conductivity at low concentration which enhances process performance in many applications. But the author's investigation was MQL on turning in AISI 9310 steel with vegetable oil-based cutting fluid. Mao et al. [13] investigated nanofluid performance in grinding with MQL environment. The analysis was varying the nanofluid concentration with other parameters. The finding was higher concentration of nanofluid reduces the grinding force, tool wear, surface roughness. Vasu and Kumar [11] mixed 1%  $\text{Al}_2\text{O}_3$  nanoparticles with TRIM E709 emulsifier to form nanofluid and used as cutting fluid in MQL environment for machining EN31 steel at low speed cutting for his investigation. Subhash et al. [14] considered two kinds of nanofluid as 1% and 4%  $\text{Al}_2\text{O}_3$  nano particles separately blended with Max Mist ST-2020 vegetable oil and used them for turning in a lathe of Nicrofer C263 superalloy in MQL environment to study the nanofluid roll in turning that material. Since the cutting zone heat reduction and good surface finish are main objectives, alumina has good thermal conductivity and good tribological characteristics. The enhanced functional behaviour, wear resistance, and fatigue life of high chromium steel components are depending heavily on their higher surface quality [15]. The Taguchi-coupled grey relational analysis has been used to determine the best turning parameters for the multiperformance characteristics in the turning process. To do this, an interchangeable two-phase straight cemented tungsten carbide-cobalt mixed (WC-Co) insert grade (CSTC—K20) tool has been developed. While cutting speed, feed rate, and depth of cut were regarded as the controllable process parameters, flank wear and surface finish were considered as performance attributes. Three process parameters were considered at four levels in the Taguchi L16 orthogonal array used to arrange the experiments [16]. The process parameters were predicted for obtaining the best surface finish in surface grinding of EN24 steel. The prediction model was developed from ANOVA results of response surface methodology [17]. Based on the cross section sensitivity and matching

TABLE 1: Chemical test results of EN31 workpiece.

S. no.	Description of the constituent	Wt.%
1	Silicon	0.20
2	Carbon	0.93
3	Phosphorus	0.333
4	Manganese	0.59
5	Chromium	1.08
6	Sulphur	0.025
7	Iron	Remaining

restrictions of solid end mills, an iterative optimization approach was developed for the bearing and geometric parameters of grinding wheels [18]. This research interest is unique. As the flood cooling type environment is still obvious in much industry, this work tried to enrich flood cooling environment by suspending alumina nanoparticles for investigating nanofluid performance in high-speed surface grinding on EN31 steel at high wheel speed. Conventionally, the nanofluids were utilized in minimum quantity lubricant (MQL) type lubrication system to achieve cutting zone temperature reduction. But they cannot be reused. This investigation considered nanofluids in the flood cooling system and could be reused multiple times, so the coolant cost will be less than MQL.

## 3. Experimental Design

The EN31 steel is high-speed grounded by three different machining environments: dry (natural flow atmospheric air cooling), with the use of conventional coolant and with the use of nanofluid. Taguchi full factorial design was employed to conduct the experiments to observe the cutting zone temperature and surface roughness on grounded materials. The results were compared. The thermal analysis was done based on the experimented observations and presented. The DOE Taguchi full factorial design is employed for the experimental design. The work piece tested chemically to ensure its originality of EN31 steel. The tested values are presented in Table 1. The factors and responses considered for the experimental design are furnished in Tables 1–3. The constant parameters of the experimental setup are furnished in Table 4. Taguchi full factorial design for the case is furnished in Tables 5–7.

## 4. Machining Environment

**4.1. Dry Machining.** The dry machining practices exist for meeting product requirements economically because the cutting fluid consumes more cost. Dry machining means there is no cutting fluid used during the machining process. The temperature rise of the cutting tool is very high when dry machining induces reduction of tool wears and tool life. The chips generated at dry machining do not wash away, and they cause deterioration on the machined surface.

**4.2. Wet Machining.** Wet machining is the one in which the cutting fluid is used. Here, the eco-friendly cutting fluid TIRM SOL LC sf branded general-purpose emulsion and

TABLE 2: DOE: factors and amp—levels.

Factors	Level 1	Level 2	Level 3	Level 4
Feed (mm/sec)	100	120	150	175
Depth of cut ( $\mu\text{m}$ )	10	20	30	40
Machining environment	No coolant (dry)	Cutting fluid	Nanofluid	-

TABLE 3: DOE: response.

	Response	Unit
1	Cutting zone temperature	Degree centigrade ( $^{\circ}\text{C}$ )
2	Surface roughness (Ra)	Microns ( $\mu\text{m}$ )

TABLE 4: Constant factors in the experiments.

	Constant factors	Specification
1	Peripheral velocity of cutting fluid	32 m/s, 0.5 mm from the wheel surface
2	Cutting velocity	29830 mm/sec
3	Wheel speed (rpm)	2850 rpm

TABLE 5: Taguchi full factorial design: dry machining environment.

Run	Experimental design		Observation	
	Operating parameters		Surface temperature	Surface roughness
	In feed ( $\mu\text{m}$ )	Feed (mm/sec)		
1	10	100	708.34	0.246
2	10	100	732.44	0.348
3	10	100	734.94	0.418
4	20	100	741.56	0.572
5	20	100	720.08	0.320
6	20	100	743.06	0.420
7	30	100	744.10	0.546
8	30	100	753.68	0.668
9	30	100	730.14	0.422
10	40	100	753.02	0.500
11	40	100	756.06	0.694
12	40	100	767.72	0.820

TABLE 6: Taguchi full factorial design: machining with conventional coolant.

Run	Experimental design		Observation	
	Operating parameters		Surface temperature	Surface roughness
	In feed ( $\mu\text{m}$ )	Feed (mm/sec)		
1	10	100	406.78	0.240
2	10	100	422.40	0.334
3	10	100	433.16	0.406
4	20	100	442.92	0.508
5	20	100	417.56	0.296
6	20	100	431.58	0.368
7	30	100	444.12	0.460
8	30	100	451.18	0.498
9	30	100	428.02	0.368
10	40	100	442.28	0.420
11	40	100	452.24	0.534
12	40	100	462.16	0.602

TABLE 7: Taguchi full factorial design: machining with nanofluid as coolant.

Run	Experimental design		Observation	
	Operating parameters		Surface temperature	Surface roughness
	In feed ( $\mu\text{m}$ )	Feed (mm/sec)		
1	10	100	210.04	0.230
2	10	100	229.28	0.264
3	10	100	240.42	0.366
4	20	100	248.84	0.422
5	20	100	224.16	0.256
6	20	100	236.04	0.312
7	30	100	247.90	0.404
8	30	100	261.32	0.448
9	30	100	237.34	0.274
10	40	100	248.18	0.326
11	40	100	255.18	0.410
12	40	100	272.08	0.466

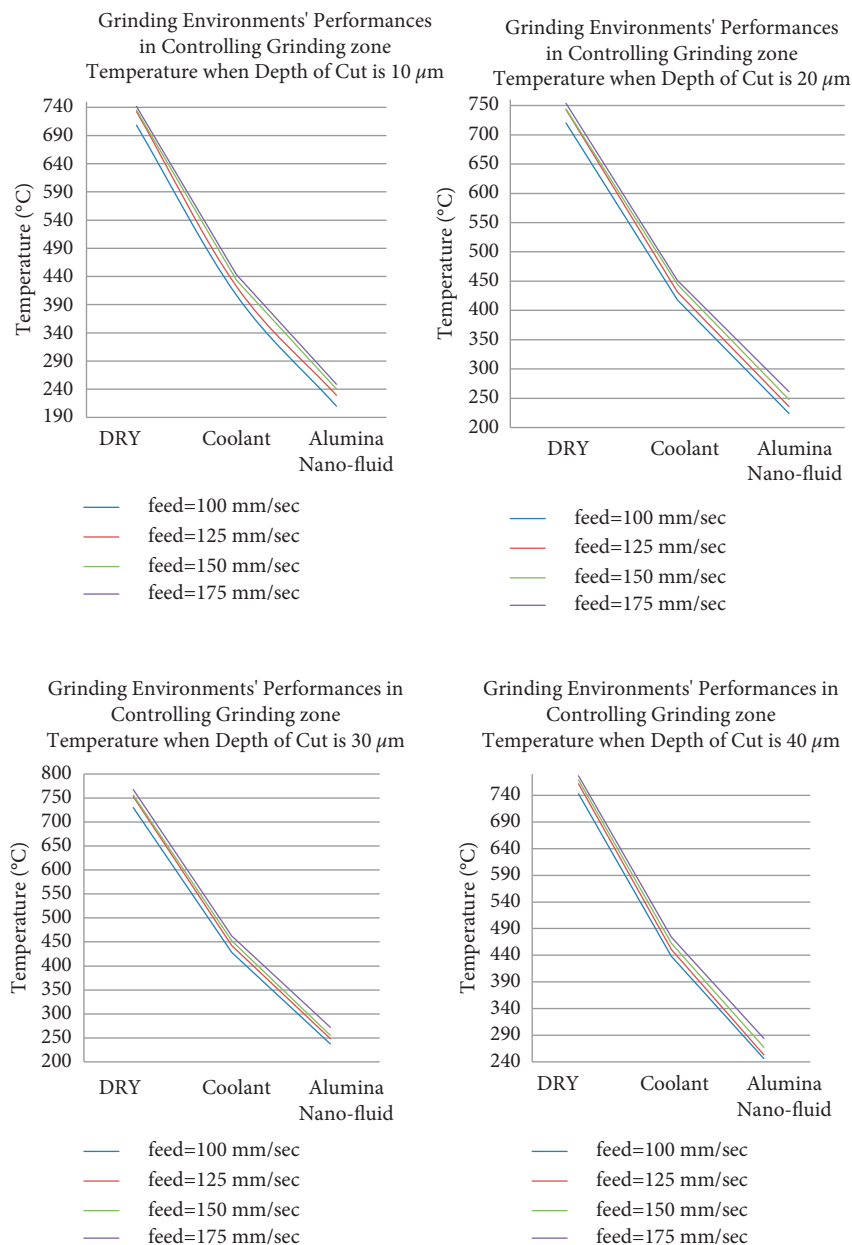


FIGURE 1: Grinding environments' performances in downsizing the cutting zone temperature in constant depth of cut and various feeds.

TABLE 8: Temperature reduction by coolant and lubricant at constant DoC.

DoC Feed mm/sec	10 $\mu\text{m}$		20 $\mu\text{m}$		30 $\mu\text{m}$		40 $\mu\text{m}$	
	Wet than dry (%)	Nanofluid than wet (%)	Wet than dry (%)	Nanofluid than wet (%)	Wet than dry (%)	Nanofluid than wet (%)	Wet than dry (%)	Nanofluid than wet (%)
100	42.57	48.37	42.01	46.32	41.38	44.55	40.96	43.87
125	42.33	45.72	41.92	45.31	41.27	43.89	40.79	43.87
150	41.06	44.50	40.31	44.18	40.18	43.57	39.81	42.23
175	40.27	43.82	40.14	42.08	39.80	41.13	38.96	40.09

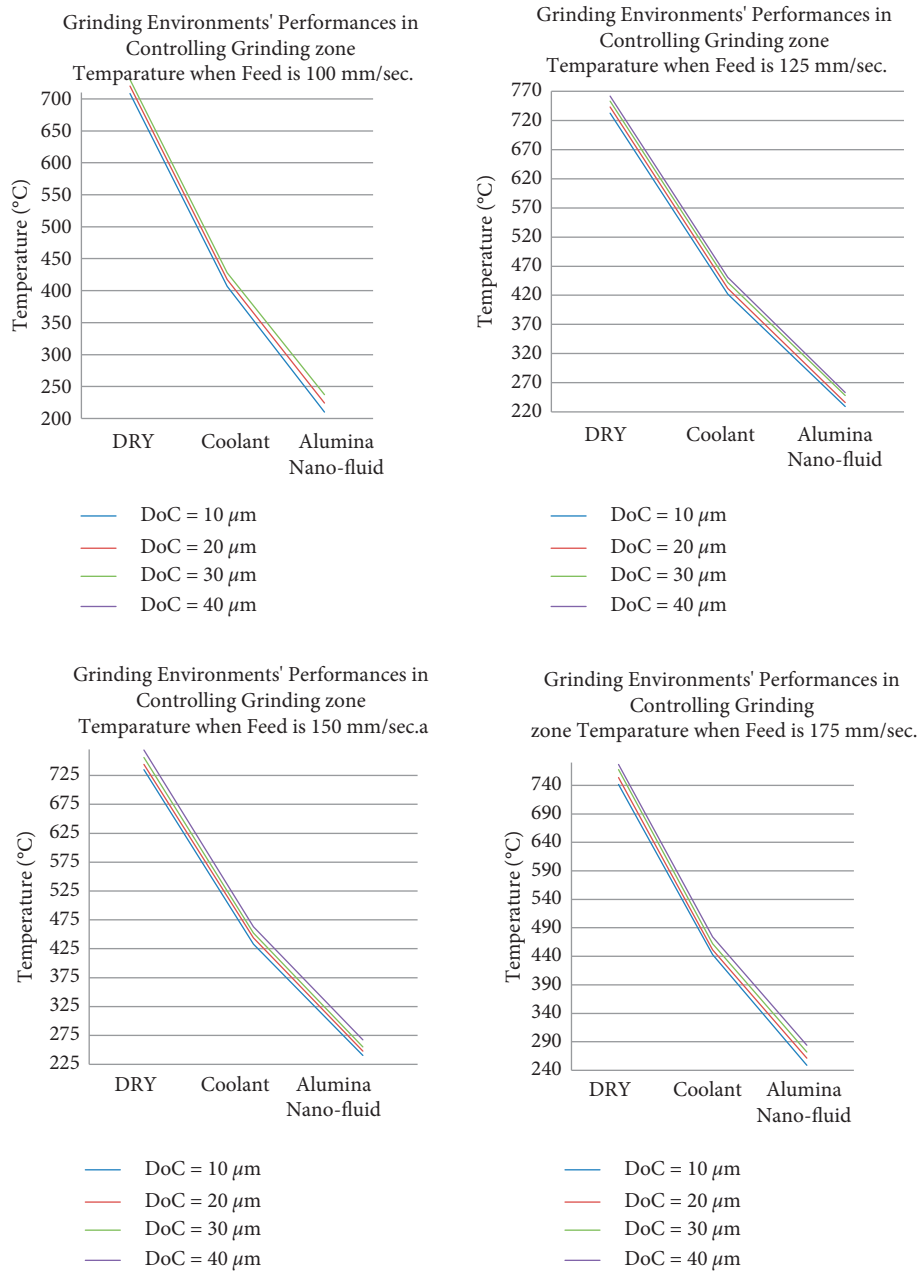


FIGURE 2: Cutting zone temperature reduction performance of machining environment at constant feed.

nonchlorinated, siloxane-free emulsifier is used. Since it is heavy duty cutting, the mixing ratio 1 : 10 was preferred. The emulsions are suspensions of oil droplets in water and have a milky

appearance with an oil droplet size in the range 0.005 mm to 0.002 mm. They will provide good cooling with moderate lubricity and overcome demerits highlighted in the literature.

TABLE 9: Temperature reduction by coolant and lubricant at constant feed.

Feed DoC ( $\mu\text{m}$ )	100 mm/sec		125 mm/sec		150 mm/sec		175 mm/sec	
	Wet than dry (%)	Nanofluid than wet (%)	Wet than dry (%)	Nanofluid than wet (%)	Wet than dry (%)	Nanofluid than wet (%)	Wet than dry (%)	Nanofluid than wet (%)
10	42.57	48.37	42.33	45.72	41.38	44.55	40.96	43.87
20	42.01	46.32	41.92	45.31	41.27	43.89	40.79	43.87
30	41.38	44.55	41.27	43.89	40.18	43.57	39.81	42.23
40	40.96	43.87	40.79	43.87	39.80	41.13	38.96	40.09

4.3. *Nanofluid*. Since nano  $\text{Al}_2\text{O}_3$  particles have superior tribological and antitoxic properties reported by Jung et al. [19], it is preferred in this study. Based on the literature, the percentage of mixing is 1% which is customary practice for investigation. Here, the alumina nanopowder is mixed with TIRM SOL LC sf cutting fluid in the ratio of 1 : 100, that is, one gram of alumina nanopowder for 100 grams of TIRM SOL LC sf cutting fluid by weight. After mixing, the fluid was stirred continuously about 8 to 9 hours in a magnetic stirrer for reducing a particle size about 5 nm and homogeneous mixing of nanopowder with cutting fluid. Then, the fluid is used as wet coolant with water in the ratio of 1 : 10. The prepared nanofluids were used in the flood form during experimentation.

4.4. *The Work Piece*. Based on the demand of its applications including dice ball and roller bearings, swaging dies spinning tools, punches, taps, ejector pins, gauges, and cylindrical, conical, and needle rollers, the EN31 steel is preferred for this study. EN31 steel is most commonly used high carbon steel which poses a good quality for wear resisting machine parts and for press tools. The work piece size is  $50 \times 50 \times 10$  mm (with centrally drilled with depth of 5 mm for temperature measurement).

## 5. Experimentation

The experimentation is to investigate the influence of machining environments and nanofluid performance evaluation in high wheel speed (29830 mm/sec) surface grinding; the other factors are feed (mm/sec) and depth of cut (microns). The measure of performance is the surface roughness in  $\mu\text{m}$  and cutting zone temperature in degree centigrade. The omega makes HH801 A dual input K/J digital thermometer with thermocouple accuracy.  $\pm 1.1^\circ\text{C}$  is employed for measuring temperature. The K-type mode is used for the measurement. The work piece has a drilled hole of 5 mm deep from bottom and the thermocouple end attached. The temperature measurements are up to 5 mm deep of from the surface. The Taylor Hobson Surtronic3+ contact type profile meter was employed in surface roughness measurement with 0.8 mm cut of length, and the sampling number is five. Initially, the dry grinding environment is considered. The minimum feed 100 mm/sec was set and was kept constant, and the depth of cut varied from  $10 \mu\text{m}$  to  $40 \mu\text{m}$  with the step of  $10 \mu\text{m}$ . Then, the feed is increased to 125 mm/sec, 150 mm/sec, and finally 175 mm/sec. For each feed setting, the trials are conducted with four different depth-of-cut

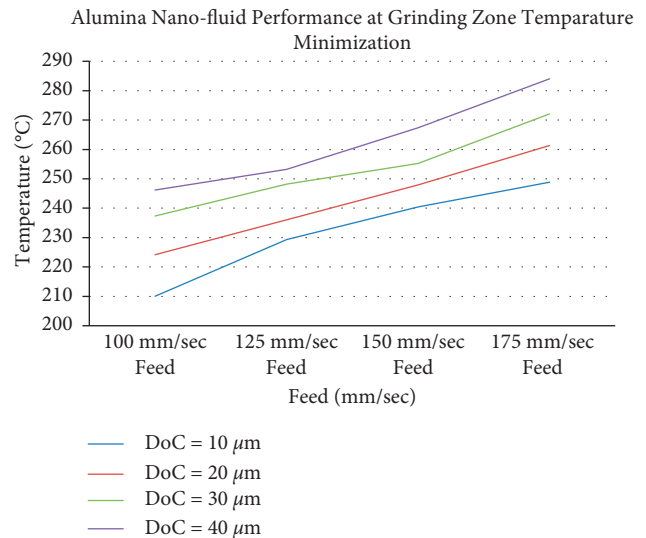


FIGURE 3: Alumina nano-fluid performance in downsizing grinding zone temperature.

settings say  $10 \mu\text{m}$ ,  $20 \mu\text{m}$ ,  $30 \mu\text{m}$ , and  $40 \mu\text{m}$ . These settings were repeated for wet cooling environment and nanofluid environment. Each trial is repeated five times, and the temperature and roughness values were recorded. The average of values is considered for minimizing the observation error. The experimental setting and observed values are tabulated in Tables 5–7 as responses for the experimental design. Table 5 is observation at dry machining environment, Table 6 is for conventional coolant (TIRM SOL LC sf), and Table 7 is for nanofluid machining environment.

## 6. Result and Discussion

The cutting zone temperature reduction is the primary objective of this work. It is observed that the cutting zone temperature variation is significant with respect to the grinding environment, feed, and depth of cut in which the cutting zone temperature with respect to grinding environment is most significant. At first, the depth of cut is kept constant and varying machining environment and feed. The behavior is plotted in Figure 1 such as first row graphs are when the depth of cut is  $10 \mu\text{m}$  and  $20 \mu\text{m}$ , the second row is when the depth of cut is  $30 \mu\text{m}$  and  $40 \mu\text{m}$ . The percentage of heat reduction was computed. The surface temperature was found higher in dry than in nanofluid environment. Hence, Table 8 shows the

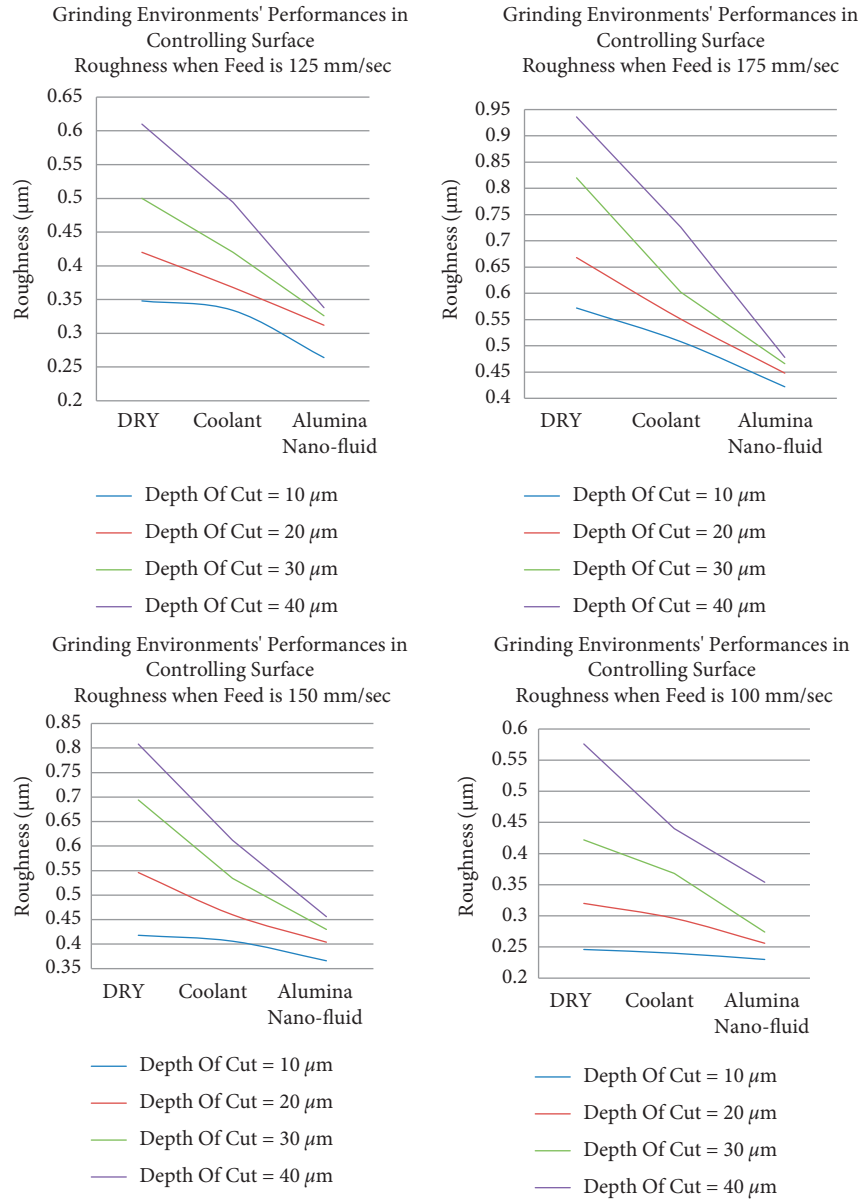


FIGURE 4: Grinding environments' performances in controlling surface roughness at constant feed upgrading surface finish.

TABLE 10: Surface roughness reduction by coolant and lubricant at constant feed.

Feed DoC (µm)	100 mm/sec		125 mm/sec		150 mm/sec		175 mm/sec	
	Wet than dry (%)	Nanofluid than wet (%)	Wet than dry (%)	Nanofluid than wet (%)	Wet than dry (%)	Nanofluid than wet (%)	Wet than dry (%)	Nanofluid than wet (%)
10	2.44	4.17	4.02	20.96	2.87	9.85	11.19	16.93
20	7.50	13.51	12.38	15.22	15.75	12.17	25.45	10.04
30	12.80	25.54	16.00	22.38	23.05	19.48	26.59	22.59
40	23.61	19.55	19.02	31.58	24.26	25.49	22.44	34.16

percentage of reduction for each case. The average reduction of temperature was considered for the calculation in percentage. It was the ratio of average of temperature reduced by wet machining ( $avg. T_{dry} - avg. T_{wet}$ ) to the

average of temperature ( $avg. T_{dry}$ ) in the conventional method (dry machining) by using equation (3). The comparison of nanofluid performance by using the ratio of average of temperature ( $avg. T_{wet} - Avg. T_{Nf}$ ) reduced



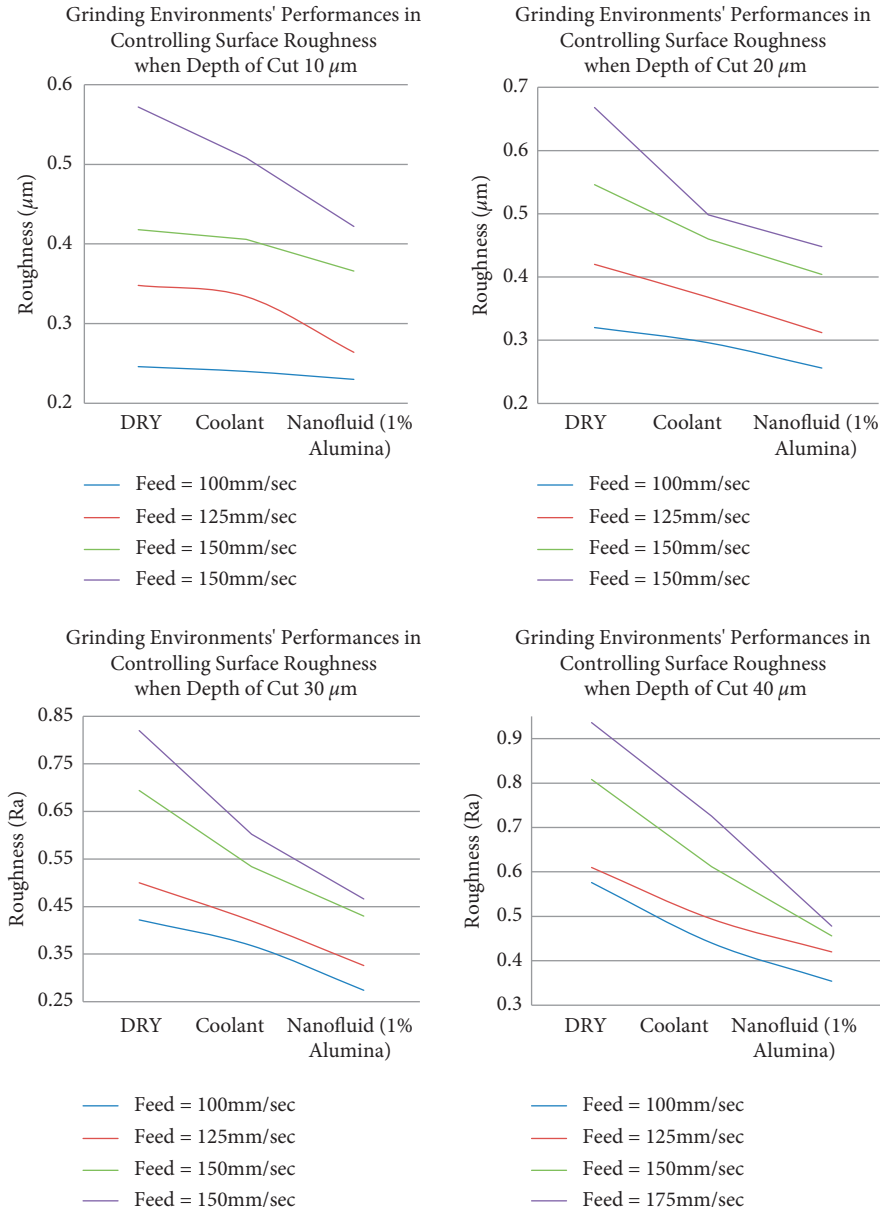


FIGURE 5: Grinding environments' performances in controlling surface roughness at a constant depth of cut.

by nanofluid to the average of temperature ( $avg. T_{wet}$ ) observed with the use of the conventional method (conventional coolant) by using equation (4).

percentage of reduction from dry to wet

$$= \frac{avg. T_{dry} - avg. T_{wet}}{avg. T_{dry}} \times 100. \quad (1)$$

percentage of reduction from wet to Nf

$$= \frac{avg. T_{wet} - avg. T_{Nf}}{avg. T_{wet}} \times 100. \quad (2)$$

Similarly to the behaviour at constant feed rate, the temperature reduction performance by varying the depth of cut and machining environment was considered. The

graphical representation is presented in Figure 2. The first row is the surface temperature with respect to depth of cut and cutting fluid and lubricant used at a constant feed of 100 and 125 mm/sec, and the second row is when 150 mm/sec  $i$  and 175 mm/sec. The percentage of temperature reduction for the abovesaid cases is consolidated in Table 9. From Figure 2 and Table 9, it is evident that the nanofluid temperature reduction is significant than conventional cutting fluid.

The nanofluid performance with respect to various feed and depth of cut was analysed. The surface temperature increases with increase of DoC or feed (refer Figure 3). But in all the cases, the temperature was maintained by nanofluid considerably very lesser than conventional cutting fluid.

The upgrading performance of surface finish can be measured in terms of degree of downsizing the surface

TABLE 11: Surface roughness reduction by coolant and lubricant at a constant depth of cut.

DoC	10 $\mu\text{m}$		20 $\mu\text{m}$		30 $\mu\text{m}$		40 $\mu\text{m}$	
	Wet than dry (%)	Nanofluid than wet (%)	Wet than dry (%)	Nanofluid than wet (%)	Wet than dry (%)	Nanofluid than wet (%)	Wet than dry (%)	Nanofluid than wet (%)
100	2.44	4.17	7.50	13.51	12.80	25.54	23.61	19.55
125	4.02	20.96	12.38	15.22	16.00	22.38	19.02	9.72
150	2.87	9.85	15.75	12.17	23.05	19.48	24.26	25.49
175	11.19	16.93	25.45	10.04	26.59	22.59	22.44	34.16

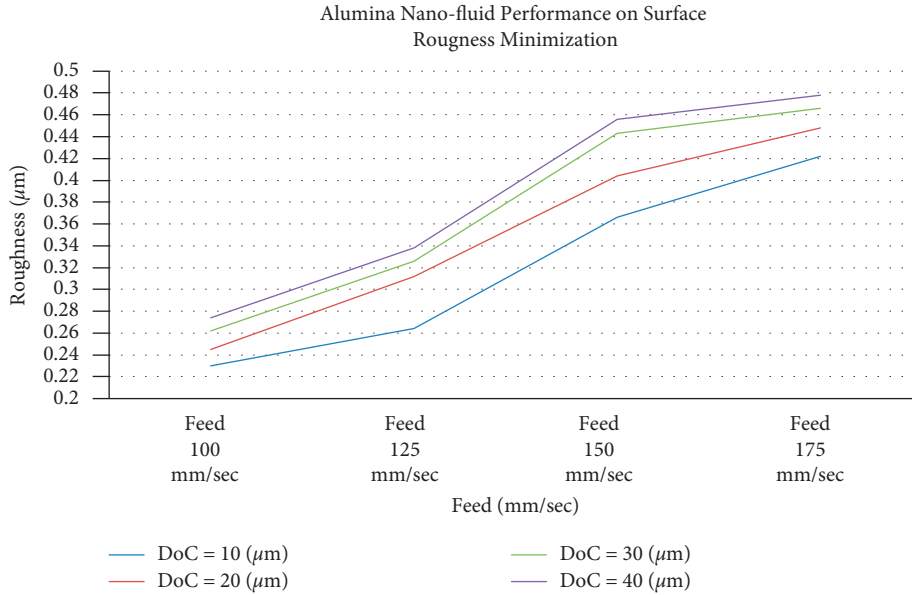


FIGURE 6: Alumina nanofluid performance on surface roughness minimization.

roughness. In general observation, the surface roughness reduction is significant with respect to machining environment. The analysis is performance of machining environment at constant feed rate and constant depth of cut. Figures 4 furnishes the graphical representation of machining environment behaviour with constant feed rate of 100 mm/sec and 125 mm/sec (first row) and 150 mm/sec and 175 mm/sec (second row). The percentage of roughness reductions is consolidated in Table 10 for constant feed rate cases. The average reduction of surface roughness was

considered for the calculation in percentage. It was the ratio of average of surface roughness reduced by wet machining ( $Avg. Ra_{dry} - Avg. Ra_{wet}$ ) to the average of surface roughness ( $Avg. Ra_{dry}$ ) in the conventional method (dry machining) by using equation (1). The comparison  $n$  of nanofluid performance by using the ratio of average of surface roughness reduced by nanofluid ( $Avg. Ra_{wet} - Avg. Ra_{Nf}$ ) to average of surface roughness ( $Avg. Ra_{wet}$ ) observed with use of conventional grinding method (conventional coolant) by using equation (2).

$$\text{Percentage of reduction from dry to wet} = \frac{Avg. Ra_{dry} - Avg. Ra_{wet}}{Avg. Ra_{dry}} \times 100, \quad (3)$$

$$\text{Percentage of reduction from wet to Nf} = \frac{Avg. Ra_{wet} - Avg. Ra_{Nf}}{Avg. Ra_{wet}} \times 100. \quad (4)$$

The roughness reduction performances were analysed with respect to various feeds and machining environments at constant DoC (depth of cut). Figure 5 is graphical illustration of the same, i.e., in first row graphs are performance

of grinding environments with respect to various feed at 10  $\mu\text{m}$  and 20  $\mu\text{m}$  DoC; similarly, the second row is for 30  $\mu\text{m}$  and 40  $\mu\text{m}$  DoCs. Roughness reduction in percentage is presented in Table 11.

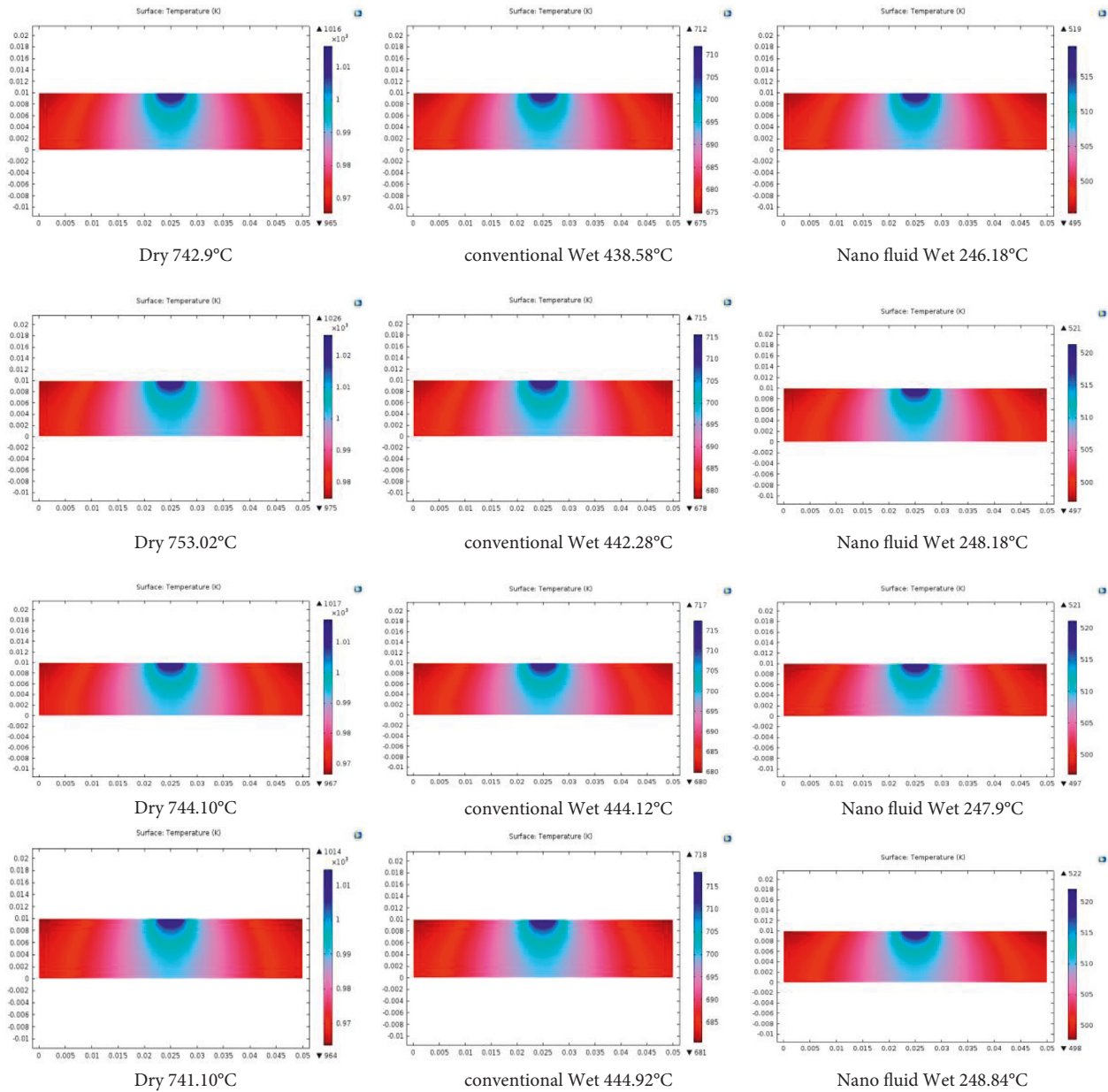


FIGURE 7: FEM: thermal analysis results. The first column is dry machining, the second column is conventional wet machining, and the third column is nanofluid wet machining.

Figure 6 shows the nanofluid performance with respect to feed and depth of cut. The increase of MRR (both depth of cut and feed rate) increases the surface roughness. But the maximum roughness  $0.48 \mu\text{m}$  is acceptable, that is, better surface finish than conventional coolant performance. Hence, it is obvious that the nanofluid coolant out performs better than conventional coolant significantly in improving surface finish as well as temperature

## 7. Thermal Analysis

The purpose of the finite element method heat transfer modeling and analysis is used for analysing energy partition in work piece. This model traces the heat distribution in the work piece. The finite element model was created by COMSOL Multiphysics 5.0 package to analyze heat distribution on the work. The heat was measured at the center of the work piece through thermo couple. The measured values are used in the FEM to observe the

behavior in the work piece. The surrounding temperature is considered as 30°C or 303 K, and the peripheral velocity is 32 m/s with 0.5 mm from surface. The forced convection is at the top surface of the natural convection on side and the conductive heat transfer at the bottom of the work piece. The meshed geometry has 5032 domain elements and 240 boundary elements. The output of the FEA is presented in Figure 7.

## 8. Conclusion

The experimental investigation of alumina nanofluid (as cutting fluid) for high-speed grinding of EN31 steel in reduction of surface roughness and surface temperature was discussed, and the following are the findings:

- (i) The two extreme parameters settings are as follows: all inputs are low and high. At low depth of cut of 10  $\mu\text{m}$  and low feed rate of 100 mm/sec, the nanofluid-based grinding reduced surface temperature by 48.37% than conventional coolant and lubricant.
- (ii) At high depth of cut of 40  $\mu\text{m}$  and high feed rate of 170 mm/sec, the temperature reduction performance with the use of alumina nanofluid was observed as 40.09% than conventional cutting fluid.
- (iii) At constant feed rate averagely 45.63.69%, 44.85%, 43.56%, and 42.24%, temperature reduced at feed rates 100, 125, 150, and 175 mm/sec, respectively, than use of conventional coolant for grinding EN31 steel at various depth cuts of 10, 20, 30, and 40  $\mu\text{m}$  in each feed rate.
- (iv) The surface finish performance is also appreciable at low and high MRR settings. The surface roughness reduction at low and high parameters setting are 4.17% and 34.16%, respectively.
- (v) The average surface roughness reduction by alumina nanofluid than conventional cutting fluid 15.69%, 17.07%, 16.75%, and 20.93% for the feed rates 100, 125, 150, and 175 mm/sec, respectively, for various depth cuts of 10, 20, 30, and 40  $\mu\text{m}$ .
- (vi) The thermal analysis reports were presented, and the fluid was kept the surface temperature in safe limit.

## Data Availability

The data used to support the findings of this study are included in the article. Further data or information required can be available from the corresponding author upon request.

## Disclosure

This work was performed as a part of the Employment Hawassa University, Ethiopia.

## Conflicts of Interest

The authors declare that they have no conflicts of interest.

## Acknowledgments

The authors appreciate the technical assistance to complete this experimental work from the Department of Mechanical Engineering, Faculty of Manufacturing, Institute of Technology, Hawassa University, Ethiopia.

## References

- [1] S. Malkin and C. Guo, "Thermal analysis of grinding," *CIRP Annals*, vol. 56, no. 2, pp. 760–782, 2007.
- [2] S. Paul and A. B. Chattopadhyay, "The effect of cryogenic cooling on grinding forces," *International journal of machine tools & manufacture*, vol. 36, pp. 63–72, 1996.
- [3] E. K. Henriksen, "Chip breaking—a study of three dimensional chip flow," *American Society of Mechanical Engineers*, vol. 53, pp. 53–59, 1953.
- [4] P. Suresh, S. D. Mc Donald, and M. S. Dargusch, "Effects of coolant pressure on chip formation while turning Ti-6Al-4V alloy," *International Journal of Machine Tools and Manufacture*, vol. 49, pp. 739–743, 2009.
- [5] Z. Chen, A. Atmadi, D. A. Stephenson, and S. Y. Liang, "Analysis of cutting fluid aerosol generation of environmentally responsible machining," *Annals of CIRP*, vol. 49, no. 1, pp. 53–56, 2000.
- [6] F. Klocke and G. Eisenblatter, "Dry cutting," *Annals of CIRP*, vol. 106, pp. 68–73, 1997.
- [7] P. S. Sreejith and B. Ngoi, "Dry machining: machining of the future," *Journal of Materials Processing Technology*, vol. 101, no. 1-3, pp. 287–291, 2000.
- [8] E. Brinksmeier, C. Heinzel, and M. Wittmann, "Friction, cooling and lubrication in grinding," *Annals of CIRP*, vol. 48, no. 2, 1999.
- [9] X. C. Tan, F. Liu, H. Cao, and H. Zhang, "A Decision making framework model of cutting fluid selection for green manufacturing and a case study," *International Journal of Machine Tools and Manufacture*, vol. 129, pp. 467–470, 2002.
- [10] S. N. Jung, L. Pil-Ho, and W. L. Sang, "A study on machining and environmental characteristics of micro-drilling process using nanofluid minimum quantity lubrication," in *Proceedings of the ASME 2011 International Manufacturing Science and Engineering Conference*, vol. 2, Corvallis, Oregon, USA, June 2011.
- [11] V. Vasu and K. M. Kumar, "Analysis of nanofluids as cutting fluid in grinding EN-31 steel," *Nano-Micro Letters*, vol. 3, no. 4, pp. 209–214, 2011.
- [12] M. M. A. Khan, M. Mithu, and N. Dhar, "Effects of minimum quantity lubrication on turning AISI 9310 alloy steel using vegetable oil-based cutting fluid," *Journal of Materials Processing Technology*, vol. 209, no. 15-16, pp. 5573–5583, 2009.
- [13] C. Mao, J. Zhang, Y. Huang, Z. Hongfu, H. Xiangming, and Z. Zhixiong, "Investigation on the effect of nanofluid parameters on MQL grinding, materials and manufacturing processes," vol. 28, no. 4, pp. 436–442, 2013.
- [14] C. B. P. Subhash, C. S. P. Rao, and J. Kishore, "Role of MQL and NANO fluids on the machining of NICROFER C263," in *Proceedings of the 5th international & 26th all India manufacturing Technology, Design and Research Conference (AIMTDR 2014)*, vol. 363, pp. 1–3, Guwahati, Assam, India, December 2014.
- [15] V. Ajitanshu, "Chaturvedi shashi kant. Optimizing machining process of E31 steel for improved surface roughness," *Invertis Journal of Science & Technology*, vol. 12, no. 4, pp. 153–164, 2019.

- [16] Z. Hussain, "Multi performance optimization in machining of EN31-535A99SS with interchangeable straight cemented tungsten carbide-cobalt mixed (WC-Co) insert grade (CSTC—K20) using Taguchi coupled grey relational analysis," *SN Applied Sciences*, vol. 2, p. 197, 2020.
- [17] R. Sanjeevi, G. A. Kumar, and B. R. Krishnan, "Optimization of machining parameters in plane surface grinding process by response surface methodology," *Materials Today Proceedings*, vol. 37, pp. 85–87, 2021.
- [18] Y. Li, G. Ding, X. Changjiu, N. Yangcheng, and J. Lei, "An iterative optimization algorithm for posture and geometric parameters of grinding wheel based on cross-section sensitivity and matching constraints of solid end mills," *Journal of Manufacturing Processes*, vol. 79, 2022.
- [19] S. N. Jung, L. Pil-Ho, C. Li, and W. L. Sang, "An experimental study on micro grinding process with nano fluid minimum quantity lubrication," *International Journal of Precision Engineering and Manufacturing*, vol. 13, pp. 331–338, 2012.

## *Retraction*

# **Retracted: Research on the Innovation of Procurement Mode of Nanomaterials Based on E-Commerce**

### **Advances in Materials Science and Engineering**

Received 26 December 2023; Accepted 26 December 2023; Published 29 December 2023

Copyright © 2023 Advances in Materials Science and Engineering. This is an open access article distributed under the Creative Commons Attribution License, which permits unrestricted use, distribution, and reproduction in any medium, provided the original work is properly cited.

This article has been retracted by Hindawi, as publisher, following an investigation undertaken by the publisher [1]. This investigation has uncovered evidence of systematic manipulation of the publication and peer-review process. We cannot, therefore, vouch for the reliability or integrity of this article.

Please note that this notice is intended solely to alert readers that the peer-review process of this article has been compromised.

Wiley and Hindawi regret that the usual quality checks did not identify these issues before publication and have since put additional measures in place to safeguard research integrity.

We wish to credit our Research Integrity and Research Publishing teams and anonymous and named external researchers and research integrity experts for contributing to this investigation.

The corresponding author, as the representative of all authors, has been given the opportunity to register their agreement or disagreement to this retraction. We have kept a record of any response received.

### **References**

- [1] B. Song and X. Wang, "Research on the Innovation of Procurement Mode of Nanomaterials Based on E-Commerce," *Advances in Materials Science and Engineering*, vol. 2022, Article ID 2415668, 9 pages, 2022.



## Research Article

# Research on the Innovation of Procurement Mode of Nanomaterials Based on E-Commerce

Baorui Song<sup>1</sup> and Xiaozhi Wang<sup>2</sup> 

<sup>1</sup>Office of Higher Education Research, Hebei Petroleum University of Technology, Chengde 067000, Hebei, China

<sup>2</sup>Department of Management Engineering, Hebei Petroleum University of Technology, Chengde 067000, Hebei, China

Correspondence should be addressed to Xiaozhi Wang; [cdpc\\_wxz@cdpc.edu.cn](mailto:cdpc_wxz@cdpc.edu.cn)

Received 13 June 2022; Revised 14 July 2022; Accepted 3 August 2022; Published 28 August 2022

Academic Editor: K. Raja

Copyright © 2022 Baorui Song and Xiaozhi Wang. This is an open access article distributed under the Creative Commons Attribution License, which permits unrestricted use, distribution, and reproduction in any medium, provided the original work is properly cited.

With the rapid development of science and technology, the proportion of nanomaterials is increasing. With the advantages of height, strength, high density, and lightweight, nanomaterials have become the preferred manufacturing materials in many industries. In the procurement business of e-commerce, the utilization rate of nanomaterials is getting higher and higher. However, due to the long manufacturing cycle, high consumption loss, and high transportation damage rate of nanomaterials, there are often many problems in the procurement process. In this paper, we use the methods of case investigation and experimental research to study the innovation of procurement mode of nanomaterials in e-commerce. The data show that the use of nanomaterials has become the first choice of many manufacturers and suppliers and has a more and more frequent trend in the use process. Nanomaterials are suitable for industrial application due to their low transportation and storage costs and high procurement efficiency. However, at present, nanomaterials need further innovation to achieve more applications. In this paper, the procurement model and marketing model are innovated to make the e-commerce procurement business of nanomaterials more convenient. From these studies, this paper concludes that the most important thing for the procurement of nanomaterials is to find out the customers' needs, and then according to the user specifications of nanomaterials, achieve the best logistics and distribution methods in the transportation process. The innovation of the e-commerce procurement mode of nanomaterials can greatly facilitate the development of business. Under the innovative mode, the transportation cost and procurement efficiency have been greatly improved, about 2 points higher than before, and the procurement value has also increased by 3 points to more than 6 points. At the same time, the innovation of e-commerce procurement mode of nanomaterials can make the related upstream and downstream industrial chain reach a very saturated state and make the scientific and technological innovation and procurement salesman in the industry more smooth and reliable.

## 1. Introduction

The research direction of this paper is to explore the innovation of nanomaterial procurement mode of e-commerce. E-commerce is the purchase mode of most people nowadays, and it has a trend of more and more frequent use. In the operation of enterprises, the use of e-commerce platforms for business development is also a very common phenomenon. For example, the enterprise's inquiry, transaction, order placing, documentary, transaction, customs declaration, shipment, and other links can be carried out through the e-commerce platform. In the

procurement business, more and more enterprises use e-commerce platforms to purchase the products they need. This procurement mode is not only high efficiency, low cost, and wide range but also can cooperate and communicate with enterprises. Promote the normal and healthy operation of the company's business upstream and downstream. Many enterprises have made high profits in the procurement business of e-commerce. Therefore, the innovation of e-commerce procurement mode of nanomaterials has become a very popular business development direction and research direction in recent years.

In the research of e-commerce nano material procurement mode innovation, many foreign researchers have made a lot of exploration. Procek et al. In his research,  $m$  used interview method and literature research method to analyze and summarize the purchasing data on many websites. Finally, the results show that the innovation of procurement mode of nanomaterials is based on the traditional procurement mode, using modern high-tech products, purchasing products on the e-commerce platform, and then greatly reducing the company's procurement cost, resulting in the cost advantage, win the competition [1]. In his research literature, Ding et al. used the case study method to make an investigation and case study in different nanomaterial suppliers, calculated and analyzed the procurement costs of different suppliers and concluded that the enterprises that use e-commerce procurement mode innovation have achieved good results in procurement cost and labor cost. It can enable the company to obtain cost-effective advantages in a short period of time, as well as certain advantages in cost, so as to be in a favorable position in the competition [2]. Chen et al. In his research,  $J$  used a large number of case studies to collect and sort out the purchase data of nanomaterials from major e-commerce platforms. After careful sorting and analysis, it is concluded that the use of e-commerce platform for nanomaterial procurement mode innovation can enable the diversified resources of e-commerce platform to combine with manufacturers and suppliers to achieve cooperation and complementarity. The purpose of e-commerce is to bring convenience of e-commerce to manufacturers and form a win-win situation, which is conducive to industrial upgrading and improving profits [2].

A large number of scholars in China have also carried out in-depth research on this subject and obtained a large number of research results. In its literature, Gkika et al. used the case comparison method to compare a large number of companies and suppliers that need to use nanomaterials. It is concluded that the enterprises that take the lead in using nanomaterials are obviously better than those enterprises that do not use nanomaterials in terms of cost control, logistics and transportation, and labor costs. This advantage greatly reduces the operating costs of these enterprises to a large extent, which makes these enterprises in an advantageous position in the competition, and finally wins in the competition [3]. Verkasalo et al. in research, using the experimental analysis method, the benefits of several enterprises using e-commerce in the procurement of nanomaterials are analyzed. A series of data are sorted out in the operation status and financial status and statements of many enterprises. It is concluded that the use of e-commerce platforms in the procurement of nanomaterials can get sufficient guarantee in the supplier's stability quotient. The supplier's nanomaterials use materials that meet international standards so that enterprises can obtain stable profits in operation [4]. Hernández et al. used the experimental research method in their literature to study the frequency of e-commerce platforms used in the procurement business of nanomaterials and the frequency of suppliers using e-commerce platform. It was concluded that the use of

e-commerce platforms in the procurement business of nanomaterials can make the operation state of enterprises more stable and high profits. Let the enterprise be in the dominant position in the supply chain [5]. However, the procurement of nanomaterials involves many aspects, and there are many factors that affect the procurement cost and value. These studies do not take into account the comprehensiveness of the procurement process and the complexity of the procurement environment.

This paper uses the case study method and experimental research method to get the purchase proportion of nanomaterials by using e-commerce from the data of logistics cost and storage cost of many enterprises, selects cases from multiple suppliers for comparison and analysis, and concludes that using e-commerce platform to purchase nanomaterials can greatly reduce the transportation process and make the procurement process more convenient. At the same time, this paper analyzes and studies the procurement data of nanomaterials from multiple e-commerce platforms, and concludes that purchasing nanomaterials on e-commerce platforms and innovating the procurement mode can let enterprises choose the best among multiple choices, reduce the cost of supply chain and increase the stability. This research can provide expansion space for the application of e-commerce platforms, and also provide targeted guidance for the innovation and upgrading of nanomaterial procurement.

## 2. Innovative Research and Design of Nanomaterials Procurement Mode in E-Commerce

### 2.1. Innovative Design of Nanomaterials Procurement in E-Commerce

2.1.1. *Innovation of Nanomaterial Purchasing Market in E-Commerce.* Market innovation refers to the behavior that enterprises promote the change of market composition and the creation of market mechanisms from a micro perspective, and expand and occupy new markets with the development of new products, so as to meet new needs. Market innovation needs to measure the preference and attention of various customers for competitive products on the basis of the competitive product market after the enterprise determines its own strategic innovation, so as to rebuild a set of product marketing innovation modes in the market. Through the positioning innovation of the market, enterprises can establish a good image in the minds of the market and consumers, and reconstruct vivid image innovation by using more distinct and unconventional advantages [6, 7].

E-commerce platform also needs to use excellent resources and technology for the overall strategy, give full play to their own characteristics and advantages, use the characteristics of the market is very large, and customer service their own disadvantages and various risks. From the analysis of various factors and strategies in this paper, we can find that there are still many opportunities for this innovation. We can use the market demand to further innovate the

business model of the platform. We can also use the e-commerce platform's integrated services and product points to innovate the market positioning for the comprehensive demand of import and export trade and retail [8, 9].

*2.1.2. Business Strategy Innovation of E-Commerce.* Business strategy refers to the enterprise in order to achieve its own sales objectives, on the basis of analyzing the internal and external conditions of the market, using the mode of optimization advantage and innovation strategy, so that the enterprise can realize its own value in the competition and development [10, 11]. In order to achieve their business objectives and achieve their own development, enterprises generally adopt product strategy, market strategy, and development strategy [12].

After the innovation of the business model of e-commerce platform, the overall strategy is to promote the search between platform users to generate more economic benefits and then to generate more platform users. The competitive strategy used is to provide customers with more affordable products and services. The basic strategies are as follows: (1). Customers, who use platform products provide a complete set of solutions; (2). Enhance the value of various products owned by customers; and (3). Provide more efficient logistics and lower the threshold for customers to purchase products [13, 14].

*2.1.3. Product Value Innovation of E-Commerce.* The value innovation of products themselves is a method for enterprises to create the most valuable products for all households and win the competition by investigating customers and meeting their needs under the condition of determining the senior value demand and value orientation. The significance of product value innovation is obvious [15, 16]. Innovation is the driving force of development, and product value innovation is the driving force of enterprise development. Through product value innovation, we can enhance the competitiveness of products, broaden the market and establish a good brand [17]. There are many ways of product value innovation, which can be roughly divided into the following:

- (1) The unmet needs of customers mainly refer to the sales process and service process of products
- (2) It refers to the expectation of customers for products, and purchases and inquiries about their purchase of nanomaterials by mobile phones
- (3) It refers to the relationship between the customer and the company so that the platform can give customers a sense of trust and solve their worries and needs in a timely manner [18, 19]
- (4) It refers to the production of higher quality products, to provide customers with quality products and services

## *2.2. Innovative Design of Nanomaterial Procurement Module for E-Commerce*

*2.2.1. Innovation of Marketing Mode.* The innovation of marketing mode refers to a series of promotion strategies formed by the company in accordance with the different

market environment by using its own conditions and strength in the products operated by itself. For example: reducing prices, advertising marketing, channel innovation, and a series of innovative models. And the marketing modes include experiential marketing, one-to-one marketing, global localization marketing, relationship marketing [20], brand marketing, and in-depth marketing. In order to break through the sales volume of nanomaterial products and promote their products to the users, who need them [21, 22].

The marketing strategies of nanomaterials can be used as follows:

- (1) Using their own employees to carry out media publicity, each employee can publicize 10 to 30 people for the company, and the cumulative publicity wave can reach 2.4 million [23, 24]
- (2) All kinds of integral promotion modes, simple and multi-choice promotion modes, such as low-cost combination sales, good quality product portfolio promotion, and so on
- (3) Use the lowest price and low-cost operation mode to promote and sell

*2.2.2. Resource Integration and Innovation.* Resource integration and innovation mean that the company combines and allocates all resources according to its growth strategy and market demand, and establishes its core competitiveness by seeking the best combination of resource allocation and customer demand [25, 26].

- (1) Fully integrate the passenger and cargo resources of China Eastern Airlines, and take the passenger and cargo products as the main subsidy products of the platform.
- (2) Integrate all nanomaterials e-commerce companies into the platform. The businesses that have not yet been integrated into the platform include "direct delivery of origin" and "duty-free products of nanomaterials company." Among them, "direct delivery origin" is an e-commerce company of China Eastern Airlines cargo company, which is responsible for purchasing fruits, world-famous seafood, milk, and alcohol. B2c sales to domestic customers can deliver foreign fresh food to foreign customers within 48 hours [27]. China Eastern Airlines duty-free shop is an e-commerce company affiliated with China Eastern Airlines duty-free shop. Passengers on international and regional routes can log in to the site in advance to purchase duty-free items, which are then delivered to passengers by flight attendants. The above two e-commerce websites have specific business platform integration, which can increase the visits of platform customers and enrich platform products.
- (3) Fully integrate the internal talents of the company. The company has more than 80000 employees and a large number of talents with platform service ability.

The company can continuously provide human resources for the platform by selecting skilled and knowledgeable employees on the Internet for training.

*2.3. E-Commerce Procurement Process Optimization Design of Nanomaterials.* This paper improves the general e-commerce procurement process of small and medium-sized enterprises. The improved special procedures are as follows:

- (1) Define procurement requirements: conduct a comprehensive evaluation of materials and change the original method of identifying materials according to the contract and experience.
- (2) Issue long-term material requirements: use e-commerce platform to release the company's long-term material requirements. In order to create conditions for joint procurement, the company must not only find the purchasing alliance in the market but also communicate with the company itself when the purchasing alliance is needed. Improve the strength of the alliance.
- (3) Develop general procurement specifications: the difference between the general procurement specification and the central procurement specification is that when a company chooses a procurement alliance, it has another standard different from the central procurement specification.
- (4) Trading: different from the previous understanding of the demand for purchasing alliances in the market, the common market takes place in the form of pure participation. Trade and negotiation require the company to make a clear procurement plan, carefully choose to cooperate with the purchasing alliance and determine the company's position in the purchasing alliance through negotiation. Take the initiative to maximize the benefits of general contracts based on e-commerce platforms.
- (5) Sign long-term order agreement: sign long-term order agreements with e-commerce platforms and suppliers, and establish partnerships to optimize the company's supply chain.
- (6) Share material design with purchasing alliance: if you want to cooperate with purchasing alliance for a long time, you need to share purchasing information and establish a strategic partnership with purchasing alliance.
- (7) Placing orders on an e-commerce platform.
- (8) Commodity monitoring.
- (9) Receive goods for inspection, storage or monitoring, and exchange procedures.

*2.4. Optimization of Nanomaterials Procurement Dispersion Process in E-Commerce*

- (1) Since it is the era of integrated supply chain management mode, the integrated supply chain mode

breaks through the boundaries of various enterprises, connects the upstream supply chain and the downstream supply chain, and forms a complete and unified business system. The collaborative work of the supply chain strengthens the cooperation between enterprises and establishes a win-win situation between enterprises. The profit maximization of common demand. In the management of the company, the relationship between the game and cooperation has become a clear division of labor in the supply chain.

The enterprise integrates the information among the common links. For the e-commerce of nanomaterials companies, the information systems and resources that should be integrated are no longer unified because of the lack of upstream and downstream information transmission. At present, the operation of material information is very rich. It covers all aspects of the company's business. E-commerce platform integrates the existing material information system and supply chain management platform. It unifies the architecture of each platform and standardizes the internal process of the information system. When the business development is not affected, it is necessary to avoid the lengthy process as much as possible, reduce the input work, and finally strengthen the integrated monitoring and preventive measures of the system. To further improve the integrity of the entire information platform.

- (2) As the division of labor in today's society is very clear, we should fully realize that it is impossible for a super large company to control the whole upstream and downstream links in the current market. The upstream companies of nanomaterials company have established some suppliers and large equipment companies related to industrial materials by means of acquisition and reorganization, but in practice, the price is too high and the products are not competitive in the market. Therefore, it is the best strategy for large integrated companies to establish strategic alliances between them.

Management system between suppliers: the relationship between construction companies and suppliers has changed from a simple engineering cooperation relationship to a platform management cooperation relationship between enterprises. It is not possible to start from the short-term interests of enterprises and let the long-term interests of the company suffer losses. The cooperation relationship between companies is from active cooperation to giving full play to the overall advantages of the supply chain, breaking through the constraints of enterprise resources, making the supply and marketing relationship become a new type of company cooperation relationship, so as to better control the sales cost and management cost in a certain range.



The management system of suppliers at all levels needs to match a certain form for effective assessment and cooperation. Especially for the existing foundation providers of qualitative analysis, a certain amount of quantitative analysis should be added to reduce the uncertainty factors of procurement departments at all levels, including supply uncertainty, demand uncertainty, cost uncertainty, and external environment uncertainty. The differences and assessment criteria between suppliers at all levels are not to set different weights, but also to comprehensively judge the performance of suppliers, including the value of various dimensions such as price, quality, and service.

- (3) There are many steps in the management of the supply chain, among which the level of logistics management has a great impact on the efficiency of the whole supply chain, and has a great effect on the efficiency and production efficiency of enterprises. It mainly includes product engineering, product technology assurance, procurement, production control, inventory control, warehouse management, and distribution management. Nanomaterials company is a large chemical enterprise. On the one hand, it needs to change the logistics mode that only depends on suppliers and project departments, on the other hand, it also needs to make full use of the role of logistics in the whole project. In the whole project, logistics can greatly reduce the total cost of the enterprise and speed up the capital turnover of the enterprise. Reduce inventory backlog and promote profit margin. Enterprises can use futures leverage appropriately to reduce the purchase cost to a certain range.
- (4) Enterprises can use the conversion transportation strategy. For nanomaterials, there is a big price change trend in a certain supply cycle, so the use of logistics centers should be reduced as much as possible. That is the cost of transshipment in the process of supply chain management. The classic distribution strategy can also be used for products with a stronger structure. Through the company's large-scale production, the cost of products can be greatly reduced. Because the centralized purchase plan has too much pressure on the inventory, the secondary allocation can be carried out according to the progress of the project. In the logistics center, information integration can also be used to integrate logistics resources.

### 3. Experimental Research on the Innovation of Nanomaterials Procurement Mode in E-Commerce

*3.1. Experimental Background.* In today's rapid development of the information technology environment, most enterprises have adapted to the Internet business model. The development speed of e-commerce is amazing. In the

e-commerce procurement business of nanomaterials, many suppliers and manufacturers have obtained a large profit space and innovative procurement mode in the e-commerce platform. In this paper, the procurement business of nanomaterials in e-commerce is analyzed and studied.

#### 3.2. Experimental Methods

*3.2.1. Case Study Method.* In this paper, the transaction data of several suppliers (tmall mall, JD mall, Alibaba mall) and manufacturers are collected, and the case study method is used to study the procurement mode innovation of suppliers in the aspects of transportation, storage and trading of nanomaterials. Obtained in the nanomaterials of e-commerce procurement mode innovation research materials.

*3.2.2. Experimental Research Method.* This paper studies and analyzes the material cost, capital cost, labor cost, storage cost, and other data of several manufacturers in the process of purchasing nanomaterials. The experimental research method is used to sort out and study the experimental research data of several manufacturers, and the latest data of e-commerce business in purchasing nanomaterials is obtained.

*3.2.3. Data Analysis.* This paper analyzes the data of several e-commerce companies, and combs and studies all the procurement business information of nanomaterials in e-commerce platforms. Let the purchase business model innovation of nanomaterials have data support.

*3.3. Experimental Data Collection.* This paper uses the case study method, experimental research method, and experimental data analysis method to study the innovation of e-commerce procurement mode of nanomaterials. After using the procurement mode innovation, the procurement efficiency of many enterprises has increased by an average of 3 percentage points. Most nanomaterial suppliers and manufacturers are satisfied with the e-commerce procurement mode innovation above 80 points, and the satisfaction degree reaches 80%. Most manufacturers will eventually choose to purchase nanomaterials on the e-commerce platform.

### 4. Experimental Analysis of E-Commerce Nanomaterials Procurement Mode Innovation

*4.1. Experimental Analysis of Nanomaterial Logistics Innovation.* The experiment of this paper is to optimize and innovate the logistics packaging process of nanomaterials, reduce the logistics cost of nanomaterials to a reasonable range, and then improve the efficiency of logistics and transportation, improve the procurement output rate of nanomaterials in e-commerce, and innovate the logistics e-commerce procurement mode of nanomaterials. The specific data are shown in Figure 1.

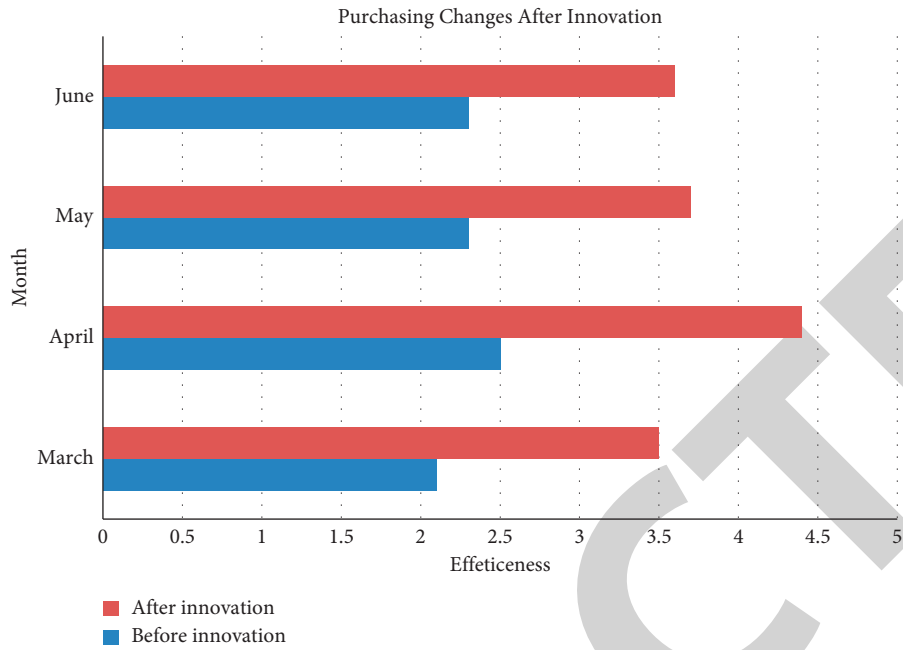


FIGURE 1: Analysis of nanomaterials logistics innovation experiment.

Through the experiment, it can be seen from the above figure that the procurement efficiency and quantity of the platform have been greatly improved by using nanomaterials in e-commerce procurement innovation business from March to June. Especially in April, both the efficiency and purchasing quantity suppliers reached the value of 4.4. It can be seen that the e-commerce procurement business using nanomaterials can not only greatly improve the procurement efficiency of enterprises but also reduce the use of human and material resources in the implementation process. To a great extent, it can reduce the cost of enterprises and greatly enrich the production efficiency and sales volume of enterprises. It is now a better procurement strategy, through the use of this strategy, enterprises and upstream and downstream cooperation, as well as the game of competitors, can achieve a relatively good state. Specifically reflected in the market competition, under this strategy, the core competitiveness of enterprises has been significantly improved and can occupy a favorable position in the market.

**4.2. Innovative Experimental Analysis on the Transport Process of Nanomaterials.** Due to the high quality and density of nanomaterials, the transportation loss of nanomaterials needs to be further reduced and confirmed when the transportation is very purchased. When enterprises transport and purchase nanomaterials, they should place nanomaterials in special equipment for transportation. This will minimize the consumption in the process of purchasing and transportation. The specific data are shown in the following Figure 2:

Through the abovementioned experiments, we can see that the transportation cost and procurement efficiency of several groups are greatly improved after the logistics and

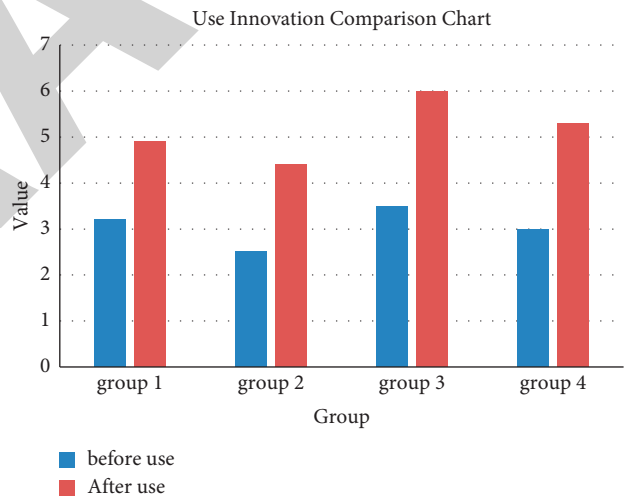


FIGURE 2: Innovative experimental analysis of the transportation process of nanomaterials.

procurement innovation using nanomaterials. It is about 2 points higher than before. Especially after the third group used logistics and procurement innovation, the procurement value increased by 3 points to more than 6. It can be seen that enterprises can reduce the cost expenditure in all aspects after using the innovative technology of purchasing and logistics of nanomaterials, so as to achieve the degree of fine operation. Let the enterprise's cost and sales and procurement process are greatly reduced. Let the enterprise's procurement and transportation costs will be reduced a lot so that enterprises can obtain more profits in cooperation with upstream and downstream suppliers, and make enterprises have more profit space when competing with similar enterprises.



**4.3. Experimental Analysis of Nanomaterials Procurement in Various E-Commerce Platforms.** In this paper, we use many types of experiments in the procurement of nanomaterials. Among them, we let the procurement companies of nanomaterials purchase on various e-commerce platforms. Finally, we can see that the platform has the highest procurement efficiency and the lowest cost. In this experiment, we use several groups to purchase in tmall mall, Jingdong Mall, and Alibaba mall. Finally, we get the specific information of this experiment from the data given by several groups. The data are shown in Figure 3.

From the above figure, we can see that there are more companies using small shopping mall to purchase nanomaterials. The proportion of companies using Jingdong shopping mall to purchase nanomaterials is relatively small, and the largest proportion is Alibaba mall, with the purchase rates reaching 32%, 23%, 26%, and 28%, respectively. It can be seen that most companies use Alibaba mall when purchasing nanomaterials. Because today's e-commerce platform is very many, users will often use one of the shopping malls to purchase. Therefore, for enterprises in the development of their own procurement needs and platforms for nanomaterials, it is best to choose a formal and large-scale mall so that the quality is guaranteed and the after-sales service is done well.

**4.4. Experimental Analysis on Procurement Rating of Nanomaterials.** In this paper, the quality of nanomaterials purchased on each e-commerce is graded. Four groups are used to grade the suppliers of nanomaterials in tmall mall, Jingdong Mall, and Alibaba mall. In order to be able to specifically detect that shopping mall's purchase quality is the most reliable, the highest efficiency, and the logistics are the most guaranteed. Finally, the purchase scores of nanomaterials of these e-commerce platforms can be evaluated. The specific data are shown in Figure 4.

As can be seen from the figure, Alibaba mall has the highest rating among the four companies, while tmall mall and Jingdong Mall are generally rated low. Among them, the evaluation of company 2 on Alibaba reached more than 40 points, and the evaluation of company 4 on Alibaba was also close to 40 points. It can be seen that at present, most enterprises purchase nanomaterials on Alibaba, and the recognition is also very high. Alibaba has played a great role in the procurement of nanomaterials, while tmall mall and Jingdong Mall are mostly used as backup options for these enterprises. In case of commodity shortage or strong demand, we will choose the nanomaterials of tmall mall and Jingdong Mall.

**4.5. Experimental Analysis of Nanomaterial Suppliers.** Procurement of nanomaterials is an important part of production, inventory, and sales from the perspective of suppliers. Enterprises should obtain convenience and efficiency in procurement. A certain agreement should be reached with the supplier to keep the price unchanged

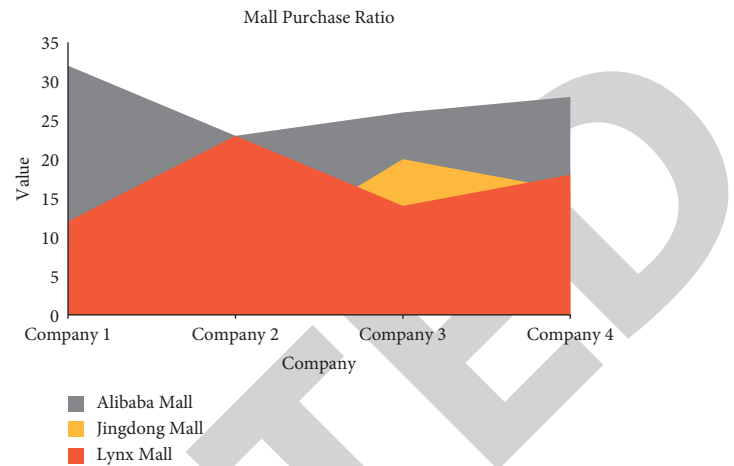


FIGURE 3: Experimental analysis of the use of nanomaterials purchase on various e-commerce platforms.

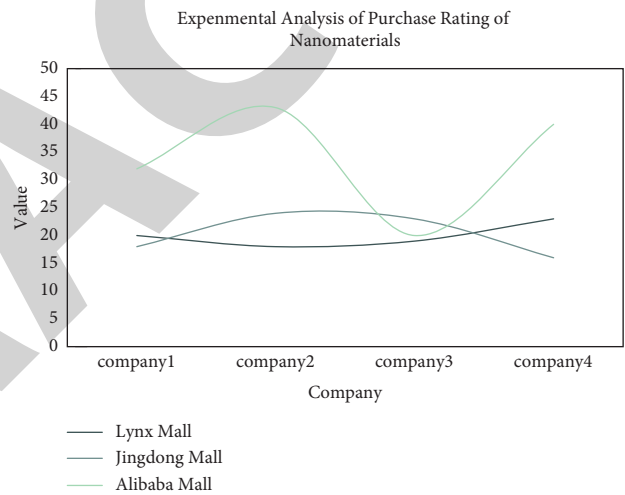


FIGURE 4: Experimental analysis of purchase rating of nanomaterials.

during the supply process. The following article will list three suppliers and survey their satisfaction with them. The specific data are shown in Table 1.

It can be seen from the above table that the satisfaction of supplier 1 and supplier 3 reaches 80%–100, reaching 6 and 8. However, the suppliers whose satisfaction reaches 60%–80% are mainly suppliers 1 and 2. It can be seen that most enterprises are still relatively satisfied with the quality and satisfaction of nanomaterials of suppliers, but generally do not reach a high value. Supplier 2 is the highest supplier whose satisfaction reaches 40%–60%. It can be seen that the satisfaction of suppliers still needs to be improved. It is necessary to improve the service quality in the important links of production, inventory, and sales. It can be seen from the table that most companies are satisfied with the suppliers of nanomaterials. In the e-commerce business of nanomaterials procurement in China, innovation is still a problem that needs to be solved.

TABLE 1: Experimental analysis of nanomaterial purchasing suppliers.

Supplier	Satisfaction 80%–100	Satisfaction 60%–80%	Satisfaction 40%–60%	Satisfaction 20%–40%	Satisfaction 0%–20%
Company 1	6	12	4	2	1
Company 2	4	8	10	3	2
Company 3	8	6	9	2	1

## 5. Conclusion

In this paper, the innovation of procurement mode of nanomaterials is studied, and the demand of suppliers and manufacturers for nanomaterials and e-commerce platforms to provide such services are taken as the basis of the research. By analyzing the purchasing data of nanomaterials on e-commerce platform, it is concluded that most suppliers and factories are satisfied with the innovation of this procurement mode.

This paper analyzes and studies the data of purchasing nanomaterials on e-commerce platforms by several factories and suppliers, and concludes that it is very in line with their own interests and competitive comparative advantages to using e-commerce platforms to purchase nanomaterials for suppliers.

In this paper, by using the procurement strategy of nanomaterials in many factories, the transportation cost of the plants is reduced a lot, and the efficiency and convenience of procurement are also greatly improved. In this paper, through the multi-angle research on the manufacturer, supplier, and e-commerce platform, it is concluded that using e-commerce platforms to purchase nanomaterials can keep a certain cost advantage and comparative advantage in the fierce competition, and keep a certain share in the domestic and foreign markets. Although this paper has made deep research on the innovation of nanomaterial procurement mode based on e-commerce, there are still some limitations in this experiment. In future work, it will continue to improve and improve the research quality.

## Data Availability

This article does not cover data research. No data were used to support this study.

## Conflicts of Interest

The authors declare that they have no conflicts of interest.

## References

- [1] M. Procek, A. Stolarczyk, T. Pustelny, and E. Maciak, "A study of a QCM sensor based on TiO<sub>2</sub> nanostructures for the detection of NO<sub>2</sub> and explosives vapours in air," *Sensors*, vol. 15, no. 4, pp. 9563–9581, 2015.
- [2] J. N. Ding, M. J. Chen, J. H. Qiu, and N. Yuan, "Photovoltaic properties of ferroelectric solar cells based on polycrystalline BiFeO<sub>3</sub> films sputtered on indium tin oxide substrates," *Science China Physics, Mechanics & Astronomy*, vol. 58, no. 3, pp. 1–6, 2015.
- [3] D. A. Gkika, C. Kontogoulidou, J. W. Nolan et al., "Nano - patents and literature frequency as statistical innovation indicator for the use of nano - porous material in three major sectors: medicine, energy and environment," *Journal of Engineering Science and Technology Review*, vol. 9, no. 5, pp. 24–35, 2016.
- [4] E. Verkasalo, R. Hänninen, and H. Heräjärvi, "Finnish research, development and innovation programme: wood Materials and Products in the Development of Bio-Economy (MAT programme)," *Advanced Materials Research*, vol. 376, no. 1, pp. 146–147, 2015.
- [5] Pe. a-Hernández, Rodrigo, M. Marques, and K. Hilmi, "Genome-wide targeting of the epigenetic regulatory protein CTCF to gene promoters by the transcription factor TFII-I," *Proceedings of the National Academy of Sciences of the United States of America*, vol. 112, no. 7, pp. 677–686, 2015.
- [6] E. C. Arvaniti, M. C. G. Juenger, S. A. Bernal et al., "Physical characterization methods for supplementary cementitious materials," *Materials and Structures*, vol. 48, no. 11, pp. 3675–3686, 2015.
- [7] S. Ghazinoory, F. Saghafi, and S. Kousari, "Ex-post evaluation of scenarios: the case of nanotechnology societal impacts," *Quality and Quantity*, vol. 50, no. 3, pp. 1349–1365, 2016.
- [8] J. Alin, M. Rubino, and R. Auras, "Effect of the solvent on the size of clay nanoparticles in solution as determined using an ultraviolet-visible (UV-vis) spectroscopy methodology," *American Political Science Review*, vol. 65, no. 1, pp. 161–171, 2015.
- [9] C. C. Xu, Y. Wang, L. Li, Y. J. Wang, L. F. Jiao, and H. T. Yuan, "Hydrothermal synthesis mechanism and electrochemical performance of LiMn<sub>0.6</sub>Fe<sub>0.4</sub>PO<sub>4</sub> cathode material," *Rare Metals*, vol. 38, no. 1, pp. 29–34, 2019.
- [10] E. Magaña, Y. Luo, and A. E. Morishige, "Engineering defects to enable cost-effective solar cells," *American Chemical Society Division of Fuel Chemistry Preprints*, vol. 61, no. 1, p. 204, 2016.
- [11] S. Marzocco, L. Calabrone, S. Adesso et al., "Anti-inflammatory activity of horseradish (*Armoracia rusticana*) root extracts in LPS-stimulated macrophages," *Food & Function*, vol. 6, no. 12, pp. 3778–3788, 2015.
- [12] X. Xu, D. Shahsavari, and B. Karami, "On the forced mechanics of doubly-curved nanoshell," *International Journal of Engineering Science*, vol. 168, Article ID 103538, 2021.
- [13] X. Bai, "Research on credit evaluation model of C to C E-commerce based on trust influence factors," *Journal of Computational and Theoretical Nanoscience*, vol. 14, no. 1, pp. 189–194, 2017.
- [14] D. J. Armaghani, E. T. Mohamad, and E. Momeni, "An adaptive neuro-fuzzy inference system for predicting unconfined compressive strength and Young's modulus: a study on Main Range granite," *Bulletin of Engineering Geology and the Environment*, vol. 74, no. 4, pp. 1301–1319, 2015.
- [15] M. L. Howe, S. R. Garner, E. Threadgold, and L. J. Ball, "Priming analogical reasoning with false memories," *Memory & Cognition*, vol. 43, no. 6, pp. 879–895, 2015.
- [16] E. W. M. Stienen, A. Brenninkmeijer, and W. Courtens, "Intra-specific plasticity in parental investment in a long-lived single-prey loader," *Journal of Ornithology*, vol. 156, no. 3, pp. 1–12, 2015.

## *Retraction*

# **Retracted: Based on the Application Practice of Multifunctional Nanomaterials in Art Design and Industrial Manufacturing Concept**

### **Advances in Materials Science and Engineering**

Received 26 December 2023; Accepted 26 December 2023; Published 29 December 2023

Copyright © 2023 Advances in Materials Science and Engineering. This is an open access article distributed under the Creative Commons Attribution License, which permits unrestricted use, distribution, and reproduction in any medium, provided the original work is properly cited.

This article has been retracted by Hindawi, as publisher, following an investigation undertaken by the publisher [1]. This investigation has uncovered evidence of systematic manipulation of the publication and peer-review process. We cannot, therefore, vouch for the reliability or integrity of this article.

Please note that this notice is intended solely to alert readers that the peer-review process of this article has been compromised.

Wiley and Hindawi regret that the usual quality checks did not identify these issues before publication and have since put additional measures in place to safeguard research integrity.

We wish to credit our Research Integrity and Research Publishing teams and anonymous and named external researchers and research integrity experts for contributing to this investigation.

The corresponding author, as the representative of all authors, has been given the opportunity to register their agreement or disagreement to this retraction. We have kept a record of any response received.

### **References**

- [1] W. Cai and Y. Li, "Based on the Application Practice of Multifunctional Nanomaterials in Art Design and Industrial Manufacturing Concept," *Advances in Materials Science and Engineering*, vol. 2022, Article ID 1653828, 11 pages, 2022.

## Research Article

# Based on the Application Practice of Multifunctional Nanomaterials in Art Design and Industrial Manufacturing Concept

Wensi Cai <sup>1</sup> and Yuze Li<sup>2</sup>

<sup>1</sup>Science and Engineering, The University of Edinburgh, Edinburgh EH8 9YL, UK

<sup>2</sup>Adam Smith Business School, University of Glasgow, Glasgow G12 8QQ, UK

Correspondence should be addressed to Wensi Cai; [wcai201@gcu.ac.uk](mailto:wcai201@gcu.ac.uk)

Received 26 May 2022; Revised 12 July 2022; Accepted 1 August 2022; Published 27 August 2022

Academic Editor: K. Raja

Copyright © 2022 Wensi Cai and Yuze Li. This is an open access article distributed under the Creative Commons Attribution License, which permits unrestricted use, distribution, and reproduction in any medium, provided the original work is properly cited.

Design is the broad application of discovering new materials and technologies. Nanomaterials have been widely used in product design as a new type of material. The rapid development of nanotechnology is bound to trigger a new design revolution. Combining user needs, design concepts, and material selection, this paper discusses the relationship between user needs and nanoproducts and user needs and nanomaterials. In this paper, the design requirements and related properties of nanomaterials are put forward through the study of the hydration rate of nanomaterials after adding cement, optical microscopy, scanning electron microscopy, and morphology analysis. The effect of the addition of ultrafine materials on the dissolution of ions during cement hydration was studied by ICP technology. The experimental results in this paper show that with the development of the distance, the concentration of calcium ions gradually decreases, and the order of calcium ion concentration is No. 3 tank > No. 4 tank > No. 5 tank. The diffusion of calcium ions was enhanced after the incorporation of nanomaterials, and the diffusion ability of NT to calcium ions was stronger than that of NS group.

## 1. Introduction

With the increase of social demand and the continuous deepening of nanomaterials research, magnetic nanomaterials stand out from many nanomaterials due to their excellent magnetic properties and broad application prospects, which have attracted the attention of many scholars. In recent years, magnetic nanomaterials have emerged one after another and are widely used in magnetic separation, information storage, biomedicine, and other fields and have achieved fruitful results. After years of exploration and challenges, researchers on the nanometer road have gradually discovered that the synthesis of multifunctional nanomaterials with stable performance and wide operating range is of great meaning to the development of nanomaterials in the future. In a simple way, this places higher demands on the overall design of the material.

With the continuous development and progress of the social economy, people have put forward higher-level requirements for the use of new materials in product design. Nanomaterials are a relatively new type of materials, which are more and more widely used in product design. However, when applying nanomaterials to product design, it is necessary to analyze the needs of users. On the basis of fully considering the needs of users, nanomaterials are reasonably used in product design to design products with both performance and appearance, win the love of users, and then increase the market share of products. With the industrialization of society, the development of urban science and technology, and the rapid development of infrastructure construction, the transformation of cement-based materials in industrial production has gradually become a hot topic in the field of building materials. In recent years, adding nanoparticles to cement mortar or concrete for better performance has become a research hotspot.

The innovation of this paper lies in the application of multifunctional nanomaterials to the concept of art design and industrial manufacturing, which is innovative and experimental.

## 2. Related Work

More and more researchers are incorporating multifunctional nanomaterials into art design and industrial manufacturing concepts. Rzayev emphasized the ability of polymer brushes as highly adjustable building blocks for forming structural nanomaterials through molecular templates, solution aggregation, and melt self-assembly. He stressed recent research results in the synthesis of discrete nanoobjects, micelle structures, and periodic nanomaterials from bottle brush copolymers and provided a brief discussion of future opportunities for polymer science [1]. Smith and Gambhir address the physicochemical composition/design of nanomaterials through lenses of physical properties that produce contrast signals for homologous imaging modalities [2]. Using a combination of macrocanonical Monte Carlo (GCMC) simulations and ab initio QM calculations, Lithoxoo et al. investigated the H<sub>2</sub> adsorption capacity of single-walled silicon nanotubes (SWSINT) in an armchair structural model [3]. Nanomaterials have been widely used as reagents for therapeutic and diagnostic (i.e., therapeutic) applications. Huang and Lovell's efforts have turned from exploring new materials in vitro to engineering materials that work in more relevant animal disease models, increasing the likelihood of clinical translation [4]. Zheng et al. first described the mode of action of silver nanoparticles (Ag-NPs) in disrupting bacterial outer membranes and their intracellular components, which enables them to exhibit broad-spectrum antibacterial effects [5]. Sadegh et al. recall the role of nanomaterials as useful wastewater adsorbents [6]. Wang et al. reviewed the research status of nanostructured photocatalysts for water disinfection, including 0D, 1D, and 2D (low-dimensional) nanostructures. They systematically summarized and discussed its synthesis method, characterization, and photocatalytic bacterial inactivation performance. They particularly emphasized the development of new conceptual directions for natural materials, especially to accelerate practical industrial applications [7]. Poorly crystallized calcium silicate hydrate (C-S-H) is the main binding phase in Portland cement concrete. Li et al. investigated experimentally and systematically the impacts of adding anatase phase nanotitanium dioxide, silica nanoparticles, graphene oxide (GO), and multiwalled carbon nanotubes (CNT) on the co-crystallization and patterns of C-S-H [8]. However, the shortcomings of these studies are that the model construction is not scientific enough and the data is not well prepared to adapt to more complex situations.

## 3. Multifunctional Nanomaterials and Related Methods

### 3.1. Nanomaterials

*3.1.1. Definition of Nanomaterials.* Nanomaterials refer to materials whose size ranges from 1 to 100 nm. Since nanomaterials have nanoscale sizes, in general, the properties of nanomaterials, such as physical properties, electrical

properties, optical properties, and magnetic properties, are very significantly different from those of conventional materials. Many nanomaterials are catalytic, adsorptive, and highly reactive.

*3.1.2. Application of Nanomaterials.* In the past few decades, nanomaterials have been extensively researched and developed, and have been successfully applied in the fields of catalysis, medicine, sensors, and biology. Nanomaterials have a relatively large specific surface area due to their small size, so they have strong adsorption capacity and reactivity. In particular, it has also received extensive attention in water treatment and wastewater treatment. Moreover, the flow properties of nanomaterials in solution are very high. It has been reported that heavy metals, organic pollutants, inorganic anions, and bacteria can be successfully removed by many kinds of nanomaterials [9].

*3.1.3. Application of Nanomaterials in Product Design.* Figure 1 shows the user requirements for using nanomaterials in product design.

*(1) Demand for Product Features.* In terms of product demand, most users hope that the product has the functions of energy saving, environmental protection, cleanliness and sanitation, and speed. For example, nano toothpaste not only has the cleaning function of ordinary toothpaste, but also nano hydroxyapatite free in nano toothpaste can repair teeth. When using nano-zinc dioxide in the refrigerator coating, people require the refrigerator to have general refrigeration and insurance functions, as well as the functions of sterilization and bacteria inhibition, which can absorb peculiar smells caused by food deterioration and odor. In nano skin care products, in addition to the usual functions, skin care products should also have the function of reaching the deep layers of the skin and repairing damaged skin [10]. The application of car paint made of nanomaterials can enhance the hardness of the car surface and enhance the wear resistance of the paint. Moreover, the angle of visible light of nano-carbon dioxide will change with the change of sunlight, which can reduce light pollution. Nano-ceramic knives are "sharp" unmatched by ordinary props, and can meet people's needs for knife functions [11].

*(2) Demand for Product Safety and Durability.* People pay more attention to whether the product will cause harm to the body when using the product in recent years and put forward higher requirements for the safety of the product. The use of nanomaterials in product design can meet people's requirements in this regard [12]. In products such as nano tooth sound, nano skin care products, nano clothes and pants, people's skin and cells directly contact the products. At this time, people not only require the product to have functions that ordinary products do not have, but also require that the product will not produce side effects and will not damage the human body. For products that come into direct contact with food, such as nano cling film and nano knives, not only should they have commonly used functions,



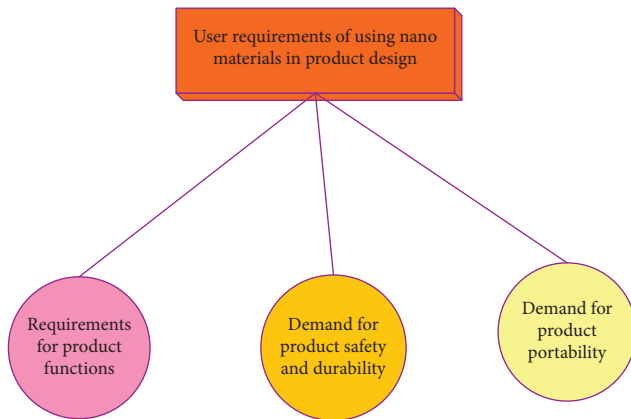


FIGURE 1: User requirements for using nanomaterials in product design.

but they should also have no chemical reaction to cause food deterioration, or leave harmful substances on the surface of food, so as not to cause damage to the human body.

(3) *The Need for Product Portability.* As we all know, nanomaterials have the characteristics of light weight, and products made of nanomaterials also have the characteristics of light weight, easy portability, and strong plasticity, which can meet people's needs for portability. For example, the thickness of solar cells made of nanomaterials is only 2–6 nm, which is not only small, but also light and thin, and is very convenient to carry. Electronic display screens made of nanomaterials have good flexibility, light weight, and strong bending resistance, and users can carry them with them when they use them [13].

3.1.4. *The Characteristics of Using Nanomaterials in Product Design.* A schematic diagram of the characteristics of using nanomaterials in product design is shown in Figure 2.

(1) *People Are More Demanding in terms of Product Performance Feedback.* Due to the special properties of nanomaterials and the influence of small molecules, nanomaterials can directly penetrate into biological cells and produce effects. It is precisely because of the above characteristics that people put forward higher requirements on the "rapidity" of nanoproducts; that is, compared with ordinary products, nanoproducts should quickly perform the functions that people need [14]. For example, by adding nanomaterials to the device for loosening drugs, the drug can quickly pass through the skin surface, reach the body's circulation, and quickly exert the function of treating diseases. The feedback time is long, which is favored by most people.

(2) *Nano Products Are "Fine."* The size of nanomaterials is small, and the products made by using nanomaterials are also relatively small, allowing users to accurately grasp the relevant laws of the onlooker world. For another example, a drug delivery device made of nanomaterials is smaller in size than red blood cells so that the drug can lead to corresponding cells through blood circulation and achieve the

effect of saving and curing people. This nano-drug delivery device does not damage healthy cells and can relieve the pain of patients during the treatment process [15].

(3) *Paying Attention to the Physical Structure of Nanomaterials in the Design of Nanoproducts.* The structure used in the aforementioned nanodrug delivery device is a nano-multi-walled carbon tube half-deep cup structure. When treating cancer patients, related drugs can be put into the deep cup. For example, the fineness of nanometer is one ten millionth of that of hair, and it has good toughness and elasticity. In medical virus research, the virus is attached to the top of the nanoscale, and the weight of the virus can be recorded according to the amplitude of the weighing rod so as to facilitate the identification of the virus and then re-search drugs or methods based on this.

(4) *Nanoproducts Pursue Cleanliness and Hygiene.* In the clean and hygienic functions of nanoproducts, it mainly includes the following two aspects: first, the products made of nanomaterials can prevent pollution and dust by themselves; second, some nanomaterials have the function of sterilization. These characteristics of nanomaterials are mainly determined by the following conditions: first, the molecules of nanomaterials are extremely small, and the scale is smaller than that of dust particles, so that dust particles cannot adhere to the surface of nanomaterials, resulting in a "lotus effect" and self-purification effect. Secondly, nanomaterials have photocatalytic effects [16]. Under the condition of light, the chemical activity of nanomaterials will be enhanced, and redox reactions will occur with the organic matter attached to its surface so that the organic matter becomes water or  $\text{CO}_2$  achieves the decontamination effect [17].

(5) *It Has Special Mechanical Properties.* Due to the influence of mechanical properties, ordinary knives are relatively brittle and are often chipped or even broken during use. Adding nanomaterials to the tool can effectively increase the toughness and elasticity of the tool. The application of nano-zinc dioxide to spray the surface of the refrigerator can enhance the firmness of the refrigerator and prolong the service time of the refrigerator.

3.1.5. *Application-Oriented Products of Nanomaterials.* Knives are tools that are often used in the kitchen. As shown in Figure 3(c), nano-ceramic knives are knives made of nanomaterials, which are so called because they are similar to ceramics. The main raw material for making nano-ceramic knives is nano-zirconia. Nano-zirconia has no heavy metal components contained in ordinary knives, is non-toxic, safe, and does not have any adverse effects on the human body [18].

As shown in Figure 3(d), the refrigerator is most frequently used in daily life, and people are accustomed to stuffing all kinds of food into this small space. But over time, this leads to spoilage of food and odors between different foods; refrigerators are easy to breed germs (bacteria) and



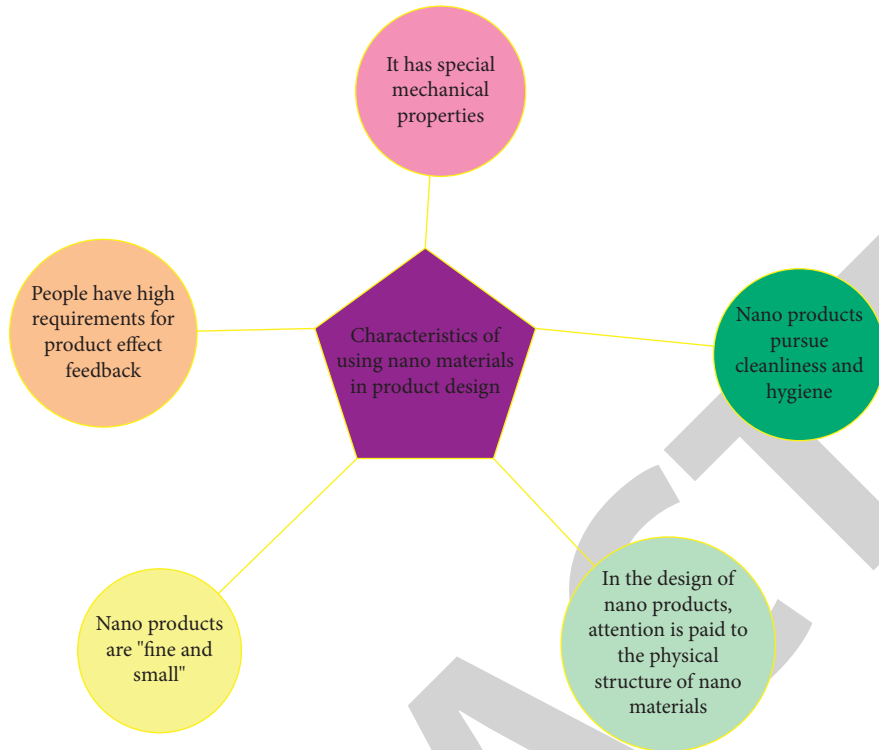


FIGURE 2: Characteristics of nanomaterials used in product design.



(a)



(b)



(c)



(d)

FIGURE 3: Applied products of nanomaterials. (a) Nano waterproof material, (b) nano titanium dioxide car paint, (c) nano-ceramic cutting tool, and (d) nano-refrigerator coating.

produce unpleasant odors. The general treatment method is to regularly clean and clean the refrigerator to keep it in a clean state. The refrigerator coated with nano-ZnO can effectively solve this headache. The refrigerator has effective bactericidal and bacteriostatic functions, which can effectively reduce the growth of bacteria in food and reduce unpleasant odors.

Nano-titanium dioxide is nontoxic and harmless, has good compatibility with automobile paint, and has good transparency to visible light. Due to its high refractive index and high luminescent activity, it can absorb UV radiation and thus is a good automotive colorant [19], as shown in Figure 3(b).

**3.1.6. Synthesis of Nanomaterials.** The preparation methods of nanomaterials can be roughly divided into physical methods, chemical methods, and other methods. Among them, physical methods include pulverization method, deposition method, and sputtering method. Chemical methods include sol-gel method, precipitation method, evaporative solvent pyrolysis method, redox method, and solvothermal method. Figure 4 is a method for preparing nanoparticles.

**3.1.7. Characterization of Nanomaterials.** In order to explore the mysteries of the nano-world, the structure and properties of nanoparticles must be characterized. The characterization of nanomaterials is the modern analysis and detection technology and related theoretical knowledge about particle composition, structure, morphology, and so on. Usually, we use inductively coupled plasma emission spectroscopy (ICP-AES), scanning electron microscopy (SEM), transmission electron microscopy (TEM), atomic force microscopy (AFM), X-ray diffraction (XRD), and X-ray photoelectron spectroscopy (XPS) to obtain the composition, particle size, morphology, structure, and interface of nanoparticles to characterize materials. The average particle size, particle size distribution, composition, and interface of nanomaterials all affect their physico-chemical properties. Figure 5 shows the commonly used characterization methods for nanomaterials.

**3.2. BP Neural Network Algorithm.** The historical summary of neural network development can be divided into four stages, namely, the enlightenment period from 1891 to 1968, the low tide period from 1968 to 1981, the revival period from 1981 to 1985, and the occurrence period of the new era from 1985 to the present. The neural network has experienced several periods of development and continuous improvement, and there are currently more than 40 neural network models [20]. Among them, the more typical neural networks are adaptive resonance theory networks network, back propagation neural network (BP neural network), cellular neural network, multilayer forward propagation network (BOP network), and so on.

Artificial neural network is a highly nonlinear dynamic system with the ability of self-organization, self-adaptation, and parallel information processing, so it has been widely

used in intelligent control, intelligent information processing, and other fields. With the continuous development of industrial production and agricultural engineering at the current stage, the objects in control become more and more complex, which requires matching with higher control requirements. The traditional control methods can no longer meet the requirements of industrial production and agricultural engineering control at the present stage. With the continuous in-depth study of control theory and a large number of theories used in practice, this makes the control theory develop in a more perfect direction, which requires some intelligent control algorithms and theories to be applied to it. The rapid development and application of neural network has made people pay more attention and research on it.

**3.2.1. The Establishment of BP Neural Network.** The structure diagram of the BP neural network PID control system designed in this paper is as follows: a 3-layer BP neural network is used (Figure 6). Its structure is as follows: 4 input neurons, 5 intermediate layer neurons, and 3 output layer neurons. The selection of neurons in the output layer is the adjustment parameters  $S_q, S_u, S_o$  of the PID.

**3.2.2. Forward Propagation Process.** According to the designed network, the input and output of each layer can be obtained.

The input and output of the network input layer are

$$H_T^1 = A(T) (T = 1, 2, 3, 4). \quad (1)$$

The input and output of the hidden layer of the network are

$$\text{net}_u^2(S) = \sum_T^D K_{uv}^2 H_T^1, \quad (2)$$

$$H_u^2(S) = g(\text{net}_u^2(S)) (u = 1, 2, 3, 4, 5). \quad (3)$$

Among them,  $K_{uv}^2$  is the weighting coefficient of the hidden layer.

The input and output of the network output layer are

$$\text{net}_L^3(S) = \sum_{u=0}^D K_{uv}^3 H_u^2(S), \quad (4)$$

$$H_L^2(S) = g(\text{net}_L^3(S)) (L = 1, 2, 3). \quad (5)$$

Among them, (1), (2), and (3) are used to represent each layer of the network.

Since this paper studies the direction of chlorination process control, it can be determined that the output of the network is three adjustable parameters  $S_q, S_u, S_o$ , and the activation function of the output layer neurons is selected as a nonnegative sigmoid function:

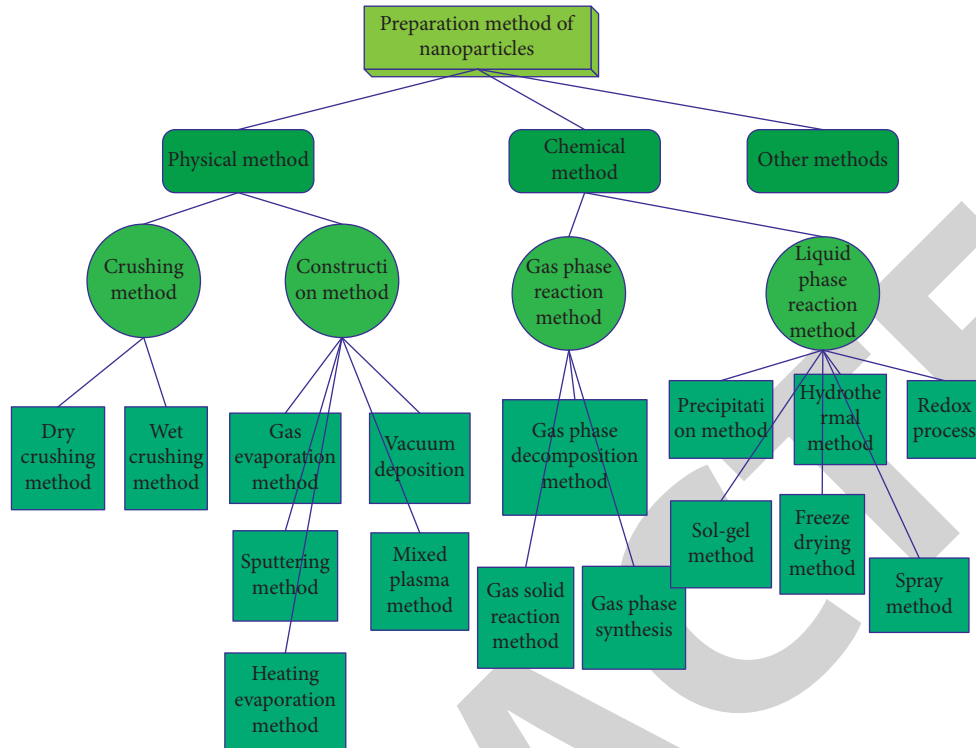


FIGURE 4: Nanoparticle preparation method.

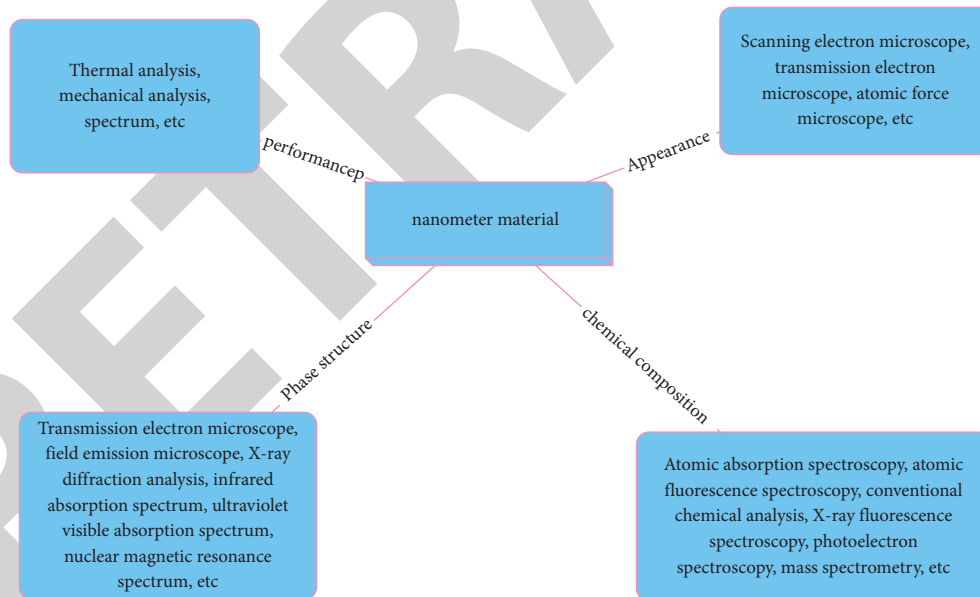


FIGURE 5: Nanomaterials characterization techniques.

$$H_1^3(S) = S_q, \tag{6}$$

$$H_2^3(S) = S_u, \tag{7}$$

$$H_3^3(S) = S_o, \tag{8}$$

$$f(A) = \frac{e^A}{e^A + e^{-A}}. \tag{9}$$

3.2.3. *Backpropagation Process.* Selecting the output performance indicator function of the network is as follows:

$$E(S) = \frac{1}{2}(rink(S) - yout(S))^2. \tag{10}$$

The weight correction function of the network adjusts the weight coefficient of the network according to the gradient descent method in the core correction process of the BP neural network. That is, the weighting coefficient is adjusted in the negative direction according to the output

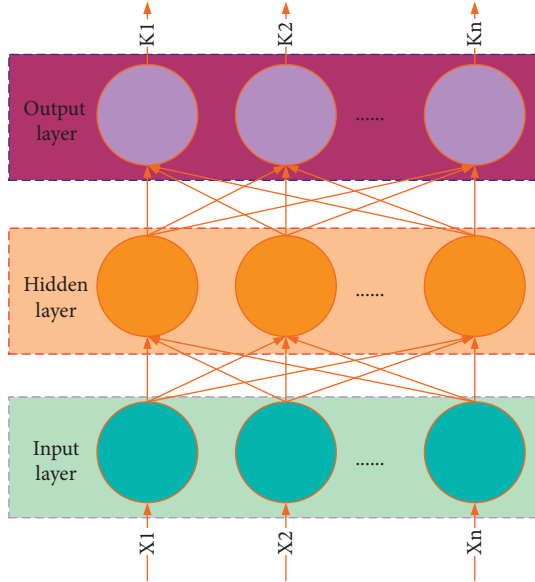


FIGURE 6: Forward neural network model.

performance index function value, and in order to prevent the network from falling into a local minimum, a learning rate  $\eta$  is added, and a global minimum inertia term is used to quickly converge the search.

$$\Delta K_{Lu}^3(S) = -\eta \frac{\partial E(S)}{\partial K_{Lu}^3} + \alpha \Delta K_{uv}^3(S-1). \quad (11)$$

Among them,  $\alpha$  is the inertia coefficient.

The partial derivatives for the correction function are as follows:

$$\frac{\partial E(S)}{\partial K_{Lu}^3} = \frac{\partial E(S)}{\partial B(S)} \cdot \frac{\partial B(S)}{\partial \Delta W(S)} \cdot \frac{\partial \Delta W(S)}{\partial H_L^3(S)} \cdot \frac{\partial H_L^3(S)}{\partial net_L^3(S)} \cdot \frac{\partial net_L^3(S)}{\partial K_{uv}^3(S)}, \quad (12)$$

$$\frac{\partial net_L^3(S)}{\partial K_{uv}^3(S)} = H_u^2(S). \quad (13)$$

Among them,  $\partial B(S)/\partial \Delta W(S)$  cannot be known. This paper decides to use its sign function to approximate replacement by consulting relevant information so that the learning rate  $\eta$  is adjusted for calculation compensation [21].

From the above calculation, the modified partial derivative formula of each output neuron can be obtained:

$$\frac{\partial \Delta W(S)}{\partial H_1^3(S)} = e(S) - e(S-1), \quad (14)$$

$$\frac{\partial \Delta W(S)}{\partial H_2^3(S)} = e(S), \quad (15)$$

$$\frac{\partial \Delta W(S)}{\partial H_1^3(S)} = e(S) - 2e(S-1) + e(S-2). \quad (16)$$

The learning algorithm for synthesizing the weights of the output layer of the available network is

$$\Delta K_{Lu}^3(S) = \alpha \Delta K_{Lu}^3(S-1) + \eta \delta_L^3 H_L^2(S), \quad (17)$$

$$\delta_L^3 = e(S) \operatorname{sgn} \left[ \frac{\partial B(S)}{\partial \Delta W(S)} \right] \cdot \frac{\partial \Delta W(S)}{\partial H_L^3(S)} \cdot f'(net_L^3(S)). \quad (18)$$

**3.3. Basic Principles of Convolutional Neural Networks.** Convolutional Neural Network (CNN), as the name suggests, should come from neuroscience or biology, and it does. At present, CNN has a wide range of applications and has made outstanding contributions in many application directions, but the most interesting research field is the field of image processing [22]. The basic principles of CNN in image processing are described in detail below. Figure 7 shows the simplest structure of a typical convolutional neural network. The input image is color, can be expressed in the form of RGB three-channel, and the size can be expressed as  $3 \times 28 \times 28$ . After convolution and pooling, it finally reaches the fully connected layer. After the fully connected layer, a classification function, such as Softmax, can be connected.

First and foremost, to a machine (computer, etc.), each image is a sequence of points (pixels) in a specific order. If the order or color of the pixels is changed, the image also changes. Basically, the machine transforms the pixels of the image into a matrix and stores the color code for each locus pixel. So, every image the machine “sees” is a matrix of numbers. According to this principle, we can represent the image in the form of a digital matrix for the machine to recognize. Since different pictures will form different digital matrices, the computer can easily recognize it. So how to effectively represent the image in the form of a digital matrix and make the machine recognize it in a simple, efficient, and feasible way. After several generations of scientists’ efforts, the convolutional neural network (CNN) came into being [23].

Convolutional neural networks are different from ordinary neural networks. Their main difference is that convolutional neural networks have a feature extractor, which consists of convolutional layers and subsampling layers. A convolutional layer of a convolutional neural network often contains multiple feature planes (Feature Map), and there are multiple neuron components on each feature plane, and these components are arranged in a rectangle [24].

## 4. Experimentation of Multifunctional Nanometers for Industrial Manufacturing Ideas

**4.1. The Effect of Nanoparticles on the Hydration Process of Industrially Manufactured Cement.** In order to better reflect the influence of different nanoparticles on the cement hydration process in this experiment,  $\text{SiO}_2$  nanoparticles with a particle size of 20 nm and  $\text{TiO}_2$  nanoparticles with a particle size of 10 nm were selected. In order to reduce the influence

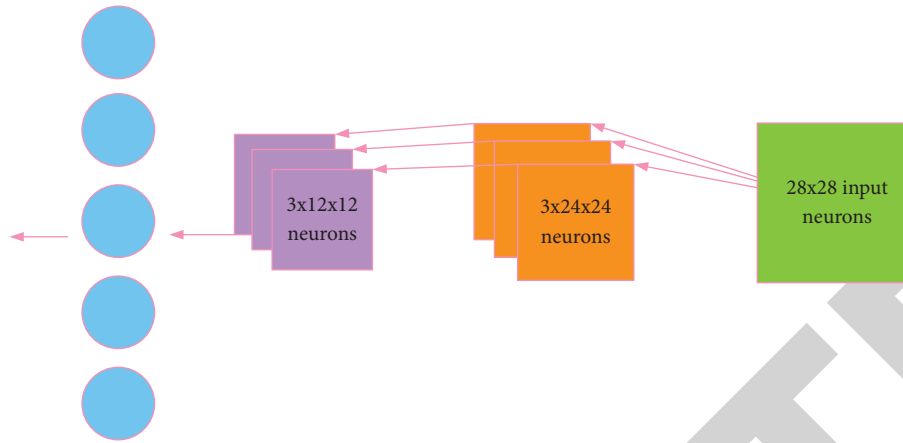


FIGURE 7: Schematic diagram of the basic principle of convolutional neural network.

of impurities in cement, Portland cement with less impurities is selected. The mineral composition of Portland cement is shown in Table 1. In order to reflect the hydration reaction of cement under the condition of different dosages of nanoparticles, three different dosages were selected for the two nanomaterials, which were 0.1 wt%, 1 wt%, and 5 wt%, respectively (the dosage in this experiment is relative to the mass of water). In order to clearly observe the hydration growth process of cement particles, the water-cement ratio was set to 10:1. The mix ratio design is shown in Table 1 [25].

**4.2. Scanning Electron Microscope Observation of Cement Hydration Products.** In this experiment, in order to observe the morphology of cement hydration products more clearly, a higher water-cement ratio  $W/B = 10:1$  was selected. At the same time, the influence of nanomaterials on the early hydration of cement is relatively significant, so the early 12 h, 24 h, and 3 d were selected as the age for the comparison of the morphology of the hydration products. In order to better illustrate the effect of nanomaterials on the hydration of  $C_3S$ , three additional groups of  $C_3S$  hydration groups without nanomaterials and those with nanomaterials were additionally set. The mix design of this experiment is shown in Table 2.

**4.3. Test Process.** The calcium ion concentrations in the five tanks at each time point were accumulated to obtain the dissolution amount of calcium ions during the cement hydration process. Figure 8(a) shows the dissolved calcium ion concentration at three time points during the hydration process of Portland cement doped with different nanomaterials. The three samples were the blank group without nanomaterials, the group with 1% NS, and the group with 1% NT. The three time periods are 5 min, 15 min, and 30 min in the early stage. It can be found that after the dissolution time of 5 min, the dissolved calcium ion concentration in the group doped with nanomaterials is higher than that in the control group. The dissolved concentration of the NS group was 2.38 times that of the control group, while the dissolved

TABLE 1: Mix design of water-cement ratio.

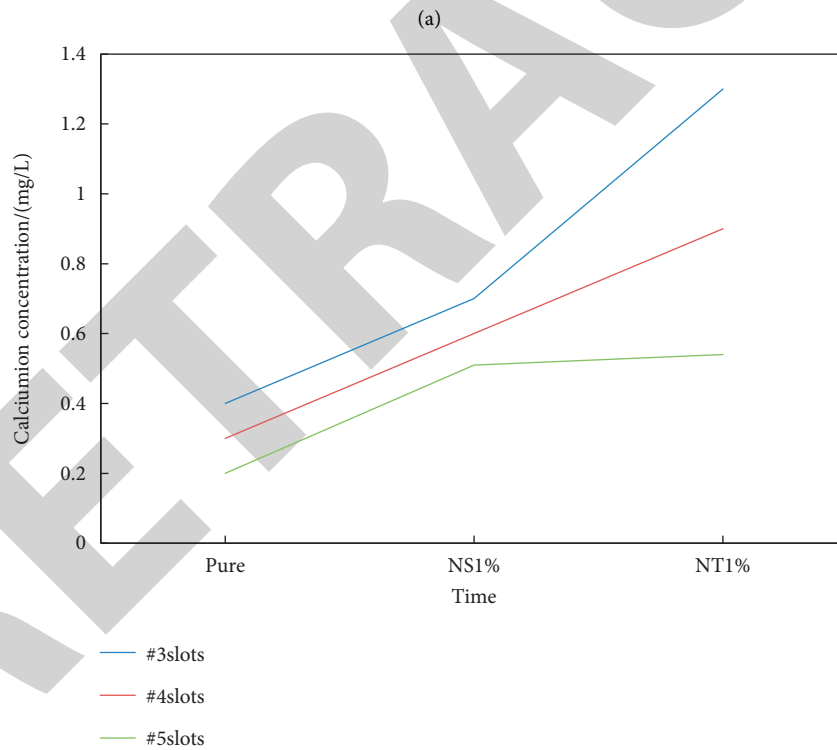
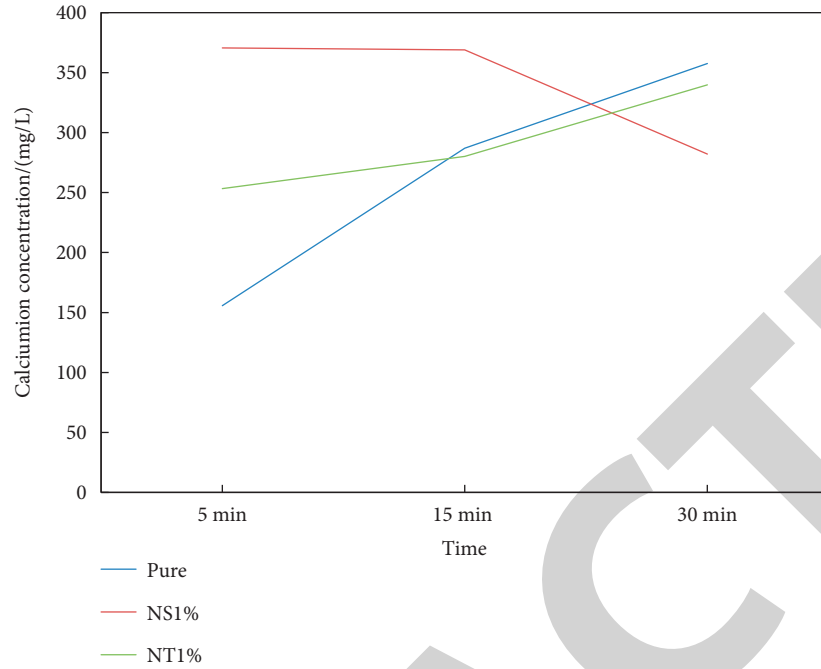
Sample	Cement (g)	Water (g)	NS or NT (%)
10Pure	3	30	0
10NS0.1%	3	30	0.1
10NS1%	3	30	1
10NS5%	3	30	5
10NS0.1%	3	30	0.1
10NS1%	3	30	1
10NS5%	3	30	5

TABLE 2: Test mix ratio of tricalcium silicate and Portland cement hydration products with different nano-content materials.

Sample	W/B	$C_3S$	Cement	NS	NT
$C_3SPure$	10	0.6 g	—	—	—
$C_3SNS1%$	10	0.6 g	—	1%	—
$C_3SNT1%$	10	0.6 g	—	—	1%
CPure	10	—	5 g	—	—
CNS1%	10	—	5 g	1%	—
CNS5%	10	—	5 g	6%	—
CNT1%	10	—	5 g	—	1%
CNT5%	10	—	5 g	—	6%

concentration of the NT group was 1.63 times that of the control group. It can be seen that the dissolution effect of NS on calcium ions is better than that of NT. However, at 15 min, the calcium ion concentrations of the control group and NT group were basically the same, while the calcium ion concentration of the NS group did not change with the concentration at 5 min. It can be found that, during this period, the dissolution rate of calcium ions in the NS group was basically balanced with its reaction rate, while the rate of dissolution of calcium ions in the NT group was significantly lower than that of the control group. At 30 min, the calcium ion concentration decreased significantly due to the reaction between NS and calcium ions, and the dissolution rate of calcium ions in the control group was still higher than that in the NT group.

The measured calcium ion concentration was simultaneously scaled up to the undiluted concentration for



(b)

FIGURE 8: Cement ion dissolution and calcium ion diffusion rate diagram. (a) The concentration of calcium ions dissolved in cement hydration with different nanomaterials. (b) The diffusion rate of calcium hydrate in cement doped with different nanomaterials.

comparison. Figure 8(b) is the concentration of calcium ion diffusion during the hydration process of cement mixed with different nanomaterials at 5 min. The three groups represent the undoped nanomaterial group, the 1% NS doped group, and the 1% NT doped group, respectively. The reaction times are 5 min, 15 min, and 30 min, respectively. Since both the

No. 1 and No. 2 tanks contain the migration of cement particles, the No. 3, No. 4, and No. 5 tanks are selected as the calibration tanks for ion diffusion. It can be seen that with the increase of distance, the concentration of calcium ions gradually decreases, and the order of calcium ion concentration is slot 3 > slot 4 > slot 5. The diffusion of calcium ions



was enhanced after the incorporation of nanomaterials, and the diffusion ability of NT to calcium ions was stronger than that of NS group.

## 5. Discussion

Nanomaterials are one-dimensional (0.1~100 nm) materials in three-dimensional space. Nanomaterials have attracted more and more attention due to their advantages such as nanometer size effect, quantum effect, surface effect, and interface effect [26]. Through the natural effects of these nanomaterials, nanomaterials have unique properties in the fields of mechanics, heat, optics, and electromagnetism.

Since the early 1980s, nanomaterials have been known as “the most promising materials in the twenty-first century,” and together with information technology and biotechnology, they have become one of the three pillars and strategic commanding heights of social and economic development in the twenty-first century. At present, the product design industry has achieved extensive development. In the process of product design, more and more designers apply nanomaterials to it, which largely meets the needs of users for products.

Nanoparticles, as a nanomaterial, have a high surface area, and they are not fully coordinated on the particle surface, thereby increasing the active centers on the surface. The combination of nanotechnology and biotechnology gives rise to nanotechnology and uses nanotechnology to solve biological problems.

## 6. Conclusions

In this paper, the effects of two nanomaterials on cement hydration rate, hydration product morphology, and ion dissolution and diffusion were compared. The main results are as follows: effects of adding two different nanomaterials on cement hydration rate, hydration products, hydration ion solubility, and ion diffusion capacity. The main test method used in this paper is to observe the effects of different dosages of nanomaterials on the hydration rate of Portland cement by using a super-depth optical digital microscope. In this paper, scanning electron microscopy was used to observe the effect of different nanomaterials on the morphology of hydration products of tricalcium silicate and Portland cement. In this paper, the plasma emission spectrometer was used to detect the effect of different nanomaterials on the ion dissolution and ion diffusion ability of Portland cement.

## Data Availability

No data were used to support this study.

## Conflicts of Interest

The authors declare that there are no conflicts of interest regarding the publication of this article.

## References

- [1] J. Rzayev, “Molecular bottlebrushes: new opportunities in nanomaterials fabrication,” *ACS Macro Letters*, vol. 1, no. 9, pp. 1146–1149, 2012.
- [2] B. R. Smith and S. S. Gambhir, “Nanomaterials for in vivo imaging,” *Chemical Reviews*, vol. 117, no. 3, pp. 901–986, 2017.
- [3] G. P. Lithoxoos, J. Samios, and Y. Carissan, “Investigation of silicon model nanotubes as potential candidate nanomaterials for efficient hydrogen storage: a combined ab initio/grand canonical Monte Carlo simulation study,” *Journal of Physical Chemistry C*, vol. 112, no. 43, pp. 16725–16728, 2008.
- [4] H. Huang and J. F. Lovell, “Advanced functional nanomaterials for theranostics,” *Advanced Functional Materials*, vol. 27, no. 2, pp. 1603524–1603524.22, 2017.
- [5] K. Zheng, M. I. Setyawati, D. T. Leong, and J. Xie, “Antimicrobial silver nanomaterials,” *Coordination Chemistry Reviews*, vol. 357, no. FEB, pp. 1–17, 2018.
- [6] H. Sadegh, G. A. M. Ali, V. K. Gupta et al., “The role of nanomaterials as effective adsorbents and their applications in wastewater treatment,” *Journal of Nanostructure in Chemistry*, vol. 7, no. 1, pp. 1–14, 2017.
- [7] W. Wang, G. Li, D. Xia, T. An, H. Zhao, and P. K. Wong, “Photocatalytic nanomaterials for solar-driven bacterial inactivation: recent progress and challenges,” *Environmental Sciences: Nano*, vol. 4, no. 4, pp. 782–799, 2017.
- [8] H. Li, T. Du, H. Xiao, and Q. Zhang, “Crystallization of calcium silicate hydrates on the surface of nanomaterials,” *Journal of the American Ceramic Society*, vol. 100, no. 7, pp. 3227–3238, 2017.
- [9] Y. Liu, L. Tian, X. Tan, X. Li, and X. Chen, “Synthesis, properties, and applications of black titanium dioxide nanomaterials,” *Science Bulletin*, vol. 62, no. 6, pp. 431–441, 2017.
- [10] X. Liu, F. Zhang, X. Jing et al., “Complex silica composite nanomaterials templated with DNA origami,” *Nature*, vol. 559, no. 7715, pp. 593–598, 2018.
- [11] G. Bo, L. Chang, H. Chenglong et al., “Effect of Mg and RE on the surface properties of hot dipped Zn–23Al–0.3 Si coatings,” *Science of Advanced Materials*, vol. 11, no. 4, pp. 580–587, 2019.
- [12] M. Hu, Z. Yao, and X. Wang, “Graphene-based nanomaterials for catalysis,” *Industrial & Engineering Chemistry Research*, vol. 56, no. 13, pp. 3477–3502, 2017.
- [13] K. L. Garner, S. Suh, and A. A. Keller, “Response to comments on “assessing the risk of engineered nanomaterials in the environment: development and application of the nanoFate model,”” *Environmental Science & Technology*, vol. 52, no. 9, p. 5511, 2018.
- [14] X. Zhang, Q. Yan, E. B. Hassan, J. Li, Z. Cai, and J. Zhang, “Temperature effects on formation of carbon-based nanomaterials from kraft lignin,” *Materials Letters*, vol. 203, no. sep.15, pp. 42–45, 2017.
- [15] P. Liu, K. Zhu, Y. Gao, H. Luo, and L. Lu, “Recent progress in the applications of vanadium based oxides on energy storage: from low dimensional nanomaterials synthesis to 3D micro/nano structures and free standing electrodes fabrication,” *Advanced Energy Materials*, vol. 7, no. 23, pp. 1700547–1700547.24, 2017.
- [16] X. Xu, D. Shahsavari, and B. Karami, “On the forced mechanics of doubly-curved nanoshell,” *International Journal of Engineering Science*, vol. 168, Article ID 103538, 2021.
- [17] R. Kumar, A. Umar, G. Kumar, and H. S. Nalwa, “Antimicrobial properties of ZnO nanomaterials: a review,” *Ceramics International*, vol. 43, no. 5, pp. 3940–3961, 2017.

## *Retraction*

# **Retracted: Clinical Application of Graphene Composite in Internal Fixation of Ankle Fracture in Sports**

### **Advances in Materials Science and Engineering**

Received 26 December 2023; Accepted 26 December 2023; Published 29 December 2023

Copyright © 2023 Advances in Materials Science and Engineering. This is an open access article distributed under the Creative Commons Attribution License, which permits unrestricted use, distribution, and reproduction in any medium, provided the original work is properly cited.

This article has been retracted by Hindawi, as publisher, following an investigation undertaken by the publisher [1]. This investigation has uncovered evidence of systematic manipulation of the publication and peer-review process. We cannot, therefore, vouch for the reliability or integrity of this article.

Please note that this notice is intended solely to alert readers that the peer-review process of this article has been compromised.

Wiley and Hindawi regret that the usual quality checks did not identify these issues before publication and have since put additional measures in place to safeguard research integrity.

We wish to credit our Research Integrity and Research Publishing teams and anonymous and named external researchers and research integrity experts for contributing to this investigation.

The corresponding author, as the representative of all authors, has been given the opportunity to register their agreement or disagreement to this retraction. We have kept a record of any response received.

### **References**

- [1] X. Xu, R. Wang, D. Zhang, and Y. Feng, "Clinical Application of Graphene Composite in Internal Fixation of Ankle Fracture in Sports," *Advances in Materials Science and Engineering*, vol. 2022, Article ID 2504511, 9 pages, 2022.

## Research Article

# Clinical Application of Graphene Composite in Internal Fixation of Ankle Fracture in Sports

Xiaowei Xu <sup>1,2</sup>, Rongna Wang,<sup>2</sup> Dachao Zhang <sup>1</sup> and Yingge Feng<sup>2</sup>

<sup>1</sup>Institute of Physical Education, Henan University, Kaifeng 475001, Henan, China

<sup>2</sup>Sports Beauty and Labor Center, Zhejiang Shuren University, Hangzhou 310015, Zhejiang, China

Correspondence should be addressed to Dachao Zhang; zhangdachao2003@126.com

Received 19 May 2022; Revised 11 July 2022; Accepted 25 July 2022; Published 25 August 2022

Academic Editor: K. Raja

Copyright © 2022 Xiaowei Xu et al. This is an open access article distributed under the Creative Commons Attribution License, which permits unrestricted use, distribution, and reproduction in any medium, provided the original work is properly cited.

The ankle joint consists of the tibia, the fibrous lower end, and the talus. Osteoporotic fractures and deboning are common injuries in orthopaedic surgery, often due to abnormal disorders following an ankle fracture. Various fractures can occur depending on the shape, size, and position of the foot at the time of the injury. With the continuous development of science and the continuous improvement of modern sports level, scientists and sports workers worldwide recognize the importance of applying new materials in sports equipment. Composite material is a combination of multiphase combination material. In short, two or more components with different properties and different forms are used in a multimaterial combination of composite means. The organic combination of related scientific equipment and composite materials promotes the development of sports equipment and the probability of reducing sports injury. The function of the existing graphene composite is analyzed and applied, and the combination of graphene composite and sports is realized theoretically. The clinical application of graphene composite in sports is studied to promote sports development. This article mainly studies the clinical application of graphene composite in ankle fracture internal fixation in sports. It is found that with the increasingly mature application of graphene rubber composite, graphene fiber composite, and other graphene composite materials, it can be widely used in all aspects of sports equipment. Graphene composite materials can be used more easily in sports equipment. In this article, the thermal material conversion algorithm, Schrodinger equation in quantum mechanics, and the use method of graphene composite materials are used to study the clinical application of graphene composite in the internal fixation of ankle joint fracture in sports. The frequent injury and instability of ankle and knee joints are signs of ankle and knee joint injury. The main factors that affect the instability of ankle and knee function are the comprehensive effects of motion range, muscle force valgus, and body feeling, and graphene composite materials are widely used in the internal fixation of ankle joint fracture in sports. The results show that graphene composite can be used in sports equipment and has a great space and high feasibility through the analysis of four groups of sports equipment. It shows that advanced materials play a very important role in the research of sports equipment.

## 1. Introduction

Graphene is a two-dimensional crystal composed of carbon atoms with only one layer of atomic thickness. Since its first discovery in 2004, graphene composites have been a hot research object all over the world. In recent years, the USA, South Korea, Spain, and China have made breakthroughs in the manufacture and application of graphene and its derivatives. Graphene has many properties that other materials do not have. Graphene is light, strong, and tough. It has good strength, flexibility, electrical and thermal conductivity, and

other properties. It is the material with the highest thermal conductivity so far and has very good thermal conductivity. Graphene derivatives also attract the great attention of scientists all over the world. There are many kinds of graphene derivatives, and their physical and chemical properties are also different. Graphene oxide, graphene-based nanocomposites, free amino graphene, and graphene rubber have been widely used.

Competitive sports has always been the front line of the application of high-tech composite materials, from track and field to swimming, from competition to training, from the

electronic timer to “shark skin” swimsuit, from “bird’s nest,” “water cube” to blood lactic acid detector, from electronic science to material science, from architecture to biochemistry. As we all know, scientific composite material is the first productivity, and sports scientific composite material is the first productivity of sports development and progress. Zhang Shan’s research shows that China has been in a period of rapid development in sports science since 1992. The coverage of sports science research in China is more and more extensive, the cross integration of sports science and related disciplines is deepening, and new disciplines are emerging. In this context, graphene materials, a new field of science and technology, will be combined with the field of sports.

With the invention of various derivatives of graphene, graphene can form a graphene-filled polymer, polymer graphene compound with layered structure, and functional polymer compound composites through the interaction of various polymers, which can be used as a substitute for graphene for carbon fiber modification. It can also be used in rubber to improve many properties of rubber. Wu J thought that under mild conditions, graphene oxide is reduced and self-assembled into a three-dimensional network, while  $\text{Fe}^{2+}$  is transformed into  $\text{Fe}_2\text{O}_3$  and deposited on the graphene network. This structure is conducive to the diffusion of electrolyte and the electron transfer between  $\text{Fe}_2\text{O}_3$  and collector, which makes the composite have high capacitance performance.  $\text{Fe}_2\text{O}_3$ /chemically transformed graphene composite has a higher specific capacitance than the saturated calomel electrode at the working potential of 0~1 V, which provides a simple and easy method for the preparation of asymmetric supercapacitor cathode materials, but there is a lack of specific data [1]. Park et al. thought that the uniform aqueous suspension of chemically modified graphite sheet with good conductivity was prepared, and the graphene composite with high conductivity was prepared by reducing chemically modified polystyrene graphene oxide. The graphite oxide was dispersed in water, and the uniform aqueous suspension containing chemically modified graphite sheet was prepared, and the chemical reactions of graphene oxide sheets suspended in water with potassium hydroxide and hydrazine were studied. In the research process, the uniform suspension of conductive graphene sheet was prepared, but the necessary experimental data were lacking [2]. Domantas believed that graphene has high carrier mobility, conductivity, flexibility, and optical transparency and is widely used in microelectronics and macroelectronics. This kind of stretchable device is characterized by a serpentine bilayer film composed of gold mesh and gold doped graphene, which forms an effective electrochemical interface for the stable transmission of electrical signals. Temperature, humidity, glucose and pH sensors, and polymer microneedles, which can be proved by thermally activated transdermal drug delivery, lack numerical analysis [3]. According to Mohamadi, a general strategy for synthesizing two-dimensional macromolecular brushes is proposed. They can be dissolved in solvents in the form of single molecules, with strong processability, and their molecular brushes have high density, high solubility, and low features such as viscosity and conductivity. Functional genes

such as epoxy groups can also be introduced into the brush arm as needed, which uses a micron-scale flake graphene superplanar monoatomic layer as the macromolecular skeleton, and more than 10 polymer chains are covalently connected to the nanosheets through radical polymerization, resulting in a large 2D brush arm density of 1.59 from polar to nonpolar  $\times 10^4$  arms per hour  $\mu$ ; M2 single-sided graphene has high solubility, low intrinsic viscosity, and good conductivity. If necessary, it can contain a large number of epoxy groups and other functional groups, but some discussions are not accurate [4].

The innovation of this article lies in the use of the thermoelectric material conversion algorithm, the Schrodinger equation in quantum mechanics, and the use of graphene composite materials to study the clinical application of graphene composite materials in the internal fixation of ankle fractures in sports. Based on this point, the application of graphene composite material in sports equipment and exploring the application scope, mode, and feasibility of graphene composite material in sports will pave the way for future practical applications.

## 2. How to Use Graphene Composites

**2.1. Graphene.** Compared with traditional single materials, composite materials have high specific strength and modulus, high-temperature performance, size stability, and chemical stability. Graphene is a kind of single-layer hybrid carbon atom, arranged in hexagonal form, such as a two-dimensional crystal, in which the carbon atoms are arranged periodically in the form of six-dimensional rings. The length of the C-C bond between the carbon atom and carbon atom is connected by a covalent bond, and the thickness of the graphene monolayer is about 0.335 nm [5]. The special geometry makes graphene show strong physical and chemical properties than other carbon-based materials, mainly in the following aspects: (1) between graphite sheets  $\pi$ - $\pi$ . The structure makes the electron show excellent conductivity, and the rapid electron conduction speed makes graphene regarded as quasigold [6]. Meanwhile, the unique carrier fluid characteristics make it can observe the quantum Hall effect at room temperature; (2) graphene exhibits excellent mechanical properties due to the small bond length of C-C bond; (3) graphene has good transparency due to its lamellar structure, so it has good optical properties. Graphene absorbs about 2.3% over a wide wavelength range and appears almost transparent. Applying a magnetic field can convert the optical properties of graphene nanoribbons, and the response is tuned to the terahertz range. When the intensity of the incident light exceeds a certain threshold, graphene’s absorption saturates.

These have made graphene widely concerned in the fields of supercapacitor, photocatalysis, biosensor, and dye-sensitized cell; graphene is shown in Figure 1.

### 2.2. Thermoelectric Material Conversion Algorithm

**2.2.1. Performance Test of Composite Membrane.** The maximum efficiency  $F$  of thermoelectric conversion is

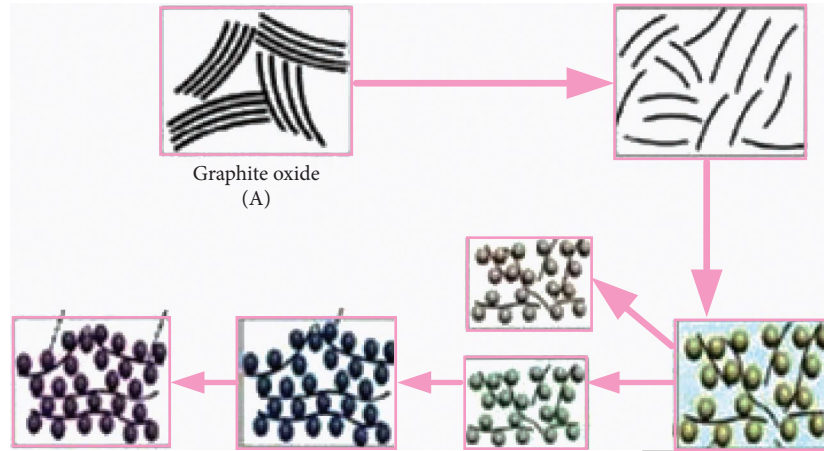


FIGURE 1: Graphene materials.

determined by two factors. The first factor is the efficiency of the Carlo cycle; the second factor is determined by the nature of the thermoelectric material itself, which is generally expressed by thermoelectric performance, which depends on Seebeck coefficient, conductivity A, and thermal conductivity ( $k = B + V$ ) [7, 8]. The performance parameters of these materials determine the thermoelectric performance of the materials. For the case of a small temperature difference, the maximum conversion efficiency F of thermoelectric power generation can be expressed as follows:

$$H = \frac{saL}{k} = \frac{saL}{b + v}, \quad (1)$$

$$f = \frac{W - M}{L} \cdot \frac{(1 + H)^{1/2} - 1}{(1 + H) + W/M}$$

In order to achieve the optimal thermoelectric performance of thermoelectric materials, multiple mutually restricted parameters must be optimized at the same time [9]. According to the definition of characterization thermoelectric quality factor, the optimal thermoelectric performance requires the following conditions: high Seebeck coefficient, high conductivity, and low thermal conductivity. However, these three parameters restrict and couple with each other and cannot be optimized independently [10]. Therefore, achieving high thermoelectric efficiency in traditional bulk materials is a great challenge. For metals or degenerate semiconductors, the Seebeck coefficient can be calculated by a simple electron transport model:

$$a = mbu, \quad (2)$$

where  $m$  is the carrier concentration,  $B$  is the effective mass of the carrier,  $e$  is the charge amount of the elementary charge, and  $l$  is the Planck constant [11, 12].

**2.2.2. Schrodinger Equation in Quantum Mechanics.** In quantum mechanics, the state of a particle can be described by a wave function, which should follow certain rules. According to the motion behavior of particle potential energy field  $v(r)$ , the wave function of the particle is

proposed, which should satisfy the following differential equation:

$$-\frac{f^2}{2n} \nabla^2 + h(x) = f \frac{a}{at}, \quad (3)$$

where  $F$  is the Planck constant and  $N$  is the mass of particles. In quantum mechanics, this “simple” equation used to describe the motion law of microparticles has a high position if the electric field acting on the microsystem is independent of time [13]. The separation variable method can be used to solve the following problem:

$$v(r, t) = k(r)h(t). \quad (4)$$

**2.2.3. Microparticle.** The left side is only related to the coordinate  $R$ , while the right side is only related to the time  $T$ .  $R$  and  $T$  are independent variables. Therefore, the equation can be satisfied only when both sides are equal to a constant at the same time. Let the constant be  $g$ . The above equation is decomposed into two equations as follows:

$$h(t) = Bl^{\frac{ig}{k}}. \quad (5)$$

It can be seen from the obtained relationship that the constant  $e$  represents the energy of the corresponding wave function in the state described by the system. When  $E$  has a certain value, the corresponding state is called the constant state, and  $V(R, t)$  is called the constant state wave function. Moreover, the probability flux density in the constant state is independent of time and is only a function of the spatial coordinates. For the Schr of the double electrons, the probability flux density in the constant state is not related to the time  $\ddot{o}$  Dinge equation:

$$\Delta F^{GL} = GL(L\Delta F^G + G\Delta F^L). \quad (6)$$

In general, the materials studied contain a large number of particles, which is the reason why it is difficult to solve the equation of state of multiparticle system through quantum mechanics [14].

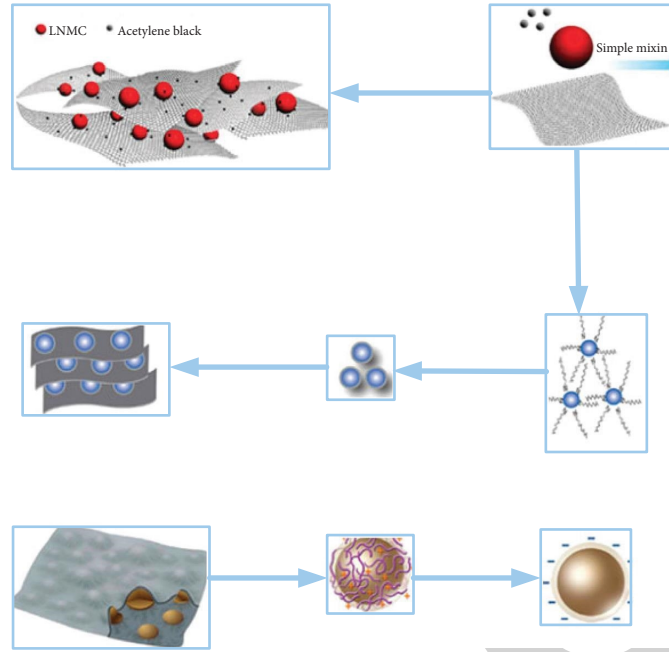


FIGURE 2: Compound material.

2.3. *Composite Materials.* The special process in the preparation of graphite oxide is as follows: put 1.5 g plastic graphite and 9 g potassium permanganate into a 250 ml gold bottle, multiply the prepared mixed acid solution by the same method, and then slowly add it into the bottle. This process is carried out in the refrigerator and bathroom. After a period of time, the bottle will rise and then slowly adjust the accelerator temperature; the mixture was heated to 50°C and stirred at this temperature for 12 hours; then the brownish purple liquid was obtained [15, 16]. After the above work, cool the liquid mixture to room temperature, and add 200 ml of liquid to it, and the color gradually turns yellow. After the second washing with hydrochloric acid and the second washing with water, the pH value will be about 7. Finally, set the time to wait after the completion, and take the oxidized liquid [17]. There is a record. In order to reduce the oxidation process, we prepared a reduction diagram. For the specific operation, see the preparation of the ITO electrode, as shown in Figure 2.

Chitosan is soluble in rare organic acids and inorganic acids such as acetic acid, formic acid, and phosphoric acid but insoluble in sulfuric acid, nitric acid, water, and alkaline solution. Acetic acid is one of the most commonly used solvents. The essence of chitosan dissolution is to dissolve positively charged polyelectrolyte chitosan in acid. Chitosan solution should be used and prepared on-site, which is easily affected by temperature, pH value, concentration, and other factors [18].

2.4. *Calculate the Forces Acting on All Particles.* The force between atoms is calculated by the set cut-off radius and the selected potential function, which is the key to determining the accuracy of the calculation results [19]. The atomic motion in MD is based on Newton's equation of motion:

$$m \frac{d^2 r}{dt^2} = -\nabla m, \quad (7)$$

where  $m$  is the potential energy between atoms, generally, the interaction between silicon atoms is described by semiempirical SW potential function, which is specially created by Stillinger and Weber for silicon:

$$m(1, \dots, N) = \sum_i h(i) + \dots + h_N(1 \dots N) h(r) = mk(r/a). \quad (8)$$

The interaction of the above calculation is repeated to make the system enter the steady state [20]. Then increase the simulation time, repeat the above process, and record the position and velocity of the atom:

$$a(t + \Delta t) = -\nabla r(t). \quad (9)$$

### 3. Related Experiments of Ankle Fracture Internal Fixation in Sports

3.1. *Graphene Rubber.* Rubber is an important material, which is indispensable and irreplaceable in the national economy and high technology. It has the characteristics of reversibility and high elasticity. It can produce large deformation under the action of external force and can recover quickly after removing the external force. It has been widely used in many fields. In recent years, the traditional rubber industry has been difficult to meet the high-performance requirements of the high-tech composite industry, transportation, aerospace, and so on. Nanofillers and rubber composites manufacturing nanofillers have become an effective way to obtain high-performance rubber compounds, which also leads to the development of graphene rubber. At present, graphene rubber has been used in general rubber



materials and special rubber materials. General rubber is a group of elastic materials first applied in the field of the national economy, also known as special synthetic rubber materials. It is used in harsh application conditions and various special synthetic rubber properties and applications. One of these two rubbers has a wide range of applications and good comprehensive performance, and the other has some special properties, which can be very strong for one situation—applicable, but not universally applicable.

**3.2. Ankle Fracture in Sports.** The data of 130 patients with an ankle fracture and graphene composite fixation in our hospital were collected, including 80 males and 50 females, with an average age of 35 years. The preoperative trauma history, physical examination, imaging data, and intra-operative findings of the patients were collected, and the imaging images were analyzed by Digimizer measurement software, as shown in Table 1.

The ankle joint is an important load joint and movement joint. The ankle joint is composed of the lower end of the tibia and fibula. The lower end of the tibia is the medial protrusion of the ankle joint, and the lower end of the fibula is the lateral protrusion. Because it is difficult to develop ligaments directly in X-ray and CT films, the diagnosis of ligaments injury should be carried out through indirect manifestations; that is, the talus tilt test is positive, which should be compared with the healthy side, as shown in Table 2.

**3.3. Statistical Methods.** The mean value of the test data was processed, and SPSS statistical software was used to process and analyze the data in Windows 10.0. The one-way ANOVA method was used to measure the knee proprioception (bending angle, extension angle) and Taekwondo group, walking group, table tennis group, and control group, as shown in Figure 3.

**3.4. Graphene Fiber.** Industry insiders believe that with the growing demand for sports equipment, fiber-reinforced composites will become the mainstream sports equipment industry in the 21st century. People perform a heating step on sic fibers in a vacuum environment and/or an inert gas environment, heat up to the decomposition temperature of silicon, and then keep warm. The graphene fibers are obtained and then applied to various fields. Graphene fibers are a new type of carbon fiber developed in recent years with natural graphite as the initial raw material. The liquid crystal dope of graphene nanosheets is assembled in one-dimensional order by wet spinning. Fiber-reinforced composites have the characteristics of lightweight, high strength, and high performance. Graphene fiber has the characteristics of high strength, high elastic modulus, good corrosion resistance, free design, and convenient processing, which can be widely used in sports equipment, showing a unique charm. The existing fiber materials mainly include ordinary glass fiber, high-strength glass fiber, high-strength polyethylene fiber, and high-strength vinyl fiber. There are many kinds of sports equipment, including the use of fiber composite

TABLE 1: Ankle fracture in sports.

Baseline data	Number of people	$x$	$P$
Gender	130	6.43	0.991
Male	80	7.12	0.002
Female	50	43.25	0.005
Age	35	44.35	0.115
Right	110	41	0.664
Wrong	0	3.3	0.321

TABLE 2: Lauge–Hansen classification of ankle fractures in sports.

	X-ray analysis	Ankle fracture fixation
SAD	21	10
SER	11	16
PAB	40	30
PRE	32	26
Unable to type	30	28
No fracture	11	66

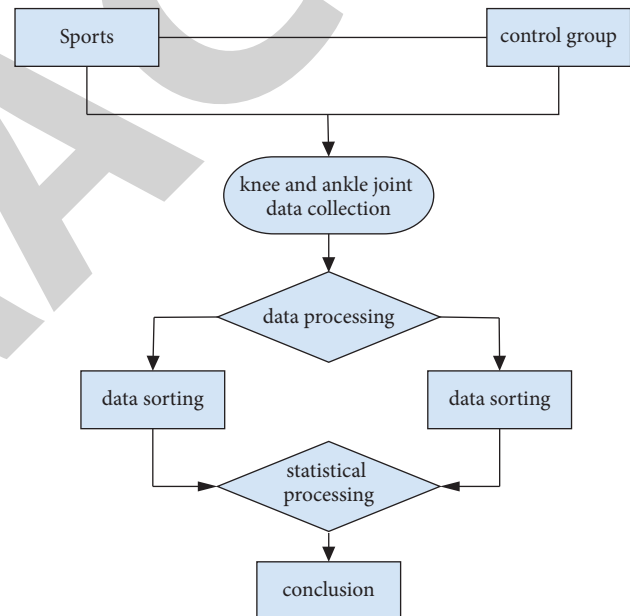


FIGURE 3: Flowchart of sports experiment.

materials: golf clubs, tennis rackets, bicycles, and skis. With the continuous expansion of the application of graphene in recent years, the application prospect of graphene fiber in sports equipment is very broad. In addition, since graphene fiber composites can also provide excellent mechanical, electrical, thermal, radiation protection, antibacterial, and other functional properties, the graphene/fibers manufactured by the functional composite fibers and related textile products have a wide range of applications in superconducting and conductive clothing materials, antibacterial medical materials, biomedical textile materials, flame retardant materials, and lightweight fiber-based thermal and conductive composite materials. Graphene fiber and carbon fiber are also dominated by carbon, and their physical and chemical properties are very similar to carbon fiber, so they are very comparable.

TABLE 3: Subject information.

	Age	Training years	Eg weight
Taekwondo group	20.67 ± 2.40	4.67 ± 2.12	15.12 ± 3.50
Walking group	23.87 ± 0.39	7.89 ± 3.31	3.45 ± 3.86
Table tennis group	7.67 ± 9.12	5.43 ± 0.14	10.67 ± 1.05
Control group	9.69 ± 5.10	1.08 ± 0.40	19.44 ± 6.40

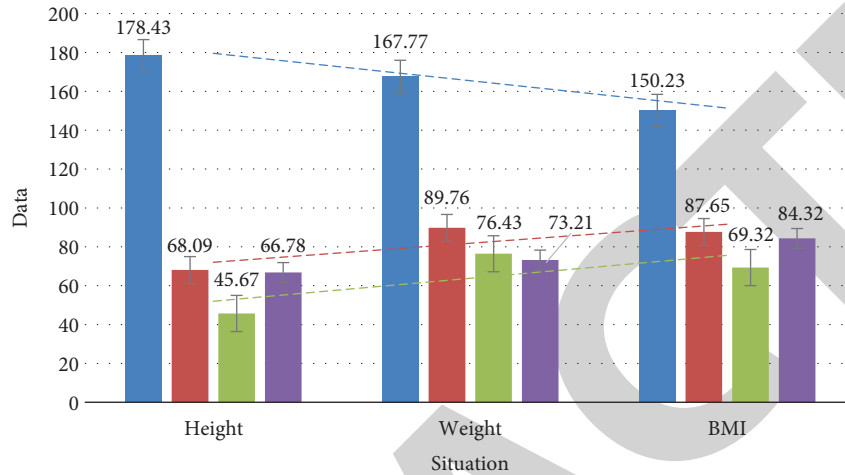


FIGURE 4: Comparison of VEGF content in granulation tissue of two groups before and after treatment.

#### 4. Experimental Analysis of Clinical Application of Ankle Fracture Internal Fixation in Sports

4.1. Comparison of Different Sports. The results showed that there was no significant difference in age and BMI among the three groups; there were significant differences in height and weight between the Taekwondo group and other groups; there was a significant difference in height between the table tennis group and other groups. Due to the different actual training conditions of various sports, the number of years of professional training has not been used as an index for analysis and comparison, as shown in Table 3.

The blood supply, sensation, and activity of the extremities were examined after anesthesia. The patients with ligament or meniscus injuries should be repaired during the operation. If it is difficult to repair this operation, the patient should be repaired under arthroscopy. After the operation, the affected limb was bandaged and raised routinely. On the third day after the operation, the patient was required to move the injured joint and toe weight-bearing exercise gently on the bed within the tolerable range if the wound healed satisfactorily, as shown in Figure 4.

For patients with more bone defects, serious osteoporosis, and serious ligament injury, long leg supports can be fixed for 2 to 3 weeks. From one week after the operation, the injured joints can be restored and trained. According to the imaging review data, the healing of fractures is observed dynamically. The limb joints are partially loaded 8–10 weeks after the operation. Under the condition of no complaints, the injured joints can be partially loaded. The load intensity is gradually

TABLE 4: Cell proliferation.

Movement direction	Dominant side	Nondominant side	P value
Ankle flexion	0.56 ± 0.07	0.47 ± 0.29	0.33
Ankle extension	0.44 ± 0.12	0.32 ± 0.11	0.21
Ankle varus	4.12 ± 0.01	1.22 ± 0.12	0.11
Ankle valgus	5.21 ± 0.07	3.25 ± 0.53	0.54

TABLE 5: Some aspects of graphene composites in sports.

Serial number	Project
1	Ice and snow
2	Archery
3	Track and field
4	Rowing
5	Sailing
6	Racing

increased. After the fracture healing is satisfied, the internal fixator is removed.

4.2. Comparison between the Sensory Superior Side and the Nondominant Side of Ankle in Golf. The average sensory mean of the ankle body in the superior and nondominant sides of the Taekwondo group was larger than the rear, and the ankle extended backward. The slope body entered the fibula joint nest, and the bone moved upward and outward to adapt to the change in the width of the ankle fossa slope. The healing of fork bone limits the activity of the ankle joint. Most patients who are cured have no clinical symptoms,

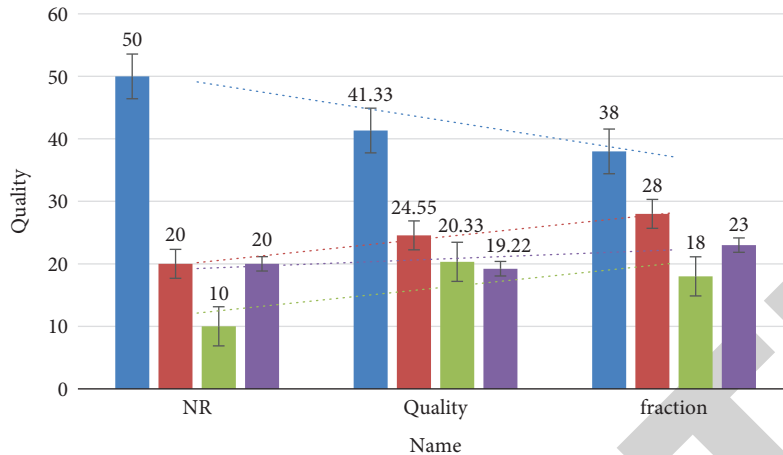


FIGURE 5: Formulation quality of graphene materials.

even if they are limited in ankle joint activity. They have no influence on daily life. After sports, the ankle function healing needs appropriate treatment significance difference, as shown in Table 4.

According to Table 4, the weight, hardness, and balance of the club are the three main factors affecting the handle and distance of the club. Different golf clubs have different effects on the hitting results, which directly affect the performance of the golfer. The weight of the club body is a very important factor for the golfer's feeling of the club. The lighter the club body is, the smaller the overall weight of the club is. The heavier the club body is, the greater the total weight of the club is. The change in the total weight of the club will directly bring changes to the feel of the club. The weight of the rod is also a very important factor affecting the stroke distance.

**4.3. Prospects of Application of Graphene Composites in Sports Equipment.** The pole vault made of graphene carbon fiber composite and glass fiber composite is light and elastic, which can be used to jump higher. With the continuous development of chemical technology, nylon and metal rod have been used one after another; a lighter and more elastic graphene fiber rod has been developed. The graphene fiber rod has been improved to ensure certain fracture toughness. Alloy rod is a development trend. Based on previous studies, graphene magnesium matrix composites have strong maximum recovery energy and sufficient energy storage capacity, which can ensure the springback of the rod. Graphene carbon fiber composite and glass fiber composite can also be made into high jump crossbars, which will not produce bending deformation, is not easy to break, and is more accurate and safe. Adding graphene carbon fiber composite to the sole of carbon fiber sole running shoes can further reduce the weight of the sole, as shown in Table 5.

Half a year after the graphene production line was put into operation, its main product was multilayer graphene with a thickness of 3 nm. Then the raw material cost of a single shoe was calculated as follows: assuming that the weight of a single shoe was 200 g, in which the proportion of graphene natural rubber composite was 36.8%, and the mass

fraction of graphene in graphene natural rubber composite was 0.85%, and the actual amount of graphene in a single shoe was about 0.63 g. It can be seen that the cost has decreased by 99.5%. And with the progress of scientific composite materials, the application of high-tech sports equipment in professional competitions is less and less affected by the cost. Athletes from all over the world are willing to invest a lot of money in the research of training methods and sports equipment. It can be said that there is no cost barrier in the application of graphene composite sports equipment in high-level professional competitions. And for amateur sports enthusiasts and the general public, the cost increase of graphene sports equipment is not obvious. With the continuous improvement of the level of graphene composites, the decline of the cost of graphene composites is the development trend, as shown in Figure 5.

With the price of graphene itself declining, the cost of adding graphene rubber composite to a basketball shoe has shown a rapid downward trend. This downward trend is the premise that graphene rubber composite sports equipment can be generally accepted by the public. Only when the general public can afford it can it be widely promoted. The analogy to other sports equipment is the same, as shown in Figure 6.

Developing highly skilled systems to assess the effects of the musculoskeletal injury on balance has been attempted to quantify static and dynamic proprioception. The evaluation method is based on the fact that the injury will damage the proprioception of the joint, resulting in decreased feedback from the lateral ligament afferent nerve and increased body swing. The graphene sports equipment that can be used in competitive sports such as basketball shoes can be extended to mass sports, and almost all mass sports can use graphene sports equipment, The prospect of graphene composites is shown in Figure 7:

If athletes want to achieve brilliant results in sports, their body control ability and body's feeling for space are very important. However, the stability of the body depends in part on the body's sensory mechanical receptors on the skin, muscles, tendons, joint capsule, and ligaments to transmit the message. Therefore, the mechanical receptors located on

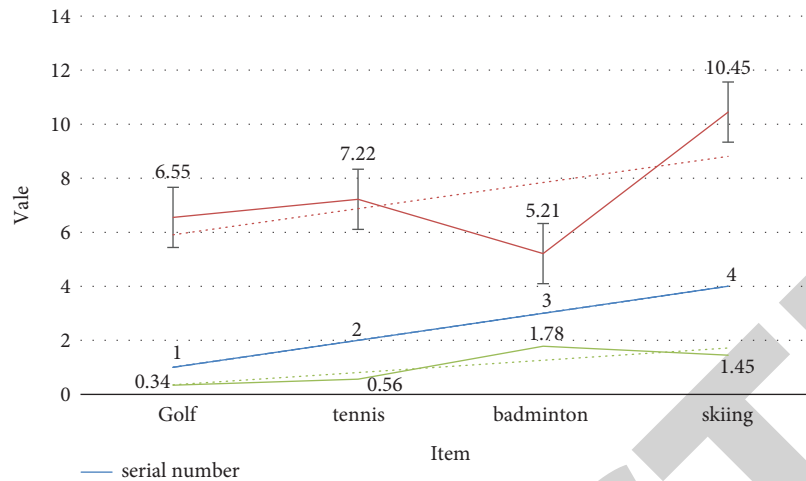


FIGURE 6: Graphene equipment project.

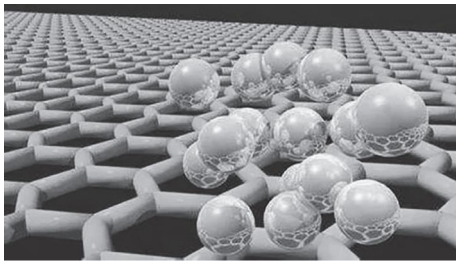


FIGURE 7: Prospect of graphene composites (<https://alturl.com/5fuj7>).

the ankle capsule and ligament can reflect the changes in joint position and direction and acceleration of limbs. These receptors also provide messages from static posture, movement, and muscle strength.

## 5. Conclusion

In this article, we use the thermoelectric material conversion algorithm, the Schrodinger equation in quantum mechanics, and the use of graphene composite materials to study the clinical application of graphene composite materials in ankle fracture internal fixation in sports. Graphene rubber composite materials and graphene fiber composite materials are used in competitive sports. Archery, racing, and many other projects have great application prospects. In the future, with the mature development of graphene rubber composites, the sports equipment that can be used in rubber materials can be replaced with graphene rubber composites. Through the understanding of the current application direction of graphene and the preliminary calculation of the application cost of graphene, the development direction of graphene composite sports equipment is determined. Graphene composites have broad application prospects in sports equipment. With the development of graphene composites, the cost of graphene is rising. It has gradually developed from 10 times higher than gold to 1000 yuan/kg. In addition, for the professional athletes or sports teams participating in

the Olympic Games, world championships, and other international competitions, the cost of sports equipment has not been an obstacle to improving sports performance. Therefore, the application of graphene composites in the field of sports equipment will not be affected by the cost.

## Data Availability

No data were used to support this study.

## Conflicts of Interest

The authors declare that there are no conflicts of interest regarding the publication of this article.

## References

- [1] J. Wu, A. Zhou, Z. Huang, L. Li, and H. Bai, "A facile method to prepare three-dimensional Fe<sub>2</sub>O<sub>3</sub>/graphene composites as the electrode materials for supercapacitors," *Chinese Journal of Chemistry*, vol. 34, no. 1, pp. 67–72, 2016.
- [2] S. Park, J. An, R. D. Piner et al., "Aqueous suspension and characterization of chemically modified graphene sheets," *Chemistry of Materials*, vol. 20, no. 21, pp. 6592–6594, 2008.
- [3] H. Lee, T. K. Choi, Y. B. Lee et al., "A graphene-based electrochemical device with thermoresponsive microneedles for diabetes monitoring and therapy," *Nature Nanotechnology*, vol. 11, no. 6, pp. 566–572, 2016.
- [4] L. Kan, Z. Xu, and C. Gao, "General avenue to individually dispersed graphene oxide-based two-dimensional molecular brushes by free radical polymerization," *Macromolecules*, vol. 44, no. 3, pp. 444–452, 2011.
- [5] W. Tao, H. Da, Y. Zhi et al., "A review on graphene-based gas/vapor sensors with unique properties and potential applications," *Nano-Micro Letters*, vol. 8, no. 002, pp. 95–119, 2016.
- [6] J. Liu, G. Chen, and M. Jiang, "Supramolecular hybrid hydrogels from noncovalently functionalized graphene with block copolymers," *Macromolecules*, vol. 44, no. 19, pp. 7682–7691, 2011.
- [7] X. Chen and N. Ye, "Graphene oxide-reinforced hollow fiber solid-phase microextraction coupled with high-performance liquid chromatography for the determination of cephalosporins

## Retraction

# Retracted: An Artificial Intelligence Mechanism for the Prediction of Signal Strength in Drones to IoT Devices in Smart Cities

### Advances in Materials Science and Engineering

Received 20 June 2023; Accepted 20 June 2023; Published 21 June 2023

Copyright © 2023 Advances in Materials Science and Engineering. This is an open access article distributed under the Creative Commons Attribution License, which permits unrestricted use, distribution, and reproduction in any medium, provided the original work is properly cited.

This article has been retracted by Hindawi following an investigation undertaken by the publisher [1]. This investigation has uncovered evidence of one or more of the following indicators of systematic manipulation of the publication process:

- (1) Discrepancies in scope
- (2) Discrepancies in the description of the research reported
- (3) Discrepancies between the availability of data and the research described
- (4) Inappropriate citations
- (5) Incoherent, meaningless and/or irrelevant content included in the article
- (6) Peer-review manipulation

The presence of these indicators undermines our confidence in the integrity of the article's content and we cannot, therefore, vouch for its reliability. Please note that this notice is intended solely to alert readers that the content of this article is unreliable. We have not investigated whether authors were aware of or involved in the systematic manipulation of the publication process.

Wiley and Hindawi regrets that the usual quality checks did not identify these issues before publication and have since put additional measures in place to safeguard research integrity.

We wish to credit our own Research Integrity and Research Publishing teams and anonymous and named external researchers and research integrity experts for contributing to this investigation.

The corresponding author, as the representative of all authors, has been given the opportunity to register their agreement or disagreement to this retraction. We have kept a record of any response received.

### References

- [1] M. R. A. Refaai, V. S. N. C. H. Dattu, H. S. Niranjana Murthy, P. Pramod Kumar, B. Kannadasan, and A. Diriba, "An Artificial Intelligence Mechanism for the Prediction of Signal Strength in Drones to IoT Devices in Smart Cities," *Advances in Materials Science and Engineering*, vol. 2022, Article ID 7387346, 13 pages, 2022.



## Research Article

# An Artificial Intelligence Mechanism for the Prediction of Signal Strength in Drones to IoT Devices in Smart Cities

Mohamad Reda A. Refaai <sup>1</sup>, Vinjamuri S. N. C. H. Dattu,<sup>2</sup> H. S. Niranjana Murthy,<sup>3</sup>  
P. Pramod Kumar,<sup>4</sup> B. Kannadasan,<sup>5</sup> and Abdi Diriba <sup>6</sup>

<sup>1</sup>Department of Mechanical Engineering, College of Engineering, Prince Sattam Bin Abdulaziz University, Alkharj 16273, Saudi Arabia

<sup>2</sup>Department of Mechanical Engineering, Aditya Engineering College, East Godavari, Surampalem, Andhra Pradesh, India

<sup>3</sup>Department of Electronics and Instrumentation Engineering, Ramaiah Institute of Technology, Bangalore, Karnataka 560054, India

<sup>4</sup>Department Computer Science and Artificial Intelligence, SR University, Warangal, Telangana, India

<sup>5</sup>Department of Civil Engineering, B. S. Abdur Rahman Crescent Institute of Science and Technology, Chennai, Tamil Nadu 600048, India

<sup>6</sup>Department of Mechanical Engineering, Mizan-Tepi University, Tepi, Ethiopia

Correspondence should be addressed to Mohamad Reda A. Refaai; drengrefaai@gmail.com and Abdi Diriba; abdi@mtu.edu.et

Received 6 May 2022; Revised 8 June 2022; Accepted 18 June 2022; Published 24 August 2022

Academic Editor: K. Raja

Copyright © 2022 Mohamad Reda A. Refaai et al. This is an open access article distributed under the Creative Commons Attribution License, which permits unrestricted use, distribution, and reproduction in any medium, provided the original work is properly cited.

Drones, the Internet of Things (IoT), and Artificial Intelligence (AI) could be used to create extraordinary responses to today's difficulties in smart city challenges. A drone, which would be effectively a data-gathering device, could approach regions that become complicated, dangerous, or even impossible to achieve for individuals. In addition to interacting with one another, drones must maintain touch with some other ground-based entities, including IoT sensors, robotics, and people. Throughout this study, an intelligent approach for predicting the signal power from a drone to IoT applications in smart cities is presented in terms of maintaining internet connectivity, offering the necessary quality of service (QoS), and determining the drone's transmission range offered. Predicting signal power and fading channel circumstances enables the adaptable transmission of data, which improves QoS for endpoint users/devices while lowering transmitting data power usage. Depending on many relevant criteria, an artificial neural network (ANN)-centered precise and effective method is provided to forecast the signal strength from such drones. The signal strength estimations are also utilized to forecast the drone's flight patterns. The results demonstrate that the proposed ANN approach has an excellent correlation with the verification data collected through computations, with the determination of coefficient  $R^2$  values of 0.97 and 0.98, correspondingly, for changes in drone height and distances from a drone. Furthermore, the finding shows that signal distortions could be considerably decreased and strengthened.

## 1. Introduction

Drones are often referred to as unmanned aircraft systems. The drone is a flying robot, and it can be remotely controlled or flown automatically using software-controlled systems. It works in conjunction with sensitive devices and the global positioning system (GPS). Drones are now in demand for testing and multiple applications because of their versatility and capability to be used in a broad variety of applications,

such as control, security, observation, and the rapid surveillance of inaccessible terrain. Furthermore, it is an alternative technology that enhances the ability of first responders to reach the areas of environmental disaster and carry out rescue operations. It can assist in emergency preparedness situations, such as medicine distribution, forest fire extinguishing, vital infrastructure preservation and testing, coastal surveillance, and police upgrades, and it can help meet the public safety standards of urban areas.



There are many different types of novel technologies that can be accessed by drones, depending on the type of activities being performed. Nonetheless, they are commonly used in the military. Drones are now used in a variety of areas, including commercial and civilian applications, such as disaster and crisis management, surveillance, hostility, rescue and search operations, temporary relay networks, civil defense, remote and agriculture sensing, wind assessment, and so on. Also, the most advanced applications of drones nowadays are their participation in smart urban areas. Real estate, infrastructure, communications, and marketing are some of the businesses offered in Smart Urban. The advantages of Smart Urban extend to everybody, including companies, people, government, ecology, and more [1]. Because of their agility, mobility, and adaptability, drones are often used in a variety of attributes. Drone user tools play a key role, especially in packaging delivery, remote sensing, and access management. As flying drones require cellular infrastructure, low-latency communications and seamless connectivity are achievable. The 5<sup>th</sup> generation new radio and extensive term evolution cellular technologies are capable of providing robust security and management over a wide variety of high-speed, secure wireless connections to drone operations.

Compared to fixed terrain base stations, such as WiFi for information gathering, drones have the advantage of being quick to use. They can also get closer to IoT devices, capture large amounts of device data (high data rate), and provide flying communications. Moreover, the drone system enables LoS to reduce shadow and signal interference. Furthermore, connection and range concerns are often a barrier to gathering accurate information from the IoT framework. because of its flexibility, mobility, and strong communication connectivity, the drone is able to go to IoT device sites and create energy-effective networks, minimizing IoT device power consumption. The data obtained will then be sent to the nearest base station (BS) [2]. The link between public security and the Internet of Things (IoT) was explored, and the IoT-based Smart City classification was presented. The usage of IoT technology in urban cities will lead to variations and developments in security, economy, public utility monitoring, and transportation [3]. The Smart City is a complex structure, largely built by Communications and Information Technology (ICT), with the aim of making metropolitan residences more desirable, practical, and ideal locations for corporate growth. App developers, professional firms, citizens, government, and open specialized companies inquire about networking, and staging engineers are key stakeholders in the Smart City. Figure 1 depicts the various services of smart cities. Furthermore, the smart urban cycle includes many ICT innovations, phases of development, maintenance and management sites, communal applications, and specific financial and social KPIs (key performance indicators). As a result, IoT platforms play an important role in building a broader multifaceted foundation [4].

Smart urban initiatives can accurately solve the problem of ensuring a greener environment by developing and implementing low carbon emissions technology. Many

governments around the world (e.g., Japan, USA, EU, and others) have planned and implemented smart city plans to successfully address any growing difficulties. To satisfy the expectation of a smart city, it is essential to properly control the analysis of the effective use of communication and information technology data, communication systems, and the efficient use of a complicated strategy to achieve the safe and smooth functioning of a modern city [5]. As per statistics, the worldwide urban population is anticipated to reach 70% or 75% by 2052, depending on the source. This rate of urbanization will have significant effects on the environment, administration, and the safety of towns. Several governments have advocated the notion of urban cities to properly control resources and enhance energy usage to deal with the dramatic rise in urbanization [6]. The concept of smart cities starts with the improvements needed to provide more efficient and timely services to residents. To solve this problem, drones offer tremendous potential for rapid transition from early planning to the real universe, as well as assist urban dwellers in improving living conditions. The timing of creating automation for corporate and average citizen activities requires an understanding of the specifics of certain requirements set out for their owners. Traffic flow management, which is organized in urban areas, requires the automata to be gradually solidified with a precise route design and be more sophisticated than other methods. As the metropolitan population is dense, automatons will be equipped with attack sensors, GPS data, and computerized maps [7]. Figure 2 shows the architecture of IoT (Internet of Things).

The technologies of smart city opportunities vary from broadening the substructure capability to producing innovative assistance, from emanations reduction to engaged people, from decreasing error rates to enhancing judgment making, and from continuing to support maintainable growth to enhancing commercial venture and city effectiveness. Among the most prominent technologies in the field of smart cities are the autonomous vehicles (AV), robots, big data, 5G, 3D printing, blockchain, cloud computing, Internet of Things (IoT), virtual reality (VR), artificial intelligence (AI), and digital twins. While some of these techniques are important in making human cities smarter, AI paired with this technology has considerable promise to report the current urbanization concerns. Moreover, AI is often regarded as the most revolutionary innovation of humans [8]. The Internet of Things (IoT) is a modern management movement in the field of information technology, and it has the potential to revolutionize many human activities. There are many approaches to using this method that have been researched and used around the world. Scientists are identifying cases where IoT principles are used for fully automated operations. The Internet of Things (IoT) is the greatest essential and noteworthy component of maximum smart urban implementation that is capable of generating large amounts of data [9]. IoT devices, including cameras and other sensors, are scattered across many smart city applications to gather information about the surrounding atmosphere. These devices are often little and have a low battery lifespan, and hence, they cannot

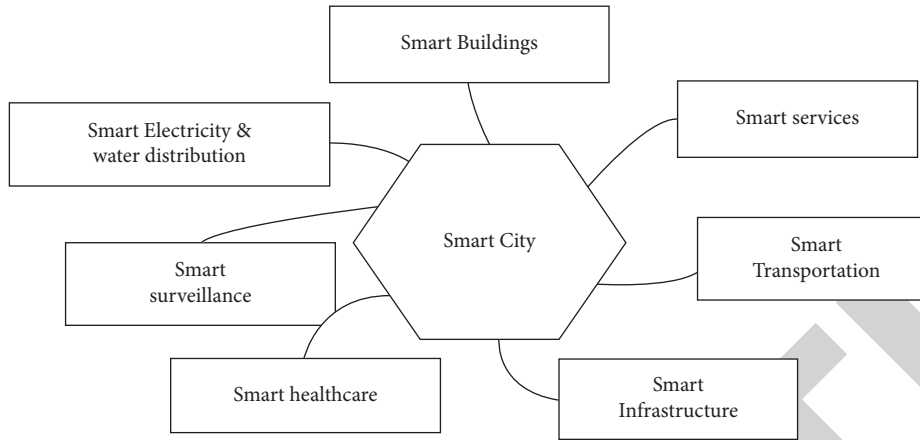


FIGURE 1: Smart city's various services.

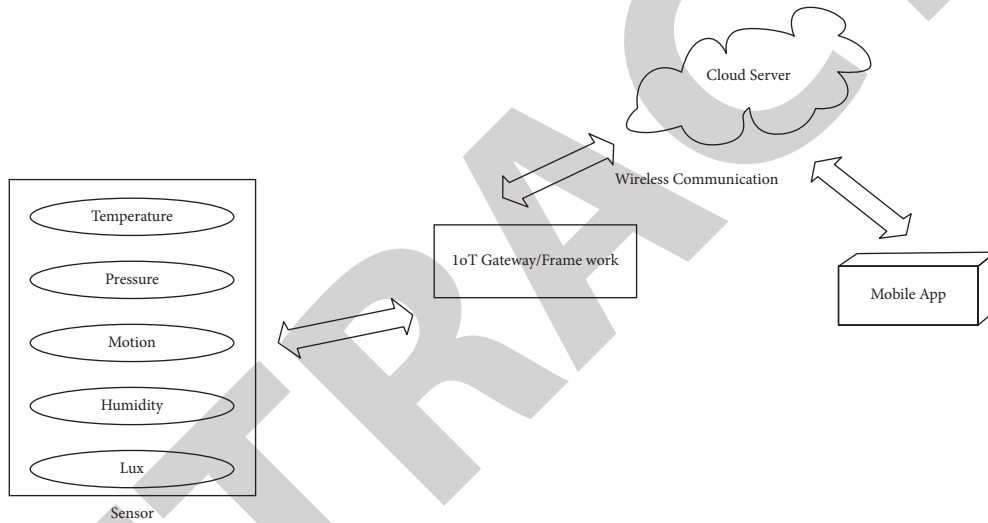


FIGURE 2: IoT structural design.

transfer signals over long distances. As a result, drones are essential for energy savings, and QoS is maintained to collect information from IoT devices installed in a wide range of applications [10]. Because IoT-based techniques have been extensively employed in smart cities, whereby vast volumes of information are created and sent, it is challenging to properly comprehend the information from a complicated world and deliver efficient operational measures in response. The artificial neural network is a potentially developing method that takes a long-term objective into deliberation and provides the greatest system mechanism for time-variant system dynamics. Figure 3 shows the Internet of Things application in various fields.

Among such large and complex pieces of information, it is difficult to accurately select the most efficient and accurate functions. To achieve optimal judgment, modern approaches, including machine learning, artificial intelligence, and deep reinforcement learning, can be used to make highly relevant evaluations of massive data. Previous strategies take into account the need for full-time targeting and lead to better or closer control options. The accuracy and reliability

of the above procedures could be additionally improved by raising the quantity of training data used to improve their learning skills, and consequently, the ability to make their own decisions [11]. The artificial neural network approach is more effective and precise for predicting the drone signal strength based on drone altitude, path losses, and many other related features that have been described. The effect of ANN on human everyday lives is growing with each day. The basis of daily human employment is fast changing in response to ANN, which is influencing the conventional perspective on human thought and responses to the environment. How could new legislation be drafted to guard the present and coming generations from the harmful consequence of ANN, although maximizing its helpful consequences to humanity? Moreover, how can AI-assisted instructions and rules be considered to promise economic and social development? The study has developed an effective criminality detection approach for a smart urban area based on neural networks. Likewise, the study presented a machine learning-based framework that may be utilized to forecast incidents and provide responses prior to their

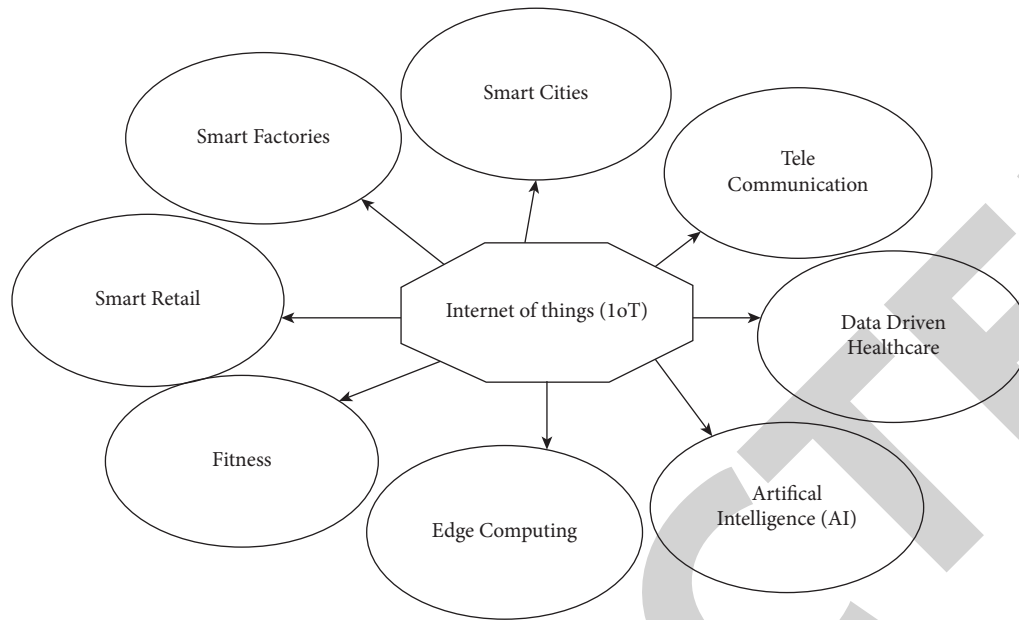


FIGURE 3: Application of IoT in various field.

occurrence [12]. Figure 4 depicts the working arrangement of an artificial neural network (ANN).

The potential benefits of ANN for urban areas are still deliberated in the literature, especially in the setting of urban cities, which are facilitated by strategies for delivering community, technology, productivity, improvement, livelihoods, sustainability, well-being, convenience, effective management, and planning. Although there are a number of papers on the subject, no scholarly book exists that gives a complete evaluation of the expanding literature. This study analyzes the literature to explore how ANN can help build urban cities. This study uses a complete literature review on the issue of “ANN and Smart City” as its methodological technique. ANN is an excellent tool for managing and analyzing a wide range of data to facilitate business choices. It is especially true when combined with IoT, which is an internet-based technology that enables a wide range of sensors to communicate in a network without human involvement. Using technologies, including blockchain, fog computing, and cloud storage, AI has the ability to capture, store, and distribute data, automating the data management process and eliminating demand intermediaries, thereby maximizing profits. Moreover, AI can expand the constancy and performance of IoT devices, resulting in better network connectivity. As a result, information exchange will increase and innovation and entrepreneurship will be encouraged [13]. ANN can be used to identify patterns in databases, improve the information management process, enhance the complete performance of the information managing system, and recognize cyber-attacks and other inefficiencies. The use of ANN is feasibility to do away with the necessity for people to repeatedly engage in commercial activities, mainly trusting on care, decreasing

potential costs, and releasing capital to the most creative or advanced industries [14].

## 2. Related Works

The incredible technical advancements of the twenty-first century have brought a plethora of intriguing and practical answers to nearly any issue imaginable by man. Investigators have been driven to the IoT technology in current years because its trends have shown to make people’s lives easier, cities smarter, and the planet a good residence for living. Nevertheless, technological advancement necessitates a large amount of energy, as well as the development of massive amounts of e-waste and toxic pollutants. The study examined the approaches and tactics that can increase life performance and make the world better, greener, more sustainable, and safer to reside in. The study particularly emphasized green IoT as a means of establishing a smart and sustainable environment via effective resource usage, reduced energy consumption, reduced pollution, and waste creation. This study is an excellent resource for anybody interested in learning about the most recent trends on the subject of green IoT. The study also showed the enabling ICT resources (WSN, RFID, M2M, communicating network, and internet) that have significantly improved the capabilities for green IoT. Concerning the significant elements of ICT, all objects nearby people will be cleverer to accomplish any activities individually, enabling different kinds of green contacts among objects and humans, as well as amongst the objects themselves, whereby the bandwidth consumption is the most, harmful pollution is minimized, and energy demand is ideally lowered. Another aspect of this study in which researchers highlighted the critical utilization of green IoT for the modern and green world was a study of the

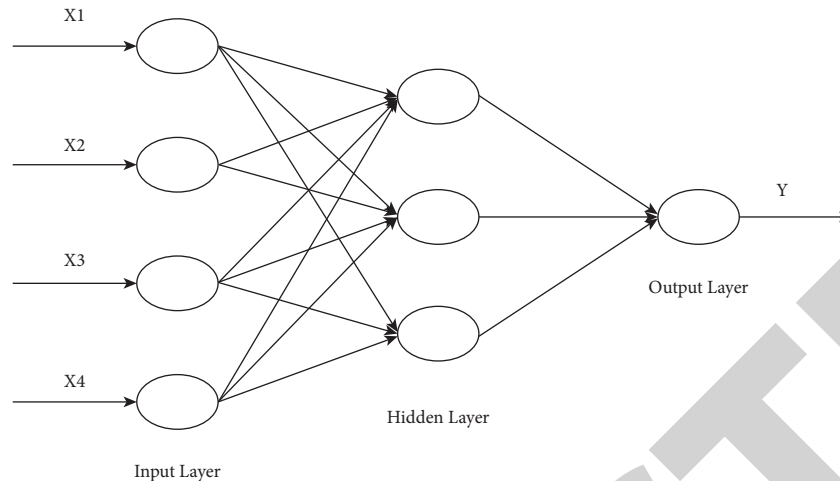


FIGURE 4: The arrangement of artificial neural network approach.

various diverse fields of green IoT in multiple industries. The study also outlines the obstacles and potential upcoming research areas in the route of green IoT development for a smarter and greener environment. The research focused on developing green IoT and creating cities better through the use of smart systems for power effectiveness. Yet, the integration of drones and IoT devices in this research has not been realized to its maximum potential [15].

Because of great flexibility and cheap cost, unmanned drones now play an essential part in a wide range of applications. One of the most important tasks in achieving dependable UAV connectivity is to examine the propagation properties of the channel. In this research, the study offers machine learning-based route loss models for the UAV air-to-air (AA) case. A ray-tracing program is used to create specimens for several paths in a common urban setting, and variable Tx and Rx UAV heights are properly considered. On the basis of the training phase, two machine-learning techniques, namely random forest and KNN, are used to develop a predictive model. The estimated accuracy of trained models is evaluated on the testing dataset using metrics, including root mean square error and mean absolute error. Simultaneously, two estimation techniques for evaluation are offered. It is demonstrated that machine learning-based systems may deliver good predictive performance while maintaining appropriate computing performance in the AA situation. Furthermore, random forest beats all other systems and has the lowest error rates. Additional research is being conducted to assess the effects of five distinct factors on route loss. It is shown that route accessibility is critical for path loss. The outcomes revealed that route accessibility is the most important factor. Propagation distances and altitude have also had a significant impact. Because UAV AA communications is a new dynamic, channel modeling and route loss estimation in such a situation are still in their early stages. Several machine learning-based models, such as ANN and SVR, should be introduced in ongoing growth. Special techniques should also be considered to validate the generalization characteristics of these systems. Lastly, assessment studies in the

AA case should be performed. Further data is predicted to increase the effectiveness and affordability of machine learning-based route loss predictions [16].

Drones in flight may be utilized for a variety of purposes and services, ranging from monitoring to package transportation. Cellular systems must offer dependable wireless access to drone user devices to guarantee the strong performance and safety of drone operations. Currently, they are developing mobile networks that have been mainly created and improved for supplying ground user equipment, producing flexibility, and resolving cloud trouble. In this study, a novel handover method for a cellular connecting drone system is designed to support strong wireless capabilities and mobility support for drone-UEs. HO choices are continuously improved using a Q-learning algorithm, employing methods from reinforcement learning, to deliver effective flexibility and scalability in the sky. The research demonstrated how the network may balance the number of HOs with the acquired signal intensity by altering the weighting of these parameters in the optimization method. The simulated findings show that, as compared to the baseline HO method in which the drone continuously links to the greatest cell, the suggested technique can considerably decrease the number of HOs while retaining a stable connection. Continued studies might go into a number of different areas. To begin, the current architecture only analyzes drone motion in 2D. Allowing 3D drone movement will be a logical expansion. The testing region and flight paths examined in this work are quite small. It will be instructive to see if the results hold true for bigger testing locations and longer flight paths with a broader pool of potential cells. The suggested method and simulation results depend on the RSRP measure. Another noteworthy involvement will be the addition of new variables to the model [17].

With an explosive increase of multiple drone operations ranging from infrastructure observation to package delivery options, integrating UAS with smart city transportation networks has become a true challenge that necessitates completely innovative and maintainable (secure, safe, with minimal ecological power and lifespan cost) strategies. The

fundamental goal of this suggested alternative is to define paths as desirable and ordered trajectories and execute them autonomously. The worldwide GPS common set with accompanying GIS mapping provides the airspace structure and fixed paths. The idea implementation necessitates additional research and answers, such as drone trajectories monitoring, via an autonomous trajectory tracking control scheme and autonomous conflict identification, resolution, safe drone following, and formation flight choices. The study presents such hypothetical designs and provides some validation testing results. Drones will be linked to the agencies and a planned trajectory to provide them with accurate data on the trajectory and corridor. The agencies will create predetermined or preferred paths using trajectories components. Drones may employ traditional GPS, acoustic, infrared, and optical sensors for locating and sophisticated navigation. The accurateness is achieved by including specific indicators in the infrastructure. The concept of safe drone use in a city environment and the potential for secure integration of drone traffic into the overall intelligent urban transportation system. In fact, the application of this notion necessitates more practically to employ a diverse range of methodologies [18].

Urban areas utilize modern technologies of information and communications to increase the effectiveness of urban services and power efficiency. Drones, in this aspect, may be used to assist multiple services, including traffic analysis, selection/rescue, and monitoring, by connecting with a variety of smart items, including sensors. Protecting such interactions is essential in making sound judgments, and it necessitates the use of effective cryptographic techniques. Moreover, the development of these protocols should take into account the flexibility and short battery life of drones and the restricted resource of smart devices. This study presents a set of cryptography algorithms for dealing with 3 different transmission schemes, such as one-to-many, one-to-one, and many-to-one. Researchers develop an efficient certificateless signcryption tag key encapsulation mechanism (eCLSC-TKEM) for one-to-one encryption that provides a verified key exchange protocol, nonrepudiation, and user revocation. By decreasing the computational cost of the smart object, eCLSC-TKEM decreases the time necessary to create public keys between a drone and a smarter object. The study presents a certificateless multi-recipient encryption method for one-to-many communication that permits a drone to effectively produce sensitive data to several smart devices. The study offers a certificateless data aggregation mechanism for many-to-one, which enables drones to quickly gather information from hundreds of smart things. In addition, for effectiveness, the study presents a dual channeling mechanism that enables several smart objects to perform this protocol at the same time. eCLSC-TKEM is evaluated using parking guidance managing testing. It also demonstrated the GPU-accelerated effectiveness of CL-MRES and CLDA on a board with a graphics-processing section. To perform properly, this approach necessitates application improvements and specialized client-server apps [19].

The present biometric systems in most drone-based apps suffer from real-time lag difficulties and security weaknesses for attackers. To solve such difficulties, the study proposes a

low-latency safe security mechanism for drones in Smart Urban based on the blockchain. The research utilizes a zone-based design in drones' networks and a customized decentralized consensus termed as drone-based delegation proof of stake for drones between areas in a modern city, which does not need reauthentication. The suggested architecture intends to improve safety and minimize latencies on the Internet of Drones. Furthermore, the study compares the system framework to existing peer models initially done for IoD to establish its reliability and scalability authentication capacity. The testing findings clearly indicate that, compared to the existing pattern, the suggested architecture not only has a small packet delay, maximum throughput, and low end-to-end delay but also could identify 97.5 percent of hostile drone assaults while flying [20].

### 2.1. The Mechanism for Signal Propagation between Drones and IoT Systems.

A drone is operated and kept flying in a certain direction. It receives data from operators on the surface who monitor the drones as they go. They recognize individual objects and assist drones in reaching precise positions using signal power. Multiple processes affect the traveling signals in distance. The analysis of signal strength is perhaps the most significant aspect of transmission. Such events have an impact on the signal intensity amongst drones, agents, or IoT systems on the surface. As a result, the signal would achieve the target very weakly [21]. As a result, when constructing the transmission and receiver, certain occurrences must be factored into the equation. The signal intensity is affected by the drone's altitude, length, and route losses. The signal route losses occur as a result of the information taking a multipath and arriving at varying times. The signals route losses vary depending on the influence of the environment. Because of a major towering building in a city, the transmission distance is extremely high [22]. Furthermore, it is minor in the suburbs and even smaller in rural areas. Reflections, refraction, and dispersion, as well as transmission weakening, are all the effects of the surroundings. Whenever a propagated signal collides with a large-scale object, it is called reflection. Whenever a propagated signal channel is interrupted by a sharp object between the transmission and reception, the transition occurs.

The application of drones aiding IoT devices is depicted in Figure 5. When a propagating signal deviates from such a direct route, scattering occurs. As a result, the scattered signals are caused by a curved surface and a small thing. The effective communication among drones and surface operators or IoT systems and the base center units is determined by characteristics, including radiation intensity and signal power [23]. The signal strength and radiation strength are affected by the covering community and surrounding environment. The possibility of covering and the total rates for various IoT devices are delivered by drones. Additionally, installing drones improves wireless transmission availability. A stable channel among the drone and ground-based facilities is required for every drone-based service to be effective [24]. As a result, the drone is among the aerial robots that have piqued people's curiosity for a range of smart cities.

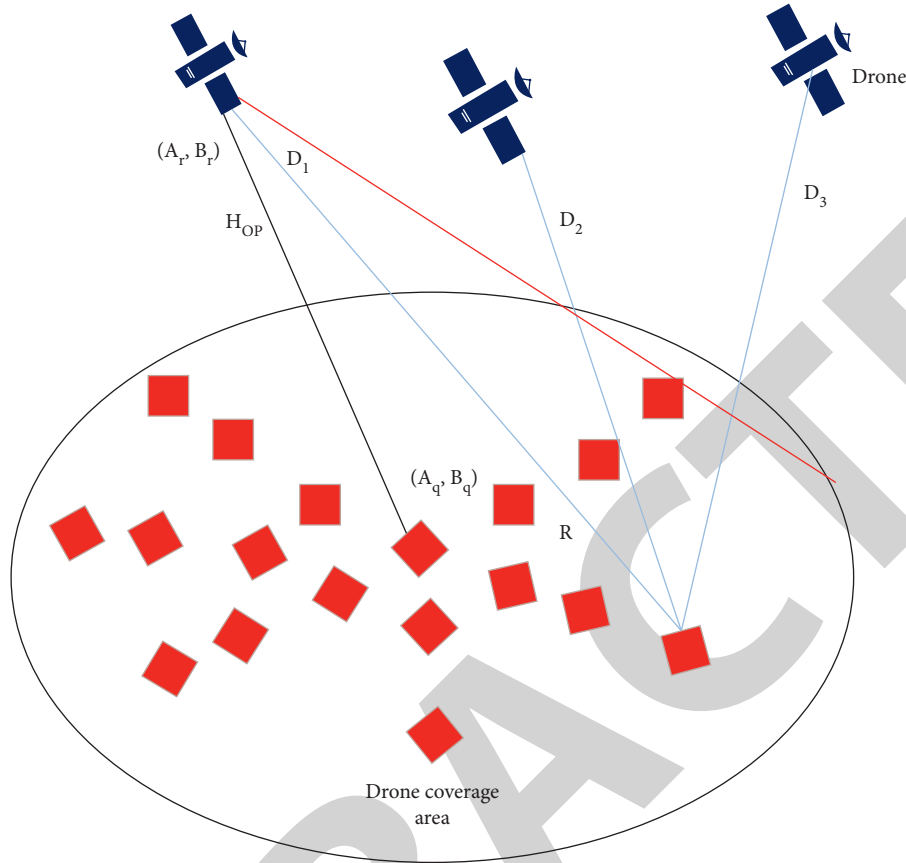


FIGURE 5: Drone into IoT application.

It is not simply a plane in the sky. It is a computer with a network infrastructure that includes a space component, a ground segment, and a communications system that connects both.

**2.2. Signal Strength.** To preserve signal strength at the receivers, the signal strength between the access point and smartphone should be greater than the significance level. Similarly, the signal strength should not be too great since it will generate a cochannel interfering with some other smartphone channels that use the same frequencies. The intensity of the transmitted power is affected by route losses, as well as transmission and reception settings. The strength of the received data determines the level of the call. The signal strength is affected by external factors and median degradation [25]. On the one side, essential propagation models show that the total RSS strength drops nonlinearly as transmission distance. Path loss, on the other hand, refers to how much signal intensity is lost throughout transmission from the transmitter and the receiver. The propagation model suggests the average RSS for transmission and receiver based on detachment spacing and the variance of signal strength in a specified place. They seem to be suitable for determining the transmitter network coverage of a transmitter and characterizing signal strength more than a significant disconnection distance between transmission and

receiver. Signal distortion and route loss can be predicted using propagation algorithms. The propagation path losses that are generated across all losses faced by the signals throughout their transmission from the base station (BS) towers to the smartphone network or mobile station (MS) are critical restricting elements in coverage estimation [26]. The knowledge of path loss could be utilized to control system efficiency or coverage. The Hata option is designed to anticipate the propagation characteristics by investigating and analyzing the HAP propagation path. The Hata concept is a path loss that is based on empirical data.

$$l_p(b^d)X + Y\log(d_i). \quad (1)$$

Here,  $d_i$  is the distance in kilometers and  $X$  is the constant loss, which is determined by the frequencies  $f_r$  in megahertz, and therefore, it is given in equations (2) and (3).

$$X = 70.62 + 18.25 \log(f_r) - 14.71 \log(b_h) - x(m_h), \quad (2)$$

$$Y = 51.8 - 5.42 \log(b_h). \quad (3)$$

The altitude of the ground station antennas in meters is given by  $b_h$ . The elevation of a wireless station antenna in meters is measured in  $hm$ . In Bdm,  $x(m_h)$  is the association coefficient, which is provided in the following:



$$x(m_h) = [2.1 \log(f_r) - 1.8]m_h - [1.43 \log(f_r) - 0.7]. \quad (4)$$

QoS is a term that describes how well a system performs, and it is used to assign a set of characteristics that represent measurable qualitative characteristics. Path loss is an important factor in improving wireless communication's QoS.

Signal strength out of a drone at various ranges: in the first case, the drone position is given. Use the ANN model for forecasting signal strength out from the drone distribution point. Based on a fixed drone placement, the ideal coverage area should be determined along with the manner in which IoT sensors attached to the drone while maintaining excellent QoS should be maintained. IoT devices' communication power would be lowered as a result.

The drone's height is considered to remain constant in this case, and the transmitted signal from the drone is calculated depending on the distance between the drone and the floor IoT devices [27]. The approach is depicted in Figure 6. These forecasts were important for calculating a drone's range and the number of drones necessary to keep maximum coverage and ensure QoS in a particular geographical region.

**2.3. Drone Coverage and Movement.** Among a drone's constraints are its operating height. Signal strength is important for determining the appropriate height for a drone's flight route, and IoT devices seem to be more approachable throughout this area. The drone should span every IoT device in the approach and interact through a significant relation to collect information from each IoT system. In the specific application, information obtained from IoT devices reveals a covering challenge [28]. The positioning of the drones has an impact on the connection link between the drone and the IoT devices within a specific application, and the connectedness has an impact on system performance. Drone movement patterns are thus an important piece of technology for enhancing network connections and coverage within approaches [29]. The angular, tractor, circular, and square movement patterns have been identified. In analyzing connection speeds, the tradeoff between flying drone patterns and processing times must be taken into account. By reducing the total of unavailable devices connected to the network, the drone's movement pattern could increase the coverage. As a result, better drone movement could be obtained if an appropriate place is determined, which is one of the goals of the work. Because of the drones' low - power consumption, they must conduct movement and communications efficiently. As a result, drones must autonomously alter their locations to achieve the desired connection speed for IoT systems while conserving energy. It links to the BS having strong signal strength using a deep learning algorithm that reduces the number of handoffs with such a modest degradation of signal strength. Movement maintenance, on the other hand, is not taken into account since it does not handle BS, numerous drones, or phone devices. The drones could receive data from IoT devices and cover various possible applications from such a fixed-known route to regulate the drone altitude. Drone movement and

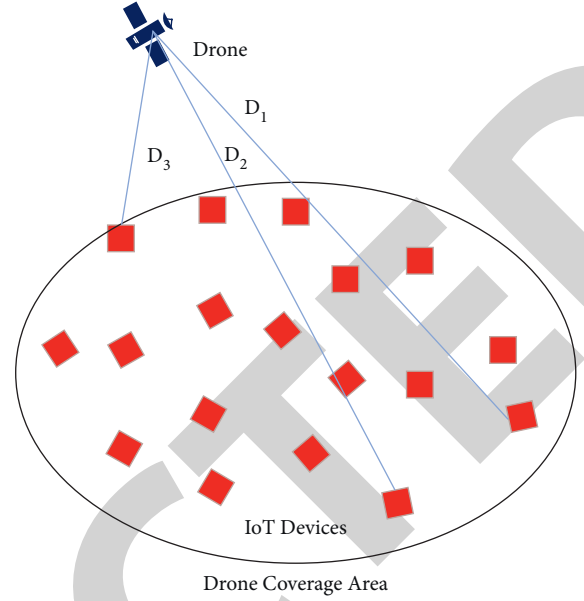


FIGURE 6: Signal quality at various distances.

position could be modified, allowing the drone to advance toward that IoT framework and obtain sustainable power conservation when connecting [30]. The major goal is to assist effective drone movement by ensuring the good QoS performance of IoT systems in the framework and increasing the signal strength of the drones.

$$md_A = d_i 10 \left[ \frac{ss_r[d_i] - ss_r[md_A]}{10^*} \right], \quad (5)$$

here  $ss_r$  is at a reference distance of  $d_i$ .  $md_A$  denotes the actual distance in between drones' location and the IoT devices, and it is the path coefficient. The ideal height  $O^h$  for the drones ranges from  $\min_h$  to  $\max_h$ , as shown in the following:

$$O^h = a_{h \in \min_h, \max_h} \min \left[ \sqrt{\sum_{t=1}^T |d_{it}^2 - h^2 - r|^2} \right], \quad (6)$$

here  $d_p$  is the distances between the drones at positions  $(An; Bn)$  on trajectories  $T$  and the standard IoT device  $(Am; Bm)$  in the approaches, as determined by signal strength. The distance between the drone and  $L$  IoT devices at trajectories location  $(An; Bn)$  is provided as follows:

$$r = \sqrt{d_{imx}^2 + O^{h2}}, \quad (7)$$

$d_{imx}$  is the distance between the drones location at  $T$  trajectories point  $(An; Bn)$  and the IoT devices in the application region.

The received signal intensity is dynamically upgraded with different drone positions, and ANN is used to forecast drone movement. The illustrations of drones flying at different ranges are shown in Figure 7. The ideal transmission range of the drones from various heights could be predicted

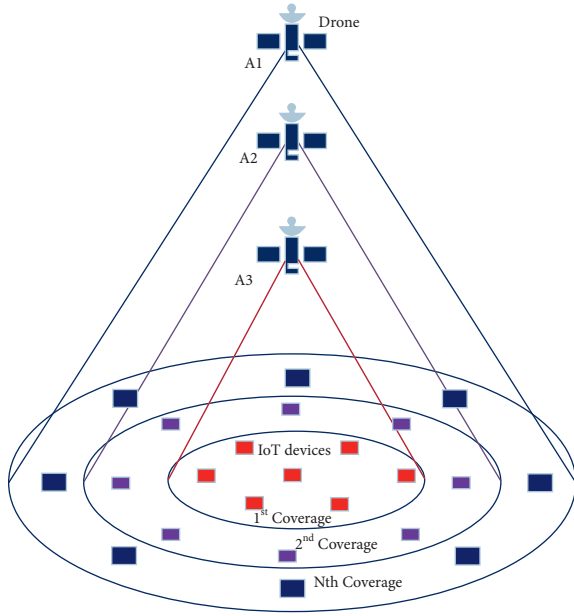


FIGURE 7: Strength of signal in various heights.

in this scenario of predicting signal strength at various positions.

### 3. Proposed Methodology

Drones are flying electronics that fly through the air. It really has sparked a strong interest for usage in various situations. Drones are important in wireless transmission in a variety of transitory situations, including disasters, transportation, sales, emergency surveillance, vehicle tracking, and athletics. As a result, drones could indeed intelligently carry out tasks in a variety of fields to benefit society, market, and administration, such as greater resolution picture quality, lower costs, faster response, the ability to fly in almost any situation, the ability to be nearer to areas of monotonous study, and for use in dangerous activities. The signal strength must be estimated to use an accurate approach to enhance transmitting and receiving architecture. An ANN is presented for anticipating the precise signal from various altitudes and distances.

$$b_{p1}(n) = [b_p(n) \dots b_{p20}(n)]. \quad (8)$$

All that should be initialized in equation is as follows: (8) the center value  $c_v(0)$ , the span value  $s_v sv(0)$ , the weight vector  $b_p(0)$ , and the expectation  $b11(0) = b21(0)$ .

The formulas used to calculate the hidden layer output, output, and error in equations (9) and (10) are as follows:

$$S_p = r \left[ \sum_{x=1}^L b_{py(n)A_y} \right], \quad p = 1, 2; L = 20, \quad (9)$$

$$u_p = d_p - S_p, \quad (10)$$

here  $d_p \in [0, 1]$  is the required layout, and the weights are updated as follows 11:

$$b_{py}(n+1) = b_{py}(n) - \alpha_b u_p A_y. \quad (11)$$

Update the center and span momentum, where  $\alpha_b$  indicates the weight and  $\alpha_c$  indicates the centre learning rates, respectively, in equations (12) and (13).

$$cv_{xy}(n+1) = cv_{xy}(n) + \alpha_c \frac{A_y}{sv} (a_x - cv_{xy}(n)) \sum u_p b_{py}(n), \quad (12)$$

$$sv(n+1) = sv(n) - \frac{2\alpha_{sv} A_y}{sv(n)} \ln A_y \sum u_p b_{py}(n). \quad (13)$$

The data needed to create an appreciative drone communications system will be processed by ANN. The goal of the ANN approach is to quickly and successfully manage the link between drones, IoT devices, grounded robotics, and users. ANN is made of a number of neurons that are organized in a specific way, as seen in Figure 8. Distance ( $d_i$ ), height ( $a_h$ ), frequencies ( $f_r$ ), and path loss are among the inputs ( $l_p$ ). The buried layer's total is equal to the outputs. The outputs determine and evaluates the signal strength appreciation (S).

The input layer only serves as an entrance point for the input signal. It does not do any analysis. The hidden layer is composed of many Gaussian functions that act as random finite elements, allowing the input sequence to be expanded over the hidden layer region. It is a nonlinear transition from the input vector to the hidden state region. The output layer produces an output sequence by linearly combining the hidden layer outputs.

The following is how the ANN learning method operates: mostly on terminals linking the input layer and the hidden layer, the neural network is initialized with appropriate initialization. The initial set of input variables is then sent to the ANN. It processes the data and provides an outcome. Backpropagation is used to transmit the error between the generated output and the support vectors backwards further into system, and the weights are changed to reduce the error. The function is conducted repeatedly for every one of the training instances, and the final weights are saved as a guideline for sustainable forecasts on unknown data. The MSE, RMSE, and coefficient determination (R2) parameters are common error measurements for neural network learning tasks. It should be noted that such a method of utilizing the ANN for prediction problems linked to wireless communication technology was already demonstrated to be successful. In a prior study, the findings indicated that utilizing ANN to forecast transfer between the earthly communications network and HAP had been the most effective method for making an appropriate choice regarding RSS. The data based on the Hata parameter estimation are generated for the training and evaluation of the proposed ANN model enabling signal strength forecasting. The metrics of distance, frequency, path loss (PL), and RSS and spaces are calculated, which are presented as inputs to the ANN throughout training and

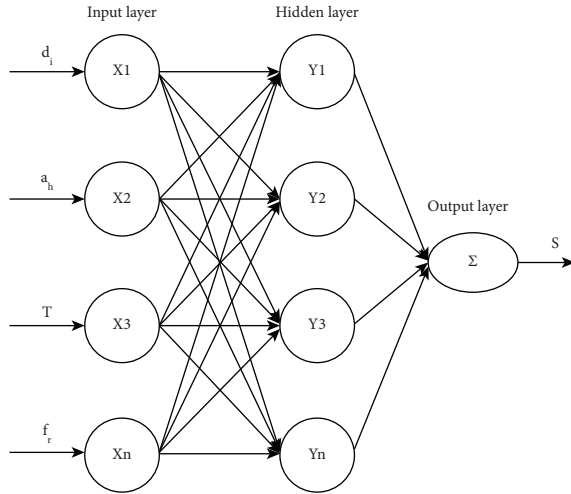


FIGURE 8: Prediction with ANN.

validation. Following ANN's output of a signal strength rating depending on the input model parameters, that value is then compared with the RSS frequency for determining error metrics and weight modification utilizing back-propagation techniques.

The whole ANN training, calibrating, verification, and installation work-flow, as well as the necessary data pre-processing stages, are depicted in Figure 9. In the first phase, the proposed method is initialized and information is preprocessed, after which all variables are combined. The ANN network is adjusted for the set of input layer neurons, hidden unit nodes, and training algorithm, and standard weighting are initialized. ANN is trained in the calibrating phase by analyzing the input variables and intended output (signal strength). The method is considered the final model once error parameters are minimized. The mean square error (MSE), root means square error (RMSE), and coefficient determination ( $R^2$ ) measures are used in the evaluation of training models.

**3.1. Evaluation of Performance.** The trained ANN model on the generated dataset and measuring the inaccuracy in the estimates provided an early evaluation of the suggested technique's effectiveness. The three main parameters had been used to calculate the standard errors: MSE, RMSE, and  $R^2$ . MSE stands for mean square error, and a number around 0 indicates a high-performing algorithm equation (14). The root-mean-square error (RMSE) is defined as the square root of the sample mean instant of the distinctions among simulated and experimental numbers, or the quadratic mean among those variations, with numbers near zero indicating a viable system equation (15). The determination coefficient ( $R^2$ ) is a measurable statistic of the data's resemblance to the linear regression line. The  $R^2$  score ranges from 0 to 1, with 0 indicating that such analysis includes minimal variance in the data and 1 indicating that its prediction is flawless.  $R^2$  values that are nearer to zero are clearly preferable to equation (16).

$$\text{Means square Error} = \frac{1}{a} \sum_{x=1}^a (B_x - A_x)^2, \quad (14)$$

$$\text{Root Mean squared error} = \sqrt{\frac{1}{a} \sum_{x=1}^a (B_x - A_x)^2}, \quad (15)$$

$$\text{Rgression metrics} = 1 - \frac{\sum_{x=1}^a (B_x - (1/n) \sum_{x=1}^a A_x)^2}{\sum_{x=1}^a (B_x - A_x)^2}. \quad (16)$$

After the model's primary measuring performance on gathered information, it must have been assessed once more with noisy data applied to the entire data. It was performed to verify that the theory was strong enough to be used in specific circumstances.

#### 4. Result and Discussion

The effectiveness of the suggested ANN approach for signal strength forecasting is evaluated throughout this article. The algorithm has been trained and finished according to the flowchart, and it is being used to make RSS estimations. Because many real-world data that would be fed into the algorithm following implementation would have been unclear, it was thought necessary to assess the model's stability in the presence of imbalanced datasets. The author starts with a collection of IoT systems in well-known possible applications in a smart city and then assumes that such a drone will be in a specific spot to the application region's IoT systems. The drone's flight speed is ignored as well as the time it takes to get there in this situation. The suggested ANN could accurately forecast signal strength, including all IoT systems in various areas and altitudes from the drones with minimal computing performance, according to the findings. The ANN is trained for 100 rounds offline. The suggested method's assessment measures MSE, RMSE, and  $R$  are computed. In the other instance, a collection of IoT gadgets is attached to a drone, which moves through a series of places. The MSE, RMSE, and  $R$  evaluation metrics are calculated for the suggested approach once more. When drones are put at a high elevation, they can accommodate a greater number of IoT devices, however, every IoT system must use more capabilities to achieve adequate signal strength for communications with the drones. As a result, it is essentially a tradeoff between the variety of devices a drones could operate and the energy requirements of specific IoT devices. If the drone's location is specified, it is simple to calculate how many IoT system may be used to receive the signal strength throughout this circumstance. For information collection through IoT devices, ANN is used to anticipate drone movements in trajectories based on signal strength based on movement drones. Based on the prior signal strength, the next point in the path could be anticipated. As a result, the following IoT devices inside the drone's path could be prepared to relay collected information to the drone whenever the drone is within the range

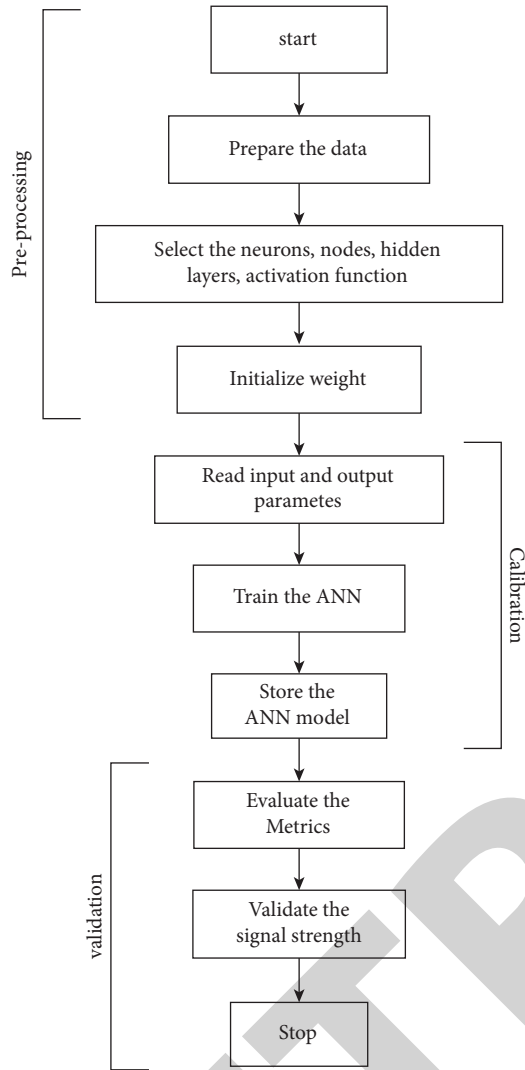


FIGURE 9: Flowchart proposed ANN process.

TABLE 1: Calculation of proposed method measurements.

Method	Mean squared error	Root-MSE	Regression
Various altitude	13.52	2.68	0.97
Various length	1.72	1.24	0.98

of the device. As a result, every IoT system would save a considerable amount of energy by not having to keep its wireless connection on most of the times.

For the training and testing sets, the analytical measures of MSE, RMSE, and R2 are performed to analyze the strongest ANN technique for estimating signal intensity distribution compared to the input variables. The outcomes of the suggested ANN method are shown in Table 1. They include various error measurement numbers. In terms of ANN predictive performance, the R2 values of 0.97 and 0.98 were obtained in the case of various height and distance circumstances, correspondingly. Figure 10 depicts the graphical representation on ANN metrics. In numerous scenarios, the total R2 values reveal that such levels are

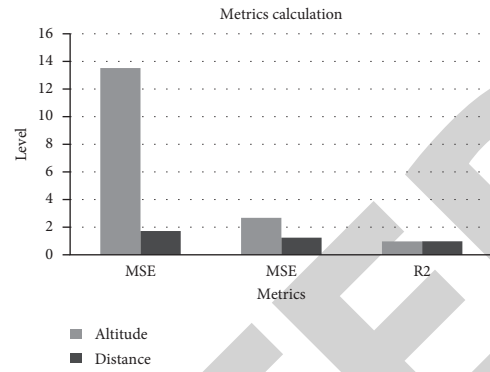


FIGURE 10: Graphical representation of ANN measurements.

significant enough to enable highly accurate results of the ideal signal traveling from the drones to a gadget in smart city environments. The projected quantities have also been evaluated with their ground-truth equivalents, yielding a median percentage of error of 1.10% across all projections. Finally, the amount of time required for the system to generate one prediction was assessed, and the algorithm was capable of doing it in 11 milliseconds. Such a prediction speed was determined on a desktop computer with average specs, and hardware implementations will undoubtedly be much quicker.

When the drone has been regarded stable at various distances, ANN estimated the signal strength from the drone once again. The drone was placed in a particular place, sample was gathered for various ranges to the IoT device, and then an artificial neural network (ANN) was used to forecast the connection depending on signal strength at various distances. The ANN projections for signal strength were found to agree with the observed data output. Moreover, uncertainty was applied to the input data, and assessments are performed to determine the reliability of the suggested ANN for implementation in real-world applications. The signal strength forecast is caused by the movement of drones at various heights across ground-based IoT systems. The effectiveness of the ANN model was assessed using the assessment measures MSE, RMSE, and R2. The maximum level of the regression model ( $R2 = 0.98$ ) indicates that the proposed approach has a greater accuracy. Real-time drone trajectory adjustments help to improve connection reliability and deliver higher QoS for the drone network coverage. The flying-path is found to alter in response to the signal strength. ANN accurately predicts the drone's position for a particular signal strength parameter, and it could also anticipate the next position derived from the previous one. As a result, the ability to forecast drone flight paths and identify drone network coverage can help meet the need to sustain performance.

While it may seem that including the path loss in the learning algorithm for the suggested ANN is unnecessary because all of the parameters around which it is reliant are indeed taken into account as independent features in the training phase, it was meant to give the ANN layout for such an implementation to the succeeding flexibility. In this

scenario, the numbers are actually influenced by certain factors, such as  $d_i$  and  $f_r$ . It might not be the case for many other path loss approaches, which could be reliant on variables that were not included in the ANN model. It is especially relevant for nondeterministic systems. With the current growth in research efforts to achieve the highest accuracy machine learning algorithm for route loss, the paper's suggested technique is more relevant.

## 5. Conclusion

Artificial intelligence (AI) combined with the connectivity of drones and the Internet of Things (IoT) may there be major interaction and complicated solutions to today's issues.

- (i) As a result, it is seen as a miniature of IoT, and it is already starting to effectively replace linked devices at fixed locations. IoT devices are not capable of sending information across great distances. Furthermore, combining drones and IoT devices would provide a resolution to today's issues.
- (ii) Fast (real-time) and accurate calculation of the RSS from the drones at the base stations is required for effectively operating drones beyond a wide geographical region with a multitude of nodes. The signal strength is forecasted efficiently and accurately depending on height, loss rate, and distance utilizing ANN.
- (iii) The use of artificial neural networks (ANNs) is critical in the training of large amounts of data in a short amount of time. It also makes accurate predictions and recognizes decisions. The MSE, RMSE, and R-squared measurements were used to assess the suggested technique's effectiveness.
- (iv) At a variety of heights and distances, the ANN-based signal strength method produces accurate forecasts with RMSE values of 2.68 percent and 1.24 percent, respectively. The acquired results demonstrated that the suggested ANN may be used in a real-world IoT scenario to predict an RSS from a drone.

## Data Availability

The data used to support the findings of this study are included within the article. Further data or information is available from the corresponding author upon request.

## Conflicts of Interest

The authors declare that there are no conflicts of interest regarding the publication of this paper.

## Acknowledgments

The authors appreciate the supports from Mizan Tepi University, Ethiopia, for the research and preparation of the manuscript. The authors thank Prince Sattam bin Abdulaziz

University for providing assistance to complete this work. This research work is not funded by any organization.

## References

- [1] M. Alzenad, A. El-Keyi, and H. Yanikomeroglu, "3-D placement of an unmanned aerial vehicle base station for maximum coverage of users with different QoS requirements," *IEEE Wirel. Commun. Lett.*, vol. 7, no. 1, pp. 38–41, 2017.
- [2] M. Mozaffari, W. Saad, M. Bennis, and M. Debbah, "Mobile unmanned aerial vehicles (UAVs) for energy-efficient Internet of Things communications," *IEEE Transactions on Wireless Communications*, vol. 16, no. 11, pp. 7574–7589, 2017.
- [3] Y. Mehmood, F. Ahmad, I. Yaqoob, A. Adnane, M. Imran, and S. Guizani, "Internet-of-things-based smart cities: recent advances and challenges," *IEEE Communications Magazine*, vol. 55, no. 9, pp. 16–24, 2017.
- [4] Q. Wu and R. Zhang, "Common throughput maximization in UAV-enabled OFDMA systems with delay consideration," *IEEE Transactions on Communications*, vol. 66, no. 12, pp. 6614–6627, 2018.
- [5] R. Petrolo, V. Loscri, and N. Mitton, "Towards a smart city based on cloud of things, a survey on the smart city vision and paradigms," *Trans. Emerg. Telecommun. Technol.*, vol. 28, no. 1, p. e2931, 2017.
- [6] Y. Liu, C. Yang, L. Jiang, S. Xie, and Y. Zhang, "Intelligent edge computing for IoT-based energy management in smart cities," *IEEE Netw.*, vol. 33, no. 2, pp. 111–117, 2019.
- [7] X. Sun and N. Ansari, "EdgeIoT: mobile edge computing for the internet of things," *IEEE Communications Magazine*, vol. 54, no. 12, pp. 22–29, 2016.
- [8] R. Arbolino, L. De Simone, F. Carlucci, T. Yigitcanlar, and G. Ioppolo, "Towards a sustainable industrial ecology: implementation of a novel approach in the performance evaluation of Italian regions," *Journal of Cleaner Production*, vol. 178, no. 3, pp. 220–236, 2018.
- [9] F. M. Al-Turjman, "Information-centric sensor networks for cognitive IoT: an overview," *Annales des Telecommunications*, vol. 72, no. 1, pp. 3–18, 2017.
- [10] Z. Dawy, W. Saad, A. Ghosh, J. G. Andrews, and E. Yaacoub, "Toward massive machine type cellular communications," *IEEE Wireless Communications*, vol. 24, no. 1, pp. 120–128, 2016.
- [11] S. D. Ramchurn, P. Vytelingum, A. Rogers, and N. R. Jennings, "Putting the 'smarts' into the smart grid: a grand challenge for artificial intelligence," *Communications of the ACM*, vol. 55, no. 4, pp. 86–97, 2012.
- [12] S. Chackravathy, S. Schmitt, and L. Yang, "Intelligent Crime Anomaly Detection in Smart Cities Using Deep Learning," in *Proceedings of the 2018 IEEE 4th International Conference on Collaboration and Internet Computing (CIC)*, pp. 399–404, Philadelphia, PA, USA, October 2018.
- [13] M. Chen, Y. Miao, X. Jian, X. Wang, and I. Humar, "Cognitive-LPWAN: towards intelligent wireless services in hybrid low power wide area networks," *IEEE Trans. Green Commun. Netw.*, vol. 3, no. 2, pp. 409–417, 2018.
- [14] R. H. Hariri, E. M. Fredericks, and K. M. Bowers, "Uncertainty in big data analytics: survey, opportunities, and challenges," *J. Big Data*, vol. 6, no. 1, pp. 1–16, 2019.
- [15] S. H. Alsamhi, O. Ma, M. Ansari, and Q. Meng, "Greening internet of things for greener and smarter cities: a survey and future prospects," *Telecommunication Systems*, vol. 72, no. 4, pp. 609–632, 2019.



## *Retraction*

# **Retracted: Molecular Dynamics Simulation Calculation Method for Elasticity and Plasticity of Metal Nanostructures**

### **Advances in Materials Science and Engineering**

Received 26 December 2023; Accepted 26 December 2023; Published 29 December 2023

Copyright © 2023 Advances in Materials Science and Engineering. This is an open access article distributed under the Creative Commons Attribution License, which permits unrestricted use, distribution, and reproduction in any medium, provided the original work is properly cited.

This article has been retracted by Hindawi, as publisher, following an investigation undertaken by the publisher [1]. This investigation has uncovered evidence of systematic manipulation of the publication and peer-review process. We cannot, therefore, vouch for the reliability or integrity of this article.

Please note that this notice is intended solely to alert readers that the peer-review process of this article has been compromised.

Wiley and Hindawi regret that the usual quality checks did not identify these issues before publication and have since put additional measures in place to safeguard research integrity.

We wish to credit our Research Integrity and Research Publishing teams and anonymous and named external researchers and research integrity experts for contributing to this investigation.

The corresponding author, as the representative of all authors, has been given the opportunity to register their agreement or disagreement to this retraction. We have kept a record of any response received.

### **References**

- [1] K. Zeng and K. Chen, "Molecular Dynamics Simulation Calculation Method for Elasticity and Plasticity of Metal Nanostructures," *Advances in Materials Science and Engineering*, vol. 2022, Article ID 6264256, 11 pages, 2022.



## Research Article

# Molecular Dynamics Simulation Calculation Method for Elasticity and Plasticity of Metal Nanostructures

**Kunrong Zeng**  and **Kaifeng Chen** 

*Department of Basic Science, Jiaozuo University, Jiaozuo 454000, Henan, China*

Correspondence should be addressed to Kunrong Zeng; [zengkunrong@zcmu.edu.cn](mailto:zengkunrong@zcmu.edu.cn)

Received 15 June 2022; Revised 23 July 2022; Accepted 28 July 2022; Published 21 August 2022

Academic Editor: K. Raja

Copyright © 2022 Kunrong Zeng and Kaifeng Chen. This is an open access article distributed under the Creative Commons Attribution License, which permits unrestricted use, distribution, and reproduction in any medium, provided the original work is properly cited.

With the rapid development of nanotechnology, surface plasmon (SP) of metal nanostructures has become one of the research hotspots in the research of information science, physics, biology, materials science, chemistry, and other interdisciplinary fields. Surface plasmon research is an emerging discipline. In this paper, based on the CPU algorithm and the GPU algorithm for the extraction of pressure and single-atom average potential energy, time tests and error analysis of different molecular scales are carried out. The analytical results show that the absolute and relative errors of pressure and single-atom average potential energy extraction increase with the molecular scale. When the molecular scale reaches 100k, the errors of pressure and single-atom average potential energy reach 0.32 and 0.052, respectively. However, compared with the pressure and single-atom average potential energy extracted by the CPU algorithm, the error of the results extracted by the GPU algorithm is only 1.55% and -1.45%.

## 1. Introduction

As early as 1902, the “Wood anomaly” was found in the reflection spectrum of metal gratings. In 1941, anomalous reflections could be explained by electromagnetic wave patterns on the surface of metal grating structures. In 1956, when analyzing the phenomenon of energy loss caused by electrons passing through metallic materials, researchers identified this loss as a so-called plasma. This is due to the collective oscillation of free electrons. In 1957, when electrons passed rapidly through thin metal films, researchers discovered that energy loss occurred not only in the plasma, but also at other frequencies. They predicted the existence of surface plasmons, and experiments in 1959 confirmed these theoretical results. They first proposed the concept of surface plasmons and gave a relationship with dispersion in 1960. The researchers investigated the resonance conditions in this mode. In 1968, two scholars proposed the attenuated total reflection method. The surface plasmon wave is excited by prism coupling, and the resonance of metal surface plasmon is observed.

Surface plasmons (SPs) have attracted much attention in recent years. It has even become a separate discipline: Plasmonics. It has been hundreds of years since it was thought to be the first (1902) experimental observation of the surface plasmon phenomenon, and it has been mathematically predicted that surface waves propagate on metal surfaces with limited electrical conductivity. During this period, due to the limitation of science and technology, this field has not been able to develop very well, until it has developed rapidly with the development of nanophotonics, biomedicine, energy, and other related fields in recent years. In particular, the development of optoelectronic devices is advancing by leaps and bounds. Compared with traditional electronic devices, optoelectronic devices have the characteristics of high precision, low power consumption, and fast propagation speed. With the development of science and technology, the size of optoelectronic devices is getting smaller and smaller, but the size is finally limited to the micro-nano level. This is mainly due to some anomalous phenomena when light transmits through nanometer-sized objects, such as abnormal light transmission, surface

fluorescence enhancement, and surface-enhanced Raman scattering. Surface plasmons are essentially formed by the collective oscillation of free electrons in the conduction band near the Fermi level of the metal surface driven by a specific electromagnetic field, which is a type of electromagnetic surface wave.

The resonance of Fano is due to the interference of dark and light on the surface plasmons in metallic nanostructures. The luminophore of a surface plasmon is a mode with a finite dipole moment that can be activated under the conditions of incident light. Therefore, it is a bright superradiant state with broad spectral lines and large interfaces. The behavior of zero static dipole moment is a sub-emissive state that cannot be directly activated by incident light, and its linewidth is small. Therefore, in the case of high radiation, dark resonances can be activated by bright resonance states to reduce radiation losses. Since the resonance of Fano is highly sensitive to changes in the actual medium environmental index, the resonance of Fano metal nanoparticles has also been extensively studied in designing highly sensitive effective chemical effect indices. Over the past few years, many people have studied Fano resonance. However, it is still a challenge to obtain Fano resonances with narrow linewidth and high spectral contrast at the same time.

## 2. Related Work

In this paper, some techniques are studied based on the molecular dynamics simulation calculation method of elasticity and plasticity of metal nanostructures. It is necessary to fully apply these techniques to research in this field. Reddy AP observed that the addition of nano-sized SiCp particles in an aluminum alloy matrix results in excellent mechanical and physical properties and interfacial properties of nanocomposites [1]. Shtertser et al. stated that metal matrix composites containing nanoscale carbon (nanotubes, graphene, etc.) were of great interest from the perspective of developing materials with improved mechanical properties [2]. Nguyen et al. investigated mixed oleylamine and oleic acid as a liquid matrix for sputtered metal nanoparticles and the effect of mixed liquid composition on particle size, homogeneity, and colloidal and oxidative stability [3]. Korotchenkov developed the theory of plasmonic exciton coupling for metallic nanocylindrical gratings [4]. Albrecht et al. believed that multifunctional metal nanoparticles (NPs) of multimetallic nanoparticles were essential to facilitate nanomaterial-based applications [5]. Ganesan et al. believed that molecular dynamics (MD) was an important tool that can provide significant benefits for structure-based drug design [6]. Gastegger et al. believed that machine learning has become an invaluable tool in many fields of research. In the current work, he exploited this ability to predict highly accurate molecular infrared spectra with unprecedented computational efficiency [7]. Bandrauk et al. believed that attosecond science is an emerging and rapidly developing field of research. Among them, molecular dynamics is studied on the time scale of several attoseconds [8]. Yeh et al. investigated the tensile deformation of semi-crystalline polyethylene (PE) at two different strain rates and

temperatures by molecular dynamics simulations [9]. Wang et al. believed that molecular dynamics simulations were used to study water desalination through functionalized nanoporous graphene membranes [10]. Loco et al. presented the realization of a Born-Oppenheimer (BO) hybrid quantum mechanics/molecular mechanics (QM/MM) molecular dynamics (MD) strategy using density functional theory (DFT) and polarized AMOEBA force fields [11].

## 3. Molecular Dynamics Simulation Calculation Method of Metal Nanostructures

**3.1. Metal Nanostructure Research.** When light of a specific wavelength is radiated to the interface between the metal and the medium, the electromagnetic waves interact with the free electrons on the metal surface. During the interaction, if the frequency of the light wave approaches the resonant frequency of the free surface electrons, large-scale collective oscillations occur. Such surface electromagnetic waves are generated by the rational interaction of free electrons and light waves on metal surfaces. The exponential drop indicates that the surface plasmons are oriented perpendicular to the surface and propagate along the surface of the metallic medium [12].

Surface plasmons have two modes. Localized surface plasmons (LSPs) are a mode located on the surface of metal nanostructures. Surface plasmon polaritons (SPPs) propagating along metal-dielectric interfaces are another mode.

Localized surface plasma: resonance occurs when the frequency of the incident light wave coincides with the oscillation frequency of free electrons on the metal surface, and the metal interacts strongly with the incident frequency of the electromagnetic wave. Surface plasmon resonance (SPR) refers to the state of resonance in which energy from an electromagnetic field can be converted into free collective electron kinetic energy on a metal surface. The electromagnetic field on the metal surface can get very big benefits. Since this phenomenon is limited by the size of the structure, localized surface plasmons (LSPs) are free electron oscillations on metal surfaces.

Surface plasmon polaritons: surface plasmon polaritons are electromagnetic oscillations formed on a metal surface by free electrons and photons, where the interaction of free electrons and electromagnetism results in electron-dense waves propagating along the metal surface. Such surface plasmons can propagate long distances along the surface of metal nanoparticles [13]. Due to the ohmic heating effect of the metal, its energy drops rapidly, resulting in a rapid reduction in its propagation distance. The SPP electric field strength decays exponentially with increasing distance from the metal surface.

The schematic diagram of surface plasmon propagation on metal and dielectric surfaces is shown in Figure 1.

Surface plasmons are electromagnetic evanescent waves propagated along the metal surface by the interaction of free electrons with an electromagnetic field. The surface plasmon shown in Figure 1 propagates along the surface of the metal-dielectric structure, which clearly shows an exponential decay trend in the direction perpendicular to the propagation.

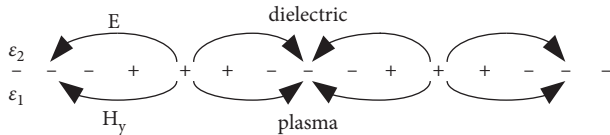


FIGURE 1: Schematic diagram of surface plasmon propagation on metal and dielectric surfaces.

Surface plasmons can also be excited in other geometries. It is not only excited in dielectric-metal planar interfaces, such as voids and metal particles of various topologies [14]. Localized surface plasmons (LSPs) are surface plasmons that represent bounded geometries. The frequencies of LSPs in the electrostatic approximation can be determined by appropriate boundary conditions of the Laplace formula. In order to ignore the retardation effect, the wavelength corresponding to the frequency of the LSPs must be larger than the characteristic size of the system. A schematic diagram of a uniform sphere in an electrostatic field is shown in Figure 2.

In Figure 2, a metal sphere has radius  $R$ , the center is at the origin, and  $\epsilon(\omega)$  is the dielectric function. Nonlinear plasmonic surface excitation is achieved by utilizing nonlinear metal processes to achieve matched phase and plasmonic surface excitation. The directional excitation of the plasmonic surface does not require any special external structures or excitation devices, but simply exploits nonlinearities. The reason why the plasmonic surface can be separated from the excitation beam by a filter is that the wavelength of the excitation beam is different from that of the plasmonic surface produced by nonlinear excitation [15]. The Otto and Kretschmann excitation devices are commonly used in linear excitation devices, as shown in Figure 3.

Figure 3 is the Kretschmann and Otto excitation devices, both of which are linear excitations. The Kretschmann excitation device cannot directly activate the plasma surface because the light wave vector in air is smaller than that of the plasma surface. In order to activate the plasmonic surface, the wave vector of the plasmonic surface can only appear at the lower refractive index between the parallel components along the metal and the medium. The total reflection angle of the wave at this time of the prism is smaller than the incident angle of light passing through the high refractive index. The Otto excitation device is a total reflection device. It generates comfortable waves in prisms and aerodynamic structures, and generates surface plasmons by exciting small channels between prisms and metal films.

### 3.2. Molecular Dynamics Simulation Calculation Method.

The understanding of multiple systems by electrons and nuclei is a dynamic molecular simulation. Computers are simulating nuclear motion. According to the nature and structure of the computer system, it simulates the motion of atoms and molecules under Newton's laws [16]. The flow chart of the molecular dynamics simulation method is shown in Figure 4.

The basic principle of molecular dynamics simulation is to first give a certain number of particles, and initialize the coordinates and velocities of these particles to simulate a

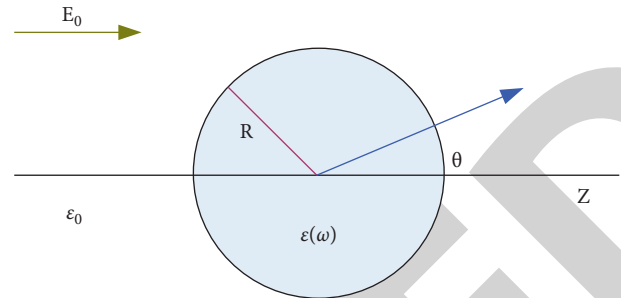


FIGURE 2: Schematic diagram of a uniform sphere in an electrostatic field.

system similar to the actual material. Through the interaction between particles, the physical and chemical properties of all particles in the system are calculated at specific time intervals to determine whether the entire system has reached an equilibrium state [17]. When the system reaches the equilibrium state, the physical and chemical properties of the material can be obtained according to the simulated system.

Cutoff radius: when the nearest mirror method is introduced in the calculation, the concept of cutoff radius needs to be considered to calculate the force between particles.

Periodic boundary conditions: the object simulated by the molecular dynamics method can be a cluster composed of dozens to hundreds of atoms, but it may also encounter a macroscopic object with a very large number of particles. Periodic boundary condition (PBC) is a kind of boundary condition, which reflects how to use the boundary condition to replace the influence of the surrounding (environment) by the selected part (system).

Integral step size: in molecular dynamics simulation calculation, how to choose the appropriate integration step size so that the calculation can save time without losing the accuracy of the calculation results is a very important part.

Nearest mirror method: when calculating the interatomic force, the nearest mirror method is used to make the atomic force at the edge of the model more complete, thereby eliminating the boundary effect [18].

The key to computer molecular dynamics on parallel computers is the molecular dynamics simulation algorithm. Data analysis shows that the calculation of particle interaction forces in molecular dynamics calculations occupies approximately 90% of the entire simulation time. This shows that the parallelization of the molecular dynamics algorithm mainly solves the parallelization of force calculation and its realization on parallel computers.

Molecular dynamics receives microscopic information, such as the position, velocity, and orientation of each particle, at times different from Newton's equations, and macroscopic properties are derived using methods that apply average time. These calculations are separate from each other. The nature of molecular dynamics facilitates parallel implementation because the objects of computation are particle positions and forces. Force decomposition, atomic decomposition, and spatial decomposition are three methods for parallel computing molecular dynamics [19].

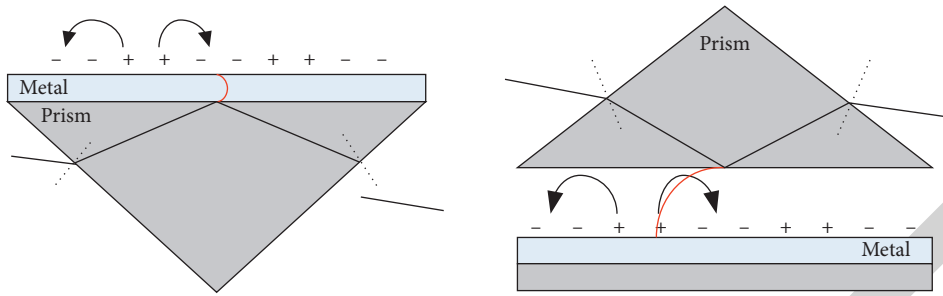


FIGURE 3: Linearly excited surface plasmon device.

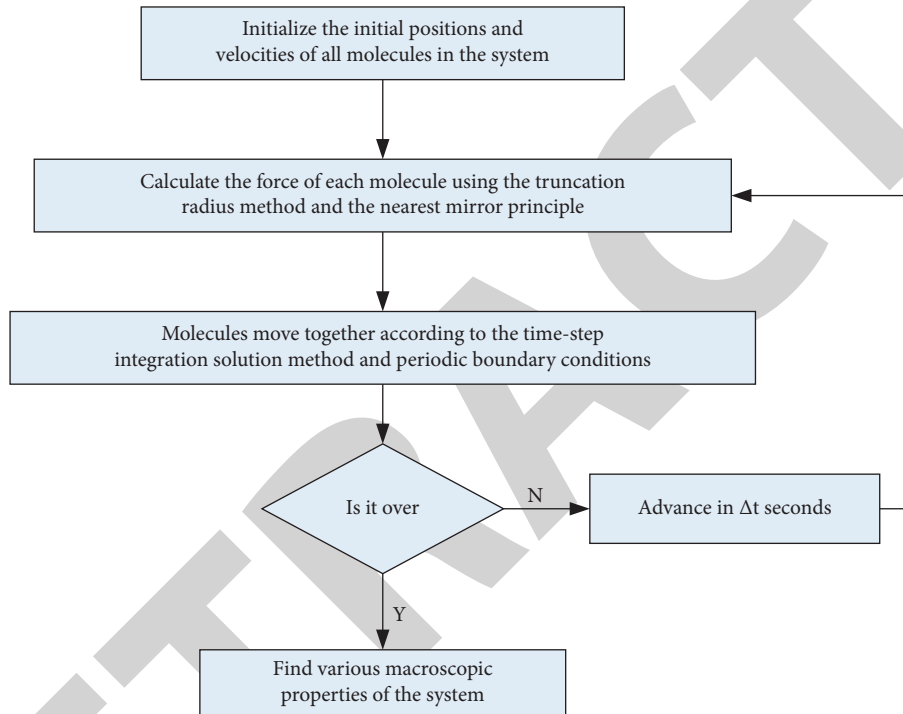


FIGURE 4: Flow chart of the molecular dynamics simulation method.

Force decomposition: it not only reduces communication costs, but also has the advantages of atomic decomposition. This can be explained with subblocks instead of partition matrices.

Atomic decomposition method: the atoms to be calculated are assigned to different processors for calculation. During the simulation process, the speed and position coordinates of the atoms are constantly updated, regardless of the physical space where the atoms are actually located.

Spatial decomposition method: the locality of the force calculation occurs due to the use of truncation.

The above several molecular dynamics parallel algorithms have their own advantages and disadvantages. The atomic decomposition method is the most direct, and the force decomposition algorithm is more complicated in force calculation. The key to the spatial decomposition algorithm lies in the realization of the data structure and the control of the load balance. The United States has a relatively mature product in molecular dynamics parallel computing [20].

## 4. Experiments and Results of Molecular Dynamics Simulation Calculations of Metal Nanostructures

*4.1. Theoretical Model and Simulation Method of Metal Nanostructures.* Simulation is the use of a model to reproduce the essential process that occurs in the actual system, and it helps study the existing or designed system through experiments on the system model, also known as simulation. The 3D-FDTD method is used to perform relevant simulation calculations, and the calculation model is divided into calculation areas according to Figure 5. The FDTD region division of the scattering problem is shown in Figure 5.

The Raman scattering spectra of DA molecules and the SERS spectra near Ag NPs dimers were simulated and calculated by the DFT method for the analysis of the SERS enhancement mechanism [21, 22]. This work is mainly done using the software Gaussian 09, using the B3LYP hybrid exchange correlation function and the LanL2DZ basis set. The geometry of the molecule was optimized before the

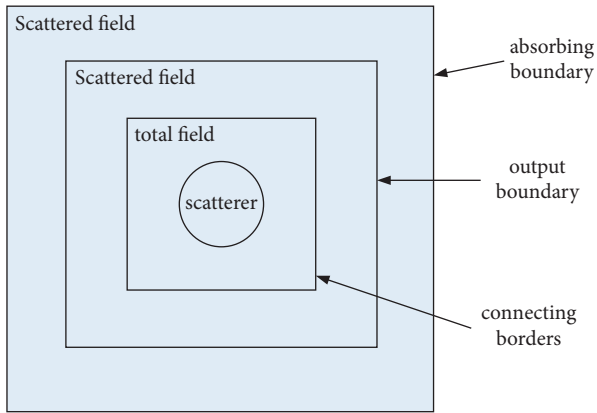


FIGURE 5: FDTD region division for the scattering problem.

calculation, and the correction factor used in the simulation calculation was 0.981.

In order to more accurately calculate the SERS enhancement factor of Ag NPs dimers, DDA, Mie scattering, and FDTD methods were used to simulate the optical properties of Ag NPs dimers. This is mainly due to the extinction spectrum and the distribution of the local electric field. The excitation wavelength used in the calculations is 532 nm, which corresponds to the actual experimental conditions. The excitation direction of the excitation light plane wave is along the direction of the long axis of the dimer. The relevant calculations of DDA are all calculated using the DDSCAT 7.3 package. The results of the Mie scattering simulation of the absorption, scattering, and extinction spectra of Ag NPs and the FDTD simulation of the local electric field distribution were calculated using a script file written by MATLAB software [23].

Regarding the adsorption process of molecules on the surface of Ag NPs, the adsorption model can be used for reference.

The degree of coverage of the Ag NPs dimer surface by the molecule to be tested can be represented by  $\theta$ , and the relationship between the SERS spectrum obtained by the experiment and the coverage degree can be expressed as

$$\theta = \frac{I_{Cs}}{I_{\max}} \quad (1)$$

In  $I_{Cs}$  is the intensity of the Raman peak to be analyzed at the concentration.  $I_{\max}$  is the saturation value of the SERS intensity at the same peak position. Combining the above two formulas, we get

$$I_{Cs} = I_{\max} \left( \frac{MC_S}{1 + MC_S} \right) \quad (2)$$

The binding constant  $M$  was used as a fitting parameter to fit the functional relationship between the Raman peak area and analyte concentration. The binding constant  $M$  is related to the Gibbs adsorption free energy ( $\Delta G$ ) as follows:

$$\Delta G = -RT \ln(M) \quad (3)$$

$M$  is the ideal gas constant with a value of 8.3143 kJ/kmol \* M, and  $T$  is the temperature in M. The temperature condition in the experiment is 25°C, which is 298.15 M.

To evaluate the utility and specificity of this method, 5 interferors (phenethylamine, tryptophan, tyrosine, levodopa, and bovine serum albumin) were tested for selectivity under the same conditions. With DA concentration of 300 nM and other species concentrations of 1  $\mu$ M, the SERS intensity of Ag NP dimer containing 300 nM DA at 767  $\text{cm}^{-1}$  was about 5 times higher than that of the five species. The selective experiment of DA detection based on SERS technology is shown in Figure 6.

As can be seen from Figure 6, these interfering species did not show a significant enhancement of SERS intensity even at high concentrations. To further confirm the specificity of this method, these five interfering chemicals were mixed as standard samples for DA detection. The obtained experimental results further confirmed the good selectivity of DA detection. Therefore, this method has good specific identification for the detection of DA.

#### 4.2. Molecular Dynamics Simulation Method and Conclusion.

The molecular dynamics simulation process generally includes the following steps: 1. It is necessary to establish the research object, establish a model according to the research object, and set the initial coordinate value and initial velocity of the atom or molecule through the initial temperature and structural characteristics required by the model; 2. It is necessary to select an appropriate simulation time step; 3. It is necessary to select an appropriate potential energy function between atoms; 4. It is necessary to determine the relevant parameters such as boundary conditions, integration algorithm, and ensemble, then start the calculation, and finally process the calculation results through the relevant software to extract the relevant parameters [24, 25].

Two aspects are generally considered when selecting boundary conditions. On the one hand, in order to reduce the amount of computation, the simulated system needs to be as small as possible. At the same time, in order to avoid the disturbance caused by dynamics to the greatest extent, the simulation system needs to be built larger to ensure statistical reliability. On the other hand, the coupling of volume change, stress balance, strain characteristics, etc. with reality needs to be considered from the actual physical nature.

The important characteristics of molecular dynamics simulation are that the motion is relatively independent, the time is long, the action can be superimposed and the short-range correlation is large, and the molecular information is simple. According to these characteristics, GPU simulation is very suitable for molecular dynamics simulation.

GPU is short for Graphics Processing Unit. CUDA extends C in five main ways: (1) The function type classifier, which determines whether the function is executed on the host side or the device side, and whether the function is called on the host side or the device side. (2) The variable type is used to define the type of memory stored by the variable. (3) Built-in vector types, CUDA provides vector types such as char1, uchar1, char2, uchar2, short1, ushort1, short2, ushort2, short3, and ushort3. (4) Four built-in variables. BlockIdx and threadIdx are used to identify threads



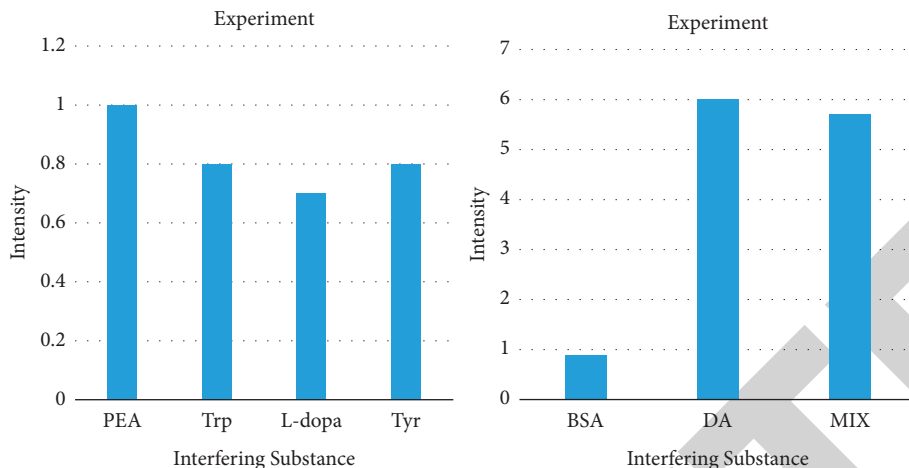


FIGURE 6: Selectivity experiment of DA detection based on SERS technology.

and thread blocks, and griddim and blockdim are used to size grid and thread blocks. 5. It introduces the  $\llcorner\llcorner\llcorner\llcorner$  operator, such as  $\text{Test}\llcorner\llcorner\llcorner\llcorner(a, b, c)$ , to specify the dimensions of the thread block and grid block, and to pass parameters to the Kernel function. The CUDA variable description table is shown in Table 1.

CUDA provides three variable-type qualifiers: `_device_`, `_shared_`, and `_constant_`. The variable-type qualifier `_device_` has a different meaning than the function-type qualifier `_device_`. `_device_` declares a variable located on the device. At most one of `_shared_` and `_constant_` can be used with the `_device_` qualifier to specify which memory space the variable belongs to. `_constant_` can be used with `_device_`. `_shared_` can optionally be used with `_device_`. The CUDA memory model is shown in Figure 7.

It can be seen from Figure 7 that during program execution, a thread can access data from multiple memory areas. Each thread has its own local and shared memory. Each thread block has a shared memory. All threads in the network can access the same global memory.

Each SM (Streaming Multiprocessor) of the GPU has thousands of registers, each SM has multiple SPs (Streaming Processors), and all the work is processed on the SPs. GPU threads cannot directly access the system main memory, and the accessed data must be stored in the GPU device memory. The on-chip GPU cache is read-only and does not cause coherency issues. The main function of the tower is to reduce the number of memory accesses, not to delay memory accesses. The GPU device memory space is shown in Figure 8.

It implements CPU and GPU algorithms to extract pressure and average potential energy of individual atoms on a PC for CPU, time, and error analysis at different molecular scales. The calculation time is the average of multiple experimental results. The running times of the CPU and GPU algorithms for pressure extraction and single-atom average potential energy extraction are shown in Tables 2 and 3.

It can be seen from Tables 2 and 3 that as the system scale increases, the GPU-based thermodynamic extraction rate also increases. When the number of molecules reaches a certain number, the computational efficiency is not

significantly improved. Compared with the CPU, the GPU can achieve a 190-fold acceleration effect.

The error analysis of the GPU algorithm relative to the CPU algorithm for pressure extraction and single-atom average potential energy extraction is shown in Figures 9 and 10.

It can be seen from the combined data in Figures 9 and 10 that the absolute and relative errors of pressure and single-atom average potential energy extraction increase with the increase in molecular scale. When the molecular scale reaches 100k, the errors of pressure and single-atom average potential energy reach 0.32 and 0.052, respectively. However, compared with the pressure and single-atom average potential energy extracted by the CPU algorithm, the error of the results extracted by the GPU algorithm is only 1.55% and -1.45%. This is because this lab does not support double-precision floating-point operations. If double-precision floating-point calculation can be added, the problem of error accumulation can be effectively avoided, and the calculation results can be made more accurate while obtaining better performance.

## 5. Molecular Dynamics Simulation Analysis of Metal Nanostructures

*5.1. Surface Plasmons in Metal Nanostructures.* Surface plasmons are electromagnetic oscillations with surface charges and electromagnetic waves, mainly composed of free electrons and photons coupled. Based on the action of the external electric field,  $1/\tau$  represents the probability of collision of free electrons per unit time.  $\tau$  is the relaxation time, which has nothing to do with the speed or position of the electron. Thermal equilibrium is achieved by generating collisions using the surrounding environment and electrons. Based on the action of the external field, the formula of motion of a single free electron can be expressed as

$$x \frac{dm^2}{dt^2} + xy \frac{dm}{dt} = -eE. \quad (4)$$



TABLE 1: CUDA variable description.

Variable declaration		Memory	Scope	Lifetime
<code>_device_local_</code>	<code>Int LocalVar;</code>	Local memory	Thread	Thread
<code>_device_shared_</code>	<code>Int SharedVar;</code>	Shared memory	Block	Block
<code>_device_</code>	<code>Int GlobalVar;</code>	Global memory	Grid	Program
<code>_device_constant_</code>	<code>Int ConstantVar;</code>	Constant memory	Grid	Program

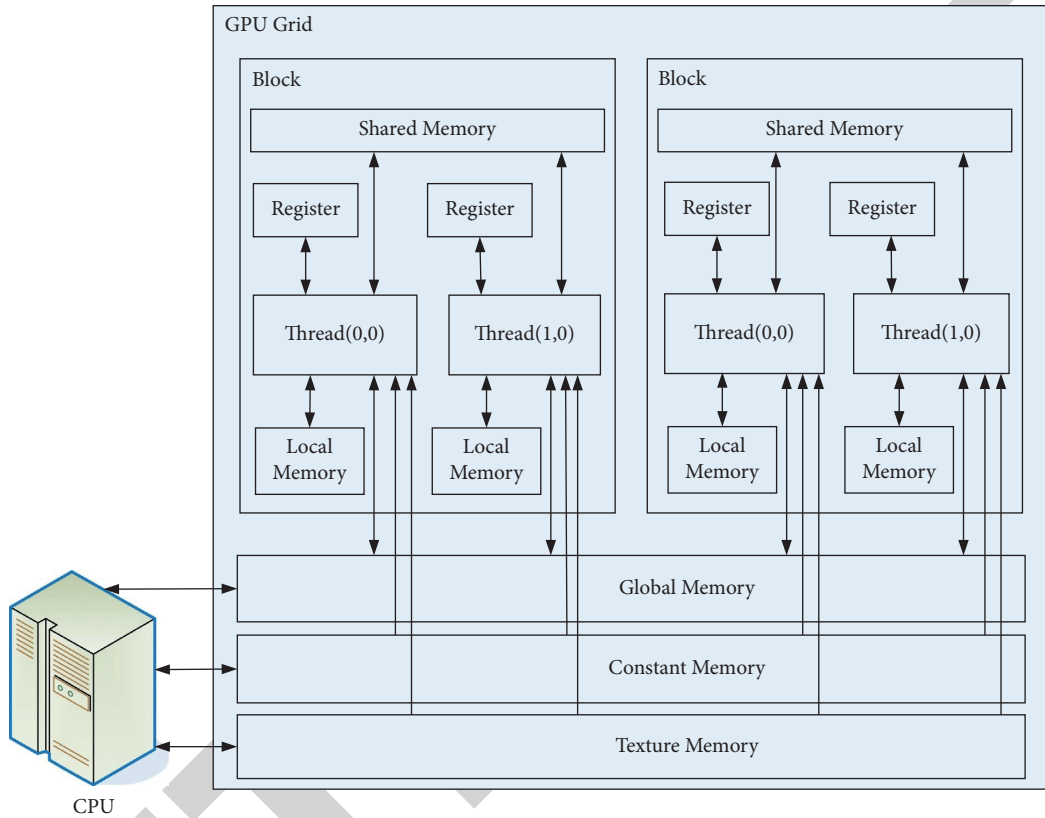


FIGURE 7: CUDA memory model.

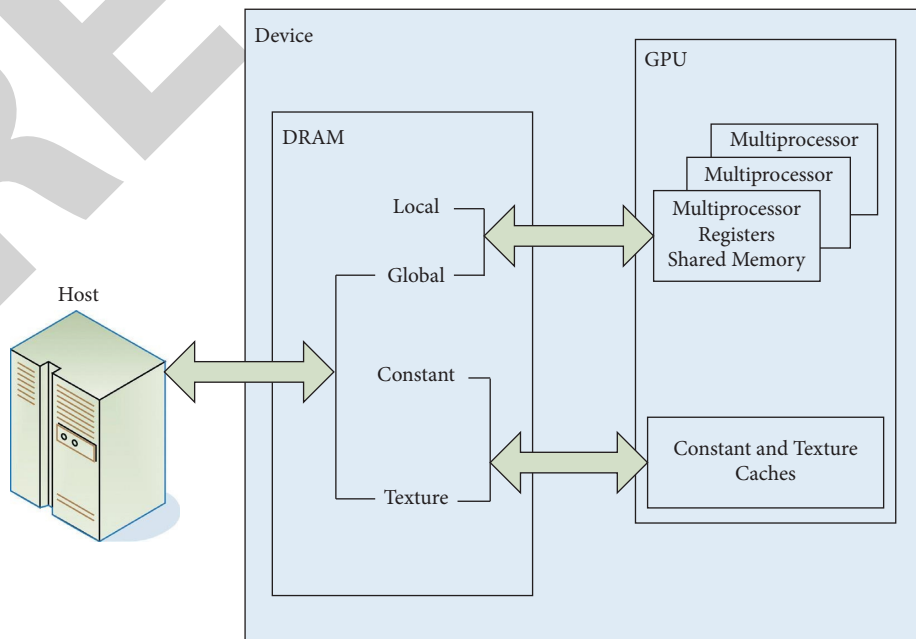


FIGURE 8: GPU device memory space.

TABLE 2: CPU algorithm and GPU algorithm running time for pressure extraction.

Particle numbers	CPU (ms)	GPU (ms)	GPU(Opt) (ms)
6400	907	19	16
12800	3556	72	33
25600	14009	282	79
38400	31228	657	173
51200	55048	1158	299
76800	123181	2563	673
102400	219337	4563	1173

TABLE 3: Running time of CPU algorithm and GPU algorithm for single-atom average potential energy extraction.

Particle numbers	CPU (ms)	GPU (ms)	GPU(Opt) (ms)
6400	907	19	16
12800	3556	72	33
25600	14009	282	79
38400	31228	657	173
51200	55048	1158	299
76800	123181	2563	673
102400	219337	4563	1173

Among them,  $m$  represents the displacement of free electrons, and  $e$  represents the elementary charge. Assuming that the electric field  $E$  is in the form of a harmonic of  $E_0 e^{-i\omega t}$ , the particular solution to the formula of motion is

$$m(t) = m_0 e^{-i\omega t}. \quad (5)$$

Substituting formula (5) into formula (4) yields

$$m(t) = \frac{e}{x(\omega^2 + i\gamma\omega)} E(t). \quad (6)$$

The polarization strength  $P = -nex$  is obtained as

$$P = \frac{ye^2}{x(\omega^2 + i\gamma\omega)} E. \quad (7)$$

According to the relationship  $D = \epsilon_0 E + P$  between the electric displacement vector  $D$  and  $P$ , we can get

$$D = \epsilon_0 \left( 1 - \frac{\omega_p^2}{\omega^2 + i\gamma\omega} \right) E, \quad (8)$$

$\omega_p^2 = ne^2/\epsilon_0 m$  is the surface plasmon oscillation frequency of the free electron gas. The relative permittivity of the metal is

$$\epsilon(\omega) = 1 - \frac{\omega_p^2}{\omega^2 + i\gamma\omega} = \epsilon_1(\omega) + i\epsilon_2(\omega). \quad (9)$$

It can be seen from the above formula that the real part  $\epsilon_1(\omega)$  and the imaginary part  $\epsilon_2(\omega)$  of the complex permittivity of metals can be expressed as

$$\epsilon_1(\omega) = 1 - \frac{\omega_p^2 \tau^2}{1 + \omega^2 \tau^2}, \quad (10)$$

$$\epsilon_2(\omega) = \frac{\omega_p^2 \tau}{\omega(1 + \omega^2 \tau^2)}.$$

Based on the relevant properties of the metal,  $\omega < \omega_p$  will be assumed in the discussion. As  $\omega \tau \gg 1$  tends to higher frequencies, the losses are negligible since the losses are relatively small. The imaginary part of  $E(\omega)$  is relatively small, and hence it can be regarded as a real number. The dielectric constant of lossless free electrons is obtained as

$$\epsilon(\omega) = 1 - \frac{\omega_p^2}{\omega^2}. \quad (11)$$

As  $\omega_p$  tends to lower frequencies,  $\omega \ll \tau^{-1}$ , then  $\epsilon_2 \gg \epsilon_1$ , and  $E(\omega)$  the real and imaginary parts are approximately equal:

$$y \approx k = \sqrt{\frac{\epsilon_2}{2}} = \sqrt{\frac{\tau \omega_p^2}{2\omega}}. \quad (12)$$

The metal has a strong absorption capacity in the frequency range, and the absorption coefficient is  $\alpha$ :

$$\alpha = \sqrt{\frac{2\omega_p^2 \tau \omega}{c^2}}. \quad (13)$$

In the free electron gas model, when  $\omega \gg \omega_p$ ,  $\epsilon \rightarrow 1$ . The response of metals in this frequency range depends mainly on free electrons in the  $s$  state. Therefore, for  $d$ -level noble metals close to the Fermi level (such as Au, Ag, Cu, etc.), the model in this frequency range needs to be corrected because noble metals contain positive ions, and positive ions produce remanent polarization effects. Therefore, the polarization caused by the electron oscillation can be expressed as

$$P_{\infty} = \epsilon_0 (\epsilon_{\infty} - 1). \quad (14)$$

The dielectric constant at this time can be obtained as

$$\epsilon(\omega) = \epsilon_{\infty} - \frac{\omega_p^2}{\omega^2 + i\gamma\omega}. \quad (15)$$

In summary, the metal-free electron gas model can well explain the dielectric response of metals in a wide frequency range.

**5.2. Molecular Dynamics Numerical Simulation Analysis.** Numerical simulation techniques are commonly used to study various "field" problems, including stress fields, displacement fields, temperature fields, electromagnetic fields, and more. The research questions can be summarized as: It solves his domain equations (differential

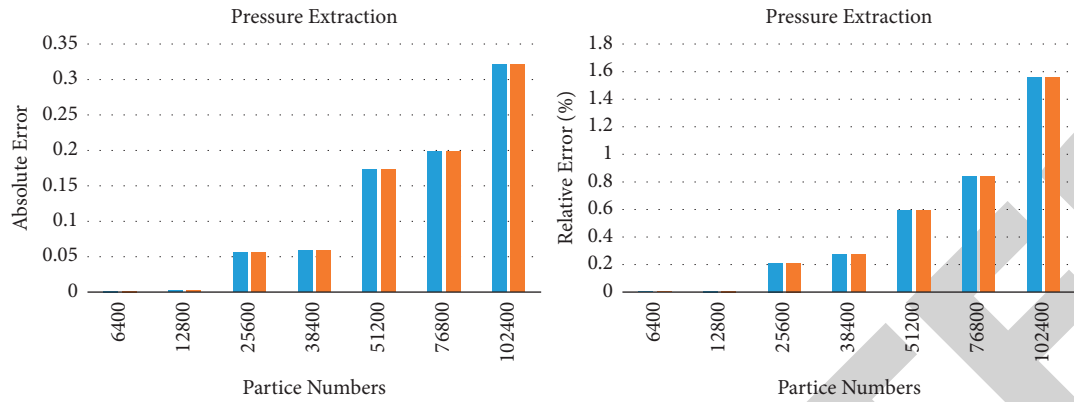


FIGURE 9: Error analysis of the GPU algorithm for pressure extraction relative to the CPU algorithm.

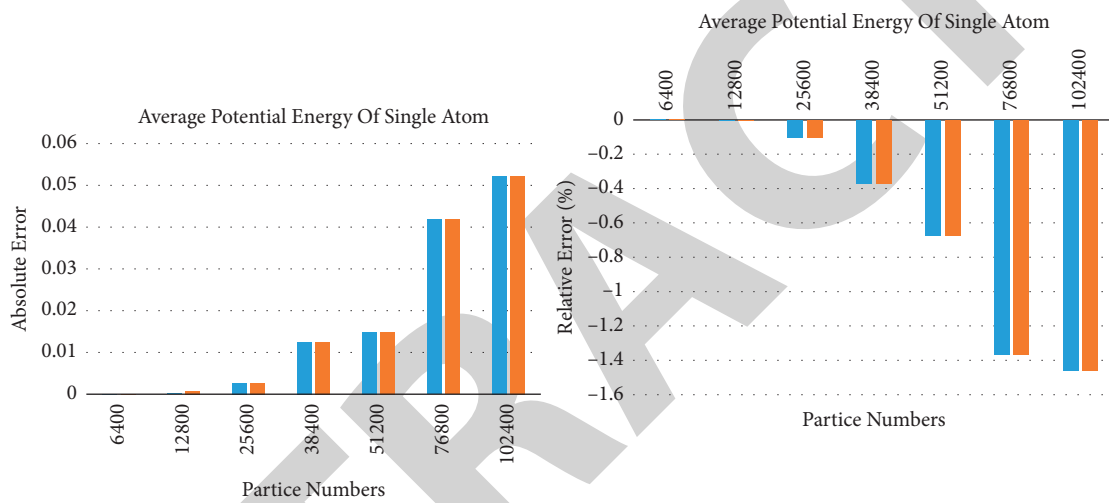


FIGURE 10: Error analysis of the GPU algorithm relative to the CPU algorithm for single-atom average potential energy extraction.

equations or partial differential equations) under certain conditions. In some cases, the process of solution is relatively simple, and the existence of boundary rules makes the solution more precise. In most cases, the resolution process is complex and needs to be simplified. In some cases, numerical simulation techniques are employed to resolve. Due to the existence of Maxwell's equations, the study of electromagnetic fields has been deeply developed and can be well applied to various fields. Composite metal nanostructures are usually complex and it is difficult to solve Maxwell's equations precisely. Therefore, in most cases, in order to solve the electromagnetic field accurately, it is necessary to use some numerical simulation method. The commonly used methods are the finite element method, discrete element method, and time domain finite difference method. The plate and shell problem is suitable for using the boundary element method developed in recent years. However, there are some limitations in use. At present, the most widely used numerical simulation methods are the time domain finite difference method and the finite element method.

Finite difference time domain (FDTD) is a very common method for calculating electromagnetic fields in the time domain.

The finite element method (FEM) is a numerical method for approximately solving boundary value problems (systems of partial differential equations) in mathematical physics. It decomposes a complex problem into several related tiny units, sets an approximate solution with parameters in each unit, and then solves the equations of each unit simultaneously and as a whole through mutual relationships. The finite element method has been more widely used in electromagnetic field calculation due to its high precision and suitability for complex geometries. It is good at solving multiband electromagnetic control coupling and multiphysics coupling problems, and was even used in aircraft design in the 1950s.

Molecular dynamics is a discrete model system consisting of a large number of interacting particles, each of which has a mass. Its position is represented by a geometric point, and its motion follows Newton's equations of motion. Newtonian mechanics takes the particle as the research object and focuses on the relationship of force. When dealing with the problem of the particle system, it emphasizes considering the force on each particle separately, and then infers the motion state of the entire particle system. It utilizes kinetic calculations to describe the behavior of each particle to represent the behavior of

the system directly or through statistics and combinations.

It assumes that a system consists of  $N$  particles, and the state of this system is marked by the particle's position 1 and momentum 2 or velocity 3.

The energy of the system is 1, and its formula of motion is

$$\frac{\partial}{\partial t} p_a = - \frac{\partial}{\partial r} H. \quad (16)$$

Or

$$\frac{\partial}{\partial t} r_a = - \frac{\partial}{\partial p} H. \quad (17)$$

In practical applications, the above formula can be transformed into Newton's formula

$$H = \frac{1}{2} \sum_{a=1}^N x_a v_a^2 + V(\{r_a\}), \quad (18)$$

$$x_a \frac{d^2}{dt^2} r_a = - \frac{\partial}{\partial r_a} V(\{r_a\}),$$

$x_a$  is the mass of particle  $a$ , and  $V(\{r_a\})$  is the interaction potential between particles.

Molecular dynamics is to decompose a continuous process into multiple discrete time steps  $t_0, t_1, t_2, t_3, \dots$ . In each step, the above formula is used to obtain the trajectory of the system state evolution to space.

$$\{r_1, p_a\}_{t_0}, \{r_a, p_a\}_{t_1}, \{r_a, p_1\}_{t_2}, \dots \quad (19)$$

In turn, the value  $Q(\{r_a, p_a\})$  of other physical quantities of interest can be calculated.

## 6. Conclusions

With the advancement of science and technology, molecular dynamics simulation methods have been applied more and more. The research on molecular dynamics simulation calculation methods is also of great significance for promoting the current scientific development. In chemical engineering, although they are mostly used in thermodynamic studies, studies on transport properties are also taking off. In the field of materials, previous methods can only give the positions of atoms. However, with the development of the first molecular dynamics method, it can simultaneously give the structure and properties of the ground state of the crystal, and also provide a reference for the design of composite materials. In the case of drugs, the actual composition of cell membranes is more complex and cannot be considered in much detail in current simulation calculations. In contrast to the past, however, molecular dynamics simulation methods allow the study of drug-membrane interactions at the atomic level. Molecular dynamics technology has received more and more attention in different countries. Molecular dynamics simulations are expected to be used for more sophisticated studies and become more widespread in the future.

## Data Availability

Data sharing is not applicable to this article as no new data were created or analyzed in this study.

## Conflicts of Interest

The authors declare no conflicts of interest.

## Acknowledgments

This work was supported by Higher Vocational School Program for Key Teachers from Department of Education of Henan Province, China (2019GZGG042).

## References

- [1] A. Prasad Reddy, P. Vamsi Krishna, R. Narasimha Rao, and N. Murthy, "Silicon carbide reinforced aluminium metal matrix nano composites-A review," *Materials Today Proceedings*, vol. 4, no. 2, pp. 3959–3971, 2017.
- [2] A. A. Shtertser, D. V. Dudina, V. Y. Ulianitsky et al., "Metal-nanocarbon composite coatings produced by detonation spraying with in situ carbon generation," *Journal of Thermal Spray Technology*, vol. 30, no. 7, pp. 1837–1849, 2021.
- [3] M. T. Nguyen, K. Wongrujipairoj, H. Tsukamoto et al., "Synergistic effect of the oleic acid and oleylamine mixed-liquid matrix on particle size and stability of sputtered metal nanoparticles," *ACS Sustainable Chemistry & Engineering*, vol. 8, no. 49, Article ID 18167, 2020.
- [4] A. V. Korotchenkov, "Coupling of quantum-well excitons to plasmons in one-dimensional metal nanocylinder gratings," *Semiconductors*, vol. 54, no. 11, pp. 1506–1508, 2020.
- [5] W. Albrecht, E. Bladt, H. Vanrompay, J. D. Smith, S. E. Skrabalak, and S. Bals, "Thermal stability of gold/palladium octopods studied in situ in 3D: understanding design rules for thermally stable metal nanoparticles," *ACS Nano*, vol. 13, no. 6, pp. 6522–6530, 2019.
- [6] A. Ganesan, M. L. Coote, and K. Barakat, "Molecular dynamics-driven drug discovery: leaping forward with confidence," *Drug Discovery Today*, vol. 22, no. 2, pp. 249–269, 2017.
- [7] M. Gastegger, J. Behler, and P. Marquetand, "Machine learning molecular dynamics for the simulation of infrared spectra," *Chemical Science*, vol. 8, no. 10, pp. 6924–6935, 2017.
- [8] A. D. Bandrauk, J. Manz, and M. Vrakking, "Attosecond molecular dynamics," *Chemical Physics*, vol. 366, no. 1-3, p. 1, 2009.
- [9] I. C. Yeh, J. W. Andzelm, and G. C. Rutledge, "Mechanical and structural characterization of semicrystalline polyethylene under tensile deformation by molecular dynamics simulations," *Macromolecules*, vol. 48, no. 12, pp. 4228–4239, 2015.
- [10] Y. Wang, Z. He, K. M. Gupta, Q. Shi, and R. Lu, "Molecular dynamics study on water desalination through functionalized nanoporous graphene," *Carbon*, vol. 116, no. Complete, pp. 120–127, 2017.
- [11] D. Loco, L. Lagardère, S. Caprasecca, F. Lipparini, B. Mennucci, and J. P. Piquemal, "Hybrid QM/MM molecular dynamics with AMOEBA polarizable embedding," *Journal of Chemical Theory and Computation*, vol. 13, no. 9, pp. 4025–4033, 2017.
- [12] J. Zhang, Y. Hong, M. Liu, Y. Yue, Q. Xiong, and G. Lorenzini, "Molecular dynamics simulation of the interfacial thermal resistance between phosphorene and silicon substrate,"

## *Retraction*

# **Retracted: Construction of Nanomaterials and the Role of Rutin in the Treatment of Cerebral Hemorrhage**

### **Advances in Materials Science and Engineering**

Received 26 December 2023; Accepted 26 December 2023; Published 29 December 2023

Copyright © 2023 Advances in Materials Science and Engineering. This is an open access article distributed under the Creative Commons Attribution License, which permits unrestricted use, distribution, and reproduction in any medium, provided the original work is properly cited.

This article has been retracted by Hindawi, as publisher, following an investigation undertaken by the publisher [1]. This investigation has uncovered evidence of systematic manipulation of the publication and peer-review process. We cannot, therefore, vouch for the reliability or integrity of this article.

Please note that this notice is intended solely to alert readers that the peer-review process of this article has been compromised.

Wiley and Hindawi regret that the usual quality checks did not identify these issues before publication and have since put additional measures in place to safeguard research integrity.

We wish to credit our Research Integrity and Research Publishing teams and anonymous and named external researchers and research integrity experts for contributing to this investigation.

The corresponding author, as the representative of all authors, has been given the opportunity to register their agreement or disagreement to this retraction. We have kept a record of any response received.

### **References**

- [1] X. Li and Z. Gao, "Construction of Nanomaterials and the Role of Rutin in the Treatment of Cerebral Hemorrhage," *Advances in Materials Science and Engineering*, vol. 2022, Article ID 7044153, 11 pages, 2022.

## Research Article

# Construction of Nanomaterials and the Role of Rutin in the Treatment of Cerebral Hemorrhage

Xin Li <sup>1</sup> and Zhenzhong Gao<sup>2</sup>

<sup>1</sup>Neurosurgery Department Associate Chief Physician, Yangzhou Hongquan Hospital, Yangzhou 225200, Jiangsu, China

<sup>2</sup>Department of Neurosurgery, First Affiliated Hospital of Hainan Medical University, Haikou 570100, Hainan, China

Correspondence should be addressed to Xin Li; 3170400017@caa.edu.cn

Received 16 June 2022; Revised 18 July 2022; Accepted 23 July 2022; Published 18 August 2022

Academic Editor: K. Raja

Copyright © 2022 Xin Li and Zhenzhong Gao. This is an open access article distributed under the Creative Commons Attribution License, which permits unrestricted use, distribution, and reproduction in any medium, provided the original work is properly cited.

Cerebral hemorrhage generally refers to nontraumatic cerebral parenchymal hemorrhage. In China, about 20%–30% of all stroke in a month after the mortality rate can be as high as 40%. And most of the survivors have obvious neurological dysfunction, to the patient's family and society from all walks of life caused great psychological pressure, which will seriously affect the human physical and mental health. This article aims at studying the construction of nanomaterials and the role of rutin in the treatment of ICH. It first introduces the characteristics of nanomaterials; nanomaterials have some special effects based on their special internal structural properties and surface states. These effects derive many physical and chemical properties that general substances do not possess, such as optical, electrical, magnetic, catalytic, and photocatalytic properties. A simple analysis of cerebral hemorrhage then gives the nanomaterials the first-principles algorithm. Practical application of nanomaterials is a class of nanomaterials, which have many strange chemical characteristics such as special light, electric, magnetic, thermal, mechanical, mechanical physical, and chemical characteristics. Then, the nanocomposite of rutin electrochemical detection is analyzed, and finally rutin and analog brain drug dynamics is discussed. The experimental results showed that the RSD of samples at room temperature, freeze-thaw cycles, and long-term stability of the mice were less than 5.0%, and the stability of mouse brain tissue homogenate samples completely meets the requirements of troxerutin, rutin, and troxerutin aglycone.

## 1. Introduction

Patients with cerebral hemorrhage often have a sudden onset due to emotional agitation and exertion, and the early mortality is very high. Most of the survivors have sequelae of varying degrees of motor impairment, cognitive impairment, and speech and swallowing disorders. Cerebral hemorrhage is one of the most serious refractory diseases that endanger people's lives. Its high case fatality rate and great mortality rate have brought a heavy burden to Chinese residents. In recent years, investigations have shown that stroke has surpassed cardiovascular disease and malignant cancer as the first fatal factor in Chinese adults, and cerebral hemorrhage is the second largest type of stroke, accounting for 10%–15% of all stroke. And the proportion of stroke in China is as high as 20%–30% and some even more than 50%.

This article aims at studying the construction of nanomaterials and the role of rutin in the treatment of ICH. Cerebral hemorrhage is one of the most serious refractory diseases that endanger people's lives. Its high case fatality rate and great mortality rate have brought a heavy burden to Chinese residents. Investigation in recent years has shown that stroke has surpassed cardiovascular disease and malignant cancer. As the first fatal factor of Chinese adults, it may be able to greatly shorten the treatment time window after stroke and get symptomatic treatment in an early stage, which has an open prospect of clinical transformation. This article aims at studying the construction of nanomaterials and the role of rutin in the treatment of ICH, in order to make a certain contribution in the treatment of ICH.

The innovations of this article are as follows. (1) The characteristics of nanomaterials are analyzed. (2) The first-



principles algorithm for nanomaterials is proposed. (3) The intracerebral pharmacokinetics of Troxerutin and its analogs are investigated experimentally.

## 2. Related Work

According to the progress of foreign research, different researchers have a corresponding cooperative research on the construction of nanomaterials and cerebral hemorrhage: Jiao et al. summarized the research work based on the impact of bile salt on the self-assembly of micro- and nanomaterials and related research worldwide. Dye molecules are considered ideal substrates for the construction of functional nanomaterials; as biosurfactants, bile salts are commonly used to assist in the synthesis of micronanomaterials. To gain a more comprehensive and deeper understanding of the preparation of micronanomaterials in the presence of bile salts, the research provides a solid foundation for exploring future applications [1]. Rincón-Morantes et al. aim at gathering different experiences using nanomaterials to stabilize or improve the mechanical and geotechnical properties of soils used in road construction, especially those related to manufacturing nanofibers for soils, finding that its applications in the road field will be studied and developed by different types of solutions [2]. Seevakan and Sheeba study and document applicable nanotechnology products that can enhance the overall competitiveness of the construction industry. The application of nanotechnology in architecture will focus on: (1) lighter and stronger structural composites, (2) low maintenance coatings, (3) better adhesive performance, (4) reduced heat transfer and insulation of flame retardants, (5) structurally related nanosensor [3]. The Lim et al. study aimed to investigate the possibility of using these carbon-based nanomaterials as building materials. The structural and electrical properties of cemented composites were studied based on carbon-based materials such as multiple, single, carbon nanotubes, graphene nanosheets, and conductive graphite powder. Microstructural analysis was also performed by noncovalent functionalization of carbon-based nanomaterials to check for dispersion [4]. The purpose of the Michael study is to evaluate resource utilization following the implementation of a treatment regimen for mild traumatic brain injury (TBI). Patients with isolated mild TBI both before and after the implementation of a mild TBI treatment regimen were retrospectively reviewed. Efficient care is critical in modern medicine, and this study shows that mild TBI treatment options significantly reduce resource utilization without compromising patient safety [5]. Target tissue dissection is an ultrasound-based treatment modality that relies on the generation of targeted cavitation bubble clouds that mechanically separate tissue. The purpose of the Sukovich et al. study is to investigate the in vivo feasibility of using tissue analysis techniques to produce localized destructive damage in the porcine brain, including dose requirements and safety. Lesions confined to the gyrus cannot cause the significant bleeding or edema response [6] at the treatment site. However, these scholars did not study the construction of nanomaterials and the role of rutin in the treatment of cerebral hemorrhage, but only unilaterally discussed its significance.

## 3. Construction of Nanomaterials and the Role of Rutin in the Treatment of Cerebral Hemorrhage

*3.1. Characterization of the Nanomaterials.* Small-scale effect is also known as small volume effect. When the scale of nanoparticles and transfer electron wavelength or superconducting coherent wavelength are under the same physical scale, even more periodic boundary conditions were broken, the temperature, magnetism, optical absorption, boundary thermal resistance, chemical reactivity, catalytic change, and the effect of nanomaterials have also opened up a wide range of new application fields [7]. Nanostructure is a new system constructed according to certain rules on the basis of nanoscale material units.

Surface effect refers to the change in the ratio of the number of molecules to the total atomic order on the nanoparticle surface as the particle size decreases or increases rapidly. Because the application of nanomaterials is gradually smaller, the number of surface atoms increased rapidly, so the surface area and surface free energy of nanoparticles also increased rapidly, and the surface atoms field environment and binding freedom are different between the atoms. The surface molecules between there are no adjacent atoms, so many hanging bonds have unsaturated, which is easy to combine between other atoms and stabilize it, that show a strong catalytic activity [8].

Quantum size effect is that the particle scales down to a value, around the fermi electron level from quasi-continuous electron-level into discrete electron-level special phenomenon. At the discrete quantization level, the electron shock of nanomaterials produced many specific properties, such as electron-specific catalytic and photocatalytic characteristics [9].

The structure determines the properties. Because nanomaterials have a different internal structure and surface state from general substances, they will have special properties different from general substances, such as fluorescence properties, adsorption properties, and catalytic properties. Because nanomaterials based on their special internal structural properties and surface state will cause it to have some special effects, these effects derive many physical and chemical properties that general substances do not have, such as optical, electric, magnetic, catalytic, and photocatalytic properties [10]. The catalytic properties based on nanomaterials have been widely concerned and applied in various fields of production and life, such as the detection of heavy metal ions in water, degradation of sewage and organic dyes, sensitive detection of biomolecules, detection of toxic gases in the air (such as carbon monoxide and nitric oxide), and detection of additives in food. Sensors based on the properties of nanomaterials can achieve selective and highly sensitive detection [11]. Compared with conventional materials, nanomaterials have greatly improved toughness, strength, and hardness, so they are widely used in aviation, aerospace, navigation, oil drilling, and other fields. The nanomaterial assembly structure is shown in Figure 1.

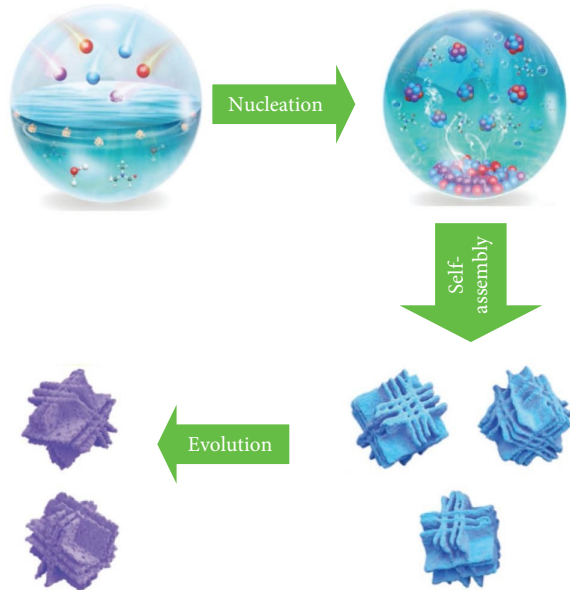


FIGURE 1: Nanomaterial assembly structure.

**3.2. Cerebral Hemorrhage.** Cerebral hemorrhage is a typical neurological disease. It is a high lethality, high mortality disease. But due to the developed social economy and further improvement of public quality of life, the age of hemorrhagic stroke is increasingly young. Scientific research confirmed that the average annual prevalence of hemorrhagic stroke is about 60-80-0/100000 people, accounting for 20%–30% of the ischemic stroke; the month after the average death rate of more than 40%, 3/4 of cerebral hemorrhage survivors lost life and work ability to varying degrees. Hypertension diseases are also the most common cause of cerebral hemorrhage. Head trauma, congenital cerebrovascular malformation, anticoagulation, or thrombolytic therapy are also the more common causes of cerebral hemorrhage. The primary principle of ICH treatment is to keep quiet, stabilize blood pressure, prevent continued bleeding, appropriately reduce intracranial pressure, prevent cerebral edema, and maintain the balance of water, electrolyte, blood sugar, and body temperature according to the situation. Age, genetic factors, smoking, alcohol abuse, eating habits, obesity, and diabetes are all risk factors for cerebral hemorrhage [12]. Hypertensive intracerebral hemorrhage often occurs in 50 to 70-year-old males, which is slightly more likely to occur in winter and spring; it usually occurs during activities and emotional agitation, and there is no warning before bleeding. Half of the patients had severe headache, vomiting was common, and blood pressure increased significantly after hemorrhage. As shown in Figure 2, cerebral hemorrhage will not only cause somatic motor function and swallowing function, and discourse dysfunction, but also lead to major obstacles to cognitive function, including attention, memory function, action function, and learning and other different dysfunctions, which severity affect the patient's health process and survival ability [13]. Intracerebral hemorrhage refers to hemorrhage caused by rupture of blood vessels in the nontraumatic brain parenchyma. The most common

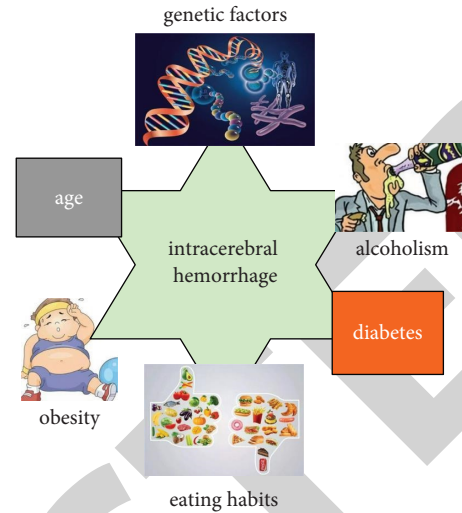


FIGURE 2: Causes of intracerebral hemorrhage.

causes are hypertension, cerebral arteriosclerosis, intracranial vascular malformations, etc., which are often induced by exertion, emotional agitation, and other factors. Therefore, most of the onset occurs suddenly during activities. Clinically, the onset of cerebral hemorrhage is very rapid, mainly manifested as disturbance of consciousness, limb hemiplegia, aphasia, and other nervous system damage.

**3.3. First-Principles Calculation of Nanomaterials.** Nanomaterials have many strange characteristics such as special light, electricity, magnetic, thermal, mechanical, and other physical and chemical characteristics, which makes nanotechnology quickly enter into all scientific research studies by a large number of physicists and chemists; nanomaterials gain home and abroad scholars' general attention. It has become the global hot topic of scientific research. Physicists are interested in nanomaterials because of their special electromagnetic properties, and material chemists are interested in their physical and chemical activities and their potential value, while material scholars are interested in its hardness, strength, and flexibility [14–16]. Undoubtedly, the new nanotechnology based on nanomaterials will have a huge and profound impact on the economic development and social progress in today's world. Therefore, the scientific research of nanomaterials is of great importance. Among them, carbon nanomaterials are one of the most popular scientific research materials [17]. Figure 3 is the manufacturing process of nanometer.

When dealing with the related problems of the micro-multiparticle system, the basic starting point is to solve the following equation of the system:

$$K\psi(l, L) = W\psi(l, L), \quad (1)$$

where  $\psi(l, L)$  as the wave function of the system and  $K$  is the Hamiltonian operator of the molecular system, which can be expressed as

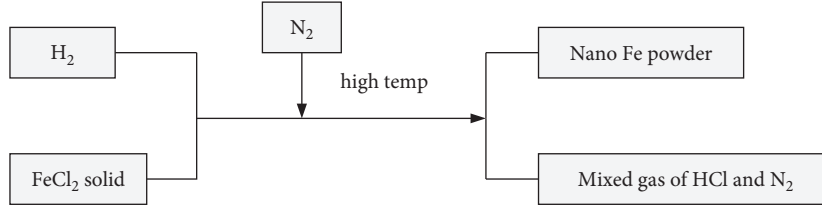


FIGURE 3: Nanofabrication process.

$$K(l, L) = U_w(l_n) + R_{ww}(l_n) + U_P(L_N) + R_{PP}(L_N) + R_{Pw}(l_n, L_N) = - \sum_n \frac{k^2}{2q_w} \nabla_{l_n}^2 + \frac{1}{2} \sum_{n,m} \frac{w^2}{|l_n - l_m|} \quad (2)$$

$$\sum_n \frac{k^2}{2Q_N} \nabla_{L_N}^2 + \frac{1}{2} \sum_{N,M} \frac{C_N C_M w^2}{|L_N - L_M|} - \sum_{N,n} \frac{C_n w^2}{|l_n - L_N|}$$

where  $q_w$  is the mass of the electron,  $l$  is the electron position coordinate,  $Q_N$  is the nuclear mass, and  $L$  is the nuclear position coordinate. The meanings of the five terms of the Hamiltonian operator are the electron kinetic energy term, the Coulomb action between the electrons, the nuclear kinetic energy term, the action between the nucleus, and the action term between the electron and the nucleus, respectively [18].

When using this equation to solve specific problems, there are many problems to be addressed. However, for many nanosystems, rigorously precisely solving the equations in many-particle systems is still a difficult career-long thing [19].

The so-called first-principles method: starting from quantum mechanics, using numerical solution equations, all the physical and chemical properties of the system can be studied. The first-principles method can provide the electronic structure characteristics of the system, but also can describe the bond damage and reconstruction, as well as electronic rearrangement process (such as chemical reaction). Because the principle method usually gives the highest accuracy calculation method, in principle, it only requires the type and position between molecules as input, and can accurately estimate all the physical and chemical properties of the molecular system [20].

**3.3.1. The Born–Oppenheimer Approximation.** The Born–Oppenheimer approximation is a commonly used approximation method for solving quantum mechanical equations of systems involving electrons and nuclei. In the Born–Oppenheimer approximation,

(a) Electronic equation of motion is given as

$$K_w \psi_w(l, L) = W_w \psi_w(l, L), \quad (3)$$

where  $\psi_w$  is the wave function for the electron, and  $K_w$  is the Hamiltonian operator for the electron, which can be expressed as

$$K_w = U_w(l_n) + R_{ww}(l_n) + R_{Pw}(l_n, L_N). \quad (4)$$

(b) Equation of nuclear motion is given as

$$K_P \psi_P(l, L) = W_P \psi_P(l, L), \quad (5)$$

where  $\psi_P$  is the wave function of the electron, and  $K_P$  is the Hamiltonian operator of the nucleus, which can be expressed as

$$K_P = U_P(L_N) + R_{PP}(L_N) + W_e. \quad (6)$$

(c) A brief discussion of the Born–Oppenheimer approximation is given as follows:

The Born–Oppenheimer approximation is a very useful approximation, causing very small errors. Compared to other approximations that must be used to solve the multi-electron problem, the errors can usually be ignored. If the electron motion and nuclear motion interactions are strong (electron-vibration coupling), it must be considered, which generally use the perturbation theory [21].

**3.3.2. Hartree–Fock Approximation.** Under the Born–Oppenheimer approximation, the Hamiltonian operator of the electrons in the system can be expressed as

$$K(l, L) = - \sum_n \frac{k^2}{2q_w} \nabla_{l_n}^2 + \frac{1}{2} \sum_{n,m} \frac{w^2}{|l_n - l_m|} - \sum_{n,m} \frac{C_N w^2}{|l_n - L_N|}. \quad (7)$$

We know that the key point in solving these differential equations is to calculate the Coulomb term between

electrons. Without examining the Pauli incompatibility principle between electrons and atoms, Hartree sees all electrons as operating in a mean potential field formed with other atoms, so that the situation of each atom can be explained only by the wavefunction of a single atom. Therefore, the multi-electronic problem of this treatment system can be simply approximated by treating the single-atom problem [22].

Therefore, the wave function form of the system can also be written as a continuous product form of the single-electron wave function form:

$$\psi(l) = \prod_n \varphi_n(l_n). \quad (8)$$

Thus, the total energy of the system can be expressed as

$$W = \langle \psi | K | \psi \rangle = \sum_n \langle \varphi_n(l_n) | K_n | \varphi_n(l_n) \rangle. \quad (9)$$

We know that Pauli's incompatibility principle can also be examined in the Hartree equation. Therefore, Fock has

modified the Hartree equation to change the wave function of the whole system from product type to Slater determinant, so that the system wave function satisfies the Pauli principle:

$$\psi \equiv \frac{1}{\sqrt{P!}} \begin{pmatrix} \varphi_1(a_1) & \varphi_2(a_1) & \cdots & \varphi_P(a_1) \\ \varphi_1(a_2) & \varphi_2(a_2) & \cdots & \varphi_P(a_2) \\ \cdots & \cdots & \cdots & \cdots \\ \varphi_1(a_P) & \varphi_2(a_P) & \cdots & \varphi_P(a_P) \end{pmatrix}_{a_n = (l_n, \delta_n)}. \quad (10)$$

$l_n$  and  $\delta_n$  are the coordinates and spin indicators of the electrons, respectively.

Among them,

$$\varphi(a_n) = \varphi(l_n, \delta_n) = \varphi(l_n \cdot \delta_n). \quad (11)$$

Therefore, the total energy of the system can be expressed as

$$W = \langle \psi | K | \psi \rangle = \sum_n \int dl \varphi_{n,\delta}^*(a_n) \left[ -\frac{1}{2} \nabla^2 + D_{ext} \right] \varphi_{n,\delta}(a_n) + \frac{1}{2} \sum_{n,m} \int dl_n dl_m \frac{\varphi_n^*(a_n) \varphi_m^*(a_m) \varphi_m(a_n) \varphi_n(a_m)}{|l_n - l_m|} \\ + \frac{1}{2} \sum_{n,m} \int dl_n dl_m \frac{\varphi_n^*(a_n) \varphi_m^*(a_m) \varphi_m(a_m) \varphi_n(a_n)}{|l_n - l_m|}. \quad (12)$$

Correspondingly, the Schrodinger equation for a single electron can be expressed as

$$\left[ -\frac{k^2}{2q} \nabla^2 + D_{ext}(l) \right] \varphi_n(a_n) + \sum_{n \neq m} \int dl_m \frac{|\varphi_m(a_m)|^2}{|l_n - l_m|} \varphi_n(a_n) - \sum_{n \neq m} \int dl_m \frac{\varphi_m^*(a_m) \varphi_n(a_n)}{|l_n - l_m|} \varphi_m(a_n) \\ = \sum_m \varphi_{nm} \varphi_m(a_n). \quad (13)$$

In conclusion, the Hartree-Fock equation is an adiabatic approximation for the multi-electron interaction system; that is, the electrons run in the average potential field of the nucleus. And then, the Hartree-Fock approximation considers the incompatibility principle of the electron and Pauli system and then transforms the multi-electron problem into a single electron in a certain effective potential field.

**3.4. Structure and Properties of Graphene.** With its unique electronic structure and properties, graphene is an ideal two-dimensional electronic system discovered by humans so far. Graphene is the thinnest and lightest, yet

the strongest nanometer film material in the world. Figure 4 shows the process of making graphene.

The surface of graphene is almost fully transparent, absorbing only 23% of the light, so its thermal conductivity is 5300 W/m \* K. At this temperature, its electron migration speed is 15000 cm<sup>2</sup>/V \* s, which is the nanomaterials with the least resistivity temperature coefficient known. Meanwhile, graphene also has a room-temperature quantum Hall effect and magnetic forces. These physico-chemical properties of graphene are derived from its peculiar electronic structure. Graphene is a carbon molecule made at sp<sup>2</sup>. The honeycomb single-layer plane two-dimensional crystal is similar to the single-carbon source of graphite, as shown in Figure 5. Therefore, graphene should

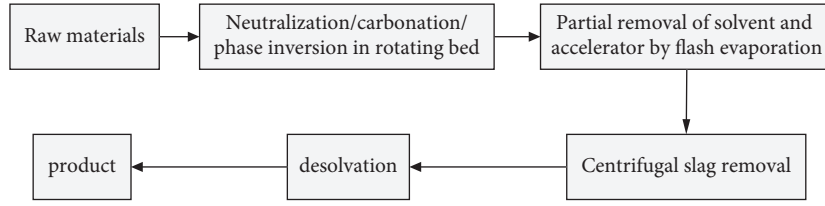


FIGURE 4: Graphene production process.

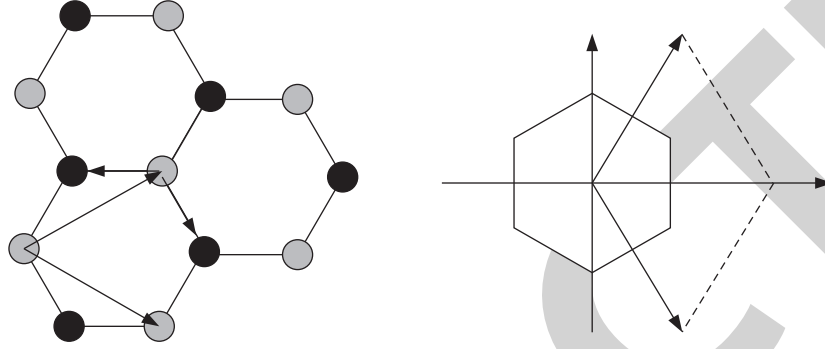


FIGURE 5: Electronic band energy structure of graphene.

be considered a planar polycyclic aromatic hydrocarbon molecular lattice structure.

As we can see from the lattice structure of graphene, it is composed of two sublattices  $X$  and  $Y$  interspersed, and the two lattice targets can be expressed as

$$x_1 = \frac{x}{2} (3, \sqrt{3}), \quad (14)$$

$$x_2 = \frac{x}{2} (3, -\sqrt{3}),$$

where  $x = 1.42^\circ X$  is the C-C bond length in graphene. The inverted target of its inverted space can be expressed as

$$y_1 = \frac{2\pi}{3x} (1, \sqrt{3}), \quad (15)$$

$$y_2 = \frac{2\pi}{3x} (1, -\sqrt{3}).$$

In addition, there are two very important high-symmetry points  $R$  and  $R'$  in the Brillouin region of graphene, whose corresponding coordinates are

$$R = \left( \frac{2\pi}{3x}, \frac{2\pi}{3\sqrt{3}x} \right), \quad (16)$$

$$R' = \left( \frac{2\pi}{3x}, -\frac{2\pi}{3\sqrt{3}x} \right).$$

Using a simple tight-binding approximation to investigate the small molecule interaction between the closest and

subclose relatives, the Hamiltonian  $T$  of graphene can be defined as

$$T = -s \sum (x_{\delta,n}^+ y_{\delta,m} + T.v.) - s' \sum (x_{\delta,n}^+ x_{\delta,m} + y_{\delta,n}^+ y_{\delta,m} + T.v.), \quad (17)$$

where  $x_{\delta,m}$  ( $x_{\delta,n}^+$ ) and  $y_{\delta,m}$  ( $y_{\delta,n}^+$ ) represent the generation and annihilation operators of the sublattices  $X$  and  $Y$ . The band structure of graphene can be calculated from the tight-binding theory:

$$W_{\pm}(h) = \pm s \sqrt{3 + g(h)} - s' g(h),$$

$$g(h) = 2 \cos(\sqrt{3} h_b x) + 4 \cos\left(\frac{\sqrt{3}}{2} h_b x\right) \cos\left(\frac{3}{2} h_b x\right). \quad (18)$$

It is clear that graphene at two high-symmetry points  $H$  and  $H'$  attachments, with a conical band structure, presents a linear dispersion relationship that can be approximately expressed as

$$W_{\pm}(u) = \pm s c_G |u| + T \left( \left( \frac{u}{H} \right)^2 \right), \quad (19)$$

where  $c_G \approx 10^6 m/s$  are the Fermi velocities near  $H$  and  $H'$ , and these high-symmetry points  $H$  and  $H'$  are called the Dirac points of graphene.

#### 4. Nanomaterials and Their Role in the Treatment of Cerebral Hemorrhage

##### 4.1. Electrochemical Detection of Rutin by Nanocomposites.

Lutin, also known as vitamin P, belongs to flavonoids and is widely found in the leaves of some plants such as Sophora

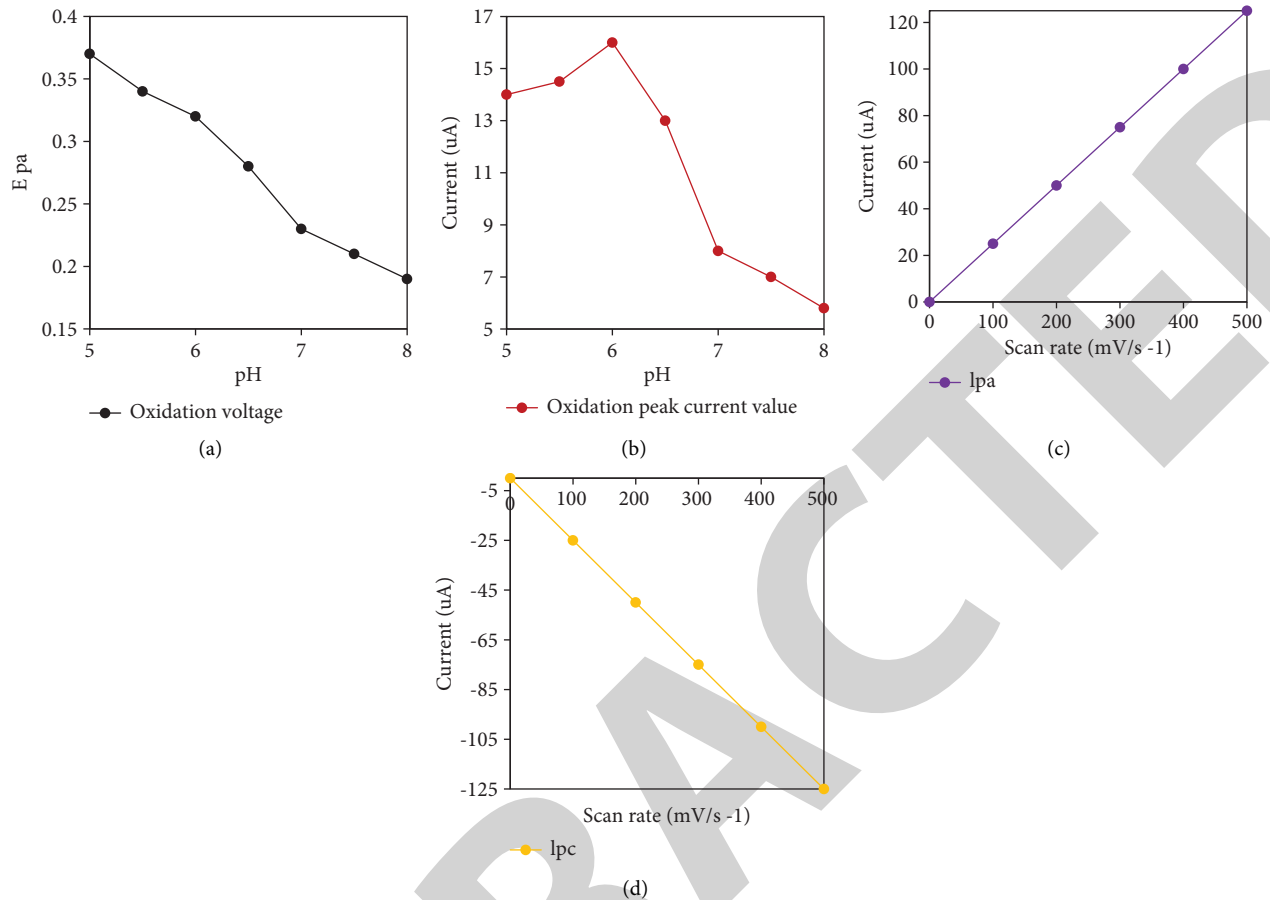


FIGURE 6: The linear relationship between oxidation voltage, current, and pH value and the linear relationship between redox peak current and scan rate.

TABLE 1: Comparison of rutin determination results with different electrodes.

Electrode	Line range ( $\mu\text{M}$ )	LOD ( $\mu\text{M}$ )
Au/en/MWNTs <sup>a</sup> /GCE <sup>b</sup>	0.047–0.096	0.031
GR/CILE <sup>c</sup>	0.06–1	0.023
IL/GCE	0.2–1	0.08
PtNPs/RGO/GCE	0.056–102.61	0.02

japonica rice and buckwheat. Rutin is usually considered a kind of active therapeutic drugs to prevent and treat diseases such as hypertension and cerebral hemorrhage. Meanwhile, and as a natural drug, rutin has obvious antibacterial, antiallergic, antioxidant, and other physical and chemical properties. However, the overdose of rutin drugs can produce serious side effects and pose a threat to human life safety. Therefore, the development of simple, economical, and sensitive rutin detection methods is of great significance for human health. So far, the laboratory detection methods used in rutin include HPLC, reverse-phase HPLC, UV visible spectrophotometry, and chemical luminescence method, but some of these methods are complicated pre-detection and require a long detection time; on the contrary, the electrochemical method is convenient, and has characteristics such as quick response, low detection limit, and

good stability; therefore, compared with these common methods, electrochemical detection method is a good choice for Rutin detection [23].

We experimentally explored the effect of solution pH on the electrochemical reaction during rutin detection. As can be seen in Figure 6, a clear linear relationship between the oxidative voltage and pH with solution pH increases, and the number of electron transport and proton transfer is the same during the redox process of rutin. In addition, the relationship curve between the solution pH value and the oxidation peak current value can also be seen. When the pH value of the solution is less than 6.0, rutin is hydrolyzed into rhamnose, glucose, and cutin under acidic conditions, so the oxidation peak current is lower to detect than the other oxidation ones. When the pH value of the solution is greater than 6.0, the oxidation peak current also appears decreasing, possibly because the flavonoids' parent core is damaged under alkaline conditions, which affects the electrochemical catalysis of rutin. Therefore, we chose pH = 6.0 as the best pH value for the detection solution.

As can be seen from Figure 6, the redox current of rutin is correlated with the sweep speed, while the peak potential of the redox peak is slightly changed, and a good linear relationship between the oxidation peak current and the pH value is shown. The linear relationship between them proves



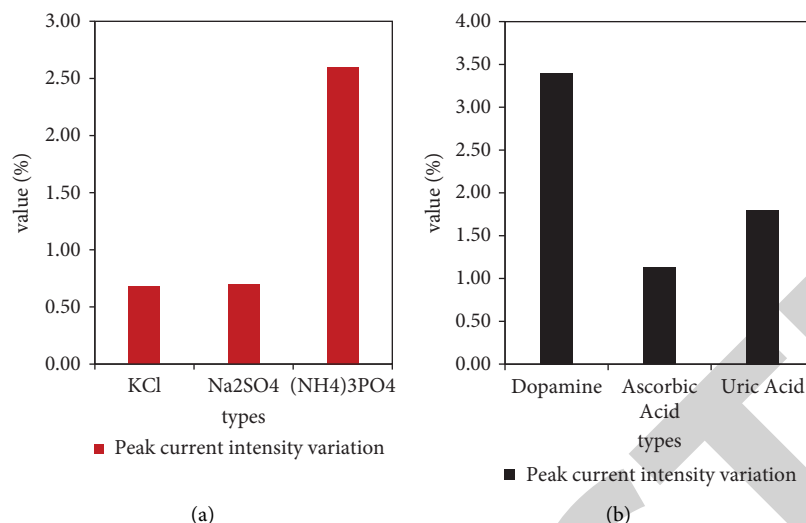


FIGURE 7: Response results of PtNPs/RGO/GCE in rutin solution to interfering ions.

that the catalytic reaction of rutin on a platinum/graphene-modified glass carbon electrode is an adsorption-controlled process.

Under the appropriate experimental conditions, we used the differential pulse voltammetry of the prepared electrode. In the range of 0.057–102.59  $\mu\text{M}$ , the oxidation peak current value of rutin and the concentration of rutin solution were positively correlated and showed a two-stage linear relationship. In the concentration range of 0.57–5.47  $\mu\text{M}$ , the oxidation peak current increases rapidly; with the concentration of rutin increasing from 5.47  $\mu\text{M}$  to 102.59  $\mu\text{M}$ , the oxidation peak current slows down, and the minimum detection limit of the electrode reaches 0.02  $\mu\text{M}$  ( $S/N=3$ ), which is much lower than the other reported detection results. As shown in Table 1, it proves that our platinum/graphene-modified glass carbon electrode shows good detection performance for rutin.

In the repetitive test, five prepared PtNPs/RGO/GCE electrodes were tested for cyclic voltammetry in 10  $\mu\text{M}$  rutin solution, with the relative standard deviation of the oxidation peak current of 1.5%, showing good repeatability of the electrodes. In addition, the prepared electrode was placed at room temperature for one week and tested every other day after the results of DPV, whose oxidation peak current value remained at 91.08% of the initial value, showing good stability of the prepared electrode. To study the anti-interference properties of PtNPs/RGO/GCE, we added 10 times the concentration of KCl, Na<sub>2</sub>SO<sub>4</sub>, and NH<sub>4</sub> to 10  $\mu\text{M}$  rutin solution; PO<sub>4</sub>, DA, AA, UA, glucose, and no obvious interference peak, as shown in Figure 7, indicating that the prepared electrode has good anti-interference performance. The recovery rate on PtNPs/RGO/GCE is 98.60%, 106.25%, and 98.90%, respectively, which shows that the prepared electrode can be effectively applied to the detection of the rutin content in commercial rutin tablets.

The composite graphene nanochip material is modified and applied to rutin detection. During the electrochemical detection of rutin, platinum nanoparticles/graphene

TABLE 2: Mobile phase ratios.

Time (min)	Mobile phase ratio	
	Methanol	0.1% formic acid water
0	34	64
2.5	34	64
4.5	49	49
6.5	34	64

composites effectively enhance the electrochemical catalytic response and improved detection performance compared with pure platinum and graphene, probably due to its large flexural area, strong conductivity, and catalytic activity. In the preparation of the electrode, the measurement range of rutin is 0.057–102.59  $\mu\text{M}$ , and the minimum measurement limit is 0.02  $\mu\text{M}$ . Meanwhile, the electrode also showed good repetition, stability, and interference resistance. This indicates that the described method for rutin detection and the prepared electrodes have great potential applications in the actual rutin detection.

#### 4.2. Intracerebral Pharmacokinetics of Trekrutin and Analogs

**4.2.1. Experimental Materials.** Clean-grade healthy mice, male and generally weighing between 18 g and 22 g, were purchased at a laboratory animal management center at a medical institution. Mice were housed in a plastic feeding cage, bedding was replaced once the other day, and water was consumed freely, after 1 week of temperature 22~25°C and humidity around 40%~60%.

**4.2.2. Experimental Method.** Internal standard material: quercetin; chromatographic analysis column: ® (50 mm × 2.1 mm, 1.7 m); flow phase: acetamide: 0.1% formic acid water; gradient elution, as shown in Table 2. Flow rate: 0.3 mL·min<sup>-1</sup>; column temperature: 30°C; mass of inflow sample: 1 L.

TABLE 3: Investigation of brain tissue matrix effect.

Samples	Concentration (ng * ml <sup>-1</sup> )	Matrix effect (%)	RSD(%)
Troloxerutin	10	93.1	1.3
	50	90.6	
	200	91.5	
Rutin	10	91.5	1.6
	50	92.4	
	200	91.4	
Troloxerutin aglycone	10	92.8	1.1
	50	91.1	
	200	90.7	

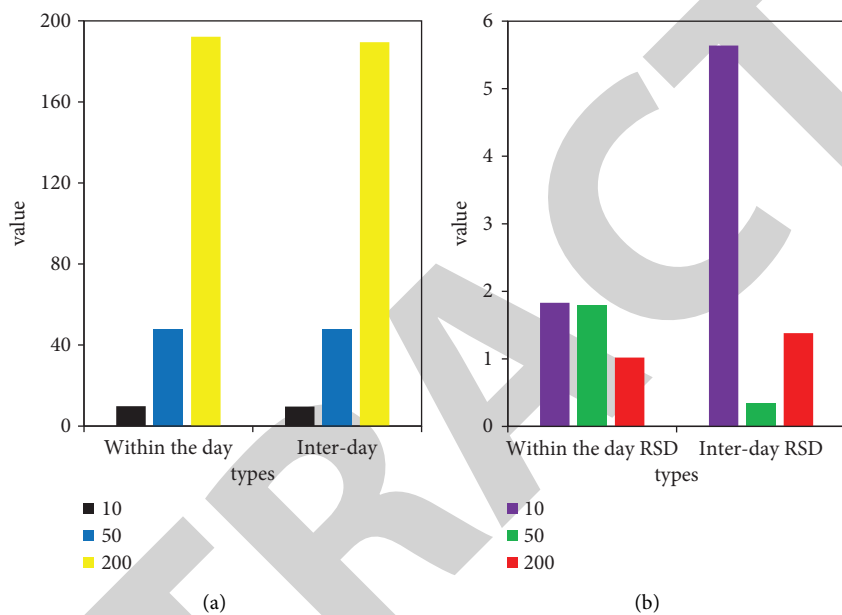


FIGURE 8: Extraction precision of troloxerutin in mouse brain tissue.

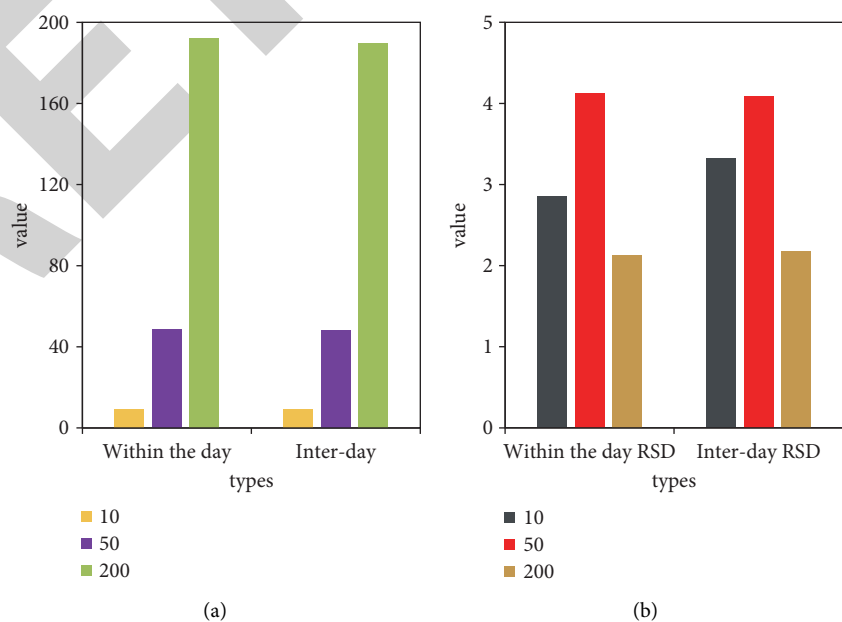


FIGURE 9: The extraction precision of rutin in mouse brain tissue.

TABLE 4: Extraction precision of troxerutin aglycone in mouse brain tissue.

Concentration (ng/mL)	Within the day (ng * mL <sup>-1</sup> )	RSD (%)	Interday (ng/mL)	RSD (%)
10	9.51	1.95	9.37	2.87
50	49.17	2.51	48.96	98.2
200	196.08	1.24	194.15	98.7

12.5 mg of troxerutin, rutin, and troxerutin aglycone were taken as the reference product, weighed accurately, and put into a 50-mL brown volumetric flask. It was hydrolyzed with an acetylpropylamine ultrasonic tube and fixed to volume to prepare a stock solution with a content of about 250  $\mu\text{g} * \text{mL}^{-1}$ , which was frozen and stored in a refrigerator at 4°C for later use.

200 L of blank brain tissue was taken and blow-dried with nitrogen, and a series of 200 L of troxerutin, rutin, and troxerutin aglycone were added to prepare low, medium, and high concentrated water solvents of 10,50,200  $\text{ng} * \text{mL}^{-1}$  and 72  $\text{ng} * \text{mL}^{-1}$ . The aqueous solution ( $n=6$ ) is the difference between the peak building area measured and the peak area measured with the same content in the blank EP tube.

**4.2.3. Results.** The brain tissue matrix has less influence on troxerutin, rutin, and troxerutin aglycone and internal target; the mean matrix effect is between 90% and 100%; and the RSD is less than 2%, which can be considered to have basically no matrix effect. The specific results are shown in Table 3.

The extraction recovery rate meets the requirements of pharmacokinetics. Intraday and daytime precision suggested that the RSD of tretin and rutin at high, medium, and low concentrations was <6.0%. The specific results are shown in Figures 8 and 9 and Table 4.

Room temperature, freeze-thaw cycles, and long-term stability were investigated, and the results showed that the RSD of rutin and low concentrations was less than 5.0%, and the stability of troxerutin, rutin, and troxerutin aglycone met the requirements.

## 5. Discussion

Rutin has antioxidative effect against the decline of antioxidant capacity caused by the decline of endogenous estrogen. At present, the pharmacokinetics reports of troxerutin, rutin, and troxerutin aglycone are mostly detected in the blood concentration, and there is no literature on the concentration determination of trekrutin and analogs in brain tissue or brain pharmacokinetics, and the detection methods are mostly HPLC. The liquid mass combination combines the characteristics of chromatography and mass spectroscopy, which combines the high separation of chromatography and the high-resolution characteristics of mass spectrometry. It has recently become a tool with high sensitivity and high specificity, and is widely used for biological sample analysis and pharmacokinetic research. In general, the mass spectrometry detection method mostly selects the MRM (multireaction monitoring) method, and

the MRM method has higher sensitivity, stronger specificity, and lower quantitative limit. In the first-level full scanning of trekrutin and analogs, it was not easy. When secondary fragment ion scanning, it was found that rutin is the same at the ion source, and too low voltage to test ionization will cause low response, and high voltage of source cracking will also cause low response; multiple groups of voltage were tried. Finally, we choose 3.49 kV capillary voltage, and used acetpropylamine and low strength formic acid as the flow phase peak tail and facilitate ionization, and then, a better peak shape and mass spectrum response were gotten.

## 6. Conclusions

Triccludin, rutin, and triccluditidine in the mouse brain tissue were extracted by methanol protein precipitation, and the UPLC-M S/MS analysis method of triccludin and analogs was first established and successfully used for the brain pharmacokinetic study of triccludin and analogs in the mouse brain tissue. The tail vein injection of troxerutin, rutin, and troxerutin aglycone peaked rapidly and eliminated more slowly in the brain. It is much higher than the other two drug groups, suggesting that the least polar logP crosses the BBB, providing a reference to study the structure of drugs passing through the BBB. However, due to the limitations of time and technology, we have not carried out research on the deeper application of rutin. We will carry out further experiments to explore this in the follow-up.

## Data Availability

No data were used to support this study.

## Conflicts of Interest

The authors declare that they have no conflicts of interest.

## References

- [1] J. Jiao, G. Xu, and X. Xin, "Effect of bile salts on self-assembly and construction of micro-/nanomaterials," *Acta Physico-Chimica Sinica*, vol. 35, no. 7, pp. 684–696, 2019.
- [2] J. F. Rincón-Morantes, O. J. Reyes-Ortiz, and J. C. Ruge-Cárdenas, "Review of the use of nanomaterials in soils for construction of roads," *Respuestas*, vol. 25, no. 2, pp. 213–223, 2020.
- [3] K. Seevakan and B. Sheeba, "Applications of nanotechnology and nanomaterials in construction," *International Journal of Pure and Applied Mathematics*, vol. 119, no. 12, pp. 6275–6286, 2018.
- [4] K. M. Lim, S. Y. Yun, and J. H. Lee, "Electrical conductivity of cementitious composites mixed with carbon-based nanomaterials used as a construction material," *Journal of the*

## *Retraction*

# **Retracted: Investigation of Insulation Properties Using Microwave Nondevastating Methodology to Predict the Strength of Polymer Materials**

### **Advances in Materials Science and Engineering**

Received 26 December 2023; Accepted 26 December 2023; Published 29 December 2023

Copyright © 2023 Advances in Materials Science and Engineering. This is an open access article distributed under the Creative Commons Attribution License, which permits unrestricted use, distribution, and reproduction in any medium, provided the original work is properly cited.

This article has been retracted by Hindawi, as publisher, following an investigation undertaken by the publisher [1]. This investigation has uncovered evidence of systematic manipulation of the publication and peer-review process. We cannot, therefore, vouch for the reliability or integrity of this article.

Please note that this notice is intended solely to alert readers that the peer-review process of this article has been compromised.

Wiley and Hindawi regret that the usual quality checks did not identify these issues before publication and have since put additional measures in place to safeguard research integrity.

We wish to credit our Research Integrity and Research Publishing teams and anonymous and named external researchers and research integrity experts for contributing to this investigation.

The corresponding author, as the representative of all authors, has been given the opportunity to register their agreement or disagreement to this retraction. We have kept a record of any response received.

### **References**

- [1] A. Gopalan, S. Ramesh, P. Nirmala et al., "Investigation of Insulation Properties Using Microwave Nondevastating Methodology to Predict the Strength of Polymer Materials," *Advances in Materials Science and Engineering*, vol. 2022, Article ID 1673263, 9 pages, 2022.

## Research Article

# Investigation of Insulation Properties Using Microwave Nondevastating Methodology to Predict the Strength of Polymer Materials

Anitha Gopalan <sup>1</sup>, S Ramesh <sup>1</sup>, Nirmala P <sup>1</sup>, Govindaraj Ramkumar <sup>1</sup>,  
Satyajeet Sahoo <sup>2</sup>, S. Agnes Shifani <sup>3</sup> and S. Arockia Jayadhas <sup>4</sup>

<sup>1</sup>Department of Electronics and Communication Engineering, Saveetha School of Engineering, SIMATS, Chennai 602105, Tamil Nadu, India

<sup>2</sup>Department of Electronics and Communication Engineering, Vignan's Foundation for Science, Technology and Research (Deemed-to-be University), Vadlamudi, Guntur, Andhra Pradesh 522213, India

<sup>3</sup>Department of Electronics and Communication Engineering, J. P College of Engineering, Vagaikulam 628102, Tamil Nadu, India

<sup>4</sup>Department of EECE, St. Joseph University in Tanzania, Dar es Salaam, Tanzania

Correspondence should be addressed to S. Arockia Jayadhas; [arockia.jayadhas@sjuit.ac.tz](mailto:arockia.jayadhas@sjuit.ac.tz)

Received 6 July 2022; Revised 13 July 2022; Accepted 19 July 2022; Published 12 August 2022

Academic Editor: K. Raja

Copyright © 2022 Anitha Gopalan et al. This is an open access article distributed under the Creative Commons Attribution License, which permits unrestricted use, distribution, and reproduction in any medium, provided the original work is properly cited.

The study was extended and developed to predict the roughness of polymer-based materials using the latest data mining techniques. Different types of particles are used in polymer-based materials, which characterize the roughness of polymer-based materials. The research study focused on predicting the roughness of bulk polymer materials using fly ash. Fly ash is an alternative material that is used to replace both cement and fine aggregate to some extent. Particles such as silica fume, limestone, and slag have been used in place of concrete, but flash has received more attention than other elements. It is important to express the insulation properties of polymer materials using the microwave nondevastative method. Finally, this article concludes by predicting the strength of polymer materials by measuring insulation properties using the microwave nondevastative method.

## 1. Introduction

The basic mixture of accumulation and lake is defined as concrete. Water and the binding material mix to form polymer concrete granules and these particles recombine with the accumulating material to form a rock structure. Due to the chemical reaction of water and the bonding material, the stone becomes a little harder and stronger. The roughness of polymer concrete increases with the age of the polymer concrete and the amount of mixing and curing affects the roughness in compression [1]. This also includes mixing, treating, inserting, and inspecting the concrete. Most of the construction process uses high roughness concrete. Polymer concrete has a superior blend of presentation and consistency

requirements known as high roughness concrete. Typically, polymer concrete is said to have a strong point when it is set for 28 days. Therefore, different countries have different mixing ratios and terminologies to define polymer concrete as high roughness concrete [2].

There are 24 types of polymer concrete used for construction purposes, and in this case, the most commonly used polymer concrete will be discussed. These are bearing concrete, normal strength concrete, ultrahigh performance polymer concrete, and polymer concrete. In this polymer, the concrete plays an important role, the aggregates bond with the polymer rather than with the cement, helping to reduce the void volume in the aggregate. Polymer concrete is divided into three types:

impregnated concrete, partially impregnated polymer concrete, and polymer cement concrete [3].

Cement is the most expensive ingredient in polymer concrete mixes. When the cost of cement increases, the cost of polymer concrete also increases; the only way to reduce the cost of polymer concrete is to reduce the cost of cement or substitute another material instead of cement particles. Most research studies have been done to reduce or replace cement particles. Materials such as slag, silica fume, and limestone are some of the powdered materials that replace cement particles. The main purpose of cement in polymer concrete is to fix each fine or coarse aggregate and the cement paste is filled between the aggregate particles [4]. The former depends on the specific surface of the accumulator and the aggregate depends on the porosity of the accumulator. In some cases, polymer concrete is recycled and used again, but this reduces the roughness of the concrete.

Polymer concrete materials contain defects, cracks, defects, and inhomogeneities and to find these defect patterns in polymer concrete materials, different types of techniques have been used. This technique is classified into two types: devastating methods and nondevastating methods. The devastating type evaluation technique has many advantages over the nondevastating type evaluation method [5]. The main advantage of the devastating method is that it is less expensive and has good drilling conditions compared to nonmetallic materials, but the major disadvantage of devastating methods is that they cannot come into contact with the microwave sensor. This is remedied by the method of the nondevastating type. This method is accompanied by the insulating properties of metals and polymer concrete [6, 7].

The paper explores predicting the roughness of a polymer concrete material with the replacement of fly ash in the place of cement using a neural network. This also defines the insulation properties of concrete. The introduction part defines the overall basic nature of polymer concrete and the predicted rate. Section 2 rolls around the related work done based on the prediction level and the effect of ration in a polymer concrete material. The scope of the work is determined in Section 3 and the experimental work is defined in Section 4 and then it is concluded in the last section.

## 2. Related Works

To predict the compressive roughness of the polymer concrete of slump, the authors of [6] proposed a method using a neural network. This method defines the roughness of the concrete, mostly the research study deals with higher roughness. Although a fly ash content lower than 25% of the total cement content is a regular, when it is used in concrete, high volume fly ash polymer concrete (HVFA) is not widely used due to the perceived low forces in young children. Corresponding bottles were used during this process to estimate the roughness of HVFA polymer concrete in place at an early age and to confirm the expected mature forces. The results showed that the roughness of the standard and field hardened cylinders underestimates the roughness of the existing concrete. The high temperature defines the mass characteristics of the structural element. This increases the

reasonable place of the construction, roughness, and match cured cylinders.

Previously issued tentative data on the impact of nuclear radioactive on the assets of ordinary polymer concrete are canalized and 2 are evaluated. Neutron radioactive with a crore fence greater than  $1 \times 10^{19}$  n/cm may have an adverse effect on the roughness of the polymer concrete and the elasticity of ball joints [8]. The thermal expansion coefficient, thermal conductivity, and shielding assets of polymer concrete are largely unaffected by radioactivity. Radioactive damage is mainly caused by mesh defects in the cumulative, resulting in increased cumulative and polymer concrete volume. Various cumulative factors present a different radioactive resistance, so the selection of appropriate cumulative is the important parameter of frost in the design of a radioactive-resistant concrete.

The compressive roughness of polymer concrete is the most commonly used criterion for polymer concrete production. However, compression testing of the roughness of polymer concrete samples is a complex and time-consuming task [9]. Therefore, forecasting resistance prior to polymer concrete installation is highly necessary. This study presents the application effort of the neural network technique to predict the compression resistance of polymer concrete as a function of the proportions of the polymer concrete mixture. The data set of a combination of different industries was needed for the training and testing data and they also require trial and error for forecasting the compressive roughness [10].

*2.1. Scope of Research.* The research study is based on the prediction of the strength of polymer concrete using the neural network and then on the study of insulation properties of polymer concrete using the nondevastating microwave method.

## 3. Materials and Methods

The analysis was done on polymer concrete with coal fly ash and glass fibers. The following raw materials were used to prepare the concrete: cement, fly ash, river aggregate, gravel, and glass fibers. A very small round particle is combined together and they are known as the coal ash, and they also contain amorphous glass and crystalline phases. The diameter of the concrete is said to be 0.01 to 400  $\mu\text{m}$ . The main property of coal is the grey color powder substance and the presence of pozzolanic assets. The pozzolanic assets are said to have high binding capacity and this is mostly used in the preparation of concrete and concrete mixed products. Table 1 defines the features of the coal ash used for the experimental analysis. The management concrete composition was grade C25/30: cement 360  $\text{kg}/\text{m}^3$  (of that 100 percent was replaced with coal fly ash), diameter 0–4 metric linear unit in an exceedingly amount of 803.16  $\text{kg}/\text{m}^3$ , diameter 4–8 metric linear unit in an exceedingly amount of 384.12  $\text{kg}/\text{m}^3$ , diameter 8–16 metric linear unit in an exceedingly amount of 558.72  $\text{kg}/\text{m}^3$ , water one hundred eighty  $\text{L}/\text{m}^3$ , and superplasticizer kind Cervus sika ViscoCrete-1040 in an exceedingly indefinite quantity



TABLE 1: Features of coal ash.

Element	Coal ash (Wt %)	At %
CL	17.18	26.90
NL	01.35	01.81
OL	37.55	44.15
NaL	00.70	00.57
MgL	0.55	00.42
AL	13.10	09.15
SiL	18.40	12.35
SL	00.72	00.42
LL	01.75	0.85
CaL	03.18	01.50
TiL	01.72	00.69
FeL	04.01	01.36
Matrix	Alteration	ZAF

of one. 4% of the cement weight. Close to the management combination, a variety of thirteen mixes were established by employing a turned focused composed program of second order, with 2 variables. The overall range of tests was statistically established taking into consideration the number of freelance variables, the sort of analysis that was done and therefore the style of experimental setup that was chosen. The following 2 variables were chosen for the input: length and indefinite quantity of optical fiber. The dosages of glass fibers were between zero, 25%, and 1.75% of the concrete mass; therefore, the lengths were between five metric linear units and thirty five metric linear units. The experimental matrix contains a variety of thirteen experiments (13 mixes).

The table represents the mass percentage (Wt) and atomic number (At) and L represents the layer to which the chemical properties are determined. In different amounts, the glass fiber is added to mix the concrete. The percentage of the fiber was between 0.25% and 1.75% weight of concrete and the length of the fiber was between 5 mm and 35 mm. The yarn strength is determined as the properties of the fiber and it is about 76.6 N and the loop strength is about 101.86 N [10]. The aggregate was different types of natural sand and river gravel, and the diameter is of 4–8 mm and 8–16 mm. By different parameters like aggregate, water, cement, and other materials, the mechanical assets of the concrete were affected. Hence, by influencing the coal ash and the fiberglass, the workable strength of the concrete can be evaluated [11].

In Figure 1, factors affecting concrete properties are illustrated. The mechanical properties of concrete are mainly influenced by this type of factor. By mixing the aggregate with cement, coal ash, and water, the concrete is prepared, and the glass fiber was introduced into the fresh mixed particle before the final process. Then, the concrete is transformed into the mold and kept at a condition of 20°C. This is a normal temperature to be kept in. As polymer concrete use a polymer binder instead of cement and other aggregate particles, they are totally different from the conventional type of concrete. Although it may be used in construction such as conventional polymer concrete [12], it has several unique features that make it more durable than

conventional concrete. Polymeric concrete has the following properties:

*Curing property:*

The hardening effect is quick at ambient temperatures between –18 and 40°C (0 to 104°F). Polymer concrete develops 70% resistance after a day of hardening at room temperature while conventional polymer concrete gains only 20% of its 28-day resistance in a day.

*Strength:*

Polymer concrete has high tensile strength, bending strength, compression strength, and good abrasion resistance compared to cemented concrete.

*Durability:*

Polymer concrete provides good long-term durability of concrete with regard to freezing and thawing cycles and chemical attacks, as it reduces chloride and salt intrusion.

*Lightweight:*

When polymers are used in concrete, light polymer concrete is produced.

*3.1. Bond-Slip Characteristics of Polymer-Concrete.* The load end and the slip end are essentially the same, but they are somewhat delayed in moving the free end [13]. Hence, the complete improvement is often merely segmented into 3 stages [14].

Tables 2 and 3 define the relationship between the moisture strength and bonding strength. When the concrete is totally saturated, increasing the chemical compound density has very little result on the bond strength.

*3.2. Neural Network Model Design Process.* For predicting the strength of the concrete, the error propagation and the recall algorithm is used because this method can proficiently solve the variable problems in the system. The step-by-step process for the expansion of ANN has been designed. To predict the strength of the polymer concrete material, single ANN architecture is used. Based on the research design, cement is replaced by fly ash and the mixture is made of fine aggregate and coarse aggregate. By using the neural network method, the strength of the polymer concrete is predicted and the microwave nondestructive method is used to define the insulation properties of the concrete [15]. To blend the polymer concrete, the ribbon mixture is made and then they are mixed together to form concrete. Specific representation is made for the polymer concrete mix such as specific gravity and fineness modulus of sand and coarse are 2.64, 2.2, and 2.81, 6.5, respectively.

The neural network developed in this research comprises seven variable quantities in the input layer and two variables in the output layer and is represented in Figure 2 [16]. The main problem is choosing the hidden layer to any extent and this depends on the number and training design quality; this helps to analyze the optimal sum of the hidden layers. The rate of components used in this study is given below:

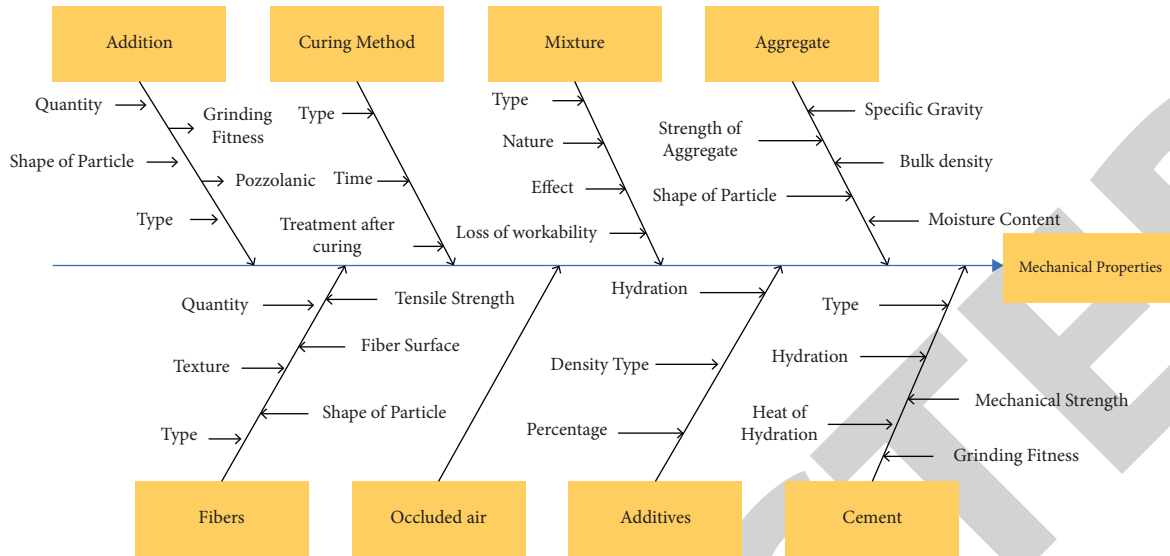


FIGURE 1: Factors affecting concrete properties.

TABLE 2: Moisture strength.

Number	Temperature (°C)	Moisture (%)	Average moisture (%)
1-3	0	0	0
		0	0.99
		0.9	
13-15	0	1.04	0.83
		1.12	
		0.96	
25-27	0	0.48	1.3
		1.09	
		0.95	
37-39		1.20	
		1.80	

TABLE 3: Bonding strength.

No	Temperature (°C)	Bond strength (MPa)	Avg. bond strength (MPa)
1-3	0	0.43	0.49
		0.57	
		0.48	
13-15	0	0.39	0.72
		0.45	
		0.10	
25-27	0	0.30	0.20
		0.65	
		1.13	
37-39		0.28	
		0.2	
		0.11	

No of input element = 7  
 No of hidden layer = 2  
 No of first hidden layer = 5

No of second hidden layer = 3

No of output layer = 2

Based on the binding, the mixture has to be blend for 2 minutes to get a perfect mixture. To make the polymer concrete, a cube sample is taken and it is casted using the steel molds, and to replace the fly ash in the place of cement or sand, a table vibrator is used. The following equation is used to predict the strength of the polymer concrete material [17]. Five features were involved in the modeling process of the neural networks; they are data acquisition, architecture, learning process, and testing. During the testing process, certain errors could occur and they are expressed in terms of root mean square and the expression is as follows:

$$RMS = \sqrt{\left(\frac{1}{d}\right) * \sum_i |v_i - p_i|} \tag{1}$$

Despite the variance and the mean absolute percentage error, the sum of the square error are analyzed using the following expression:

$$R^2 = 1 - \left(\frac{\sum_i (v_i - p_i)}{\sum_i (p_i)^2}\right),$$

$$Mean\ Absolute\ Percentage\ Error = \left(\frac{p - v}{p}\right) * 100,$$

$$Sum\ of\ Square\ Error = \sum_i (v_i - p_i)^2. \tag{2}$$

In which,  $v$  denotes the value of the target,  $p$  denotes the value of output, and  $d$  is the pattern design. From the outside environment, the information is received by the input layer neurons and the information transmitted is passed to the hidden layer. Passing the information to the hidden layer does not require any performance calculation [18]. The

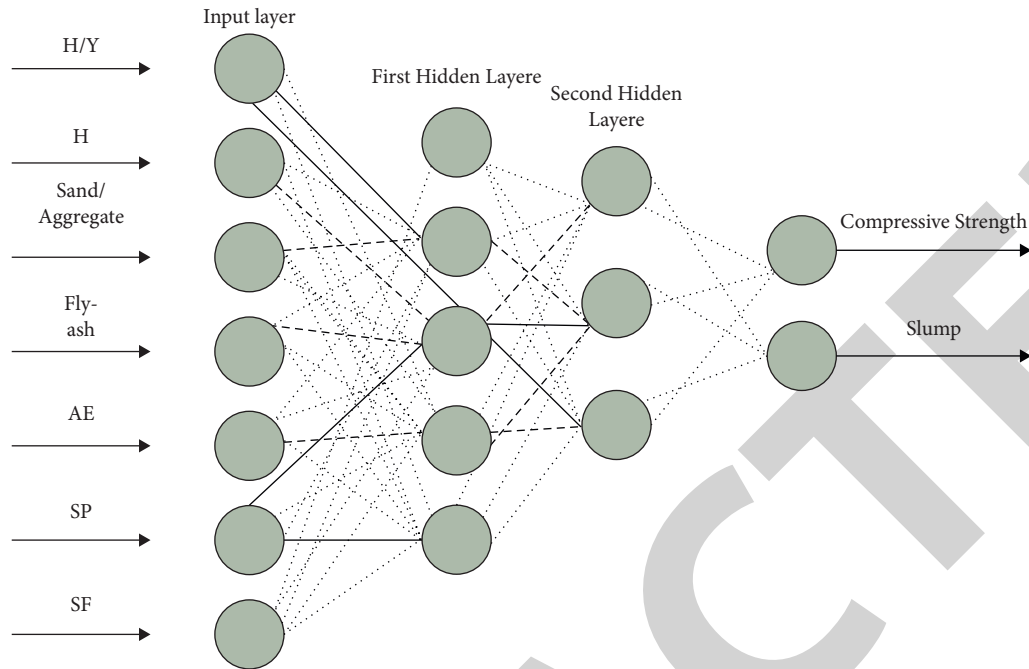


FIGURE 2: Neural network model.

incoming information in the hidden layer is performed and the useful information is extracted to recreate the mapping process from the input space. The input layer is interrelated by the weight. The network prediction is produced to the outside world by the output neurons. For choosing the neurons in the hidden layer, there is no general rule or process that has to be done. The quality of the training pattern is influenced by the choice of the hidden layer [19].

**3.3. Technique of Radio Wave Nondestructive Monitoring.** To detect the 1–100 kHz radio frequency range, nondestructive radio wave monitoring is used. The radio wave frequency is categorized into two different methods; they are the parallel plate electrode system and mobile insulation robe sensor. The first method is widely used in the medical laboratory and research units and the second method is used in designing the surface sensor and this sensor is lightweight and simple [20]. This method is widely used in the surface sensor because this could provide data at different points. In this research study, the nonconductor properties of polymer concrete material are determined via the microwave non-destructive method which is a part of the MDPS technique.

The microwave nondestructive testing is an important method related to the electrical method in which the utilization of microwave frequency is done. The alternating current or the electromagnetic wave with the frequencies range of 300 MHz and 300 GHz is termed as microwave. The microwave non-destructive system uses the frequency range of about 7–15 GHz. The good conducting material contains a short penetrating range than other conducting materials and the microwave nondestructive method is widely used in nonmetallic materials [21]. There are two types of microwave non-destructive methods: free space microwave method and waveguide

technique. The far-field region operation is carried out in the free space microwave method and the near-field region operation is carried out in the waveguide technique [22]. The waveguide technique involves flexible coaxial lines, quadrilateral waveguide, microstrip lines, and crack cavity resonator as probes. This method uses horn antenna as it is a contactless system and Figure 3 shows the representation of free space microwave test method. The system uses the MNDT for the estimation of polymer concrete materials.

Using two horn antennas, the free space microwave test method is done, and for blistering and getting rays, an open-ended rectangular waveguide is used. From the sample, the distance of the horn is calculated and it is done by using the frequency range. In the center of the coils, a sample holder holds the test material. It is important to align the position of the sample holder and the antenna position. In all directions, the two antennas are symmetric to each other and this is done to eradicate the dissimilarities of the incident and reflected waves. The horn antenna used here could focus on the spot of each polymer concrete material. A flat-convex lens mounted back-to-back in a conical antenna in this one convex lens provides the electromagnetic plane wave and the next one shows the focus of electromagnetic radiation. Nearly, 8–12.50 GHz frequency range is observed and it is said that the same technique can be used to predict the frequency of about 7.5 to 40 GHz.

## 4. Result and Discussion

The water ingestion of concrete-based materials connects with their own permeability and it is higher once the permeability is bigger. Correlation of water retention rate and its effects of standard administration test on mortars/cements solidified with three-layer nongovernmental association [23].

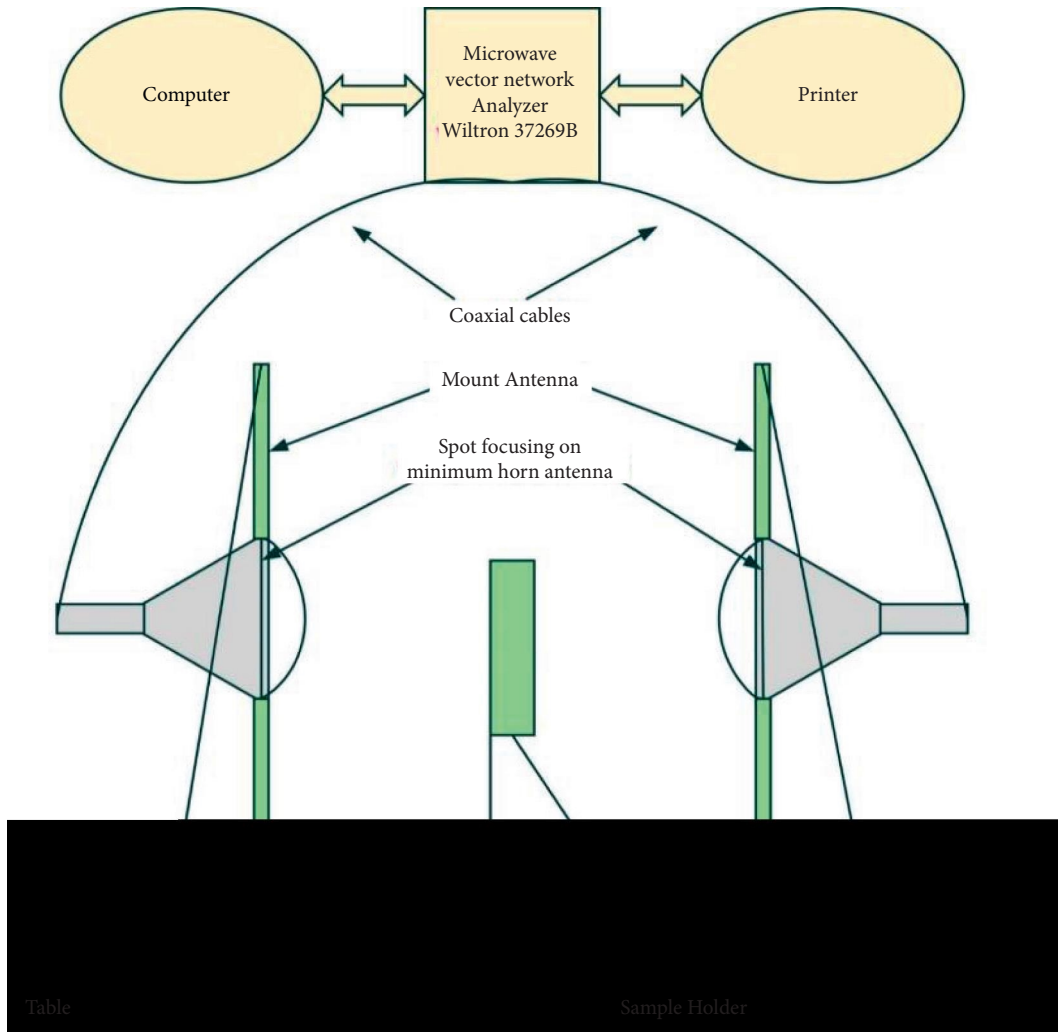


FIGURE 3: Free space microwave method.

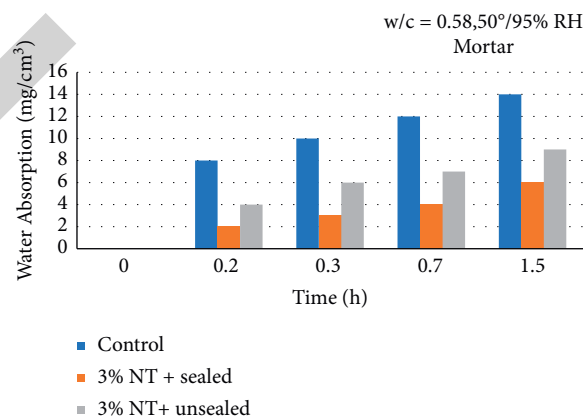


FIGURE 4: Time vs. water absorption of trial data with 50°C.

For unlocked mortars, water retention greatness connection at 1.5 h decreases by or so four-hundredth, while that of fixed may downsize by around 50–60% contrasted and the administration test. Also, from

the trial data of 50°C and 20°C, as shown in Figures 4 and 5 clearly increasing the regular interaction temperature could not uniquely work on the smallness of mortars.

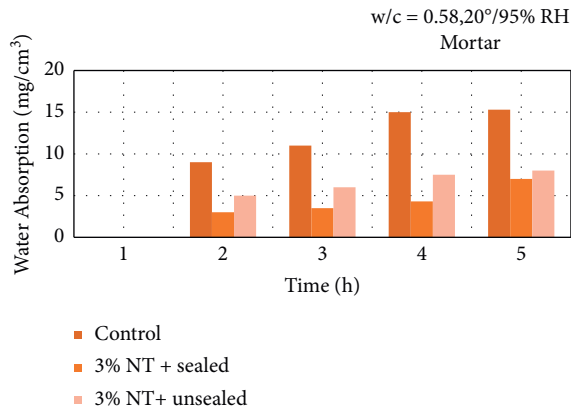


FIGURE 5: Time vs. water absorption of trail data with 50°C.

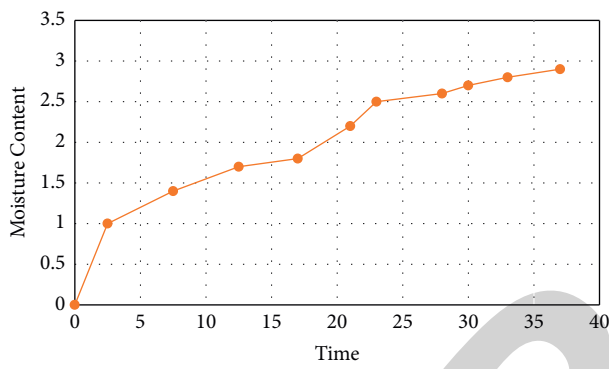


FIGURE 6: Moisture growth.

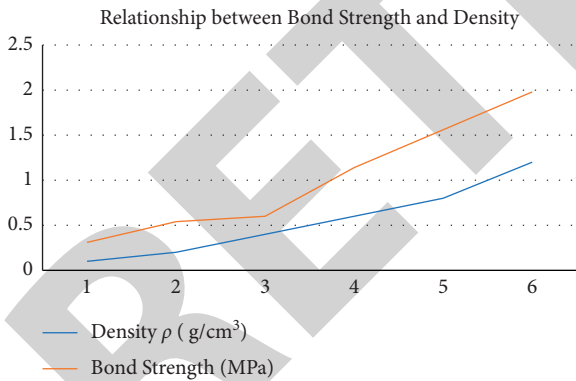


FIGURE 7: Relationship between bond strength and density.

TABLE 4: Relationship between the bond strength and density.

Density $\rho$ (g/cm <sup>3</sup> )	0.1	0.2	0.4	0.6	0.8	1.2
Bond strength (MPa)	0.3	0.5	0.6	1.1	1.5	1.9

Figure 6 shows the moisture growth content in the concrete. The cracks in the concrete are fully saturated for a prolonged immersion of time. In this research method, the sample used having high strength and the measure in the moisture content is shown in Figure 4. This shows that as the

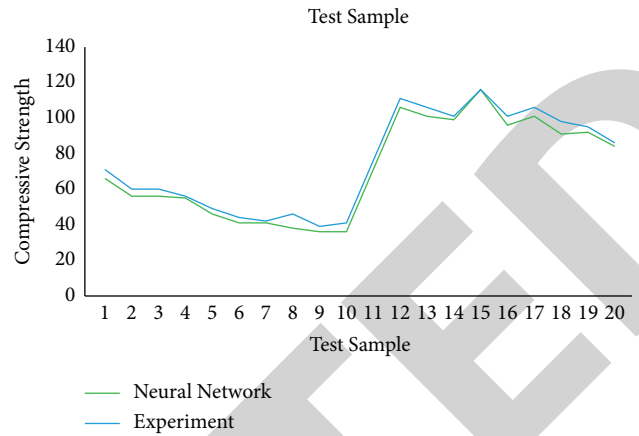


FIGURE 8: Test sample.

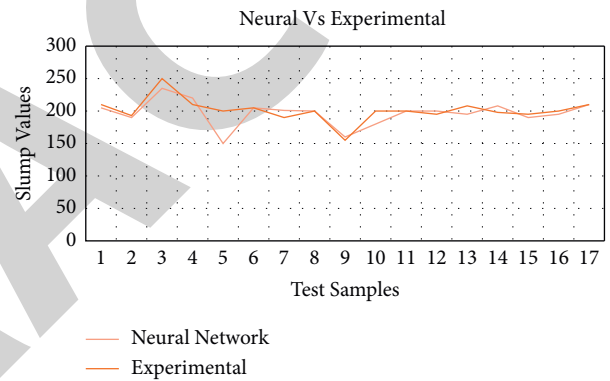


FIGURE 9: Neural vs. experimental.

time increases, the moisture content in the concrete starts to grow, while soaking in the water the moisture rises to the peak in the initial stage and then slows down after 24 hours. Consequently, the moisture content corresponding to the 24-hour immersion period can be considered as the saturated moisture content (approximately 2.66%)

Figure 7 illustrates the relationship between bond strength and density. The research study analyzes the strength of the polymer and the concrete under 25°C and in dry conditions. Table 4 defines the relationship between the bond strength and density.

Figures 8 and 9 show the graphical representation of the comparison between the neural network and the experimental compressive strength and the slump values. The numerical value for both the compressive and slump value is calculated by the training and tests, such as root mean square and variance. Based on the proposed neural network model, the mean absolute square value is 2.61710% and 660954; in the training set, the value is 1.956210% and 5.78225% for the compressive strength of polymer concrete material. The value for variance is about 100.897% and 100.257% for the compressive polymer concrete strength and the training set is about 99.91% and 99.3455%. The variance, mean square,

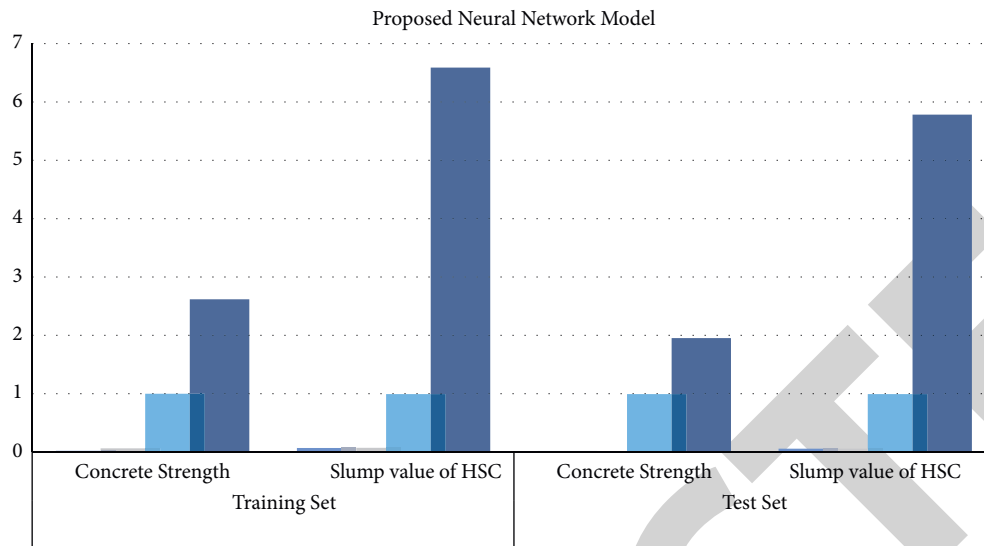


FIGURE 10: Proposed neural network model.

and square root are tested for both the compressive strength and the slump value of the polymer concrete material.

Figure 10 shows the proposed neural network model. The comparison between the concrete strength and the slump value of HSC is plotted against the training set and test set. In each set, the slump value in the training set is high when compared to the other set and the concrete strength remain constant for both the training set and test set.

## 5. Conclusion

The study describes the prediction of compressive strength of polymer-based materials and a nondestructive method is used to predict the insulating properties of polymer-based materials. The strength of polymer concrete is predicted using a neural network and by performing a predictive computation. The fly ash replacement and the preparation of polymer-based materials are explained by schematic diagrams and followed by the determination of the neural network layer for the significant strength of the polymer. The strength prediction of polymer concrete is performed and the results are tabulated based on a comparison between the neural network and the experimental setup. A training and test set was determined for the neural network system, and then, a nonharmful microwave method was performed to represent the electrical insulation and microwave frequency properties of the polymeric elementary particles. The main advantage is that by replacing cement with fly ash, the cost of the polymer can be significantly reduced. The strength frequency of polymer concrete was determined by the free-space microwave method. Overall, the study design provides a better standard for predicting the strength of polymer concrete and the insulating properties of the base polymer are studied by nondamaging microwave methods.

## Data Availability

The data used to support the findings of this study are included within the article.

## Conflicts of Interest

The authors declare that there are no conflicts of interest regarding the publication of this article.

## Acknowledgments

The authors would like to express their gratitude towards Saveetha School of Engineering, Saveetha Institute of Medical and Technical Sciences (formerly known as Saveetha University), for providing the necessary infrastructure to carry out this work successfully.

## References

- [1] T. Phoo-Ngernkham, C. Phiangphimai, N. Damrongwiriyanupap, S. Hanjitsuwan, J. Thumrongvut, and P. Chindaprasirt, "A mix design procedure for alkali-activated high-calcium fly ash concrete cured at ambient temperature," *Advances in Materials Science and Engineering*, vol. 2018, Article ID 2460403, 12 pages, 2018.
- [2] S. Behranvand and V. Behranvand, "Polymeric nanoparticles: recent development in synthesis and application," *Express Polymer Letters*, vol. 10, no. 11, pp. 895–913, 2016.
- [3] R. Bedi, R. Chandra, and S. Singh, "Mechanical properties of polymer concrete," *Journal of Composites*, vol. 2013, Article ID 948745, 12 pages, 2013.
- [4] Nirmala, "Artificial intelligence to analyze the performance of the ceramic-coated diesel engine using digital filter optimization," *Advances in Materials Science and Engineering*, vol. 2021, Article ID 7663348, 10 pages, 2021.
- [5] F. Deng, Y. He, S. Zhou, Y. Yu, H. Cheng, and X. Wu, "Compressive strength prediction of recycled concrete based on deep learning," *Construction and Building Materials*, vol. 175, pp. 562–569, 2018.
- [6] K. Kovler, "Does the utilization of coal fly ash in concrete construction present a radiation hazard?" *Construction and Building Materials*, vol. 29, pp. 158–166, 2012.
- [7] B. N. Ganguly, *Nanomaterials in Bio-Medical Applications: A Novel Approach*, Materials Research Foundations, Millersville, PA, USA, 2018.



## *Retraction*

# **Retracted: A Multisensor Data Fusion Based Anomaly Detection (Ammonia Nitrogen) Approach for Ensuring Green Coastal Environment**

### **Advances in Materials Science and Engineering**

Received 26 December 2023; Accepted 26 December 2023; Published 29 December 2023

Copyright © 2023 Advances in Materials Science and Engineering. This is an open access article distributed under the Creative Commons Attribution License, which permits unrestricted use, distribution, and reproduction in any medium, provided the original work is properly cited.

This article has been retracted by Hindawi, as publisher, following an investigation undertaken by the publisher [1]. This investigation has uncovered evidence of systematic manipulation of the publication and peer-review process. We cannot, therefore, vouch for the reliability or integrity of this article.

Please note that this notice is intended solely to alert readers that the peer-review process of this article has been compromised.

Wiley and Hindawi regret that the usual quality checks did not identify these issues before publication and have since put additional measures in place to safeguard research integrity.

We wish to credit our Research Integrity and Research Publishing teams and anonymous and named external researchers and research integrity experts for contributing to this investigation.

The corresponding author, as the representative of all authors, has been given the opportunity to register their agreement or disagreement to this retraction. We have kept a record of any response received.

### **References**

- [1] C. Qu, Z. Zhou, Z. Liu, S. Jia, L. Ma, and M. I. Sheela L, "A Multisensor Data Fusion Based Anomaly Detection (Ammonia Nitrogen) Approach for Ensuring Green Coastal Environment," *Advances in Materials Science and Engineering*, vol. 2022, Article ID 4632137, 6 pages, 2022.

## Research Article

# A Multisensor Data Fusion Based Anomaly Detection (Ammonia Nitrogen) Approach for Ensuring Green Coastal Environment

Chong Qu,<sup>1,2</sup> Zhiguo Zhou,<sup>3</sup> Zhiwen Liu,<sup>3</sup> Shuli Jia,<sup>4</sup> Liyong Ma ,<sup>5</sup>  
and Mary Immaculate Sheela L <sup>6</sup>

<sup>1</sup>School of Information and Electronics, Beijing Institute of Technology, Beijing, China

<sup>2</sup>Automation, Engineering Department, Shanghai Marine Diesel Engine Research Institute, Shanghai, China

<sup>3</sup>School of Information and Electronics, Beijing Institute of Technology, Beijing, China

<sup>4</sup>Automation Engineering Department, Shanghai Marine Diesel Engine Research Institute, Shanghai, China

<sup>5</sup>School of Science and Engineering, Harbin Institute of Technology, Weihai, China

<sup>6</sup>DEAN-FESAC, Pentecost University, Accra, Ghana

Correspondence should be addressed to Liyong Ma; [liyongma2@gmail.com](mailto:liyongma2@gmail.com) and Mary Immaculate Sheela L; [misheela@pentvars.edu.gh](mailto:misheela@pentvars.edu.gh)

Received 14 May 2022; Revised 9 June 2022; Accepted 15 June 2022; Published 11 August 2022

Academic Editor: K. Raja

Copyright © 2022 Chong Qu et al. This is an open access article distributed under the Creative Commons Attribution License, which permits unrestricted use, distribution, and reproduction in any medium, provided the original work is properly cited.

Great changes have been brought about by the coastal environment when the economy develops rapidly. Coastal environmental monitoring is the basis and technical guarantee for coastal environmental protection supervision and management. It is one of the important tasks to detect and timely discover coastal seawater anomalies. Usually, a single sensor cannot determine whether the coastal environment or ship operation is an anomaly. Recently, an unmanned surface vehicle for coastal environment monitoring was developed, and stacked autoencoders are used for seawater anomaly detection using multisensor data fusion methods. The multisensor data of pH, conductivity, and ammonia nitrogen are employed to judge the anomaly of seawater. The mean, standard deviation, mean square root, and normalized power spectrum features of multisensor data are extracted, and a stacked autoencoder is employed to fuse these features for anomaly detection. The proposed method is feasible and effective for anomaly detection of coastal water quality and ship operation. Compared with other commonly used methods, the proposed method has a higher recall, precision, and *F1* score performance.

## 1. Introduction

The coastal environment is closely related to human life. With the rapid economic development around the world, great changes have been brought about in the coastal environment. In particular, the increasing environmental degradation, including coastal environmental pollution, is increasingly threatening human health. Environmental monitoring has always been one of the most effective ways for mankind to control environmental pollution, and it is also an essential key step in environmental governance. Coastal environmental monitoring is the basis and technical guarantee for coastal environmental protection supervision and management. The types and concentrations of

pollutants in coastal waters can be measured and compared through real-time monitoring of the coastal environment, which can provide scientific and quantitative data for coastal environmental protection. In recent years, more and more automated methods for real-time monitoring of water quality have been studied. Anomaly detection of different types of water quality has been studied [1–7], some of the main types of research literature are listed in Table 1, and the corresponding main methods are also listed in the table. Artificial intelligence methods are increasingly used in these studies. Also, there are few studies on the quality anomaly detection of water in coastal environments. This automatic monitoring is completed by various sensors. Usually, a single sensor cannot determine whether the coastal environment is

TABLE 1: Anomaly detection for different water types.

Content	Anomaly detection method
Groundwater level	Artificial neural network [1]
Surface water quality	Bayesian autoregressive [2]
Aquaculture water	Density clustering [3]
Wastewater	One-class classifier [4]
Drinking water	Direct measurement [5]

abnormal and whether the ship's state is abnormal [8–11]. How to comprehensively use these sensors to provide environmental anomaly detection and anomaly detection of ship equipment itself is a practical problem that needs to be solved.

Recently, an unmanned surface vehicle (USV) for coastal environment monitoring was successfully developed by the author team [8–10]. A data platform was developed and deployed on the ship [11]. The data platform stores various sensor data in a distributed manner. These sensors collect a large amount of data on coastal environment data and ship power, propulsion, and navigation data. The ship mainly completes regular ecological monitoring of water quality and pollution. Conduct surveillance monitoring of important continental source sewage outlets and coastal projects along the coast. The ship is equipped with biological testing, microbial testing, hydrological measurement, and water quality monitoring equipment. The ship is equipped with a multiparameter water quality analyzer, flow meter, and automatic sampler with a volume of 5L. The marine hydrological parameters that the ship can monitor include wind speed, direction, flow rate, flow direction, ambient temperature, and atmospheric pressure. Water quality biological state measurements include solvent oxygen, pH value, salinity, and various nitrates. It is also equipped with an acoustic doppler current profiler (ADCP) and single beam side-scan sonar. The ship is equipped with a global positioning system (GPS), video surveillance, automatic navigation, and an intelligent data platform, which can upload data to the shore data center. It has the functions of autonomous navigation, and it supports all navigation and sampling tasks through remote intelligent control. The ducted propeller is used to effectively waterproof grass, branches, fishing nets, and other foreign objects.

Water quality monitoring is an important part of coastal environmental monitoring. An anomaly means that the data monitored by the sensor does not conform to the usual pattern. One situation is that the value of the seawater quality index exceeds the normal range, and the other is that the change of the data does not conform to the change law of the context, but the value does not exceed the normal range. The former is easy to judge, while the latter is more difficult to detect. Generally, abnormal seawater quality cannot be judged by single-sensor data. Stacked autoencoders are used for seawater anomaly detection using multisensor data fusion methods. The multisensor data of pH, conductivity, and ammonia nitrogen are fused to judge the anomaly of seawater. As a kind of autonomous navigation equipment, an unmanned vessel's anomaly detection of equipment and navigation data is also one of the necessary functions. This

paper also studies multisensor anomaly detection based on power propulsion and navigation data in an unmanned ship based on an autoencoder. Artificial intelligence (AI) has been rapidly developed, and AI has made great progress in recent years and has achieved great success in the fields of classification, recognition, and anomaly detection [12–17]. Autoencoder is an unsupervised machine learning method of AI. Autoencoder is employed for anomaly detection by multisensor data fusion in this paper.

The innovation of this research is as follows. Firstly, a fusion method employing stacked autoencoders is proposed, and the method is applied to anomaly detection. Secondly, anomaly detection applications for coastal water quality and the operation of UAVs are described. Compared with other commonly used methods, the proposed method has a higher recall, precision, and  $F1$  score performance.

## 2. Methods

Autoencoder has received extensive attention in the field of machine learning and has been successfully used in data dimensionality reduction, feature extraction, fault diagnosis, and other fields. Autoencoder is trained to learn a reconstruction close to its original input. By using the hidden representation of the autoencoder as the input of another autoencoder, the autoencoders are stacked to form a deep autoencoder. Anomaly detection based on an autoencoder is a semisupervised learning method based on deviation, which is especially suitable for tasks such as anomaly detection. In the anomaly detection task, there are a lot of normal data, and the sample data of anomaly data are less, which is not statistically significant. Stacked autoencoders that combine deep networks and autoencoders can better realize the effective expression of data in low-dimensional feature spaces through hierarchical learning [13–17].

*2.1. Autoencoder.* The architecture of the standard autoencoder is illustrated in Figure 1. It has a fully symmetrical network architecture. The network is symmetrical with the hidden layer as the center, and the two sides of the network are the input and output layers. When the hidden layer in the middle is used as the axis of symmetry, an encoder,  $h = f(X)$  and a decoder,  $y = f(h)$  are formed with the preceding input layer and the subsequent output layer, respectively. In which, the input is  $X$ , the hidden layer weight is  $h$ , the output is  $y$ , and the activation function is  $f$ .

The hidden layer in the autoencoder can be regarded as a feature layer, especially when the hidden layer node number is smaller than the node number of the input and output layers, the autoencoder is called an under-complete autoencoder. At this time, the autoencoder forces the learning of the low-dimensional representation of the input data to capture the most significant features in the data. In particular, when a linear activation function is used, the under-complete autoencoder performs a linear transformation. It is equivalent to linear dimensionality reduction

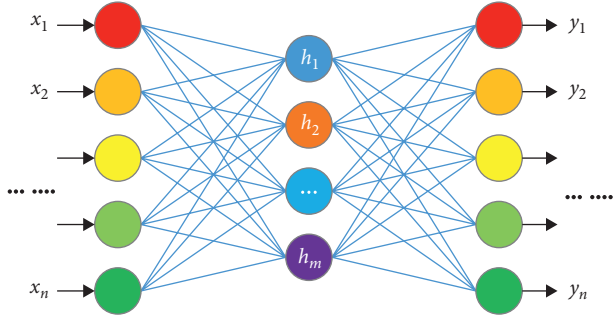


FIGURE 1: The architecture of autoencoder.

approaches, such as principal component analysis (PCA) and singular value decomposition (SVD) [18]. Denote weights as  $\mathbf{W}$  and bias as  $\mathbf{b}$ , the encoder can be expressed as  $z = W_E X + b_E$ , and the decoder as  $z = W_D X + b_D$ . Autoencoder obtains the feature expression through the minimum error between the output and input obtained by reconstruction. The error function is defined as the second norm of input and output, which is

$$J_{AE} = \frac{1}{2N} \sum \|X - Y\|_2^2. \quad (1)$$

Batch gradient descent is used to solve this optimization problem [19]. To prevent overfitting of the training data, a regularization term is added to the objective function to punish the overlearning of weights and parameters [20, 21], and the error function is

$$J = J_{AE} + J_r, J_r = \frac{\lambda}{2} \left( \|\mathbf{W}_D\|_F^2 + \|\mathbf{W}_E\|_F^2 \right), \quad (2)$$

where  $\|\cdot\|_F$  is the Frobenius norm, and  $\lambda$  is the coefficient of weight decay.

**2.2. Stacked Autoencoder.** When the features of standard autoencoders are cascaded, each autoencoder is used to continue to obtain the output of the new feature by the previous autoencoder, and a stacked autoencoder is obtained. When the number of stacked layers is large, direct training will encounter great difficulties. Generally, the method of training layer by layer is used to solve it. The first layer of the autoencoder is separated for independent training. After the first layer of self-encoder training is completed, the input of the second layer of an encoder is connected to the hidden layer output of the first layer of the self-encoder to form a new network for training. By analogy, the subsequent layers of autoencoders are sequentially added to the trained autoencoders network for training, until all network layers are added to complete the training. After the stacked autoencoder training is completed, the center hidden layer as the symmetry axis of the network architecture is used to connect the classifier. The features of the hidden layer are employed to distinguish the abnormal and normal samples.

**2.3. Anomaly Detection with Stacked Autoencoder.** The data acquired by the sensor is time series data. The sequence data

collected by the sensor are segmented, and then, features are extracted for each segment. After the features extracted from the segmented data of multiple sensors are combined into one vector data, the vector data are input to the stacked autoencoder [17]. The final reconstruction error is calculated by stacking autoencoders. By analyzing the distribution of the reconstruction error of the normal detection data, the boundary threshold of the normal error can be determined, so that the reconstruction error can be used for anomaly detection. This anomaly detection scheme is illustrated in Figure 2.

Feature extraction from the time series of sensors is the key to data fusion and anomaly detection. In this article, the time-domain and frequency-domain characteristics of the time series are extracted and combined as the input of the autoencoder. The features calculated from the time-domain series include mean, standard deviation, and mean square root and denote sensor data series as  $x_i$ , the length of the series as  $N$ , and average as  $\bar{x}$ .

$$f_1 = \frac{1}{N} \sum_{i=1}^N x_i, f_2 = \sqrt{\frac{1}{N} \sum_{i=1}^N (x_i - \bar{x})^2}, f_3 = \sqrt{\frac{1}{N} \sum_{i=1}^N x_i^2}. \quad (3)$$

Then, the segmented sensor data are decomposed into four layers with wavelet, and the following normalized power spectrum is also selected features

$$f_4^k = \frac{\sum_{j=1}^M P_{kj} \ln P_{kj}}{\ln M}, \quad (7)$$

where  $M$  is the frequency components number and  $P_{kj}$  is the probability density of the  $j$ th frequency component of the  $k$ th decomposed subsignal,  $k=0, 1, \dots, 15$ .

### 3. Experimental Results and Discussion

To obtain more accurate water quality detection results, the abnormal detection of coastal water quality uses the data of three sensors, which are pH value, conductivity, and ammonia nitrogen. pH value is measured with pH meter PHSJ-6L (Inesa Instrument, China). Online digital conductivity detection instrument KM-SAL-01 (KingMill Tech. Co, China) is employed for conductivity detection. Also, ammonia nitrogen is measured with the instrument HY-YDCG-Y01 (Haiyan Electronics, China).

Every sensor samples once every 20 minutes and 3 sampling data are obtained per hour. Considering the sequence characteristics of the data, anomaly detection is carried out in hours. The hourly data include the sampling data of the previous hour, the current hour, and the next hour. That is, the hourly data include 9 sampling values. Each sensor input of anomaly detection is 28 data composed of these 9 sampling values and 19 features obtained by the calculation method described in 2.2. The data of three sensors form a 28x3 matrix, which is used as the input of the autoencoder. After the autoencoder is trained, whether the output is abnormal by reconstructing the error.

There are 4,500 normal data and 300 abnormal data in the data set. Part of the abnormal data comes from actual data, and the other part comes from simulation data. The



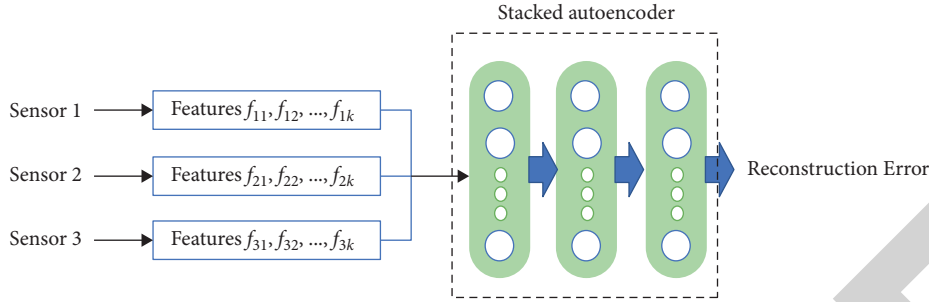


FIGURE 2: Data fusion anomaly detection scheme.

TABLE 2: Different method comparison for anomaly detection of seawater quality.

Method	Recall	Precision	Accuracy	Specificity	F1 score
One class SVM	0.783	0.746	0.970	0.982	0.764
Isolation forest	0.867	0.852	0.982	0.990	0.860
Proposed	1.000	0.938	0.996	0.996	0.968

normal data and abnormal data in the data set are randomly selected according to 4:1 to determine the training sample set and the test sample set. The training sample set is used to train the autoencoder, and the test sample set is used to test with the trained autoencoder and compare performance indicators.

To compare different methods, three indicators are used to evaluate results, and they are recall, precision, accuracy, specificity, and F1 score [12, 13]. Among them, the F1 score is a comprehensive indicator that can more comprehensively reflect the performance of the method. When an anomaly is judged as an anomaly, it is marked as P; otherwise, it is marked as N. When this judgment is correct, it is marked as T; otherwise, it is marked as F. These indicators are calculated as follows:

- (i)  $\text{Recall} = \text{TP}/(\text{TP} + \text{FN})$
- (ii)  $\text{Precision} = \text{TP}/(\text{TP} + \text{FP})$
- (iii)  $\text{Accuracy} = (\text{TP} + \text{TN})/(\text{TP} + \text{TN} + \text{FP} + \text{FN})$
- (iv)  $\text{Specificity} = \text{TN}/(\text{TN} + \text{FP})$
- (v)  $\text{F1-Score} = 2\text{PrecisionRecall}/(\text{Precision} + \text{Recall})$

Two other commonly used anomaly detection methods are applied, and the results are used to evaluate detection performance. One is the one-class support vector machine (OCSVM) method [2]. Also, another one is the isolation forest (IF) method [7]. The training set is used to build the models of these methods, and the 900 normal data and 60 abnormal data in the test set are used to test these methods, and the results are listed in Table 2.

Some anomaly examples are illustrated in Figure 3. A, B, and C are an anomaly, while D, E, and F are not an anomaly. Our proposed method provides correct results while the OCSVM method and IF method incorrectly mark D as an anomaly and OCSVM also marked E and F as anomalies. The judgment error of the two methods is due to insufficient use of all sensor information, and only the fluctuation of one sensor data is judged as abnormal. By observing the data and

the figure, it is shown that the proposed method is the best one. The method proposed in this article surpasses the other two methods in every index. It has the best anomaly detection performance when it is compared with other methods and evaluated with all the indicators.

The proposed anomaly detection method is also applied to ship operation. Two sensor data are used, and they are the sailing angle and speed of the ship. The actual data of one-day sailing are used for anomaly detection with the proposed method. The anomaly detection results are shown in Figure 4.

The data in Figure 4 are compared and analyzed with the actual ship operating status. The ship suddenly found a moving float while cruising, so it carried out quick obstacle avoidance operations. It is manifested in the curve data that there are two rapid angle changes at high speed, and these changes correspond to two steering operations. Therefore, the anomaly detection results are correct.

This research is different from the existing water quality anomaly monitoring [1–7] in that anomaly detection is realized through the ship's intelligent platform. This method can be integrated into the ship's intelligent system, thereby providing more options for the automatic recording and analysis of anomaly detection results. For example, after detecting an abnormal seaside environment, the smart ship can automatically cruise and detect the area to locate the range of the abnormal area.

The real-time water quality detection method can solve the problem of full coverage of water quality monitoring in coastal waters so that data in the time and space dimensions can be obtained. The artificial intelligence method based on the autoencoder provided in this paper only uses normal data for learning and training. A large amount of normal data is easy to obtain, but it is very difficult to obtain abnormal data. Such methods are very important for anomaly detection. The method also shows

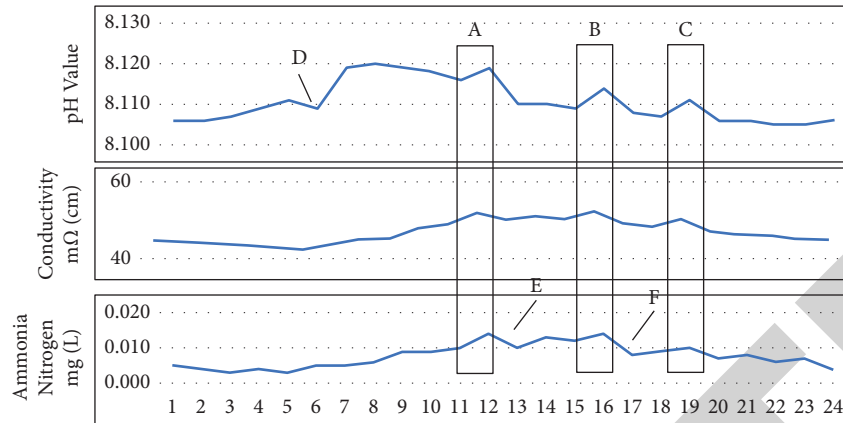


FIGURE 3: Coastal water quality anomaly detection.

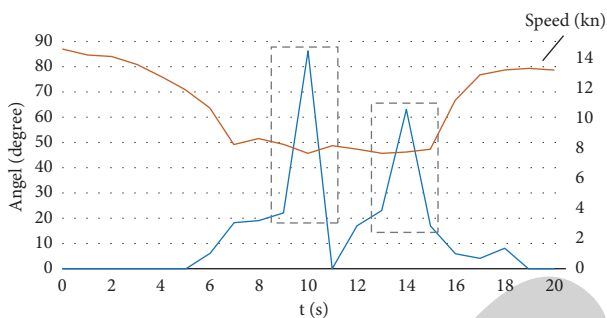


FIGURE 4: Anomaly detection results of ship operation.

advantages over existing methods in terms of performance such as accuracy.

#### 4. Conclusions

An anomaly detection method is developed for coastal environment monitoring ships. Multisensor data fusion based on an autoencoder is employed for anomaly detection of seawater quality and ship operation. For the autoencoder that has completed the training, its calculation amount is not large when it is applied, and the calculation of the result can be completed within 1 second. Therefore, the proposed method in this paper is real time.

With the help of a smart ship platform and intelligent method, real-time monitoring and abnormal detection of the coastal environment are achieved. In future research, further factors affecting coastal water quality will be considered, such as coastal rainfall, river flow, surrounding factories, and residents' activities.

With the application of real-time environmental detection based on USV, people can more completely monitor the quality and detect the anomaly of coastal water at different times and in different areas in time. On the one hand, the detection and response speed of water anomalies will be greatly improved. On the other hand, some seasonal or periodic abnormal changes will be found, and the sources and effects of these changes will be

further studied. People will gain a deeper understanding of the relationship between the environment and human activities.

#### Data Availability

The data used to support the findings of this study are included within the article.

#### Conflicts of Interest

The authors declare that there are no conflicts of interest regarding the publication of this paper.

#### Acknowledgments

The publication of this research work is only for the academic purpose of Pentecost University, Accra, GHANA.

#### References

- [1] M. Hosseini and R. Kerachian, "A data fusion-based methodology for optimal redesign of groundwater monitoring networks," *Journal of Hydrology*, vol. 552, no. 1, pp. 267–282, 2017.
- [2] J. Liu, J. Gu, H. Li, and S. Carlson, "Machine learning and transport simulations for groundwater anomaly detection," *Journal of Computational and Applied Mathematics*, vol. 380, no. 1, Article ID 112982, 2020.
- [3] Y. Zhang, X. Hua, and X. Sun, "Study on density clustering based anomaly detection for aquaculture water," in *Proceedings of the 7th International Conference on Computing and Artificial Intelligence*, pp. 227–232, ACM Press, Tianjin China, April 2021.
- [4] C. Bourelly, A. Bria, L. Ferrigno et al., "A preliminary solution for anomaly detection in water quality monitoring," in *Proceedings of the IEEE International Conference on Smart Computing*, Article ID 9239635, IEEE Press, Bologna, Italy, September 2020.
- [5] Z. Shi, C. Chow, R. Fabris, J. Liu, and B. Jin, "Applications of online UV-vis spectrophotometer for drinking water quality monitoring and process control: a review," *Sensors*, vol. 22, no. 8, Article ID 2987, 2022.
- [6] U. Ahmed, R. Mumtaz, H. Anwar, S. Mumtaz, and A. M. Qamar, "Water quality monitoring: from conventional



## *Retraction*

# **Retracted: Preparation and Supercritical CO<sub>2</sub> Foaming of Modified Nanocrystalline Cellulose Reinforced Polylactic Acid Bionanocomposites**

### **Advances in Materials Science and Engineering**

Received 26 December 2023; Accepted 26 December 2023; Published 29 December 2023

Copyright © 2023 Advances in Materials Science and Engineering. This is an open access article distributed under the Creative Commons Attribution License, which permits unrestricted use, distribution, and reproduction in any medium, provided the original work is properly cited.

This article has been retracted by Hindawi, as publisher, following an investigation undertaken by the publisher [1]. This investigation has uncovered evidence of systematic manipulation of the publication and peer-review process. We cannot, therefore, vouch for the reliability or integrity of this article.

Please note that this notice is intended solely to alert readers that the peer-review process of this article has been compromised.

Wiley and Hindawi regret that the usual quality checks did not identify these issues before publication and have since put additional measures in place to safeguard research integrity.

We wish to credit our Research Integrity and Research Publishing teams and anonymous and named external researchers and research integrity experts for contributing to this investigation.

The corresponding author, as the representative of all authors, has been given the opportunity to register their agreement or disagreement to this retraction. We have kept a record of any response received.

### **References**

- [1] D. Chen, P. Zhang, J. Wang, and D. Gao, "Preparation and Supercritical CO<sub>2</sub> Foaming of Modified Nanocrystalline Cellulose Reinforced Polylactic Acid Bionanocomposites," *Advances in Materials Science and Engineering*, vol. 2022, Article ID 2805670, 14 pages, 2022.

## Research Article

# Preparation and Supercritical CO<sub>2</sub> Foaming of Modified Nanocrystalline Cellulose Reinforced Polylactic Acid Bionanocomposites

Dan Chen <sup>1</sup>, Ping Zhang,<sup>2</sup> Jiajun Wang,<sup>3</sup> and De Gao<sup>2</sup>

<sup>1</sup>Taizhou Vocational College of Science and Technology, Taizhou 318020, Zhejiang, China

<sup>2</sup>Ningbo Institute of Technology Zhejiang University, Ningbo 315100, Zhejiang, China

<sup>3</sup>Zhejiang Sci-Tech University, Hangzhou 310000, Zhejiang, China

Correspondence should be addressed to Dan Chen; [chend@tzvcst.edu.cn](mailto:chend@tzvcst.edu.cn)

Received 21 May 2022; Revised 21 June 2022; Accepted 5 July 2022; Published 10 August 2022

Academic Editor: K. Raja

Copyright © 2022 Dan Chen et al. This is an open access article distributed under the Creative Commons Attribution License, which permits unrestricted use, distribution, and reproduction in any medium, provided the original work is properly cited.

The solution casting method was used to prepare polylactic acid/modified nanocrystalline cellulose (PLA/mNCC) composites, and the effects of the mNCC content on the morphology, thermal characteristics, and rheological properties of the PLA nanocomposite were examined. The PLA microcellular foaming nanocomposite was prepared using supercritical CO<sub>2</sub> foaming. Furthermore, the foaming conditions were optimized, and the effect of NCC surface modification, as well as the content and interfacial force of nanoparticles, on the foaming efficiency and cell pattern of composites was examined. The results suggested that a sufficient number of nanoparticles increased the nucleation site for foaming and played a vital role in heterogeneous nucleation in the foaming system. An ideal microcellular foaming material with an average cell diameter of 6.97 μm and a cell density of 6.05 × 10<sup>9</sup> cells/cm<sup>3</sup> was prepared when the foaming temperature was 110°C, the foaming pressure was 18 MPa, the incubation period was 2 h, and the mNCC content was 6%.

## 1. Introduction

Microcellular foaming plastics exhibit a wide range of excellent properties, including lightweight, strong moisture absorption, high impact strength, good thermal insulation and sound insulation, and high specific strength. Thus, microcellular foaming plastics are suitable for a variety of applications, including cushion packaging, food packaging, structural materials, and sound insulation [1–3]. Polystyrene (PS), polyurethane (PU), polyvinyl chloride (PVC), and poly(methyl methacrylate) (PMMA) foams are the most prevalent polymer foam materials nowadays. The achievement of biodegradability and recycling of these systems remains a significant challenge. Additionally, the inevitable depletion of fossil fuels and growing environmental concerns encourage researchers to develop biodegradable polymer foams to replace the petroleum-based materials currently employed [4–7].

Poly(lactic acid) (PLA) is a thermoplastic polymer made from the renewable agricultural raw material corn. It is well-known for its renewability, biodegradability, high mechanical strength, thermoplastic properties, and low cost [8–10]. It has a wide range of uses in a variety of fields, most notably in the packaging and biomedical sectors [11–14]. PLA has also been employed to develop foaming materials with microcellular structures. PLA, on the other hand, has low melt strength, a restricted processing window, a low foaming rate, and a poor cell pattern, all of which make it difficult to produce [15]. Several previous studies have demonstrated that adding nanoparticles (e.g., cellulose nanocrystals, clay, talc, or silica) significantly improves the foaming efficiency of PLA [16–18]. The nanoparticles not only improve the melt strength of the material but also play the role of heterogeneous nucleation during the foaming process. Lin et al. [19] prepared PLA/NCC/PEG microcellular foam material using nanocrystalline cellulose (NCC) as a nucleating agent. The findings demonstrated

that NCC acted as a heterogeneous nucleation agent during the foaming process. The volume expansion rate of foam increased as the NCC concentration increased, whereas cell diameter decreased and cell density increased. Ameli et al. [20] found that nanoclay improved the crystallinity and melt strength of PLA, significantly improved its foaming behavior, and promoted the refinement and uniform distribution of cells. Wang et al. [21] prepared PLA/graphite foam-up nanocomposite with a density of  $0.7\text{ g/cm}^3$  and a uniform microporous structure by using nanographite to facilitate the crystallization of PLA and increase its viscoelasticity.

NCC is an organic nanoparticle that is naturally occurring and sustainable. It has a large specific length and diameter as well as a high strength. NCC modification not only can increase the melt strength of PLA but also can improve foaming performance and broaden its application range. Additionally, both PLA and NCC are formed from biomass and can be biodegraded following their use [22–24]. However, due to the high hydrophilicity of the NCC polyhydroxyl groups, they readily agglomerate in the PLA matrix, and hence the surface hydrophobic modification of NCC was typically performed [25]. Modification techniques that were often utilized included physical adsorption modification [26–29], esterification modification properties [30–33], graft copolymerization [34–37], and silane coupling agent modification [38–41]. The modified NCC could be more uniformly dispersed in the polymer matrix and played an effective role as nanoparticles. Kasa et al. [42] and Ali et al. [43] used solution casting to successfully prepare acetylation-modified NCC and PLA nanocomposites. Acetylated NCC exhibits increased dispersion in polymer matrixes, indicating that the acetylation reaction enhanced NCC's capability to be used as a reinforcing material in PLA. Jiang et al. [44] used cetyltrimethyl ammonium bromide-modified NCC and found that the surface modification of NCC improved the dispersion state of NCC in the natural rubber matrix as well as the interfacial interaction between natural rubber and NCC.

The purpose of this study was to produce a completely biodegradable PLA microcellular foaming nanocomposite. First, the hydrophobicity of nanocrystalline cellulose was increased by acetylation, and then a solution casting approach was used to produce a polylactic acid/modified nanocrystalline cellulose (PLA/mNCC) nanocomposite. Investigations were carried out on the effects of mNCC at various concentrations on the morphology, thermal characteristics, and rheological properties of a PLA nanocomposite. Finally, the foaming of PLA nanocomposite was studied using supercritical  $\text{CO}_2$  foaming. The foaming process parameters including temperature, pressure, and time were optimized, and the effects of surface modification of NCC, nanoparticle content, and interfacial force on the foaming performance and cell pattern of composites were explored.

## 2. Experimental

**2.1. Materials.** Polylactic acid (PLA), 2003D, with a molecular weight ( $M_n$ ) of ca.  $2.15 \times 10^4\text{ g mol}^{-1}$  (determined using an Ubbelohde viscosity meter at  $25^\circ\text{C}$  with chloroform as the solvent), was acquired in pellet form from Natureworks Co.

PLA pellets were dried in a vacuum oven at  $70^\circ\text{C}$  for 12 h. NCC was supplied by the Beijing Nanocrystalline Cellulose Technology Research and Development Centre of China International Tourism and Trade Co. Ltd. (China). NCC had a diameter of 20–50 nm and a length of 200–500 nm. Ningbo Fangxin Co. Ltd. (China) provided  $\text{CO}_2$  with a purity of 99%. Sinopharm Chemical Reagent Co. Ltd. (China) provided the acetic acid, perchloric acid, acetic anhydride, ethyl alcohol, and dichloromethane used in this study. No additional purification was performed on any reagents.

## 2.2. Methods

**2.2.1. Modification of NCC by Acetylation.** Acetic acid, perchloric acid, and acetic anhydride (1 g of NCC to 25 mL of toluene, 20 mL of acetic acid, 0.1 mL of perchloric acid, and 7 mL of acetic anhydride) were added to the toluene ultrasonic solution of NCC and stirred at room temperature for 1 h. The mixture was then poured into ethanol to precipitate a white flocculent precipitate that was centrifuged and washed three times with ethanol and deionized water to yield an acetic anhydride-modified NCC aqueous solution. The mixture was then freeze-dried to a constant weight to yield a white solid powder, which was named acetic anhydride-modified NCC (mNCC) [45].

**2.2.2. Preparation of PLA Nanocomposite.** The solvent casting approach was used to prepare PLA/mNCC nanocomposites [46]. The resultant mNCC aqueous solution was replaced with a solution to produce mNCC  $\text{CH}_2\text{Cl}_2$  solution, which was ultrasonically dispersed in an ice-water bath. After that, a certain amount of PLA was dissolved in a 10% mNCC  $\text{CH}_2\text{Cl}_2$  solution at  $40^\circ\text{C}$ . After the mixture had been well mixed, it was ultrasonically dispersed and then placed in a vacuum oven for 1 h before being cast on the film. The mixture was vacuum dried before being hot-pressed into a sheet to produce composites with mNCC concentrations of 0%, 2%, 4%, 6%, and 8%, indicated as PLA, PLA/mNCC-2, PLA/mNCC-4, PLA/mNCC-6, and PLA/mNCC-8, respectively.

**2.2.3. Supercritical  $\text{CO}_2$  Foamed PLA Nanocomposite.** The PLA nanocomposite sample was placed in the foaming chamber. The switch was tightened after the air in the chamber had been removed.  $\text{CO}_2$  was continuously injected into the chamber to adjust the pressure, causing the  $\text{CO}_2$  to reach a supercritical state. The temperature was maintained, and the material was soaked in supercritical  $\text{CO}_2$  for a certain time. Then, the pressure was quickly released, and the material was placed in an ice-water bath to cool and shape to obtain a PLA microcellular foaming nanocomposite as shown in Figure 1.

## 2.3. Characterization

**2.3.1. Characterization of the Cross-Sectional Morphology of a PLA Nanocomposite.** Field emission scanning electron microscopy (FE-SEM; S-4800, Hitachi, Japan) was used to

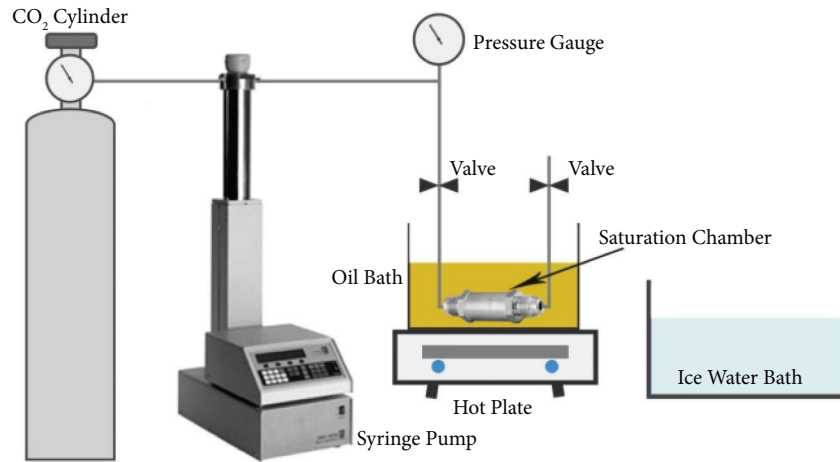


FIGURE 1: Supercritical CO<sub>2</sub> foaming process.

examine the cross-sectional morphology of a PLA nanocomposite. The samples were quenched and brittle cracked in liquid nitrogen before being sprayed with gold (platinum) and examined using an FE-SEM.

**2.3.2. Thermal Stability Analysis of PLA Nanocomposite.** The thermal stability of PLA nanocomposite was analyzed using a thermogravimetric analyzer (TGA; SDT Q600, TA Corporation, USA). In a nitrogen atmosphere, 1 mg of PLA nanocomposite was subjected to thermogravimetric analysis. The gas flow rate was set to 20 mL/min; the temperature range was set to room to 600°C; and the heating rate was set to 10°C/min.

**2.3.3. Dynamic Thermomechanical Analysis of PLA Nanocomposite.** The dynamic thermomechanical analysis (DMA) of PLA nanocomposite was performed using a dynamic thermomechanical analyzer (Q800, TA, USA) operating at a frequency of 10 Hz, a temperature range of -50 to 100°C, and a heating rate of 3°C/min. The experimental sample had a dimension of 30 mm × 5 mm and a thickness of 1 mm.

**2.3.4. Analysis of the Rheological Properties of a PLA Nanocomposite.** A rotational rheometer (Physica MCR301, Anton Paar, Austria) was used to determine the rheological properties of a PLA nanocomposite. The sample was a disc with a thickness of 1 mm and a diameter of 25 mm. The temperature throughout the test was 170°C, and the frequency ranged from 0.01 to 100 Hz. The sample must be dried prior to the test.

**2.3.5. Characterization of PLA Microcellular Foaming Nanocomposite Sections Using Scanning Electron Microscopy.** The microstructure of the PLA microcellular foaming nanocomposite cell was characterized by scanning electron microscopy (SEM; TM1000, Hitachi, Japan). The foaming material samples were quenched and brittle cracked with liquid nitrogen, then sprayed with gold (platinum), and examined under SEM.

**2.3.6. Cell Diameter of PLA Microcellular Foaming Nanocomposite.** The cell diameter of the PLA microcellular foaming nanocomposite was statistically examined using the particle size distribution calculating software Nano Measurer. The SEM images of the cells were counted multiple times, and the average value was taken to ensure the accuracy of the statistics.

**2.3.7. Density of PLA Microcellular Foaming Nanocomposite.** The density of PLA microcellular foaming nanocomposite was assessed using the capillary pycnometer method [47], which used the density of water to calculate the buoyancy method. Following (1), the density of foaming material samples was estimated. Each group of samples was measured three times, and the findings were calculated based on the average of the three measurements.

$$\rho_{foam} = \frac{m\rho_{water}}{m + m_1 - m_2}, \quad (1)$$

where  $\rho_{foam}$  is the sample density, g/cm<sup>3</sup>;  $\rho_{water}$  is the water density (obtained by the mass-to-volume ratio of water in the pycnometer), g/cm<sup>3</sup>;  $m$  is the mass of the sample;  $m_1$  is the mass of the water after filling the pycnometer; and  $m_2$  is the mass of the pycnometer containing the water and the sample.

**2.3.8. Volume Expansion Rate of PLA Microcellular Foaming Nanocomposite.** The volume expansion rate of a PLA microcellular foaming nanocomposite can be calculated using the following formula:

$$V_f = \frac{V_{foam}}{V} = \frac{m/\rho_{foam}}{m/\rho} = \frac{\rho}{\rho_{foam}}, \quad (2)$$

where  $V_f$  is the volume expansion rate of the sample, that is, the foaming ratio, in cm<sup>3</sup>;  $V_{foam}$  and  $V$  are the volumes of foamed and nonfoamed materials, in cm<sup>3</sup>, respectively; and  $\rho_{foam}$  and  $\rho$  are densities of foamed and nonfoamed materials, in g/cm<sup>3</sup>, respectively.



**2.3.9. Cell Density of PLA Microcellular Foaming Nanocomposite.** The cell density of PLA microcellular foaming nanocomposite is commonly represented in terms of the number of cells per unit volume, and the formula for calculating it is shown in the following equation [48, 49]:

$$N = \left(\frac{n}{A}\right)^{(3/2)} \times V_f, \quad (3)$$

where  $N$  is the cell density of the foaming material, in cells/cm<sup>3</sup>;  $A$  is the area of the area used for analysis in the SEM image, in cm<sup>2</sup>;  $n$  is the number of cells in the area used for analysis in the SEM image; and  $V_f$  is the volume expansion rate of the foaming material, that is, the foaming ratio, in cm<sup>3</sup>.

### 3. Results and Discussion

**3.1. Morphology of PLA Nanocomposite.** FE-SEM was used to investigate the PLA nanocomposite's cross-sectional morphology. The cross-sectional morphology of mNCC composites with varying contents is shown in Figure 2. The section of pure PLA is smooth and flat, as illustrated in Figure 2, which is distinct from that of other composites. Although the mNCC was equally dispersed throughout the PLA matrix, as the mNCC content increased, a small amount of agglomeration formed as a result of the hydrogen bonding interaction between the unmodified hydroxyl groups on the surface of the NCC [50].

**3.2. Thermal Stability Analysis of PLA Nanocomposite.** The TGA technique was employed to investigate the thermal degradation of the PLA nanocomposites. According to the TG and DTG curves in Figure 3, the neat PLA and PLA nanocomposites began to lose weight when exposed to temperatures between 300 and 400°C. The onset weight loss temperature of the nanocomposites continued to decrease with the addition of the mNCC. The nanocomposite's lower thermal degradation performance was mostly related to the NCC's low thermal stability [51, 52]. While the PLA nanocomposites demonstrated a lower thermal decomposition capability than pure PLA, their initial weight loss temperature remained above 300°C, which meets the requirements for a wide variety of applications.

**3.3. Dynamic Thermomechanical Analysis of PLA Nanocomposite.** Figure 4 illustrates the storage modulus  $E'$  and loss factor  $\tan\delta$  curves of PLA and its nanocomposites as a function of temperature. As shown in Figure 4(a), when the temperature was lower than 45°C, the increase in storage modulus  $E'$  with mNCC concentration could be attributed to the formation of cross-linked structures, an increase in crystallinity (more ordered regions developed), and better mNCC dispersion in the PLA matrix, which resulted in improved mNCC adhesion [48]. The storage modulus  $E'$  of PLA and its nanocomposites reduced dramatically with increasing temperature between 45°C and 70°C because of the glass transition.

The effect of mNCC content on the loss factor of PLA nanocomposite is shown in Figure 4(b). As observed, the loss factor ( $\tan\delta$ ) in the PLA nanocomposites' glass transition region reduced as mNCC concentration increased, and the nanocomposites' loss factor ( $\tan\delta$ ) was significantly less than that of pure PLA. Pure PLA contained a single transition peak, but as mNCC was added, more prominent double peaks appeared gradually, demonstrating that mNCC can cause crystallization of PLA [52]. Furthermore, changes in mNCC content had a negligible effect on the glass transition temperature of PLA nanocomposite [53].

**3.4. Analysis of the Rheological Properties of a PLA Nanocomposite.** We investigated the dynamic rheological properties of PLA nanocomposites. At 170°C, Figure 5 illustrates the frequency dependence of the storage modulus  $G'$ , the loss modulus  $G''$  and the complex viscosity  $\eta^*$  of the PLA/mNCC nanocomposites. As found, when the mNCC content was increased, both the storage modulus and the loss modulus increased, with the storage modulus approaching the loss modulus in the low-frequency region, suggesting that the PLA/mNCC nanocomposite had become more viscoelastic as the mNCC content was increased [54].

Furthermore, the  $\eta^*$  in the low-frequency region of PLA remained relatively constant as the scanning frequency  $\omega$  was increased, similar to a Newtonian fluid, whereas the PLA/mNCC composites exhibited relatively clear shear-thinning behavior. The complex viscosities of the PLA/mNCC nanocomposites were found to be greater than those of pure PLA and increased as the mNCC content increased. The high viscosities of the polymer matrix with nanometric cellulose fillers were attributed to filler-filler interactions via hydrogen bonding as well as an excellent filler-matrix interfacial interaction. As a result, the flow restrictions of the PLA chains were caused by the strong interaction between the mNCC and the PLA molecules, which increased the melt viscosity of the PLA/mNCC nanocomposites [55]. However, the complex viscosity of the PLA/mNCC-8 nanocomposite did not increase considerably, which could be attributed to the agglomeration of the high content nanofiller. These findings are in accordance with the SEM micrographs.

**3.5. Effect of Foaming Process Conditions on Composites Cell Pattern.** The effects of foaming processing parameters such as foaming temperature, foaming pressure, and incubation time on the cell pattern of composites were explored using PLA/mNCC-6 composites as the research object.

Figure 6 illustrates cross-sectional SEM images of the foamed PLA/mNCC foaming material after a 2 h incubation period and a foaming pressure of 16 MPa at various foaming temperatures. It was found that the foaming material produced by composites at a foaming temperature of 110°C had the most homogeneous cells, the smallest size, and the most complete shape in the range of 90–150°C. Figure 7 shows the influence of various foaming temperatures on the average cell diameter and density of the foaming material, as well as

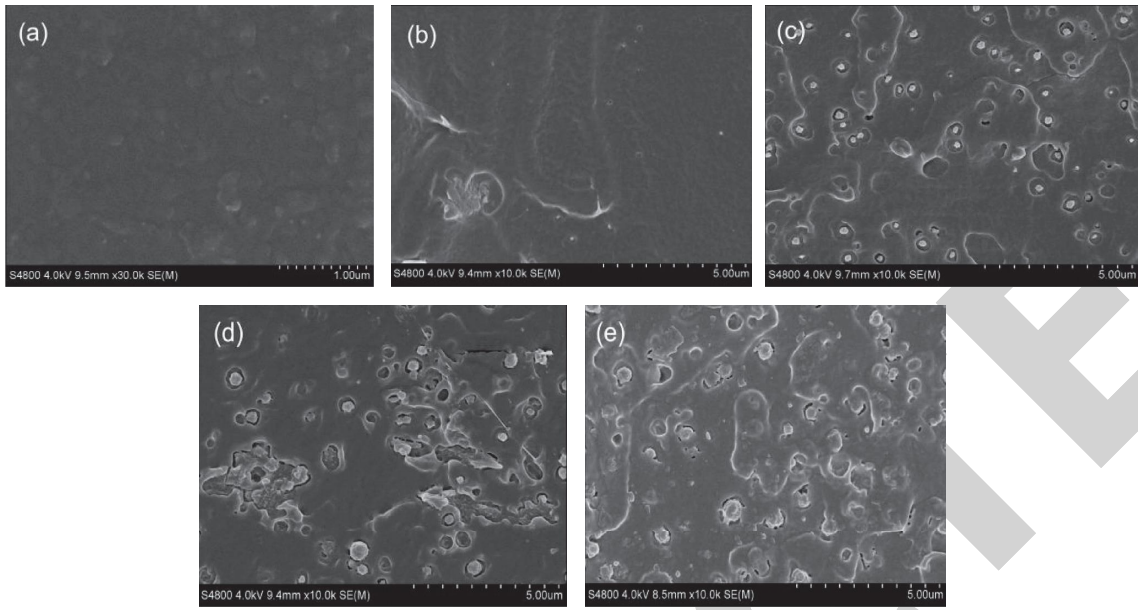


FIGURE 2: FE-SEM micrographs of the PLA nanocomposites: (a) pure PLA, (b) PLA/mNCC-2, (c) PLA/mNCC-4, (d) PLA/mNCC-6, and (e) PLA/mNCC-8.

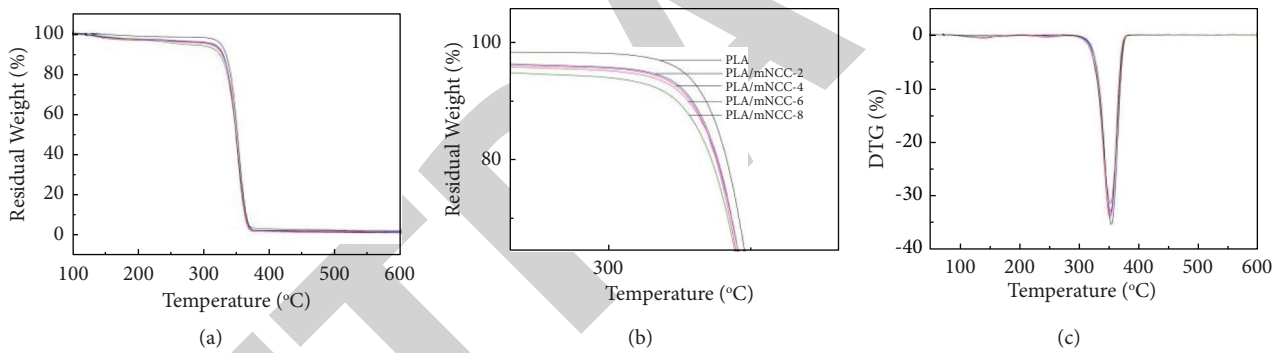


FIGURE 3: Thermal decomposition of the pure PLA and PLA nanocomposites at a heating rate of  $10^{\circ}\text{C min}^{-1}$  under nitrogen.

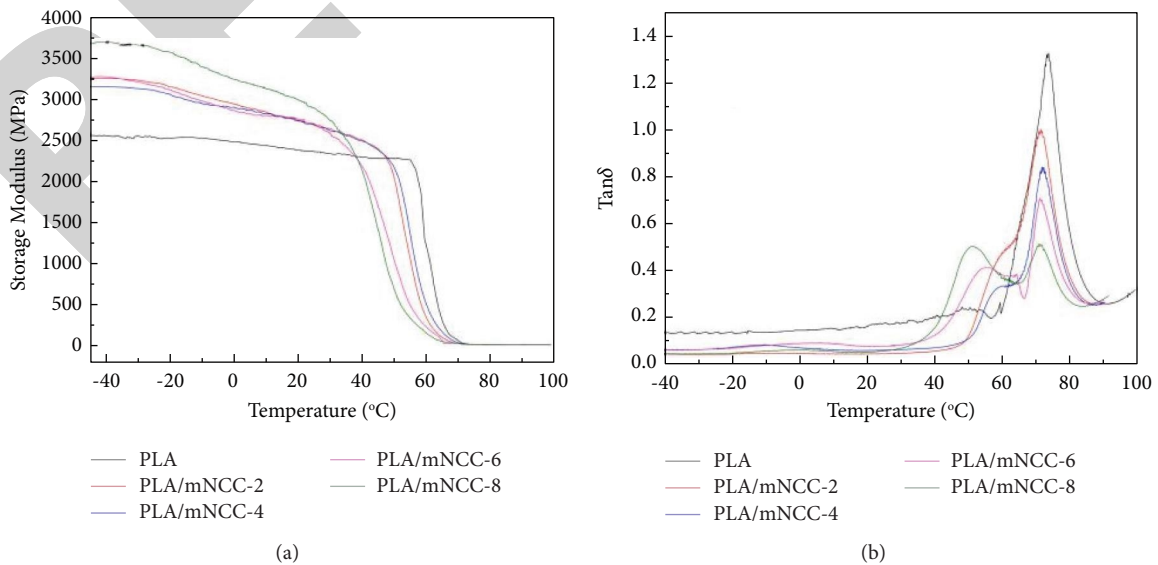


FIGURE 4: Dynamic thermomechanical analysis of PLA and its nanocomposites: (a) storage modulus and (b) loss factor.



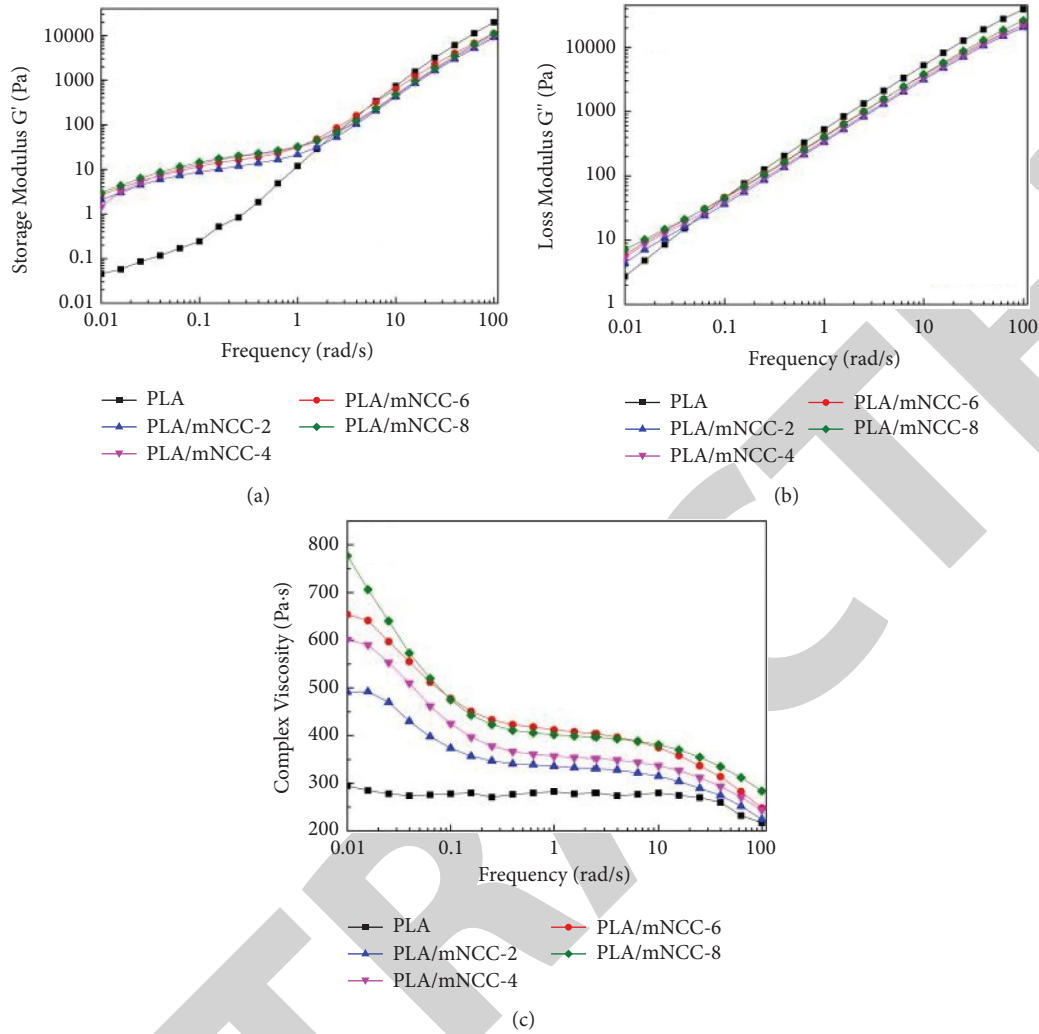


FIGURE 5: Dynamic rheological behaviors of the PLA nanocomposites (test temperature 170°C): (a) storage modulus  $G'$ , (b) loss modulus  $G''$ , and (c) complex viscosity  $\eta^*$ .

the foam density and volume expansion rate. It was observed that the cell density was greatest at a foaming temperature of 110°C.

The foaming temperature had a considerable effect on the cell pattern of the composites, as demonstrated. It was observed that when the foaming temperature was lower, the diffusion rate of  $\text{CO}_2$  in the polymer matrix was slow. As a result, the dissolution equilibrium could not be reached, and the distribution was not uniform, resulting in partial material foaming.  $\text{CO}_2$  slowly diffused into the polymer matrix and reached dissolution equilibrium as the temperature increased, resulting in the completion of the foaming process, which gradually improved the cell structure. Increasing the temperature resulted in a decrease in melt strength and a decrease in surface tension, which caused the cells to squeeze one another, causing the cells to grow larger, merge, and rupture. In addition, the size of the cells became irregular, and the density of the cells also decreased. Rapid depressurization and cooling molding allowed the comparatively low foaming temperature of 110°C to be rapidly decreased to below the system's glass transition temperature  $T_g$  in a short

time, resulting in a relatively short cell growth time and a small and even cell size.

Figure 8 illustrates cross-sectional SEM images of the foamed PLA/mNCC foaming material at a temperature of 110°C and incubation period of 2 h under the influence of various foaming pressures. Figure 9 shows a trend diagram showing the effect of varying foaming pressures on the average cell diameter and density of the foaming material, as well as the density of the foam and the rate of volume expansion. When the foaming pressure was low, it was noticed that the  $\text{CO}_2$  did not reach dissolution equilibrium in the polymer matrix, the number of nucleation was low, and an unfoamed area appeared in the composites. The cell pattern was poor, and the size was not uniform. The solubility of  $\text{CO}_2$  in the polymer matrix increased progressively as the foaming pressure increased, as was the rate of bubble nucleation; the cell diameter of the foaming material dropped; and the cell size distribution became more uniform. Meanwhile, after saturation of the matrix with high-pressure  $\text{CO}_2$ , the molecular chain movement was accelerated; the viscosity of the composite melt lowered; the nucleation and growth resistance

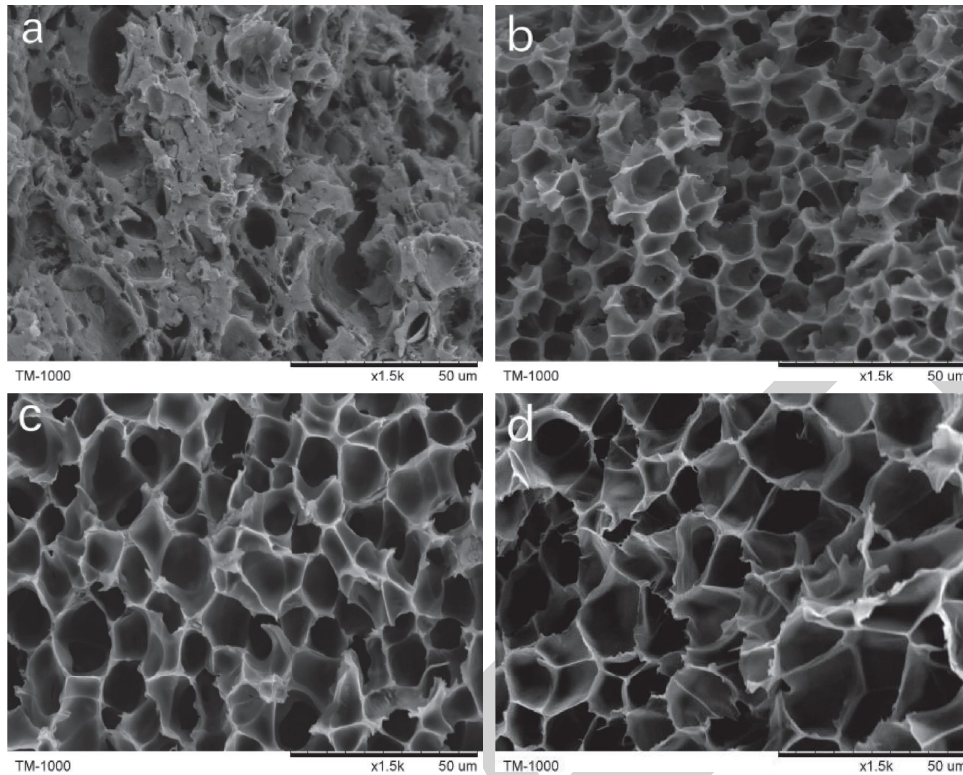


FIGURE 6: Cell structure of foaming material at different foaming temperatures (2 h, 16 MPa): (a) foaming temperature 90°C, (b) foaming temperature 110°C, (c) foaming temperature 130°C, and (d) foaming temperature 150°C.

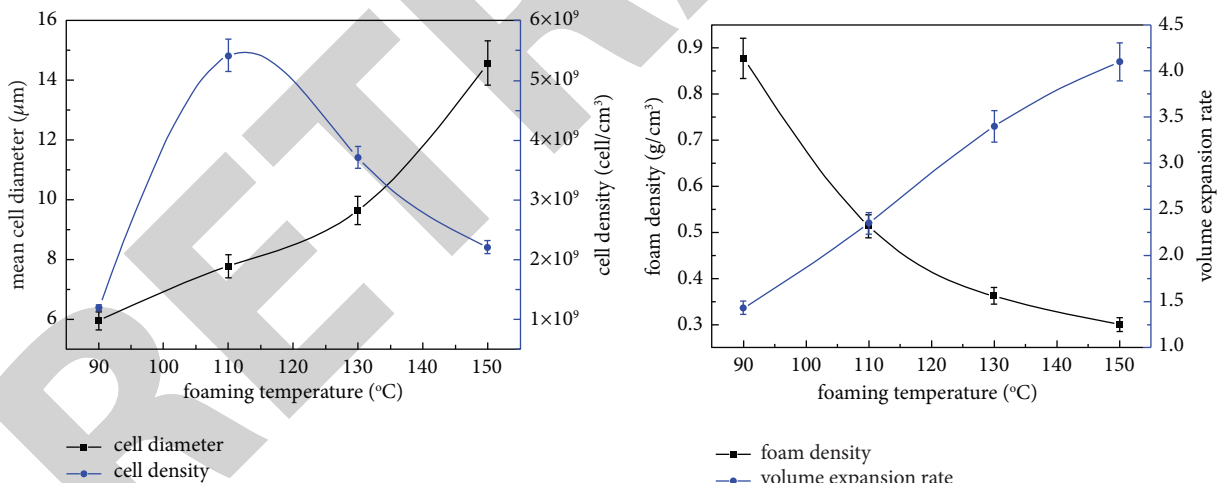


FIGURE 7: Effect of different foaming temperatures on foaming of composites (2 h, 16 MPa).

of cells were decreased; and the cell structure was enhanced. Therefore, when the foaming pressure was 18 MPa in the 12–18 MPa research range, the cell size was reduced, and the cell structure was relatively excellent.

Figure 10 depicts cross-sectional SEM images of foamed PLA/mNCC foaming material with a foaming temperature of 110°C and a foaming pressure of 16 MPa at various incubation times. Figure 11 depicts a trend diagram illustrating the effect of various incubation times on the average cell diameter and density of the foaming material, as well as

the foam density and volume expansion rate. It was found that after approximately 2 h of incubation, the dissolved CO<sub>2</sub> in the polymer matrix achieved saturation and that further extension of the incubation time had minimal influence on the cell structure.

*3.6. Influence of NCC Surface Modification on Composites Cell Pattern.* The cell pattern, diameter, and density of PLA/mNCC and PLA/NCC microcellular foaming nanocomposite

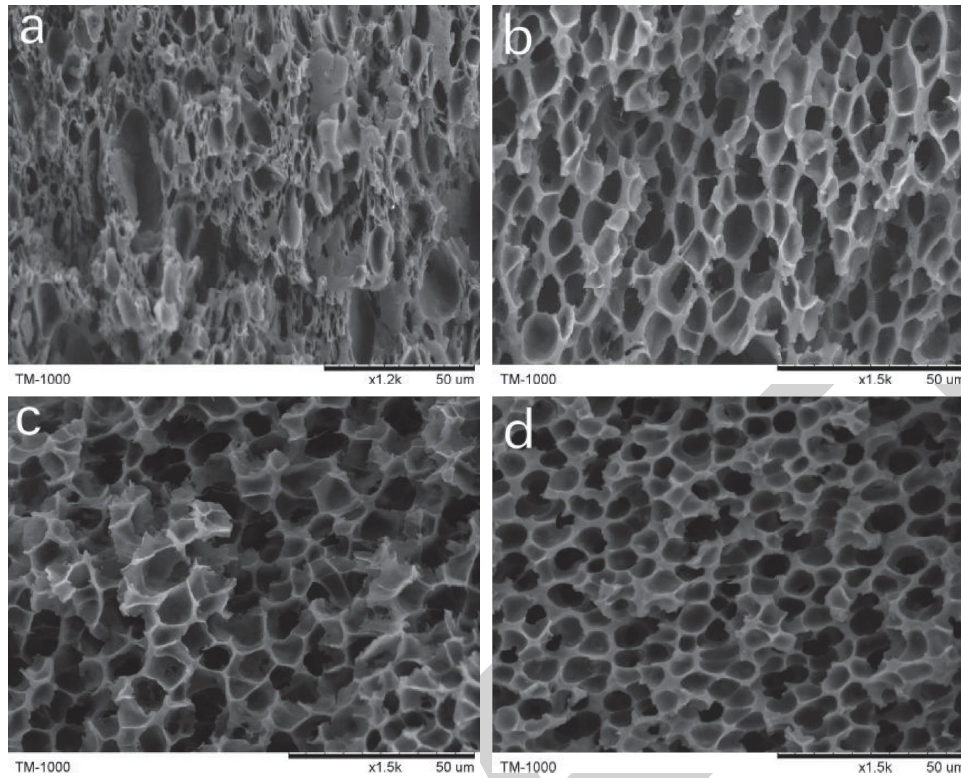


FIGURE 8: Cell structure of foaming material under different foaming pressure (2 h, 110°C): (a) foaming pressure 12 MPa, (b) foaming pressure 14 MPa, (c) foaming pressure 16 MPa, and (d) foaming pressure 18 MPa.

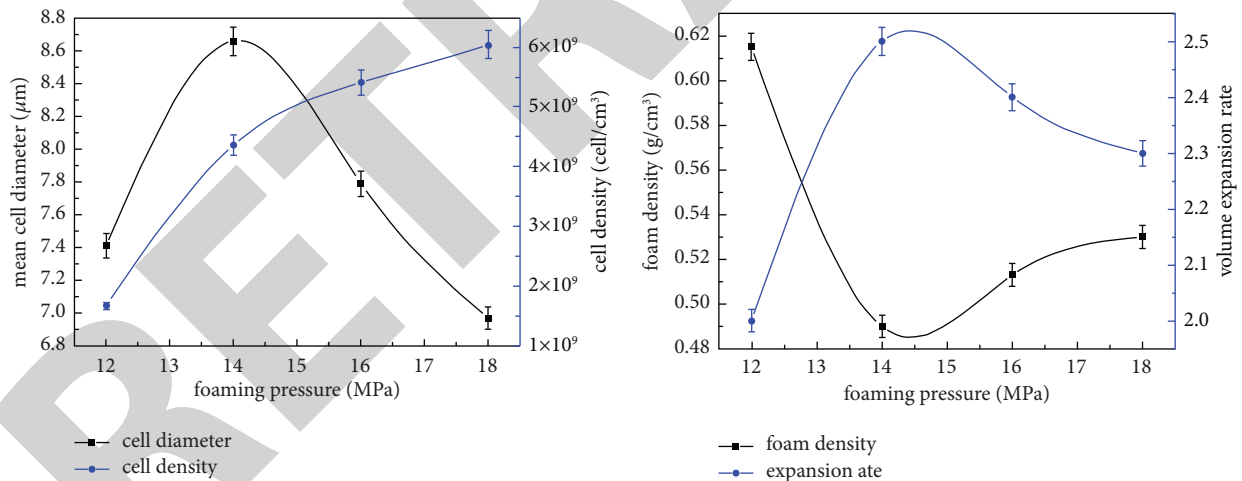


FIGURE 9: Effect of different foaming pressure on foaming of composites (2 h, 110°C).

were compared in Figures 12 and 13 under the same foaming conditions (110°C, 18 MPa, 2 h). It was found that when nanoparticles were added at a concentration of 2% and 6%, the average cell diameter of the PLA/mNCC microcellular foaming nanocomposite was significantly smaller, the average cell density was considerably greater, and the cell pattern was markedly better than that of the PLA/NCC microcellular foaming nanocomposite. This was primarily owing to the difference in dispersion state and interaction of the nanofillers with the PLA matrix generated by the different surface characteristics of NCC and mNCC. Nanoparticle aggregation

or their strong interaction with the PLA matrix typically lowers their nucleation effectiveness. More nucleation sites can be provided by enhanced nanoparticle dispersion, which necessitates improved phase adhesion. Improved polymer-particle compatibility, on the other hand, is deleterious to nucleation since weak phase interfaces are typically favored for heterogeneous nucleation during physical foaming. Acetylation may increase the interfacial interaction between PLA and NCC particles, resulting in a more uniform distribution of mNCC in PLA than in NCC. The decreased aggregation and increased effective filling of the filler particles



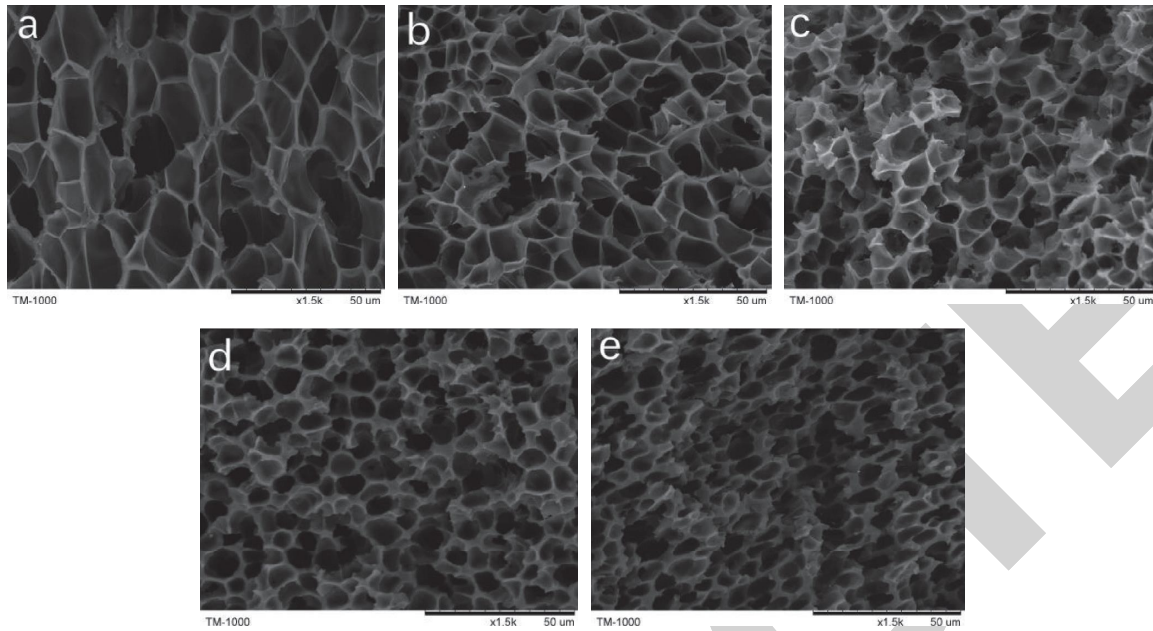


FIGURE 10: Cell structure of foaming material under different incubation times (110°C, 16 MPa): (a) foaming time 0.5 h, (b) foaming time 1 h, (c) foaming time 2 h, (d) foaming time 4 h, and (e) foaming time 8 h.

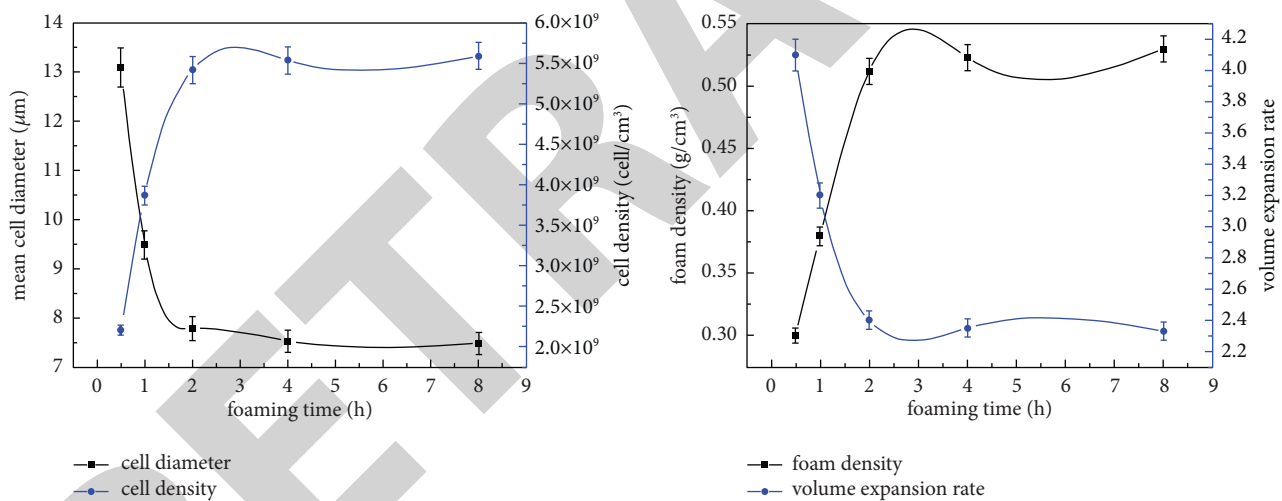


FIGURE 11: Effects of different incubation times on foaming of composites (110°C, 16 MPa).

indicate that the PLA/mNCC contained more additional nucleation sites. This may compensate for the loss in nucleation capacity of each NCC particle induced by surface acetylation, resulting in increased nucleation efficiency of the PLA/mNCC nanocomposites [17, 56].

**3.7. Influence of Content and Interfacial Force of mNCC on Composites Cell Pattern.** The pure PLA and PLA/mNCC composites were microcellular foamed using supercritical CO<sub>2</sub> at 110°C for 2 h, and the cross-sectional structure and cell pattern of the microcellular foam material were studied using SEM, as shown in Figure 14. The average cell diameter and density of foaming material were analyzed and compared in Figure 15. It was discovered that the PLA/mNCC

foaming nanocomposite had a significantly improved cell pattern compared to pure PLA. When the nanoparticle concentration was less than 6%, increasing the mNCC content resulted in a decrease in the average cell diameter of the foaming material and a more homogeneous size distribution. Furthermore, the cell pattern was improved; the wall thickness was enhanced; and the cell structure was optimized. This was because mNCC acted as a heterogeneous nucleating agent in the compound foaming system. During the foaming process, the free energy barrier to be overcome in heterogeneous nucleation was lower than that in homogeneous nucleation; cell nucleation was easier; and the number of nucleation sites in heterogeneous nucleation was determined by the number of nucleation attachment points in the composite [49]. Therefore, as the mNCC

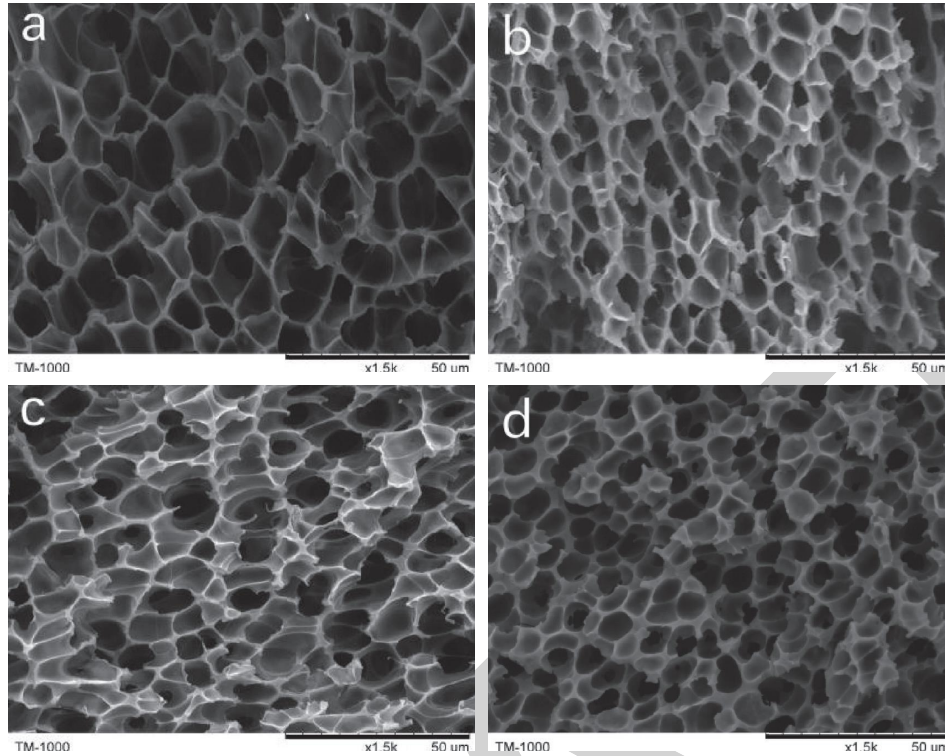


FIGURE 12: Comparative analysis of PLA foaming nanocomposite cell structures (110°C, 18 MPa, 2 h): (a) PLA/NCC-2, (b) PLA/NCC-6, (c) PLA/mNCC-2, and (d) PLA/mNCC-6.

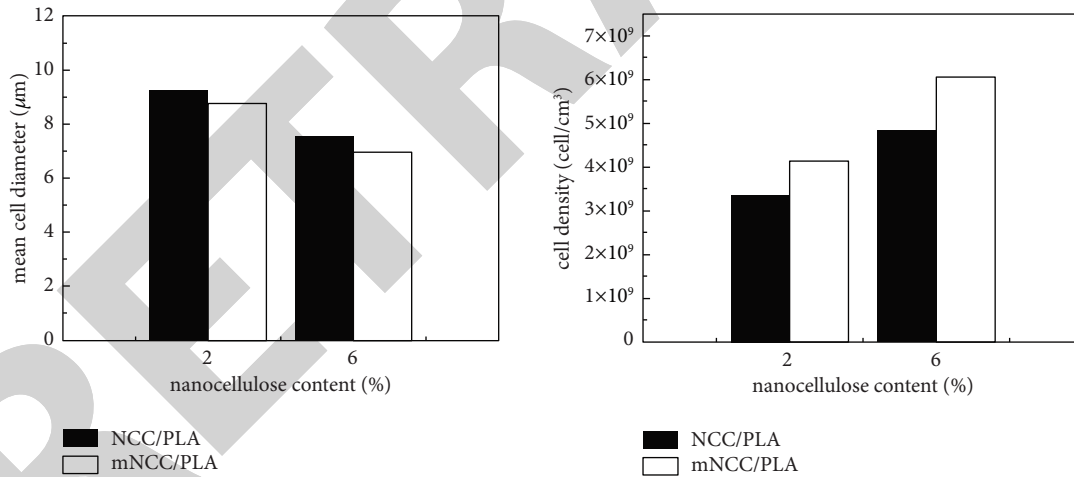


FIGURE 13: Average cell diameter and cell density (110°C, 18 MPa, 2 h of PLA foaming nanocomposite).

content increased, the number of nucleation sites increased, and the cell density increased accordingly. However, when the mNCC content was increased to 8%, neither the average cell diameter nor the cell density rose considerably, indicating that the cell structure remained comparable to that of the 6% content. This was mostly due to the high mNCC content, which resulted in an increase in the number of unreacted hydroxyl groups on the surface, which led to a little agglomeration, resulting in mNCC clusters distributed throughout the PLA matrix. Since the number of nucleation sites was lowered in comparison to single mNCC, there was no substantial increase in nucleation sites.

To conduct a more detailed examination of the effect of mNCC on the foaming process of composites, the interfacial at the nucleation site was determined as a force [57]:

$$\begin{aligned}
 N &= Cf \exp \left[ \frac{-16\pi r^3}{3(\Delta P)^2 k_B T} \right] \Rightarrow \log N \\
 &= -\frac{16\pi}{3k_B T} \times \frac{r^3}{(\Delta P)^2} + \log Cf,
 \end{aligned} \tag{4}$$

where  $N$  is the cell density, in cell/cm<sup>3</sup>;  $C$  is the concentration of CO<sub>2</sub> and/or the concentration of heterogeneous

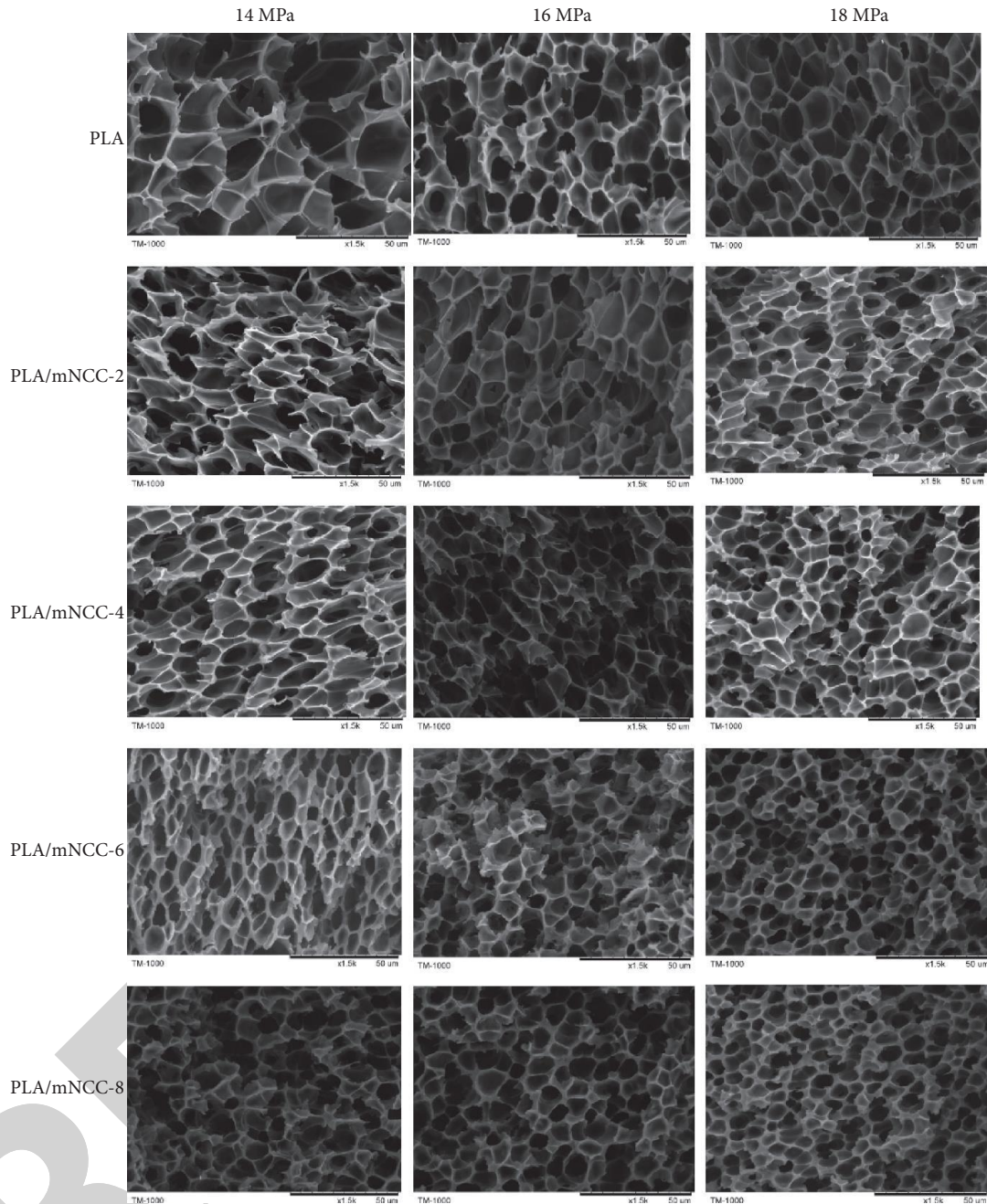


FIGURE 14: Cell structures of different pressures and different nanoparticle content foaming nanocomposite (110°C, 2 h).

nucleation sites;  $f$  denotes the collision frequency of  $\text{CO}_2$ ;  $r$  denotes the interfacial tension, in  $\text{mJ}/\text{m}^2$ ;  $\Delta P$  is the foaming pressure, MPa;  $k_B$  is Boltzmann constant,  $\text{J}/\text{K}$ ; and  $T$  is the absolute foaming temperature, K.

The logarithm of the cell density was supposed to be linear with the parameter  $\Delta P^2$  in classical nucleation theory. As indicated in formula (4), the nucleation site's interfacial force can be determined using the slope of the regression line. The regression line's vertical shift was associated with the number of nucleation sites or the concentration of  $\text{CO}_2$  molecules and may have been influenced by cell merger, which was not incorporated in the equation.

The slopes of the regression line for pure PLA and pure PLA nanocomposite are listed in Figure 16. The interfacial force of each material nucleation site is calculated using the slope and formula as follows:  $3.59 \text{ mJ}/\text{m}^2$  for pure PLA,  $2.96 \text{ mJ}/\text{m}^2$  for PLA/mNCC-2,  $2.62 \text{ mJ}/\text{m}^2$  for PLA/mNCC-4,  $2.81 \text{ mJ}/\text{m}^2$  for PLA/mNCC-6, and  $2.88 \text{ mJ}/\text{m}^2$  for PLA/mNCC-8. As can be observed, the interfacial force between the PLA nanocomposite and pure PLA was significantly less than that of pure PLA at the nucleation site. The addition of mNCC decreased the nucleation site's interfacial force and increased nucleation efficiency, owing to the greater interaction between the carboxyl groups and  $\text{CO}_2$  produced on



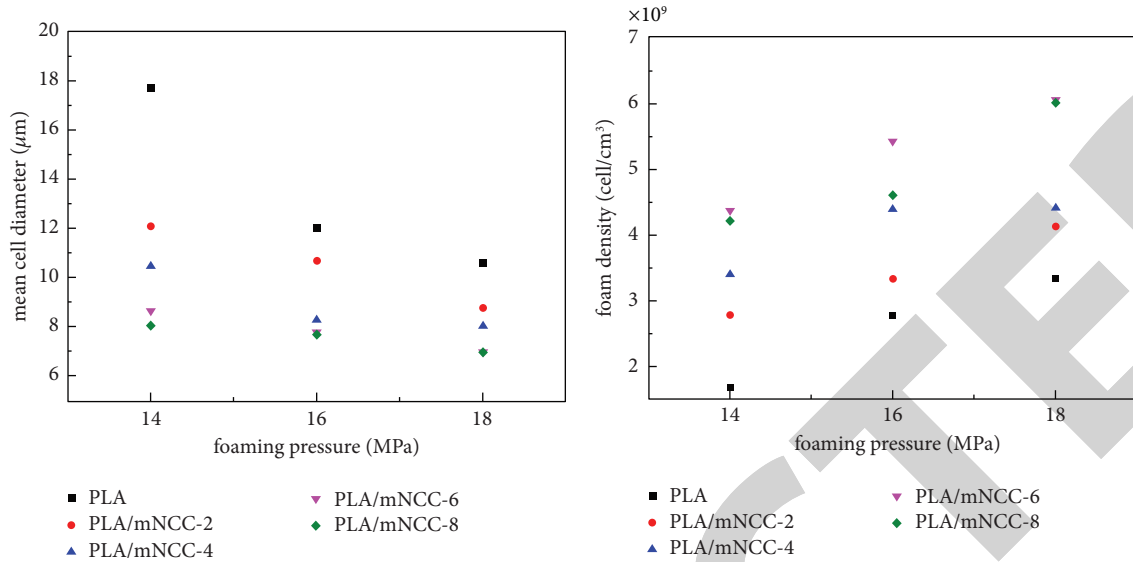


FIGURE 15: Average cell diameter and cell density of foaming nanocomposite under different pressure and nanoparticle content (110°C, 2 h).

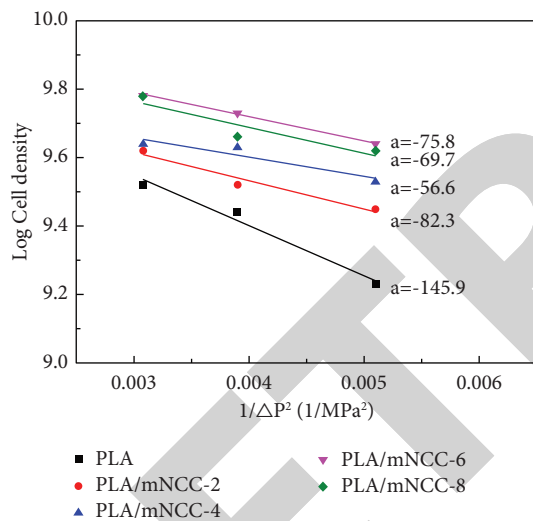


FIGURE 16: Logarithmic relationship between parameter  $1/\Delta P^2$  and cell density of pure PLA and composites.

the surface of the mNCC. However, as the mNCC concentration increased, agglomeration occurred; the nucleation site decreased; the interfacial force remained constant; and the nucleation efficiency remained constant.

#### 4. Conclusions

The solution casting approach was used to successfully prepare a PLA/mNCC nanocomposite. However, when the mNCC content increased, the agglomeration phenomenon became more evident. The addition of mNCC did not affect the thermal weight loss of composites and had a negligible effect on the glass transition temperature  $T_g$  of the material, as determined by thermal analysis, dynamic thermo-mechanical analysis, and rheological test. The storage modulus  $G'$ , loss modulus  $G''$ , and complex viscosity  $\eta^*$  of

composites increased as the mNCC content increased, and the storage modulus increased more dramatically, approaching the loss modulus in the low-frequency region, indicating that mNCC restricted the motion of the PLA macromolecular chain and significantly improved the melt viscoelasticity of composites.

The foaming process parameters such as temperature, pressure, and time were optimized using supercritical  $\text{CO}_2$  foamed PLA and its nanocomposites, and the effects of surface modification of NCC and mNCC content on the foaming performance and cell pattern of composites were compared. The addition of an appropriate amount of mNCC increased the nucleation site for foaming and acted as a heterogeneous nucleation agent in the foaming system. In the aforementioned research range, the average cell diameter was  $6.97 \mu\text{m}$ , and the cell density reached  $6.05 \times 10^9 \text{ cells/cm}^3$  under the conditions of a foaming temperature of  $110^\circ\text{C}$ , foaming pressure of 18 MPa, incubation period of 2 h, and mNCC content of 6%, indicating that the material was an ideal microcellular foaming material.

#### Data Availability

The data that support the findings of this study are available from the corresponding author upon reasonable request.

#### Conflicts of Interest

The authors declare that they have no known conflicts of interest or personal relationships that could have appeared to influence the work reported in this paper.

#### Authors' Contributions

All authors listed have made a substantial, direct, and intellectual contribution to the work and approved it for publication.

## Acknowledgments

The study was supported by Science and Technology Plan Project of Taizhou City, Zhejiang Province, China (21gyb38), and the visiting engineer project of Zhejiang Province, China.

## References

- [1] A. Jennifer, J. Villamil, N. Le Moigne et al., "Foaming of PLA composites by supercritical fluid-assisted processes: a review," *Molecules*, vol. 25, no. 15, p. 3408, 2020.
- [2] S. Standau, C. Zhao, S. Murillo Castellón, C. Bonten, and V. Altstädt, "Chemical modification and foam processing of polylactide (PLA)," *Polymers*, vol. 11, no. 2, p. 306, 2019.
- [3] Y. Wang, Y. Song, J. Du, Z. Xi, and Q. Wang, "Preparation of desirable porous cell structure polylactide/wood flour composite foams assisted by chain extender," *Materials*, vol. 10, no. 9, p. 999, 2017.
- [4] M. T. Zafar, S. Kumar, R. K. Singla, S. N. Maiti, and A. K. Ghosh, "Surface treated jute fiber induced foam microstructure development in poly(lactic acid)/jute fiber biocomposites and their biodegradation behavior," *Fibers and Polymers*, vol. 19, no. 3, pp. 648–659, 2018.
- [5] L. M. Matuana and O. Faruk, "Effect of gas saturation conditions on the expansion ratio of microcellular poly(lactic acid)/wood-flour composites," *Express Polymer Letters*, vol. 4, no. 10, pp. 621–631, 2010.
- [6] H. Naguib, R. Reza, B. Cochrane, H. Naguib, and C. Lee Patrick, "Fabrication and characterization of melt-blended polylactide-chitin composites and their foams," *Journal of Cellular Plastics*, vol. 47, no. 3, pp. 283–300, 2011.
- [7] W. Ding, *Development of Poly(lactic Acid)/Cellulose Nanofiber Biocomposite Foams*, Ph.D Thesis, University of Toronto, Canada, CA, USA, 2016.
- [8] Y. Zhang, Lu Cui, H. Xu et al., "Poly(lactic acid)/cellulose nanocrystal composites via the Pickering emulsion approach: rheological, thermal and mechanical properties," *International Journal of Biological Macromolecules*, vol. 137, pp. 197–204, 2019.
- [9] C. Xu, J. Chen, D. Wu, Y. Chen, Q. Lv, and M. Wang, "Polylactide/acetylated nanocrystalline cellulose composites prepared by a continuous route: a phase interface-property relation study," *Carbohydrate Polymers*, vol. 146, pp. 58–66, 2016.
- [10] W. Wan, S. Zhou, and Y. Zhang, "Parallel advances in improving mechanical properties and accelerating degradation to polylactic acid," *International Journal of Biological Macromolecules*, vol. 125, no. C, pp. 1093–1102, 2019.
- [11] N. Pal, P. Dubey, P. Gopinath, and K. Pal, "Combined effect of cellulose nanocrystal and reduced graphene oxide into polylactic acid matrix nanocomposite as a scaffold and its antibacterial activity," *International Journal of Biological Macromolecules*, vol. 95, pp. 94–105, 2017.
- [12] P. Dhar, S. S. Gaur, and N. Soundararajan, "Reactive extrusion of polylactic acid/cellulose nanocrystal films for food packaging applications: influence of filler type on thermo-mechanical, rheological, and barrier properties," *Industrial & Engineering Chemistry Research*, vol. 56, no. 16, pp. 4718–4735, 2017.
- [13] T. Kuang, F. Chen, L. Chang, and Y. Zhao, "Facile preparation of open-cellular porous poly (l-lactic acid) scaffold by supercritical carbon dioxide foaming for potential tissue engineering applications," *Chemical Engineering Journal*, vol. 307, pp. 1017–1025, 2017.
- [14] N. Alvarado, J. Romero, A. Torres et al., "Supercritical impregnation of thymol in poly(lactic acid) filled with electrospun poly(vinyl alcohol)-cellulose nanocrystals nanofibers: development an active food packaging material," *Journal of Food Engineering*, vol. 217, pp. 1–10, 2018.
- [15] E. Vatansever, D. Arslan, and M. Nofar, "Polylactide cellulose-based nanocomposites," *International Journal of Biological Macromolecules*, vol. 137, pp. 912–938, 2019.
- [16] Z. Han, Y. Zhang, W. Yang, and P. Xie, "Advances in microcellular foam processing of PLA," *Key Engineering Materials*, vol. 717, pp. 68–72, 2016.
- [17] Y. Qiu, Q. Lv, D. Wu, and W. Xie, "Cyclic tensile properties of the polylactide nanocomposite foams containing cellulose nanocrystals," *Cellulose*, vol. 25, no. 3, pp. 1795–1807, 2018.
- [18] S. Sekhar Borkotoky, T. Ghosh, P. Bhagabati, and V. Katiyar, "Polylactic acid/modified gum Arabic (MG) based microcellular composite foam: effect of MG on foam properties, thermal and crystallization behavior," *International Journal of Biological Macromolecules*, vol. 125, pp. 159–170, 2018.
- [19] M. X. Lin, P. P. Zou, and P. Zhang, "Study on foaming properties of PLA/NCC microcellular foam materials," *Engineering Plastics Application*, vol. 41, no. 10, pp. 90–95, 2013.
- [20] A. Ameli, M. Nofar, D. Jahani, G. Rizvi, and C. B. Park, "Development of high void fraction polylactide composite foams using injection molding: crystallization and foaming behaviors," *Chemical Engineering Journal*, vol. 262, no. C, pp. 78–87, 2015.
- [21] G. Wang, G. Zhao, S. Wang, and L. Zhang, "Injection-molded microcellular PLA/graphite nanocomposites with dramatically enhanced mechanical and electrical properties for ultra-efficient EMI shielding applications," *Journal of Materials Chemistry C*, vol. 6, no. 25, pp. 6847–6859, 2018.
- [22] J. Lu, C. Sun, K. Yang, K. Wang, and Y. Jiang, "Properties of polylactic acid reinforced by hydroxyapatite modified nanocellulose," *Polymers*, vol. 11, no. 6, Article ID 1009, 2019.
- [23] A. Karimian, H. Parsian, and M. Majidinia, "Nanocrystalline cellulose: preparation, physicochemical properties, and applications in drug delivery systems," *International Journal of Biological Macromolecules*, vol. 133, pp. 850–859, 2019.
- [24] D. I. Simangunsong, T. H. A. Hutapea, and H. W. Lee, "The effect of nanocrystalline cellulose (NCC) filler on polylactic acid (PLA) nanocomposite properties," *Journal of Engineering and Technological Sciences*, vol. 50, no. 4, pp. 578–587, 2018.
- [25] J. Lu, J. Lang, Na Wang, X. Wang, P. Lan, and H. Zhang, "Preparation and thermostability of hydrophobic modified nanocrystalline cellulose," *Nordic Pulp and Paper Research Journal*, vol. 36, no. 1, pp. 157–165, 2020.
- [26] K. Sakakibara, H. Yano, and Y. Tsujii, "Surface engineering of cellulose nanofiber by adsorption of diblock copolymer dispersant for green nanocomposite materials," *ACS Applied Materials & Interfaces*, vol. 8, no. 37, pp. 24893–24900, 2016.
- [27] K. S. Kontturi, K. W. Biegaj, and A. Mautner, "Noncovalent surface modification of cellulose nanopapers by adsorption of polymers from aprotic solvents," *Langmuir*, vol. 33, no. 23, pp. 5707–5712, 2017.
- [28] A. G. D. Souza, G. F. D. Lima, and R. Colombo, "A new approach for the use of anionic surfactants: Nanocellulose modification and development of biodegradable nanocomposites," *Cellulose*, vol. 27, no. 10, pp. 5707–5728, 2020.
- [29] Y. Yan, H. Amer, T. Rosenau, C. Zollfrank, and o., "Dry, hydrophobic microfibrillated cellulose powder obtained in a

## *Retraction*

# **Retracted: Utilization of Flex Controlled Robotics on Prosthetic Hand instead of Damaged Body Parts**

### **Advances in Materials Science and Engineering**

Received 26 December 2023; Accepted 26 December 2023; Published 29 December 2023

Copyright © 2023 Advances in Materials Science and Engineering. This is an open access article distributed under the Creative Commons Attribution License, which permits unrestricted use, distribution, and reproduction in any medium, provided the original work is properly cited.

This article has been retracted by Hindawi, as publisher, following an investigation undertaken by the publisher [1]. This investigation has uncovered evidence of systematic manipulation of the publication and peer-review process. We cannot, therefore, vouch for the reliability or integrity of this article.

Please note that this notice is intended solely to alert readers that the peer-review process of this article has been compromised.

Wiley and Hindawi regret that the usual quality checks did not identify these issues before publication and have since put additional measures in place to safeguard research integrity.

We wish to credit our Research Integrity and Research Publishing teams and anonymous and named external researchers and research integrity experts for contributing to this investigation.

The corresponding author, as the representative of all authors, has been given the opportunity to register their agreement or disagreement to this retraction. We have kept a record of any response received.

### **References**

- [1] M. R. A. Refaai, A. Elfasakhany, P. Rajalakshmy, B. Chandra Saha, A. S. Prakaash, and D. Basheer, "Utilization of Flex Controlled Robotics on Prosthetic Hand instead of Damaged Body Parts," *Advances in Materials Science and Engineering*, vol. 2022, Article ID 3496122, 7 pages, 2022.

## Research Article

# Utilization of Flex Controlled Robotics on Prosthetic Hand instead of Damaged Body Parts

Mohamad Reda A. Refaai <sup>1</sup>, Ashraf Elfakhany,<sup>2</sup> P. Rajalakshmy,<sup>3</sup> Bikash Chandra Saha,<sup>4</sup> A. S. Prakaash,<sup>5</sup> and Dadapeer Basheer <sup>6</sup>

<sup>1</sup>Department of Mechanical Engineering, College of Engineering, Prince Sattam Bin Abdulaziz University, Alkharj 16273, Saudi Arabia

<sup>2</sup>Mechanical Engineering Department, College of Engineering, Taif University, Taif 21944, Saudi Arabia

<sup>3</sup>Department of Robotics Engineering, Karunya Institute of Technology and Sciences, Coimbatore 641114, Tamil Nadu, India

<sup>4</sup>Cambridge Institute of Technology, Ranchi, Jharkhand 835103, India

<sup>5</sup>Department of Mathematics, Panimalar Institute of Technology, Chennai 600123, Tamil Nadu, India

<sup>6</sup>Department of Mechanical Engineering, Haramaya Institute of Technology, Haramaya University, Dire Dawa, Ethiopia

Correspondence should be addressed to Mohamad Reda A. Refaai; [refaai.mraworks@yahoo.com](mailto:refaai.mraworks@yahoo.com) and Dadapeer Basheer; [dadapeer.basheer@haramaya.edu.et](mailto:dadapeer.basheer@haramaya.edu.et)

Received 10 April 2022; Revised 29 April 2022; Accepted 18 May 2022; Published 9 August 2022

Academic Editor: K. Raja

Copyright © 2022 Mohamad Reda A. Refaai et al. This is an open access article distributed under the Creative Commons Attribution License, which permits unrestricted use, distribution, and reproduction in any medium, provided the original work is properly cited.

Scientists have researched human anatomy and biology to produce human-like prosthetic hands. In the absence of a hand, prosthetics assist in reestablishing independence and confidence. Prosthetic hands are limited in functionality and cost. A low-cost anthropomorphic prosthetic hand was designed. With five independently operated fingers and powered thumb roll movement, the design is unlike anything else on the market. This research aims to provide a cheaper alternative to the market's robotic prostheses. Inability to use limbs causes psychological and physical issues for amputees. Arduino, an open-source microprocessor, was used to build a prototype prosthetic hand. An Android app allows users to select a hand motion to circumvent myoelectric prosthesis control mechanisms. The Arduino uses this data to power servos that individually trigger each finger.

## 1. Introduction

A prosthesis is a medical device that substitutes a missing body part due to damage, disease, or congenital disorders. A transradial prosthesis, or below elbow (BE) prosthesis, replaces the arm between the elbow and the wrist. They can be practical or purely cosmetic, depending on their purpose. An amputee who undertakes a lot of manual labour may choose a hook prosthesis. Opting for a cosmetic prosthesis means sacrificing functionality for a more natural appearance (fast-changing field). Currently, only a few specialists need to know this. The demand for bionic hands is expected to expand as technology progresses. An ancient hook prosthesis gave way to today's bionic limb. We describe modern prosthetic hands' primary functionalities. However, bionic prostheses still lag behind biological prostheses. A bionic

hand that can fully duplicate or even surpass the human hand's intrinsic capabilities is the ultimate goal of bionic limb research.

Develop a highly versatile upper body prosthetic device that overcomes the current prosthetics' cost and usability issues. This saves money and frustration for myoelectric prosthesis users. The Arduino uses this data to power servos that individually trigger each finger. Cheap materials and ubiquitous technology like cellphones make it easy for amputees to purchase new prosthetics.

This project develops an anthropomorphic robotic hand that can handle objects with minimal human input. This study attempts to create a prosthetic hand that is as natural and easy to use as a person's biological limb. Nearly 6,000 upper limb amputations occur annually in India, leaving many disabled. Aside from the pain caused by curious

onlookers, these injuries can severely impede daily activities. Prosthetics have mechanical hooks and pincers that are useful but not adaptable. Amputees' abilities have improved with recent technologies like the i-Limb and bebionic prosthetic hands, yet consumers still find the user interface confusing and restricted ("i-Limb Ultra," 2014). However, they are substantially more expensive than their predecessors, which many potential customers deem unnecessary. Develop a highly versatile upper body prosthetic device that overcomes the current prosthetics' cost and usability issues. An anthropomorphic robotic hand can decide the ideal grip for an object and execute it with minimal human input. This study attempts to create a prosthetic hand that is as natural and easy to use as a person's biological limb. Simply take an object and tell the gadget to close. Choosing and executing a grip pattern will be instinctive. Plastics and low-cost manufacturing processes like laser cutting and 3D printing will be used to reduce costs. The IRIS system can also be utilized as a gripper for modular robot platforms. Our method allows a robot to hold different items without altering them. Input ports for the IRIS controller's grip and release are already connected to the robot leads. It could be modified to communicate with a robot platform through USB.

With the advent of consumer 3D printers, 3D manufactured prosthetics have gained popularity and utility. Free printable hand models are obtainable on the open-source library called Thingiverse. Unlike typical prosthetics, which can cost tens of thousands of dollars, these alternatives are affordable. Personalized prostheses are now more affordable than typical operations. Control is important in high-end prosthetics, aside from cost. In electromyography, electrical impulses from an amputee's residual muscles are read and mimicked. Electromyography can be used by people with or without forearm muscles, although it is complicated and incorrect. For the average amputee, a 3D-printed hand that works with everyday items like phones is essential. It is much easier to use a smartphone than myoelectric or motion-detecting. Also, consumer robotic hands have developed in recent years. Users from all across the world can now access thousands of 3D-printed hands. These prostheses may be easily resized and reintegrated into the control system for toddlers and teenagers. Despite meeting most of its goals, this project had a few snags. Stress-generated palm cracks owing to slight hand printing errors. Acetone was utilized to soften leftover ABS filament before rehabilitating cracks. Initially, the fishing line rotated beneath the servo arms. We used eyeglass screws in the servo blade holes to increase the rotation distance. A larger circumference than diameter prevents further finger traction. Instead of around the servo screws, the fishing line would often wrap underneath them, preventing proper closure. For sealing the arm's internal piping, the plastic or O ring was placed. The fishing line was threaded through the ring's openings. Another issue was the hand's inability to rest. Rubber bands were employed to fix it. Rubber bands held the servos from dragging their fingers into the palm. Thinner elastic bands restore the finger movement by replacing the rubber bands. It would not work if the hinge joints were nylon. Molding and curing silicone

joints may be gone. The original arm's outer shell fit the servos perfectly. Enlarging the casing solved the problem.

The project's main purpose is to improve amputees' quality of life by constructing a human-like prosthetic arm. Data capture and transmission mechanisms are examined. This breakthrough paves the way for a prosthetic limb that works with the human nervous system. Unlike a normal prosthesis that only provides motion, this design aims to provide tactile feedback to the nervous system. The hand's physical structure has been developed for simplicity of assembly using traditional coordinate reference systems. It now has only six degrees of freedom while retaining some vital hand motions. A one-finger model was constructed. With this model, you can grasp anything with force. A Visual Basic package to manipulate the model and display the project's potential was produced. The project was built in two stages due to its intricacy. As part of a holistic approach, a model based on the human nervous system was created. The simplified model is meant to highlight optimal design and functionality. This ensured that design flaws were addressed in both designs.

In this work [1], the aim is to craft humanoid artificial appendages that mimic biological counterparts. Although much has changed since the days of the wooden peg leg, modern orthoses and prostheses cannot be employed in daily activities [2]. In the Dextrus Hand, each finger is controlled by a string and servomotor, allowing the hand to grip the object perfectly. However, some robotic hands move the fingers in unison, with only one motor and string controlling all fingers [3]. 2.2" SEN-10264 Flex Sensors were used here. They may measure the bend by measuring the sensor's resistance. The applied resistance is 25k Ohms at rest and 125 k Ohms at the maximum bend, weaved into the glove. As per them [4], there are 5 pressure sensors attached to the fingertips of the robotic hand and 5 servomotors attached to the sensor glove. Each servomotor is responsible for providing stopping force to each finger. The servomotor and the corresponding finger are connected by two strings.

It is hard to act as precisely as a human. Picking up an egg, for example, requires precise strength control to avoid breaking or dropping it. Shoelace tying requires a robotic hand and outstanding coordination. Both flex sensor gloves and robotic hands must meet technical requirements. Unlike losing a leg, the functional limits following hand loss are catastrophic. Hand loss is caused by trauma, dysvascularity, and neoplasia. Men lose their hands more than women, with 67 percent of upper limb amputees being male. Upper limb amputations occur most frequently between the ages of 16 and 54. This patient group has significant functional demands and high expectations of a prosthetic limb. Modern prosthetic hands are designed to look and feel like natural limbs. Although the bionic hand has lately been praised as a victory of engineering excellence, it is still inferior to the actual thing and so faces challenges in gaining acceptance among upper limb amputees. These issues prohibit the prosthetic hand from achieving its ultimate goal: user acceptability [5-7]. It consists of a suitable motor and a position sensor. It also necessitates a complex controller [8], often a dedicated servomotor module. Servomotors are not a



specific type of motor, but rather a motor appropriate for use in closed-loop control systems. Servomotors are utilized in robotics, CNC, and automated manufacturing. Most current servomotors are built around a single manufacturer's controller module. Controllers can also be built around microcontrollers to save money in high-volume applications. They are tiny, light, and powerful. Servos can rotate around 180 degrees (90 in each direction) and are similar to ordinary ones. You can control them with any servo code, hardware, or library. It is good for novices who wish to move items without developing a motor controller with feedback and gearbox. This project intends to provide a less expensive alternative to the robotic prostheses now available on the market.

## 2. Software Approach to Design Prosthetic Hand

The hand prosthesis could be made available for universities and other relevant individuals to use as a mechanical evaluation and study of research in the future. When it comes to being utilized as a demonstration tool, the prototype is practically finished. Many people are investigating the use of increased electrical signals or brainwave nerve mapping to operate prosthetic devices, which is becoming increasingly popular. There are no devices available that are designed to emulate the shape and function of the human hand or that can be easily adjusted. The control code would be made available to the public as open source. The Arduino is a popular hobbyist and professional tool that may be connected serially to a computer via a USB connection. This is why the microcontroller was chosen; it is simple to work with and easy to understand. On the controls side, users may want to experiment with adding extra touch and grip sensors to see if they can increase the performance of their prosthetic hands [9–11]. Create innovative fingertip forms that can be made from a variety of materials in order to investigate how they affect the user experience on the mechanical side of things. Even if they are working on a more advanced solution, a design team needs to get their hands on something quickly so they can have a sense of what is expected of them. Figure 1 shows the master module and Figure 2 shows the slave module of this process.

**2.1. Arduino IDE.** Arduino is a single-board computer corporation, project, and user community that uses open-source hardware and software, and a built-in microcontrollers for developing digital devices and interactive things that can sense and control physical and digital objects. The project's products are open-source hardware and software licensed under the LGPL or GPL [12–15] allowing anybody to produce Arduino boards and distribute software. Arduino boards are available commercially assembled or as DIY kits.

**2.2. Mobile App.** Any computer software that runs on a phone, tablet, or watch is a mobile app. It is worth noting that mobile web browsers are often used instead of mobile

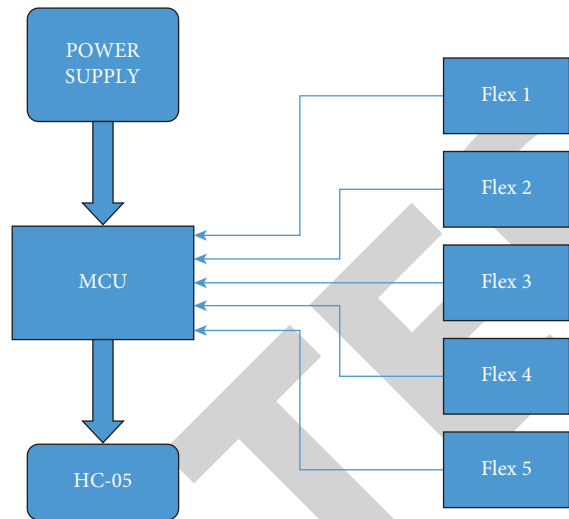


FIGURE 1: Block diagram of microcontroller in the master module.

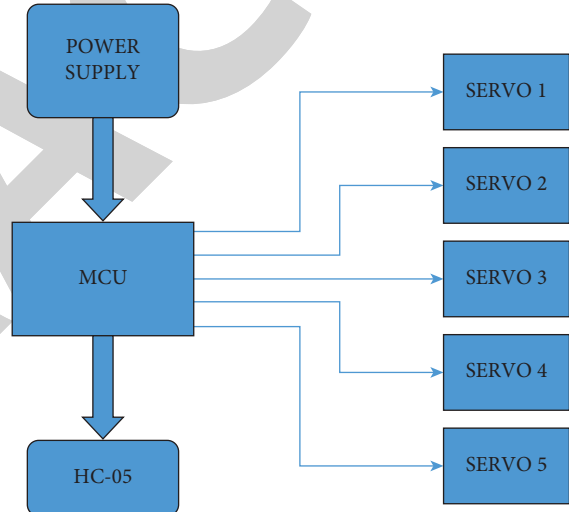


FIGURE 2: Block diagram of microcontroller in the slave module.

devices to access mobile applications. Figure 3 shows the mobile application.

## 3. Flex Sensor Interface Gloves

A flex sensor is a mechanical device that offers varied resistance after being bent. Figures 4(a) and 4(b) show the flex sensor interfaced in glove and finger gesture detection using the sensor. It is feasible to measure the resistance of a flex sensor by feeding a voltage through it and into an analogue input on an Arduino UNO board. Moreover, potentiometer is also called as variable resistor. Resistive carbon components make up flex sensors. A flex sensor is a changeable printed resistor on a flexible thin substrate. It creates output resistance proportional to the bent angle of the substrate [16–20]. It is obvious that when a flex sensor's bend angle increases, so does the resistance. A flex sensor's flat state has nominal resistance. The resistance increases with the radius. The variations of the parameters using the flex sensor are given in Figure 5.



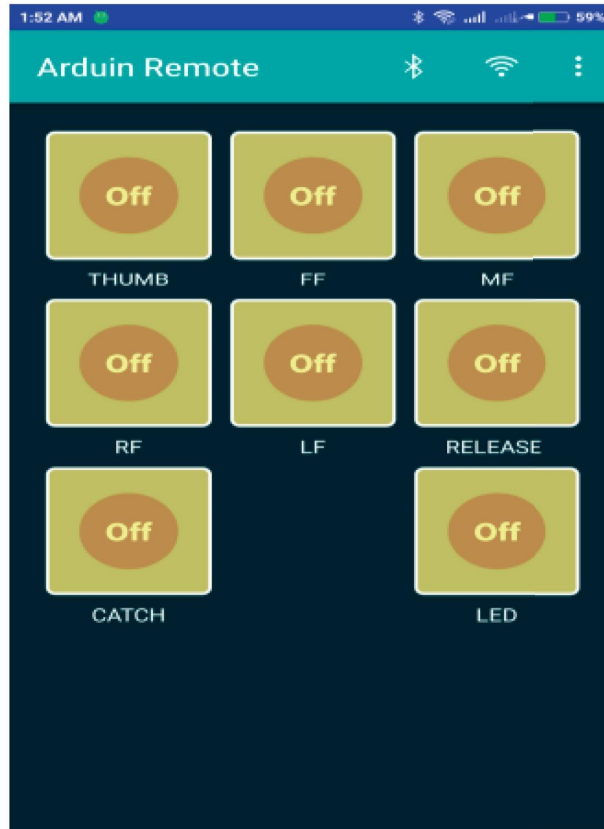


FIGURE 3: Mobile application.

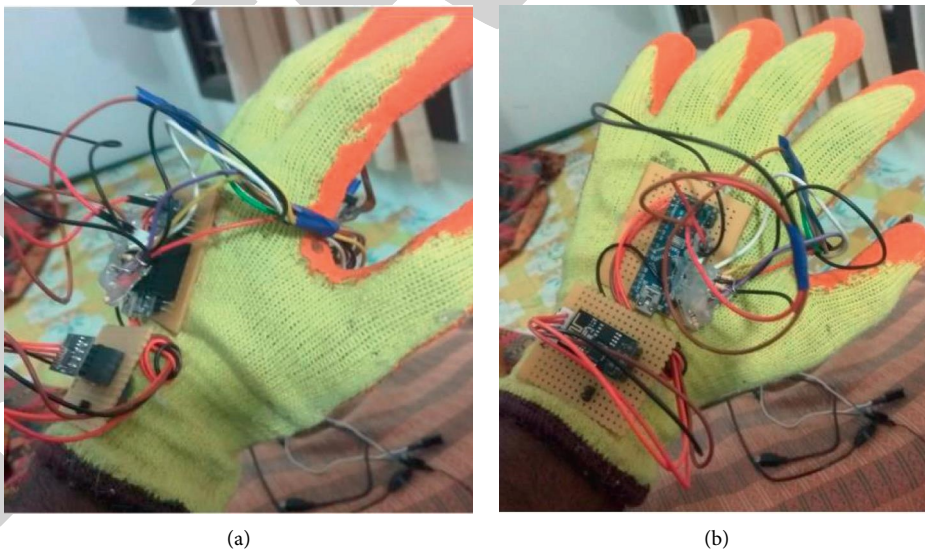


FIGURE 4: (a) Flex sensor interfaced in glove. (b) Human finger gesture detection using flex sensor.

#### 4. Results and Discussion

Demand for bionic hands is projected to grow as technology advances, necessitating a broader knowledge. The modern bionic limb has come a long way from the centuries-old hook prosthesis. We describe how current prosthetic hands artificially duplicate the human hand's key functions.

Despite great developments, bionic prostheses are inferior to organic prostheses. Finally, we outline significant research areas that could lead to vast increases in bionic limb capability that could one day fully mimic or even surpass the biological hand's inherent capabilities and develop a highly versatile upper body prosthetic device that overcomes the challenges of cost and usability of today's commercially

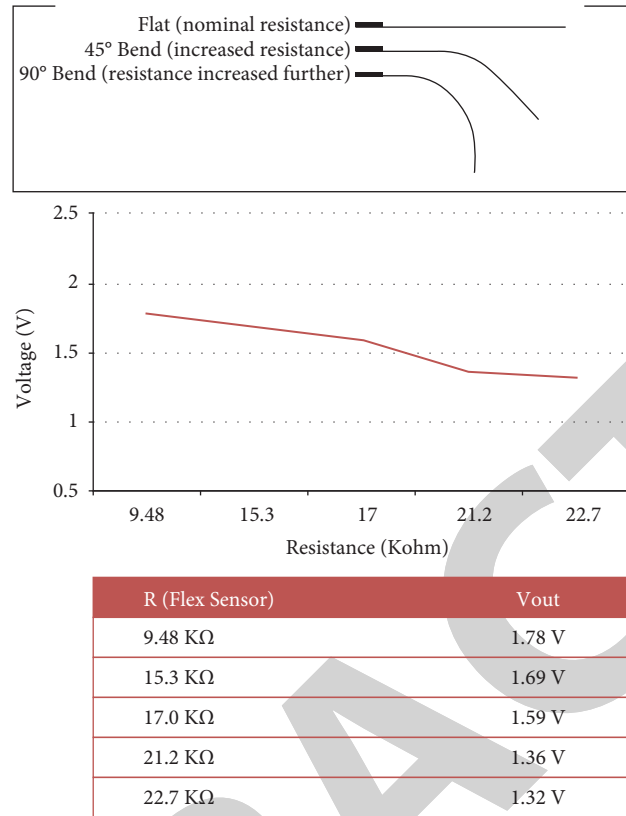


FIGURE 5: Flex sensor variation.

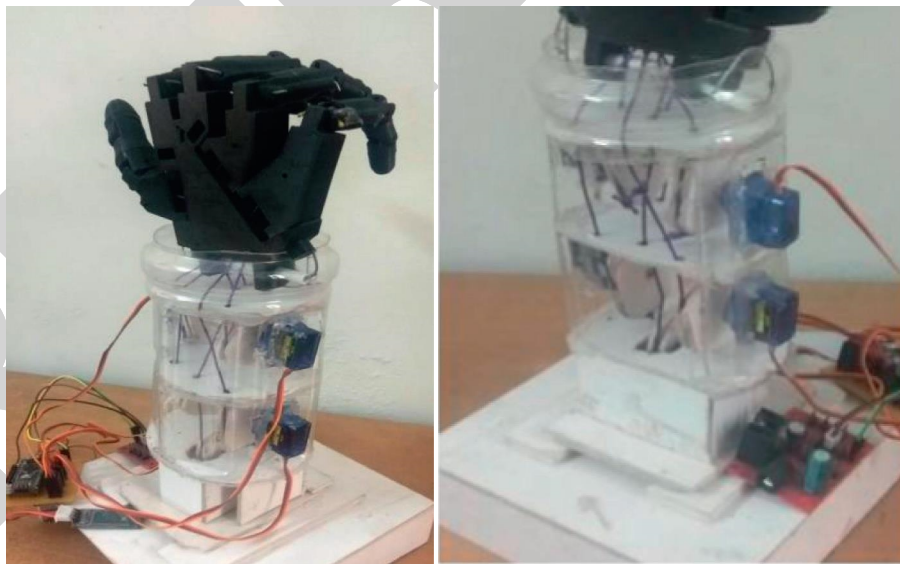


FIGURE 6: Pulley string action.

available prostheses. For myoelectric prostheses, the user can select a gesture via an Android smartphone application, saving money and frustration. The Arduino receives this information from the phone and uses it to power servos that independently trigger each finger. As a result of low-cost materials and the use of popular electronics such as cell phones, amputees may afford to purchase cutting-edge

prosthetics with relative ease. The pulley string action is given in Figure 6.

PWM controls the position of each servo motor. The motors are controlled by transmitting data from a PC to the appropriate motor controller over a serial line. The data sent down the serial line contains both the intended location and the requested motor number. This data is delivered to all motor

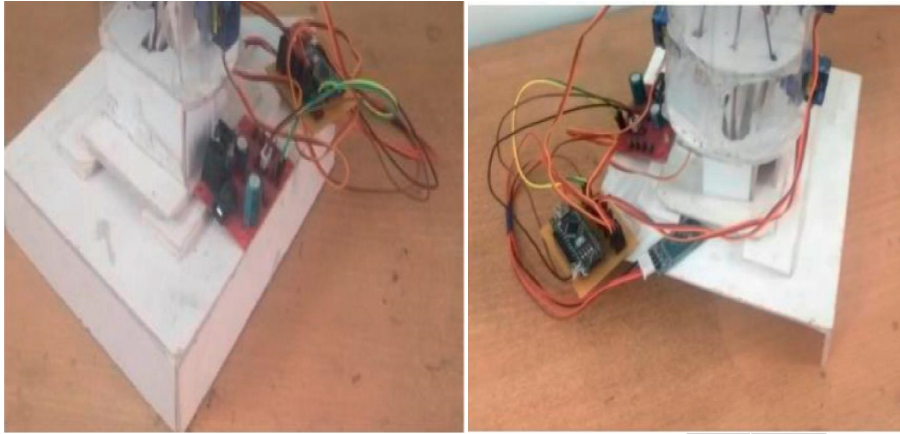


FIGURE 7: Power supply and microcontroller interface with servo.

control circuits in a daisy-chain configuration. Each control circuit's microcontroller checks the desired motor's number against its own. It converts the requested location into a pulse width signal and sends it to the motor until each circuit receives a new position request. If it is not needed, the controller keeps sending the last requested signal. Each microcontroller includes two timers; one to keep the motor in place and the other to run the microcontroller, including data collection. Each motor thus requires a microcontroller. The circuit next translates the signal into the proper pulse output to hold the motor in place. To demonstrate the system's real-time nature, a Visual Basic simulation was created that displays the model's motions on the screen. The simulation uses the same data as the model and displays the desired outcome so that the actual and desired outputs can be compared [21, 22].

The finished prototype has 5 servos coupled to pulleys and strings to move the 3D-printed fingers. The servos are coupled to the strings and pulleys to move the 3D-printed fingers. Connectors link the joints. The 3D-printed elements are linked together with myothreads. They are connected via pulleys. This project uses an Arduino NANO microcontroller. A 16MHz quartz crystal and 14 digital input/output pins show the Arduino NANO pinout schematic. It connects the robotic hand and sensor glove by obtaining signals from the flex sensor in the sensor glove and the pressure sensor on the robotic hand. The power supply supplies 5V to the servo and the Arduino board. Bluetooth data transmission and reception require 5V. The power supply and microcontroller interface with servo are given in Figure 7.

## 5. Conclusion

This work created a complete prosthetic hand prototype. It outperformed contemporary offerings in terms of functionality.

- (i) Compound thumb gearboxes enable powered articulated thumb roll actuation. This technique is unique; it uses serial Bluetooth communication between master and slave to detect finger movement. Serial communication is used between the transmitter and receiver.

- (ii) In order to facilitate programming and algorithm development, a long-term test platform has been built. It is no longer necessary to look for ultra-precision industrial components because of the readily available hobby and remote control industry components available today.
- (iii) Because designers are neither directly responsible for research and development costs nor concerned with the final cost of a high-end item, large corporations have developed a standard strategy for researching and constructing new systems for their products. When an individual creates a novel system, they might challenge existing design and manufacturing methods to produce an equal product faster and easier.
- (iv) In the future, robots will be widely used in every engineering industry reducing human efforts.

## Data Availability

The data used to support the findings of this study are included within the article. Further data or information is available from the corresponding author upon request.

## Conflicts of Interest

The authors declare that there are no conflicts of interest regarding the publication of this article.

## Acknowledgments

The authors appreciate the supports from Haramaya University, Ethiopia, for providing help during the research and preparation of the manuscript. This work is also supported by Taif University researchers supporting project number (TURSP-2020/40), Taif University, Taif, Saudi Arabia.

## References

- [1] K. H. Ng, V. Nazari, and M. Alam, "Can prosthetic hands mimic a Healthy human hand?" *Prosthesis*, vol. 3, no. 1, pp. 11-23, 2021.

## *Retraction*

# **Retracted: The Influence of Chemically Treated Hemp Fibre on the Mechanical Behavior and Thermal Properties of Polylactic Acid Made with FDM**

### **Advances in Materials Science and Engineering**

Received 26 December 2023; Accepted 26 December 2023; Published 29 December 2023

Copyright © 2023 Advances in Materials Science and Engineering. This is an open access article distributed under the Creative Commons Attribution License, which permits unrestricted use, distribution, and reproduction in any medium, provided the original work is properly cited.

This article has been retracted by Hindawi, as publisher, following an investigation undertaken by the publisher [1]. This investigation has uncovered evidence of systematic manipulation of the publication and peer-review process. We cannot, therefore, vouch for the reliability or integrity of this article.

Please note that this notice is intended solely to alert readers that the peer-review process of this article has been compromised.

Wiley and Hindawi regret that the usual quality checks did not identify these issues before publication and have since put additional measures in place to safeguard research integrity.

We wish to credit our Research Integrity and Research Publishing teams and anonymous and named external researchers and research integrity experts for contributing to this investigation.

The corresponding author, as the representative of all authors, has been given the opportunity to register their agreement or disagreement to this retraction. We have kept a record of any response received.

### **References**

- [1] N. I. Haroon Rashid, R. Meenakshi Reddy, A. R. Venkataramanan et al., "The Influence of Chemically Treated Hemp Fibre on the Mechanical Behavior and Thermal Properties of Polylactic Acid Made with FDM," *Advances in Materials Science and Engineering*, vol. 2022, Article ID 6953136, 9 pages, 2022.

## Research Article

# The Influence of Chemically Treated Hemp Fibre on the Mechanical Behavior and Thermal Properties of Polylactic Acid Made with FDM

N. I. Haroon Rashid,<sup>1</sup> R. Meenakshi Reddy,<sup>2</sup> A. R Venkataramanan,<sup>3</sup> Melvin V. D. Poures,<sup>4</sup> A. Thanikasalam,<sup>5</sup> Ashraf Elfasakhany,<sup>6</sup> and Agonafir Alemayehu <sup>7</sup>

<sup>1</sup>Department of Aerospace Engineering, B.S.A.R. Crescent Institute of Science and Technology, Vandalur, Chennai, Tamilnadu, India

<sup>2</sup>Department of Mechanical Engineering, G. Pulla Reddy Engineering College, Kurnool, Andhra Pradesh, India

<sup>3</sup>Department of Mechanical Engineering, Sona College of Technology, Salem 636005, TamilNadu, India

<sup>4</sup>Department of Thermal Engineering, Saveetha School of Engineering, Saveetha Institute of Medical and Technical Sciences, Chennai, Tamil Nadu, India

<sup>5</sup>Department of Mechanical Engineering, Academy of Maritime Education and Training (AMET-Deemed to be University) ECR-Kannathur, Chennai 603 112, Tamil Nadu, India

<sup>6</sup>Mechanical Engineering Department, College of Engineering, Taif University, P.O. Box 11099, Taif 21944, Saudi Arabia

<sup>7</sup>Department of Mechanical Engineering, Mizan Tepi University, Ethiopia

Correspondence should be addressed to Agonafir Alemayehu; [agonafir@mtu.edu.et](mailto:agonafir@mtu.edu.et)

Received 15 May 2022; Revised 16 June 2022; Accepted 23 June 2022; Published 5 August 2022

Academic Editor: K. Raja

Copyright © 2022 N. I. Haroon Rashid et al. This is an open access article distributed under the Creative Commons Attribution License, which permits unrestricted use, distribution, and reproduction in any medium, provided the original work is properly cited.

Reinforcement with natural fibre has become a common place in a range of industries in the modern day. A polymer matrix can, however, boost the strength of the reinforcing element. When it comes to natural fibres and polymers, they simply do not mix because of their different hydrophobic and hydrophilic properties. However, because the polymer matrix is designed to be hydrophobic, the natural fibres are hydrophilic. This issue can now be rectified with alkalization and a silane binding agent. This technique of modifying natural fibres may result in both rise in surface roughness and a reduction in water attraction and moisture content. In this research, the effects of alkaline and silane treatment were demonstrated using mechanical testing and Fourier transform infrared spectroscopy (FTIR). DSC and TGA tests were used to assess the materials' chemical compositions and thermal properties. In comparison to other composites, those with a 2 percent silane treatment showed improved strength performance. Hemp fibre composites are expected to achieve great performance in industrial applications by enduring chemical treatment.

## 1. Introduction

The reduction of petroleum resources has prompted engineers and other professionals to pay more attention to this issue. When incineration releases toxic gas into the atmosphere, it provides a viable alternative for developing sustainable natural polymer composites [1]. Carbon and glass fibres are the fundamental ingredients in advanced polymer composites, which are widely used in the aerospace,

automotive, and construction sectors [2, 3]. As a result, it was found that these fundamental materials are rarely, if ever, reusable. Replacements for petroleum-based and synthetic-based fibres have been introduced [4]. As far as natural fibre qualities go, they are fairly similar to those of synthetic fibres, and high rigidity and good mechanical properties are among many other qualities [5]. Natural fibres provide a lots of benefits over synthetic fibres and glass fibres, including biodegradability, nontoxicity, and a CO<sub>2</sub> neutral life cycle [6].



Researchers and industrial engineers are encouraged to continue their work on natural fibres because of their ability to protect the environment as well as other advantages such as reduced machine wear and no health risks, excellent sound absorption, and reduced equipment wear as well as better energy recovery and good thermal insulation are some of the advantages of using lightweight composite materials [7–9]. Impact resistance and modulus are two of the most important aspects of rigidity, as are strength and durability, and are just a few of the mechanical attributes that natural fibres possess in abundance. Natural fibres can be used in a variety of industrial settings because of their unique qualities. All kinds of things from windows and doors to railroad sleepers and furniture to automobile dashboards and brake linings are included. Natural fibres include fibres made from plants, animals, and minerals [10, 11]. Lignocellulosic or cellulosic fibre, also referred to as plant fibre, are widely used in the industrial sector. Natural fibres such as PALF, hemp, sisal, jute, hemp, flax, ramie, and wood can be used to reinforce biodegradable or nonbiodegradable polymers. In addition to being biodegradable and readily available in tropical regions, hemp fibre (HF) is an excellent substitute for synthetic fibres [12, 13]. Due of its rapid growth and its inexpensive cost, the demand for hemp plants were extremely strong. Hemp bast's mechanical properties make it an attractive fibre for researchers and scientists. Natural fibres such as flax and hemp, as well as hemp bast, are popular choices. As a common material for biodegradable products in areas including automotive and aerospace sectors, marine, and packaging industries, natural fibre has been advocated by researchers and scientists [14, 15]. Lightweight and strong, natural fibres are an excellent choice for clothing. Plastics are now used in nearly every industry [16]. Thermoplastic polymers are commonly utilized in high-tech applications, but their reduced temperature stability and strength mean that they may not be suitable for all situations [17]. Plastics such as PLA, a renewable and biodegradable basic polymer in the polyester family, have been shown to be safe for the environment, humans, and animals. Several reactive groups, most of which are made up of biopolymers, are ideal for combining natural fibres with matrix polymers [18, 19].

Hemp and other natural fibres have an inherent hydrophilic quality. To put it another way, this feature states that because they include cellulose structures that contain hydroxyl groups (-OH), the moisture content may rise over time [20–22]. When a structure is too wet, it might swell and become unstable, which can lead to cracks, among other things. While it may be desirable for a fibre to be able to adhere to a polymer matrix, this trait can have an adverse effect on the test findings [23, 24]. As a result, low inter-phase bonding may lead to inferior mechanical properties, low strength, and a limited service life for the product. Researchers believe that increasing the mechanical characteristics of biocomposites by applying a surface modification may be a solution to these hydrophilic and hydrophobic issues [25]. When it comes to modifying a

surface, sodium hydroxide immersion can be an effective tool, according to [26]. While removing natural fibre wax and oil, this process may also increase the fiber's surface roughness. It has been established that alkaline treatment and the use of a silane coupling agent have no effect on surface modification. It is possible to enhance the interfacial bonding between natural fibres and polymer matrixes by using a coupling agent; for example, compared to other surface treatments, silane is an excellent and superior coupling agent for fiber-polymer interlocking adhesion [27]. Chemical bonding in natural fibres and polymer matrixes are also affected.

An experiment by [28] employed hemp fibre and PALF composites to explore the impact of surface treatment. Fibres that had been treated with alkaline-silane and silane were all examined in this study [29]. Researchers found that a complete alkaline treatment can remove all fibre impurities, depending on alkali concentration and soaking time, according to their findings. Surface treatment can increase the strength of composite materials. All of the categories in Table 1 show that natural fibres outperform synthetic fibres.

Research into natural fibre production is a relatively young field of study. Many companies and researchers are interested in natural fiber-reinforced polymer biocomposites made with ecologically friendly FDM technology. Usual fibres in the filament of FDM have drawn the attention of various rivals and market platforms. Acrylonitrile butadiene styrene (ABS) is the most often used polymer in FDM [30]. However, it is still not advised that a thermoplastic polymer be used as the primary material for FDM. Strength and stiffness are two of polymer's most critical mechanical qualities. Many bio-based polymers have had their mechanical properties examined in an effort to improve FDM technology, as previously mentioned [31]. Because of their stability, acrylonitrile butadiene styrene and polylactic acid are common building materials. PLA was the most commonly used thermoplastic in this process. PLA is biodegradable, recyclable, and it has a melting point of 145–160 degrees Celsius [32]. Because of its high tensile strength and limited thermal stability, PLA is a biopolymer that resists crystallization. It is created by fermentation of a recyclable product. In addition, PLA is drawing interest because of its biodegradability and renewable nature [33]. Natural fibres such as hemp can also be used as reinforcement when PLA is mixed with PLA using a traditional method. Optimization of fibre loading and chemical treatment of the reinforcement could affect the mechanical properties of the product. As a result, PLA-coated natural fibres are brittle and need to be stored and fed from dried feedstock [34].

After a 24-hour NaOH treatment, natural fibres were subjected to varying concentrations of a silane coupling agent which was maintained at (1 to 2%, respectively) before being evaluated in this study. This study focuses on the mechanical characteristics of hemp fiber-strengthened PLA mixtures that are being chemically treated [35, 36]. Alkaline and silane treatment impacts on surface amendment have also been investigated [37].



TABLE 1: Fibre distinctive values for tensile strength, Young's modulus, elongation (%), and density.

Fibre	Tensile strength (MPa)	Young's modulus (GPa)	Elongation (%)	Density (g/cm <sup>3</sup> )
Cotton	290–810	5.2–11.8	3.1–11	1.6–1.8
Jute	385–805	10–28.1	1.17–1.7	1.4–1.7
Flax	337–1500	28.4	1.3–3.4	1.5–1.7
Hemp	500–850	71.2	1.7–4.2	1.48–1.52
Sisal	350–650	8–37	2.1–15	1.35–1.6
E-glass	2100–3400	71–74	2.6–3.5	2.52–2.56
Carbon (standard)	3300–4700	235–475	1.5–1.7	1.5–1.62
Hemp	920	54	1.7	1.3–1.54
PALF	160–16354	61–83.5	1.7–2.5	1.78

TABLE 2: Parameters for preparing silane concentrations.

S. No	Parameter	Explanation
1	PLA	Neat polymer
2	Untreated	Untreated hemp fibre composites
3	1% silane	1wt % concentration of silane + 7% concentration of alkalinity hemp fibre composites
4	2% silane	2wt % concentration of silane + 7% concentration of alkalinity hemp fibre composites
5	3% silane	3wt % concentration of silane + 7% concentration of alkalinity hemp fibre composites

TABLE 3: Orientation of mixtures.

Specimens	Composite weight in grams	Fibre weight in grams 3 wt%	Matrix weight in grams 97 wt%
All specimens	550	12.5	537.5

## 2. Alkaline Therapy Methodology

Randomly sized hemp fibre powder between 100 and 650 microns was subjected to alkaline treatment in this experiment. Concentration of sodium hydroxide in the sodium hydroxide solution was 6 percent for 24 hours. Hemp fibres were treated with alkaline and then thoroughly cleaned under running water before being dried in an oven at 110°C for 24 hours.

**2.1. Silane Treatment.** The next step is to apply a silane link mediator to the surface. In this treatment, APS (amino-propyltriethoxy silane) was liquified in a solution containing 65 percent methanol and 35 percent water at concentrations of 1 percent, 2 percent, and 3 percent, respectively. 30 minutes of vigorous agitation followed. A silane solution was used to soak the hemp fibre for three hours before drying it in an oven at 120 degrees Fahrenheit for 24 hours to eliminate all of the fiber's moisture content. Silane concentration, plain polymer, and untreated hemp fibre samples were categorised according to Table 2 silane concentrations.

**2.2. Composite Mixture.** According to the law of combination formulation in Table 3, hemp fibre and polymer composite were created. An equation has been used to determine the weight of components in composites in order to obtain their composition in equation.

$$\begin{aligned} &\text{Weight \% of Element} \times \text{Weight of composites} \\ &= \text{Weight of elements.} \end{aligned} \quad (1)$$

**2.3. Extrusion of a Polymer Fibre.** Table 4 shows the properties of filament composites produced by a twin screw extruder, and Figure 1 shows the schematic view of the twin screw extruder.

**2.4. Sample Extrusion.** The nozzle's temperature, the bed's temperature, and the infill percentage all have to be considered. The option that controls the solid infill was previously set to 100% in-line form. The upper and lower layers of the shell's parameter have three repeated numerical layers, whereas the shell itself has two layers. In comparison, the first layer had a layer height of 0.27 mm. The quality of the printed samples was also influenced by the printing speed. There is an 80 m/s difference between the print head speed and the print speed in this printing procedure.

## 3. Sample Characterization

**3.1. Mechanical Test.** The biodegradable composites' mechanical characteristics were evaluated using the tensile test. After doing a tensile test, researchers can determine mechanical properties. Type 1 is one of three "dog bone" samples available. ASTM D638 was used for the testing in this investigation. Using a load cell rated at 5 kN and 50 mm span, this typical test achieves a crosshead speed of 1 mm/min. The UTM was used to evaluate the tensile properties of composites.

An equation can be used to determine exactly strong a single fibre is

TABLE 4: Extrusion-related constraint.

Samples	Melting temperature (°C)	Screw speed (rpm)
PLA	220	27
Untreated fibre	200	31
1% silane	208	27
2% silane	208	27
3% silane	208	27

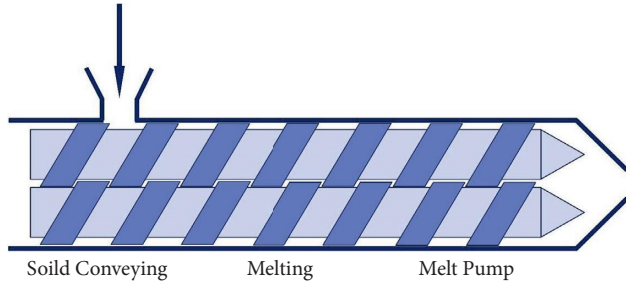


FIGURE 1: Twin screw extruder.

$$\sigma = \frac{F}{A}, \quad (2)$$

where  $\sigma$  is the tensile strength of the fibre (Pa), and cross-sectional area ( $A$ ) equals cross-sectional area ( $F$ ) in newtons ( $m^2$ ). The 3-point bending test was agreed out in line with ASTM D790. By means of this conventional testing procedure, the crosshead speed is 1 mm/min. The crosshead's speed is 1 mm/min with a load cell of 5 kN throughout this routine testing. One sample was tested at a time by the Universal Testing Machine for every one of the aforementioned categories. The sample size required by the ASTM standard is 100103 mm, with a 50 mm swath.

Equation can be used to determine the flexural strength of a single fibre

$$\sigma = \frac{3 PL}{2bd^2}. \quad (3)$$

Here,  $\sigma$  is flexural strength of the fibre (Pa),  $P$  is highest force at break ( $N$ ),  $L$  is support length (mm),  $b$  is the thickness (mm), and  $d$  is the deepness of the beam tested (mm).

**3.2. Thermo Gravimetric Analysis (TGA).** Before being transformed into composites, the deterioration of the hemp fibre was examined using thermogravimetric analysis. A filament specimen and a TA instruments machine are used in this study. Before manufacturing composites, the TGA was employed to regulate the breakdown of hemp fibres at high temperatures. Following the ASTM D3850 standard, TA equipment and a filament specimen are used for this analysis. Temperatures ranged from 10°C to 900°C, temperature range, with an average rate of 10 C/min heating.

**3.3. Fourier Transform Infrared Spectrometry (FTIR).** In terms of finding out which surface treatment belongs to which functional group, FTIR was performed on five

separate samples utilizing the Jasco FT/IR-6100 on untreated powder at 1 percent silane, 2 percent silane, and 3 percent silane. All spectra were taken in the 4000  $cm^{-1}$  to 400  $cm^{-1}$  wavelength range.

## 4. Results and Discussion

**4.1. Mechanical Test.** Mechanical testing was used to assess the tensile and flexural strength and Young's modulus of the material. Interfacial bonding may affect the strength of composites in a variety of ways. Good outcomes may be obtained by a well-balanced distribution of stress.

According to [38], tensile stress can be viewed as a single form of stress acting in a single direction (1-D). The results of this examination could show whether or not the sample has a good or bad interfacial bond. In order to get the most out of the tensile test, it is necessary to endure it.

There were threetypes of hemp fibres used in this experiment: untreated and treated. Processes of alkali and silane immersion were employed in the treatment of hemp fibres for use in clothing. One, two, and three percent silane solution concentrations were utilized in the experiment. It is possible to remove contaminants, lignin, and hemicellulose from the hemp fibre using alkaline treatment, but the concentration of alkali and the length of immersion must be taken into consideration. An excellent tensile strength result may be achieved by tolerating alkali and silane treatment, according to this article. The results shown in Figure 2 are from the untreated hemp fibres' investigational outcomes.

In accord with the ASTM D638 standard, the tensile test was carried out. In comparison to the neat polymer and untreated fibre, the graph overhead indicates that the treated fibre has excellent strength. It may be stated that surface treatment resulted in superior mechanical performance compared to untreated fibres. Because the fibre utilized in this experiment is in a powder form known as isotropous, it lacks an exact alignment and therefore cannot be used in this experiment. Following that is a comparison of different concentrations of silane treatment, which clearly reveals that silane treatment at 3% (56.25 MPa) is most effective compared to 1 percent (55.81 MPa) and 2 percent (57.46 MPa). The best tensile strength was found at 1% silane content, according to the research. Adding fibres to PLA increased the plastic's mechanical qualities, according to the results. Lignocellulose and hemicellulose were efficiently removed while retaining better interfacial contact among the matrixes and fibres, according to these findings. Because of fibre breakage and chemical degradation, a higher silane concentration could reduce the tensile strength of the fibres, resulting in a reduction in tensile strength. The hydrophilic characteristic of the fibre also reduced the strength of composites, despite the lower concentration of impurities. Lower concentrations may not be effective, according to earlier studies on the optimum concentration. As opposed to 3 percent and 5 percent, [25] found that a silane concentration of 1 percent produced the best composite strength and binding. [17] investigated the effect of silane concentration on fiber-reinforced polymer composites made from maize stalks. A larger concentration of silane may alter fibre

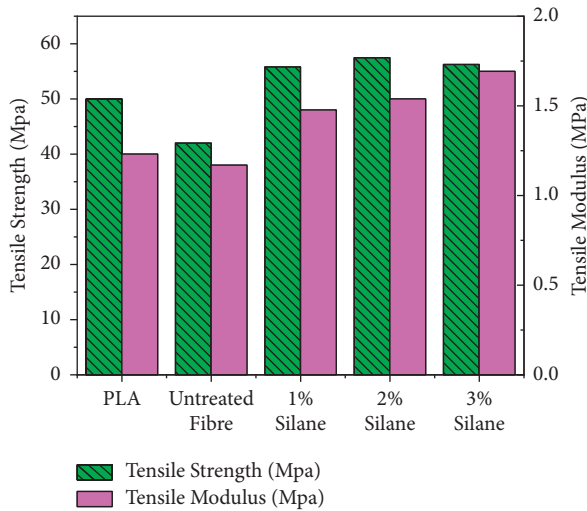


FIGURE 2: Results of composites tensile strength, MPa, and tensile modulus, MPa.

surface properties and lessen the unique fibre feature; hence, this study's findings suggest that a concentration of 1 percent is the best. [21] published another work in which he examined the effects of various concentrations on the tensile and impact test results of a mechanical test. According to the mechanical test, a concentration of 1 percent silane is the best option for treatment. Because silane is an acidic solvent, it will erode the fiber's original structure and strength if used in large quantities. Researchers reported that on the surface fiber has the ability to change concentration, time, and effect [24]. As [24] reported, higher concentration and longer immersion time resulted in a decrease in fibre standard's bursting strength. As shown in the graphs above, the treated fibres are stronger than their untreated counterparts.

Composites can be damaged during production, according to a review of the scientific literature. The difference in performance between treated and untreated fibre composites could be due to surface cleaning, as treated fibre aids in the adhesion of the two phases and increases the overall strength of composites. Tests on flexure were required to determine how well the material would hold up in a load before the break point was reached. The material's modulus of elasticity was measured by placing a supported beam between two supports and applying a load there. If the composites can handle bending loads and deformation before breaking or deforming, flexural testing is used. According to the criteria of the ASTM D790 standard, a flexural test was conducted. Polymer, untreated fibre, and silane-treated fibre are all included in this flexural test. However, Figure 3 shows that 2.0 percent silane had the second-highest flexural modulus (86.41 MPa), although only one percent of it had the same strength (83.5 MPa). PLA's strength (61.1 MPa) was the lowest of any of the composites evaluated when evaluated to treated counterparts (49.46 MPa). When a force was applied to a silane-treated fibre, the dispersion stress was sufficient to maintain interfacial bonding. Composites can be damaged during production, according to a review of the scientific literature.

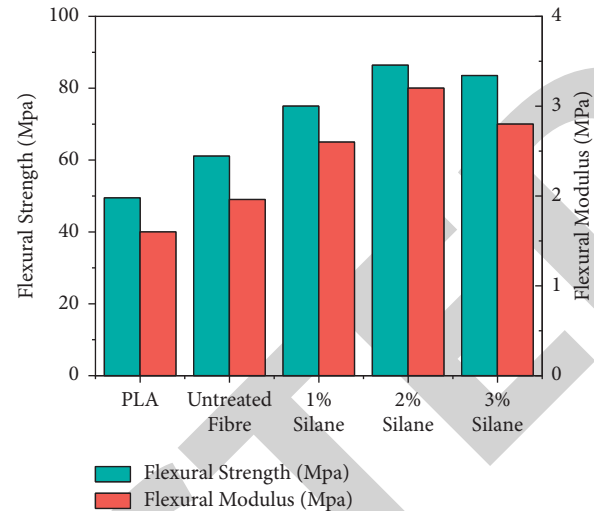


FIGURE 3: Flexural strength (MPa) and flexural modulus (MPa).

The difference in performance among treated and untreated fibre composites could be owing to surface cleaning, as treated fibre aids in the adhesion of the two phases and enhances the overall strength of composites. In order to measure the material's strength and resistance to distortion under stress, a flexural test was conducted. The material was arranged as a supported beam between two supports and subjected to a point load for bending and flexural stress measurements. To find out if the composites can be twisted and distorted without breaking, this kind of testing is carried out. The flexural test was performed in accord with the ASTM D790 standard. Polymer, untreated fibre, and silane-treated fibre are all included in this flexural test. Figure 3 indicates that 1.0 percent silane has the highest flexural modulus (83.8 MPa), whereas 2.0 percent silane has the second-highest (83.8 MPa) (81.4 MPa). PLA exhibited the lowest strength (58.7 MPa) of any of the composites tested when compared to treated composites (49.4 MPa). Silane was employed to improve the treated fiber's interfacial bonding and dispersion stress.

**4.2. Results of Flexural Modulus (MPa) and Flexural Strength (MPa) for Composites (MPa).** A high flexural modulus (3162.2 MPa) was found for 2-percent silane in comparison to other composites and plain polymers when measuring the modulus. Hemp fibre composites can be successfully made with a silane content of 2%. This could be due to a lack of fiber-polymer contact or inadequate dispersion of the fibre toward the matrix, both of which resulted in limited load transmission for the untreated polymer. The bonding between the two phases of a composite rises as the strength of the composite increases (reinforced and polymer matrix). A chemical treatment can also be achieved for interlocking composites, which is different from conventional composites and neat polymers. A silane concentration of 2% can be used to make hemp fibre composites. No data were found to support the untreated polymer's lack of interfacial connection with fibre or poor fibre dispersion toward the

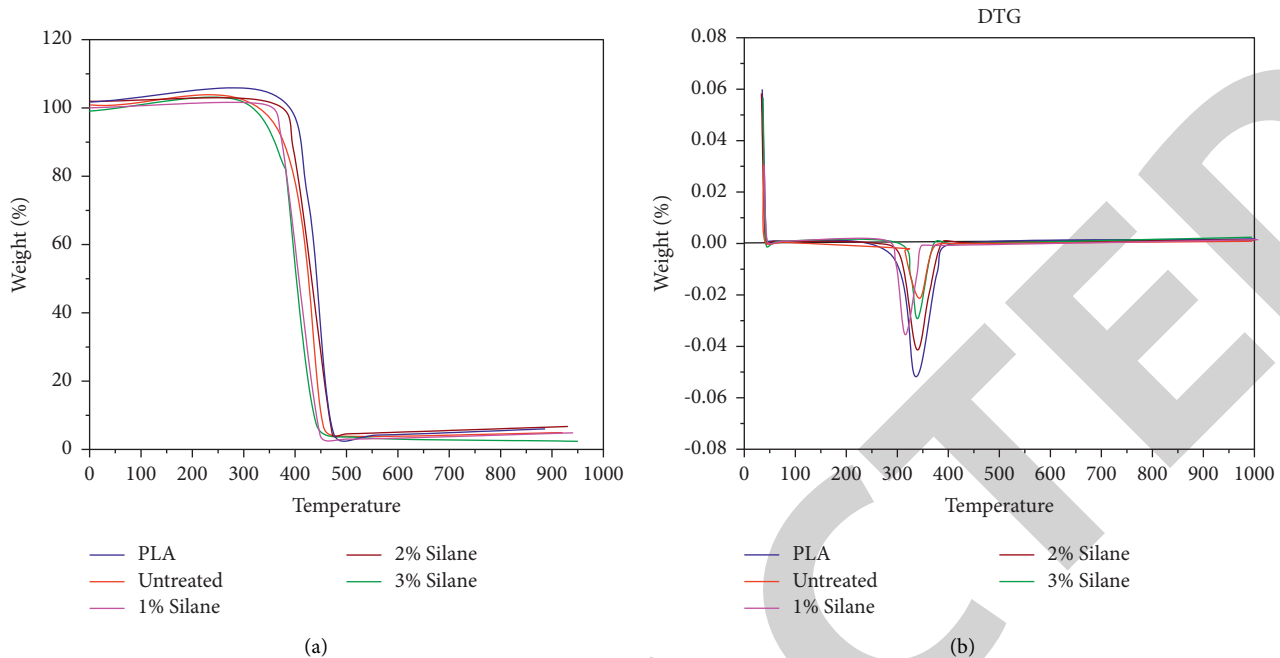


FIGURE 4: (a) Thermogravimetric analysis (TGA) and (b) difference thermogravimetry (DTG) results of composites.

matrix, both of which lead to insufficient load transmission. The bonding between the two phases of a composite rises as its strength increases (reinforced and polymer matrix). By enduring the optimum concentration of chemical treatment, it is also possible to produce effective interlocking composites. Good surface treatment parameters resulted in strong and elastic results in any test, which was found by researchers.

The interfacial adhesion between the hemp fibre silane coupling agent and the fibres was found to improve the tensile capacities of the complex samples after the treatment. The active agent of silanol will be generated as long as the trialkoxysilane is in contact with water ( $H_2O$ ). This silanol structure was organically dumped on the hemp surface in order to form a siloxane bond between the hemp and the silane binding agent. Incorporating PLA resin into a functional hemp surface can improve fiber-matrix adhesion. Hemp substrate is transformed into silanol via water-mediated reaction between trialkoxysilane and trialkoxysilane ( $H_2O$ ). To create a siloxane bond with the silane coupling agent, this silanol complex was condensed and applied to the hemp surface. A functional hemp surface can be achieved by incorporating organofunctional groups into the PLA resin, which reacts with the fibres and enhances their adherence.

**4.3. Thermogravimetric Analysis (TGA).** Figures 4(a) and 4(b) show the TGA and DTG protocols used to evaluate PLA, untreated hemp fibre composites, and treated hemp fibre composites in a nitrogen atmosphere for thermal stability, thermal decomposition, and mass changes. Because of the unique properties of thermoplastics, which allow for both recycling and reusing, thermal degradation is necessary for studying the breakdown of composites. High-

temperature resistance of the composite can be assessed using this approach. Composites degrade under nitrogen air, as shown by TGA and DTG. At specific temperatures, five samples were taken and began to deteriorate. [35] described three stages of decomposition: initial, intermediate, and final. Phase one involved evaporating the moisture, and second phase was employed to remove chemical content such as lignin and hemicellulose, leaving less than 10% of the original weight as final residue.

The first phase deprivation of hemp fiber-reinforced PLA composites occurs between 10 and 300°C in TGA analysis. Fibres begin to lose moisture as it evaporates in this phase, and the weight loss now stands at less than 9%. When heated to 300–400 degrees Celsius, the chemical conformation of fibres such as cellulose, hemicellulose, pectin, and lignin began to degrade. This is owing to the high temperatures that are practical to the hemp fibre during the manufacturing process. Fibres in the hemispheres deteriorated first before lignin (which is more stable) and the rest. Experimentation revealed that in composites containing 2% silane, breaking the functional group needed a high temperature. Finally, after reaching the highest temperature, the residual composites underwent the final stage of processing.

**4.4. Fourier Infrared Spectroscopy Is Used to Perform Chemical Analyses.** The FTIR spectrum revealed the presence of cellulose, hemicellulose, and lignin among other substances. A good example is the C–O stretch-1 group. Untreated lignin was clearly seen in the data at 1000–1300  $cm^{-1}$  peak. Fibre lignin is detected at a peak of 1028  $cm^{-1}$ , and 6 percent NaOH is detected at a high of 1030  $cm^{-1}$  in the data. 8 percent NaOH reveals a peak of 1028  $cm^{-1}$  in the treated fibre, while fibre lignin displays a peak of 1028  $cm^{-1}$  in the

TABLE 5: Extrusion parameters.

Parameters	Untreated	7% NaOH	1% silane	2% silane	3% silane
Lignin	1028	1022	1032	1034	1032
Cellulose CH <sub>2</sub>	2821	3144	3242	3244	3245
Hydroxyl group -OH	3100–3300	3100–3300	3100–3300	3100–3300	3100–3300
Stretching N-H	3128–3140	3100–3128	—	—	—
Ethyl carbonyl group C=O	1618	1612	1608	1608	1608
Hemicellulose CH	2814–2816	2904	2904	2912	2312
Absorption of water	1584	1502	1434	1434	1434
Si-C stretching bond silane	8821	831.2	822.6	910–920	910–920
Ester carbonyl group C=O	1619	1601	1602	1602	1602

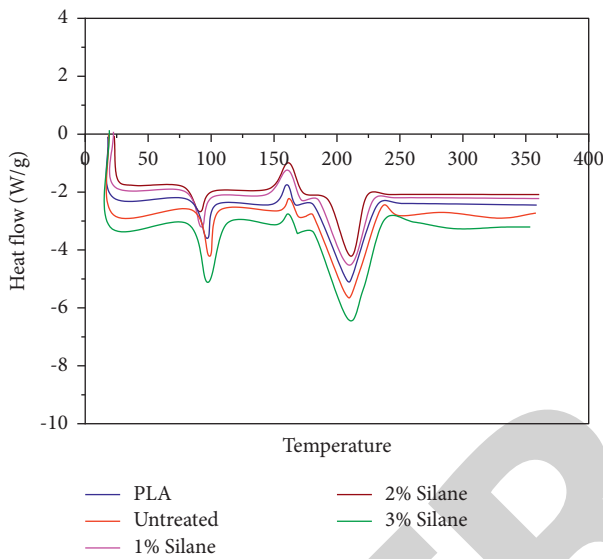


FIGURE 5: Differential scanning calorimetry (DSC).

untreated fibre. There was lignin in the range of 1028–1031  $\text{cm}^{-1}$  based on the declining wave number. This indicates that the lignin has been reextracted from the fibre. The extrusion parameters of the composites are given in Table 5.

Theoretically, the highest concentrations of hemicellulose and cellulose (CH and  $-\text{CH}_2$ ) can be found in the range of 2864  $\text{cm}^{-1}$  to 2931  $\text{cm}^{-1}$ . Hemicellulose can be found in concentrations ranging from 2864  $\text{cm}^{-1}$  to 3012  $\text{cm}^{-1}$  in untreated fibres, while cellulose reaches a maximum concentration of 2924  $\text{cm}^{-1}$ . Hemicellulose concentrations of 3012 and 3406  $\text{cm}^{-1}$  have been found in untreated fibres. Hemicellulosic fibres that have been treated with alkaline treatment and 1 percent silane had hemicellulose concentrations of 2912  $\text{cm}^{-1}$  and 3412  $\text{cm}^{-1}$  for cellulose, respectively. A peak at 3436  $\text{cm}^{-1}$  for hemicellulose indicates no significant difference between fibres treated with sodium hydroxide and 1 percent silane and fibres treated with sodium hydroxide and 3 percent silane, while the peak for cellulose, NaOH, and 2 percent silane is 2912  $\text{cm}^{-1}$ . The peak of 3436  $\text{cm}^{-1}$  demonstrated no difference.

The temperature values of the raw polymer, untreated hemp fiber-reinforced PLA composites, and treated ones are demonstrated in Figure 5 and Table 6, correspondingly. As a result, the data have been compiled in Table 6. In graph reading, exothermic and endothermic processes are the most

TABLE 6: DSC data.

Constraints	Thermal characteristics		
	T <sub>g</sub> °C	T <sub>cc</sub>	T <sub>m</sub>
PLA	61.4	122.4	152.3
Untreated hemp/PLA	61.03	117.3	151.3
1% silane hemp/PLA	62.60	119.4	154.3
2% silane hemp f/PLA	60.80	119.2	154.2
3% silane kenaf/PLA	58.40	117.2	151.9

important terms to know. The exothermic peak for the PLA polymer is the crystallization temperature; the endothermic peak is the melting temperature of 151.23°C and the degradation temperature of 298.75°C.

The T<sub>g</sub> of Poly(lactic acid) (59.12°C), untreated (59.01°C), at 1 percent silane (62.19°C), 2 percent silane (59.32°C), and 3 percent silane treated hemp fibre composites is shown in the DSC curves of PLA mixtures with untreated, 1 percent silane, 2 percent silane, and 3 percent silane of treated hemp fibre composites (57.04°C). Thermography demonstrates that the polylactic acid polymer chains did not crystallize entirely in untreated 1 percent silane, 2 percent silane, and 3 percent silane fibre composites, as shown in the temperature high of hemp fibre composites. According to the data, the crystallization temperatures were 116.21°C, 119.38°C, 119.46°C, and 117.32°C. Composites and plain PLA have very different melting points. The melting points of untreated (148.62°C), 1 percent silane (151.8°C), 2 percent silane (153.6°C), and 3 percent silane can be found in the following table (151.20°C). It appears that the hemp fibre has no effect on PLA composite melting temperatures in the 1C region, indicating that processing temperatures are unaffected by this material. Each parameter's degradation temperature ranged from 292.41°C to 297.5°C. This occurred as a result of the PLA degrading the polymer chain and hydrogen elements being lost as a result of the rupture. An important consideration prior to printing is the filament's thermal characteristics. This is owing to the fact that the filament's thermal qualities must be taken into consideration when printing. The mechanical properties of the samples will be affected if the heat energy is insufficient during the procedure. As a result, the precise melting temperature will help ensure a consistent dispersion of fibres and polymers during extrusion.



## 5. Conclusions

For a long time, various researchers have been attempting to figure out the best approach to strengthen materials with natural fibres. However, this work examines the mechanical and physical characteristics of hemp fiber-polymer PLA mixtures that have been mixed in various ways to reinforce a polymer matrix.

- (i) Among the many advantages of FDM is its ability to construct a wide range of complicated shapes and geometries, as well as low manufacturing costs. This analysis investigates the impact of chemical treatment on hemp fibre using mechanical and physical tests. A dual screw extruder was employed to produce a 3D printer filament containing 2.5 weight percent hemp fibre and a PLA polymer.
- (ii) Naked polymer (PLA without fibre component), silane-treated hemp fibre mixtures, and untreated hemp fibre composites were generated by researchers in this study. The testing used ASTM-printed samples, and the outcomes contain data. After cellulose, hemicellulose, and lignin have been treated with a 7 percent alkali solution, the interfacial connection between the two phases can be strengthened by adding 2% silane concentration.
- (iii) High levels of silane have been shown to damage fibres in this experiment. It has been shown that 3 percent silane is weaker than 2 percent silane because it is the most concentrated form of silane available. Because of their poor interfacial bonding and inability to evenly transfer stress over the surface, untreated natural fibre composites have the lowest strength of all composites. Silane concentration for natural fibre surface treatment is the most critical factor in achieving high strength in application development for natural fibre modifying composites.

## Data Availability

The data used to support the findings of this study are included within the article. Further data or information is available from the corresponding author upon request.

## Conflicts of Interest

The authors declare that there are no conflicts of interest regarding the publication of this paper.

## Acknowledgments

The authors appreciate the supports from Mizan-Tepi University, Ethiopia, for providing help during the research and preparation of the manuscript. This work was also supported by the Taif University researchers supporting project number (TURSP-2020/40), Taif University, Taif, Saudi Arabia.

## References

- [1] M. A. Rahuman, S. S. Kumar, R. Prithivirajan, and S. G. Shankar, "Dry sliding wear behavior of glass and jute fiber hybrid reinforced epoxy composites," *International Journal of Engineering Research and Development*, vol. 10, no. 11, pp. 46–50, 2014.
- [2] V. Mohanavel, S. Suresh Kumar, J. Vairamuthu, and B. NagarajaGanesh, "Influence of stacking sequence and fiber content on the mechanical properties of natural and synthetic fibers reinforced penta-layered hybrid composites," *Journal of Natural Fibers*, vol. 12, pp. 1–13, 2021.
- [3] Y. Liu, J. Xie, N. Wu, L. Wang, Y. Ma, and J. Tong, "Influence of silane treatment on the mechanical, tribological and morphological properties of corn stalk fiber reinforced polymer composites," *Tribology International*, vol. 131, pp. 398–405, 2019.
- [4] A. Oushabi, S. Sair, F. O. Oudrhiri Hassani, Y. Abboud, O. Tanane, and A. El Bouari, "The effect of alkali treatment on mechanical, morphological and thermal properties of date palm fibers (DPFs): study of the interface of DPF-Polyurethane composite," *South African Journal of Chemical Engineering*, vol. 23, pp. 116–123, 2017.
- [5] M. Asim, M. Jawaid, K. Abdan, and M. R. Ishak, "Effect of alkali and silane treatments on mechanical and fibre-matrix bond strength of kenaf and pineapple leaf fibres," *Journal of Bionics Engineering*, vol. 13, no. 3, pp. 426–435, 2016.
- [6] D. P. Sreenivasan, A. Sujith, A. N. Asokan, and C. Rajesh, "Dielectric properties of composites of natural rubber and KeratinFibre from chicken feather," *Fibers and Polymers*, vol. 22, pp. 1–14, 2021.
- [7] V. S. Sreenivasan, D. Ravindran, V. Manikandan, and R. Narayanasamy, "Influence of fibre treatments on mechanical properties of short Sansevieria cylindrica/polyester composites," *Materials & Design*, vol. 37, pp. 111–121, 2012.
- [8] A. M. M. Edeerozey, H. M. Akil, A. B. Azhar, and M. I. Z. Ariffin, "Chemical modification of kenaf fibers," *Materials Letters*, vol. 61, no. 10, pp. 2023–2025, 2007.
- [9] R. Siakeng, M. Jawaid, H. Ariffin, S. M. Sapuan, M. Asim, and N. Saba, "Natural fiber reinforced polylactic acid composites: a review," *Polymer Composites*, vol. 40, no. 2, pp. 446–463, 2019.
- [10] R. Mahjoub, J. M. Yatim, A. R. M. Mohd Sam, and S. H. Hashemi, "Tensile properties of kenaf fiber due to various conditions of chemical fiber surface modifications," *Construction and Building Materials*, vol. 55, pp. 103–113, 2014.
- [11] Hm. Akil, M. F. Omar, A. A. M. Mazuki, S. Safiee, Z. A. M. Ishak, and A. A. Bakar, "Kenaf fiber reinforced composites: a review," *Mater. Des.* vol. 32, no. 8, pp. 4107–4121, 2011.
- [12] N. Saba, M. T. Paridah, and M. Jawaid, "Mechanical properties of kenaf fibre reinforced polymer composite: a review," *Construction and Building Materials*, vol. 76, pp. 87–96, 2015.
- [13] S. Sreenivasan, S. Sulaiman, B. Baharudin, M. K. A. Ariffin, and K. Abdan, "Recent developments of kenaf fibre reinforced thermoset composites: review," *Materials Research Innovations*, vol. 17, no. sup2, pp. s2–s11, sup2, 2013.
- [14] N. Sgriccia, M. C. Hawley, and M. Misra, "Characterization of natural fiber surfaces and natural fiber composites," *Composites Part A: Applied Science and Manufacturing*, vol. 39, no. 10, pp. 1632–1637, 2008.
- [15] R. Vijay, "Extraction and characterization of vetiver grass (*Chrysopogon zizanioides*) and kenaf fiber (*Hibiscus*



## *Retraction*

# **Retracted: Control of Material Procurement Cost of Enterprises under the Background of the Low-Carbon Economy**

### **Advances in Materials Science and Engineering**

Received 26 December 2023; Accepted 26 December 2023; Published 29 December 2023

Copyright © 2023 Advances in Materials Science and Engineering. This is an open access article distributed under the Creative Commons Attribution License, which permits unrestricted use, distribution, and reproduction in any medium, provided the original work is properly cited.

This article has been retracted by Hindawi, as publisher, following an investigation undertaken by the publisher [1]. This investigation has uncovered evidence of systematic manipulation of the publication and peer-review process. We cannot, therefore, vouch for the reliability or integrity of this article.

Please note that this notice is intended solely to alert readers that the peer-review process of this article has been compromised.

Wiley and Hindawi regret that the usual quality checks did not identify these issues before publication and have since put additional measures in place to safeguard research integrity.

We wish to credit our Research Integrity and Research Publishing teams and anonymous and named external researchers and research integrity experts for contributing to this investigation.

The corresponding author, as the representative of all authors, has been given the opportunity to register their agreement or disagreement to this retraction. We have kept a record of any response received.

### **References**

- [1] Y. Ma, "Control of Material Procurement Cost of Enterprises under the Background of the Low-Carbon Economy," *Advances in Materials Science and Engineering*, vol. 2022, Article ID 5643665, 12 pages, 2022.

## Research Article

# Control of Material Procurement Cost of Enterprises under the Background of the Low-Carbon Economy

Yan Ma 

Accounting and Finance, Xi'an Peihua University, Xi'an 710000, Shaanxi, China

Correspondence should be addressed to Yan Ma; mayan@peihua.edu.cn

Received 24 May 2022; Revised 1 July 2022; Accepted 7 July 2022; Published 31 July 2022

Academic Editor: K. Raja

Copyright © 2022 Yan Ma. This is an open access article distributed under the Creative Commons Attribution License, which permits unrestricted use, distribution, and reproduction in any medium, provided the original work is properly cited.

With the increasing prominence of global warming and serious resource consumption, the low-carbon economy has become a new growth point for the world economy and is widely recognized by all sectors of society. Purchasing cost control management is generally regarded as an applied management discipline with important theoretical, operational, time, and management roles. Due to China's rapid economic development, high energy consumption, heavy pollution, and high emissions have resulted in catastrophic environmental damage. In recent years, the public's awareness of environmental protection has increased, and the requirements for enterprises to reduce pollution and energy consumption have increased, and environmental issues have become more and more important in China's economic development strategy. Based on the background of a low-carbon economy, this article studies the energy consumption of company's buildings and weights the suppliers of building raw materials. The maximum value, CI value, and CR value of the quality factor were 7.3379, 0.0566, and 0.0429, respectively.

## 1. Introduction

The rapid development of science and technology has improved human's ability to understand and shape nature, but it has also weakened the relationship between humans and nature, resulting in increasingly intensified conflicts between the ecological environment, natural resources, and economic and social development. Climate change has become a major challenge that threatens human survival and development and has attracted great attention from all countries. Climate change with global warming as the main feature has led to a series of natural disasters, threatening the survival of all living things, and is a serious crisis for human survival and development. In this case, reducing greenhouse gas emissions has become an important tool to deal with the crisis, which has given birth to a low-carbon economy.

Observations and theoretical studies have proved that the main reason for changes in greenhouse gas concentrations is inappropriate human activities. Global warming is caused by the massive consumption of fossil energy in pursuit of maximum economic profit. To solve

this problem, theoretical research must be carried out from the perspective of economy, people's ideas, production, and lifestyle. Economically speaking, on the one hand, it is necessary to study low-carbon technologies to improve energy efficiency and optimize the energy structure. On the other hand, it is necessary to study policies and measures to encourage greenhouse gas emission reduction and, at the same time, to solve the externality problems brought about by politics, environment, and society.

The innovation of this article is that it starts from the relevant theories of procurement cost management and systematically summarizes the relevant content of procurement cost, strategic cost, and value chain cost management. In the supply chain management environment, strategic suppliers are identified through supplier evaluation, and strategic partnerships are established to integrate the supply chain of the industry and further optimize resource allocation. All parties involved are beneficiaries, enhancing the competitive advantages of both parties and reducing procurement costs, which is conducive to the healthy development of the entire supply chain.

## 2. Related Work

Regarding the low-carbon economy, relevant scientists have done the following research. On the basis of a low-carbon economy, Lou et al. proposed a coordinated operation model of EV and system aiming at minimizing power generation cost, CO<sub>2</sub> emission cost, and V2G service subsidy. The new model comprehensively considers the relevant constraints such as electric vehicle driving demand, carbon emission quota, and carbon trading mechanism. A case study based on a test system demonstrates the rationality and effectiveness of the model [1]. Chen studied the performance impact of e-commerce, international hotel chains, local hotel chains, and green certification on carbon emission reduction of international tourism hotels. Over enough time, the environmental and economic performance of green-certified hotel groups have improved. According to the recommendation of the operation policy, the international hotel chain group and e-commerce outperformed the local hotel chain, and he discussed how to maintain the continuous improvement of the low-carbon performance of the hotel industry [2]. Faerber et al. outlined how current distribution network pricing can be modified to enable the transition to smart grids in a low-carbon economy. He highlighted multiple trade-offs between innovative pricing approaches and regulatory principles, which may be addressed by political decisions on how to recover or socialize costs. Privacy legislation serves as an enabler for new approaches to network governance and potentially reduces costs for consumers. This suggests that the focus of future network pricing should be on the services and functions provided by the grid rather than the commodity electricity itself [3]. Dou built a cone model, focusing on the analysis of basic factors such as low-carbon technology innovation, carbon emissions trading, carbon finance, and low-carbon policies, to provide a theoretical basis for low-carbon economic practice. The results show that low-carbon technology innovation is the foundation of low-carbon economic development, and carbon emission trading is the key to low-carbon economic development. The development of a low-carbon economy requires corresponding conditions such as carbon finance and low-carbon policies [4]. Duarte et al. assessed the dynamic paths and medium-term environmental impacts of certain consumer-oriented measures using a dynamically computable general equilibrium model. They assessed the dynamic impact of more efficient technologies on electricity consumption and the use of transportation services in terms of both environmental and economic effects. The findings confirm the role of technological improvements in delivering positive outcomes for the environment, as well as the importance of the rebound effect across the economy. Through a detailed study of energy use resulting from increased household energy consumption efficiency, the reduction in per capita emissions is consistent with economic growth [5]. Winiewski and Kistowski assessed the role and importance of agriculture and rural areas in the development of a low-carbon economy at the local level based on the concept of sustainable development. Based on model solutions developed during the implementation of the low-carbon development pilot project, they diagnosed the possibility of maintaining or improving carbon dioxide absorption capacity and reducing greenhouse gas emissions from

agricultural land and soil. They determined the specific goals, operating principles, and the main body of low-carbon rural development of the low-carbon economy [6]. Holm et al. examined how vocational education and training and higher education can be enablers of a green and low-carbon economy. They chose three main areas: decentralized renewable energy production, use of organic by-products, and improving the energy efficiency of properties. Results were presented at workshops where green economy knowledge supply chains in selected areas were developed. It is important to discover collaborations between different fields and educational levels, as new skills often appear at the interface [7]. The above studies provide a detailed analysis of the application of a low-carbon economy and corporate material procurement costs. It is undeniable that these studies have greatly promoted the development of the corresponding fields. We can learn a lot from methodology and data analysis. However, there are relatively few studies on corporate material procurement costs in the field of low-carbon economy, and it is necessary to fully apply these algorithms to research in this field.

## 3. Control Methods of Enterprise Material Procurement Cost

*3.1. Low-Carbon Economy.* A low-carbon economy refers to a form of economic development under the guidance of the concept of sustainable development, through technological innovation, institutional innovation, industrial transformation, new energy development, and other means, to minimize the consumption of high-carbon energy such as coal and oil, reduce greenhouse gas emissions, and achieve a win-win situation for both economic and social development and ecological, environmental protection. Low-carbon economy combines the concepts of low-carbon and economy. It is understood literally that lower-carbon (greenhouse gas) emissions mean that in the process of economic development, companies must do their best to minimize or stop their reliance on carbon-containing fuels, for example, by improving energy efficiency, strengthening technological self-innovation, and developing new energy. The economy maintains the sustainability of development and the stability of economic growth in the process of implementing the low-carbon path [8, 9]. That is to say, the emerging concept of the low-carbon economy cannot exclude long-term economic growth, and its concept of sustainable development that takes into account social and environmental benefits undoubtedly represents the form of future economic development. The starting point of a low-carbon economy is to count carbon sources and footprints. There are three important sources of carbon dioxide, the most significant of which is thermal power emissions.

A low-carbon economy is a form of economic development that follows the principle of sustainable development, with the characteristics of “three highs and three lows.” The three highs refer to high efficiency, high performance, and high benefits, and the three lows refer to low pollution, low energy consumption, and low emissions. From an economic point of view, a low-carbon economy is a macroeconomic production mode that increases the cost of

carbon emissions as a constraint. Under the guidance of the concept of a low-carbon economy, economic development should follow the combination of economic benefits and environmental benefits. The realization of economic benefits requires that the GDP growth rate in the implementation of a low-carbon economy should be greater than zero, that is, to achieve positive economic growth. The realization of environmental benefits requires reforms and innovations from multiple perspectives such as technology, system, energy, and finance [10]. For countries with different development levels, there are certain differences in the realization scale of a low-carbon economy. Developed countries need to follow the development goals of an absolute low-carbon economy, while developing countries should take relative low-carbon development and ensure economic growth as the basic goal. Figure 1 shows a schematic diagram of low-carbon economic activities and their mechanisms.

The realization of a low-carbon economy is closely related to the adjustment of the industrial structure and the innovation of industrial technology. The primary industry agriculture and the tertiary industry service industry have low-carbon emission levels. The secondary industry, including industry, construction, and other industries, consumes a lot of energy and is the main source of carbon emissions. The development of the industrial structure is generally in line with the economic level of the country. For developed countries, the tertiary industry has become the main body of their economic structure, and the secondary industry with high energy consumption and high-carbon emissions can be transferred to developing countries. However, for developing countries, due to the need for economic development, it is necessary to stimulate the growth of the national economy through industrial development, so the adjustment of their industrial structure is carried out gradually and limitedly [11–13]. In the reality of China, the development of the tertiary industry should be encouraged under the premise of taking into account economic development. At the same time, it will carry out technological innovation for the development of industrial industries with high energy consumption and comprehensively utilize various technologies of environmental protection and energy saving, such as clean coal technology, carbon dioxide capture, and storage technology, and carbon neutral technology, which are used in various industries such as energy-saving vehicles, green buildings, environmental protection facilities, energy-saving materials, and environmental protection recycling. At the same time, it will increase the use of clean energy, replace the combustion of coal, oil, and other energy sources, and reduce carbon dioxide emissions. Figure 2 shows the haze situation in some cities.

Carbon finance is a general term for various financial activities, mechanisms, and systems aimed at reducing greenhouse gas emissions [14]. It mainly includes investing and financing carbon emission rights trading and related financial derivatives. Carbon finance is a financial market resulting from the combination of low-carbon economy-related industries and financial capital. By conducting market transactions, on the one hand, the total amount of

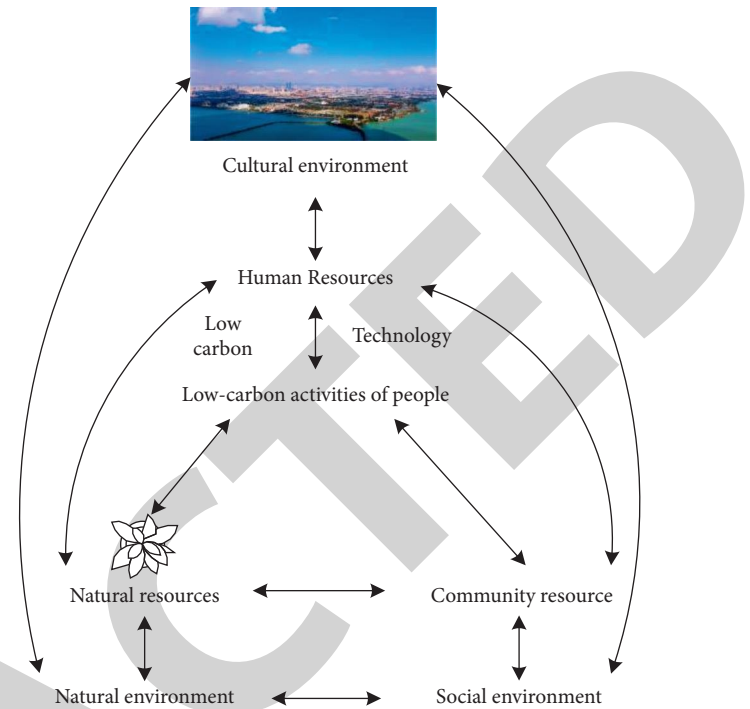


FIGURE 1: Schematic diagram of low-carbon economic activities and their mechanism of action.

carbon emissions is controlled, and on the other hand, economic value is created for enterprises with carbon credits [15, 16]. Carbon finance has two definitions: narrow and broad. The carbon financial market, in the narrow sense, mainly refers to the carbon emission rights trading market, including the general carbon spot market and its derived carbon futures and carbon options. The standard it defines is that the subject matter of the transaction is a direct carbon credit or carbon emission right. In a broad sense, the carbon financial market refers to various investment and financing activities to achieve carbon emission reduction, so it covers a wide range. Investment, consultation, guarantee, financing, and credit related to low-carbon economic projects all belonging to the broad scope of carbon finance [17–19]. A low-carbon economy means not only that the manufacturing industry should accelerate the elimination of energy-intensive, high-polluting backward production capacity and promote energy-saving and emission-reducing scientific and technological innovation but also that the public should be guided to reflect on which habitual consumption patterns and lifestyles are bad hobbies that waste energy and increase pollution, so as to fully explore the huge potential of energy-saving and emission-reducing in the service industry and consumer life. One of the important ways to shift to a low-carbon economy and lifestyle is to quit the hobby of “convenience consumption” at the cost of high energy consumption.

The global climate resource is a typical public good, and production companies emit carbon dioxide into the environment but do not need to pay for this behavior, resulting in the lack of restrictions on greenhouse gas emissions. Due

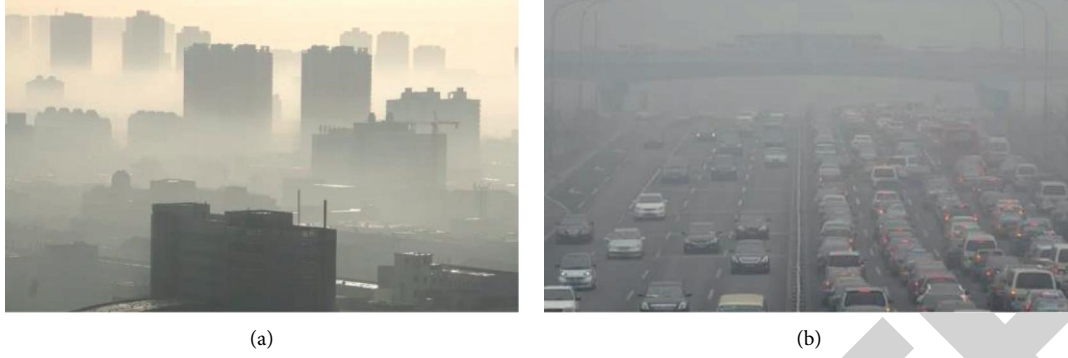


FIGURE 2: Smog in some cities.

to the difficulty of supervision and control, simply using political means or coercive means cannot solve the global carbon emission control problem. Introducing the theory of public goods, we can depublic goods of climate resources and convert them into nonpublic goods by pricing carbon dioxide emission rights [20]. Carbon emission rights that become nonpublic goods can be used for trading, making carbon emission rights exclusive and competitive. With the fluctuating transaction price of the market mechanism, for production enterprises, carbon emission rights become one of the costs of production and need to be included in cost accounting. This avoids the waste of resources, limits the excessive emissions of high-polluting enterprises, compensates for the technology development cost of low-carbon energy-saving industries, and realizes the low-carbon economic development route of controlling carbon emissions, energy conservation, and emission reduction [21].

$$W_{\text{mat}} = \sum_{u=1}^b a_u \times L_u \times (1 - x_u), \quad (1)$$

$$W_{\text{tran}} = \sum_{u=1}^b S_u \times a_u \times L_{\text{tran}},$$

$W_{\text{mat}}$  is the carbon emissions in the production stage of building materials;  $a_u$  is the the amount of building materials;  $L_u$  is the carbon emission factor of building materials;  $x_u$  is the recovery factor of building materials.

$$W_{\text{cons}} = W_{\text{mac}} + W_{\text{pro}},$$

$$W_{\text{max}} = \sum_{u=1}^a (R_{\text{max}u} \times E_{\text{mac}u} \times W_{\text{mac}u}), \quad (2)$$

$$W_{\text{pro}} = \sum_{v=1}^b (E_{\text{day}v} \times R_{\text{tot}v} \times L_{\text{eney}v}),$$

$W_{\text{cons}}$  is the carbon emissions in the construction phase;  $a$  is the type of machinery required for the project;  $R_{\text{mac}u}$  is the the total number of workbench shifts;  $b$  is the number of temporary measures.

$$W_{\text{utili}} = \left( \sum_{u=1}^b R_{\text{ener}u} \times L_{\text{ener}u} \right) \times N, \quad (3)$$

$W_{\text{utili}}$  is the carbon emissions in the operation phase;  $N$  is the service life of the building;  $L_{\text{ener}u}$  is the carbon emission factor of energy.

$$W_s = W_{\text{dis}} + W_{\text{dis.tran}} + W_{\text{recy}},$$

$$W_{\text{dis}} = \sum_{u=1}^b W_{s,u} \times L_{s,u}, \quad (4)$$

$$W_{\text{rec}} = a_{\text{tot}} \times x_{\text{rec}} \times (L_{\text{rec.pro}} - L_{\text{rec.mat}}),$$

$W_s$  is the carbon emissions at the disposal stage of buildings;  $L_{s,u}$  is the carbon emission factor of construction;  $x_{\text{rec}}$  is the recycling ratio of materials.

$$T_x = \frac{\bar{T}_d + \bar{T}}{2} + \frac{1/b \sum_{u=1} T_d + \bar{T}}{2}, \quad (5)$$

$$T_g = \frac{\bar{T}_h + \bar{T}}{2} = \frac{1/b \sum_{u=1} T_h + \bar{T}}{2},$$

$\bar{T}$  is the average limit;  $T_d$  is the advanced average.

$$w = m_0 + cm, \quad (6)$$

$w$  is the indicator matrix;  $c$  is the regression coefficient;  $m, m_0$  are the influencing factors.

$$W_d = \bar{V} + Z_x D, \quad (7)$$

$Z_x$  is the standard normal distribution probability density value.

$$T_Z = \sum_{u=1}^b (T_u \times P_u), \quad (8)$$

$$T_X = \sum_{u=1}^b (T_u \times K_u),$$

$T_Z$  is the total annual building energy consumption of the building;  $T_X$  is the building heating energy consumption.

$$\begin{aligned} \frac{1}{2} c_{lu} v_u \Delta m_u &= g_1 (e_{1,x} - e_1) + \frac{\delta_1}{\Delta m} (r_2 - r_1), \\ \left( \frac{1}{2} c_{lu} v_{u-1} \Delta m_{u-1} + \frac{1}{2} c_{lu} v_u \Delta m_u \right) \frac{dr_u}{d\tau} &= \frac{\delta_{u-1}}{\Delta m_{u-1}} (r_{u-1} - r_i), \end{aligned} \quad (9)$$

$c_{lu}$  is the certain pressure and heat capacity of the differential layer;  $v_u$  is the density of the differential layer;  $r_u$  is the node temperature.

The development and realization of a low-carbon economy are inseparably related to carbon finance. First of all, the realization of related technologies to promote the development of a low-carbon economy requires financial support and assistance. The related technologies to develop a low-carbon economy have large investments, high costs, and a long investment recovery period. Promoting the development of a low-carbon economy requires financing through the role of financial leverage to promote the development of a low-carbon economy. Taking carbon emission rights trading as an example, enterprises that implement low-carbon technologies can implement energy conservation and emission reduction to obtain carbon emission indicators, and relevant indicators can be converted into economic benefits through trading, thereby improving the source power of enterprises to develop low-carbon related technologies [22].

Secondly, the existence of the carbon financial market makes the mechanism arrangement of energy conservation and emission reduction for enterprises more flexible. For enterprises with different production characteristics in different industries, carbon emission reduction has different costs. When the cost of independent carbon emission reduction is higher than the transaction cost of carbon emission rights, enterprises can simplify the emission reduction process and achieve emission reduction goals through the transaction of carbon emission rights. When the cost of independent carbon emission reduction is lower than the transaction cost of carbon emission rights, enterprises can use their own low-carbon technology to obtain financial benefits. As an effective financial tool, carbon finance realizes the spontaneous adjustment of the market so that different types of enterprises can achieve emission reduction goals through appropriate channels, reduce the contradiction between industrial development and low-carbon emission reduction, and promote the harmonious development of the low-carbon economy [23].

Finally, the existence of a carbon financial market is the economic motivation for realizing the path of low-carbon development. Through the construction of the carbon trading mechanism, carbon assets have a unified measurement standard and have become one of the components of the cost-benefit measurement of enterprises. Through the pricing and circulation of carbon assets that can be used for trading, the financial capital and the real economy are linked. Through the existence of the carbon financial market, carbon emission reduction has become a standardized financial tool, which can effectively measure the development effect of a low-carbon economy and open up the channel for

low-carbon technology to create economic value. As a result, the development path of the low-carbon economy is transformed from voluntary or compulsory behavior of enterprises or individuals to capital-oriented market behavior, which has irreplaceable value for promoting the rapid development of the low-carbon economy. Figure 3 shows the low-carbon economic development model framework.

The concept of a low-carbon economy and its good construction expression can be mainly started from four aspects. (1) The change of basic concept shows that social members have a good acceptance of the term low-carbon economy because factors such as economy, environment, and national policy orientation make people have a better life concept and are willing to pursue a better way of life. This way of life is based on the characteristics of three highs and three lows, and it is reflected in the change of the basic concept of the enterprise, that is, the company's members and relevant stakeholders. (2) Policy orientation and institutional innovation: the low-carbon economy has put forward requirements for the social and national systems and policies to realize the transformation of the industry. It is necessary to convert high-carbon emissions in the industry into low-carbon emissions as much as possible, and the decomposition into enterprises is mainly reflected in the characteristics of environmental protection, greenness, and safety in the enterprise system. (3) Development of new energy: this feature shows that the low-carbon economy requires that the solution to the energy crisis should be based on increasing scientific research efforts to develop new energy sources and to minimize the use of nonrenewable energy sources or energy consumption. This is reflected in enterprises as appropriate investment in scientific research to open up new market channels. (4) Technology innovation: this proposes to the society actively innovating technologies including energy saving and emission reduction, which can not only improve the efficiency of energy utilization and reduce pollution emissions but also improve their own image and thus enhance the competitiveness of enterprises. The development of a low-carbon economy is closely related to people's living habits and the environment. Its rapid development can promote the generation of new technology standards and the improvement of advanced culture, the transformation of national industries, and the thinking of enterprises on the concept of a low-carbon economy, which will enable enterprises to obtain more opportunities and sustainable development space.

**3.2. Enterprise Material Procurement Cost.** Strategic management is the use of strategy to manage the entire enterprise and is a series of business management operations that combine daily business decisions with long-term planning decisions. Enterprises must strengthen strategic awareness, strategic thinking, and strategic management. The so-called procurement specifically refers to the purchase of certain products or services from external enterprises (also what we usually call suppliers) in order to meet the needs of daily operation and sustainable production and development in



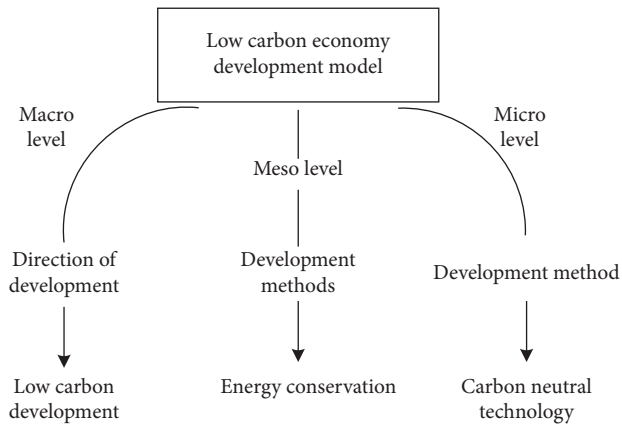


FIGURE 3: Low-carbon economic development model framework.

the course of business operations. The so-called procurement cost refers to the related expenses involved and incurred by the enterprise in the procurement process, including labor costs, machinery costs, material costs, logistics costs, and corresponding sales management fees. To a certain extent, procurement cost is an indispensable factor in the procurement process of production and living materials, and it is a very important measure and standard in the process of production and operation. Therefore, when an enterprise controls its own costs, especially its procurement costs, in addition to controlling its own raw materials, it also needs to consider other costs incurred in the process of raw material procurement, including labor and sales management costs. The so-called procurement cost control, that is to say, in the entire process of purchasing raw materials, reducing the size of procurement costs for corporate procurement activities, is the first issue that needs to be paid attention to in corporate procurement cost control. In order to achieve these goals, enterprises can adopt various modes of procurement, including commissioned customization, third-party outsourcing procurement, and commissioned processing procurement. Its fundamental purpose is to reduce costs, improve efficiency, and provide high-quality and low-cost raw materials for the production and operation of enterprises [25].

Specifically, the influencing factors of enterprise procurement cost mainly include the following aspects: determine the specific type of enterprise procurement activities. That is to say, whether the raw material procurement activities of enterprises occur regularly or only one time. If the company's raw material procurement activities are frequent, then the company should formulate a corresponding procurement plan according to its current type of procurement activities. On the contrary, if it is only a one-time procurement activity, the enterprise should also formulate a specific procurement plan for one-time procurement [26]. And according to the constant changes in the company's procurement activities, it continuously adjusts the plan to achieve a good interaction between the company's procurement plan and the type of procurement and specifically measures the relationship between the company's raw material procurement quantity and the total cost. This factor

is mainly a factor that must be considered for the needs of the bargaining game in the process of purchasing activities. Only when the procurement quantity of the enterprise matches the procurement cost, the procurement activity of the enterprise is highly efficient; otherwise, it is inefficient [27]. The cooperation relationship between enterprises and suppliers is related to the size of the procurement cost. Only by long-term cooperation between the two can a long-term cooperation relationship and a long-term cooperation mechanism of sharing risks be established, thereby improving the cooperation relationship and cooperation efficiency between the two, preventing the procurement activities of enterprises from being affected by the external market environment. According to the theory of the whole life cycle, any product must go through a complete life cycle from survival to extinction—initial growth period, growth period, maturity period, and extinction period. In different life cycles, the production demand of enterprises for raw materials is different, which requires enterprises to constantly analyze their own life cycle stages and explore a scientific and reasonable demand cost structure [28]. Figure 4 shows the specific steps of procurement cost control optimization.

Enterprises can use a variety of different methods to optimize and control their procurement costs. These control strategies specifically include management and control of raw material shipping and miscellaneous costs, forecasting of raw material purchase prices, raw material storage costs, and raw material out-of-stock costs. To a certain extent, procurement cost is an indispensable factor in the procurement process of production and living materials, and it is a very important measure and standard in the process of production and operation [29–32]. Therefore, when an enterprise controls its own costs, especially its procurement costs, in addition to controlling its own raw materials, it also needs to consider other costs incurred in the process of raw material procurement, including labor and sales management costs. Changing its cost management methods through changes in purchasing methods, specifically, companies can outsource the procurement of raw materials so that companies can concentrate on doing what they are good at. In this case, the enterprise's procurement management model can be further deepened.

The value chain is the process of value creation that can be carried out in the process of enterprise operation. In the process of production and operation, the company conducts a series of activities such as product design and production, sales, and after-sales. It is mainly divided into two categories: basic activities and auxiliary activities [33]. After years of development, the value chain view has gradually developed and matured and has become an important basic theory to guide enterprise management innovation. The value chain diagram is shown in Figure 5.

Basic activities include input-output and after-sales activities. It mainly includes the logistics of purchasing goods, not only the process of supply chain management but also strengthening the cooperative relationship between supply chains, including the collection and storage of various materials, and the activities of checking and receiving

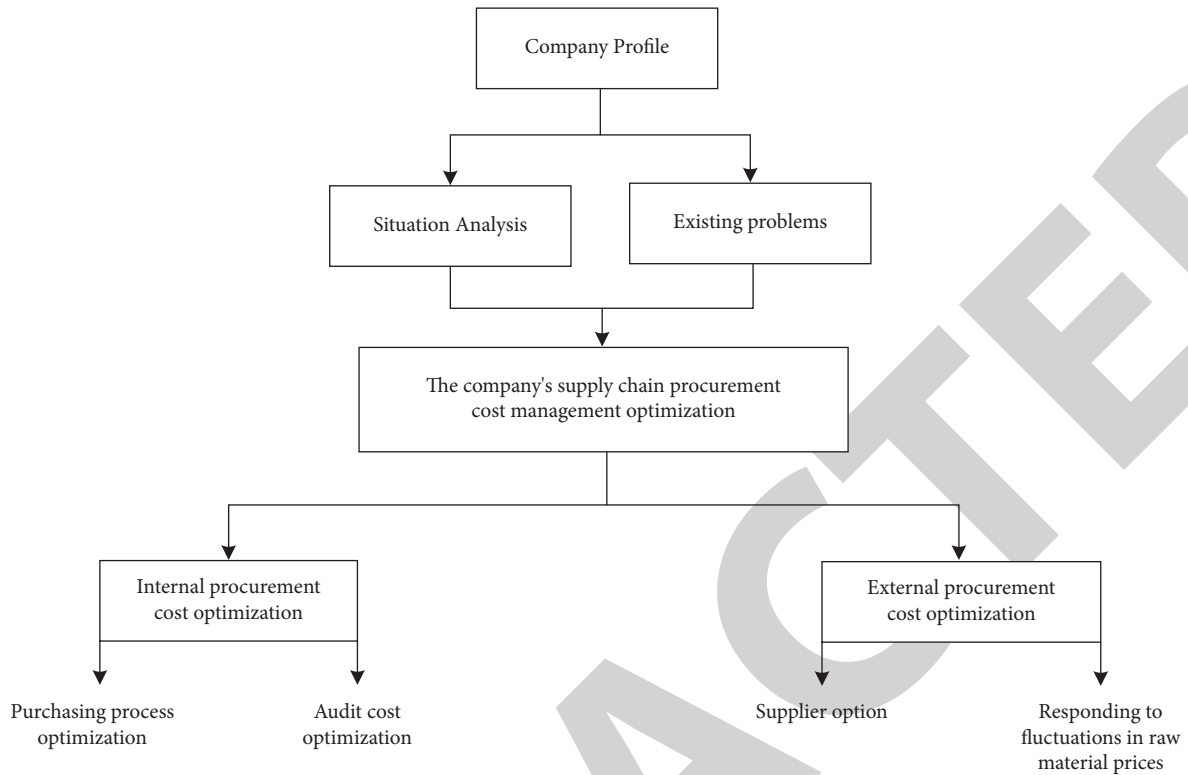


FIGURE 4: The specific steps of purchasing cost control optimization.

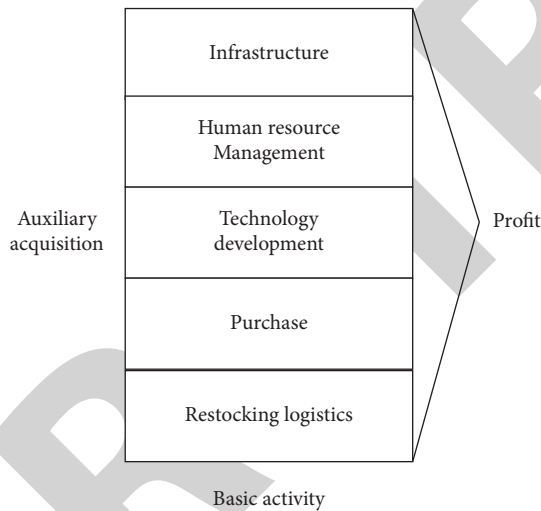


FIGURE 5: Value chain diagram.

warehouses. Production includes the process of producing and processing materials, including the entire process from raw materials to product cost. Shipping logistics includes all activities required to collect, store, and distribute finished products. Sales involves stimulating consumers to buy products through various guiding activities, including advertising marketing, and channel marketing and conducting product sales activities through pricing and promotion. After-sales service includes both the process of maintaining products and services and enhancing value formation through services, including repair and maintenance, as well

as the development of service activities such as maintenance [34].

#### 4. Control Experiment of Material Purchasing Cost in Enterprises

Business office buildings refer to buildings that provide office space for some business activities. They are located in relatively advantageous geographical locations. Most of them are located in the central business district and adopt unified property management. The energy consumption of commercial office buildings refers to the energy consumption input from the outside during the operation of heating, cooling, ventilation, air conditioning, and lighting, as well as the energy consumption of office equipment and elevators to maintain the building environment and building functions. Figure 6 shows the total global carbon emissions in recent years and the carbon emissions from the construction industry in recent years. From the data in Figure 6, it can be seen that it is imminent to reduce the carbon emissions of buildings, especially the carbon emissions of commercial office buildings that occupy a certain share of the buildings.

The dynamic energy consumption calculation method refers to the calculation method of hourly building energy consumption in order to meet the environmental requirements such as indoor temperature and humidity under the condition of hourly changes in meteorological parameters, personnel density, and heat source. The dynamic energy consumption calculation method is based on dynamic energy consumption simulation. It can improve the accuracy of

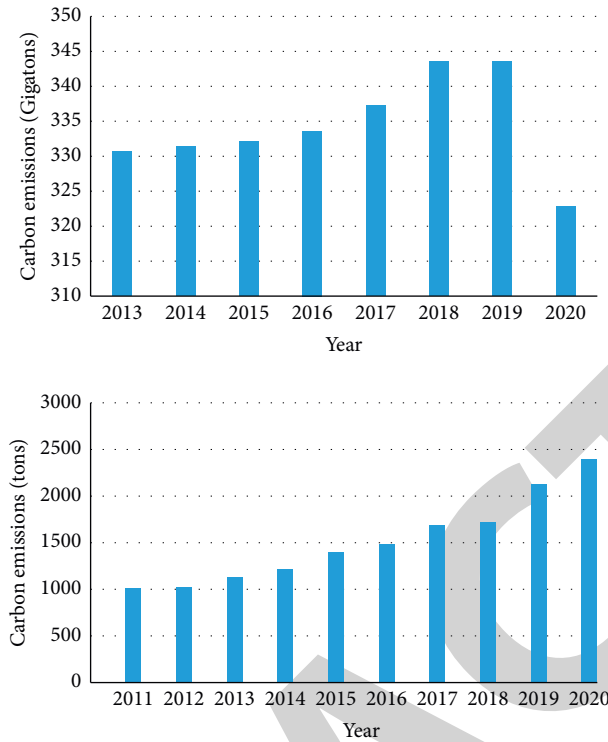


FIGURE 6: Total global carbon emissions in recent years.

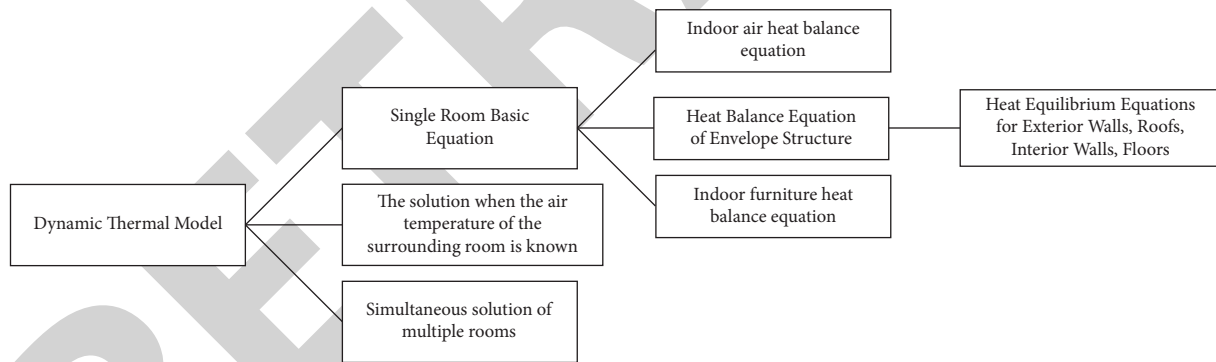


FIGURE 7: Dynamic thermal model system.

energy consumption calculation, but the premise is to establish a complex heat transfer equation. The dynamic thermal model system is shown in Figure 7.

The air conditioning heating and air conditioning cooling of a commercial office building in a certain province share the same system, which provides central cooling and heating for the building. Therefore, the energy consumption of building heating and air conditioning is all included in the electricity consumption, and it is not easy to calculate the heating energy consumption separately. For commercial office buildings that are heated using municipal heat network heat exchange or boiler heating, it is easier to calculate the heating energy consumption separately. For heating in

this way, the heating energy consumption can be calculated separately. Tables 1 and 2 show the basic information about commercial office buildings in the province.

Tables 3 and 4 show the basic information of municipal thermal commercial office buildings.

The software can present hourly meteorological parameters (temperature, humidity, solar radiation, wind speed, wind direction, etc.) and ensure that the daily values of each item are close to the source data. After the meteorological simulation, the statistical values of each meteorological element and the hourly meteorological data of the city were calculated. As shown in Figure 8, the annual temperature distribution and direct solar radiation intensity

TABLE 1: Basic information on commercial office buildings.

Serial number	Completion time	Construction area	User count	Building energy efficiency standards	Air conditioning method
1	2019	22000	485	Not energy-efficient	Chiller
2	2018	18700	350	Not energy-efficient	Split air conditioner
3	2012	5800	600	Not energy-efficient	Chiller
4	2012	10000	200	Not energy-efficient	Chiller
5	2015	20815	256	Not energy-efficient	Chiller

TABLE 2: Annual building energy consumption.

Year	Air conditioning area	Power consumption	Natural gas consumption	LPG consumption
2018	16158	49.72	18.18	850
2019	16158	48.25	16.07	930
2020	16158	42.83	10.4	950

TABLE 3: Basic information on municipal thermal commercial office buildings.

Serial number	Completion time	Construction area	User count	Building energy efficiency standards	Air conditioning method
1	2004	51460	2500	Not energy-efficient	Split air conditioner
2	2018	16877	350	Not energy-efficient	Chiller
3	2016	12000	300	Not energy-efficient	Chiller
4	2005	39000	500	Not energy-efficient	Chiller
5	2003	50000	1000	Not energy-efficient	Chiller

TABLE 4: Annual building energy consumption.

Year	Air conditioning and heating area (m <sup>2</sup> )	Power consumption	Natural gas consumption	Hot water
2018	51540	242	48.18	26.21
2019	51540	230	46.7	26.75
2020	51540	182	40.4	24.87

statistics are shown. The annual temperature is below 0°C for a total of 875 hours, and the year-round temperature is above 25°C for a total of 234 hours.

It can be seen that the construction of commercial office buildings consumes a lot of energy. When enterprises purchase building materials and energy supply materials, they can make improvements and build an importance judgment matrix to analyze the data. It is scored by buyers with many years of purchasing experience and experts in supplier selection, based on the average score obtained by the expert group. As shown in Figures 9 and 10, the indicator weights and CR values under the supplier evaluation factor are shown. It can be seen that the weights are all less than 0.1, and the consistency test passes.

According to the idea of strategic cost management, it is necessary to strengthen supplier cost analysis, conduct peer review activities with competitors, and control procurement costs. The main purpose is to carry out the main management and control of competitors in order to achieve a dominant competitive position in price control factors. The management and control of the company’s procurement are mainly carried out by the internal management department. If the procurement cost is to be fully controlled, it is not enough to rely solely on improving the internal management methods. In practice, it is necessary

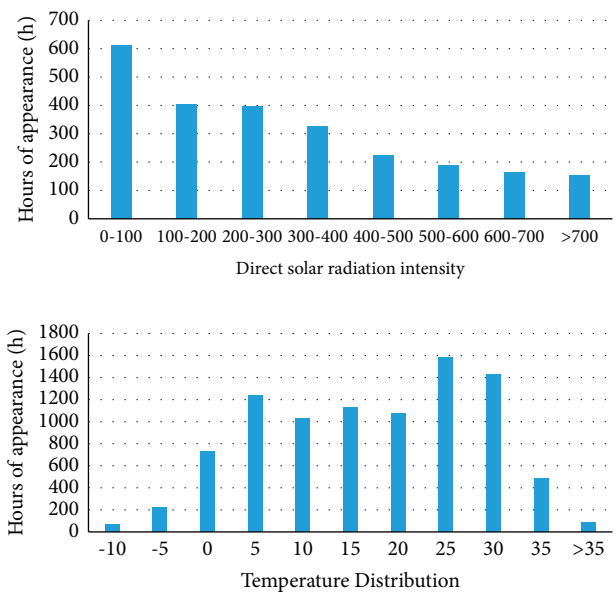


FIGURE 8: Statistical chart of direct solar radiation intensity.

to conduct a comprehensive analysis of the supplier’s products, understand its relevant information, understand the supplier’s product cost according to the relevant

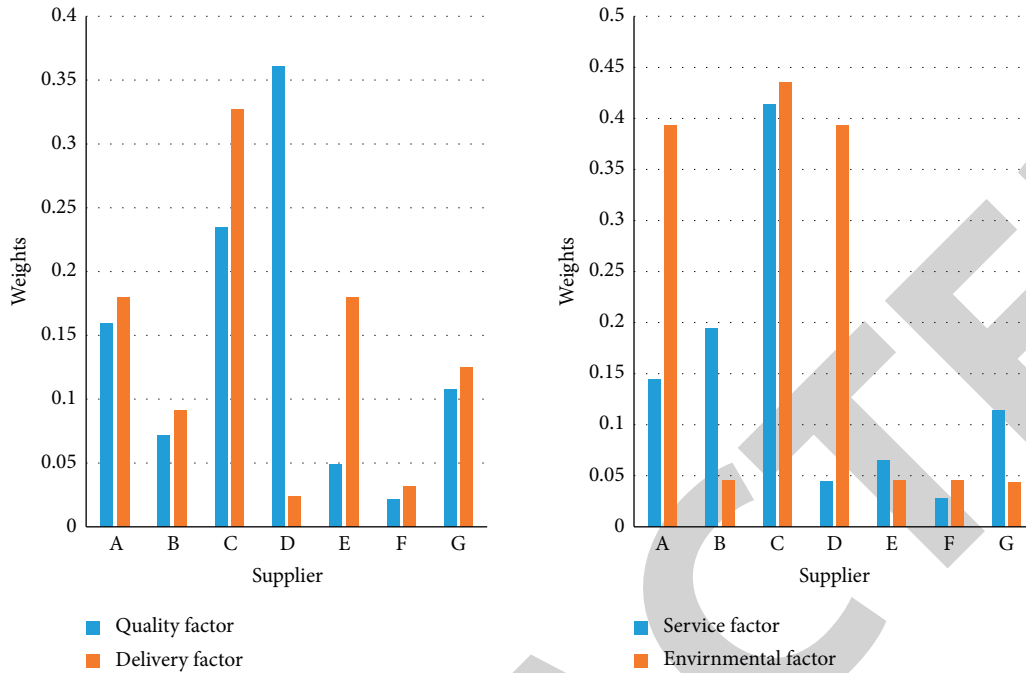


FIGURE 9: Weights of indicators under supplier evaluation factors.

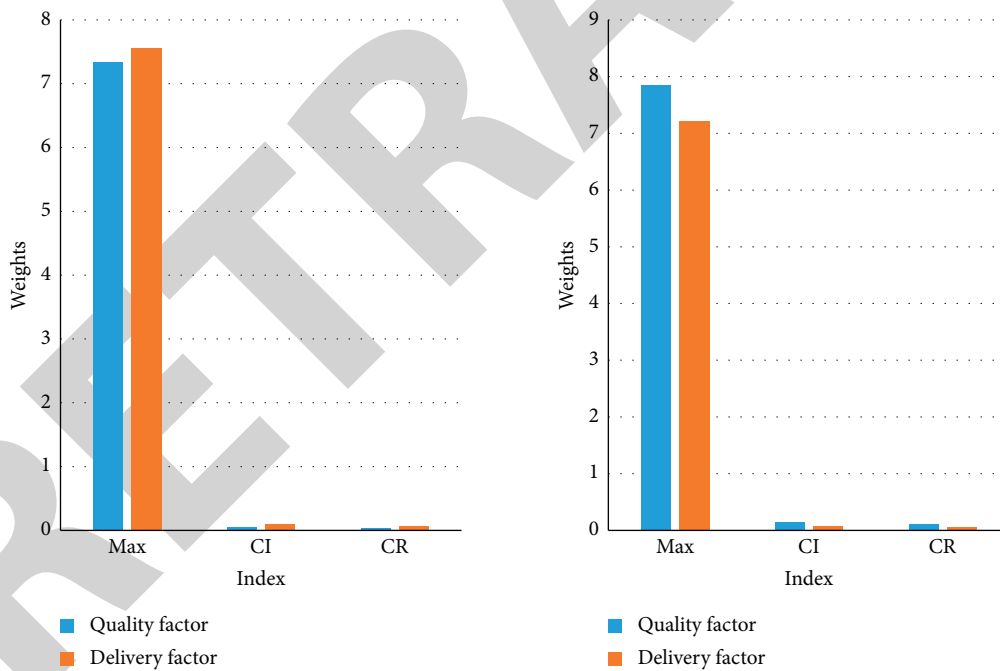


FIGURE 10: CR values for supplier evaluation factors.

information, and then point out the main direction of controlling the procurement cost. For the overall optimization and management of the procurement business, the corresponding management process technology is adopted, and the corresponding business management is continuously revised, thereby ensuring the improvement of the corresponding management capabilities and the clarification of job responsibilities and the improvement of the procurement management efficiency.

### 5. Discussion

Through the development of supplier management inventory and early intervention work, the coordination between suppliers and enterprises can be ensured, and the ability can be effectively shared, thereby providing certain conditions for reducing procurement costs, thus achieving win-win cooperation between suppliers and enterprises. Setting up special institutions to carry out corresponding project

tracking and services, especially in the process of research and development, can carry out comprehensive technical updates, strengthen mutual information communication and coordination between supply chain enterprises, and speed up the implementation of projects. In terms of products, material approval has been focused on, and acceptance management has been strengthened in terms of quality. The quality assurance work is mainly completed by the supplier, which has passed the relevant quality approval and inspection and supervision procedures to ensure the quality level of the materials. The supplier's production conditions and quality control system have become an important prerequisite for material quality management.

Improving customer management effect can improve supplier relationships and actively establish strategic partnerships between suppliers. The procurement personnel of enterprises not only need to strengthen the price control of material procurement but also actively strengthen the alliance of strategic partners. Through mutual cooperative production and management, we actively compress the production cycle and the production cost of products, seize the market more quickly with the lowest price, and achieve a win-win situation. It should actively build strategic partnerships with suppliers, improve the stability of material supply through stable cooperative relationships, and at the same time, through the establishment of cooperative relationships, extend the payment period, and maximize the interests of the strategic alliance from the overall situation. This kind of strategic partnership can save the company a lot of human resources and material resources and play a great role in controlling procurement costs.

## 6. Conclusion

Low-carbon economy is an ecological economy based on market activities. Its development requires the support of certain institutions, and it is necessary to strengthen human survival and development capabilities to achieve a state of self-sufficiency and self-realization, achieve comprehensive resource conservation, and reduce the social costs and overall benefits of human survival and development. Therefore, the study of developmental patterns should be an integrated process, the result of overlapping and intersecting across disciplines, requiring holistic thinking and a systematic approach to achieve holistic impact. This article proposes to actively build a strategic partnership with suppliers and improve the stability of material supply through stable cooperative relationships. At the same time, through the establishment of cooperative relationships, the payment period is extended, and the interests of the strategic alliance are maximized from the overall situation. In terms of raw material procurement, since China Telecom's media procurement market has just started, in the process of specific case studies, there is a lack of corresponding authoritative measurement standards, and it is difficult to carry out effective cost optimization and comparative analysis. These issues need to be further studied and discussed on the basis of continuous study and practice and on the premise of perfecting the system. Future research on the evaluation

system of corporate culture must be strengthened and based on the practice of corporate development.

## Data Availability

No data were used to support this study.

## Conflicts of Interest

The authors declare that the research was conducted in the absence of any commercial or financial relationships that could be construed as potential conflicts of interest.

## References

- [1] S. Lou, L. Zhang, and Y. Wu, "Coordination operation of electric vehicles and power system under low-carbon economy," *Diangong Jishu Xuebao/Transactions of China Electrotechnical Society*, vol. 32, no. 5, pp. 176–183, 2017.
- [2] L. F. . Chen, "Green certification, e-commerce, and low-carbon economy for international tourist hotels," *Environmental Science and Pollution Research*, vol. 26, no. 18, Article ID 17965, 2018.
- [3] L. A. Faerber, N. Balta-Ozkan, and P. M. Connor, "Innovative network pricing to support the transition to a smart grid in a low-carbon economy," *Energy Policy*, vol. 116, pp. 210–219, 2018.
- [4] X. Dou, "Low carbon technology innovation, carbon emissions trading and relevant policy support for China's low carbon economy development," *International Journal of Energy Economics and Policy*, vol. 7, no. 2, pp. 172–184, 2017.
- [5] R. Duarte, J. Sanchez-Choliz, and C. Sarasa, "Consumer-side actions in a low-carbon economy: a dynamic CGE analysis for Spain," *Energy Policy*, vol. 118, pp. 199–210, 2018.
- [6] P. Winiewski and M. Kistowski, "Agriculture and rural areas in the local planning of low carbon economy in light of the idea of sustainable development - results from a case study in north-central Poland," *Fresenius Environmental Bulletin*, vol. 26, no. 8, pp. 4927–4935, 2017.
- [7] T. Holm, P. Vennervirta, T. Pöykkö, E. Hameenoja, and N. Teirasvuo, "Identification of skills needed for central areas of green and low-carbon economy, for the needs of labor market, in Finland," *European Journal of Sustainable Development Research*, vol. 1, no. 1, pp. 1–8, 2017.
- [8] M. N. Islam Sarker, M. A. Hossin, J. Anusara, B. Chanthamith, and N. Kumar, "Practices of low carbon economy in China: challenges and opportunities for economic development," *Low Carbon Economy*, vol. 09, no. 01, pp. 18–32, 2018.
- [9] L. Yin, X. Li, L. Gao, C. Lu, and Z. Zhang, "A novel mathematical model and multi-objective method for the low-carbon flexible job shop scheduling problem," *Sustainable Computing: Informatics and Systems*, vol. 13, no. 3, pp. 15–30, 2017.
- [10] B. Yang, "China's low-carbon economy development and carbon finance market supervision mechanism," *Low Carbon Economy*, vol. 08, no. 04, pp. 97–105, 2017.
- [11] O. Wisesa, A. Andriansyah, and O. Ibrahim Khalaf, "Prediction analysis for business to business (B2B) sales of telecommunication services using machine learning techniques," *Majlesi Journal of Electrical Engineering*, vol. 14, no. 4, pp. 145–153, 2020.
- [12] C. A. Tavera Romero, D. F. Castro, J. H. Ortiz, O. I. Khalaf, and M. A. Vargas, "Synergy between circular economy and



## *Retraction*

# **Retracted: Effect of SiC Particle Incorporated Dielectric Medium on Electrical Discharge Machining Behavior of AA6061/B4Cp/SiCp AMCs**

### **Advances in Materials Science and Engineering**

Received 6 April 2023; Accepted 6 April 2023; Published 19 April 2023

Copyright © 2023 Advances in Materials Science and Engineering. This is an open access article distributed under the Creative Commons Attribution License, which permits unrestricted use, distribution, and reproduction in any medium, provided the original work is properly cited.

*Advances in Materials Science and Engineering* has retracted the article titled “Effect of SiC Particle Incorporated Dielectric Medium on Electrical Discharge Machining Behavior of AA6061/B4Cp/SiCp AMCs” [1] due to significant overlap with a previously published article by different authors [2].

### **References**

- [1] J. Khajuria, N. Nagabhooshanam, P. Sharma et al., “Effect of SiC Particle Incorporated Dielectric Medium on Electrical Discharge Machining Behavior of AA6061/B4Cp/SiCp AMCs,” *Advances in Materials Science and Engineering*, vol. 2022, Article ID 2661158, 9 pages, 2022.
- [2] S. G. Iyyappan, R. Sudhakarapandian, and M. Sakthivel, “Influence of silicon carbide mixed used engine oil dielectric fluid on EDM characteristics of AA7075/SiCp/B4Cp hybrid composites,” *Materials Research Express*, vol. 8, no. 8, 2021.

## Research Article

# Effect of SiC Particle Incorporated Dielectric Medium on Electrical Discharge Machining Behavior of AA6061/B4Cp/SiCp AMCs

Johny Khajuria,<sup>1</sup> N. Nagabhooshanam,<sup>2</sup> Pankaj Sharma,<sup>3</sup> Atul Kumar,<sup>4</sup> Santosh Kumar Sahu,<sup>5</sup> Peyyala Sree Devi,<sup>2</sup> and Kuma Gowwomsa Erko <sup>6</sup>

<sup>1</sup>Department of Mechanical Engineering, Mahant Bachittar Singh College of Engineering and Technology, Jammu, Jammu and Kashmir, India

<sup>2</sup>Department of Mechanical Engineering, Aditya Engineering College, ADB Road, Aditya Nagar, Surampalem 533437, Andhra Pradesh, India

<sup>3</sup>Department of Mechanical Engineering, JECRC University, Jaipur, India

<sup>4</sup>Department of Mechanical Engineering, SET, Mody University of Science and Technology, Lakshmanagarh, Sikar 332311, Rajasthan, India

<sup>5</sup>Department of Mechanical Engineering, Veer Surendra Sai University of Technology, Burla 768018, Odisha, India

<sup>6</sup>Department of Mechanical Engineering, Ambo University, Ambo, Ethiopia

Correspondence should be addressed to Kuma Gowwomsa Erko; [kuma.gowwomsa@ambou.edu.et](mailto:kuma.gowwomsa@ambou.edu.et)

Received 1 May 2022; Accepted 8 June 2022; Published 21 July 2022

Academic Editor: K. Raja

Copyright © 2022 Johny Khajuria et al. This is an open access article distributed under the Creative Commons Attribution License, which permits unrestricted use, distribution, and reproduction in any medium, provided the original work is properly cited.

In this work, it was observed that using motor oil as the dielectric fluid when producing AA6061/SiCp/B4Cp hybrid composites provided wealth from waste. In these studies, modifications in silicon carbide (SiC) concentration, electrode (copper and brass), current, pulse time, and reinforcing weight percentage were tested. Surface roughness and machined hardness are measured and reported for each removed piece of the material. The bridging effect of silicon carbide particles raised the material removal rate (MRR), while a thorough dielectric fluid flush enhanced the Ra value. On the machined topography, the oil carbon content left dark smudges. Machining performance is superior to that of copper electrode-processed specimens. The MRR, TWR, and Ra all rise as the discharge current and pulse duration increase. Because there is no remelted layer, composites with low machining surface hardness had better finishes. The parameters were optimized using the TOPSIS approach, and it was observed that the efficiency of machining was enhanced by utilizing engine oil by the concentration of 4 gl<sup>-1</sup>. Moreover, during machining, optimized parameters like pulse on time 36 seconds, current 4 Amps, and also a brass electrode.

## 1. Introduction

Standard machining methods were useless in composite materials because of the occurrence of strengthening elements [1]. EDM and other unconventional methods of machining are frequently used to attain high precision and accuracy. The key aims of the EDM are MRR, TWR, and Ra. Process variables such as electrical current, pulse on time, and tool material are all significant in determining machining characteristics [2, 3]. Machine tools can be made from a

variety of materials, including copper, brass, graphite, Cu-W, and ZrC. The correct tool and workpiece combination must be determined to optimise machining performance [4–6]. It is possible to increase machine output by mixing foreign particles into the dielectric fluid [7].

There have been several research altering the particle size, powder materials, and powder concentration [8]. Powders including SiC, B<sub>4</sub>C, Al<sub>2</sub>O<sub>3</sub>, and graphite are commonly used in PMEDM. Adding powder particles, according to the majority of findings, reduces the gap growth

and thus raises MRR [9–11]. Because of the homogeneous distribution of discharge energy, an improvement in MRR was attained. Short circuits are formed when powder particles are added above the limit, resulting in a significant decrease in MRR. Hong et al. [12] tested the kerosene dielectric by adding chromium powder to it. Results show that the addition of chromium powder to dielectric fluid raises material removal rate and surface roughness by 45 and 68%. Abdudeen et al. [13] investigated the dielectric fluid breakdown using powders for four distinct materials. The breakdown of dielectric was reduced when the concentration of powder was increased [14–16].

In terms of dielectric fluids, hydrocarbon, vegetable, and synthetic oil-based fluids are maximum and frequently used [13, 17]. Dielectric fluids such as kerosene, EDM oil, and deionized water are the most common. Machined by these traditional fluids, poisonous gas is released into the environment [18–20]. HSS-M35 was machined using argon, nitrogen, and air as dielectric media by [21]. Nitrogen and argon gas was found to be the finest dielectric medium for removing more material and producing the highest surface quality. Imran et al. [22] used distilled water and paraffin oil as dielectric media to manufacture AA6061 aluminium alloy. Using purified H<sub>2</sub>O as dielectric resulted in a thicker white coating than using paraffin oil. Larger globules and surface pitting have been noticed under paraffin medium, according to the report as well [23–25].

Dielectric fluid properties of Jatropha biodiesel were examined by [26]. If you compare it to synthetic EDM oil, it performs better than kerosene in terms of machining, but it performs worse than kerosene in terms of cutting. Pure water and kerosene can be used as the dielectric medium to mill high-carbon and high-chromium steel, according to [27–29]. In this machining method, copper, graphite, and brass tools were employed, and the current and pulse duration were both dynamically modified. Carbon was thought to be deposited on the surface of machines that were operated in kerosene environment [30]. When specimens were fabricated in distilled water using a graphite tool, the MRR was larger and the Ra was lower. Deionized tap water was employed by the authors of [31] as an electric discharge medium. A decrease in surface quality was found as a result of machining that resulted in craters. Dielectric fluid made from multiwall carbon nanotubes and mixed with Kusum edible oil by the authors of [32] was utilized by them to manufacture EN-31.

The multicriteria decision-making (MCDM) technique is used in TOPSIS to be preferred because they resemble the deal scenario [33, 34]. When it came to solving a material election problem, TOPSIS was one of the most effective MCDM techniques. Finding the top solution and the nastiest solution yielded the top and worst values [35]. Finding these two perfect values led to the discovery of the optimum parameters. Four separate process parameters were varied by their EDM experiments [36]. The TOPSIS technique was used to discover the ideal process parameters for abrasive water jet machining and powder mixing to electric discharge drilling [37, 38]. Numerous studies using a variety of dielectric fluids and powders in combination with electric

TABLE 1: Chemical composition of AA6061.

Zn	Mn	Cu	Mg	Fe	Al
0.24	0.85	0.24	0.92	0.04	Remaining

discharge machining have been published, according to scientific research [39–41]. There has never been any research on unused engine oil as a dielectric fluid. These projects sought to make money from waste by using engine oil as dielectric fluid for EDM on AA6061 hybrid composites [42].

## 2. Materials and Methods

The matrix material was AA6061, which is employed in the fabrication of aerospace structural parts because of its weldability and dimensional stability, and it is excellent for a wide range of diverse uses. Its element percentage is shown in Table 1. An average particle size of 5  $\mu\text{m}$  was chosen as strengthening for the SiC and B4C materials. Modified stir casting was used to create the composite. In a graphite receptacle, the alloy was heated to 850°C. At 1000 rpm, the mixture is agitated for 180 seconds after injecting preheated SiC and B4C particles. Before reheating the composition to 850°C, the same was cooled to 420°C for 120 seconds and violently agitated. Engineering composites of various weight percentages have been made using the same method for releasing the charge into the preheated die steel. Figure 1 shows a schematic view of the electrical discharge machine.

The dielectric was made up of copper and brass, with different concentrations of SiC powder (0, 4, and 8  $\text{gl}^{-1}$ ) added to improve the machining properties. Table 2 depicts the dielectric characteristics of the used engine oil obtained from the automotive exhibition room. A mechanical stirrer, submersible flushing pump, and a 12-liter tank make up the PMEDM tank [43]. The variables' ranges were determined through preliminary tests. We assumed that all of our studies would display a steady discharge. Table 3 depicts the values of the input variables. Several responses are recorded, including MRR, TWR, Ra, and surface hardness (SH). For each trial, the machining time was set at 10 minutes. The specimen Ra was determined using an SJR210 surface roughness tester, which measured it 10 times and averaged the results. The Rockwell hardness testing machine was used to evaluate the surface hardness value following machining in accordance with ASTM standard E18. The TOPSIS (Technique for Order of Preference by Similarity to Ideal Solution), a multicriteria decision analysis optimization method, was used to discover the ideal process parameter value as follows:

$$\text{material removal rate} = (W_b - W_a), \quad (1)$$

$$\text{tool wear rate} = (T_b - T_a). \quad (2)$$

## 3. Results and Discussion

When powder concentration is 4  $\text{gl}^{-1}$ , the MRR increased, and when it was 8  $\text{gl}^{-1}$ , the MRR decreased. Particles suspended in a space between a tool and its workpiece will

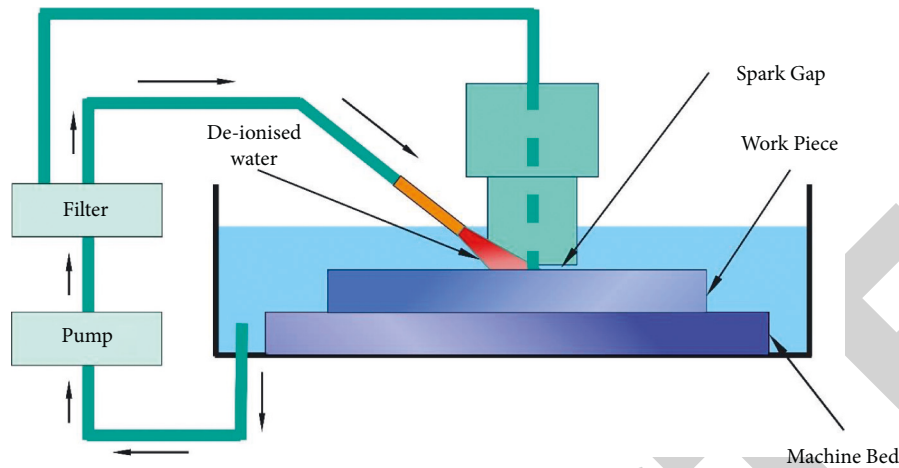


FIGURE 1: Schematic view of the electrical discharge machine.

TABLE 2: Dielectric fluid properties.

Property	Electrical discharge machining oil	Engine oil after used	Remarks
Strength (KVA)	47	65	Strength raises the efficiency of machining
Colour	Clear	Black	The workpiece is invisible
Carbon (%)	9	97	Black dot deposition on the surface of the machine due to carbon content
Flashpoint (°C)	>93	188	Enhancing the safety of work by higher flash point
Thermal conductivity (Wm <sup>-1</sup> k <sup>-1</sup> )	0.114	0.140	Heat dissipation raises due to thermal conductivity
Density (kg m <sup>-3</sup> )	830	876	Blushing expands the density
Viscosity at 45°C (mm <sup>2</sup> /s)	2.46	2.5	Heat transfer raises due to low viscosity
Specific heat (kJ kg <sup>-1</sup> K <sup>-1</sup> )	2.12	1.824	Specific heat is less in used oil compared to EDM oil

TABLE 3: Levels of process parameters.

Parameter	Levels
Current	2, 4, 6 A
Electrode material	Copper, brass
Powder concentration	0, 4, 8 gl <sup>-1</sup>
Pulse on time	12, 24, 36µs
Dielectric fluid	Used engine oil
Work piece	AA6061/SiC/B <sub>4</sub> C
Voltage	32V
The weight percentage of composite	5, 10, 15 wt. %

increase spark frequency and intensity if applied a voltage. As a result, the MRR will rise. Table 4 illustrates the results of the inquiry. The findings were in line with prior research. As the spark gap widened further, more heat was released due to an increase in powder concentration. Machining the workpiece was not possible due to insufficient heat generated, thereby decreasing the MRR. With copper electrodes, samples cut with brass tools had a lower MRR.

In addition, it was discovered that the current MRR climbed until a saddle point of 4 A, at that time began to fall again. MRR increased more rapidly because the current flowed through a denser plasma channel and had a higher intensity, which naturally rises as the current increases as shown in Figure 2. As current flows across the plasma

channel, MRR lowers. For a current of 6 A, however, the MRR was larger when the powder concentration was 4 gl<sup>-1</sup>. Plasma channels shrink and produce greater heat as spark gaps increase owing to powder addition, according to this theory. Because of this, melting and vaporization are accelerated, increasing MRR. MRR was maximum at a powder concentration of 4 gl<sup>-1</sup>. According to the data, the MRR decreases as the weight % of strengthening particles increases.

Copper electrodes, as seen in Figure 3, have a lower TWR than brass electrodes. This decrease in TWR was nominally lower for electrodes with greater melting temperatures because of the material's physical characteristics. As a result, copper has a lower TWR than brass due to its higher melting point. TWR decreases until it reaches the saddle point of 4 gl<sup>-1</sup> and then begins to rise again. From the result, TWR can easily reduce due to the bulk of the negative ions passing over the process gap. Short circuits develop by increasing the powder concentrations, resulting in a rise in TWR. Increased discharge current erodes a greater amount of electrode material, increasing TWR. Increasing the pulse-on-time causes a raise in spark energy and an increase tool wear rate as previously noted. At an outlet current of 2 A, a pulse on time of 15 s, and a concentration of powder of 4 gl<sup>-1</sup>, TWR was determined to be modest. tolerable work ratio (TWR) is minimum for composites with 5 and 10%

TABLE 4: EDM experimental results of AA7075 hybrid composites.

S. no.	Tool	Concentration of the powder	Current	Pulse on time	% of weight	Material removal rate	Tool wear rate	Surface roughness	Hardness	Material removal rate	Expected values		
											Tool wear rate	Surface roughness	Hardness
1	Cu	0	2	12	5	292	59	4.35	94	300.9	52.9	4.8	89.6
2	Cu	0	4	24	10	342	72	4.4	97	321.6	69.9	5.1	94.7
3	Cu	0	6	36	15	343	83	5.30	103	346.6	78.4	5.9	101.8
4	Cu	4	2	12	10	332	44	2.12	89	367.3	49.1	2.6	88.3
5	Cu	4	4	24	15	403	63	3.60	97	393.8	60.7	3.7	93.4
6	Cu	4	6	36	5	507	71	3.66	84	488.4	79.6	3.7	85.1
7	Cu	6	2	12	10	393	69	4.72	91	374.5	64.6	4.8	86.9
8	Cu	6	4	24	15	334	76	5.12	95	346.8	69.6	5.2	97.9
9	Cu	6	6	36	5	294	69	4.84	99	275.6	66.7	5.1	98.5
10	Br	0	2	12	5	297	83	5.67	96	292.7	87.7	5.7	97.3
11	Br	0	4	24	10	325	86	3.82	93	306.9	85.7	4.1	91.2
12	Br	0	6	36	15	395	88	4.29	97	302.4	87.7	4.9	94.0
13	Br	4	2	12	15	327	68	2.51	90	336.1	67.9	2.6	89.4
14	Br	4	4	24	5	443	74	1.73	85	469.1	74.5	1.4	85.7
15	Br	4	6	36	10	352	73	2.14	95	356.3	68.9	2.4	91.5
16	Br	6	2	12	10	379	79	3.98	95	356.9	78.5	4.4	94.0
17	Br	6	4	24	15	284	84	3.92	96	292.3	79.3	4.3	97.6
18	Br	6	6	36	5	304	77	4.17	91	307.8	72.4	4.6	89.9

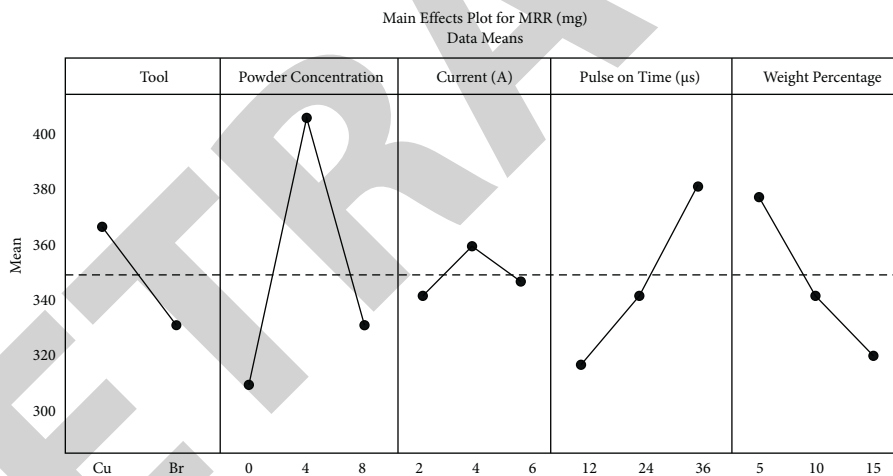


FIGURE 2: Differences in MRR concerning diverse process parameters.

reinforcing particles, but it rapidly rises when samples with 15% reinforcing particles are machined.

Figure 4 shows that the addition of SiC powder to the dielectric phase considerably reduces Ra. The distance separating the electrode and the workpiece widens as the particles are added. There are no more “globules” or “layers” of remelted material to be formed, which helps to increase the Ra of the gap. As a result of the increased strength of the powder, the gap distance grows even further, which reduces heat generation. As a result, the quality of the surface is lowered because of the production of voids and microcracks. A greater Ra value is created as the discharge strength is raised, and the surface is creating pits. The even distribution of discharge energy provided by 4 gl<sup>-1</sup> particles results in a finer surface finish. Because of the greater spark bombardment caused by the longer pulse-on-time, the surface’s

Ra value increased. Composites have a deteriorating surface quality with increasing weight fractions. Micropits emerge on the surface when reinforcing substances are removed from the surface during machining, which is consistent with prior observations.

Hardness values before machining ranged from 86, 93 to 97 HRB for composites containing 5, 10, and 15% reinforcing particles. A higher weight percentage led to higher hardness readings because of the presence of hard ceramic fragments. Machining composites with powder particles at 4 gl<sup>-1</sup> results in a loss of hardness as shown in Figure 5. The surface quality is raised by a more significant spark gap generated by the silicon carbide particles, reducing the production of remelted layers. The machined surface’s hardness changes when reinforcing particles are removed from the surface.

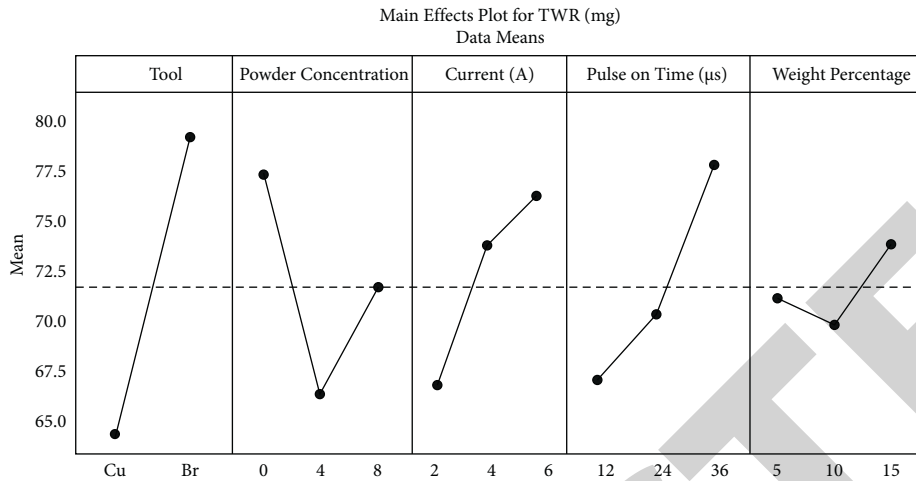


FIGURE 3: Differences in tool wear rate with respect to diverse process parameters.

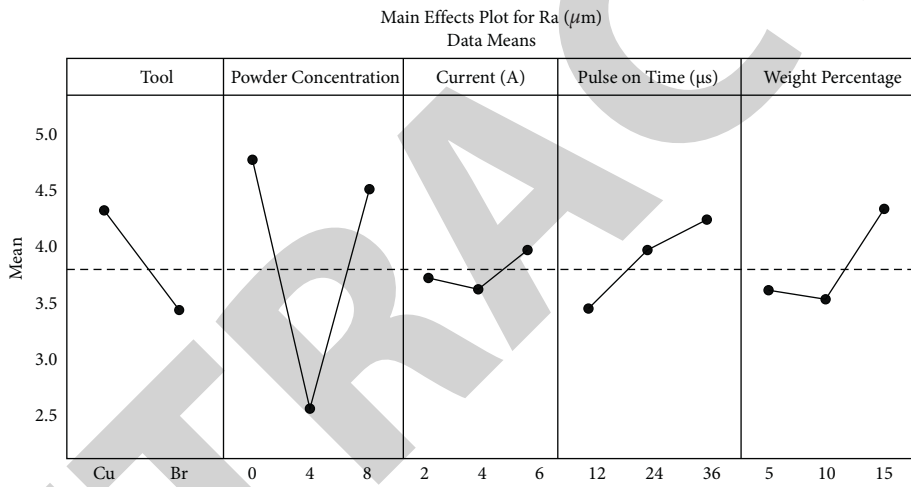


FIGURE 4: Differences in the roughness of surface with respect to diverse process parameters.

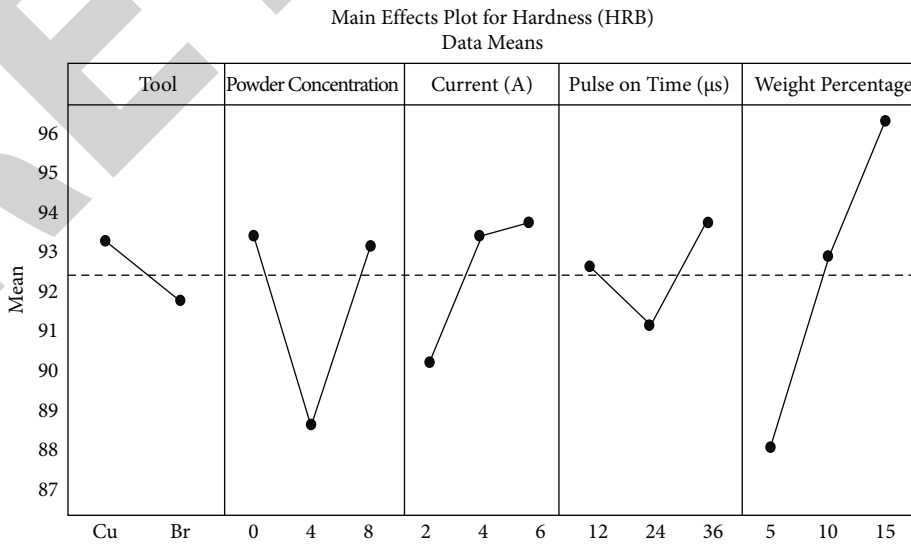


FIGURE 5: Differences in machined surface hardness concerning diverse process parameters.



TABLE 5: Enhanced values in investigational data set and technique for the order of preference by similarity to ideal solution.

Normalized matrix			Normalized decision matrix by weight			$P^+$	$P^-$	Pi	Rank
0.19321	0.78654	0.264558	0.06453	0.063454	0.12586	0.08	0.05	0.42	17
0.21674	0.228765	0.294875	0.08548	0.067416	0.11256	0.09	0.04	0.33	8
0.21724	0.264324	0.318748	0.08570	0.087124	0.125763	0.10	0.03	0.22	13
0.26340	0.168304	0.129588	0.09423	0.057861	0.053475	0.04	0.10	0.80	5
0.28243	0.199345	0.216590	0.10182	0.067543	0.187602	0.06	0.07	0.63	2
0.35346	0.257528	0.219147	0.12416	0.085197	0.183560	0.06	0.08	0.64	6
0.26107	0.218765	0.287365	0.096628	0.073482	0.112316	0.08	0.05	0.41	14
0.23103	0.241685	0.306361	0.083819	0.079502	0.116834	0.09	0.04	0.28	10
0.20223	0.221349	0.288545	0.073868	0.074356	0.116234	0.09	0.04	0.32	16
0.21260	0.296812	0.234585	0.076524	0.096557	0.131249	0.11	0.02	0.10	15
0.22523	0.283912	0.228826	0.081735	0.092867	0.082546	0.08	0.05	0.42	18
0.20234	0.306544	0.256510	0.075196	0.099688	0.101227	0.09	0.04	0.31	9
0.22657	0.238453	0.153482	0.082169	0.072830	0.063824	0.06	0.08	0.64	3
0.31124	0.261287	0.114098	0.108210	0.086154	0.149146	0.04	0.10	0.80	4
0.24321	0.231496	0.132034	0.087769	0.078526	0.092416	0.05	0.09	0.71	1
0.26015	0.237889	0.238608	0.093565	0.087409	0.084341	0.07	0.05	0.47	12
0.19796	0.272347	0.234812	0.072767	0.089825	0.099683	0.09	0.05	0.39	7
0.20167	0.248721	0.249612	0.076314	0.085153	0.094216	0.08	0.05	0.38	11
Wt.			0.43	0.4	0.4				
Eigen values			0.124268	0.058753	0.048523				
			0.072768	0.098769	0.131249				

Remelted layers are formed when the powder is added to composites while they are being machined, which makes the globules less stable. As a result of the high pulse on time, most of the molten material is deposited again on the surface due to insufficient flushing. Adding SiC particles to the dielectric fluid remedied this issue by increasing the spark gap and allowing for adequate flushing. The experimental data used in the prediction calculation was used to determine the regression coefficients of the second-order equation. This study indicated that the difference between actual and projected results was less than five percent.

#### 4. Surface Topography

The occurrence of carbon in wasted engine oil had discovered to be the cause of black patches on the composite surface. Due to the irregular spreading of discharge energy, a significant fracture was detected on the surface; the acquired data are exactly matched to the experimental data, as shown in the Figure 5. It is possible to discern globules, remelted layers, and deeper pits all over the surface, all of which significantly impair the surface. The surface topography at a higher magnification of 2000x, reveals craters, tiny holes, and micropits. Because of this, the surface roughness value was increased by approximately 20  $\mu\text{m}$ . Machined composites have a reduced hardness because they lack a remelted layer on the surface. The spark gap's surface quality improves because melting debris is washed away by the extra space between the electrode and the workpiece. Other researchers have made similar discoveries. There is an increase in the production of carbon black spots, fracturing, and pitting at higher magnifications. This is compensated for by a higher spark frequency. Thus, for fine-finish machining of hybrid composites, an increased spark gap was shown to be preferable.

4.1. TOPSIS. Due to identifying the optimum possible mixing of parameters, the Technique for Order of Preference by Similarity to the Ideal Solution (TOPSIS) optimization approach was applied. Because policymakers and end-users are both involved, this solution has an advantage. There were 18 experiments with three responses, thus a crucially in a matrix form of  $18 \times 3$  has been produced as displayed in Table 4. As a first step, data sets are normalized by equations (3) and (4). The normalizing matrix is  $B_{ij}$ , where  $i$  denotes the number of experiments and  $j$  is the number of responses. As a result, these normalized matrices were used to generate a weighted normalized judgment matrix  $C_{ij}$  as follows:

$$B_{ij} = \frac{A_{ij}}{\sum \sqrt{()}} \quad (3)$$

$$C_{ij} = w_j * B_{ij} \quad (4)$$

To calculate eigen values, the weighted normalized decision matrix is weighted, with  $\mathcal{E}^+$  being the highest value and  $\mathcal{E}^-$  being the lowest value in equation (5). According to formula (6), for nonbeneficiary qualities, the calculation was reversed.

For beneficiaries,

$$\mathcal{E}^+ = \text{Max}(C_{ij})_{i=1}^n, \mathcal{E}^- = \text{Min}(C_{ij})_{i=1}^n \quad (5)$$

For nonbeneficiaries,

$$\mathcal{E}^+ = \text{Min}_{i=1}^n, \mathcal{E}^- = \text{Max}(C_{ij})_{i=1}^n \quad (6)$$

Using this equation, we were able to determine the optimal  $P^+$  and ideal in the nastiest  $P^-$  solutions in equation (7). According to equation (8) indicated in Table 5, the dispersion between ideal and nonideal is determined.

$$(P^+, P^-) = \sum \sqrt{(C_{ij} - \xi^+)^2 + (C_{ij} - \xi^-)^2}, \quad (7)$$

$$O^i = \left( \frac{P^-}{P^+ + P^-} \right). \quad (8)$$

It was discovered that the discharge current of 4 A and also pulse on time of 45  $\mu$ s were the ideal parametric values when the electrode was brass and the powder mixture concentration was 4  $\text{gl}^{-1}$ .

## 5. Conclusion

Hybrid composites were successfully fabricated using AA6061/SiCp/B4Cp and dielectric fluid based on motor oil. A range of variables, including dielectric powder concentration, pulse time, and electrode material, was used to analyze machining performance. Following research, the following conclusion was reached:

- (1) The bridging activity of SiC particles increased spark frequency and energy strength, improving MRR. When an amount is applied beyond the saddle point, short circuit occurs. Brass-tool manufactured specimens exhibited the highest MRR when compared to copper-tool manufactured specimens. This raises the MRR by increasing discharge current and pulse on time, which increases plasma channel density and spark energy.
- (2) With the increased spark gap, the flushing of dielectric fluid enhances surface quality when suspended SiC particles are present. Due to bombardment and surface blitzkrieg, the Ra value raises with raising pulse on time and current. When increased beyond the threshold, this results in reduced heat generation and the formation of voids and pits.
- (3) Its higher melting point makes it possible for the copper electrode to have a more efficient total work rate (TWR). SiC particles reduce TWR by reducing the mobility of negatively charged ions across the gap. TWR rises in proportion to longer pulse on times and higher discharge currents.
- (4) The mechanical characteristics of composites are adversely affected by increases in wt.% of reinforcing elements. In terms of machining surface hardness, remelted layer and globule formation have a greater impact than normal. Higher surface quality can be achieved with lower machined hardness specimens.
- (5) Carbon in the used engine oil causes a black spot on the machined surface. Surface features such as pits, remelted layers, crater valleys, and globules were apparent. Adding SiC particles reduce surface roughness by preventing the creation of the remelted layer. The surface quality deteriorates when the length of the crater valley is extended by SiCp at a concentration of 6  $\text{gl}^{-1}$ .
- (6) The TOPSIS optimization technique is used to optimize the input variables. Current, 6 amps; pulse on

time, 45  $\mu$ s; and brass tool are the best process variables for the machining of AA6061/SiCp/B4Cp underutilized engine oil dielectric medium.

## Data Availability

The data used to support the findings of this study are included within the article. Further dataset or information is available from the corresponding author upon request.

## Conflicts of Interest

The authors declare that there are no conflicts of interest regarding the publication of this paper.

## Acknowledgments

The authors appreciate the support from Ambo University, Ethiopia, for the research and preparation of the manuscript. The authors appreciate the support from the Veer Surendra Sai University of Technology, Aditya College of Engineering, and JECRC University for the assistance in completing this work.

## References

- [1] P. Sivaprakasam, J. Udaya Prakash, P. Hariharan, and S. Gowri, "Micro-electric discharge machining (Micro-EDM) of aluminium alloy and aluminium matrix composites - a review," *Advances in Materials and Processing Technologies*, vol. 2021, pp. 1–16, 2021.
- [2] T. Sathish, V. Mohanavel, K. Ansari et al., "Synthesis and characterization of mechanical properties and wire cut EDM process parameters analysis in AZ61 magnesium alloy + B4C + SiC," *Materials*, vol. 14, no. 13, p. 3689, 2021.
- [3] M. U. Gaikwad, A. Krishnamoorthy, and V. S. Jatti, "Investigation and optimization of process parameters in electrical discharge machining (EDM) process for NiTi 60 Mater," *Res. Express*, vol. 6, Article ID 6065707, 2019.
- [4] K. Mausam, K. Sharma, G. Bharadwaj, and R. P. Singh, "Multi-objective optimization design of die-sinking electric discharge machine (EDM) machining parameter for CNT-reinforced carbon fibre nanocomposite using grey relational analysis," *Journal of the Brazilian Society of Mechanical Sciences and Engineering*, vol. 41, pp. 1–8, 2019.
- [5] R. Ranjith, P. Tamilselvam, T. Prakash, and C. Chinnsamy, "Examinations concerning the electric discharge machining of AZ91/5B4CP composites utilizing distinctive electrode materials," *Materials and Manufacturing Processes*, vol. 34, no. 10, pp. 1120–1128, 2019.
- [6] D. Purusothaman, R. S. Suresh Kumar, and B. G. Sivakumar, "Optimization of process parameter in machining inconel 800 by electrical spark eroding machine," *Journal of Chemical and Pharmaceutical Sciences*, vol. 9, no. 2, pp. 974–977, 2016.
- [7] H. K. Kansal, S. Singh, and P. Kumar, "Technology and research developments in powder mixed electric discharge machining (PMEDM)," *Journal of Materials Processing Technology*, vol. 184, no. 1-3, pp. 32–41, 2007.
- [8] A. Y. Joshi and A. Y. Joshi, "A systematic review on powder mixed electrical discharge machining," *Heliyon*, vol. 5, pp. 1–12, Article ID e02963, 2019.
- [9] G. Talla, S. Gangopadhyay, and C. Biswas, "State of the art in powder-mixed electric discharge machining: a review,"

- Proceedings of the Institution of Mechanical Engineers - Part B: Journal of Engineering Manufacture*, vol. 231, no. 14, pp. 2511–2526, 2017.
- [10] S. Tripathy and D. K. Tripathy, "Optimization of process parameters and investigation on surface characteristics during EDM and powder mixed EDM," *Innovative Design and Development Practices in Aerospace and Automotive Engineering*, Springer, Singapore, pp. 385–391, 2017.
  - [11] M. C. Nguyen, L. A. Tung, B. T. Danh et al., "Influence of input factors on material removal rate in PMEDM cylindrical shaped parts with silicon carbide powder suspended dielectric," *Key Engineering Materials*, Trans Tech Publications Ltd, vol. 861, , pp. 129–135, 2020.
  - [12] T. T. Hong, N. V. Cuong, B. T. Danh et al., "Multi-Objective optimization of PMEDM process of 90CrSi alloy steel for minimum electrode wear rate and maximum material removal rate with silicon carbide powder," *Materials Science Forum*, Trans Tech Publications Ltd, vol. 1018, , pp. 51–58, 2021.
  - [13] A. Abdudeen, J. E. Abu Qudeiri, A. Kareem, T. Ahammed, and A. Ziout, "Recent Advances and Perceptive Insights into Powder-Mixed Dielectric Fluid of EDM," *Micromachines*, vol. 11, Article ID 11754, 2020.
  - [14] A. P. Tiwary, B. B. Pradhan, and B. Bhattacharyya, "Influence of various metal powder mixed dielectric on micro-EDM characteristics of Ti-6Al-4V Mater," *Manuf. Processes*, vol. 34, 2019.
  - [15] S. S. Kumar, T. Varol, A. Canakci, S. T. Kumaran, and M. Uthayakumar, "A review on the performance of the materials by surface modification through EDM," *Int. J. Lightweight Mater. Manuf.*, vol. 4, 2021.
  - [16] N. A. J. Hosni and M. A. Lajis, "Experimental investigation and economic analysis of surfactant (Span-20) in powder mixed electrical discharge machining (PMEDM) of AISI D2 hardened steel," *Machining Science and Technology*, vol. 24, no. 3, pp. 398–424, 2020.
  - [17] S. Jeavudeen, H. S. Jailani, and M. Murugan, "Powder additives influence on dielectric strength of EDM fluid and material removal," *International Journal of Machining and Machinability of Materials*, vol. 22, no. 1, pp. 47–61, 2020.
  - [18] J. E. A. Qudeiri, A. Zaiout, A. H. I. Mourad, M. H. Abidi, and A. Elkaseer, "Principles and characteristics of different EDM processes in machining tool and die steels SNApl," *Science*, vol. 2020, Article ID 102082, 2020.
  - [19] X. Li, D. Wei, Q. Li, and X. Yang, "Study on effects of electrode material and dielectric medium on arc plasma in electrical discharge machining," *International Journal of Advanced Manufacturing Technology*, vol. 107, no. 11–12, pp. 4403–4413, 2020.
  - [20] B. Singaravel, K. C. Shekar, G. G. Reddy, and S. Deva Prasad, "Performance Analysis of Vegetable Oil as Dielectric Fluid in Electric Discharge Machining Process of Inconel 800 Mater," *Sci. Forum* 97877-83, Trans Tech Publications Ltd, vol. 978, , 2020.
  - [21] S. Fattahi and H. Baseri, "Analysis of dry electrical discharge machining in different dielectric mediums," *Proceedings of the Institution of Mechanical Engineers - Part E: Journal of Process Mechanical Engineering*, vol. 231, no. 3, pp. 497–512, 2017.
  - [22] M. Imran, S. M. Rahmanshah, S. Mehmood, and R. Arshad, "EDM of aluminum alloy 6061 using graphite electrode using paraffin oil and distilled water as dielectric medium," *Adv. Sci. Technol. Research*, vol. 11, 2017.
  - [23] M. Yunus Khan, P. Sudhakar Rao, and B. S. Pabla, "Investigations on the feasibility of Jatropha curcas oil based biodiesel for sustainable dielectric fluid in EDM process," *Materials Today Proceedings*, vol. 26, pp. 335–340, 2020.
  - [24] M. Patel GowdruChandrashekarappa, S. Kumar, D. Y. Pimenov, and K. Giasin, "Experimental Analysis and Optimization of EDM Parameters on HcHcr Steel in Context with Different Electrodes and Dielectric Fluids Using Hybrid Taguchi-Based PCA-Utility and CRITIC-Utility Approaches," *Metals*, vol. 2021, Article ID 11419, 2021.
  - [25] T. Muthuramalingam, "Effect of diluted dielectric medium on spark energy in green EDM process using TGRA approach," *Journal of Cleaner Production*, vol. 238, Article ID 117894, 2019.
  - [26] R. Bajaj, A. R. Dixit, and A. K. Tiwari, "Machining performance enhancement of powder mixed electric discharge machining using Green dielectric fluid," *Journal of the Brazilian Society of Mechanical Sciences and Engineering*, vol. 42, pp. 1–20, 2020.
  - [27] S. H. Mousavi-Nasab and A. Sotoudeh-Anvari, "A Comprehensive MCDM-Based Approach Using TOPSIS, COPRAS and DEA as an Auxiliary Tool for Material Selection Problems," *Materials & Design*, vol. 121, 2017.
  - [28] V. S. Viswanth, R. Ramanujam, and G. Rajyalakshmi, "Performance study of eco-friendly dielectric in EDM of AISI 2507 super duplex steel using Taguchi-fuzzy TOPSIS approach," *International Journal of Productivity and Quality Management*, vol. 29, no. 4, pp. 518–541, 2020.
  - [29] R. Nadda, R. Kumar, T. Singh, R. Chauhan, A. Patnaik, and B. Gangil, "Experimental investigation and optimization of cobalt bonded tungsten carbide composite by hybrid AHP-TOPSIS approach," *Alexandria Engineering Journal*, vol. 57, no. 4, pp. 3419–3428, 2018.
  - [30] J. Jayaraj, R. Sundaresan, and S. Chinnamuthu, "Multi-criteria decision of W-powder mixed electro discharge drilling parameters using TOPSIS approach," *Mechanics*, vol. 25, pp. 52–56, 2019.
  - [31] N. Yuvaraj and M. Pradeep Kumar, "Multiresponse optimization of abrasive water jet cutting process parameters using TOPSIS approach Mater," *Manuf. Processes*, vol. 30, 2015.
  - [32] T. C. Wang and H. D. Lee, "Developing a fuzzy TOPSIS approach based on subjective weights and objective weights," *Expert Systems with Applications*, vol. 36, 2009.
  - [33] V. Tao Le, "The influence of additive powder on machinability and surface integrity of SKD61 steel by EDM process," *Materials and Manufacturing Processes*, vol. 36, no. 9, pp. 1084–1098, 2021.
  - [34] M. A. Razak, A. M. Abdul-Rani, A. A. Aliyu et al., "The potential of improving the Mg-alloy surface quality using powder mixed EDM," *Progress in Engineering Technology. Advanced Structured Materials*, Springer nature, Switzerland, pp. 43–53, 2019.
  - [35] P. N. Huu, "Study of the effects of process parameters on tool wear rate in powder mixed electrical discharge machining by Taguchi method," *Science and Technology Development Journal*, vol. 20, pp. 55–60, 2017.
  - [36] C. Prakash, H. K. Kansal, B. S. Pabla, and S. Puri, "Experimental investigations in powder mixed electric discharge machining of Ti35Nb – 7Ta – 5Zrβ-titanium alloy Mater," *Manuf. Processes*, vol. 32, 2017.
  - [37] M. V. Chame, P. Swaminadhan, and M. S. Bembde, "Optimization of process parameters of powder mixed dielectric EDM for MRR and Ra," *Optimization*, vol. 4, pp. 1039–1041, 2017.
  - [38] K. Dhakar and A. Dvivedi, "Dry and near-dry electric discharge machining processes," *Materials Forming, Machining*

## *Retraction*

# **Retracted: Experimental Studies on Mechanical and Thermal Properties of Polyester Hybrid Composites Reinforced with Sansevieria Trifasciata Fibers**

### **Advances in Materials Science and Engineering**

Received 26 December 2023; Accepted 26 December 2023; Published 29 December 2023

Copyright © 2023 Advances in Materials Science and Engineering. This is an open access article distributed under the Creative Commons Attribution License, which permits unrestricted use, distribution, and reproduction in any medium, provided the original work is properly cited.

This article has been retracted by Hindawi, as publisher, following an investigation undertaken by the publisher [1]. This investigation has uncovered evidence of systematic manipulation of the publication and peer-review process. We cannot, therefore, vouch for the reliability or integrity of this article.

Please note that this notice is intended solely to alert readers that the peer-review process of this article has been compromised.

Wiley and Hindawi regret that the usual quality checks did not identify these issues before publication and have since put additional measures in place to safeguard research integrity.

We wish to credit our Research Integrity and Research Publishing teams and anonymous and named external researchers and research integrity experts for contributing to this investigation.

The corresponding author, as the representative of all authors, has been given the opportunity to register their agreement or disagreement to this retraction. We have kept a record of any response received.

### **References**

- [1] R. Premkumar, K. Sathish Kumar, J. Maniraj et al., “Experimental Studies on Mechanical and Thermal Properties of Polyester Hybrid Composites Reinforced with Sansevieria Trifasciata Fibers,” *Advances in Materials Science and Engineering*, vol. 2022, Article ID 8604234, 6 pages, 2022.

## Research Article

# Experimental Studies on Mechanical and Thermal Properties of Polyester Hybrid Composites Reinforced with *Sansevieria Trifasciata* Fibers

R. Premkumar,<sup>1</sup> K. Sathish Kumar,<sup>1</sup> J. Maniraj,<sup>1</sup> A. Felix sahayaraj,<sup>1</sup> I. Jenish,<sup>2</sup> Fayaz Hussain ,<sup>3</sup> Nidhal Ben Khedher,<sup>4,5</sup> Walid Aich,<sup>4</sup> and V. Suresh <sup>5</sup>

<sup>1</sup>Department of Mechanical Engineering, Kalaingar Karunanidhi Institute of Technology, Coimbatore 641402, Tamilnadu, India

<sup>2</sup>Department of Applied Mechanics, Seenu Atoll School, Ministry of Education, Addu, Maldives

<sup>3</sup>Faculty of Integrated Technologies, Universiti Brunei Darussalam, Brunei Darussalam

<sup>4</sup>Department of Mechanical Engineering, College of Engineering, University of Ha'il, Ha'il 81451, Saudi Arabia

<sup>5</sup>Laboratory of Thermal and Energetic Systems Studies (LESTE), National School of Engineering of Monastir, University of Monastir, Monastir 5000, Tunisia

Correspondence should be addressed to V. Suresh; [suresh.velse@sharafuddin.edu.mv](mailto:suresh.velse@sharafuddin.edu.mv)

Received 31 March 2022; Accepted 10 June 2022; Published 12 July 2022

Academic Editor: K. Raja

Copyright © 2022 R. Premkumar et al. This is an open access article distributed under the Creative Commons Attribution License, which permits unrestricted use, distribution, and reproduction in any medium, provided the original work is properly cited.

In the recent decades, natural fiber reinforced composite (NFRC) plays a vital role in most of the engineering applications including automobile and structural. The demand for novel natural fiber increasing steeply in recent times. Current research work aimed to develop hybrid *sansevieria trifasciata* fiber (HSTF)/polyester composite, and researchers combined untreated *sansevieria trifasciata* fibers (USTFs) with NaOH treated sisal fibers (NSTFs) and combined them with a polyester matrix. The reinforced effect of HSTFs was shown to be superior to that of NSTFs. It has the tensile strength of 48.47 MPa, the flexural strength of 69.17 MPa, and the impact strength of 16.34 kJ/m<sup>2</sup>. The thermal behaviour of the composite increased because of chemical treatment and hybrid composition. Polyester/HSTFs show superior mechanical properties compared to other developed samples.

## 1. Introduction

Because of their superior mechanical properties and biodegradability, polyester and natural fiber composites have gotten a lot of attention. Polyester is a high-modulus, and high-strength polymer used as a matrix in most of the polymer-based composites [1, 2]. Natural fibers are environmentally friendly fibers derived from natural sources because natural fiber reinforced composites (NFRCs) are completely biodegradable in soil. In addition to that, NFRC has merits such as recyclability, low density, and cheap cost over man-made fibers [3]. NFRC is frequently used in automobile and structural parts due to its lower weight, biodegradable, and higher specific strength [4–7]. To increase fiber compatibility, certain techniques for pretreatment were applied, such as physical explosion, thermal treatment,

chemical treatment, and so on [7, 8]. While these approaches improved matrix fiber bonding, enhancing the roughness of the surface, and the mechanical behavior (tensile, flexural, and impact strength). Even though chemical treatment enhances the matrix fiber bonding, it causes fibers to fracture rather than pull out when subjected to mechanical stress [9–11]. In the meantime, the hybrid composite of chemically treated and untreated sisal fiber-reinforced polylactic acid showed superior quality than the other composition [12]. Indran et al. [13] reported that a high NaOH concentration and a longer soaking time caused fiber degradation, disrupted fiber structure, and reduced fiber strength. Furthermore, following NaOH treatment, reduces the thickness of fiber due to the removal of hemicelluloses, lignin, and other contaminants [14, 15]. When the fiber penetrates into the polymer matrix, fracture strength is mainly depending

on the fiber volume and length of the fiber. Generally, fibers predominantly exhibit the following failure mechanisms, namely, delamination, fiber pull-out, and fiber fracture [16, 17]. The cissus quadrangularis stem fiber (CQSF) has more physical and chemical properties. It has the cellulose content of nearly 82% [13]. Though it has adequate properties because of poor bonding the mean strength was not as much as expected. But, the treated cissus quadrangularis stem fiber (CQSF) reinforced polyester composite produced high tensile and flexural strength and also found minimum delamination while fracturing [18]. The thermal and tribological behaviour of the CQSF/Epoxy have been identified as good as compared to other composite materials [9]. It indicates that the thinner the fibers in the composite, the poorer the mechanical qualities. In this study, certain untreated sansevieria trifasciata fibers (USTFs) were combined with NaOH-treated sansevieria trifasciata fibers (NSTFs) to create hybrid sansevieria trifasciata fibers (HSTFs), which were then put into a polyester matrix to form polyester/HSTF composites. Sansevieria trifasciata fiber (STF) is derived from the leaf of the sansevieria trifasciata plant, which is abundantly farmed in South Asia.

The hybrid STFs reinforced polyester is a new composition for this fiber. It has not been done in any other studies. In this paper only, the performance analysis of HSTFs/polyester composite has been discussed. The plant of STFs was shown in Figure 1. Low density, high relative strength, and biodegradability are only a few of the benefits of STFs. The inclusion of USTFs was intended to reduce the drawbacks of fiber surface modification through chemical treatment and improve the performance of STF reinforced polyester composites, particularly mechanical properties.

## 2. Experimental Methods

**2.1. Materials.** Covaiseenu chemicals supplied the polyester. Table 1 lists the compositions of the prepared polyester composite material. Sansevieria trifasciata fibers were collected from the local region of Coimbatore district as in Figure 1, Tamilnadu, India. Table 2 shows the composition and mechanical parameters of sansevieria trifasciata extracted fiber. In NaOH Treatment of STFs, hemicelluloses, lignin, and other tiny molecular components in STFs may be removed by NaOH treatment. With a cutting machine, the STF is converted to short fibers (fiber length-40 mm). The STFs were then immersed in a 5% NaOH solution for the duration of 3 hours. Finally, NaOH treated STFs were cleaned with pure water and dried in the open air for 48 hours.

**2.2. Sample Preparation.** Polyester, NSTFs, and USTFs were all dried for 4 hours at 80°C. To make HSTFs, treated fibers were mixed with untreated fiber in the 1 : 1 ratio. The treated and untreated fibers are given in Figure 2. The polyester was poured and compounded with the STFs at room temperature. According to Table 1, three types of samples were created: polyester/USTF (A1), polyester/NSTFs (A2), and polyester/HSTFs (A3). The sample images showed in Figure 3. Temperature and pressure for compression moulding



FIGURE 1: Sansevieria trifasciata plant.

TABLE 1: List of prepared materials.

Sample code	Description	USTF (%)	NSTF (%)	Matrix (%)
Sample A1	USTF/ Polyester	30	0	70
Sample A2	NSTF/ Polyester	0	30	70
Sample A3	HSTF/ Polyester	15	15	70

were 30°C and 10 MPa, respectively. For the tensile test, dumbbell-shaped specimens (75 × 4 × 1 mm, parallel portion 25 mm) were made, while rectangular specimens (80 × 10 × 4 mm) were prepared for the flexure and impact tests, respectively.

**2.3. Mechanical Examination.** The composites' tensile and flexural characteristics were tested with the aid of the Instron Universal Testing Machine (Instron: model-5565). An Izod Impact Tester was used to conduct the impact testing. The samples were prepared according to the ASTM standard for the comparison purpose [18].

**2.4. Thermal Characteristics.** A TGA was performed on the composites using a Thermogravimetric Analyser (model: STA 409) to determine their thermal stability. The sample used for this experiment is powder form and the temperature is raised by 10°C/min in presence of nitrogen gas. The maximum temperature for this experiment is 700°C.

**2.5. Morphological Study.** A scanning electron microscope was employed to examine the matrix fiber adhesion in the developed samples. The gold coating was used over the surface of the sample where the fracture took place. The gold coating increased the conductivity of the electron which means the image is very clear.

## 3. Results and Discussion

**3.1. Mechanical Characteristics.** Figures 4–6 show the mechanical properties of the developed samples. The tensile strength (32.53 MPa), flexural strength (61.42 MPa), and impact strength (11.42 KJ/m<sup>2</sup>) of polyester/USTFs are reported, meanwhile, those of polyester/NSTFs are tensile



TABLE 2: Numerical results after the experiment.

Sample code	Tensile strength (MPa)	Tensile modulus (GPa)	Flexural strength (MPa)	Flexural modulus (GPa)	Impact strength (KJ/m <sup>2</sup> )
Sample A1	32.53	2.15	61.42	2.42	11.42
Sample A2	45.26	2.56	66.73	3.16	13.15
Sample A3	48.47	2.72	69.17	3.33	16.34



FIGURE 2: Extracted fiber with untreated and NaOH treated.

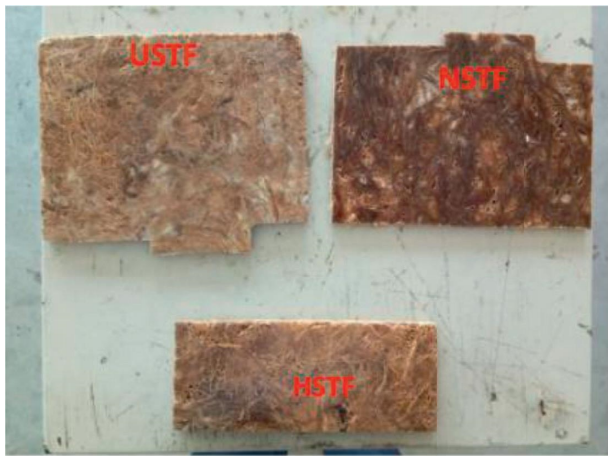


FIGURE 3: Prepared composite materials.

strength (45.26 MPa), flexural strength (66.73 MPa), and impact strength (13.15 KJ/m<sup>2</sup>), which are higher than neat polyester with USTFs. It demonstrates that polyester and NSTFs are compatible, as well as NSTF dispersion in a polyester matrix. The tensile and flexural modulus of the USTF sample are 2.15 and 2.42 GPa, whereas the tensile and flexural modulus of the treated sample shows 2.56 and 3.16 GPa, respectively, superior than the neat polyester with the USTFs sample. It might be because the modulus of STFs is superior than the plain polyester sample, or because the microstructure of polyester composites changes when STFs are added. As a result, further research into crystal morphology is required. Hybrid sample HSTF sample properties are good compared to other developed composites. The hybrid samples show flexural strength and modulus values

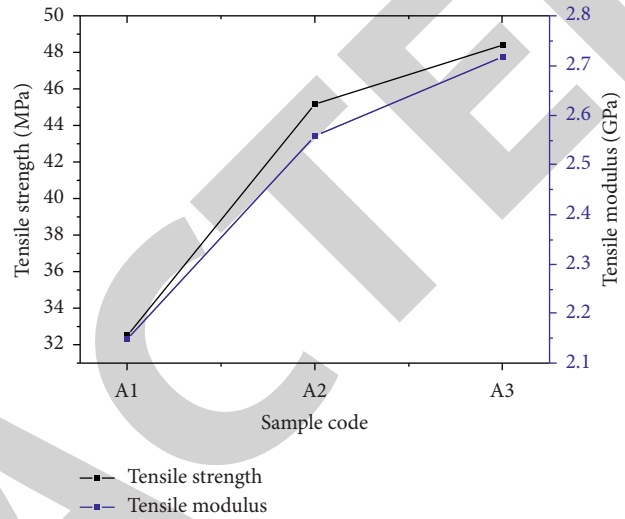


FIGURE 4: Tensile strength and modulus results.

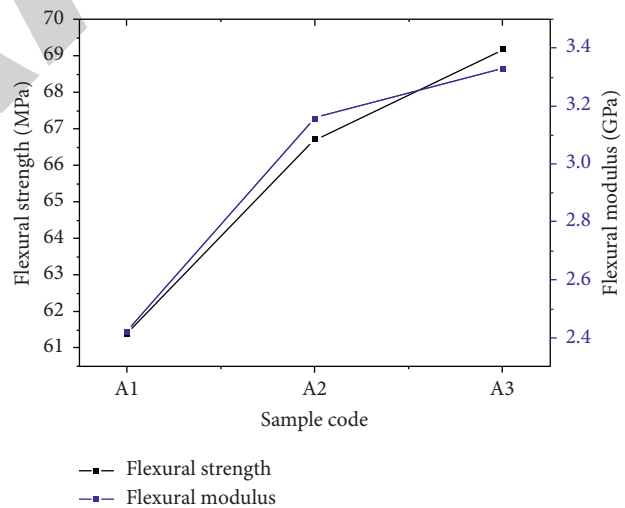


FIGURE 5: Flexural strength and modulus results.

of 69.17 and 3.3 GPa, respectively, which are 3.65% and 5.37% greater than polyester/NSTFs. Polyester/HSTFs have tensile strengths and moduli of 48.47 MPa and 2.72 GPa, respectively, which are 7.09% and 6.25% greater than polyester/NSTFs. The impact strength trends are also obtained, as illustrated in Figure 6. Polyester/HSTFs have 16.34 KJ/m<sup>2</sup> impact strength, which is 24.2% greater than polyester/NSTFs. There are three basic reasons why polyester/HSTFs have superior mechanical qualities than polyester/NSTFs. First, as discussed in the introduction, it is owing to the synergistic action of USTFs and NSTFs. STFs

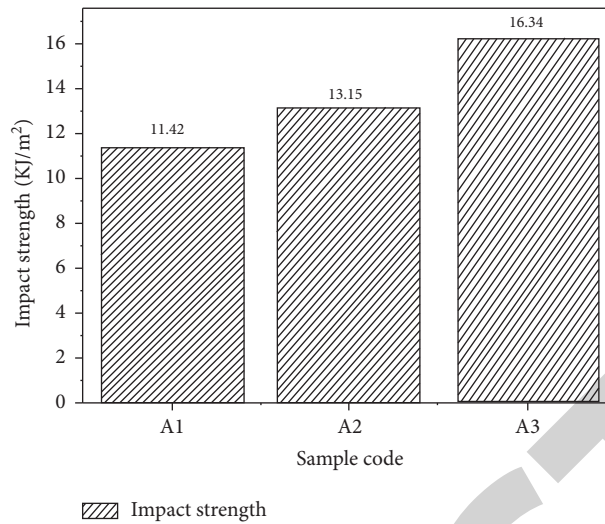


FIGURE 6: Impact strength results.

are having a hollow cellulose structure bonded with lignin and hemicelluloses. Cellulose and hemicelluloses are the primary parts of the plant cell walls, meanwhile, lignin fills the gaps between the cellulose fibrils, bonding both cellulose and other elements. The cell walls thicken as a result of the lignification process, and the carbohydrate is protected against chemical and physical harm. The natural cellulose structure was depolymerized by alkali treatment. Furthermore, during the NaOH treatment procedure, fibers are reversed and twined, as seen in mechanical characterization. Tensile strength may be reduced due to torsional stresses. Furthermore, NSTFs have a poorer dispersion in the polyester matrix than USTFs. USTFs may help to mitigate the problems of surface treatment, while also preserving the benefits of STF and improving the performance of polyester composites. Second, certain chemicals in the untreated STFs may have stimulated the development of a new crystal (beta) with higher mechanical characteristics. Lignin may aid in the nucleation and development of crystals [19]. Canetti discovered that the nucleating action of lignin formed a  $\beta$ -crystal of PP while keeping the original  $\beta$ -crystal. Third, fibers' lignin, wax, and other components may be advantageous for the inclusion of fibers and matrix. Because of its high dispersion, lignin is often utilized as a binder [20]. Rozman et al. [21] discovered that composites using lignin as a compatibilizer have better flexural characteristics than control composites [21]. According to previous investigations, hemicelluloses have also been shown to be effective in changing the cellulose microstructure due to their hydrophobicity. When hemicelluloses are removed, the comparatively flexible cellulose, hemicelluloses, cellulose link is replaced with the stiffer cellulose, cellulose bond, preventing stress redistribution and lowering strength qualities. As a result of combining NSTFs with USTFs, some valuable fiber components may be retained, improving composite interface qualities.

**3.2. Thermogravimetric Analysis (TGA).** Table 3 thermal properties of the developed polyester and STFs reinforced polyester composites. The weight percentage of polyester/

USTFs and polyester composites began to rapidly decrease between 398°C which is mostly due to material deterioration. When the thermal degradation commenced, a second transition occurred between 360 and 380 degrees Celsius. From the TGA results, it was clear that the polyester with untreated fiber was more thermally stable. The fibers and polyester were exposed to heat and friction throughout the composites preparation process, resulting in thermal deterioration. As a consequence, the thermal stability of polyester/USTFs composites decreased when compared to plain polyester. Polyester/HSTFs also had greater thermal degradation temperature, indicating that polyester/HSTFs had superior thermal stability than polyester/NSTFs. In comparison to polyester/NSTFs composite, it can be determined that polyester/HSTFs composite has a more stable chemical structure. Another reason might be that the NaOH treatment has damaged the fiber structure. Another reason is that polyester/HSTFs have a greater crystallinity than other materials. Furthermore, the residual weight percentages of the three components differed from one another. The polyester/HSTFs composite contained the highest residues, while straight polyester had the least. Because of the SFs as reinforcement, polyester/SFs composites had a greater heat resistance than plain polyester, and HSTFs had a superior heat resistance than NSTFs.

**3.3. SEM Analysis.** Figure 7 shows the morphological analysis of developed samples. Fibers in the polyester matrix are randomly oriented, as shown in Figures 7(a) and 7(b). Polyester/HSTFs seemed to have a different microstructure. The SEM picture of polyester/HSTFs in Figure 7(a) was obtained at 750X zoom level. It was found that only fewer cavities indicating that more fibers were bonding together. Figure 7(b) shows tearing fibers, indicating that the strength of SFs was considerably reduced as a result of the NaOH treatment. The number of cavities in the SEM image of polyester/HSTFs (Figure 7(b)) reduced, indicating that removing fibers from the matrix was more difficult and

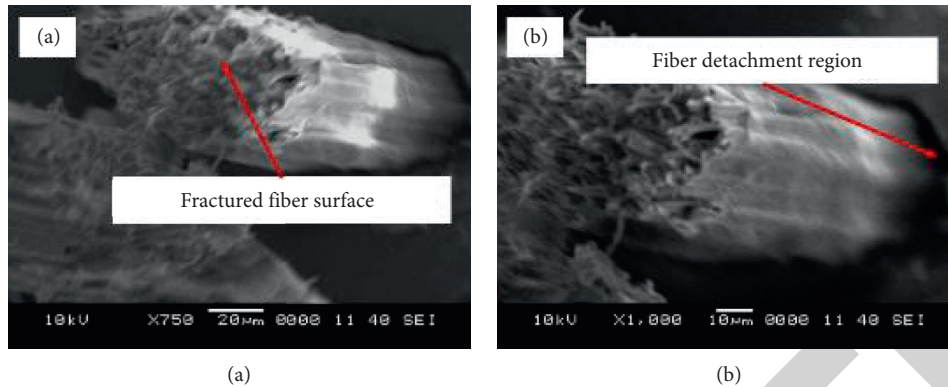


FIGURE 7: Morphology of polyester/HSTFs composite after tensile test.

TABLE 3: Thermal stability of the prepared samples.

Sample code	Initial degradation temp (°C)	Weight loss (%)	Final degradation temp (°C)	Weight loss (%)	Final residue (%)
Sample A1	398.52	31.14	—	—	58.01
Sample A2	268.16	34.82	355.14	24.74	30.15
Sample A3	282.24	37.59	388.24	23.68	28.34

interface strength was enhanced. This indicated that some chemicals in the USTFs had a good impact on interface strength. Figure 7(b) shows a crisp image of polyester/HSTFs magnified 1000 $\times$ . The smooth fracture surface can be visible, which might indicate that certain USTFs were stronger than NSTFs and so served as reinforcement.

#### 4. Conclusion

Using HSTFs as reinforcement instead of NSTFs might greatly enhance the mechanical and thermal characteristics of polyester composites. Polyester/HSTFs composite had 7.09%, 3.65%, and 24.2% greater in tensile strength, flexural strength, and impact strength compared to other compositions. Excellent matrix fiber interfacial bonding which might contribute to improved mechanical and thermal properties. The thermal residuals amount decreased in the hybrid composite and the decomposition temperature increased to 388.24°C in this composition due to hybridization and chemical treatment. Matrix fiber adhesion of polyester/HSTFs sample was better than that of polyester/NSTFs, according to SEM studies. Chemical treatment and hybridization increased the bonding strength due to the removal of wax and excessive oxides content in the outer surface of the fiber [22].

#### Data Availability

The data used to support the findings of this study are included within the article. Further data or information is available from the corresponding author upon request.

#### Conflicts of Interest

The authors declare that there are no conflicts of interest regarding the publication of this paper.

#### Acknowledgments

This research has been funded by the Scientific Research Deanship at the University of Ha'il, Saudi Arabia through project number RG-22 057.

#### References

- [1] L. Prabhu, V. Krishnaraj, S. Sathish, S. Gokulkumar, M. R. Sanjay, and S. Siengchin, "Mechanical and acoustic properties of alkali-treated sansevieria ehrenbergii/camellia sinensis fiber-reinforced hybrid epoxy composites: incorporation of glass fiber hybridization," *Applied Composite Materials*, vol. 27, no. 6, pp. 915–933, 2020.
- [2] T. Raja, V. Mohanavel, S. Suresh Kumar, S. Rajkumar, M. Ravichandran, and R. Subbiah, "Evaluation of mechanical properties on kenaf fiber reinforced granite nano filler particulates hybrid polymer composite," *Materials Today Proceedings*, vol. 59, pp. 1345–1348, 2022.
- [3] A. Felix Sahayaraj, M. Muthukrishnan, and M. Ramesh, "Experimental investigation on physical, mechanical, and thermal properties of jute and hemp fibers reinforced hybrid polylactic acid composites," *Polymer Composites*, vol. 43, no. 3, pp. 2854–2863, 2022.
- [4] G. V. Vigneshwaran, I. Jenish, and R. Sivasubramanian, "Design, fabrication and experimental analysis of pandanus fibre reinforced polyester composite," *Advanced Materials Research*, vol. 984-985, pp. 253–256, 2014.
- [5] P. K. Panda, J. Jebastine, M. Ramarao, S. Fairouz, C. K. Reddy, and O. Nasif, "Exploration on mechanical behaviours of hyacinth fibre particles reinforced polymer matrix-based hybrid composites for electronic applications," *Advances in Materials Science and Engineering*, vol. 2021, Article ID 4933450, 10 pages, 2021.
- [6] R. Ganesamoorthy, R. M. Reddy, T. Raja, P. K. Panda, S. H. Dhoria, and O. Nasif, "Studies on mechanical properties of kevlar/napier grass fibers reinforced with polymer matrix

## *Retraction*

# **Retracted: Mechanical and Morphological Studies of *Sansevieria trifasciata* Fiber-Reinforced Polyester Composites with the Addition of SiO<sub>2</sub> and B<sub>4</sub>C**

### **Advances in Materials Science and Engineering**

Received 26 December 2023; Accepted 26 December 2023; Published 29 December 2023

Copyright © 2023 Advances in Materials Science and Engineering. This is an open access article distributed under the Creative Commons Attribution License, which permits unrestricted use, distribution, and reproduction in any medium, provided the original work is properly cited.

This article has been retracted by Hindawi, as publisher, following an investigation undertaken by the publisher [1]. This investigation has uncovered evidence of systematic manipulation of the publication and peer-review process. We cannot, therefore, vouch for the reliability or integrity of this article.

Please note that this notice is intended solely to alert readers that the peer-review process of this article has been compromised.

Wiley and Hindawi regret that the usual quality checks did not identify these issues before publication and have since put additional measures in place to safeguard research integrity.

We wish to credit our Research Integrity and Research Publishing teams and anonymous and named external researchers and research integrity experts for contributing to this investigation.

The corresponding author, as the representative of all authors, has been given the opportunity to register their agreement or disagreement to this retraction. We have kept a record of any response received.



### **References**

- [1] P. Hariprasad, M. Kannan, C. Ramesh et al., “Mechanical and Morphological Studies of *Sansevieria trifasciata* Fiber-Reinforced Polyester Composites with the Addition of SiO<sub>2</sub> and B<sub>4</sub>C,” *Advances in Materials Science and Engineering*, vol. 2022, Article ID 1634670, 5 pages, 2022.



## Research Article

# Mechanical and Morphological Studies of *Sansevieria trifasciata* Fiber-Reinforced Polyester Composites with the Addition of SiO<sub>2</sub> and B<sub>4</sub>C

P. Hariprasad,<sup>1</sup> M. Kannan,<sup>1</sup> C. Ramesh,<sup>1</sup> A. Felix Sahayaraj,<sup>1</sup> I. Jenish ,<sup>2</sup> Fayaz Hussain,<sup>3</sup> Nidhal Ben Khedher,<sup>4,5</sup> Attia Boudjemline,<sup>6</sup> and V. Suresh <sup>7</sup>

<sup>1</sup>Department of Mechanical Engineering, Kalaingar Karunanidhi Institute of Technology, Coimbatore 641402, Tamilnadu, India

<sup>2</sup>Department of Applied Mechanics, Seenu Atoll School, Addu, Ministry of Education, Maldives

<sup>3</sup>Faculty of Integrated Technologies, Universiti Brunei Darussalam, Brunei Darussalam

<sup>4</sup>Department of Mechanical Engineering, College of Engineering, University of Ha'il, Ha'il 81451, Saudi Arabia

<sup>5</sup>Laboratory of Thermal and Energetic Systems Studies (LESTE) at the National School of Engineering of Monastir, University of Monastir, Monastir 5000, Tunisia

<sup>6</sup>Department of Industrial Engineering, College of Engineering, University of Ha'il, Ha'il 81451, Saudi Arabia

<sup>7</sup>Department of Biotechnology, Sharafuddin School, Hithadhoo, Postal Code 19020, Maldives

Correspondence should be addressed to V. Suresh; [suresh.velse@sharafuddin.edu.mv](mailto:suresh.velse@sharafuddin.edu.mv)

Received 31 March 2022; Accepted 6 June 2022; Published 11 July 2022

Academic Editor: K. Raja

Copyright © 2022 P. Hariprasad et al. This is an open access article distributed under the Creative Commons Attribution License, which permits unrestricted use, distribution, and reproduction in any medium, provided the original work is properly cited.

The impact of SiO<sub>2</sub> and B<sub>4</sub>C on mechanical and morphological studies of *Sansevieria trifasciata* fiber (STF) reinforced in polyester composites is investigated in this study. STF fibers are reinforced with polyester composites with the addition ceramic fillers such as SiO<sub>2</sub> and B<sub>4</sub>C in various weight fractions to improve tensile, flexural, and impact characteristics. The morphological properties are studied with the help of scanning electron microscopy (SEM). The improved mechanical properties were tensile strength (44.92 MPa), flexural strength (103.58 MPa), and impact strength (27.4 kJ/m<sup>2</sup>) obtained for 20 wt.% STF fiber and 15 wt.% SiO<sub>2</sub> reinforcement with the polyester matrix. The mechanical characteristics of the composites were significantly influenced by increasing SiO<sub>2</sub> up to 15 wt.%.

## 1. Introduction

Natural fiber-reinforced composites (NFRC) have been more important in specialized applications ranging from sports to biomedicine and the military in recent decades. Automotive industries, sporting goods, and structural components are dominated by composites derived from petroleum-based synthetic fibers. Synthetic fibers are often used in a variety of sectors due to their excellent mechanical qualities and inexpensive cost. These fibers, on the other hand, have several drawbacks, including high cost, causing environmental pollution by emitting greenhouse gases [1]. When petroleum-based goods are burned, a large quantity of CO<sub>2</sub> is released into the atmosphere. Natural fibers are

gradually replacing petroleum-based fibers due to concerns about the environment, sustainability, and the need for biodegradable and energy-efficient products [2, 3]. Jute, sisal, kenaf, and hemp are some of the frequently used natural fibers [4–7]. Natural fibers derived from plants are mostly composed of various elements (cellulose, hemicellulose, lignin, etc.) [8, 9]. Compared to synthetic fibers, natural fibers have numerous advantages including light density, low cost, simple availability, biodegradability, recyclability, easy processing, and minimum health concerns [10, 11]. Meanwhile, they need to improve the following properties such as matrix fiber adhesion, thermal stability, and mechanical strength [12]. When compared to synthetic fiber composites, poor matrix fiber adhesion is

the major reason for inferior mechanical properties. Since researchers' primary aim was improving matrix fiber bonding by doing various chemical modification techniques [13, 14], various chemical treatments are used to treat natural fibers in order to improve their interfacial contact with the matrix [15, 16]. Furthermore, adding ceramic fillers to resin improves the mechanical characteristics of composite materials, resulting in increased efficiency and cost savings [1, 17–20]. When compared to composites without silica, mudar/snake grass/polyester composites with silica had 1.5 and 1.08 times the tensile strength and modulus, respectively [18, 21]. The flexural and impact properties of jute/B4C have been improved by adding 30 and 10% wt.% jute and alumina, respectively [22, 23]. The inclusion of silica raised the impact values of bamboo fiber-reinforced composites up to a certain point, beyond which they dropped [24, 25]. B<sub>4</sub>C and SiO<sub>2</sub> are often employed as possible fillers for different thermoset composites since they are the least expensive of all ceramics. The current study looks at how SiO<sub>2</sub> and B<sub>4</sub>C affect the morphological and mechanical characterization of STF fiber reinforced with polyesters. Five samples were fabricated by varying the ceramic fillers in terms of weight proportions from 0–20%.

## 2. Materials and Methods

**2.1. Materials.** STF leaf fibers were collected and extracted from the local region of the Coimbatore district. The cellulose content of this fiber is around 56% and high hemicellulose of 35% with a low lignin content of 6% [26]. The better composite is obtained from the base of the finer since the fiber performance is comparatively good. So, the expectation on the fiber composite is unavoidable. The required ceramic filler and chemical SiO<sub>2</sub>, B<sub>4</sub>C, polyester resin, and catalyst (MEKP) were procured from Covaiseenu chemicals, Coimbatore. Testing and characterizations were done at KIT-Kalaignar Karunanidhi Institute of Technology, Coimbatore. The images of the fillers such as B<sub>4</sub>C and SiO<sub>2</sub> are shown in Figures 1 and 2.

**2.2. Treatment with Chemicals.** Poor interface bonding is thought to be a typical issue with polymer matrix composites. This problem can be rectified by doing chemical treatment. The most commonly used surface treatment is NaOH for removing unwanted materials such as dust and wax from the surface of the fiber which improves the fiber-matrix bonding. This strengthens the interfacial connection between natural fibers and matrix, which increases the composite's overall mechanical properties. The fiber was rinsed with clean water to remove contaminants and dirt. The rinsed fibers were dried in the open air for 24 hours, then subjected to treatment for 3 hours in NaOH solutions. After that, the fibers were dried in an oven at 80°C for 4 hours. Alkaline solutions have the effect of removing hydroxyl groups from the fiber. FRC's interface strength and mechanical properties have also been significantly increased by alkaline treatment.

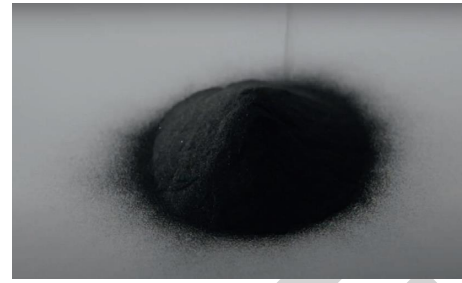


FIGURE 1: Image of B<sub>4</sub>C.



FIGURE 2: Image of SiO<sub>2</sub>.

**2.3. Composite Preparation.** The selection of fiber and volume fractions is the major factor that impacts the mechanical performance of the fabricated samples. To manufacture the composites, current research employs an STF short fiber (20%) reinforced in a polyester resin (60 wt %) as a continuous phase, with the addition of 20% of ceramic fillers such as SiO<sub>2</sub> and B<sub>4</sub>C. The mold is polished first, and then wax is added to the surface to make it easier to remove the composite from the mold. An electromagnetic stirrer evenly agitates the polyester resin distributed with ceramic fillers. The ceramic filler polyester resin was poured into the mold. Subsequently, the mold was placed in a compression molding setup. The temperature was kept at 30°C, the pressure was kept at 35 bar, and it was maintained in the same conditions for 60 minutes. The samples were subjected to post-curing for 120 minutes. The manufacturing approach and process layout of composites are very unique and certain.

**2.4. Characterization of the Prepared Composite with Different Experiments.** In the present study, tensile (ASTM D3039) and flexural tests (ASTM D790) are performed using a computer-controlled universal testing machine (UTM). Tensile and flexural tests were performed on specimens with dimensions of 250 × 25 × 3 mm and 125 × 12.7 × 3 mm, respectively. Both experiments were carried out at a crosshead velocity of 20 cm/min. The notched impact strength was measured by the Charpy impact testing procedure. The ASTM D 256 impact test standard was used, and the specimen dimensions were 60 × 12 mm. Using the flexural test results, the following equation is used to calculate the interlaminar shear strength.

$$ILSS = \frac{3F}{4bt}, \quad (1)$$



TABLE 1: Prepared composite materials.

Sample code	Matrix	Fiber	SiO <sub>2</sub>	B <sub>4</sub> C
C1	60	20	20	0
C2	60	20	15	5
C3	60	20	10	10
C4	60	20	5	15
C5	60	20	0	20

TABLE 2: Derived results from the experiment.

Sample code	Tensile strength	Flexural strength	Impact strength	ILSS
C1	38.15	88.32	19.4	3.41
C2	44.92	103.58	27.4	4.11
C3	43.46	99.09	23.2	3.67
C4	37.73	95.28	21.7	3.43
C5	35.60	84.73	16.6	2.99

where  $F$  is the braking load in  $N$  and  $b$  and  $t$  are the specimen's cross-sectional dimensions.

SEM is used to examine the specimens' fracture surface morphology. The fiber and matrix interface strength were determined using SEM analysis. Specimens were painted silver on an aluminum counterfoil before the morphological study, which was then sputtered with gold. During the observation of the sample, the coating inhibits the buildup of static electrical load. Testing was carried out at standard atmospheric conditions. The prepared sample list is displayed in Table 1 and the obtained results are summarized in Table 2.

### 3. Results and Discussion

**3.1. Tensile Strength.** Figure 3 depicts the impact of SiO<sub>2</sub> and B<sub>4</sub>C on the tensile properties of STF FRC. The inclusion of ceramic fillers in the composites significantly increased the tensile strength, according to the findings. This was found up to 15% SiO<sub>2</sub> because the polyester matrix transmits stress to ceramic fillers, resulting in an increased tensile strength. However, owing to the incongruity between SiO<sub>2</sub> and polyester with the STF fiber, the tensile strength of this content falls over an excess addition leads to poor matrix fiber bonding.

**3.2. Flexural Strength.** The effect of the addition of ceramics fillers in STF/polyester composites is shown in Figure 3. The flexural strength was determined to be the highest at 15 wt.% SiO<sub>2</sub> and 20 wt.% STF fibers' reinforcement. The flexural strength varies between 84.73 MPa and 103.58 MPa as the amount of SiO<sub>2</sub> varies between 0 and 20 wt.%. This improvement may be attributed to SiO<sub>2</sub> in polyester, which significantly increases agglomeration resulting in poor mechanical properties. Enhanced flexural strength of ceramics-filled composites might be attributed to the composites' improved resistance to fracture initiation and

propagation. The composites' flexural strength and modulus are improved as a consequence. There is a decline in the impact strength beyond this 15%.

**3.3. Impact Strength.** Impact energy steadily rises in the composites until it reaches 15 wt.% and 20 wt.% STF (Figure 3). Because of the increase in SiO<sub>2</sub> from 0 to 20 wt.%, the composite's impact strength rose from 2.99 kJ/m<sup>2</sup> to 4.11 kJ/m<sup>2</sup>. The use of ceramic fillers improved the composites' capacity to absorb impact energy. The impact strength falls beyond 15 wt.% SiO<sub>2</sub> content owing to agglomeration and a weak contact to the matrix. The poor impact strength reduces the dimensional stability of developed composites. This is the reason behind the drop in impact strength when the SiO<sub>2</sub> filler addition goes beyond 15 wt.%.

**3.4. Interlaminar Shear Strength (ILSS).** Sample C2 has a greater ILSS than the other samples as seen in Figure 3. This demonstrates that the polyester resin improves the adherence of the fillers and STF fiber. Furthermore, increasing the percentage of SiO<sub>2</sub> in the STF fiber from 0% to 20% enhances the ILSS, but increasing B<sub>4</sub>C causes a drop in ILSS. The ILSS of a composite with 20% SiO<sub>2</sub> content drops from 4.11 MPa to 3.41 MPa without fail. This might be due to incompatibility of the ceramic filler with the fiber, as well as a lack of saturation of 20 wt.% SiO<sub>2</sub> with polyester.

**3.5. SEM Analysis.** According to SEM examination, a composite containing 15% SiO<sub>2</sub> may be homogeneously distributed in polyester because the uniform distribution matrix fiber bonding increased significantly. Mechanical properties were increased up to 15% SiO<sub>2</sub> concentration. When SiO<sub>2</sub> concentration rises beyond 15 wt.%, agglomerates form, resulting in a reduced bonding strength. Beyond 15 wt.% SiO<sub>2</sub> concentration, reduced bonding

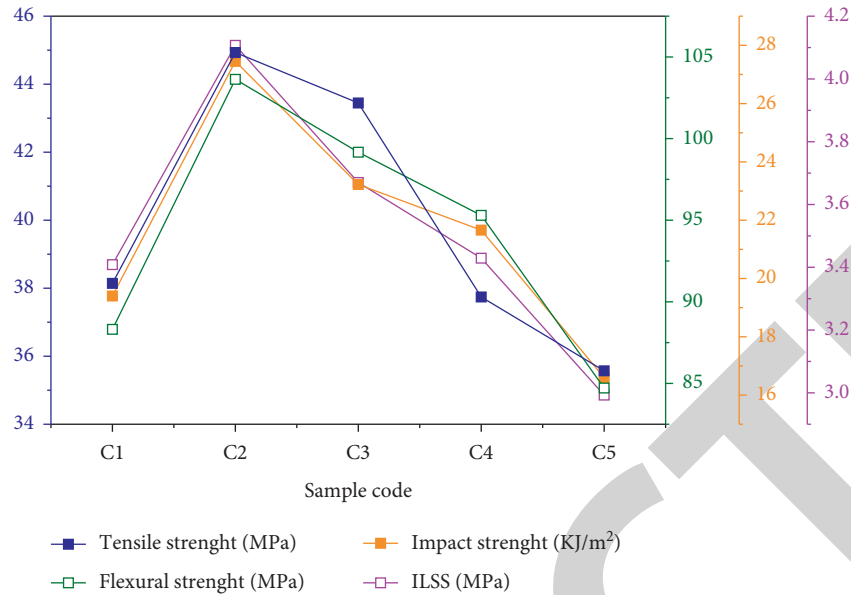


FIGURE 3: Mechanical test result after the experiment.

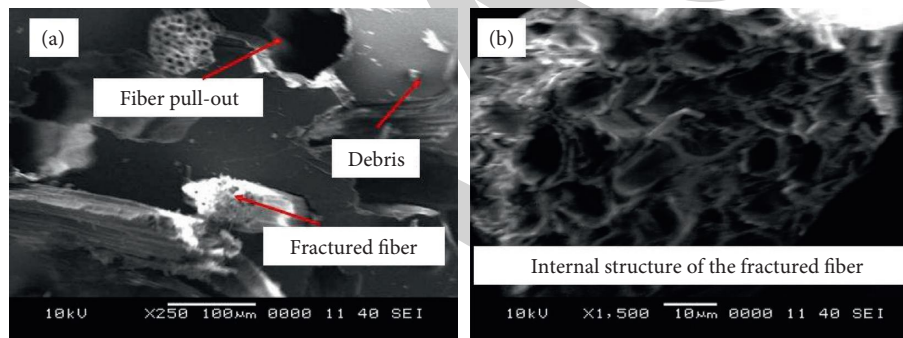


FIGURE 4: SEM images after tensile test. (a) SiO<sub>2</sub> 15 wt.%. (b) SiO<sub>2</sub> 20 wt.%.

between fibers and fillers with polyester shows deterioration in mechanical characteristics. Figure 4 shows SEM images of the fractured samples.

#### 4. Conclusion

The experimental study of the effects of SiO<sub>2</sub> and B<sub>4</sub>C on the mechanical characterization of STF polyester composites yielded the following results: The addition of SiO<sub>2</sub> and B<sub>4</sub>C to STF fiber improves tensile, flexural, and impact strength greatly. When 0–20 wt.% SiO<sub>2</sub> and B<sub>4</sub>C were combined with STF fibers, it was discovered that 15 wt.% SiO<sub>2</sub> produced the best mechanical qualities. Mechanical characteristics are reduced when the SiO<sub>2</sub> level exceeds 15% by weight. Increases in the ILSS have been seen when SiO<sub>2</sub> is added to the STF fiber from 0 to 15%; however, a drop in the ILSS has been observed when B<sub>4</sub>C is increased. The fiber fracture mechanism has been studied by using SEM images and shows good transfer of the resin over the fiber interlaminar structure. As a result of their superior mechanical

characteristics, the produced composites may be inferred to be a low-cost, lightweight, and environmentally friendly brake pad composite.

#### Data Availability

The data used to support the findings of this study are included within the article. Further data or information is available from the corresponding author upon request.

#### Conflicts of Interest

The authors declare that there are no conflicts of interest regarding the publication of this paper.

#### Acknowledgments

This research has been funded by the Scientific Research Deanship at the University of Ha'il, Saudi Arabia through project number RG-22 057.

## *Retraction*

# **Retracted: Experimental Investigation on the Average Surface Roughness (Ra) of AlSi10Mg Alloy Manufactured by Laser Powder Bed Fusion Method**

### **Advances in Materials Science and Engineering**

Received 26 December 2023; Accepted 26 December 2023; Published 29 December 2023

Copyright © 2023 Advances in Materials Science and Engineering. This is an open access article distributed under the Creative Commons Attribution License, which permits unrestricted use, distribution, and reproduction in any medium, provided the original work is properly cited.

This article has been retracted by Hindawi, as publisher, following an investigation undertaken by the publisher [1]. This investigation has uncovered evidence of systematic manipulation of the publication and peer-review process. We cannot, therefore, vouch for the reliability or integrity of this article.

Please note that this notice is intended solely to alert readers that the peer-review process of this article has been compromised.

Wiley and Hindawi regret that the usual quality checks did not identify these issues before publication and have since put additional measures in place to safeguard research integrity.

We wish to credit our Research Integrity and Research Publishing teams and anonymous and named external researchers and research integrity experts for contributing to this investigation.

The corresponding author, as the representative of all authors, has been given the opportunity to register their agreement or disagreement to this retraction. We have kept a record of any response received.

### **References**

- [1] M. R. A. Refaai, D. Prakash, K. G. Jaya Christiyana, D. Prasad, E. Archana, and A. S. Shata, "Experimental Investigation on the Average Surface Roughness (Ra) of AlSi10Mg Alloy Manufactured by Laser Powder Bed Fusion Method," *Advances in Materials Science and Engineering*, vol. 2022, Article ID 5874875, 5 pages, 2022.

## Research Article

# Experimental Investigation on the Average Surface Roughness (Ra) of AlSi10Mg Alloy Manufactured by Laser Powder Bed Fusion Method

Mohamad Reda A. Refaai <sup>1</sup>, D. Prakash,<sup>2</sup> Jaya Christiyana K G,<sup>3</sup> DVSSSV Prasad,<sup>4</sup> E. Archana,<sup>5</sup> and Agegnehu Shara Shata <sup>6</sup>

<sup>1</sup>Department of Mechanical Engineering, College of Engineering, Prince Sattam Bin Abdulaziz University, Alkharj 16273, Saudi Arabia

<sup>2</sup>Centre for Excellence in Energy and Nano Technology, Department of Mechanical Engineering, S.A. Engineering College, Chennai 77, Tamil Nadu, India

<sup>3</sup>Department of Mechanical Engineering, M S Ramaiah Institute of Technology, Bengaluru, Karnataka 560054, India

<sup>4</sup>Department of Mechanical Engineering, Aditya College of Engineering, Surampalem, Andhra Pradesh 533437, India

<sup>5</sup>Department of Computer Science Engineering, Panimalar Institute of Technology, Chennai, Tamil Nadu 600123, India

<sup>6</sup>Faculty of Mechanical Engineering, Arba Minch Institute of Technology, Arba Minch University, Ethiopia

Correspondence should be addressed to Mohamad Reda A. Refaai; [refaai.mraworks@yahoo.com](mailto:refaai.mraworks@yahoo.com)

Received 10 April 2022; Accepted 4 May 2022; Published 7 July 2022

Academic Editor: K. Raja

Copyright © 2022 Mohamad Reda A. Refaai et al. This is an open access article distributed under the Creative Commons Attribution License, which permits unrestricted use, distribution, and reproduction in any medium, provided the original work is properly cited.

AlSi10Mg alloy is an extensively utilised material having good mechanical qualities. The laser powder bed fusion procedure has been applied for fabricating the aluminium alloy (AlSi10Mg) plates in this research. Different exposure periods and scan techniques were applied in this work to measure the average roughness. Results demonstrate that the energy density grew and roughness reduced at first and then improved. Furthermore, there were considerable differences in roughness throughout the created faces. At 125 J/mm<sup>3</sup> and 180 J/mm<sup>3</sup>, excellent surface quality was attained. By this experiment, it was noticed that the direction of scan, wiper movement, and gas flow are the key parameters.

## 1. Introduction

Since 1985, additive manufacturing of metals and alloys has attracted researchers and industrial experts. Huge efforts have been made to prove several aspects of this metal production procedure, including the technological aspect [1], the metallurgical aspect [2], and the design aspect [3]. Laser powder bed fusion, sometimes known as laser fusion, is a technique that uses lasers to fuse powders in a bed. SLM has become one of the most used methods of laser melting [4]. In real-time practice, the laser bed fusion method has been used in the production of a number of products such as steel [5], titanium [6], nickel [7], and aluminium alloys which are some of the real-time examples. The capacity to

manufacture unique components without the use of part-specific equipment is one of the advantages of LPBF technology. Laser powder bed fusion is a well-known innovative technology for developing and manufacturing high-performance components for aerospace and automotive applications [8]. Aluminium alloys are attracting attention as construction material for parts with a high strength-to-weight ratio, low cost, and damage tolerance [9]. In comparison to alloys such as stainless steel SS 316L, Inconel 718, and titanium alloy (Ti6Al4V) [5], the printability of aluminium alloy is inferior [10]. Due to a slight change in phase 2 and solidus temperature near the two series, six series, and seven series of superalloys, only near-eutectic casting alloys like AlSi12 and AlSi10Mg are relatively simple to produce.

As a result, one of the solutions to this issue is the introduction of different Al alloys which are specifically developed for the laser powder bed fusion process, primarily through silicon addition [11].

This study examined the properties of laser power ( $P$ ), scan speed ( $S$ ), and hatch on the mechanical properties and microstructure of a high thermal conductivity aluminium matrix 6063 produced by laser powder bed fusion. Around crack, the element dispersion and grain misorientation were examined. The bulk of cracks were found to just be parallel to the property's direction. By raising the scanning speed, the crack density was reduced. The directed fracture causes anisotropy in mechanical characteristics [12]. Several materials appropriate for this process, notably aluminium alloys, appear to be in demand in the industry. This study used laser powder bed fusion to perform a thorough examination of the machinability of aluminium six series alloys. The influence of process parameters on the microstructure A9618 specimens, particularly improved preheating process [13], was investigated.

Additive manufacturing is the technical term for printing technology, a computer-controlled technique that produces three-dimensional things by layering materials in levels. Additive manufacturing such as 3D printing enables the creation of novel parts with complicated structures and also latest design alternatives for difficult components. On the other hand, high surface roughness is a significant constraint [14]. Surface roughness is an important parameter in the manufacturing of any metallic components. Aluminium magnesium metal matrix composites were fabricated by using the laser powder bed fusion. The conversion from a computer-aided design model to stereolithography and the choice of process parameters significantly affected roughness in this study [15]. From the previous works, it was observed that additive manufacturing is one of the new technologies that allows to manufacture complex-shaped metallic parts. This study looks into the effect of laser powder bed fusion process parameters on surface roughness during manufacturing an aluminum alloy (AlSiMg10 alloy).

## 2. Materials and Methods

The equipment used for this research is EOSINT M290 three-dimensional printing machine. The machine is controlled by a ytterbium laser (wavelength 1080 nm) and a laser power (450 W). This laser method is better than micro-machining because it burns material away instead of moving it to other parts of the object. The schematic of the laser powder bed fusion process is depicted in Figure 1 [16].

For laser focusing, a concentrated spot size of  $90\ \mu\text{m}$  can be employed. Here deflection of laser is provided by two galvanometric scanning mirrors. The procedure can be carried out in an argon environment with a low oxygen level of less than 0.13%. In order to remove the byproducts, this environment within the chamber is cycled and filtered through filter. Figure 2 depicts an aluminium alloy that was created utilising the additive manufacturing process. Table 1 shows the STL setting values used for the experiment [17].

The AlSi10Mg alloy is made up of aluminium alloyed with silicon with a mass fraction of up to 10%, limited

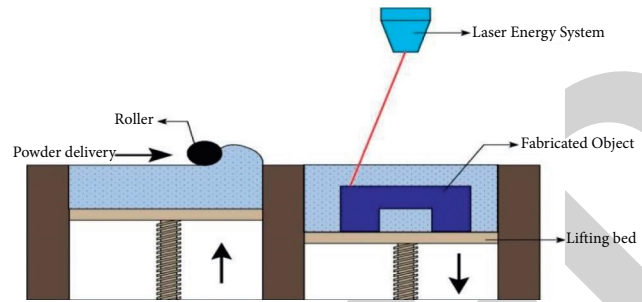


FIGURE 1: Schematic involved in laser powder bed fusion process.

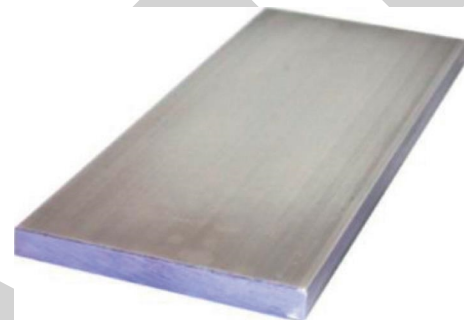


FIGURE 2: Fabricated aluminium alloy samples.

quantities of magnesium, and other negligible components. The addition of silicon makes the alloy tougher and harder than pure aluminium due to the development of  $\text{Mg}_2\text{Si}$  precipitate. Due to the spontaneous production of an oxide layer on the surface of the aluminium alloy, the material has a good corrosion resistance, which can be further increased by chemical oxidation treatment [18]. The process parameters for aluminium alloy samples are shown in Table 2.

## 3. Result and Discussion

**3.1. Deviation between STL Model and AlSi10Mg Alloy.** The STL files were matched to the samples produced. The results of the variance between the STL model and the actual result are listed in Table 3.

Sample 1 and sample 4 have the greatest variances. In general, there is a bigger variation at the lower level near the edges in all samples. Thermal stress or a parameter setup error can both cause this discrepancy. The edge operation is linked to the contour operation in some LPBF software, and some of the parameters that control the contour operations also influence the edge procedure [19]. The maximum allowed distance from the edge scanning path to a prototype is represented by a function of the offset values.

**3.2. Surface Roughness ( $R_a$ ) at Different Zones.** From Table 4, it was noted that minimum surface roughness was obtained in zone 3. The previous layer's surface roughness, which is comparable to the layer thickness, on the other hand, can cause interference also with blade. Figure 3 depicts the

TABLE 1: STL setting values.

Samples	Number of triangles	Dimension file (MB)	Angle (degrees)	Deviation control (mm)
1	2078	102	30	0.0613
2	4534	31	10	0.0254
3	79003	1.60	0.5	0.0024

TABLE 2: Process parameters used for aluminium samples.

Parameter	Condition
Power (P) (W)	175–375
Scan speed (mm/sec)	400–1000
Hatch distance (mm)	0.10–0.14
Energy density (J/mm <sup>3</sup> )	54.2–114.6

TABLE 3: The deviation between STL model and AlSi10Mg alloy.

Trial	Deviation (mm)
Sample 1	0.1267
Sample 2	0.0768
Sample 3	0.0497
Sample 4	0.0921

TABLE 4: The result of surface roughness (Ra) in different zones.

Sample no.	Roughness zones			
	1	2	3	4
1	12.43	10.43	4.65	14.54
2	11.89	11.65	3.91	15.56
4	10.78	12.09	2.87	16.87

surface roughness of the manufactured metal sheet measured in different zones [20, 21].

Furthermore, the recoating blade pushes a lot of powders against the sharp end of the part being produced, causing dynamic pressure. It is possible that the difference between samples 2 and 4 is related to their differing orientations [22]. Walls made along the Y-axis, or parallel to the blade, are more sensitive to force produced by interaction between the part and the blade than walls formed along the X-axis. As a result, to shorten the contact length, the part must be rotated at a moderate angle.

#### 4. Effect of Process Parameters on Surface Roughness

In this investigation, laser power, scan speed, hatching distance, and energy density were selected as process parameters. Surface roughness was measured at various zones on the fabricated AlSi10Mg alloy surfaces. Mitutoyo surface

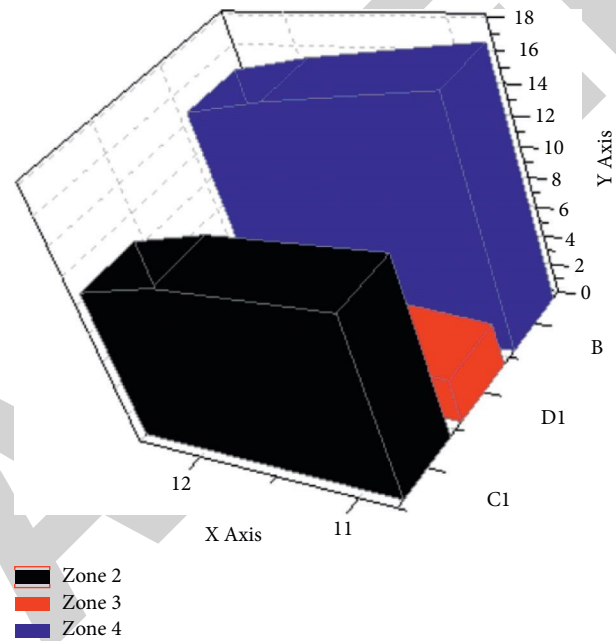


FIGURE 3: Surface roughness obtained in different zones for the fabricated aluminium alloy (AlSi10Mg alloy).

roughness testing equipment was used to evaluate the surface roughness at various zones [13, 23]. Table 5 shows the average surface roughness obtained during the fabrication of AlSiMg10 alloy using the laser powder bed fusion process.

Even though the optimised process effectively reduced the roughness of the LPBF-produced part, variations in other surfaces were not eliminated. The “filleting effect” and “stair stepping impact” have been attributed to the phenomena of the Ra on the top face being considerably smaller than the Ra on the side in laser powder bed fusion-produced components with an angle of inclination. From Table 5, it was observed that the surface roughness obtained was 15.82  $\mu\text{m}$ . In this current work, scan speed is the significant parameter which reduces the surface roughness. The hatch offset is frequently chosen to decrease porosity in the LPBF process, although this results in steps on the sides between interlayers. As shown in Figure 4, When components are created horizontally, enough powder is obtained and adheres to the bottom surface melt pool, resulting in a rough side inside the part [24].



TABLE 5: Average surface roughness (Ra) obtained during the laser powder bed fusion process.

Experimental trial	Power (W)	Scan speed (mm/sec)	Hatching distance (mm)	Energy density ( $J/mm^3$ )	Surface roughness (Ra)
1	100	400	0.10	75	16.45
2	100	600	0.12	50	15.67
3	100	800	0.14	100	14.67
4	180	400	0.10	100	15.67
5	180	600	0.12	75	15.89
6	180	800	0.14	50	16.06
7	360	400	0.10	50	15.93
8	360	600	0.12	100	16.12
9	360	800	0.14	50	15.95

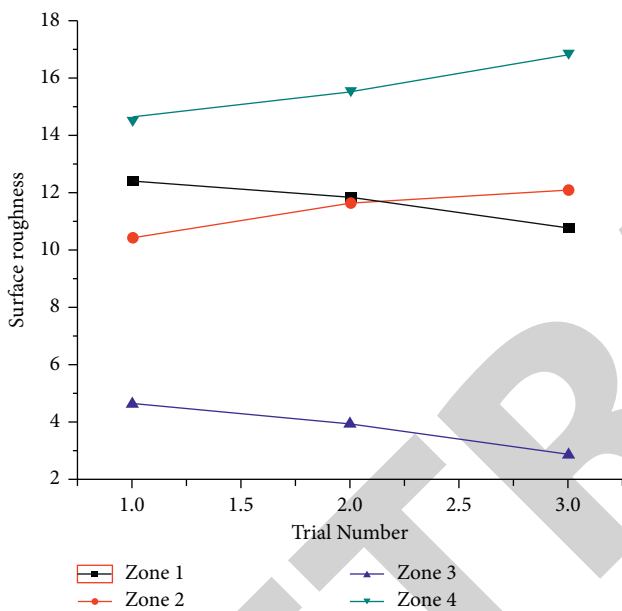


FIGURE 4: Surface roughness measurement in different zones.

## 5. Conclusion

In this work, AlSiMg10 workpiece was fabricated using the laser powder bed fusion process. Surface roughness at different zones (zones 1, 2, 3, and 4) of the fabricated samples was evaluated. From this work, it was observed that the average surface roughness obtained was  $15.92 \mu\text{m}$ . It was concluded that the scanning speed is the significant process parameter which affects the surface roughness.

## Data Availability

The data used to support the findings of this study are included within the article. Further data or information is available from the corresponding author upon request.

## Conflicts of Interest

The authors declare that there are no conflicts of interest regarding the publication of this paper.

## Acknowledgments

The authors appreciate the support from Arba Minch University, Ethiopia, for the research and preparation of the manuscript. The authors thank Prince Sattam Bin Abdulaziz University, S.A. Engineering College, and M.S. Ramaiah Institute of Technology for providing assistance to complete this work.

## References

- [1] A. Paolini, S. Kollmannsberger, and E. Rank, "Additive manufacturing in construction: a review on processes, applications, and digital planning methods," *Additive Manufacturing*, vol. 30, Article ID 100894, 2019.
- [2] A. Aversa, G. Marchese, A. Saboori et al., "New aluminum alloys specifically designed for laser powder bed fusion: a review," *Materials*, vol. 12, no. 7, Article ID E1007, 2019.
- [3] M. K. Thompson, G. Moroni, T. Vaneker et al., "Design for additive manufacturing: trends, opportunities, considerations, and constraints," *CIRP Annals*, vol. 65, no. 2, pp. 737–760, 2016.
- [4] A. Gisario, M. Kazarian, F. Martina, and M. Mehrpouya, "Metal additive manufacturing in the commercial aviation industry: a review," *Journal of Manufacturing Systems*, vol. 53, pp. 124–149, 2019.
- [5] P. Bajaj, A. Hariharan, A. Kini, P. Kürnsteiner, D. Raabe, and E. A. Jäggle, "Steels in additive manufacturing: a review of their microstructure and properties," *Materials Science and Engineering A*, vol. 772, Article ID 138633, 2020.
- [6] L.-C. Zhang and H. Attar, "Selective laser melting of titanium alloys and titanium matrix composites for biomedical applications: a review," *Advanced Engineering Materials*, vol. 18, no. 4, pp. 463–475, 2016.
- [7] C. Y. Yap, H. K. Tan, Z. Du, C. K. Chua, and Z. Dong, "Selective laser melting of nickel powder," *Rapid Prototyping Journal*, vol. 23, no. 4, pp. 750–757, 2017.
- [8] W. A. Rafael de Moura Nobre, H. R. Oliveira, R. B. Falcao et al., "Role of laser powder bed fusion process parameters in crystallographic texture of additive manufactured Nb–48Ti alloy," *Journal of Materials Research and Technology*, vol. 14, pp. 484–495, 2021.
- [9] M. Ravichandran, V. Mohanavel, T. Sathish, P. Ganeshan, S. Suresh Kumar, and R. Subbiah, "Mechanical properties of AlN and molybdenum disulfide reinforced aluminium alloy matrix composites," *Journal of Physics: Conference Series*, vol. 2027, no. 1, Article ID 12010, 2021.

## *Retraction*

# **Retracted: Optimization of Process Parameter on AA8052 Friction Stir Welding Using Taguchi's Method**

### **Advances in Materials Science and Engineering**

Received 26 December 2023; Accepted 26 December 2023; Published 29 December 2023

Copyright © 2023 Advances in Materials Science and Engineering. This is an open access article distributed under the Creative Commons Attribution License, which permits unrestricted use, distribution, and reproduction in any medium, provided the original work is properly cited.

This article has been retracted by Hindawi, as publisher, following an investigation undertaken by the publisher [1]. This investigation has uncovered evidence of systematic manipulation of the publication and peer-review process. We cannot, therefore, vouch for the reliability or integrity of this article.

Please note that this notice is intended solely to alert readers that the peer-review process of this article has been compromised.

Wiley and Hindawi regret that the usual quality checks did not identify these issues before publication and have since put additional measures in place to safeguard research integrity.

We wish to credit our Research Integrity and Research Publishing teams and anonymous and named external researchers and research integrity experts for contributing to this investigation.

The corresponding author, as the representative of all authors, has been given the opportunity to register their agreement or disagreement to this retraction. We have kept a record of any response received.

### **References**

- [1] P. Sharma, S. Baskar, P. Joshi et al., "Optimization of Process Parameter on AA8052 Friction Stir Welding Using Taguchi's Method," *Advances in Materials Science and Engineering*, vol. 2022, Article ID 3048956, 8 pages, 2022.

## Research Article

# Optimization of Process Parameter on AA8052 Friction Stir Welding Using Taguchi's Method

Pankaj Sharma,<sup>1</sup> S. Baskar,<sup>2</sup> Puneet Joshi,<sup>3</sup> T. A. Raja,<sup>4</sup> Santosh Kumar Sahu,<sup>5</sup> Medapati Sreenivasa Reddy,<sup>6</sup> and M. Rudra Naik<sup>7</sup> 

<sup>1</sup>Department of Mechanical Engineering, JECRC University, Jaipur, India

<sup>2</sup>Centre for Excellence in Energy and Nano Technology, S.A. Engineering College, Chennai 600077, India

<sup>3</sup>Department of Electrical Engineering, Rajkiya Engineering College, Ambedkar Nagar, Uttar Pradesh 224122, India

<sup>4</sup>Department of Agricultural Statistics & Economics, Sher-e-Kashmir University of Agricultural Sciences and Technology, Srinagar, Jammu and Kashmir 190025, India

<sup>5</sup>Department of Mechanical Engineering, Veer Surendra Sai University of Technology, Burla, Odisha 768018, India

<sup>6</sup>Department of Mechanical Engineering, Aditya Engineering College, Surampalem 533437, East Godavari District, Andhra Pradesh, India

<sup>7</sup>Department of Electro-Mechanical Engineering, Arba Minch University, Sawla Campus, Arba Minch, Ethiopia

Correspondence should be addressed to M. Rudra Naik; [rudra.naik@amu.edu.et](mailto:rudra.naik@amu.edu.et)

Received 5 April 2022; Accepted 4 May 2022; Published 14 June 2022

Academic Editor: K. Raja

Copyright © 2022 Pankaj Sharma et al. This is an open access article distributed under the Creative Commons Attribution License, which permits unrestricted use, distribution, and reproduction in any medium, provided the original work is properly cited.

The Taguchi method of experimental design was employed in this study to scrutinize the impact of welding processing factors, including rotating speed, travelling speed, and pin profile on ultimate tensile strength, microhardness, and impact strength of the Friction Stir Welded AA 8052 joint. The S/N values for each process specification were calculated using an orthogonal array of L9 design. The 1150 rpm and 28.5 mm/min were the greatest tensile strength, microhardness, S/N evaluation parameters, respectively, and a used cylinder pin. A combination of 1150 rpm and 32.5 mm/s and a conical cylindrical pin provided the best impact toughness results. According to the analysis of variance, the spinning speed, travel feed, and pin shape had a 37.34% impact on ultimate strength and a further 34.33% impact on microhardness. A second set of tests verified the findings, with tensile strength of 349.96 MPa, hardness of 115.31 H, and impact strength of 7.95 kJ.

## 1. Introduction

Light aluminum alloy welding has always been a difficult task for designers, producers, and technicians alike [1]. High thermal buildings, such as a high thermal growth coefficient, high thermal conductivity, greater oxidation, and concretion contractions, as well as a developed solubility of hydrogen and other gasolines in the molten stage, provide several obstacles for the joining process [2, 3]. Hot cracking occurs in the weld zone (dissolved region) due to the dispersion of alloying elements through compaction, which reverses the heat process influence and generates an extremely crude microstructure, leading in poor mechanical qualities of a joint [4]. The welding framework

may be utilized in the aircraft industry to reduce the amount of light we consume [5].

For nonconsumable devices, friction stir weld can be utilized to solder a most difficult creation than the bottom material. As a joining invention for metal joints, friction stir weld has various advantages, including the elimination of faults such porosity and insufficient blend and filler materials, which decreases manufacturing costs [6, 7]. The mechanical qualities of friction stir weld of Al and its own combinations are superior to those of ordinary fusion welds since the joints are defect-free [8]. Friction stir weld processing stipulations on microstructure growth have been the subject of numerous studies and comparisons between friction stir weld and standard blend methods such as TIG

and MIG connected Al composites structures have been thoroughly examined [9, 10]. To ensure high-quality joined junctions, friction stir weld relies on shared plan and source geometry of equipment [11]. This is because these specifications have a significant impact on heat flow and product flow design, as well as on the creation of microstructures [12]. Many published papers have looked at the effects of friction stir weld guidelines on the metallurgical and mechanical characteristics of various low weight aluminum alloy junctions [13, 14]. Only a few research studies have focused on formalizing and optimizing the influence of Friction stir weld handing out conditions on the metallurgic and mechanical characteristics of alike and distinct aluminum joints. The Taguchi method of experimentation methodology is beneficial for optimizing the parameters of the procedures. In addition, it demonstrates how well each parameter contributes to the overall goal of the process. For example, upright pressure has a greater impact on joint tensile strength than any of the other three welding criteria in friction stir weld of A319 directed alloy (travel velocity, rotating speed, and vertical centre force), whereas a few papers have shown that spinning speed has the greatest impact on joint tensile strength over both vertical pressure and travel speed [15]. Moreover, the formalization and optimization of welding standards will also reduce the cost of welding processes for both identical and different Al alloys joints, in addition to being more convenient [16–18]. These parameters were tested on AA8052 metals to see if they affected the flexibility, solidity, impact stamina, and superior disorder in the abrasion mix assembly process for 8052 joints, and the results showed that they had a significant effect in all of those areas [19]. Using orthogonal array design, the process parameters, rotating speed, travel speed, and pin shape, are fine tuned for finding ultimate tensile strength, microhardness, and impact strength of AA8052 material joints.

## 2. Experimental Procedure

In order to build the structure, we used AA8052 alloy plates of 5 mm thickness. Corrosion-resistant 8052 alloy is an excellent choice for big maritime buildings, such as tanks for LNG ships, since it is very resistant to saltwater and salt spray. The 100 mm × 60 mm partitions of the aluminum 8052 lightweight plates were actually used. The tool's rotational speed (950, 1150, and 1450 rpm) and 26, 32.5, and 41 travel speed (mm/min) are used as welding recommendations. FSW (square butt joint) joints were formed using an H13 steel welding tool with pins made up cylinder pin with flutes, con, and triangular pins. Table 1 shows the FSW factors and strategy levels.

The FSW factors of AA 8052 metals were improved using Taguchi's L9 orthogonal array of practices. Rotating speed (W), travel feed (V), and tool geometry were chosen as the FSW guidelines for this study. Strength, hardness, and impact resistance are all output properties. Analysis of the sound-to -noise ratio was carried out for each and every procedure criterion. Use of signal-to-noise analysis helped to keep desired features as stable as possible. This resulted in

more accurate and similar values for ultimate tensile strength, impact strength, and hardness [20]. To advance the mechanical of joints for certain alloys, this study sets out to conduct experiments. Formula (1) was employed to compute the S/N ratio, which displays the quality attributes:

$$\frac{s}{y} = -10 \log \left( \frac{1}{n} \sum_{i=1}^R \frac{1}{y_i^2} \right). \quad (1)$$

By employing Taguchi's L9 orthogonal array of methods, we were able to enhance the FSW properties of aluminum 8052. Device pin geometry and rotational speed (W) were used as the FSW criteria for this study. Output qualities include hardness, elasticity, and abrasion resistance. For each and every method criterion, the S/N (signal-to-noise ratio) was evaluated [21, 22]. Stability was maximized through the application of signal-to-noise analysis. More precise and comparable data for UTS, impact strength, and hardness were obtained as a result of this process. This study sets out to undertake experiments in order to enhance the mechanical characteristics of joints for certain alloys. Utilizing formula (1), the S/N ratio was calculated, which shows the quality characteristics.

## 3. Results and Discussion

**3.1. Ultimate Tensile Strength.** The highest attainable UTS was 352.49 MPa for practice 4 (1150 rpm, 26 mm/min). In addition, for an example prepared from the weld problem in Experiment 9 (1450 rpm, 41 mm/min, triangular pin), the lowest UTS. There was a weld zone fracture in all of the samples. Table 2 shows the results of tensile testing.

**3.2. Analysis of Sound-to-Noise Ratio.** By this analysis, the ultimate tensile strength of a residential property was examined as one of the factors that affect the FSW. Alloy FSW junction tensile strength was a primary objective in this investigation [23]. With the "far higher is actually much better" premise in mind, the goal is to have the highest possible UTS values for all variables. Using L9 orthogonal selection design less weight aluminum alloy 8052 joints, the S/N ratio of corresponding studies is shown in Table 3. The welding example was the only one to fail the tensile test.

If the signal-to-noise ratio is higher, the FSW process will be more effective. As a result, the most model S/N really worth is the optimal level of processing requirements. Consequently, 1150 rpm rotational speed, 26 mm/min travel speed, and CWF resource pin geometries are the optimal levels of the process criteria. In Figure 1, the S/N ratio gives the most important role.

Figure 1 shows that the sound-to-noise ratio of spinning speed rises between 950 rpm and 1150 rpm and subsequently falls between 1150 rpm and 1450 rpm, indicating that the optimal rotating speed is in fact 1150 rpm. Sound-to-noise ratio of welding travelling speed drops between 26 mm/min and 32.5 mm/min and then rises from 32.5 to 41 mm/min; thus, the ideal welding speed is 41.5. As shown by the S/N ratio data obtained from the resource pin profile page, the

TABLE 1: FSW factors and strategy levels.

S. No.	Factors code	Level 1	Level 2	Level 3
1	Rotating speed (W) (rpm)	950	1150	1450
2	Travelling speed (V) (mm/min)	26	32.5	41
3	Tool geometry	Cylinder pin with flutes (CWF)	Tapered cylinder pin profile (Con)	Triangular pin profile (TRI)

TABLE 2: Results of tensile testing.

S. No	Rotational speed (W)	Travel speed (V)	Tool geometry	Ultimate tensile strength (UTS) (MPa)
1	950	26.0	CWF	344.24
2	950	32.5	Con	313.72
3	950	41.0	TRI	327.52
4	1150	2560	CWF	352.49
5	1150	32.5	Con	320.04
6	1150	41.0	TRI	335.28
7	1450	26.0	CWF	330.38
8	1450	32.5	Con	327.19
9	1450	41.0	TRI	306.44

TABLE 3: S/N ratio of AA8052 joints.

S. no	Rotational speed (W)	Travel speed (V)	Tool geometry	Ultimate strength (MPa)	Tensile ratio
1	950	26.0	CWF	345	50.7701
2	950	32.5	Con	314	49.9453
3	950	41	TRI	328	50.2386
4	1150	26.0	CWF	353	50.8785
5	1150	32.5	Con	320	50.1329
6	1150	41.0	TRI	335	50.5264
7	1450	26.0	CWF	330	50.3164
8	1450	32.5	Con	327	49.6621
9	1450	41.0	TRI	306	49.8851

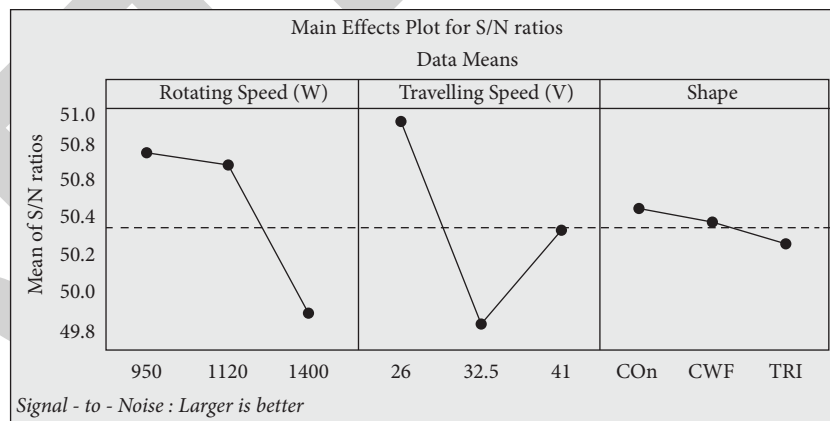


FIGURE 1: Main effects plot on sound-to-noise ratio.

FSW joint is substantially more durable when it is supported by cylinder pins with flues.

3.3. ANOVA. The influence of each process parameter was studied using ANOVA. It evaluates a set of experimental data is impacted by various operational conditions. NOVA is active to examine the impact of distinct

course principles on the UTS of a material [24]. Using the F-test, the quantity of each weld parameter that affects the UTS of a 8052 aluminum metals junction is shown in Table 4.

In Table 4, the P market value directs the possibility of uncontrollability of processing conditions, whereas the F market value shows the amount of relationship between manageable process requirements and optimal ultimate

TABLE 4: Analysis of variance for mean.

Source	DF	Adj SS	Adj MS	F-test	P
Rotating speed	2	0.47946	0.239722	37.32	0.027
Travelling speed	2	0.83328	0.416592	64.85	0.016
Tool pin profile	2	0.01456	0.007268	1.14	0.468
Error	2	0.01286	0.006426		
Total	8	1.34002			

tensile strength [25]. It is chosen to have the highest possible  $F$  value, the lowest possible  $P$  value, and the factor that has a 5% chance of occurring as an important constraint for a better joint quality. The rotating speed contributes 37.34% to the trip speed, while the pin geometry accounts for 13% of the travel speed. Together, these two factors account for 64.86% of the travel speed. So, it is apparent that travel speed is the most significant factor in maximizing ultimate tensile strength.

**3.4. Weld Zone's Hardness.** Table 5 summarizes the results of measuring the microhardness of the AA8052 welded connections with a micro-Vickers hardness tester. According to this data, the sample of the eighth practice (1450 rpm, 32.5 mm/min) had the greatest microhardness of 117.

**3.5. Analysis of Sound-to-Noise Ratio.** During this specific investigation, microhardness was measured to be one of the most desirable unique features that were used to optimize the constraints of FSW. We wanted the highest possible hardness, so we embraced the "larger is truly better" philosophy when doing our analyses with the S/N ratio. In Table 6, there are the S/N ratios of microhardness of AA 8052 connections based on L9 orthogonal arrangement studies.

The optimum S/N and best microhardness values were achieved by utilizing a spinning speed of 1150 rpm, a travelling speed of 26 mm/min, and a cylinder pin with flutes as the device pin profile.

As can be seen in Figure 2, the S/N ratio of rotating speed declines between 950 rpm and 1450 rpm, making 950 rpm the optimal rotational speed with the highest S/N ratio. When travelling at a speed between 32.5 and 41 mm/min, the signal-to-noise ratio falls from 32.5 to 26. Thus, the ideal speed for travelling is 32.5 mm/min. The optimum resource pin account is CWF when the S/N ratio on the device pin profile page is cylindrical pin with flute to downside and then condensed from CWF to TRI.

**3.6. Analysis of Variance.** It is actually done to figure out how well certain process rules for microhardness work. In friction stir welding, the microhardness of welded 8052 aluminum joints is measured using an  $F$ -test to determine the relative importance of various parameters [26]. According to Table 7, each manageable parameter has a significant impact via pillar  $F$ .

Table 7 shows that travel speed accounts for 51.31% of the total, while rotational speed accounts for 34.23%. As a

result, it is clear that the trip speed is more important than any other AA8052 alloy parameter for controlling residential properties such as microhardness since it pays the biggest dividends in achieving maximum microhardness.

**3.7. Impact Strength.** The Charpy test apparatus was employed to compute the impact strength of the AA8052 weld joints, and the findings are indicated in Table 8. Experiment 3 (950 rpm, 41 mm/min, TRI), test 5 (1150 rpm, 32.5 mm/min, Con), and practice 1 (950 rpm, 26 mm/min, CWF) showed that the greatest feasible impact strength was 7 J, while the lowest possible impact durability was 3.8 J.

**3.8. Analysis of Sound-to-Noise Ratio.** As a result of this investigation, influence strength was deemed to be one of the best symbolic buildings from which the guidelines for friction stir welding were optimized [27]. When using the S/N ratio, the "larger is actually better" approach was used since the maximum influence toughness was preferred. S/N ratios for friction stir bonded 8052 aluminum metals' joints depend on L9 orthogonal arrangement design and are shown in Table 9. The highest S/N market value was really 1150 rpm, 32.5 mm/min, and also downside with the most process conditions.

Spinning at 1150 rpm, travel at 32.5 mm/s, and a tool pin profile page for a conical cylinder pin were the perfect process specifications with the maximum S/N value (Con).

To summarize, the best rotational rate is 1400 rpm, which has the highest marketplace value, as the S/N ratio of rotating velocity rises from 950 rpm to 1450 rpm. Figure 3 shows the main effects plot on the S/N ratio. Trip velocity should be 41 mm/min because the sound-to-noise ratio of travelling velocity rises from 26 to 41 mm/min. S/N tool pin account ratios decline from CWT resources [28], improve from CWF resources, and then fall from TRI pin S/N ratios, as shown in Figure 3.

**3.9. ANOVA.** It is used to assess the impact strength of precise processing requirements on long-term toughness. Column F of Table 10 shows the % addition to each controllable constraint that has been found to have a substantial impact on the impact stamina of bonded AA 8052 joint in FSW.

According to Table 10, the tool pin geometry accounts of the total addition, while rotating speed subsidizes 4.29% and travel speed contributes 5.12% of the total contribution. Accordingly [29], the maneuver pin profile page demonstrates that the finest addition to obtaining extreme impact strength is the pin's position on the device.



TABLE 5: Results of the Vickers hardness test.

S. no	Rotational speed (W)	Travel speed (V)	Tool geometry	Vickers hardness number (HV)
1	950	26	CWF	116.35
2	950	32.5	Con	109.68
3	950	41	TRI	113
4	1150	26	CWF	117
5	1150	32.5	Con	116.35
6	1150	41	TRI	109.68
7	1450	26	CWF	113
8	1450	32.5	Con	117
9	1450	41	TRI	116.35

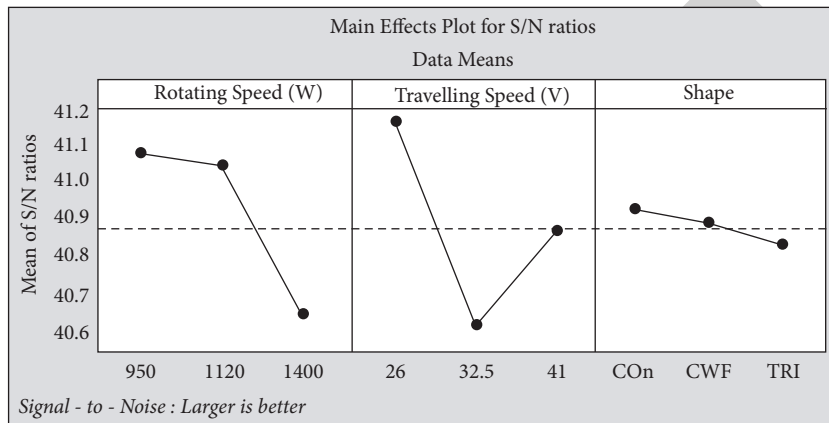


FIGURE 2: Main effects plot on sound-to-noise ratio.

TABLE 6: Sound-to-noise ratios of AA8052 joints.

S. no	Rotational speed (W)	Travel feed (V)	Tool pin geometry	Vickers hardness number (HV)	SN ratio
1	950	26	CWF	116.35	41.35
2	950	32.5	Con	109.68	40.82
3	950	41	TRI	113	40.80
4	1150	26	CWF	117	41.06
5	1150	32.5	Con	108	41.36
6	1150	41	TRI	112.67	40.69
7	1450	26	CWF	110.67	40.89
8	1450	32.5	Con	105	40.42
9	1450	41	TRI	108	40.67

TABLE 7: ANOVA for mean.

Source	DF	Adj SS	Adj MS	F-test	P
Rotating speed	2	0.2734	0.1367	34.15	0.029
Travelling speed	2	0.4103	0.2052	51.29	0.018
Tool pin profile	2	0.0047	0.0024	0.59	0.635
Error	2	0.0078	0.0040		
Total	8	0.6962			

TABLE 8: Impact strength test results.

S. no	Rotating speed (W)	Travelling speed (V)	Tool pin geometry	Impact strength (Joules)	S/N ratio
1	950	26.0	CWF	3.8	11.6581
2	950	32.5	Con	5	13.9429
3	950	41	TRI	7	16.6544
4	1150	26.0	CWF	5	13.7318
5	1150	32.5	Con	7	17.1980
6	1150	41.0	TRI	4.8	13.5793
7	1450	26.0	CWF	6.8	16.6047
8	1450	32.5	Con	5	13.7318
9	1450	41.0	TRI	5.6	15.2598

TABLE 9: S/N ratio of AA 8052 joints.

S. no	Rotating speed (W)	Travelling speed (V)	Tool pin geometry	Impact strength (Joules)	S/N ratio
1	950	26.0	CWF	3.7	11.6691
2	950	32.5	Con	5	13.9339
3	950	41	TRI	7	16.6544
4	1150	26.0	CWF	5	13.7318
5	1150	32.5	Con	7	17.1960
6	1150	41.0	TRI	4.8	13.5773
7	1450	26.0	CWF	6.8	16.6047
8	1450	32.5	Con	5	13.7318
9	1450	41.0	TRI	5.6	15.2598

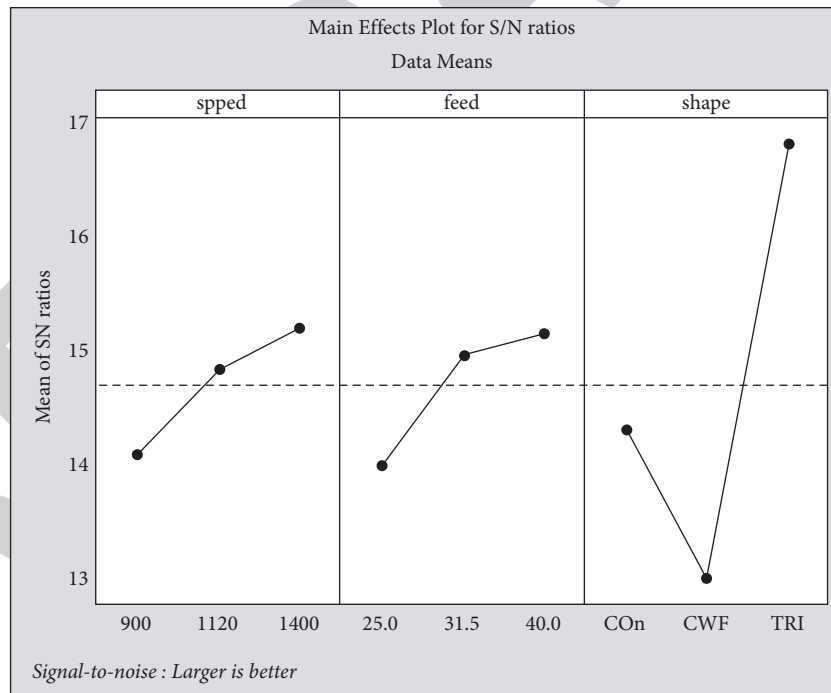


FIGURE 3: Main effects' plot on S/N ratio.

TABLE 10: ANOVA for mean.

Source	DF	Adj SS	Adj MS	F-test	P
Rotating speed	2	1.9447	0.9724	4.29	0.188
Travelling speed	2	2.3163	1.1582	5.12	0.165
Tool pin profile	2	22.6984	11.3493	50.10	0.021
Error	2	0.4532	0.2266		
Total	8	27.4124			

## 4. Conclusions

- (i) Impact strength of AA8052 alloy joints can be measured using rotational speed, travel speed, and tool pin profile of 1150 rpm, 32.5 mm/min, and conical tool pins. These values were also found to be ideal for measuring ultimate tensile strength and microhardness. These conditions resulted in ultimate tensile strength and toughness measurements of 143.59 MPa and 117 J for the joint.
- (ii) ANOVA was found to have a substantial impact on individual weld performance. It was found that the best technique parameters for maximum ultimate tensile strength were rotating speed of 1150 rpm, travel speed of 26 mm/min, and cylinder pin with flutes' tool profile (CWF). Rotating speed makes up 37.34% of the total ultimate tensile strength, while travel speed makes up 64.86%, tool pin profile makes up 1.154%, and so on. As a result, ultimate tensile strength is most strongly influenced by travel speed.
- (iii) Rotating speed is 1150 rpm, travel speed is 26 mm/s, and tool pin profile is CWF, all of which work together to produce the highest possible microhardness. Rotational speed accounts for 34.23%, travel speed for 51.31%, and tool pin shape for 59% of the total contribution to achieving maximal microhardness. As a result, travel speed has a greater impact on microhardness than any other component.
- (iv) Impact strength is best achieved with rotating speed of 1150 rpm, travel speed of 32.5 mm/s, and a tool pin profile with a concave cross section. Rotational speed contributes 43.9%, travel speed contributes 6.3%, and tool pin profile contributes 50.12% to achieving maximum impact strength.
- (v) Thus, the tool pin profile has the greatest impact on the strength of the tool.

## Data Availability

The data used to support the findings of this study are included within the article. Further data or information are available from the corresponding author upon request.

## Conflicts of Interest

The authors declare that there are no conflicts of interest regarding the publication of this article.

## Acknowledgments

The authors appreciate the supports from Arba Minch University, Ethiopia, for providing help during the research and preparation of the manuscript. The authors thank JECRC University, Rajkiya Engineering College, and S.A. Engineering College for providing assistance to complete this work.

## References

- [1] N. Abdulwadood, B. Sahin, and N. Yildirim, "Effect of welding parameters on the mechanical properties of dissimilar aluminum alloys 2024-T3 to 6061-T6 joints produced by friction stir welding," *Nigde Univ. Muhendis. Bilim. Degisti*, vol. 3, pp. 1–11, 2012.
- [2] D. K. Rajendran, G. B. Kannan, and S. Muthukumaran, "Investigation on the mechanical and wear properties of aluminium-magnesium bimetallic composite fabricated by friction stir processing technique," *Transactions of the Indian Institute of Metals*, vol. 71, no. 5, pp. 1247–1255, 2018.
- [3] Y. Zhang, Y. Chen, D. Yu, D. Sun, and H. Li, "A review paper on effect of the welding process of ceramics and metals," *Journal of Materials Research and Technology*, vol. 9, no. 6, ISSN 2238-7854, Article ID 16236, 2020.
- [4] V. Mohanavel, M. Ravichandran, and S. Suresh Kumar, "Optimization of tungsten inert gas welding parameters to," *Materials Today Proceedings*, vol. 5, no. 11, pp. 25112–25120, 2018, Part 3.
- [5] X. Wang, K. Wang, Y. Shen, and K. Hu, "Comparison of fatigue property between friction stir and TIG welds," *Journal of University of Science and Technology Beijing Mineral Metallurgy, Material*, vol. 15, no. 3, pp. 280–284, 2008.
- [6] K. Mariyappan, K. Praveen, S. S. Kumar, K. Kadambanathan, S. Rajamanickam, and R. Vignesh, "Characterization of brass/steel plates joined by friction stir welding," *International Journal of Engineering & Technology*, vol. 7, no. 3, pp. 366–368, 2018.
- [7] F. Gharavi, K. A. Matori, R. Yunus, and N. K. Othman, "Corrosion behavior of friction stir welded lap joints of AA6061-T6 aluminum alloy," *Materials Research*, vol. 17, no. 3, pp. 672–681, 2014.
- [8] G. N. ShivaKumar and G. Rajamurugan, "Friction stir welding of dissimilar alloy combinations-a review," *Proceedings of the Institution of Mechanical Engineers - Part C: Journal of Mechanical Engineering Science*, vol. 2022, Article ID 095440622110, 2022.
- [9] M. M. Moradi, H. Jamshidi Aval, R. Jamaati, S. Amir Khanlou, and S. Ji, "Microstructure and texture evolution of friction stir welded dissimilar aluminum alloys: AA2024 and AA6061," *Journal of Manufacturing Processes*, vol. 32, pp. 1–10, 2018.
- [10] V. K. S. Jain, J. Varghese, S. Muthukumaran, and S. Muthukumaran, "Effect of first and second passes on microstructure and wear properties of titanium dioxide-reinforced aluminum surface composite via friction stir processing," *Arabian Journal for Science and Engineering*, vol. 44, no. 2, pp. 949–957, 2018.
- [11] V. S. Gaikwad and S. Chinchankar, "Mechanical behaviour of friction stir welded AA7075-T651 joints considering the effect of tool geometry and process parameters," *Advances in Materials and Processing Technologies*, vol. 2021, pp. 1–19, 2021.
- [12] G. Rambabu, D. Balaji Naik, C. H. Venkata Rao, K. Srinivasa Rao, and G. Madhusudan Reddy, "Optimization of friction stir welding parameters for improved corrosion resistance of AA2219 aluminum alloy joints," *Defence Technology*, vol. 11, no. 4, pp. 330–337, 2015.
- [13] A. Boşneag, M. A. Constantin, E. Nițu, and M. Iordache, "Friction Stir Welding of three dissimilar aluminium alloy used in aeronautics industry," *IOP Conference Series: Materials Science and Engineering*, vol. 252, no. 1, Article ID 012041, 2017.

## *Retraction*

# **Retracted: Investigation on Durability Behavior of Fiber Reinforced Concrete with Steel Slag/Bacteria beneath Diverse Exposure Conditions**

### **Advances in Materials Science and Engineering**

Received 26 December 2023; Accepted 26 December 2023; Published 29 December 2023

Copyright © 2023 Advances in Materials Science and Engineering. This is an open access article distributed under the Creative Commons Attribution License, which permits unrestricted use, distribution, and reproduction in any medium, provided the original work is properly cited.

This article has been retracted by Hindawi, as publisher, following an investigation undertaken by the publisher [1]. This investigation has uncovered evidence of systematic manipulation of the publication and peer-review process. We cannot, therefore, vouch for the reliability or integrity of this article.

Please note that this notice is intended solely to alert readers that the peer-review process of this article has been compromised.

Wiley and Hindawi regret that the usual quality checks did not identify these issues before publication and have since put additional measures in place to safeguard research integrity.

We wish to credit our Research Integrity and Research Publishing teams and anonymous and named external researchers and research integrity experts for contributing to this investigation.

The corresponding author, as the representative of all authors, has been given the opportunity to register their agreement or disagreement to this retraction. We have kept a record of any response received.

### **References**

- [1] M. Kumar M, V. L. Sivakumar, S. Devi V, N. Nagabhooshanam, and S. Thanappan, "Investigation on Durability Behavior of Fiber Reinforced Concrete with Steel Slag/Bacteria beneath Diverse Exposure Conditions," *Advances in Materials Science and Engineering*, vol. 2022, Article ID 4900241, 10 pages, 2022.

## Research Article

# Investigation on Durability Behavior of Fiber Reinforced Concrete with Steel Slag/Bacteria beneath Diverse Exposure Conditions

Madhan Kumar M,<sup>1,2</sup> Vidhya Lakshmi Sivakumar,<sup>1</sup> Subathra Devi V,<sup>3</sup>  
N. Nagabhooshanam,<sup>4</sup> and Subash Thanappan <sup>5</sup>

<sup>1</sup>Department of Civil Engineering, Saveetha School of Engineering, SIMATS, Chennai, Tamilnadu, India

<sup>2</sup>Department of Civil Engineering, Saveetha Engineering College, Chennai, Tamilnadu, India

<sup>3</sup>Director CIRA Technology Pvt. Ltd., Chennai 602105, Tamilnadu, India

<sup>4</sup>Department of Mechanical Engineering, Aditya Engineering College (A), Aditya Nagar, A D B Road, Surampalem, Andhra Pradesh, India

<sup>5</sup>Department of Civil Engineering, Ambo University, Ambo, Ethiopia

Correspondence should be addressed to Subash Thanappan; [subash.thanappan@ambou.edu.et](mailto:subash.thanappan@ambou.edu.et)

Received 10 April 2022; Accepted 5 May 2022; Published 31 May 2022

Academic Editor: K. Raja

Copyright © 2022 Madhan Kumar M et al. This is an open access article distributed under the Creative Commons Attribution License, which permits unrestricted use, distribution, and reproduction in any medium, provided the original work is properly cited.

One of society's most perplexing concerns is trash management. Among them is steel slag, which is obtained from steel mills and is used in the building industry as a partial substitution ingredient in concrete. To ensure that the concrete lasts the desired service life without deteriorating, bacteria (*Bacillus subtilis*) are introduced to ensure that the construction performs as planned. The research is focused on the M30 grade concrete mix specified in the Indian Standard Code. Concrete specimens containing fiber, steel slag, and bacteria are subjected to a variety of environmental conditions, including extreme, extremely severe, severe, moderate, and mild. The ultrasonic pulse velocity, sorptivity, water absorption, rapid chloride penetration, and acid resistance characteristics of the fiber-reinforced bacterial concrete are compared to those of regular concrete specimens.

## 1. Introduction

The 30 million tonnes of steel slag waste have been generated from the steel manufacturing industry every year in India. Utilizing this waste as a useful product in construction industry will reduce the over mining of natural resources. A single way of application can give the solutions for two problems such as waste management and depletion of natural resources. Steel slags are available in various sizes that can be used as substitute materials for fine and coarse aggregates in concrete. The properties of the steel slag such as size, shape, density, specific gravity, color, and appearance are compared to the conventional aggregates. Among all the properties, the water absorption of steel slag is slightly more than the normal coarse aggregates as, the micropores of the

steel slag absorb greater portion of water from its surface [1]. The by-product of steel manufacturing plant is called steel slag and is used as a boosting material in clayey soil to improve the SBC of the soil [2]. Steel slag can be added as a basic ingredient material in concrete as well as a supplement material in cement for binding [3]. The depth of penetration of water in steel slag aggregate is higher in coarse form and lower in fine form while using in concrete. The same can be rectified by immersing the aggregate in water before using it into concrete [4]. The steel slag aggregate concrete having high resistivity to various imposed loads to avoid surface cracking in such a way that the particle binding in it [5]. Other than Blast Furnace Slag, the ferrous slag produced from the steel extraction producing major pollution element to the environment especially which leads leachate. Only

Blast Furnace and other nonferrous slags can be used for construction [6]. Utilization of steel slag in various construction activities and other raw materials-related products are reducing the management of waste due to slag and generating new job opportunities [7]. Some of the localized failure in conventional concrete can be reduced by replacing conventional aggregate with steel slag aggregate, since these aggregates having high resistivity to failures [8]. Replacing the steel slag and ceramic waste aggregates with optimized percentage can be improving the durability property of concrete compare than the conventional concrete, the percentage of replacement [1]. The self-healing property of the concrete can be improved by mixing the *Bacillus subtilis* with conventional concrete as liquid form with concentration  $0.7 \times 10^7$  cells/ml. These are the lab-cultured bacteria with incubated at 30°C for 7 days [9]. Replacement of microsilica % in cement with *B. subtilis* giving good improvement in self-compacting property of the concrete, in addition to it improving the strength and durability of the concrete [10]. The replacement of 50% of conventional fine and coarse aggregate in concrete with addition of 1.5% of steel fiber increasing the workability and strength of the concrete by 30% when compared to the control concrete mix [11]. The performance of steel slag in very severe condition is good. Hence, it can be used for various practical applications in constructions where the atmospheric conditions are severe to very severe [12]. *B. subtilis* bacteria observing the moisture from the concrete and generating the calcium carbonate precipitation as a by-product which healing the surface and internal crack on the concrete by itself [13]. Steel slag aggregate can be used in concrete as economical and sustainable alternative material in concrete at different percentages to get the better strength in compression and tension [14]. Concrete specimen with and without cold joints subjected to continuous drying, wetting, freezing and thawing effects up to 900°C, and tested for weight losses of sample resulting the good strength on both the types of concrete [15]. Ultrasonic wave passes through the specimen of stones used for construction to test the physical properties with economical NDT method, The detailed internal structure and strength of stones from various locations are identified easily based on the receiving side velocity [16]. Ceramic waste materials are crushed and used as a waste powder in cement and their crystalline structure with porosity tested, the durability of the mortar specimen tested based on the chloride and sulphate attack [17]. The lab-cultured *B. subtilis* bacteria were used in fly ash concrete, the calcium precipitation was examined and evidenced using SEM analysis. The final result shows effective in minimizing sorptivity in concrete specimen in the presence of FA [18]. The ceramic waste powder replaced as a waste particle in cement mortar and their microstructure was analyzed using scanning electron microscopy, after 90 days the compressive strength result shows 40% replacement gave better performance [19]. The optimization technique used in this project can be found out by the exact percentage of substitution of steel slag in concrete. In which we could convert the waste materials in to useful products with new opportunities of jobs. Here an attempt was made with steel slag as a

replacement material for coarse aggregate and various durability properties under various exposure conditions are investigated. The suitable mix with optimal performance in various durability conditions was identified.

## 2. Manufacturing Materials and Methods

The basic ingredients for manufacturing the concrete as aggregates are crushed stone and river sand. They are selected based on their properties such crushing strength, impact value, specific gravity, water absorption, according to the Indian Standard Code 383–1996. The values of the abovementioned properties are compared with the standard values also. The main thing observed from the comparative study of properties of materials is absorbing the water by steel slag aggregate, which is 3%. But the value of water absorption of normal aggregates is 1–2%. The 53 grade Ordinary Portland Cement (OPC) is used as a binding material in concrete manufacturing process and is tested based on the IS code BIS 1489 Part–1. The basic properties of steel fiber used in this research have been listed in Table 1 such as density, aspect ratio, length, and diameter. As well as the shape of the fiber is zig-zig one to get the better binding with the basic ingredients of concrete. The liquid form of lab-cultured *B. subtilis* bacteria is used as a healing material in concrete. The hardened concrete properties such as characteristic compressive strength, split tensile strength, and flexural strength has been tested as per the IS Code 456–2000.

### 2.1. Properties of Materials

**2.1.1. Steel Slag and Coarse Aggregate.** The basic properties of normal and steel slag aggregate have been compared and listed in Table 1 with the specific properties required for concrete manufacturing process. A grade steel slag coarse aggregate was used as a replacement material in concrete with the different trial replacement such as 30, 40, 50, and 60%. Based on the previous study related to this research, the optimum value of replacement of steel slag as coarse aggregate is 50%. The detailed particle size distribution analysis for the steel slag aggregates also done, and the results shown in particle size distribution curve Figure 1.

**2.1.2. Steel Fiber.** In this research, zig-zag shaped steel fibers with 30 mm length and 0.5 mm diameter have been used as a reinforcement material to improve the tensile strength of the concrete. According to the literature review, 3% of the steel fiber by weight was used in every mold. The dispersion of the fiber was checked using wash out test and the uniformity of the fiber dispersion were observed. The properties of fiber have been listed in Table 2.

**2.1.3. Bacteria.** *B. subtilis* bacteria from the bacillus group was widely used in this research as a healing agent. *B. subtilis* is a bacterium having rod shape and the outer core of it can withstand in extreme conditions of environment.



TABLE 1: Properties of steel slag and normal coarse aggregate.

Properties	Normal coarse aggregate	Steel slag	Standard values
Impact value in $J/m^2$	9	25	<45
Cursing strength in $N/mm^2$	36	62	<45
Attrition (%)	5	4	<2
Specific gravity	2.8	3.5	2.5–2.7
Water absorption (%)	1–2	3	0.1–2.0

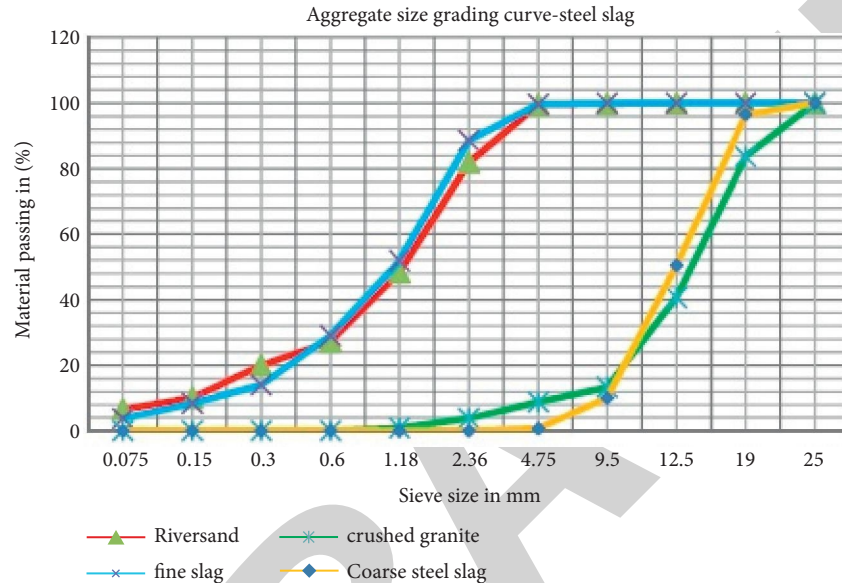


FIGURE 1: Particle size distribution of steel slag with normal aggregate.

TABLE 2: Properties of steel fiber.

Properties	Description
Diameter (mm)	0.5
Length (mm)	30
Aspect ratio	60
Ultimate tensile strength (Mpa)	900
Elastic modulus (Gpa)	210
Density	7850 ( $kg/m^3$ )
Shape	Zig-zag

(1) *Preservation of Bacteria before Culturing.* The *B. subtilis* bacteria were preserved in Luria Bertani Agar Medium and Luria Bertani Broth Medium. It forms irregular dry white colonies on nutrient media, and then they are incubated at the temperature of 30°C in a BOD incubator.

(2) *Culturing of Bacteria.* The bacteria are capable enough to produce the calcium carbonate on media with calcium course (Calcium Lactate). According to the supplier’s recommendations, the *B. subtilis* were cultured in both agar and liquid media. The Petri dishes, flasks, and nutrient medium were sterilized before adding the bacterial strains, then the media is prepared according to the specifications provided below and cooled to room temperature (25°C). Then the culture was incubated at 30°C in the BOD incubator. The detailed list of preparation of media for *B. subtilis* is listed in Table 3.

2.2. *Mix Design.* The quantity of the materials can be derived exactly to achieve the required strength and durability of concrete by using mix design. There are different methods of mix design such as ACI method, BIS method, and DOI method. In this research, BIS method of mix design were used based on the IS code 10262–2009. The mix design was derived for M30 grade concrete in this research to achieve the effective quantity of material. Based on the mix design, the resulting mix ratio is 1 : 1.97 : 3.24 with water cement ratio of 0.54 to get target compressive strength. To test the various durability of concrete, the following two specimens were made for both conventional concrete and steel slag replaced fiber reinforced bacterial concrete. The standard dimensions for the cube is 150 × 150 × 150 mm, and the cylinder is 100 mm dia with 150 mm depth. In this research, the optimum percentage of the replacement of steel slag as coarse aggregate is 50%, which is optimized with the trial mix of replacement of steel slag as coarse aggregate starting from 30% up to 60% with 10% increment. The cubes and cylinders are casted with 50% replacement of steel slag as coarse aggregate in addition to its 30 ml *B. subtilis* and 3% of steel fiber by weight to each cube. As per previous research, the quantity of bacteria added to the concrete is limited to 30 ml, if the quantity increased more than that precipitation of calcium exceeding the allowable limit in concrete, which caused the over deposition of the products on the surface. As well as increasing the percentage of the fiber more than 3%

TABLE 3: Preparation of media for *B. subtilis*.

Luria Bertani agar		Broth (LBB) medium, Miller (M1151/M1245)	
Compounds	Quantity	Compounds	Quantity
Casein enzymic hydrolysate	10.0 g	Casein enzymic hydrolysate	10.0 g
Yeast extract	5.0 g	Yeast extract	5.0 g
Sodium chloride	10.0 g	Sodium chloride	10.0 g
Distilled water	100 ml	Distilled water	100 ml
Agar	15.0 g		

resulting in the increase of self-weight of the concrete. After 24 hours, the specimens are demolded and cured in next 28 days. The designation for the specimens to test durability properties are follows. AA<sub>Mild</sub>, AA<sub>Moderate</sub>, AA<sub>Severe</sub>, AA<sub>Very Severe</sub>, AA<sub>Extreme</sub> and BB<sub>Mild</sub>, BB<sub>Moderate</sub>, BB<sub>Severe</sub>, BB<sub>Very Severe</sub>, BB<sub>Extreme</sub>. Where AA represents Conventional Concrete and BB steel slag replaced fiber reinforced bacterial concrete.

**2.3. Exposure Conditions.** According to Indian Standard Code 456-2000 (Clause 8.2.2.1 and 35.3.2) the concrete durability conditions were tested based on the following five exposure conditions such as extreme, very severe, severe, moderate, and mild. The concrete specimens were placed directly to atmosphere for mild exposure conditions. Specimens were placed under the water, in order to meet the moderate exposure conditions. In case of severe exposure conditions, the concrete specimens was under continuous wetting and drying conditions. The specimens are buried under the subsoil to check the exposure conditions under very severe. For extreme exposure conditions, the specimens directly placed in chemicals or acids. Figure 2 shows the above mentioned five exposure conditions of concrete specimens.

### 3. Fresh Concrete Properties

**3.1. Workability.** This research deals with the concrete mix of 1 : 1.97 : 3.24 and water cement ratio of 0.54. According to this mix, the concrete cubes were casted for all the tests as well as the workability of the fresh mix are good with true slump value. In this research, steel slag used as a partial replaced coarse aggregate and the workability of steel slag concrete also less. In order to increase the workability, the steel slag is immersed in water before use.

**3.2. Hardened Concrete Properties.** The hardened concrete properties tested such as compressive strength, flexural strength, and split tensile strength. The abovementioned tests have been done for the 7 days and 28 days cured specimens with three trials to get the optimum value and suitable percentage of substitution of steel slag. In addition to that the below-listed hardened concrete tests were done to test the durability properties in the steel slag concrete with different exposure conditions such as extreme, very severe, severe, moderate, and mild.

**3.3. Ultrasonic Pulse Velocity Test (UPV).** In the given concrete specimen of size 150 × 150 × 150 mm, the ultrasonic waves were passed through it with the help of transmitter and received on other side. If, the received ultrasonic pulse velocity value is 4.5 and more than that; the quality of the concrete is in excellent condition. If the value lies between 3 and 4.5, then the quality of the concrete is good. In case of the value less than 3, then the quality of the concrete is doubtful. These are the derived parameters as per the IS 13311 (Part-1)-1992 with the unit of measurement of mm/s. The pulse velocity can be calculated with the ratio of distance traveled by time taken. The detailed experimental set up of Ultrasonic Pulse Velocity test method as shown in Figure 3.

**3.4. Rapid Chloride Penetration Test (RCPT).** The RCPT used to find the amount of chloride penetration into the concrete specimen by passing the electric current through the concrete specimen with 100 mm diameter and 50 mm thick with 6 hours as per ASTM C 1202 as show in Figure 4. In this test throughout the time period 60 V of electricity will be maintained. In which the two leads, one submerged with sodium chloride solution of 3% and another end immersed with sodium hydroxide solution with 0.3 N. The amount of electric charge passed through the specimen will be calculated based on the formula given below in Coulombs (Q) in (1).

$$Q = \frac{900}{100} (I_0 + 2I_{30} + 2I_{60} \dots + 2I_{360}). \quad (1)$$

### 3.5. Acid Resistance Test

**3.5.1. Acid Attack-Hydrochloric Acid (HCl).** In order to check the acid resistance of steel slag concrete, the specimens are immersed in hydrochloric acid. A total of 28 days water-cured specimens of size 150 × 150 × 150 mm are immersed in the solution for the period of 90 days and the specimen weights will be compared based on the weight loss before and after immersed in the acid. Figure 5 shows the specimen immersed in Hcl.

**3.5.2. Acid Attack-Sulfuric Acid (H<sub>2</sub>SO<sub>4</sub>).** The concrete specimens of extreme exposure conditions can be tested by immersing in acid solutions for a particular period and measuring the weight of the compared specimens in which 0.1 normality sulfuric acid will be used in a container to immerse the concrete cube specimen for the period of

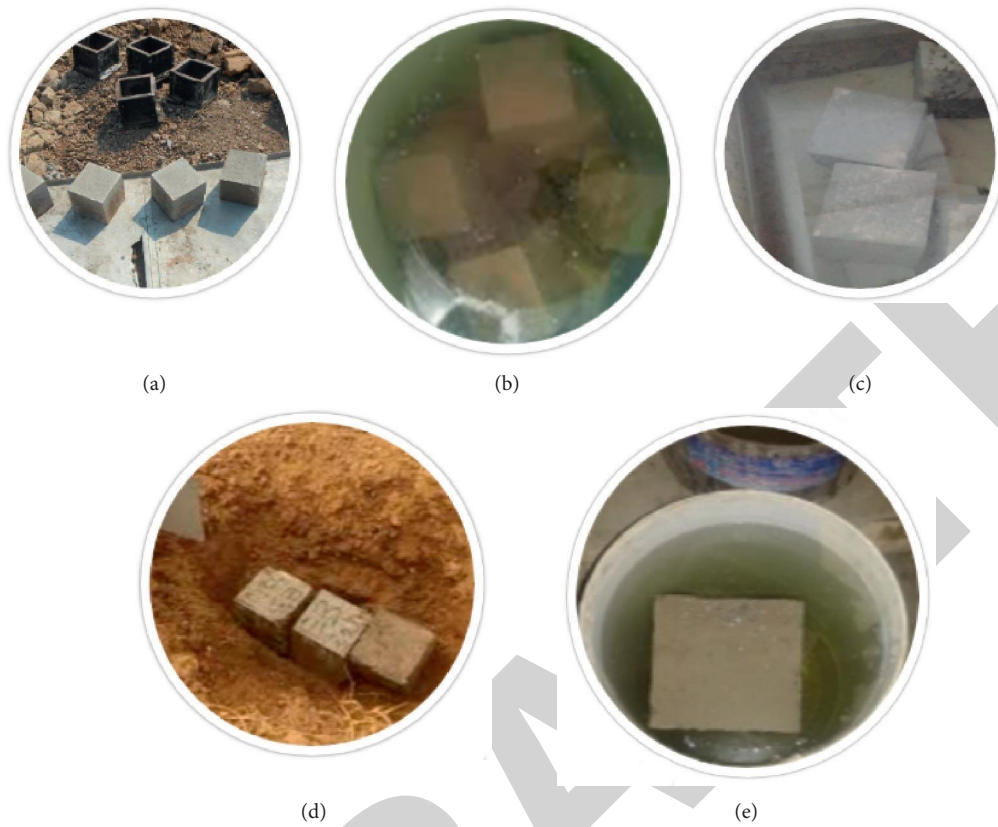


FIGURE 2: (a) Mild. (b) Moderate. (c) Severe. (d) Very severe. (e) Extreme conditions.



FIGURE 3: UPV test.



FIGURE 4: RCPT.



FIGURE 5: Specimen immersed in Hcl.

90 days. The weight loss of the concrete cube before and after immersion in acid is found and analyzed based on IS 456: 2000, Clause 8.2. Figure 6 shows the specimen immersed in  $H_2SO_4$ .

**3.6. Sorptivity Test.** The water absorbing rate of the concrete specimen is determined by Sorptivity test. This test is used to analyze the internal voids and micropores in concrete. The specimen used for this test is a cylindrical specimen with the dimensions of 50 mm diameter and 100 mm height. ASTM C 1585-4 standards are the criteria used to conduct the Sorptivity test. The specimen needs to be prepared at  $110^\circ C$  for a period of one day, then 24 hours cooling in a room temperature, and then placed in the test setup. In order to





FIGURE 6: Specimen immersed in  $H_2SO_4$ .

maintain the unidirectional water flow, the specimen coated with water proofer on its circumference. The water will be absorbed by capillary action and its weight gain measured every half an hour. The Sorptivity is calculated based on the formula as in (2) given below and also shown in Figure 7:

$$K = \frac{W}{(A \cdot x \cdot ml/mm^2/\sqrt{\min})}, \quad (2)$$

where  $W$  = weight of water absorbed (ml),  $A$  = cross sectional area of specimen ( $mm^2$ ),  $t$  = time in minutes,  $k$  = Sorptivity coefficient.

## 4. Results and Discussion

**4.1. Ultrasonic Pulse Velocity Test.** Based on the test conducted for the specimens of various exposure conditions in both conventional and steel slag replaced fiber-reinforced bacterial concrete, the test results are shown in Figure 8. Ultrasonic waves are passed through 150 mm side cube and the velocity is calculated using the time taken for the ultrasonic waves to travel a particular distance. Quality of concrete depends on the velocity of ultrasonic waves. When the velocity is less than 3, the concrete is categorized as poor; between 3 and 4.5, it is good; and greater than 4.5, it is excellent. According to the test results, the steel slag replaced fiber-reinforced concrete having the value of UPV between 3 and 4.5, and categorized as good; meanwhile, the value is greater than the conventional concrete. It shows that the internal structure and durability of the steel slag fiber-reinforced bacterial concrete is better than the conventional concrete in all exposure conditions. The test result shows that the concrete can withstand and perform well in the application of high acidity area. So the fiber-reinforced bacterial steel slag concrete can be utilized to construct the chemical industries, other plants related to acid applications and the area where the atmosphere and geotechnical conditions are acidic in nature. In extreme exposure conditions, steel slag fiber-reinforced bacterial concrete performs better than the conventional concrete.

**4.2. Rapid Chloride Penetration Test.** Electric current has been passed via the specimen placed in the Rapid Chloride Penetration Test (RCPT) setup to determine the amount of

penetrability of chloride content through the specimen. When the value of electric charge is 100 coulombs, the amount of chloride penetrability will be negligible. The penetrability of chloride is low, when the value of electric charge passed through the specimen is between 1000 and 2000 as per the codal provision. The chloride ion penetrability for both normal concrete and fiber-reinforced steel slag concrete is less than 2000 coulomb for all the exposure conditions, which is shown in Figure 9. The steel slag fiber-reinforced concrete specimen with very severe exposure conditions resisting 7.5% better than the other exposure conditioned specimens and conventional concrete specimen.

### 4.3. Acid Resistance Test

**4.3.1. Acid Attack-Hydrochloric Acid (HCl).** We know that, the concrete is alkaline in nature. The alkalinity in concrete is producing better strength while binding with the aggregates. In order to find the resistivity to acid solutions, the specimens are immersed in hydrochloric acid and sulfuric acid and weighted according to Indian Standard Code. The  $150 \times 150 \times 150$  mm size specimen has been immersed in HCl acid of 0.1 N for the duration of 90 days. The attack of the acid to the specimen can be observed by the weight loss percentage. The percentage of the various weight loss of SS concrete and conventional concrete are shown in Figure 10. From the test results, the concrete is performing well in hydro chloric acid than the sulfuric acid. The graph shows that the steel slag concrete with moderate, very severe, and extreme exposure conditions are good in acid attack of HCl acid than the other two exposure conditions. The result shows SS fiber-reinforced concrete having 70% more acid attack resistivity than the conventional concrete under all exposure conditions.

**4.3.2. Acid Attack-Sulfuric Acid ( $H_2SO_4$ ).** According to IS 456-2000, the standard cube of size  $150 \times 150 \times 150$  mm is used in this test. The different exposure conditioned cubes are immersed in the acid container with 0.1 N for the duration of 90 days. The weight reduction of concrete cube specimens takes place while performing the test. The loss of weight of concrete specimens are shown in Figure 11 under various exposure conditions. According to the test results, moderate and very severe exposure conditioned specimens have less weight loss percentage, which is less than 3% compared to the other exposure conditions. The result shows that steel slag fiber-reinforced concrete having very good resistivity to sulfuric acid compared to conventional concrete, which is 65% more resistant to losing weight than the conventional concrete.

**4.4. Sorptivity Test.** The test results of coefficient of Sorptivity to the steel slag fiber-reinforced concrete with conventional concrete are shown in Figure 12. The graph shows the capillary action in the steel slag concrete is lesser than the normal concrete in which steel slag concrete with severe and

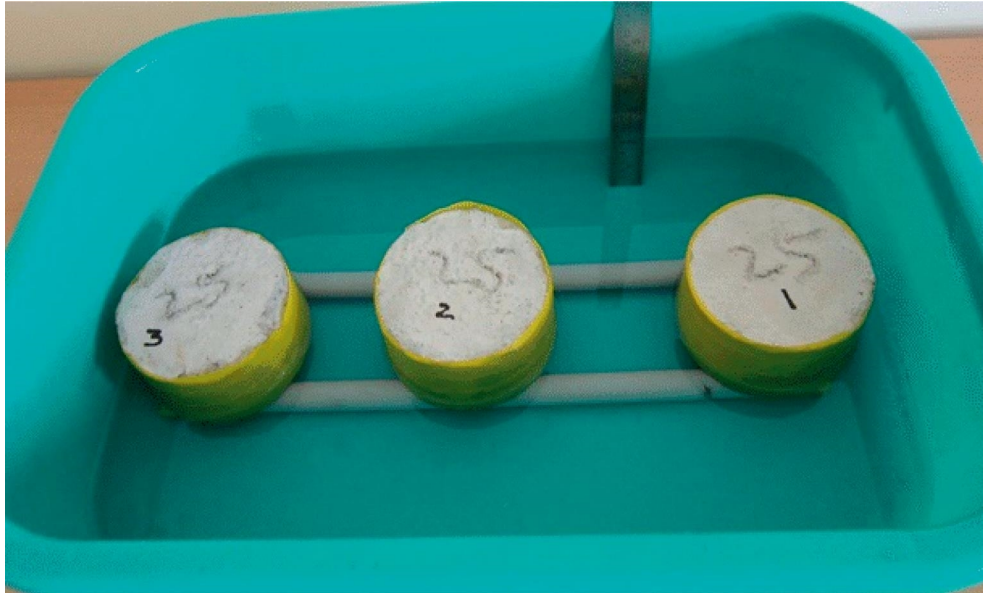


FIGURE 7: Sorptivity test.

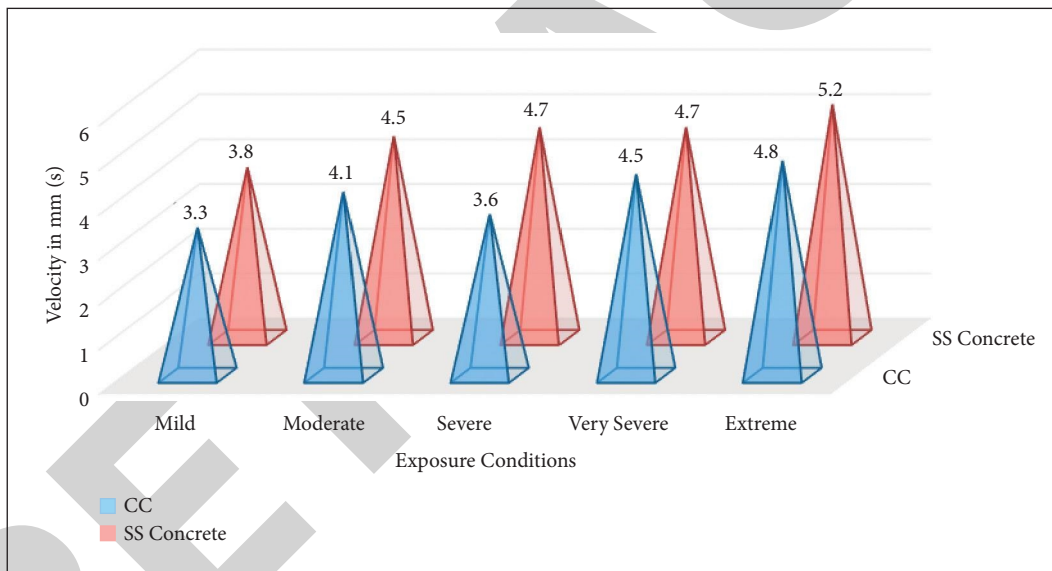


FIGURE 8: UPV of CC and steel slag concrete for different exposure conditions.

extreme exposure conditions are performing better than the other exposure conditions. The lesser value of coefficient of Sorptivity shows the lower percentage of capillary action and porosity. The presence of zig-zag-shaped fibers with replacement of steel slag decreases the porosity in the concrete, which results in the reduction of capillary action in steel slag concrete and improving the resistance of flow of water

through itself. The materials inside the concrete mix are packed well with a lesser number of pores than the conventional concrete. According to the test results, the value of coefficient of sorptivity is 10.67% less in steel slag fiber-reinforced concrete than the normal concrete. This shows the capillary action of SS concrete is better than the normal concrete.

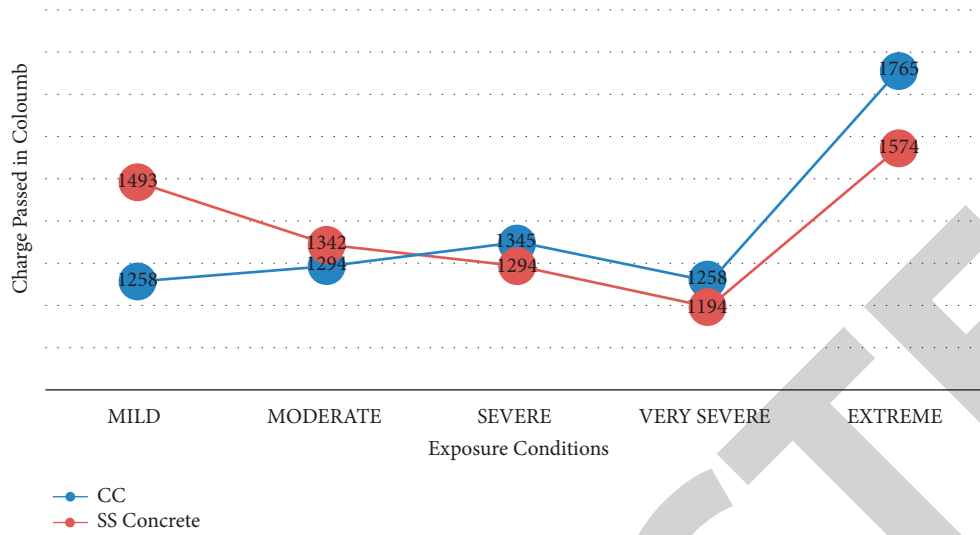


FIGURE 9: RCPT test results for CC and SS concrete.

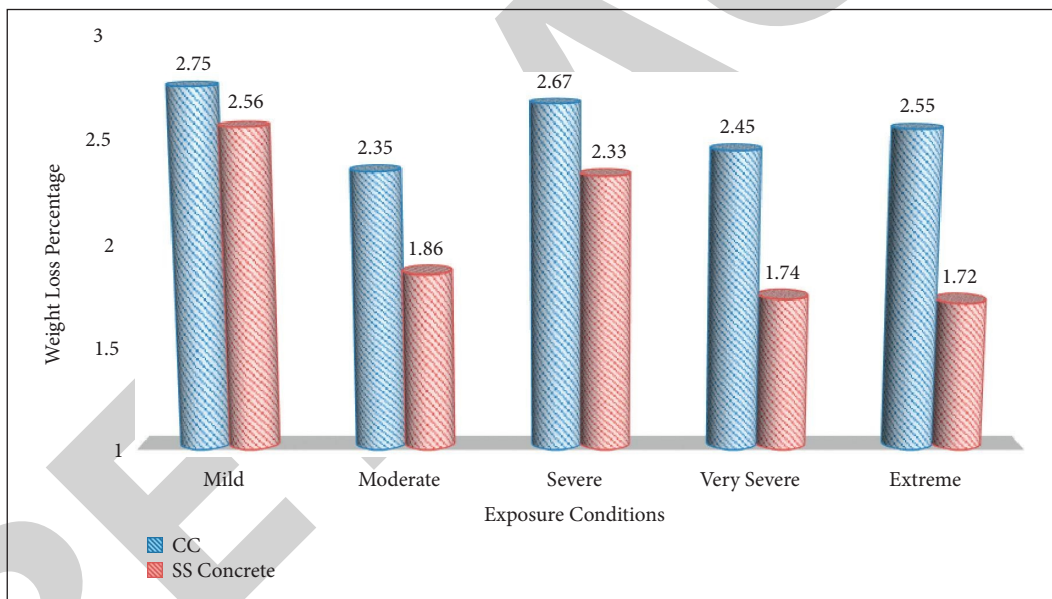


FIGURE 10: Comparison of weight loss percentage of CC and SS concrete in HCl acid attack.



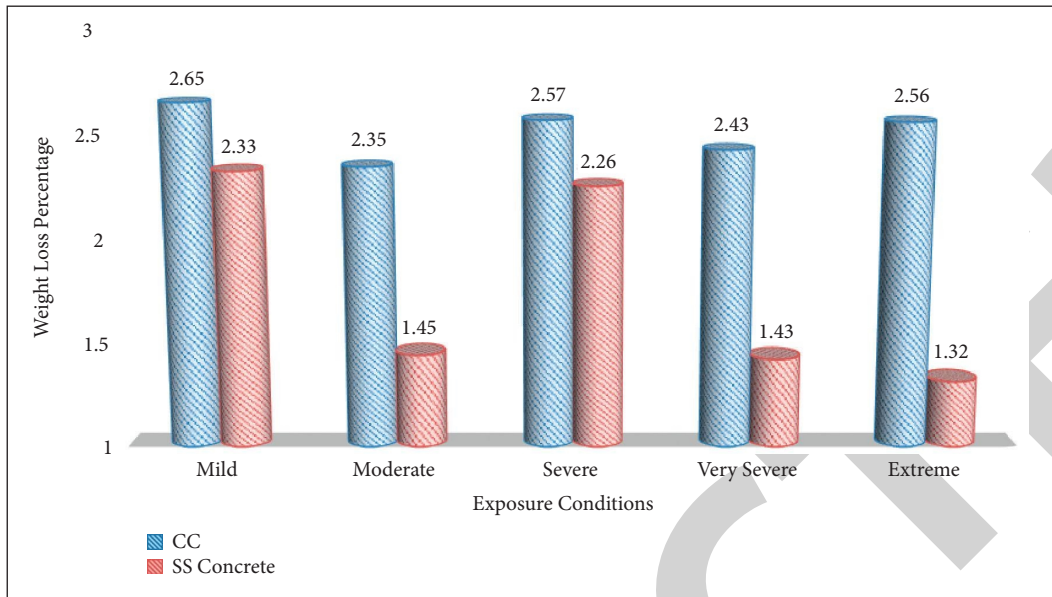


FIGURE 11: Comparison of weight loss percentage of CC and SS concrete in  $H_2SO_4$  acid attack.

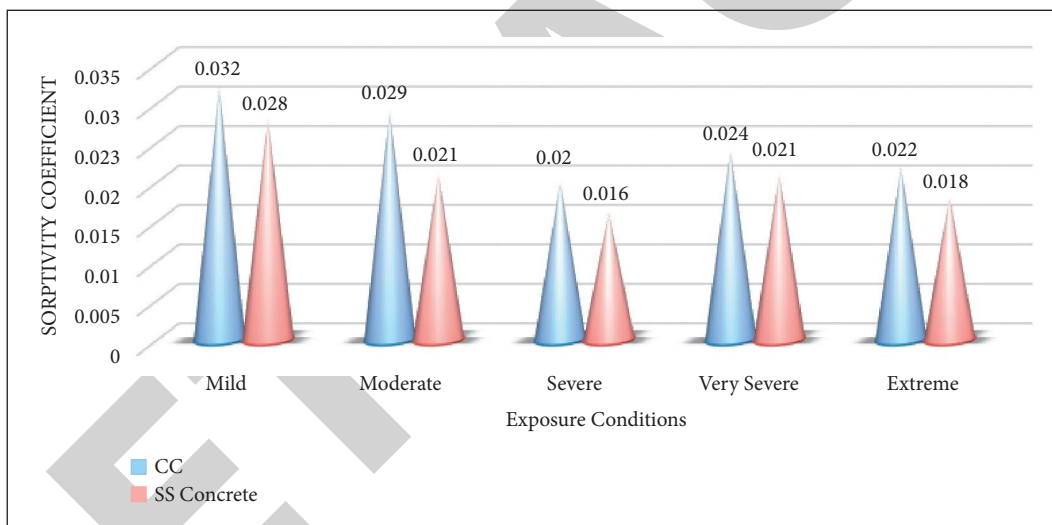


FIGURE 12: Sorptivity coefficient for CC and SS concrete.

## 5. Conclusion

The analysis of durability properties of M30 grade concrete with partial replacement of steel slag as coarse aggregate (50% replacement of coarse aggregate), steel fiber, and bacteria under various exposure conditions has been done. The finding from the experimental analysis listed as follows:

- (i) Steel slag having greater water absorption property than conventional aggregate, it can be negligible before mixing into concrete by saturating the steel slag aggregates.
- (ii) Steel slag concrete with extreme exposure conditions having better durability than conventional concrete. The UPV test shows the velocity of SSC at extreme exposure is having around 95% at the

receiving side. It results in the good quality when compared to other conditions with less than 90% receiving velocity.

- (iii) The percentage of rate of penetration of chloride through the concrete mass is very less in SS concrete, with very severe exposure condition with less than 4%. On the other hand, both conventional and other exposure conditioned SS concrete have the penetrability of more than 5%.
- (iv) In the acid attack test, SS concrete with very severe and extreme exposure conditions has 65–70% more resisting capacity in both the acids ( $HCl$  &  $H_2SO_4$ ) than the conventional concrete.
- (v) According to the Sorptivity test result, the coefficient of Sorptivity is 10% less in SS concrete with